ANNUAL MEETING 2022

ISMRM Benelux CHAPTER

14TH ANNUAL MEETING
25th of April, 2022
MECC, Maastricht

BRUKER
Canon
PRODRIVE TECHNOLOGIES
scannexus
skope

MR SOLUTIONS
PHILIPS
SIEMENS Healthineers
Tesla Dynamic Coils

ABSTRACT BOOK

Sponsors

The organising committee would like to thank all the sponsors of this year's ISMRM Benelux meeting for their kind contributions.

GOLD

PHILIPS

MR SOLUTIONS

Tesla Dynamic Coils

SIEMENS Healthineers

SILVER

BRUKER

Canon

PRODRIVE TECHNOLOGIES

scannexus

skope

BRONZE

icometrix
MEASURABLY BETTER

PROEFSCHRIFTMAKEN

Improved ΔR_2^* calculation through voxelwise subtraction for MRI-based dosimetry of holmium-166 transarterial radioembolization

M.W.M. van Wijk[1], J. Roosen[1], L.E.L. Westlund Gotby[1], M.J. Arntz, M.J.R. Janssen[1], D. Lobeek[1], G.H. van de Maat[2], C.G. Overduin[1], J.F.W. Nijsen[1]

[1] Department of Medical Imaging, Radboud Institute for Health Sciences, Radboud university medical center, Nijmegen, The Netherlands; [2] Imaging & Software Solutions, Quirem Medical B.V., Deventer, The Netherlands

Synopsis: Transarterial radioembolization (TARE) is a treatment for liver cancer, during which radioactive microspheres are administered through the hepatic artery. Microspheres containing holmium-166 enable MRI-based dosimetry, based on subtraction of pre- and post-treatment R_2^* values. This subtraction is performed using a mean pre-treatment R_2^* value. This does however not take pre-existing differences of R_2^* values into account, introducing an error in the dosimetry. In this work a voxelwise subtraction method is presented, using deformable registration to transform the pre-treatment R_2^* map to the post-treatment R_2^* map, enabling voxel-by-voxel subtraction. This method does take R_2^* differences into account and improves MRI-based dosimetry.

Introduction: Transarterial radioembolization (TARE) is a locoregional treatment for liver malignancies. During TARE, beta-emitting microspheres (containing yttrium-90 (^{90}Y) or holmium-166 (^{166}Ho)) are injected into the hepatic artery, and lodge in the liver microvasculature where they mostly irradiate the tumours. A key characteristic of the ^{166}Ho microspheres is their paramagnetic property, enabling MR imaging and dosimetry. MRI-based dosimetry of ^{166}Ho microspheres is based on a local increase of the transverse relaxation rate (R_2^*)[1]. To quantify this increase, a multi gradient echo (MGRE) sequence is acquired before and after treatment, from which R_2^* maps can be calculated. Subtraction of the pre- and post-treatment R_2^* map leads to a ΔR_2^* map, which corresponds to the distribution of the ^{166}Ho microspheres in the tissue. The ΔR_2^* map is proportional to the absorbed dose, and therefore a dose map can be constructed. However, finding ΔR_2^* using a direct voxel-to-voxel subtraction of pre- and post-treatment R_2^* values is challenging due to the deformability of the liver. Therefore a mean pre-treatment R_2^* value is computed to perform the subtraction in the current workflow. The drawback of this method is that the heterogeneity of R_2^* values before treatment is not taken into account, leading to inaccuracies in the estimated dose distribution[2]. In this work we aim to increase the accuracy in the dose quantification by using a deformable registration algorithm to enable a voxelwise subtraction of the R_2^* maps.

Methods: A MGRE was acquired directly before and after ^{166}Ho TARE for six patients. Furthermore, a SPECT/CT was acquired of all patients two days after TARE, which was used to compare to MRI-based dosimetry. To quantify pre-existing R_2^* differences between tumour and healthy liver tissue, pre-treatment R_2^* values were analyzed. Conventional quantification of the MR images was performed using the mean subtraction method (mean method), during which a mean pre-treatment R_2^* was subtracted from the post-treatment R_2^* map. This quantification was executed in a research version of the clinically used software for ^{166}Ho dose evaluation (Q-Suite™ 2.0, Quirem Medical, Deventer, The Netherlands), of which the steps can be seen in Figure 1. For the newly developed voxelwise subtraction method (VW method) the same workflow was followed, but the subtraction step was replaced by in-house developed code, as can be seen in Figure 1 as well. Pre-treatment imaging and R_2^* maps were mapped to the post-treatment imaging and R_2^* maps using an automatic affine registration followed by a deformable registration using symmetric normalization and mutual information, as implemented in the SyN algorithm of the Advanced Normalization Tools (ANTs) Python package[3,4]. Thereafter, the ΔR_2^* map was obtained by a voxelwise subtraction of the post-treatment and pre-treatment ΔR_2^* maps. The accuracy of the registration was scored using the Dice Similarity Coefficient (DSC).

Results: Pre-treatment R_2^* values were lower in tumours (mean 38.6 s^{-1}, range: 24.4 – 54.7 s^{-1}) than in healthy liver tissue (mean 55.7 s^{-1}, range: 41.4 – 73.8 s^{-1}), while the mean R_2^* of the total liver volume was 48.4 s^{-1} (range: 34.5 – 68.3 s^{-1}). Two examples of pre-treatment R_2^* distributions are visualized in Figure 2. Image registration resulted in an increase of mean DSC of 0.83 (range: 0.70 – 0.88) to 0.95 (range: 0.92 – 0.97). Mean dose for both MRI-based quantification methods are stated in Table 1. For all patients, voxelwise subtraction-based dose maps yielded a higher tumour dose (mean increase of 9.7%) and lower healthy liver dose (mean decrease of 16.9%) compared to the mean method. ^{166}Ho-SPECT dosimetry showed a lower tumour dose than the MRI-based methods (mean 63.3 Gy, range 22.0 – 89.3 Gy), and a healthy liver dose higher than the VW method but lower than the mean method (mean 33.3 Gy, range 20.0 – 51.0 Gy). The mean whole liver dose was comparable for all dosimetry methods. Voxelwise subtraction-based dose maps visually corresponded better to SPECT-based dose maps, as can be seen in Figure 3.

Discussion: The ability to perform MRI-based dosimetry after TARE is one of the unique characteristics of the ^{166}Ho microspheres. In this work, we have presented a robust alternative for the current method of calculating the ΔR_2^* map, based on voxelwise subtraction, improving the accuracy of MRI-based dosimetry. As opposed to the mean method, the VW method takes local differences in the pre R_2^* values into account for the dosimetry. Quantification of these local differences resulted in a substantially lower mean R_2^* in tumours compared to healthy liver tissue and whole liver values. This leads to an underestimation of the tumour dose, and an overestimation of the healthy liver dose when the mean method is used. Furthermore, the VW method shows better visual comparability to SPECT/CT than the mean method. We therefore argue that the VW method is intrinsically superior to the mean method, provided that the image registration prior to subtraction is performed adequately.

Conclusion: The VW method enables a voxelwise pre- and post-treatment subtraction by using deformable registration, and presents an accurate alternative to the currently implemented mean method for MRI-based dosimetry of ^{166}Ho microspheres.

References:

1. Seppenwoolde JH, Nijsen JF, Bartels LW, Zielhuis SW, van Het Schip AD, Bakker CJ. Internal radiation therapy of liver tumors: qualitative and quantitative magnetic resonance imaging of the biodistribution of holmium-loaded microspheres in animal models. Magn Reson Med. 2005;53(1):76-84.
2. van de Maat GH, Seevinck PR, Elschot M, Smits ML, de Leeuw H, van Het Schip AD, et al. MRI-based biodistribution assessment of holmium-166 poly(L-lactic acid) microspheres after radioembolisation. Eur Radiol. 2013;23(3):827-35.
3. Avants BB, Tustison NJ, Song G, Cook PA, Klein A, Gee JC. A reproducible evaluation of ANTs similarity metric performance in brain image registration. Neuroimage. 2011;54(3):2033-44.
4. Tustison NJ, Cook PA, Holbrook AJ, Johnson HJ, Muschelli J, Devenyi GA, et al. The ANTsX ecosystem for quantitative biological and medical imaging. Sci Rep. 2021;11(1):9068.

Acknowledgments / Funding Information: Continue on this line

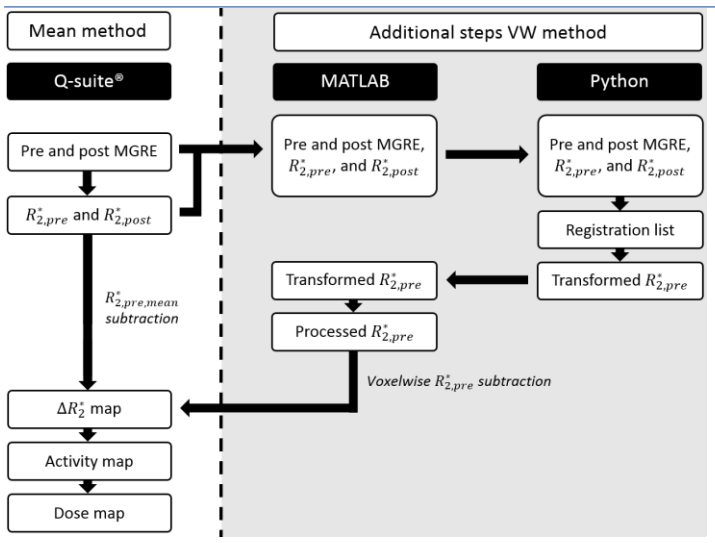

Figure 1: Workflow of the post-processing as implemented in Q-suite (white background) and the additional post-processing for the voxelwise (VW) subtraction method (grey background). In the conventional workflow a mean pre-treatment R_2^* is calculated and subtracted from all post-treatment R_2^* values. For the voxelwise method the transformed pre-treatment R_2^* values are subtracted voxelwise from the post-treatment R_2^* values. MGRE = multigradient echo sequence.

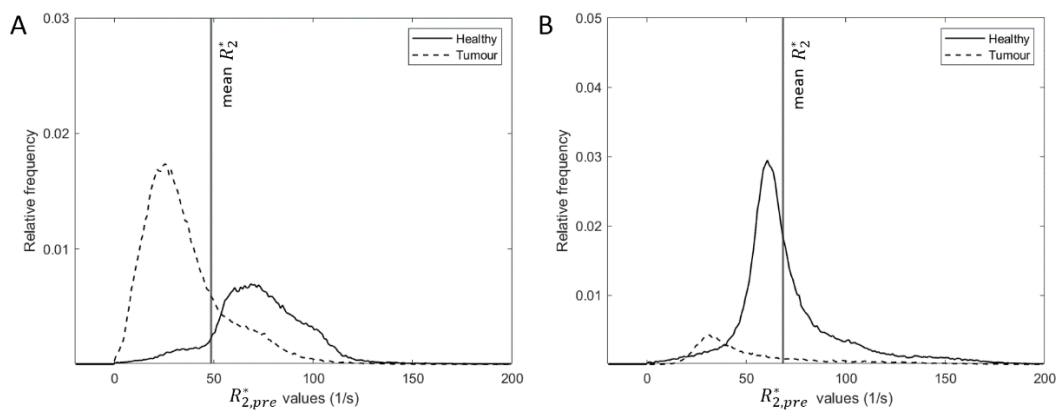

Figure 2: R_2^* distributions before treatment of patient 1 (A) and patient 4 (B) classified as either originating from tumours or healthy liver tissue. Additionally, the mean R_2^* value of the entire liver volume is visualized. In general, the mean R_2^* of the entire liver volume gives an overestimation of the tumour R_2^* values.

Table 1: Mean dose per volume of interest as calculated through the mean method and the VW method. Difference indicates the percentual difference between the VW method and the mean method. Data is presented as mean with range between brackets.

	Mean method	**VW method**	**Difference**
Mean total liver dose (Gy)	45.2 (30.0 – 54.0)	43.5 (26.0 – 55.0)	-3.7% (-13.3% – 4.2%)
Mean healthy liver dose (Gy)	35.4 (28.0 – 47.5)	29.8 (15.0 – 44.5)	-16.7% (-55.9% – 0.0%)
Mean tumour dose (Gy)	71.3 (23.0 – 110.3)	78.1 (25.8 – 125.0)	9.7% (4.6% – 15.9%)

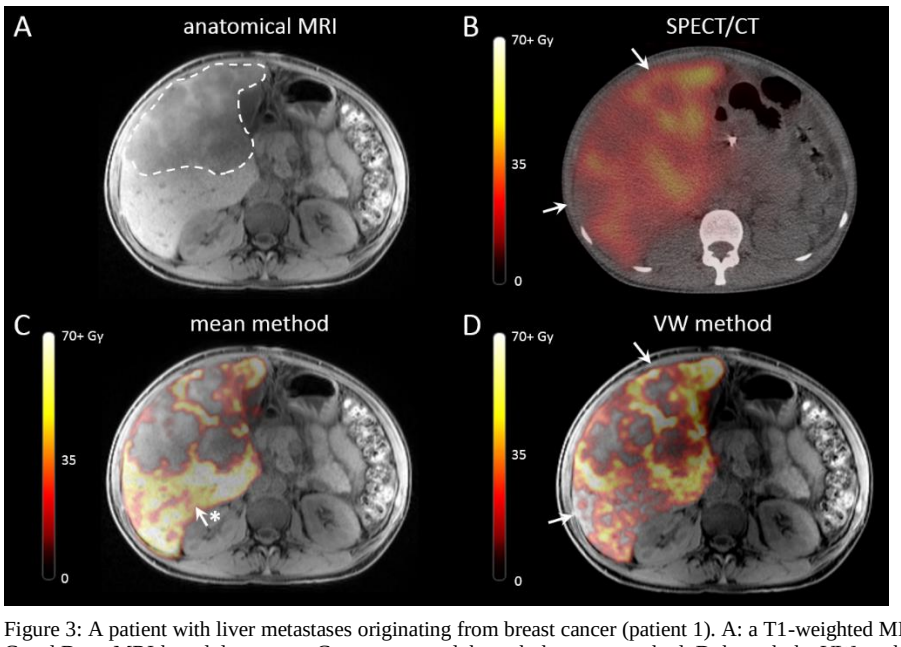

Figure 3: A patient with liver metastases originating from breast cancer (patient 1). A: a T1-weighted MRI in which the tumour is delineated with a dashed line. B: ^{166}Ho-SPECT fused with a low-dose CT. C and D are MRI-based dose maps, C was generated through the mean method, D through the VW method. The arrow with asterisk (Figure 3C) indicates the overestimation of the dose in the healthy liver tissue for the mean method as compared to the SPECT images. Other arrowheads indicate similarities between the dose map resulting from the VW method and the SPECT images.

Amyloid burden and vascular risk factors correlate with regional cerebral blood flow in a cognitively unimpaired population

B. E. Padrela [a], L. Lorenzini [a], L. E. Collij [a], M. ten Kate [a], A. den Braber [b], J. Tomassen[b], B. van Berckel [a], P. J Visser [b], F. Barkhof [a, d], J. Petr [c], H. J.M.M. Mutsaerts [a]

[a] Department of Radiology and Nuclear Medicine, Amsterdam Neuroscience, Amsterdam University Medical Center, Location VUmc, Amsterdam, the Netherlands. [b] Alzheimer Center, Department of Neurology, Neuroscience Campus Amsterdam, VU University Medical Center, Amsterdam, the Netherlands.
[c] Helmholtz-Zentrum Dresden-Rossendorf, Institute of Radiopharmaceutical Cancer Research, Dresden, Germany. [d] Queen Square Institute of Neurology and Centre for Medical Image Computing (CMIC), University College London, London, UK. [e] Department of Biological Psychology, Vrije Universiteit Amsterdam, Amsterdam, The Netherlands

Synopsis: Studying the association between cerebral blood flow (CBF), amyloid burden, and vascular risk factors in a cognitively unimpaired elderly population could clarify the role of CBF as a biomarker of cognitive decline. In 196 cognitively unimpaired participants, regional CBF was associated with regional amyloid-PET Centiloid. Vascular risk scores as measured by the Framingham risk score combined with amyloid Centiloid values were associated with increased CBF in vascular territories. Longitudinally, global CBF changes were associated with baseline precuneus amyloid burden.

Introduction: Recent findings indicate considerable overlap between cerebrovascular disease and Alzheimer's disease (AD), suggesting additive or synergistic effects of both pathologies on cognitive decline[1,2]. Perfusion imaging holds great promise for detecting alterations in neuronal functioning at early stages of cognitive decline[3] since adequate cerebral blood flow (CBF) is essential to maintain neuronal metabolism and brain function. Supply and demand of blood flow in the brain can be affected by, respectively, the loss of vascular health and the decrease of neuronal activity — as a consequence of AD[4]. This study investigates to what extent the vascular and AD components affect CBF and how they interact with each other. We hypothesize that the amyloid burden in early-accumulation regions[5,6] and vascular risk factors are related to brain perfusion alterations in an elderly cognitively unimpaired (CU) population.

Methods: A total of 196 CU participants, aged 70±7.3 years; 57% female, were included from the EMIF-AD PreclinAD[7] Twin60++ cohort. Four years after baseline, 135 participants were scanned again with an identical scanner, scanner software, and scan protocol. The cardiovascular risk profile for each participant was summarized using the Framingham score index[8]. Amyloid-PET using the [18F]flutemetamol radiotracer was used to image cortical amyloid burden and quantified using the Centiloid method[9] globally and for four early amyloid accumulation regions of interest (ROIs) obtained from the LEAP atlas[10,11]: Early Frontal Gyrus —orbital frontal + basal frontal — Precuneus, Superior Frontal Gyrus, and Lingual Gyrus (Figure 1). Whole-brain 3D T1-weighted and 2D EPI Arterial Spin Labeling (ASL) images were obtained using a 3T PET-MRI Ingenuity scanner (Philips Healthcare, Best, The Netherlands). After visual quality-control, 172 baseline and 117 follow-up scans were included. Image processing was performed with ExploreASL[12]. Mean regional CBF was assessed in the total gray matter (GM) and in the same four amyloid-based ROIs. Additionally, we investigated the mean CBF in the vascular territories [13] (Figure 1) that overlapped with these ROIs (Figure 2).

All statistical analyses were performed in R 3.3.1 using generalized estimating equations (GEEs). Cross-sectionally, we first examined the relation between Centiloid and CBF values in early amyloid accumulation regions[5,6]. Second, we examined the association between the amyloid ROIs with the spatially overlapping vascular territories CBF (Figure 2), including the association between global GM CBF values and global Centiloid. Analyses were adjusted for age, sex, and twin dependency. For both analyses, we studied the interaction between Centiloid and Framingham scores on CBF in the same regions. In the longitudinal analysis (n=117), we examined whether *global* and *regional* amyloid burden at baseline predicts global GM CBF at follow-up.

Results: We found significant associations between regional Centiloid and CBF in corresponding regions from the LEAP atlas (Table 1). A significant interaction between amyloid and Framingham on CBF was found only for the Lingual Gyrus ROI ($p=0.003$). Both global and regional associations were found between global Centiloid with Framingham scores and CBF values for all of the vascular territories except for the MCA proximal region (Table 2). No significant association between global Centiloid at baseline and total CBF changes was found. Regionally, linear models detected no significant predictors, however, using quadratic models, Precuneus Centiloid significantly predicted total CBF changes over time ($p = 0.0285$, $\Delta QIC = 187$) (Figure 3).

Discussion: We found regional amyloid burden in AD signature regions to be associated with altered CBF in cognitively intact individuals. Interestingly, the interaction between amyloid Centiloid values and Framingham Risk scores was associated with vascular territory CBF values, suggesting the importance of vascular risk factors when studying CBF in the context of cognitive decline. The missing association between the Early Frontal Centiloid region and MCA proximal territory could be explained by the susceptibility artifact in the orbitofrontal cortex in the 2D EPI ASL acquisition used. Unexpectedly, we observed an increase in vascular territories CBF with increasing Centiloid; which could be explained by compensatory mechanisms at the beginning of amyloid accumulation[14]. From the longitudinal assessment, we found an association between total CBF change over time and Precuneus Centiloid values at baseline, which is one of the first AD-related regions for amyloid accumulation and atrophy[15]. However, these results might be driven by outliers as we have only had a few participants with high amyloid load in this CU cohort. This work demonstrates the potential value of the joint analysis of regional CBF, cardiovascular risk scores, and amyloid burden. Future work will include the investigation of their joint impact on cognitive performance.

References: 1. Atterms *et al.*, 2014, *BMC Med.* ; 2. Bangen *et al.*, 2014 *Front. Aging Neurosci. ;* 3. Wieranga *et al.*, 2014 ; 4. Butterfield, 2019, *Nat Rev Neurosci.* ; 5. Mattson *et al.*, 2014 *Brain.* ; 6. Collij *et al.*, 2020 *Neurology* ; 7. Konijnenberg *et al.*, 2018 *Alzheimers. Res. Ther* ; 8. Wilson *et al.*, 1998, *Circulation* ; 9. Klunk *et al.*, 2015. *Alzheimers. Dement* ; 10. Wolz *et al.*, 2010 *Neuroimage* ; 11. Lopes Alves *et al.*, 2020, *Alzheimers. Dement* ; 12. Mutsaerts *et al.*, 2020, *Neuroimage* ; 13. Mutsaerts *et al.*, 2015, *PLoS One* ; 14. Hahn *et al.*, 2019, *Cereb. Cortex* ; 15. Thomas *et al.*, 2019, *AJNR Am. J. Neuroradiol.*

Acknowledgments: BP, JP, and HM are supported by the EU Joint Program for Neurodegenerative Disease Research, provided by the Netherlands Organisation for health Research and Development and Alzheimer Nederland (DEBBIE JPND2020-568-106).

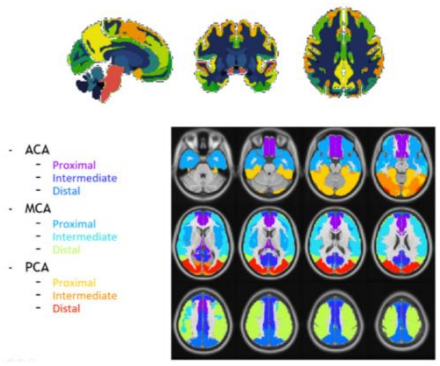

Fig. 1: *LEAP atlas (top) and Vascular Territories atlas (bottom). ACA: Anterior Cerebral Artery; MCA: Middle Cerebral Artery: PCA: Posterior Cerebral Artery.*

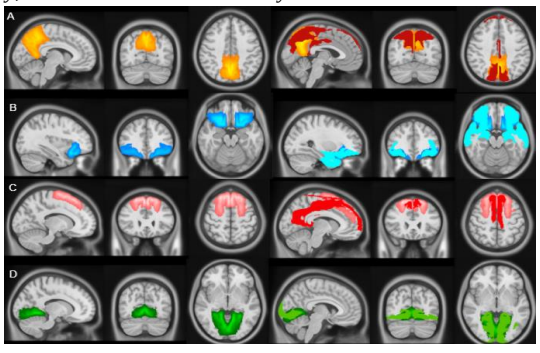

Fig. 2: *Centiloid regions (columns 1-3) and spatially matching vascular territories (columns 4-6): A) Precuneus (orange) and ACA distal (red) B) Orbital frontal (blue) and MCA proximal (light blue); C) Superior Frontal Gyrus (pink) and ACA intermediate (red); D) Lingual Gyrus (green) and PCA intermediate (light green).*

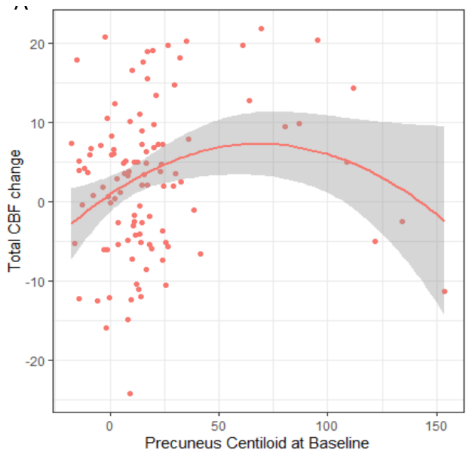

Fig.3. *Quadratic model adjusted for the correlation between Precuneus Centiloid values at baseline and Total CBF change over time.*

		Model parameters	
		Linear	
Predictor (Amyloid)	**Dependent (regional CBF)**	***β***	***p***
Early Frontal Gyrus	Early Frontal Gyrus	-0.129	<0.001**
Early Frontal Gyrus x Framingham	Early Frontal Gyrus	0.01	0.08
Precuneus	Precuneus	-0.042	<0.001**
Precuneus x Framingham	Precuneus	0.0009	0.06
Superior Frontal Gyrus	Sup Frontal Gyrus	-0.0016	<0.001**
Superior Frontal Gyrus x Framingham	Sup Frontal Gyrus	0.0141	0.007*
Lingual Gyrus	Lingual Gyrus	-0.16	<0.001**
Lingual Gyrus x Framingham	Lingual Gyrus	0.054	0.003**

Table 1: *GEE results are shown for the association between regional amyloid values at baseline and CBF — with or without correction for Framingham risk factors. x indicates interaction effect. * indicates significance (p<0.05) and ** significance after Bonferroni correction (p<0.05/8). There were no independent associations between Framingham and CBF (p>0.05).*

		Model statistics	
		Linear GEEs	
Predictor (Amyloid)	**Dependent (CBF vascular territories)**	***β***	***p***
Global	Total GM	0.017	0.6
Global x Framingham	Total GM	0.016	0.046 *
Early Frontal Gyrus	MCA proximal	0.004	0.8
Early Frontal Gyrus x Framingham	MCA proximal	0.008	0.09
Precuneus	ACA distal	0.02	0.4
Precuneus x Framingham	ACA distal	0.013	0.041*
Superior Frontal Gyrus	ACA intermediate	0.007	0.7
Superior Frontal Gyrus x Framingham	ACA intermediate	0.012	0.044*
Lingual Gyrus	PCA intermediate	0.07	0.3
Lingual Gyrus x Framingham	PCA intermediate	0.05	0.002**

Table 2: *GEE results are shown for the association between regional amyloid values at baseline and CBF in the vascular territory regions — with or without correction for Framingham risk factors. x indicates interaction effect. * indicates significance (p<0.05) and ** significance after Bonferroni correction (p<0.05/8).*

Sleep and waste clearance:
The association of sleep quality with an 7T IVIM imaging derived proxy of interstitial fluid

M.M. van der Thiel[1,2], G.S. Drenthen[1,2], P.H.M. Voorter[1,2], T. Feiweier[3], I.H.G.B Ramakers[2,4], W.H. Backes[1,2,5], J.F.A. Jansen[1,2,6]

[1]Department of Radiology & Nuclear Medicine, Maastricht University Medical Center, Maastricht, the Netherlands; [2]School for Mental Health & Neuroscience, Maastricht University, Maastricht, the Netherlands; [3]Siemens Healthcare, Erlangen, Germany; [4]Department of Psychiatry & Neuropsychology, Maastricht University, Maastricht, the Netherlands; [5]School for Cardiovascular Disease, Maastricht University, Maastricht, the Netherlands; [6]Department of Electrical Engineering, Eindhoven University of Technology, Eindhoven, the Netherlands

Synopsis: Cerebral clearance is most active during sleep, therefore reduced sleep quality might induce impaired clearance function. Interstitial fluid (ISF) washes waste products from in-between cells through the parenchyma and its volume is found to be regulated by the sleep-wake cycle. Assessment of the ISF-fraction through IVIM can be a potential, non-invasive method to determine sleep-related variations in ISF, without contamination of parenchymal or microvascular diffusion. The current exploratory study investigates the potential of the IVIM-derived ISF-fraction to assess ISF-volume changes in relation to sleep by examining whether these changes are driven by actual hours of sleep or self-reported sleep quality.

Introduction

Recently, spectral decomposition of the intravoxel incoherent motion (IVIM) signal revealed an additional, intermediate, component between the two traditional components (microvascular and parenchymal diffusion)[1]. The fraction of this component (f_{int}) is argued to reflect interstitial fluid (ISF) within the parenchyma and was suggested to relate to cerebral clearance.[1,2] The ISF plays a crucial part in the cerebral clearance system, as it washes the waste products through the parenchyma.[3]

Cerebral clearance is most active during sleep,[4,5] therefore reductions in sleep quality might induce impaired clearance function.[6] ISF expands during sleep, which facilitates the clearance of waste products from in-between the cells, while the ISF-volume reduces again in awake states.[6,7] Previous diffusion studies have observed alterations in general diffusivity measures dependent on sleeping patterns and support the role of underlying ISF-volume on altered clearance.[8-10] Decreased diffusivity measures (i.e., axial, radial, and mean diffusivity) were found after sleep deprivation[8,9] and a lower apparent diffusion coefficient was found in awake states as compared to sleep.[10] However, previous studies have neither examined the effects of long-term subjective sleep deprivation on cerebral diffusivity, nor have they investigated alterations in ISF-volume by specifically isolating the ISF diffusion signal from parenchymal and microvascular diffusivity.

Therefore, the current exploratory study investigates the potential of f_{int} as a marker to non-invasively assess ISF-volume changes in relation to sleep by examining whether these changes are associated to the actual hours of sleep or self-reported sleep quality.

Methods

MRI acquisition: Twenty healthy elderly subjects underwent high-field MRI (7T research system, Siemens Healthcare, Erlangen, Germany) using a 32-element channel phased-array head coil. Diffusion MR images (acquired with a prototype sequence) and anatomical T_1-weighted were acquired for all subjects (Table 2).
Image analysis: Diffusion Trace images were calculated and corrected for susceptibility induced distortions (topup, FSL version 6.0.1),[11] motion and eddy currents (ExploreDTI version 4.8.4).[12] Hereafter, images were smoothed with a 3mm FWHM Gaussian kernel (fslmaths, FSL).[13]

Anatomical T_1-weighted images were automatically segmented into gray matter (GM) and white matter (WM) using Freesurfer (version 5.1.0). Resulting masks were coregistered to IVIM image space (FLIRT, FSL).[14]

Spectral analysis using non-negative least squares (NNLS) was conducted to analyse the IVIM data in a voxel-wise manner.[1] The intermediate diffusion component was identified as $1.5*10^{-3}$<Diffusivity<$4.0*10^{-3}$ mm^2/s (Figure 1), and the contribution of the intermediate component to the total signal was determined by quantifying the ISF-volume fraction (f_{int}), while correcting for T_1- and T_2-relaxation effects.[1] To solve the NNLS, 80 basis functions were used, logarithmically spaced between $.1*10^{-3}$ and $200*10^{-3}mm^2/s$. Additionally, a regularisation smoothing constraint was added, allowing a misfit between 2% and 2.5%. The median value of f_{int} was extracted for WM and GM.

***Sleep questionnaire*:** Sleep quality over the last month was assessed by using the Pittsburgh Sleep Quality Index (PSQI).[15] In addition to the clinically used total PSQI (sum of all 7 components), two specific PSQI components were examined: Subjective sleep quality (PSQI 1) and Sleep duration (PSQI 3).

***Statistics*:** Pearson correlations were computed between the PSQI scores and f_{int} for WM and GM (IBM SPSS statistics version 25). To check for potential confounding influences, the analysis was repeated while adjusting for age and time of MRI-acquisition (in minutes after the previous midnight) using partial correlations.

Results

The sample characteristics and descriptive statistics of the PSQI and IVIM measures are summarized in Table 1.
A significant negative association is found between PSQI 1 (subjective sleep quality) and WM f_{int} (R=-.454, p=.045), where a worse reported sleep quality relates to lower WM f_{int} (Figure 2) (Table 3). After adjusting for age and time of MRI-acquisition, this association remains to show a trend towards significance (R=-.437, p=.061). No other significant associations were found (Table 3).

Discussion

The current explorative study identified a lower IVIM-derived proxy of ISF-volume (f_{int}) in the WM of subjects who reported a subjective feeling of long-term sleep deprivation. This association was effectively independent of age and the time of MRI-acquisition. A reduction in ISF-volume leaves less space for waste products to be cleared from in-between the cells. Thereby, the findings of this study are supportive of an association between sleep function and cerebral clearance.

Our findings are in line with previous studies that show reduced general diffusivity measures after sleep deprivation.[8,9] However, by isolating ISF from contamination of blood and parenchymal diffusivity, the current study was able to specifically assess ISF-volume alterations in relation to sleep deprivation measurements.

Interestingly, only the self-reported subjective sleep quality and not the actual hours of sleep, was found to be associated to the ISF-fraction. In contrast to the hours of sleep, the sleep quality represents sleep disturbances while accounting for intra-individual variations in need for sleep. The need to correct for intra-individual differences in sleep requirements is thereby further highlighted.[16-18] Furthermore, the total PSQI score does not seem sensitive enough to pick up intra-individual sleep variation in relation to ISF-volume.

Our findings highlight the potential of the IVIM-derived ISF-fraction as a non-invasive method to measure ISF alterations related to sleep disturbances. More data is currently being acquired, which will allow for more detailed investigation of the effects of potential confounding factors on the association between self-reported sleep and the ISF-volume.

References

1.Wong S, Backes W, Drenthen G, et al. Spectral Diffusion Analysis of Intravoxel Incoherent Motion MRI in Cerebral Small Vessel Disease. Journal of Magnetic Resonance Imaging. 2019.
2.van der Thiel MM, Freeze WM, Verheggen IC, et al. Associations of increased interstitial fluid with vascular and neurodegenerative abnormalities in a memory clinic sample. Neurobiology of Aging. 2021;106:257-267.
3.Abbott NJ. Evidence for bulk flow of brain interstitial fluid: significance for physiology and pathology. Neurochemistry International. 2004;45(4):545-552.
4.Jessen NA, Munk ASF, Lundgaard I, Nedergaard M. The glymphatic system: a beginner's guide. Neurochemical research. 2015;40(12):2583-2599.
5.Reddy OC, van der Werf YD. The Sleeping Brain: Harnessing the Power of the Glymphatic System through Lifestyle Choices. Brain Sciences. 2020;10(11):868.
6.Mendelsohn AR, Larrick JW. Sleep facilitates clearance of metabolites from the brain: glymphatic function in aging and neurodegenerative diseases. Rejuvenation research. 2013;16(6):518-523.
7.Xie L, Kang H, Xu Q, et al. Sleep Drives Metabolite Clearance from the Adult Brain. Science. 2013;342(6156):373-377.
8.Elvsåshagen T, Norbom LB, Pedersen PØ, et al. Widespread Changes in White Matter Microstructure after a Day of Waking and Sleep Deprivation. PLOS ONE. 2015;10(5):e0127351.
9.Bernardi G, Cecchetti L, Siclari F, et al. Sleep reverts changes in human gray and white matter caused by wake-dependent training. NeuroImage. 2016;129:367-377.
10.Demiral ŞB, Tomasi D, Sarlls J, et al. Apparent diffusion coefficient changes in human brain during sleep–Does it inform on the existence of a glymphatic system? Neuroimage. 2019;185:263-273.
11.Andersson JL, Skare S, Ashburner J. How to correct susceptibility distortions in spin-echo echo-planar images: application to diffusion tensor imaging. Neuroimage. 2003;20(2):870-888.
12.Leemans A, Jeurissen B, Sijbers J, Jones D. ExploreDTI: a graphical toolbox for processing, analyzing, and visualizing diffusion MR data. Paper presented at: Proc Intl Soc Mag Reson Med2009.
13.Jenkinson M, Beckmann CF, Behrens TE, Woolrich MW, Smith SM. FSL. Neuroimage. 2012;62(2):782-790.
14.Jenkinson M, Bannister P, Brady M, Smith S. Improved optimization for the robust and accurate linear registration and motion correction of brain images. Neuroimage. 2002;17(2):825-841.
15.Buysse DJ, Reynolds III CF, Monk TH, Berman SR, Kupfer DJ. The Pittsburgh Sleep Quality Index: a new instrument for psychiatric practice and research. Psychiatry research. 1989;28(2):193-213.
16.Mercer PW, Merritt SL, Cowell JM. Differences in reported sleep need among adolescents. Journal of Adolescent Health. 1998;23(5):259-263.
17.Ursin R, Bjorvatn B, Holsten F. Sleep Duration, Subjective Sleep Need, and Sleep Habits of 40- to 45-Year-Olds in the Hordaland Health Study. Sleep. 2005;28(10):1260-1269.
18.Landry G, Best J, Liu-Ambrose T. Measuring sleep quality in older adults: a comparison using subjective and objective methods. Frontiers in Aging Neuroscience. 2015;7(166).

Acknowledgments / Funding Information: This research was supported by Alzheimer Nederland (research grant WE.03-2018-02).

Table 1. This table displays the sample characteristics and descriptive statistics of the PSQI and IVIM measures. Mean (standard deviation) are reported unless stated otherwise.
Abbreviations: IVIM = intravoxel incoherent motion, D_{int} = interstitial fluid diffusion, f_{int} = interstitial fluid fraction, PSQI = Pittsburgh Sleep Quality Index, BMI = Body mass index.

Participant characteristics (n=20)	
Age (years)	65.08 (7.70)
Male, n (%)	7 (35.0)
BMI	.0025 (.00043)
Alcohol per week, mean [range] (units)	3.03 [0 - 14]
Smoking, n (%)	Never smoked: 10 (50) Past smoker: 10 (50)
Sleep measures	
PSQI 1 *Subjective sleep quality, mean [range]*	.8 [0 – 2]
PSQI 3 *Sleep duration, mean [range]*	1.1 [0 – 3]
PSQI Total *Sum of all 7 PSQI components, mean [range*	5.5 [1 - 12]
IVIM measures	
White matter D_{int} $(x10^{-3}\ mm^2/s)$ f_{int} (%)	1.946 (.084) 15.02 (1.66)
Gray matter D_{int} $(x10^{-3}\ mm^2/s)$ f_{int} (%)	1.992 (.083) 14.55 (1.58)

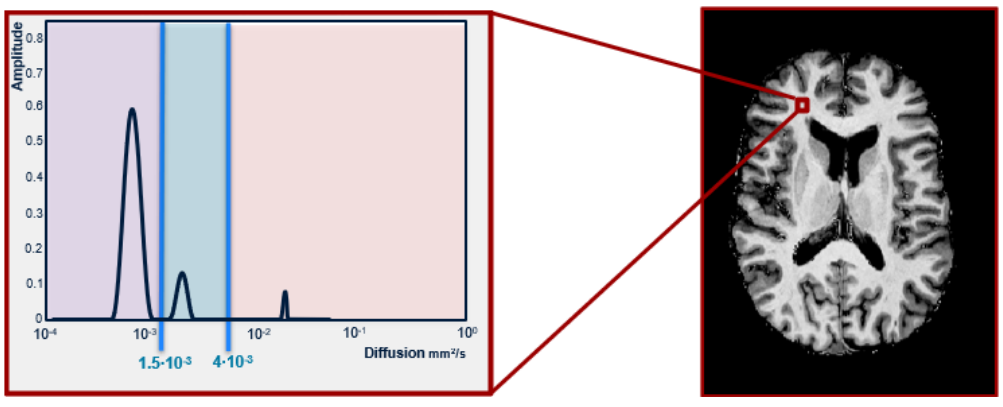

Figure 1. A simulated example of a diffusion spectrum of a voxel in the white matter is shown. The spectrum is divided into the three microstructural compartments (i.e., parenchymal, intermediate and microvascular compartment), showing the intermediate diffusion component in the middle.
purple = parenchymal diffusion range, blue = intermediate diffusion range, pink = microvascular pseudodiffusion range.

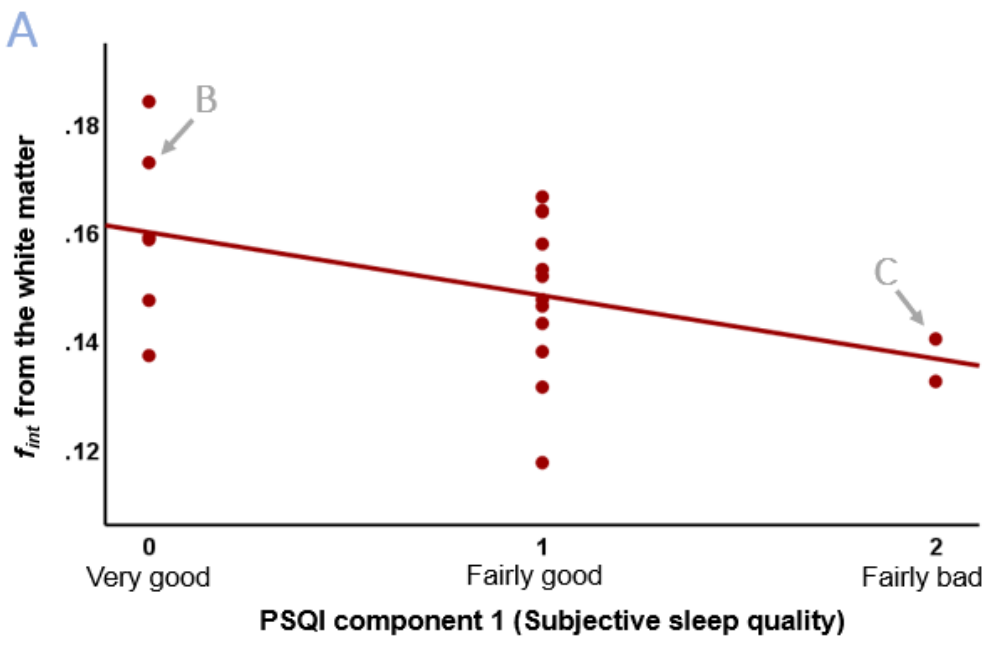

Table 2. This table summarizes the acquisition parameters of the sequences used.
Abbreviations: IVIM, intravoxel incoherent motion; TR, repetition time; TE, echo time; TI, inversion time; EPI, echo planar imaging.

Acquisition parameters	**IVIM**	**T_1-weighted**
Scan mode	multi-shot spin-echo EPI	MP2RAGE
Dimension	2D	3D
TR [ms]	22800	5000
TE [ms]	57.6	2.47
TI [ms]	2330	TI 1: 900 TI 2: 2750
Acquisition matrix	128x128x32	240x320x320
Acquired voxel size [mm³]	1.5x1.5x3.5	0.7x0.7x0.7
Acceleration factor	2	3
b-values [s/mm²]	0,5,10,15,20,30,40,50, 60,100,200,400,800,1000	
Diffusion sensitization directions	3 orthogonal directions	

Table 3. Pearson correlations of f_{int} with the subscales (PSQI 1 and PSQI 3) and total score (sum of all 7 PSQI components) of the PSQI.
Abbreviations: f_{int} = interstitial fluid fraction, PSQI = Pittsburgh Sleep Quality Index, R = Pearson correlation.
*** p < 0.05.**

	ISF-volume fraction (f_{int})			
	Gray matter		*White matter*	
PSQI measures (n = 20)	*R*	*p*-value	*R*	*p*-value
PSQI 1 *Subjective sleep quality*	-.292	.211	**-.454**	**.045***
PSQI 3 *Sleep duration*	.036	.879	-.119	.616
PSQI Total *Sum of 7 components*	-.075	.755	-.233	.322

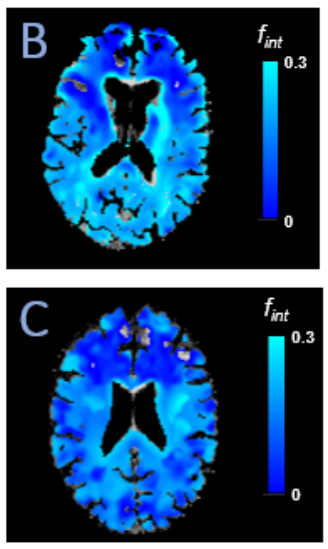

Figure 2. Scatterplot of f_{int} from the white matter with PSQI component 1 scores (subjective sleep quality during the past month) **(A)**. A least-square linear regression line is added for visualization. Arrows point to the participants used to present exemplary f_{int} maps of the whole parenchyma overlaid on the anatomical T_1-weighted image in native IVIM space, i.e., a subject with a low PSQI 1 score and high white matter f_{int} **(B)** and a subject with a high PSQI 1 score and low white matter f_{int} **(C)**.

Abbreviations: f_{int} = interstitial fluid fraction, PSQI = Pittsburgh Sleep Quality Index (PSQI).

Increased Pulsatility Index of Perforating Arteries as Novel 7T Marker in Sporadic Cerebral Small Vessel Disease – Results of ZOOM@SVDs Study.

SDT Pham[1], H. van den Brink[2], T. Arts[1], JCW Siero[1], J Hendrikse[1], JJM Zwanenburg[1], GJ Biessels[2] on behalf of the SVDs@Target consortium

[1]Department of Radiology, [2]Department of Neurology and Neurosurgery, Brain Center, University Medical Center Utrecht, Utrecht University, the Netherlands

Synopsis: We assessed blood-flow velocity measurements on 7T MRI as a potential disease marker for cerebral small vessel disease (SVD). Two-dimensional phase-contrast velocity measurements were performed in perforating arteries of the basal ganglia (BG) and white matter of the centrum semiovale (CSO) in patients with sporadic SVD and age- and sex-matched controls. Pulsatility index (PI) was significantly higher in the BG, in patients (0.45 [0.41–0.49] vs. 0.36 [0.30–0.41] in controls) (p=0.02). In the CSO, similar number of vessels, mean velocity, and PI were observed between patients and controls. BG pulsatility could be a potential marker for SVD.

Introduction: Cerebral small vessel diseases (SVDs) account for most hemorrhagic strokes, a quarter of the ischemic strokes and approximately 45% of dementia cases, alone or together with other neurodegenerative disorders[1]. In 70% of the people over 65, manifestations of SVDs can be found on brain MRIs[2]. Despite the large health burden of SVDs, there is still no treatment for SVDs with a proven efficacy due to the limited understanding of the mechanisms behind SVDs.

Current biomarkers of SVDs such as visible MRI manifestations (i.e. lacunes, white matter hyperintensities, enlarged perivascular spaces, microbleeds), microstructural changes to white matter measured with diffusion tensor imaging, or blood-based biomarkers are primarily reflective of irreversible SVDs-related damage to parenchymal tissue. SVDs impact small vessel function of pial and parenchymal arteries as observed in animal models[3]. New MRI techniques at 7T MRI allow for measuring the small vessel function in humans directly at the small vessels themselves[4]. These measures have potential as biomarkers for SVDs to give more insight in the disease mechanisms.

The ZOOM@SVDs[5] study was a prospective observational cohort study part of the SVDs@target collaborative program. One of the aims of this study was to assess which aspects of small vessel function measured at 7T MRI are affected in patients with Cerebral Autosomal Dominant Arteriopathy with Subcortical Infarcts and Leukoencephalopathy (CADASIL) and in patients with a sporadic form of SVD. Here we present the first results of small vessel blood-flow velocity and pulsatility measurements in patients with sporadic SVD and matched controls.

Methods: An overview of the ZOOM@SVDs study design has been published[5]. 46 patients with sporadic SVD and 22 matched healthy controls had successful 7T MRI brain scans. Subjects were scanned on a Philips 7T MRI with a 32-channel head coil. The blood-flow velocity measurements were performed in the small perforating arteries at the level of the centrum semiovale (CSO) and the basal ganglia (BG) using a two-dimensional phase-contrast (2D-PC) MRI acquisition (Figure 1). The following scan parameters were used: field of view CSO: 230x230 mm^2, BG: 170x170 mm^2; reconstructed spatial resolution CSO/BG: 0.2x0.2x2.0 mm^3; TR/TE CSO: 29/16 ms, BG: 28/15 ms; velocity encoding CSO: 4 cm/s, BG: 20 cm/s; acquired temporal resolution CSO/BG: 112 ms; 13 reconstructed heart phases, scan duration: 5 minutes for a heart rate of 60 bpm.

The 2D-PC images were analyzed to assess the cerebral perforating artery density ($N_{density}$) (number of perforating arteries/cm^2), mean blood-flow velocity (V_{mean}), and pulsatility index (PI). The PI was defined as $vPI = \frac{V_{max}-V_{min}}{V_{mean}}$, where V_{max}, V_{min}, and V_{mean}, are the maximum, minimum, and mean of the normalized and averaged velocity trace over the cardiac cycle (Figure 1). Analysis of the 2D-PC images was performed as described previously[6–8]. The region of interest (ROI) in the CSO was segmented automatically for the total white matter (TWM) and normal appearing white matter (NAWM) (Figure 2). ROIs in the BG were drawn manually. All statistical analyses were corrected for age and comparison of PI was corrected for V_{mean}.

Results: Controls were matched with patients based on age and sex. Mean age of the patients and controls were 63 and 65 years respectively. All controls had successful CSO and BG scans. 46 (100%) and 44 (96%) patients had successful CSO and BG scans respectively. In the BG we found similar $N_{density}$ (mean difference: 0.01 vessels/cm^2; p=0.69), lower V_{mean} (mean difference: 0.15 cm/s; p=0.55), and significantly higher PI (mean difference: 0.09; p=0.02), in patients when compared to controls (Table 1). In the CSO we found similar $N_{density}$, V_{mean}, and PI in the NAWM and TWM between patients and controls (Table 2).

Discussion: Patients with sporadic SVD had a higher velocity pulsatility in the BG when compared to healthy matched controls. No differences in the CSO outcome measures between controls and patients were found. The increased velocity pulsatility index we found in the BG in sporadic SVD is also in accordance with previous results in lacunar stroke patients[9] and with other findings of an increase pulsatility index in the internal carotid or middle cerebral arteries in cerebrovascular diseases[10,11]. The measurements in sporadic SVD are very comparable to the CADASIL patients in the ZOOM@SVDs cohort[12]. It is known that SVDs can manifest in small vessels as loss of smooth muscle cells, fibrinoid necrosis, narrowing of the lumen, and thickening of the vessel wall[13], which could be parts of the mechanism behind the increased velocity pulsatility index. With these results we signify the potential for 2D-PC blood-flow velocity measurements to be a direct signature of the disease in the small perforating arteries. These disease markers could also potentially be associated with disease burden or progression. The strength of these markers is that they are a direct reflection of small vessel function rather than small vessel damage.

Conclusion: The ZOOM@SVDs study showed the potential for 7T MRI 2D-PC blood-flow velocity measurements as small vessel function markers in monogenic and sporadic forms of SVD. The strength of these markers is that they are derived directly from the small vessels themselves, which could help contribute to unraveling the mechanisms behind SVDs.

References:

1. Wardlaw JM, Smith C, Dichgans M. Small vessel disease: mechanisms and clinical implications. Lancet Neurol. 2019;18(7):684-696.

2. Debette S, Schilling S, Duperron M-G, et al. Clinical Significance of Magnetic Resonance Imaging Markers of Vascular Brain Injury: A Systematic Review and Meta-analysis. JAMA Neurol. 2019;76(1):81-94.

3. Dabertrand F, Krøigaard C, Bonev AD, et al. Potassium channelopathy-like defect underlies early-stage cerebrovascular dysfunction in a genetic model of small vessel disease. Proc Natl Acad Sci. 2015;112(7):E796-E805.

4. Zwanenburg JJM, Van Osch MJP. Targeting cerebral small vessel disease with MRI. Stroke. 2017;48(11):3175-3182. doi:10.1161/STROKEAHA.117.016996

5. van den Brink H, Kopczak A, Arts T, et al. Zooming in on cerebral small vessel function in small vessel diseases with 7T MRI: Rationale and design of the "ZOOM@SVDs" study. Cereb Circ - Cogn Behav. 2021;2:100013.

6. Geurts L, Biessels GJ, Luijten P, et al. Better and faster velocity pulsatility assessment in cerebral white matter perforating arteries with 7T quantitative flow MRI through improved slice profile, acquisition scheme, and postprocessing. Magn Reson Med. 2018;79(3):1473-1482.

7. Arts T, Meijs TA, Grotenhuis H, et al. Velocity and Pulsatility Measures in the Perforating Arteries of the Basal Ganglia at 3T MRI in Reference to 7T MRI. Front Neurosci. 2021;15:480.

8. Arts T, Siero JCW, Biessels GJ, et al. Automated Assessment of Cerebral Arterial Perforator Function on 7T MRI. J Magn Reson Imaging. 2021;53(1):234-241.

9. Geurts LJ, Zwanenburg JJM, Klijn CJM, et al. Higher Pulsatility in Cerebral Perforating Arteries in Patients with Small Vessel Disease Related Stroke, a 7T MRI Study. Stroke. 2019;50(1):62-68.

10. Shi Y, Thrippleton MJ, Blair GW, et al. Small vessel disease is associated with altered cerebrovascular pulsatility but not resting cerebral blood flow. J Cereb Blood Flow Metab. 2020;40(1):85-99.

11. Shi Y, Thrippleton MJ, Marshall I, et al. Intracranial pulsatility in patients with cerebral small vessel disease: a systematic review. Clin Sci. 2018;132(1):157-171.

12. van den Brink H, Arts T, Kopczak A, et al. Novel 7T Markers of Small Vessel Function in CADASIL. Manuscript in preparation.

13. Pantoni L. Cerebral small vessel disease: from pathogenesis and clinical characteristics to therapeutic challenges. Lancet Neurol. 2010;9(7):689-701.

Acknowledgments / Funding Information: We want to thank all study participants for participating in the ZOOM@SVDs study. Furthermore, we want to thank all partners of the SVDs@target collaborative program for their efforts in the field of SVDs. ZOOM@SVDs is part of SVDs@target that has received funding from the European Union's Horizon 2020 research and innovative program under grant agreement No. 666881. JCWS and SDTP are funded by the UMCU Brain Center Young Talent Fellowship 2019.

Figure 1: A) Two-dimensional phase contrast (2D-PC) slice planning at the level of the centrum semiovale (CSO) and basal ganglia (BG) on a 3D T_1-w image. B) Magnitude image of a 2D-PC image of the CSO. Perforators are marked in red. C) Magnitude image of a 2D-PC image of the BG. Perforators are marked in red. D) Average velocity trace over the cardiac cycle of the perforating arteries in the CSO. E) Average velocity trace over the cardiac cycle of the perforating arteries in the BG.

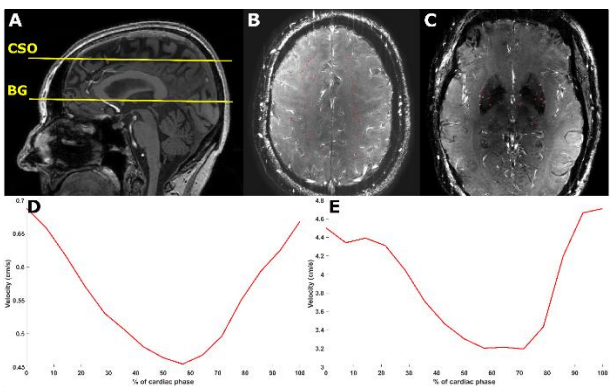

Figure 2: A) Region of interest (ROI) of the white matter automatically segmented in the two-dimensional phase contrast (2D-PC) slice at the level of the centrum semiovale (CSO). B) ROI manually drawn in the 2D-PC slice at the level of the basal ganglia (BG).

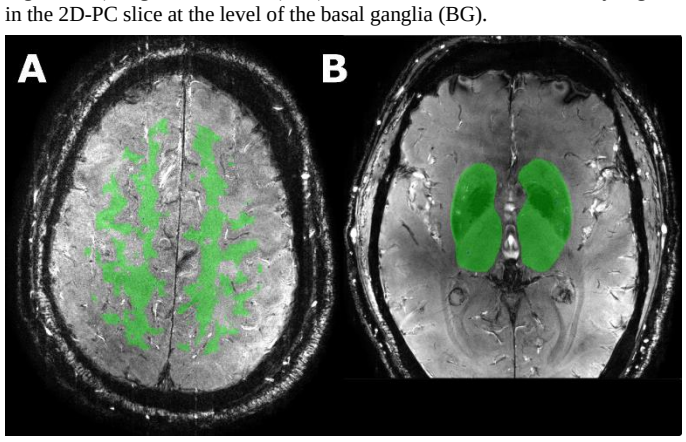

Table 1: Blood-flow velocity measurements of the perforating arteries in the basal ganglia (BG). $N_{density}$ = density of detected perforators given in amount detected/cm^2; V_{mean} = mean blood-flow velocity of the perforating arteries given in cm/s; CI = confidence interval. Values are given in mean with 95% CI. A p-value < 0.05 indicates statistical significance.

Basal Ganglia	Controls (n = 22)	Patients (n = 44)	p-value
$N_{density}$ (mean #/cm^2 [95% CI])	0.92 [0.80 – 1.04]	0.91 [0.83 – 0.99]	0.69
V_{mean} (cm/s [95% CI])	3.87 [3.59 – 4.16]	3.72 [3.52 – 3.93]	0.55
Pulsatility Index (mean [95% CI])	0.36 [0.30 – 0.41]	0.45 [0.41 – 0.49]	0.02

Table 2: Blood-flow velocity measurements of the perforating arteries in the semioval center (CSO) for the total white matter (Top) and the normal appearing white matter (Bottom). $N_{density}$ = density of detected perforators given in amount detected/cm^2; V_{mean} = mean blood-flow velocity of the perforating arteries given in cm/s; CI = confidence interval. Values are given in mean with 95% CI. A p-value < 0.05 indicates statistical significance.

Centrum semiovale Total white matter	Controls (n = 22)	Patients (n = 46)	P-value
$N_{density}$ (mean #/cm^2 [95% CI])	2.28 [1.90 – 2.65]	2.23 [1.90 – 2.56]	0.91
V_{mean} (mean cm/s [95% CI])	0.64 [0.60 – 0.68]	0.65 [0.62 – 0.69]	0.70
Pulsatility Index (mean [95% CI])	0.32 [0.27 – 0.37]	0.35 [0.31 – 0.38]	0.39
Centrum semiovale Normal appearing white matter	**Controls (n = 22)**	**Patients (n = 46)**	**P-value**
$N_{density}$ (mean #/cm^2 [95% CI])	2.27 [1.90 – 2.64]	2.23 [1.90 – 2.56]	0.91
V_{mean} (cm/s [95% CI])	0.64 [0.60 – 0.68]	0.66 [0.62 – 0.69]	0.65
Pulsatility Index (mean [95% CI])	0.32 [0.27 – 0.37]	0.36 [0.32 – 0.39]	0.33

High temporo-spatial resolution VASO reveals differential laminar reactivity to event-related stimuli at 7T

S. Dresbach[1], R. Huber[1] , R. Goebel[1]
[1]Faculty of Psychology and Neuroscience, Maastricht University, Maastricht, NL, Maastricht, Netherlands

Synopsis: Due to its high specificity, VASO plays a major role in laminar fMRI. To mitigate its lower sensitivity compared to GE-BOLD researchers mostly employ block-designs to increase SNR. Here, we developed a VASO sequence with a short TR (895ms volume acquisition) and showed that it provides the means to capture layer-specific haemodynamic responses with high spatio-temporal resolution. During event-related stimulation, we show reliable responses in visual and somatosensory cortices. Furthermore, the short TR and high specificity of VASO enabled us to show differences in laminar reactivity and onset times, thus demonstrating the high value of event-related designs using CBV-based fMRI.

Purpose: FMRI at ultra high resolutions lends the possibility to investigate the human brain at the mesoscopic scale (Dumoulin, 2016). A key feature at this level is the organization of cortical layers. While the commonly used GE-BOLD is biased towards the cortical surface, non-BOLD contrasts like Vascular Space Occupancy (VASO) have a higher specificity to the underlying microvasculature (Huber, 2017). However, this comes at the cost of lower sensitivity. Nevertheless, researchers have successfully used experimental conditions with long blocks of stimulation (~30s, e.g. Huber, 2017, but also see Persichetti, 2020). The possibility to employ short paced stimulation designs would widen the range of neuroscientific insights to be gained.The goal of the current study was:

- To develop and test a VASO sequence protocol with a short TR which provides the means to capture layer-specific haemodynamic responses with high temporal resolution (895 ms volume acquisition Trs).
- To characterise the sub-millimeter detection sensitivity of block and event-wise stimulation.
- To investigate the generalizability of different stimulus modalities (vision and somatosensation).

Methods: Data-acquisition: 4 participants underwent scanning using a 'classical' MAGNETOM 7T scanner (Siemens Healthineers, Erlangen, Germany), equipped with a 32-channel head coil at Scannexus (Maastricht, The Netherlands). All functional scans were performed with slice-selective slab-inversion VASO (SS-SI VASO, Huber, 2014) and a nominal resolution of 0.9mm isotropic (16 slices TI1/TI2/TR/TE = 50/825/1720/18 ms, partial fourier factor = 6/8, flip angle = 26°, FLASH GRAPPA 3, bandwidth =1266Hz/Px, FoV = 133 mm, Fig1 B). Slice position and orientation were chosen individually for each subject and covered the calcarine sulci and as much of the right postcentral gyrus as possible (Fig1 A). Finally, whole brain anatomical images (0.7mm isotropic) were acquired using MP2RAGE (Marques. 2010).

Paradigm: During block-stimulation runs (2 runs of ~12 minutes), flickering checkerboards were presented at 16Hz and, concurrently, 5 digit-tips (left hand) were stimulated (30s on-off block design) by means of a piezoelectric vibrotactile stimulator (mini PTS system, Dancer Design, UK). During subsequent event-stimulation runs (2-4 runs of ~12 minutes), we presented the same visio-tactile stimuli for 2s per trial with inter-trial intervals (ITIs) between 3 and 10s chosen from a uniform distribution, resulting in 84 trials per run. These highly irregular ITIs were chosen to accurately capture the haemodynamic responses of BOLD and VASO. The stimulation pattern was generated once and then used for all runs in order to allow averaging.

Data-processing: Motion- and BOLD-correction was applied using ants-Registration and LAYNII, respectively. GLM-analyses were performed in FSL (contrast: stimulation vs rest), ROIs were manually drawn in FSLeyes and layering was performed on spatially upsampled data (factor 5 in-plane) using LAYNII (Huber, 2021). Finally, the ROIs were used to generate event-related averages (ERAs) by extracting timecourses from 4 TRs before and 8 TRs after stimulation and averaging them using custom python-scripts. For analysis code, see: https://bit.ly/3qdZCBG.

Results and Discussion: Here, we discuss the results in visual cortices. For blocks, z-maps show clear responses in all participants (Fig2 A). ERAs for both VASO and BOLD show the expected sustained response which is stronger for BOLD than for VASO (Fig2 B). Z-scores increase strongly towards the cortical surface for BOLD but less for VASO (Fig2 C). For unimodal responses to long stimuli, a peak in middle layers would be expected for VASO (under the assumption that the nulled blood has been drained between volume TRs). Possibly, the signal increase we see towards the surface for VASO and BOLD reflects the multimodal input from tactile stimulation. When averaging multiple runs, we also obtained reliable z-maps for event-related stimuli (Fig3 A) and ERAs that follow the expected temporal pattern, with clear peaks, initial dips and undershoots (Fig3 B). Importantly, the general response pattern stabilizes after averaging about 20 event-trials (Fig4 B), showing its suitability for the use in neuroscientifically valuable designs due to high efficiency. Still, the event-related results show a reliable, but lower detection sensitivity compared to the block design data (as seen by the less pronounced maps in Fig3 A vs. Fig2 A, lower signal change Fig3 B vs. Fig2 B and lower z-scores in Fig4 C). Importantly, Fig3 D shows earlier responses for middle and deep layers in VASO, which demonstrates its high value for depth-dependent analyses. The slow venous hemodynamic filter in BOLD, however, cannot capture these differences in our data.

Similar results were obtained in the somatosensory cortex (S1, see Fig5). Note, that here we found higher z-scores for event-wise stimulation in VASO (Fig5 D).

Conclusion and Summary: Here, we characterize the applicability of SS-SI VASO with event-related stimulation. With a short 895 ms volume acquisition TRs, we were able to capture the haemodynamic response for VASO and BOLD within a few average trials. Furthermore, the short TR and high specificity of VASO enabled us to show subtle laminar-dependent timing differences of neural processing and vascular reactivity features. Here, deep and middle layers showed the earliest responses in VASO but not BOLD. We believe that this shows the added value of employing shorter stimulation periods using VASO, which greatly increases the range of possible design choices for CBV-based laminar fMRI.

Acknowledgements

- Laurentius Huber was funded by from the NWO VENI project 016.Veni.198.032.
- Sebastian Dresbach is supported by the 'Robin Hood' fund of the Faculty of Psychology and Neuroscience and the department of Cognitive Neuroscience
- Scanning was supported by FPN (faculty of psychology and neuroscience) via the MBIC grant scheme. Scanning was performed at the facilities of Scannexus B.V. (Maastricht, Netherlands).

References

- Dumoulin, S. O., Fracasso, A., van der Zwaag, W., Siero, J. C. W., & Petridou, N. (2018). Ultra-high field MRI: Advancing systems neuroscience towards mesoscopic human brain function. NeuroImage, 168(September 2016), 345–357. https://doi.org/10.1016/j.neuroimage.2017.01.028
- Huber, L., Ivanov, D., Krieger, S. N., Streicher, M. N., Mildner, T., Poser, B. A., … Turner, R. (2014). Slab-selective, BOLD-corrected VASO at 7 tesla provides measures of cerebral blood volume reactivity with high signal-to-noise ratio. Magnetic Resonance in Medicine, 72(1), 137–148. https://doi.org/10.1002/mrm.24916
- Huber, L., Handwerker, D. A., Jangraw, D. C., Chen, G., Hall, A., Stüber, C., … Bandettini, P. A. (2017). High-Resolution CBV-fMRI Allows Mapping of Laminar Activity and Connectivity of Cortical Input and Output in Human M1. Neuron, 96(6), 1253-1263.e7. https://doi.org/10.1016/j.neuron.2017.11.005
- Huber, L. (Renzo), Poser, B. A., Bandettini, P. A., Arora, K., Wagstyl, K., Cho, S., … Gulban, O. F. (2021). LayNii: A software suite for layer-fMRI. NeuroImage, 237(April), 118091. https://doi.org/10.1016/j.neuroimage.2021.118091
- Marques, J. P., Kober, T., Krueger, G., van der Zwaag, W., Van de Moortele, P. F., & Gruetter, R. (2010). MP2RAGE, a self bias-field corrected sequence for improved segmentation and T1-mapping at high field. NeuroImage, 49(2), 1271–1281. https://doi.org/10.1016/j.neuroimage.2009.10.002
- Persichetti, A. S., Avery, J. A., Huber, L., Merriam, E. P., & Martin, A. (2020). Layer-Specific Contributions to Imagined and Executed Hand Movements in Human Primary Motor Cortex. Current Biology, 1–5. https://doi.org/10.1016/j.cub.2020.02.046

Acknowledgments / Funding Information: Continue on this line

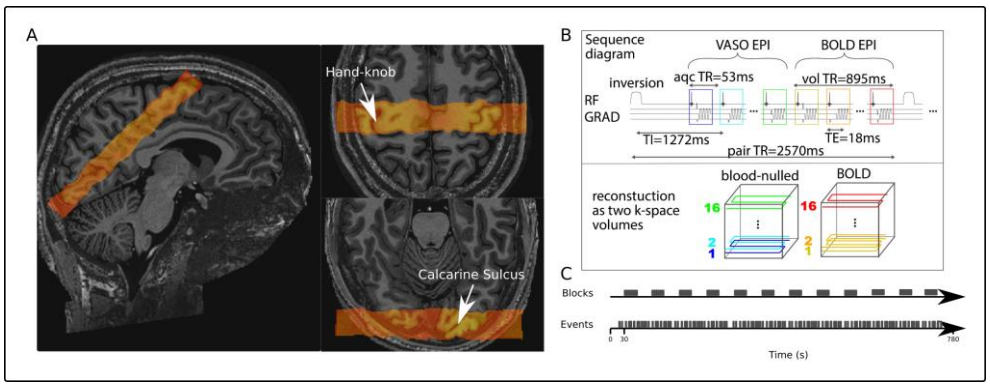

Fig1. Experiment Information. A) Slab coverage registered to and overlaid on whole-brain MP2RAGE and anatomical landmarks guiding slab-selection B) Sequence diagram C) Schematic stimulation paradigm for blocks and event-related stimulation.

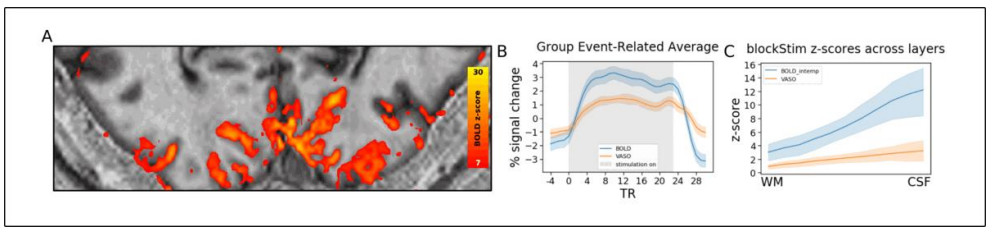

Fig2. Block stimulation results and ROIs. A) BOLD Zmap and resulting layer-ROIs flipping back and forth based on block stimulation for a representative participant. B) Group-level event-related averages showing the BOLD and VASO signal change across all layers in response stimuli with a duration of 30s. C) Group-level layer profiles (z-scores) for BOLD and VASO. Shaded area around graphs: 95% confidence interval across trials.

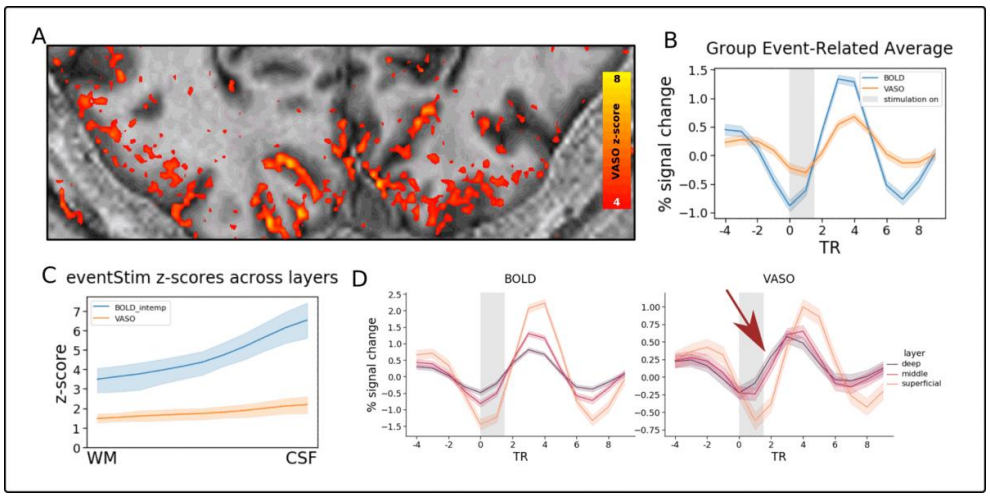

Fig3. Event-wise stimulation results. A) VASO Zmap of 4 averaged runs and layer ROI (based on block simulation) flipping back and forth for a representative participant. B) Group-level ERA showing the BOLD and VASO signal change across layers in response stimuli with a duration of 2s. C) Group-level layer profiles (z-scores) for BOLD and VASO in response to event-wise stimulation. D) Layer-effect for response onset for VASO but not for BOLD. Shaded area around graphs: 95% confidence interval across trials.

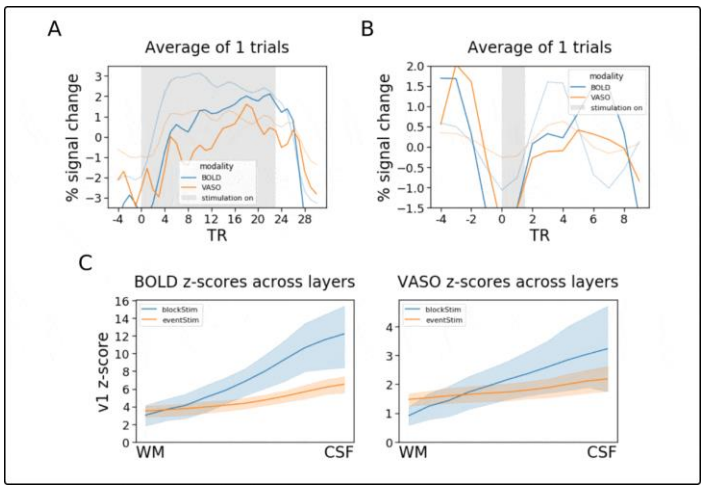

Fig4. Incremental averaging of trials and z-score comparison. Animations showing the incremental convergence on the mean signal change for one run of a representative participant. Each frame depicts the ERA of a given number of trials for block- A) and event-wise B) stimulation in darker hue and the run average in lighter hue. C) Comparison between z-scores for block- and event-wise stimulation separately for BOLD and VASO.

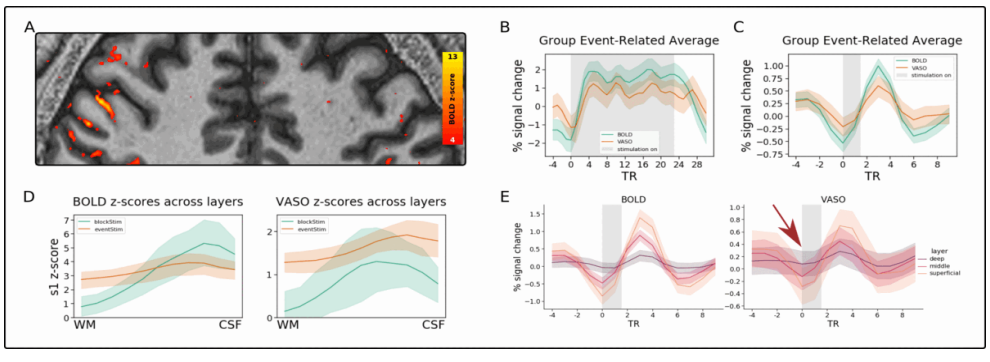

Fig5. Tactile stimulation results. A) BOLD Zmap and layer-ROI in S1 based on block stimulation for a representative participant. B) Same as Fig2B but for ROI in S1 C) Same as Fig3B but for ROI in S1 D) Comparison between group layer profiles in S1 (z-scores) in response to block- and event-wise stimulation for BOLD and VASO E) Trend towards layer-effect (within error bars) in S1 for response onset for VASO but not for BOLD. Shaded area around graphs: 95% confidence interval across trials.

Longitudinal Fixel-Based Analysis of diffusion MRI in the zQ175 Huntington's disease mouse model

N. Vidas-Guscic[a,b], J. van Rijswijk[a,b], J. Van Audekerke[a,b], B. Jeurissen[b,c], S. Missault[a,b], D. Pustina[d], H. Tang[d], R. Cachope[d], L. Liu[d], C. Dominguez[d], I. Munoz-Sanjuan[d], A. Van der Linden[a,b], M. Verhoye[a,b]

[a]Bio-Imaging Lab, University of Antwerp, Antwerp, Belgium, [b]μNEURO Research Centre of Excellence, University of Antwerp, Antwerp, Belgium, [c]Vision-Lab, University of Antwerp, Antwerp, Belgium, [d]CHDI Management/CHDI Foundation, Princeton, NJ, United States of America

Synopsis

Huntington's disease (HD) is a neurodegenerative disorder that affects motor and cognitive abilities. In this study, we present the outcome of a longitudinal multi-shell DWI investigation of the zQ175 HD mouse model using the diffusion tensor, diffusion kurtosis, and fixel-based analysis. This study reveals that, microstructural deficits are observed at an early stage of disease and mainly affect the diffusion tensor in corpus callosum and kurtosis in caudate putamen and grey matter, while fiber cross-section is reduced in major fiber bundles. At a late stage, many white matter fiber bundles show deficits that are indicative of differential myelination and potential axonal pathology.

Summary of main findings

Fixel-based analysis and diffusion kurtosis analysis reveal white and gray matter pathology at 6 and 11 months in the zQ175 Huntington's disease mouse model.

Introduction

Huntington's disease is a progressive genetic neurological disease that affects the motor and cognitive abilities.[1] Biomarkers are crucial to distinguish different stages of the disease and to test potential HD treatments. Diffusion weighted imaging (DWI) and the commonly applied diffusion tensor imaging (DTI) analysis have already revealed structural deficits in human HD patients and animal models compared to healthy controls.[2] Previously, we have demonstrated the presence of structural deficits in the zQ175 mouse model in a moderate stage of Huntington's disease using DWI. In this longitudinal study, we investigated (1) at what disease stages the structural changes occur in the brain of zQ175 HD mice and (2) how these deficits change between disease stages.

Methods

29 HD mice ($zQ175^{+/-}$) and 29 healthy control littermates ($zQ175^{-/-}$) were investigated at 3, 6 and 11 months of age (premanifest, disease onset and moderate manifest stage respectively) using multi-shell diffusion MRI. Animals were anesthetized with 1-2% isoflurane in a mixture of N_2 and O_2 during handling and image acquisition. Body temperature and breathing rate were monitored. Diffusion imaging was performed on a 7T Pharmascan 70/16 USR horizontal MR system (Bruker, Germany) using a multi-shell (b= 700, 1200 and 2800 s/mm^2; δ= 4ms, Δ= 12ms) two-shot spin echo DW-EPI sequence with 60 unique diffusion directions across each shell (TE/TR= 23/7000ms). Per scan, 3 b_0 images were acquired. Each scan contained 16 horizontal slices (500μm slice thickness) with an in-plane resolution of (200x200)μm^2 and a matrix size of [108x100]. Images were pre-processed using Gibbs ringing correction and denoising (MRtrix3.0),[4] motion- and distortion correction (FSL6.0), and bias-field correction (ANTs).[5] Voxel-level modelling was performed using multi-tissue constrained spherical deconvolution[6] in MRtrix3.0. A study-specific population template of the white matter (WM), gray matter (GM) and cerebrospinal fluid (CSF) compartment was built across all ages using iterative non-linear registration in ANTs. Data was statistically compared in Mrtrix3.0 using a fixel-wise two sample t-test. A similar processing pipeline was used before fitting the diffusion data to the DKI model, from which both diffusion tensor and kurtosis metrics were extracted. A voxel-wise two sample t-test was performed on the diffusion/kurtosis maps using FSL6.0 randomise.[7] Mean values for each metric were extracted for Huntington vulnerable regions-of-interest (ROI) and statistically compared using a linear mixed model to test for age, genotype, and interaction effects, followed by FDR correction.

Results

Voxel and fixel-wise analysis demonstrate widespread significant differences between $zQ175^{-/-}$ (WT) and $zQ175^{+/-}$ (HD) mice at 6 and 11 months of age (Fig.1). White matter structures have lower fractional anisotropy (FA) and axial diffusivity (AD), and increased RD at 11 months of age in $zQ175^{+/-}$ mice. Gray matter structures demonstrate widespread increased mean kurtosis (MK) and axial kurtosis (AK) at 6 months, while at 11 months MK and AK are decreased. In white matter fiber tracts, fiber bundle cross-section is lower in $zQ175^{+/-}$ mice at 6 and 11 months of age.

Region-of-interest analysis of the diffusion tensor and kurtosis metrics in corpus callosum (CC), caudate putamen (CPu) and motor cortex which are relevant regions in HD pathology, shows that in $zQ175^{+/-}$ mice FA is lower, and RD increased in the CC at 6 and 11 months. No genotype differences except increases of mean kurtosis (MK) are found for the CPu. However, in the motor cortex MD and AD significantly decreased at 6 and 11 months (Fig.2-3), and FA significantly decreased at 11 months. The Tract-of-interest analysis reveals that FD increased and FC decreased in CPu at 3 months of age (Fig.4), which is earlier than the diffusion tensor and kurtosis metrics. FD and FC significantly decreased in CC, and FC significantly decreased in CPu at 6 and 11 months. FC significantly decreased in the motor cortex at 6 months.

Discussion & Conclusion

This longitudinal characterization of the $zQ175^{+/-}$ HD mouse model reveals that most structural deficits are present at 6 months of age when the animals exhibit their first motor deficits (Fig.5). At this stage, the structural phenotypes are best captured by decrease of FA and increase of RD in CC, increase of MK and decrease of FC in CPu, and decrease of FD and/or FC in major fiber bundles. At the moderate manifest stage (11 months), pathology has a more widespread effect on white matter fiber bundles, displayed as a decrease in FA and increase in RD, suggesting differential myelination. At the moderate manifest stage, the increase in the kurtosis parameters is no longer present, while FD, FC and FDC remain decreased, which suggests that the microstructural complexity and axon bundle density and cross-section are reduced. The non-linear changes in FA and kurtosis metrics are counterintuitive, however, such changes have been reported in fMRI in HD.[8,9] DTI studies in Parkinson's disease, which is also a neurodegenerative motor disorder, suggest potential (early) compensatory mechanisms could be involved.[10] Immunohistochemistry is planned to investigate what is causing these microstructural deficits.

References

1. Bates, G. P. *et al.* Huntington disease. *Nat. Rev. Dis. Prim.* **1**, 1–21 (2015).
2. Estevez-Fraga, C., Scahill, R., Rees, G., Tabrizi, S. J. & Gregory, S. Diffusion imaging in Huntington's disease: comprehensive review. *J. Neurol. Neurosurg. Psychiatry* jnnp-2020-324377 (2020).
3. Raffelt, D. A. *et al.* Investigating white matter fibre density and morphology using fixel-based analysis. *Neuroimage* **144**, 58–73 (2017).
4. Tournier, J. D. *et al.* MRtrix3: A fast, flexible and open software framework for medical image processing and visualisation. *Neuroimage* **202**, 116137 (2019).
5. Tustison, N., Avants, B., Cook, P., Zheng, Y., Egan, A., Yushkevich, P. & Gee, J. N4ITK: Improved N3 Bias Correction. IEEE Transactions on Medical Imaging, **29**, 1310-1320 (2010).
6. Jeurissen, B., Tournier, J.D., Dhollander, T., Connelly, A. & Sijbers, J. Multi-tissue constrained spherical deconvolution for improved analysis of multi-shell diffusion MRI data. *Neuroimage* **103**, 411-426 (2014).
7. Winkler, A. M., Ridgway, G. R., Webster, M. A., Smith, S. M. & Nichols, T. E. Permutation inference for the general linear model. *Neuroimage* **92**, 381–397 (2014).
8. Pini, L., Jacquemot, C., Cagnin, A., Meneghello, F., Semenza, C., Mantini, D. & Vallesi, A. Aberrant brain network connectivity in presymptomatic and manifest Huntington's disease: A systematic review. *Human Brain Mapping* **41**, 256-269 (2020).
9. Gregory, S., Long, J.D., Tabrizi, S.J. & Rees, G. Measuring compensation in neurodegeneration using MRI. *Curr Opin Neurol* **30**, 380-387 (2017).
10. Moghaddam, H.S., Dolatshahi, M., Mohebi, F., Aarabi, M.H. Structural white matter alterations as compensatory mechanisms in Parkinson's disease: A systematic review of diffusion tensor imaging studies. *J Neurosci Res.* **98**, 1398-1416 (2020).

Acknowledgments / Funding Information: Continue on this line

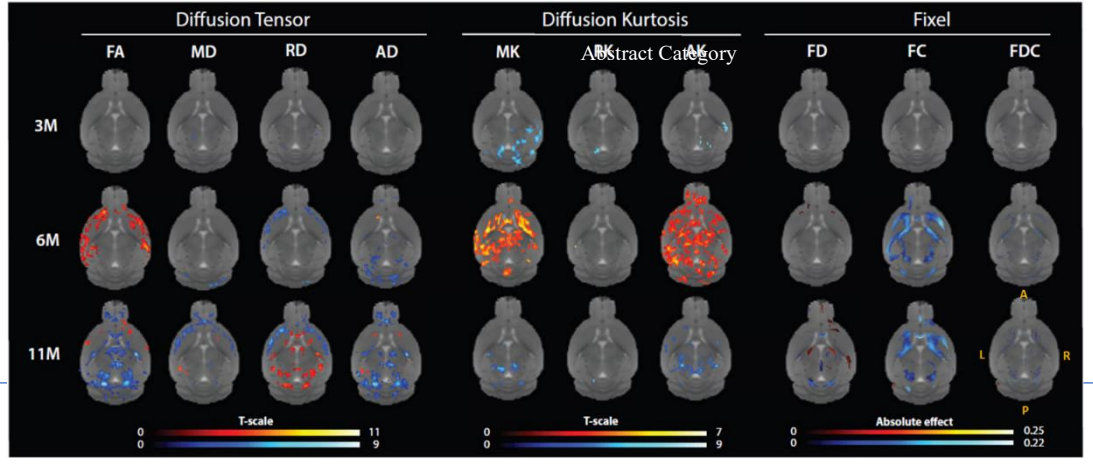

Figure 1: Voxel-wise diffusion tensor and kurtosis analysis and fixel-based analysis reveal structural deficits in different stages of HD progression. Significant voxels ($P_{TFCE\text{-}FWE} < 0.05$ for diffusion tensor and kurtosis) and fixels ($P_{CFE\text{-}FWE} < 0.05$) are overlaid on a T2-weighted template in horizontal view at -2.68mm Bregma. Hot T-scales and absolute effect scale indicate an increase in zQ175$^{+/-}$ (HD) mice compared to zQ175$^{-/-}$ (WT) animals, while cool scales indicate a significant decrease.

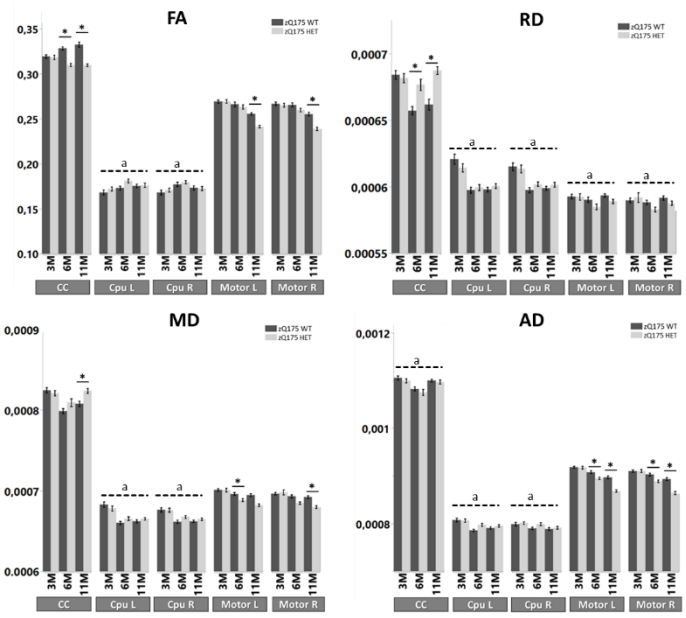

Figure 2: ROI-based analysis of diffusion tensor data in HD relevant regions. Analysis is performed separately for fractional anisotropy (FA), radial diffusivity (RD, 10^{-3} mm^2/s), mean diffusivity (MD, 10^{-3} mm^2/s), and axial diffusivity (AD, 10^{-3} mm^2/s). zQ175$^{-/-}$ (WT) mice are shown in dark gray and zQ175$^{+/-}$ (HD) animals are shown in light grey. Asterisks indicate significant post-hoc differences (P<0.05) between genotypes per timepoint. Dotted lines labelled **a** indicate significant main effects of age (P<0.05), regardless of genotype. Error bars indicate the SEM.

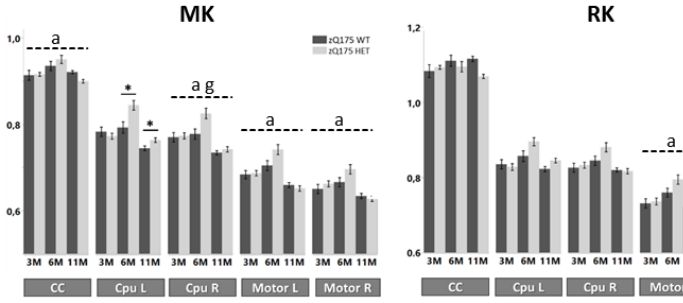

Figure 3: ROI-based analysis of diffusion kurtosis data in HD relevant regions. Analysis is performed separately for mean kurtosis (MK), radial kurtosis (RK) and axial kurtosis (AK). zQ175$^{-/-}$ (WT) mice are shown in dark gray and zQ175$^{+/-}$ (HD) animals are shown in light grey. Asterisks indicate significant post-hoc differences (P<0.05) between genotypes per timepoint. Dashed lines indicate a significant (P<0.05) main effect of age (**a**) or genotype (**g**). Error bars indicate the SEM.

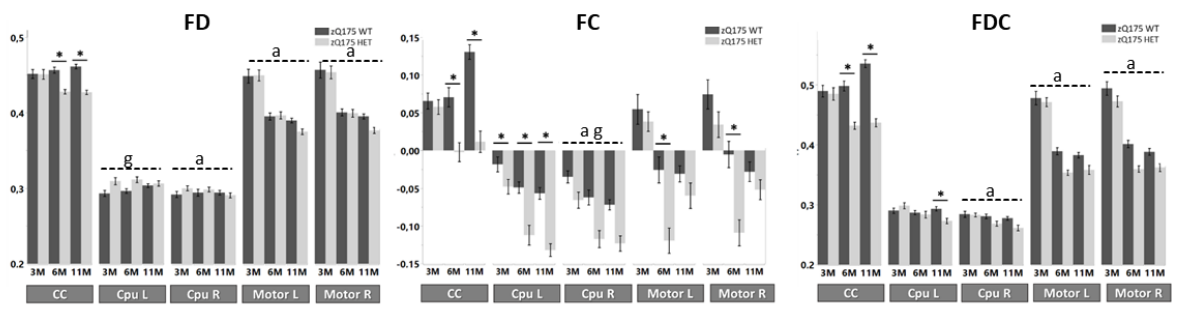

Figure 4: Tract-based comparison of fixel-based data in five HD relevant regions. Analysis is performed separately for fiber density (FD), fiber cross-section (FC) and fiber density x cross-section (FDC). zQ175$^{-/-}$ (WT) mice are shown in dark gray and zQ175$^{+/-}$ (HD) animals are shown in light grey. Asterisks indicate significant post-hoc differences (P<0.05) between genotypes per timepoint. Dashed lines indicate a significant (P<0.05) main effect of age (**a**) or genotype (**g**). Error bars indicate the SEM.

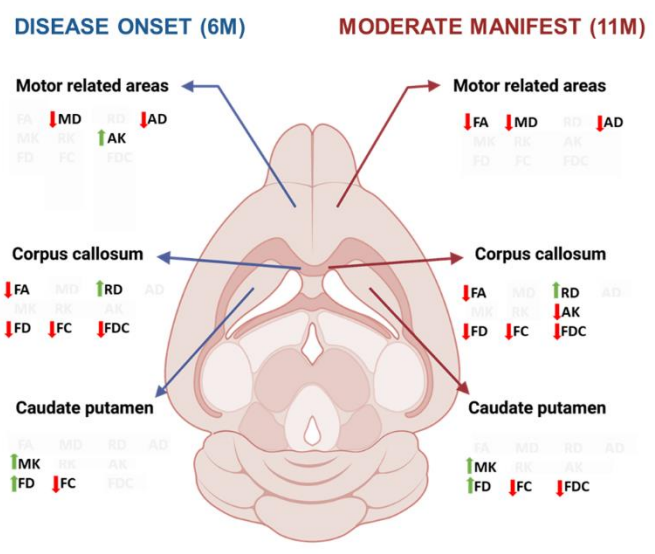

Figure 5: Schematic overview of pathological micro-and microstructural features in HD relevant regions. Comparisons are summarized from figures 2 – 4. Left side: changes in diffusion parameters in disease onset. Right side: changes in diffusion parameters in the moderate manifest stage. Significantly different parameters are paired with arrows indicating an increase (green) or decrease (red) for a specific metric. Figure created with BioRender.com.

Impaired brain perfusion and cerebrovascular reactivity in the zQ175 mouse model of Huntington's Disease, a longitudinal pCASL-MRI study

T. Vasilkovska[1,2], V. Vanreusel[1], S. Salajeghe[1], J. Van Audekerke[1,2], L. Hirschler[3], D. Pustina[4], R. Cachope[4], H. Tang[4], L. Liu[4], C. Dominguez[4], I. Munoz-Sanjuan[4], A. Van der Linden[1,2], M. Verhoye[1,2]

[1]Bio-Imaging lab, University of Antwerp, Antwerp, Belgium; [2]μNEURO Research Centre of Excellence, University of Antwerp, Antwerp, Belgium; [3]C.J. Gorter Center for High Field MRI, Leiden University Medical Center, Leiden, the Netherlands; [4]CHDI Management/CHDI Foundation, Princeton, NJ, USA

Synopsis: Abnormal cerebral vasculature and consequent diminished cerebrovascular function have been shown to play a role in Huntington's Disease (HD). However, how these impairments reflect on cerebral blood flow (CBF) dynamics and vascular reactivity (CVR) have been poorly understood. Towards this, we performed a longitudinal study measuring CBF and CVR, using pCASL, in the zQ175 KI Huntington's disease (HD) mouse model at pre-manifest (3/4.5 months), disease onset (6 months) and manifest (9 months) stage. Our results demonstrate decreased CBF under CO2 challenge at disease onset and decreased CVR in manifest HD stage in the zQ175 KI mice compared to age-matched controls.

Introduction: Huntington's Disease (HD) is an autosomal, dominantly inherited neurodegenerative (ND) disease with an abnormal expansion of the CAG (cytosine-adenine-guanine) repeat in the huntingtin gene. Despite the known genetic background, HD pathomechanisms are still not fully understood, limiting the possibility of a successful therapy thus far. Brain perfusion, cerebrovascular functional and anatomical integrity have been shown to be compromised in ND diseases, such as HD. More specifically, in manifest HD patients, hypoperfusion is markedly reduced in cortical and basal ganglia brain regions[1], whereas recent, preliminary findings in pre-symptomatic HD have shown cerebrovascular reactivity (CVR) alterations in subcortical white matter areas[2]. This raises the potential of using vascular-based changes as a biomarker which can allow for probing new therapeutic strategies.

In order to better characterize perfusion dynamics at different stages of HD and explore the potential of a cerebrovascular biomarker, we used the zQ175 KI heterozygous (HET) model which mimics the human HD progression the closest[3], with motor deficits starting at 6 months, marked as disease symptom onset[4]. Hence, in our study, we sought to investigate cerebral blood flow (CBF) and CVR changes in the zQ175 HET HD mouse model using pseudo-Continuous Arterial Spin Labelling (pCASL) MRI.

Methods: Longitudinal pCASL MRI was performed on a 7T Bruker scanner on two different cohorts of wild-type (WT, n=10) and HET (n=10) zQ175 DN mice in different conditions, at 2 separate scan moments: (1) measuring plain perfusion under baseline (66% N2 and 33% O2) at 3, 6 and 9 months, (2) assessing CVR (%ΔCBF between baseline and CO2 challenge) via measuring perfusion under baseline (100% O2) and CO2 challenge (90% O2 10% CO2) at 4.5, 6 and 9 months of age. Mice were anesthetized with a combination of 0.4% isoflurane and medetomidine (0.05mg/kg s.c. bolus; 0.01mg/kg/h s.c. infusion). The physiological parameters were monitored and kept stable throughout the scan procedure. pCASL scans were acquired 40 min post bolus for 7 minutes during baseline (both conditions), 7 minutes under CO2 challenge and 3.5 minutes under recovery (Fig. 1, A). Preceding the pCASL acquisition, a time-of-flight angiogram was acquired to define the labelling position, a labelling efficiency map as well as a pCASL scan in order to determine the optimal phase steps for the labelled and control RF pulse. The pCASL sequence[5] is a spin echo (SE) EPI with labelling time of 3000ms, post label delay (PLD) of 200ms, TR/TE 3450/19.5ms. 120/120/60 label and control images are acquired (60/60/30 CBF measures) in baseline/challenge/recovery, for 5 coronal slices with a spatial resolution of 0.26 x 0.39 x 0.8 mm^3. Absolute CBF was quantified using a T1 map (estimated from an extra slice-selective Inversion Recovery acquisition) and calculated using the single compartment model6. Realignment, co-registration to a T1 weighted image, spatial normalization and in-plane smoothing of the label/control images was performed using SPM12 software. A study-based template was created in ANTs. ROI- based analysis (RBA) was performed using pre-defined regions of interest (ROI) from which mean CBF values per subject were extracted. Two-sample T-tests on the distributions of CBF and CVR data of WT and HET mice were performed with FDR correction ($p<0.05$) in GraphPad Prism 9.2. Explorative voxel-based analysis (VBA) to reveal - at each age - local differences in CBF and CVR between WT and HET mice was performed in SPM12 using two-sample t-tests with $p<0.01$, uncorrected.

Results: At disease symptom onset (6 months), RBA demonstrates a significant lower perfusion in HET mice during 100% O2 baseline condition in the piriform cortex, and - more robust - significant lower CBF during CO2 challenge across multiple brain regions (Fig.2.A) with no significant CVR changes present. This is in line with the VBA maps that display lower CBF in the same regions and conditions (Fig.2.B). At a manifest disease stage (9 months), the dynamic profiles of brain averaged CBF from baseline to CO2 challenge demonstrate a smaller increase in CBF in HET compared to WT mice (Fig.1.B), which is in accordance with the RBA where the retrosplenial cortex has lower CBF under CO2 challenge (Fig.3.A). An overall lower CVR is present in HET across different brain areas (Fig.3.A), while no CBF changes were detected in 100% O2 baseline conditions. The VBA maps display differences in the same line as the RBA with an overall lower CBF and %ΔCBF in HET (Fig.3.B). Even though perfusion measurements under normoxic condition did not show any statistically significant difference between both groups at any age, at 9 months, both RBA and VBA analysis showed a trend in higher CBF in several brain regions (Fig.4.A, B).

Discussion and Conclusion: Our main findings demonstrate that, in zQ175 HET mice, at disease symptom onset, there is lower perfusion under CO2 challenge and impaired CVR at a manifest stage. The compromised vascular response indicates aberrations at the level of the neurovascular unit, potentially as a consequence of mutant huntingtin (mHTT) depositions within blood vessels7 and different cell types, such as smooth muscle cells, astrocytes8 or pericytes. This study highlights the relevance of assessing CBF and CVR alterations as a prospective biomarker which can be used for evaluating efficacy of future therapies that aim at lowering mHTT or targeting different vascular components.

References:

1. Chen JJ, Salat DH, Rosas HD. Complex relationships between cerebral blood flow and brain atrophy in early Huntington's disease. Neuroimage. 2012;59(2):1043-1051. doi:10.1016/j.neuroimage.2011.08.112

2. Chan ST, Mercaldo ND, Kwong KK, Hersch SM, Rosas HD. Impaired Cerebrovascular Reactivity in Huntington's Disease. Front Physiol. 2021 Jul 21;12:663898

3. Menalled L., Kudwa AE, Miller S, et al. Comprehensive behavioral and molecular characterization of a new knock-in mouse model of Huntington's disease: zQ175. PLoS One. 2012; 7(12): e49838.

4. Heikkinen T, Bragge T, Bhattarai N, Parkkari T, Puoliväli J, Kontkanen O, Sweeney P, Park LC, Munoz-Sanjuan I. Rapid and robust patterns of spontaneous locomotor deficits in mouse models of Huntington's disease. PLoS One. 2020 Dec 28;15(12):e0243052.

5. Hirschler L, Debacker CS, Voiron J, et al. Interpulse phase corrections for unbalanced pseudo-continuous arterial spin labeling at high magnetic field. Magn Reson Med. 2018;79(3):1314-1324

6. Buxton, R. B. Quantifying CBF with arterial spin labeling. J Magn Reson Imaging. 2005; 22, 723-726

7. Drouin-Ouellet J, Sawiak SJ, Cisbani G, Lagacé M, Kuan WL, Saint-Pierre M, Dury RJ, Alata W, St-Amour I, Mason SL, Calon F, Lacroix S, Gowland PA, Francis ST, Barker RA, Cicchetti F. Cerebrovascular and blood-brain barrier impairments in Huntington's disease: Potential implications for its pathophysiology. Ann Neurol. 2015 Aug;78(2):160-77.

8. Hsiao HY, Chen YC, Huang CH, Chen CC, Hsu YH, Chen HM, Chiu FL, Kuo HC, Chang C, Chern Y. Aberrant astrocytes impair vascular reactivity in Huntington disease. Ann Neurol. 2015 Aug;78(2):178-92.

Acknowledgments / Funding Information: Continue on this line

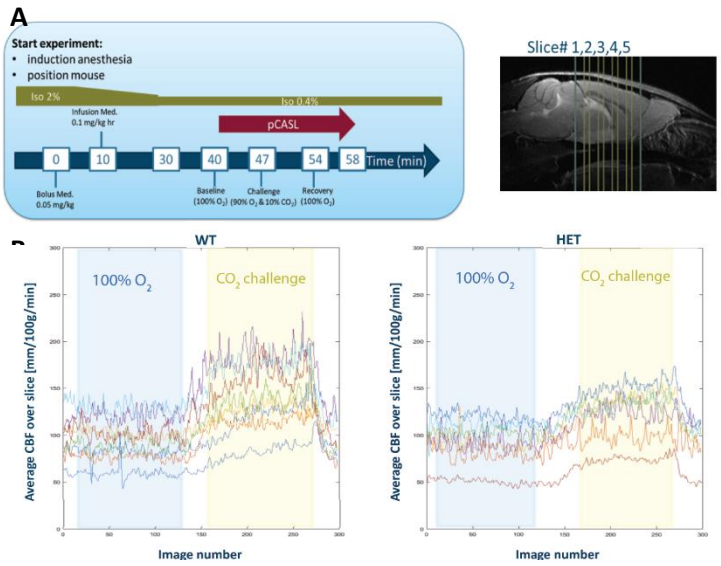

Fig.1: (A) Acquisition scheme for pCASL with CO2 challenge (left) and the anatomical position of the 5 coronal slices (right); (B) Example of the average CBF across time during baseline (blue insert) and CO2 challenge (yellow insert) conditions for both WT and HET mice.

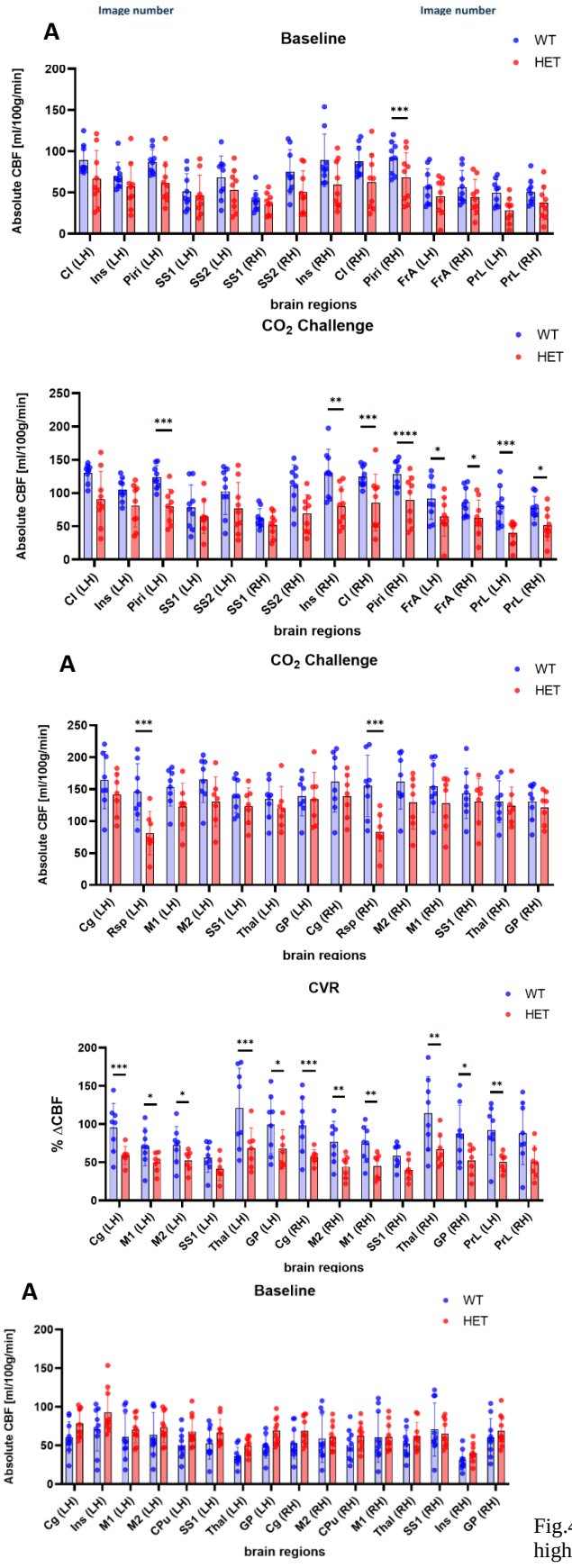

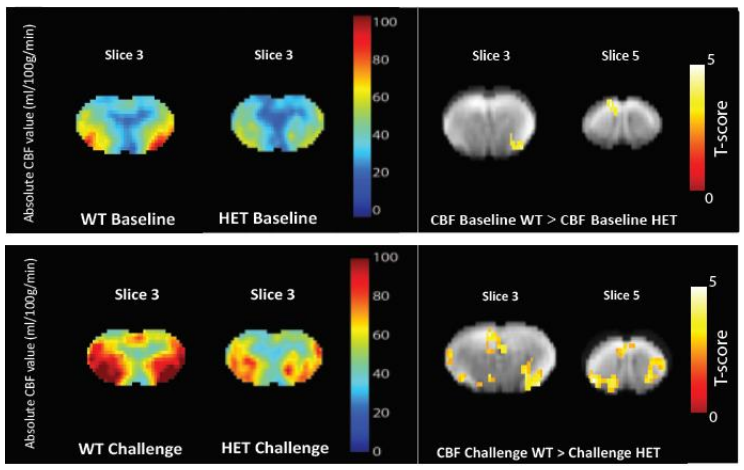

Fig.2: (A) ROI-based analysis at 6 months of age demonstrates under 100% O2 baseline, significant lower CBF in Piriform Cortex (Piri) in HET compared to WT mice, while under CO2 challenge multiple regions show significant lower CBF in HET; (B) Mean CBF maps for both WT and HET under 100% O2 baseline and CO2 challenge and VBA statistical maps demonstrating decreased CBF in the same ROIs as (A) in HET in both conditions; Two-sample T-test for RBA with $p<0.05$ (FDR corrected) and VBA statistical maps with $p<0.01$ (uncorrected)

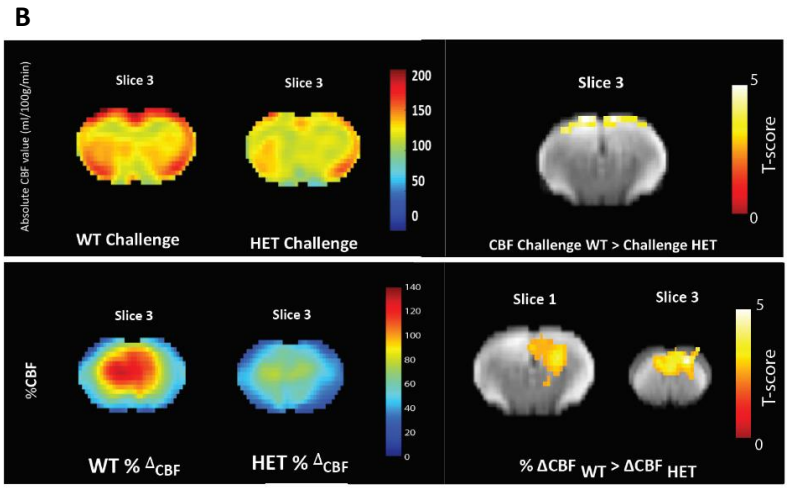

Fig.3: (A) ROI-based analysis at 9 months of age demonstrates under CO2 challenge, significant lower CBF in Retrosplenial Cortex (Rsp) in HET compared to WT mice, while the CVR shows significant lower %ΔCBF in multiple regions in HET; (B) Mean CBF maps for both WT and HET under CO2 challenge and CVR and VBA statistical maps demonstrating lower CBF and lower CVR in HET in the same ROIs as (A) ; Two-sample T-test for RBA with $p<0.05$ (FDR corrected) and VBA statistical maps with $p<0.01$ (uncorrected)

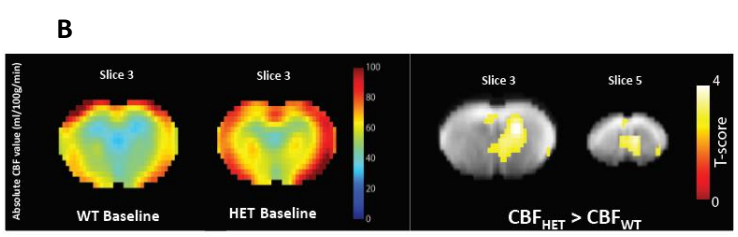

Fig.4: (A) ROI-based analysis of perfusion under normoxic condition at 9 months of age shows only a trend of higher CBF in HET in several regions compared to WT mice; (B) Mean CBF maps for both WT and HET and VBA statistical map demonstrating higher CBF in HET compared to WT mice; Two-sample T-test for RBA with $p<0.05$ (FDR corrected) and VBA statistical maps with $p<0.01$ (uncorrected)

Measurement of renal perfusion using ASL-MRI and renal oxygenation using BOLD-MRI in dogs: a pilot study

A. Hillaert[1], K. Vanderperren[1], P. Pullens[2-4]

[1]Department of Morphology, Imaging, Orthopedics, Rehabilitation and Nutrition, Ghent University, Merelbeke, Belgium; [2]Department of Radiology and Nuclear Medicine, Ghent University Hospital, Ghent, Belgium; [3] Ghent Institute for functional and Metabolic Imaging, Ghent University, Ghent, Belgium; [4]Institute of Biomedical Engineering and Technology (IBiTech), Ghent University, Ghent, Belgium

Synopsis: ASL- and BOLD-MRI have shown great potential in humans and rodents. To date, however, these techniques have not been used to image the canine kidney. Therefore, renal blood flow (RBF) and relaxation rate (R2*) were assessed using ASL and BOLD sequences on a beagle at 3T to examine the feasibility of both techniques in dogs. Mean RBF was 263.3 ± 39.0 and 277.4 ± 83.3 ml/100g/min in the right and left kidney, respectively. Mean R2* in the right kidney was 22.6 (range 14.8 - 36.8) s^{-1}. This pilot-study demonstrates the feasibility of ASL- and BOLD-MRI for renal assessment in dogs.

PURPOSE

Renal disorders are a common problem, in both humans and companion animals. In dogs, the prevalence of chronic kidney disease alone is estimated to be between 0.5 and 7% [1]. Previous studies in veterinary medicine have urged the need for better methods that can diagnose kidney diseases and elucidate the pathophysiological process [2,3]. Current methods to assess canine kidney function (e.g. renal biomarkers in blood and urine) are cumbersome and ineffective to detect early kidney damage [3-5].

Noninvasive magnetic resonance imaging (MRI) methods like arterial spin labeling (ASL) MRI and blood oxygenation level dependent (BOLD) MRI show great potential to address these challenges. Both techniques rely on an endogenous contrast to assess renal perfusion and renal tissue oxygenation, respectively [6]. Unlike contrast-enhanced ultrasound, which usually takes single plane images, ASL- and BOLD-MRI characterize the entire kidney.

Functional MRI measures in combination with standard anatomical images allow comprehensive characterization of the kidney [6]. To date, ASL- and BOLD-MRI have been used in humans and rodents[7], but has not been used to image the canine kidney. Therefore, the purpose of this study was to determine whether a scan protocol could be composed to visualize renal perfusion and renal tissue oxygenation in dogs.

METHODS

A healthy Beagle (male, 3 years, 10 kg) was scanned in dorsal recumbency on a Siemens PrismaFit 3T. Before the MRI scan, the dog was deprived of water and food for 5 and 12 hours, respectively. Sedation was achieved with administration of butorphanol (0.2 mg/kg, i.v.). Anesthesia was induced with propofol (4 mg/kg, i.v.) and maintained with inhalation of isoflurane (2%) in 100% oxygen. Midazolam (0.2 mg/kg, i.v.) was supplemented because of superficial breathing. To evaluate perfusion, a multi-TI FAIR QTIPS ASL scan with background suppression was performed (Siemens WIP ASP 1023H), with TIs ranging from 250 to 2500ms, Bolus length 1000ms. TR/TE 4500/23.58ms, matrix 64x64, 8 oblique coronal 8mm slices, 272x136mm FOV, 5 measurements per TI. Afterwards a second single-TI FAIR ASL was performed with TI=2000ms, 30 measurements. RBF maps are calculated on the scanner. Segmentation and statistics were done with FSL (https://fsl.fmrib.ox.ac.uk/). A multi-echo GRE sequence with 12 equally spaced echo times (TR 70ms/TEs 4.20:4.20:50.40ms), matrix 96x96, FOV 180x180, four 4mm slices, was used to generate BOLD contrast. A 15 sec breath-hold was induced by applying end-expiratory positive pressure with the breathing balloon. R2* maps were calculated with T2Processor (https://github.com/gifmi) in Matlab R2019a, and the TLCO (Twelve-Layer Concentric Objects) method[8] was used to calculate mean R2* in the cortex and medulla.

RESULTS

In dogs, the kidneys are oriented oblique in two axes in the abdomen, which makes positioning more challenging compared to humans (Fig 1). Fig 2 shows multi-TI FAIR QTIPS perfusion weighted images. Based on these data, a TI of 2000 ms was chosen to be optimal. Fig 3 shows the Renal Blood Flow (RBF) map, scaled from 0 to 500 ml/100g/min. Mean (sd) RBF in the R kidney was 263.3(39.0), in the L kidney 277.4 (83.3) ml/100g/min. There is a clear distinction in RBF between the cortex and medulla. Fig 4 shows R2*. Mean R2* in twelve concentric layers is from outside to inside; 30.2, 24.0, 20.7, 19.4, 16.8, 15.2, 14.2, 17.2, 20.9, 23.5, 36.8 and 32.8 s^{-1} respectively.

DISCUSSION

Canine renal perfusion MRI can be performed on a clinical scanner. The ASL voxel size was relatively large in this experiment, so future experiments are needed to see if this can be reduced.

ASL-MRI derived RBF seems comparable to the true RBF in healthy dogs obtained by an ultrasonic flow-probe [9]. Lee et al. (2020) divided the renal arterial flow measured with the ultrasonic flow-probe on the renal artery by the renal cortical volume quantified on CT images to calculate the true RBF of the kidney [9]. The researchers reported a mean RBF of 246.28 and 273.68 mL/min/100g versus an RBF of 263.3 and 277.4 mL/min/100g in this study [9]. Furthermore, Renal Blood Flow values are in a similar range as human renal perfusion (mean RBF of 229 ± 41 ml/min/100g) [10].

Using induced breath-hold, BOLD data of good quality can be obtained. Positioning of the imaging plane in a dog is more challenging than in human, because of the orientation of the kidneys in the abdomen. As for ASL-MRI, the measurements obtained with BOLD-MRI in dogs were in proximity of to those in humans. In humans, the mean R2* in the outer concentric layers ranged from 23.4 to 27.9 s^{-1} and from 30.7 to 31.9 s^{-1} in the inner concentric layers, while the mean R2* of all layers was 28.1 ± 4.5 s^{-1}, which is in line with the values obtained in this experiment [8].

CONCLUSION

In this study, we demonstrate the feasibility of ASL- and BOLD-MRI for quantification of renal perfusion and tissue oxygenation in dogs by a tailored scan protocol. However, further optimalisation for better image quality is necessary. RBF values are very similar to reference RBF values obtained with ultrasonic flow probes. Both ASL- and BOLD-MRI may contribute to an improved diagnosis of renal diseases and clarification of underlying pathophysiological processes. The canine model can also be used to validate renal ASL in humans.

REFERENCES

1. Lund EM, Armstrong PJ, Kirk CA, et al. Health status and population characteristics of dogs and cats examined at private veterinary practices in the United States. J Am Vet Med Assoc. 1999;214(9):1336–41.

2. Miyagawa Y, Takemura N, Hirose H. Assessments of factors that affect glomerular filtration rate and indirect markers of renal function in dogs and cats. J Vet Med Sci. 2010;72(9):1129–36.

3. Von Hendy-Willson E V & Pressler B M. An overview of glomerular filtration rate testing in dogs and cats. Vet. J. 2011;188(2):156–165.

4. Schneider M. Ultrasound Contrast Agents. In: Kiessling F, Pichler BJ, editors. Small Animal Imaging. Berlin, Heidelberg: Springer; 2011. p. 219–29.

5. Kazmierski B, Deurdulian C, Tchelepi H, et al. Applications of contrast-enhanced ultrasound in the kidney. Abdom. Radiol. 2018;43(4):880–898.

6. Selby NM, Blankestijn PJ, Boor P et al. Magnetic resonance imaging biomarkers for chronic kidney disease: a position paper from the European Cooperation in Science and Technology Action PARENCHIMA. Nephrol. Dial. Transplant. 2018;33(suppl_2):ii4–ii14.

7. Ku M-C, Fernández-Seara MA, Kober F, Niendorf T: Noninvasive Renal Perfusion Measurement Using Arterial Spin Labeling (ASL) MRI: Basic Concept. In Preclinical MRI of the Kidney: Methods and Protocols. Edited by Pohlmann A, Niendorf T. New York, NY: Springer US; 2021:229–239. [Methods in Molecular Biology]

8. Piskunowicz M, Hofmann L, Zuercher E, et al.: A new technique with high reproducibility to estimate renal oxygenation using BOLD-MRI in chronic kidney disease. Magnetic Resonance Imaging 2015; 33:253–261.

9. Lee SK, Jang Y, Jung JW, et al. Comparison of Renal Blood Flow Using Maximum Slope-Based Computed Tomography Perfusion and Ultrasound Flow Probe in Healthy Dogs. Front Vet Sci. 2020;7(541747).

10. Gillis KA, McComb C, Foster JE, et al. Inter-study reproducibility of arterial spin labeling magnetic resonance imaging for measurement of renal perfusion in healthy volunteers at 3 Tesla. BMC Nephrol. 2014;15(23):1–10.

Acknowledgments / Funding Information: Funding was provided by the Special Research Fund of Ghent University, Belgium (BOF grant 01D27919). The authors thank research assistant Stephanie Bogaert and the colleagues of the Department of Morphology, Imaging, Orthopedics, Rehabilitation and Nutrition, and the Small Animal Department for their assistance during the MRI scan, and Dr. Bernd Kühn (Siemens Healthcare AG, Erlangen, DE) for providing the ASL WIP sequence.

Figure 1. Positioning of the imaging plane for FAIR ASL overlayed on coronal and axial T2 HASTE images. In dogs, the kidneys are oriented oblique in two axes in the abdomen, which makes positioning more challenging compared to humans.

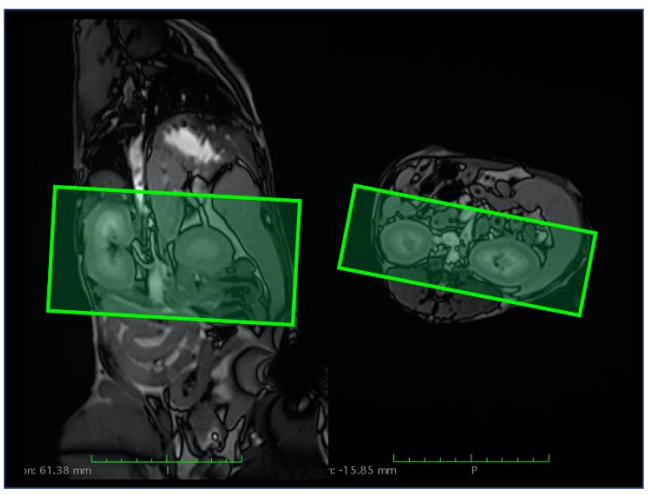

Figure 2. Perfusion-Weighted images of the multi-TI experiment. The highest perfusion signal is observed at TI=2000ms.

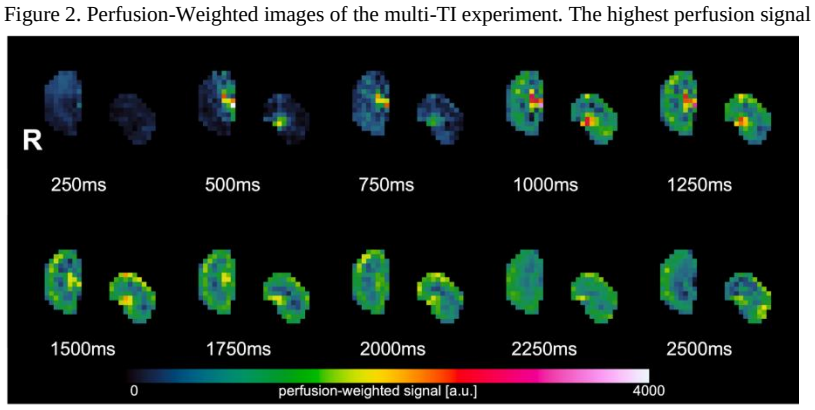

Figure 3. Renal Blood Flow (RBF) map. Mean cortical perfusion is 263 ml/100g/min in the right kidney, 277 ml/100g/min in the left kidney.

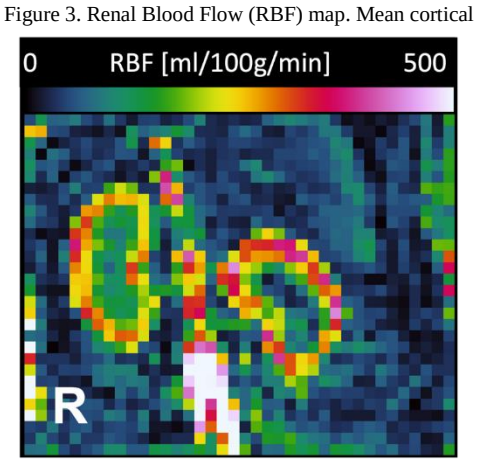

Figure 4. R2* map (A), TLCO layers (B) and R2* in each layer (C). 1 represents the outer layer, 12 the inner layer. Mean R2* ranges from 14.2 to 36.8 s^{-1}, with an average R2* of 22.6 s^{-1}.

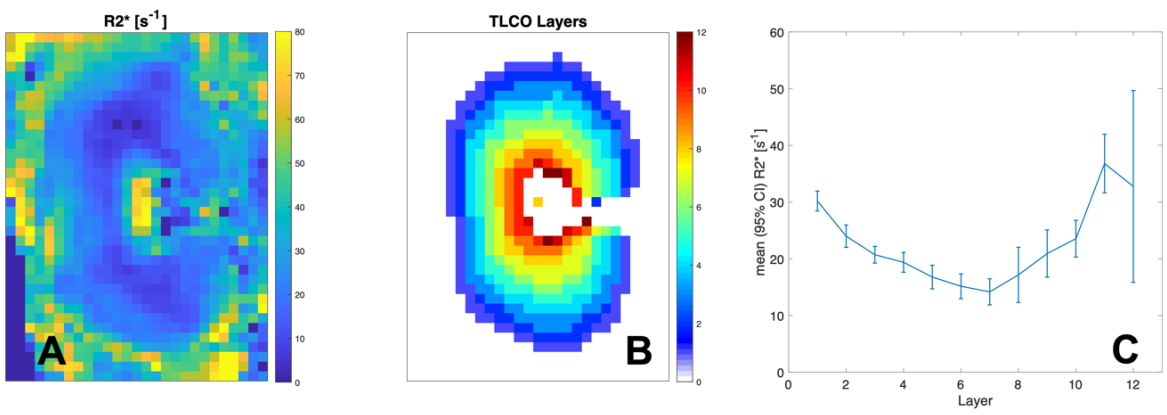

Evaluation of Placenta Oxygenation and Perfusion in A Rat Model of Fetal Growth Restriction Using Quantitative T2* Mapping and 3D DCE-MRI

Fatimah Al Darwish[1], Bram Coolen[1], Fieke Terstappen[2], Caren van Kammen[2], Lindy Alles[1], Titia lely[2], Raymond Schiffelers[2], and Gustav Strijkers[1]

[1]Biomedical engineering and physics, Amsterdam University Medical Center, Amsterdam, Netherlands; [2]University Medical Center Utrecht, Utrecht, Netherlands

Synopsis: Developing preclinical imaging techniques in the field of preeclampsia is essential to test the effectiveness of new therapeutic approaches. We applied T2* weighted and three -dimensional dynamic contrast-enhanced MRI in a pregnant rat model of reduced uterine perfusion pressure (RUPP) to test their feasibility and ability to detect differences in placental oxygenation and perfusion in RUPP rats compared to control. These techniques produced high-quality data that enabled the assessment of oxygenation and perfusion parameters. Oxygenation was decreased in RUPP placenta; however, perfusion parameters did not reveal differences, which requires further investigations.

Purpose: Preeclampsia (PE) and fetal growth restriction (FGR) are pregnancy-related systemic syndromes driven by placenta dysfunction, in which oxygen and nutrient supply to the fetus is insufficient. For preclinical research on placental dysfunction and possible therapeutic strategies, the reduced uterine perfusion pressure (RUPP) rat model has been established[1]. Two important outcome measures for the assessment of placenta dysfunction are placental oxygenation and perfusion. The purpose of this study was to develop a preclinical MRI protocol to assess rat placental oxygenation and perfusion using quantitative T2* mapping three-dimensional dynamic contrast enhanced (3D DCE) MRI, respectively, and to establish whether these techniques can measure differences between healthy and RUPP placentas in the rat.

Methods:

Animal experiment:

Pregnant Sprague Dawley rats were subjected to sham (n=5) or RUPP (n=6) surgery on gestational day (GD) 13. The RUPP model was achieved by clipping the ovarian arteries and abdominal aorta, intended to reduce the blood supply to the uterus. Animals were scanned at GD 19 on a 7T MRI scanner (MR Solutions, Guildford, UK). The MRI session consisted of T2-weighted anatomical imaging for localizing the placentas, followed by T2* weighted MRI for placental and fetal oxygenation assessment, and 3D-DCE MRI for perfusion assessment.

T2* MRI:

Quantitative T2* maps were based on a respiratory gated multi-slice multi-gradient-echo sequence with the following parameters: TR = 130 ms, TE0 = 2.2 ms, echo-spacing = 2.2 ms, number of echoes = 8, flip-angle = 30o, FOV = 60 x 60 mm2, matrix = 192 x 192, slice thickness = 1.2 mm, number of slices = 3-5, acquisition time = 3-5 min.

3D-DCE MRI:

Dynamic contrast-enhanced MRI was based on a 3D RF-spoiled gradient-echo sequence with the following parameters: TR = 8 ms, TE = 2 ms, flip-angle = 25o, FOV = 60 x 60 x 60 mm3, matrix = 128 x 96 x 96. K-space filling was done using a pseudo-radial scheme in the two phase-encoding directions and a tiny golden-angle increment of 16.95o between successive spokes (Fig. 1B). The pseudo-radial acquisition was repeated for 11 minutes. Subsequently, data was reconstructed with a temporal resolution of 22 seconds using a compressed sensing reconstruction algorithm with a total variation regularization in the temporal domain.

Results: A typical T2-weighted anatomical scout scan is shown in Figure 2A along with representative examples of T2* weighted images from different fetuses (Fig. 2B) and their corresponding quantitative T2* maps (Fig 2C). For one case (Fig. 2D), the series of T2*-weighted images is given demonstrating the excellent image quality and delineation of several fetal organs at the different echo times. No further registration was needed in calculating the T2* maps. Figure 3 shows that the oxygenation status, as reflected by the R2* (1/T2*) values, was significantly lower in the maternal placental layer of the RUPP rats comparing to sham rats (p=0.01). However, no statistically significant differences between RUPP and sham rats were identified in the fetal placental layer, nor in the fetal brain or liver.

3D dynamic contrast enhanced imaging of rat placentas was feasible and provided full coverage to cope with the complex arrangement of the placentas in the abdomen. The temporal enhancement starting from the central arterial canal on the maternal side to the fetal side and back to the maternal side can be appreciated from the 3D DCE time series (Fig. 3). Resulting signal intensity-time curves were analyzed semi-quantitatively by assessing the initial area under the curve (AUC) after signal normalization (Fig 5). No significant differences between the RUPP and sham rats were observed.

Discussion: The MRI protocols used in this study produced high-quality T2* mapping and high-temporal resolution 3D DCE MRI that can be used to study placenta oxygenation and perfusion parameters in pregnant rats. Most previous human and animal studies focus on the changes in T2*-weighted signals in response to a respiratory challenge[2]. Our study showed that quantitative T2* differences can be detected at baseline between RUPP and sham groups. The decrease in placenta T2* reflects a change in oxygenation, in keeping with the found in the human placenta in fetal growth restriction and other animal models of preeclampsia3,4. 3D DCE quality remained good up to temporal resolutions of 20-25 seconds. Although this allowed us to perform an AUC analysis of the contrast agent uptake, this did not reveal the expected differences between RUPP and sham rats. This can have different reasons, including the position of the fetuses in the uterine horns, variability in fetal and placental weights, variability in litter size, and variability in phenotype severity. These sources of variability made the distinction more difficult to be detected. In the future, we will focus on implementation of improved quantitative DCE modeling to overcome some of these issues, e.g., by making use of reference region models[5] to prevent the need for fast arterial input function (AIF) measurements. Finally, we would like to validate our MRI protocol with alternative techniques, such as photoacoustic imaging and contrast-enhanced ultrasound.

Conclusion: T2* mapping and 3D DCE-MRI can be successfully applied in pregnant rats to study changes in oxygenation and perfusion. Our rat model of fetal growth restriction showed significant changes in oxygenation, whereas differences in perfusion parameter were not observed.

References:

1. Li J, LaMarca B, Reckelhoff JF. A model of preeclampsia in rats: The reduced uterine perfusion pressure (RUPP) model. *Am J Physiol - Hear Circ Physiol*. 2012;303(1). doi:10.1152/ajpheart.00117.2012

2. Sørensen A, Hutter J, Seed M, Grant PE, Gowland P. T2* weighted Placental MRI: Basic research tool or an emerging clinical test of placental dysfunction? *Ultrasound Obstet Gynecol*. 2019;55(3):293-302. doi:10.1002/UOG.20855

3. Sinding M, Peters DA, Frøkjær JB, et al. Placental magnetic resonance imaging T2* measurements in normal pregnancies and in those complicated by fetal growth restriction. *Ultrasound Obstet Gynecol*. 2016;47(6):748-754. doi:10.1002/UOG.14917

4. Collinot H, Marchiol C, Lagoutte I, et al. Preeclampsia induced by STOX1 overexpression in mice induces intrauterine growth restriction, abnormal ultrasonography and BOLD MRI signatures. *J Hypertens*. 2018;36(6):1399-1406. doi:10.1097/HJH.0000000000001695

5. Yankeelov TE, Luci JJ, Lepage M, et al. Quantitative pharmacokinetic analysis of DCE-MRI data without an arterial input function: a reference region model. *Magn Reson Imaging*. 2005;23(4):519-529. doi:10.1016/J.MRI.2005.02.013

Acknowledgments / Funding Information: No acknowledgement found.

A. MRI parameters

Imaging parameter	T2W	T2* mapping	3D-DCE
Acquisition plane	Coronal	Coronal	-
Repetition time (ms)	2500	130	8
Echo time (ms)	30	2.2	2
echo-spacing	-	2.2	-
number of echoes	-	8	-
Flip angle (°)	90	30	25
Matrix size	256 x 256	192 x 192	128 x 96 x 96
Field of view (mm^2)	90 x 90	60 x 60	60 x 60
Slice thickness (mm)	1.2	1.2	60
Slice gap (mm)	0.5	0.2	-
Signal average	4	8	1
Total acquisition time (min)	10	3-5	11

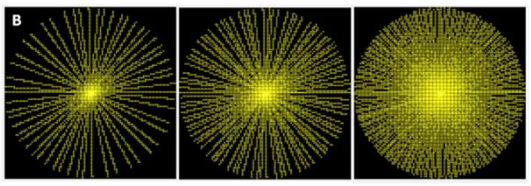

Figure 1. A) MRI protocol parameters. **B)** K-space pseudo-radial filling scheme for 3D-DCE.

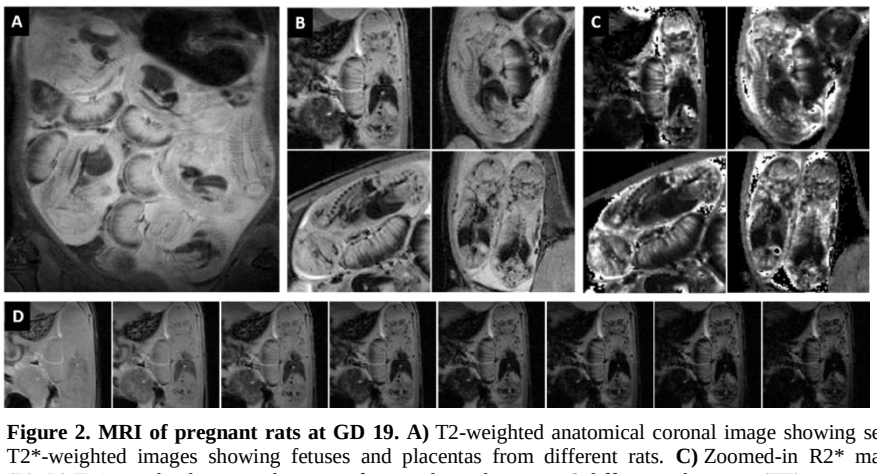

Figure 2. MRI of pregnant rats at GD 19. A) T2-weighted anatomical coronal image showing several fetuses and placentas. **B)** Zoomed-in T2*-weighted images showing fetuses and placentas from different rats. **C)** Zoomed-in R2* maps of the same T2*-weighted images in (B). **D)** T2*-weighted images showing a fetus with its placenta at 8 different echo times (TE).

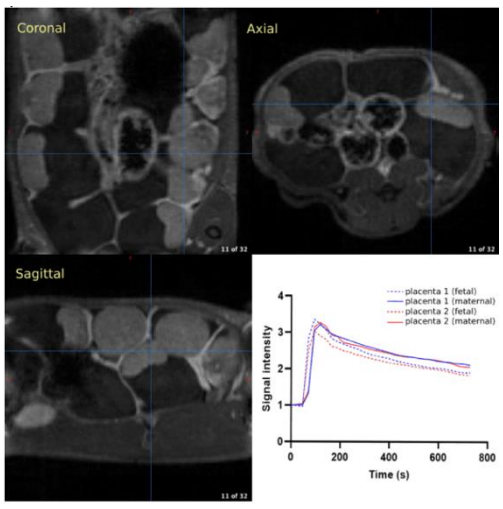

Figure 3: Three-Dimensional Dynamic contrast enhancement MRI. DCE MRI in three planes (coronal, axial and sagittal) showing the arrival of the contrast to the placentas. Lower right: Signal intensity time curve during contrast injection at selected placentas.

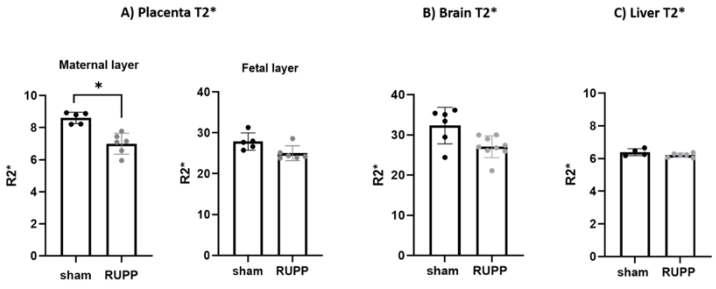

Figure 4. Comparison of R2* values between RUPP and sham rats. A) R2* in placentas maternal and fetal layers **(B)** and **(C)** R2* values of fetal brain and liver respectively. **Figure 5.** AUC of dynamic contrast enhancement time curves in maternal and fetal placental layers.

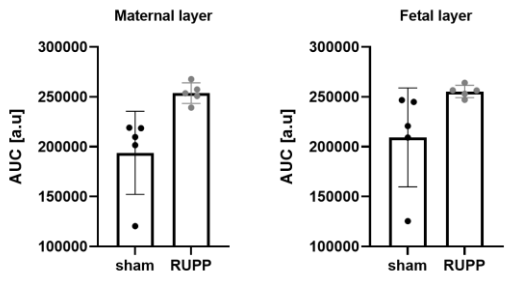

Figure 5: AUC of dynamic contrast enhancement time curves in maternal and fetal placental layers.

To what extent is DSC-MRI able to detect subtle blood-brain barrier leakage in cerebral small-vessel disease?

E.P. Elschot[1,2], W.H. Backes[1,2,4], J.J.A. de Jong[1,2], G.S. Drenthen[1,2], S.M. Wong[1], J. Staals[3,4], R.J. van Oostenbrugge[2,3,4], R.P.W. Rouhl[3], J.F.A. Jansen[1,2,5].

[1]Departments of Radiology and Nuclear Medicine, Maastricht University Medical Center+, Maastricht, the Netherlands; [2]School for Mental Health and Neuroscience, Maastricht University, Maastricht, the Netherlands; [3]Department of Neurology, Maastricht University Medical Center+, Maastricht, the Netherlands; [4]CARIM School for Cardiovascular Diseases, Maastricht University, Maastricht, the Netherlands; [5]Department of Electrical Engineering, Eindhoven University of Technology, Eindhoven, the Netherlands;

Synopsis:
This study investigated to what extent blood-brain barrier (BBB) leakage (1) can be measured with DSC-MRI and (2) is influenced by perfusion. In vivo DCE (golden-standard) and DSC data of patients with cerebral small vessel disease (cSVD) and elderly controls were used, as well as simulations of signal curves. DSC-MRI, in contrast to DCE-MRI, is not sensitive enough to measure subtle leakage in cSVD. Further research is required to better disentangle perfusion effects from leakage, and therefore correction methods should be used with caution for measuring subtle leakage.

Introduction:
Blood-brain barrier (BBB) impairment was previously linked to several pathologies, including cerebral small vessel disease (cSVD)[1]. Traditionally, BBB integrity is assessed by dynamic contrast-enhanced (DCE) MRI, which can measure subtle BBB leakage[2]. Recently, it has been suggested that (single-echo) dynamic susceptibility contrast (DSC) MRI can be used not only to assess cerebral blood volume (CBV), and flow (CBF), but also leakage of contrast agent (CA) across the BBB[3,4]. When CA leaks into the parenchyma, the DSC signal is affected by both T1- and T2*-effects. The most well-known method to correct for these leakage effects is the Boxerman-Schmainda-Weisskoff (BSW) model[5], which is often applied in substantially leaking brain tumors. This model uses a reference concentration curve derived from non-leaking voxels. However, it does not account for perfusion effects, e.g. variations in mean transit time between healthy and diseased tissue. Therefore, Leigh et al. adapted the BSW-model to incorporate arrival time correction (ATC)[6]. The current golden-standard measurement for BBB leakage, DCE-MRI, is time-consuming (>20 min), whereas DSC-MRI scans are short (ca. 2 min) and already provides information on perfusion. Therefore, DSC-MRI could be an attractive alternative for BBB leakage detection. However, it is unclear whether DSC-MRI is suitable for detecting subtle brain leakage. This study investigated to what extent BBB leakage (1) can be measured with DSC-MRI and (2) is influenced by perfusion. In vivo DCE (golden-standard) and DSC data of cSVD patients and elderly controls were used, as well as computer simulations.

Methods:
MRI acquisition: DCE- and single-echo DSC-MRI data were acquired in 15 cSVD patients and 12 elderly controls at 3T (Philips Achieva TX)[7]. Additionally, T1-weighted and T2-weighted sequences were acquired for anatomical reference (Table 1).

Simulations: A realistic, non-leaking DSC relaxation curve was mimicked based on in vivo data. The leakage fraction (K2) was incorporated according to the BSW-method (Equation 1), after which noise (derived from in vivo data) was added. K2 values were calculated from 100 simulated curves for each K2 value, where values above the limit of quantification (LOQ) (SNR≥10) were assumed reliable.

Data analysis: Both DCE and DSC images were corrected for subject motion (FSL). Voxel-specific leakage rates (K_i) were obtained from the DCE-MRI data using Patlak modeling and histogram correction[2] to represent the ground-truth BBB leakage level. The DSC-derived leakage fraction was obtained voxel-wise using two methods: the basic BSW-method[5] (Equation 1), and the extended BSW-model correcting for ATC[6] (Equation 2). Furthermore, CBV and CBF maps were calculated using an arterial input function from manually selected voxels in the middle cerebral artery[8].

$$\Delta\tilde{R}2^*(t) = K1\overline{\Delta R2^*}(t) - K2_{BSW}\int_0^t \overline{\Delta R2^*}(t')\,dt' \quad (1)$$

$$\Delta\tilde{R}2^*(t)_{ATC} = \overline{\Delta R2^*}(t) - K2_{ATC}\int_0^t \overline{\Delta R2^*}(t')\,dt', \text{ with } \Delta\tilde{R}2^*(t)_{ATC} = \gamma\overline{\Delta R2^*}\left(\frac{t+\tau}{\alpha}\right) \quad (2)$$

With K1 = proportional constant, $\overline{\Delta R2^*}$ = average concentration from non-enhancing voxels, and γ, α and τ = ATC parameters for scaling in height and width, and shifting respectively.

Segmentation of the normal-appearing white matter (NAWM) and gray matter (GM) was performed using Freesurfer[9]. White matter hyperintensities (WMH) were semi-automatically segmented from the NAWM[10]. Region masks were co-registered to DCE and DSC image space.

Statistics: To compare the outcome measures between all ROIs, within-subject ANOVAs with subsequent post-hoc analyses and Bonferroni correction were conducted ($p<0.05$ is significant). The relationship between K2 and perfusion measures was assessed using Pearson's correlation.

Results:
Simulations: Figure 1 shows how increasing K2 values change the shape of the relaxivity-time curves. Note that two curves with very low K2 values (<0.01 min^{-1}) can barely be distinguished after noise addition. Simulations showed that K2 can be measured up to the LOQ of $4*10^{-3}$ min^{-1} (Figure 2).

Data analysis: Post-hoc analyses identified a significantly higher K_i in the NAWM compared to GM ($p=0.012$) and WMH compared to NAWM and GM (both $p<0.001$) (Figure 3A). $K2_{BSW}$ did not significantly differ between regions ($F=-0.377$, $p=0.557$) (Figure 3B). However, after ATC, post-hoc analyses revealed a significantly lower leakage fraction ($K2_{ATC}$) in the NAWM compared to GM and WMH compared to NAWM and GM (all $p<0.001$) (Figure 3C). Further analyses revealed that the ATC scaling factor γ had a significant negative correlation with DSC-derived perfusion measures ($r=-0.512$, $r=-0.491$ and $r=-0.517$ for $K2_{ATC}$, CBV, and CBF respectively, $p<0.001$).

Discussion:
Two DSC analysis methods were evaluated for detecting subtle BBB leakage. In line with previous research[11], the DCE-derived leakage rate K_i was found to be significantly elevated in WMH compared to NAWM and GM. From simulations, a detection limit for K2 was determined at $4*10^{-3}$ min^{-1}. For the leakage fraction obtained with the BSW-method ($K2_{BSW}$), no significant differences were found between tissue types, which is in line with these values being lower than the detection limit obtained from simulations. After performing ATC, the leakage fraction ($K2_{ATC}$) became lower in WMH compared to other tissue types. Interestingly, the perfusion parameters CBV, CBF, and the ATC scaling factor γ, varied in a parallel way over the various tissue types, which could indicate that the ATC correction method introduces obfuscating perfusion effects. We therefore argue that the BSW-method, with or without ATC correction, is not suited for the detection of subtle leakage.

Conclusion:
DSC-MRI, in contrast to DCE-MRI, is not sensitive enough to measure subtle leakage in cSVD. Further research is required to better disentangle perfusion effects from leakage, and therefore correction methods should be used with caution for measuring subtle leakage.

References: 1. Zhang CE, Wong SM, van de Haar HJ, et al. Blood-brain barrier leakage is more widespread in patients with cerebral small vessel disease. Neurology. 2017;88(5):426-432; 2. Haar HJ, Jansen JFA, Jeukens CRLPN, et al. Subtle blood-brain barrier leakage rate and spatial extent: Considerations for dynamic contrast-enhanced MRI. Med Phys. 2017;44(8):4112-4125; 3. Dewey BE, Xu X, Knutsson L, et al. MTT and blood-brain barrier disruption within asymptomatic vascular WM lesions. Am J Neuroradiol. 2021;42(8):1396-1402; 4. Etherton MR, Wu O, Cougo P, et al. Sex-specific differences in white matter microvascular integrity after ischaemic stroke. Stroke Vasc Neurol. 2019;4(4):198-205; 5. Boxerman JL, Schmainda KM, Weisskoff RM. Relative Cerebral Blood Volume Maps Corrected for Contrast Agent Extravasation Significantly Correlate with Glioma Tumor Grade , Whereas Uncorrected Maps Do Not. Ajnr Am J Neuroradiol. 2006;27(4):859-867; 6. Leigh R, Jen SS, Varma DD, Hillis AE, Barker PB. Arrival Time Correction for Dynamic Susceptibility Contrast MR Permeability Imaging in Stroke Patients. Herholz K, ed. PLoS One. 2012;7(12):e52656; 7. Wong SM, Jansen JFA, Zhang CE, et al. Blood-brain barrier impairment and hypoperfusion are linked in cerebral small vessel disease. Neurology. 2019;92(15):e1669-e1677. 8. Zaharchuk G. Theoretical basis of hemodynamic MR imaging techniques to measure cerebral blood volume, cerebral blood flow, and permeability. Am J Neuroradiol. 2007;28(10):1850-1858; 9. Fischl B, Salat DH, Busa E, et al. Whole brain segmentation: Automated labeling of neuroanatomical structures in the human brain. Neuron. 2002;33(3):341-355; 10. de Boer R, Vrooman HA, van der Lijn F, et al. White matter lesion extension to automatic brain tissue segmentation on MRI. Neuroimage. 2009;45(4):1151-1161; 11. Li Y, Li M, Zhang X, et al. Higher blood-brain barrier permeability is associated with higher white matter hyperintensities burden. J Neurol. 2017;264(7):1474-1481.

Acknowledgments / Funding Information: This work is part of the program Translational Research 2 with project number 446002509, funded by ZonMw/Epilepsiefonds Nederland

Table 1. This table summarizes the acquisition parameters of the sequences used in this study. FLAIR, Fluid Attenuated Inversion Recovery; DCE, Dynamic Contrast Enhanced; GRE, Gradient Echo; DSC, Dynamic Susceptibility Contrast; PRESTO, PRinciples of Echo Shifting using a Train of Observations; DSI, Dynamic Scan Interval; TR, repetition time; TE, echo time; TI, inversion time; FA, Flip Angle.

Acquisition parameters	T_1w	T_2w	DCE FAST	DCE SLOW	DSC
Scan mode		FLAIR	saturation prepared fast GRE		PRESTO
TR [ms]	8.3	4800	5.6	5.6	20
TE [ms]	3.8	299	2.5	2.5	30
TI [ms]	800	1650	-	-	-
DSI [s]	-	-	3.2	30.5	1.56
FA [degree]	8	90	30	30	8
Acquisition matrix [mm³]	256x256x160	250x256x180	256x200x50	256x256x100	240x190x105
Voxel size [mm³]	1x1x1	1x1x1	2x2x5	1x1x2	1.9x1.9x3.5
Acceleration factor	-	-	2	2	-
Number of volumes	-	-	29 (9 pre-contrast)	45 (3 pre-contrast)	75 (11 pre-contrast)

Figure 2. Calculation of K2 values from 100 simulated relaxation-time curves for each K2 value. According to the limit of quantification (SNR≥10), K2 values lower than $4*10^{-3}$ min^{-1} are assumed no longer reliable.

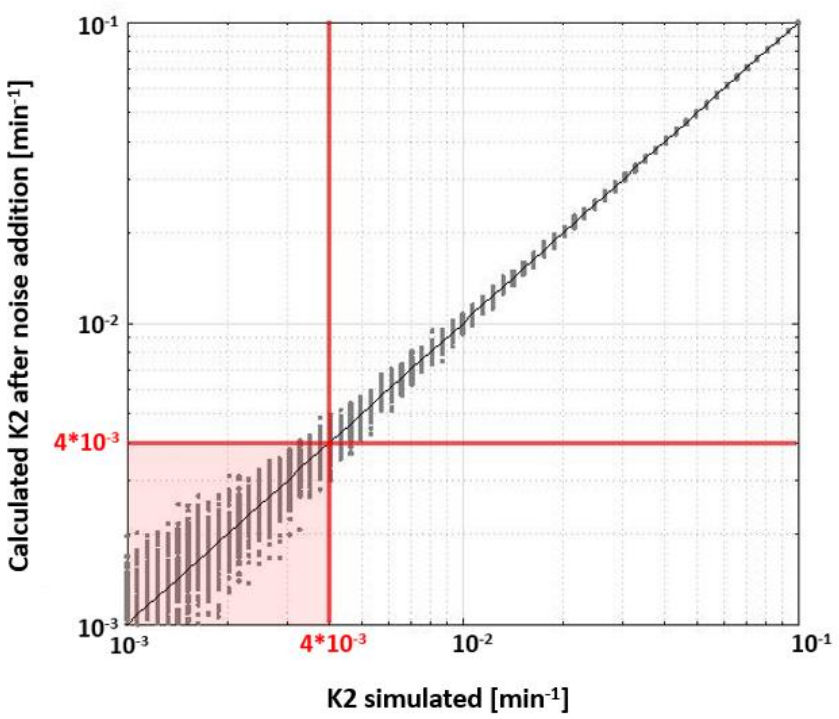

Figure 1: (A) Simulated relaxation-time curves obtained from the NAWM of an in vivo dataset. (B) After the addition of realistic noise levels, obtained from the same in vivo dataset, curves with low K2 values (<0.01 min^{-1}) can no longer be distinguished.

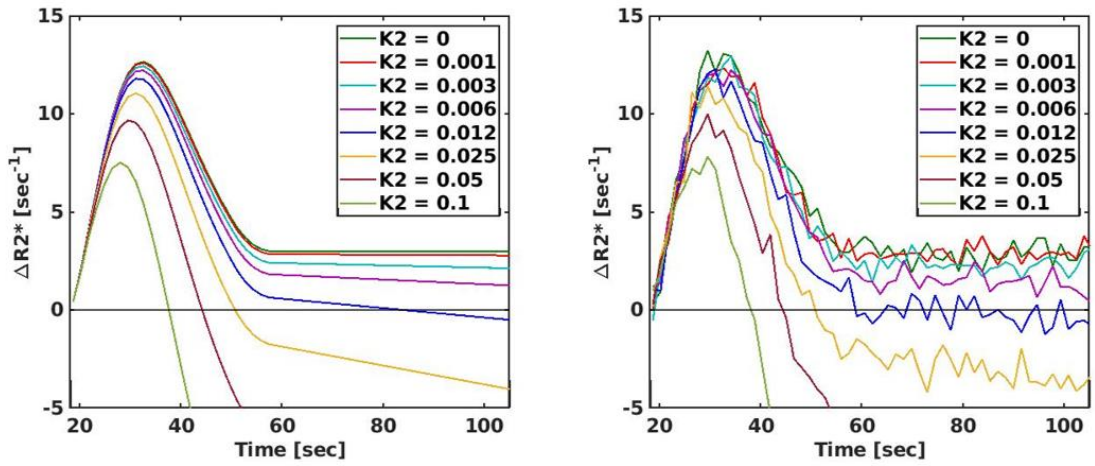

Figure 3: Histograms of (A) the (golden-standard) DCE-derived leakage rate K_i, (B) the DSC-derived leakage fraction obtained with the basic BSW-method ($K2_{BSW}$) and (C) the DSC-derived leakage fraction obtained with the extended BSW-model correcting for ATC ($K2_{ATC}$), for the different tissue types.

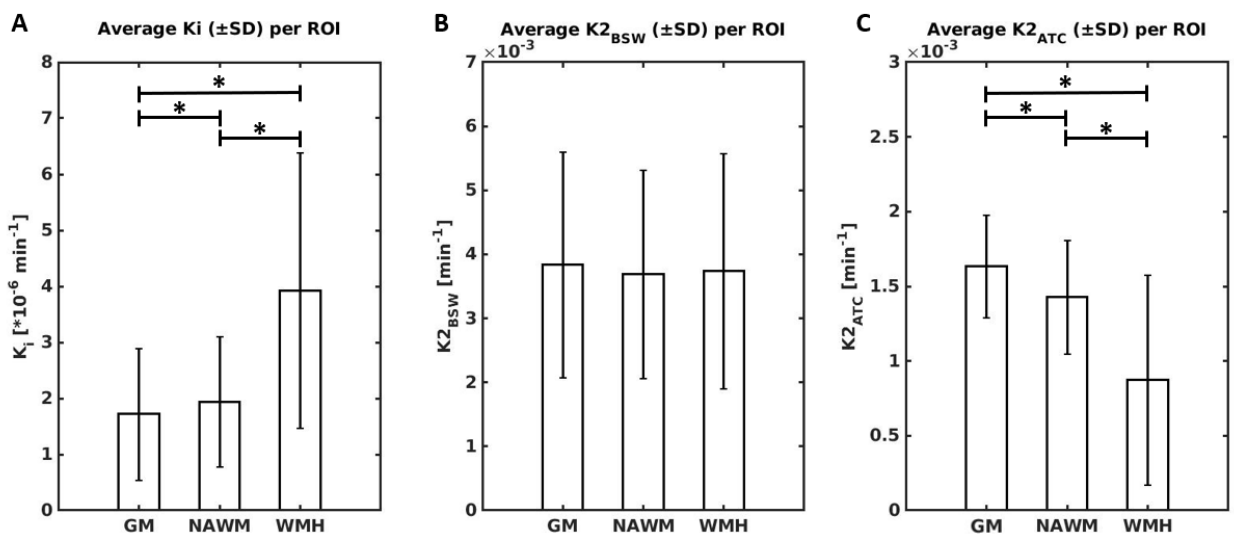

Influence of Arterial Transit Time Delay in Arterial Spin Labeling on Differentiating Tumor Progression and Pseudo-Progression in Glioblastoma

Daniëlle van Dorth[1], Janey Jiang[2,3], Bárbara Schmitz-Abecassis[1], Robert J. I. Croese[4,5], Martin J. B. Taphoorn[4], Marion Smits[6], Johan A. F. Koekkoek[4], Linda Dirven[4], Jeroen de Bresser[2], Matthias J. P. van Osch[1]

[1]C. J. Gorter Center for High-Field MRI, Department of Radiology, Leiden University Medical Center, Leiden, Netherlands; [2]Department of Radiology, Leiden University Medical Center, Leiden, Netherlands; [3]Department of Radiology, HagaZiekenhuis, Den Haag, Netherlands; [4]Department of Neurology, Leiden University Medical Center, Leiden, Netherlands; [5]Department of Neurology, Haaglanden Medical Center, Den Haag, Netherlands; [6]Department of Radiology and Nuclear Medicine, Erasmus MC, University Medical Center, Rotterdam, Netherlands

Synopsis: In the clinical follow-up of glioblastoma patients, presence of delayed arterial transit times (ATT) could affect the evaluation of ASL perfusion data. In this retrospective study the influence of the presence and severity of ATT-artifacts on perfusion assessment and differentiation between tumor progression and pseudo-progression were studied. The results show that the presence of ATT-artifacts lowers the agreement between radiological evaluation of DSC-MRI and ASL, although the severity of ATT-artifacts did not have significant influence. In conclusion, detection of ATT-artifacts is important as it could affect radiological evaluation of ASL-data. Future work aims to include additional quantitative perfusion measures.

Purpose: Arterial Spin Labeling (ASL) and Dynamic Susceptibility Contrast MRI (DSC-MRI) are commonly used techniques to measure perfusion in patients with glioblastoma. Perfusion MRI is especially helpful in distinguishing tumor progression from pseudo-progression[1,2,3,4]. The consensus approach for ASL is pCASL with a single post-labeling delay (PLD)[5] of 1800ms, in which the resulting images can be affected by arterial transit time (ATT) artifacts[6]. When the ATT is prolonged, not all labeled spins have arrived in the tissue leading to underestimation of perfusion, which could affect clinical assessment. Therefore, the two research questions of this study are:

1. Does the presence of ATT-artifacts impact the assessment of perfusion, i.e. are ASL maps in lesser agreement with DSC-MRI when delayed transit times are present?
2. Do delayed ATTs influence the radiological evaluation of ASL perfusion maps?

Methods: In this retrospective, single-center study data were analyzed from 64 adult patients (Table 2) with histologically confirmed glioblastoma who received postoperative radio(chemo)therapy. The study was performed in accordance with local IRB-regulations. ASL scans were made ±3 months post-radiotherapy either with 2D pCASL with 1600ms labeling-duration (LD) and 1525ms (first slice) – 2120ms (last slice) PLD, or with 3D pCASL 1800ms/1800ms (LD/PLD).

The data was evaluated by a neuroradiologist based on three scores:

1. The presence/absence of ATT-artifacts were scored as well as their severity (%).
2. Perfusion score: ASL and DSC perfusion of the enhancing tumor lesion were scored as increased or as normal/decreased. Scores were made per lesion (78 in total), focusing on the nodular part.
3. Radiological score: ASL and DSC perfusion maps were separately interpreted on a 7-point scale with 1 representing definite tumor progression and 7 definite pseudo-progression.

The concordance between the DSC and ASL scans in radiological score was tested by a sign test (threshold of $p<0.05$) both for patients grouped based on presence versus absence as well as on severity of ATT-artifacts (1-50% versus 50-100%, thus excluding patients without ATT-artifacts).

Results: Figure 1 shows example ASL images with different levels of delayed ATT-severity. The total number of patients with ATT-artifacts present was 52 (81.3%) with 14 showing severe ATT-artifacts.

Table 1 shows an overview of the perfusion assessment when patients were grouped according to presence/absence of ATT-artifacts.

In the presence of ATT-artifacts, for 35 patients (67.3%) the radiological score showed agreement between ASL and DSC. In the absence of ATT-artifacts, this was the case for 7 patients (58.3%). The sign test showed a significant difference in the scoring of the ASL and DSC scans in the presence of ATT-artifacts ($p = 0.013$, median (IQR) ASL = 3.00 (3.00-6.00), median (IQR) DSC = 5.00 (3.00-6.00)), whereas in the absence of ATT-artifacts no significant difference was found ($p = 0.375$, median (IQR) ASL = 3.00 (2.00-5.75), median DSC = 4 (2.25-5.75)). Figure 2 shows Bland-Altman and correlation plots for the radiological scores.

For minor ATT-artifacts, exact agreement between ASL and DSC scores was found for 26 patients (68.4%), see Figure 3. For severe ATT-artifacts, this was the case for 9 patients (64.3%). In case of minor ATT-artifacts, a significant difference ($p = 0.039$, median (IQR) ASL = 3.00 (3.00-6.00), median (IQR) DSC = 5.00 (3.00-6.00)) was found between ASL and DSC scores, while for severe artifacts no significant difference was found ($p = 0.375$, median (IQR) ASL = 5.00 (2.75-5.25), median (IQR) DSC = 5.00 (3.00-6.00)).

Discussion: In this study the influence of a delayed ATT on the perfusion assessment and radiological evaluation of glioblastoma was investigated. Main findings were: 1) In 81% of the patients ATT-artifacts were present; 2) The perfusion assessment showed reasonable agreement between ASL and DSC with little influence of the presence of ATT-artifacts, although ASL had a minor tendency to overestimate perfusion compared to DSC; 3) The presence, but not the severity of ATT-artifacts affected the radiological evaluation of ASL scans.

First, it should be recognized that even when using settings close to the recommended settings, in a large number of patients ATT-artifacts were observed. Second, the relative perfusion scores were for most patients in agreement with DSC-scores, but when in disagreement ASL had the tendency to overestimate perfusion. This finding was, however, independent of the presence of ATT-artifacts. When looking at the radiological interpretation, a statistically significant difference was found between the scoring on DSC and ASL when ATT-artifacts were present. Furthermore, the correlation analysis showed that the ASL evaluation tended slightly more towards tumor progression than for DSC in agreement with the tendency to overestimate perfusion. This could possibly be explained by the apparent increased signal on the ASL scan caused by label present within large arteries. The limited influence of delayed ATT-severity could be explained by the fact that only 14 patients were present in the highest severity group, as opposed to 38 patients with low severity. Furthermore, acknowledgement of severe ATT-artifacts could have caused a bias in the radiological evaluation.

Conclusion: The presence of delayed ATT in ASL-data seems to impact the radiological evaluation of ASL-data towards tumor progression (as compared to the DSC evaluation), whereas in patients without ATT-artifacts ASL and DSC provide more similar radiological scores. Future work aims to include additional quantitative perfusion data.

References:

1. Fatterpekar GM, Galheigo D, Narayana A, Johnson G, Knopp E. Treatment-related change versus tumor recurrence in high-grade gliomas: A diagnostic conundrum - Use of dynamic susceptibility contrast-enhanced (DSC) perfusion MRI. Am J Roentgenol. 2012;198(1):19-26. doi:10.2214/AJR.11.7417

2. Radenkovic S, Jovanovic M, Stosic-Opincal T, et al. Differentiation between progression and pseudoprogression by arterial spin labeling MRI in patients with glioblastoma multiforme. JBUON. 2017;22(4):1061-1067.

3. van Dijken BRJ, van Laar PJ, Smits M, Dankbaar JW, Enting RH, van der Hoorn A. Perfusion MRI in treatment evaluation of glioblastomas: Clinical relevance of current and future techniques. J Magn Reson Imaging. 2019;49(1):11-22. doi:10.1002/jmri.26306

4. Manning P, Daghighi S, Rajaratnam MK, et al. Differentiation of progressive disease from pseudoprogression using 3D PCASL and DSC perfusion MRI in patients with glioblastoma. J Neurooncol. 2020;147(3):681-690. doi:10.1007/s11060-020-03475-y

5. Alsop DC, Detre JA, Golay X, et al. Recommended Implementation of Arterial Spin-Labeled Perfusion MRI for Clinical Applications: A Consensus of the ISMRM Perfusion Study Group and the European Consortium for ASL in Dementia. doi:10.1002/mrm.25197

6. Grade M, Hernandez Tamames JA, Pizzini FB, Achten E, Golay X, Smits M. A neuroradiologist's guide to arterial spin labeling MRI in clinical practice. Neuroradiology. 2015;57(12):1181-1202. doi:10.1007/s00234-015-1571-z

Acknowledgments / Funding Information: We are thankful to NWO domain AES (project 17079) and Medical Delta Cancer Diagnostics 3.0 for their support.

Table 2. Clinical information.

Male patients, n (%)	37 (57.8%)
Age at follow-up MRI (years ± SD)	60.1 ± 12.7
KPS score, median (range)	90 (80-100)
Surgery, n (%) • ***Resection*** • ***Biopsy***	 • 53 (82.8%) • 11 (17.2%)
Second surgery, n (%)	11 (17.2%)
Radiotherapy dose, n (%) • ***40 Gy*** • ***45 Gy*** • ***60 Gy***	 • 8 (12.5%) • 8 (12.5%) • 48 (75%)
Temozolomide chemotherapy, n (%)	52 (81.3%)

Table 1. Perfusion assessment, displaying number of lesions. A) ATT-artifacts are present: sensitivity = 92.8%, specificity = 71.1%. B) ATT-artifacts are not present: sensitivity = 100%, specificity = 71.4%.

A	**DSC normal**	**DSC increased**
ASL normal	27	2
ASL increased	9	26

B	**DSC normal**	**DSC increased**
ASL normal	5	0
ASL increased	2	7

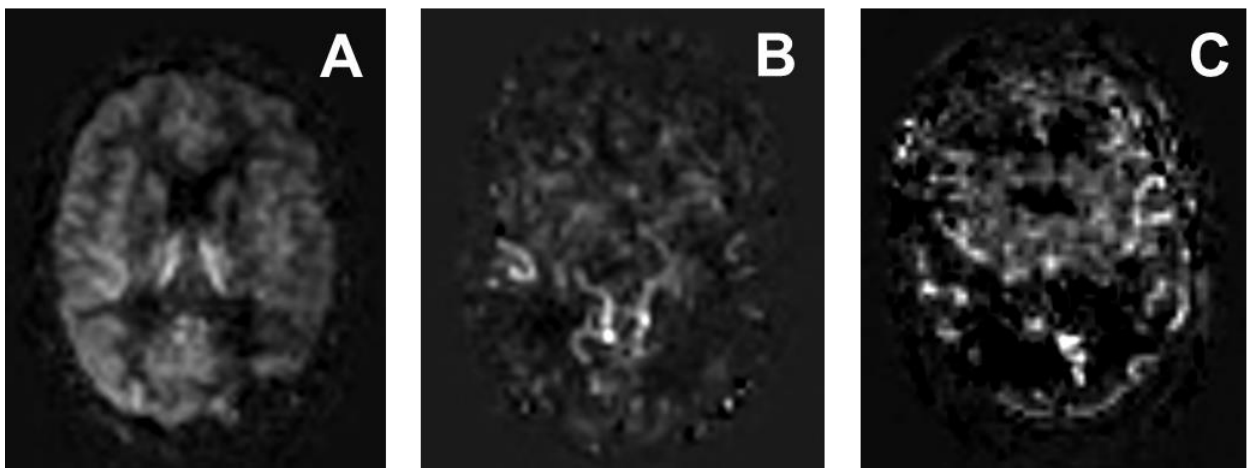

Figure 1. ASL images of A) 57 year-old female without ATT-artifacts; B) 68 year-old male with moderate ATT-artifacts; C) 71 year-old female with severe ATT-artifacts. In C) the signal in the large vessels is clearly visible.

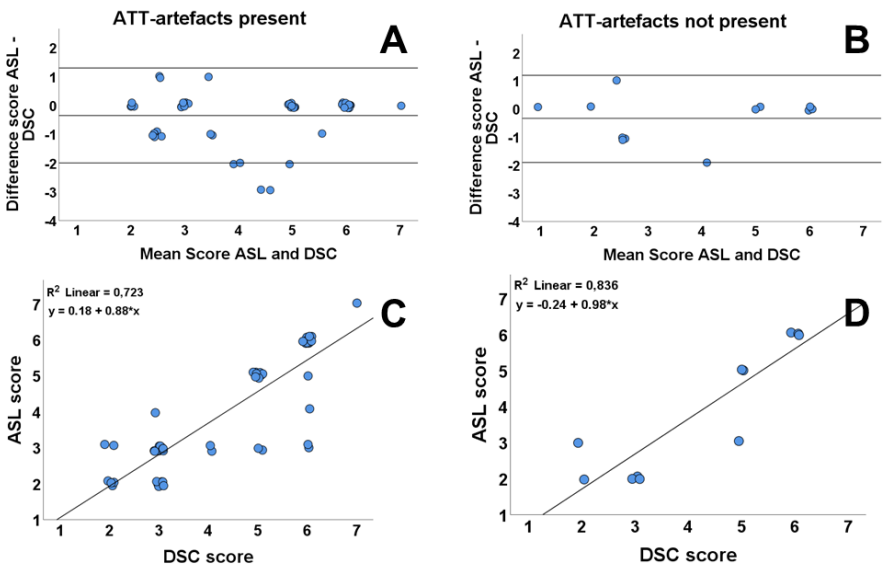

Figure 2. Bland Altman plots (+/- 1.96 SD) in patients with (A) and without (B) ATT-artifacts. Correlation plots in patients with (C) and without (D) ATT-artifacts, showing significant correlations (Spearman's rho = 0.850 versus 0.902) between the radiological evaluation on ASL and DSC scans ($p < 0.01$ in both cases). Scores are a 7-point scale, with a score of 1 representing definite tumor progression and a score of 7 definite pseudo-progression.

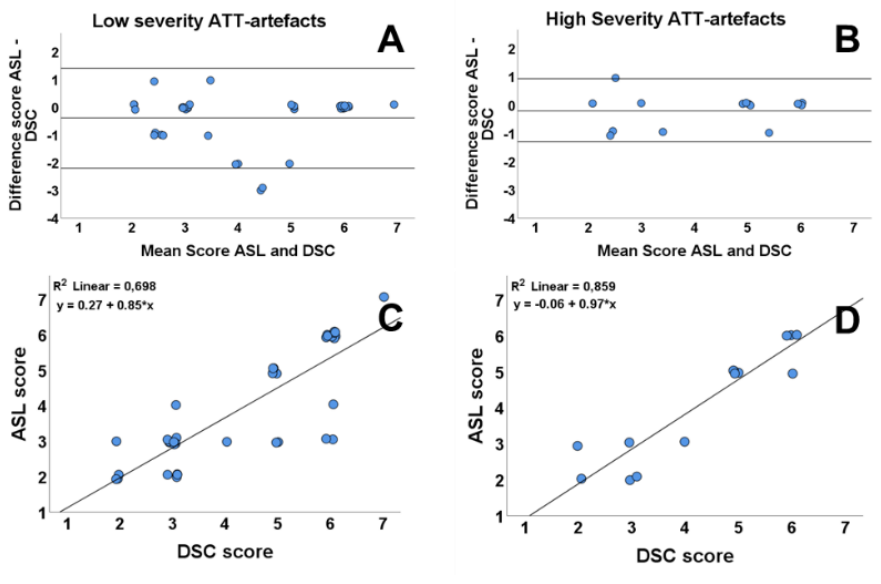

Figure 3. Bland Altman plots (+/- 1.96 SD) in patients with minor (A) and severe (B) ATT-artifacts. Correlation plots in patients with minor (C) and severe (D) ATT-artifacts, showing significant correlations (Spearman's rho = 0.835 versus 0.914) between the radiological evaluation on ASL and DSC scans ($p < 0.01$ in both cases). Scores are a 7-point scale, with a score of 1 representing definite tumor progression and a score of 7 definite pseudo-progression.

Correlation of vessel size and cerebral blood volume measurements in glioma genetic subtypes

F. Arzanforoosh[1,2], S.R. Van Der Voort[1,2], F. Incekara[1,3], A. Vincent[3] , M. van den Bent[2,3], M. Smits[1,2], E.A.H. Warnert[1,2]

[1]Department of Radiology and Nuclear Medicine, Erasmus MC, Rotterdam, Netherlands; [2]Erasmus MC Cancer Institute, Erasmus MC, Rotterdam, Netherlands; [3]Department of Neurology, Erasmus MC, Rotterdam, NL, the Netherlands

Synopsis

Deep insight about tumor microvasculature is important for diagnosis and progression of glioma patients. Relative Cerebral Blood Volume (rCBV) and vessel size are two parameters, derived from perfusion MRI, used for evaluation of tumor microvasculature in glioma. In this study, we investigated the clinical value of both rCBV and vessel size and their correlation for three subgroups of glioma based on the recent 2021 World Health Organisation (WHO) classification scheme. The result showed that neither rCBV nor vessel size differed significantly between glioma subtypes, though correlation of these two parameters sheds light on the microvasculature characteristics of each subgroup.

Background and Purpose: The creation of new blood vessels, angiogenesis, plays a critical role in glioma development. The formation of irregular vasculature is not only varying between various glioma subtypes, but changes in the underlying vasculature can also herald malignant transformation (1). In particular in light of the recent 2021 WHO classification scheme, early and accurate diagnosis of glioma or malignant transformation is of utmost importance for prognosis and treatment decision making.

The most commonly assessed imaging biomarker of tumor vasculature is rCBV coming from dynamic susceptibility contrast (DSC) MRI. Although previous work illustrated that increased rCBV corresponds to increased malignancy in diffuse glioma, in practice this does not hold when oligodendroglioma - as defined in the WHO 2021 classification scheme - are included (2). This type of tumor is known for its "chicken wire" vasculature, which in turn can lead to high rCBV values (3).

When extending DSC MRI to assess simultaneous acquisition of T_2 and T_2* weighted images to follow the passage of a gadolinium-based contrast agent (GBCA) through the cerebral vasculature, vessel size imaging (VSI) can be done, that has the potential to add information about microvascular structure. We explored using VSI in addition to rCBV to assess three diffuse glioma subtypes present within the WHO 2021 glioma classification.

Materials and Methods: A retrospective dataset consisting of 38 patients with confirmed non-enhancing glioma was used and classified in three groups: **Oligo/IDH^{MUT}&1p/19q^{-}**, **Astro/IDH^{MUT}**, and **Glioblastoma/IDH^{WT}** (4). All patients underwent 3T MRI scanning (GE, Milwaukee, WI, USA) prior to surgery. For DSC MRI, Hybrid EPI (HEPI) was used with following parameters: 122 repetitions, TR: 1500m, FOV: 15 slices, voxel size: 1.88x1.88x4.00 mm^3, TE(GRE): 18.6 ms and TE(SE): 69 ms, with administration of 7.5ml of GBCA (Gadovist, Bayer, Leverkusen, GE). A pre-load bolus of equal size was administrated 5 minutes before the DSC scan was acquired. Diffusion weighted imaging (2 b-values: 0, 1000 s/mm^2, voxel size: 1x1x3 mm^3 and TE/TR of 63/5000 ms) was done to estimate the apparent diffusion coefficient (ADC) required for VSI. High resolution T1-weighed pre- and post-contrast (voxel size: 1x1x0.5 mm^3; TE/TR: 2.1/6.1 ms), T2 (voxel size: 0.5x0.5x3.2 mm^3; TE/TR: 107/10000 ms), and FLAIR (voxel size: 0.6x0.5x0.5 mm^3; TE/TR: 106/6000 ms) images were acquired and used for tumor segmentation.

Estimates of mean vessel size and normalized rCBV maps were made according to previously described methods (5,6). HD-GLIO was used to generate tumor regions of interest (ROI) for all patient . Average tumor vessel size, normalized rCBV, and ADC were calculated for each group of patients. Additionally, correlation analysis was performed between rCBV and vessel size for each subgroup.

Results: Patient information is summarised in Table 1. Figure 1 shows an example slice of ADC, rCBV and vessel size maps for three patients, each selected from one subgroup. The average of the microvascular parameters (rCBV, vessel size) and ADC are presented in figure 2 for each patient and each group. In **Oligo/IDH^{MUT}&1p/19q^{-}**, rCBV was significantly higher compared to **Astro/IDH^{MUT}** ($p < 0.05$, unpaired t-test), but equal to **Glioblastoma/IDH^{WT}.** A trend of increased vessel size was found for **Oligo/IDH^{MUT}&1p/19q^{-}** and **Astro/IDH^{MUT}** compared to **Glioblastoma/IDH^{WT}**, but no significant differences were found. Vessel size and rCBV showed strong correlation in **Glioblastoma/IDH^{WT}** (r=0.82, p=0.02), moderate correlation in **Oligo/IDH^{MUT}&1p/19q^{-}** (r=0.56, p=0.01) and no correlation in **Astro/IDH^{MUT}** (r=0.17, p=0.57) (Fig. 3).

Discussion: The result of this study on nonenhancing glioma suggests that rCBV and vessel size alone cannot distinguish between three subgroups based on the 2021 WHO guidelines. However, combining these two parameters and measuring the correlation of these two parameters sheds light on the microvasculature characteristics of each subgroup.

Intuitively it might be expected that vessel size and rCBV are positively correlated, however this correlation is modulated by the vessel density. In other words, in an area with densely packed microvessels, slight change in vessel diameters can result in a considerable change in rCBV, whereas in an area with low vessel density, change in vessel diameters may lead to no or limited change in rCBV. **Oligo/IDH^{MUT}&1p/19q^{-}** with high rCBV and high VSI showing a moderate relationship between these two parameters, might be reflecting high vessel density. Low density might be present within the **Astro/IDH^{MUT}**, as we see no correlation - while in **Glioblastoma/IDH^{WT}** our findings indicate high vessel density. Note that this would be in line with the histopathological findings in (3).

Future work validating these results should include histology measurements of vessel size and mean vessel density of targeted biopsies of tumor tissue based on rCBV and vessel size and investigation of the clinical applicability of VSI in glioma imaging diagnostics.

Reference:

1. Lebelt A, Dziecioł J, Guzińska-Ustymowicz K, Lemancewicz D, Zimnoch L, Czykier E. Angiogenesis in gliomas. *Folia Histochem Cytobiol* (2008) **46**: doi:10.2478/v10042-008-0009-4
2. Louis DN, Perry A, Wesseling P, Brat DJ, Cree IA, Figarella-Branger D, Hawkins C, Ng HK, Pfister SM, Reifenberger G, et al. The 2021 WHO Classification of Tumors of the Central Nervous System: a summary. *Neuro Oncol* (2021) **23**:1231–1251. doi:10.1093/neuonc/noab106
3. Guo H, Kang H, Tong H, Du X, Liu H, Tan Y, Yang Y, Wang S, Zhang W. Microvascular characteristics of lower-grade diffuse gliomas: investigating vessel size imaging for differentiating grades and subtypes. *Eur Radiol* (2019) **29**:1893–1902. doi:10.1007/s00330-018-5738-y
4. van der Voort SR, Incekara F, Wijnenga MMJ, Kapas G, Gardeniers M, Schouten JW, Starmans MPA, Tewarie RN, Lycklama GJ, French PJ, et al. Predicting the 1p/19q codeletion status of presumed low-grade glioma with an externally validated machine learning algorithm. *Clin Cancer Res* (2019) doi:10.1158/1078-0432.CCR-19-1127
5. Arzanforoosh F, Croal PL, van Garderen KA, Smits M, Chappell MA, Warnert EAH. Effect of Applying Leakage Correction on rCBV Measurement Derived From DSC-MRI in Enhancing and Nonenhancing Glioma. *Front Oncol* (2021) **11**: doi:10.3389/fonc.2021.648528

Acknowledgments / Funding Information: Continue on this line

6. Kiselev VG, Strecker R, Ziyeh S, Speck O, Hennig J. Vessel size imaging in humans. *Magn Reson Med* (2005) **53**:553–563. doi:10.1002/mrm.20383

Figure 1: Example MRI images of three patients of **Oligo/IDH^{MUT}&1p/19q^{-}** (A), **Astro/IDH^{MUT}** (B) and **Glioblastoma/IDH^{W}** (C). The images from left to right respectively are: T2W FLAIR; T2W FLAIR overlaid with tumor ROI, apparent diffusion coefficient (ADC), relative cerebral blood volume (rCBV), and vessel size.

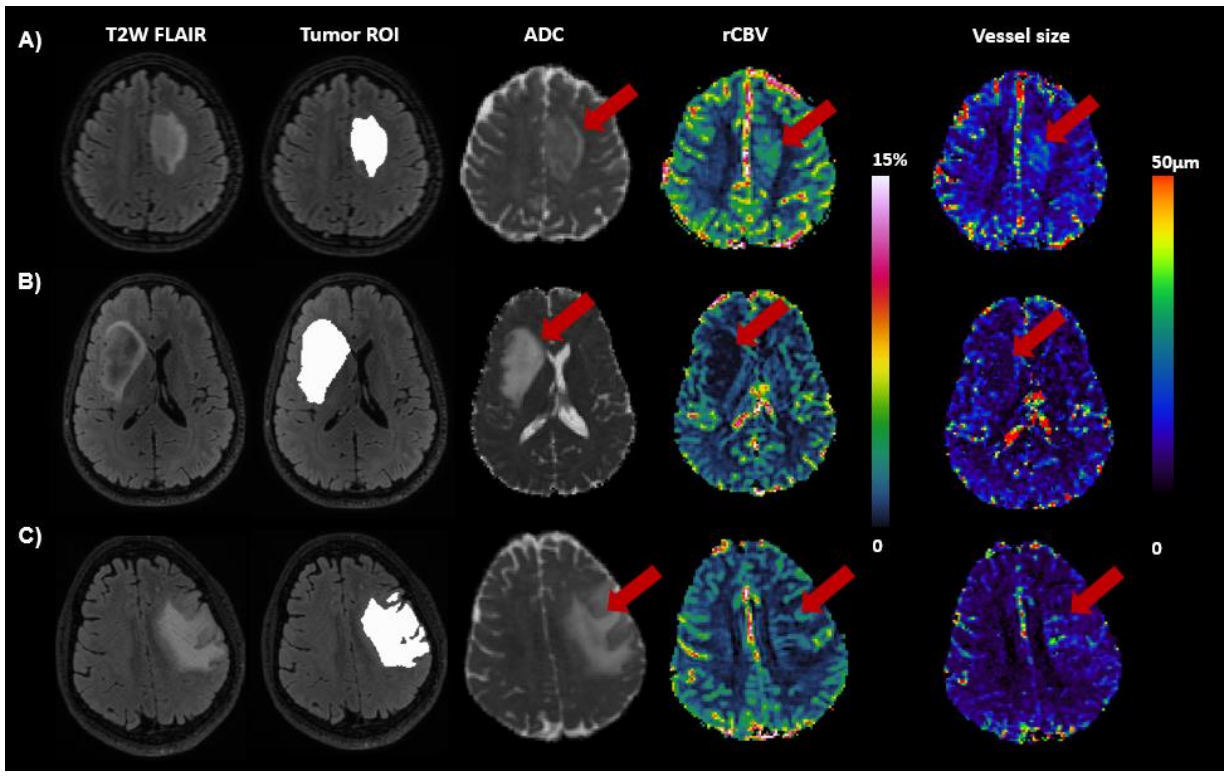

Figure 2: Scatter plot of ADC, rCBV and Vessel Size (VS) with mean bar for three subtypes of gliomas. * *Significantly different, $p < 0.05$, unpaired t-test.*

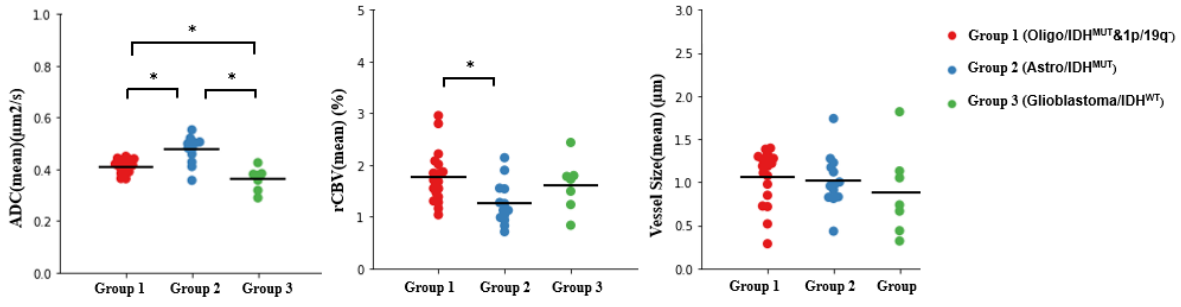

Figure 3: correlation between vessel size and rCBV for three subtypes of gliomas

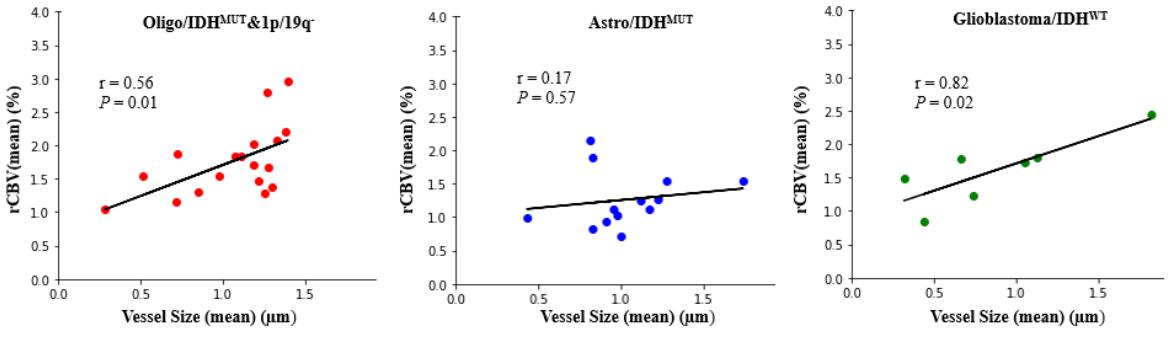

Table 1: Summary of clinical description of patients in the dataset.

Group	Grade 2	Grade 3	Grade 4	Total	gender	age
Oligo/IDH^{MUT}&1p/19q^{-}	15	3	-	18	13M / 5F	40±12
Astro/IDH^{MUT}	9	4	-	13	5M / 8F	36±8
Glioblastoma/IDH^{WT}	1	2	4	7	7M / 0F	60±10

Towards reproducible Arterial Spin Labelling in the myocardium: Impact of blood T1 time and imaging readout parameters

M. Božić-Iven[1,2], S. Rapacchi[3], I. Pierce[4], G. Thornton[4], Q. Tao[2], L.R. Schad[1], T. Treibel[4], S. Weingärtner[2]

[1]Computer Assisted Clinical Medicine, Heidelberg University, Mannheim, Germany; [2]Department of Imaging Physics, Delft University of Technology, Delft, The Netherlands; [3]Faculté de Médicine, Université Aix-Marseille, Marseille, France; [4]Barts Heart Centre, Barts Health NHS Trust, London, United Kingdom

Synopsis: Despite promising results, clinical translation of myocardial arterial spin labelling (myoASL) is hampered by insufficient reproducibility and robustness. We investigated the influence of physiological and sequence parameters on FAIR-myoASL in simulations as well as phantom experiments, and developed a correction method based on separately acquired T1 maps. Our simulation and phantom results show acquisition related MBF differences, potentially undermining the reproducibility of myoASL measurements. Inaccuracies between true and reconstruction blood T1, further render the sequence susceptible to heart rate variations, particularly for larger T1 mismatch. Using accurate blood T1 times in reconstruction may improve robustness and reproducibility.

Introduction

The clinical gold standard for detection of myocardial ischemia is first pass myocardial perfusion imaging[1], where the distribution of an exogenous contrast agent is tracked using T1 weighted imaging. However, the use of contrast agents limits repeated use and its clinical applicability. Arterial spin labelling (ASL), on the other hand, relies on magnetically labelled blood as an endogenous contrast and has proven effective in quantifying neurovascular perfusion[2]. In cardiac applications, however, several challenges are faced, such as a complex anatomy and high levels of physiological noise[3]. Although myoASL and positron emission tomography based myocardial blood flow (MBF) were shown to agree[4], insufficient robustness and reproducibility hinder widespread clinical translation. In this work, we sought to investigate the influence of physiological and sequence parameters on the reproducibility of myoASL based perfusion. Further, we sought to develop a correction method based on precedingly acquired T1 maps to increase robustness of myoASL.

Methods

Numerical Simulations: Bloch simulations were performed to investigate the effect of physiological and sequence parameters for bSSFP and spGRE based myoASL. For both imaging readouts, the acquisition flip angle (FA), matrix size, and delay between tag and control image (C-T delay) were varied. Moreover, varying RR intervals, i.e. different effective inversion times (TI), were simulated, with a blood volume fraction of 0.14 and in-flow rate of 0.8ml/g/min.

FAIR-myoASL sequence: Imaging was performed across two 3T scanners (Magnetom Skyra/Prisma, Siemens Healthineers, Erlangen Germany). For all measurements, a double ECG-gated Flow Alternating Inversion Recovery (FAIR) ASL sequence[4,5] was implemented (Fig.1). For the control and tag image, a selective and global adiabatic inversion pulse was applied, respectively, during mid-diastole. Image acquisition (bSSFP/spGRE) followed in mid-diastole of the successive heartbeat.

Phantom and In vivo Measurements: In total, one pair of baseline images (no inversion) and 5/6 (phantom/in vivo) control-tag pairs were acquired with 8mm slice-thickness and 2x2mm/1.7x1.7mm base resolution (phantom/in vivo). MOLLI[6] was used for T1 mapping in phantom and in vivo. Phantom experiments were performed with varying RR intervals, FAs and C-T delays in a NiCl2-doped agarose phantom. In-vivo images of 4 healthy subjects (4 male, 39±4.7 years) were obtained with a 6s C-T delay in 12-18s long breath-holds per image pair depending on the heart rate.

Data analysis: After groupwise registration[7], mistriggered control-tag image pairs were excluded. Buxton's model[8] was used for MBF reconstruction, where control and tag signal are corrected with respective TI and blood T1 time (T1B). Previous in vivo studies relied on a fixed literature based value for T1B (~1700ms)[4,5,9]. Here, individual MOLLI-T1B times were used in a second reconstruction method to obtain perfusion maps and septal MBF. In simulations T1B was varied, while in phantom the model T1 was varied. Mean MBF values were obtained by averaging MBF over all ASL pairs and subjects.

Results

Simulated MBF values were constant (3.5/2.3 ml/g/min bSSFP/GRE) for varying heart rates when simulation and reconstruction T1B were identical. When "true" and reconstruction T1B differ, however, the obtained MBF values were highly heart rate dependent. This effect was more pronounced for lower heart rates and is observed in both bSSFP and GRE (Fig. 2a). For higher FAs and matrix sizes, bSSFP based MBF continuously increased. In GRE, MBF decreased to zero for FAs of 30° and beyond (Fig. 2b). For larger matrix sizes, MBF increased in bSSFP and continuously decreased in GRE (Fig. 2c). With varying C-T delay (Fig. 2d), MBF values showed almost no deviation from values simulated with the global inversion pulse acting on fully recovered magnetization (infinite delay).

Phantom data depicts similar trends, where MBF difference due to T1B mismatch was stronger for lower heart rates (Fig. 3a). MBF values in bSSFP increased with increasing FA, while in GRE the values increased until 18°, then decreased and stayed constant after 35°. bSSFP based MBF remained constant over the entire range of matrix sizes, whereas GRE based MBF continuously decreased with increasing matrix size. For varying C-T delay, MBF remained largely constant in bSSFP and GRE.

In vivo perfusion maps are shown in Fig. 4a for bSSFP and GRE acquisition. Septal MBF was 1.53±1.04ml/min/g(bSSFP) /1.9±1.55ml/min/g(GRE) with fixed T1B, whereas with adaptive T1B MBF was 1.46±0.97ml/min/g (bSSFP) /1.81±1.44ml/min/g (GRE) Fig. 4b.

Discussion

Our simulation and phantom results show that sequence parameters such as FA and matrix size lead to MBF differences, potentially eroding the reproducibility of myoASL. Due to the impact of the readout, effect were particularly pronounced for a large mismatch between reconstruction and true T1B. Moreover, MBF values show a heart rate dependence when true and model T1B differ. Without correction, this may lead to measuring spurious MBF changes in stress and rest conditions. The effect of varying C-T delay on MBF values is negligible in comparison, indicating that 6s may suffice despite long T1B. Both in bSSFP and GRE, simulated and phantom MBF values as well as MBF maps match previously reported perfusion values[4,5]. The use of adaptive instead of fixed T1B yields slightly more robust reconstruction of myoASL based perfusion.

Conclusions

MyoASL shows residual sensitivity to sequence parameters and potentially HR dependence. This may reduce the reproducibility in clinical use and corrupt stress/rest performance. Simulations show that the use of accurate blood T1 time may mitigate this effect for improved robustness.

References

1. Qayyum, A. A., & Kastrup, J. (2015). Measuring myocardial perfusion: the role of PET, MRI and CT. Clinical radiology, 70(6), 576-584.
2. Chen, Y., Wang, D. J., & Detre, J. A. (2011). Test–retest reliability of arterial spin labeling with common labeling strategies. Journal of Magnetic Resonance Imaging, 33(4), 940-949.
3. Jao, T., & Nayak, K. (2019). Analysis of physiological noise in quantitative cardiac magnetic resonance. Plos one, 14(8), e0214566.
4. Zun, Z., Wong, E. C., & Nayak, K. S. (2009). Assessment of myocardial blood flow (MBF) in humans using arterial spin labeling (ASL): feasibility and noise analysis. Magnetic Resonance in Medicine: An Official Journal of the International Society for Magnetic Resonance in Medicine, 62(4), 975-983.
5. Do, H. P., Jao, T. R., & Nayak, K. S. (2014). Myocardial arterial spin labeling perfusion imaging with improved sensitivity. Journal of Cardiovascular Magnetic Resonance, 16(1), 1-6.
6. Messroghli, D. R., Radjenovic, A., Kozerke, S., Higgins, D. M., Sivananthan, M. U., & Ridgway, J. P. (2004). Modified Look-Locker inversion recovery (MOLLI) for high-resolution T1 mapping of the heart. Magnetic Resonance in Medicine: An Official Journal of the International Society for Magnetic Resonance in Medicine, 52(1), 141-146.
7. Tao, Q., van der Tol, P., Berendsen, F. F., Paiman, E. H., Lamb, H. J., & Van Der Geest, R. J. (2018). Robust motion correction for myocardial T1 and extracellular volume mapping by principle component analysis-based groupwise image registration. Journal of Magnetic Resonance Imaging, 47(5), 1397-1405.
8. Buxton, R. B., Frank, L. R., Wong, E. C., Siewert, B., Warach, S., & Edelman, R. R. (1998). A general kinetic model for quantitative perfusion imaging with arterial spin labeling. Magnetic resonance in medicine, 40(3), 383-396.
9. Lu, H., Clingman, C., Golay, X., & Van Zijl, P. C. (2004). Determining the longitudinal relaxation time (T1) of blood at 3.0 Tesla. Magnetic Resonance in Medicine: an Official Journal of the International Society for Magnetic Resonance in Medicine, 52(3), 679-682.

Acknowledgments / Funding Information: Continue on this line

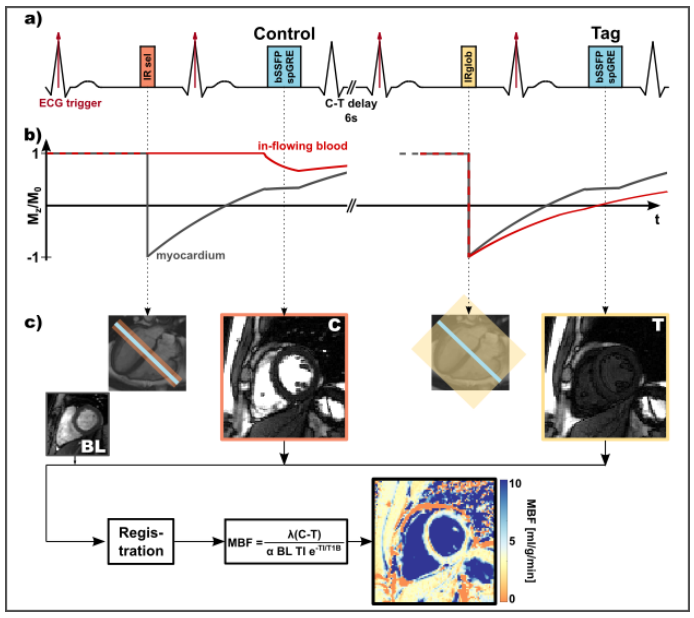

Figure 1: **Sequence Diagram**. **(a)** Diagram of the double ECG-gated Flow-Alternating Inversion Recovery myocardial ASL (FAIR-myoASL) sequence. Control and tag images are acquired after a selective and global inversion pulse during mid-diastole, respectively, with a 6s delay in between. **(b)** During control image acquisition non-inverted blood flows into the myocardium, while in the tag image inverted blood flows in. **(c)** Registered control and tag images are processed with a baseline image to obtain myocardial blood flow values.

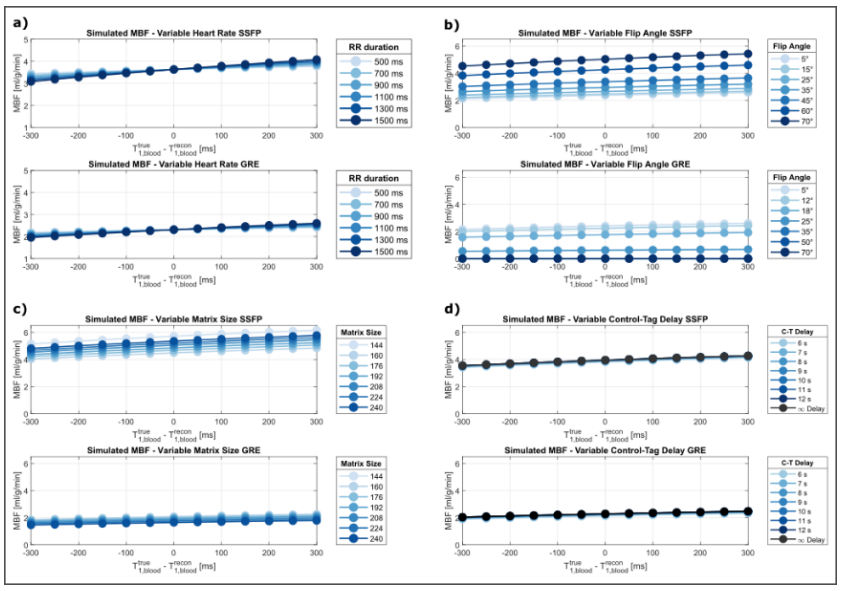

Figure 2: **Numerical Simulations**. **(a)** Simulated myoASL-MBF for varying simulated and fixed reconstruction blood T1 (1700 ms) for bSSFP/GRE readouts. Larger T1 inaccuracy renders the sequence more susceptible to heart rate variations. Varying sequence parameters, such as the flip angle **(b)** and matrix size **(c)** lead to further differences in MBF. Variations in the delay between tag and control image **(d)** result in only minimal deviation of MBF values compared to values obtained with simulated infinite delay.

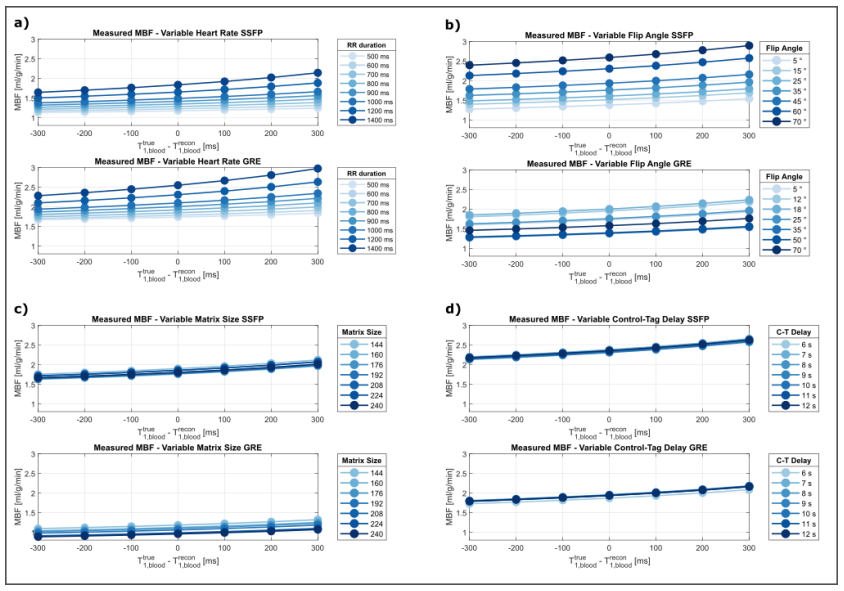

Figure 3. **MyoASL-MBF obtained in phantom** (vial T1: 1800ms) with bSSFP and GRE readout plotted against the difference in vial and reconstruction T1 time of blood: For **(a)** varying RR (500-1500ms), **(b)** acquisition flip angle (5°-70°), **(c)** matrix size (144x144-240x240, resolution 1.7x1.7mm2), and **(d)** delay between tag and control image. MBF values exhibit stronger variation in RR duration with increasing difference in T1, and show a flip-angle and matrix-size dependence.

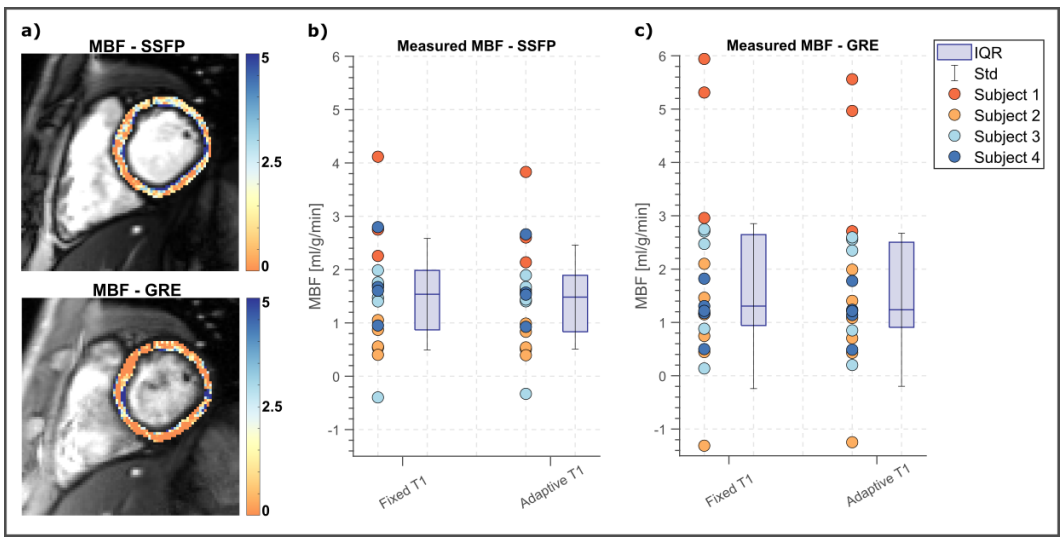

Figure 4: **In vivo MBF maps and septal MBF. (a)** Pixelwise average myoASL-MBF maps for one subject in bSSFP and GRE readout (TR/TE 3.3/1.65ms/3.4/3.1ms (bSSFP/GRE), GRAPPA-factor 2, Partial Fourier 6/8). **(b)** Mean septal MBF values reconstructed with fixed and adaptive blood T1 for bSSFP and **(c)** GRE readout for all subjects (blue: interquartile range). The standard deviation (black) was similar in bSSFP and GRE, but smaller for adaptive T1 times.

An Adaptive Target Field Framework for Complete Low Field MRI System Design

B. de Vos[1], R.F. Remis[1], A.G. Webb[1,2]

[1]C.J. Gorter Center for High Field MRI, Leiden University Medical Center, Leiden, Netherlands, [2]Circuits and Systems, Delft University of Technology, Delft, Netherlands

Synopsis

In this work a low field point-of-care system design framework is created using target field methods for all of the hardware components. A new target field method for Halbach-based magnet optimization with variable ring diameter and spacing is derived. Magnet, gradient and RF are combined into a single framework which includes a feedback loop for dealing with the component interdependencies. The result is a pipeline which with a few user inputs can create an optimal magnet, gradient and RF design in minutes.

Introduction

Low-cost portable low field point-of-care systems can be designed for particular applications based on specific interdependent hardware requirements[1-4]. In this work an iterative framework including feedback is created to design the optimal Halbach-based magnet, gradient and RF coils such that a set of user-specified imaging requirements are met. In order to achieve this most efficiently we use target-field (TF) methods, which have been commonly used in gradient coil design[5-10], and occasionally in RF coil design, but not in Halbach array-based permanent magnet design: a new mathematical model was derived to achieve this. Combining these methods results in a unique framework that, with minimum input, can design an entire low field MRI system within minutes.

Methods

Magnet design using a TF approach: TF approaches rely on specifying the desired field (gradient, B_0 or RF) within a certain region and finding an analytical relationship with respect to the source quantity.

Starting from the quasi-static Maxwell's equations an integral representation for the magnetic field in terms of a continuous cylindrical Halbach magnetization is derived. The continuous magnetization is discretized to represent individual magnets. The magnets are located within rings of variable radii and spacing. The goal is to obtain a set of ring radii $\mathbf{r}$ and ring spacings $\mathbf{d}$ such that $\mathbf{b}_T - \mathbf{b}_z(\mathbf{r},\mathbf{d})=\mathbf{0}$. Here $\mathbf{b}_T$ is the vector containing the prescribed field values inside the desired region and $\mathbf{b}_z(\mathbf{r},\mathbf{d})$ is the vector containing the field values due to chosen radii and spacing vectors. This non-linear problem is solved using a standard Newton optimization scheme[11] and constraints are applied to the radii and spacings to ensure practical solutions.

Iterative system design: The above TF approach for magnets is combined with previously derived TF methods for gradient and RF coil design[5,6] to create the iterative design framework illustrated in Figure 1. Given the user inputs, a system is designed which is as compact as possible, has the strongest possible magnet and which has sufficient homogeneity with regards to the gradient strength-dependent readout pixel bandwidth specified by the spatial resolution.

The initial guess for the field strength and number of rings is found by taking the most compact design given the minimum radius and a length/diameter ratio of 1.7 (based on previous literature). Next, power optimized gradient coils (with dimensions determined by the magnet) are designed. Using the efficiency [$Tm^{-1}A^{-1}$], the maximum current from the gradient amplifier, and the targeted resolution, the readout pixel bandwidth is compared with the blurring effect of ΔB_0. If the magnet inhomogeneities dominate, the model loops back to magnet design, the target B_0 is decreased by 2%, and ring diameters and separation distance are optimized to create a more homogeneous (but larger) magnet. This process is repeated until the desired spatial resolution is reached. If the user-specified minimum B_0 is reached before this, additional magnet rings are added and the pipeline is restarted. If adding rings creates a magnet longer than the specified maximum, inputs such as the spatial resolution need to be relaxed. In the final step after convergence, the RF coil is designed using a uniform TF oriented in the axial direction over the ROI. The RF pulse duration must be sufficiently short to excite the entire ROI, and there is a final check that this is possible with the modelled Q value and the power available from the RF amplifier.

Results

To demonstrate the potential of the framework an adult neuroimaging system was designed. The input parameters are shown in Figure 2.

For a 300 mm clear bore, the inner magnet layer diameter is set to 320 mm. The initial uniform ring spacing of 25 mm combined with a length/diameter ratio of 1.7, dictates that 23 rings constitute the initial setup. The output of the first pipeline iteration is shown in the first column of Figure 3. The B_0 inhomogeneity is higher than the readout pixel bandwidth and so the magnet design iterates with B_0 successively decreased in steps of 2%. The second column shows that when the minimum specified B_0 (50 mT) is reached, the required magnet homogeneity is still not obtained and so additional magnet rings are added. The iterative process continues until a solution is determined with a 25-ring magnet producing a 53 mT field (third column): the magnet designs corresponding to the columns are also shown in Figure 3. Figure 4 shows the ΔB_0 vs Newton iterations during the last step prior to the pipeline obtaining a solution. Figure 5 shows the final output of the framework: the gradient coils, magnet and RF coil are shown separately and combined in one assembly.

Conclusion and Discussion

A novel TF approach for Halbach-based magnet design is combined with RF and gradient coil methods, creating an integrated model which includes component interdependencies, amplifier specifications, and spatial resolution. The result is a very fast optimization framework which can be used to design an entire low field MRI system. The next step is to build in additional passive shimming to relax the homogeneity requirements of the basic magnet.

References:

1. Nakagomi M, et al. Development of a Small Car-Mounted Magnetic Resonance Imaging System for Human Elbows Using a 0.2 T Permanent Magnet. J Magn Reson (2019) 304:1–6. doi:10.1016/j.jmr.2019.04.017.
2. He Y, et al. Use of 2.1 MHz MRI Scanner for Brain Imaging and its Preliminary Results in Stroke. J Magn Reson (2020) 319:106829. doi:10.1016/j.jmr.2020.106829
3. O'Reilly T, et al. Three-dimensional MRI in a Homogenous 27 cm Diameter Bore Halbach Array Magnet. J Magn Reson (2019) 307:106578. doi:10.1016/j.jmr.2019.106578
4. Cooley C, et al. A portable scanner for magnetic resonance imaging of the brain. Nat Biomed Eng (2020). https://doi.org/10.1038/s41551-020-00641-5.
5. de Vos B, et al. Gradient Coil Design and Realization for a Halbach-Based MRI System," in IEEE Transactions on Magnetics, vol. 56, no. 3, pp. 1-8, March 2020, Art no. 5100208, doi: 10.1109/TMAG.2019.2958561.
6. de Vos B, et al. Design, characterisation and performance of an improved portable and sustainable low-field MRI system. Frontiers in Physics (2021). https://doi.org/10.3389/fphy.2021.701157
7. Turner R. A Target Field Approach to Optimal Coil Design. J Phys D: Appl Phys (1986) 19:L147–L151. doi:10.1088/0022-3727/19/8/001
8. Turner R. Minimum Inductance Coils. J Phys E Sci Instrum (1988) 21:948–52. doi:10.1088/0022-3735/21/10/008
9. Forbes LK, Crozier S. A Novel Target-Field Method for Finite-Length Magnetic Resonance Shim Coils: I. Zonal Shims. J Phys D: Appl Phys (2001) 34:3447–55. doi:10.1088/0022-3727/34/24/305
10. Forbes LK, Crozier S. A Novel Target-Field Method for Finite-Length Magnetic Resonance Shim Coils: II. Tesseral Shims. J Phys D: Appl Phys (2002) 35:839–49. doi:10.1088/0022-3727/35/9/303
11. Nocedal, J, Wright, SJ (2006). Numerical optimization. Springer series in operations research.

Acknowledgments / Funding Information: Simon Stevin Meester Prize, ERC Advanced Grant 101021218 PASMAR

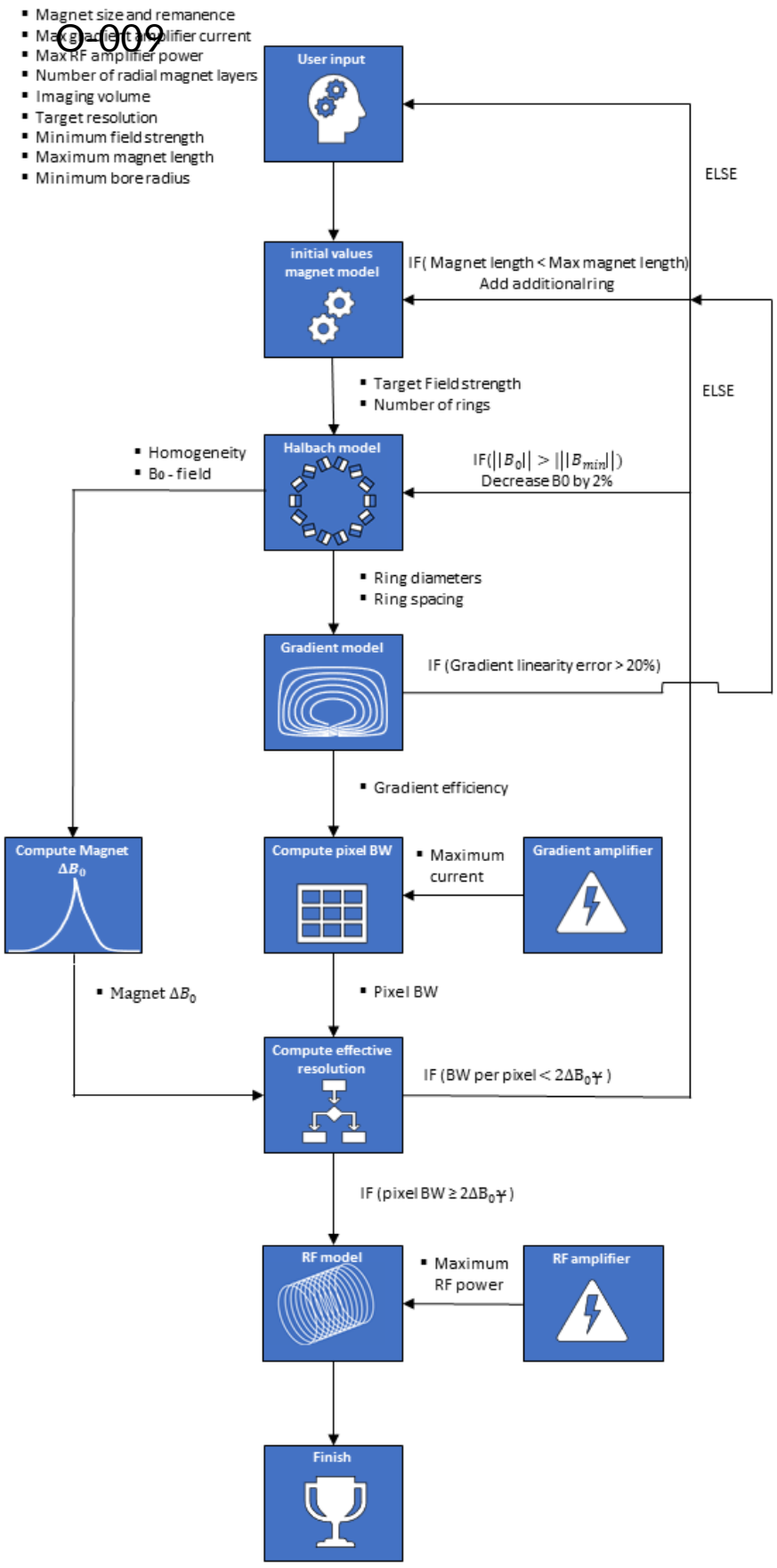

Figure 1: Flowchart of the system design methodology including the feedback loop.

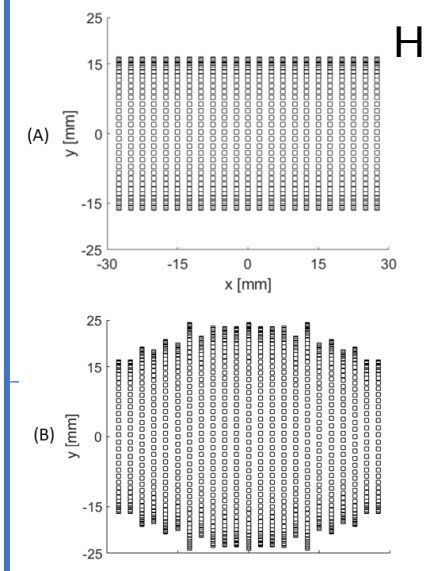

		(A) Initial design	(B) Minimum B0 reached	(C) Final convergence
	Target B0 [mT]	55	50	53
	Number of rings	23	23	25
Output	Magnet length [mm]	550	550	552
Output	Magnet Homogeneity over DSV [ppm]	53461	3713	810
Output	Gradient BW [Hz/pixel]	578	578	573
Output	$\Delta B_0 \gamma$ [Hz]	46797	2524	280

Figure 3: Left) Table showing the key output parameters for three events during the design framework: (A) the initial compact design from which the pipeline starts the iterations. (B) the magnet design after iterating to the user specified minimum target field strength of 50 mT. (C) The improved design after the number of rings is increased. Right) The magnets corresponding columns (B) and (C). Only the inner radial layer of magnets is shown for clarity.

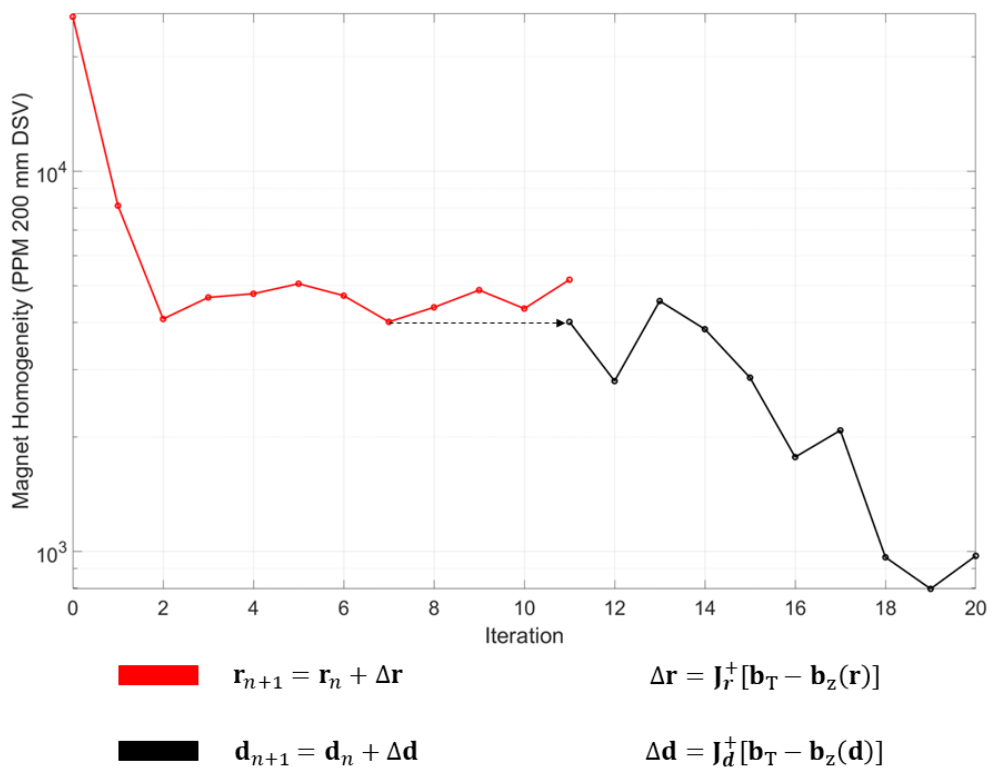

Figure 4: The homogeneity in PPM per Newton iteration step for the final magnet design discussed in the results section. The ring radii optimization is shown in red and ring spacing in black. The Newton update scheme is shown below the figure: Δr/d can be calculated by taking the Moore-Penrose inverse of the Jacobian matrix which holds the derivatives with respect to each radius/spacing for every target point in space. This is multiplied with the target field vector minus the system vector. The minimum and maximum ring spacing and diameter constraints are included in this scheme.

Input parameters	
Target DSV [mm]	200
Number of radial magnet layers	2
Maximum magnet length [mm]	600
Minimum bore radius	150
I max [A]	30
Resolution [mm]	1
Magnet size (LxWxH) [mm]	12x12x12
Magnet remanence [T]	1.1
Minimum field strength	50 mT

Figure 2: Table containing the input parameters of the design framework for the adult size

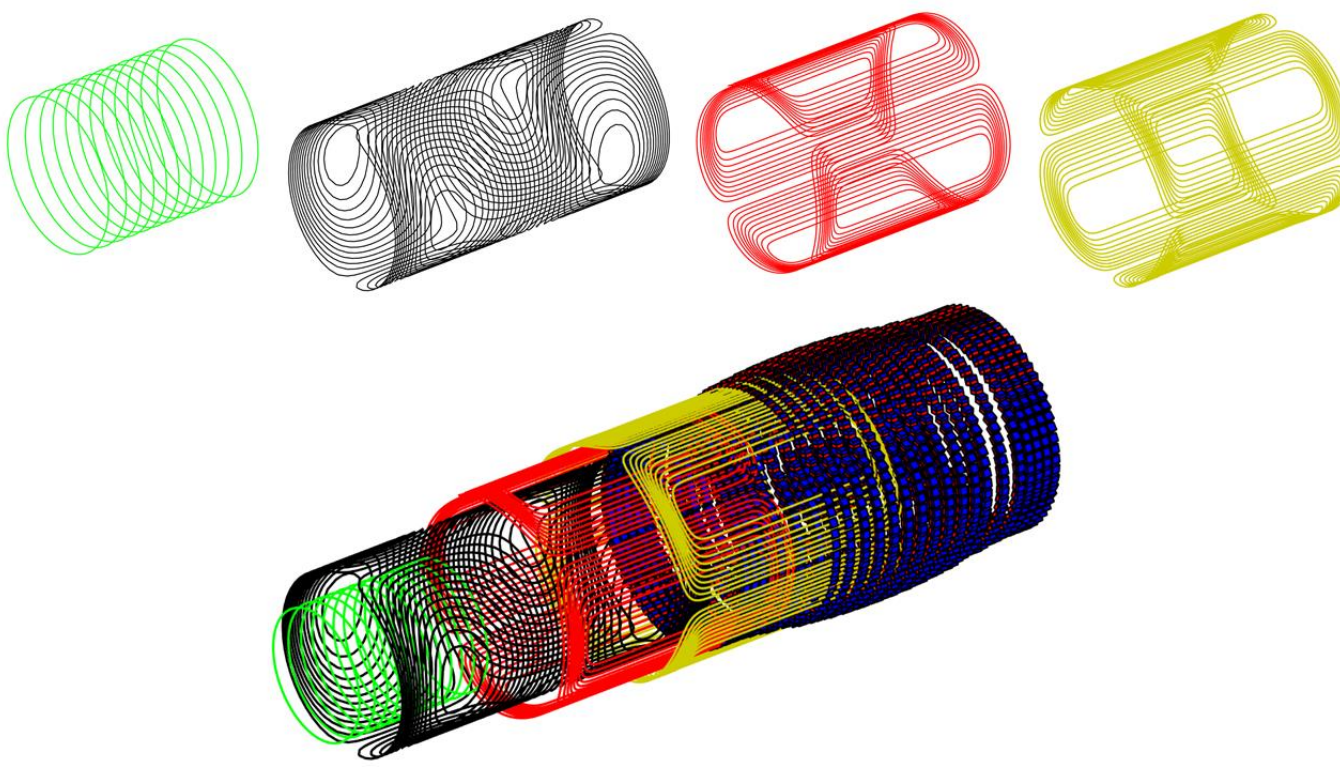

Figure 5: Visualization of the framework output. The gradient coils, Magnet and RF-coil are shown separately as well as together in a telescopic view. RF co (green), x-gradient (black), z-gradient (red), y-gradient (yellow), magnet (blue&red)

Reducing MRI acoustic noise burden with Predictive Noise Cancelling

P. Šiurytė[1], J. Tourais[1] , S. Weingärtner[1]
[1]Department of Imaging Physics, TU Delft, Delft, Netherlands;

Synopsis: Acoustic noise in MRI is a main source of patient anxiety, with noise levels reaching up to 130 dB. In this work, a low-cost solution is proposed, combining active noise cancelling and direct sequence noise prediction from the scanner gradient inputs. The prediction is based on the linearity between the derivative of the gradient coil input and corresponding acoustic noise. A proposed Predictive Noise Cancelling demonstrated an in-bore noise reduction up to 10 dB despite the system imperfections.

Purpose: Acoustic noise in MRI is a main contributor to patient discomfort, with sound pressure levels up to 130 dB[1]. In addition to presently used passive earplugs or headphones, silent MRI sequences or hardware solutions have been proposed. However, silent sequences often trade-off scan time or acquisition quality, and hardware upgrades are cost intensive[2-3]. Active noise cancelling, i.e. using simultaneously applied anti-noise, has also been explored[4], but is limited to the application of repetitive sequences only[5]. While this performs well in fMRI studies, clinical scan protocols contain distinct scan sequences and are therefore not suited for active noise cancelling. In this work, we present a versatile solution by combining the anti-noise approach with a direct noise prediction from the scanner gradient inputs, termed predictive noise cancelling (PNC). We describe a low cost setup for in-bore noise cancelling and evaluate its potential for noise attenuation.

Methods: An acoustic setup was constructed, placing a custom speaker box and amplifier outside the scanner room and attaching a hose to channel the sound inside the bore (see fig. 1). The full setup consisted of the speaker system, optical fiber microphone (Phonoptics), function generator (Tektronix, AFG31002) and a PC for signal processing. All signals were recorded at 44.1 kHz sampling rate, filtered to 0.3-6 kHz and processed using Matlab and LabVIEW.

The noise prediction was based on a linear time-invariant model, utilizing linearity between acoustic noise $p(t)$ and the scanner gradient input derivative $g`(t)$. In frequency domain, this is expressed as $P_{x/y/z}(f) = H_{x/y/z}(f) \cdot G`(f)$, where $H_{x/y/z}(f)$ represents a measured system transfer function[6-8].

A calibration sequence was designed for a 3T Philips system, consisting of triangular gradient pulses with a 0.14 ms rise time and 20 mT/m amplitude. 20 such blips were played out with a 3 s repetition time and used as trigger pulses (see fig. 2, black pulses). Firstly, these trigger pulses were followed by a single-gradient pulse, used to estimate the transfer functions. Next, the same pulse noise was predicted, to evaluate the maximum expected noise reduction values. Using an acoustic signal from the trigger pulses, the predicted noise was triggered to estimate the absolute latency and synchronize the system. In the final step, the anti-noise signal played out simultaneously with a scanner pulse (dashed lines in fig. 2).

Two output corrections were needed to achieve noise cancellation. Firstly, a distortion introduced by the speaker-hose system to the sound was corrected by including channel equalization. The equalizer calculates the inverse transfer function of the system from the input of the scanner pulse and a recorded playback (indicated as EQ in fig. 2). Secondly, clock mismatch between the recording device and the scanner causes the output signals to dephase. This accumulative latency was estimated based on the train of 20 trigger pulses. All recorded signals were accordingly resampled.

After the calibration steps, a prediction was applied to the components of a spoiled GRE sequence (see fig. 4, left). Theoretical maximum reduction values were estimated based on ideal equalizer and alignment conditions. The predicted anti-noise was triggered using the previously used trigger pulse. Live reduction data was acquired with 6 repetitions for each gradient coil.

Results: A clock mismatch of 12.2 us per second was measured and used to resample the signals. The calibration pulse noise $P_{x/y/z}(f)$, gradient input derivative $G`(f)$ and the derived transfer functions $H_{x/y/z}(f)$ are shown in fig. 3. For the calibration pulses, estimated theoretical maximum reduction was 21 dB, assuming ideal conditions. The achieved live noise reduction for calibration pulses was 7.16 dB, 8.27 dB and 7.29 dB for X, Y and Z coils accordingly.

For a spoiled GRE sequence, the estimated theoretical maxima were 9.99 dB, 13.52 dB and 9.85 dB for X,Y and Z coils respectively. Experimentally, this translated to mean values of 7.01± 0.31 dB, 6.42 ± 2.04 dB and 9.28 ± 0.26 dB reduction. An example acquisition is illustrated in fig. 5.

Discussion: Initial results with PNC using a low cost setup demonstrated noise attenuation comparable to the setting achieved in repetitive sequences or with cost intensive gradient hardware upgrades[2-3].

Equalizer imperfections were the main obstacle in achieving the stated theoretical estimates. Iterative equalizers can be applied for improved channel correction, and MRI compatible speakers can be employed. This will be explored in future studies to further improve noise attenuation.

Considerable noise reduction was achieved for individual gradient components. It is likely, however, that combining the gradients would result in attenuated reduction[9]. A segmentation of the transfer functions in terms or slew rate and/ or amplitude could help achieve stronger noise cancelling in future experiments.

Conclusion: First results of Predictive Noise Cancelling show a promise of active noise attenuation. Despite system imperfections, up to 10 dB noise reduction was presented based on a linear time-invariant prediction model, and further optimized setups may achieve even higher attenuation based on the theoretical maximum. Predictive noise cancelling, therefore, bears great promise as a cost effective solution to improve patient comfort without the need for new or modified scanner hardware.

References:

1. McJury, M. J. (2021). Acoustic Noise and Magnetic Resonance Imaging: A Narrative/Descriptive Review. Journal of Magnetic Resonance Imaging.
2. Segbers, M., Rizzo Sierra, C. V., Duifhuis, H., & Hoogduin, J. M. (2010). Shaping and timing gradient pulses to reduce MRI acoustic noise. Magnetic resonance in medicine, 64(2), 546-553.
3. Katsunuma, A., Takamori, H., Sakakura, Y., Hamamura, Y., Ogo, Y., & Katayama, R. (2001). Quiet MRI with novel acoustic noise reduction. Magnetic Resonance Materials in Physics, Biology and Medicine, 13(3), 139-144.
4. Goldman, A. M., Gossman, W. E., & Friedlander, P. C. (1989). Reduction of sound levels with antinoise in MR imaging. Radiology, 173(2), 549-550.
5. Optoacoustics, OptoActive II. https://www.optoacoustics.com/medical/optoactive-ii Accessed on November 10, 2021.
6. More, S. R., Lim, T. C., Li, M., Holland, C. K., Boyce, S. E., & Lee, J. H. (2006). Acoustic noise characteristics of a 4 Telsa MRI scanner. Journal of Magnetic Resonance Imaging: An Official Journal of the International Society for Magnetic Resonance in Medicine, 23(3), 388-397.
7. Sierra, C. V. R., Versluis, M. J., Hoogduin, J. M., & Duifhuis, H. (2008). Acoustic fMRI noise: linear time-invariant system model. IEEE Transactions on Biomedical Engineering, 55(9), 2115-2123.
8. Wu, Z., Kim, Y. C., Khoo, M. C., & Nayak, K. S. (2014). Evaluation of an independent linear model for acoustic noise on a conventional MRI scanner and implications for acoustic noise reduction. Magnetic resonance in medicine, 71(4), 1613-1620.
9. Šiurytė, P., Tourais, J., Weingärtner, S. (2021). MRI Acoustic Noise: Limits of the Linear Time-Independent Model. ESMRMB, 2021

Acknowledgments / Funding Information: S.W. acknowledges funding from the 4TU Precision Medicine program, an NWO Start-up STU.019.024, and ZonMW OffRoad 04510011910073

Figure 1. Experimental predictive noise cancelling setup. The speaker box was constructed by placing a woofer on the left side of the wooden cabinet (top left), filling walls with acoustic wool padding and sealing it with silicon (bottom left). On the right side of the box, a funnel was fixed to attach to a rubber hose (top right), transporting the sound into the scanner room (bottom right).

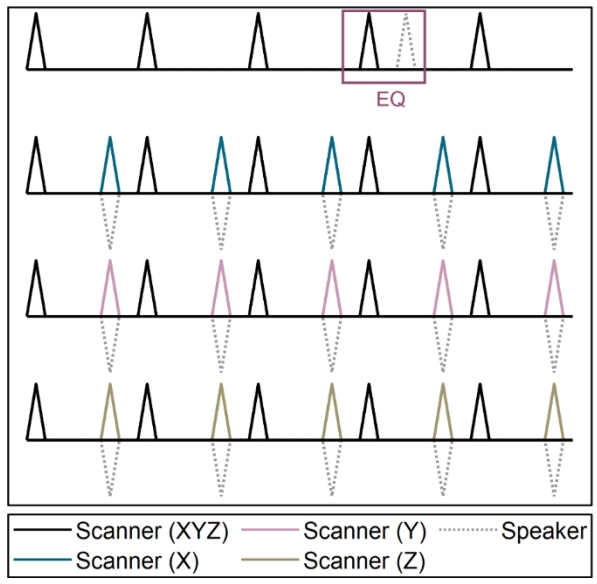

Figure 2. Calibration sequence scheme. All pulses have 20 mT/m amplitude and 0.14 ms rise time. Black pulses are played out on all 3 coils simultaneously, and are used as an acoustic trigger. Coloured pulses represent single-gradient scanner pulses used to derive the transfer functions, while dashed lines under those indicate an anti-noise in the last calibration step. Equalizer (EQ) inputs are also indicated, where dashed pulse shows a speaker playback of the recorded trigger pulse.

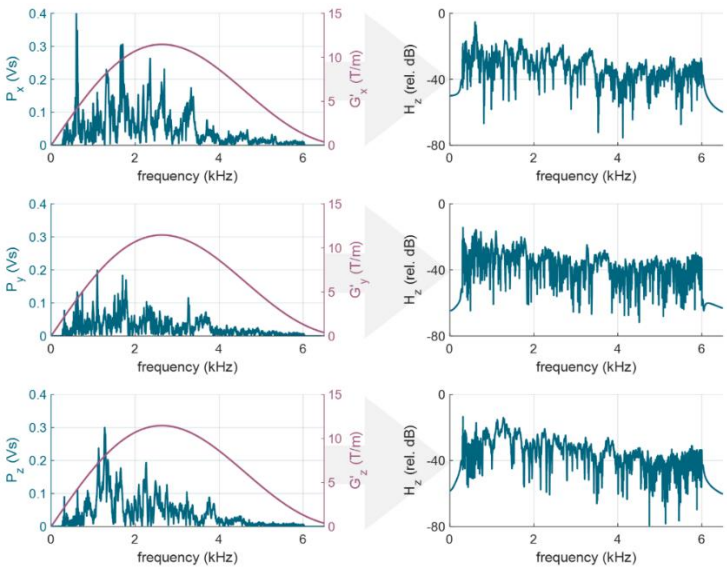

Figure 3. Derivation of the transfer functions $H_{x/y/z}(f) = P_{x/y/z}(f) \,/\, G\,`(f)$. Calibration pulse noise $P(f)$ is illustrated on the left (blue), along with a gradient derivative $G`(f)$ of a triangular pulse (pink). Corresponding transfer functions are plotted in relative dB scale on the right.

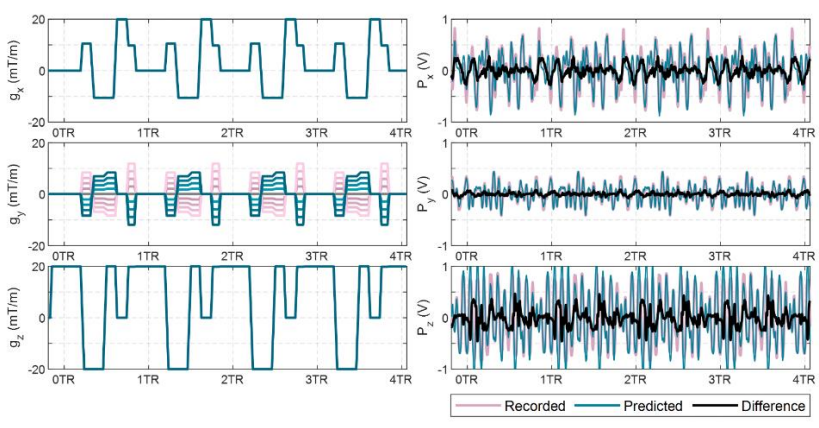

Figure 4. Spoiled GRE sequence gradient inputs (left). Measurement gradient was arbitrarily assigned to X coil, phase gradient to Y coil and slice selection gradient to Z coil. The corresponding noise prediction along with the original and the attenuated sequence noise is also shown (right). Sequence TR/TE = 10.6/6.4 ms and total length - 10 s.

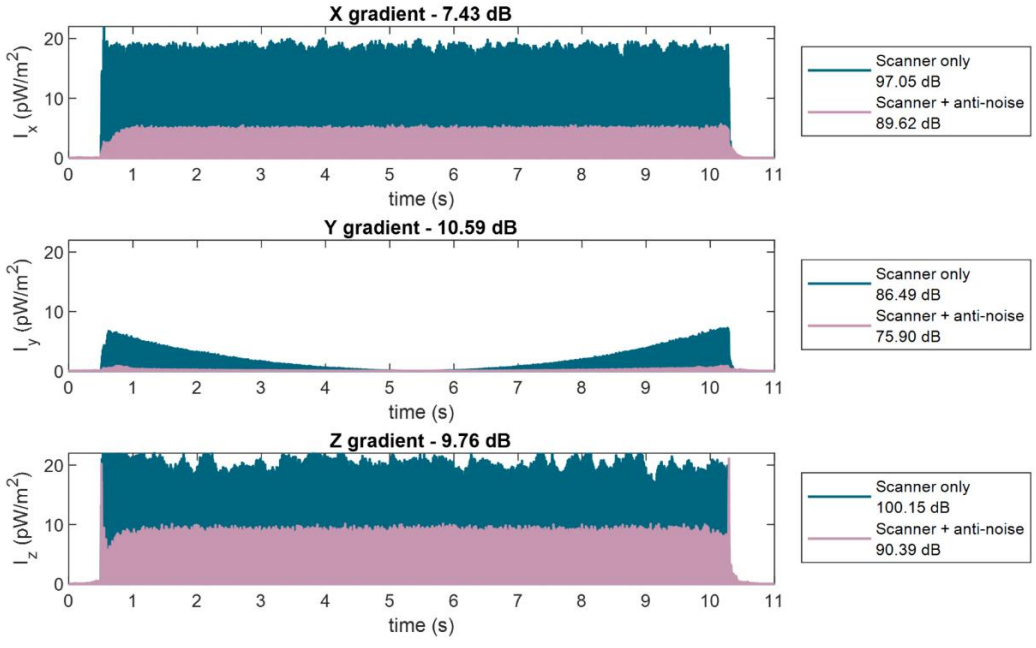

Figure 5. Live FFE sequence noise reduction results. Sound intensities are plotted for scanner sequence components (blue) and for scanner noise with simultaneous anti-noise output (pink). Up to 90% signal intensity reduction is shown. The reference intensity was assumed as I_0 = 1 pW/m^2.

Ultra-high field done ultra-fast: Enhancing Wave-CAIPI using an single-axis insert head gradient

Thomas Roos[1,2,3], Edwin Versteeg[1] & Jeroen Siero[1]
[1]Highfield research group, University Medical Center Utrecht, Utrecht, Netherlands
[2]Delft University of Technology, Delft, Netherlands
[3]Spinoza Centre for Neuroimaging, Amsterdam, Netherlands

Synopsis: Acceleration techniques like SENSE have enabled significant decreases in scan time, but the G-factor penalty on SNR limits attainable accelerations.

Wave-CAIPI lowers this G-factor by spreading aliasing and taking advantage of the coil sensitivity distributions. A high performance single-axis insert gradient is utilised to increase the attainable wave amplitudes and thereby increasing the effectivity of Wave-CAIPI.

Simulations and 7T phantom & in-vivo acquisitions show significant improvements in G-factor when using Wave-CAIPI, especially when utilizing the higher performance of the insert gradient. Not only are the G-factors lower but also show increased spreading and lack hard edges, allowing for even faster acquisitions.

Introduction

In recent years, acceleration techniques like SENSE and GRAPPA have enabled significant decreases in scan time, but even with the advance of ultra-high field scanners and their increased SNR, the penalty on SNR from √R and G-factor limit attainable accelerations.

Improved methods like CAIPI, BPE and Wave-CAIPI[1] have been developed that try to lower this G-factor by spreading aliasing over the FOV and taking advantage of the coil sensitivity distributions. Previous work has predicted that Wave-CAIPI can benefit from using a high-performance insert gradient[2], even when it only contains a single axis[3].

Purpose

To reduce the G-factor penalty on SNR in highly accelerated scans by utilising Wave-CAIPI on a high performance single-axis head insert gradient, thereby allowing for even faster acquisitions without compromising on quality.

Methods

To study the effectivity of Wave-CAIPI with increased wave amplitudes on a single axis, simulations are performed and then validated in both phantom and in-vivo brain acquisitions on a 7T MRI scanner (Philips, Best, The Netherlands) with 32ch head coil (Nova Medical, Wilmington, USA).

The chosen sequence is designed for SWI and consists of a whole-brain 3D GRE with a resolution of 0.8mm^3 over a FOV of 256x192x256mm, with $T_R/T_E/\alpha$/BW = 43[ms]/20[ms]/14°/285[Hz]. The acquisition duration is reduced to 2min42sec by accelerating 16-fold, 4 times in both Y- &Z-axes, using SENSE and two types of Wave-CAIPI.

Wave-CAIPI is created by introducing a FOV/2 shift and 10 periods of sinusoidal waves on both Y-& Z-axes. The Z-axis wave is given a 90° phase offset to produce a cosine during the readout. The whole-body gradient specifications limit the wave amplitude to 9 [mT/m] and that amplitude is therefore played out on the Y-axis. The insert gradient produces the Z-axis wave and since previous work has shown that Wave-CAIPI efficiency improves with higher wave amplitudes[4], the higher performance of the insert gradient is used to double the amplitude of the Z-axis wave to 18 [mT/m] in the simulations and phantom acquisitions. To remain under auditory limits, a factor of 1.7x and thus 15.3 [mT/m] waves are utilised in the in-vivo acquisitions. A secondary 1x reference acquisition is acquired for direct comparison with the higher performance waves.

Reconstruction is performed using an in-house developed NUFFT-based pipeline implemented in MATLAB complemented by MRecon (GyroTools, Zurich, Switzerland) and BART[5]. The real-time scanner behaviour and all resulting gradient waveforms are reproduced and convolved with a GIRF[6] captured previously using a field camera[7] (Skope, Zurich, Switzerland). For scans that just utilise the whole-body gradients the resulting trajectory suffices, but the insert gradient produces a B0 offset when not positioned perfectly on iso-center and therefore requires a PSF scan to measure and correct that offset. Sensitivity maps are calculated using ESPIRiT[8] on a low-resolution reference acquisition. 18 iterations of CG-SENSE[9] with L_2-regularisation produce the final reconstruction.

Simulations are created from a generated 3D phantom and acquired sensitivity maps. The phantom is multiplied by the sensitivities to produce ideal coil images. Noise is added to create a 14dB SNR and simulated K-space is calculated from those images using a NUFFT on trajectories taken from the reconstruction pipeline above.

Finally, G-factor maps are created for all reconstructions using the pseudo multiple replica method[10] that performed the entire reconstruction 50 times with additional simulated noise.

Results

The G-factor analysis results for the simulations, phantom and in-vivo acquisitions that are depicted in figure 2 to 4 respectively, show a consistent pattern that is quantified in the table of figure 5.

The Wave-CAIPI acquisition shows very significant reduction in G-factor over the SENSE acquisition. The enhanced (1.7x or 2x) Wave-CAIPI acquisition consistently improves over the regular Wave-CAIPI acquisition and shows even lower G-factor values. The vendors SENSE implementation shows a similar pattern in G-factor to our SENSE implementation, but achieves slightly different results in which our implementation performs better on the phantom acquisition and the vendor SENSE shows favourable in-vivo G-factors. Exemplar slices show slight folding artefacts in the SENSE acquisitions, which are not visible in the Wave-CAIPI acquisitions. However, the phantom Wave-CAIPI reconstructions show a ghost in the readout dimension that increases with increasing wave amplitude.

Discussion

Wave-CAIPI shows significant and consistent improvements in all acquisition types, not only are the absolute G-factor values themselves lower, they also show geometrical spreading and therefore lack the hard edges that frequently cause visible artefacts.

The enhanced performance of the insert gradient enhanced the effect of Wave-CAIPI by further lowering the G-factor and increasing the spreading. The increase in wave amplitude slightly increased an artefact in the phantom acquisition, probably due to the higher sensitivity for imperfections in the trajectory and coil sensitivities produced by the pipeline that is tailored to in-vivo data. The chosen wave frequency limited the in-vivo capability of the gradient insert due to auditory limits, but that is reducible by changing frequency and could be completely eliminated by going above 20khz.

Conclusion

Wave-CAIPI significantly reduces the G-factor penalty on accelerated scans. While the high-performance single-axis insert head gradient shows clear improvements of the performance of Wave-CAIPI in the studied sequence, faster acquisitions are now feasonable (with increased R and shorter readouts, such as EPI) and have even larger potential performance benefits.

References

1. Bilgic, Berkin, et al. "Wave-CAIPI for highly accelerated 3D imaging." Magnetic resonance in medicine 73.6 (2015): 2152-2162.
2. Versteeg, Edwin, et al. "A plug-and-play, lightweight, single-axis gradient insert design for increasing spatiotemporal resolution in echo planar imaging-based brain imaging." NMR in Biomedicine 34.6 (2021): e4499.
3. Monreal Madrigal, Alejandro. "Ultra fast MRI acquisition at 7 Tesla: Implementation of Wave-CAIPI with a high efficiency head insert gradient coil." (2020).
4. Wang, Haifeng, et al. "Parameter optimization framework on wave gradients of Wave-CAIPI imaging." Magnetic resonance in medicine 83.5 (2020): 1659-1672.
5. Uecker M, Ong F, Tamir JI, et al. Berkeley Advanced Reconstruction Toolbox. Annual Meeting ISMRM, Toronto 2015, In: Proc. Intl. Soc. Mag. Reson. Med 2015;23:2486.
6. Vannesjo, Signe J., et al. "Gradient system characterization by impulse response measurements with a dynamic field camera." Magnetic resonance in medicine 69.2 (2013): 583-593.
7. Wilm, Bertram J., et al. "Higher order reconstruction for MRI in the presence of spatiotemporal field perturbations." Magnetic resonance in medicine 65.6 (2011): 1690-1701.
8. Uecker, Martin, et al. "ESPIRiT—an eigenvalue approach to autocalibrating parallel MRI: where SENSE meets GRAPPA." Magnetic resonance in medicine 71.3 (2014): 990-1001.
9. Pruessmann, Klaas P., et al. "Advances in sensitivity encoding with arbitrary k-space trajectories." Magnetic Resonance in Medicine: An Official Journal of the International Society for Magnetic Resonance in Medicine 46.4 (2001): 638-651.
10. Robson, Philip M., et al. "Comprehensive quantification of signa-tlo-noise ratio and g-factor for image-based and k-space-based parallel imaging reconstructions." Magnetic Resonance in Medicine: An Official Journal of the International Society for Magnetic Resonance in Medicine 60.4 (2008): 895-907.

Figure 1: Two photos of the utilized insert gradient; the left photo (A) shows the coil during construction with the integrated birdcage transmit coil exposed and the right photo (B) is taken with the coil on the patient table showing the inside of the 32-channel receive array.

	5^{th}Percentile		Mean		95^{th}Percentile	
	$G-$factor	%−change	$G-$factor	%−change	$G-$factor	%−change
Simulation						
SENSE	0.66	–	1.06	–	1.65	–
Wave-CAIPI	0.65	−1.4%	0.92	−12.6%	1.31	−20.5%
Wave-CAIPI 2x	0.64	−3.3%	0.89	−15.6%	1.21	−26.9%
Phantom						
Vendor SENSE	1.39	–	1.67	–	2.25	–
SENSE	0.72	−48.0%	1.07	−36.0%	1.71	−24.2%
Wave-CAIPI	0.69	−50.0%	0.92	−44.9%	1.13	−49.9%
Wave-CAIPI 2x	0.71	−49.2%	0.92	−45.2%	1.10	−51.3%
In-vivo						
Vendor SENSE	0.91	–	1.23	–	1.78	–
SENSE	0.81	−11.0%	1.34	+8.16%	1.82	+2.8%
Wave-CAIPI	0.71	−21.0%	1.12	−9.65%	1.53	−13.4%
Wave-CAIPI 1.7x	0.68	−25.3%	1.02	−17.1%	1.40	−20.8%

Figure 5: Table with quantified results of G-factor analysis from all types of simulations, phantom & in-vivo acquisitions.

The three depicted metrics are the 5 percentile, mean and 95 percentile of G-factor values taken over their entire respective 3D volume.
Each metric is also shown as a percentage change from the (vendor) SENSE acquisition.

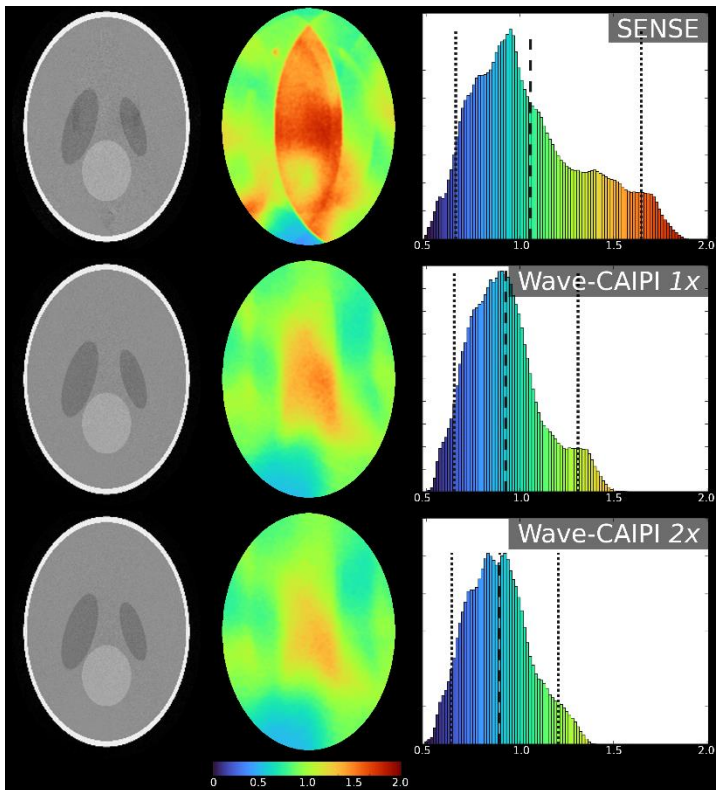

Figure 3: Results of the simulations for three types of acquisitions; **SENSE**, **Wave-CAIPI 1x** & **Wave-CAIPI 2x** from *top to bottom, as marked in the figure*.

The **2x** acquisition utilises the higher performance available with the insert gradient and doubles the Z-axis waves over the **1x** acquisition. The left column depicts an exemplar image slice, the middle column the G-factors over that slice with colorbar below and the right column contains the histogram of G-factors from the entire 3D volume.

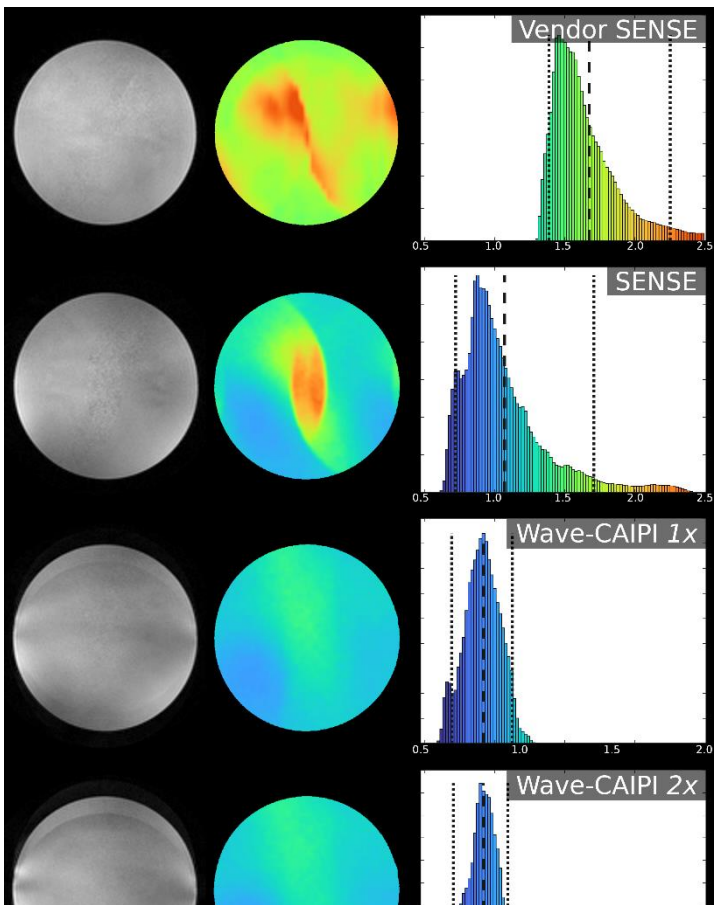

Figure 3: Results of the phantom acquisitions for four types of acquisitions; **Vendor SENSE**, **SENSE**, **Wave-CAIPI 1x** & **Wave-CAIPI 2x** from *top to bottom, as marked in the figure*.

The **2x** acquisition utilises the higher performance available with the insert gradient and doubles the Z-axis waves over the **1x** acquisition. The left column depicts an exemplar image slice, the middle column the G-factors over that slice with colorbar below and the right column contains the histogram of G-factors from the entire 3D volume.

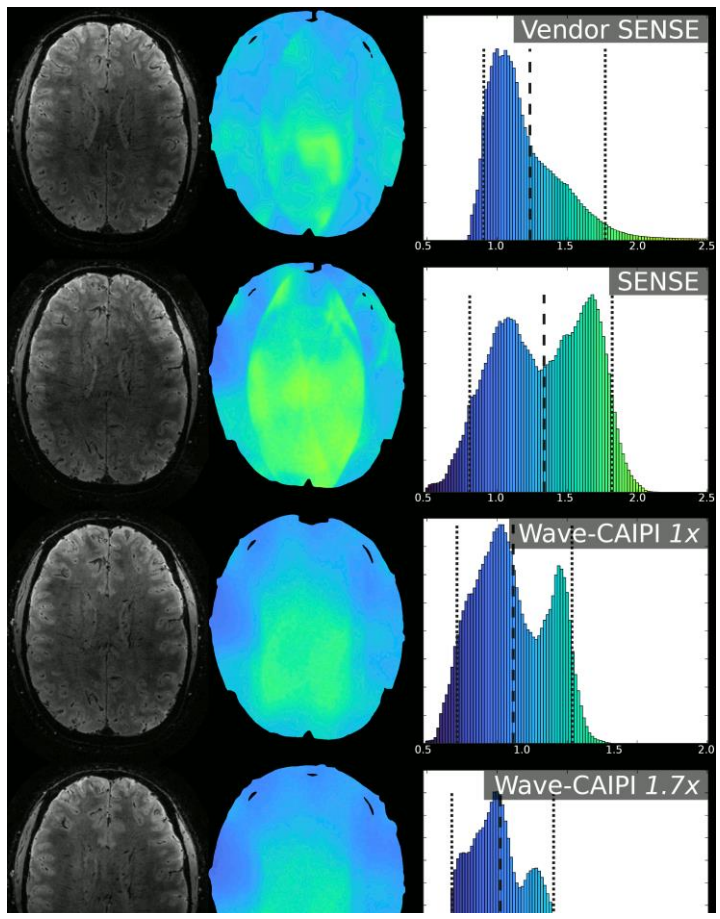

Figure 4: Results of the in-vivo acquisitions for four types of acquisitions; **Vendor SENSE**, **SENSE**, **Wave-CAIPI 1x** & **Wave-CAIPI 1.7x** from *top to bottom, as marked in the figure*.

The 1**.7x** acquisition utilises the higher performance available with the insert gradient and doubles the Z-axis waves over the **1x** acquisition. The left column depicts an exemplar image slice, the middle column the G-factors over that slice with colorbar below and the right column contains the histogram of G-factors from the entire 3D volume.

Short-TE diffusion-MRI by combining strong gradients with ultrasonic readout

Aris van Ieperen[1,2], Chantal Tax[1,3], Dennis Klomp[1], Bas Vermulst[2], Jeroen Siero[1,4], Joost van Straalen[5], Martijn Heintges[5], and Edwin Versteeg[1]

[1]Radiology, University Medical Center Utrecht, Utrecht, Netherlands, [2]Electromechanics & Power Electronics, Eindhoven University of Technology, Eindhoven, Netherlands, [3]CUBRIC, School of Physics and Astronomy, Cardiff University, Cardiff, United Kingdom, [4]Spinoza Centre for Neuroimaging, Amsterdam, Netherlands, [5]Prodrive Technologies B.V., Son, Netherlands

Synopsis: For high-resolution diffusion-MRI, strong gradients combined with fast readout are desired. In this study, we propose a gradient system architecture for such strong gradients and fast readouts without nerve stimulation by implementing a filter topology that allows for both low and high frequency gradient waveforms. Two gradient inserts with different specifications are realized and two proposed modulation strategies are implemented in the amplifier firmware. Field measurements demonstrated the desired dual-mode capability of the system. With one gradient insert, a gradient amplitude of 300 mT/m and slew rates well above 10.000 T/m/s can be reached with only 500A&330V as amplifier output.

Purpose: Diffusion-weighted MRI can probe the architectural configuration of tissue microstructure, yet requires very strong gradients, particularly when considering tissues with short T_2 relaxation times. While whole body designs that facilitate gradients up to 300 mT/m have been developed [1], they suffer from relatively slow ramp times that avoid peripheral nerve and cardiac stimulation, and require a significant physical footprint. Moreover, as these designs are specifically targeted towards high field strengths, they are suboptimal during the echo planar imaging (EPI) readout. In this paper we propose a new gradient system architecture, for which typical gradient amplifier hardware can be employed. The proposed approach enables seamless switching between two modes, one for strong gradients and one for ultrasonic readout. The method is experimentally verified, demonstrating that a diffusion gradient followed by a 20 kHz readout is feasible and significantly reduces the sound pressure levels and nerve stimulation associated with an EPI readout.

Methods: The proposed gradient system architecture, shown in Figure 1, consists of a typical gradient amplifier and a modified, distributed output filter. Additionally, the gradient amplifier modulation scheme is adapted to cater two modes of operation: one using conventional pulse-width modulation (PWM) with reference tracking, and one fixed frequency modified sine wave operation with amplitude control, to allow strong gradients and ultrasonic readout respectively.

Combining a resonant filter with the gradient head coil results in a third-order LCL filter. By using a capacitor in parallel with the system's gradient coil, the filter is capable of handling DC current, which enables low frequency gradient waveforms. Additionally, the filter is tuned such that the resonance frequency is around 20 kHz to allow an ultrasonic EPI readout, according to

$$\omega_{\mathrm{res}} = \sqrt{\frac{L_1+L_2}{L_1 L_2 C}}. \quad (1)$$

By utilizing the amplifying characteristic of the resonance, the high slew rates (up to 10.000 T/m/s) for the 20 kHz operation are provided. Additionally, a hybrid feed-forward and feedback control method is proposed that significantly improves the performance of the overall system, as depicted in Figure 2. The first gradient coil was paired with an off-the-shelf gradient amplifier (Prodrive, Netherlands), Here, the proposed modulation strategies were implemented in the amplifier firmware to enable the amplifier to produce high frequency waveforms as well as low frequency gradient waveforms. The proposed gradient architecture was evaluated by measuring the gradient amplitude with a field camera (Skope, Switzerland). During these measurements, the setup was controlled by an external waveform generator that was triggered by the MR-system (Philips Achieva 7T, Netherlands). As a proof-of-principle and to ensure that the signals of the field camera do not become completely dephased by the typical long diffusion pulses, we used a relatively short “diffusion” pulse (1ms), followed by the 20 kHz EPI readout (10ms).

Results: Two insert gradients were built, the first one with inductances of the Y- and Z gradient of 30.46 and 38.24 μH and efficiencies of 0.095 and 0.3 mT/m/A, and the second insert gradient with inductances of the Y- and Z gradient of 61.07 and 261.65 μH and efficiencies of 0.095 and 0.60 mT/m/A respectively. The frequency response function of the designed LCL filter for the input voltage to gradient insert voltage and current is shown in Figure 3. The voltage over the insert gradient is attenuated by a factor two for the low frequency region (below 1 kHz) and amplified at the resonance frequency of 20 kHz by a factor 21. Figure 4ab show the amplifier current for a diffusion gradient and ultrasonic readout, respectively. These measurements demonstrate that both the low frequency diffusion gradient as well as the high frequency readout currents can be provided to the gradient coil. Despite the high amplification factor of the resonant coil, we could reach steady-state of the silent EPI train in 0.5 ms due to the proposed control scheme. Figure 4c shows the measured field for a low diffusion pulse followed by the silent readout of 40 mT/m. Figure 5 presents the TE achievable for a given diffusion weighting (characterized by the b-value), leveraging the strong gradients and ultrasonic readout of the insert compared to state-of-the-art gradient setups.

Discussion and Conclusion: We have demonstrated a setup which operates the gradient system in dual-mode, to generate a low frequency gradient pulse followed by an ultrasonic readout. The proposed control algorithm of the ultrasonic readout reduced the rise time of the field amplitude significantly, as can be seen in Figure 5 by comparing the HF-startup time with the damped oscillation time at the end of the sequence (0.5 and 2.0 ms respectively). The control algorithm of the diffusion pulse can be further improved by tuning the control parameters. Depending on the properties of the gradient insert and the used amplifier, gradient amplitude of 300 mT/m at 500 A can be obtained for the Z-gradient, and both Y and Z gradients could be driven well above a 10.000 T/m/s during the silent EPI readout. The combination of wave encoding and EPI readout opens up avenues for high accelerations and resolution while reducing g-factor and artifacts [2].

References:

1) D. K. Jones, D. C. Alexander, R. Bowtell, M. Cercignani, F. Dell’Acqua, D. J. McHugh, K. L. Miller, M.Palombo, G. J. M. Parker, U. S. Rudrapatna, and C. M. W. Tax, “Microstructural imaging of the human brain with a ‘super-scanner’: 10 key advantages of ultra-strong gradients for diffusion MRI,” NeuroImage,vol. 182, no. May, pp. 8–38, 2018.2)

2) J. Cho, C. Liao, Z. Zhang, W.-c. Lo, J. Xu, O. Beker, K. Setsompop, and B. Bilgic, “Highly Accelerated EPI with Wave Encoding and Multi-shot Simultaneous Multi Slice Imaging,”Proc. Int. Soc. Magn. Reson.Med., p. submitted, 2020.

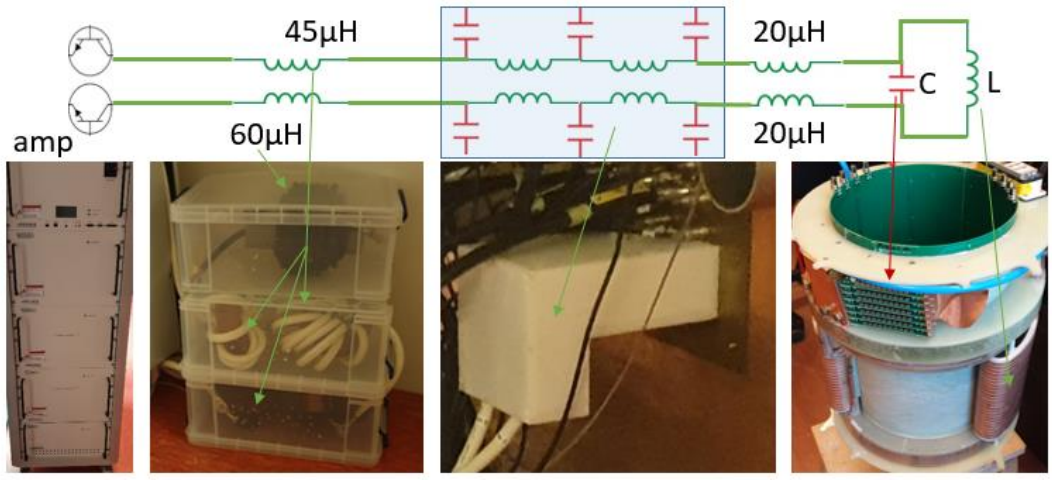

Figure 1. Schematic overview of the distributed output filter of the gradient amplifier towards the gradient coil. Left, the commercial gradient amplifier (Prodrive) with manually removed output filter and updated firmware; second, the first stage of inductance to partially match the inductance of the gradient coil; third, the RF cage filter with limited voltage threshold; right, inside the magnet room the second part of matching inductor followed by the insert gradient coil with inductance (L) and parallel capacitor bank (C).

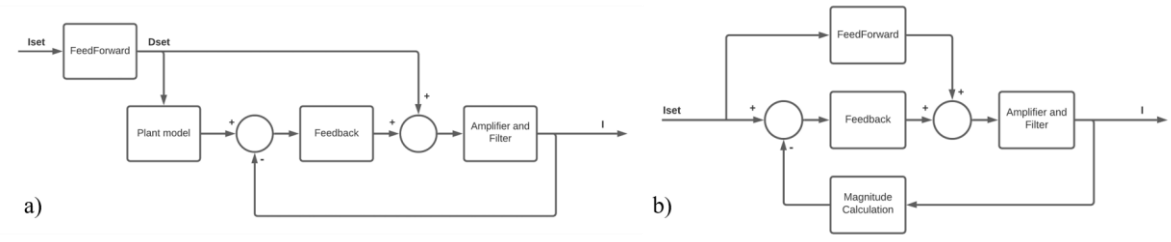

Figure 2. Schematic overview of the proposed control methods, (a) for the pulse-width modulation (PWM) with reference tracking and (b) for the fixed frequency modified sine wave operation with amplitude control.

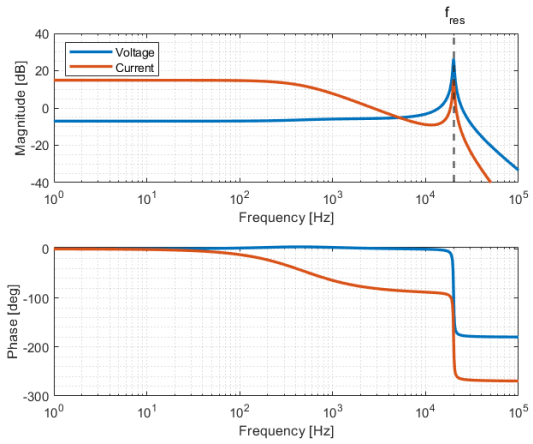

Figure 3. Frequency response function of input voltage to gradient insert voltage and current with the resonance frequency at 20 kHz.

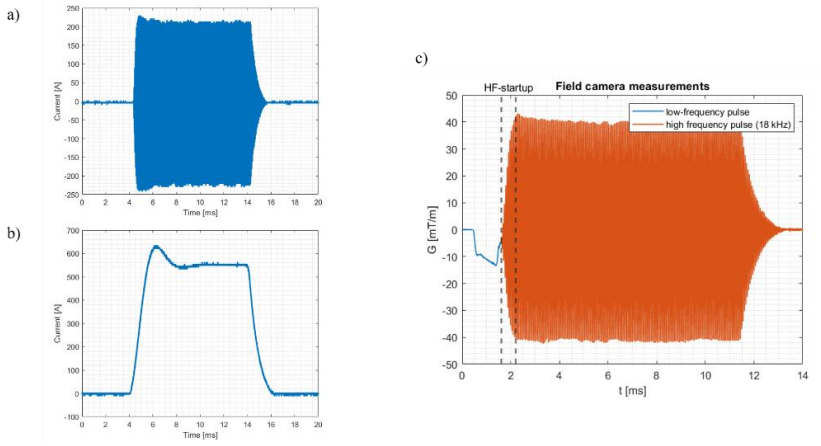

Figure 4. Amplifier current for (a) a diffusion gradient and (b) ultrasonic readout. (c) Field as measured by the field camera fora diffusion gradient followed by ultrasonic readout.

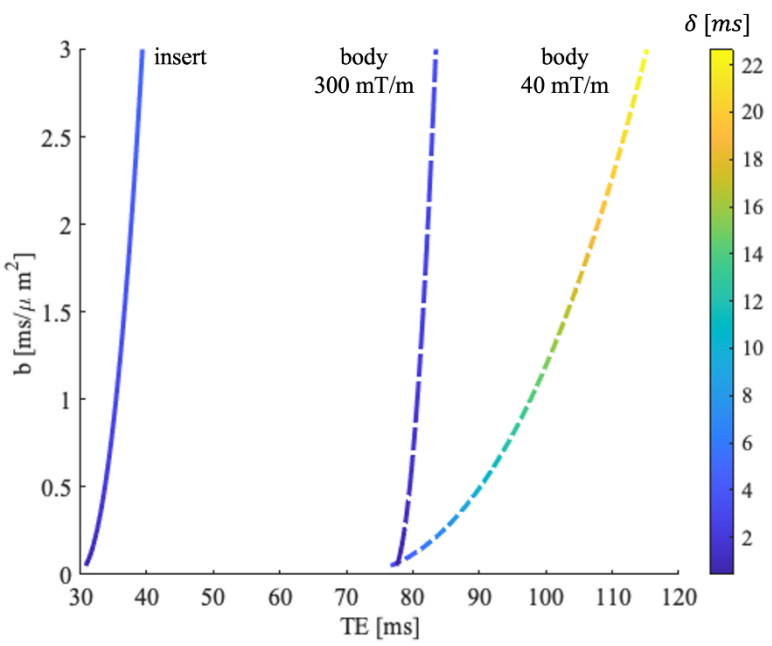

Figure 5. Diffusion weighting ($b = \gamma^2 G^2 \left(\delta^2 \left(\Delta - \frac{\delta}{3}\right) + \frac{\sigma^3}{30} - \left(\frac{\delta\sigma^2}{6}\right)\right)$, with G=diffusion pulse gradient strength, Δ=separation between pulses ,δ=pulse duration, σ=rise time) vs echo time (TE) for different setups. FOV=265 mm, resolution=2 mm, no partial Fourier. The insert leverages the 300 mT/m gradient strength and 1300 T/m/s slew rate for diffusion weighting, and a proof-of-principle ultrasonic readout during an EPI train with body gradients (dutation = 23 ms). The other setups have slew rate 83.3 T/m/s and 200 T/m/s, respectively, with convetional readout (duration = 63.5 ms).

Brain tissue segmentation on 3D-FLAIR weighted images in multiple sclerosis

S. Noteboom[1], M.D. Steenwijk[1], D.R. van Nederpelt[2], E.M.M. Strijbis[3], B. Moraal[2], F. Barkhof[2,4], J.J.G. Geurts[1], M.W.A. Caan[5], H.Vrenken[2], M.M. Schoonheim[1]

Departments of [1]Anatomy and Neurosciences, [2]Radiology and Nuclear Medicine and [3]Neurology, MS Center Amsterdam, Amsterdam Neuroscience, Amsterdam UMC, Vrije Universiteit Amsterdam, Amsterdam, The Netherlands, [4]Institutes of Neurology and Healthcare Engineering, UCL London, London, UK, [5]Department of Biomedical Engineering & Physics, Amsterdam UMC, location AMC, The Netherlands

Synopsis: Conventional brain segmentation approaches typically require high resolution 3D-T1 weighted images, which are often unavailable in clinical multiple sclerosis (MS) protocols. Recently, SynthSeg was released which allows 3D-FLAIR to be used for segmentations. This study compared segmentation on 3D-FLAIR with SynthSeg to segmentation performance in the same patients on 3D-T1 (SynthSeg, FastSurfer and SAMSEG). Brain segmentation was performed on 100 patients with 3D-T1 and 3D-FLAIR images from research and clinical datasets. ICC results showed good comparability for brain tissue, ventricle and grey matter assessments in research data. In clinical data only good comparability was found for ventricle segmentation.

Purpose: Accelerated brain tissue loss occurs from the earliest stages in multiple sclerosis (MS) and is associated with disability and cognitive impairment[1]. Brain volumetric measurements on MRI provide important imaging markers for disease progression and evaluating therapeutic effects[2]. To date, these imaging markers are primarily used as outcome measures in research and clinical trials. Clinical protocols commonly focus on 3D-FLAIR over 3D-T1 imaging, while most segmentation methods are only compatible with the latter[3]. To overcome this issue, new segmentation approaches have been developed that work on other MRI contrasts and lower resolutions. The recently developed convolutional neural network (CNN)-based segmentation software SynthSeg showed promising results in brain tissue segmentation of contrasts other than 3D-T1, but performance on 3D-FLAIR remains to be validated[4]. The aim of this study was to investigate agreement between 3D-T1 weighted brain volumetrics and SynthSeg-based volumetrics on 3D-FLAIR.

Methods: To evaluate the agreement of brain volumetric measurements on 3D-T1 and 3D-FLAIR images, 100 MRI examinations from 100 MS patients were selected. MRI data were acquired on two 1.5 T systems (Siemens Magnetom Sola, Siemens Avanto) and three 3.0 T systems (Siemens Magnetom Vida, GE Discovery MR750, GE Signa HDxT). From each scanner, 20 MRI examinations were included. The dataset contained both research and clinical datasets. Research imaging protocols contained a 3D-T1 weighted sequence (FSPGR) without contrast and 3D-T2 weighted FLAIR sequence. Clinical imaging protocols contained a 3D-T1 weighted sequence with or without contrast (T1 SPACE FS, T1 FLASH) and a 3D-T2 weighted FLAIR sequence. Segmentation was performed on 3D-T1 weighted images using FastSurfer, SAMSEG (cross-sectional pipeline for MS patients) and SynthSeg.4-6 3D-FLAIR weighted images were segmented with SynthSeg only. Brain, ventricular, cortical grey matter (GM), total deep grey matter (DGM) and thalamic volumes were compared between 3D-T1 and 3D-FLAIR based segmentations with calculation of the intraclass correlation coefficient (ICC; two way-mixed model, absolute agreement). Thalamic volume was assessed in addition to DGM given its known strong clinical predictive value in MS.7 Analyses were performed separately on the research data (n=40, GE scanners) and the clinical data (n=60, Siemens scanners). An example of a research and a clinical MRI exam with their corresponding segmentations are shown in **Figure 1**.

Results: In the research data, good (ICC>0.8) agreement was found between 3D-FLAIR segmentation and all 3D-T1 segmentations for most assessed brain structures (**Table 1**). Only poor agreement was found for SAMSEG on brain and thalamic volumes. In clinical data, ICC calculations showed good agreement between SynthSeg on 3D-FLAIR and SynthSeg on 3D-T1 for all measures, i.e. brain, ventricle, cortex, deep grey matter and thalamic volumes (**Table 1**). However, agreement between SynthSeg on 3D-FLAIR and 3D-T1-based FastSurfer and SAMSEG segmentation was poor for cortical and deep grey matter volumes. FastSurfer and SAMSEG on 3D-T1 displayed lower volumes of these structures compared to the 3D-Flair segmentation (**Figure 2**). Total brain volume agreement for FastSurfer with SynthSeg on 3D-Flair was good, but poor for SAMSEG. Only ventricular volumes were highly comparable between methods in the clinical dataset. FastSurfer missed parts of the brain in some cases with poor grey/white matter contrast, an example is shown in **Figure 3**.

Discussion: In this study, SynthSeg was used to determine volumetric measurements on 3D-FLAIR images, which were compared to 3D-T1 measurements using three automated segmentation approaches. SynthSeg achieved high agreement between 3D-T1 and 3D-FLAIR based segmentation in both research and clinical datasets. However, specific variations in agreement were observed, showing especially a lower agreement with SAMSEG. The segmentations of FastSurfer and SAMSEG may not have been the best reference in the clinical dataset, since these methods typically require high quality images with sufficient grey matter/white matter contrast, which might not always be the case for the 3D-T1 in clinical protocols. In the 3D-T1 and 3D-FLAIR images from research protocols, a high agreement was found between 3D-T1 segmentations (FastSurfer and SynthSeg) and SynthSeg 3D-FLAIR segmentation for all structures, while SAMSEG showed poorer agreement. Therefore, 3D-FLAIR segmentation with SynthSeg is a promising approach for volumetric measurements in MS patients, but further validation is required.

Conclusion: Brain, cortical, ventricular and deep grey matter volume assessments on 3D-FLAIR weighted images with SynthSeg show good agreement to 3D-T1 segmentation with FastSurfer and SynthSeg in high quality research data. In clinical data only ventricular volume could be reliably measured on 3D-FLAIR weighted images in MS patients. Future studies should validate this finding to enable FLAIR-based volumetric measurements in clinically acquired MRI data.

References

1. Roosendaal SD, Bendfeldt K, Vrenken H, et al. Grey matter volume in a large cohort of MS patients: relation to MRI parameters and disability. Multiple Sclerosis Journal 2011;17:1098-1106.

2. De Stefano N, Airas L, Grigoriadis N, et al. Clinical relevance of brain volume measures in multiple sclerosis. CNS drugs 2014;28:147-156.

3. Rocca MA, Battaglini M, Benedict RH, et al. Brain MRI atrophy quantification in MS: from methods to clinical application. Neurology 2017;88:403-413.

4. Billot B, Greve DN, Puonti O, et al. SynthSeg: Domain Randomisation for Segmentation of Brain MRI Scans of any Contrast and Resolution. ArXiv 2021;abs/2107.09559.

5. Cerri S, Puonti O, Meier DS, et al. A contrast-adaptive method for simultaneous whole-brain and lesion segmentation in multiple sclerosis. NeuroImage 2021;225:117471.

6. Henschel L, Conjeti S, Estrada S, Diers K, Fischl B, Reuter M. Fastsurfer-a fast and accurate deep learning based neuroimaging pipeline. NeuroImage 2020;219:117012.

7. Eshaghi A, Prados F, Brownlee WJ, et al. Deep gray matter volume loss drives disability worsening in multiple sclerosis. Annals of neurology 2018;83:210-222.

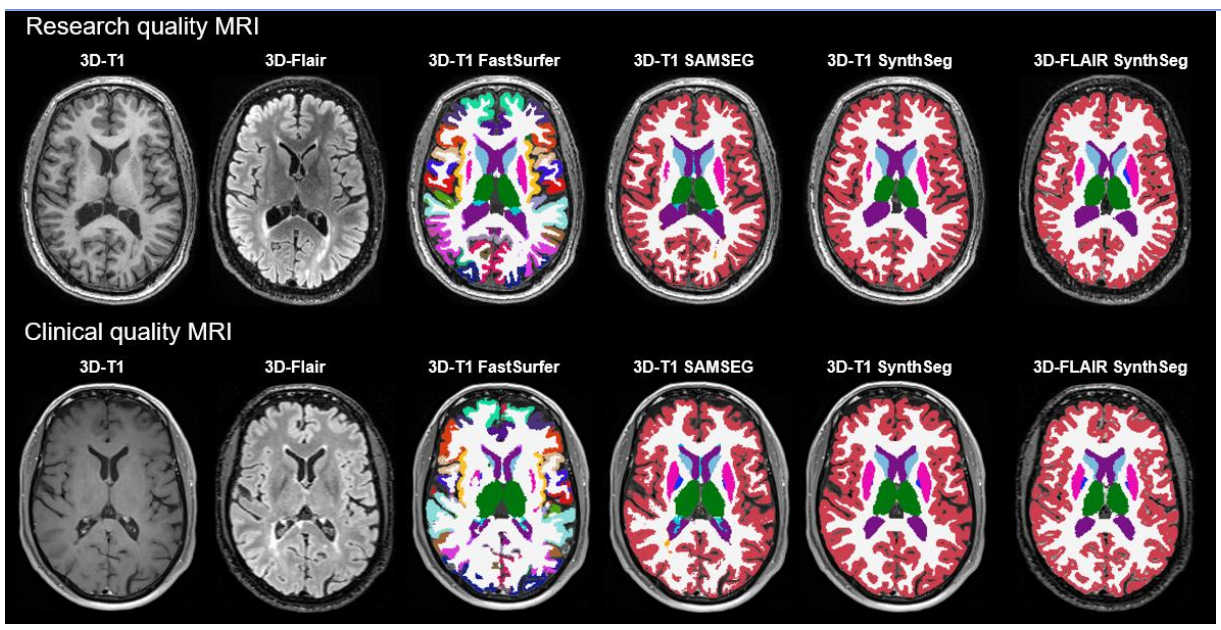

Figure 1. Example of brain segmentation on research and clinical quality MRI with various automated segmentation approaches.

	Research data (n=40)					**Clinical data (n=60)**				
	ICC SynthSeg 3D-FLAIR					***ICC SynthSeg 3D-FLAIR***				
Reference	**Brain**	**Ventricle**	**Cortex**	**DGM**	**Thalamus**	**Brain**	**Ventricle**	**Cortex**	**DGM**	**Thalamus**
FastSurfer 3D-T1	0.952	0.989	0.832	0.862	0.867	0.909	0.939	0.134	0.495	0.772
SAMSEG 3D-T1	0.733	0.883	0.921	0.873	0.581	0.721	0.956	0.579	0.552	0.552
SynthSeg 3D-T1	0.994	0.988	0.800	0.959	0.935	0.969	0.996	0.897	0.985	0.978

Table 1. Absolute agreement (ICC) between 3D-FLAIR and 3D-T1 based volumes of brain, ventricles, cortex, deep grey matter (DGM) and thalamus.

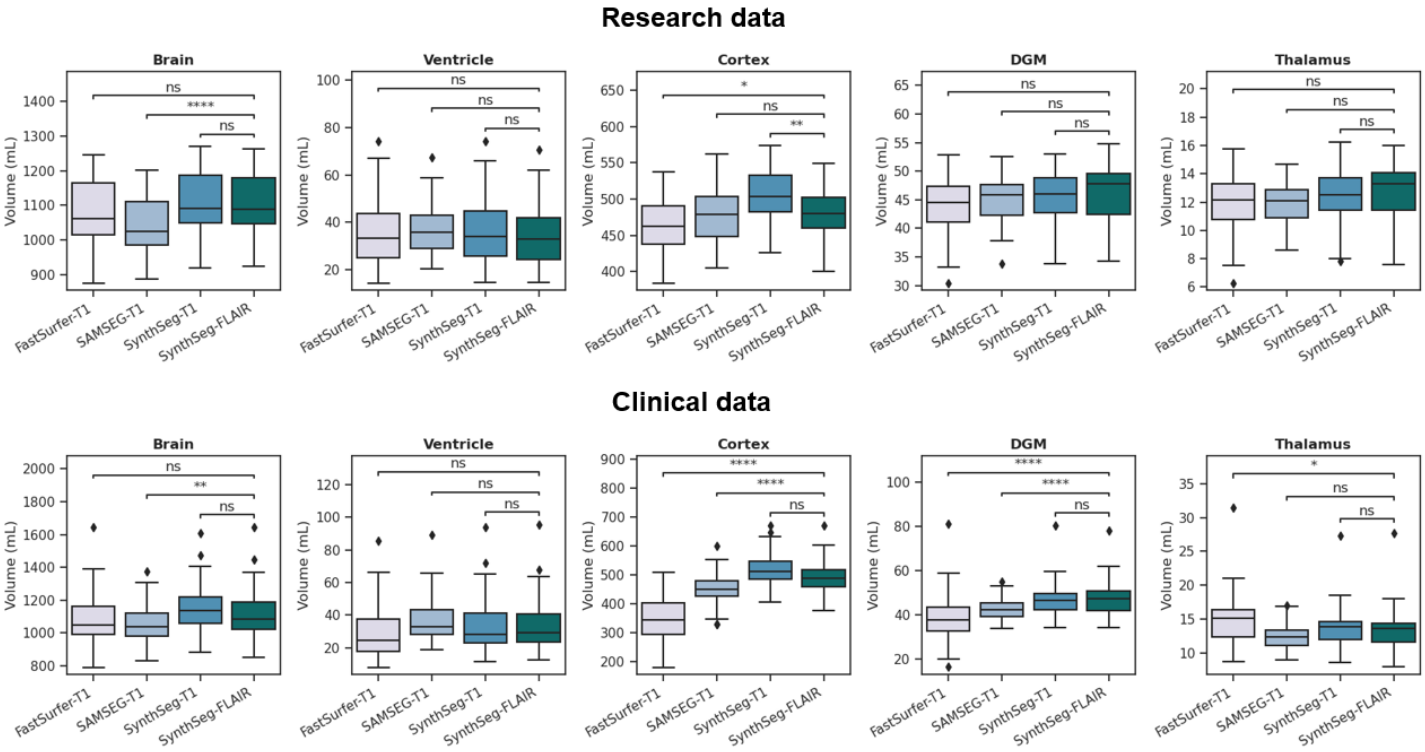

Figure 2. Volumes of brain, ventricle, cortex, DGM and Thalamus for the four assessed segmentation methods. Paired t-tests SynthSeg on 3D-FLAIR vs. other methods: ns = not significant, *p<0.05, **p<0.01, ***p<0.001, ****p<0.0001, Bonferroni corrected.

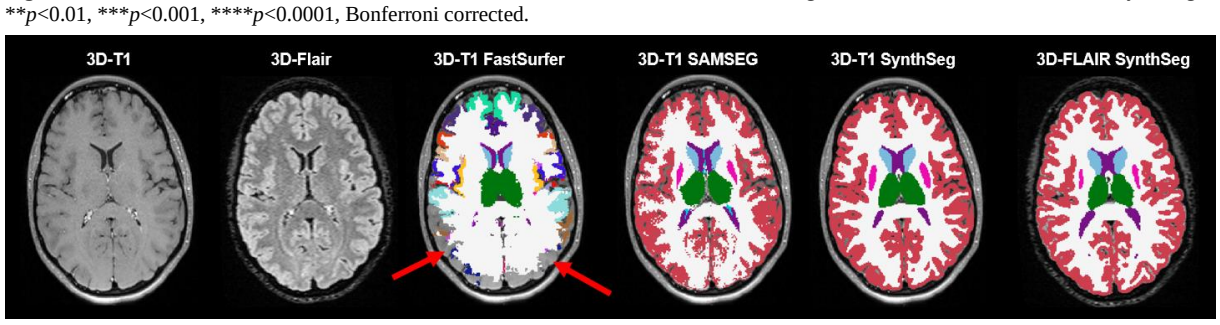

Figure 3. Example of brain segmentation on clinical MRI data where FastSurfer misses part of the brain and cortex.

7T metabolic MRI in focal epilepsy

S.M. Jacobs[1], Z. Shams[1], E.C. Wiegers[1], J.P. Wijnen[1], D.W. Klomp[1], E. Versteeg[1], J.C.W. Siero[1,2], A. Mühlebner[3,4], W. Van Hecke[3], P. van Eijsden[5], P.A. Robe[5], M. Zijlmans[5,6], A.G. van der Kolk[1,7]

1. Department of Radiology and Nuclear Medicine, University Medical Center Utrecht, Utrecht, the Netherlands; 2. Spinoza Centre for Neuroimaging Amsterdam, Amsterdam, the Netherlands; 3. Department of Pathology, University Medical Center Utrecht, Utrecht, the Netherlands; 4. Department of Pathology, Amsterdam University Medical Center, location AMC, Amsterdam, the Netherlands; 5. UMC Utrecht Brain Center, Department of Neurology and Neurosurgery, University Medical Center Utrecht, Utrecht, Netherlands; 6. Stichting Epilepsie Instellingen Nederland (SEIN), Heemstede, the Netherlands; 7. Department of Radiology, Radboud University Medical Center, Nijmegen, the Netherlands.

Synopsis: In this clinical study, we combined different (metabolic) MRI sequences at 7T to characterize focal epileptogenic lesions, and uncover potential metabolic markers that could help identifying the culprit lesion in MRI-negative epilepsy patients. Using QSM, we observed increased iron deposition in the affected hippocampus of two HS patients that was not found in the contralateral hippocampus, neither in a suspected HS patient with no abnormal tissue, nor in matched healthy volunteers. No increased iron deposition was found in patients with FCD or matched healthy volunteers. No significantly different metabolite ratios between patients and healthy volunteers were found using SV ^{1}H-MRS.

Introduction: Epilepsy surgery is an effective therapy for drug-resistant epilepsy[1,2], and surgery is more successful in patients with epileptogenic lesions detected with structural MRI. About 20-30% of patients with focal epilepsy show no structural abnormalities, i.e., are MRI-negative[3]. Surgery can be effective if an epileptic focus can be defined in another way. Metabolic MRI can visualize underlying metabolic pathways associated with disease, especially when applied at ultrahigh field with its increased SNR and spectral dispersion to help us identify epileptogenic lesions that cannot be detected with structural MRI.

Several potential metabolic markers for epileptogenic lesions that can be imaged with metabolic MRI have been reported in recent years. For instance, glutamate, associated with mitochondrial and metabolic injury inducing seizures in patients with epilepsy, and locally increased concentrations have been found in MRI-negative epileptogenic lesions.[4] Also iron accumulation, a potential marker of oxidative stress, has been found in hippocampal sclerosis (HS) and focal cortical dysplasia (FCD) using histopathological staining.[5] The metabolic phenotype – or 'profile' – of epileptogenic lesions will likely consist of a combination of metabolites, some of which may not even have been found using in vivo imaging techniques.

In this preliminary clinical trial, we aim to find (combinations of) metabolic markers of epileptogenic lesions that can be detected with 7T metabolic MRI, using glutamate-CEST (GluCEST), quantitative susceptibility mapping (QSM) and single-voxel (SV) ^{1}H MRS, and validate these with histopathology. This abstract discusses the imaging results of QSM and ^{1}H MRS in the first five patients compared to five healthy volunteers.

Methods: Five patients (aged 23-48 years; three females) and five healthy volunteers (aged 24-27 years; two females) were included. All patients were diagnosed with focal epilepsy with an epileptogenic lesion on structural MRI and/or positron emission tomography and were scheduled for surgical treatment. This clinical trial was approved by our IRB; all participants gave written informed consent.

MRI examination

All participants underwent one 7T (Philips, Best, the Netherlands) MRI examination with a 32-channel head coil (Nova Medical) the day prior to their surgery. Next to QSM and SV ^{1}H MRS (sLASER), a high-resolution T_1-weighted sequence was acquired for FOV planning; see **Table 1** for acquisition parameters. The FOV in healthy volunteers was matched with the lesion location in the patients; for MRS, a TE of 36 ms was used in HS patients (N=3) and matched volunteers, and a TE of 110 ms was used in the FCD patients (N=2) and matched volunteers. Final diagnosis was based on histopathology.

Post-processing & data analysis

QSM data was post-processed with the SEPIA tool using Laplacian-based phase unwrapping, variable-kernel SHARP background field removal and the iLSQR method for computing the susceptibility maps. MRS data was analyzed using LCModel with a simulated basis set.[6] No correction for T_1 or T_2 relaxation times was applied. Metabolite ratios with respect to total creatine, with a Cramér Rao Lower Bound of <20% for N≥2 per different TE were reported (**Figure 2**; **Table 2**). QSM images were analyzed qualitatively for differences in iron deposition; a Wilcoxon-signed rank test was used to compare differences in metabolite ratios between epileptogenic lesions and healthy brain tissue.

Results:

QSM

The two patients with histopathologically confirmed HS showed increased iron deposition in the affected hippocampus, while the third HS patient did not show abnormal iron deposition in either hippocampus (**Figure 1**); this patient however turned out not to have abnormal tissue. None of the matched healthy volunteers nor the patients with FCD showed increased iron deposition in either hippocampus or respective lesions of interest.

^{1}H MRS

Some differences in metabolite ratios between HS and the contralateral hippocampus in the two histopathologically confirmed HS patients could be seen, though not statistically evident. We also found no evident differences in metabolite ratios between HS patients and healthy volunteers. This same result was found in the FCD patients and their matched healthy volunteers.

Discussion & conclusion: In this clinical study, we combined different (metabolic) MRI sequences at 7T to characterize focal epileptogenic lesions, and uncover potential metabolic markers that could help identifying the culprit lesion in MRI-negative epilepsy patients. Using QSM, we observed increased iron deposition in the affected hippocampus of two HS patients that was not found in the contralateral hippocampus, nor in a patient with suspected HS with no abnormal tissue, nor in matched healthy volunteers. These results support previous findings of increased iron deposition using susceptibility-weighted imaging and histopathology in mesial temporal lobe epilepsy (TLE)[5,7]; however, contrary to previous histopathology-based literature, no increased iron deposition was found in patients with FCD. Two studies at 7T using MRS in epilepsy patients showed variable metabolite ratios: both increased (FCD) and 'normal' (TLE) GABA levels were found, and no differences in glutathione and glutamate/glutamine.[8,9] The same lack of statistically significantly different metabolite ratios was found in our five patients; however, our very small sample size precludes any final conclusions. Ongoing patient inclusion will increase our sample size, allowing for more robust statistical analyses of our QSM and MRS data. Combining these with planned GluCEST data acquisition in the same patients could lead to an even stronger profiling of the metabolic phenotype of epileptogenic lesions.

References:

1. Lamberink HJ, Otte WM, Blümcke I, et al. European Epilepsy Brain Bank writing group; study group; European Reference Network EpiCARE. Seizure outcome and use of antiepileptic drugs after epilepsy surgery according to histopathological diagnosis: a retrospective multicentre cohort study. Lancet Neurol. 2020 Sep;19(9):748-757.

2. Dwivedi R, Ramanujam B, Chandra PS, et al. Surgery for Drug-Resistant Epilepsy in Children. N Engl J Med. 2017 Oct 26;377(17):1639-1647.

3. Nguyen DK, Mbacfou MT, Nguyen DB, et al. Prevalence of nonlesional focal epilepsy in an adult epilepsy clinic. Can J Neurol Sci 2013; 40: 198–202.

4. Davis KA, Nanga RPR, Das S, et al. Glutamate imaging (GluCEST) lateralizes epileptic foci in non-lesional temporal lobe epilepsy. Sci Transl Med 2015;7:309ra161.

5. Zimmer TS, Ciriminna G, Arena A, et al. Chronic activation of anti-oxidant pathways and iron accumulation in epileptogenic malformations. Neuropathol Appl Neurobiol. 2019;10.1111/nan.12596.

6. Shams Z, van der Kemp WJM, Emir U, et al. Comparison of 2-Hydroxyglutarate Detection With sLASER and MEGA-sLASER at 7T. Front Neurol. 2021 Sep 7;12:718423.

7. Zhang Z, Liao W, Bernhardt B, et al. Brain iron redistribution in mesial temporal lobe epilepsy: a susceptibility-weighted magnetic resonance imaging study. BMC Neurosci. 2014;15:117. Published 2014 Nov 21.

8. Gong T, Liu Y, Chen Y, et al. Focal cortical dysplasia in epilepsy is associated with GABA increase. Neuroimage Clin. 2021;31:102763.

9. Gonen OM, Moffat BA, Desmond PM, et al. Seven-tesla quantitative magnetic resonance spectroscopy of glutamate, γ-aminobutyric acid, and glutathione in the posterior cingulate cortex/precuneus in patients with epilepsy. Epilepsia. 2020 Dec;61(12):2785-2794.

Acknowledgments / Funding Information: We would like to thank neurosurgeons dr. P.C. van Rijen, drs. P.H. Gosselaar and nurse specialist Janine Ophorst-van Eck of the University Medical Center Utrecht for their contribution to this study.

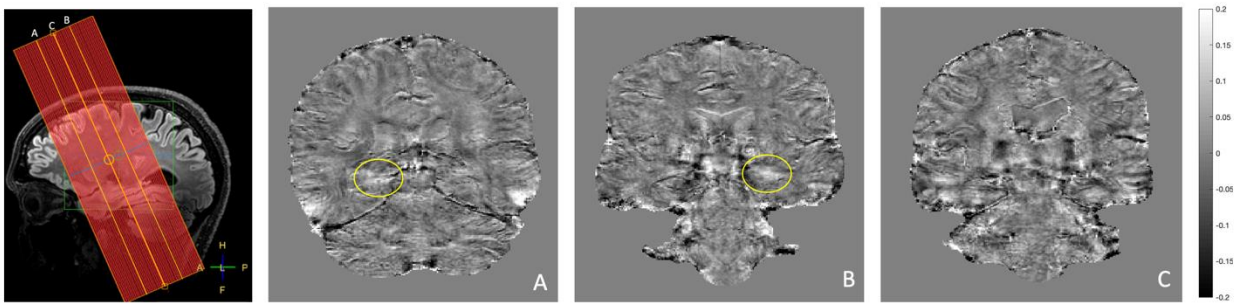

Figure 1: QSM images of all three patients with suspected HS, slice location indicated by yellow lines; HS patients 1 and 2 were confirmed with histopathology and show iron deposition in the right hippocampus tail (A) and the left hippocampus head (B), respectively, indicated by yellow circle, while the 3rd patient shows no difference / abnormal iron deposition between hippocampi (C).

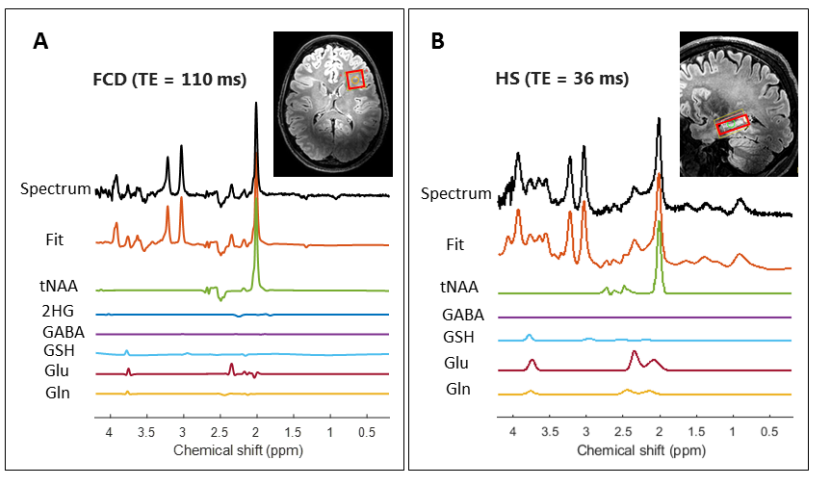

Figure 2: Example of fitted spectra of patient with HS (A) and patient with FCD (B).

Sequence	Scan time (min)	TE (ms)	TR (ms)	NSA	FOV (mm)	Recon voxel size (mm³)	Flip angle	Water suppression
T_1-weighted	05:02	Shortest (2.2)	6.2	1	240x240x160	0.5	5	-
QSM*	05:31	4.3/5/29 (TE_1/ΔTE/TE_6)	43		256x224x80	0.8	15	
SV ^{1}H-MRS sLASER	05:35	36 110 ms	5000	64	Differed per subject		-	VAPOR (300 Hz)

Table 1: Acquisition parameters; * = flow compensated gradient echo sequence.

Diagnosis	Age (y)	Sex	Histopathology	L/R	Asp	Glx	GSH	mI+Gly	tCho	tNAA	Tau	Scyllo
HS (right)	48	M	HS type I, Wyler grade 4	L	0.464 (16%)	1.358 (5%)	0.134 (13%)	1.109 (3%)		1.158 (2%)	0.402 (7%)	8.9E-02 (8%)
				R	0.795 (12%)	1.413 (5%)	0.198 (10%)	1.306 (2%)		1.069 (2%)	0.394 (8%)	0.107 (7%)
HS (left)	28	F	HS type I, Wyler grade 3	L	0.444 (19%)	1.758 (3%)	0.218 (7%)	1.270 (2%)		1.283 (2%)	0.363 (7%)	5.9E-02 (12%)
				R	4.141 (12%)	1.735 (4%)	0.118 (14%)	1.124 (2%)		1.376 (1%)	0.438 (6%)	7.9E-02 (8%)
HS (right)	32	M	Negative	L	0.692 (16%)	1.661 (6%)	0.172 (16%)	1.283 (3%)		1.174 (3%)	0.430 (10%)	0.102 (11%)
Healthy volunteer (matched for HS)	24	F	N/A	L	0.738 (15%)	1.681 (4%)	0.234 (9%)	1.150 (3%)	N/A	1.168 (2%)	0.266 (13%)	5.9E-02 (16%)
				R	0.626 (14%)	1.586 (4%)	0.123 (14%)	1.147 (3%)		1.293 (2%)	0.330 (9%)	5.5E-02 (14%)
Healthy volunteer (matched for HS)	24	M	N/A	L	0.296 (30%)	1.697 (5%)	0.155 (16%)	1.182 (3%)		1.204 (2%)	0.571 (6%)	8.6E-02 (11%)
				R	0.476 (15%)	1.640 (4%)	0.152 (10%)	1.167 (2%)		1.230 (1%)	0.454 (5%)	5.3E-02 (11%)
Healthy volunteer (matched for HS)	26	M	N/A	L	0.332 (25%)	1.764 (4%)	0.129 (16%)	1.042 (3%)		1.215 (2%)	0.505 (6%)	9.2E-02 (9%)
				R	0.834 (13%)	1.871 (5%)	0.225 (11%)	1.486 (3%)		1.312 (2%)	0.460 (8%)	7.6E-02 (12%)
FCD (left)*	26	F	FCD type IIb	L		1.614 (5%)		1.124 (9%)	0.674 (4%)	2.828 (4%)	8.7E-02 (41%)	
FCD (right)*	23	F	FCD type IIb	L		1.101 (4%)		0.531 (4%)	0.630 (3%)	4.357 (2%)	0.108 (24%)	
				R		1.058 (7%)		0.631 (4%)	0.748 (4%)	3.736 (2%)	0.164 (15%)	
Healthy volunteer (matched for FCD)*	27	M	N/A	L	N/A	1.526 (5%)	N/A	0.694 (9%)	0.774 (2%)	4.233 (2%)	0.135 (16%)	N/A
				R		1.322 (6%)		0.678 (4%)	0.761 (2%)	3.805 (2%)	0.162 (15%)	
Healthy volunteer (matched for FCD)*	25	F	N/A	L		1.280 (5%)		0.775 (3%)	0.643 (2%)	3.576 (2%)	0.155 (11%)	
				R		1.210 (6%)		0.850 (3%)	0.626 (2%)	3.713 (2%)	0.153 (15%)	

Table 2: Fitted metabolite ratios to total creatine with Cramér Rao Lower Bounds <20% for N≥2 per different echo time. * = echo time of 110 ms; Asp = aspartate; tCr = total creatine; Gly = glycine; Glx = glutamate + glutamine; GSH = glutathione; mI = myo-inositol; tCho = total choline; NAA = n-acetylaspartate; Tau = taurine ; Scyllo = scyllo-inositol.

CBV-sensitive layer-fMRI in the human auditory cortex at 7T: Challenges and capabilities

L.K. Faes[1], O.F. Gulban[1,2], B.A. Poser[1], F. De Martino[1], L. Huber[1]
[1]Department of Cognitive Neuroscience, Maastricht University, Maastricht, The Netherlands; [2]Brain Innovation, Maastricht, The Netherlands

Synopsis: Laminar-specific fMRI with CBV-sensitive VASO is valuable for neuroscientific questions on hierarchical information processing.
While VASO fMRI has already proven its utility in other brain areas, it has not yet been successfully applied in the auditory cortex due to several additional technical challenges in this region. Here, we explore multiple sequences and their effectiveness to mitigate these challenges. Our purpose is to develop an experimental setup that future neuroscientific studies can be built on. Ultimately, we found a stable parameter set for the usage of layer-fMRI VASO in the auditory cortex and validated it in a group of participants.

Purpose: Laminar-specific fMRI with blood volume sensitive VASO methods allows neuroscientists to address research questions of hierarchical information processing across brain areas without unwanted large draining vein effects.
While layer-fMRI VASO has been used for visual and sensory-motor areas before, its application in the auditory system is challenged by many sequence constraints (Fig. 1):

I. Inflow contaminations by non-nulled blood;
II. Limited B_1^+-efficiency for the inversion of z-magnetization;
III. Physiological noise variation across segments in the common VASO 3D-EPI acquisitions;
IV. Evolution of non-steady-state magnetization in inversion recovery sequences with silent gaps;
V. Generally low sensitivity compared to GE-BOLD, due to the lack of signal amplification at the large draining veins.

The purpose of the study was to explore a wide parameter space of advanced sequence approaches that can mitigate these challenges. We sought to find a good parameter set for performing layer-fMRI experiments in the auditory cortex. The sequence approaches that we investigated include:

1. 2D-EPI, 3D-EPI[1], and MB-EPI-VASO[2];
2. Multi-shot and single-shot schemes for GRAPPA auto-calibration signal data[3,4];
3. Multiple orientations (coronal vs. sagittal) and timing (faster and slower than cardiac cycle);
4. Advanced adiabatic inversion pulses with B_1^+-insensitive adjustable inversion efficiency[5] and non-adiabatic M_z-'rest' pulses[6].

Methods: Scanning was performed on a MAGNETOM "classic" 7T scanner (Siemens Healthineers) with MRI-compatible earbuds (Sensimetrics) for presentations of sounds in the scanner. For simultaneous acquisition of BOLD and VASO, an SS-SI-VASO sequence was used[7,8].
A total of 21.5 hours of scanning was done:

- Six hours of phantom scanning was done to validate the correct implementation of the above mentioned sequence approaches.
- 7.5 hours of in-vivo scanning across 4 sessions was performed to find optimal parameters (Fig. 1).
- Four two-hour sessions were performed to validate the stability of the chosen sequence approach (Fig. 2) in experienced and in naive participants.

The spatial resolution was between 0.8-0.9 mm iso, with readout TRs of 0.77-1.70 s and inversion delays of 0.75-0.90 s, resulting in BOLD-VASO.
Functional runs of the chosen sequence consisted of 20 TRs without auditory stimulation, alternating with 20 TRs of sounds. Thirteen blocks were presented per run, resulting in a total duration of approximately 13 minutes per run. The sounds were described by the participants as "chipmunks from space" (task recording: https://youtu.be/TGX_Ulbv9wA). The scan protocol pdfs are available on Github (https://layerfmri.page.link/auditory_VASO_pdfs). We are happy to share the sequences used in this work via SIEMENS C2P. Data processing**:** Motion corrected (SPM) data were sorted by contrast and corrected for BOLD contamination (LayNii). Equi-volume layerification was performed with LN2_LAYERS[9]. Block design activation z-scores were quantified with FSL Feat and are presented as an overlay to the inherently T_1-weighted mean VASO images (Fig. 3-4).

Results and Discussion: During the first ten hours of scanning, we found that each and every one of the challenges in layer-fMRI VASO at the auditory cortex can be partially accounted for by means of advanced sequence approaches and FOV compromises. We tested the reproducibility of our findings with 2D and 3D acquisition protocols of BOLD and VASO by applying the identical sequence and task settings in the same volunteers in four additional two-hour sessions. We find that both acquisition approaches (2D and 3D) and contrasts (VASO and BOLD) reveal significant activation in the primary auditory cortex (Fig. 3). Layer-profiles of VASO have the largest activation in slightly deeper cortical depths compared to BOLD. In the BOLD data, the signal increases towards the superficial surface. The results are consistent across sessions and participants (Fig. 4).

Summary and Conclusion: While layer-fMRI VASO has become popular in many cortical areas, until now it has never been successfully applied in the human auditory cortex. This is in contrast to GE-BOLD readouts, which have been applied in the auditory cortex with success already 10, 11. Here, we described why VASO layer-fMRI is so challenging in this area and we present a combination of sequence approaches as well as a good parameter set for successful layer-fMRI VASO without venous biases in the auditory cortex. This study has built the groundwork that future neuroscience-focused application studies can be based on.

References:

1. Poser BA, Koopmans PJ, Witzel T, Wald LL, Barth M. Three dimensional echo-planar imaging at 7 tesla. *Neuroimage*. 2010;51(1):261-266. doi:10.1016/j.neuroimage.2010.01.108
2. Huber L, Ivanov D, Guidi M, et al. Functional cerebral blood volume mapping with simultaneous multi-slice acquisition. Neuroimage. 2016;125:1159-1168. doi:10.1016/j.neuroimage.2015.10.082
3. Polimeni JR, Bhat H, Witzel T, et al. Reducing sensitivity losses due to respiration and motion in accelerated echo planar imaging by reordering the autocalibration data acquisition. Magn Reson Med. 2016;75(2):665-679. doi:10.1002/mrm.25628
4. Talagala SL, Sarlls JE, Liu S, Inati SJ. Improvement of temporal signal-to-noise ratio of GRAPPA accelerated echo planar imaging using a FLASH based calibration scan. Magn Reson Med. 2016;75(6):2362-2371. doi:10.1002/mrm.25846
5. Norris DG. Adiabatic radiofrequency pulse forms in biomedical nuclear magnetic resonance. *Concepts Magn Reson Part B Magn Reson Eng*. 2002;14(2):89-101. doi:10.1002/cmr.10007
6. Lu H. Magnetization "reset" for non-steady-state blood spins in Vascular-Space-Occupancy (VASO) fMRI. *Proc 16th Annu Meet ISMRM*. 2008;16(1):2008. http://cds.ismrm.org/ismrm-2008/files/00406.pdf
7. Lu H, Golay X, Pekar JJ, van Zijl PCM. Functional magnetic resonance imaging based on changes in vascular space occupancy. *Magn Reson Med*. 2003;50:263-274. doi:10.1002/mrm.10519
8. Huber L, Ivanov I, Krieger SN, Streicher MN, Mildner T, Poser BA, Moller HE, Turner R. Slab-selective, BOLD-corrected VASO at 7 Tesla provides measures of cerebral blood volume reactivity with high signal-to-noise ratio. *Magnetic resonance in medicine*, 2014;72.1: 137-148.
9. Huber L, Poser BA, Bandettini PA, et al. LAYNII: A software suite for layer-fMRI. *Neuroimage*. 2021;237:118091. doi:10.1016/j.neuroimage.2021.118091
10. De Martino F, Moerel M, Ugurbil K, Goebel R, Yacoub E, Formisano E. Frequency preference and attention effects across cortical depths in the human primary auditory cortex. *Proc Natl Acad Sci*. 2015;112(52):16036-16041. doi:10.1073/pnas.1507552112
11. Moerel M, De Martino F, Kemper VG, et al. Sensitivity and specificity considerations for fMRI encoding, decoding, and mapping of auditory cortex at ultra-high field. *Neuroimage*. 2018;164(March):18-31. doi:10.1016/j.neuroimage.2017.03.063

the principles expressed in the Declaration of Helsinki.

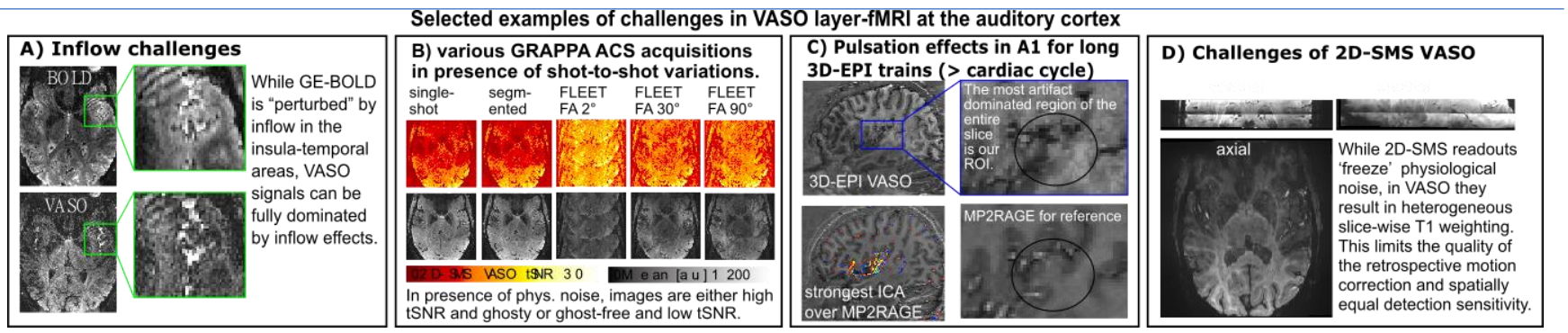

Figure 1: Selected challenges of performing layer-fMRI VASO in the auditory cortex at 7T:
The blood vessels close to the auditory cortex are challenging on so many levels. A) They result in dominating inflow contaminations, B) they impose physiological noise within the GRAPPA auto calibration signal, C) they evoke signal changes that are in the order of magnitude as structural and functional VASO contrast, D) common approaches that would minimize these effects impose other VASO-related problems.

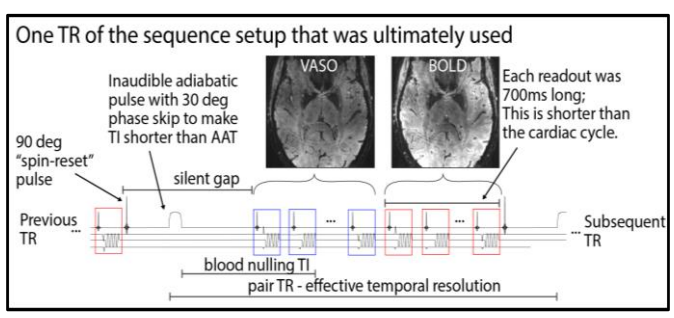

Figure 2: Schematic sequence diagram and the adaptation for VASO application in the auditory cortex at 7T:
The sequence setup that was found to be most suitable is an axial acquisition with spin-reset pulses at the end of each readout. A TR-FOCI pulse with phase skip was used for efficient inversion of a single channel head-Tx NOVA coil. Readout blocks were kept as short as possible at the cost of coverage. The inherent silent sequence dead times in VASO were exploited for auditory task presentation.

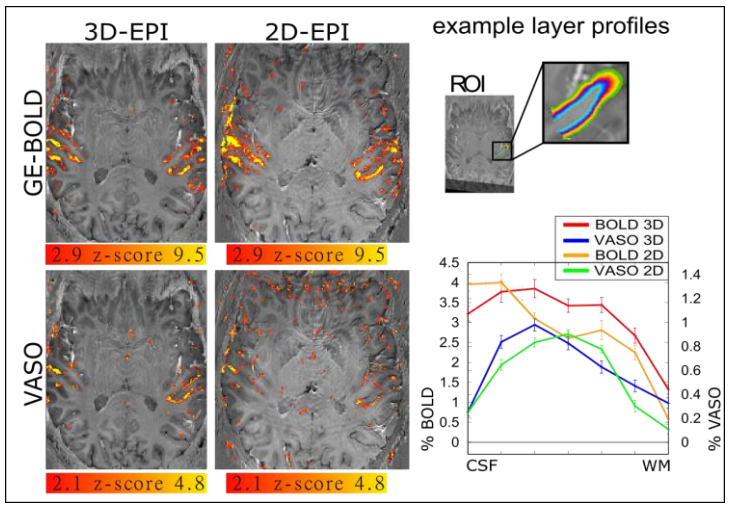

Figure 3: Representative activation results
Activation maps of GE-BOLD and VASO for 3D-EPI and 2D-EPI (no SMS). We find that the fast protocol with readout durations of 700ms and a thin slab with 12 slices at 0.9mm iso can detect significant activation changes. For BOLD, z-scores are generally larger with 2D-EPI in the activation maps, while for VASO, z-scores are larger for 3D-EPI. As expected, layer-profiles for GE-BOLD are slightly shifted towards the surface.

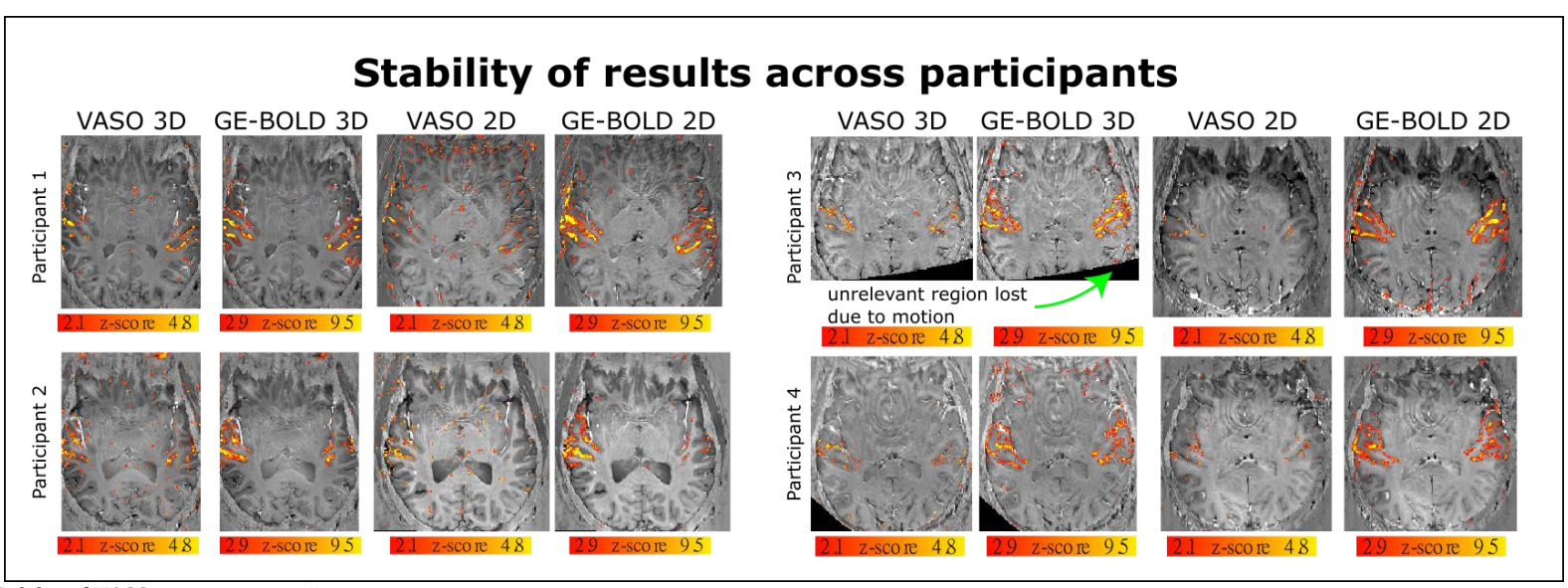

Figure 4: Stability of VASO activation across 4 participants
It can be seen that the sequence approaches investigated here provide enough sensitivity to provide layer-fMRI results in the auditory cortex. Two of the participants were naive to fMRI scanning and two of them were experienced fMRI participants. There is an indication that 3D-EPI provides more activation for VASO than 2D-EPI. And 2D-EPI provides more activation for BOLD than 3D-EPI. VASO is less sensitive than BOLD.

Accelerated respiratory-resolved 4D-MRI with separable spatio-temporal neural networks

M.L. Terpstra[1,2], M. Maspero[1,2], J.J.C. Verhoeff[1,2], C.A.T. van den Berg[1,2]

[1]Deparment of Radiotherapy, University Medical Center Utrecht, Utrecht, Netherlands; [2]Computational Imaging Group for MR Diagnostics & Therapy, University Medical Center Utrecht, Utrecht, Netherlands

Synopsis: Four-dimensional (4D) respiratory-resolved imaging is crucial for managing respiratory motion in radiotherapy, enabling irradiation of highly mobile tumours. However, acquiring high-quality 4D-MRI requires long acquisition (typically ≥5 minutes) and long iterative reconstructions, limiting treatment efficiency. Recently, deep learning has been proposed to accelerate undersampled MRI reconstruction. However, it has not been established whether deep learning may reconstruct high-quality 4D-MRI from accelerated acquisitions. This work proposes a small deep learning model that exploits the spatio-temporal information present in 4D-MRI, allowing to split the reconstruction into two separated branches, enabling high-quality retrospectively-accelerated 4D-MRI acquired in ~60 seconds and reconstructed in 16 seconds.

Introduction:

Four-dimensional (4D) respiratory-resolved imaging is crucial for managing respiratory motion in radiotherapy, enabling accurate irradiation of highly mobile tumours[1], and facilitating treatment adaptation based on daily motion[2]. However, obtaining high-quality 4D-MRI requires long acquisition (typically ≥5 minutes) and long iterative reconstructions limiting treatment efficiency. Recently, deep learning (DL) has been proposed to accelerate undersampled MRI reconstruction[3], demonstrating its potential also for 4D-MRI[4]. However, it has not been established whether DL may reconstruct high-quality 4D-MRI from accelerated acquisitions. Reconstructing complete 4D-MRI volumes with a single model requires performing 4D convolutions, which is an expensive operation that may result in an overly large model, e.g., >100M trainable parameters. Training such large models requires specialized hardware and large training datasets while being prone to overfitting. Previous research[5,6,7] showed that separating spatial and temporal information is a powerful technique, leading to efficient DL architectures. We propose using a model that exploits the spatio-temporal information present in 4D-MRI, allowing to split the reconstruction into two separated branches. Also, we perform 2D convolutions rather than training a single model that performs 3D convolutions. Such models have few parameters, leading to low memory usage, fast inference, and low risk of overfitting. We investigate the performance of 2D+t models, studying whether they may enable high-quality accelerated 4D-MRI acquisition and reconstruction.

Materials and methods:

Data preparation: Twenty-seven patients with lung cancer included in an IRB-approved study were imaged in free-breathing during Gadolinium injection on a 1.5T MRI (MR-RT, Philips Healthcare) using a fat-suppressed golden-angle radial stack-of-stars T1-w GRE thorax MRI for approximately five minutes (resolution=2.2x2.2x3.5mm^3, FOV=350x350x270mm^3, slice direction=feet-head). K-space was retrospectively sorted in 10 respiratory bins based on the relative amplitude of the self-navigation signal present in radial k-space[8]. Complex XD-GRASP[9] reconstructions with total variation over the respiratory phases (λ=0.03) served as the target image. Accelerated complex NUFFT-adjoint images were reconstructed[10] by undersampling the sorted bins with acceleration factors R_{4D}=1, 2, 4, 8, and 10, simulating an acquisition of approximately T_{acq}=300, 150, 60, 30, and 25 seconds long, respectively. This corresponded to an undersampling factor per bin of $R_{Nyquist}$ = 4, 8, 16, 32, and 40, respectively. For evaluation purposes, we computed deformation vectors fields (DVFs) between every respiratory phase and the end-exhale state using a free-form deformation algorithm[11].

Model architecture: The proposed model will reconstruct a 2D+t respiratory-resolved volume y with n_p phases using a spatial and a temporal branch. The spatial branch learns a volume Ψ by performing $1\times c_x\times c_y$ complex convolutions, while the temporal branch learns a volume Ξ by performing $n_p\times 1\times 1$ complex convolutions. The 4D reconstruction is then achieved by learning $y_{t+1}=y_t+\Psi\Xi$ for every slice **(Figure 1)**. We implemented an iterative model[12] with residual connections between y_{t+1} and y_t, using four iterations to learn complex XD-GRASP reconstructed slices from complex NUFFT-reconstructed slices of 4D-MRI. Each iteration used a spatial and a temporal branch with five complex convolution layers, employing a cardioid non-linear activation function[13] (c_x=c_y=3). In total, the model has approximately 238,000 trainable parameters.

Training and experiments: Ten models with identical architectures were trained on axial and sagittal slices, one for every undersampling factor R_{4D}. Every model was trained on 17 patients, evaluated on five, and tested on five other patients. Models were optimized using the AdamW optimizer (lr=10^{-3}, weight-decay=10^{-4}) with a batch size of 3, minimizing the hybrid magnitude SSIM/⊥-Loss[14] for 20 epochs.

Evaluation: Models were evaluated on all patients in the test set using the magnitude SSIM of the full 4D reconstruction compared to the XD-GRASP reconstruction and the end-point error (EPE) of DVFs obtained with the free-form deformation against the XD-GRASP DVFs. Statistical significance ($p<0.05$) was established using a paired t-test.

Results and discussion:

The models were trained in ~6 hours using ~18GB memory, and inference took ~16 seconds for full 4D-MRI. Using the proposed deep learning model significantly improved image quality **(Figure 2)**, demonstrating that spatio-temporally decomposed models can effectively reconstruct high-quality 4D-MRI. Compared to XD-GRASP, the average SSIM of non-accelerated 4D-MRI (R_{4D}=1) increased from 0.82±0.01 ($\mu\pm\sigma$) using NUFFT reconstructions to 0.92±0.02 with our model. Image quality is significantly increased for accelerated reconstructions **(Figure 3)**. For R_{4D}=4, the acquisition time decreased to ~60s, while the mean EPE decreased from 1.80±0.92 mm for NUFFT reconstructions to 0.85±0.43 mm (**Figure 4**), although blurring can be observed in the DL reconstructions. Using R_{4D}>4 reduces reconstructed image quality and shows decreased motion magnitude. However, considering an EPE<1mm as clinically acceptable, reconstructions up to R_{4D}=4 may be justified, allowing for accurate motion estimation with a retrospective acquisition time T_{acq}≈60s. No significant differences were found between axial and sagittal reconstructions for motion estimation. However, models evaluated on axial images show higher image reconstruction quality than models evaluated on sagittal images **(Figure 5)**. Future work will investigate model performance on prospectively undersampled MRI and comparison to not spatio-temporally decomposed models. Using high-quality accelerated 4D-MRI could shorten the acquisition time, increasing patient comfort and improving treatment throughput. Moreover, it could enable accelerated high-quality time-resolved imaging[15].

Conclusion:

We have presented a small deep learning model for 4D-MRI reconstruction that splits the spatio-temporal information into two separated branches. Retrospectively-accelerated 4D-MRI (T_{acq}≈60s) was reconstructed in 16s with high quality, enabling accurate motion estimation compared to XD-GRASP (EPE<1mm).

References:

[1] Korreman et al. "Image-guided radiotherapy and motion management in lung cancer" Br J Radiol. 2015

[2] Stemkens et al. "Nuts and bolts of 4D-MRI for radiotherapy." PMB 63.21 (2018)

[3] Hammernik et al. "Learning a variational network for reconstruction of accelerated MRI data" MRM 79.6 (2017)

[4] Freedman et al. "Rapid 4D-MRI reconstruction using a deep radial convolutional neural network: Dracula." Radiotherapy and Oncology 159 (2021)

[5] Huttinga et al. "Prospective 3D+t non-rigid motion estimation at high frame-rate from highly undersampled k-space data: validation and preliminary in-vivo results" Proc. Intl. Soc. Mag. Reson. Med. 27 (2019)

[6] Kofler et al. "Spatio-temporal deep learning-based undersampling artefact reduction for 2D radial cine MRI with limited training data" IEEE TMI 39.3 (2019)

[7] Küstner, Thomas, et al. "CINENet: deep learning-based 3D cardiac CINE MRI reconstruction with multi-coil complex-valued 4D spatio-temporal convolutions." Scientific reports 10.1 (2020)

[8] Stemkens et al. "Optimizing 4-dimensional magnetic resonance imaging data sampling for respiratory motion analysis of pancreatic tumors" IJROBP 91.3 (2015)

[9] Feng et al. "XD-GRASP: golden-angle radial MRI with reconstruction of extra motion-state dimensions using compressed sensing." MRM 75.2 (2016)

[10] Fessler and Sutton. "Nonuniform fast Fourier transforms using min-max interpolation." IEEE transactions on signal processing 51.2 (2003)

[11] Beare et al. “Image Segmentation, Registration and Characterization in R with SimpleITK”, J Stat Softw 86.8 (2018)

[12] Adler et al. "Solving ill-posed inverse problems using iterative deep neural networks" IP 33.12 (2017)

[13] Virtue et al. "Better than real: Complex-valued neural nets for MRI fingerprinting." IEEE ICIP (2017)

[14] Terpstra et al. "Rethinking complex image reconstruction: ⊥-loss for improved complex image reconstruction with deep learning" Proc. Intl. Soc. Mag. Reson. Med. 29 (2021)

[15] Feng et al. "MPnRAGE: A Magnetic Resonance SIGnature MAtching framework for real-time volumetric imaging" MRM 84.3 (2020)

Acknowledgements / Funding information: This work is part of the research program HTSM with project number 16354, which is (partly) financed by the Netherlands Organisation for Scientific Research (NWO) and Philips Healthcare. We gratefully acknowledge the support of NVIDIA Corporation with the donation of the Quadro RTX 5000 GPU used for prototyping this research.

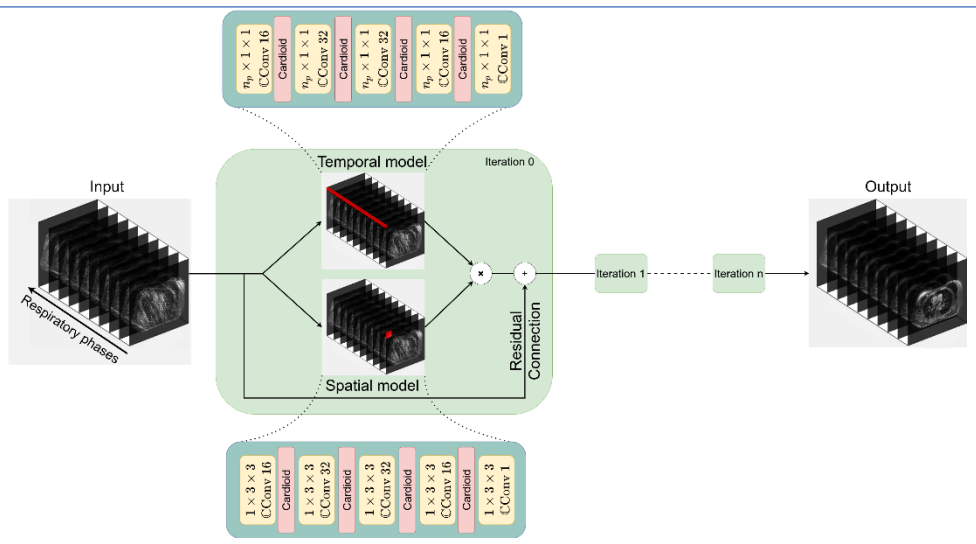

Figure 1: Model architecture. The model uses a complex 2D+t volume y_0 with n_p respiratory phases. Then, one branch extracts temporal information in a volume Ξ by performing $n_p \times 1 \times 1$ complex convolutions, while the other branch extracts a volume Ψ containing spatial information by performing $1 \times 3 \times 3$ complex convolutions. The final output of one iteration is $y_{t+1}=y_t+\Xi\Psi$. In total, four iterations were used.

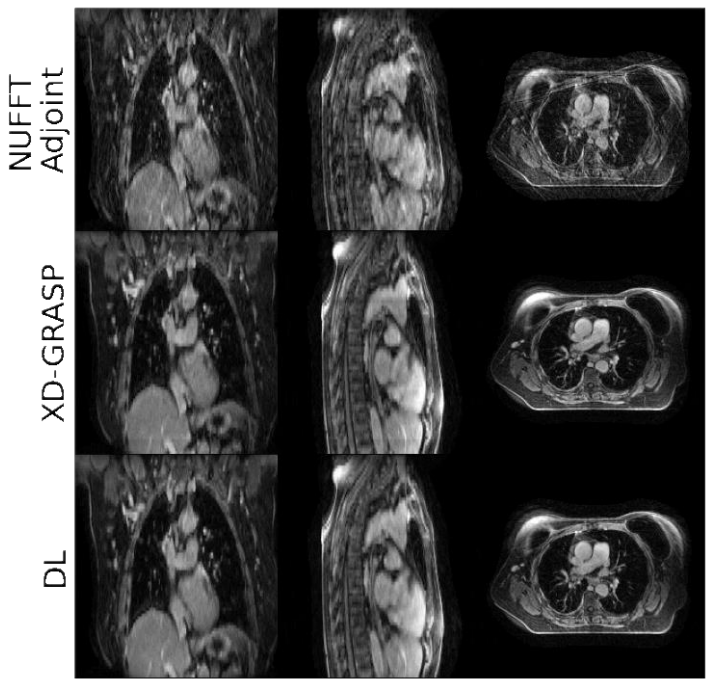

Figure 2: Example reconstruction with R_{4D}=1. Here, a patient (female, 71 years old, T3N0M0 squamous cell-carcinoma) from the test set is shown. Top row shows the NUFFT-adjoint reconstruction, middle row the XD-GRASP reconstruction, and the bottom row shows the deep learning reconstruction. The acquisition time was approximately 5 minutes. Average SSIM increased from 0.81 using NUFFT adjoint reconstructions to 0.94 with DL reconstructions compared to XD-GRASP, while the EPE decreased from 0.98 mm to 0.38 mm.

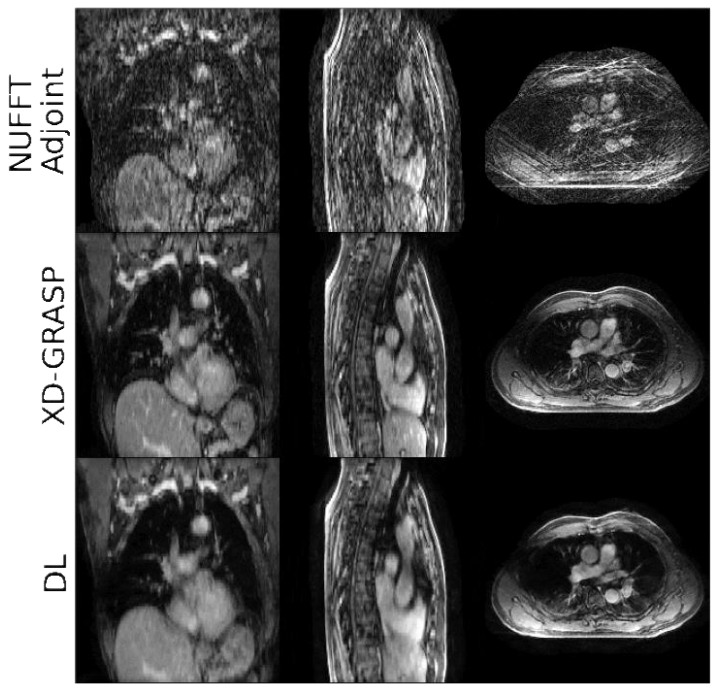

Figure 3: Example reconstruction with R_{4D}=4. Here, a patient (male, 72 years old, T4N1M0 small-cell carcinoma) from the test set is shown. Top row shows the NUFFT-adjoint reconstruction, middle row the XD-GRASP reconstruction, and the bottom row shows the deep learning reconstruction. The acquisition time was approximately 1 minutes. Average SSIM increased from 0.63 using a NUFFT-adjoint reconstruction to 0.87 with DL reconstructions compared to XD-GRASP, while the EPE decreased from 1.87 mm to 1.10 mm.

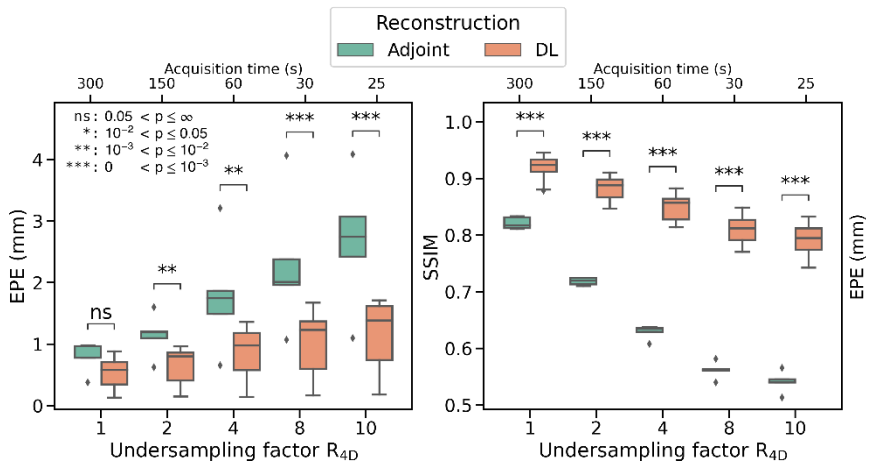

Figure 4: Deep learning results. Comparison between NUFFT-adjoint reconstructed 4D-MRI (Adjoint) and 4D-MRI reconstructed with the proposed deep learning model (DL) for multiple undersampling factors R_{4D}. Deep learning significantly increases the SSIM and reduces the EPE compared to XD-GRASP for accelerated and non-accelerated MRI.

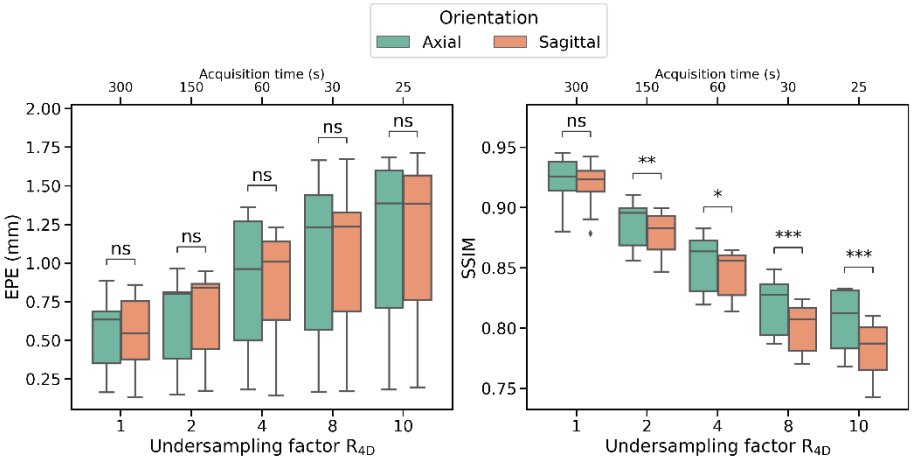

Figure 5: Orientation comparison. Comparison between deep learning models evaluated on axial images and models evaluated sagittal images for multiple undersampling factors R_{4D}. For motion estimation, there is no difference between the two orientations. Axial models show higher image quality compared to XD-GRASP at high undersampling factors (R_{4D}>1) than sagittal reconstructions.

Assessment of pessary position using upright MR imaging of patients with pelvic organ prolapse

Lisan M. Morsinkhof, Anique T.M. Grob, Lianne Straetemans, and Frank F.J. Simonis[1]
1.Magnetic Detection & Imaging, University of Twente, Enschede, Netherlands 2.Multi-Modality Medical Imaging, University of Twente, Enschede, Netherlands

Synopsis: Pessary treatment for pelvic organ prolapse (POP) has a success rate of only 63% and its working mechanism remains unclear. This study applies upright MRI to gain insight into pessary. Patients were scanned in supine and upright position. The pessary was located under the inferior pubic bone in 7 out of 9 patients in upright position, opposed to 1 out of 9 in supine position. This indicates that the pubic bone does not (solely) contribute to the supporting mechanism. The use of upright MRI contributes to knowledge about the working mechanism of the pessary.

Introduction: Pelvic organ prolapse (POP) is a common condition in elderly women, with a prevalence of 11% between the ages of 45-85 years in the Netherlands[1]. A pessary is a relatively simple and cheap device to treat POP. However, the success rate after 3 months is only 63%[2]. Success factors on pessary fitting are described, but are mainly based on global physical factors (e.g. previous hysterectomy, overweight, hiatal circumferences). A universally accepted view on the working mechanism of a pessary, including support tissue, is lacking. This is most easily proved by the variation in the position and effect of a pessary portrayed in scientific papers and patient information folders. Little research has been done to better understand the actual position of the pessary and the location of the prolapsed organs before and after pessary insertion. Since physical examination, typically done in supine position, is unable to present us with a 3D multicompartment view, imaging is needed.
Magnetic Resonance Imaging (MRI) allows for multicompartment pelvic imaging. There are currently a few low-field MRI scanners available that provide the opportunity to scan patients in different body positions[3,4]. Since the amount of prolapse in upright position is significantly larger than in supine position[5], this technique is crucial for a realistic evaluation of the working mechanism of a pessary.
This research aims to determine the position and orientation of the pessary in patients with POP in upright position and compare this to the position and orientation in supine position, to obtain a better understanding of its working mechanism.

Methods: In this study in total 15 patients wearing their ring shaped pessary for at least three months will be scanned in upright and supine position using a 0.25T MRI scanner (Esaote SpA, Genoa, Italy). Until now, 9 patients were scanned, all between 16:00 and 18:00[4], and emptied their bladder 15 minutes before the scan. A multi-slice T2-weighted fast spin echo was acquired in the sagittal plane, using the following parameters: TE/TR: 25/3480 ms, flip angle: 90°, reconstructed resolution: 1.3×1.3 mm^2, slice thickness: 5 mm, number of slices: 11, total scan time: ≈2 min.
On the acquired scans the distance between the most inferior part of the pessary and the Pelvic Inclination Correction System (PICS) reference line[6] was measured (d_{pess}) and compared between upright and supine position using the Wilcoxon signed-rank test. Furthermore, the angle between the pessary and the PICS (α_{pess}) was measured and compared between upright and supine position.

Results: As can be seen in Figure 1, the pessary can be clearly seen on the MR image. The figure also shows an overview of the drawn lines and calculated variables. The PICS line originates at the inferior pubic point and descends from there in 8 out of 9 patients. This means that when the pessary is located lower than the PICS line, the pessary is also located lower than the inferior pubic point.
Figure 2a shows an overview of d_{pess} of all patients in supine and upright position. It can be seen that in upright position the pessary is located lower in all patients, with a median (min, max) descent of 1.8 (1.2, 2.6) cm (p = 0.008). The lowest point of the pessary is located lower than the PICS line in1 out of 9 patients in supine position, and in 7 out of 9 patients in upright position. A scan be seen in Figure 2B, there is only a slight change in α_{pess} between supine and upright position, varying from increase to decrease. The median (min, max) difference between upright and supine is -5 (-16, 1) degrees (p = 0.16).

Discussion: The difference in α_{pess} between supine and upright position is small, but there is a significant descent of the pessary observed in all patients in upright position. Furthermore, the lowest point of the pessary is located lower than the inferior pubic point in 7 out of 9 patients, indicating that there has to be at least an additional support mechanism of the pessary than solely the pubic bone, as was hypothesized before[7]. This phenomenon can only be observed when patients are in the upright position, indicating that imaging in this position is of importance for further evaluation of the working mechanism of the pessary in patients with POP.
This research was performed using 2D sagittal images on which the PICS and the pessary angle were used as parameters to analyze the pessary position. 3D analysis would enable research into additional parameters that may be useful to investigate the working mechanism of the pessary, such as the position and orientation in the coronal and transverse plane and the relationship between the pessary position with reference to the pelvic organs.

Conclusion: This research showed a descent of the pessary in upright body position compared to supine, and the difference in position relative to the PICS line and inferior pubic point. A pessary position lower than the inferior pubic point indicates that the pubic bone does not (solely) contribute to the support of the pessary. Upright MRI gives more insight into the working mechanism of a pessary in patients with POP in its most relevant body position.

References:
1. Slieker-ten Hove MCP, Pool-Goudzwaard AL, Eijkemans MJC, Steegers-Theunissen RPM, Burger CW, Vierhout ME. Symptomatic pelvic organ prolapse and possible risk factors in a general population. Am J Obstet Gynecol. 2009; 200(2):184.e1-184.e7.
2. Manzini C, Morsinkhof LM, van der Vaart CH et al. Parameters associated with unsuccessful pessary fitting for pelvic organ prolapse up to three months follow-up: a systematic review and meta-analysis. Int Uroynecol J 2021 (in press).
3. Williams HG, Cooper A, Hodgen L at al. Upright pelvimetry using MRI for the prediction of birth associated cephalo-pelvic disproportion following induction of labour. Proc Intl Soc Mag Reson Med 28 (2020);submission 2571
4. Morsinkhof LM, Grob ATM, Veenstra van Nieuwenhoven AL, Simonis FFJ, Upright MR imaging of daily variations in pelvic organ position for assessment of pelvic organ prolapse. Proc Intl Soc Mag Reson Med 29 (2021);submission 3691
5. Grob ATM, Heuvel J olde, Futterer JJ, et al. Underestimation of pelvic organ prolapse in the supine straining position, based on magnetic resonance imaging findings. Int Urogynecol J 2019;30(11):1939-1944.
6. Betschart C, Chen L,Ashton-Miller JA, DeLancey JOL. On pelvic reference lines and the MR evaluation of genital prolapse: A proposal for standardization using the Pelvic Inclination correction system. Int Urogynecol J. 2013; 24(9):1421-1428.
Acknowledgments / Funding Information
7. Hong CX, Meer E, Cioban M et al. Position and orientation of vaginal pessaries in situ on magnetic resonance imaging. Int Urogynecol J. 2021.

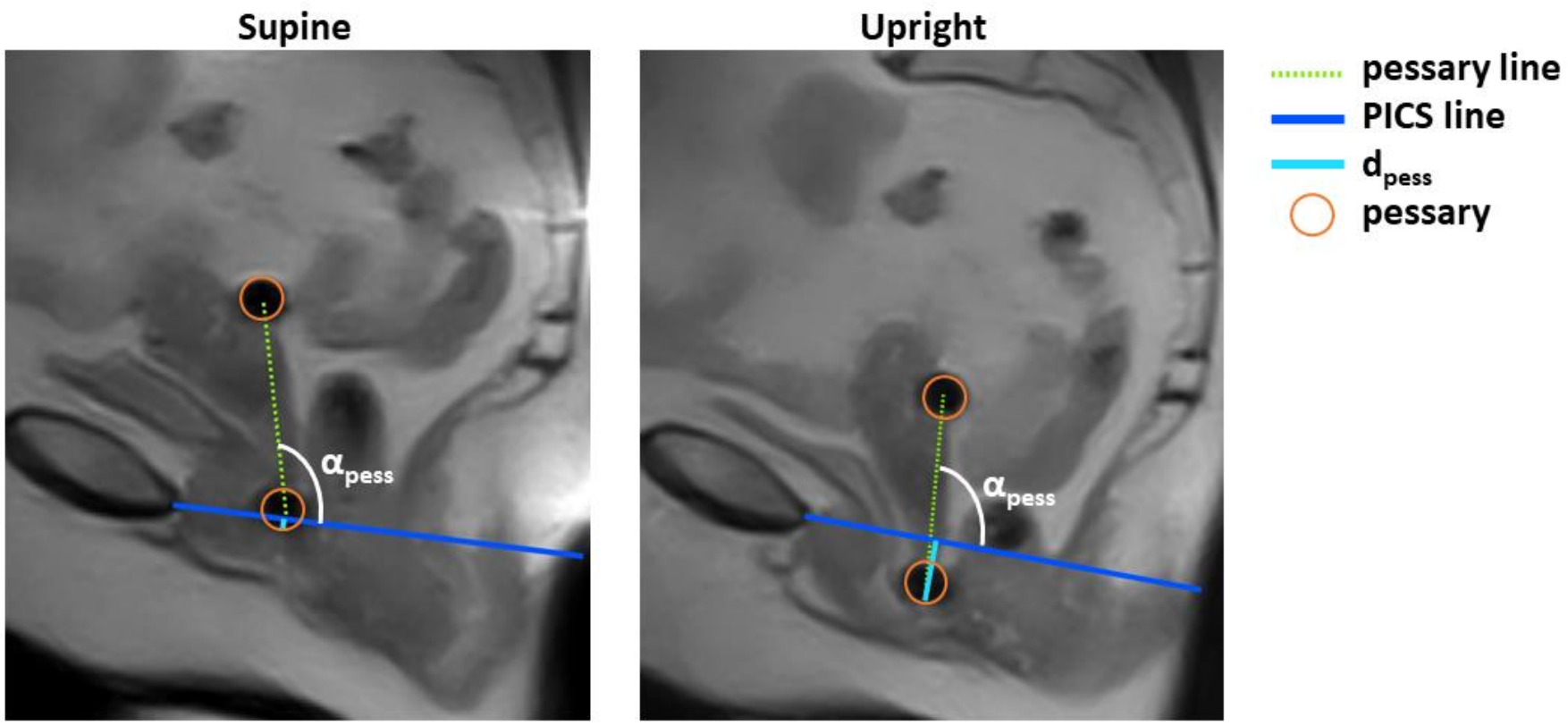

Figure 1. Sagittal MR scans of a patient with a ring pessary in supine and upright position. The pessary line and PICS line are used to measure d_{pess} and α_{pess}. The pessary is clearly visible and descends in upright position compared to supine.

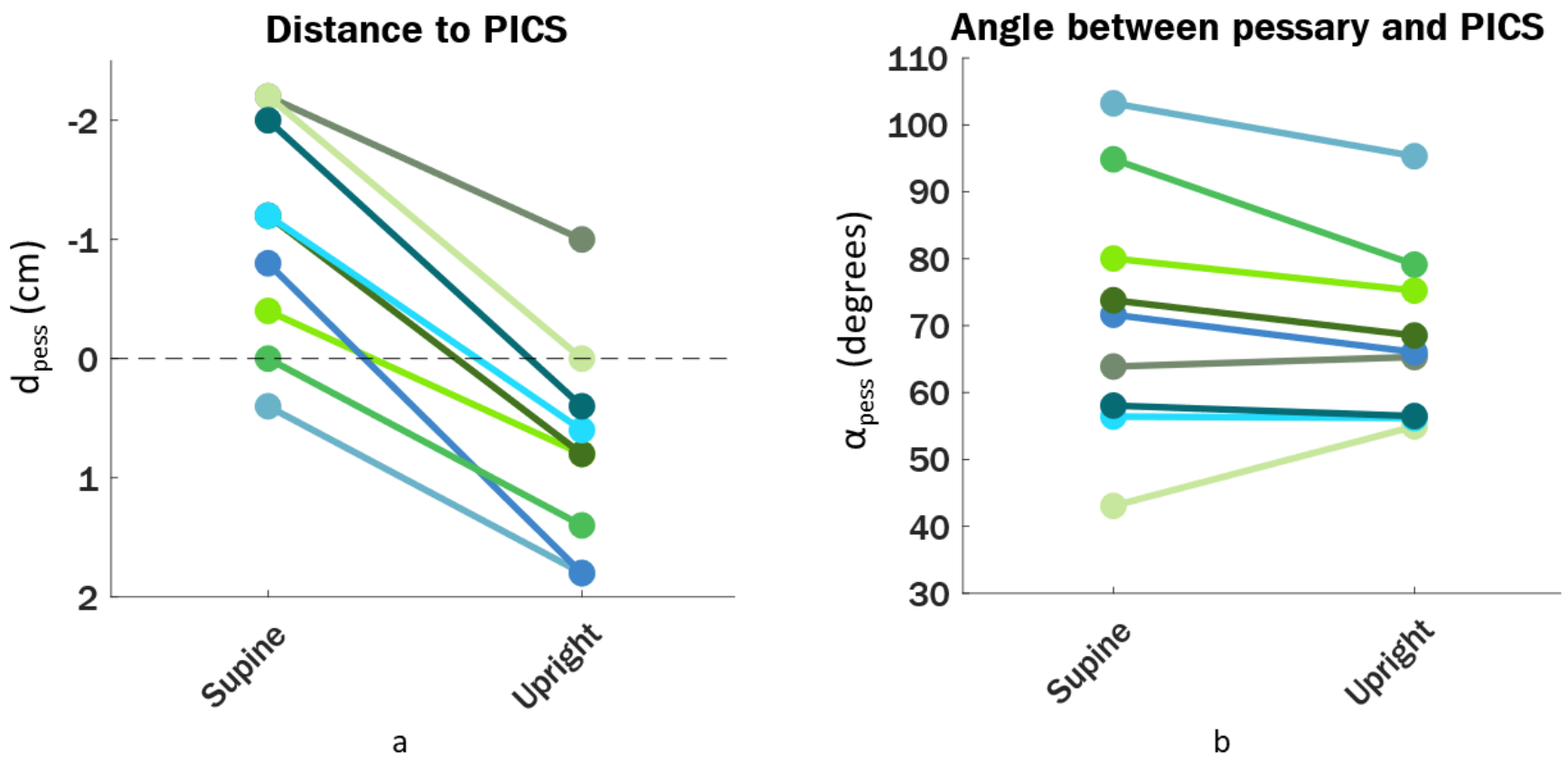

Figure 2. Measured parameters of all patients in supine and upright position a) The distance of the pessary to the PICS reference line. The pessary is located lower in upright position in all 9 patients. The lowest point of the pessary is located lower than the PICS line in 1 out of 9 patients in supine position and in 7 out of 9 patients in upright position. b) The angle of the pessary with respect to the PICS line changes only slightly between body positions without any specific direction.

Breathing task paradigm to improve the quality of pancreatic Magnetic Resonance Elastography

N.P.M.Wassenaar[1], A. van Schelt[1], E.M. Schrauben[1], R. van der Woude[2], J.E. de Jong[2], J.L. Nelissen[1], H.W.M. van Laarhoven[3], J. Guo[4], I. Sack[4], J.H. Runge[1], A.J. Nederveen[1], J. Stoker[1]

[1] Department of Radiology and Nuclear Medicine, Amsterdam University Medical Centers, University of Amsterdam, Amsterdam, the Netherlands [2] University of Twente, Enschede, the Netherlands [3] Cancer Center Amsterdam, Department of Medical Oncology, Amsterdam University Medical Centers, University of Amsterdam, Amsterdam, the Netherlands [4] Department of Radiology, Charité - Universitätsmedizin Berlin, corporate member of Freie Universität Berlin, Humboldt-Universität zu Berlin, and Berlin Institute of Health, Berlin, Germany

Synopsis: Free-breathing acquisition of pancreatic MR elastography can potentially introduce errors in stiffness reconstruction. In this study, breathing tasks are introduced during interleaved and reversed slice order MRE acquisition to determine if the quality of MRE increases. The shear-wave speed and octahedral shear strain signal-to-noise-ratio in the pancreas did not significantly change when using breathing tasks. However, the stability of the pancreas location over time increases when using breathing tasks combined with reversed slice ordering as well as the octahedral shear strain signal-to-noise-ratio in the whole abdomen. Future research should focus on comparing shear-wave speed reproducibility of both MRE methods.

Introduction: Pancreatic MR Elastography (MRE) can detect viscoelastic changes in the course of pancreatitis or pancreatic cancer[1,2]. Both breath-hold and free-breathing (FB) MRE is possible, the latter preferable in sick patients unable to suspend their breath multiple times. However, FB-MRE acquisition can lead to a mismatch in pancreatic location over multiple phase-offsets, potentially introducing errors in stiffness reconstruction.

Using a breathing task (BT) paradigm timed such that MRE acquisition for a given slice occurs during the same respiratory phase could potentially increase MRE quality without limiting the temporal and spatial resolution. We investigated the impact of BTs on pancreatic MRE by evaluating the pancreatic location over multiple phase-offsets. Furthermore, the influence of BTs on the octahedral shear strain signal-to-noise-ratio (OSS-SNR) and shear-wave speed (SWS) was determined.

Methods:

Study protocol: Nine healthy volunteers (♂=3,♀=6, mean age 27±2 years) were included. Subjects fasted four hours prior to MRI examination. BTs were created in ePrime (version 3.0,PST Inc.,Sharpsburg,PA,USA) and followed a natural breathing pattern(Figure 1). The breathing period was equal to TR and phase-offset delay, and instructions were synchronized with the sequence using a TTL pulse. This way, each slice with varying phase-offset is acquired at the same respiratory phase.

MRI measurements: Multi-slice multi-frequency spin-echo echoplanar imaging (SE-EPI) MRE images were acquired with a 3.0T MRI scanner (R.5.7.1.1,Ingenia,Philips,Best,the Netherlands). Mechanical vibrations were introduced using four compressed-air driven MRE transducers at four vibrational frequencies (MRE_{freq}=30,40,50,60Hz)[2]. Motion encoding gradients (MEG) were applied along three orthogonal directions. Three different MRE acquisitions were recorded(Table 1). In FB-MRE scans, no BTs were displayed and standard interleaved slice ordering was used. For the two MRE scans using synchronized BTs, interleaved (BT-Int) and reversed central slice ordering (BT-Rev) were performed(Figure 1). BT-Rev was used to test if central slices containing the pancreas within the multi-slice acquisition were scanned during end-expiration.

*Analysis and statistics:*To determine the stability of the pancreas location over phase-offsets for the three MRE scans, the pancreas was manually delineated in three slices aimed at head, body and tail on the magnitude MRE images for eight phase-offsets at 30 and 50 Hz. The mean dice similarity coefficient (DSC) of all combinations of the regions of interest (ROI) of all three slices was calculated. To test for differences between BT-Int and BT-Rev, the DSC for each slice was compared. Magnitude images of BT-Int and BT-Rev were visually compared to investigate the influence of slice order on image quality. The whole pancreas was delineated on mean magnitude MRE images (mean over phase-offsets, MEG directions, frequencies). These ROIs were used to determine the pancreatic OSS-SNR and pancreatic SWS which was calculated with kMDEV inversion[3]. The OSS-SNR was also calculated over the whole abdomen. Repeated measures ANOVA with pairwise comparison and Bonferroni correction was used for statistical analysis. Image analysis and statistical analysis were performed in Matlab (R2021a,Mathworks,Natick,MA,USA) and SPSS (version 26,IBM,Armonk,NY,USA).

Results: Mean values of DSC, SWS and OSS-SNR are shown in Table 2. Compared with FB, DSC was significantly higher for BT-Rev (p=0.026), while no significant difference was found for DSC between BT-Int and BT-Rev or FB and BT-Int. No significant differences were found between the MRE scans for pancreatic SWS and OSS-SNR. However, OSS-SNR in the whole abdomen significantly increased for BT-Rev compared to FB and BT-Int (p-value=0.010 and 0.014 respectively). Magnitude images over eight phase-offsets can be found in Figure 2. Comparing the magnitude image quality between BT-Int and BT-Rev, signal loss in various slices was present more pronounced in BT-Rev. Overlap images of phase-offset ROIs and corresponding elastograms are shown in Figure 3.

Discussion: Introduction of BT-Rev paradigm during pancreatic MRE significantly increases DSC compared to FB-MRE. This may be an important finding for pancreatic tumors where stromal tissue is of great interest. Pancreatic tumors can be small and a consistent location over multiple phase-offsets is needed to be able to perform sub-region analysis. Previous research showed that 2D motion correction in coronal direction improves sharpness of FB-MRE images[4]. Nevertheless, this is more difficult in an axial orientation and eddy current artifacts lead to distortions when acquiring pancreatic MRE in coronal orientation on a 3T MRI system.

BT-Rev MRE significantly improves OSS-SNR in the whole abdomen compared to FB and BT-Int, while pancreatic OSS-SNR did not significantly differ between scans. Higher abdominal OSS-SNR suggests that measurements may be more reproducible when BT-Rev is used. The pancreatic SWS did not significantly differ, and values were comparable to literature[1,2,4,5].

Magnitude image quality of BT-Int was visually higher than BT-Rev. This could be explained by signal leakage into adjacent slices typical of EPI acquisitions. Despite this finding, the increase in whole-abdomen OSS-SNR and DSC warrant future research on using BT-Rev to compare the reproducibility of SWS measurements with FB-MRE. The scan time increased two times when using BTs, giving the opportunity to acquire more/thinner slices or a higher in-plane resolution. Furthermore, future research could focus on performing motion correction in axial orientation or applying respiratory binning.

Conclusion: Although, pancreatic OSS-SNR did not improve and SWS did not significantly change, using BTs during pancreatic MRE acquisition causes a more stable pancreatic location over multiple phase-offsets leading to a higher OSS-SNR in the whole abdomen.

References:

1. Zhu L, Guo J, Jin Z et al. Distinguishing pancreatic cancer and autoimmune pancreatitis with in vivo tomoelastography. Eur Radiol. 2021 May;31(5):3366-3374. doi: 10.1007/s00330-020-07420-5. Epub 2020 Oct 30. PMID: 33125553.

2. Marticorena Garcia SR, Zhu L, Gültekin E et al. Tomoelastography for Measurement of Tumor Volume Related to Tissue Stiffness in Pancreatic Ductal Adenocarcinomas. Invest Radiol. 2020 Dec;55(12):769-774. doi: 10.1097/RLI.0000000000000704. PMID: 32796197.

3. Tzschätzsch H, Guo J, Dittmann F et al. Tomoelastography by multifrequency wave number recovery from time-harmonic propagating shear waves. Med Image Anal. 2016 May;30:1-10. doi: 10.1016/j.media.2016.01.001. Epub 2016 Jan 13. PMID: 26845371.

4. Shahryari M, Meyer T, Warmuth C et al. Reduction of breathing artifacts in multifrequency magnetic resonance elastography of the abdomen. Magn Reson Med. 2021 Apr;85(4):1962-1973. doi: 10.1002/mrm.28558. Epub 2020 Oct 26. PMID: 33104294.

5. Gültekin E, Wetz C, Braun J et al. Added Value of Tomoelastography for Characterization of Pancreatic Neuroendocrine Tumor Aggressiveness Based on Stiffness. Cancers (Basel). 2021 Oct 15;13(20):5185. doi: 10.3390/cancers13205185. PMID: 34680334.

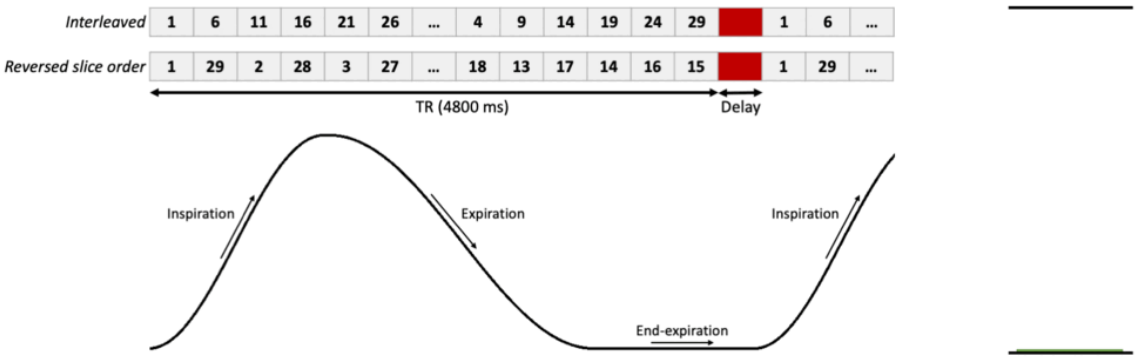

Figure 1: Breathing tasks are synchronized with the MRE sequence such that each slice will be acquired during the same breathing phase. The TR is 4800 ms and the delay varies for each mechanical frequency and phase-offset. In this study, interleaved and reversed slice order are used, shown here for 29 slices. At the right, an accelerated example of the breathing task paradigm is shown that is presented to the volunteer during the MRE scan.

Parameter	FB-MRE	BT-Int MRE	BT-Rev MRE
TR [ms]	2400	4800	4800
TE [ms]	55	55	55
Slice order	Interleaved	Interleaved	Reversed central
Scan duration [min:sec]	4:02	8:04	8:04
Breathing tasks?	No	Yes	Yes
Phase-offsets	8	8	8
Resolution [mm]	2.5x2.5x5	2.5x2.5x5	2.5x2.5x5
Number of slices	29	29	29

Table 1: Summary of the relevant MRE parameters. TRs of MRE scans with breathing tasks are longer to ensure a more natural breathing pattern.

Scan	DSC [-]		SWS pancreas [m/s]	OSS-SNR pancreas [dB]	OSS-SNR abdomen [dB]	
FB	0.68 (0.08)	†	1.24 (0.09)	3.27 (0.88)	6.65 (0.54)	
BT-Int	0.78 (0.07)		1.21 (0.08)	3.81 (0.75)	6.95 (0.45)	*, ‡
BT-Rev	0.79 (0.05)		1.17 (0.09)	3.51 (0.62)	7.22 (0.41)	

Table 2: The mean (standard deviation) of dice similarity coefficient, shear-wave speed and OSS-SNR in the pancreas and whole abdomen for the three different MRE scans (†p=0.026 , *p=0.010 , ‡p=0.014).

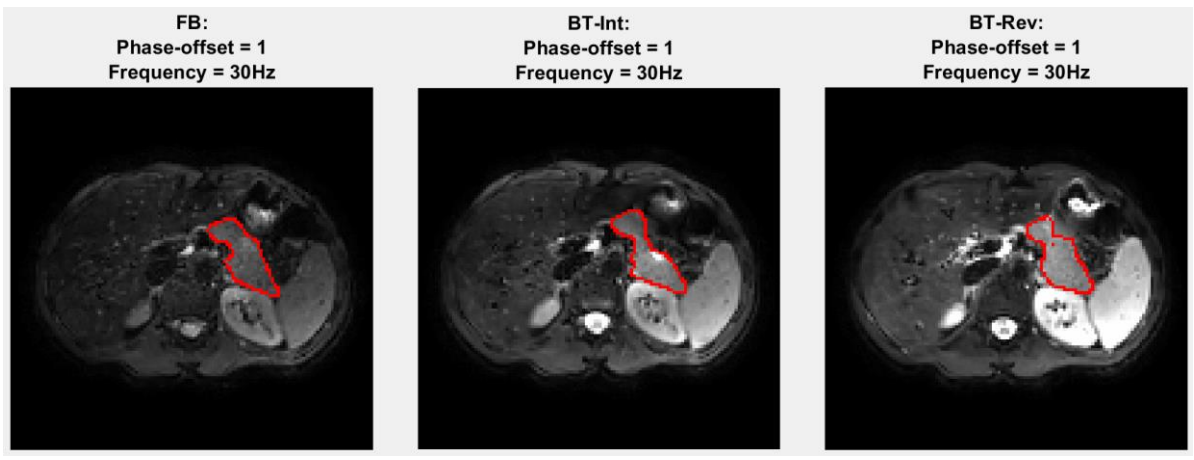

Figure 2: Magnitude MRE images for the three different scans for each phase-offset acquired at a vibrational frequency of 30 and 50 Hz. The pancreas is delineated in red. The movement of the pancreas over time can be recognized.

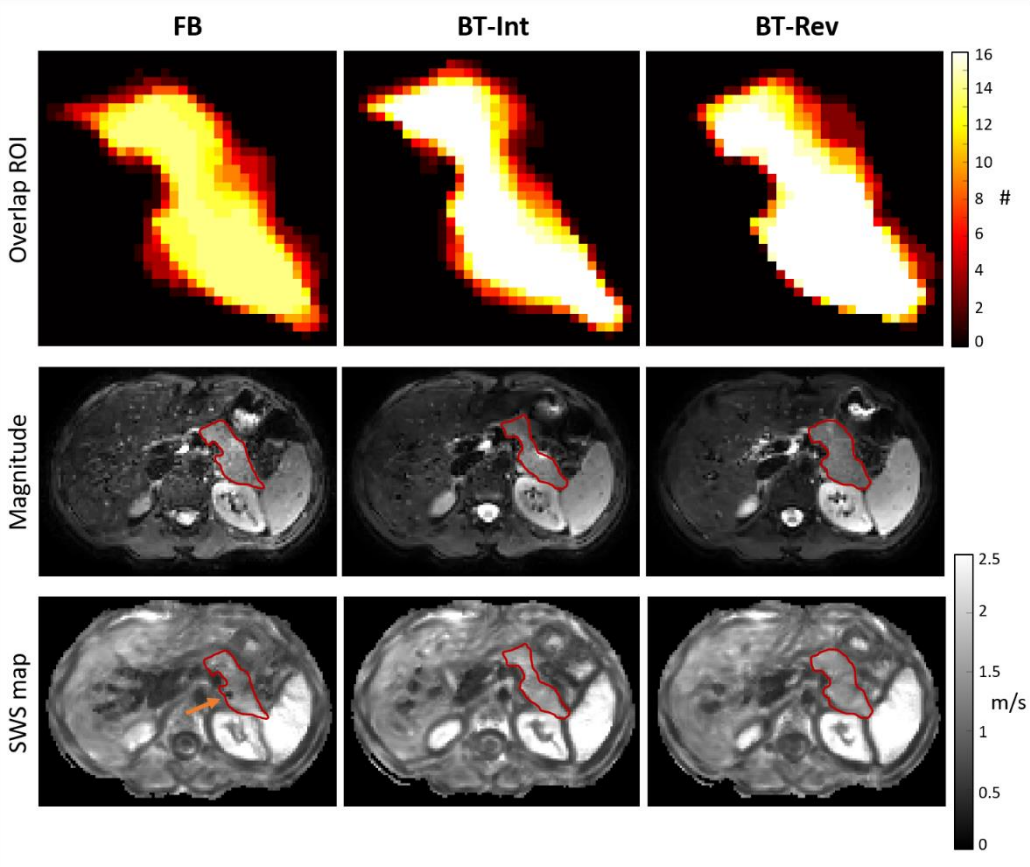

Figure 3: Top: Overlap of 16 ROIs delineated on 8 phase-offset magnitude images for 2 mechanical frequencies shown for the three different MRE scans in 1 volunteer. The image is zoomed in on pancreatic ROI. Note that for FB-MRE, the pancreas was not located in this slice for 2 phase-offsets.
Middle: Magnitude MRE images for the three MRE scans with the pancreas delineated in red.
Bottom: SWS map of the whole abdomen with the pancreas delineated in red. The orange arrow indicates signal distortion in the pancreas in the FB-MRE scan.

In-vivo ^{31}P MRSI in healthy and malignant human pancreas at 7 Tesla

L.W.F. Seelen[1,2]*, L. van den Wildenberg[1]*, A. Gursan[1], T.A. van der Velden[1], W.J.M. Gosselink[1], M. Froeling[1], W.J.M. van der Kemp[1], F.A.A. Mohamed Hoesein[3], N. Haj Mohammad[4], I.Q. Molenaar[2], H.C. van Santvoort[2], D.W.J. Klomp[1], J.J. Prompers[1]

[1]Dept. of Radiology, University Medical Center Utrecht, Utrecht, The Netherlands; [2]Dept. of Surgery, UMC Utrecht Cancer Center and St Antonius Hospital Nieuwegein: Regional Academic Cancer Center Utrecht, Utrecht University, Utrecht, The Netherlands; [3]Dept. of Radiology, University Medical Center Utrecht, Utrecht University, Utrecht, The Netherlands; [4]Dept. of Medical Oncology, UMC Utrecht Cancer Center, Regional Academic Cancer Center Utrecht, Utrecht University, Utrecht, The Netherlands

Synopsis:

Early response assessment for patients with pancreatic cancer receiving chemotherapy is limited. Detection of alterations in ^{31}P metabolite levels during treatment could change this perspective. However, to date ^{31}P MRS has not yet been demonstrated in the human pancreas *in vivo*. Here we show *in-vivo* ^{31}P MRSI data in the pancreas of healthy subjects, using a ^{31}P whole-body transmit coil in combination with a 16-channel receive array at 7T, and show moderate to good test-retest reliability. In addition, we demonstrate the feasibility of performing ^{31}P MRSI in a patient with pancreatic cancer before and after chemotherapy.

Purpose:

Pancreatic ductal adenocarcinoma (PDAC) is an aggressive malignancy with a dismal prognosis, of which the incidence is increasing.[1-3] Patients with PDAC are usually treated with chemotherapy. However, there are limitations in the assessment of early treatment response.

Phosphorus magnetic resonance spectroscopy (^{31}P MRS) is a non-invasive technique that has been shown to enable detection of early treatment-induced metabolic alterations in different tumors.[4] Nevertheless, to date ^{31}P MRS has not yet been demonstrated in the human pancreas *in vivo*. The penetration depth of commonly used ^{31}P surface coils is limited and the pancreas is located more or less in the center of the abdomen, which makes ^{31}P MRS of the pancreas extremely challenging. With the development of a ^{31}P whole-body transmit coil for a 7T MRI scanner[5] and by using a multi-channel ^{31}P receive array[6], ^{31}P signals can be measured also from deeper lying tissues in the abdomen, providing the opportunity to measure *in-vivo* ^{31}P MR spectra from the pancreas.

The first aim of this study was to determine the repeatability of ^{31}P MRSI of the pancreas of healthy subjects at 7T. Secondly, we aimed to determine the feasibility of obtaining ^{31}P MRSI data from a patient with PDAC.

Methods:

The institutional review board approved this study and all participants gave written informed consent. Ten healthy volunteers (six males and four females, age 34±12y) participated in the repeatability study. In addition, one patient with PDAC (age 27y, tumor 94mmx41mm on CT images) was included. We used a whole-body 7T MR system (Philips Healthcare, Best, NL) with an in-house designed ^{31}P whole-body birdcage transmit coil (diameter 60cm) to perform ^{31}P MRSI at 120.6 MHz.[5] In addition, a body array with 16 ^{31}P loop coils and 8 transmit-receive fractioned ^{1}H dipole antennas[6,7] was used to receive the ^{31}P signals and perform ^{1}H MRI, respectively. All healthy participants were scanned twice on the same day. The patient was also scanned twice, but on different days, i.e., before and after four cycles (8 weeks) of chemotherapy. B_0 maps were acquired for B_0 shimming and transversal and coronal T_1-weighted images were measured with the same field of view and number of slices as for ^{31}P MRSI. ^{31}P spectra were acquired with a pulse-acquire sequence with a block pulse (carrier frequency set to phosphocreatine, B_1=6μT), followed by phase encoding gradients for 3D spatial encoding. The following acquisition parameters were used: FOV=500(LR)×280(AP)×360(FH)mm^3, nominal resolution=20mm isotropic, TR/TE=60/0.56ms, FA=12°, BW=5000Hz, NSA=20, acquisition time=22:37min. Matlab R2019a (The Mathworks Inc., Natick, MA) was used to reconstruct the ^{31}P MRSI data. Principal component analysis (PCA)-based denoising was performed before applying Roemer channel combination.[8,9] A mask around the pancreatic head/body was manually drawn on the T_{1w} images. The data in the mask was quantified using AMARES in the spectroscopy fitting tool (OXSA).[10-12] The following metabolites were fitted: α-, β-, and γ-ATP, inorganic phosphate (Pi), glycerophosphocholine (GPC), glycerophosphoethanolamine (GPE), phosphocholine (PC), phosphoethanolamine (PE), nicotinamide adenine dinucleotide (NADH), uridine diphosphate glucose (UDPG), phosphatidylcholine (PtdC), and phosphocreatine (PCr). Variability was assessed with Bland-Altman analyses (coefficients of repeatability (CR) and bias), intraclass correlation coefficients (ICC), t-tests (p-value), and within-subject coefficients of variation (CoV).[13]

Results:

Figure 1 shows an example of the pancreas mask on the ^{31}P MRSI grid (in one slice) and the ^{31}P MR spectrum in one of the voxels. On average 6±2 voxels were used for quantification of pancreas ^{31}P metabolites in scan 1, and 5±2 voxels in scan 2. No significant differences were observed in ^{31}P metabolite levels between scan 1 and scan 2 of healthy subjects (p-values>0.05; Figure 2). ICC's were higher than 0.50 for most metabolites, indicating moderate (ICC=0.5-0.75) to good (ICC=0.75-0.9) repeatability, except for β-ATP, PC, PtdC. CoV's ranged from 4.95% for α-ATP to 38.83% for GPE (excluding PtdC). Bland-Altman plots of variability in relative ^{31}P metabolite levels are shown in Figure 3. In the patient, 10 voxels were selected in the pancreatic tumor before therapy and 7 voxels after therapy, of which 2 were discarded because of contamination with biliary PtdC (Figure 4). Figure 5 shows the GPC, GPE, PC, and PE levels and combined phosphodiester (PDE) and phosphomonoester (PME) levels in the individual tumor voxels in the patient before and after therapy, next to the average values in the pancreas of the healthy subjects. GPC seems higher in the patient compared to controls, and PC, PE and PME increased significantly after therapy.

Discussion and conclusion:

To the best of our knowledge, we have shown here the first *in-vivo* ^{31}P MRS data of the human pancreas. Repeatability of ^{31}P MRSI in the healthy pancreas was moderate to good and comparable to the repeatability of ^{31}P MRSI previously determined in the liver at 7T,[14] also for the lower-concentration metabolites. In addition, we have shown the feasibility of performing ^{31}P MRSI in a patient with PDAC and detected changes in PME levels in the tumor before and after four cycles of chemotherapy.

In conclusion, *in-vivo* ^{31}P MRSI of the human pancreas is feasible at 7T with the use of a ^{31}P whole-body transmit coil in combination with a ^{31}P receive array, and has potential for monitoring treatment response in pancreatic cancer.

References

1. Vincent A, Herman J, Schulick R, et al. Pancreatic cancer. Lancet. 2011 Aug 13;378(9791):607-20.
2. Siegel RL, Miller KD, Jemal A. Cancer statistics, 2020. CA Cancer J Clin. 2020 Jan;70(1):7-30.
3. Rahib L, Smith BD, Aizenberg R, et al. Projecting cancer incidence and deaths to 2030: the unexpected burden of thyroid, liver, and pancreas cancers in the United States. Cancer Res. 2014 Jun 1;74(11):2913-21.
4. Negendank W. Studies of human tumors by MRS: a review. NMR Biomed. 1992 Sep-Oct;5(5):303-24.
5. Löring J, Van der Kemp WJM, Almujayyaz S, et al. Whole-body radiofrequency coil for 31P MRSI at 7T. NMR Biomed. 2016 Jun;29(6):709-20.
6. Van Houtum Q, Mohamed Hoesein FAA, Verhoeff JJC, et al. Feasibility of 31P spectroscopic imaging at 7 T in lung carcinoma patients. NMR Biomed. 2021 May;34(5):e4204.
7. Raaijmakers AJE, Italiaander M, Voogt IJ, et al. The fractionated dipole antenna: A new antenna for body imaging at 7 Tesla. Magn. Reson. Med. 2016 Mar;75(3):1366-74.
8. Roemer PB, Edelstein WA, Hayes CE, et al. The NMR Phased Array. Magn. Reson. Med. 1990 Nov;16(2):192-225.
9. Froeling M, Prompers JJ, Klomp DWJ, et al. PCA denoising and Wiener deconvolution of 31P 3D CSI data to enhance effective SNR and improve point spread function. Magn Reson Med. 2021;85:2992-3009.
10. Vanhamme L, Van Den Boogaart A, Van Huffel S. Improved Method for Accurate and Efficient Quantification of MRS Data with Use of Prior Knowledge. Journal of Magnetic Resonance. 1997 Nov;129(1):35-43.
11. Purvis LAB, Clarke WT, Biasiolli L, et al. OXSA: An open-source magnetic resonance spectroscopy analysis toolbox in MATLAB. PLoS One. 2017 Sep 22;12(9):e0185356.
12. Purvis LAB, Clarke WT, Biasiolli L, et al. Line-width constraints in Matlab AMARES using pre-Metabolite T2 and per-Voxel Delta B0. in In Proceedings of the 22nd Annual Meeting of ISMRM, p. 2885.
13. Hyslop NP, White WH. Estimating Precision Using Duplicate Measurements. J. Air Waste Manage. Assoc. 2009 Sep;59(9):1032-9.
14. Purvis LAB, Clarke WT, Valkovič L, et al. Phosphodiester content measured in human liver by in vivo ^{31} P MR spectroscopy at 7 tesla. Magn Reson Med. 2017 Dec;78(6):2095-2105.

Acknowledgments / Funding Information: Dutch Cancer Society and Technical Sciences and St. Antonius Hospital Nieuwegein Research Fund

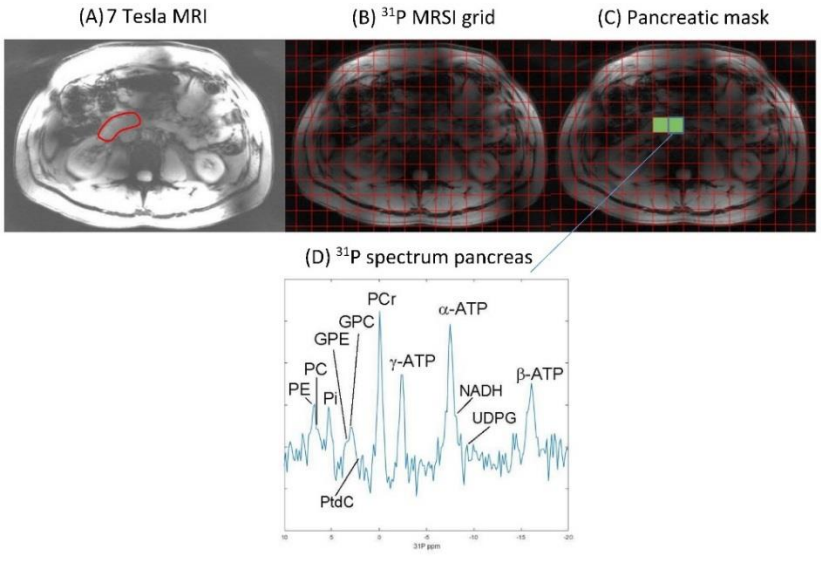

Metabolites	Scan 1	Scan 2	Statistics				
	Mean (SD)	Mean (SD)	ICC	p-value	CoV	CR	bias
α-ATP	21.81 (1.59)	22.15 (2.26)	0.85	0.48	4.95	2.82	-0.33
β-ATP	13.82 (1.58)	13.79 (1.47)	-0.63	0.98	11.71	4.65	0.02
γ-ATP	18.63 (2.59)	19.03 (3.01)	0.93	0.42	5.81	2.92	-0.40
Pi	6.60 (1.12)	7.13 (1.20)	0.60	0.20	13.07	2.38	-0.53
GPC	3.69 (0.96)	3.78 (1.08)	0.86	0.71	14.98	1.44	-0.09
GPE	2.44 (0.94)	2.14 (1.06)	0.72	0.34	35.83	1.84	0.30
PC	4.21 (0.67)	4.50 (1.26)	0.31	0.49	20.04	2.55	-0.29
PE	5.30 (0.64)	5.55 (0.94)	0.53	0.34	5.51	1.53	-0.25
NADH	7.22 (1.92)	5.90 (2.36)	0.57	0.10	27.78	4.41	1.32
UDPG	1.60 (0.50)	1.50 (0.86)	0.68	0.67	31.88	1.39	0.10
PtdC	2.37 (1.10)	1.79 (0.73)	0.00	0.20	41.68	2.58	0.58
PCr	12.28 (4.26)	12.72 (6.07)	0.82	0.75	22.01	8.21	-0.43
PME (PC+PE)	9.52 (0.78)	10.05 (2.00)	0.57	0.33	10.28	3.26	-0.54
PDE (GPC+GPE)	6.13 (1.81)	5.92 (1.84)	0.84	0.65	17.26	2.74	0.21

Figure 1: A) One slice of the transversal T_1-weighted 7T MRI of subject 5, with the pancreas indicated with the red line; B) ^{31}P MRSI grid; C) Selected voxels (green) in the pancreatic mask with in D) a ^{31}P MR spectrum of one voxel in the pancreas. No apodization was applied in the spectrum.

Figure 2: ^{31}P metabolite quantification results in the pancreatic masks of healthy subjects in scan 1 and scan 2 and the repeatability measures: intraclass correlation coefficient (ICC), t-test results (p-value), intra-subject coefficient of variance (CoV), coefficient of repeatability (CR) and bias. Obtained metabolites are expressed as percentage of the sum of all fitted signals. Combined phosphomonoester (PME) and phosphodiester (PDE) levels were calculated from the fit results of the obtained PC, PE, GPC and GPE metabolites.

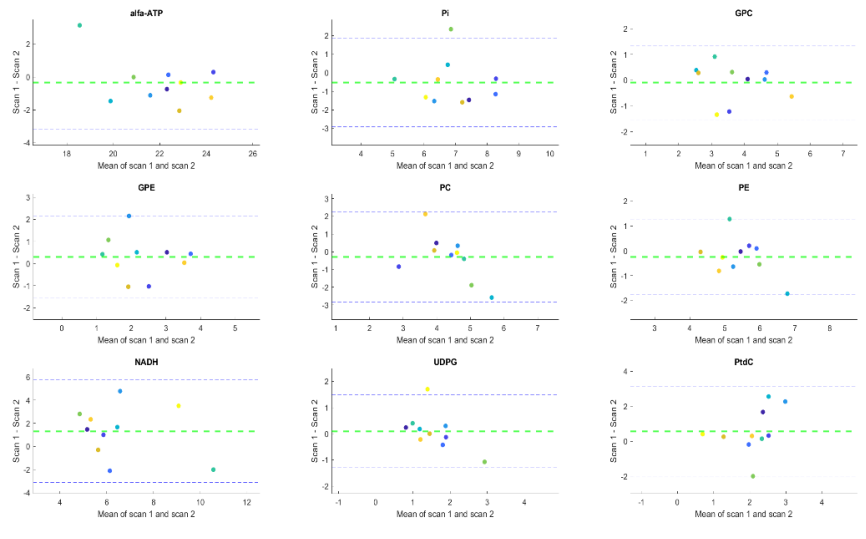

Figure 3: Bland-Altman plots of variability in relative ^{31}P metabolite levels. Each colour represents one subject. The green dashed line shows the bias from zero and the blue dashed lines mark the 95% confidence interval.

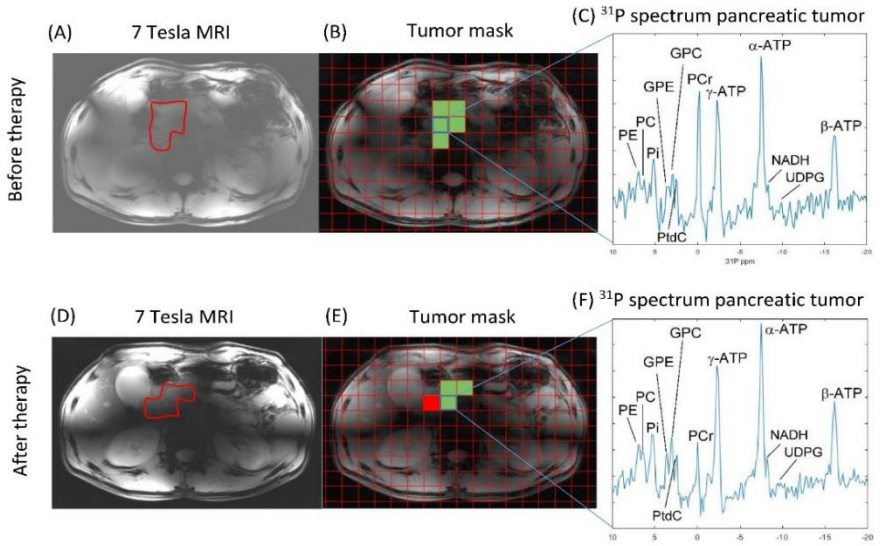

Figure 4: A/D) One slice of the transversal T_1-weighted 7T MRI of the PDAC patient, with the pancreatic tumor indicated with the red line; B/E) Selected voxels (green) in the pancreatic tumor mask with in C/F) a ^{31}P MR spectrum of one voxel in the tumor, before and after four cycles of chemotherapy. The red voxel in the tumor mask after therapy was discarded because of contamination from biliary PtdC. No apodization was applied in the spectra.

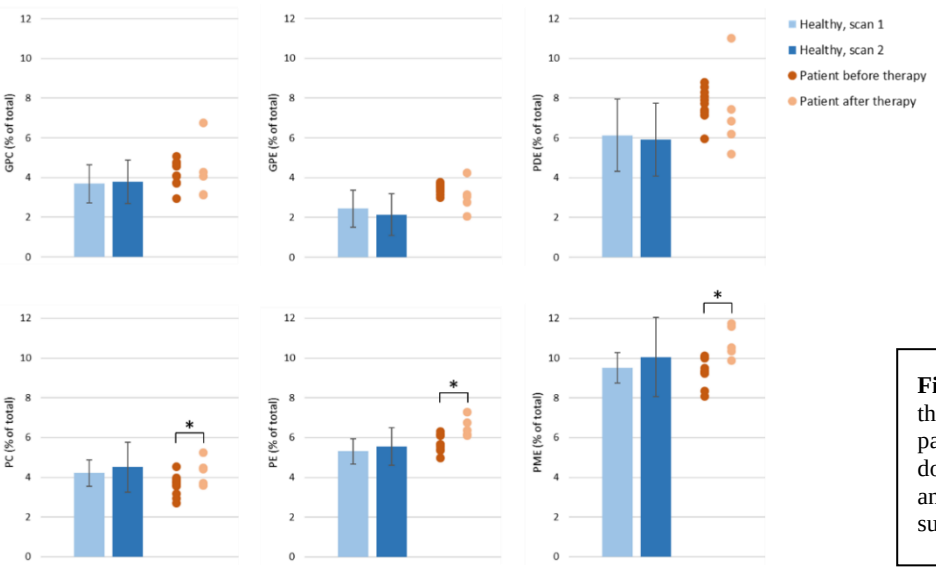

Figure 5: A comparison of the quantified GPC, GPE, PDE, PC, PE and PME levels in the pancreas of healthy subjects (average of scan 1 and average of scan 2) and in the pancreatic tumor of the patient before and after chemotherapy. For the patient, each dot represents a measurement from one voxel in the tumor (10 voxels before therapy and 5 voxels after therapy). The metabolites levels are expressed as percentage of the sum of all fitted signals. * p-value<0.05.

Joint sparsity multi-component MRF reconstruction - directly from k-space to component maps

E. Hartsema[1], M. Nagtegaal[1], K. Koolstra[2], F. Vos[1,3]
[1]Department of Imaging Physics, Delft Univerity of Technology, Delft, The Netherlands;
[2]Division of Image Processing, Department of Radiology, Leiden University Medical Center, Leiden, The Netherlands
[3]Department of Radiology and Nuclear Medicine, Erasmus MC, Rotterdam, Netherlands

Synopsis: The use of high undersampling factors and short flip angle trains leads to shorter acquisition times in MR Fingerprinting acquisitions. To obtain accurate multi-component estimates from this data advanced reconstructions are required. We study a low-rank ADMM based reconstruction method that adds a multi-component constraint to the inverse reconstruction problem (MC-ADMM). This method is combined with a joint-sparsity constraint yielding higher quality multi-component estimates with k-SPIJN than with previous methods. In simulations we observed increased stability to sequence truncation and in vivo multi-component estimates contained less noise-like effects.

Introduction: MR Fingerprinting (MRF)[1] allows for time-efficient estimation of tissue properties by sampling the MR-signal in a transient state while applying high undersampling factors. Conventionally, the data is first reconstructed to (SVD-compressed) time frame images, from which parameter estimates per voxel are obtained, e.g. T_1, T_2 and M_0-maps. This voxel-wise estimation does not take multi-component effects such as myelin water or partial voluming into account. Recently we proposed the Sparsity Promoting Iterative Joint NNLS algorithm for MRF-data(SPIJN-MRF) to obtain multi-component T_1, T_2-estimates based on a joint-sparsity constraint[2]. The estimation of multi-component fraction maps is less robust to artifacts than single-component estimations and therefore requires data with less undersampling artifacts (and thus requiring long scan times). In this work we aim to improve the image reconstruction to facilitate multi-component MRF while high undersampling factors are applied. Therefore we propose an Alternating Direction Method of Multipliers(ADMM) including multi-component constraints into the reconstruction problem. The proposed k-SPIJN method benefits from this extra regularization term that enables direct estimation of joint sparsity multi-component estimates from undersampled data.

Methods - Reconstruction methods: Essentially, multi-component effects in MRF can be modelled as a linearly weighted combination of (low rank(LR)[3]) dictionary items D (D_r, rank r). Given certain LR-images x_r, the weights of the dictionary items can be obtained by solving a non-negative least squares problem:

$$c = \underset{\hat{c}\in\mathbb{R}_{\geq 0}^{N_d\times N_n}}{\operatorname{argmin}} \|P_r D_r \hat{c} - x_r\| \tag{1}$$

in which $c \in \mathbb{R}_{\geq 0}^{N_d\times N_n}$ are estimated magnetization weights per voxel and dictionary atom, and P_r represents spatial phase variations (as excluded from the real-valued c). $P \in \mathbb{C}^{N_n}$ is pre calculated based on a LR-solution, using $r = 1$.

$$P = \frac{x_1}{abs(x_1)} \tag{2}$$

With element-wise division, after which P is mapped to r dimensions. The inverse multi-component reconstruction problem can be written as:

$$c = \underset{\hat{c}\in\mathbb{R}_{\geq 0}^{N_d\times N_n}}{\operatorname{argmin}} \|GU_r F_r S P_r D_r \hat{c} - k\|_2^2. \tag{3}$$

Where k is (multi-coil) k-space data, G a (spiral) gridding-operator, U_r a SVD-based compression-operator, F_r a Fourier-operator, S a coil-sensitivity-operator and r −underscript operators "broadcasted" to low-rank space. Since this problem cannot be solved directly in an efficient manner, we performed variable splitting as Assländer et al.[4] did for single-component MRF. Accordingly, we rewrote the MC-MRF reconstruction as an augmented Lagrangian minimization problem:

$$x_r, c, \bar{u} = \underset{\hat{x}_r, u\in\mathbb{C}^{r\times N_n}, \hat{c}\in\mathbb{R}_{\geq 0}^{N_d\times N_n}}{\operatorname{argmin}} \frac{1}{2}\|GU_r F_r S_r \hat{x}_r - k\|_2^2 + \frac{\mu}{2}\|P_r D_r \hat{c} - \hat{x}_r + u\|_2^2 - \frac{\mu}{2}\|u\|_2^2 \tag{4}$$

in which u is the scaled Lagrange multiplier and μ the coupling parameter balancing data consistency and constraint terms. Subsequently, a multi-component ADMM(MC-ADMM) (Fig. 1-upper row) was used to solve (4), alternating between:

$$x_r = \underset{\hat{x}_r\in\mathbb{C}^{r\times N_n}}{\operatorname{argmin}} \frac{1}{2}\|GU_r F_r S_r \hat{x}_r - k\|_2^2 + \frac{\mu}{2}\|P_r D_r \hat{c} - \hat{x}_r + u\|_2^2 x_r = \underset{\hat{x}_r\in\mathbb{C}^{r\times N_n}}{argmin} \frac{1}{2}\|GU_r F_r S_r \hat{x}_r - k\|_2^2 + \frac{\mu}{2}\|P_r D_r \hat{c} - \hat{x}_r + u\|_2^2 \tag{5}$$

$$c = \underset{\hat{c}\in\mathbb{R}_{\geq 0}^{N_d\times N_n}}{\operatorname{argmin}} \frac{\mu}{2}\|P_r D_r \hat{c} - \hat{x}_r + u\|_2^2 c = \underset{\hat{c}\in\mathbb{R}_{\geq 0}^{N_d\times N_n}}{argmin} \frac{\mu}{2}\|P_r D_r \hat{c} - \hat{x}_r + u\|_2^2 \tag{6}$$

$$u = u + x_r - P_r D_r c u = u + x_r - P_r D_r c \tag{7}$$

until convergence was reached. The LR-inversion problem of (5) was solved with Conjugate Gradients. Equation (6) was solved using the NNLS algorithm[5].

To reduce the number of possible solutions and regularize the multi-component problem, the Sparsity Promoting Iterative Joint NNLS (SPIJN)[2] (Fig.1-middle row) algorithm was applied, applying a joint-sparsity constraint minimizing the number of tissue components, i.e. in a voxel as well as spatially, regularizing the number of non-zero component-maps c_i. The sparsity term $N_c = \sum_{i=1}^{N}\|c_i\|_0$ was implemented by combining dictionary reweighting [6] and ℓ_1^2-regularization[7] with SPIJN regularization parameter $\lambda = 0.15$.

The number of employed dictionary atoms is reduced by the joint-sparsity constraint. This facilitates that in an iterative scheme the actually used dictionary and component maps can be restricted to non-zero elements to improve problem conditioning. The resulting reconstruction scheme will be referred to as k-SPIJN(Fig.1-lower row).

Methods – experiments: Experiments were performed with a gradient-spoiled SSFP-MRF acquisition[8] with a flip angle train of length 400 (and truncated in numerical experiments)[9] and using TR=15ms,TE=4ms. Dictionary signals were simulated using EPG's[10](T_1=100ms-5.2s, T_2=10ms-3s 5%-increments). A constant-density spiral with a undersampling factor 32 was used. The Brainweb phantom [11],incorporating partial voluming of white matter(WM), gray matter(GM) and CSF, was used in numerical simulations to verify the implemented methods and sensitivity to ADMM-parameters. Geometric mean T_1 and T_2-values were evaluated for error analysis. In vivo brain scans were performed on a 3.0 T Philips Ingenia (Best, The Netherlands) MR-scanner with a 32-channel head coil (FOV=240×240mm^2, in plane resolution 1×1mm^2 and 5mm slice thickness). Acquisition with a single flip angle train and 5/32 repeats were performed (delay time 6s). Both for numerical and in vivo experiments joint sparsity multi-component estimates were obtained by 1) LR-inversion and subsequently SPIJN 2) MC-ADMM and subsequently SPIJN and 3) k-SPIJN.

Results and discussion: In numerical simulations the MC-ADMM showed a fast convergence behaviour (Fig. 2), after which we fixated $\mu = 2 \times 10^{-3}$ in further experiments. When sequence lengths were truncated from 400 to 300 and 200 time-points, obtained estimations showed increasing errors and errors in WM and GM became dominant in LR-inversion estimates at N=200(Fig. 3. k-SPIJN showed lower errors than MC-ADMM estimates. Estimated magnetization fraction maps with different reconstruction methods are shown in Fig. 4 and Fig.5 for undersampling factors 5/32 and 1/32 respectively. All reconstructions yielded fraction maps corresponding to WM, GM and CSF. Also, myelin water fraction maps were estimated (shortest T_1, T_2 values, first column), but an increased noise propagation was observed in the MC-ADMM+SPIJN estimates compared to k-SPIJN. For 5/32-undersampling 2 CSF-like components were estimated as observed before[2,12], while 1/32-undersampling yielded 1 CSF component. This was not directly related to the used regularization parameter.

Conclusion: The k-SPIJN reconstruction method is able to obtain myelin water fraction maps from highly undersampled MRF-data, which was not possible with previous methods, with relatively short flip angle trains, reducing acquisition time.

References

1. Ma, D.; Gulani, V.; Seiberlich, N.; Liu, K.; Sunshine, J. L.; Duerk, J. L.; Griswold, M. A.Nature2013,495, 187–192, DOI:10.1038/nature11971.
2. Nagtegaal, M. A.; Koken, P.; Amthor, T.; Doneva, M.Magnetic Resonance in Medicine2020,83, 521–534, DOI:10.1002/mrm.27947.
3. McGivney, D. F.; Pierre, E.; Ma, D.; Jiang, Y.; Saybasili, H.; Gulani, V.; Griswold, M. A.IEEE Transactions on Medical Imaging2014,33, 2311–2322, DOI:10.1109/TMI.2014.2337321.
4. Assl ̈ander, J.; Cloos, M. A.; Knoll, F.; Sodickson, D. K.; Hennig, J.; Lattanzi, R.MagneticResonance in Medicine2018,79, 83–96, DOI:10.1002/mrm.26639.
5. Lawson, C. L.; Hanson, R. J.,Solving least squares problems; SIAM: 1974.
6. Tropp, J. A.Signal Processing2006,86, 589–602, DOI:10.1016/j.sigpro.2005.05.031.
7. Foucart, S.; Koslicki, D.IEEE Signal Processing Letters2014,21, 498–502, DOI:10.1109/LSP.2014.2307064.
8. Jiang, Y.; Ma, D.; Seiberlich, N.; Gulani, V.; Griswold, M. A.Magnetic Resonance inMedicine2015,74, 1621–1631, DOI:10.1002/mrm.25559.
9. Sommer, K.; Amthor, T.; Koken, P.; Meineke, J.; Doneva, M. InProc. Intl. Soc. Mag. Reson.Med. 25, ISMRM: Honolulu, USA, 2017; Vol. 25, p 1491.
10. Hennig, J.Journal of Magnetic Resonance1988,78, 397–407, DOI:10 . 1016 / 0022 -2364(88)90128-X.
11. Collins,D. L.; Zijdenbos,A. P.; Kollokian, V.; Sled, J. G.; Kabani, N. J.; Holmes, C. J.;Evans, A. C.IEEE Transactions on Medical Imaging1998,17, 463–468, DOI:10.1109/42.712135.
12. Nagtegaal, M. A.; Koken, P.; Amthor, T.; de Bresser, J.; Madler, B.; Vos, F.; Doneva, M.NeuroImage2020,219, 117014, DOI:10.1016/j.neuroimage.2020.117014.

Acknowledgments / Funding Information: This research was partly funded by the Medical Delta consortium, a collaboration between the Delft University of Technology, Leiden University, Erasmus University Rotterdam, Leiden University Medical Center and Erasmus Medical Center. The authors want to thank Peter Börnert for fruitful discussions and Peter Koken, Mariya Doneva and Thomas Amthor for providing the MRF patch.

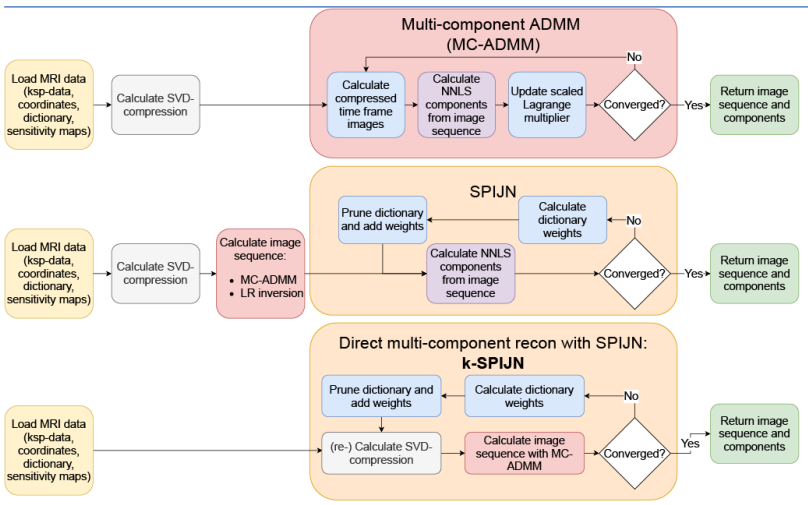

Figure 1. A schematic overview of the here proposed reconstruction methods. Low rank Multi-component ADMM (MC-ADMM) reconstructs low rank images with a multi-component constraint. SPIJN[2] allows for joint-sparsity multi-component estimates from (low rank) images. k-SPIJN directly reconstructs joint-sparsity multi-component maps from undersampled k-space MRF data.

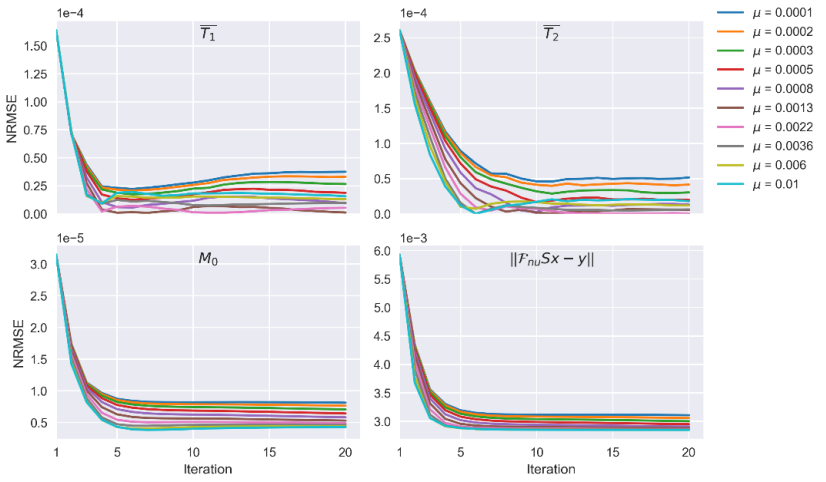

Figure 2. Convergence plots for different values of the ADMM coupling parameter. The ADMM loop was performed with 20 Conjugate gradient iterations per outer iteration. A numerical BrainWeb phantom was used as ground truth and the root mean square error (RMSE) is evaluated over the complete image. Geometric mean T_1 and T_2 were derived from the obtained component maps.

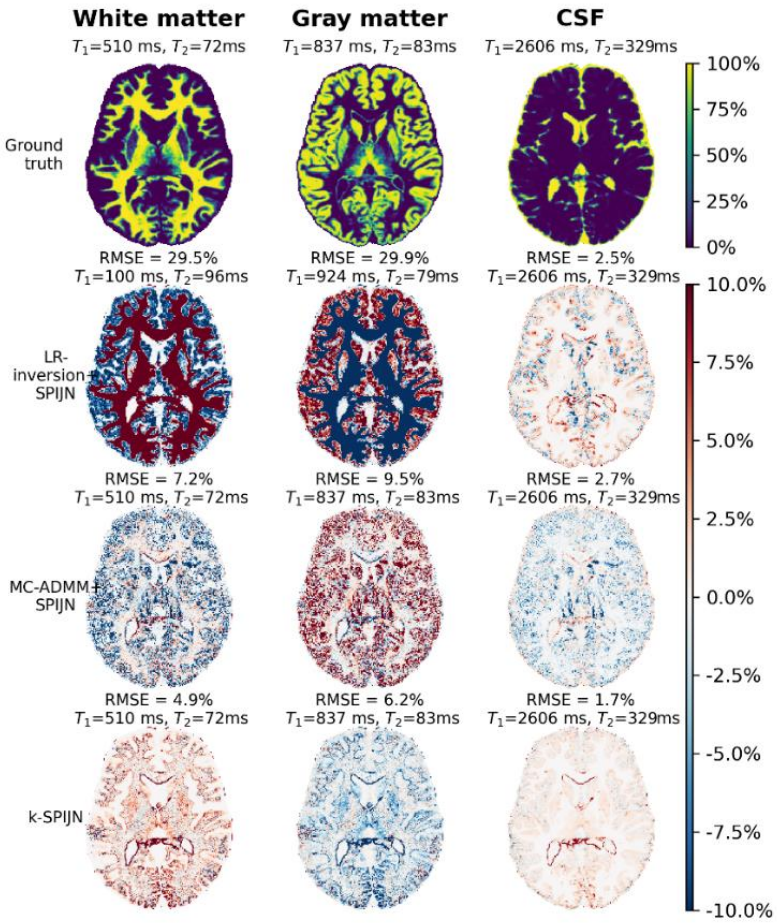

Figure 3. Obtained error maps for multi-component tissue segmentations using different reconstruction methods (lower 3 rows). A numerical BrainWeb phantom was used as ground truth (upper row) and an MRF sequence of length 200 was used. Root mean square errors (RMSE) were computed over the whole slice. Estimated and ground truth relaxation times are reported above each map.

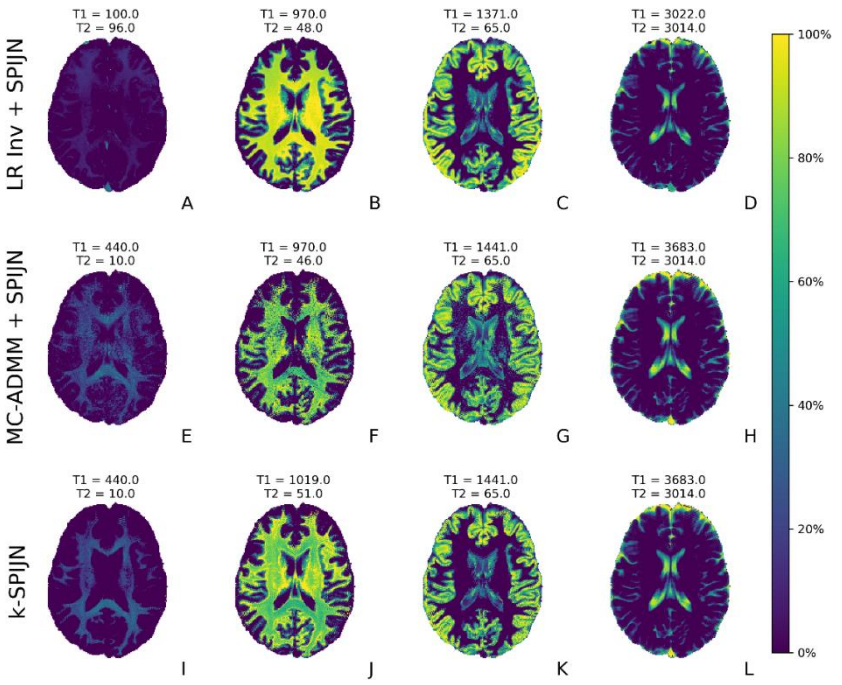

Figure 4. Estimated magnetization fraction maps and tissue components from R=5/32 undersampled data for sequence length 400 with 3 different reconstruction methods. The estimated components (structurally and matched relaxation times) relate to myelin water, WM, GM and CSF (columns from left to right). In general there is structural similarity between estimates, but k-SPIJN shows less noise especially in white matter.

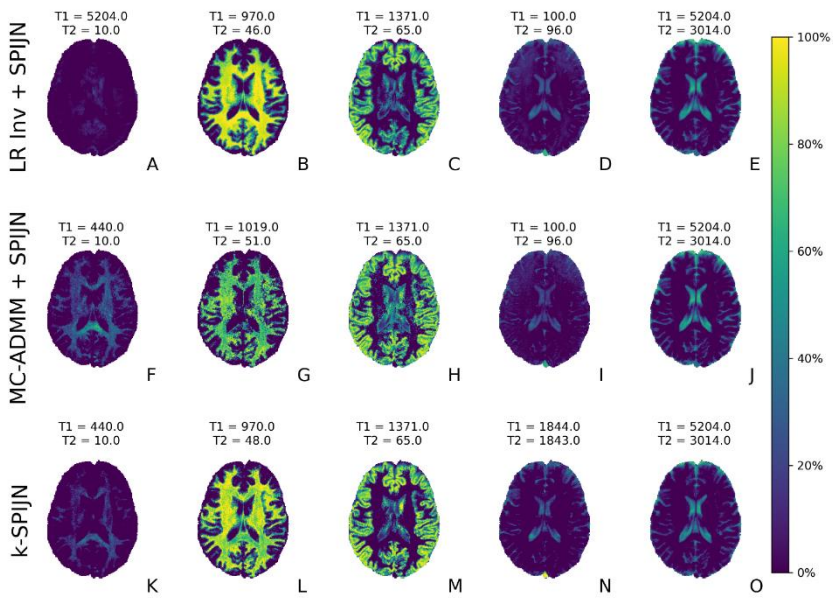

Figure 5. Estimated magnetization fraction maps and tissue components from R=1/32 undersampled data for sequence length 400 with 3 different reconstruction methods (rows). The estimated components (structurally and matched relaxation times) relate to myelin water, white matter, gray matter and CSF (2 components) (columns from left to right). Again differences between reconstruction techniques are most pronounced in the first 2 columns.

Eliminating limits of spatiotemporal resolution in radial stack-of-stars imaging using FID navigators and single-readout binning

I.T. Maatman[1], S. Ypma[1], M. Kachelrieß[2], Y. Berker[3], K.T. Block[4], E. Van der Bijl[5], C. Rosman[6], J.J. Hermans[1], M.C. Maas[1], and T.W.J. Scheenen[1]

[1]Department of Imaging, Radboud University Medical Centre, Nijmegen, the Netherlands; [2]Department of X-Ray Imaging and Computed Tomography, German Cancer Research Center (DKFZ), Heidelberg, Germany; [3]Clinical Cooperation Unit Pediatric Oncology, German Cancer Research Center (DKFZ), Heidelberg, Germany; [4]Department of Radiology, NYU Langone Medical Center, New York, NY, United States; [5]Department of Radiotherapy, Radboud University Medical Centre, Nijmegen, the Netherlands; [6]Department of Surgery, Radboud University Medical Centre, Nijmegen, the Netherlands

Synopsis: Motion-compensated images can be created from motion-binned undersampled radial stack-of-stars data through compressed sensing and image registration. However, for longer repetition times or many partitions, the acquisition time for one radial projection with all phase-encode steps becomes too long to sample the motion via self-gating, which leads motion artifacts. Therefore, we estimate motion from FID navigators and perform binning on a single-readout level to gain higher spatiotemporal resolutions. Our methods are tested on a motion phantom and volunteer with gridding and motion-compensated reconstructions. Our results show accurate detection of the motion signal and reduced motion blur in reconstructions.

Purpose: MRI of the thorax is challenging, as respiratory motion can induce blurring or ghosting artifacts.[1] Breath-holding limits acquisition times to approximately 15 s, precluding high spatial resolutions over large fields-of-view.

Radial sampling schemes are inherently motion robust.[2] Furthermore, if golden-angle reordering is used, radial MR data can be retrospectively gated into multiple motion states according to a motion signal.[3] A common method to extract the motion signal is to collect the data near the k-space center for projections of the total signal in the imaged volume at every $\Delta t = N_p \cdot TR$, where Np is the number of partitions and TR is the repetition time.[3-6] According to the Nyquist criterion, the detectable respiratory frequency in this case is limited to $f_s = 1/(2 \cdot N_p \cdot TR)$. For longer TR, or many partitions, the acquisition time for a full stack of partitions per radial projection becomes too long to faithfully sample the motion, leading to temporal aliasing and motion blur when binning k-space data into different motion states.

We lift this restriction by acquiring a short free-induction decay (FID) navigator at every TR, allowing single-readout binning (SRB) of the data into motion states, resolving motion frequencies up to $1/(2 \cdot TR)$. We test our method on a motion phantom and a normal breathing volunteer, reconstructing the data with a non-uniform fast Fourier transform (NUFFT) and an adapted version of the 4D motion-compensated high-dimensional total variation (MoCo-HDTV) algorithm, which is a framework for joint reconstruction and motion estimation for undersampled radial data.[6]

Methods: We acquired data of a motion phantom (Quasar MRI 4D, Modus QA, London, Canada) and volunteer with a golden-angle radial stack-of-stars spoiled gradient echo sequence[7] (Table 1) on a 3-T MR system (Prisma-Fit, Siemens Healthineers, Erlangen, Germany). The phantom contained a central oscillating gel-filled cylinder. Maximum peak-to-peak translation was set to 3 cm and the frequency of the breathing-like motion pattern was approximately 0.25 Hz. TR and N_p were chosen such that spoke angle binning (SAB), which includes all phase-encode steps per spoke orientation, was expected to lead to inaccurate motion estimates. We sampled 32 FID acquisition points in 200 µs between excitation and phase-encoding gradient as a navigator. For each spoke angle, all partitions were sampled in random order before moving to the next angle to ensure a more evenly distributed number of readouts in each partition and respiratory phase (Fig. 1).

Respiratory motion signals were extracted as the first principal components of principal component analyses (PCA) of the FID navigators and of the nine central points of every gradient-echo readout.[6,8] We calculated the correlation coefficients of the FID and gradient-echo motion signals with the reference signal of the phantom. We reconstructed the data both with NUFFTs and via an adapted version of the MoCo-HDTV algorithm.[6]

To compare SAB and SRB independent of the method of motion detection, we created reconstructions for SAB with the means of the FID navigators across the partitions as the motion signal, since Δt was too long to detect respiratory motion from the k-space center.

Results and Discussion: The FID motion signal shows a clear correspondence to the motion pattern imposed on the phantom, indicating that the rigid motion during acquisition was accurately extracted from the FID navigators (Fig. 2). Meanwhile, the gradient-echo motion signal is clearly aliased (Fig. 2). Calculated correlation coefficients of the FID and gradient-echo motion signals with respect to the reference equaled 0.98 and 0.26, respectively.

SRB resulted in reduced motion blur in NUFFT reconstructions of the phantom data, and in higher through-plane incoherence of undersampling artifacts, which may be advantageous for compressed sensing reconstructions (Fig. 3).[8]

Figure 3 also shows comparisons of the MoCo-HDTV reconstructions for the phantom data again at end-exhalation, which greatly reduce the level of undersampling artifacts, although at the cost of slight motion blur. However, SRB instead of SAB leads to an increase of the effective spatial resolution by reducing motion blur between slices. Using SRB combined with MoCo-HDTV reconstruction on in vivo data leads to a sharp depiction of anatomical structures in the thorax and abdomen at high spatial resolution (Fig. 4).

Conclusion: We showed first results for the acquisition and reconstruction of radial stack-of-stars data where the temporal resolutions for motion detection and reconstruction are increased through FID navigators and single-readout binning. Images of a moving phantom and a volunteer show reduced motion blur, and reduced and more incoherent streaking artifacts, allowing the detection of small anatomical structures in the upper abdomen in a free-breathing acquisition.

References:

1. Axel L, Summers RM, Kressel HY, et al. Respiratory effects in two-dimensional Fourier transform imaging. Radiology. 1986; 160:795-801.
2. Glover GH, Pauly JM. Projection reconstruction techniques for reduction of motion effects in MRI. Magn Reson Med. 1992; 28(2):275-89.
3. Feng L, Axel L, Chandarana H, et al. XD-GRASP: Golden-angle radial MRI with reconstruction of extra motion-state dimensions using compressed sensing. Magn Res Med. 2016; 75(2):775-88.
4. Spincemaille P, Liu J, Nguyen T. Z-intensity-weighted position self-respiratory gating method for free-breathing 3D cardiac CINE imaging. Magn Reson Imaging. 2011; 29(6):861-8.
5. Schneider M, Benkert T, Solomon E, et al. Free-breathing fat and R2*-quantification in the liver using a stack-of-stars multi-echo acquisition with respiratory-resolved modelbased reconstruction. Magn Reson Med. 2020; 84(5): 2592-2605.
6. Rank CM, Heußer T, Buzan MTA, et al. 4D respiratory motion-compensated image reconstruction of free-breathing radial MR data with very high undersampling. Magn Res Med. 2016; 77(3):0740-3194.
7. Block, KT, Uecker, M. and Frahm, J. Undersampled radial MRI with multiple coils. Iterative image reconstruction using a total variation constraint. Magn. Reson. Med. 2007; 57:1086-1098.
8. Lustig M, Donoho D, Pauly JM. Sparse MRI: the application of compressed sensing for rapid MR imaging. Magn Reson Med. 2007; 58(6):1182-1195.

Acknowledgments / Funding Information: We thank C. Schneider and U. Van der Heide of the Netherlands Cancer Institute (NKI) for providing the Quasar MRI 4D phantom.

	Phantom scan	Volunteer scan
Number of readout points	512 (2x oversampling)	512 (2x oversampling)
Number of spokes	400	500
Number of partitions	112	144
TE	2.46 ms	2.46 ms
TR	20.0 ms	7.00 ms
Δt for motion without FID nav	112 x 20 = 2240 ms	144 x 7 = 1008 ms
Δt for motion with FID nav	20 ms	7 ms
Voxel size	1.56 x 1.56 x 2.50 mm^3	1.17 x 1.17 x 2.00 mm^3
Field of view	400 x 400 mm^2	300 x 300 mm^2
Slice resolution	100%	100%
Bandwidth	698 Hz/px	1085 Hz/px
Orientation	transversal	coronal
Acquisition time	14 m 58 s	8 m 25 s

Table 1. Sequence parameters of the MR acquisitions of phantom and volunteer data. Δt for motion indicates the time interval between motion signal samples.

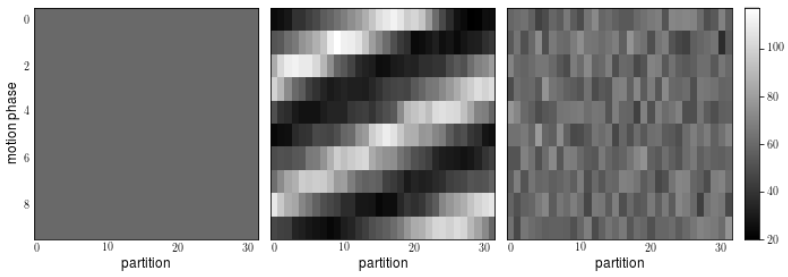

Figure 1. Distribution of the number of readouts per motion phase (for 10 unique phases) and partition for three different acquisition schemes: SAB (left), SRB with linear kz-reordering (middle image) and random kz-reordering (right). We suppress the periodicity in the distribution (middle image) by sampling partitions in random order (right).

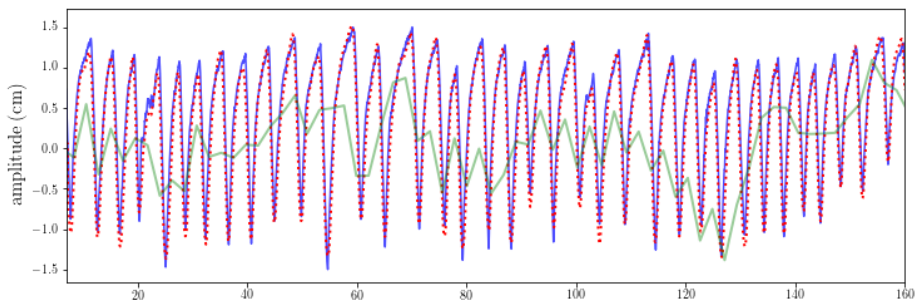

Figure 2. The phantom's reference signal (blue line), the free-induction decay navigator signal (red dotted line) and the gradient-echo signal (green line). There is a clear correspondence between the reference and the FID navigators (correlation coefficient of 0.98 with reference), apart from some under- or oversampling of motion in the end-inhalation phase. The gradient-echo signal is clearly aliased (correlation coefficient of 0.26 with reference).

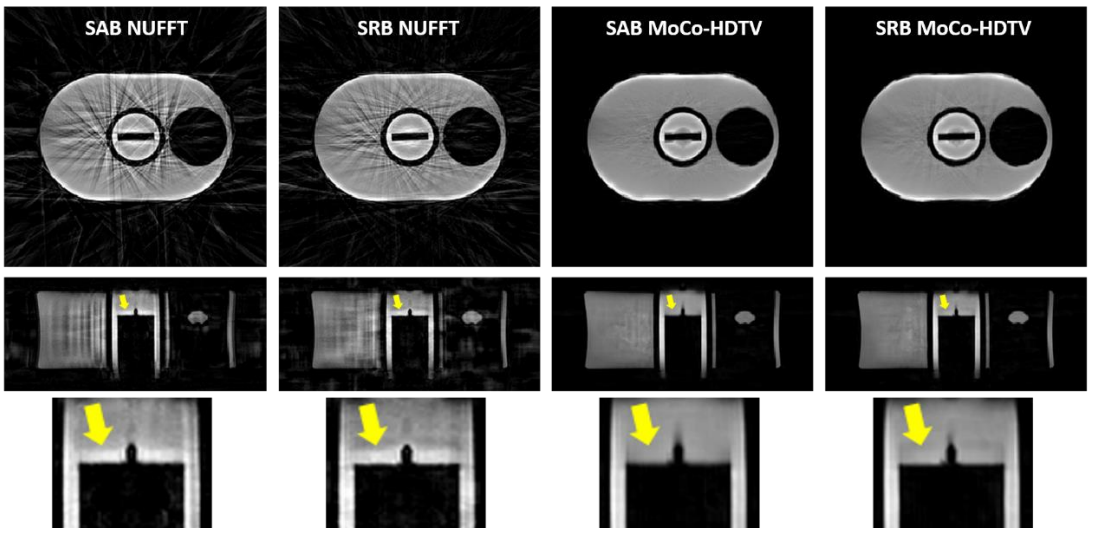

Figure 3. NUFFT and MoCo-HDTV reconstructions of the phantom data at end-exhalation with both the SAB and SRB methods. Images in the top row correspond to reconstructions in the readout plane. For images in the bottom row, the vertical axes of images correspond to the phase-encoding directions. SRB reduces the motion blur (arrows) and increases through-plane incoherence of radial streak artifacts.

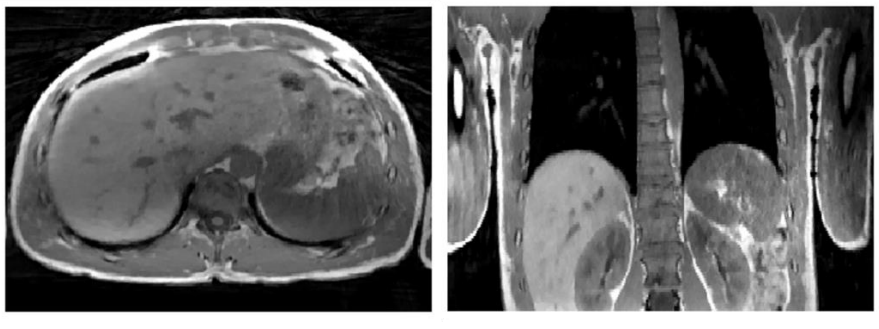

Figure 4. Transversal and coronal MoCo-HDTV reconstructions of the volunteer data with SRB. Data was acquired in coronal orientation. Contours of the diaphragm and liver are sharply delineated in both images.

Recurrent Variational Inference for fast and robust reconstruction of accelerated FLAIR MRI in Multiple Sclerosis

D. Karkalousos [1], L.C. Liebrand [1], S. Noteboom [2], Hanneke E. Hulst [2,3], F. M. Vos [4], M.W.A. Caan [1]

1 Department of Biomedical Engineering & Physics, Amsterdam UMC, University of Amsterdam, Amsterdam, Netherlands, 2 Department of Anatomy & Neurosciences, MS Center Amsterdam, Amsterdam Neuroscience, Amsterdam UMC, Vrije Universiteit Amsterdam, Amsterdam, Netherlands
3 Department of Medical, Health and Neuropsychology, Leiden University, Leiden, Netherlands 4 Department of Imaging Physics, Delft University of Technology, Delft, Netherlands

Synopsis: Robustness when applying Deep Learning methods to clinical data is crucial for accurate high-resolution reconstructions while having fast inference times. We propose the Cascades of Independently Recurrent Variational Inference Machine (CIRVIM), targeting deep unrolled optimization and enforcing data consistency for further robustness. We quantify contrast resolution of seven and half times prospectively undersampled FLAIR MRI without fully-sampled center containing Multiple Sclerosis lesions. The proposed scheme reduces inference times by a factor of 6 compared to Compressed Sensing. Lesion contrast resolution improves by approximately 13% while preserving spatial detail with enhanced sharpness compared to more blurred results of other presented methods.

Purpose: To reconstruct out-of-training-distribution high-resolution images containing Multiple Sclerosis lesions with sufficient contrast resolution and fast inference times.

Introduction: In MRI high acceleration factors can be achieved with Compressed Sensing (CS)[1] to facilitate the slow acquisition times, but the reconstruction times are relatively slow. Machine Learning (ML) can vastly reduce inference times while producing high-resolution images. Sampling significantly fewer data points results in kspace results in an aliased image in the image domain. The barrier when applying an ML method for dealiasing and denoising MRI data in the clinical setting is its robustness in generating accurate results. The main challenge is the generalization to new data, where it is unknown how to restore the fully sampled image given sparsely sampled measurements. This is known as the inverse problem of accelerated-MRI reconstruction. ML methods learn how to solve it from the data instead of applying a predefined sparsifying transform as in CS. We assess the robustness of an unrolled scheme targeting optimization by gradient descent to solve the inverse problem of accelerated-MRI reconstruction. We use pretrained networks and compare them to CS for evaluating fast high-resolution reconstructions of out-of-training-distribution clinical data of Multiple Sclerosis patients with known white matter lesions.

Methods: The Recurrent Inference Machine[2] solves the inverse problem of accelerated-MRI reconstruction through a sequence of alternating convolutional and recurrent layers. To reduce the model's complexity and, thus, inference time, we chose the Independently Recurrent Neural Network (IndRNN)[3] as an option for the recurrent layers and built an Independently Recurrent Inference Machine (IRIM). Its recurrent nature allows it to capture long-range dependencies through time steps, so robustness is assessed by increasing them. Nevertheless, training RNNs with a large number of time-steps is challenging due to often out-of-memory errors by vanishing or exploding gradients. For that purpose, we selected a general variational scheme of cascades and built RIM blocks sequentially connected. We call this method Cascades of Independently Recurrent Variational Inference Machine (CIRVIM) (Figure 1).

We trained networks on fully sampled 3D 3.0T T1-weighted brain data[2], as well as 2D FLAIR brain data[4], retrospectively undersampled up to ten times on a Gaussian distribution. The training and validation sets consisted of 3150 slices for the T1 dataset and 6750 for the FLAIR dataset. The IRIM and CIRVIM models were built with 64 channels and 8 time-steps. The cascades were tuned with selected values varying between 1 for building an IRIM and 4, 6, and 8 for building larger CIRVIM models. Parallel-Imaging Compressed Sensing (PICS) reconstructions were done using the BART toolbox[5] with l1-regularization set to 0.05 and 60 iterations (Figure 2). All experiments were performed on an NVidia Tesla V100 GPU with 32GB of memory.

The test dataset contained 18 3D FLAIR scans of relapsing remitting Multiple Sclerosis patients with known white matter lesions, prospectively undersampled with a factor of 7.5 on a Variable-Density Poisson disk distribution. Data were acquired on a 3.0T Philips Ingenia scanner (Philips Healthcare, Best, The Netherlands) in Amsterdam UMC within the scope of a more extensive, ongoing study. The local ethics review board approved this study, and patients provided informed consent prior to imaging. A fully-sampled reference scan was also acquired and used to estimate coil sensitivity maps using the caldir method of the BART toolbox. We quantified the performance by measuring contrast resolution (CR) of the lesion relative to surrounding white matter after reconstruction:

$$\mathrm{CR} = \frac{S_{\text{lesion}} - S_{\text{WM surrounding lesion}}}{S_{\text{lesion}} + S_{\text{WM surrounding lesion}}}.$$

Results: The highest scoring method on measuring contrast resolution was the CIRVIM with eight cascades trained on the FLAIR data (Figure 3). The IRIM was the fastest method requiring ~6 seconds for reconstructing a 32-coils volume from the test set with 224 slices and matrix size 223×163. The largest CIRVIM with eight cascades was six times slower, while PICS was sixteen times slower than the IRIM. PICS scored fourth-best with overall more blurred results (Figure 4). The other CIRVIMs scored comparably to PICS, with overall sharper results but not up to the level of the model with the eight cascades. Quantitative evaluation of an example reconstructed slice showed an improvement in contrast resolution of approximately 13% of the FLAIR-trained CIRVIM compared to PICS (Figure 4). The second-highest scoring model (T1-trained IRIM) showed artifacts, while other reconstructions showed more apparent blurring.

Discussion/ Conclusion: The Cascades of Independently Recurrent Variational Inference Machine (CIRVIM) target robustness through cascades for learning optimization by gradient descent. The CIRVIM built with eight cascades and trained on FLAIR data scored highest on measuring contrast resolution for reconstructing Multiple Sclerosis lesions with an undersampling factor of 7.5x. The models trained on the T1 dataset appeared to be robust in reconstructing FLAIR data. The updated inputs through the cascades can enhance performance, thus generalization to clinical data containing pathologies unseen during training. Our method showed promising generalization capabilities, preserving spatial detail on reconstructing MS lesions with enhanced sharpness in contrast to a more blurred result by CS, as well as reducing the inference times up to six times.

References:

1. Donoho, D. L. (2006) 'Compressed sensing', IEEE Transactions on Information Theory, 52(4), pp. 1289–1306. doi: 10.1109/TIT.2006.871582.
2. Lønning, K. et al. (2019) 'Recurrent inference machines for reconstructing heterogeneous MRI data', Medical Image Analysis, 53, pp. 64–78. doi: 10.1016/j.media.2019.01.005.
3. Li, S. et al. (2018) 'Independently Recurrent Neural Network (IndRNN): Building A Longer and Deeper RNN', Proceedings of the IEEE Computer Society Conference on Computer Vision and Pattern Recognition, (1), pp. 5457–5466. doi: 10.1109/CVPR.2018.00572.
4. Muckley, M. J. et al. (2020) 'State-of-the-Art Machine Learning MRI Reconstruction in 2020: Results of the Second fastMRI Challenge'. Available at: http://arxiv.org/abs/2012.06318.
5. Uecker, M. et al. (2015) 'Berkeley Advanced Reconstruction Toolbox', Proc. Intl. Soc. Mag. Reson. Med., 23.

Acknowledgments / Funding Information: This publication is based on the STAIRS project under the TKI-PPP program. The collaboration project is co-funded by the PPP Allowance made available by Health~Holland, Top Sector Life Sciences & Health, to stimulate public-private partnerships.

Also, we would like to thank Marike van Lingen and Kevin Pancras for their contribution.

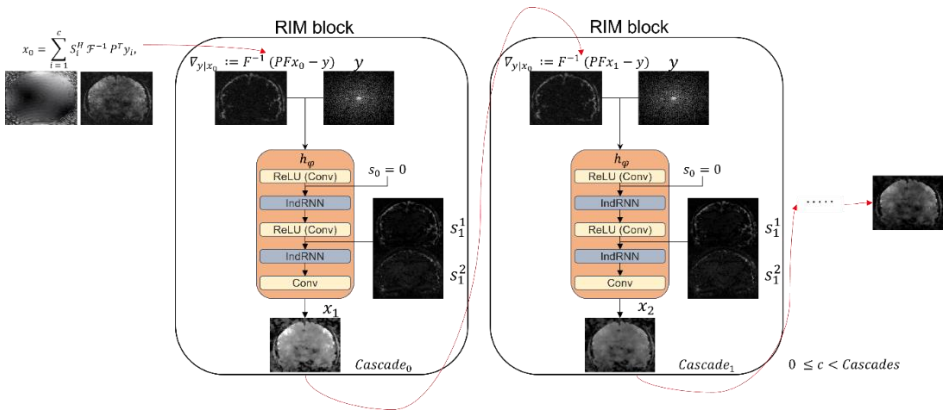

Figure 1: Sequentially connected RIM blocks form the Cascades of Independently Recurrent Variational Inference Machine (CIRVIM). The initial estimation (top-leftmost) is passed as input only to the first cascade. At every cascade, the subsampled measurements y and the computed log-likelihood gradient (top row), which is dependent on the previous estimation, are given as inputs to a RIM targeting optimization with better estimations (bottom) to produce the final estimation (middle-rightmost).

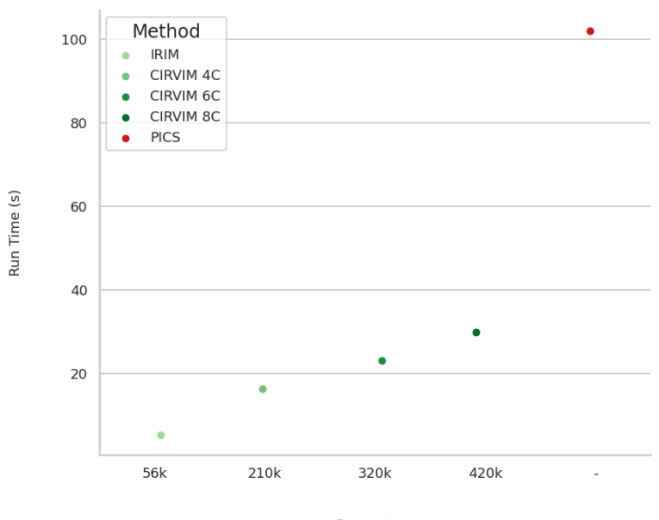

Figure 2: GPU inference times of PICS, the IRIM, and the CIRVIM with an increasing number of cascades. The y-axis represents seconds of the time to reconstruct a 32-coils volume with 224 slices and matrix size 223 x 163. Increasing the number of cascades leads to a linear increment to the inference time. The IRIM was 16 times faster than PICS, while the CIRVIM with eight cascades was ~3 times faster.

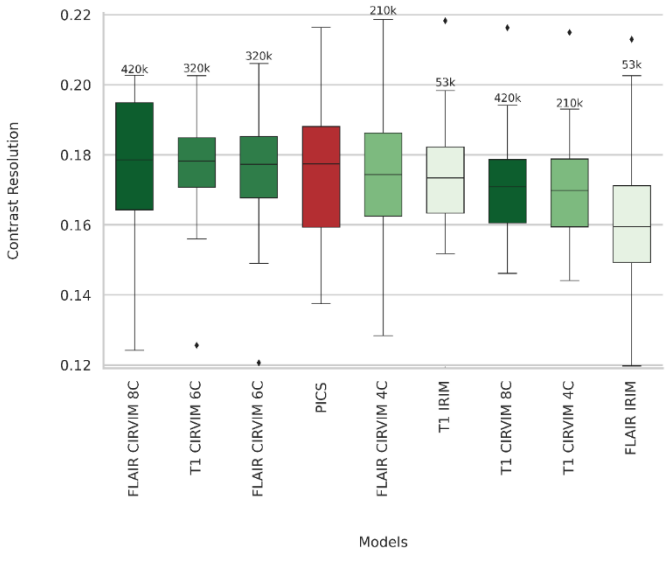

Figure 3: Evaluation of quantified contrast resolution. The x-axis, ordered from best (leftmost) to worst (rightmost), represents each model pretrained on the FLAIR and T1 datasets. On top of each bar, the number of parameters of the model is reported. The CIRVIMs with the higher numbers of cascades performed best compared to the four cascades and the IRIM, while PICS scored fourth-best.

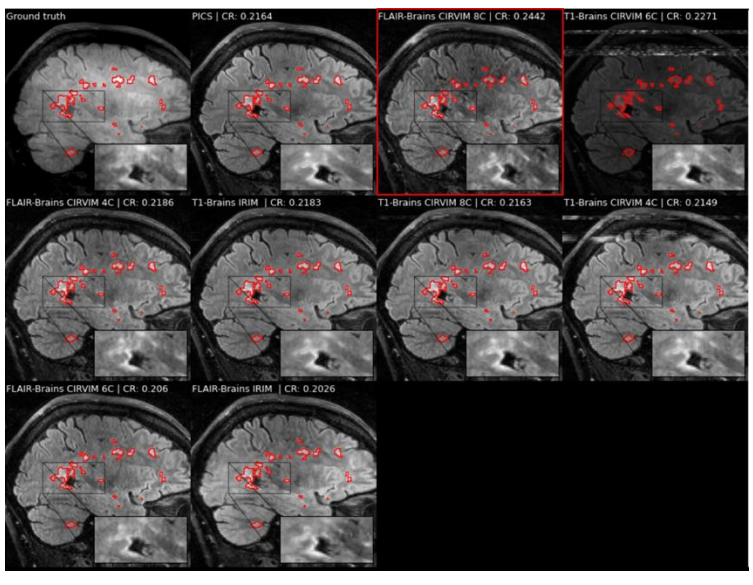

Figure 4: Reconstruction of a 7.5x prospectively undersampled FLAIR MRI slice containing Multiple Sclerosis lesions. The CIRVIM with eight cascades (first row-third image) trained on FLAIR data scored highest when quantifying contrast resolution. The best model (first row-third image, highlighted in a red square box) showed substantial difference compared to the other methods, preserving great spatial detail, without any distortions compared to the second-highest scoring model (first row-fourth image), and less blurring than all the other methods.

Accuracy and repeatability of joint sparsity multi-component estimation in MR Fingerprinting

Martijn Nagtegaal[1], Laura Nunez-Gonzalez[2], Dirk H.J. Poot[2], Jeroen de Bresser[3], Matthias J.P. van Osch[4], Juan Hernandez Tamames[1,2], Frans Vos[1,2]

1: Department of Imaging Physics, Delft University of Technology, Delft, the Netherlands
2: Department of Radiology and Nuclear Medicine Department, Erasmus MC, Rotterdam, the Netherlands
3: Department of Radiology, Leiden University Medical Center, Leiden, the Netherlands
4: C.J. Gorter Center for High Field MRI, Radiology Department, Leiden University Medical Center, Leiden, the Netherlands

Introduction

MR Fingerprinting[1] is getting increasingly more attention as a fast, multiparametric quantitative imaging method. The reduced scan-time of MRF has facilitated its applicability in research and clinical protocols. While MRF can have a rich sensitivity to a wide range of tissue properties, the relaxometry estimates are traditionally made voxel-wise, assuming a single T_1,T_2 combination per voxel. However, partial volume effects are known to hinder this so-called single component approach[2].

To cope with different tissue types within a voxel, the Sparsity Promoting Iterative Joint Non-negative least squares algorithm that was applied to MRF data[3] (SPIJN-MRF) was proposed. This approach asserted joint sparsity of the number of tissue components in a region of interest, i.e. in a voxel as well as spatially. Compared to other methods[1,4,5] this does not require a predetermined number of tissues and has less variation in tissue compositions between neighbouring voxels. In first in vivo validation, SPIJN-MRF showed to be able to obtain tissue segmentations.

The aim of this work is to evaluate the accuracy and repeatability of the SPIJN-MRF parameter estimations from highly undersampled MRF acquisitions and compare these with conventional segmentation methods.

Methods

Numerical simulations

To assess the accuracy of the SPIJN-MRF and T_1 weighted (T_1w) based segmentations 20 BrainWeb phantoms[6] were used. A gradient-spoiled MRF sequence of 1000 time points with a flip angle pattern as in[7] was simulated using EPG[8](resolution 1x1x5mm^3). T_1w-images were simulated by the BrainWeb simulator. Rician noise(SNR=100) was added to the simulated MRF and T_1w images.

In vivo acquisitions

Five healthy volunteers were scanned 8 times on a 3.0T GE MR750 MR scanner with a gradient-spoiled MRF sequence in an Institutional Review Board-approved study. Sequence settings were the same as in the simulations. 27 slices were acquired, with voxel size 1.2x1.2x5mm^3, 1mm slice gap and 256x256 voxels per slice. Total scan time was 5:54 minutes.

MRF data was reconstructed using an in-house implemented low-rank reconstruction algorithm. During reconstruction low rank images were estimated while a compression matrix was iteratively updated. The spatial L_1-norm of the L_2-norm across the component images was applied for regularization purposes.

An MRF dictionary was simulated with T_1=100ms-3s and T_2=10ms-1s with 5% step size. Synthetic T1w(sT_1w) images were calculated after single component matching with TE=25ms, TR=300ms, FA=90°.

The SPIJN-MRF partial volume segmentations were estimated by minimizing:

$$\hat{C} = \min_{C \in \mathbb{R}_{\geq 0}^{N_A \times J}} ||X - DC||_F^2 + \lambda \sum_i^N ||C_i||_0$$

in which X are the (compressed) MRF images with J voxels per time frame, D is the (compressed) dictionary with N_A atoms and C consists of N_A tissue fraction maps Ci of J voxels[3].

Data analysis

To achieve spatial correspondence FSL-FAST[9] and SPM12[10] segmentations were applied to sT1w images. SPIJN-MRF was used to obtain multi-component estimates from the MRF data. Obtained partial volume maps were registered based on sT1w-images to the ICBM152 atlas.

Six groups of MRF component maps were identified based on estimated T_1, T_2 values: myelin water(MW, T_1:100ms-500ms,T_2:9ms-20ms), white matter(WM, T_1:800ms-1050ms,T_2:50ms-100ms), gray matter(GM, T_1:1050ms-1500ms,T_2:50ms-100ms), two CSF components(T_1>2s,T_2<300ms and T_2>300ms) and *veins and arteries*(T_1:500ms-2s,T_2:200ms-1200ms). CSF components and MW and WM maps were combined for comparison with SPM12 and FSL segmentations.

The fuzzy Tanimoto coefficient (FTC) and Combined FTC (CFTC)[11] (range 0-1, where 1 is best) were used to estimate the voxelwise similarity between numerical ground truth and estimations, and between partial volume maps across days in vivo respectively. The coefficients of variation (CoV) of estimated volumes per subject, tissue and method were calculated for simulations and in vivo data. Slices showing motion artefacts were visually identified and excluded from the analysis.

Results

Numerical results

SPIJN-MRF yielded exact outcomes estimating the number of tissue component and corresponding relaxation times. The obtained segmentations were very close to the ground truth (Figure 1), while FSL and SPM12 showed a larger voxel-wise error. The relative error in volume was especially larger for SPM12.

In vivo results

SPIJN-MRF T_1 and T_2 estimates showed to be highly repeatable for WM, GM and CSF (Table 1). In comparison, myelin water showed more variation in T_1. Furthermore, T_1 estimates for CSF consistently corresponded to the longest T_1 time in the dictionary.

Magnetization fraction maps for one subject for a center slice are given in **Error! Reference source not found.**, showing a high similarity between scans, although a slight variation in MW fraction can be observed. Segmentations obtained with SPIJN-MRF, SPM12 and FSL showed clear differences (**Error! Reference source not found.**), especially in the CSF (see circles) and partial volume regions. **Error! Reference source not found.** shows the estimated CFTC and CoV for WM, GM, CSF and total brain volume (TBV) for the 5 subjects. SPM12 and FSL yielded smaller CoVs than SPIJN-MRF for WM and GM, while differences were smaller for CSF and TBV. Differences in CTFC were smaller and for CSF SPIJN-MRF showed better scores than SPM12 and FSL.

Discussion

The estimated relaxation times by SPIJN-MRF were in line with previously reported values in the literature[12], but WM (excluding MW) showed higher T_2 than GM, possibly due to the concentration of myelin water in a separate component . In simulations, SPIJN-MRF showed a very small bias in total volume estimates and very high FTC compared with SPM12 and FSL. In vivo, the SPM12 and FSL segmentations showed a very low CoV, also compared to previous studies[13,14], this could be caused by the use of sT_1w images, potentially leading to artificially increased reproducibility (and possibly at the expense of biased estimates).

Conclusion

SPIJN-MRF is able to estimate accurate and precise tissue relaxation times and partial volume maps with increased accuracy in CSF compared to conventional methods.

References

[1]D. Ma, et al, Nature 495 (2013) 187–192. [2] D.F. McGivney,et al. Magn. Reson. Imaging 0 (2019). [3] M.A. Nagtegaal,*et al* Magn. Reson. Med. 83 (2020) 521–534. [4]D. McGivney, et al, Magn. Reson. Med. (2017). [5]B. Tang, C. et al, Inverse Probl. 34 (2018) 094005. [6] B. Aubert-Broche, et al. IEEE Trans. Med. Imaging 25 (2006) 1410–1416. [7] Y. Jiang, et al, Magn. Reson. Med. 74 (2015) 1621–1631. [8] J. Hennig, J. Magn. Reson. 78 (1988) 397–407. [9] M. Jenkinson, et al, NeuroImage 62 (2012) 782–790. [10] J. Ashburner, K.J. Friston, NeuroImage 26 (2005) 839–851.[11] W.R. Crum et al,

Acknowledgments / Funding Information: This research was partly funded by the Medical Delta consortium, a collaboration between the Delft University of Technology, Leiden University, Erasmus University Rotterdam, Leiden University Medical Center and Erasmus Medical Centre. This research was partially financed by a Research Grant from GE (B-GEHC-05).

IEEE Trans. Med. Imaging 25 (2006) 1451–1461. [12] J.Z. Bojorquez,et al, Magn. Reson. Imaging 35 (2017) 69–80. [13]F. Klauschen, et al, Hum. Brain Mapp. 30 (2009) 1310–1327. [14] D.L. Tudorascu, et al, Front. Neurosci. 10 (2016) 503.

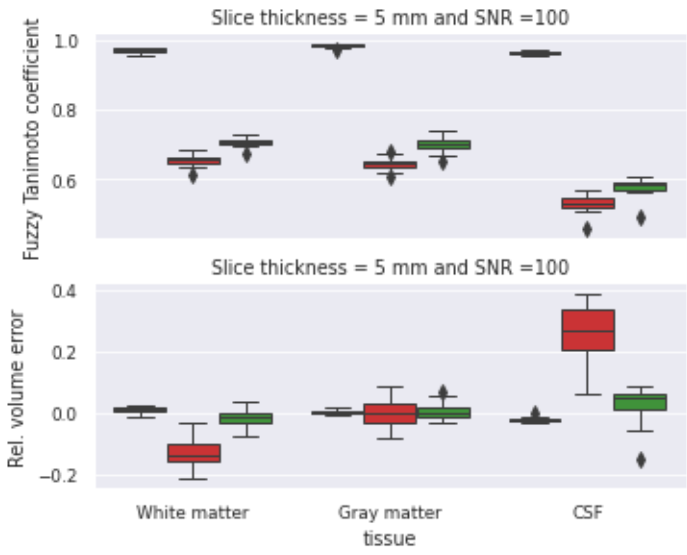

Figure 1: Accuracy of partial volume estimates in numerical simulations based on 20 BrainWeb phantoms. Voxel-wise accuracy was assessed with the fuzzy Tanimoto coefficient, accuracy of total volume estimates is compared based on the relative volume error.

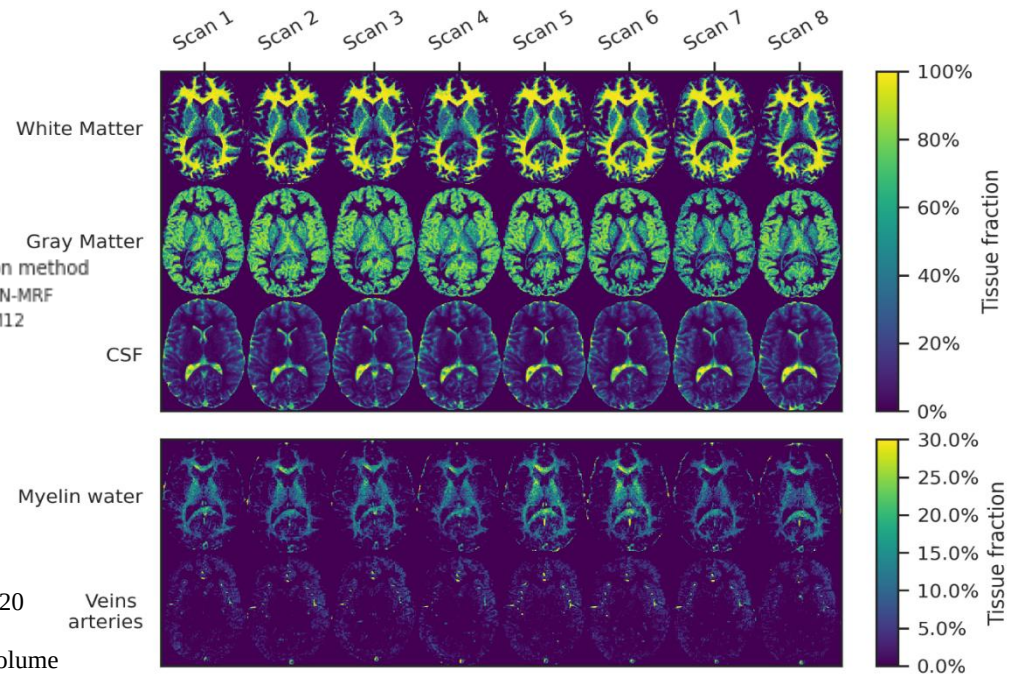

Figure 2: SPIJN-MRF maps across days and tissue types for a central slice for one subject after grouping based on relaxation time and before registration. Note that the lower two rows use a different color range for illustration purposes.

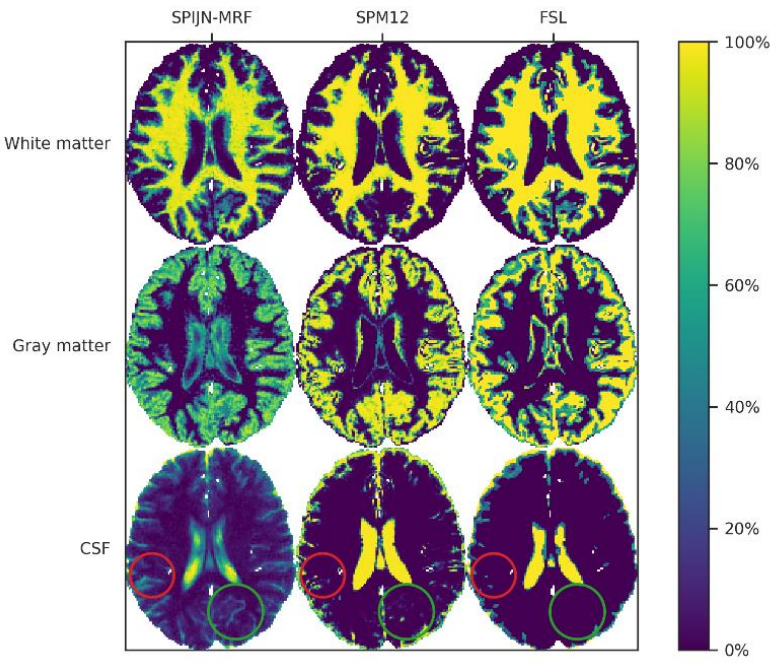

Figure 3: A representative slice showing the white matter (top), gray matter (middle) and CSF (bottom) fraction maps obtained using SPIJN-MRF (left), SPM12 (middle), and FSL (right) for one single acquisition of one subject. Red and green circles point out notable differences in CSF between methods.

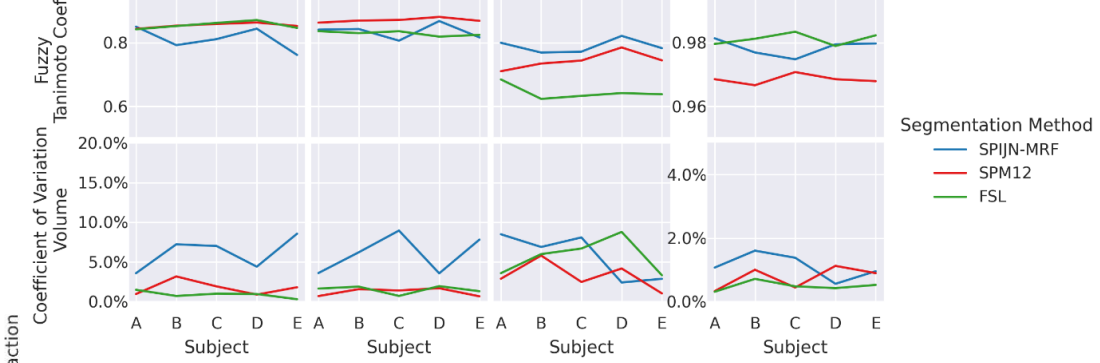

Figure 4: Combined Fuzzy Tanimoto Coefficient (CFTC) and CoV of estimated total volumes for each subject for white matter (including myelin), gray matter, CSF and total brain (white matter plus gray matter) obtained with SPIJN-MRF (blue), SPM12 (red), and FSL (green). The CFTC is a measure for voxel-wise differences, CoV shows the variation in total volume estimates. A total of 10 MRF acquisitions (out of 40) were affected by motion artefact in one or more slices. It concerned 3% of the total number of slices. These were left out of this analysis.

Table 1: Means and corresponding standard deviations of estimated T_1 and T_2 relaxation times across all 5 subjects and 8 repeated scans per tissue as well as the means of 5 intrasubject standard deviations per tissue. *T_1 or T_2 values were the minimum/maximum value represented in the dictionary, which also occurred with extended boundaries.

Tissue	**T_1 (ms)**		**T_2 (ms)**	
	Mean (Std)	**Mean Intrasubject standard deviation**	**Mean (Std)**	**Mean Intrasubject standard deviation**
White matter excluding myelin water	943.4 ± 0.0	0.0	69.2 ± 1.2	2.5
Gray matter	1383.9 ± 10.8	17.7	62.3 ± 1.2	1.7
CSF longer T_2	3042.6 ± 0.0*	0.0	1030.3 ± 0.0*	0.0
CSF shorter T_2	3042.6 ± 0.0*	0.0	149.3 ± 9.4	18.3
Myelin water	230.7 ± 20.1	34.0	10.0 ± 0.0*	0.0
Veins and arteries	876.2 ± 93.9	106.7	1030.3 ± 0.0*	0.0

Multivariate Curve Resolution (MCR) application for prostate cancer localization

A Stamatelatou[1], CG Bertinetto[2], JJ Jansen[2], GJ Postma[2], A. Heerschap[2], TWJ Scheenen[1]
[1]Medical Imaging, Radboud UMC, Nijmegen, The Netherlands; [2]Analytical Chemistry & Chemometrics, Radboud University, Nijmegen, the Netherlands

Synopsis: Three-dimensional MRSI data of the prostate was analyzed with a Multivariate Curve Resolution (MCR) approach for rapid automated localization and classification of cancer and healthy tissue. This data-driven method was used to extract common spectroscopic components without a need of prior knowledge, and compared to fitting a linear combination of prior knowledge models (LCModel). The MCR method identified components with known prostate metabolites and residual lipid and water signals Altogether, our approach can be considered as a step towards the development of an automated tool for classification of prostate MRSI spectra, avoiding subjective human intervention.

Introduction: Automated and reliable spectral evaluation is essential for the clinical use of 3D ^{1}H-MRSI of the prostate[1]. The multivariate Curve Resolution-Alternating (MCR) method aims at reconstructing the relative intensity of spectral profiles of individual chemical components within a sample[2], providing an easily interpretable model. Aim of this work is to apply the data-driven MCR method to prostate MRSI data for rapid automated localization and classification of cancer and healthy tissue, reducing the requirement for in-house expertise and improving objectiveness by avoiding subjective human intervention.

Method: We used data from 5 patients with prostate cancer (53-69 years, mean age 61 years) acquired on a 3T MR system (MAGNETOM Trio, Siemens Healthcare, Erlangen, Germany) with a body coil for transmission and an endorectal coil (MEDRAD, Pittsburgh, PA) for signal reception.

Non-water suppressed MRSI data were acquired using a semi-LASER sequence with frequency-selective refocusing and crushing of lipid signals3, optimized pulse timing for the spectral shape of citrate (TE 88ms) and a TR of 1930 ms. The water signal and sideband artefacts were removed in post-processing using the Löwner BSS algorithm4. Magnitude spectra(n=1824) in the spectral range of interest(2-4ppm) of 4 patients were used to perform MCR, which models the data **X** as a linear mixture of components: **X**=**C S**, where **C** and **S** are matrices of the pure components' relative abundances and spectral profiles respectively. These profiles are obtained by imposing mathematical constraints based on physicochemical principles. Therefore, MCR differs from other commonly used bilinear models such as Principal Component Analysis, whose components satisfy pure mathematical criteria(e.g.orthogonality) that do not necessarily relate to natural properties. The number of components in the model was estimated with Singular Value Decomposition (SVD) and initialized by entropy minimization5. The initial profiles were iteratively optimized using MCR-Alternating Least Squares (MCR-ALS)2, imposing a non-negativity constraint.

The relative intensities of each component for each voxel were normalized across all voxels from 4 patients, and mapped slice-by-slice for a qualitative validation of the model, using the histopathology reports as gold standard. The model's components were interpreted following the patterns of in-vivo prostate spectral shapes1. The component with the highest intensity in the Choline ppm region was further investigated as the most suspicious for the presence of tumor. As a second independent quantification method, spectra from all voxels were fitted with LCModel (Fig.1b, c) and the ratio (Choline+Creatine)/Citrate was calculated6. Z-score approach for both the relative intensity of the suspicious component from MCR-ALS and the LCModel's metabolite ratio was used to calculate thresholds to discriminate between healthy and cancerous spectra. Different thresholds were calculated for the peripheral zone (PZ) and the central gland (CG) of the prostates. The performance of the two methods was compared with the untested data of the 5th patient(456voxels) with a confusion matrix.

Results and Discussion: The optimal number of components, as assessed by SVD, was 4 for the training set of 4 prostate cancer patients (Fig.1). Examples of relative intensity maps of the components are presented for a slice in a patient with a tumor with Gleason score 2+3 (Fig.2) and for a patient with an aggressive tumor(Gleason score 3+4) (Fig.3). The spectral profile of component 1 has a shape similar to that of healthy prostate spectra, with high levels for Cit (2.6ppm) and low for Cho (3.2ppm) and Cre (3.03ppm). In contrast, the spectral profile of component 2, with elevated intensity in the Cho ppm range, is deemed representative for tumor spectra. Qualitatively in all 4 patients, the regions of increased levels of component 1 and 2 seemed to correlate with histopathologically healthy regions and regions with tumor tissue, respectively. Tentatively, in cases with more aggressive tumors, the intensity levels of component 2 were increased in comparison with less aggressive tumors (Fig.3). In the example of the aggressive tumor (Fig. 3), the mean value of the relative intensity of component 2 in 6 voxels located in the tumorous region was 0.87±0.05 AU, while in the second case (Fig.2) it was 0.68±0.04AU. The spectral profile of component 3 corresponded to prostate signals that were contaminated by lipids, which commonly occurs at the borders of the prostate (comp.3 in Fig.2,3). Finally, the profile of component 4 may arise from water signal that was not sufficiently removed.

The model, built on 1824 spectra from 4 patients, was applied to the 456 untested spectra of the 5th patient. The defined thresholds for component 2 from MCR-ALS (0.36AU for CG and 0.31AU for PZ) and for the metabolite ratio from LCModel (0.37AU for CG and 0.30AU for PZ) were used to classify the spectra as suspicious and non-suspicious for prostate cancer. Both methods agreed with an accuracy of 98% in classifying voxels of test patient 5 (Table 1), and the added value of MCR-ALS that prior knowledge is not required.

Conclusion: MCR-ALS can be used for the extraction of common spectroscopic components without a need of prior knowledge. The components can be used to classify prostate spectra as suspicious and non-suspicious for cancer, as well as identify lipids in the prostate. Furthermore, the results indicate the method may also assess tumor aggressiveness. Altogether, our approach can be considered as a step towards the development of an automated tool for classification of prostate MRSI spectra.

References:

1. Tayari N, Heerschap A, Scheenen TWJ, Kobus T. In vivo MR spectroscopic imaging of the prostate, from application to interpretation. Anal Biochem. 2017;529. doi:10.1016/j.ab.2017.02.001

2. De Juan A, Jaumot J, Tauler R. Multivariate Curve Resolution (MCR). Solving the mixture analysis problem. Anal Methods. 2014;6(14). doi:10.1039/c4ay00571f

3. Tayari N, Wright A, Heerschap A. Absolute choline tissue concentration mapping for prostate cancer localization and characterization using 3D 1 H MRSI without water-signal suppression. Magn Reson Med. Published online September 23, 2021.

4. Stamatelatou A, Sima DM, Van Huffel S, Van Asten JJ, Heerschap A, Scheenen TWJ. Post-acquisition water signal removal in 3D water-unsuppressed 1H-MR spectroscopic imaging data of the prostate. ISMRM Proceedings; 2021.

5. Bertinetto CG, de Juan A. Systematic comparison and potential combination between multivariate curve resolution–alternating least squares (MCR-ALS) and band-target entropy minimization (BTEM). J Chemom. 2018;32(6). doi:10.1002/cem.3000

6. Kobus T, Wright AJ, Weiland E, Heerschap A, Scheenen TWJ. Metabolite ratios in 1H MR spectroscopic imaging of the prostate. Magn Reson Med. 2015;73(1). doi:10.1002/mrm.25122

This project has received funding from the European Union's Horizon 2020 research and innovation program under the Marie Sklodowska-Curie grant agreement No 813120.

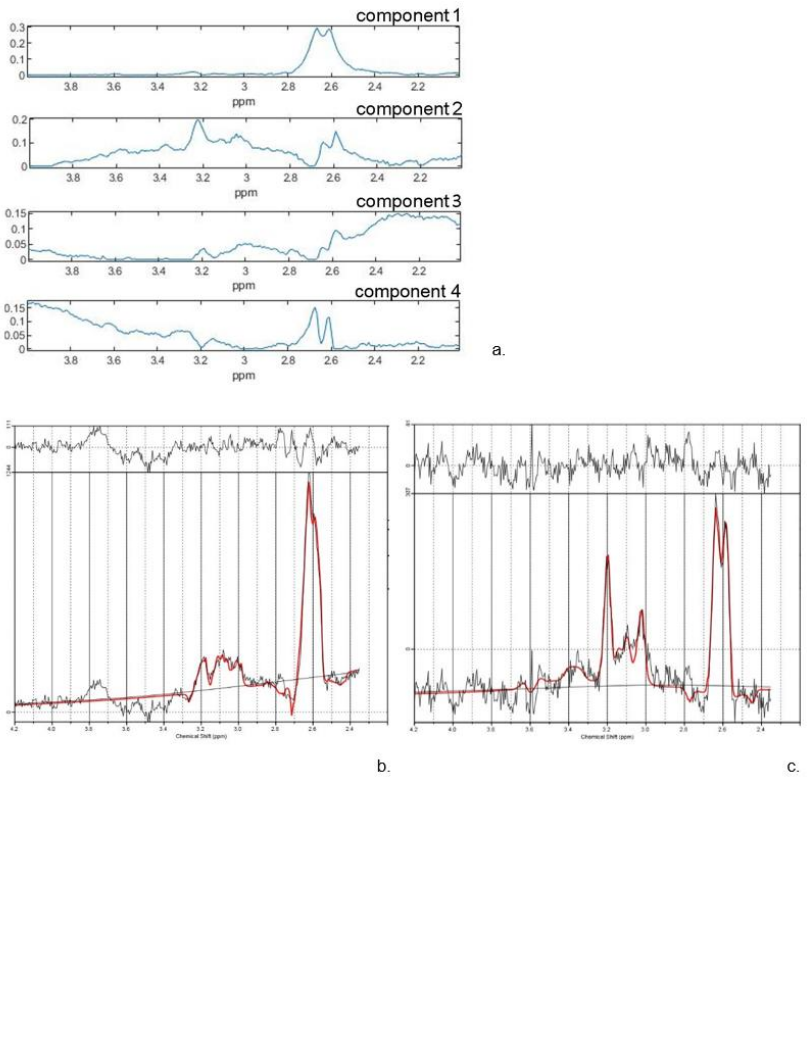

Figure 1. a. The spectral profiles of the components extracted with MCR-ALS from 4 prostate cancer patients. b. LCModel output of a healthy spectrum with high citrate levels that are also present in component 1. c. LCModel output of a cancerous spectrum, with an elevated choline signal at 3.2 ppm that can be observed in component 2.

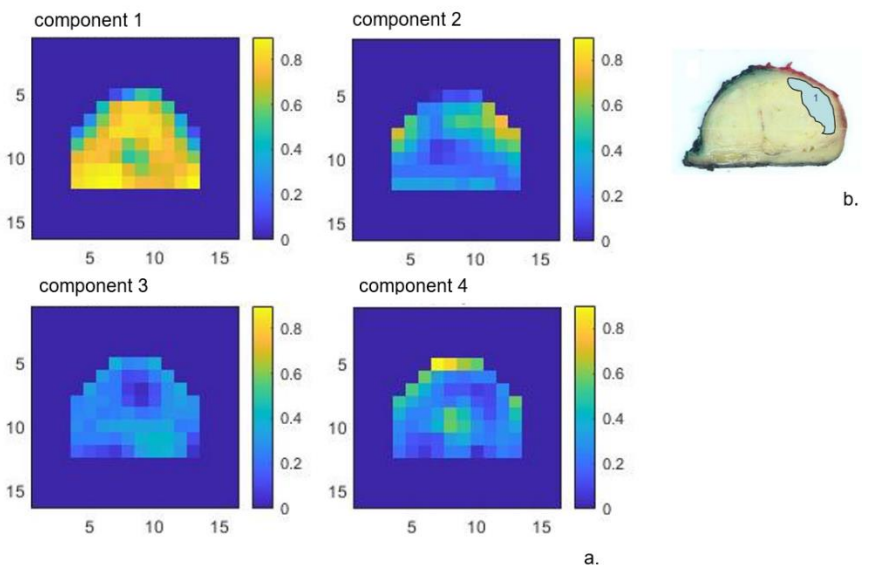

Figure 2. a. The relative intensity maps of each component in a slice of a prostate with a cancer lesion. The values are normalized across all voxels from 4 patients. b. Histopathology of the closest matching slice. A tumor is present with a Gleason score 2+3.

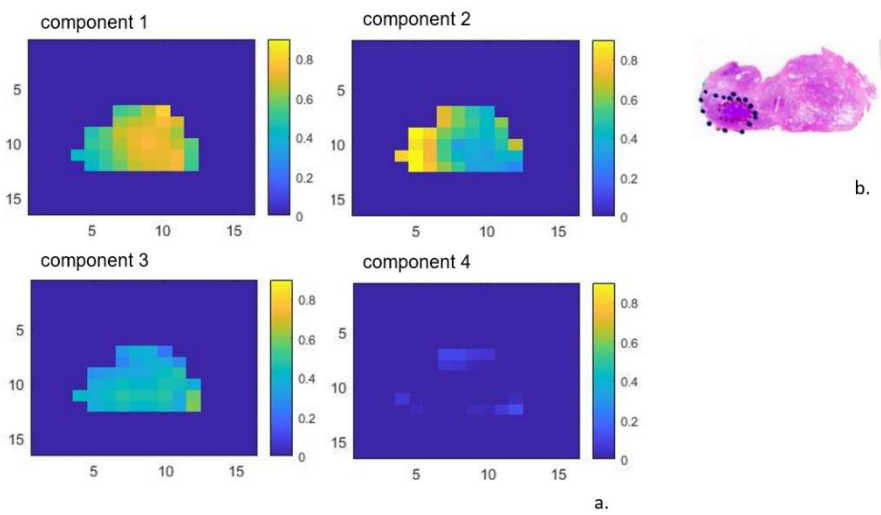

Figure 3. a. The relative intensity maps of each component in a slice of the prostate of a different patient with prostate cancer. The values are normalized across all voxels from 4 patients. b. Matching histopathology identified a tumor with Gleason score 3+4.

Table1. Confusion matrix comparing the performance of the data-driven MCR-ALS approach and LCModel fitting. Both methods had their own z-score calculated as the threshold between suspicious and non-suspicious spectra for the presence of prostate cancer.

	MCR-ALS suspicious	MCR-ALS non-suspicious
LC model output suspicious	187	0
LC model output non-suspicious	7	262

Ex vivo 7T MRI of resection specimen of oral cancer to improve margin control.

Klijs J. de Koning[1], Rob Noorlag[1], Annette van der Toorn[2], Gerben E. Breimer[3], Jan Willem Dankbaar[4], Remco de Bree[1], and Marielle E.P. Philippens[5]

1Head and Neck Surgical Oncology, University Medical Center Utrecht, Utrecht, Netherlands, 2Biomedical MR Imaging & Spectroscopy Group, University Medical Center Utrecht, Utrecht, Netherlands, 3Pathology, University Medical Center Utrecht, Utrecht, Netherlands, 4Radiology, University Medical Center Utrecht, Utrecht, Netherlands, 5Radiotherapy, University Medical Center Utrecht, Utrecht, Netherlands;

Synopsis: We validated the measured resection margins of the surgical specimens of tongue carcinoma on 7T ex vivo MRI with histopathology using T2 weighted MRI. In 3D T2wTSE (250 μm) with an acquisition time of 15-20 minutes, the resection margins was underestimated by 0.5 mm (+/- 1.3 mm). This will be developed into a clinical study with immediate re-resection during surgery to prevent adjuvant (chemo)radiotherapy, which is associated with radiation induced side effects.

Introduction

Oral squamous cell carcinoma (OSCC) is preferably treated by surgery. Its complete removal is essential for locoregional control and disease-free survival. Inadequate resection margins require adjuvant therapy such as re-resection or (chemo)radiation, which causes extra morbidity. In international literature, 30% to 85% inadequate resection margins are reported [1]. For tongue SCC, both intraoral ultrasonography (US) and magnetic resonance imaging (MRI) are reported to be very accurate in determining tumor thickness and depth of invasion preoperatively. In addition to in vivo imaging, also ex vivo imaging can help to improve the number of adequate resections. Since 7T MRI has the potential to visualize □ne details, ex vivo 7T MRI of the resection specimen of OSCC can indicate areas with close or positive resection margins for immediate re-resection [2] and by that reduce adjuvant radiotherapy treatment and eventually improve oral function and the patient's quality of life by adequate tumor resection.

Aim

A feasibility study to optimize the MRI protocol was performed in tongue tumors and compared to histopathology to build experience with ex vivo 7T MRI of resection specimen of OSCC in 10 tongue cancer patients.

Material and Methods

Ex vivo MR imaging of resection specimens was performed on a Bruker 7T MR spectrometer (BioSpec7T, Bruker, Ettlingen, Germany) interfaced with a Philips console. Multislice T2w TSE images (in plane 125 μm slice thickness 1 mm), 3D T2w TSE (250 μm) and DTI was performed (b-values: 0, 800, 1600 and 3200 s/mm, 40 directions, 1 mm). The tumor thickness and the smallest resection margins were measured in the MR images. Hematoxylin and eosin stained sections were cut every 3-5 mm and the distance between tumor outline and resection edge was measured and compared with the resection margins on MRI. In addition, MRI and histology was spatially correlated.

Results

HE stained sections and 7T MRI were compared and showed a small over-estimation of tumor thickness on MRI versus histopathology (1.2±1.0mm), while it slightly under-estimated the margin (0.5±1.2mm) (Figure 1). In addition, the tumor on HE stained sections and 3D T2 weighted TSE images were reoriented to match the histopathological sagittal slices and visually tumor extent on both 3D and multislice T2 weighted images (Figure 2). DWI showed acceptable co-localization with histopathology. Muscle □ber tracking showed the directionality of muslce □bers in the tongue. The total scan time of the three images was 30 – 45 minutes, depending on the size of the specimen.

Discussion and conclusion

The resection margins and tumor thickness on 7T MRI di□ered only slightly from that on histopathology. As the time for evaluation during surgery for immediate re-resection has to be limited, acquisition time and evaluation time has to be within 45 minutes, which means that maximum imaging time will be limited to 20-30 minutes. Therefore, either accelerated image acquisition is needed or only a single MR contrast and acquisition has to be chosen. For optimal 3D spatial correlation some re□ning using only whole mount sectioning and automatic registration between whole mount sections and MR images is desirable.

In conclusion, the close agreement between histopathology and 7T T2w images is promising for the transfer of ex vivo 7T MRI to a clinical study.

References

1. Smits, R. W., Koljenović, S., Hardillo, J. A.,Ten Hove, I., Meeuwis, C. A.,Sewnaik, A., Dronkers, E. A., Bakker Schut, T. C., Langeveld, T. P.,Molenaar, J., Hegt, V. N., Puppels, G. J. & Baaenburg de Jong, R. J. 2016.Resection margins in oral cancer surgery: Room for improvement.Head Neck, 38 Suppl 1, E2197-203.

2. Steens, S. C. A., Bekers, E. M., Weijs, W. L. J., Litjens, G. J. S., Veltien, A.,Maat, A., van den Broek, G. B., van der Laak, J. A. W. M., Futterer, J. J., vander Kaa, C. A. H., Merkx, M. A. W. & Takes, R. P. 2017. Evaluation of tonguesquamous cell carcinoma resection margins using ex- vivo MR. Int J Comput Assist RadiolSurg, 12, 821-828

Acknowledgments / Funding Information: We thank Tijl van der Velden for the technical assistance on the 7T scanner, Gerard van Vliet for the daily support and Martijn Foeling for setting up and processing of the muscle DTI.

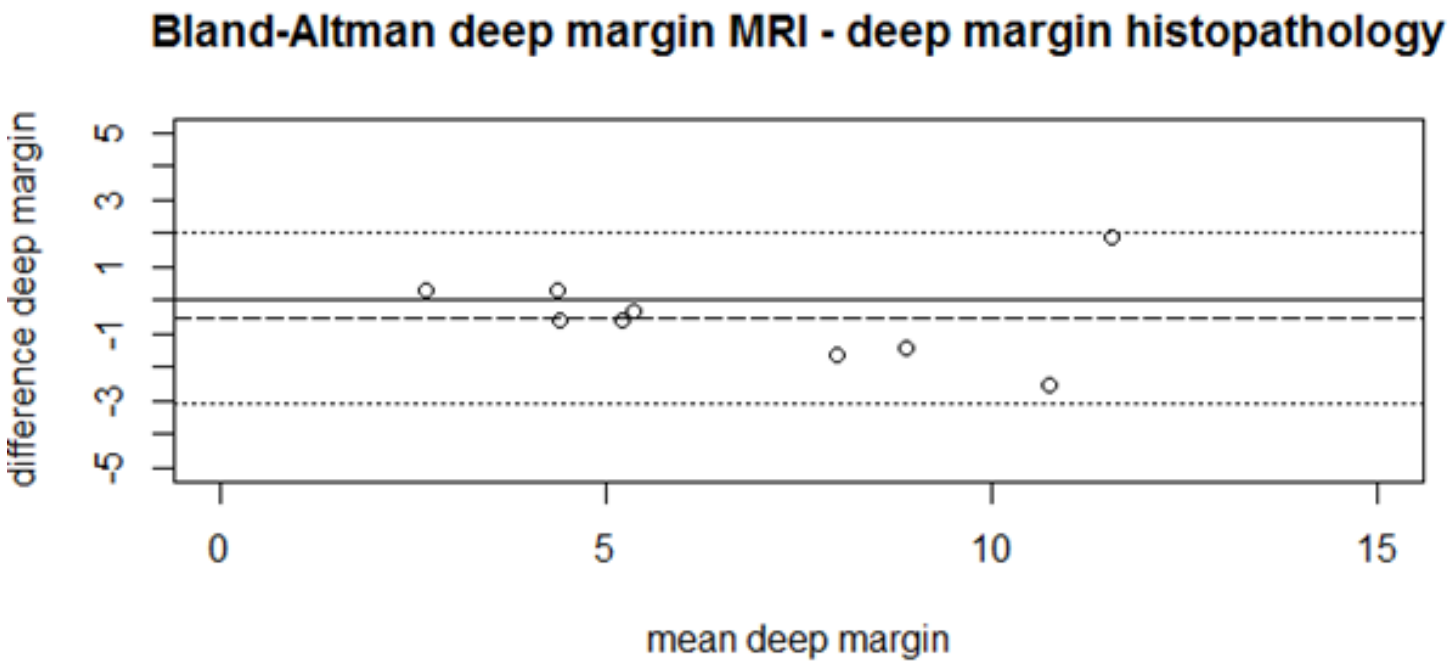

Figure 1. Bland-Altman plot of deep margins measured by MRI minus measured by histopathology. Dashed line shows the mean difference and dotted line the 95% confidence interval. As can be seen, MRI under-estimated the deep margin by 0.5mm with 95% confidence interval of 1.3 mm

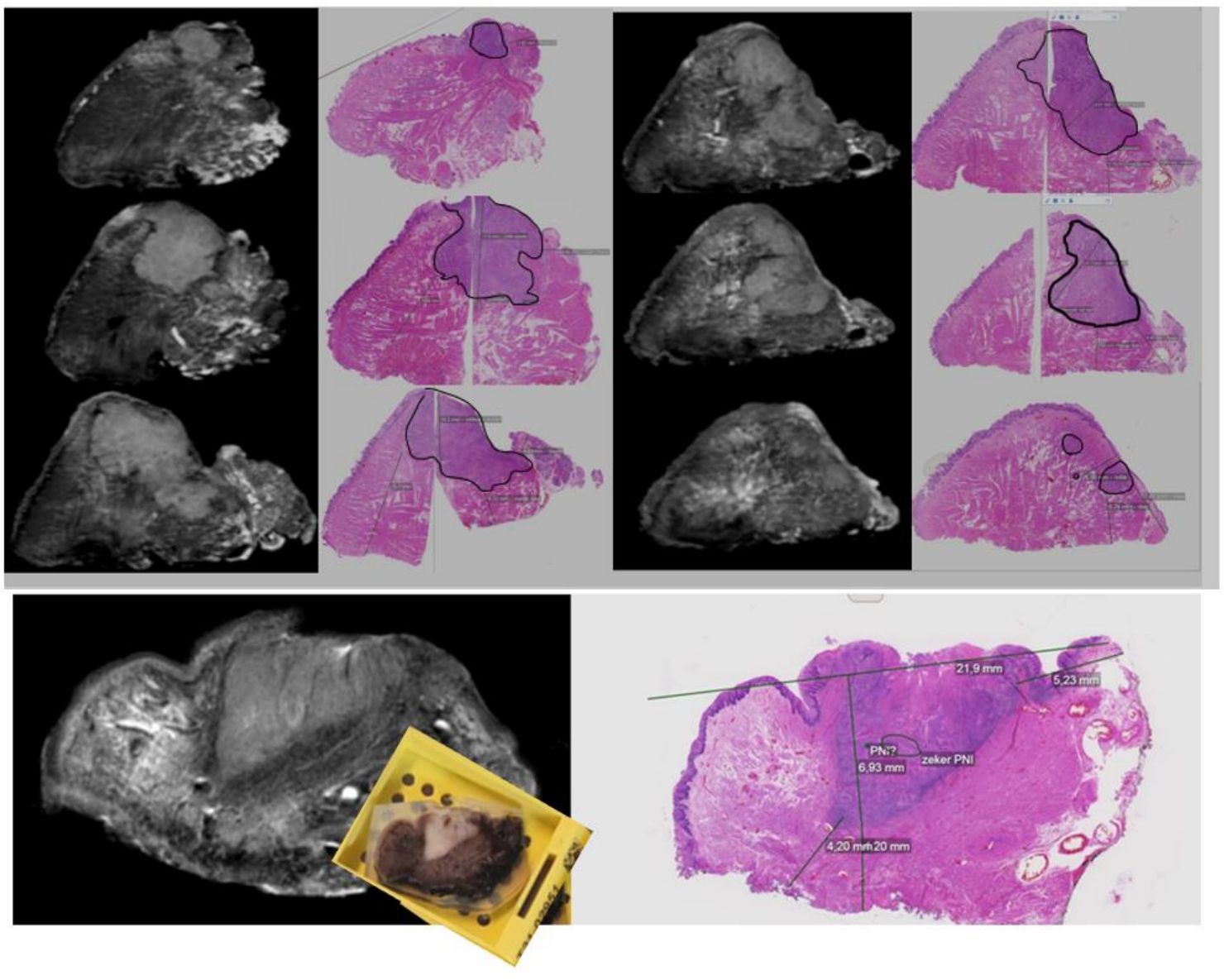

Figure 2. Two examples of the specimens of two patients with a tongue tumor. Visual evaluation shows an excellent correlation between HE-coupes and 3D T2W TSE images (upper row). Correlation between (2D) T2W TSE images. HE-coupes and macroscopic pathological images shows an excellent correlation as well (lower row).

APT-CEST Scan-Rescan Reproducibility in Healthy Volunteers and Brain Glioma Patients at 3 Tesla

Ivar J.H.G. Wamelink[1], Beatriz Padrela[1], Joost P.A. Kuijer[1], Yi Zhang[3], Frederik Barkhof[1,2], Henk J.M.M. Mutsaerts[1], Elsmarieke van de Giessen[1], Vera C. Keil[1]

[1]Department of Radiology and Nuclear Medicine, Vrije Universiteit Amsterdam Medisch Centrum, The Netherlands [2]Key Laboratory for Biomedical Engineering of Ministry of Education, Department of Biomedical Engineering, College of Biomedical Engineering & Instrument Science, Zhejiang University, Hangzhou, Zhejiang, China [3]UCL Institutes of Neurology and Healthcare Engineering, London, United Kingdom

Synopsis: Amide proton transfer (APT) chemical exchange saturation transfer (CEST) MRI is a potentially useful clinical technique to image brain tumors, but its reproducibility was not yet investigated in detail. Our 3T scan-rescan protocol on volunteers and glioma patients revealed high within-session and slightly lower in-between-session and between-day reproducibility, with highest reproducibility occipitally and centrally in the brain and lowest at the skull base. The within-session reproducibility for patients was also good, both intratumoral and extratumoral. These results show that APT-CEST at 3T MRI renders reproducible values allowing for clinical monitoring of metabolic brain tumors.

Purpose: Amide proton transfer chemical exchange saturation transfer (APT-CEST) imaging can detect increased levels of amides and peptides[1,2], which is potentially useful to detect and monitor brain tumors like gliomas[3-5]. While APT-CEST has shown promising results, its reproducibility has not yet been extensively investigated. Good reproducibility is however crucial for clinical follow-up and cut-off value determination. This study evaluates the reproducibility of APT-CEST at 3T for both healthy volunteers and glioma patients.

Methods:

Participants and Study design

21 healthy volunteers (age 39±11 yrs, 11 women) and 10 glioma patients (age: 55±15 yrs, 7 women) were scanned at 3T (Vida, Siemens, Erlangen, Germany) using a 20-channel head coil, including whole-brain 3D T1w and APT-CEST (2.8x2.8x2.8 mm resolution, 7 frequencies with MT pulses (10x 100ms at 2.5μT gaussian pulses) at ± 3.0, 3.5 and 4.0 ppm off-resonance, scan duration: 4m36s) plus a dual-echo GRE B0 map for geometric distortion correction.[6]

Healthy volunteers underwent 3 APT-CEST scan-sessions, while patients underwent one session. Each scan-session contains two consecutive APT-CEST scans and one B0-map. For a detailed description of the scan protocol see fig. 1.

Post-processing

Motion and distortion-corrected APT-CEST maps were calculated as magnetization transfer (MT) asymmetry (MTR_{asym}). APT-CEST unprocessed scans were registered to the 3D T1w images and transformed to MNI using ExploreASL and smoothed by a 3.5x3.5x3.5mm FWHM Gaussian filter. PyCharm was used to create voxelwise within-subject standard deviation (SD) maps of the difference between sessions/blocks (SD_{diff}) and further image processing.

Analysis

A neuroradiologist (VK), with 10 years of experience, manually delineated the hyperintense glioma regions-of-interest (ROIs) on the post-contrast T1w. The MTR_{asym} of tumor ROI was compared to a similarly-sized contralateral region and the between-days SD_{diff}.

SD_{diff} maps were calculated for the within-session, in-between-session, and between-day reproducibility. The within-session SD_{diff} maps of the volunteers were compared to the within-session SD_{diff} maps of the patients. Variance component analysis (Rstudio VCA) was performed for the whole brain, cortical gray matter, deep white matter, thalamus, and putamen. The normal APT-CEST values for healthy volunteers were also calculated for these masks and compared to mean tumor values. Finally, the scanning variability was related to the MTR_{asym} effect size between tumor and contralateral tissue. The effect size is given by mean_tumor_MTR_{asym} - mean_contralateral_MTR_{asym}.

Results:

APT-CEST values in healthy volunteers

Normal whole brain MTR_{asym} ranged between -0.92% and 1.96% —5^{th} and 95^{th} percentile, respectively — with a mean of 0.49% (Table 1).

SD_{diff} map

The within-session SD_{diff} maps showed a low variance within each session (fig. 2), but increased with larger time periods between scans. The mean voxelwise within-session, in-between-session and between-days within-subject SD_{diff} were 0.033 (95^{th} percentile is 0.13%), 0.064 (95^{th} percentile is 0.25%), 0.093% (95^{th} percentile is 0.36%) respectively. The variance was highest in the skull base (within-session, in-between-session, and between-days SD_{diff}: 0.57, 1.24, and 1.72%) and lowest occipitally and centrally (within-session, in-between-session, and between-days SD_{diff}: 0.06, 0.1, and 0.13% and 0.08, 0.15, and 0.22% respectively for occipital and central regions).

Covariance analysis in healthy volunteers

The total variance was unexpectedly low and appears to be mainly explained by variability between participants rather than measurement error (Table 2). The variances corroborate the visual findings shown by the SD_{diff} maps (fig. 2). Moreover, the reproducibility decreased with increasing time between scans.

Findings in glioma patients

The within-session within-subject SD_{diff} for patients was 0.024% (n=10). Intratumoral mean MTR_{asym} ranged from 0.56 to 3.11%. Contralateral same-sized ROI MTR_{asym} in healthy-appearing tissue were 0.0-0.94% (fig. 3). For GBM (n=7), the mean MTR_{asym} value of the tumors was 2.27% whereas the mean contralateral MTR_{asym} value was 0.75. The effect size between GBMs and contralateral tissue is 1.52. The SD_{diff} is 6% of the effect size when considering the between-days SD_{diff} in the healthy volunteers.

Discussion: These findings show that APT MTR_{asym} measurements have good reproducibility for healthy volunteers even over longer periods of time in a clinical setting. Note that the mean between-days session SD_{diff} was much smaller than the absolute APT-CEST values. However, focal signal inhomogeneity in areas close to the skull base can be an issue.

The in-between scan variance can be caused by the correction of B0 inhomogeneity and potentially also by registration errors.

Tumors expectedly showed larger APT-CEST values than healthy tissue. The effect size between tumors and healthy tissue was large compared to the mean between-days within-subject SD_{diff}. Tagao et al. used a similar scanning protocol and found comparable results.[7] However they looked at mean tumor APT-CEST values, while we also performed a voxel-wise reproducibility analysis on healthy volunteers, which allows for more general conclusions concerning broader clinical applications.

Conclusion: The current study demonstrates that APT-CEST results have a very high consistency between scan timepoints for the entire brain and masked regions including tumor at 3T. APT-CEST can therefore be recommended for clinical applications in the brain including monitoring and cut-off value determination.

References:

1. Zhou, J., Lal, B., Wilson, D. A., Laterra, J. & van Zijl, P. C. M. Amide proton transfer (APT) contrast for imaging of brain tumors. *Magn. Reson. Med.* **50**, 1120–1126 (2003).

2. Zhou, J., Payen, J.-F., Wilson, D. A., Traystman, R. J. & van Zijl, P. C. M. Using the amide proton signals of intracellular proteins and peptides to detect pH effects in MRI. *Nat. Med.* **9**, 1085–1090 (2003).

3. Zou, T. *et al.* Differentiating the histologic grades of gliomas preoperatively using amide proton transfer-weighted (APTW) and intravoxel incoherent motion MRI. *NMR Biomed.* **31**, (2017).

4. Jiang, S. *et al.* Amide proton transfer-weighted magnetic resonance image-guided stereotactic biopsy in patients with newly diagnosed gliomas. *Eur. J. Cancer* **83**, 9–18 (2017).

5. Dou, W. *et al.* Chemical exchange saturation transfer magnetic resonance imaging and its main and potential applications in pre-clinical and clinical studies. *Quant. Imaging Med. Surg.* **9**, 1747–1766 (2019).

6. Zhang, Y. *et al.* Whole-brain chemical exchange saturation transfer imaging with optimized turbo spin echo readout. *Magn. Reson. Med.* **84**, 1161–1172 (2020).

7. Togao, O. *et al.* Scan-rescan reproducibility of parallel transmission based amide proton transfer imaging of brain tumors. *J. Magn. Reson. Imaging* **42**, 1346–1353 (2015).

Acknowledgments / Funding information:

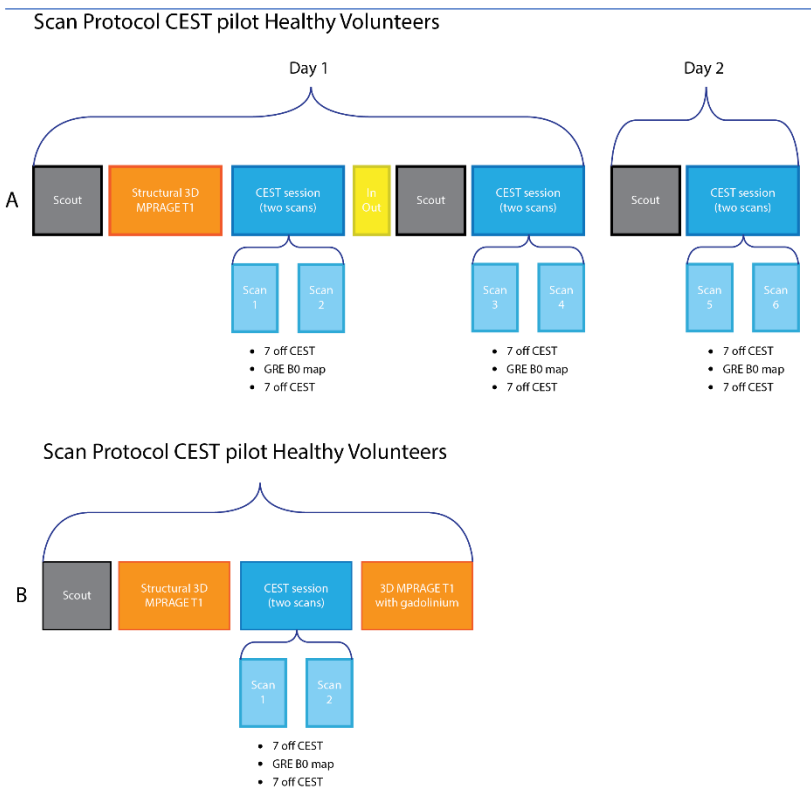

Figure 1. A. Scan protocol for the healthy volunteers. B. Scan protocol for the patients. A session contains two consecutive APT-CEST scans and one B0 map. (A) Scans: 1 = baseline, 2 = scan directly after the baseline — i.e., 1-2 = within-session reproducibility — scan 4 is a scan 30 min after the first — i.e., 1-4 = between-session reproducibility — scan 6 = another day — i.e., 1-6 = between-day reproducibility. (B) Glioma patients underwent one session.

Table 1. APT-CEST values in healthy volunteers

	Whole brain	Cortical gray matter	Deep white matter	Putamen	Thalamus
Mean (%)	0.49	1.06	0.42	0.95	1.39
5th percentile (%)	-0.92	-0.02	-0.24	0.44	0.96
95th percentile (%)	1.97	2.31	1.15	0.14	1.88

Table 1. Mean, 5th percentile, and 95th percentile APT-CEST MTR_{asym} values of different brain structures in healthy volunteers.

Table 2. Percentage of total variance

	Whole brain	Cortical gray matter	Deep white matter	Putamen	Thalamus
Total variance (MTR_{asym} %)	**0.0028**	**0.0068**	**0.0050**	**0.015**	**0.0079**
Factor subject	55%	70%	58%	52%	57%
Factor day	28%	17%	24%	28%	11%
Factor session	**7%**	**6%**	**9%**	**14%**	**23%**
Factor within-session	10%	7%	9%	6%	9%

Table 2. Variance components shown for factors subject, day, session, and within-session. If we take an example tumor MTR_{asym} of 2% and contralateral healthy tissue of 0.5%, the total variance is relatively low.

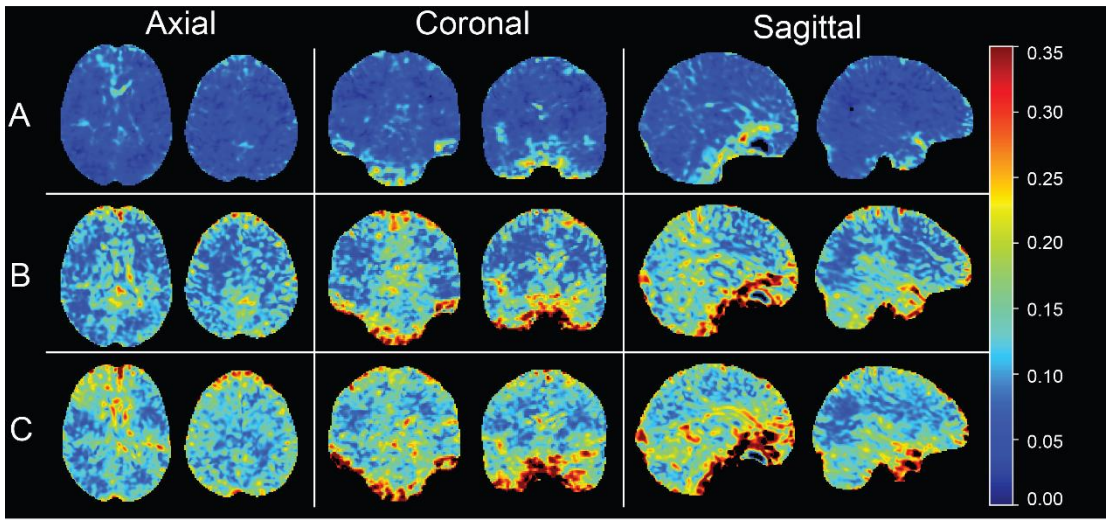

Figure 2. Standard deviation (SD) maps of the within-subject difference between scan sessions 1-2, 1-4, and 1-6 (rows A, B, and C, respectively), for all participants (n=21). Higher SD of the difference means lower reproducibility. Note how the reproducibility lowers as physiological variability seems to increase with a larger time difference.

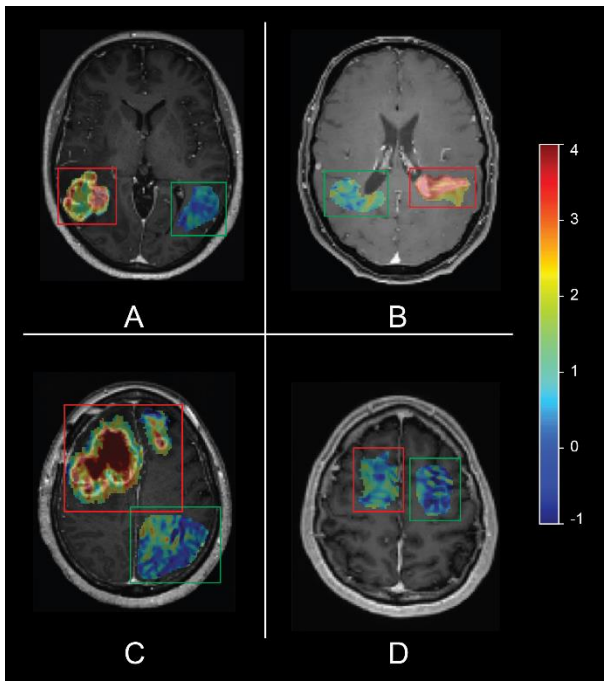

Figure 3. Single transversal APT-CEST slices of four glioblastoma patients, CEST values in color scale projected on the post-contrast T1w image, within the tumor ROI only. Red and green boxes are positioned around the tumor and contralateral ROIs, respectively. Note the heterogeneous hyperintensity in the tumorous regions on the T1 when compared to the contralateral region (A-C). D shows the APT-CEST value of a non-enhancing GBM.

Deep learning DCE-MRI parameter estimation: Application in pancreatic cancer

T.Ottens[1], S.Barbieri[2], M.Orton[3], R.Klaassen[4], H.W.M van Laarhoven[4], H.Crezee[5], A.J.Nederveen[1], O.J.Gurney-Champion[1]

[1]Department of Radiology and Nuclear Medicine, Cancer Center Amsterdam, Amsterdam UMC, University of Amsterdam, Netherlands; [2]Centre for Big Data Research in Health, UNSW, Sydney, Australia; [3]Department of Radiology, The Royal Marsden NHS Foundation Trust and The Institute for Cancer Research, London, United Kingdom; [4]Department of Medical Oncology, Cancer Center Amsterdam, Amsterdam UMC, University of Amsterdam, Netherlands; [5]Department of Radiation Oncology, Cancer Center Amsterdam, Amsterdam UMC, University of Amsterdam, Netherlands

Synopsis: Quantitative physiological perfusion parameters can be obtained from dynamic contrast-enhanced (DCE)-MRI. Conventionally, fitting is done with the non-linear least squares (NLLS) approach. However, the NLLS-fit suffers from long processing times and results in noisy parameter maps. In this work, we implemented a physics-informed gated recurrent unit (GRU) network with attention layers for estimating physiological parameters using the extended Tofts model. In simulations, we show it outperforms NLLS with more accurate and precise parameter maps. We show our method produced substantially less noisy parameter maps than NLLS in a fraction of the time in pancreatic cancer patients.

Introduction: Dynamic contrast-enhanced (DCE)-MRI is a promising technique for quantifying tissue perfusion. Conventionally, tracer-kinetic (TK) modelling is done with non-linear least squares (NLLS) fitting. However, the NLLS-fit has long processing times and results in noisy parameter maps.

Recently, deep neural networks have been explored to quickly estimate the physiological parameters from DCE-MRI. However, these networks focussed on acceleration but not on outperforming NLLS, and only were applied to brain DCE. Moreover, most approaches were specific to a fixed acquisition length and unsuited for long-range temporal dependencies.

Hence, we developed a novel network that utilizes a gated recurrent unit (GRU) combined with attention layers to predict physiological parameters from DCE-MRI. We validated it in simulations and applied it to DCE data from pancreatic ductal adenocarcinoma (PDAC). The GRU network handles input with different acquisition lengths and the attention layers allow handling long-range temporal dependencies.

Methods: We investigated two types of networks for estimating the extended Tofts TK parameters from DCE data: temporal and spatiotemporal. The temporal networks predict the physiological parameters based on the concentration time curve per voxel while the spatiotemporal networks use convolutions to include spatial information. Our temporal networks were a Fully Connected Network (FCN; 4 layers, width: [320,160,80,40]), a Long Short-Term Memory (LSTM) and the GRU (Figure 1). Our spatiotemporal network was a CNN, as introduced by Ulas et al., 2019.

We used an unsupervised physics-informed loss function that was the mean-squared-difference between the input data and forward extended Tofts modelling of the returned TK-parameters. Training parameters were: batch size 256/8 (temporal/spatial-temporal), ADAM optimizer, 50 epochs, an adaptive learning rate that started at 1e-3 and was multiplied by 0.1 every time validation loss was not improved for 3 consecutive epochs.

Simulations: We constructed a synthetic dataset of 500,000 concentration curves with added noise (Signal-to-Noise Ratio [SNR] ranging from 5-100). Concentration curves were simulated using the extended tofts model with random values for extravascular extracellular space (v_e) [0-0.7], plasma volume fraction (v_p) [0-0.05] and rate constant for efflux of gadolinium (k_{ep}) [0-2]. Data acquisition was simulated for 160 dynamics at 1.75s per frame. The precision was quantified by the standard deviation of the errors and the accuracy was quantified by the absolute mean errors between the predicted and ground truth parameters. In additional simulations, we varied the acquisition length from 80-160 time points to assess whether the GRU could handle different lengths.

In vivo: The best performing temporal network and the CNN were evaluated in 31 patients with PDAC, of which 16 received repeated baseline (test-retest) scans and 15 received a scan before and after chemo-radiotherapy. We used a 3D T1-weighted spoiled ultrafast gradient echo sequence with: FOV=400x400x75mm^3, resolution=2.5mm^3, TR/TE=3.2/2.0s, FA=20°, Sense=3.6/1.5, frame-rate=1.75s and 100 dynamic scans. We used the root-mean-square error (RMSE) and structure similarity index measure (SSIM) to assess the performance of the networks. Repeatability was determined with a Bland-Altman analysis of the test-retest dataset. Then, the treated patients were added to determine the potency to detect significant changes in individual patients receiving treatment.

Results: Simulations: All networks showed higher precision and accuracy compared to the NLLS-fit for SNR values up to 40 (Figure 2), particularly for v_e. The GRU outperformed the FCN when different acquisition lengths were used (Figure 2). Considering the flexibility to acquisition length and the smaller systematic errors in the k_{ep} and v_p parameter, the GRU was selected for in vivo evaluation.

In vivo: The CNN and GRU both showed less noisy parameter maps than the NLLS-fit in vivo (Figure 3), especially for v_e. There was little difference between the networks on SSIM and RMSE (Figure 4), where GRU had a marginally higher SSIM and lower RMSE than NLLS-fit, suggesting it more accurately describes the data. All networks were substantially faster than NLLS-fit. The GRU had similar repeatability as the NLLS-fit (Figure 5). The test-retest precision of the k_{ep} and v_e parameters from the CNN were better (tighter 95% confidence interval), while the variation in patients receiving treatment remains similar, suggesting CNN was best at picking up treatment effects.

Discussion: We successfully implemented several neural networks for predicting pharmacokinetic parameters from DCE data. These networks are superior to the conventional NLLS-fit. With simulations, we showed that our suggested networks are more accurate and precise for typical SNR. Our networks perform good in vivo, with less noisy parameter maps and similar (GRU) to better (CNN) repeatability. Finally, our networks are substantially faster than conventional approaches.

Results suggest that the addition of spatial information allows the CNN to outperform the GRU in vivo. However, we see an increased v_p in the liver for the CNN in Figure 3. Without simulations, it is hard to determine whether this is a systematic error of the CNN or alternative methods. Furthermore, our GRU is able to perform well on data from any acquisition length, whereas the CNN is limited to a fixed length. Therefore, we suggest using the GRU until the CNN is further improved and validated.

Conclusion: Our networks for analyzing DCE output more accurate and precise parameter estimates than conventional NLLS fitting in a fraction of the time. This opens the way for clinical DCE.

Acknowledgments / Funding Information: Continue on this line

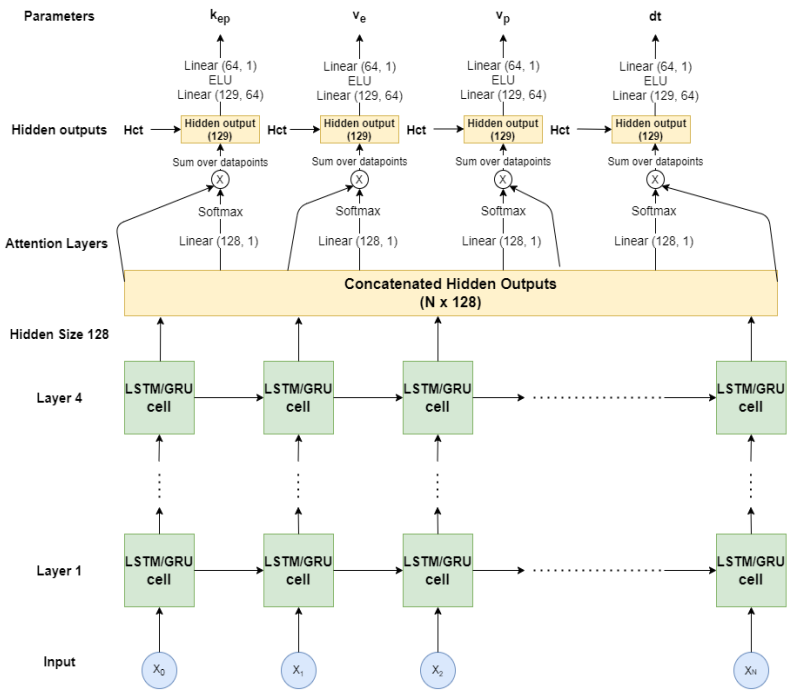

Figure 1. LSTM/GRU architecture for predicting DCE-MRI parameters from one concentration curve with N datapoints. Attention is added to include intermediate information from hidden outputs.

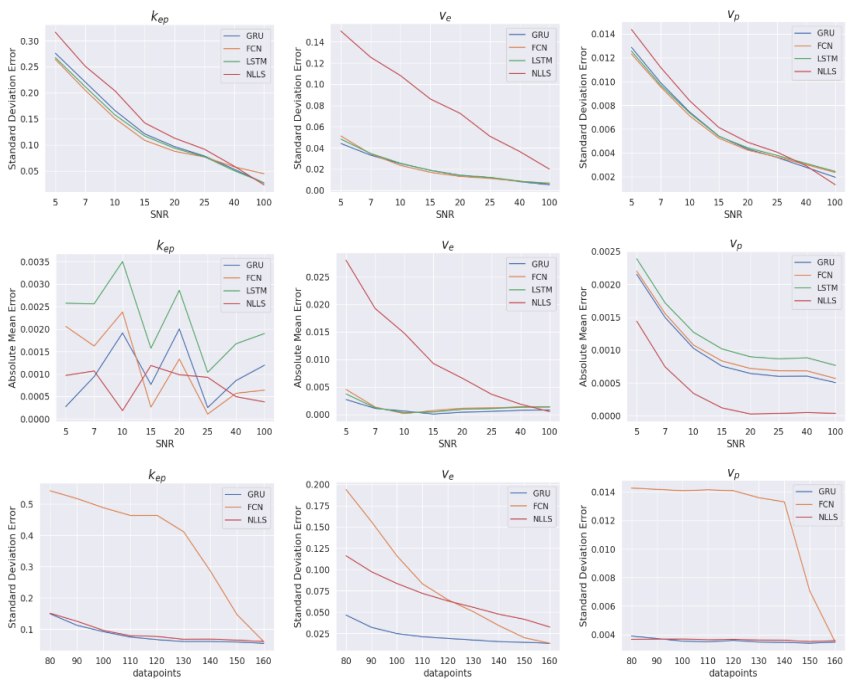

Figure 2. Standard deviation error (top) and absolute mean error (middle) of the networks on all physiological ground truth parameters. Bottom row shows the standard deviation error of the networks on predicting the ground truth parameters for varying datapoints.

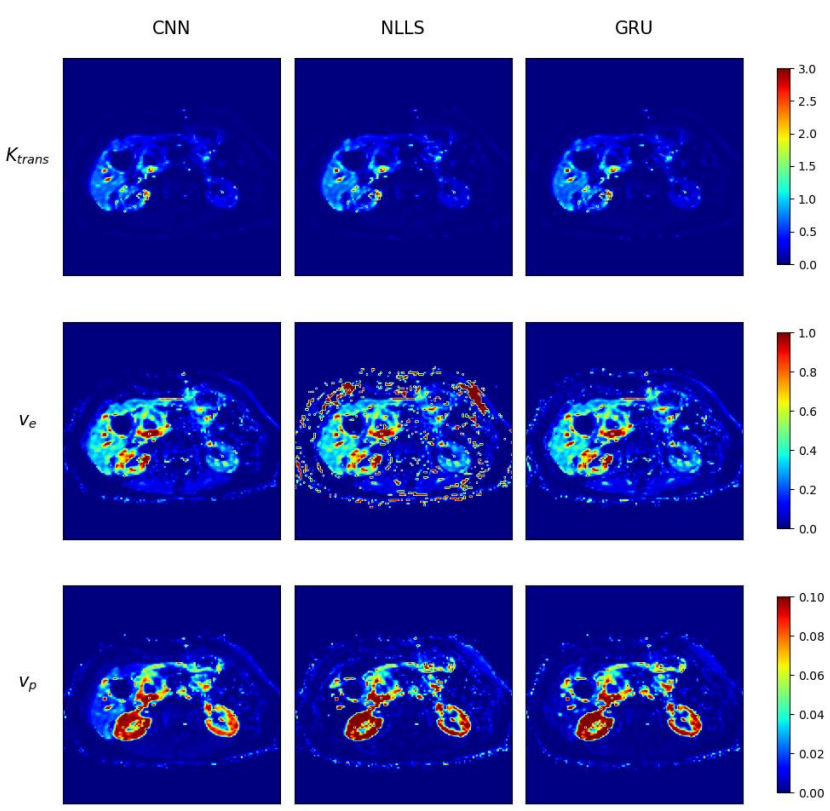

Figure 3. Parameter maps of a slice of the abdominal region created by 3 different models:

Network	SSIM	RMSE	nRMSE (%)	Time per slice (s)	Type
NLLS	0.805	0.271	0.312	61.71	-
GRU	0.807	0.270	0.312	0.68	Temporal
CNN	0.800	0.272	0.323	0.43	Spatiotemporal

Figure 4. Evaluation of the NLLS, GRU and CNN on our patient dataset.

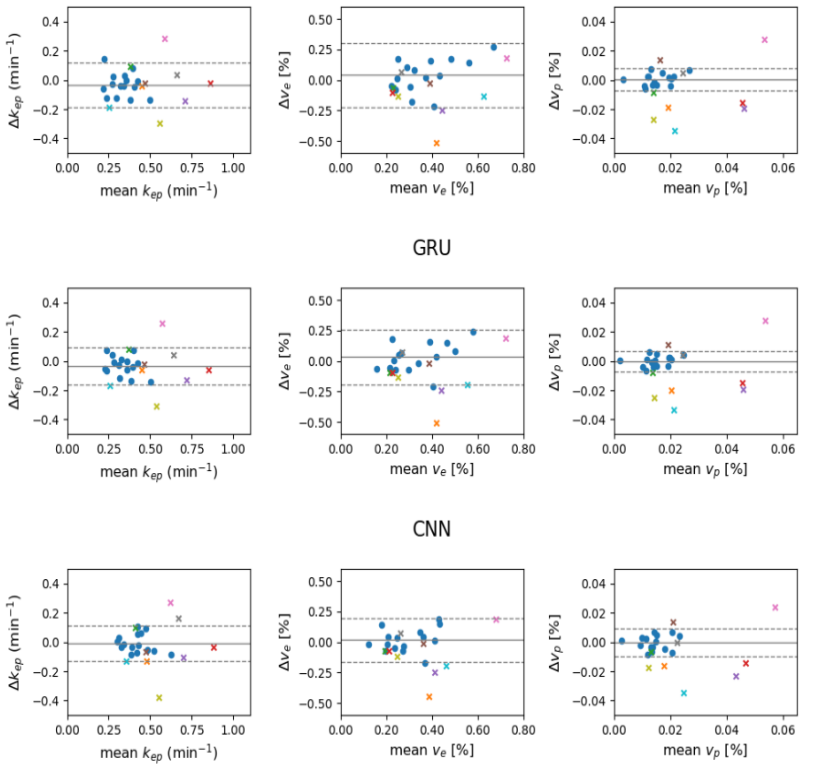

Figure 5. Bland-Altman plots of the neural network approaches to fitting of the physiological parameters of DCE-MRI concentration curves. The mean and difference is shown between the intersession repeatability patients (blue dots) and the mean and difference between pre- and post-treatment patients who received chemoradiation therapy (colored crosses).

Non-steady-state sequences for multi-parametric MRI need to be evaluated in the context of gradient-encoding

Miha Fuderer[1,2], Oscar van der Heide[1,2], Hongyan Liu , Cornelis A.T. van den Berg[1,2], and Alessandro Sbrizzi[1,2]
[1]Computational Imaging Group for MR Diagnostics and Therapy, Center for Image Sciences, University Medical Center Utrecht, Utrecht, Netherlands, [2]Department of Radiology, Division of Imaging and Oncology, University Medical Center Utrecht, Utrecht, Netherlands

Synopsis: In non-steady-state multi-parametric quantitative MRI (e.g. MR-STAT or MR Fingerprinting (MRF)), it is a non-trivial task to devise good sequences of time-varying flip angles. Recent work addresses this issue, albeit assuming a single-voxel approach, i.e. the k-space encoding is not taken into account when optimizing. In this work we show, using examples from MR-STAT reconstructions and using a Cramer-Rao based BLAKJac analysis, that two apparently similar sequences can have vastly different outcomes when applied in an actual (2-dimensional) measurement setup - showing that the context of encoding is very relevant.

Purpose: In MR-STAT[1] as well as in MR Fingerprinting[2] (MRF) and in Hybrid-state imaging[3], flip angle trains are usually time-varying. This gives many degrees of freedom to devise good sequences of flip angles, which is a non-trivial task. Recent work addresses this issue[3-9], albeit assuming a single-voxel approach, i.e. the k-space encoding is not taken into account when optimizing. In the context of MR-STAT multi-parametric reconstructions, in this study we use experiments as well as BLAKJac[12], an analytical framework to analyze the combined effects of RF and gradient-encoding, to show that two sequences with equivalent performance in a single-voxel approach can have vastly different outcomes when applied in an actual (2-dimensional) measurement setup.

Methods: Single-slice (2D) MR-STAT scans were made of a phantom setup and of a volunteer. The phantom setup consisted of 16 vials of the Eurospin II phantom set[10] plus one kiwifruit in order to visually assess the rendition of high spatial frequencies. In addition, a single-voxel scan (without encoding gradients) was done of on a homogenous central slice of vial 7 of the set.
We used a Cartesian pseudo-SSFP sequence on a 3T scanner (Philips Elition), with TR=10ms and TE=5ms. we define two RF tip angle patterns, called "Incoherent" and "Coherent", as shown in fig. 1. The latter is chosen to be in-sync with the phase-encoding pattern. These two have almost identical performance based on a single-voxel Cramer-Rao based analysis (see table 1).
For the 2D scans, the acquisition voxel size was 1mm x 1mm, slice thickness of 5mm, with a Field Of View of 224mm, requiring 224 phase-encoding steps. The set of phase-encoding steps was repeated 5 times in order to allow MR-STAT reconstruction[11] of maps of proton density, T1 and T2. In total, 1120 readout-lines were acquired. This setup was re-scanned 10 times which led to 10 separate reconstructions, in order to allow for an estimate of standard deviations in the resulting maps.

In the single-voxel scans, the phase-encoding was switched off. The readout-gradient was still active, to obtain more measurement points over a homogenous region of the tube. The slice thickness was chosen to 1.5mm. This was 20 times re-scanned and re-reconstructed. For the phantom scans (2D and single-voxel), standard deviations (SD) were calculated per voxel over the 10 (or 20) re-scans. These SD were averaged over regions of interest (ROI) for all the vials for 2D. Concurrently, a Cramer-Rao based BLAKJac analysis was applied to predict the outcomes of the standard deviations.

Results: The Cramer-Rao based BLAKJac analysis results are provided in table 1, indicating that the two sequences are expected to have identical performance on single-voxel, yet to be different by a factor of 3 to 7 on a 2D measurement.
The results of the single-voxel scan are summarized in the left half of table 2. The differences in SD between the Coherent and Incoherent sequences are not significant.
Figure 2 shows the phantom results, showing very poor rendition of the Coherent sequence. In addition, the measured standard deviations - averaged over all vials - is 2.9 times (T1) resp. 3.7 times (T2) higher on the Coherent sequence compared to "Incoherent". This ratio is slightly smaller than predicted; this is due to early stopping of the iteration of the Coherent sequence, which has not reached a stable result after 50 iterations, while "Incoherent" usually stabilizes already after 6 iterations.
Figure 3 shows the in-vivo results. The measured standard deviation, averaged over the whole image, is a factor of 2.0 (T1) resp. 2.4 (T2) higher for the Coherent sequence compared to "Incoherent". Also the bias (deviation from literature values) is substantially higher.

Discussion: The two test sequences of RF angles perform similarly in a single-voxel setup, as was predicted by the Cramer-Rao based analysis. In the absence of phase-encoding, the calculated performance is identical.
Yet, in the context of gradient-encoding, it really does matter whether the RF sequence shows incoherence with the phase-encoding pattern or whether it synchronizes to it. Without incoherence, all spatial frequencies are measured under almost identical sensitivities to T1 and T2, which makes the inversion problem ill-posed. Indeed, in the context of encoding, the Coherent sequence shows roughly 3 times more noise than the Incoherent sequence, as predicted by BLAKJac.

Conclusion: A sequence that is optimal in a single-voxel approach might be suboptimal in a setup where phase-encoding (or, encoding in general) is applied. So the Cramer-Rao based analysis has to take the encoding pattern into account, which is effectively done by our BLAKJac analysis.

References:

1. A. Sbrizzi et al, “Fast quantitative MRI as a nonlinear tomography problem”, Magnetic Resonance Imaging 46(2018): 56-63 O. van der Heide et al, NMR in Biomedicine, 202;33:e4251
2. Ma D, Gulani V, Seiberlich N, et al. Magnetic resonance fingerprinting. Nature, 2013;495187–495192.
3. Assländer J, Novikov DS, Lattanzi R, Sodickson DK, Cloos MA. Hybrid-state free precession in nuclear magnetic resonance. COMMUNICATIONS PHYSICS (2019) 2:73
4. K.Sommer, T.Amthor, M.Doneva, P.Koken, J.Meineke, P.Börnert. Towards predicting the encoding capability of MR fingerprinting sequences. Magnetic Resonance Imaging, Volume 41, September 2017, Pages 7-14.
5. Bo Zhao, Justin P. Haldar, Kawin Setsompop, Lawrence L. Wald. Maximum Likelihood Reconstruction for Magnetic Resonance Fingerprinting. Conf Proc IEEE Eng Med Biol Soc. 2016 August ; 2016: 453–456.
6. Bo Zhao, Justin P. Haldar, Congyu Liao, Dan Ma, Yun Jiang, Mark Griswold, Kawin Setsompop, Lawrence L. Wald. Optimal Experiment Design for Magnetic Resonance Fingerprinting. Conf Proc IEEE Eng Med Biol Soc. 2016 August ; 2016: 453–456.
7. Ouri Cohen, Matthew Rosen. Algorithm comparison for schedule optimization in MR fingerprinting. Magnetic Resonance Imaging, Volume 41, September 2017, Pages 15-21
8. Mickevicius, Nencka, Paulson. Reducing the Dimensionality of Optimal Experiment Design for Magnetic Resonance Fingerprinting. https://ui.adsabs.harvard.edu/abs/2020arXiv201000674M/abstract
9. Philip K. Lee et al. Flexible and efficient optimization of quantitative sequences using automatic differentiation of Bloch simulations. Magn Reson Med. 2019;82:1438–1451
10. TO5, Eurospin II test system, Scotland
11. Oscar van der Heide, A. Sbrizzi, P. Luijten, C.A.T. van den Berg. High-resolution in vivo MR-STAT using a matrix-free and parallelized reconstruction algorithm. NMR in Biomedicine. 2020;33:e4251
12. M. Fuderer, O. van der Heide, A. Sbrizzi, C.A.T. van den Berg. BLAKJac - A computationally efficient noise-propagation performance metric for the analysis and optimization of MR-STAT sequences. Proc. Intl. Soc. Mag. Reson. Med. 29 (2021), 3059.

Acknowledgements / Publication Information: [illegible]

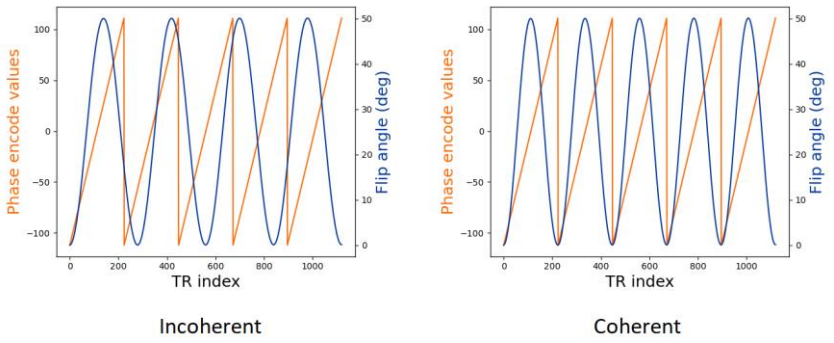

Figure 1: two sequences of 1120 RF pulses: both are sinusoidaly varying from 0 degrees to 50 degrees, with an RF phase of 0. The "Incoherent" sequence has 4 lobes, while "Coherent" has 5 lobes and is thereby in-sync with the phase-encoding pattern.

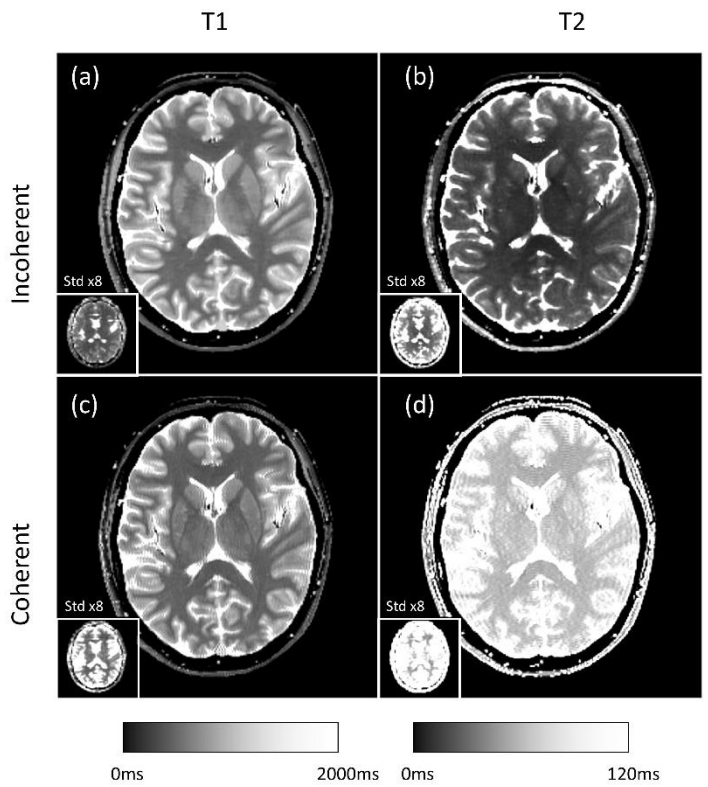

Figure 3: volunteer results, Incoherent (a,b) vs. Coherent (c,d). The small inset shows the localized standard deviation, multiplied by 8; these insets show that the deviations are higher in the Coherent sequence for all brain regions.

BLAKJac predicted deviations (a.u.)	Single-voxel		With encoding	
	T1	T2	T1	T2
Incoherent	5.3	4.2	6.2	4.5
Coherent	5.3	4.2	17.8	32.3

Table 1: The Cramer-Rao based analysis (BLAKJac) prediction of noise standard deviation values (arbitrary units) on T1- and T2-maps for the two sequences; this indicates that the Incoherent sequence is greatly superior to the Coherent sequence when taking encoding into account.

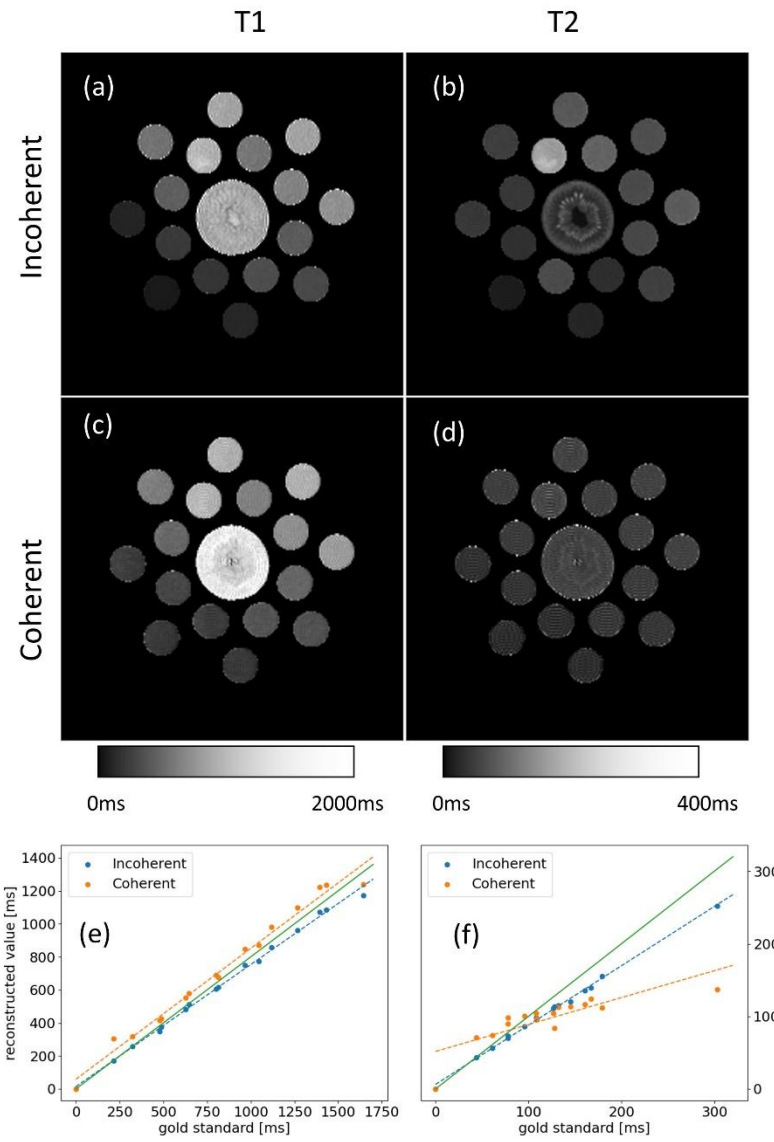

(g) Standard deviations

	T1	T2
Incoherent	73ms	7.6ms
Coherent	210ms	28 ms

Figure 2: phantom results for the Incoherent sequence (a,b) and the Coherent sequence (c,d). Figures (a), (c) and (e) refer to T1 maps, (b), (d) and (f) to T2. From (d) and (f), it is apparent that the Coherent sequence gives a very poor rendition of T2 values with substantially higher noise levels (g)

Measured	Single-voxel Mean ± stddev		2D averaged std.dev	
	T1	T2	T1	T2
Incoherent	583.1 ± **9.1**ms	71.5 ± **0.8**ms	**73**ms	**7.6**ms
Coherent	587.6 ± **8.1**ms	70.6 ± **0.85**ms	**210**ms	**28**ms

Table 2: in the single-voxel setup (absence of phase-encoding), noise standard deviations have been calculated over 20 different acquisitionreconstruction combinations. They show almost equivalent performance for the two sequences. The right half shows the noise levels in the 2D experiment, i.e. with gradient-encoding: the standard deviation has been calculated over the measurements and then averaged over all vials.

The Relative Contribution of the Vascular Architecture and Reactivity to the BOLD signal Formation

Emiel C. A. Roefs[1], Wouter Schellekens[1], Mario G. Báez-Yáñez[1], Alex A. Bhogal[1], Jeroen C.W. Siero[1,2], and Natalia Petridou[1]
[1]Radiology department, Center for Image Sciences, UMC Utrecht, Utrecht, Netherlands, [2]Spinoza Center for Neuroimaging, Amsterdam, Netherlands

Synopsis: In this study, we investigate the vascular contribution to the BOLD signal by comparing purely non-neuronal-related changes in the BOLD signal induced by gas manipulations with neuronal-related hemodynamic changes in the BOLD signal for different vascular compartments. Different vascular compartments were targeted by employing gradient-echo and spin-echo in combination with cortical depth estimations and pial vein segmentations. Our findings suggest that the increase in macro-vascular baseline venous blood volume ($CBVv_0$) is the main contributor to the large GE-BOLD signal increase towards the pial surface and that normalization for this $CBVv_0$-dependence is possible using a hyperoxia breathing task.

Introduction: The Blood-Oxygen-Level-Dependent (BOLD) signal[1,2] reflects neuronal activity indirectly via changes in local venous oxygen saturation regulated by neurovascular coupling; changes in local cerebral blood flow and volume in response to neuronal activity. This complicates the interpretation of the BOLD signal as a direct representation of neuronal activity since it may also reflects signals having vascular origins. This confounding influence increases when measuring at the laminar scale; particularly since vascular architecture and density change across cortical depth[3-5]. Therefore, quantifying the contribution of different vascular compartments to the BOLD signal is crucial. We estimate the contributions of pial veins, intra-cortical veins, and micro-vessels with respect to cerebrovascular reactivity (CVR) and venous blood volume capacity ($CBVv_0$). The hemodynamic response functions (HRF) were estimated following brief visual stimulations, while non-neuronal hemodynamic changes were induced by CO_2 and O_2 administration. The different vascular compartments were targeted by employing spin-echo (SE)-BOLD, whose sensitivity is weighted predominantly to the capillaries, and gradient-echo (GE)-BOLD, which is sensitive to all vessel sizes[6,7]. A hyperoxia normalization method is proposed to correct for $CBVv_0$.

Methods:
Six healthy volunteers participated in a 7T fMRI session, while performing a hypercapnic (+3, +5, +8, and +10mmHg $PetCO_2$) and hyperoxic (+350mmHg $PetO_2$) breathing task using a RespirAct™ device combined with brief visual stimuli (black/white random orientation patterns on a grey background of 0.2s duration, ISI: 3-20s) (Fig.1.). Functional volumes were acquired with GE-EPI (voxel size=1.0mm^3, TR/TE=850/27ms, FA =50°, and FOV=7x128x128mm) and SE-EPI (voxel size=1.5mm^3, TR/TE=850/50ms, FA=130°, and FOV=7.5x190x190mm) covering the early visual areas using two 16-channel high-density surface coils.

Cortical laminae (top, middle, deep) were segmented from T1-weighted scans (Fig.2.c) using LayNii[8]. Pial veins were segmented from T2*-weighted anatomical volumes based on their dark appearance and susceptibility difference using two tools, BrainCharter[9] and Nighres[10], which worked complementary (Fig.2.a,d). These pial veins and laminae were linearly warped to functional space giving a probability for each cortical depth level to be present in each voxel (Fig.2.e.).

A General Linear Model was used to obtain estimates of the percent BOLD signal increase following hyperoxia and hypercapnia, using the end-tidal gas traces ($\Delta PetCO_2$) as regressors. The estimated weights correspond with the O_2-response ($CVRo_2$) and $CVRco_2$ in %ΔBOLD/mmHg. Subsequently, the HRF curves were estimated with a Finite Impulse Response[11-13]. These HRFs were quantified with the amplitude and time-to-peak (TTP). The estimated HRF amplitudes were divided by the amplitude of the $CVRo_2$ to account for $CBVv_0$ dependence14 in the BOLD signal and extract the neuronal component of the HRF[15-17].

Results: We found that the magnitude of $CVRo_2$ was higher for GE (mean=0.017, se=0.002) compared to SE (mean=0.010, se=1e-4) with increasing difference from deeper laminae to top laminae and pial veins ($F_{(1,5)}$=13.2, p=0.014). Additionally, a linear increase in $CVRo_2$ towards the pial surface was observed for GE (z=-7.8, p_{Holm}<0.001) and SE (z=-2.8, p_{Holm}=0.006). A similar trend was observed for $CVRco_2$ for GE (z=-7.8, p_{Holm}<0.001), but not for SE (z=-1.6, p_{Holm}<0.15). For the estimated HRFs to the visual task, we found larger HRF amplitudes for GE (mean=2.05, se=0.18) in comparison with SE (mean=0.91, se=0.8) ($F_{(1,5)}$=40.7, p=0.001). HRF amplitudes are linearly increasing towards the pial surface for GE (z=-8.3, p_{Holm}<0.001) but not for SE (z=-1.7, p_{Holm}=0.096). The $CBVv_0$ normalized HRF amplitudes showed no difference between sequences ($F_{(1,5)}$=6.0, p=0.056), but an inverse relationship across cortical depth was found; decreasing from deeper laminae towards the pial surface (z=3.1, p_{Holm}=0.005). No difference was observed in TTP between scan sequence ($F_{(1,4)}$=0.21, p=0.67) nor across cortical depth ($F_{(3,15)}$=2.44, p=0.105)

Discussion: We investigated the contribution of micro-vessels, intra-cortical veins, and pial veins to the BOLD signal formation during visual stimulation and different breathing tasks. We found an increase in relative macro-vascular $CBVv_0$ from deeper laminae to top laminae and pial veins, as measured by the GE-$CVRo_2$ compared with SE-$CVRo_2$ (Fig.4.). Hypercapnia mainly affected the macro-vasculature and to a lesser extent the capillaries, as seen by the $CVRco_2$ (Fig.4.), suggesting that vessel reactivity is proportional to vessel size or composition. The well-known GE HRF amplitude increase towards the pial surface was observed[17-19], and was extended in this study with the pial veins, which displayed an even more prominent increase (Fig.5.). Drainage effects could be another factor contributing to this HRF amplitude increase. However, in this study, no significant differences in TTP (Fig.5.) were observed between sequences nor across cortical depth suggesting that the $CBVv_0$ was the main contributor to the GE-BOLD HRF amplitude which is consistent with recently published models[20]. No difference in normalized HRF amplitude was found between GE and SE (Fig.5.). This implies that the $CBVv_0$ contribution of the macro-vasculature is reduced, and the signal changes rather reflect the visual task, making the $CBVv_0$-normalization preferable for investigation of brain metabolism.

Conclusion: We found that the BOLD signal from the macro-vasculature, as measured with GE-BOLD, is affected by $CBVv_0$ as we observed a linear HRF amplitude increase from deeper laminae to top laminae and pial veins, which coincides with an increase in $CVRo_2$. In contrast, the SE-BOLD contained limited purely vascular contributions. Therefore, the BOLD signal caused by the micro-vasculature predominantly reflects neuronal processes. Normalization of GE-BOLD signals by $CBVv_0$ yields a similar laminar profile as SE-BOLD.

References: [1] S. Ogawa, T.-M. Lee, A. R. Kay, and D. W. Tank, “Brain magnetic resonance imaging with contrast dependent on blood oxygenation,” proceedings of the National Academy of Sciences, vol. 87, no. 24, pp. 9868–9872, 1990. [2] K. K. Kwong, J. W. Belliveau, D. A. Chesler, I. E. Goldberg, R. M. Weisskoff, B. P. Poncelet, D. N. Kennedy, B. E. Hoppel, M. S. Cohen, and R. Turner, “Dynamic magnetic resonance imaging of human brain activity during primary sensory stimulation.,” Proceedings of the National Academy of Sciences, vol. 89, no. 12, pp. 5675–5679, 1992. [3] H. M. Duvernoy, S. Delon, and J. Vannson, “Cortical blood vessels of the human brain,” Brain research bulletin, vol. 7, no. 5, pp. 519–579, 1981. [4] F. Reina-De La Torre, A. Rodriguez-Baeza, and J. Sahuquillo-Barris, “Morphological characteristics and distribution pattern of the arterial vessels in human cerebral cortex: a scanning electron microscope study,” The Anatomical Record: An Official Publication of the American Association of Anatomists, vol. 251, no. 1, pp. 87–96, 1998. [5] H. Duvernoy, S. Delon, and J. Vannson, “The vascularization of the human cerebellar cortex,” Brain research bulletin, vol. 11, no. 4, pp. 419–480, 1983. [6] J. Budde, G. Shajan, M. Zaitsev, K. Scheffler, and R. Pohmann, “Functional mri in human subjects with gradient-echo and spin-echo epi at 9.4 t,” Magnetic resonance in medicine, vol. 71, no. 1, pp. 209–218, 2014. [7] T. Q. Duong, E. Yacoub, G. Adriany, X. Hu, K. Uˇgurbil, and S.- G. Kim, “Microvascular bold contribution at 4 and 7 t in the human brain: gradient-echo and spin-echo fmri with suppression of blood effects,” Magnetic Resonance in Medicine: An Official Journal of the International Society for Magnetic Resonance in Medicine, vol. 49, no. 6, pp. 1019–1027, 2003. [8] L. R. Huber, B. A. Poser, P. A. Bandettini, K. Arora, K. Wagstyl, S. Cho, J. Goense, N. Nothnagel, A. T. Morgan, J. Van Den Hurk, et al., “Laynii: a software suite for layer-fmri,” NeuroImage, vol. 237, p. 118091, 2021. [9] M. Bernier, S. C. Cunnane, and K. Whittingstall, “The morphology of the human cerebrovascular system,” Human brain mapping, vol. 39, no. 12, pp. 4962–4975, 2018. [10] J. M. Huntenburg, C. J. Steele, and P.-L. Bazin, “Nighres: processing tools for high-resolution neuroimaging,” GigaScience, vol. 7, no. 7, p. giy082, 2018. [11] C. Goutte, F. A. Nielsen, and K. Hansen, “Modeling the hemodynamic response in fmri using smooth fir filters,” IEEE transactions on medical imaging, vol. 19, no. 12, pp. 1188–1201, 2000. [12] G. H. Glover, “Deconvolution of impulse response in event-related bold fmri1,” Neuroimage, vol. 9, no. 4, pp. 416–429, 1999. [13] B. Bai, P. Kantor, and A. Shokoufandeh, “Effectiveness of the finite impulse response model in content-based fmri image retrieval,” in International Conference on Medical Image Computing and Computer-Assisted Intervention, pp. 742–750, Springer, 2007. [14] P. A. Bandettini and E. C. Wong, “Effects of biophysical and physiologic parameters on brain activation-induced r2* and r2 changes: simulations using a deterministic diffusion model,” International Journal of Imaging Systems and Technology, vol. 6, no. 2-3, pp. 133–152, 1995. [15] D. Bulte, P. Chiarelli, R. Wise, and P. Jezzard, “Measurement of cerebral blood volume in humans using hyperoxic mri contrast,” Journal of Magnetic Resonance Imaging: An Official Journal of the International Society for Magnetic Resonance in Medicine, vol. 26, no. 4, pp. 894– 899, 2007. [16] P. A. Chiarelli, D. P. Bulte, R. Wise, D. Gallichan, and P. Jezzard, “A calibration method for quantitative bold fmri based on hyperoxia,” Neuroimage, vol. 37, no. 3, pp. 808–820, 2007. [17] J. R. Polimeni, B. Fischl, D. N. Greve, and L. L.Wald, “Laminar analysis of 7 t bold using an imposed spatial activation pattern in human v1,” Neuroimage, vol. 52, no. 4, pp. 1334–1346, 2010. [18] C. J. Gauthier, C. Madjar, F. B. Tancredi, B. Stefanovic, and R. D. Hoge, “Elimination of visually evoked bold responses during carbogen inhalation: implications for calibrated mri,” Neuroimage, vol. 54, no. 2, pp. 1001–1011, 2011. [19] J. C. Siero, N. F. Ramsey, H. Hoogduin, D. W. Klomp, P. R. Luijten, and N. Petridou, “Bold specificity and dynamics evaluated in humans at7 t: comparing gradient-echo and spin-echo hemodynamic responses,” PLoS One, vol. 8, no. 1, p. e54560, 2013. [20] M. Havlicek and K. Uludaˇg, “A dynamical model of the laminar bold response,” NeuroImage, vol. 204, p. 116209, 2020.

Acknowledgments / Funding Information: This work was supported by the National Institute of Mental Health of the National Institutes of Health under award number R01MH111417.

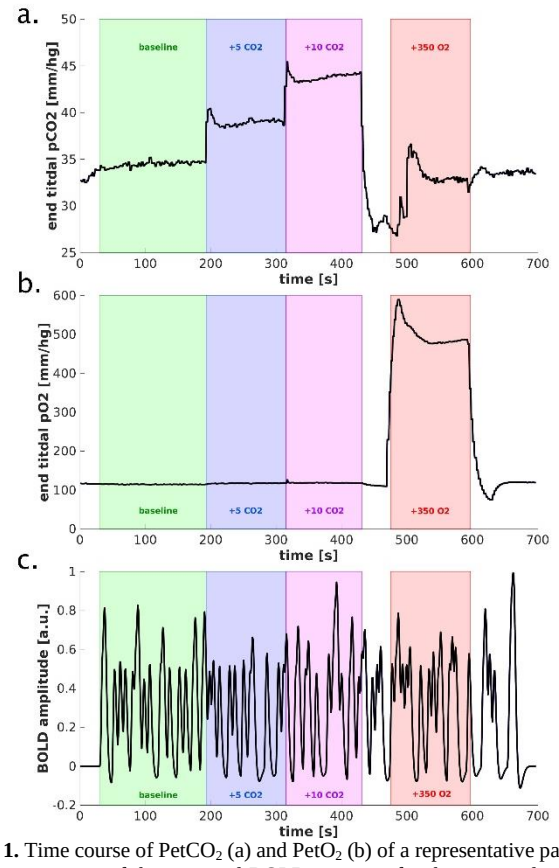

Fig. 1. Time course of $PetCO_2$ (a) and $PetO_2$ (b) of a representative participant and time course of the expected BOLD response for the event-related visual task (c). Colors indicate the different gas breathing task (green = baseline (gas mixture resembling room-air), blue =+5$PetCO_2$, purple = +10$PetCO_2$, and red = +350$PetO_2$).

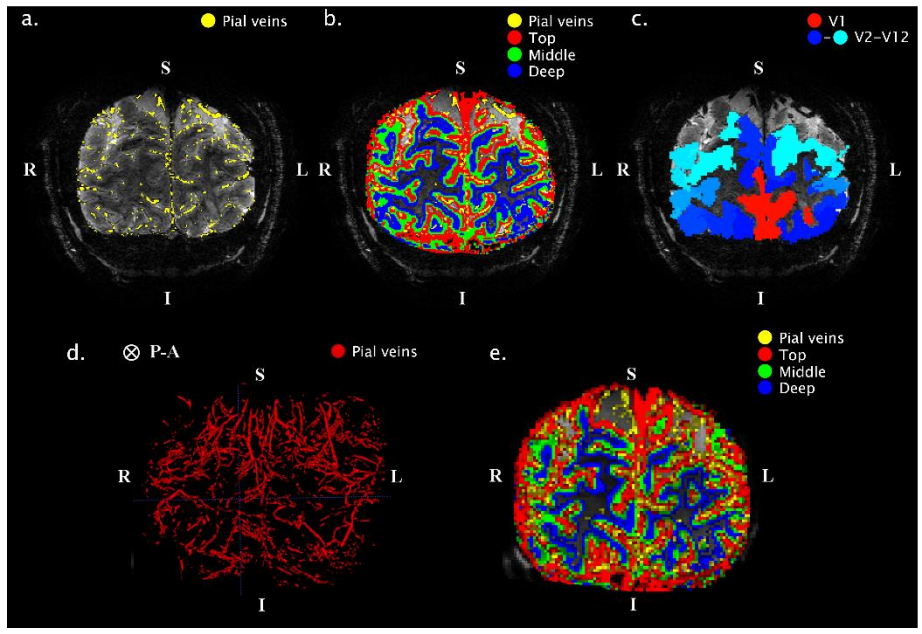

Fig. 2. Top row: Pial veins mask (a), cortical laminae as measure of cortical depth together with pial veins (b), and visual area mask (c) superimposed on the T2*-weighted scan. Bottom row: Posterior view of 3D render of the pial vein mask (d) and probability mask of cortical depth levels, where each pixel-color is a weighted combination of the four measures of cortical depth, superimposed on functional image (e).

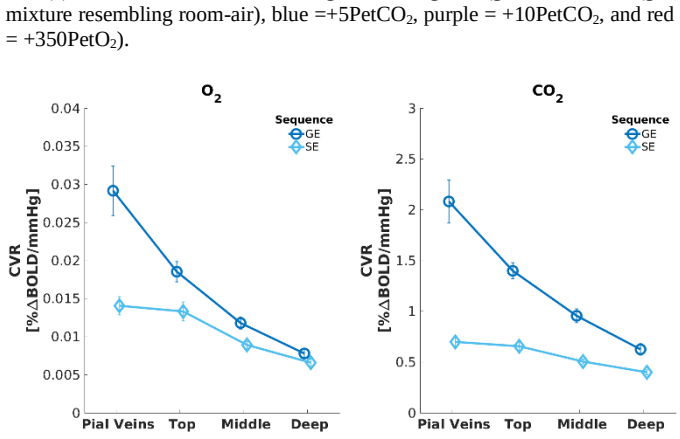

Fig. 3. Mean CVR to O_2* (left panel) and CO_2 (right panel) breathing tasks acquired with GE (dark blue) and SE (light blue). The error bars refer to the standard error of the mean (SEM) across participants. *Reactivity to O_2 is strictly no vascular reactivity.

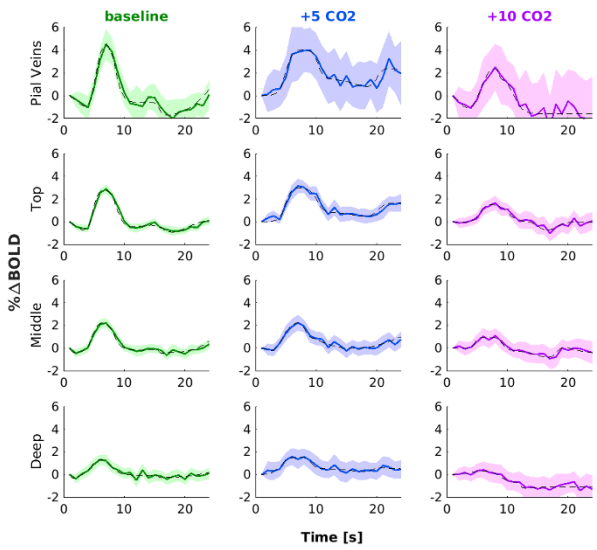

Fig. 4. Example of the estimated HRF for a representative participant visualized across cortical depth for two hypercapnic gas conditions acquired with the GE-BOLD sequence. Shading indicates the 95%-confidence interval. For this participant, it is clearly visible that the HRF amplitude falls off towards the WM (deep laminae) and during hypercapnia compared with baseline.

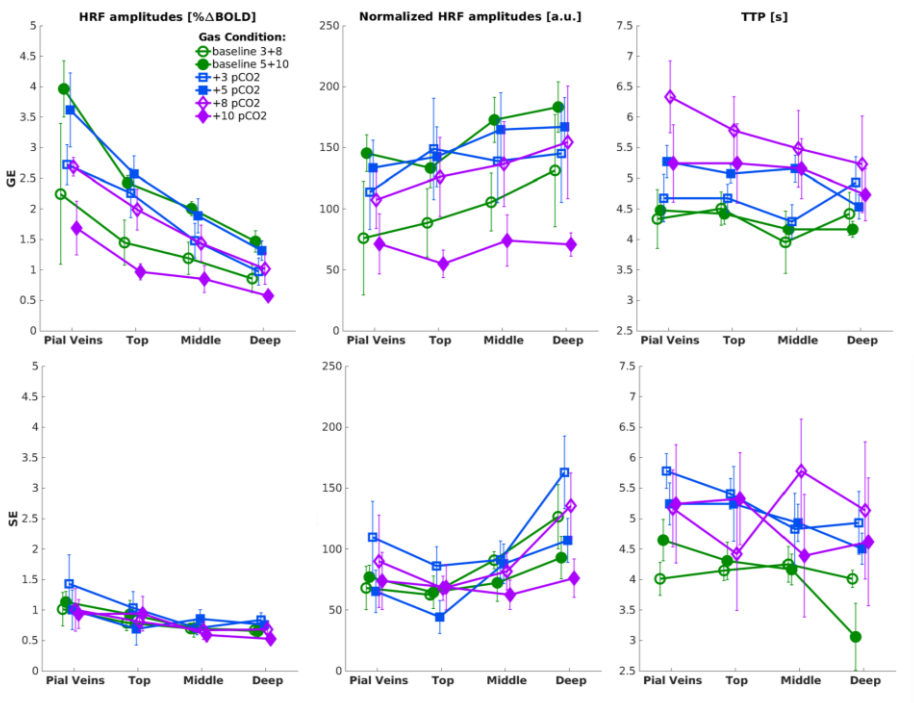

Fig. 5. Quantification of the HRFs averaged across subjects for GE (top row) and SE (bottom row): HRF amplitudes (left column), for $CBVv_0$ normalized HRF amplitudes (middle column) and TTP (right column), colors and markers indicate different breathing tasks. The error bars refer to the standard error of the mean (SEM) across participants. Note that the +3,+8-run was not performed by all

Combining the benefits of 3D acquisitions and spiral readouts in VASO fMRI

Alejandro Monreal[1], Ruoyun Emily Ma[1], Renzo Huber[1],Denizhan Kurban[1] , Nicolas Boulant[2], Benedikt A. Poser[1]

[1]Faculty of Psychology and Neuroscience, Maastricht University, Maastricht, NL; [2]CEA NeuroSpin, Gif-sur-Yvette, France

Synopsis: VASO fMRI can provide beneficial localization specificity and quantifiability compared to the commonly used BOLD contrast. Previous work has also shown the benefits of using spiral readouts compared to Cartesian.

In this work, we explore the benefits of 3D stack of spirals readouts and compare it with the current state of the art 3D-EPI readouts for VASO fMRI. The sequence implementation is done using Pulseq, images were reconstructed using gpuNUFFT; functional analysis with an openly available pipeline. We find that a tSNR efficiency improvement of a factor of 2.5 over EPI is achieved using the proposed spiral implementation.

Introduction: It has previously been shown that fMRI methods that measure cerebral blood volume such as, VAscular Occupancy (VASO) [1] can outperform the most commonly used BOLD techniques with respect to its physiological interpretability and its localization specificity; this is especially the case at UHF and at a high spatial resolution (<1.5 mm) [2]. Some of the main limitations of VASO are BOLD contamination (which affects the VASO contrast), limited detection sensitivity, and temporal sampling efficiency. For the BOLD contamination, it has been shown that a BOLD-corrected VASO image can be obtained by means of dynamic division of concomitantly acquired control images [3]. To overcome the limitations set by low temporal sampling efficiency, previous work has suggested combining the efficiency of spiral k-space sampling with simultaneous multi-slice acquisitions [4]. For high-resolution fMRI, however, 3D readouts can be advantageous over 2D [2].

The purpose of this study is to combine the benefits of 3D acquisitions and the efficiency of spiral readouts to obtain VASO images at sub-second TR. This is possible using a 3D stack of spirals (SOSP) readout which has previously been advocated as an efficient framework for BOLD fMRI [5]. Here, we demonstrate that fMRI with VASO contrast can be obtained using SOSPs, allowing for shorter echo times to improve temporal SNR, remove BOLD contamination and reduce acquisition time.

Methods: A 3D stack of spirals SS-SI VASO method was implemented using Pulseq [6], a framework that allows for rapid prototyping and implementation of sequences in the scanner. For BOLD contamination correction, a BOLD weighted control image was acquired right after the VASO one [2]. The VASO inversion was implemented by means of a 10 ms TR-FOCI pulse [7] applied 900 ms before the first excitation pulse of the spiral-out readout module. The sequence diagram used in this work is shown in Figure 1.

To confirm the stability of the novel sequence setup, a healthy volunteer was scanned using a 7T scanner, SIEMENS Healthineers while performing a motor task (block-design). Two different scenarios were tested: 1) low-resolution with parameters of 1.4x1.4x1 mm^3, 24 slices, TR_{vol}=767 ms, TE=2.5 ms, TI_1=1283 ms with in-plane acceleration of 2.2 and 2) high-resolution: 0.9x0.9x1.0 mm^3, 24 slices, TR_{vol}=1381 ms, TE=2.5 ms, TI_1=1590 ms with in-plane acceleration of 2.2. As a reference, a Cartesian 3D-EPI [8] VASO was acquired with the same task and spatial resolution. The desired voxel size, coverage, inversion delay and acceleration was matched to the protocols of SOSPs. In order to (partly) account for the lower sampling efficiency of the Cartesian readout compared to spirals, partial Fourier imaging of 6/8 was used. The TE and TR of the Cartesian readout were kept as short as possible with TR_{vol}/TE=2319/20 ms (for low-resolutions) and TR_{vol}/TE=3400/36 ms (for high-resolutions), respectively. The image reconstruction was performed using the open-source software gpuNUFFT [9] and a CG-SENSE reconstruction. For functional analysis, the openly available VASO pipeline [https://github.com/layerfMRI] consisting of Motion correction, BOLD correction and conventional quality measures (tSNR, mean, GLM statistics) was used to analyze both the SOSPs and 3D-EPI acquisitions.

Results and Discussion: Figure 2 shows various quality metrics of the low-resolution SOSPs data. Figures 3 and 4 show the activation maps obtained from the low and high-resolution acquisitions respectively. Figure 5 shows that for both low and high-resolution acquisitions a higher tSNR efficiency can be obtained with the proposed implementation. Especially in the thermal noise dominated regime of the high-resolution VASO, the spiral approach outperforms the Cartesian sampling by a factor of 2.5. This is expected, as from cumulative gains of improved signal sampling, including shorter echo times with reduced T2*-decay and faster sampling with more images per unit of time. Without full integration of off-resonance correction in the spiral reconstruction scheme yet, the signal appears blurrier in the SOSPs compared to the Cartesian 3D EPI. Note however that this form of blurring refers to the signal only, not the noise. Thus, we do not expect that the tSNR estimates presented here are affected by this.

Summary and Conclusion: In this work, we have shown that a fast implementation of a VASO fMRI with a 3D-SOSPs readout can be achieved using Pulseq. The preliminary results indicate that with the current implementation activation maps can be obtained at sub-second TR with considerable high tSNR. Even though spiral sampling allows for flexible acquisitions of fMRI data, the reconstruction is more challenging compared to conventional Cartesian sampling. Further work will focus on correcting for off-resonances, optimizing the spiral trajectory, implementing acceleration in the kz direction, and reconstruction speed up. With this, we expect to be able to observe all the benefits of combining the efficiency of spirals and 3D acquisitions applied to VASO fMRI. We believe that the developed acquisition and analysis tools will be useful tools for future mesoscopic fMRI experiments at UHF, including the human 9.4T and 11.7T scanners available to this project.

References:

1. Lu, Hanzhang, et al. 2003. “Functional Magnetic Resonance Imaging Based on Changes in Vascular Space Occupancy.” MRM 50: 263–74.
2. Huber, L., et al. (2018). “Techniques for blood volume fMRI with VASO: From low-resolution mapping towards sub-millimeter layer-dependent applications.” NeuroImage, 164, 131–143.
3. Huber, Laurentius et al. 2014. “Slab-Selective, BOLD-Corrected VASO at 7 Tesla Provides Measures of Cerebral Blood Volume Reactivity with High Signal-to-Noise Ratio.” MRM 72(1): 137–48.
4. Zahneisen, B., Poser, B. A., Ernst, T., & Stenger, A. V. (2014). Simultaneous Multi-Slice fMRI using spiral trajectories. NeuroImage, 92, 8-18.
5. Hu, Y., & Glover, G. H. (2007). Three-dimensional spiral technique for high-resolution functional MRI. MRM 58(5), 947-951.
6. Layton, K. J., et (2017). Pulseq: a rapid and hardware-independent pulse sequence prototyping framework. MRM 77(4), 1544-1552.
7. Hurley AC, Al-Radaideh A, Bai L, et al. Tailored RF pulse for magnetization inversion at ultrahigh field. MRM 2010;63(1):51-58.
8. Poser BA, Koopmans PJ, Witzel T, Wald LL, Barth M. Three dimensional echo-planar imaging at 7 tesla. Neuroimage. 2010;51(1):261-266.
9. Knoll, F., Schwarzl, A., Diwoky, C., & Sodickson, D. K. (2014). gpuNUFFT-an open-source GPU library for 3D regridding with direct Matlab interface. In International Society for Magnetic Resonance in Medicine: Scientific Meeting & Exhibition (pp. 4297-4297).

Acknowledgments / Funding Information: This work has been funded by the H2020 FET-Open AROMA grant agreement no. 88587. Benedikt Poser is also funded by the NWO VIDI grant 16.Vidi.178.052, the National Institute for Health grant R01MH/111444 (PI David Feinberg). Renzo Huber was funded from the NWO VENI project 016.Veni.198.032.

Combining the benefits of 3D acquisitions and spiral readouts in VASO fMRI

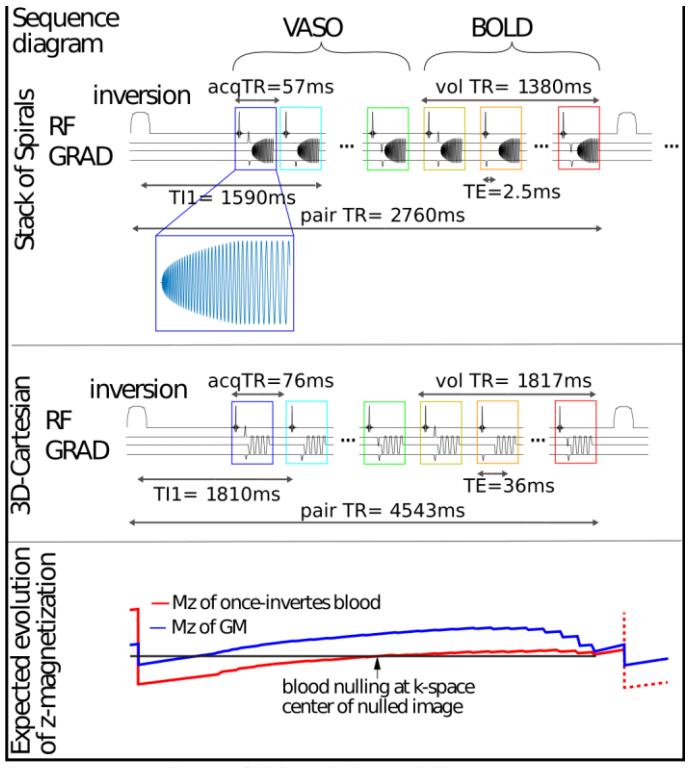

Figure 1: Sequence diagram of high-resolution acquisitions:
Upper: sequence diagram of high-resolution SOSP acquisition. A TR-FOCI inversion pulse is applied 900ms before the excitation of the first volutume. A BOLD weighted volume is obtained after the VASO one for further BOLD correction.
Middle: Sequence diagram of high-resolution 3D Cartesian acquisition.
Lower: Excpected evolution of z-magnetization of once inverted blooad and Gray Matter. The k-space center is acquired at the blood nulling point.

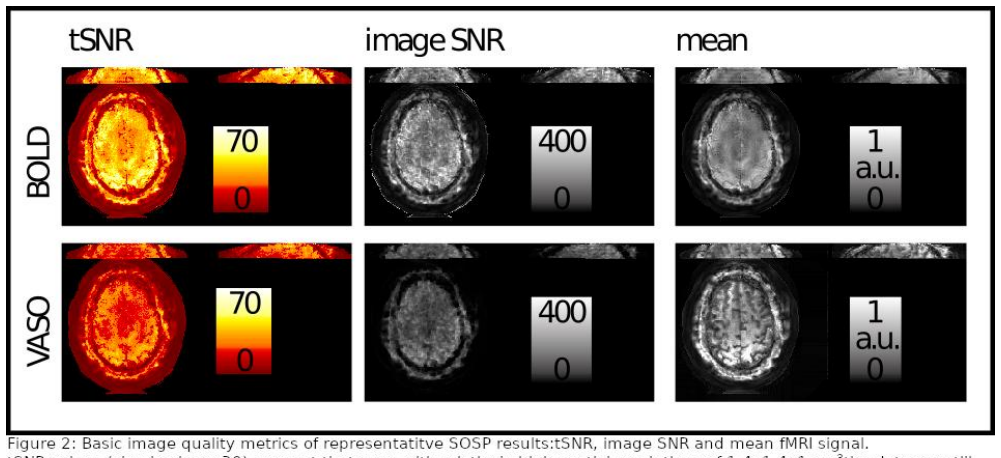

Figure 2: Basic image quality metrics of representatitve SOSP results:tSNR, image SNR and mean fMRI signal.
tSNR values (clearly above 30) suggest that even with relatively high spatial resolutions of 1.4x1.4x1mm³the data are still not fully in the thermal noise dominated regime. The temporal mean image shows the characteristic T1 weighting of VASO, as excpected. Note, that unlike conventional fMRI data, the short TEs of spiral acquisitions result in a relatively strong fat ring arouund the brain

Figure 3: Activation maps, VASO and BOLD signal of low-resolution stack of spiral:
Temporal signal traces follow the task blocks as excpected. Note that VASO is a negative CBV contrast with an expected signal decrease during activity. The representative results shown here highlight the high functional detection sensitivity of the implemented samping approach. Three 30 sec task blocks are sufficent to capture significalt CBV changes in the cortex at 1.4x1.4x1mm³ resolution

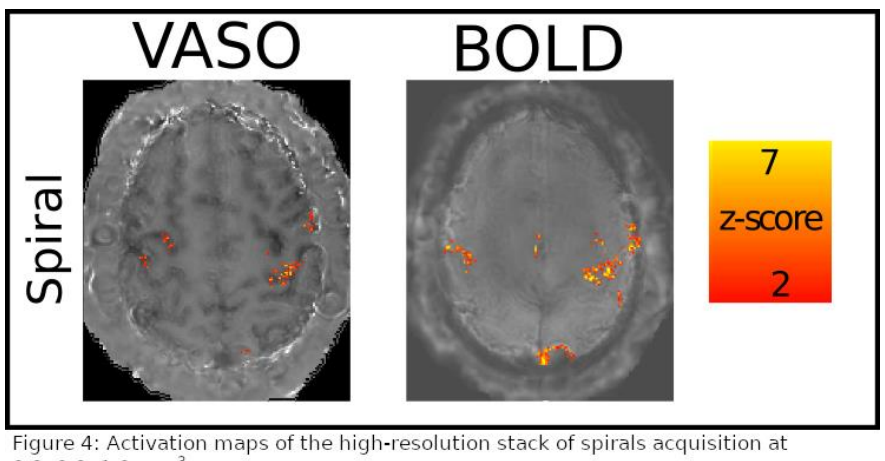

Figure 4: Activation maps of the high-resolution stack of spirals acquisition at 0.9x0.9x1.0 mm³
Activation maps were also obtained with the high-resolution acquisition. It can be seen that the high sapling efficiency of the spiral readout provides suffcient detection sensitivity to capture functional C changes at sub-millimeter resolutions

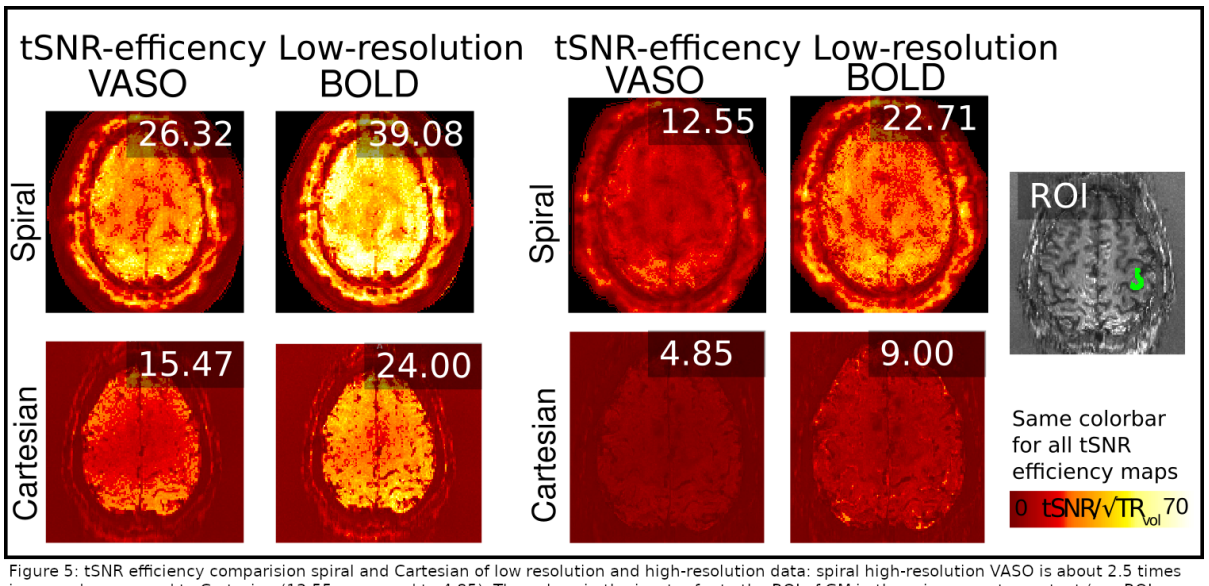

Figure 5: tSNR efficiency comparision spiral and Cartesian of low resolution and high-resolution data: spiral high-resolution VASO is about 2.5 times improved comprared to Cartesian (12.55 compared to 4.85). The values in the inset refer to the ROI of GM in the primary motor cortext (see ROI inset).

VASO fMRI USING 2D-SMS SPIRAL READOUTS

Denizhan Kurban[1], Renzo Huber[1],Gilad Liberman[2], Dimo Ivanov[1], Benedikt A Poser[1]

[1]Maastricht Brain Imaging Centre, Faculty of Psychology and Neuroscience, Maastricht University, Maastricht, the Netherlands

[2]Athinoula A. Martinos Center for Biomedical Imaging, MGH, Boston, MA, United States

Synopsis: High-resolution blood volume-sensitive fMRI VASO can capture functional signal changes with high localization specivity compared to conventional BOLD sequences. However, it suffers from reduced sampling efficiencies and lower detection sensitivity. Here, we overcome these limitations by combining VASO contrasts with the high efficiency of multi-echo enabled spiral k-space sampling and CAIPI-optimized SMS acceleration. We find that spiral sampling enables faster VASO acquisitions than possible with Cartesian EPI sampling. For high spatial resolutions (1.25mm), we confirm that the proposed method is insensitive to large draining veins while having more stable fMRI signals (higher tSNR).

INTRODUCTION

Blood-volume-sensitive (VASO) fMRI[1] can be advantageous compared to conventional GE-EPI-based BOLD methods, especially at ultra-high field or when high spatial resolution is required. VASO provides improved spatial specificity down to the level of cortical layers and columns, and allows the quantification of meaningful physiological parameters. Its neuroscientific application, however, is limited by BOLD-contrast contamination and temporal sampling inefficiency. VASO fMRI acquisitions are conventionally performed with Cartesian EPI readouts, which put limits on the shortest echo time (TE) and readout durations achievable, especially for high resolution studies.

To overcome these VASO fMRI limitations, specifically to achieve faster acquisitions at a shorter echo time, free of BOLD contamination, we combined the efficiency of spiral k-space sampling and SMS[2] acceleration with blood-volume-sensitive VASO contrast. We used two different spiral readout schemes to perform interleaved VASO-BOLD acquisitions to explore the feasibility of VASO fMRI with 2D-SMS spiral readout at ultra-high field. The flexibility and efficiency of spiral readouts have been previously demonstrated at 7T, including BOLD fMRI acquisitions[3,4,5]. Spiral sampling enables faster VASO acquisitions than previously possible for given resolution and coverage requirements. Furthermore, for high spatial resolution we show that the proposed method is less sensitive to large draining veins; which allows for better separation of fMRI signals from 'kissing' gyri, e.g. as in sensory and motor cortex.

METHODS

Two spiral readout schemes were implemented in a slice-selective slab inversion (SS-SI) VASO[6] sequence in the vendor-provided IDEA environment (VB17A-UHF) (Figure 1): 1) dual-echo spiral out-in readout for simultaneous acquisition of VASO and BOLD contrasts at $2mm^3$ iso, nominal TE_1/TE_2=2.5ms/27.5ms, TR_{VASO}=1350ms, TR_{BOLD}=350ms 24 slices, SMS-factor=2. 2) High resolution spiral-out readout at $1.25x1.25x1.2mm^3$ resolution, TE=2.5ms, TR_{VASO}=1500ms, TR_{BOLD}=500ms, 30 slices, SMS-factor=2. Data was acquired on a 7T Siemens scanner (SIEMENS Healthineers). Cartesian acquisitions with matched parameters were also performed ($TE_{2mm}/TE_{highres}$=11/19ms). The VASO specific inversion was implemented by means of a 10 ms TR-FOCI pulse 950 ms before the first excitation pulse of the readout module. 9-minute runs were acquired with a visuo-motor functional block-design task (30/30 TRs ON/OFF). The image reconstruction of the spiral data was performed with Minimal Linear Network reconstruction that is trained on session-specific B_0 maps [7]. No smoothing was applied during any stage of the analysis in SPM (MOCO), AFNI, FSL (for GLM), and LayNii (for profile plot). We applied a T2* deblurring in the pre-processing of the spiral data (Figure 4).

RESULTS

Figure 2 shows the mean image and tSNR maps of the VASO time series, corrected for BOLD contamination. Compared to Cartesian acquisitions, spiral acquisitions at very short TE show superior temporal stability for the VASO contrast. The difference between the tSNR of spiral and Cartesian acquisitions is especially highlighted in the high resolution acquisitions as the Cartesian EPI TE becomes longer. For the dual-echo VASO-BOLD acquisitions we show that the visuomotor task leads to strong signal changes in both CBV and BOLD. In the high resolution VASO acquisitions, spiral images resulted in stronger activation maps compared to Cartesian images (figure 3B). Additionally, VASO shows higher spatial specificity compared to BOLD (figure 3C): this is visible in the profiles as two separate activations for M1 and S1 in the VASO signal, whereas the BOLD signal generates an unspecific peak over sensory and motor cortices.

DISCUSSION AND CONCLUSIONS

We combined non-Cartesian spiral readouts with blood volume sensitive VASO contrast preparations and showed the feasibility of such technique in a task-based fMRI experiment at 7T. The proposed approach provides superior signal stability, unprecedented sampling efficiency (sub-second TRs), and avoids unwanted sensitivity to large veins. The technique might become a valuable tool for neuroscientific applications that require high spatio-temporal resolutions. Extension of the proposed 2D approach to 3D stack-of-spirals is desirable as benefits of 3D VASO acquisitions have previously been shown[8].

REFERENCES

1- Lu, Hanzhang, Xavier Golay, James J Pekar, and Peter C M van Zijl. 2003. "Functional Magnetic Resonance Imaging Based on Changes in Vascular Space Occupancy." Magnetic Resonance in Medicine 50: 263–74.

2- Setsompop, K., Gagoski, B. A., Polimeni, J. R., Witzel, T., Wedeen, V. J., & Wald, L. L. (2011). "Blipped-controlled aliasing in parallel imaging for simultaneous multislice echo planar imaging with reduced g-factor penalty. Magnetic Resonance in Medicine." 67(5), 1210–1224. doi:10.1002/mrm.23097

3- Engel, M., Kasper, L., Barmet, C., Schmid, T., Vionnet, L., Wilm, B., & Pruessmann, K. P. (2018). "Single-shot spiral imaging at 7 T." Magnetic Resonance in Medicine 80(5), 1836–1846.

4- Kasper, Lars; Engel, Maria; Heinzle, Jakob; Mueller-Schrader, Matthias; Reber, Jonas; Schmid, Thomas et al. (2019): "Advances in Spiral fMRI. A High-resolution Study with Single-shot Acquisition." In bioRxiv. DOI: 10.1101/842179.

5- Kurban, D., Liberman, G., Kashyap, S., Ivanov, D., Poser, AB. (2019) "Dual-echo simultaneous multi-slice spiral acquisition for concurrent CBF and BOLD fMRI at 7T." Proceedings of ISMRM, Montreal

6- Huber, Laurentius et al. 2014. "Slab-Selective, BOLD-Corrected VASO at 7 Tesla Provides Measures of Cerebral Blood Volume Reactivity with High Signal-to-Noise Ratio." Magnetic Resonance in Medicine 72(1): 137–48.

7- Liberman G, Poser BA. "Minimal Linear Networks for Magnetic Resonance Image Reconstruction." NatSciRep (accepted; SREP-19-06395B)

8- Huber, L., Ivanov, D., Handwerker, D. A., Marrett, S., Guidi, M., Uludağ, K., … Poser, B. A. (2018). "Techniques for blood volume fMRI with VASO: From low-resolution mapping towards sub-millimeter layer-dependent applications." NeuroImage, 164, 131–143. doi:10.1016/j.neuroimage.2016.11.039

9- Huber L, Guidi M, Goense JBM, et al. (2015). The magnitude point spread function is an inadequate measure of T2*-blurring in EPI. *Proc Int Soc Magn Reson Med*.;23:2056.

10- Kasper L, Engel M, Barmet C, et al. (2018). Rapid anatomical brain imaging using spiral acquisition and an expanded signal model. Neuroimage.;168:88-100.

11. Shao X, Guo F, Shou Q, et al. Laminar perfusion imaging with zoomed arterial spin labeling at 7 Tesla. bioRxiv. 2021:1-20. https://doi.org/10.1101/2021.04.13.439689.

Acknowledgments / Funding Information: Funding support: LH NWO VENI 016.198.032, BAP, DK VIDI 016.178.052,
We thank Christopher J Wiggins from Scannexus (Maastricht, NL) for his enthusiastic support of this project.

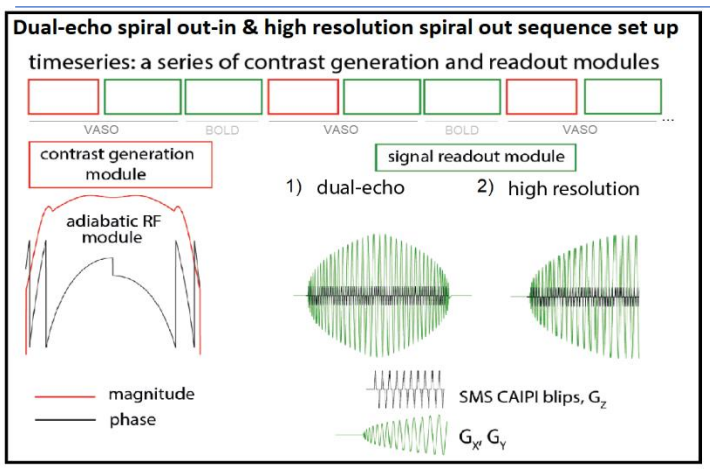

Figure 1 (above): Sequence setup: Two different spiral readout modules (shown in green) were implemented after a VASO contrast generation module (shown in red). The readout modules were run twice to acquire interleaved VASO and BOLD volumes. For efficient SMS unaliasing, CAIPI shifts were played out during the signal acquisition along the spiral trajectories.

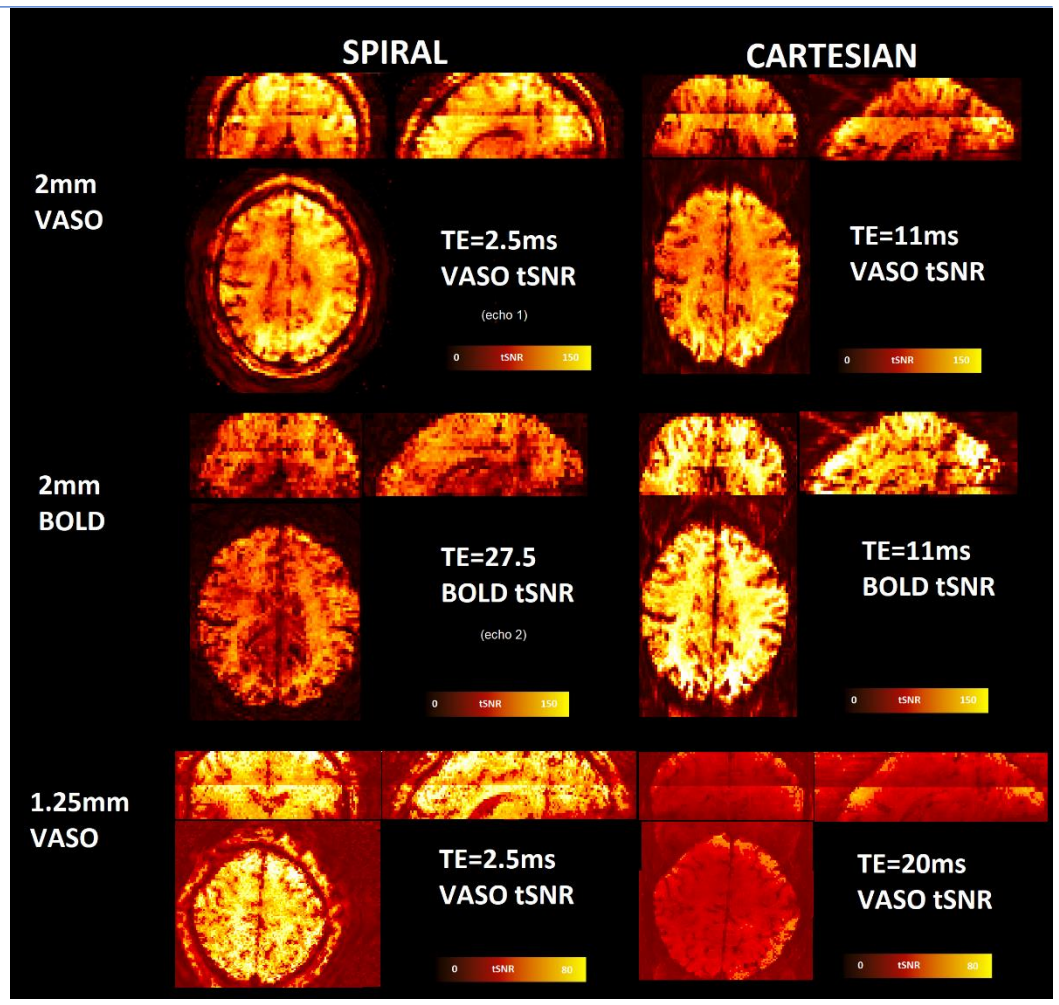

Figure 2 (rigjht): Voxel-wise tSNR maps of the low resolution dual-echo spiral VASO and BOLD and high resolution VASO acquisitions. Comparisons to the reference Cartesian acquisitions are shown on the right side

Figure 3 (below): A)VASO and BOLD activation maps obtained from the low resolution dual-echo spiral acquisitions. The VASO data refer to the first echo, the BOLD data refer to the second echo.B) Comparison of the high resolution spiral and Cartesian VASO acquisitions. Note the larger scaling of the z-score color code.C) BOLD and VASO activation maps in the motor cortex, obtained with the spiral acquisitions. The activation projection from an ROI in sensorimotor cortex shows the higher spatial specificity of VASO compared to BOLD.

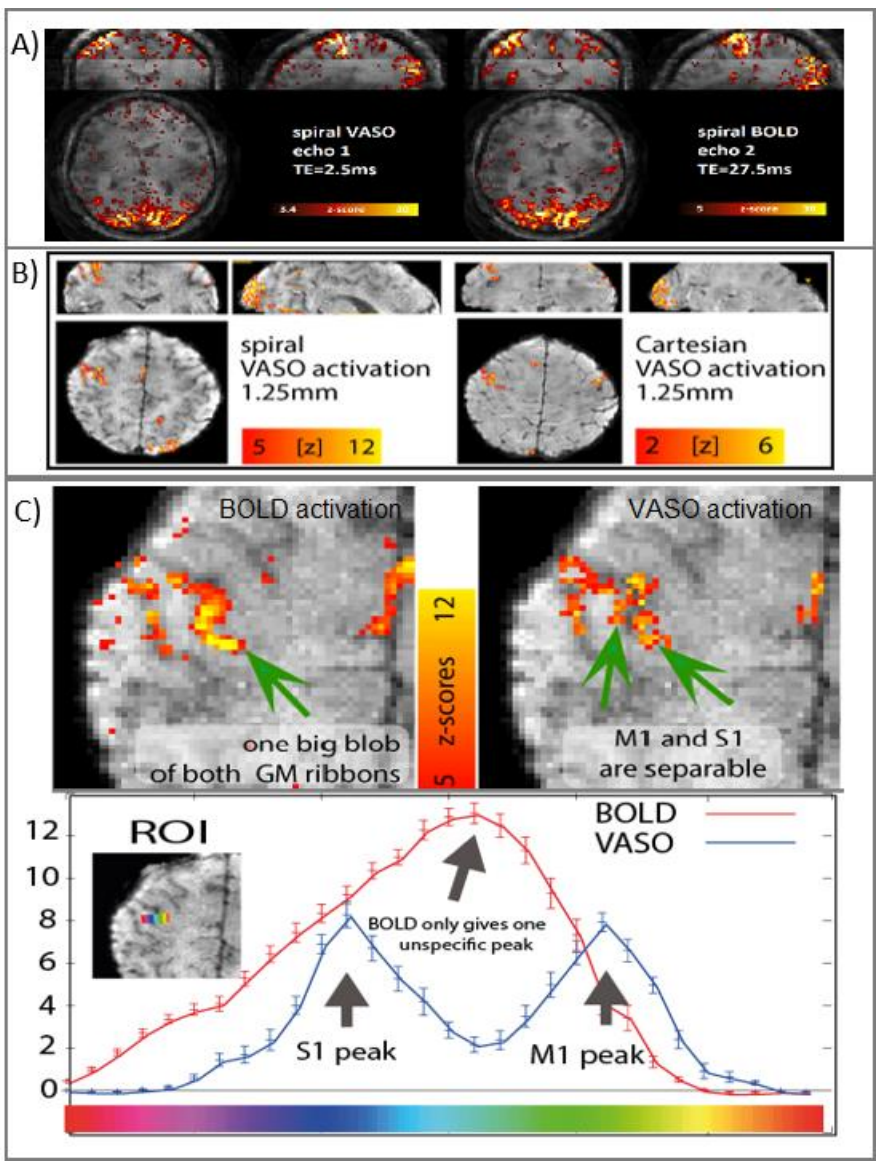

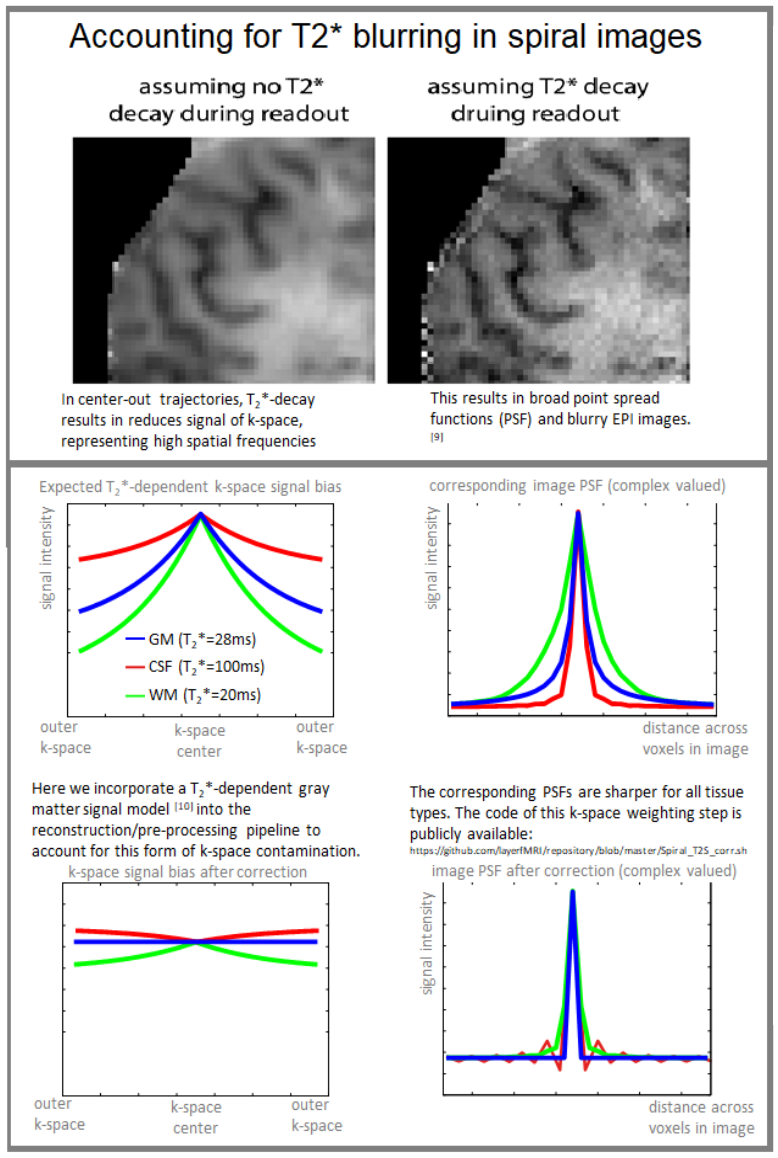

Figure 4. Implementation of a T2* blurring correction of spiral images. The top panels depict the expected broadening of the imaging point spread function for center-out spiral trajectories with T2*-decay during the echo-planar readout. We included such T2*-decays into the signal model [11] to retrospectively account for T2*-blurring. This approach allowed us to retain the high-resolution signal fidelity of the VASO contrast (at the cost of noise amplification).

Extra-ocular muscle volume, $T2_{water}$ and fat fraction are slightly increased in patients with myasthenia gravis

Kevin R. Keene[1,2], Jan. J. G. M. Verschuuren[1], Irene C. Notting[3], Martijn R. Tannemaat[1], Jan-Willem M. Beenakker[2,3],Hermien E. Kan[2]

1. Leiden University Medical Center, Department of Neurology, The Netherlands
2. Leiden University Medical Center, C.J. Gorter Center for High Field MRI, Department of Radiology, The Netherlands
3. Leiden University Medical Center, Department of Ophthalmology, The Netherlands

Synopsis

Quantitative MRI of the extra-ocular muscles might have diagnostic value and play a role in therapeutic monitoring in myasthenia gravis (MG). Our data show a slight increase in volume, fat fraction and $T2_{water}$ in extra-ocular muscles of MG patients compared to controls. Volume and fat fraction changes were most pronounced in chronic MG patients, $T2_{water}$ changes were most pronounced in recently diagnosed and untreated MG patients. The absence of gross structural changes implies that eye muscle weakness might be reversible, even in chronic patients with residual ophthalmoplegia.

Abstract

Introduction

Quantitative MRI of the eye muscles, or the extra-ocular muscles (EOM), might have diagnostic value and play a role in therapeutic monitoring in myasthenia gravis (MG).[1] Diplopia, double vision, is a hallmark of myasthenia gravis and caused by relative weakness of the four recti eye muscles (lateral rectus [LR], medial rectus [MR], inferior rectus [IR] and superior rectus [SR]) in this synaptic disease.[2] In Chronic progressive external ophthalmoplegia, a mitochondrial disease with EOM involvement, atrophy and fat replacement of the EOM was previously observed.[3] Quantitative MRI of the EOM was shown to be feasible in a small group of patients.[4] Now we aimed to explore structural differences of the eye muscles in a large group of myasthenia gravis (MG) patients using quantitative MRI and compared this to healthy controls and CPEO patients.

Methods

18 recently diagnosed MG (58±20yrs), 18 chronic MG (51±17yrs), 11 seronegative MG (58±8yrs), 5 CPEO patients (52 ± 12yrs) and 11 healthy controls (58±13yrs) were scanned at 7T (Philips). Scans included a 3-point-Dixon (TE/TR/FA/ΔTE:2.4ms/10ms/3°/0.33ms) and two multi-echo spin-echo (ME-SE) sequences (20 echoes, ΔTE/TR: 9m/4000ms) planned perpendicular on the EOM for each eye. Example scans for EOM volume and fat fraction measurements are demonstrated respectively in figure 1A and 1B. MR-scans were semi-automatically 3D-segmented to determine EOM volume and fat fractions (FF) (figure 1C). Data from the Dixon acquisition were fitted using an in-house developed water-fat separation Matlab script. $T2_{water}$ data obtained by fitting the ME-SE echoes using a dictionary fitting method using extended phase graph (EPG) algorithms including B1 in the model.[5,6] Measurements were compared between CPEO, MG groups and healthy controls groups using an ANOVA per EOM with Tukey post-hoc analysis. A separate ANOVA was performed including only the healthy controls and MG groups to test whether the MG groups differ from the healthy controls. Correlations between qMRI measurements were tested using Pearson correlations, after pooling the MG groups. The $T2_{water}$ between the left and the right orbit was compared using an independent T-test.

Results

Differences in volume between healthy controls, CPEO and MG groups were observed (e.g. respectively for MR, 569±129, 603±106, 635±140, 520±85 and 442±114 mm^3, healthy controls, recent MG, chronic MG, seronegative MG and CPEO, $p<0.01$, figure 2). The volume differences where overall IR>MR>LR. For the CPEO patients post-hoc tests showed the volume of the LR, MR and the SR to be significantly smaller than the other groups. Fat fraction was slightly elevated in CPEO and all MG groups, (e.g. respectively for LR, 12±2%, 15±4%, 15±5%, 12±3% and 20±10%)., figure 3) and were overall SR>IR>LR. In CPEO patients the fat fraction was significantly higher than the other groups for all four EOM. A positive correlation between EOM volume and fat fraction was present for the SR ($r=0.41$, $p < 0.0001$) and the IR ($r=0.24$, $p < 0.05$) in MG patients. On the contrary, a strong negative correlation between EOM volume and fat fraction was observed in the LR ($r=-0.86$, $p < 0.005$) and MR ($r=-0.74$, $p < 0.05$) in CPEO patients. The $T2_{water}$ was significantly different between the groups in the MR and post-hoc analysis shows the difference is caused by a higher $T2_{water}$ in the recently diagnosed MG patients (respectively 25.5±2.9, 27.3±3.2, 24.6±3.6, 26.3±3.9 and 27.3±2.8 ms, $p<0.05$, figure 5). Given the high variation in the $T2_{water}$ measurements between subjects in the groups, we pooled all the muscles and found a positive correction between the fitted B1 and $T2_{water}$ ($r = 0.43$, $p<0.0001$). Additionally, we found a significant difference in $T2_{water}$ between the left and right orbit (87% and 75% respectively, $p<0.0001$).

Discussion

We show that qMRI of the EOM was able to detect subtle differences between MG patients, CPEO patients and controls. EOM volume and fat fraction was increased, most pronounced in chronic MG. No severe atrophy was observed as was expected in patients with residual ophthalmoplegia.[7] We hypothesize that the unexpected increase in EOM volume in MG is due to compensatory hypertrophy, where the muscle volume increases to compensate for the muscle weakness. The atrophy and severe fat replacement in CPEO patients was expected based on the disease pathophysiology and is in line with literature[3]. The increase in $T2_{water}$ in the MR of the recently diagnosed MG group could be due to inflammation, as complement activation has previously been shown to occur in muscles in MG[8] and these patient are immunosuppressant naive. However, a high variation in $T2_{water}$ measurements between subjects was observed that could be obscuring differences. This may be caused by B1 influences that are not fully corrected in our EPG model, given the remaining relationship between $T2_{water}$ and B1. Moreover, we observed a B1 difference between the left and right orbit, which might be explained by regional B1 variation due to the field strength and challenging orbital anatomy. Improving the EPG model for this specific case is subject of future work.

Conclusion

We observed small increases in volume and FF in eye muscles of MG patients, most pronounced in chronic MG patients. This absence of gross structural changes implies that eye muscle weakness might be reversible, even in chronic patients with residual ophthalmoplegia. Additionally, we observed an increase in $T2_{water}$ in the MR in recently diagnosed MG patients.

References

1. Verschuuren JJGM, Palace J, Erik Gilhus N. Clinical aspects of myasthenia explained. *Autoimmunity*. 2010;43(5-6):344-352. doi:10.3109/08916931003602130
2. Nair AG, Patil-Chhablani P, Venkatramani D V., Gandhi RA. Ocular myasthenia gravis: A review. *Indian J Ophthalmol*. 2014;62(10):985-991. doi:10.4103/0301-4738.145987
3. Pitceathly RDS, Morrow JM, Sinclair CDJ, et al. Extra-ocular muscle MRI in genetically-defined mitochondrial disease. *Eur Radiol*. 2016;26(1):130-137. doi:10.1007/s00330-015-3801-5
4. Keene KR, van Vught L, van de Velde NM, et al. The feasibility of quantitative MRI of extra-ocular muscles in myasthenia gravis and Graves' orbitopathy. *NMR Biomed*. 2020. doi:10.1002/nbm.4407
5. Keene KR, Beenakker JWM, Hooijmans MT, et al. T2 relaxation time mapping in healthy and diseased skeletal muscle using extended phase graph algorithms. *Magn Reson Med*. April 2020:mrm.28290. doi:10.1002/mrm.28290
6. Marty B, Baudin PY, Reyngoudt H, et al. Simultaneous muscle water T2 and fat fraction mapping using transverse relaxometry with stimulated echo compensation. *NMR Biomed*. 2016;29(4):431-443. doi:10.1002/nbm.3459
7. Mantegazza R, Antozzi C. When myasthenia gravis is deemed refractory: Clinical signposts and treatment strategies. *Ther Adv Neurol Disord*. 2018;11. doi:10.1177/1756285617749134
8. Silvestri NJ, Wolfe GI. Myasthenia gravis. *Semin Neurol*. 2012;32(3):215-226. doi:10.1055/s-0032-1329200

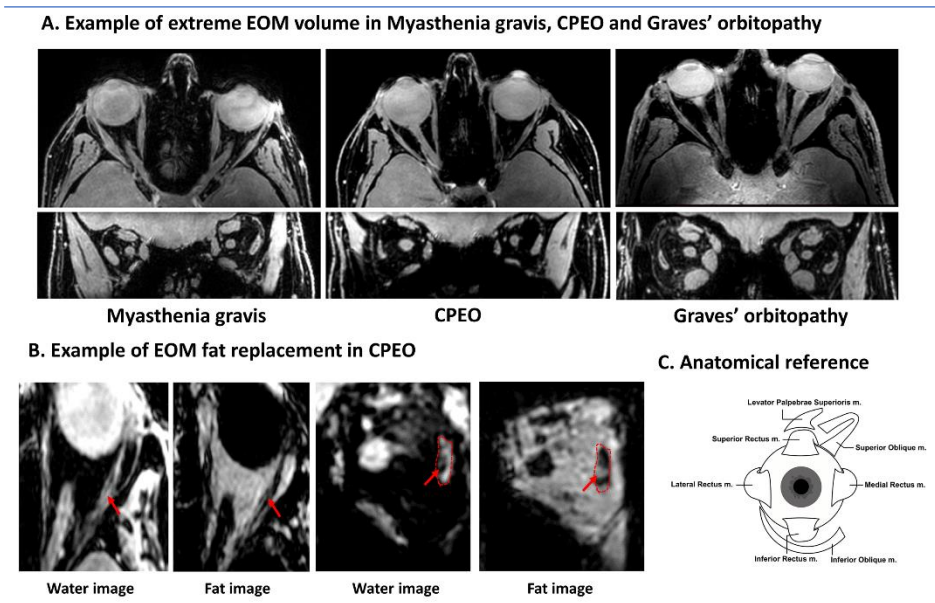

Figure 1: Dixon images depicting the eye muscles. **A:** Transverse water image on top and coronal water image below. Demonstration of volume changes in MG, CPEO and Graves' orbitopathy. Notice the decrease in eye muscle volume in CPEO and swelling in the Graves' orbitopathy patient. **B:** Example of extreme fat replacement of the eye muscles in CPEO, with the transverse water and fat image on the left and the coronal water and fat image on the right. **C:** Anatomical reference of all eye muscles.

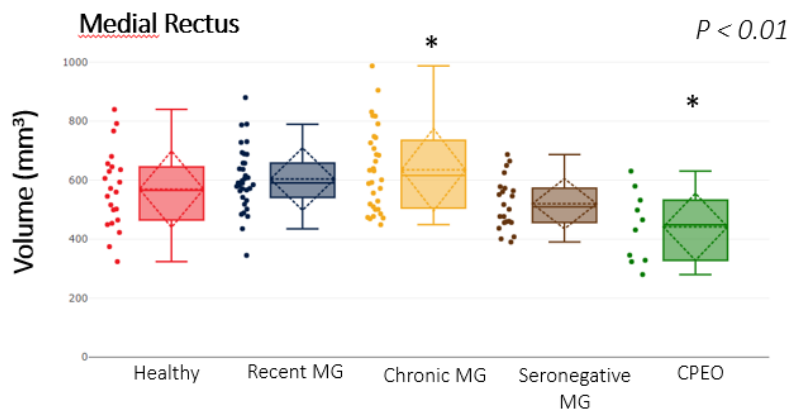

Figure 2: Muscle volume of the medial rectus eye muscle for all groups (healthy controls, recent MG, chronic MG, seronegative MG and CPEO). Increases in volume were observed for the chronic MG patients and a decrease in volume was observed for the CPEO patients (e.g. respectively for MR, 569±129, 603±106, 635±140, 520±85 and 442±114 mm^3, $p<0.01$).

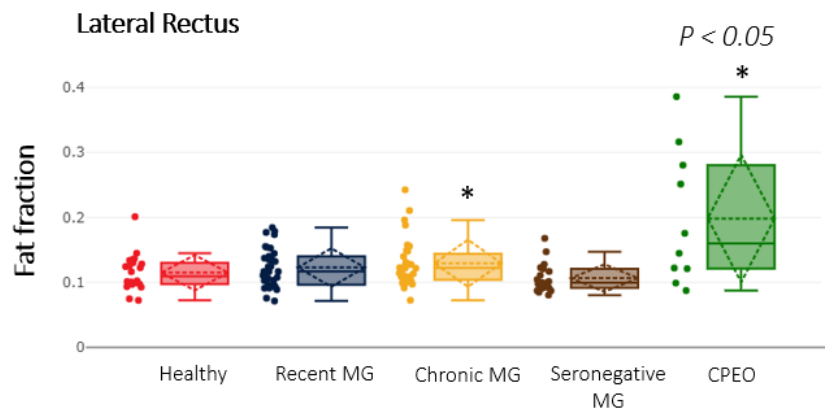

Figure 3: Fat fraction of all the superior rectus eye muscle for all groups (healthy controls, recent MG, chronic MG, seronegative MG and CPEO). Fat fractions were different between groups: slightly elevated in chronic MG patients and severely elevated in CPEO patients (e.g. respectively for LR, 12±2%, 15±4%, 15±5%, 12±3% and 20±10%).

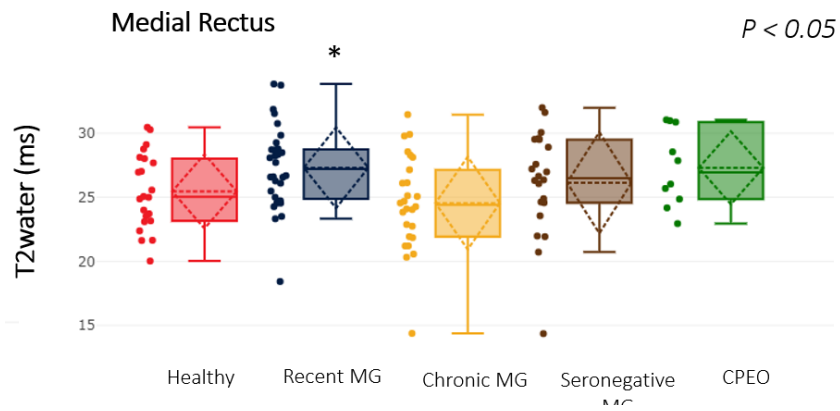

Figure 5: $T2_{water}$ of the medial rectus eye muscle for all groups (healthy controls, recent MG, chronic MG, seronegative MG and CPEO). The $T2_{water}$ was significantly different between groups in the MR and post-hoc analysis shows the difference is caused by a higher $T2_{water}$ in the recently diagnosed MG patients (respectively 25.5, 27.31, 24.55, 26.3 ms and 27.3±2.8, $p < 0.05$).

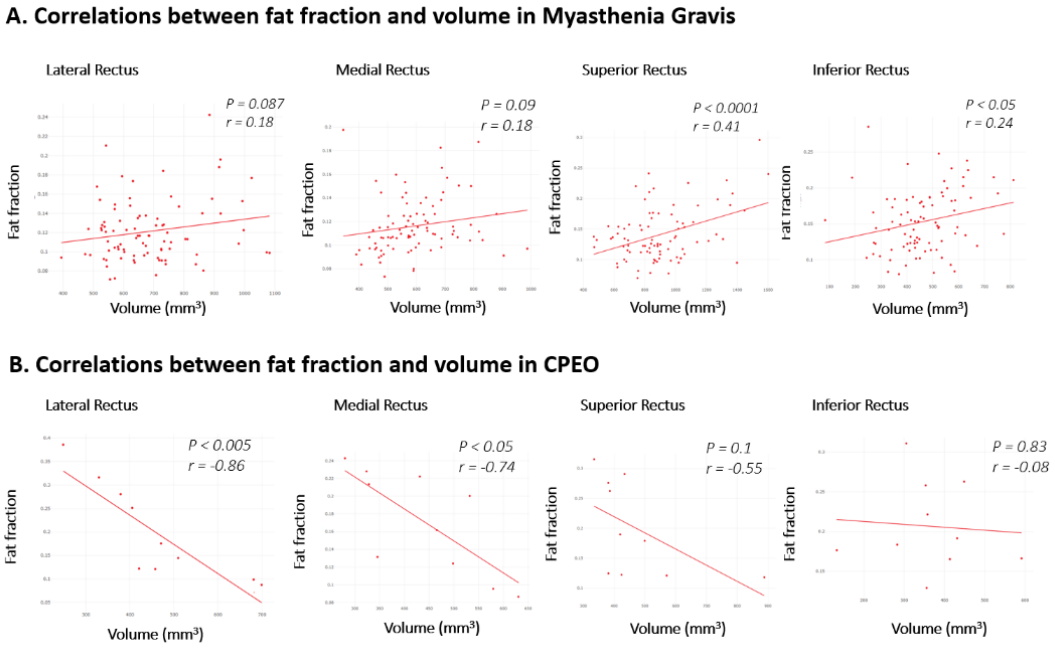

Figure 4: Correlations between eye muscle volume and fat fraction. A positive correlation between eye muscle volume and fat fraction was present for the SR ($r=0.41$, $p < 0.0001$) and the IR ($r=0.24$, $p < 0.05$) in MG patients. On the contrary, a strong negative correlation between eye muscle volume and fat fraction was observed in the LR ($r=-0.86$, $p < 0.005$) and MR ($r=-0.74$, $p < 0.05$) in CPEO patients.

Wall shear stress and velocity pulsatility in the parent artery of an unruptured intracranial aneurysm - a 7T 4D flow MRI study

RJ van Tuijl[1], YM Ruigrok[2], KM Timmins[1], BK Velthuis[1], P van Ooij[1], JJM Zwanenburg[1], IC van der Schaaf[1]
1) Department of Radiology, 2) Department of Neurology and Neurosurgery, UMC Utrecht Brain Center, University Medical Center Utrecht, Utrecht University, the Netherlands

Synopsis: The influence of maximum wall shear stress (WSSMAX) and velocity pulsatility (vPI) are extensively investigated in aortic aneurysms, but hemodynamic variation along the Circle of Willis (CoW) in patients with an unruptured intracranial aneurysm (UIA) is unknown. Thirteen patients with an UIA were scanned at 7T-MRI using 4D phase-contrast MRI, comparing hemodynamic parameters between the parent artery of the UIA and the corresponding contralateral artery. The parent vessel of the UIA showed significantly higher WSSMAX, blood-flow and velocity, and lower vPI compared to the unaffected contralateral side. This study supports a hemodynamic role in the aetiology of aneurysm formation.

Summary of main findings: Parent arteries of intracranial aneurysms show higher blood-flow, velocity and wall shear stress and lower velocity pulsatility, compared to the contralateral arteries. This suggests that hemodynamics play an etiologic role in aneurysm development.

Introduction: An unruptured intracranial aneurysm (UIA) is a saccular dilatation of a brain vessel that is at risk of rupture. Aneurysm rupture results in an aneurysmal subarachnoid hemorrhage, a subtype of stroke with poor outcome[1,2]. The number of detected UIA is growing due to the increasing number and quality of brain scans. Timely treatment can prevent aneurysm rupture, but is mostly performed in UIAs with high rupture risk[1].

Prediction of aneurysm rupture is crucial in clinical decision making in patients with an UIA. Development and growth of an unruptured IA (UIA) is a multifactorial process with hemodynamic forces such as wall shear stress being an important contributor[3]. Arteries are under constant mechanical loading from the blood pressure and flow which causes endothelial shear stress and circumferential wall stress[4]. Novel imaging techniques as 7T-MRI 4D flow imaging enable accurate and reproducible measurement and quantification of blood flow and the resulting wall shear stress (WSS), blood-flow, mean velocity and velocity pulsatility index (vPI) in the intracranial vessels[5]. Since abnormal levels of WSS are implicated in the pathogenesis of aneurysmal disease[6], relation between wall shear stress and presence of an UIA in a blood vessel may provide insight in the aetiology of UIA[7]. This study used accelerated 4D-flow imaging to compare the WSS, blood-flow, mean velocity and vPI in the intracranial parent artery containing an UIA with the corresponding contralateral artery without UIA.

Methods: This study included subjects from the 3T-MRI ERASE (**E**arly **R**ecognition of persons at high risk of **A**neurysmal **S**ubarachnoid hemorrhag**E**) study, a screening study for UIA in family members of patients with an UIA. We included patients with a detected UIA that underwent additional 7-Tesla with a four-dimensional phase-contrast-MRI (4D PC-MRI) acquisition. UIA locations were only included if there was a contralateral artery without an UIA and if the UIA was included in the 4D PC-MRI acquisition. Participants underwent 7-Tesla MRI (Philips Healthcare, Best, The Netherlands) using a volume transmit and 32-Channel receive coil (Nova Medical, Houston, United States). For this study, we used PROspective Undersampling in multiple Dimensions (PROUD) acceleration, which enables a pseudospiral k_y/k_z-plane acquisition scheme designed for incoherent undersampling with a variable sampling density[8]. The 4D PC-MRI acquisition covered the complete CoW with scan specifics as given in Table 1.

The reconstructed 4D PC-MRI datasets were analysed using CAAS MR Solutions v5.1.1 software (Pie Medical Imaging, Maastricht, The Netherlands). CAAS automatically generates the centreline and perpendicular slices along the complete CoW from the ICA towards the smaller cerebral arteries. These perpendicular slices were visually checked and automatically propagated to create volumetric flow rate traces and separate velocity and area traces over the cardiac cycle.

The blood-flow velocity pulsatility index ($vPI=(Velocity_{max}-Velocity_{min})/Velocity_{mean}$) was calculated from each velocity trace. The maximum WSS (WSS_{MAX}) was calculated using an in-house-developed software in Matlab R2016a by multiplying the wall shear rate by the dynamic viscosity of blood ($3.2x10^{-3}$ Pa·s)[9] (Figure 1). The outcome parameters WSS_{MAX}, blood-flow, vPI and mean velocity over the cardiac cycle were calculated for all patients with UIAs (Figure 2) for two ROIs: 1. parent artery of the UIA, 2. the corresponding contralateral artery. An affected (ipsilateral) side versus unaffected (contralateral) side comparison was performed for each patient using paired t-test. The statistical significance threshold was set at $p<0.05$.

Results: We included 14 patients (nine women, mean age 52 ± 12) with UIA (range 1.5 to 5 mm). One patient with a posterior inferior cerebral artery (PICA)) outside the field-of-view was excluded. Thirteen patients were included with the following UIA locations: six middle cerebral artery; three internal carotid artery (ICA); two posterior communicating artery and two anterior cerebral artery). WSS_{MAX}, blood-flow and mean velocity were statistically significantly higher, and the vPI was statistically significantly lower in the parent artery containing an UIA compared to the contralateral artery (Table 2). These results were consistent for all 13 included patients with different UIA locations.

Discussion: This study using 4D PC-MRI on ultra-high field (7T) showed different hemodynamics in the parent artery containing an UIA compared to the contralateral side without an UIA. The WSS_{MAX}, blood-flow, mean velocity and vPI are thus potentially of risk for aneurysm development, growth and/or rupture. The limitation of this study is the limited number of UIAs. All UIA were in the anterior circulation, and therefore no conclusions can be drawn regarding the posterior circulation. However, we showed significant differences in these relatively small diameters of the UIAs, and all measurements were different within the same subject. Future studies need to include a larger population, preferably with long term follow-up, with also larger UIA in both anterior- as well as posterior circulation, to study the relation between WSS, blood-flow, velocity and vPI in the parent vessels and the presence of an aneurysm.

Conclusion:

This study shows that hemodynamic changes occur in parent arteries with UIA compared to the contralateral artery without UIA. All outcome measurements (WSS_{MAX}, blood-flow and vPI) show statistically significant differences. These three hemodynamic markers in the parent arteries with UIA should be investigated further in larger population with UIA.

References:

1. Etminan N, Rinkel GJ. Unruptured intracranial aneurysms: Development, rupture and preventive management. *Nat Rev Neurol*. 2016;12(12):699-713.

2. Algra AM, Lindgren A, Vergouwen MDI, et al. Procedural Clinical Complications, Case-Fatality Risks, and Risk Factors in Endovascular and Neurosurgical Treatment of Unruptured Intracranial Aneurysms: A Systematic Review and Meta-analysis. *JAMA Neurol*. 2019;76(3):282-293.

3. Szajer J, Ho-Shon K. A comparison of 4D flow MRI-derived wall shear stress with computational fluid dynamics methods for intracranial aneurysms and carotid bifurcations — A review. *Magn Reson Imaging*. 2018;48:62-69.

4. Lu D, Kassab GS. Role of shear stress and stretch in vascular mechanobiology. *J R Soc Interface*. 2011;8(63):1379-1385.

5. Markl M, Frydrychowicz A, Kozerke S, et al. 4D flow MRI. *J Magn Reson Imaging*. 2012;36(5):1015-1036.

6. Dolan JM, Kolega J, Meng H. High Wall Shear Stress and Spatial Gradients in Vascular Pathology: A Review. *Ann Biomed Eng*. 2013;(1):1411-1427.

7. Paszkowiak JJ, Dardik A. Arterial wall shear stress: Observations from the bench to the bedside. *Vasc Endovascular Surg*. 2003;37(1):47-57.

8. Gottwald LM, Töger J, Markenroth Bloch K, et al. High spatiotemporal resolution 4D flow MRI of intracranial aneurysms at 7T in 10 minutes. *Am J Neuroradiol*. 2020;41(7):1201-1208.

9. Van Ooij P, Potters W V., Guédon A, et al. Wall shear stress estimated with phase contrast MRI in an in vitro and in vivo intracranial aneurysm. *J Magn Reson Imaging*. 2013;38(4):876-884.

Acknowledgments / Funding Information: Continue on this line

Figure 1. Delete this page if there are no figures or tables

Table 1: Scan parameters

	4D PC-MRI covering the Circle of Willis
Field-of-view	250 x 190 x 20 mm^3
Acquired Resolution	0.7 x 0.7 x 0.7 mm^3
Velocity encoding sensitivity	100 cm/s (Left-Right)
Flip angle	15°
Repetition Time	6.4 ms
Echo Time	2.0 ms
Temporal resolution for a heart rate of 60 bpm	83 ms
Scan duration for a heart rate of 60 bpm	3x 3:15 min:sec

Table 2: Outcome parameters for all included subjects calculated at the ipsilateral side (parent artery), where the aneurysm is located, and the unaffected contralateral side.

	Ipsilateral side	**Contralateral side**	**P-value**
Maximum Wall shear stress (Pa)	12.20 ± 2.18	8.62 ± 1.12	<0.001
Blood-flow (ml/s)	1.41 ± 0.45	1.05 ± 0.40	0.007
Velocity Pulsatility	0.68 ± 0.11	0.77 ± 0.09	0.002
Mean velocity (cm/s)	39.42 ± 5.93	32.61 ± 4.87	<0.001

Figure 1: Representation of the steps from 4D flow images to the analysis, whereby the red arrow points to the aneurysm location in this subject. A) 4D PC-MRI images are reconstructed and visualized over the cardiac phase with velocity scaled between 0 and 100 cm/s in this subject. B) The wall shear stress distribution along the Circle of Willis used for analysis regarding affected (ipsilateral) versus unaffected (contralateral) side.

Figure 2: Representation of the 4D flow image analysis regarding affected (ipsilateral) versus unaffected (contralateral) side using CAAS software, whereby the red arrow points to the aneurysm location in this subject. A) MRA TOF image to show the aneurysm in this subject. B) Blood-flow analysis using the CAAS software for that same subject focused on the parent artery. C) Mean velocity curves (in cm/s) for this subject in the parent (blue) and contralateral artery (orange). D) Blood-flow (in ml/s) for this subject in the parent (blue) and contralateral artery (orange).

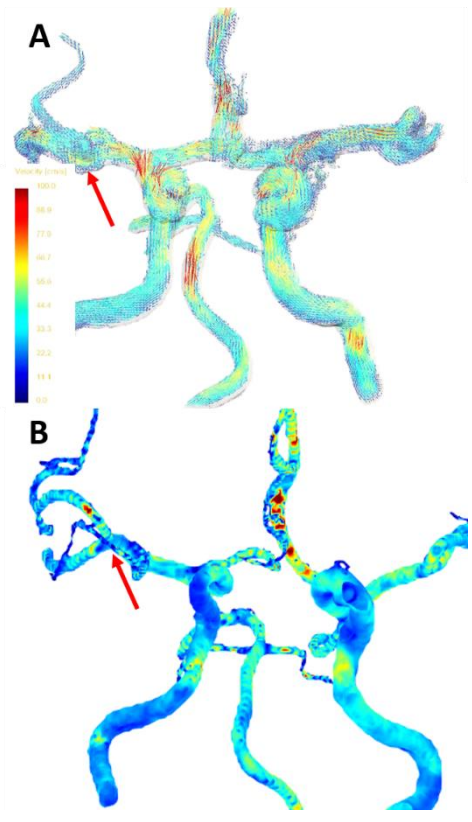

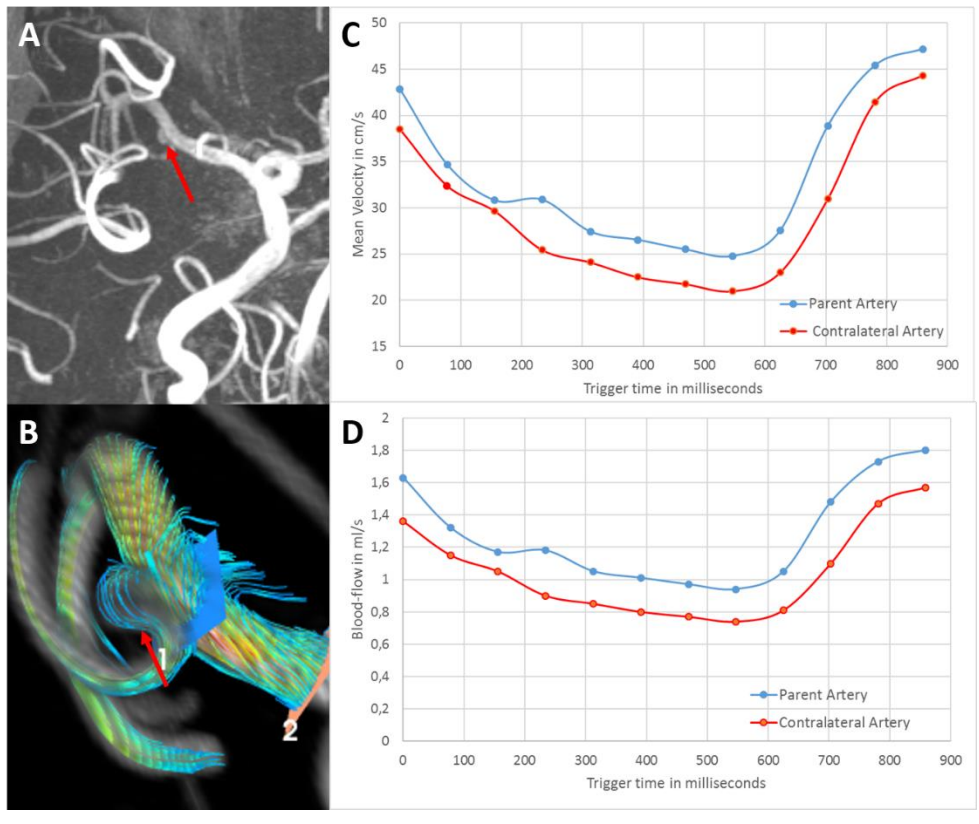

Comparision Between Multi-Contrast Atherosclerosis Characterization (MATCH) And Multi-Sequence MRI for Scoring Carotid Plaque Composition

Mohamed Kassem,[1,2] Ellen Boswijk,[2] Jochem van der Pol,[2] Rik PM Moonen,[2] Jan Bucerius,[3] Werner H Mess,[4] Robert Jan van Oostenbrugge,[1,6] Zhaoyang Fan,[7] M Eline Kooi [1,2]

[1]CARIM School for Cardiovascular Diseases, Maastricht University, Maastricht, Netherlands; [2]Department of Radiology and Nuclear Medicine, Maastricht University Medical Center, Maastricht, Netherlands; [3]Georg-August University Göttingen, Department of Nuclear Medicine, Germany; [4]Department of Clinical Neurophysiology, Maastricht University Medical Center, Maastricht, Netherlands; [5]Division of Image Processing, Department of Radiology, Leiden University Medical Center, Leiden, the Netherlands; [6]Department of Neurology, Maastricht University Medical Center, Maastricht, The Netherlands;

Synopsis: Multi-contrast Atherosclerosis Characterization (MATCH) was developed to quantify of carotid atherosclerotic plaque composition within 5 minutes' scan time. Twenty symptomatic patients with ≥2 mm carotid plaque underwent 3.0 Tesla conventional multi-sequence and MATCH MRI. Excellent agreement was obtained for scoring a Lipid-rich necrotic core (LRNC) intraplaque hemorrhage (IPH) on the MATCH images while fair for calcifications. No significant differences between MATCH and multi-sequence MRI were found in volume of LRNC, IPH and calcifications. We demonstrated excellent agreement between MATCH and multi-sequence MRI for the identification and quantification of LRNC and IPH within significant shorter time.

Background: Multi-sequence magnetic resonance imaging (MRI) is commonly used for quantification of carotid atherosclerotic plaque composition (1). Limitations are long scan time and image mis-registration errors. Multi-contrast Atherosclerosis Characterization (MATCH) was developed to overcome these limitations (2).

Aim: To compare MATCH with multi-sequence MRI for the quantification of carotid plaque components.

Methods: Twenty symptomatic patients with ≥2 mm carotid plaque underwent 3.0 Tesla multi-sequence and MATCH MRI. Image quality was scored on a 5-point scale based on vessel wall signal-to-noise ratio (SNR) and visibility of vessel wall and substructures (1, poor and 5, excellent) (3). The effective vessel wall SNR and contrast-to-noise ratio (CNR) between IPH and the muscle were calculated by dividing SNR and CNR by the acquisition time. Image analysis of the MATCH images was performed independently to that of the multi-sequence images (Figure 1). A Cohen's kappa test was used to determine agreement in the detection of plaque components using multi-sequence versus MATCH MRI. Sensitivity and specificity of MATCH in identifying plaque components were calculated using multi-sequence MRI as reference standard.

Results: One total or nearly occluded artery was excluded. The mean quality scores of the MATCH images were lower than multi-sequence images (2.4±0.5 versus 3.7±0.4; $p<0.05$), respectively. The overall effective SNR of MATCH was higher than multi-sequence protocol except for the hyper T1w images (Table 1). The mean effective CNR of intraplaque hemorrhage (IPH) on MATCH was significantly higher than that of magnetization prepared rapid acquisition gradient echo (MPRAGE) (7.2 ±4.3 versus 4.7±2.8; $p=0.007$). The scan time for MATCH and multi-sequence MRI was 7 and 39 minutes, respectively. Excellent intraobserver agreement was obtained for scoring a Lipid-rich necrotic core (LRNC) ($\kappa=0.89$) and IPH ($\kappa=0.91$) on the MATCH images while fair intraobserver agreement was observed for calcifications ($\kappa=0.32$). The sensitivity and specificity of scoring LRNC and IPH were >83% and >96% while for calcifications the sensitivity and specificity were 76% and 50%, respectively (Table 2). No significant differences between MATCH and multi-sequence MRI were found in volume of LRNC, IPH and calcifications. There was a small but significant difference in total volume of vessel wall and total volume of fibrous tissue (Figure 2).

Conclusion: We demonstrated excellent agreement between MATCH and multi-sequence MRI for the identification and quantification of LRNC and IPH. There was only fair agreement for scoring presence of calcifications. Although MATCH images showed a lower mean image quality score, short scan time and perfect co-registration are major advantages of MATCH.

References:

1. Saba L, Yuan C, Hatsukami TS, et al. Carotid Artery Wall Imaging: Perspective and Guidelines from the ASNR Vessel Wall Imaging Study Group and Expert Consensus Recommendations of the American Society of Neuroradiology. AJNR Am J Neuroradiol 2018;39:E9-E31.
2. Fan Z, Yu W, Xie Y, et al. Multi-contrast atherosclerosis characterization (MATCH) of carotid plaque with a single 5-min scan: technical development and clinical feasibility. J Cardiovasc Magn Reson 2014;16:53.
3. Yuan C, Mitsumori LM, Ferguson MS, et al. In vivo accuracy of multispectral magnetic resonance imaging for identifying lipid-rich necrotic cores and intraplaque hemorrhage in advanced human carotid plaques. Circulation 2001;104:2051-6.

Acknowledgments / Funding Information: Continue on this line

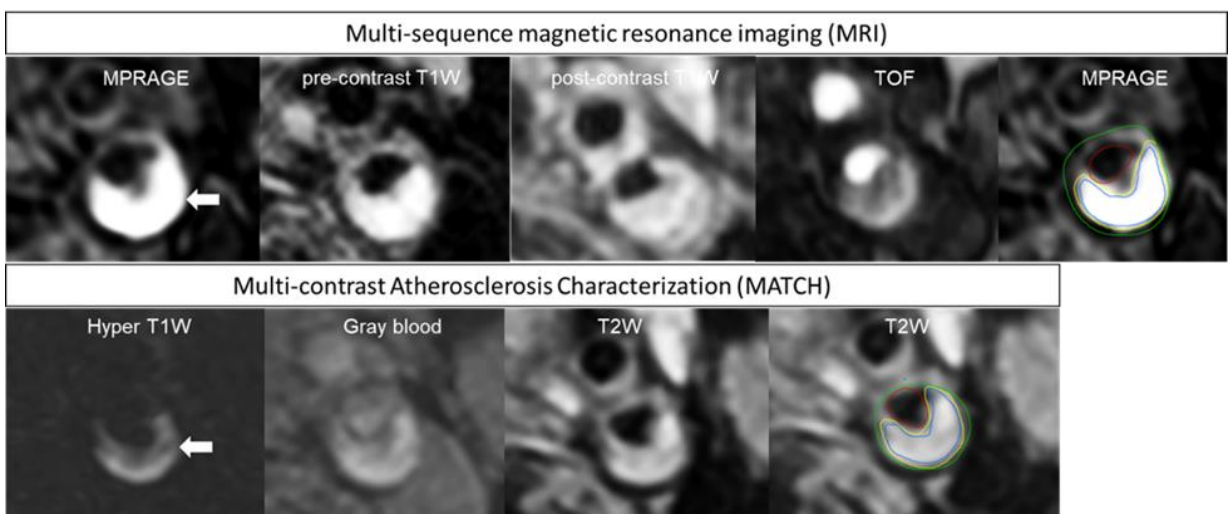

Figure 1. An example of a patient with an atherosclerotic plaque in the left carotid artery. Four multi-sequence MRI weightings are manually co-registered and shown in the upper row, while the MATCH images are inherently registered and shown in the bottom row. IPH appears hyper-intense (white arrow) on hyper T1w MATCH and on magnetization prepared rapid acquisition gradient echo (MPRAGE) images. Contours are shown on T2w MATCH and MPRAGE as follows: green for outer vessel wall, red for lumen, yellow for lipid-rich necrotic core and blue for IPH. A good agreement is shown between the contours that are delineated on the MATCH versus the multi-sequence MR images, although slight deviations can be observed.

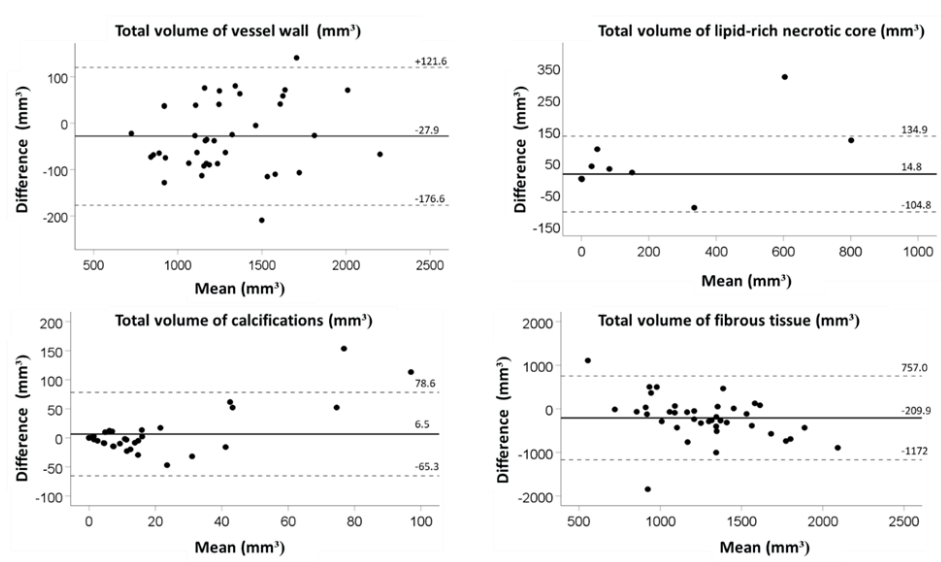

Figure 2. An example of a patient with an atherosclerotic plaque in the left carotid artery. Four multi-sequence MRI weightings are manually co-registered and shown in the upper row, while the MATCH images are inherently registered and shown in the bottom row. IPH appears hyper-intense (white arrow) on hyper T1w MATCH and on magnetization prepared rapid acquisition gradient echo (MPRAGE) images. Contours are shown on T2w MATCH and MPRAGE as follows: green for outer vessel wall, red for lumen, yellow for lipid-rich necrotic core and blue for IPH. A good agreement is shown between the contours that are delineated on the MATCH versus the multi-sequence MR images, although slight deviations can be observed.

Table 1. Comparison of the effective signal to noise ratio of the MATCH and multi-sequence images

Comparison	**Mean effective SNR± Standard error**	**P-value**
Hyper T1w vs MPRAGE	2.6±0.2 *vs* 3.9±0.2	P<0.001
Gray blood vs TOF	6.2±0.4 *vs* 4.8±0.3	P=0.008
T2w MATCH vs T1w post-contrast	6.0±0.4 *vs* 4.9±0.3	P=0.09

Table 2. Concordance between identification of intraplaque hemorrhage (IPH), lipid-rich necrotic core (LRNC), and calcifications (CA) on MATCH versus multi-sequence images.

MATCH	Multi-sequence	
	IPH -	IPH +
IPH -	**33 (97.1%)**	0
IPH +	1	**5 (83.3%)**
Total	34	5

MATCH	Multi-sequence	
	LRNC -	LRNC +
LRNC -	**27 (96.4%)**	1
LRNC +	1	**6 (85.7%)**
*Total	28	7

MATCH	Multi-sequence	
	CA -	CA +
CA -	**9 (50%)**	5
CA +	9	**16 (76.2%)**
Total	18	21

*4 carotids were excluded (contraindication of contrast injection)

A comparison of muscle pennation angles measured with DTI fiber tractography and 3D-ultrasound

L. Secondulfo[1], M. Eggelbusch[2], R. C.I. Wust[2.3] ,G. Weide[3], R. T. Jaspers[3], A. J. Nederveen[4], M. T. Hooijmans[1,4], G. J. Strijkers[1]

1Department of Biomedical Engineering and Physics, Amsterdam University Medical Centers, University of Amsterdam, The Netherlands, 2Laboratory for Myology, Department of Human Movement Sciences, Faculty of Behavioural and Movement Sciences, Vrije Universiteit Amsterdam, Amsterdam Movement Sciences, The Netherlands, 3Department of Rehabilitation Medicine, VU University Medical Center Amsterdam, Amsterdam Movement Sciences, The Netherlands, 4Department of Radiology and Nuclear Medicine, Amsterdam University Medical Centers, University of Amsterdam, the Netherlands

Synopsis: Pennation angle is an important architecture parameter to understand muscle functioning. It is commonly measured using 2D ultrasound. However, it is difficult to infer 3D muscle architecture from 2D imaging. Therefore, we compare the pennation angle measurements obtained with 3D-DTI fiber-tractography and 3D-ultrasound (3D-US). We acquired data of the Vastus Lateralis muscle in 9 healthy subjects. The mean pennation angle with 3D-US was 18.9°± 5.9°, whereas we found 33.3°±6.7° (straight fiber approximation) and 34.5°±4.8°(curved fiber fit) for DTI fiber-tractography. These differences between 3D-US and DTI could be of technical or physiological origin.

Background(133 words):

Knowledge on skeletal muscle architectural parameters, such as pennation angle, allow for a better understanding of how muscle architecture and function are related in health and disease. The most commonly used definition of pennation angle is the angle between the muscle fascicle and aponeuroses, commonly assessed using 2D B-mode ultrasound imaging[1]. However, it is challenging to align the imaging plane with the line of pull and it is generally difficult to correctly infer 3D architecture from 2D imaging. Alternatively, both Diffusion-Tensor-Imaging (DTI) and 3D-ultrasound (3D-US) facilitate a 3D assessment of muscle fiber orientations and pennation angles[2,3]. However, so far little is known about how these two modalities compare. The purpose of this study was therefore to compare the quantification of pennation angles of the Vastus Lateralis muscle using DTI fiber-tractography and 3D-US.

Methods(317 words):

MRI of the upper legs was performed in supine position with the legs stretched in nine healthy participants (age range: 22-64 years; 5 males) at 3T (Philips ingenia) using a 16-channel anterior coil and the 10-channel table posterior coil. MRI consisted of a 3-point Dixon scan as anatomical reference (FFE; TR/TE1/ΔTE=8/1.33/1.1ms, FOV=480x276 x186mm^3, voxel-size=1.5x1.5x3.0mm^3, 4 echoes) and a DTI scan (SE-EPI; 48 gradient directions, b-value=0 & 400s/mm^2, FOV=480x276x186mm^3, voxel-size=3.0x3.0x6.0mm^3, TR/TE=4630/53ms, fat-suppression: SPAIR and SSGR[4], NSA: 3) for the pennation-angle assessment (Figure 1). On the same day 3D-US acquisitions of the Vastus Lateralis muscle were obtained in the same position as for the MRI with a 5 cm 12.5MHz linear-array probe (imaging depth: 8 cm, acoustic frequency: 30Hz).

Data-analysis:

For both modalities the pennation angle was defined as the angle between the aponeurosis and the muscle fascicles passing by the central point at two third point within the muscle belly in the mid-longitudinal plane (Figure 2). More details on 3D-US pennation angle measurements were previously described[5]. DTI data were acquired in 3 stacks, joined and post-processed using QMRITools for Mathematica[6]. The post-processing consisted of denoising, registration and tensor calculation. DTI fibertracts were obtained from the fitted tensor starting in a 3 by 3 pixel Region-Of-Interest (ROI) located in the center of the muscle (settings: max angle=15°, step-size=1.5mm, FA range=[0.1-0.6] [7]) (Figure 3). Fibertracts were fitted to 1st- (linear) and 2nd-order polynomial lines. The deep aponeurosis of the Vastus Lateralis was manually segmented using ITK-snap[8], fitted to a polynomial surface after which the surface normals and tangents were calculated. The pennation angle was defined as the angle between the fitted aponeurosis surface and the fitted fibertracts at the intersection point between aponeurosis and fibers (Figure 4). For the comparison of the pennation angles between the two modalities, Bland-Altman analysis, paired t-test and the intra-class correlation coefficient (ICC) (two-way random effect, consistency agreement, multiple measurements) were used[9].

Results(111 words):

A total of nine datasets were successfully acquired and measurements of the pennation angles were calculated from both imaging modalities. The average pennation angle measured with 3D-US was 18.9°± 5.9°, whereas the pennation angles measured with the DTI fiber-tractography based approach were systematically and substantially higher, 33.3°±6.7° for the straight line fit, and 34.5°±4.8° for the 2nd order polynomial fit. The Bland-Altman analysis between 3D-US and DTI resulted in bias:-14.4° ±7.1°, LoA=[-28.4° 0.4°], p=0.0001 , ICC=0.5, 95% confidence interval= [0.5° 0.9°] for the straight line fiber fit and bias:-15.5°±6.9°, LoA=[-29.0° -2.0°], p= 0.0003, ICC= 0.3, 95% confidence interval = [0.3° 0.8°] for the 2nd order polynomial fit (Figures 4 and 5).

Discussion(240 words):

The pennation angles which were obtained with DTI fiber-tractography were larger than the ones which were obtained with 3D-US. Previous studies show values in the range between 6° and 28°[10, 11]. Although both techniques separately resulted in consistent pennation angle values, the reason for this discrepancy between techniques needs further investigation. There are a couple of reasons, both of technical and methodological nature, that could have contributed to the difference. First of all, 3D-US involves in-painting of a 3D volume by sweeping a linear ultrasound probe across the muscle and 3D position tracking with an external device, which involves several registration steps. Similarly, the DTI dataset needs registration to the anatomical DIXON data to compensate for field-inhomogeneity induced distortions of the EPI-based diffusion-weighted acquisitions. We will further investigate to which extent 3D-US and DTI Vastus Lateralis volumes match and/or whether post-processing in one of the two imaging modalities has introduced a systematic bias. Moreover, in 3D-US the analysis was done in 2D by selecting a plane in the 3D volume. Secondly, due to space limitations in the MRI, DTI and 3D-US measurements were performed in supine position with the leg stretched. The sarcomeres of the resting Vastus Lateralis, however, would be at near optimal length at 60° of knee flexion[12].The lower knee angle could have resulted in wavy and curved relaxed fibers, which is probably somewhat more difficult to quantify using 3D-US as opposed to 3D DTI.

Conclusions(40 words):

We have compared two advanced 3D imaging modalities for the assessment of pennation angle. Future research will be aimed at further investigating the nature of the differences and to assess the reliability and the applicability of the pennation angle quantification.

References:

1. Kwah, Li Khim, et al. "Reliability and validity of ultrasound measurements of muscle fascicle length and pennation in humans: a systematic review." Journal of applied physiology 114.6 (2013): 761-769.

2. Hiblar T, Bolson EL, Hubka M, Sheehan FH, Kushmerick MJ. Three dimensional ultrasound analysis of fascicle orientation in human tibialis anterior muscle enables analysis of macroscopic torque at the cellular level. In Molecular and Cellular Aspects of Muscle Contraction

3. Damon, B. M., Froeling, M., Buck, A. K. W., Oudeman, J., Ding, Z., Nederveen, A. J., Bush, E. C. & Strijkers, G. J. Skeletal muscle diffusion tensor-MRI fiber tracking: rationale, data acquisition and analysis methods, applications and future directions. Nmr Biomed 30, e3563 (2017).

4. Williams SE, Heemskerk AM, Welch EB, Li K, Damon BM, Park JH. Quantitative effects of inclusion of fat on muscle diffusion tensor MRI measurements. J Magn Reson Imaging. 2013 Nov;38(5):1292-7. doi: 10.1002/jmri.24045. Epub 2013 Feb 15. PMID: 23418124; PMCID: PMC3664247.

5. Weide, Guido, et al. "3D ultrasound imaging: Fast and cost-effective morphometry of musculoskeletal tissue." JoVE (Journal of Visualized Experiments) 129 (2017): e55943.

6. Froeling, Martijn. "QMRTools: a Mathematica toolbox for quantitative MRI analysis." Journal of Open Source Software 4.38 (2019): 1204.

7. Forsting, Johannes, et al. "Diffusion tensor imaging of the human thigh: consideration of DTI-based fiber tracking stop criteria." Magnetic Resonance Materials in Physics, Biology and Medicine 33.3 (2020): 343-355.

8. Paul A. Yushkevich, Joseph Piven, Heather Cody Hazlett, Rachel Gimpel Smith, Sean Ho, James C. Gee, and Guido Gerig. User-guided 3D active contour segmentation of anatomical structures: Significantly improved efficiency and reliability. Neuroimage. 2006 Jul 1; 31(3):1116-28.

9. IBM Corp. (2017). IBM SPSS Statistics for Windows. Armonk, NY: IBM Corp. Retrieved from https://hadoop.apache.org

10. Rutherford, O. M., and D. A. Jones. "Measurement of fibre pennation using ultrasound in the human quadriceps in vivo." European journal of applied physiology and occupational physiology 65.5 (1992): 433-437.

11. Chauhan, Bhawesh, Maher A. Hamzeh, and Antonio I. Cuesta-Vargas. "Prediction of muscular architecture of the rectus femoris and vastus lateralis from EMG during isometric contractions in soccer players." Springerplus 2.1 (2013): 1-8

12. Chen, Xuefeng, et al. "Changes in sarcomere lengths of the human vastus lateralis muscle with knee flexion measured using in vivo microendoscopy." Journal of biomechanics 49.13 (2016): 2989-2994.

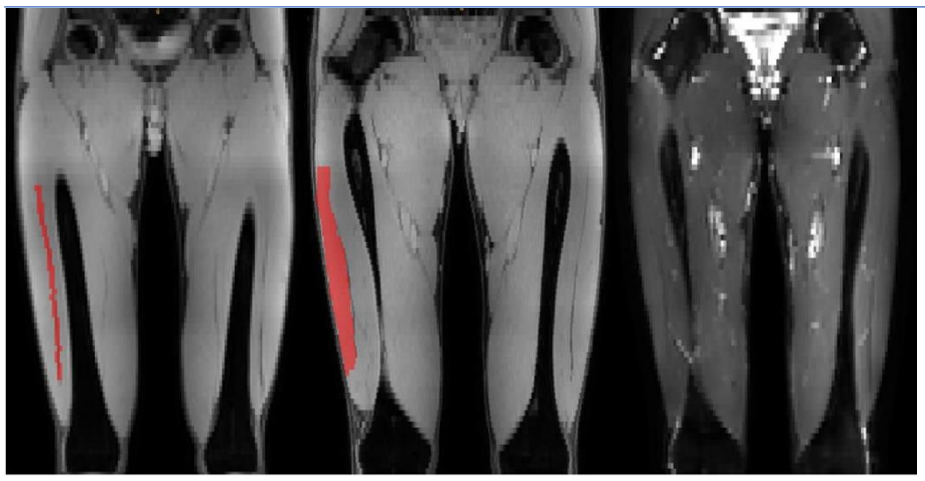

Figure 1: *MRI of a representative subject. (Left) Water Images from the Vastus Lateralis Deep Aponeurosis. (Middle) Segmentation of the Vastus Lateralis Muscle (red volume). (Right) Representative diffusion-weighted image of the same slice.*

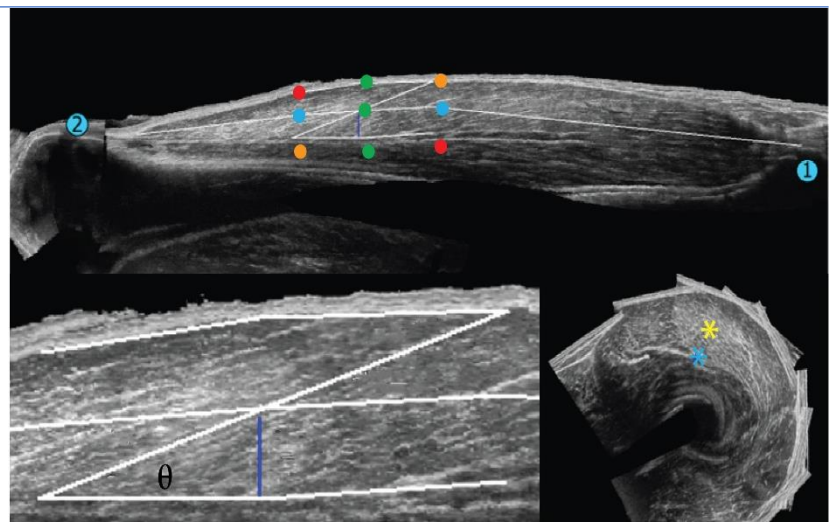

Figure 2*: 3D-US image of the Vastus Lateralis muscle. (Top) Sagittal plane. The dots show: the muscle insertion points (blue with numbers 1 and 2); the intersection points between the fascicle and the superficial and deep aponeurosis (orange); the center of the muscle and its projections on the aponeurosis (green). (Bottom left) Zoomed image on the sagittal plane at 2/3 of muscle length, indicating the pennation angle (θ) between the fascicle and the deep aponeurosis. (Right) Axial plane. The center of the muscle and its projection on the deep aponeurosis are shown with yellow and blue asterisks.*

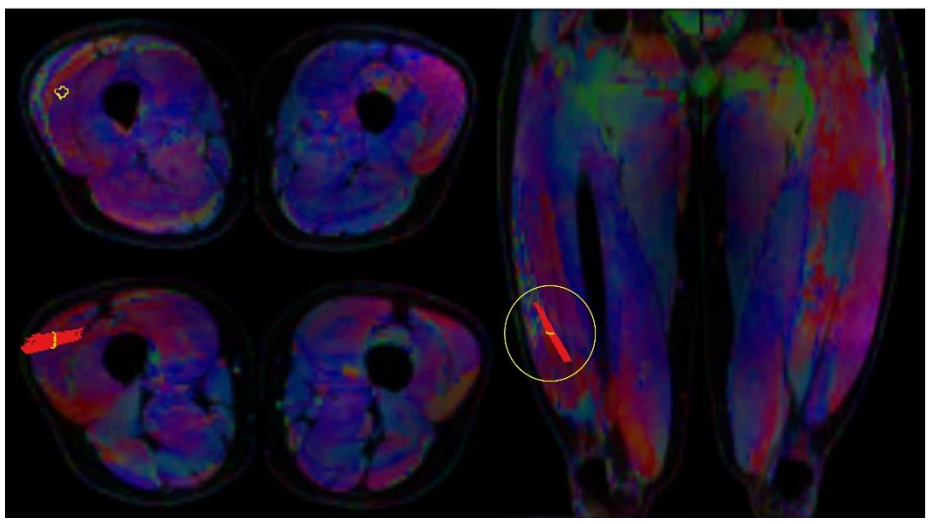

Figure 3: *Fractional anisotropy (FA) maps overlayed on Dixon water images of a representative subject of an MRI dataset with tracked fibers. (Left) Axial view with at the top: the ROI in the centre of the Vastus Lateralis muscle, at the bottom: fibertracts (in red) in the selected ROI. (Right) Coronal view with fibertracts (in red) at 2/3 of the muscle length.*

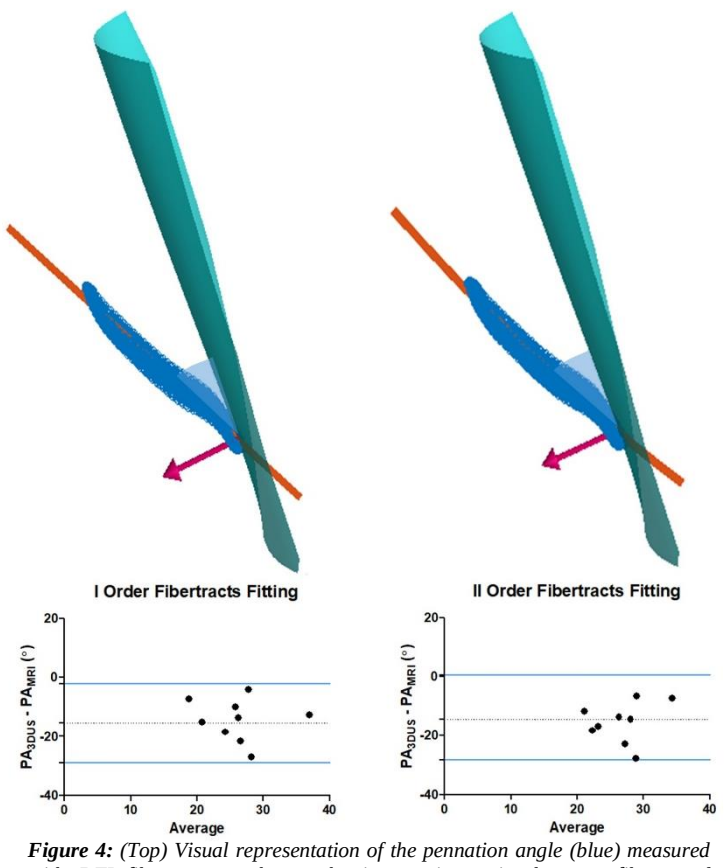

Figure 4: *(Top) Visual representation of the pennation angle (blue) measured with DTI fibertractography at the intersection point between fibers and aponeurosis surface. The green surface represents a polynomial 3D-surface fitting of the Vastus Lateralis deep aponeurosis. The orange lines are(Left) the 1st order and (Right) 2nd order fitted fibertracts (blue points). The red arrow indicated surface normal. (Bottom) Bland-Altman plot of the pennation angle measurements comparison between 3D-US and (Bottom left) 1st order and (Bottom right) 2nd order fitted DTI fibertracts.*

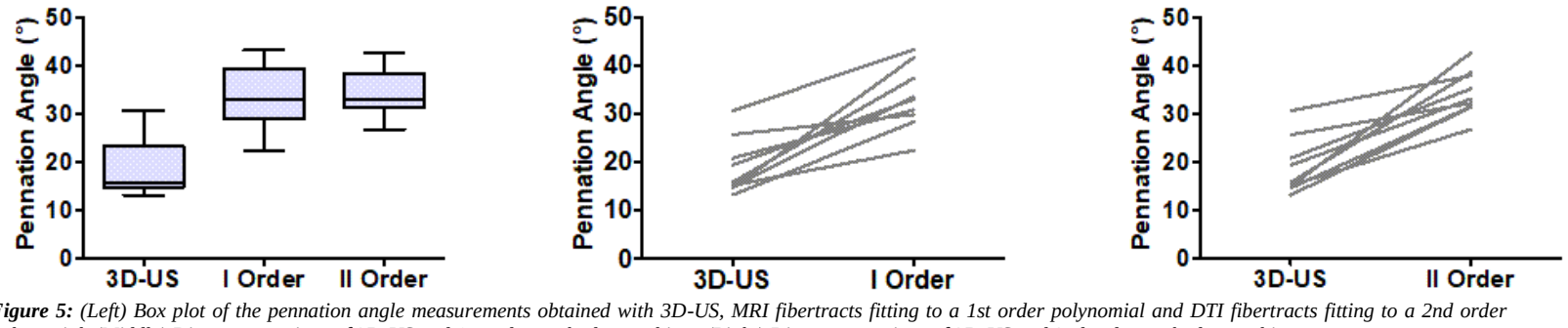

Figure 5: *(Left) Box plot of the pennation angle measurements obtained with 3D-US, MRI fibertracts fitting to a 1st order polynomial and DTI fibertracts fitting to a 2nd order polynomial. (Middle) Direct comparison of 3D-US and 1st order method per subject. (Right) Direct comparison of 3D-US and 2nd order method per subject.*

Heterogeneity of ASL perfusion MRI in low-grade paediatric glioma as imaging biomarker to assess treatment effect

L. Alic[1], S.C. Willekens[1,2], H.J. Mutsaerts[2], J. Petr[3], A.Y.N. Schouten-van Meeteren[4,5], M. Lequin[2], E.C. Wiegers[2]

[1]Magnetic Detection & Imaging Group, Technical Medical Centre, University of Twente, Enschede, the Netherlands

[2]Department of Radiology, University Medical Center Utrecht, Utrecht, the Netherlands; [3]Helmholtz-Zentrum Dresden-Rossendorf, Institute for Radiopharmaceutical Cancer Research, Dresden, Germany; [4]Department of Radiology and Nuclear Medicine, Amsterdam Neuroscience, Amsterdam University;

[5]Department of Neuro-oncology Princess Máxima Centre, Utrecht, the Netherlands

Synopsis: ASL-MRI is recognized as an option to assess potentially heterogeneous physiological processes important for tumour treatment. Therefore, we explored the heterogeneity in normalised CBF as an imaging biomarker for assessment of treatment effect in paediatric low-grade glioma (pLGG). There is a noticeable effect of chemotherapy observed as a change in texture in comparison to healthy appearing brain tissue. A high difference in texture between treated and untreated patients for non-enhancing tumour part is observed, suggesting that texture, based on co-occurrence matrices, might be suitable as an imaging biomarker for assessment of treatment effect in pLGG.

Summary of Main Findings: Heterogeneity in ASL-MRI is evaluated as an imaging biomarker for assessment of treatment effect in pLGG. Regardless of changes observed in remaining brain tissue, texture features are reflecting the change in tumour heterogeneity.

Introduction: Paediatric low-grade gliomas (pLGG) account for 30-50% of all paediatric brain tumours[1]. The presentation of pLGG varies between symptomless, motor impairment, visual impairment, endocrine deficiencies, and hypothalamic failure. Consequently, primary treatment for pLGG consist of surgical resection and/or chemotherapy depending on these clinical symptoms and tumour location. Progression of residual disease can require multiple phases of chemotherapy over the years[2]. Despite 10-year overall survival of 85-96%, management of pLGG remains challenging[3] and is considered a chronic disorder in over 50% of the cases[4]. Due to the underlying condition and/or treatment, the patients often suffer from functional, visual, and neurological impairment[5]. Arterial spin labelling (ASL) perfusion MRI assesses cerebral perfusion and is reported as an option to quantify underlying potentially heterogeneous physiological processes important in therapeutic decision making[6]. This study explores the heterogeneity in ASL-MRI as an imaging biomarker for assessment of treatment effect in pLGG.

Methods: 17 Paediatric patients with confirmed pLGG (at the following brain locations: 5 posterior fossa, 1 lateral ventricles, 8 chiasmatic, 1 suprasellar, 1 spinal cord, 1 temporal hemisphere) referred to the Princess Máxima Centre for Paediatric Oncology were included in this study: 5 untreated patients (2f/3m, age=9.4±5.0year) and 12 patients (6f/6m, age=7.3±3.4year) treated by chemotherapy. For untreated patients, MRI was acquired at baseline and for treated patients at follow-up. MRI was acquired at 1.5T or 3T Philips MRI system using a 32-channel receive head coil. Imaging protocol included a T1-weighted (T1w), T1w after gadolinium injection (T1w-c), T2-weighted (T2w), FLAIR, and pseudo-continuous ASL (PCASL). The PCASL-MRI was acquired as a 2D EPI sequence with background suppression, label duration of 1800 ms, and an initial post-label delay of 1800ms or 1525ms at 1.5T or 3T respectively.

Three-step processing framework of the structural PCASL images is illustrated by flow chart in Figure 2. Pre-processing of structural MRI involved registration to T1w images, skull-stripping by SPM12[7], and segmentation of brain structural data of normal-appearing grey matter (NAGM) and normal-appearing white matter (NAWM). Subsequently, co-registered skull-stripped structural MR images were used to segment tumour by utilising HD-GLIO[8,9] that resulted in individual tumour components: contrast enhancing (CE) and non-contrast enhancing (NCE), cyst, and necrosis.

The quality of image registration and automatic tumour segmentation was assessed in a group of ten patients randomly selected from our LGG cohort. Registration was evaluated quantitatively using manual annotations of anatomical landmarks (e.g., AC and PC) and is assessed as the root mean square error (RMSE) between individual observers. Automatic tumour segmentation was compared with a manual delineation by a radiologist and quantified by DICE coefficient[9]. PCASL-MRI was processed by ExploreASL10 into quantitative CBF and normalised by average CBF in the HAGM, producing normalised CBF (nCBF). Treatment effect was assessed by three first order statistical (FOS) features (mean, median, standard deviation) and 22 co-occurrence texture features[11-13] with a matrix size of 26 averaged over four directions. The resulting features were averaged over all slices containing the tumour and were presented separately for CE, NCE, and NAWM. A total of 25 features per ROI was ranked independently using a feature selection algorithm maximising the area between the empirical ROC curve and the classifier slope. The Wilcoxon signed-rank test was used to assess the differences between the treated and untreated patients.

Results: The checkerboard view in Figure 2A illustrates an example of registration results at the ventricles level and at the tumour level. The averaged RMSE for the two anatomical landmarks is similar for all three sequences (Figure 2B). All tumour masks produced by HD-GLIO were manually post-processed. For two tumours, HD-GLIO produced a false negative segmentation for both CE and NCE tumour masks. The remaining eight tumours had an average DICE score of 0.76 for the CE tumour mask and 0.34 for the NCE tumour masks. Figure 3 illustrates the final masks (CE, NCE, NAGM, and NAWM) and nCBF-map. Considering differentiation between treated and untreated patients, none of the FOS features demonstrate significance while a number of textual features were found significant. The most potent texture feature (i.e. cluster shade) assessing the differences between treated and untreated patients showed an average change of 109% for NCE tumour mask and 18 % change in NAWM.

Discussion & Conclusions: Quantitative validation of the registration gives a lower RMSE than the size of the AC and the PC suggesting a good registration accuracy in these paediatric patients. There is a noticeable effect of chemotherapy observed as a change in texture of NAWM. This is in line with previous studies showing that chemotherapy is associated with damage of normal-tissue in the brain[14]. The significantly higher difference in texture between treated and untreated patients for NCE suggests that texture analysis, based on co-occurrence matrices, are suitable to quantify the change in heterogeneity and therefore could potentially serve as an imaging biomarker for assessment of treatment effect in pLGG. These conclusions are also supported by previous findings in paediatric patients after radiotherapy[15].

References:

1. Ryall, S. et al. Acta Neuropathol Commun. 2020;8(1):30.
2. Lassaletta, A. et al. J Clin Oncol. 2016;34(29):3537-43.
3. de Blank, P. et al. Curr Opin Pediatr. 2019;31(1):21-7.
4. Fangusaro, J. et al. Lancet Oncol. 2020;21(6):e305-e16.
5. de Lande, R.S.V. et al. 2019;66(1):e27419.
6. Carlsson, J. et al. J Neurooncol. 2006;77(1):33-45.
7. Friston, K.J. et al. University College London. https://www.fil.ion.ucl.ac.uk/spm/doc/intro/intro.pdf.
8. Kickingereder, P. et al. Lancet Oncol. 2019;20(5):728-40.
9. Taha, A.A. et al. BMC Med Imaging. 2015;15:29.
10. Mutsaerts, H. et al. Neuroimage. 2020;219:117031.
11. Haralick R.M. et al. IEEE T Syst Man Cyb. 1973;Smc3(6):610-21.
12. Alic, L. et al. Phys Med Biol. 2011;56(6):1601-16.
13. Alic, L. et al. 3rd IEEE International Symposium on Biomedical Imaging: Nano to Macro; 6-9 April 2006; Arlington, VA, USA2006.
14. Ahles, T.A. et al. J Clin Oncol. 2012;30(30):3675-86.
15. Li, M.D. et al. J Pediatr. 2017;185:173-80 e3.

Figure 1. Delete this page if there are no figures or tables

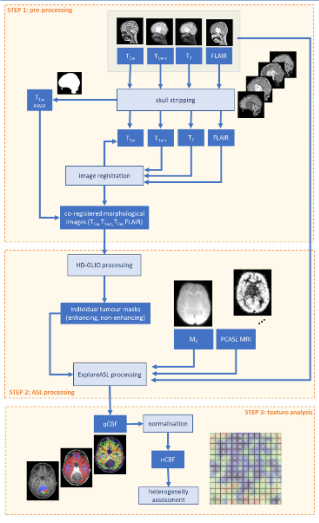

Figure 1. Flow chart illustrating the three-step processing algorithm consisting of pre-processing (image registration, scull-stripping, and segmentation of structural MRI), processing of PCASL MRI (tumour segmentation and generation of qCBF-map), and texture analysis (normalisation of qCBF and heterogeneity assessment).

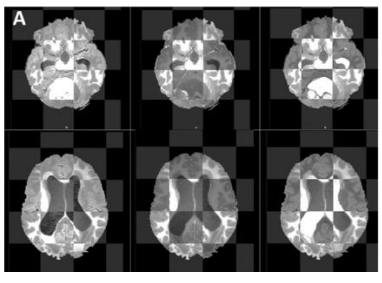

Moving images	Mean RMSE	
	Pixels	[mm]
FLAIR	2.10	1.42
T1c	2.01	1.13
T2	1.71	1.07

B

Figure 2. Final registration results illustrated by:

A: checkerboard view at tumour level (upper panel) and at ventricle level (lower panel) between T1w and following moving images: FLAIR (left column), T1c (middle column), and T2w (right column).

B: average RMSE for two anatomical landmarks

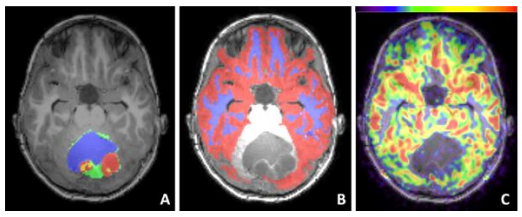

Figure 3. T1w-MRI overlaid with tumour masks (A), GM and WM mask (B), and nCBF-map (C)

A: different tumour masks: CE-red, NCE-green, cyst-blue, necrotic-yellow

B: two brain masks in the supratentorial brain region: NAGM -red, and NAWM-blue

Table 1. Groupe-wise feature ranges for treated and untreated patients. *indicate a significant difference. CE, contrast enhancing tumour; NCE non-contrast enhancing tumour; HAWM, healthy-appearing white matter.

Feature ranges (treated patients)	**CE**	**NCE**	**NAWM**
Mean nCBF– map	0.2-0.6	0.4-0.8	0.5-0.6
Median nCBF– map	0.1-0.6	0.3-0.8	0.4-0.6
STD nCBF– map	0.2-0.3	0.2-0.5	0.3-0.5
Texture – homogeneity	***0.2-1.0****	0.2-1.0	0.4-0.6
Texture – cluster shade	152.7-1504.0	***-08.0-1255.6****	***470.2-1135.0****
Texture – correlation	0.6-0.9	0.6-0.9	***0.8-0.9****

Feature ranges (not treated patients)	**CE**	**NCE**	**NAWM**
Mean nCBF– map	0.2-0.8	0.4-0.6	0.5-0.7
Median nCBF– map	0.3-0.7	0.3-0.5	0.4-0.6
STD nCBF– map	0.2-0.6	0.2-0.6	0.3-0.4
Texture – homogeneity	***0.2-0.5****	0.3-0.4	0.4-0.5
Texture – cluster shade	38.9-1080.4	***450.2-1748.4****	***402.5-730.5****
Texture – correlation	0.5-0.9	0.7-0.8	***0.8-0.9****

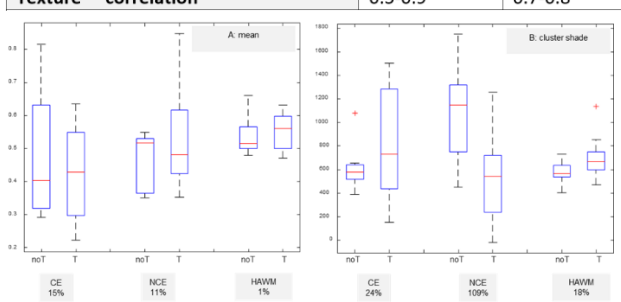

Figure 4. Boxplots illustrating the nCBF-map results as quantified by FOS feature mean in panel A, and by texture feature cluster shade in panel B. noT, untreated patients; T, treated patients

Narcosis depresses the BOLD-CVR response to acetazolamide in pediatric moyamoya vasculopathy

P.T. Deckers[1], J.C.W. Siero[23], A. Kronenburg[1], K.P.J. Braun[4], A van der Zwan[1], A.A. Bhogal[2]

[1]Neurosurgery, UMC Utrecht, Utrecht, The Netherlands;
[2]Radiology, UMC Utrecht, Utrecht, The Netherlands
[3]Spinoza Centre for Neuroimaging, Amsterdam, The Netherlands;
[4]Pediatric Neurology, WKZ/UMC Utrecht, Utrecht, The Netherlands;

Synopsis: Measuring cerebrovascular reactivity (CVR) under narcosis is underreported, while narcosis is often necessary for pediatric or cognitively impaired patients. When acetazolamide is used in awake patients, maximum CBF increase reaches a plateau after ~12min. Using ASL- and BOLD-MRI with acetazolamide we showed that for pediatric moyamoya patients the response is different. Patients under narcosis show lower CVR and reach peak CBF earlier (after around 6 minutes), after which CBF decreases again without the plateau-phase. This shows the response to acetazolamide is distinctively different between awake and narcosis patients and caution is warranted during interpretation of narcosis CVR images.

INTRODUCTION

Cerebrovascular reactivity (CVR) measurements are increasingly used for a range of diseases and indications[1–3], using gold-standard [^{15}O]H_2O-PET, or MRI based measurements (Blood Oxygen Level Dependent (BOLD) and Arterial Spin Labeling (ASL))[4–6]. Acetazolamide-injection is a commonly used vascular-stimulus[7,8]. For moyamoya vasculopathy (MMV), cerebral blood flow (CBF) and CVR measurements are essential for the indication and evaluation of revascularization[4,9]. However, MMV patients are often young or cognitively impaired, thus necessitating narcosis to prevent severe motion related artifacts[10,11].

Little has been reported on CVR in MMV under narcosis, but typically acetazolamide is used in a similar manner as in awake patients under the assumption that anesthesia does not affect the mechanisms of CVR. To test this assumption, we compared the response to acetazolamide between MMV patients under narcosis and awake, using a dynamic BOLD-series combined with multi-delay ASL (MD-ASL) before and ~15 minutes after injection of acetazolamide.

METHODS

We included all pediatric MMV patients without motion artefacts from our clinical MRI-CVR database. All patients provided written informed-consent. Narcosis was either propofol or sevoflurane, at the discretion of the anesthesiologist, using a laryngeal mask without muscle relaxants. Scans were performed at 3T (Philips) using a 32-channel receive coil (Nova Medical).

Baseline CBF measurements parameters: 5 post-labeling-delays (1206-3480ms), pCASL, multi-slice EPI, label duration=2s, voxel-size=3.75x3.75x7mm^3, 16 slices, FOV=240x240x120mm^3, TR/TE=6s/11ms, flip angle=25°, SENSE factor=2, background suppression, 24 volumes, scan-time=5min. Multi-slice gradient-echo BOLD EPI parameters: multi-band (TR=1.1s) or non-multiband (TR=2.8s), voxel-size=2.5mm isotropic, 48 slices, FOV=224x224x120mm^3, TR/TE=1.1s/35ms, flip angle=65°, SENSE factor=1.7. Acetazolamide injection (20mg/kg (max 1g)) began between 60-90 seconds after the start of the BOLD-scan. Upon completion of the BOLD-scan, a second MD-ASL scan was acquired and used for the calculation of the ASL-CVR. CBF was computed using BASIL (FSL, FMBRIB, Oxford, UK).

BOLD data were motion-corrected (MCFLIRT, FSL), distortion-corrected (TOPUP, FSL), spatially smoothed (3D Gaussian kernel, FWHM=5mm) and normalized (to Δ%BOLD). Considering the variable TRs used, all BOLD data were interpolated to TR=1s. Further timeseries analysis was performed using functions from the seeVR-toolbox (seeVR, Utrecht, NL)[13]. Cerebellar masks were applied to generate BOLD-CVR ROI time-series, which were temporally smoothed (LOESS filter, 6% window) and averaged for both groups. The mean and 95%*CI* (1.96**SEM*) was plotted. Time-to-peak (TTP), the CVR-slope of the initial linear response and the final CVR amplitude were calculated for each subject and compared using Student's t-test (Matlab, Natick, USA).

The patients' MMV-pathology will have heterogeneous spatial effects in the cerebrum. To focus primarily on the effects of the anesthesia on CVR we focused in this study on the cerebellum as this is independently perfused by the vertebrobasilar system; unaffected by MMV[12].

RESULTS

We identified 44 datasets, from 37 unique patients (23 children) and we could include eight (median age 11.8y) narcosis scans and ten (13.4y) awake scans (Table 1).

The %BOLD-change in the (unaffected) cerebellum differed significantly between narcosis and awake patients ~120s after starting the acetazolamide injection (Fig 1). The mean TTP were ~413±159s (mean/SD) and ~630±110s in narcosis and awake patients, respectively (p=0.0035, Fig 1B). The final BOLD-CVR amplitude was 0.64±0.70%BOLD for narcosis and 3.8±1.2%BOLD for awake patients (p<0.0001). The CVR-slope was 0.0070±0.0060%/s and 0.016±0.0051%/s for the narcosis and awake patients, respectively (p=0.0035, Fig 1A).

The ASL-CBF values in the cerebellum were comparable between narcosis and awake at baseline (31.5±16.3 resp. 38.4±10.3 ml/100g/min, p=0.3) but after acetazolamide-injection the CBF of awake patients was higher than narcosis patients (67.0±13.6 vs. 47.4±17.5, p=0.02). ΔCBF was higher in awake patients, but not significantly different (27.5±12.4 vs. 16.1±11.5 ml/100g/min, p=0.07, Fig. 2).

DISCUSSION

We showed a significant difference in BOLD-response in terms of the TTP, CVR-slope and amplitude parameters to acetazolamide between narcosis and awake MMV patients in the unaffected cerebellum. This was supported by ASL results, albeit less strong. This is an important finding since the effect of the anesthesia may lead to an underestimation of true CVR.

The mechanisms driving the observed differences is not directly clear and warrants further research. The anesthetic agents may pre-dilate vessels leading to a higher venous oxygen saturation and lower possible BOLD signal increase with acetazolamide[14]. However, we did not see a difference in baseline CBF-values between awake and narcosis patients. Combining ACZ with anesthesia might lead to an physiological interaction, causing more hyperventilation and deeper breathing (i.e. respiratory compensation for pH-decrease) leading to inhibition of the CBF-increase. The lower BOLD response under narcosis could also be due to anesthesia-related reductions in $CMRO_2$[14]. Here, baseline venous saturation would increase leading to less 'headroom' to evoke BOLD-contrast changes during acetazolamide-mediated increases in CBF. If true, this would mean BOLD-CVR may be underestimated under narcosis. However, the apparent reduction in the BOLD response at later time-points (after the TTP) suggest that even the post-ACZ ASL -and even [^{15}O]H_2O-PET- may be underestimating CVR under narcosis.

CONCLUSION

The use of narcosis has an substantial effect on the CVR response of patients under narcosis, leading to a lower CVR slope, a shorter TTP and lower final CVR amplitude. More research is needed for the implications of this finding, and to find the best way to measure CVR under narcosis. Until then, narcosis CVR scans using acetazolamide need to be interpreted with caution.

1. Yonas H, Smith HA, Durham SR, et al. Increased stroke risk predicted by compromised cerebral blood flow reactivity. *J Neurosurg* 1993; 79: 483–489.
2. Silvestrini M, Pasqualetti P, Baruffaldi R, et al. Cerebrovascular reactivity and cognitive decline in patients with Alzheimer disease. *Stroke* 2006; 37: 1010–1015.
3. Bacigaluppi S, Dehdashti AR, Agid R, et al. The contribution of imaging in diagnosis, preoperative assessment, and follow-up of moyamoya disease. *Neurosurg Focus* 2009; 26: E3.
4. Fierstra J, van Niftrik C, Warnock G, et al. Staging Hemodynamic Failure With Blood Oxygen-Level-Dependent Functional Magnetic Resonance Imaging Cerebrovascular Reactivity: A Comparison Versus Gold Standard ((15)O-)H2O-Positron Emission Tomography. *Stroke* 2018; 49: 621–629.
5. Fan AP, Guo J, Khalighi MM, et al. Long-Delay Arterial Spin Labeling Provides More Accurate Cerebral Blood Flow Measurements in Moyamoya Patients A Simultaneous Positron Emission Tomography / MRI Study. 2017; 2441–2449.
6. Hauser T-K, Seeger A, Bender B, et al. Hypercapnic BOLD MRI compared to H215O PET/CT for the hemodynamic evaluation of patients with Moyamoya Disease. *Neuroimage (Amst)*; 22. Epub ahead of print 2019. DOI: 10.1016/j.nicl.2019.101713.
7. Ringelstein EB, Van Eyck S, Mertens I. Evaluation of cerebral vasomotor reactivity by various vasodilating stimuli: Comparison of CO2 to acetazolamide. *J Cereb Blood Flow Metab* 1992; 12: 162–168.
8. Fierstra J, Sobczyk O, Battisti-Charbonney A, et al. Measuring cerebrovascular reactivity: What stimulus to use? *J Physiol* 2013; 591: 5809–5821.
9. Kronenburg A, Braun KPJ, Van Der Zwan A, et al. Recent advances in moyamoya disease: Pathophysiology and treatment. *Curr Neurol Neurosci Rep* 2014; 14: 1–9.
10. Kronenburg A, van den Berg E, van Schooneveld MM, et al. Cognitive Functions in Children and Adults with Moyamoya Vasculopathy: A Systematic Review and Meta-Analysis. *J stroke* 2018; 20: 332–341.
11. Scott RM, Smith ER. Moyamoya Disease and Moyamoya Syndrome. *N Engl J Med* 2009; 360: 1226–1237.
12. Delion M, Dinomais M, Mercier P. Arteries and Veins of the Cerebellum. *Cerebellum* 2017; 16: 880–912.
13. Bhogal AA. abhogal-lab/seeVR: v1.01 (v1.01). Zenodo. Epub ahead of print 2021. DOI: https://doi.org/10.5281/zenodo.5283595.
14. Szabó EZ, Luginbuehl I, Bissonnette B. Impact of anesthetic agents on cerebrovascular physiology in children. *Paediatr Anaesth* 2009; 19: 108–118.

Acknowledgments / Funding Information: Continue on this line

Table 1, Characteristics of included patients

		narcosis (n = 8)	awake (n = 10)
age (median, range)		11.8 (5.0-16.4)	13.4 (6.8-17.2)
female (n, %)		6 (75%)	6 (60%)
MMV type	MMD	3 (38%)	8 (80%)
	MMS	5 (63%)	2 (20%)
	bilateral	6 (75%)	6 (60%)
	unilateral	2 (25%)	4 (40%)
treatment	pre-operative	3 (38%)	7 (70%)
	unilateral operated	1 (13%)	1 (10%)
	bilaterally operated	4 (50%)	2 (20%)

Abbreviations: MMV = moyamoya vasculopathy, MMD = moyamoya disease (idiopathic), MMS = moyamoya syndrome.

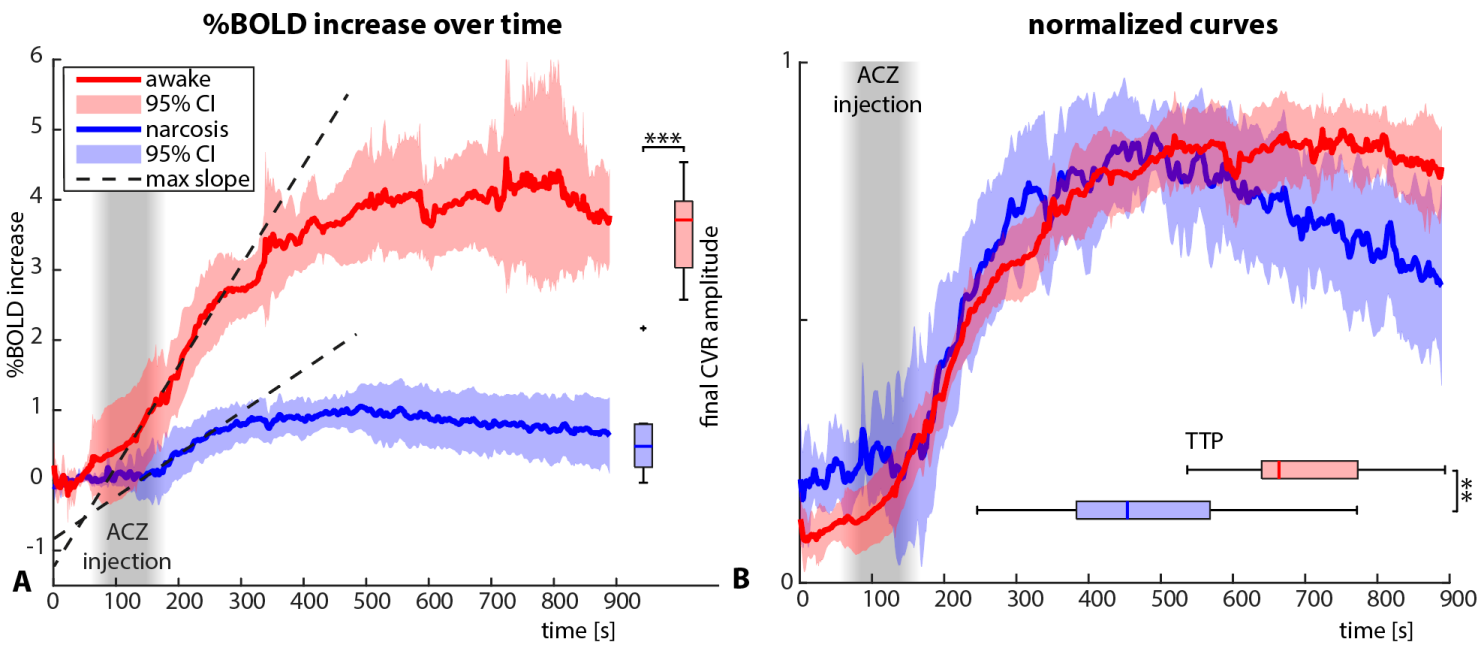

FIGURE 1 Mean timeseries of the BOLD-response of the – unaffected – cerebellum compared between narcosis and awake patients, showing %BOLD-change (A) and normalized (B). The curves show the mean of the raw data per group with the 95% confidence interval. Three metrics are compared; the maximum slope - group average for both group is shown by dotted lines -, final CVR amplitude (vertical boxplots, 1A), and the Time To Peak (TTP, horizontal boxplots, 1B). **: p<0.005, ***:p<0.0005

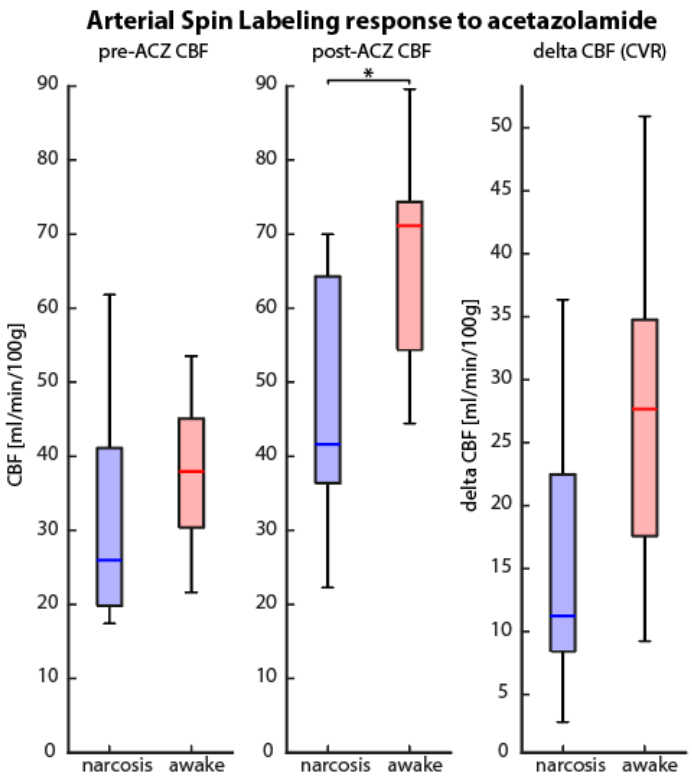

FIGURE 2 Comparison of quantified cerebral blood flow (CBF) of the cerebellum between narcosis and awake patients, measured by multidelay arterial spin labeling, before and after acetazolamide (ACZ) injection and the difference between before and after.

Quantitative MRI in Major Depressive Disorder at 7T

J.Heij[1], W. van der Zwaag[1], M.W.A. Caan[2], G. van Wingen[3], M. Aghajani[4]

[1]Spinoza Centre for Neuroimaging, Amsterdam, Netherlands; [2]Department of Biomedical Engineering, Amsterdam UMC, Netherlands, [3]Department of Psychiatry, Amsterdam UMC, Netherlands, [4]Institute of Education and Child Studies, University of Leiden, Leiden, Netherlands

Synopsis: Large scale efforts are being employed to link Major Depressive Disorder (MDD) to cortical alterations in gray and white matter, though often, limited resolution prevents conclusions regarding the source. Here we used quantitative 7T MRI to explore the myeloarchitecture of the cortex in people suffering from MDD in order to unravel potential mechanisms underlying the psychopathology of MDD. We find altered T1-profiles in the rostral ACC, lateral PFC and OFC in MDD compared to healthy controls, indicating changes in cortical myeloarchitecture. Overall, cortical T1 values were higher in MDD, suggesting lower cortical myelination.

Summary of main findings: Using ultrahigh field MRI we showed that the cortical T1-profiles of people suffering from MDD differed from those of healthy controls. Consistently higher T1-values were found in ACC, PFC and OFC, suggesting altered cortical myeloarchitecture.

Introduction: Major depressive disorder (MDD) is one of the most prevalent and debilitating psychiatric disorders, affecting hundreds of millions of people worldwide. Earlier magnetic resonance imaging studies have associated MDD with thinner cortex in the (para)limbic circuitry, including orbitofrontal cortex (OFC), medial prefrontal cortex (mPFC) and rostral anterior cingulate cortex (rACC)[1]. Quantitative imaging can potentially resolve the myelin distribution over the cortical layers and possible demyelination beyond what can be covered by volumetric analysis alone. Here, we specifically aimed to study the myeloarchitecture of the cerebral cortex using ultrahigh field MRI (7T) and quantitative multiparametric mapping (T1 and T2*). T1-variations in gray matter are for a large part explained by myelin concentration[2,3,4,5], while T2*-values are associated with iron content, brain tissue damage, and (resting state) neuronal activity[6]. Distribution of relaxation time values across the layers of the cortex could provide insights in the way structural integrity is affected by MDD.

Methods: Images of 73 individuals (14 healthy controls; 59 patients diagnosed with MDD) were acquired using a Philips Achieva 7T MRI scanner with a 32-channel head array coil. We used a submillimeter MP2RAGEME (multi-echo magnetization-prepared rapid gradient echo)[7] sequence with the following parameters: TE_1= 3 ms, $TE_{2,1-4}$ = 3, 11.5, 19, 28.5 ms, flip angles = 4°/4°, $TR_{GRE1,2}$ = [6.2 ms, 31 ms], FOV = 205×205×164 mm; nominal voxelsize = 0.7 mm isotropic. Fat-navigator based motion correction was used to improve edge definition[8]. T1-maps were computed using a look-up table[9] and T2*-maps were computed by least-squares fitting of the exponential signal decay over the multi-echo images of the second inversion. The T1-weighted anatomical image was processed following a pipeline designed to optimize laminar accuracy. Delineation of cortical areas was based on the Desikan-Killiany atlas, following the MDD-ENIGMA consortium[1]. To limit the multiple comparisons problem, we selected three ROIs that showed the highest effect sizes in the ENIGMA-study[1] (rACC, mOFC, and lPFC), which were sampled to the subjects' volumetric space and applied to the T1-/T2*-data that was sampled to 10 cortical depths using Nighres' profile sampling module, resulting in 10 values for each region for each subject. Statistical testing consisted of t-tests implemented in JASP to elucidate effects across groups.

Results: Average T1/T2*-maps sampled to the surface are shown in Figure 1A, showing the classical pattern of reduced T1/T2*-values in the sensorimotor cortex[4,6]. Figure 1B highlights the endeavors taken to improve segmentation as much as possible. Note that basing results solely on a FreeSurfer segmentation comes at the risk of underestimating T1-profiles towards to pial surface (red arrow). Given that the atlas labels of the ROIs are based on FreeSurfer's segmentation, we dilated the ROIs and multiplied them with our optimized segmentation to maximally sample the cortex. Obtained T1/T2*-values are in line with the literature and are consistent across hemispheres (any effects did not survive Bonferroni correction). Figure 2 shows the profiles of T1-/T2*-values across cortical depth in people suffering from MDD compared to healthy controls (line plots), as well as the area under the curve (AUC; distribution plots), obtained by fitting a 2nd-order polynomial to the profiles. For all ROIs, the T1-profiles of the MDD-group lie above those of the HC-group, especially at ~50% cortical depth, indicative of altered T1-distributions in this group. No statistical effects were found for T2*-parameters and these were therefore excluded from the additional parameter fit analysis. The polynomial fit analysis in T1-profiles revealed differences across groups: the A-parameter of the MDD group was greater than the healthy control group in the medial OFC (t_{60} = -2.485, p =.016) and lateral PFC (t_{60} = -2.909, p = 0.005). The B-parameter of the MDD group was decreased in the rostral ACC (t_{60} = 2.493, p = .015) and medial OFC (t_{60} = 3.018, p = .004). Only the A-parameter effect in the lateral PFC and the B-parameter effect in the medial OFC survived the Bonferroni correction for multiple comparisons with a threshold of p<0.007.

Discussion: Here, we used high resolution, motion corrected, quantitative MRI at 7T to probe detailed properties of the cortex in regions crucially implicated in MDD, e.g., the rostral ACC, medial PFC, and lateral PFC. We find alterations in characteristics of T1-, but not T2*-profiles, in patients with MDD, with reduced T1-values across the cortical ribbon, suggestive of decreased myelin content. Though UHF-MRI is desired to get the required resolution to resolve fine details, it comes with increased difficulties in segmenting delicate areas such as the prefrontal regions due to more disruptive B1-/B0-inhomogeneities. Parameters obtained from polynomial fits can be informative for the general shape of cortical profiles, but their functional implications are yet to be determined and should be complemented by other measures of shape such as the non-linearity index reflecting the amount of deviation from a linear regression fit[3]. Lastly, these results should be interpreted with caution due to the limited size of the healthy control group, but underscore the promise of quantitative 7T MRI for psychiatric applications. To overcome some of the effects this might have, future research will focus on analyses within the MDD group, to relate these parameters to disease severity and other metrics.

Conclusion: We show here the feasibility of quantitative MRI with a psychiatric application. T1-values across the cortical ribbon were altered in MDD compared to healthy controls, possibly benefiting insights in functional characterization of aberrant circuitry that underpin psychopathology.

References:

[1]Schmaal, et al., (2017) Mol Psychiatry. 22: 900-909

[2]Ferguson, et al., (2018) Neuroinformatics. 6: 181-196

[3]Sprooten, et al., (2019) NeuroImage. 185: 27-34

[4]Cohen-Adad, et al., (2012) NeuroImage. 60: 1006-1014

[5]McColgan, et al., (2021) Hum Brain Mapp; 42: 4996-5009

[6]Cho, et al. (2010) J Psychiatr Res. 44: 881-886

[7]Caan, et al., (2018) Hum Brain Mapp; 40: 1786-1798

[8]Bazin, et al., (2020) NeuroImage. 222: 117227

[9]Marquez, et al. (2010) NeuroImage. 49: 1271-1281

Acknowledgments / Funding Information: This work was supported by an Amsterdam Neuroscience Alliance Grant 2018

Figure 1. (A) Average T1-/T2*-maps projected onto FSAverage. (B) Example segmentations and challenging areas (e.g., ACC) indicated with a red arrow. (C) Average T1-/T2*-values across hemispheres for each ROI. Any effects did not survive correction for multiple comparisons. (D) Comparison of T1-/T2*-values across selected ROIs. *$p < 0.05$, **$p < 0.01$, survived Bonferroni correction. Abbreviations: ACC = Anterior Cingulate Cortex, PFC = prefrontal cortex, OFC = orbitofrontal cortex, ROI(s) = regions of interest.

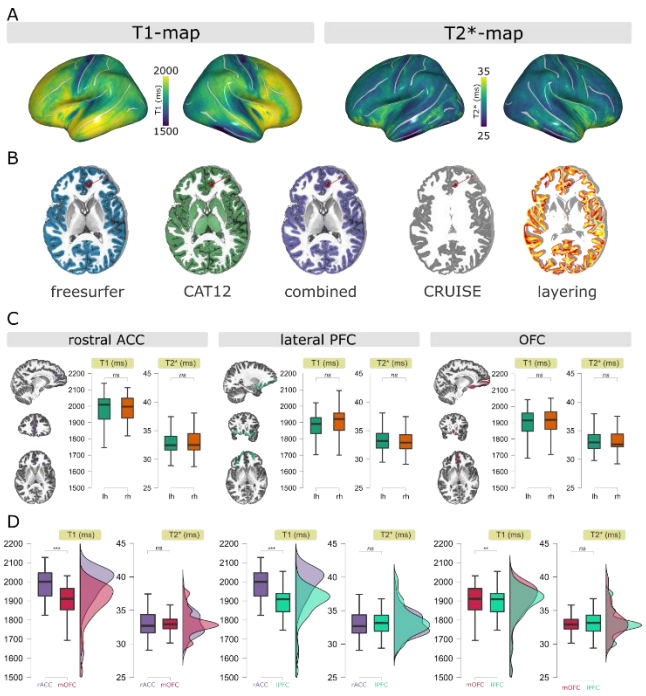

Figure 2. T1- and T2*-values across cortical depth in patients with MDD (blue) and healthy controls (grey). Dot plots represent the area-under-curve (AUC) derived from fitting a 2nd-order polynomial to the profiles.

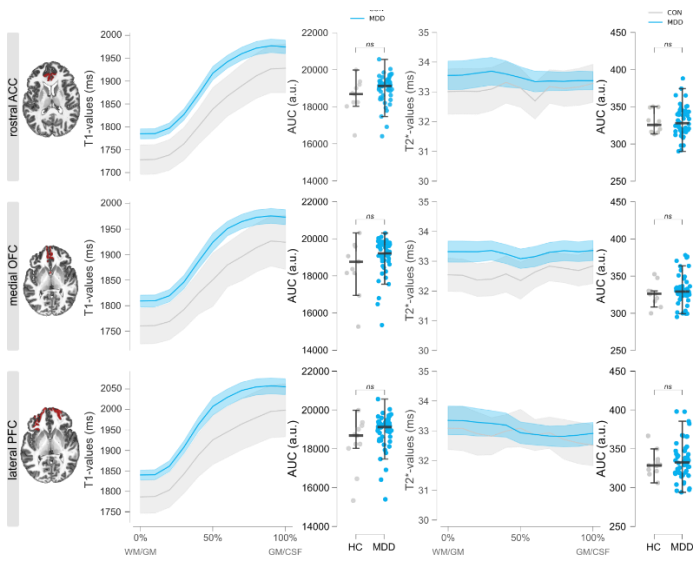

Figure 3. Characterization of profiles with parameters from the polynomial fit for each ROI. The distribution in MDD and HC is depicted in the form of dots and density. *$p < 0.05$, **$p < 0.01$, survived Bonferroni correction.

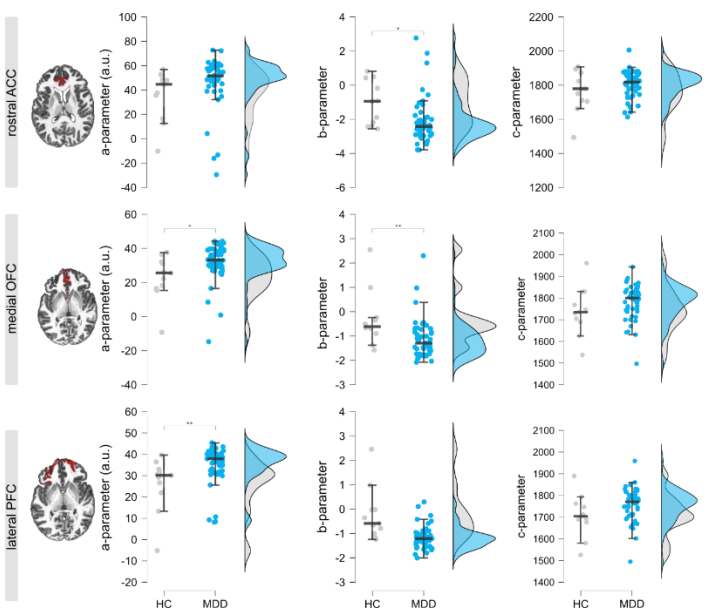

Synthetic MRI with MR-STAT: results from a clinical trial

Jordi P.D. Kleinloog[1,2], Stefano Mandija[1,2], Federico D'Agata[3], Oscar van der Heide[1,2], Beyza Koktas[1], Sarah M. Jacobs[4], Cornelis A.T. van den Berg[1,2], Jeroen Hendrikse[2], Anja G. van der Kolk[2], and Alessandro Sbrizzi[1,2]

[1]Computational Imaging Group for MR diagnostic and therapy, Center for Image Sciences, University Medical Center Utrecht, Utrecht, Netherlands, [2]Department of Radiotherapy, University Medical Center Utrecht, Utrecht, Netherlands, [3]Department of Neurosciences, University of Turin, Turin, Italy, [4]Department of Radiology and Nuclear Medicine, University Medical Center Utrecht, Utrecht, Netherlands

Synopsis: Magnetic Resonance Spin TomogrAphy in Time-domain (MR-STAT) reconstructs multiple quantitative MR parameters from a single fast scan. This quantitative information can be leveraged for several purposes, including the synthetization of clinically desired image contrasts. Preliminary results of the first clinical trial using MR-STAT in patients with neurological diseases show that the synthetically generated contrast images (i.e., T1w, T2w, PDw and FLAIR) were acceptable for diagnostic use (5-point Likert scale ≥ 3), although the score was lower compared to conventional contrasts. This highlights the potential of MR-STAT to provide synthetic contrasts on top of quantitative maps, while reducing scan time.

Introduction: A standard clinical MRI neuro-examination consists of several sequences with different image contrast weightings (e.g., T1w, T2w, proton density [PD], fluid-attenuated inversion recovery [FLAIR]), totaling an acquisition time between 15 – 20 minutes. Using the Magnetic Resonance Spin TomogrAphy in Time-domain (MR-STAT) technique, the quantitative value of T1, T2 and proton density can be extracted with one 5-minute multi-parametric whole-brain sequence (1, 2). MR-STAT consists of a transient-state Cartesian acquisition scheme and model-based non-linear inversion reconstruction. The reconstructed quantitative values can be used in diagnosis, evaluation of disease progression and treatment (3, 4). Additionally, any desired image contrast can be synthesized according to a physical signal model. The aim of this prospective cross-sectional study was to assess the diagnostic image quality of MR-STAT-generated synthetic image data sets in healthy participants and patients with neurological diseases compared to conventional images (5).

Methods: In total 50 participants (22 females) with a median age of 45 years (range: 21 – 79 years) were included: 10 healthy volunteers without a history of neurological disease and 40 patients with one of four common neurological diseases – brain tumor, epilepsy, multiple sclerosis (MS) or ischemic stroke – equally divided among these disease groups. MRI exams were performed at the University Medical Center Utrecht on a 3T MR system (Ingenia, Philips, Best, the Netherlands); all subjects underwent one MR-STAT sequence and four clinically used T1w, T2w, PD and FLAIR MRI sequences. The 5-minute-long MR-STAT sequence was a Cartesian encoded, spoiled Gradient Echo with a slowly varying flip angle preceded by a non-selective inversion pulse (2). The specific sequence parameters for MR-STAT, which was 54% faster, and conventional sequences are specified in Table 1. The reconstructed quantitative MR images were used to generate corresponding synthetic contrast images from standard signal models after denoising the parameter maps using deep learning (6). For these preliminary results, a total of 400 (4 synthetic MR-STAT and 4 conventional for each of the 50 participants) randomized images were assessed by at least two out of three blinded independent neuroradiologist (>6 years' experience). Assessment sessions included 100 unique images and were separated by a memory-washout period of at least two weeks. Images were scored for overall quality on a 5-point Likert scale, morphologic legibility and presence/absence of artifacts.

Results and Discussion: The overall image quality was acceptable for diagnostic use (Likert scale ≥ 3) for 99% of all contrasts synthesized from quantitative MR-STAT as well as for conventional serial acquisition (Table 2). However, synthetic MR-STAT images scored lower than conventional for T1w, PDw and FLAIR contrasts (the exception being T2w) (Table 2). Images synthetically generated from quantitative MR-STAT maps and conventional acquisitions of healthy participants had comparable image contrasts, an example is shown in Figure 1. Additionally, similar image quality can be observed in synthetic MR-STAT and conventional images in the relevant slice of a patient with a (a) brain tumor, (b) stroke, (c) epilepsy and (d) MS (Figure 2). However, in some patients (see Figure 2) we noticed that lesions appear hypointense in synthetic MR-STAT FLAIR images, while they are hyperintense in conventional images. Inferior image quality of synthetic image contrasts were also previously observed (7-9), but could be enhanced as shown by Hagiwara et al. (10).

Legibility of prior determined anatomic/morphologic features were similar for the synthetic and conventional images, except for the head of the caudate nucleus and the posterior limb of the internal capsule which were more legible in the synthetic MR-STAT T1w images (Table 3). The overall percentage of images with artifacts identified and characterized for conventional and synthetic MR-STAT images is shown in Table 3. In the conventional images, more motion artifacts were observed (Δ 18%) predominantly in the FLAIR contrast (Δ 50%). In contrast, more images with synthetic MR-STAT T1w contrast had white pixels/spike noise (Δ 62%), while overall more blurring (Δ 49%), susceptibility (Δ 21%) and flow effects were observed. Flow effects are intrinsic to the 2D gradient echo MR-STAT acquisition technique, while optimization of the synthetization process may reduce the blurring effects. A possible alternative to improve synthetized contrasts could be machine-learning based methods (11).

Conclusion: The synthetic MR-STAT images from a single fast scan were overall acceptable for diagnostic use, although the perceived image quality is lower and in some cases the contrast of lesions differ in FLAIR images. These results highlight the potential of MR-STAT to provide clinicians with clinically useful image contrasts within substantially reduced scan time, in addition to multi-parametric quantitative maps.

Acknowledgements: We would like to thank neuroradiologists Dr. ir. E.P.A. Vonken, Dr. J.W. Dankbaar from the University Medical Center Utrecht and Dr. V.C.W. Keil from the Amsterdam University Medical Center for assessing the MR images. Additionally, we thank Carlo Lucci from the University Medical Center Utrecht for supporting the data acquisition. This clinical trial was funded by the Netherlands Organization for Scientific Research (NWO; Demonstrator Grant 16937), and has been registered in the Netherlands Trial Register with number NL8437 (https://www.trialregister.nl/trial/8437)

References

1. Sbrizzi A, Heide OVD, Cloos M, Toorn AVD, Hoogduin H, Luijten PR, et al. Fast quantitative MRI as a nonlinear tomography problem. *Magn Reson Imaging.* 2018; 46: 56-63.
2. van der Heide O, Sbrizzi A, Luijten PR, van den Berg CAT. High-resolution in vivo MR-stat using a matrix-free and parallelized reconstruction algorithm. *NMR Biomed.* 2020; 33: e4251.
3. Murakami Y, Kakeda S, Watanabe K, Ueda I, Ogasawara A, Moriya J, et al. Usefulness of quantitative susceptibility mapping for the diagnosis of parkinson disease. *AJNR Am J Neuroradiol.* 2015; 36: 1102-8.
4. Piredda GF, Hilbert T, Granziera C, Bonnier G, Meuli R, Molinari F, et al. Quantitative brain relaxation atlases for personalized detection and characterization of brain pathology. *Magn Reson Med.* 2020; 83: 337-51.
5. Madija S, D'Agata F, Liu H, van der Heide O, Koktas B, van den Berg CAT, et al. A five-minute multi-parametric high-resolution whole-brain MR-stat exam: First results from a clinical trial. I*SMRM abstract.* 2020.
6. Iglesias JE, Dinov I, Singh J, Tong G, Tu Z. Synthetic MRI signal standardization: Application to multi-atlas analysis. *Med Image Comput Comput Assist Interv.* 2010; 81-8.
7. Blystad I, Warntjes JB, Smedby O, Landtblom AM, Lundberg P, Larsson EM. Synthetic MRI of the brain in a clinical setting. *Acta Radiol.* 2012; 53: 1158-63.
8. Tanenbaum LN, Tsiouris AJ, Johnson AN, Naidich TP, DeLano MC, Melhem ER, et al. Synthetic MRI for clinical neuroimaging: Results of the magnetic resonance image compilation (MAGiC) prospective, multicenter, multireader trial. *AJNR Am J Neuroradiol.* 2017.
9. Granberg T, Uppman M, Hashim F, Cananau C, Nordin LE, Shams S, et al. Clinical feasibility of synthetic MRI in multiple sclerosis: A diagnostic and volumetric validation study. *AJNR Am J Neuroradiol.* 2016; 37: 1023-9.
10. Hagiwara A, Otsuka Y, Hori M, Tachibana Y, Yokoyama K, Fujita S, et al. Improving the quality of synthetic FLAIR images with deep learning using a conditional generative adversarial network for pixel-by-pixel image translation. *AJNR Am J Neuroradiol.* 2019.
11. Virtue P, Tamir JI, Doneva M, Yu SX, Lustig M. Learning contrast synthesis from MR fingerprinting. *ISMRM abstract*. 2018.

Acknowledgments / Funding Information: We would like to thank neuroradiologists Dr. ir. E.P.A. Vonken, Dr. J.W. Dankbaar from the University Medical Center Utrecht and Dr. V.C.W. Keil from the Amsterdam University Medical Center for assessing the MR images. Additionally, we thank Carlo Lucci from the University Medical Center Utrecht for supporting the data acquisition.

This clinical trial was funded by the Netherlands Organization for Scientific Research (NWO; Demonstrator Grant 16937), and has been registered in the Netherlands Trial Register with number NL8437 (https://www.trialregister.nl/trial/8437)

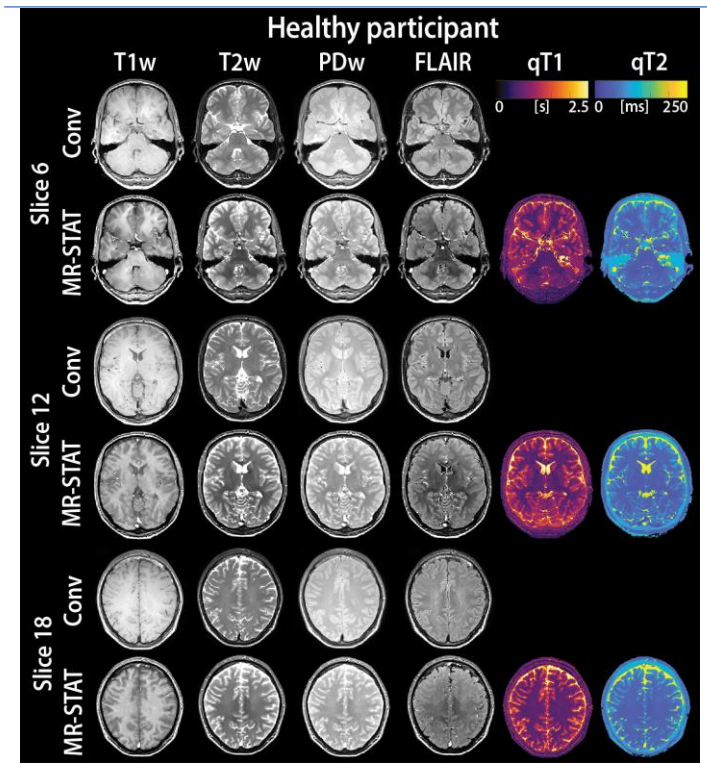

Figure 1. Comparison of T1w, T2w, PDw and FLAIR contrast images obtained from conventional (Conv) MR and synthetically generated from quantitative (q)T1 and (q)T2 maps obtained with MR-STAT. Different axial slices uniformly distributed over the longitudinal direction of one representative healthy participant.

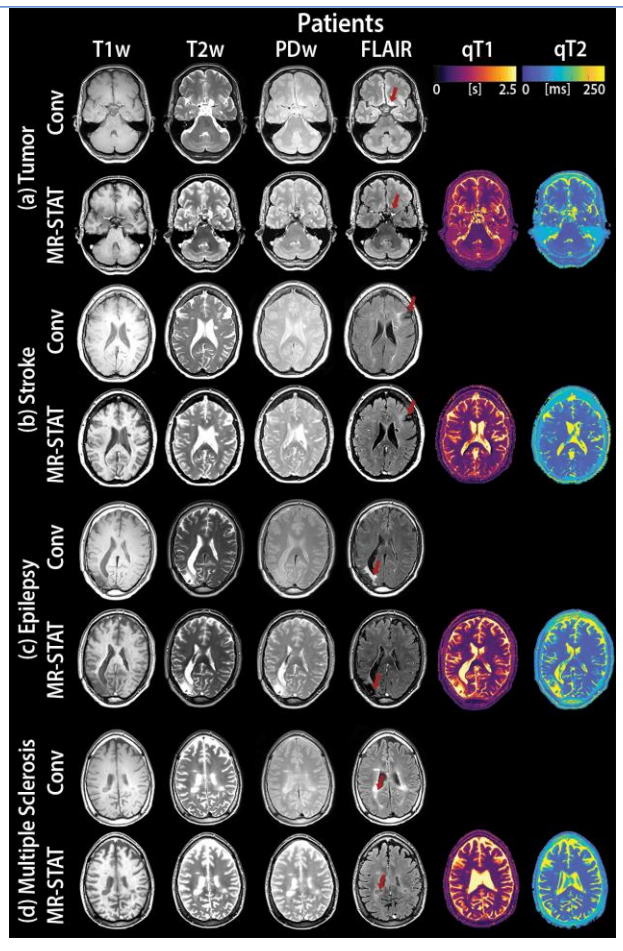

Figure 2. Comparison of T1w, T2w, PDw and FLAIR contrast images obtained from conventional (Conv)

Table 1. Prospective MRI acquisition imaging parameters

Imaging parameters	MR-STAT	T1w	T2w	PDw	FLAIR
	Spoiled-GRE	FSE	TSE	TSE	TSE
FOV (cm)	224x224x133.5 mm^3				
Resolution	1x1x3 mm^3				
Gap	1.5 mm				
Slices	30				
TR (ms)	8.9	451	3400	2800	10000
TI (ms)	-	-	-	-	2800
TE (ms)	4.7	14	80	20	120
Flip angle	Variable	70	90	90	120
TSE factor	-	-	15	14	24
Scan time	5 min	11 min			

MR-STAT: Magnetic Resonance Spin TomogrAphy in Time-domain; PDw: Proton Density weighted; FLAIR: Fluid Attenuated Inversion Recovery; GRE: Gradient Echo; FSE: Fast Spin Echo; TSE: Turbo Spin Echo

Table 3. Overall legibility of anatomic/morphologic features, and artifact identification and characterization for conventional and synthetic MR-STAT images across contrasts and participants (n = 200)[1]

Legibility of feature[2]	Conv (%)	MR-STAT (%)	Artifact type[2]	Conv (%)	MR-STAT (%)
Central sulcus	100	100	Signal-encoding artifacts		
Cerebral peduncle	100	100	Motion	18	0
Cervicomedullary junction	99	100	Infolding or wraparound	0	0
Head of caudate nucleus	81	97	White pixels/spike noise	0	16
Middle cerebrallar peduncle	100	100	Phase-encoding	3	4
Posterior limb of internal capsule	74	94	General artifacts		
			Low resolution	0	1
			Low signal-to-noise	0	0
			Poor contrast-to-noise	1	0
			Blurring	24	73
			Susceptibility	19	40

Conv: conventional MR imaging (control); MR-STAT: synthetic contrasts from quantitative MR-STAT images. [1]All data are shown as n/N%, where n is the count and N is the total reads per category. [2]Median across observers on a five-point Likert scale.

Table 2. Diagnositc image-quality ratings by contrast view and overall for conventional and synthetic images[1]

Diagnostic quality[2]	T1w		T2w		PDw		FLAIR		Overall	
	conv (%)	MR-STAT (%)	conv (%)	MR-STAT (%)	conv (%)	MR-STAT (%)	conv (%)	MR-STAT (%)	conv (%)	MR-STAT (%)
Acceptable for diagnostic use (3, 4, 5)	98	100	100	100	100	98	98	98	99	99
Excellent (rated 5)	0	0	46	0	0	0	0	0	12	0
Good (rated 4)	50	6	48	82	86	20	90	64	69	43
Acceptable (rated 3)	48	94	6	18	14	78	8	34	19	56
Unacceptable for diagnostic use (1, 2)	2	0	0	0	0	2	2	2	1	1

Conv: conventional MR imaging (control); MR-STAT: synthetic contrasts from quantitative MR-STAT images. [1]All data are shown as n/N%, where n is the count and N is the total reads per category (50 per category and 200 overall). [2]Median across observers on a five-point Likert scale.

A comparison of tractography and fMRI pre-surgical planning approaches with intraoperative mapping-based validation.

Ahmed Radwan[1,2], Louise Emsell[1,2,3,4], Evy Cleeren[5], Silvia Kovacs[6], Anais Van Hoylandt[5], Ronald Peeters[6], Steven De Vleeschouwer[2,5,7], Tom Theys[2,5,7], Patrick Dupont[2,8], Stefan Sunaert[1,2,6]

1 KU Leuven, Department of Imaging and pathology, Translational MRI, Leuven, Belgium, 2 KU Leuven, Leuven Brain Institute, Department of Neurosciences, Leuven, Belgium, 3 KU Leuven, Department of Neurosciences, Neuropsychiatry, Leuven, Belgium,

4 University Psychiatric Center (UPC) – Leuven,, Geriatric Psychiatry, Leuven, Belgium 5 Department of Neurosurgery, University Hospitals Leuven, Leuven, Belgium, 6 Department of Radiology, University Hospitals Leuven, Leuven, Belgium,

7 KU Leuven, Department of Neurosciences, Research Group Experimental Neurosurgery and Neuroanatomy, Leuven, Belgium, 8 KU Leuven, Department of Neurosciences, Laboratory for cognitive neurology, Leuven, Belgium

Synopsis: Accurate presurgical brain mapping enables preoperative risk assessment and intraoperative guidance to minimize postoperative deficits. Here we compare mapping accuracy of task-based fMRI (tbfMRI), BOLD and Functionnectome resting state fMRI (rsfMRI), DTI and constrained spherical deconvolution (CSD)-based tractography in 21 preoperative neurosurgical patients using intraoperative electrical stimulation (DES) as the ground truth for functional mapping. Accuracy was estimated based on minimum distance between MRI-based mapping and positive DES coordinates. We report that CSD outperforms DTI, and rsfMRI performs similarly to tbfMRI using DES. This demonstrates the potential benefits of using CSD and rsfMRI in clinical practice.

Introduction

Presurgical brain mapping enables preoperative risk assessment and is used for intraoperative guidance to minimize postoperative deficits [1–3]. Presurgical MRI mapping includes structural imaging, task-based fMRI (tbfMRI) for functional mapping, and diffusion tensor imaging (DTI) [4–6] scans for white matter mapping with fiber assignment by continuous tracking (FACT) [7]. TbfMRI requires adequate task-performance, which limits its applicability only to patients who are able to perform the task of interest [8,9]. DTI FACT is known to suffer from inaccuracies in the presence of complex fiber architecture 10. However, these techniques remain the mainstay of clinical presurgical MRI brain mapping despite the availability of alternatives such as resting state fMRI (rsfMRI) [11], and constrained spherical deconvolution (CSD) [12] based tractography, which address these limitations.

Here we evaluated the accuracy of a) CSD to FACT based tractography and b) tbfMRI to resting-state fMRI (rsfMRI) in preoperative neurosurgical patients. Intraoperative electrical cortical and subcortical stimulation (DES) represented the ground truth. Accuracy was estimated based on minimum distance between MRI-based mapping and positive DES coordinates.

Methods

Multimodal presurgical MRI scanning (3T Philips) was performed on 21 surgically naïve patients who were prospectively recruited (14 tumors, and 7 epilepsy). All participating patients signed written informed consent and local ethics committee approval was acquired (S61759 - Leuven/Belgium). We acquired 3D high resolution structural images (1mm isotropic), tbfMRI (1.8x1.8x3.2 mm resolution, TR 1.5s, multiband factor 2) and rsfMRI (2.2 mm isotropic resolution, TR 0.9s, multiband factor 6) and diffusion MRI (2 mm isotropic resolution) (5 b0, 128d b1200, +/- 128d b2500).

Patients underwent wake-up neurosurgery and DES (OSIRIS neurostimulator). DES points were considered positive if stimulation interfered with task performance or evoked a motor/sensory response. Spheres of 5 mm radius were constructed around positive coordinates and warped to subject-specific T1w space using FSL [13,14] and ANTs [15].

TbfMRI data were processed using a general linear model in SPM12 [16], DTI FACT tractograms of the corticospinal tract (CST) and arcuate fasciculus (AF) were manually generated using the Philips EWS clinical workstation, resulting tractograms were exported as voxel maps. Structural parcellation of the T1w images was done using VBG [17], FreeSurfer [18] and MSBP [19]. RsfMRI data was processed using the first level seed-to-voxel analysis in CONN [20] and the MSBP parcellation maps. CSD tractography was done using FWT [21]. Preprocessed rsfMRI BOLD images were also processed using the region-wise Functionnectome [22] pipeline and processed with the first level seed-to-voxel in CONN.

Tb-fMRI maps were thresholded at $p_{uncorrected} < 0.05$. All results were warped to the subject-specific T1w space using ANTs. Minimum distances were calculated between each DES point and the corresponding functional maps and/or tractograms voxel maps and used to represent mapping accuracy. A two-tailed paired t-test was used to compare DTI and CSD, and a one-way analysis of variance (ANOVA) with repeated measures was used to compare the fMRI results. Results were considered significant at $p < 0.05$. Figure 1 shows a schematic of data processing workflow.

Results

Table 1 shows summary statistics of the minimum distances and results of all tests. There was a significantly lower minimum distance between CSD fiber bundles and the DES coordinates compared to DTI bundles, indicating that CSD is more accurate than DTI FACT. There was a small difference in minimum distance between tbfMRI and rsfMRI that didn't survive Bonferroni correction, and a significant difference between tbfMRI and Functionnetcome outputs. In both cases tbfMRI was found to be the most accurate. The differences found between DTI and CSD were the largest and most significant result. Demonstrative results for the SMN, and for the language network are shown in Figures 2 and 3.

Discussion

We found a lower minimum distance between CSD tractograms and DES spheres demonstrating the added benefit of using CSD for fiber tracking compared to the clinical implementation of DTI FACT. This finding cannot be attributed solely to the CSD model however, but also to the advanced diffusion preprocessing used [23–25]. More accurate DTI results may be achievable with advanced preprocessing pipelines. In line with the literature [26–29], TbfMRI and BOLD rsfMRI showed only small and non-significant differences, confirming the reasonable accuracy of BOLD rsfMRI based localization of eloquent cortical regions. Additionally, rsfMRI can be used to investigate multiple RSNs simultaneously, making it more efficient than tbfMRI, which tends to be task-specific. This feature of rsfMRI may extend the scope of presurgical planning by additionally localising higher-order cognitive and emotional processing networks [30]. Functionnectome analysis results were less encouraging, however, this may be attributed to the presence of focal pathologies in our data, which changes the structural connectivity profile of the involved brain regions and violates the method's assumptions. However, it does show promise and this study is the first to apply the Functionnectome approach to clinical data.

Conclusion

In a neurosurgical setting, CSD outperforms DTI, and rsfMRI performs similarly to tbfMRI when using DES to localize functional brain regions. This demonstrates the potential benefits for using CSD and rsfMRI in clinical practice.

References

1.Kokkonen, S.-M. et al. Preoperative localization of the sensorimotor area using independent component analysis of resting-state fMRI. Magn. Reson. Imaging 27, 733–740 (2009).

2.Stippich, C. et al. Localizing and Lateralizing Language in Patients with Brain Tumors: Feasibility of Routine Preoperative Functional MR Imaging in 81 Consecutive Patients 1. Radiology 243, 828–836 (2007).

3.Sunaert, S. Presurgical planning for tumor resectioning. J. Magn. Reson. Imaging 23, 887–905 (2006).

4.Basser, P. J., Mattiello, J. & LeBihan, D. MR diffusion tensor spectroscopy and imaging. Biophys. J. 66, 259–267 (1994).

5.Basser, P. J., Mattiello, J. & LeBihan, D. Estimation of the effective self-diffusion tensor from the NMR spin echo. J. Magn. Reson. B 103, 247–254 (1994).

6.Pierpaoli, C., Jezzard, P., Basser, P. J., Barnett, A. & Chiro, G. D. Diffusion tensor MR imaging of the human brain. Radiology (1996) doi:10.1148/radiology.201.3.8939209.

7.Mori, S., Crain, B. J., Chacko, V. P. & van Zijl, P. C. Three-dimensional tracking of axonal projections in the brain by magnetic resonance imaging. Ann. Neurol. 45, 265–269 (1999).

8.Manan, H. A., Franz, E. A. & Yahya, N. The utilisation of resting-state fMRI as a pre-operative mapping tool in patients with brain tumours in comparison to task-based fMRI and intraoperative mapping: A systematic review. Eur. J. Cancer Care (Engl.) 30, e13428 (2021).

9.Pujol, J. et al. Clinical application of functional magnetic resonance imaging in presurgical identification of the central sulcus. J. Neurosurg. 88, 863–869 (1998).

10.Jeurissen, B., Leemans, A., Tournier, J. D., Jones, D. K. & Sijbers, J. Investigating the prevalence of complex fiber configurations in white matter tissue with diffusion magnetic resonance imaging. Hum. Brain Mapp. 34, 2747–2766 (2013).

11.Biswal, B., Yetkin, F. Z., Haughton, V. M. & Hyde, J. S. Functional Connectivity in the Motor Cortex of Resting Human Brain Using Echo-Planar MRI. https://pdfs.semanticscholar.org/693a/6e46be9b613ac5beab7313e1f0b51658dbe9.pdf (1995).

12.Tournier, J. D., Calamante, F., Gadian, D. G. & Connelly, A. Direct estimation of the fiber orientation density function from diffusion-weighted MRI data using spherical deconvolution. NeuroImage 23, 1176–1185 (2004).

13.Jenkinson, M., Beckmann, C. F., Behrens, T. E. J., Woolrich, M. W. & Smith, S. M. FSL. NeuroImage 62, 782–790 (2012).

14.Smith, S. M. et al. Advances in functional and structural MR image analysis and implementation as FSL. NeuroImage 23 Suppl 1, S208-219 (2004).

15.Tustison, N. J. et al. The ANTsX ecosystem for quantitative biological and medical imaging. Sci. Rep. 11, 9068 (2021).

16.Ashburner, J. et al. Statistical Parametric Mapping: The Analysis of Functional Brain Images. (2006).

17.Radwan, A. M. et al. Virtual brain grafting: Enabling whole brain parcellation in the presence of large lesions. NeuroImage 229, 117731 (2021).

18.Fischl, B. FreeSurfer. NeuroImage 62, 774–781 (2012).

19.Tourbier, S., Aleman-Gomez, Y., Griffa, A., Bach Cuadra, M. & Hagmann, P. sebastientourbier/multiscalebrainparcellator: Multi-Scale Brain Parcellator v1.1.1. (Zenodo, 2019). doi:10.5281/zenodo.3627097.

20.Whitfield-Gabrieli, S. & Nieto-Castanon, A. Conn: a functional connectivity toolbox for correlated and anticorrelated brain networks. Brain Connect. 2, 125–141 (2012).

21.Radwan, A. et al. An atlas of white matter anatomy, its variability, and reproducibility based on Constrained Spherical Deconvolution of diffusion MRI. 2021.10.13.464139 https://www.biorxiv.org/content/10.1101/2021.10.13.464139v1 (2021) doi:10.1101/2021.10.13.464139.

22.Nozais, V., Forkel, S. J., Foulon, C., Petit, L. & Thiebaut de Schotten, M. Functionnectome as a framework to analyse the contribution of brain circuits to fMRI. Commun. Biol. 4, 1–12 (2021).

23.Brun, L., Pron, A., Sein, J., Deruelle, C. & Coulon, O. Diffusion MRI: Assessment of the Impact of Acquisition and Preprocessing Methods Using the BrainVISA-Diffuse Toolbox. Front. Neurosci. 13, 536 (2019).

24.Ressel, V., van Hedel, H. J. A., Scheer, I. & O'Gorman Tuura, R. Comparison of DTI analysis methods for clinical research: influence of pre-processing and tract selection methods. Eur. Radiol. Exp. 2, 33 (2018).

25.Roalf, D. R. et al. The impact of quality assurance assessment on diffusion tensor imaging outcomes in a large-scale population-based cohort. NeuroImage 125, 903–919 (2016).

26.Branco, P. et al. Resting-State Functional Magnetic Resonance Imaging for Language Preoperative Planning. Front. Hum. Neurosci. 10, 1–14 (2016).

27.Cochereau, J. et al. Comparison between resting state fMRI networks and responsive cortical stimulations in glioma patients. Hum. Brain Mapp. 37, 3721–3732 (2016).

28.Hacker, C. D., Roland, J. L., Kim, A. H., Shimony, J. S. & Leuthardt, E. C. Resting-state network mapping in neurosurgical practice: a review. Neurosurg. Focus 47, E15 (2019).

29.Kumar, V. A. et al. The role of resting-state functional MRI for clinical preoperative language mapping. Cancer Imaging 20, 47 (2020).

Acknowledgments / Funding Information: Continue on this line

30.Catalino, M. P. et al. Mapping Cognitive and Emotional Networks in Neurosurgical Patients Using Resting-State Functional Magnetic Resonance Imaging. Neurosurg. Focus 48, E9 (2020).

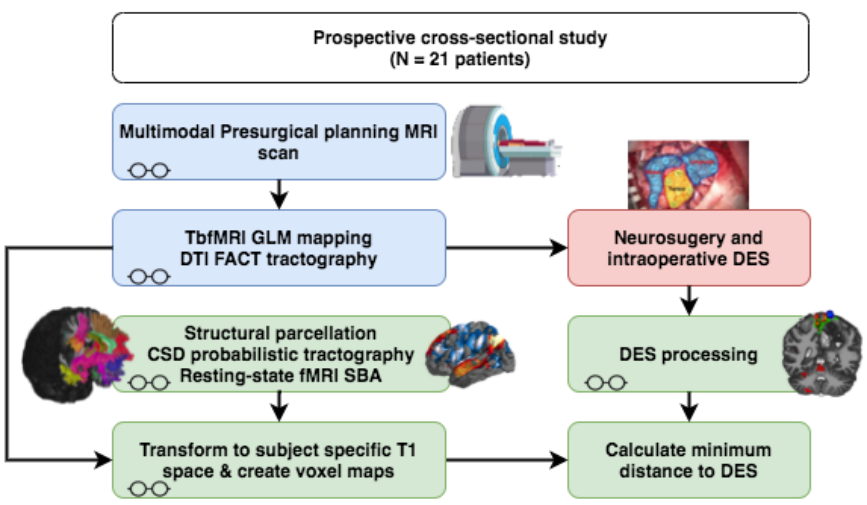

Figure 1: Schematic representation of the study outline and data processing steps. Cartoon glasses shown in the left lower corners indicate visual quality checks. Blue = clinical MRI workflow, Red = surgical intervention, Green = study analyses. TbfMRI = task-based functional MRI. DTI FACT = diffusion tensor imaging fiber assignment by continuous tracking. GLM = general linear model, DES = direct electrical stimulation, CSD = constrained spherical deconvolution, rsfMRI = resting state functional MRI.

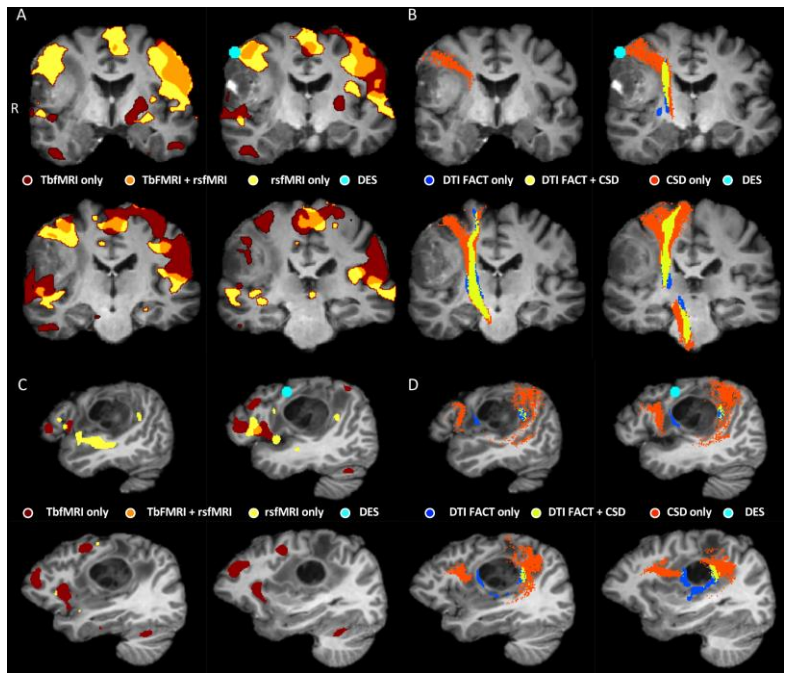

Figure 2: (A and B) Sagittal T1-weighted images from a patient with a right frontal opercular high-grade glioma. Lip motor fMRI maps from tbfMRI and BOLD rsfMRI (A), and voxel maps of the cortico-spinal tract (CST) using DTI FACT and CSD (B).(C and D) show sagittal plane images from a patient with a left fronto-parietal high-grade glioma, language fMRI and arcuate fasciculus results overlaid in differential color coding for overlap and differences. DES spheres are shown in turquoise.

Table 1: Quantitative results for minimum distances (in mm) between DES spheres and fMRI and tractography maps

1- **Functional MRI results**			
	TbfMRI	**BOLD rsfMRI**	**Functionnectome rsFMRI**
Number of datasets	34	34	34
Mean	8.146	9.525	16.899
Variance	98.029	123.926	512.528
ANOVA results	F-statistic = 4.284		p-value = 2.501^{-07}
Post-hoc paired two-tailed t-test results ($p_{bonferroni} < 0.017$)	Test1: tbfMRI vs. BOLD fMRI	Test2: BOLD vs Functionnectome rsfMRI	Test3: tbfMRI vs Functionnectome rsfMRI
T-score	2.424	3.004	2.77
p-value	0.020	0.005 *	0.009 *

2- **Diffusion MRI tractography results**		
	DTI FACT	**CSD**
Number of datasets	42	42
Mean	16.851	6.570
Variance	121.217	90.702
Paired two-tailed t-test results ($p_{uncorrected} < 0.05$)	T-score = 5.241	p-value = 5.149^{-6}

Table 1: Summary statistics of the minimum distances and results of all statistical tests. Bonferroni's corrected p-value was set to 0.017 (0.05/3). Notably, the difference between tbfMRI and rsfMRI was initially significant at an uncorrected level but did not survive the Bonferroni correction. The differences found between DTI and CSD were the largest and most significant results.

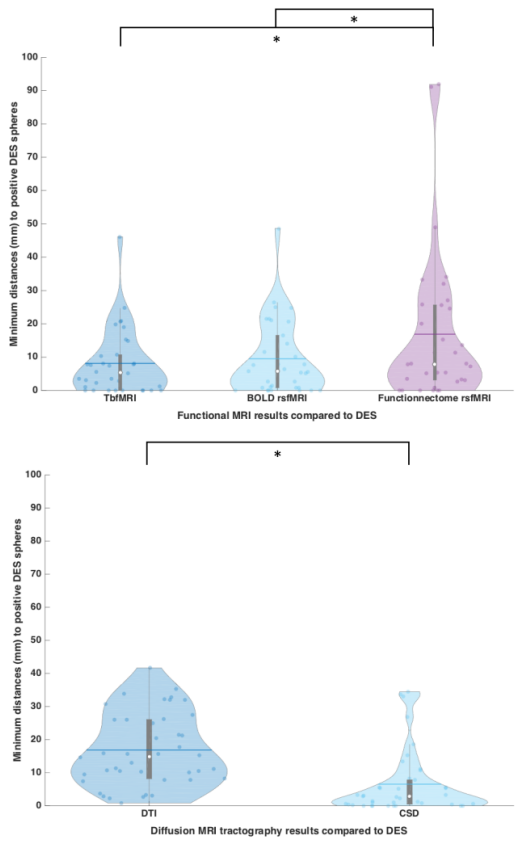

Figure 3: Violin plots of minimum distances between tbfMRI, rsfMRI and Functionnectome maps and DES sphere (top), and DTI and CSD tractography maps (bottom). Means are indicated by horizontal lines inside each violin plot. Asterisks indicate statistically significant differences. TbfMRI = task-based functional MRI, BOLD = Blood oxygen level dependent contrast, rsfMRI = resting state fMRI.

Neuromelanin MRI as biomarker for treatment resistance in first episode schizophrenia patients

M. van der Pluijm[1,2], P.N. Reijers[1], K. Wengler[3], L. de Haan[2], J. Booij[1], G. Horga[3], E. van de Giessen[1]

[1]Department of Radiology and Nuclear Medicine, Amsterdam UMC, Amsterdam, The Netherlands ; [2]Department of Psychiatry, Amsterdam UMC, Amsterdam, The Netherlands; [3]New York State Psychiatric Institute, Columbia University Medical Center, New York, USA

Synopsis: The current study assesses neuromelanin sensitive MRI (NM-MRI) as a potential biomarker for treatment resistance (TR) in first episode schizophrenia patients. NM-MRI is a novel MRI sequence, which indirectly measures dopamine synthesis. Research using positron emission tomography (PET) imaging suggest that TR patients show lower dopamine synthesis than responders. We acquired NM-MRI in 61 patients with first-episode schizophrenia. Treatment response was determined during 6 months follow-up. TR patients showed significantly lower NM-MRI signal compared to responders. These findings are in line with previous PET studies and demonstrate the potential of NM-MRI as alternative and more accessible biomarker for TR.

Purpose: Treatment resistance (TR) in schizophrenia is a major clinical problem with 20-35% of psychotic patients showing non-response to standard antipsychotic treatment[1]. A biomarker that could predict TR is needed to reduce delays in effective treatment. A well-established finding in schizophrenia, using [^{18}F]F-DOPA PET imaging, is increased striatal dopamine synthesis, but interestingly TR patients do not show this altered synthesis[2]. [^{18}F]F-DOPA however is too costly and invasive to use for TR screening. A novel neuromelanin-sensitive MRI sequence (NM-MRI), which indirectly measures striatal dopamine synthesis[3], has potential as biomarker for TR. NM-MRI signal is indeed increased in schizophrenia patients, but has not yet been evaluated in TR[4]. The current study assessed NM-MRI as a biomarker for TR and investigated if TR patients show lower NM-MRI signal than responders.

Methods: 61 first episode schizophrenia patients underwent an MRI scan at baseline. Treatment response was determined during six months follow-up. A patient was classified as TR after showing no adequate response to a minimum of two sufficiently dosed conventional antipsychotics. MRI scans were conducted on an 3 Tesla Ingenia MRI scanner equipped with a 32-channel sense head coil. T1-weighted scans were acquired for processing of the NM-MRI image (TR/TE=4.1/9.0 msec; 189 slices; FOV=84×284×170 mm; voxel size= 0.9×0.9× 0.9 mm, FA = 8°). NM-MRI scan contained a T1-weighted gradient recalled echo sequence with resonance magnetization transfer preparation pulses (TE/TR=3.9/260 msec, FA=40°, 8 slices, slice thickness=2.5 mm, in-plane resolution=0.39×0.39 mm^2, FOV=162×199 mm, NSA=2;) and was placed perpendicular to the fourth ventricle floor with coverage from the posterior commissure to halfway through the pons (Figure 1). NM-MRI signal in the Substantia Nigra (SN) was measured as contrast ratio (NMcr), with the Crus Cerebri (CC) as reference region. The toolbox described by Wengler (2020)[5] was used for processing of the NM-MRI scan. First the T1-weigthed scans were used to normalize the NM-MRI scans to MNI standard space using ANTS 2.3.1.[6] The normalized NM-MRI scans were then spatially smoothed using 3D Gaussian kernels with full-width-at-half-maximum of 1 mm. Template masks from a previous study[3] were used to obtain the signal intensity (S) of the SN and CC (Figure 2). NMcr was calculated at each voxel in the NM-MRI images as NMcr= (S_{SN} – mode(S_{CC})/ mode(S_{CC})) * 100. A One-way ANCOVA was conducted to assess group differences between TR and responders on mean NMcr controlling for age. Age was added as covariate, since neuromelanin levels in the SN show an inverted U-shaped age effect[7].

Results: At six months of follow-up 15 patients were classified as TR and 46 patients as responders. The two groups did not significantly differ on gender, IQ, use of medication, and substance use. However, the mean age of TR patients was lower than responders, t(59)= -2.876 p = 0.007. The ANCOVA revealed a significant effect of group (TR versus responder) on mean NMcr after controlling for age, $F(1,58) = 5.064$, $p = 0.028$. Age was not a significant covariate ($F(1,58) = 0.457$, $p = 0.502$). In addition no correlation was found between age and NMcr (r =0.177, p =0.172).

Discussion: Significantly lower NMcr levels were found in TR patients compared to responders. These findings are in line with the [^{18}F]F-DOPA PET studies showing lower dopamine synthesis in TR compared to responders. This study demonstrates the promise of NM-MRI as biomarker for TR although the application of NM-MRI as a predictor for TR remains uncertain given the overlap in NMcr levels between TR and responders (Figure 3). A possible explanation for this might be that binary categorizing patients as either TR or responders is not appropriate as the response to antipsychotics could be a spectrum, including a group of partial responders. This will be further assessed. In addition, we will map the regional voxelwise variation within the current template mask. The template mask is purposefully over inclusive to ensure that all SN voxels are included in the mask and conversely some voxels outside the SN might be incorrectly included. This could influence the mean signal intensity to various degree in different subjects. No correlation was found between age and NMcr. Even though neuromelanin is known to increase with age, this increase is most steeply until the age of 20. Since the mean age of our two patients groups (21.3 and 24.3 years) is slightly higher, the effect of age on our results might be limited.

Conclusion: This study demonstrated the potential of NM-MRI as a biomarker for TR in schizophrenia. Even though the results of this study show significant differences in NMcr between TR and responders, the predictive value of NM-MRI still requires further investigation.

References:

1. Farooq S, Agid O, Foussias G, Remington G. Using treatment response to subtype schizophrenia: Proposal for a new paradigm in classification. Schizophrenia Bulletin. 2013; 39(6):1169-1172.

2. Demjaha A, Murray R. M, McGuire, PK, Kapur, S., & Howes, OD. (2012). Dopamine synthesis capacity in patients with treatment-resistant schizophrenia. American Journal of Psychiatry. 2012;169(11):1203-1210.

3. Cassidy CM, Zucca FA, Girgis RR, et al. Neuromelanin-sensitive MRI as a noninvasive proxy measure of dopamine function in the human brain. Proc. Natl. Acad. Sci. U. S. A. 2019;116:5108–5117

4. Shibata E, Sasaki M, Tohyama K, et al. Use of neuromelanin-sensitive MRI to distinguish schizophrenic and depressive patients and healthy individuals based on signal alterations in the substantia nigra and locus ceruleus. Biological psychiatry. 2008;64(5):401-406.

5. Wengler K, He X, Abi-Dargham A, Horga G. Reproducibility Assessment of Neuromelanin-Sensitive Magnetic Resonance Imaging Protocols for Region-of-Interest and Voxelwise Analyses. Neuroimage 2019:1–37

6. Avants BB, Tustison N, Song G. Advanced normalization tools (ANTS). Insight j. 2009;2;1–35.

7. Xing Y, Sapuan A, Dineen RA, Auer DP. Life span pigmentation changes of the substantia nigra detected by neuromelanin-sensitive MRI. Mov. Disord. 2018;33:1792–1799 doi: 10.1002/mds.27502.

Acknowledgments / Funding Information: The study was funded by a Veni grant (91618075) from the Netherlands Organisation for Health Research and Development (ZonMw). The funders had no role in study design, data collection and analysis, decision to publish, or preparation of the manuscript.

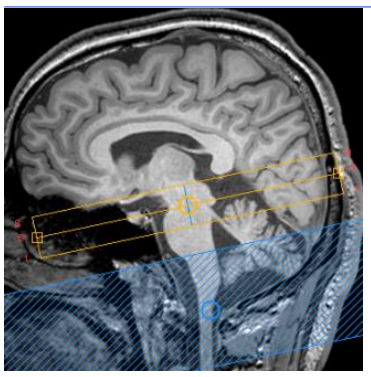

Figure 1. Example of the NM-MRI scan placement. The NM-MRI was placed perpendicular to the fourth ventricle floor with coverage from the posterior commissure to halfway through the pons.

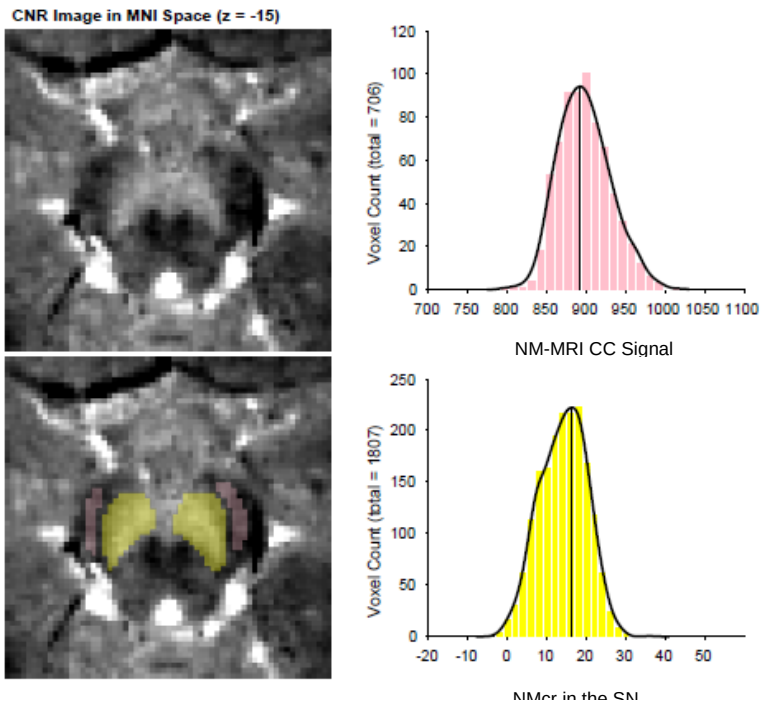

Figure 2: Spatially normalized NM-MRI image of a single subject. Template masks for the Substantia Nigra (SN) in yellow and for the Crus Cerebri (CC) in pink are overlaid onto the normalized image of a single subject. The graphs on the right are in pink the signal intensities (S) of the voxels in the CC and in yellow the neuromelanin contrast ratio (NMcr) of the voxels in the SN, calculated as $NMcr=S_{SN} - mode(S_{CC})/ mode(S_{CC})$

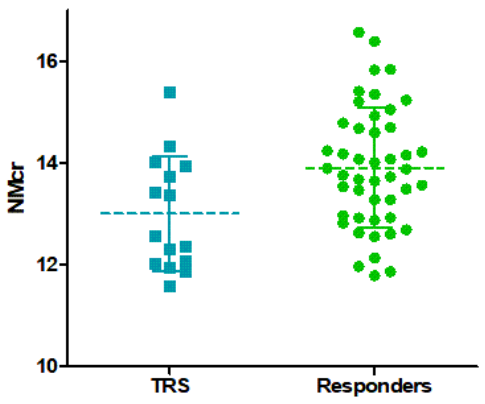

Figure 3. Neuromelanin contrast ratio (CR) of the treatment resistant (TR) and responders, with a significant difference between the TR (NMcr = 13.0) and responders (NMcr=13.9), $F(1,58) = 5.064$, $p = 0.028$.

Vital Signs, Temperature and COMFORT Scale Scores in Infants During Ultra-High-Field MR Imaging.

I.M. van Ooijen[1,2], K.V. Annink[1], J. Dudink[1], T. Alderliesten[1], F. Groenendaal[1], M.L. Tataranno[1], M. Lequin[2], J.M. Hoogduin[2], F. Visser[2], A.J.E. Raaijmakers[2,3], D.W.J. Klomp[2], E.C. Wiegers[2], M.J.N.L. Benders[1], J.P. Wijnen[2] & N.E. van der Aa[1]

[1]Department of Neonatology, University Medical Center Utrecht, Utrecht, The Netherlands; [2]Department of Radiology, University Medical Center Utrecht, Utrecht, The Netherlands; [3]Department of Biomedical Engineering, Eindhoven University of Technology, Eindhoven, The Netherlands.

Synopsis: 7T MRI in infants could improve cerebral diagnostic quality, but safety should be evaluated before standard use. In this study, twenty infants without respiratory support between term-equivalent age and 3 months corrected age, were scanned on 7T directly after 3T MRI. Vital signs (heart rate, oxygen saturation and respiratory rate), temperature (rectal, body and brain), COMFORT scale scores and adverse events were monitored throughout the process. None of these parameters changed around 7T MRI. Also, heart rate and temperature were not significantly different during 7T, compared to 3T MRI. Therefore scanning infants at 7T appears to be safe.

Introduction: Cerebral MRI in infants is usually performed on 3T. 7T MRI potentially increases the spatial resolution and improves the use of advanced imaging, such as MR spectroscopic imaging[1,2] and vascular imaging[3]. Previously, we showed that global and peak specific absorption rate (SAR) levels at 7T in an infant model do not exceed the levels in an adult model[4,5], and that hearing protection can be guaranteed[6]. Here we focus on related and additional effects: thermal heating of the infant and the potential effects of the main static magnetic field. We provide an overview of vital signs, temperature, COMFORT scale (CS) scores and adverse events (AE's) before, during and after 7T MRI.

Methods: Twenty clinically stable infants without respiratory support between term-equivalent age and 3 months corrected age, were scanned at 7T right after their clinical 3T MRI scan (both Philips Healthcare Best, The Netherlands). At 7T, a 2-channel transmit 32-channel receive head coil (Nova Medical, Wilmington, MA) was used. All infants were sedated before 3T MRI.

Vital signs (heart rate (HR), oxygen saturation (SpO2) and respiratory rate (RR)) were closely monitored during both MRI scans. HR and SpO2 were continuously measured from 1-2 hours before, until 18 hours after both MRI scans. Temperature was measured rectally before, and every 6 hours after the MRI scans until 18 hours after MRI scans. Body temperature was measured continuously during both MRI scans via a sensor attached to the abdomen. ^{1}H-MRS data was acquired (3T: PRESS, TE/TR=38/2000ms; 7T: STEAM, TE/TR=10/2000ms) from a single voxel in the left deep gray matter. From this data, brain temperature was determined by assessing the chemical shift difference between water (H_20) and N-acetyl-aspartate (NAA) (figure 1), as described before[7,8,9].

The CS[10] is a scoring system containing 6 items (alertness, agitation, crying, body movements, facial muscle tension and overall muscle tension) with a 5-point scale (1=comfortable and 5=discomfort). In general, a score ≥14 indicates discomfort. The CS was scored 1-2 hours before MRI scans, during transport after both MRI scans, and every 6 hours after the MRI scans until 18 hours after MRI scans. AE's (desaturation (SpO_2 <85%), apnea (>20 seconds episode of cessation of breathing), hypothermia (<35.5ºC), hyperthermia (>38.5ºC), bradycardia (<100 bpm), tachycardia (>200 bpm), need for interruption of scanning, stopping scans prematurely and events like regurgitation mentioned by parents after discharge) were monitored. We used the paired-samples t-test or Wilcoxon signed ranks test (for not-normal distributed data) to assess differences between 3T and 7T MRI.

Results: Table 1 shows the baseline characteristics. There was no significant difference between the HR at the end of 3T compared to the end of 7T (mean bpm: 144 and 140, respectively; Z=-0.806; p=0.420). SpO2 was significantly lower at the end of 3T compared to the end of 7T (mean SpO2: 94% and 96%, respectively; p=0.002). Temperature was stable during the whole observation period (figure 2A). Also, brain temperature did not change at 7T, compared to 3T (mean temperature: 36,1ºC and 36,0ºC, respectively; p=0.998), (figure 2B).

CS scores showed no difference during transport after 3T compared to transport after 7T (mean CS: 8.9 and 10.7, respectively; Z=-1.670; p=0.095), (figure 3). One infant showed a highly increased CS during transport after 7T MRI, most likely due to being hungry, since the infant quickly recovered after feeding. At last, no changes in AE's were reported after 7T MRI (table 2). Apnea, hypothermia, hyperthermia, bradycardia, need for circulatory or respiratory support and AE's after discharge never occurred. Desaturations were related to a premature breathing pattern, almost always already occurring before 7T MRI. Tachycardia in one infant during 7T was induced by crying and directly recovered after comforting the infant. One infant showed regurgitation of milk after 7T MRI, already occurring before MRI scans. 7T scans were paused a few times due to technical problems, movement artifacts or inadequate monitoring. Three infants cried during 3T MRI and during 7T MRI, all were comforted quickly.

Discussion and Conclusion: No changes in vital signs, temperature, CS scores and AE's were found in infants around 7T MRI. Also, HR and temperature were not significantly different during 7T, compared to 3T MRI. Brain temperature was lower compared to rectal or surface temperature, this is in line with previous studies[7,8]. We have used localized F_0 determination of water as determined automatically by the scanner prior to the metabolite scan. Even more accurate assessments may be obtained by using the non-suppressed water scan and to evaluate potential frequency drifts of NAA during the metabolite scan, or to use metabolite cycling with non-suppressed water[12]. Lower SpO2 during 3T could be caused by sedation administered before 3T MRI, with effects of sedation possibly wearing off during the 7T scan. This could possibly also lead to slightly higher comfort scores after 7T.

Ultra-high field strengths pose potential areas of risk for the infant. The SAR and sound pressure levels were previously modeled[4]. Here we show that 7T MR scanning in infants induces no significant changes in vital signs, temperature, CS scores and AE's. Therefore, 7T MRI appears to be safe in infants without respiratory support. Future research should elucidate the advantages of 7T compared to 3T MRI, possibly improving diagnostic quality.

References:

1. Van der Kolk AG, Hendrikse J, Zwanenburg JJ, Visser F, & Luijten PR. Clinical applications of 7 T MRI in the brain. Eur J Radiol. 2013;82(5):708-718.
2. Dagia C & Ditchfield M. 3 T MRI in paediatrics: challenges and clinical applications. Eur J Radiol. 2008;68(2):309-319.
3. Springer E, Dymerska B, Cardoso PL, et al. Comparison of routine brain imaging at 3 T and 7 T. Invest Radiol. 2016;51(8):469.
4. Annink KV, van der Aa NE, Dudink J, et al. Introduction of ultra-high-field MR imaging in infants: preparations and feasibility. Am J Neuroradiol. 2020;41(8):1532-1537.
5. Malik SJ, Hand JW, Satnarine R, Price AN & Hajnal JV. Specific absorption rate and temperature in neonate models resulting from exposure to a 7T head coil. Magn Reson Med. 2021.
6. Huijing ER, Wiegers, E, Klomp DWJ, et al. Damping of acoustic noise for neonatal MRI at 7 Tesla; ISMRM 2021.
7. Wu TW, McLean C, Friedlich P, et al. Brain temperature in neonates with hypoxic-ischemic encephalopathy during therapeutic hypothermia. J Pediatr. 2014;165(6):1129-1134.
8. Annink KV, Groenendaal F, Cohen D, et al. Brain temperature of infants with neonatal encephalopathy following perinatal asphyxia calculated using magnetic resonance spectroscopy. Pediatr Res. 2020;88(2):279-284.
9. Alderliesten T, de Vries LS, Staats L, et al. MRI and spectroscopy in (near) term neonates with perinatal asphyxia and therapeutic hypothermia. Arch Dis Child Fetal Neonatal Ed. 2017;102(2):F147-F152.
10. Ambuel B, Hamlett KW, Marx CM & Blumer JL. Assessing distress in pediatric intensive care environments: the COMFORT scale. J Pediatr Psychol. 1992;17(1): 95-109.
11. Pijnappel WWF, Van den Boogaart A, De Beer R & Van Ormondt D. SVD-based quantification of magnetic resonance signals. J Magn Reson. 1992; 97(1):122-134.
12. Henning A, Schär M, Kollias SS, Boesiger P & Dydak U. Quantitative magnetic resonance spectroscopy in the entire human cervical spinal cord and beyond at 3T. J Magn Reson. 2008;59(6):1250-1258.

Acknowledgments / Funding Information: I.M. van Ooijen and K.V. Annink shared first authorship; J.P. Wijnen and N.E. van der Aa shared last authorship.

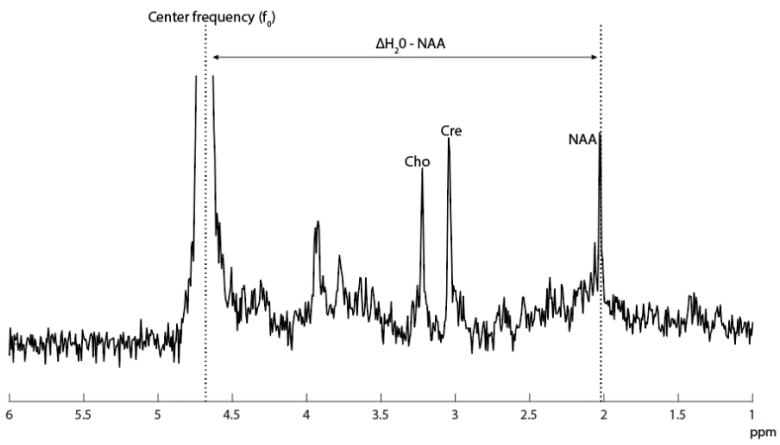

Figure 1. Spectrum of the single voxel 1H-MRS in the left deep gray matter of one infant during 7T MRI. The ppm of the H20 peak is assumed to be the center frequency (F0). The frequency offset of the NAA peak is determined using the HLVSD option, locating the fifteen highest peaks10. This was used in the formula (T = 263 + NAA × 85.76; see7), which results in a temperature (T) of 35.7ºC in the deep grey matter of this infant.

Characteristic	Infants (n = 20)
Male/female	10/10
Gestational age in weeks, *mean (sd)*	33.01 (1.54)
Birth weight in grams, *mean (sd)*	1207.25 (307,65)
Weight during scans in grams, *mean (sd)*	4280.25 (293.17)
Postmenstrual age at MRI, *mean (sd)*	44.71 (1.16)
Postnatal age at MRI in days, *mean (sd)*	80.50 (7.09)

Table 1. Baseline characteristics of the infants included in this study.

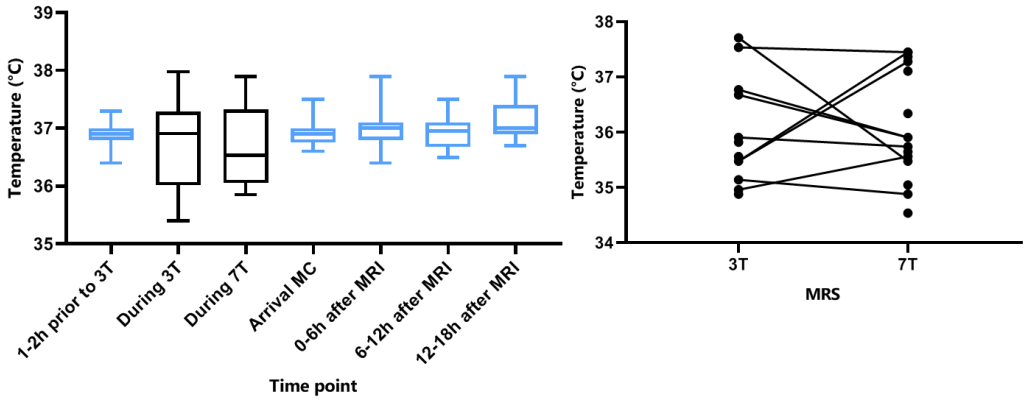

Figure 2. (A) temperature before and every 6 hours after the MRI scans until 18 hours after MRI scans measured rectally (blue), and during MRI via a sensor attached to the infants abdomen (black). (B) brain temperatures measured with 1H-MRS in the left deep gray matter at 3T and 7T.

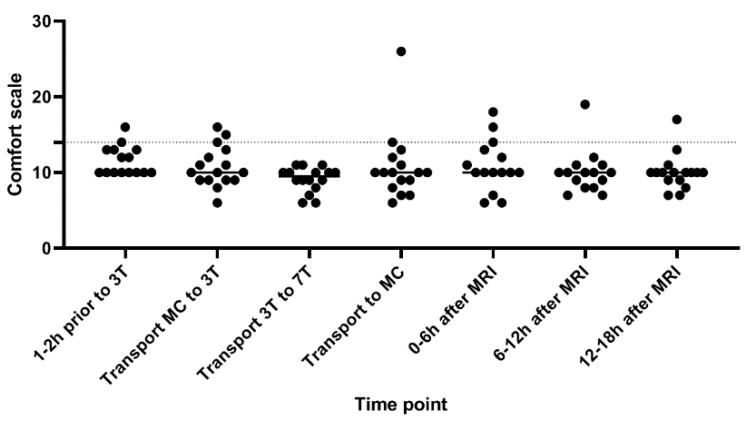

Figure 3. COMFORT scale10 scores measured 1-2 hours before MRI, during transport between MRI's and every 6 hours after the MRI scans until 18 hours after MRI scans. In general, a score of 14 or more means the baby experiences discomfort, indicated by the dotted line.

Adverse event	Before 3T (n)	During 3T (n)	During 7T (n)	After 7T (n)
Desaturation (SpO_2 <85%)	1	3	3	3
Tachycardia (>200 bpm)	1	0	1	0
Regurgitation of milk	10	1	0	1
Interruption of scanning	-	5 (3xa, 1xb, 1xc*)	7 (3xa, 1xb, 1xd, 2xe*)	-
Scan stopped prematurely	-	0	3	-

Table 2. All observed adverse events monitored throughout the study.
**a: crying but able to comfort; b: technical problems; c: movement artifacts; d: inadequate monitoring and e: other.*

GDPR compliant reuse of medical data: encouraging patients to contribute to research (video)

E. Warnert[1], S. Beun[2], N. Broeckx[3], V. Keil[4], C. Maumet[5], K. Oliver[6], J. Petr[7], J. Pinto[8], K. Van Driessche[9], I. Wamelink[4], P. Clement[2]

[1]Department of Radiology & Nuclear Medicine, Erasmus MC, Rotterdam, The Netherlands; [2]Ghent Institute for Functional and Metabolic Imaging, Ghent University, Ghent, Belgium; [3]; [4]Department of Radiology and Nuclear Medicine, Amsterdam University Medical Center, location VUmc, Amsterdam, The Netherlands; [5]Inria, Univ Rennes, CNRS, Inserm – IRISA UMR 6074, Empenn ERL U 1228, Rennes, France; [6]The International Brain Tumour Alliance, Tadworth, United Kingdom; [7]Helmholtz-Zentrum Dresden-Rossendorf, Dresden, Germany; [8]Institute of Biomedical Engineering, Department of Engineering Science, University of Oxford, United Kingdom; [9]Ghent University Hospital, Ghent, Belgium.

Synopsis

Many patients are unaware of the implications of the General Data Protection Regulation (GDPR) on their medical data, including the transparency principle stating that individuals should be informed about the use of their personal data in a clear, concise and accessible manner. In order to overcome this challenge, the COST Action 'Glioma MR Imaging' developed an animation video in 17 languages to inform patients about the importance of reuse of medical data for research and how their data is protected. It is expected that implementing this video throughout Europe will engage and educate patients and facilitate reuse of medical data.

Introduction

Data acquired for clinical purposes are often unreachable for scientific research. The General Data Protection Regulation (GDPR) in the EU introduced new safeguards to ensure patient privacy, including the transparency principle that states that information about data protection should be easily accessible in a concise and clear way, using plain language.[1,2,3] Patients are often unaware that they can become active participants in the scientific process by allowing the reuse of their medical data and that privacy protection rules guarantee safe data-sharing.

Having these challenges in mind, the European Cooperation in Science and Technology (COST) Action 'Glioma MR Imaging 2.0' (GliMR; glimr.eu) has developed an animation video that can be used to inform patients. GliMR is a network of clinicians, researchers and other stakeholders, that attempts to streamline and improve the diagnosis, prognosis, follow-up, and evaluation of treatment of brain tumours using advanced MRI techniques.[4] Previously, a joint-initiative from GliMR and the Open Brain Consent resulted in the development of a GDPR-compliant template consent form and associated data user agreement.[5] These templates are valuable tools to inform patients and healthy volunteers about data usage and sharing related privacy regulations, and facilitate the collection of consent. Unfortunately, patients are only exposed to this information when recruited specifically for scientific studies.

Therefore, GliMR released an animation video as a tool for communication towards patients, which can be used as part of the data protection strategy within hospitals and healthcare institutions across Europe.

Methods

Initially, a GDPR-specialist and hospital data protection officer were consulted to collect information about the current regulations for reuse of medical data in science. Using this information, the main messages and focus points of the animation were identified. The video had to be short, clear, visual, and have on-screen text crucial for situations in which no sound is available, e.g. in waiting rooms, as illustrated in Figure 1 and 2. Additionally, a patient testimonial format was chosen, with glioma as a case sample. These points were used to develop a video script and storyboard in English by the private video company, WellPlayed Video (Ghent, Belgium). Several versions were revised by clinicians and researchers of GliMR, the GDPR-specialist, and patient representatives assembled by the International Brain Tumour Alliance (theibta.org). Simultaneously, the script was translated by native GliMR-members into 16 additional languages: Bulgarian, Croatian, Czech, Danish, Dutch, Estonian, French, German, Greek, Italian, Norwegian, Polish, Portuguese, Romanian, Slovak, and Spanish. These translations were checked on clarity by native laypeople and patients. After recording the scripts by professional voice actors and final feedback from all involved parties, the videos were finalised. The videos were released during the International Brain Tumour Awareness Week 2021, and distributed via the GliMR-members to over 21 countries and 72 hospitals and research centers. Additionally, a press release has been released on AlphaGalileo.[6]

Results

A short and clear animation video is available in 17 languages, with and without subtitles. The video focuses on three main messages:

1. Reusing and sharing medical data for scientific purposes is possible.
2. When data is reused for scientific research, multiple safeguards are in place to keep the patients' privacy protected.
3. Medical data is needed: by sharing their medical data, each patient can make a difference to help discover more about pathologies and their cures.

The videos are publicly available under a CC-BY-ND Creative Commons license. For each language, a web page is available, which can be found via glimr.eu/gdpr-video. These web pages provide context about the video and information on its use. This information is mainly for data protection officers, healthcare professionals, clinicians and researchers who want to use the video to inform their patients.

Discussion and conclusion

Within this project, an animation video was developed to inform patients about the reuse of their medical data and the protection of their privacy. More importantly, the video tries to involve patients in medical research, by stressing the importance of their data for future scientific breakthroughs.

The video is a useful tool to comply with the transparency principle of GDPR, by providing data privacy related information in a concise, transparent and intelligible manner. In the video, clear and plain language is used, verified by laypeople and patients. It can be used for free by all types of healthcare professionals, hospitals, institutions, patient organizations and other relevant stakeholders. The video can be broadcasted in the waiting room, embedded on a website, or shared via social media. Therefore, this video can be part of the data protection strategy as the first layer of information. However, it cannot be used as the sole resource of information for patients, as it only provides an overview of the major safeguards to protect patient privacy. Each institution, hospital, and healthcare professional is responsible to provide additional layers of information and correctly implement other European, national and local privacy-related measures.

In conclusion, this video can be part of the data protection strategy of hospitals and healthcare institutions throughout Europe. The implementation of this video in daily clinical and research practice is expected to engage patients and facilitate the reuse of medical data.

References

1. GDPR.EU. General Data Protection Regulation (GDPR): Art. 12 GDPR: Transparent information, communication and modalities for the exercise of the rights of the data subject. https://gdpr.eu/. Accessed 08/11/2021.
2. GDPR.EU. General Data Protection Regulation (GDPR): Art. 13 GDPR: Information to be provided where personal data are collected from the data subject. https://gdpr.eu/. Accessed 08/11/2021.
3. GDPR.EU. General Data Protection Regulation (GDPR): Art. 14 GDPR: Information to be provided where personal data have not been obtained from the data subject. https://gdpr.eu/. Accessed 08/11/2021.
4. Clement P, Booth T, Borovečki F, Emblem KE, Figueiredo P, Hirschler L, Jančálek R, Keil VC, Maumet C, Özsunar Y, Pernet C, Petr J, Pinto J, Smits M, Warnert EAH. GliMR: Cross-Border Collaborations to Promote Advanced MRI Biomarkers for Glioma. J Med Biol Eng. 2020 Dec 3:1-11.
5. The open brain consent working group. The Open Brain Consent: Informing research participants and obtaining consent to share brain imaging data. Hum Brain Mapp. 2021 May;42(7):1945-1951.
6. European Cooperation in Science and Technology (COST). COST Action GliMR releases video to underline the crucial importance of sharing medical data. AlphaGalileo. November 5, 2021. https://www.alphagalileo.org/. Accessed 08/11/2021.

Acknowledgments / Funding Information: This publication is part of the COST Action CA18206 Glioma MR Imaging 2.0, supported by COST (European Cooperation in Science and Technology). www.cost.eu | www.glimr.eu. We would like to thank all GliMR members involved with the translations of the script and web pages: Dr. Øystein Bech-Aase, Prof. Dr. Fran Borovečki, Irène Brumer, Dr. Marco Castellaro, Marta & Maite Calvo Imirizaldu, Prof. Dr. Marek Chmelík, Patricia Clement, Asen Cvetkov, Prof. Dr. Kyrre Emblem, Alexandros Ferles, Dr. Rémi Gau, Oliver Geier, Dr. Gilbert Hangel, Prof. Dr. Otto Henriksen, Prof. Dr. Radim Jančálek, Prof. Dr. Dominik Juskanič, Prof. Dr. Vasileios Katsaros, Vera Keil, Fodor Lucian, Dr. Camille Maumet, Dr. Henk Mutsaerts, Ruben Nechifor, Dr. Wibeke Nordhøy, Dr. Elli Paal, Beatriz Padela, Maria Pelechrini, Prof. Dr. Cyril Pernet, Dr. Jan Petr, Julie Prahl, Prof. Dr. Agnieszka Sabisz, Bárbara Schmitz Abecassis, Helena Singerová, Dipl. Ing. Prof. Dr. Magdalena Stoeva, Ivar Wamelink, Dr. Esther Warnert, Eleonora Zampilli, Vivi Zoteva. Additionally, we would like to thank all patients and caregivers involved in feedback from the International Brain Tumour Alliance: Emiel Duijn and Alexandra Duijn, Jorge A Silva, Karen Glerup, Kathy Oliver, Norbert Diehm. We also thank the Patiëntenadviesraad voor Wetenschappelijk Onderzoek UZ Gent. Finally, we thank all our GliMR members who were involved in the discussions about this project during our member meetings.

Figure 1 - Still from the video, illustrating the style of the animations.

Figure 2 - Screenshot from the animation video. Key words and sentences appear as on-screen text to increase clarity in situations during which no sound can be played, for example in a general practitioner's or hospital waiting room.

High-precision MR thermometry of RF heating in the upper thigh at 7T using a multi-echo water-fat separation model

M.W.I. Kikken[1], B.R. Steensma[2], C.A.T. van den Berg[2], and A.J.E. Raaijmakers[1]
[1]1Biomedical Engineering - Medical Imaging Analysis, Eindhoven University of Technology, Eindhoven, Netherlands;
[2]Center for Image Sciences - Computational Imaging Group, University Medical Center Utrecht, Utrecht, Netherlands

Synopsis: A multi-echo MRT approach is presented for application in RF safety assessment and validation of thermal simulations. By water-fat separation, more accurate determination of the drift field is possible. The method was tested in the thigh at 7T, using multi-transmit coils. Precision and accuracy were improved considerably compared to a previous single-echo fat-referenced method (precision: 0.09 vs 0.19 °C). Comparison of measured temperature distributions to simulated counterparts show good relative agreement in three subjects for multiple RF shim settings. Strikingly, simulated heating magnitudes mostly underestimated the observed heating with varying extent, suggesting a role for subject-specific parameters, such as perfusion.

Introduction

Current guidelines[1] on RF safety in MRI are based on specific absorption rates (SAR); which does not necessarily correlate with local temperature increase[2-4]. Therefore, more insight into local temperature elevations would be highly desirable. Similar to SAR, temperature rise in MRI can be simulated. Unfortunately, these simulation models still lack solid validation[5]. MRI is capable of measuring the spatial distribution of temperature rise (MR thermometry, MRT). However, most studies on MRT show application for thermal treatments. Here, the temperature rise is considerable and often localized. Validation of thermal simulations of RF exposure requires much more precise and accurate MRT methods. First of all, compensation is required for the slow variation in field strength over time (drift field). These can be measured using field cameras[6], but this requires considerable investment. Alternatively, a fat-referenced approach[7] for drift field correction using the subcutaneous fat layer and near-harmonic 2D reconstruction[8] has been presented. However, this method (single-echo model) is highly sensitive to fat layer thickness. Ideally, not only the subcutaneous fat layer but all fat signal within the image should be used. This was demonstrated for focused ultrasound MRT, using multiple echoes to separate the water and fat signal to consequently retrieve drift fields and temperature rise[9,10]. The aim of this study is to apply the same method for measurement of RF heating. For this purpose, the method was adapted to include the Salomir method[8] within the iterative optimization (adapted multi-echo model). The resulting method was tested for the ability of measuring temperature rise in the thigh at 7T.

Results

The method as presented by Poorman et al.[10] is based on the acquisition of multi-echo images and a signal model (figure 1a). For our purpose, we replaced the basis of polynomials for the drift field by a basis of spherical harmonics. Additionally, adaptations were made to the initialization (figure 1a); where the drift field is first fitted using only regions with high fat content. Subsequently, a good initialization for the whole region of interest is acquired by applying the method of Salomir[8]. To test the adapted multi-echo model, MRT measurements were performed on the thigh and compared to thermal simulations.

Acquisition: MR scans were performed on a 7T system (Achieva, Philips Healthcare, Best, NL). Thigh imaging was performed in 3 subjects (3 male, age 22-42, BMI 18.4-24.9) where the leg was surrounded by 4 fractionated dipole antennas with receive loops (figure 1c)[11]. A subject-specific simulation model was generated for every subject and antennas were labeled with vitamin markers and placed in a plexiglass holder. For temperature measurement, spoiled 13-echo gradient echo MRT scans (TE_1 13.48 ms, $TE_{spacing}$ 0.66 ms, TR 30 ms, 2.1x2.1x8 mm^3 resolution, 170x170x8 mm^3 FOV, flip angle 11°, single-shot, cardiac triggered) were acquired for 300 dynamics (296-399 seconds): a baseline scan without heating and a heating scan, constituting a 10 kHz off-resonance block pulse to acquire an average power of 5.3 W per channel[12].

Simulations: After MRT, electromagnetic and thermal simulations (Sim4Life, ZMT, Zurich, CH) were performed on the Duke model[13]. The right thigh was replaced by a patient-specific model (figure 1d). Power and phase settings of individual channels were numerically optimized to ensure matching of measured and simulated |B1+|.

Discussion and conclusion

In the MRT images acquired without heating (figure 2), the lower temporal standard deviation over the slice demonstrates a considerably higher precision (0.09 vs 0.19 °C, averaged over all volunteers) for the adapted multi-echo model compared to the single-echo model. A similar comparison between both approaches is provided in figure 3, where reconstructed temperature and field drift distributions are shown after 300 dynamics with heating. A graph diagram of heating over time is provided for 4 voxel locations (figure 3b). Again, the precision for the adapted multi-echo model is superior. Also, the method is more accurate because of its superior drift field reconstruction; MRT scans in volunteer 3 without heating and volunteer 2 with heating clearly show a residual drift field for the single-echo correction. The results of subject-specific electromagnetic simulations show that simulated |B1+| distributions are in excellent agreement with measurements (figure 4a). Locations of heating hotspots (figures 4b/c) in measurements match with simulations in most slices and volunteers. However, the simulated heating magnitude mostly underestimates the observed heating, with the degree of underestimation varying between volunteers. The animated multi-slice heating over time (figure 5) shows the occurrence of hotspots in the bottom and top right leg regions.

Discussion and conclusion

We have adapted the multi-echo MRT methodology as presented by Poorman et al.[10] for measuring RF induced heating in MRI. The proposed method reaches higher precision and accuracy in comparison to a previous method[7,12]. This is achieved by multi-echo water-fat separation, enabling the method to assess drift field correction using the fat signal in every voxel which severely reduced the sensitivity to fat layer thickness. Future work will focus on application in other imaging targets such as brain or prostate. Also, the effect of gradient imperfections on local TE[14] and accounting for motion will be considered, which will most likely further improve precision. Finally, patient-specific perfusion properties will be explored in thermal simulations to find an explanation for the deviation in heating magnitude.

References

1. IEC. Medical electrical equipment. Part 2-33: particular requirements for the safety of magnetic resonance equipment for medical diagnosis. IEC 60601-2-33. 2015.
2. Murbach, M., Neufeld, E., Capstick, M., Kainz, W., Brunner, D. O., Samaras, T., ... & Kuster, N. (2014). Thermal tissue damage model analyzed for different whole-body SAR and scan durations for standard MR body coils. Magnetic resonance in medicine, 71(1), 421-431.
3. Simonis, F. F. J., Raaijmakers, A. J. E., Lagendijk, J. J. W., & van den Berg, C. A. T. (2017). Validating subject-specific RF and thermal simulations in the calf muscle using MR-based temperature measurements. Magnetic resonance in medicine, 77(4), 1691-1700.
4. Van Rhoon, G. C., Samaras, T., Yarmolenko, P. S., Dewhirst, M. W., Neufeld, E., & Kuster, N. (2013). CEM43° C thermal dose thresholds: a potential guide for magnetic resonance radiofrequency exposure levels?. European radiology, 23(8), 2215-2227.
5. Van den Brink, J. S. (2019). Thermal effects associated with RF exposures in diagnostic MRI: overview of existing and emerging concepts of protection. Concepts in magnetic resonance part b, 2019.
6. Le Ster, C., Mauconduit, F., Mirkes, C., Bottlaender, M., Boumezbeur, F., Djemai, B., ... & Boulant, N. (2021). RF heating measurement using MR thermometry and field monitoring: Methodological considerations and first in vivo results. Magnetic Resonance in Medicine, 85(3), 1282-1293.
7. Simonis, F. F., Petersen, E. T., Lagendijk, J. J., & van den Berg, C. A. (2016). Feasibility of measuring thermoregulation during RF heating of the human calf muscle using MR based methods. Magnetic resonance in medicine, 75(4), 1743-1751.
8. Salomir, R., Viallon, M., Kickhefel, A., Roland, J., Morel, D. R., Petrusca, L., ... & Gross, P. (2011). Reference-free PRFS MR-thermometry using near-harmonic 2-D reconstruction of the background phase. IEEE transactions on medical imaging, 31(2), 287-301.
9. Grissom, W. A., Rieke, V., Santos, J., Swaminathan, A., Pauly, J., Pauly, K. B., & McConnell, M. (2010). Hybrid referenceless and multi-baseline subtraction thermometry for monitoring thermal therapies in the heart. Journal of Cardiovascular Magnetic Resonance, 12(1), 1-2.
10. Poorman, M. E., Braškutė, I., Bartels, L. W., & Grissom, W. A. (2019). Multi-echo MR thermometry using iterative separation of baseline water and fat images. Magnetic resonance in medicine, 81(4), 2385-2398.
11. Steensma, B. R., Voogt, I. J., Leiner, T., Luijten, P. R., Habets, J., Klomp, D. W., ... & Raaijmakers, A. J. (2018). An 8-channel Tx/Rx dipole array combined with 16 Rx loops for high-resolution functional cardiac imaging at 7 T. Magnetic Resonance Materials in Physics, Biology and Medicine, 31(1), 7-18.
12. Steensma, B. R., van den Berg, C. A., and Raaijmakers, A. J., "Towards high precision thermal based RF safety assessment with cardiac triggered MR thermometry."
13. Christ, A., Kainz, W., Hahn, E. G., Honegger, K., Zefferer, M., Neufeld, E., ... & Kuster, N. (2009). The Virtual Family—development of surface-based anatomical models of two adults and two children for dosimetric simulations. Physics in Medicine & Biology, 55(2), N23.
14. Simonis, F. F., Petersen, E. T., Bartels, L. W., Lagendijk, J. J., & van den Berg, C. A. (2015). Compensating for magnetic field inhomogeneity in multigradient-echo-based MR thermometry. Magnetic resonance in medicine, 73(3), 1184-1189.

Acknowledgments / Funding Information: No acknowledgement found

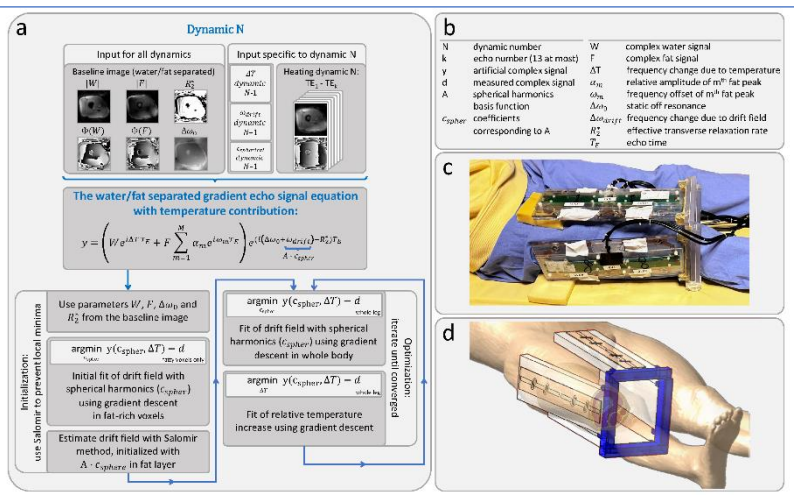

Figure 1: Schematic representation of the method to iteratiely solve temperature and drift components from the gradient echo signal equation (a). Parameter definitions are provided in (b). Essential adaptation with respect to the original method[10] is that Salomir's algorithm[8] is applied during initialization to prevent local minima caused by diffusive RF heating. Experimental imaging setup (c) where the antennas are placed in the plexiglass holder, and corresponding setup in the simulation environment (d) where the patient-specific mode is merged with the Duke model.

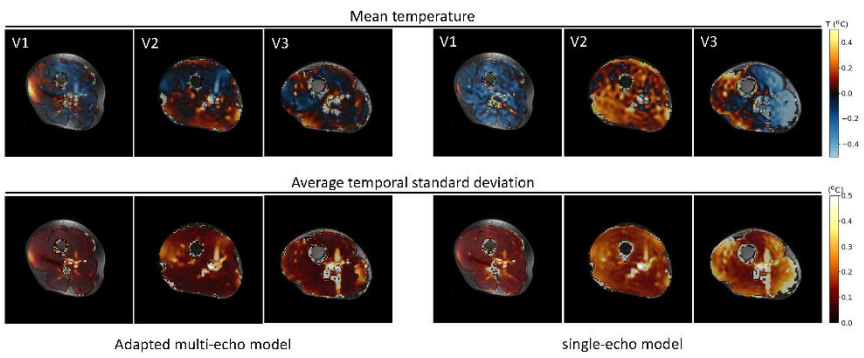

Figure 2: Spatial temperature maps without heating averaged over 300 dynamics in 3 volunteers (V1, V2 and V3) with various fat layer thicknesses; relative temperature maps were calculated both with the adapted multi-echo and the single-echo model. For each volunteer and model, a corresponding spatial map of temporal standard deviation is provided.

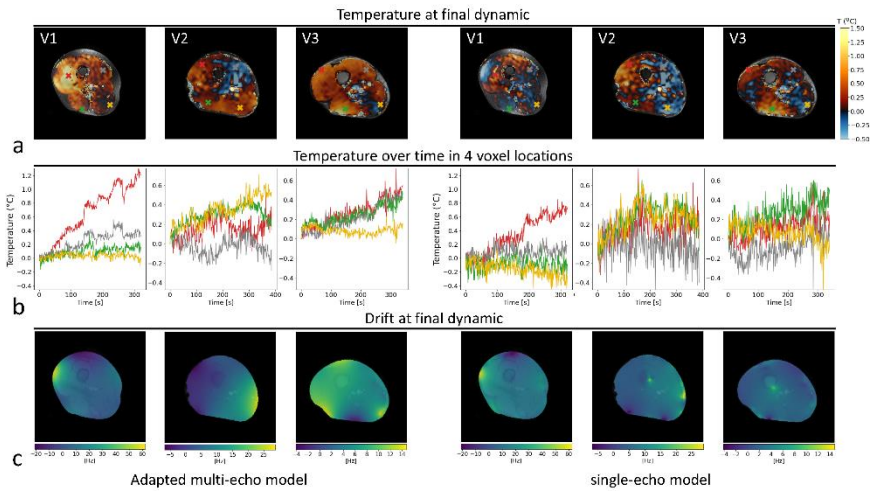

Figure 3: Spatial temperature maps after 319-385 seconds of heating with 5.3 W per channel in 3 volunteers (V1, V2 and V3) (a); relative heating maps were calculated both with the adapted multi-echo and single-echo model. A corresponding time series (b) is provided for the indicated voxel locations. The calculated drift field at the end of the series is indicated in (c).

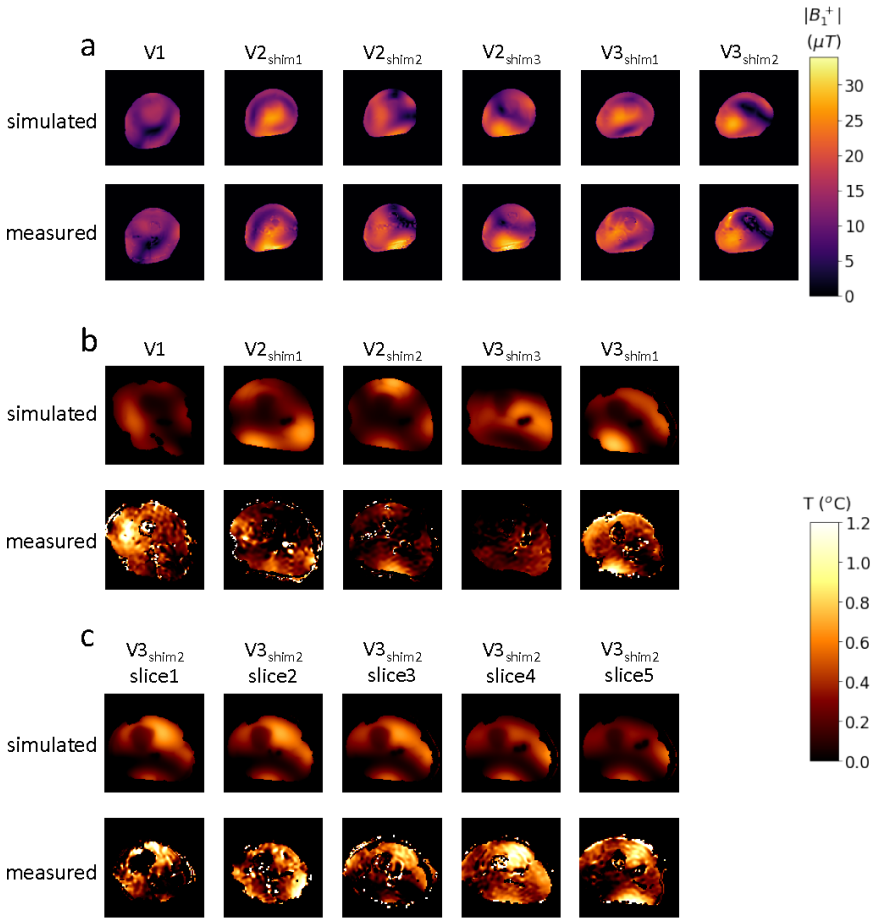

Figure 4: Measured |B1+| distributions and simulated counterparts in the central slice of 3 volunteers (a). Measured spatial heating distribution after 300 dynamics and their simulated counterparts in the central slice (b). Heating scan in volunteers 2 and 3 were performed with three and two different shim settings, respectively. For volunteer 3, the data of shim 2 was recorded with a multi-slice acquisition, for which simulated heating distributions are also provided in the corresponding slices (c).

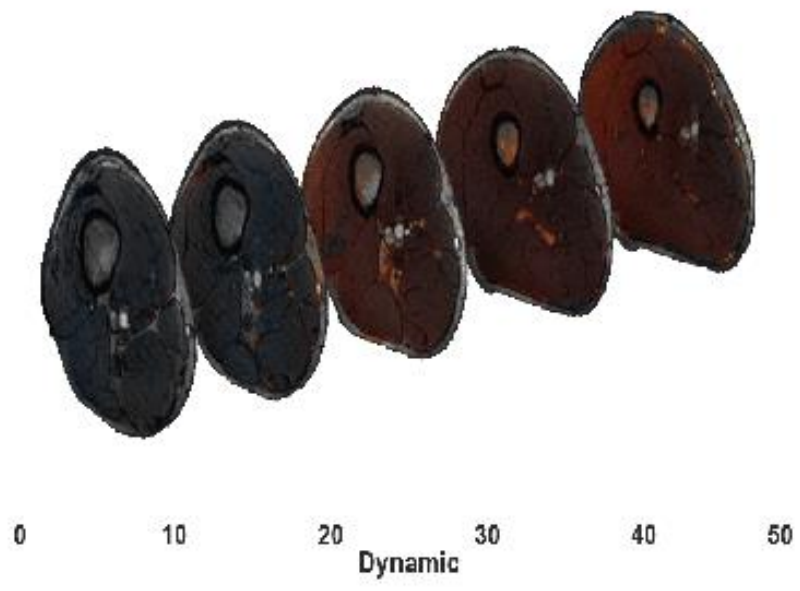

Figure 5: Animated gif representing heating distributions over a time period of 340 seconds in five 8 mm slices (slice gap of 10 mm). Heating hotspots are clearly visible in the top right and bottom region of the leg. The central slice shows the most gradual temperature increase, which is where the algorithm is most confident.

Retrospective correction of B1 field inhomogeneities in T2w 7T prostate patient data

S.D. Harrevelt[1], D. Reesink[2], A. van Lier[3], R. Meijer[3], J. Pluim[1], A.J.E. Raaijmakers[1]
[1]TU Eindhoven, Eindhoven, Netherlands; [2]Meander Medisch Centrum, Amersfoort, Netherlands, [3]UMC Utrecht, Utrecht, Netherlands

Synopsis: Prostate imaging at ultra-high fields is heavily affected by B1 field induced inhomogeneities. This not only results in unattractive images but it also might affect clinical diagnosis . To remedy this we developed a deep learning model that retrospectively corrects for the bias field. We applied this model to a clinical data set and demonstrated its performance in a qualitative manner. The results indicate that the model is able to drastically reduce the inhomogeneities in a variety of cases while the tissue contrast is generally maintained and the underlying anatomy has been successfully recovered.

Purpose: T2w prostate imaging at 7T has potential for clinical purposes because of its superior resolution and enhanced tissue contrast. In addition, the modality is indispensable for lesion localization in (X-nuclei) MR spectroscopy. However, the images suffer from B1 field induced inhomogeneities. B1 shimming[1] , TIAMO[2] and parallel transmit[3] are techniques that can reduce but not avoid these inhomogeneities. Although the imaging target can be clearly depicted, the surrounding signal voids and overall transmit and receive field inhomogeneity clearly reduce the attractiveness for clinical users. In addition, inhomogeneities may hinder the detection of anomalies and automatic image post processing methods such as segmentation become more difficult[4,5]. Reduction of these inhomogeneities is expected to improve usability and facilitate the adoption of 7T for clinical body imaging applications. For this purpose, we present a deep-learning approach to retrospectively correct 7T prostate images to alleviate the B1-field induced signal inhomogeneities.

This work is a continuation of previous work where a neural network was trained to correct multi channel acquisitions of inhomogenous prostate images[6]. With the current extension we enable retrospective application on existing clinical data sets. The performance of this approach is tested on T2w 7T images from 14 prostate cancer patients.

Methods: We consider the 7T image as the product of the underlying homogeneous image and a distribution of B1-field induced inhomogeneities, which we call the bias field. The method was developed for prostate images obtained with a transmit-receive array of eight fractionated dipole antennas[7]. We have created a training data set that mimics T2w prostate images at 7T using homogeneous clinical prostate images at 1.5T and simulated B1 field distributions at the 7T Larmor frequency, see Figure 1. A ResNet architecture and a Perceptual Style Loss were used for training, where the goal of the training was to predict the bias field from the artificial 7T input image. To obtain a bias field corrected image during inference we divide the input image by the predicted bias field from the trained neural network. This approach was preferred over predicting a homogeneous image directly to avoid that the network would be trained to fill signal voids with 'invented' tissue structures.

The trained network was applied retrospectively to T2w 7T images of 14 prostate cancer patients (age 48-72). The TSE acquisition was obtained with an RF coil array setup with eight transmit/receive fractionated dipole antennas and sixteen receive-only loop coils. A repetition time of 10s, and a TE of 140ms was used with a reconstructed pixel size of 0.28x0.28x3mm.

Results: Figure 2 displays the original and corrected images. Generally speaking, the corrected images from the deep learning model show a drastic decrease of inhomogeneity without significantly altering the contrast between fat- and muscle tissue, or of the prostate tissue itself. In mild cases, such as example 1, 5, 8 and 9, we notice an almost complete removal of the bias field and recovery of the underlying anatomy. Whereas more severe cases, where RF shimming was performed poorly such as example 11, 12 and 13, the model has difficulty in recovering the underlying anatomy and returns noise instead.

In Figure 3 we present a close-up of the same images to accurately asses the quality of the biasfield reduction around the prostate. Here we notice that in example 2, 4, 6, 12, and 14 our method is able to recover obscured parts of the peripheral which is important for asessment of extraprostatic extension.

Moreover, in example 2, 4, 6, 7 and 14 we see a great enhancement of the edges at the rectum wall, although sometimes these enhancements are accompanied by an overcompensation resulting in bright regions inside the rectum.

Discussion: The proposed method clearly improves the prostate images. B1-field induced inhomogeneities in signal intensity are removed almost completely. Please note that the method only corrects for global signal inhomogeneity but does not restore loss of local contrast because of suboptimal flip angles. As expected, the choice for the bias field as network output ensures that areas with low signal intensity have been corrected by noise amplification and not by a plausible but imaginary anatomy structure. In addition, in most cases the model does not affect tissue contrast however sometimes it does enhance the contrast of the prostate tissue as shown in example 4, 8 and 13. Remarkably, these patient images were acquired with a 24 element receive array while the method was trained on 8-channel receive fields, which apparently does not affect the performance. Note that the images were acquired in a realistic clinical work flow which sometimes resulted in suboptimal B1 shimming, e.g. 10, 11 and 12. Future work will investigate the apparent improvement in clinical usability by expert rating.

Conclusion: We have developed a method that is able to retrospectively correct the B1-field induced inhomogeneities in T2w prostate images at 7T. The model was trained on an artificial 7T data set by combining a set of clinical T2w 1.5T prostate images with simulated B1 field distributions at 7T. The model was tested using T2w 7T images from 14 prostate cancer patients. Corrected images are drastically improved with much less signal inhomogeneities while signal contrast throughout the image is preserved.

References:

1. Roemer, Peter B., et al. "The NMR phased array." *Magnetic resonance in medicine* 16.2 (1990): 192-225.

2 Orzada, Stephan, et al. "RF excitation using time interleaved acquisition of modes (TIAMO) to address B1 inhomogeneity in high-field MRI." *Magnetic Resonance in Medicine* 64.2 (2010): 327-333.

3 Rietsch, Stefan HG, et al. "Parallel transmit capability of various RF transmit elements and arrays at 7T MRI." *Magnetic resonance in medicine* 79.2 (2018): 1116-1126.

4. Chen, Jingyun, Louisa Bokacheva, and Henry Rusinek. "Image Segmentation and Nonuniformity Correction Methods." *3D Printing for the Radiologist*. Elsevier, 2022. 31-43.

5. Despotović, Ivana, Bart Goossens, and Wilfried Philips. "MRI segmentation of the human brain: challenges, methods, and applications." *Computational and mathematical methods in medicine* 2015 (2015).

6. S. Harrevelt, L. Wildenberg, D. Klomp, C.A.T. van den Berg, Josien Pluim, and Alexander Raaijmakers. "Reduction of B1-field induced inhomogeneity for body imaging at 7T using deep learning and synthetic training data.". ISMRM 2021 (2021)

7 Raaijmakers, Alexander JE, et al. "The fractionated dipole antenna: A new antenna for body imaging at 7 T esla." *Magnetic resonance in medicine* 75.3 (2016): 1366-1374

Acknowledgments / Funding Information: Continue on this line

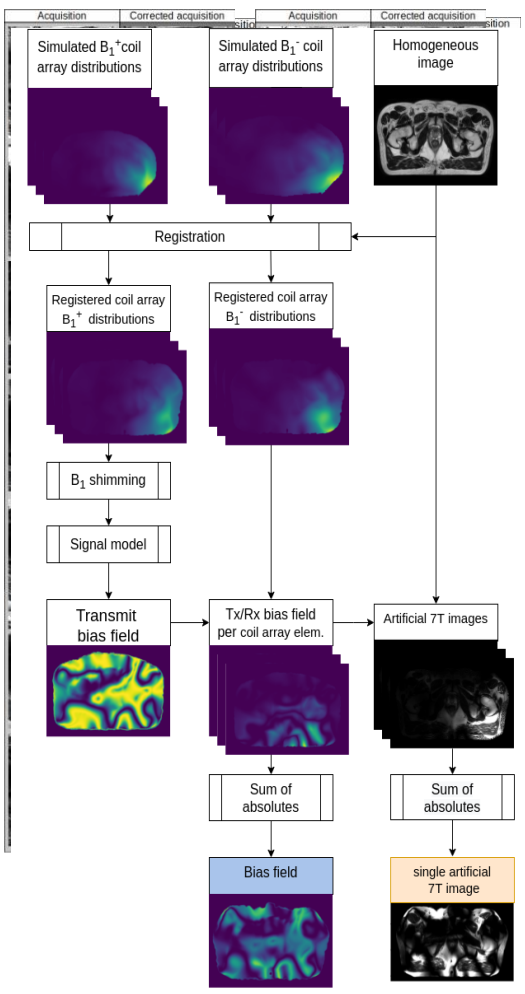

Figure 1: Results of the B1 field inhomogeneity correction on T2w 7T images of 14 prostate cancer patients. Figure presents images as obtained from the scanner accompanied by the corrected images. For each patient, only the center slice was depicted to demonstrate the performance of our model.

Figure 2: Close up of the images as presented in figure 2. This view enables more close examination of the performance of the model in the periphery of the prostate and the internal tissue structures of the prostate.

Figure 3: Schematic representation of the pipeline for creating artificial training data. Simulated 7T B1 elds of the coil array are registered to the body contour of the 1.5T prostate image, followed by a RF shimming routine on the B1+ coil distributions. Secondly, the obtained transmit eld is input to a signal model to imitate the signal of a TSE scan. By multiplying the obtained signal with the registered receive sensitivities (B1- fields) we obtained the bias eld per coil. Note that the sum-of-magnitude bias eld, in the blue colored box, is used as target image for the deep learning model. The sum-of-magnitude artificial 7T image, also in the blue colored box, is used as input image for the deep learning model

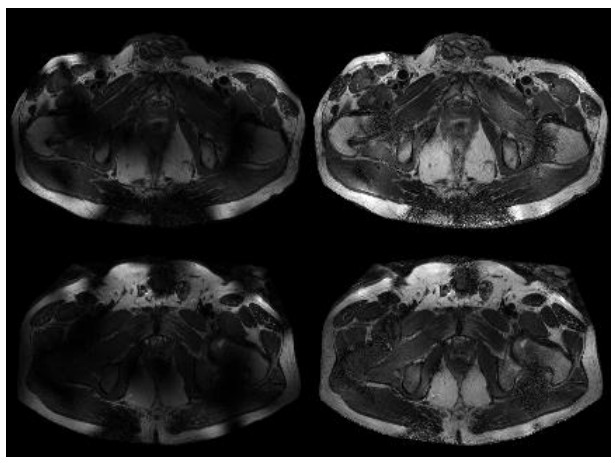

Figure 4: Animated representation of inhomogeneity correction over all slices of two selected patients

Investigating Spiral Arterial Spin Labeling with Pulseq and Field Monitoring at 7T

R. E. Ma[1], D. Ivanov[1], R. Huber[1], D. Kurban[1], B. A. Poser[1]

1, Maastricht Brain Imaging Centre (MBIC), Faculty of Psychology and Neuroscience, Maastricht University, Maastricht, the Netherlands

Synopsis: We developed several ASL sequences at 7T with a FAIR-QUIPSS II labeling scheme and various spiral readout strategies using *Pulseq*. Iterative algebraic image reconstruction was performed with CG-SENSE, using the field evolution data measured with external NMR probes. Robust performance in detecting brain's perfusion signal was observed in 2D single- and multi-band spiral acquisitions especially at relatively high spatial resolution, without the requirement for a longer scan time. 3D spiral acquisition showed reduced contrast level in perfusion maps and requires further investigation and optimization.

Investigating Spiral Arterial Spin Labeling with Pulseq and Field Monitoring at 7T

Purpose: *Pulseq*[1] is an open-source MR pulse sequence development package with direct access to all elements in MR sequences including RF pulses, gradients, ADCs and triggers, without going through the time-consuming vendor-specific sequence programming to investigate sequence behavior. Field monitoring with additional NMR probes[2] enables high-fidelity measurement of the gradient performance and therefore field correction during image reconstruction. In this study, combining the two techniques, we aimed at developing and implementing Arterial Spin Labeling (ASL) acquisitions to investigate the possibility of improving the quality of the measured perfusion signal by comparing perfusion maps from various spiral readout strategies.

Methods: FAIR-QUPISS II labeling module using a tr-FOCI inversion pulse[3] was implemented for the spiral ASL sequence using *Pulseq* in *Matlab* (The MathWorks, Inc.). The sequence diagram is shown in Fig.1.

Two resolution levels, denoted as low-res ($8.82mm^3$) and high-res ($2.43mm^3$), were chosen following an earlier study[4]. 2D single-band and multi-band CAIPI-sampled spiral[5], and 3D stack-of-spirals (SOSP) acquisitions were investigated. The acquisition parameters are listed in Fig.2. For 2D acquisitions, slices were acquired in the ascending order without gap between the neighboring slices. Same number of repetitions was measured for all acquisition strategies to facilitate the comparison afterwards. The sequences designed using *Pulseq* were compiled using a vendor-specific interpreter and executed on a 7T whole body Siemens scanner (Siemens Healthineers, Erlangen, Germany) with a 1x32 channel head coil (Nova Medical, Wilmington, MA, USA). One participant was tested with all acquisition strategies.

Field monitoring was performed after image acquisition with 16 F^{19} NMR probes (Skope, Zurich, Switzerland) placed at the iso-center of the scanner. Examples of measured 1st order field evolution are shown in Fig. 3. GPU-accelerated algebraic reconstruction with field correction of up to 2nd order based on SENSE model[6] was programmed in Matlab. Retrospective motion correction was performed using the realign function from *SPM* (SPM12, www.fil.ion.ucl.ac.uk/spm/software/spm12/). tSNR maps were computed for quality control. Relative Perfusion-weighted (PW) images, calculated as the difference between label and control images normalized to control images, were generated to evaluate the performance of perfusion signal detection for every encoding scheme.

Results:

Examples of reconstructed control images from every acquisition scheme with the corresponding tSNR maps are shown in Fig.4. High-res acquisitions showed more clearly delineated tissue boundaries compared to the low-res acquisitions. 3D SOSP acquisitions showed lower tSNR compared to that of 2D. As expected, due to 74% decrease in voxel size and 56% increase in undersampling factor, the tSNR of the high-res acquisitions was significantly lower than that of low-res acquisitions.

Fig. 5 shows the relative PW images from various acquisitions. With our parameter settings, the 3D high-res acquisition showed very noisy perfusion signal without distinguishable difference between grey and white matter and was therefore not included in the figure. Low-res single-band and multi-band acquisitions both showed perfusion signal nicely following the grey matter. Higher contrast level was seen in the multi-band images. 3D low-res acquisitions yielded similar spatial distribution of perfusion signal but with slightly lower contrast level and less blurring. The advantage of high-res acquisition can be observed in the PW images from the 2D single-band acquisitions with spatially more clearly resolved perfusion signal, albeit with a higher noise level. In addition, the 2D high-res acquisition showed the highest contrast level among all examined cases.

Discussion and Conclusion:

In this study, using *Pulseq* and field monitoring, we successfully implemented FAIR-QUIPSS II ASL acquisitions and reconstructions with spiral readouts. Different levels of resolution with 2D and 3D spiral sampling were investigated. High resolution perfusion-weighted signals were obtained with the 2D acquisition. Higher tSNR is seen in 2D acquisitions likely due to reduced physiological noise compared to the 3D scenario. The measured perfusion signal, however, showed a more complicated pattern following the change in acquisition scheme. The high perfusion signal in the 2D high-res acquisition could be linked to reduced partial volume effects. The very low contrast level in the high-res 3D acquisition compared to its 2D counterpart requires further investigation. The long readout time in the 3D approach, i.e., 24 times as long as the 2D acquisition for each slice with our parameters, could result in larger physiological noise and larger dynamic change of the local magnetic field during the imaging period. Future investigation on optimizing the 3D acquisitions shall include approaches such as reducing the imaging time per volume, flip angle optimization schemes and different sampling orders in the slice direction.

References:

1, Layton KJ, Kroboth S, Jia F et al. Pulseq: A rapid and hardware-independent pulse sequence prototyping framework. Magn Reson Med. 2016;77(4):1544-1552.

2, Barmet C, De Zanche N, Pruessmann KP. Spatiotemporal magnetic field monitoring for MR. Magn Reson Med. 2008;60:187-197.

3, Ivanov D, Poser BA, Huber L. et al. Optimization of simultaneous multislice EPI for concurrent functional perfusion and BOLD signal measurements at 7T. Magn Reson Med. 2017; 78(1): 121-129.

4, Ivanov D, Gardumi A, Haast RAM. et al. Comparison of 3T and 7T ASL techniques for concurrent functional perfusion and BOLD studies. NIMG. 2017;156:363-376

5, Zahneisen B, Poser BA, Ernst T. et al. Simultaneous multi-slice fMRI using spiral trajectories. NIMG. 2014; 92:8-18.

6, Wilm BJ, Barmet C, Pavan M. et al, Higher order reconstruction for MRI in the presence of spatiotemporal field perturbations. Magn Reson Med. 2011;65:1690-1701.

7, Hurley AC, Al-Radaideh A, Bai L, et al. Tailored RF pulse for magnetization inversion at ultrahigh field. Magn Reson Med. 2010;63(1):51-58.

8, Wong EC, Buxton RB, Frank LR. Quantitative imaging of perfusion using a single subtraction (QUIPSS and QUIPSS II). Magn Reson Med. 1998;39(5):702-708.

Acknowledgments / Funding Information: The study was supported by funding from Dutch Research Council with NWO VIDI grant 16.Vidi.178.052 (REM, DK, BAP), NWO VENI project 016.Veni.198.032 (RH), and European Research Council H2020 FET-Open AROMA grant agreement no. 88587 (BAP).

Fig. 1 Sequence diagram of FAIR-QUIPSS II ASL acquisition. The tr-FOCI inversion[7], QUIPSS II[8] saturation and imaging units are color-coded as red, purple and green, respectively, as also depicted in the images on the right for both label and control cases.

Low-res	High-res
Acquisition strategies	
2D single-band 2D multi-band 3D stack-of-spirals	2D single-band 3D stack-of-spirals
Voxel size (mm)	
(2.10 x 2.10) x 2 *(8.82 mm³)*	(1.25 x 1.25) x 1.5 *(2.34 mm³)*
In-plane undersampling factor	
1.6	2.5
Imaging slab thickness	
48mm	36mm
Common parameters	
TR/TI1/TI2/TE = 3000/700/1800/4.1 ms Echo Train Length = 25.60ms (10240 points) 50 control-label pairs Flip Angle = 60 (2D) , 10 (3D) BWTP of excitation pulse = 4.2 (2D), 25 (3D) Acquisition time: 5:00 min	

Fig. 2 Acquisition parameters for all spiral ASL acquisitions investigated in the study. In-plane resolution was calculated according to the measured FOV in k-space.

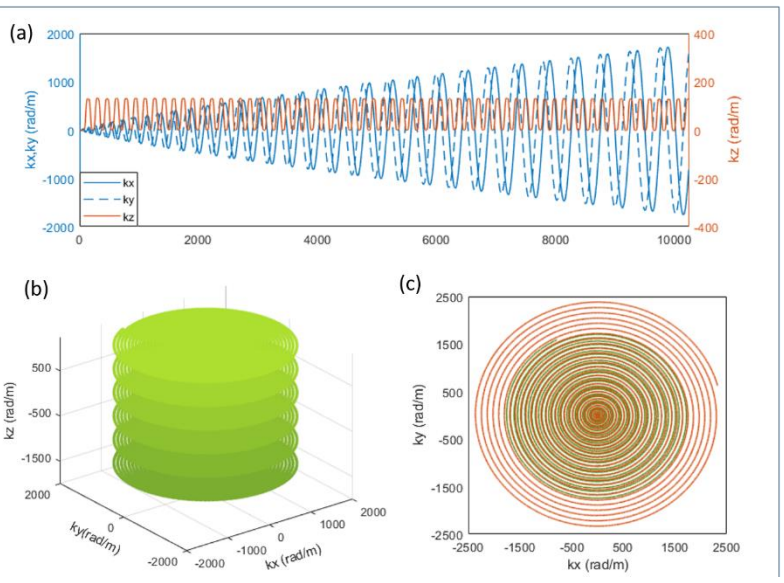

Fig. 3 Examples of measured 1st order field evolution from (a) multi-band low-res acquisition (orange kz refers to CAIPI shifting), (b) 3D stack-of-spiral acquisition and (c) low-res (green) and high-res (red) acquisition projected on kx-ky plane.

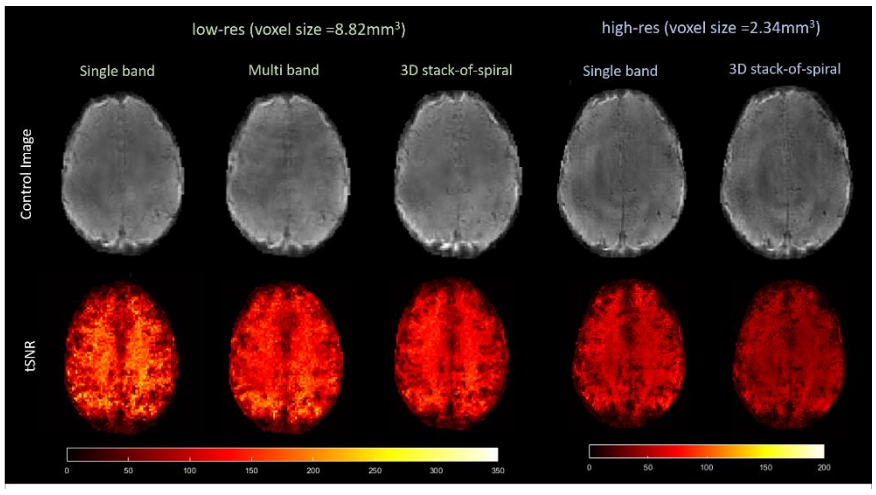

Fig. 4 Examples of control images (top row) and tSNR maps (bottom row) from low and high resolution acquisitions with various spiral encoding strategies.

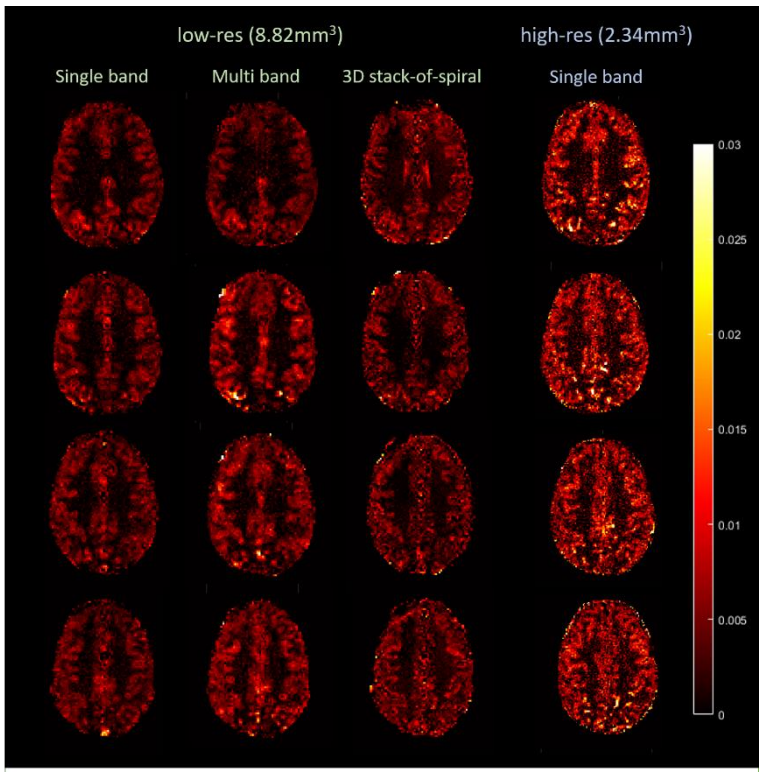

Fig. 5 Relative perfusion-weighted images from various acquisition strategies. The results from high-res 3D stack-of-spiral acquisition are not shown due to the very low contrast-to-noise ratio.

Spin-echo line-scanning at 7T

Luisa Raimondo[1], Tomas Knapen[1,2], Serge O. Dumoulin[1,3], Wietske van der Zwaag[1] and Jeroen C.W Siero[1,4]

[1]Spinoza Centre for Neuroimaging, Amsterdam, Netherlands, [2]VU University, Amsterdam, Netherlands, [3]Experimental and Applied Psychology, VU University, Amsterdam, Netherlands, [4]Radiology, University Medical Centre Utrecht, Utrecht, Netherlands

Synopsis: We implemented spin-echo line-scanning (SELINE) fMRI through a simple rotation of the spin-echo refocusing gradient to a plane perpendicular to the excited slice and removing the phase encode gradient. This technique promises a combination of high spatio-temporal resolution and specificity of functional responses to the microvasculature. We compared SELINE data to the corresponding gradient-echo version (GELINE). We demonstrate that SELINE showed much improved line selection compared to GELINE, albeit at the cost of a significant drop in functional sensitivity. The low functional sensitivity needs to be addressed before SELINE can be applied.

Summary of Main Findings: Spin-echo line-scanning (SELINE) fMRI promises a high spatiotemporal resolution in combination with specificity to microvasculature. SELINE showed much improved line selection compared to GELINE, at the cost of a drop in sensitivity.

Introduction: Neurons cluster into sub-millimeter columnar and laminar structures and neural activity occurs at millisecond resolution. The recently described gradient-echo line-scanning (GELINE) sequence achieved very high resolution in humans[1,2] across cortical depth (250µm) and time (~200ms), by sacrificing volume coverage and resolution along the cortical surface. This high spatiotemporal resolution, when combined with a method specific to microvasculature, would allow us to isolate microvessel responses and to characterize the distribution of blood flow and laminar fMRI profiles across cortical depth. Spin-echo (SE) BOLD contrast is ideal for this purpose, since it is the technique that is most dominated by microvasculature signal changes[3]. Moreover, spin-echo line-scanning (SELINE) offers beam excitation without the outer-volume suppression (OVS) pulses, which are necessary in the case of GELINE, through a simple rotation of the plane for the refocusing gradient, to a perpendicular plane. Here, we present the first implementation of SELINE for BOLD fMRI in humans at 7T. We compared the performance of SELINE with a GELINE acquisition in term of temporal signal-to-noise ratio (tSNR) and BOLD sensitivity.

Methods: We scanned 4 healthy participants at 7T MRI system (Philips, Netherlands) equipped with a 2Tx/32Rx head coil (Nova Medical, USA) and 1 participant with an 8Tx/32Rx. In addition, multiple pilots were conducted to optimize the parameters used here (Fig.1). We modified a 2D spin-echo sequence for the SELINE data acquisition (Fig.2a) where the phase-encoding in the direction perpendicular to the line was turned off: line resolution=250µm, TR=500ms, TE=50ms, fa=146°, array size=720, line thickness=2.5mm, in-plane line width=5mm, fat suppression using SPAIR. The 180° refocusing pulse was a sinc pulse with duration of 2.8ms and its gradient was moved to the phase encoding direction, to refocus only a single beam of the excited slice (Fig.2b). Pairs of crusher gradients (25mT/m, duration=1.9ms) were added around the refocusing gradient in every direction, to avoid free induction decay artefacts, while spoilers introduced at the end of the sequence eliminated residual transverse magnetization. GELINE data acquisition was based on the method we previously described[1], i.e. using OVS pulses for line excitation. A TR of 500ms, however, was used to match the SELINE acquisition. SELINE and GELINE data were reconstructed as described in Raimondo et al(1), and we also applied a NORDIC-based denoising step[4,5]. For both acquisitions, the line was positioned perpendicular to the visual cortex as much as possible. We acquired one run of functional data with each protocol, using a block design visual task consisting of a 20Hz flickering checkerboard, presented for 10s on/off. Runs lasted 6 minutes and 20s, starting with 10s baseline. For one subject 2 GELINE runs and 4 SELINE runs were acquired to increase the SNR. Functional data were analyzed using a general linear model (GLM) approach. We also calculated the tSNR across the line. Additionally, we acquired matched 2D gradient-echo (GE) and SE-EPI image series at lower spatio-temporal resolution (1.5mm isotropic, TR=2.5s), to compare functional runs of single slices and line selection images with the same visual task.

Results: Fig.2 shows the SELINE sequence (a), the signal-yielding area (b), an example coronal slice (c), the line signal distribution (LSD) image (d), with signal coming from the intersection of excited and refocused planes, and an example line-scanning acquisition (e). In Fig.3a, a representative participant's LSD profile is shown for SE and GE acquisition, obtained by averaging over all the voxels in the read-out direction of an LSD image. Notice the much sharper profile of the SELINE. Fig.3b shows the tSNR for SELINE and GELINE for the same subject. SELINE tSNR values were consistently lower than GELINE tSNR, likely driven by TE as well as differences in the profile area. SELINE acquisitions yielded very low functional responses. Fig.4 shows the beta values obtained from the GLM of 1 run of SELINE (a) and GELINE (b) and for the average of respectively 2 and 4 runs (c and d), overlaid on the acquired slices for SE and GE. Finally, Fig.5 shows the activation maps of the SE and GE-EPI slices and LSD images. SE-EPI showed lower functional responses than GE-EPI, as expected[6]. LSD functional images confirmed good beam selection, but also highlight the limited available functional signal in SELINE.

Discussion & Conclusion: We reported the first implementation of SELINE in humans at 7T and showed improved line selection without the need for OVS pulses. The improved line definition, and also the inherently lower sensitivity of SE-BOLD, led to lower tSNR and beta values compared to GELINE. We could not detect any task-driven activation in the SELINE, while GELINE showed clear activation pattern in visual cortex. In the lower resolution functional images (Fig.5), activation is barely detectable on the SE-LSD images. The SELINE acquisition has even lower SNR due to the smaller voxel volume (1.8 times lower). Hence, we conclude that the implementation of SELINE currently lacks adequate sensitivity for line-scanning fMRI. We argue that SE has a high potential for line-scanning applications due to its innate properties of line selection and microvascular selective functional contrast. Future work will aim at improving the SELINE sensitivity by incorporating a multi-echo readout, high-density surface coils[7] and averaging across more than 4 runs.

References

1. Raimondo L, Knapen T, Oliveira Ícaro AF, Yu X, Dumoulin SO, van der Zwaag W, et al. A line through the brain: implementation of human line-scanning at 7T for ultra-high spatiotemporal resolution fMRI. J Cereb Blood Flow Metab, 2021

2. Morgan AT, Nothnagel N, Petro LucyS, Goense J, Muckli L. High-resolution line-scanning reveals distinct visual response properties across human cortical layers. biorxiv, 2020

3. Siero JCW, Ramsey NF, Hoogduin H, Klomp DWJ, Luijten PR, Petridou N. BOLD Specificity and Dynamics Evaluated in Humans at 7 T: Comparing Gradient-Echo and Spin-Echo Hemodynamic Responses. PLoS ONE, 2013

4. Vizioli L, Moeller S, Dowdle L, Akçakaya M, De Martino F, Yacoub E, et al. Lowering the thermal noise barrier in functional brain mapping with magnetic resonance imaging. Nat Commun, 2021

5. Passarinho C, Raimondo L, Heij J, Knapen T, Dumoulin S, Siero JCW, van der Zwaag W. Noise removal in Line-scanning fMRI. ESMRMB 2021

6. Han S, Eun S, Cho H, Uludağ K, Kim S-G. Improvement of sensitivity and specificity for laminar BOLD fMRI with double spin-echo EPI in humans at 7 T. NeuroImage, 2021

7. Petridou N, Italiaander M, van de Bank BL, Siero JCW, Luijten PR, Klomp DWJ. Pushing the limits of high-resolution functional MRI using a simple high-density multi-element coil design. NMR Biomed, 2013

Acknowledgments / Funding Information: This study was supported by the Royal Netherlands Academy of Arts and Sciences Research Fund 2018 (KNAW BDO/3489) and the Visiting Professors Programme 2017 (KNAW WF/RB/3781) granted to the Spinoza Centre for Neuroimaging.

Figures:

N transmit channels	scan mode	TR [ms]	TE [ms]	FA [deg]	BW [Hz/pixel]	fat suppression
2	2D	500	50	146	28.89	SPAIR
8	MS	300	40	148	28.95	SPIR
8	MS	200	50	154	28.95	SPIR
8	MS	190	43	154	28.95	SPIR
8	MS	190	40	154	28.95	SPIR
8	MS	355	40	146	28.95	SPAIR
8	MS	500	50	140	28.95	SPAIR

Fig.1: pilot sequence parameters for testing the optimal SELINE acquisition parameters. MS=multi-slice.

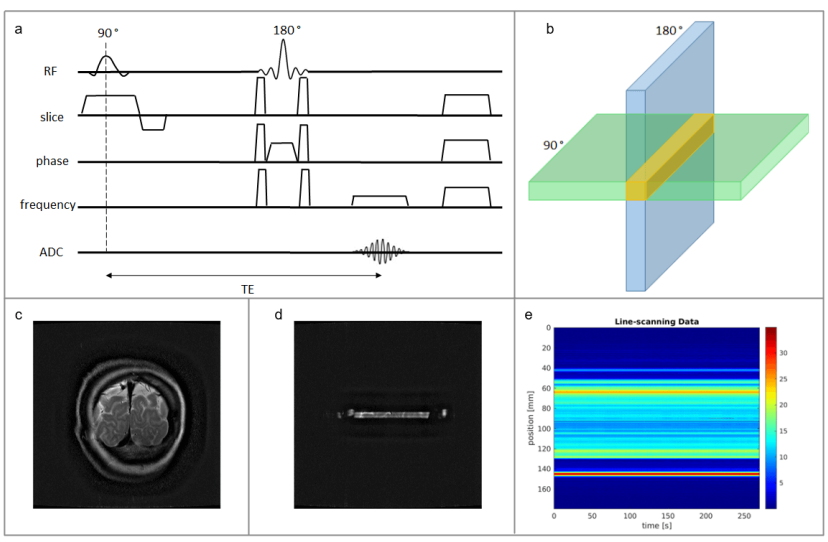

Fig.2: (a) SELINE sequence. Notice the absence of phase encoding gradients and the 2 different orientations of the 90° and 180° gradients to excite and refocus perpendicular planes (b), leading to a signal coming from a beam. (c) acquired slice with spin-echo sequence. (d) LSD image as result of the intersection of excited and refocused plane. (e) spin-echo line-scanning acquisition, plot of the signal versus position and time.

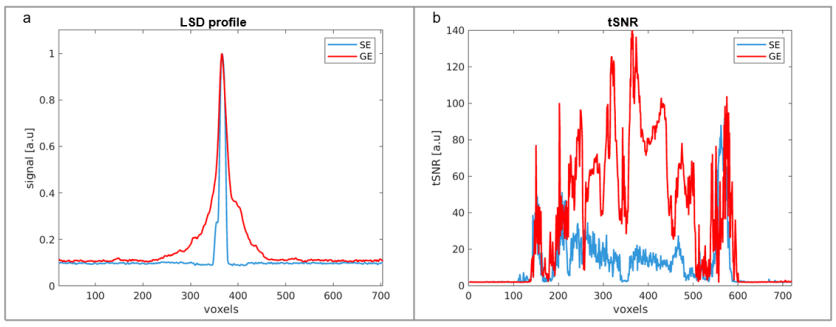

Fig.3: (a) normalized LSD profile for spin-echo (blue line) and gradient-echo (red line). Notice the improved line definition in SELINE. (b) tSNR for spin-echo line-scanning (blue line) and gradient-echo line-scanning (red line).

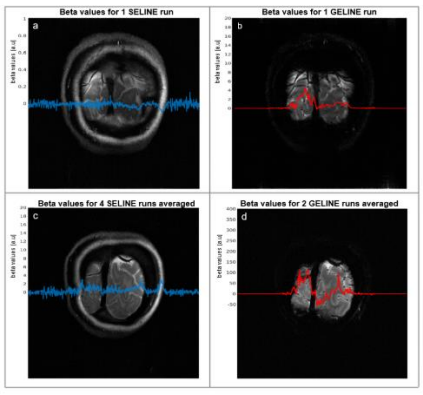

Fig.4: (a) Beta values for 1 SELINE acquisition, (b) 1 GELINE acquisition, (c) 4 runs average SELINE acquisition and (d) 2 runs average GELINE acquisition, overlaid on the acquired slices, in the same position as the line. Notice the different scaling for the four panels, and that (a,b) and (c,d) are 2 different representative participants.

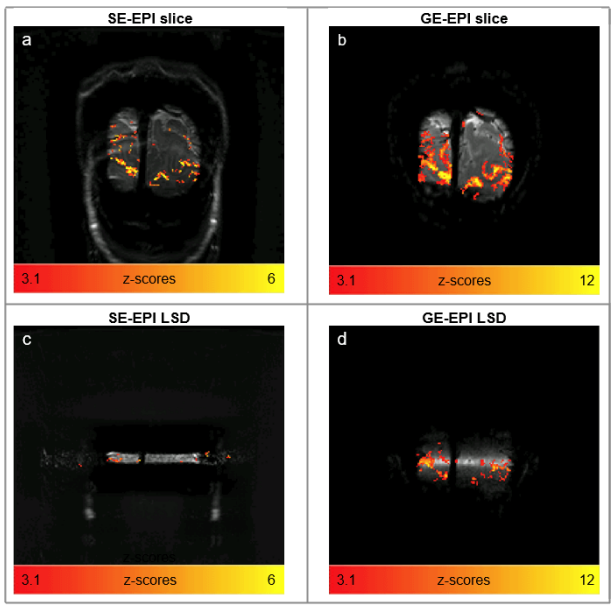

Fig.5: (a) z-scores for SE-EPI slice acquisition, (b) GE-EPI slice acquisition (c) SE LSD image acquisition and (d) GE LSD image. Spatial resolution is 1.5mm isotropic.

Whole-liver flip angle shimming at 7T using eight-channel parallel transmission kt-points pulses with FPE-DREAM B1+ mapping

B.A. Runderkamp[1], W. van der Zwaag[2], T. Roos[2], G.J. Strijkers[3], M.W.A. Caan[3], A.J. Nederveen[1]

[1]Department of Radiology and Nuclear Medicine, Amsterdam UMC, University of Amsterdam, Amsterdam, The Netherlands; [2]Spinoza Center for Neuroimaging, Amsterdam, The Netherlands; [3]Department of Biomedical Engineering and Physics, Amsterdam UMC, University of Amsterdam, Amsterdam, The Netherlands

Synopsis: Liver MRI could benefit from the increased SNR at 7T but suffers from severe flip angle inhomogeneity. In this work, eight-channel parallel transmission is used for flip angle shimming, comparing circularly polarized transmission and phase shimming with a kt-points pulse. Fourier phase-encoded DREAM is used for artifact-free B1+ mapping. With kt-points, the nominal flip angle of 8˚ could be achieved with homogeneous signal over the entire liver, while phase shimming only delivers a flip angle of approximately 4˚ with less homogeneity. Future work is directed towards use of universal slab-selective kt-points pulses to make 7T liver MRI clinically feasible.

Introduction: Liver MRI could benefit from the increased SNR at 7T. However, the B1+ wavelength decreases to abdominal dimensions at this field strength, causing flip angle (FA) inhomogeneity when using simple RF pulses in circularly polarized (CP) transmission. In this work, we use multi-channel parallel transmission for whole-liver FA homogenization comparing kt-points[1] and phase shimming. This necessitates artifact-free B1+ mapping, which was done using Fourier phase-encoded (FPE) DREAM[2,3].

Methods: Eight healthy volunteers were scanned with a 7T Philips Achieva scanner (Philips, Best, The Netherlands) using an eight-channel Tx/Rx fractionated dipole antenna body array[4] (MRCoils, The Netherlands, Figure 1c). For FPE-DREAM B1+ mapping, multiple B1+ measurements ('modes') are acquired with all channels emitting with continuously varying phase between modes according to $\exp\left(\frac{2\pi i(m-1)c}{M}\right)$, where m and c are the mode and channel number respectively and M is the total number of modes. In case M is higher than the number of channels, a weighting function is used to suppress unreliable measurements at low SNR from the overdetermined inverse problem[3]. After acquiring all modes, single-channel B1+ maps were calculated on-scanner which, together with a 2nd order B0-shimmed 3D-GRE, served as input for phase shimming and kt-points pulse calculation. To find the minimally necessary number of modes, a 35-year old male with a relatively high BMI of 28.4 was scanned with 8, 10, 13 and 16 modes. Figure 2a shows the eight-channel B1+ magnitudes and phases calculated using 13 modes and p=0.25, q=20 in the weighting function (eq. 9)[3]. Figure 2b shows single-channel B1+ magnitude maps calculated from these acquisitions. Based on these results, 13 modes were determined sufficient. Using those values, FA shimming was performed on seven volunteers (BMI 18.4-23.3, weight 50-78kg, age 26-34 years, 3 males). In volunteer 1-5, 3D-GRE scans were acquired using CP (45˚ phase increments between channels), phase shimming (except for volunteer 1) and kt-points. Additionally, intra- and inter-session kt-points repetitions were performed in four volunteers. The shimming volume-of-interest (VOI) encompassed the whole liver (see exemplary VOI in Figure 2, volunteer 5, kt-points). For phase shimming, the eight transmit-channel phase offsets were individually adapted to minimize the RF standard-deviation/(mean)^2 over the VOI, using the MRCodeTool toolbox (MRCode, The Netherlands). Kt-points pulses were calculated with five subpulses, max. blip strength = 33 mT/m, max. blip slew rate = 166 mT/m/ms and a maximum excitation k-space extent of 1/6 cm^{-1}. Channel RF amplitudes and phases and the 3D excitation k-space trajectory were calculated using an interleaved greedy-local optimization algorithm[5] in a home-built MRCodeTool extension[6] (Figure 1b). The kt-points pulses were non-selective, requiring large FOVs to cover the entire transmission volume of the antennae. All scans were acquired in a single breath-hold, as were all separate FPE-DREAM modes. Other scan settings are listed in Figure 1a. The scans were reconstructed offline using BART[7] and MRecon (Gyrotools, Zurich, Switzerland) in MATLAB. Receive B1 inhomogeneity was reduced using ANTs' N4BiasFieldCorrection[8]. Magnitude images and simulated FA distributions over the VOI were plotted to assess image quality.

Results: Figure 3 shows magnitude images in three orientations for volunteers 1-5 using CP, phase shimming and kt-points. CP shows clear signal dropouts, which are removed using phase shimming and kt-points. The kt-points scans show an increased overall contrast over phase shimming and CP. These results match with the simulations. They show that with both phase shimming and kt-points, the lowest FAs in CP can be increased, eliminating signal dropouts. Kt-points is able to deliver the nominal FA of 8˚ with a smaller FA range, while phase shimming only reaches a mean of ~4˚. The same behavior is seen in all five volunteers. Figure 4 shows good intra- and inter-session repeatability for volunteer 5. In volunteers 2 and 6, one of the scans showed signal dropouts, despite promising simulation results. Volunteer 7 reported breath-hold difficulties and showed varying B1 patterns.

Discussion: With FPE-DREAM, a homogeneous small-flip-angle whole-liver GRE can be acquired at 7T using kt-points pulses. With phase shimming, signal dropouts could be removed but with roughly half the nominal flip angle over the VOI. Occasionally, kt-points acquisitions give residual signal dropouts as shown in Figure 4. From volunteers 2 and 6 it follows that repeated acquisitions led to successful shimming, pointing at motion or inconsistent breath-holds as a possible cause. This would also explain signal dropouts in volunteer 7. The BMI values of volunteers in this study were quite low. However, Figure 2a shows that artifact-free B1+ maps and good simulation results could also be achieved on a volunteer with a higher BMI, which is promising for successful application of kt-points. This will be subject of future research, as will be the application of universal pulses[9] to avoid the time-consuming B1+ calibration phase. Finally, we intend to make the kt-points pulses slab-selective to enable smaller FOVs which, in combination with undersampling techniques like SENSE or CS[10], could increase spatial resolution.

Conclusion: With FPE-DREAM, we could acquire a homogeneous small-flip-angle whole-liver GRE at 7T using kt-points, with highly increased homogeneity and mean FA compared to phase shimming and CP.

References:

1. Cloos MA, Boulant N, Luong M, Ferrand G, Giacomini E, Le Bihan D, Amadon A. kT-points: short three-dimensional tailored RF pulses for flip-angle homogenization over an extended volume. Magn Reson Med. 2012;67(1):72-80. doi: 10.1002/mrm.22978.
2. Nehrke K, Versluis MJ, Webb A, Börnert P. Volumetric B1(+) mapping of the brain at 7T using DREAM. Magn Reson Med. 2014;71(1):246-56. doi: 10.1002/mrm.24667.
3. Tse DHY, Poole MS, Magill AW, Felder J, Brenner D, Jon Shah N. Encoding methods for B1(+) mapping in parallel transmit systems at ultra high field. J Magn Reson. 2014;245:125-32. doi: 10.1016/j.jmr.2014.06.006.
4. Raaijmakers AJE, Italiaander M, Voogt IJ, Luijten PR, Hoogduin JM, Klomp DWJ, van den Berg CAT. The Fractionated Dipole Antenna: A New Antenna for Body Imaging at 7 Tesla. Magn Reson Med. 2016;75:1366-1374. doi: 10.1002/mrm.25596
5. Grissom WA, Khalighi M, Sacolick LI, Rutt BK, Vogel MW. Small-tip-angle spokes pulse design using interleaved greedy and local optimization methods. Magn Reson Med. 2012;68(5):1553-62. doi: 10.1002/mrm.24165.
6. Roos T, Knapen T, van der Zwaag W. Reducing B1+ inhomogeneities in the brain at 7T: Pads or Parallel transmit? Proceedings of the 11th Annual Meeting ISMRM Benelux Chapter, 2019; Leiden, Netherlands
7. Uecker M. Berkeley Advanced Reconstruction Toolbox Target Audience: 2015;163(1991):25176. doi:10.1002/mrm.25176.
8. Tustison NJ, Avants BB, Cook PA, Zheng Y, Egan A, Yushkevich PA, Gee JC. N4ITK: Improved N3 Bias Correction. IEEE Trans Med Imag. 2010;29(6):1310-1320. doi: 10.1109/TMI.2010.2046908
9. Gras V, Vignaud A, Amadon A, Le Bihan D, Boulant N. Universal pulses: A new concept for calibration-free parallel transmission. Magn Reson Med. 2016;77(2):635-643. doi: 10.1002/mrm.26148
10. Lustig M, Donoho D, Pauly JM. Sparse MRI: The Application of Compressed Sensing for Rapid MR Imaging. Magn Reson Med. 2007;58:1182-1195. doi: 10.1002/mrm.21391.

a

Scan parameter	B0 map	B1 map (PE-DREAM)	CP/phase shimming/kt-points
Scan mode	3D GRE	Multislice GRE	3D GRE
FOV (mm) [RL,AP,FH]	[384,384,132]	[384,384,132]	[450,300,364]
Voxel size (mm) [RL,AP,FH]	[6,6,6]	[6,6,6]	[2.5,2.5,6.5]
In-plane recon. voxel size (mm)	6	6	1.76
TR/TE (ms)	4.0/1.41	4.0/0.99	4.0/2.1
Nominal flip angle	8°	20°	8°
Water-fat shift (pixels)	0.33	0.18	1.42
Scan duration (min:sec)	0:11.2	2:46.0 (12.8/mode × 13 modes)	0:21.1
SENSE	No	No	No
Echo train length	1	32	1
Delta TE (ms)	1	N.A.	N.A.
STEAM angle	N.A.	55°	N.A.
DREAM dT/TS	N.A	0.38/2.35	N.A.
STE TE (ms)	N.A.	1.37/-0.99/3.72	N.A.
Pulse shape			Non-selective block/ non-selective block/ kt-points scheme
Number of sub-pulses			1/1/5
Pulse duration (ms)			0.07/0.07/1.248-1.344
Nominal B1 amplitude/sub-pulse (µT)			7.41/7.41/varying

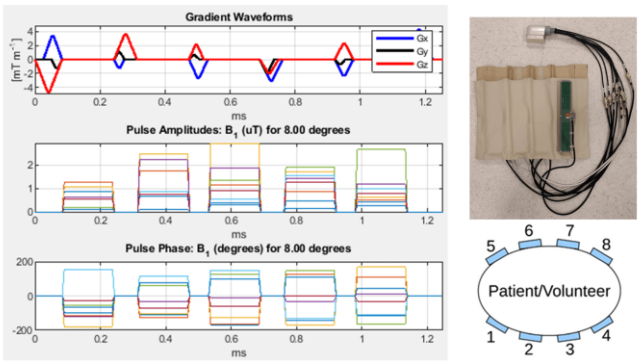

Figure 1: a) Scan parameters for B0 mapping, B1+ mapping and the scans using CP, phase shimming and kt-points. For scans utilizing kt-points, the echo time was defined as the time between the echo and the middle of the combination of sub-pulses. b) An exemplary (volunteer 2) kt-point pulse trajectory (gradient blip diagrams) and pulse amplitudes and phases. c) The eight-channel fractionated dipole antenna body array used for parallel transmission.

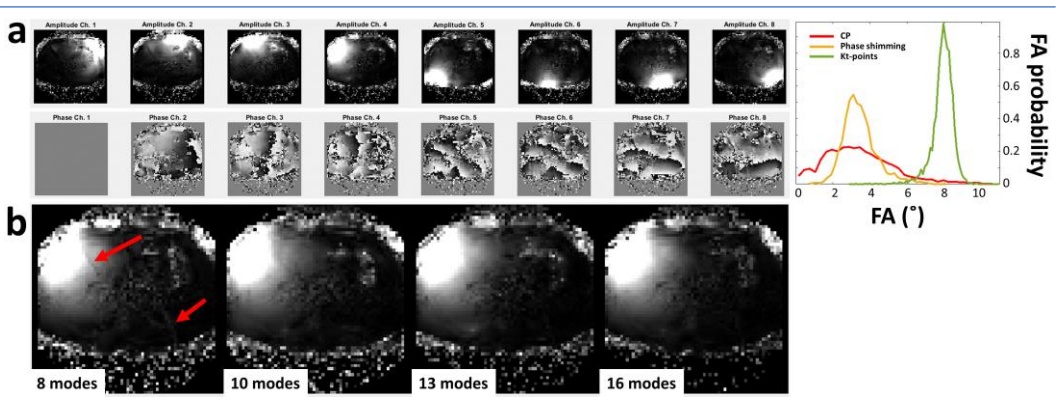

Figure 2: FPE-DREAM B1+ mapping in a volunteer with high BMI. a) Eight-channel B1+ amplitude and phase maps acquired using 13 modes (left) and corresponding whole-liver FA distribution simulations (right). The B1+ maps show no severe artifacts and the simulations show high homogeneity around the nominal FA for kt-points. b) Single-channel B1+ magnitude maps calculated from 8, 10, 13 and 16 modes. Maps calculated from 8 modes show artifacts (red arrows) that are removed when using >10 modes.

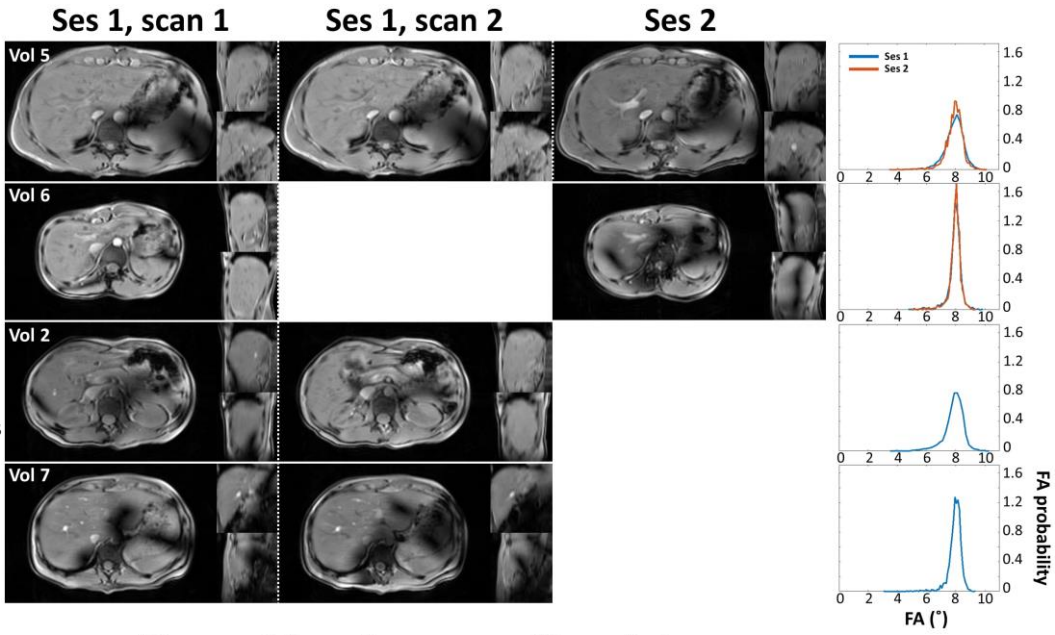

Figure 4: Robustness assessment. Magnitude images in three orientations (left) and simulations (right) of intra- and intersession kt-points repeatability tests in four volunteers. Volunteer 5 shows good repeatability in achieving whole-liver homogeneous FA. Volunteers 2, 6 and 7 show the occurrence of residual signal dropouts despite promising simulation results. Note that intra-session repetitions do not involve calculation of a new kt-points pulse and hence no separate simulation result.

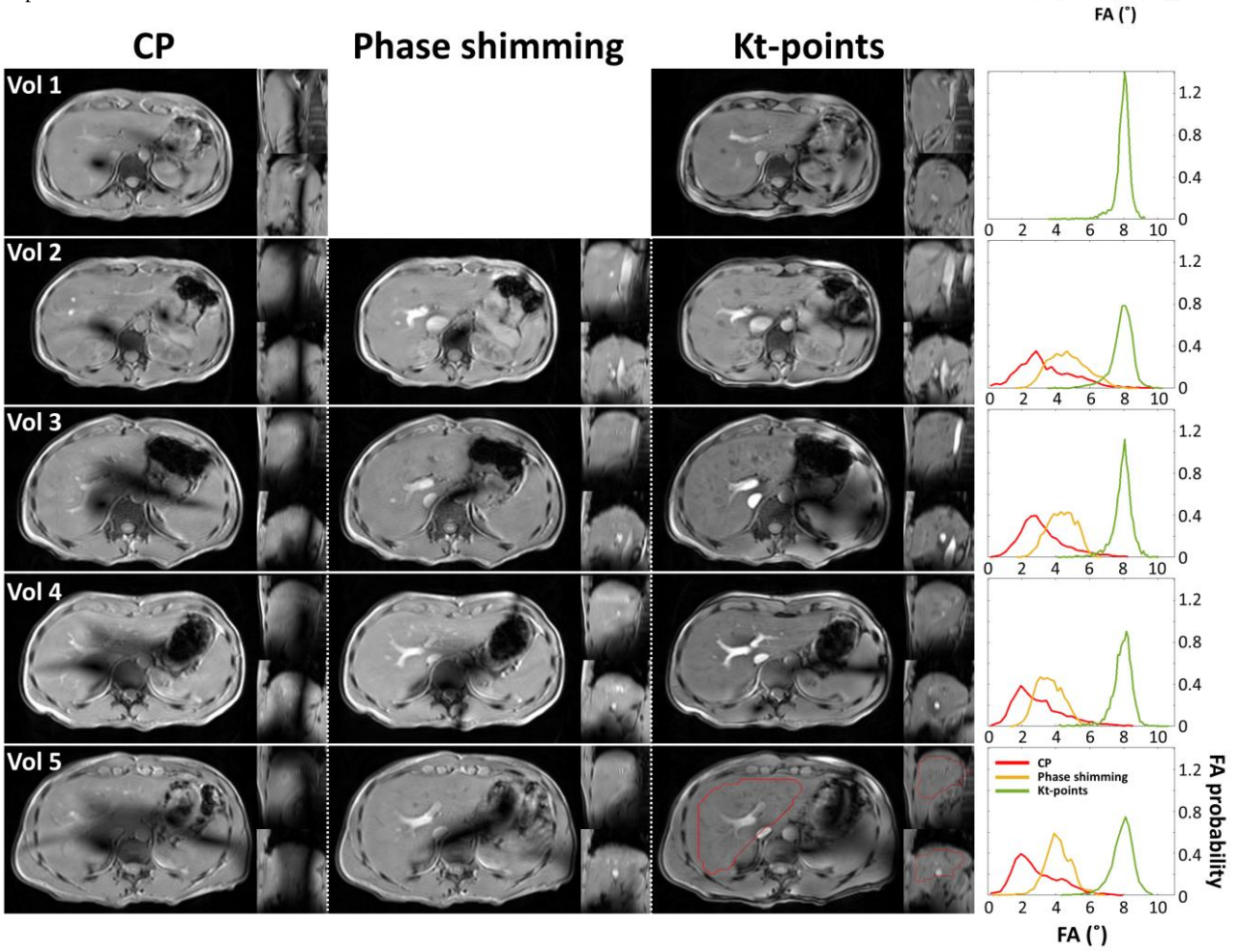

Figure 3: Magnitude images in three orientations for volunteers 1-5 using CP, phase shimming and kt-points (left). Slices are centered on the most pronounced signal dropout area in CP near the inferior vena cava. The clear signal dropouts in CP are removed using phase shimming and kt-points. Kt-points shows increased contrast over phase shimming and CP which was expected from the simulations (right). An exemplary whole-liver VOI used in pulse calculation is drawn in red (volunteer 5, kt-points).

A software-based TIAMO approach to enable high resolution large FOV body imaging at 7T ultra-high field

Jenni Schulz[1], Oliver Kraff[2], Harald H. Quick[2,3], Tom Scheenen[1,2]

[1]Dept. of Medical Imaging, Radboud UMC, Nijmegen, Netherlands; [2]Erwin L. Hahn Institute, University Duisburg-Essen, Essen, Germany; [3]High-Field and Hybrid MR Imaging, University Hospital Essen, Germany

Synopsis: Inhomogeneities across large FOVs are problematic at ultra-high field. We propose a software-based TIAMO implementation to enable similar flip angles across the body without hardware interference on the 7T MR scanner. Using an interleaved and complementary CP^{+}/CP^{2+} excitation scheme, we acquired water-selective and lipid-selective 3D GRE data at high resolution demonstrating homogeneous signal distribution across the pelvis and lower abdomen.

INTRODUCTION

Ultra-high field MRI offers high SNR and is therefore an excellent candidate for imaging small anatomical structures such as pelvic lymph nodes (LN) inside the body, which in combination with USPIO nanoparticles can aid in N-staging different types of cancer. [1] A major challenge is the decreased RF wavelength at 7T causing signal dropouts. This can in part be compensated by using RF shimming depending on the number of independent RF transmit channels. However, homogeneous RF shimming over very large field of views (FOV) remains challenging. In the past, the time interleaved acquisition of modes (TIAMO) [2] technique has been proposed to overcome the (in-)homogeneities and enabled large FOV-imaging in the body using an 8-channel parallel transmit system at ultra-high field.

TIAMO uses two complementary RF shims in an interleaved fashion to improve overall transmit homogeneity with two complementary excitations reaching similar flip angles across the body. [3]

The previous major drawback of this technique was its implementation on designated external RF hardware connected to the MR scanner, which would now interfere with warranty and maintenance issues from the MR system vendor on most recent 7T MR scanners.

In this abstract, we propose a solely software based TIAMO approach which enables high resolution and large FOV imaging at ultra-high field overcoming the mentioned inhomogeneities in the same way as the previously used hardware-based TIAMO solution. As a proof-of-concept, we show water-selective and lipid-selective 7T 3D GRE images of the pelvis.

METHODS

TIAMO was implemented into a standard pTx-capable 3D GRE sequence by modifying the phases of the individual channels of the excitation pulse in the preparation section of the sequence. Two different RF pulses were used. The first pulse was transmitting in CP^{+} mode for the individual 8 channels, the second pulse used the complementary CP^{2+} mode. Within the sequence, the two RF pulses were played out in an interleaved fashion using two average settings. Images were reconstructed using the 16 "virtual" TIAMO receive elements. [3]

Data were acquired from a healthy 47-year old male volunteer after informed consent on a 7T whole body system (Magnetom Terra, Siemens Healthcare GmbH, Germany) running on software version VE12U with a 8Tx/32Rx body-array coil [4].

After a localizer and standard B0 shimming, the high resolution protocol could be run without additional adjustments, consisting of two scans:
1. A water excitation scan with a 970 µs block pulse with transmitter frequency centered on the water resonance with the following parameters: 256 coronal partitions, 0.68 mm isotropic resolution, 384x384 matrix, 6/8 partial Fourier (PF) in phase/slice direction, BW 500 Hz/px, PAT 6, TR/TA = 16 ms/9:30 min, 5 gradient echoes with TE(1-5)=2.47/4.79/7.11/9.43/11.75 ms.
2. A lipid-selective excitation scan with the 970 µs block pulse transmitter frequency centered at the main lipid frequency. Parameters: 256 coronal partitions, 0.68 mm isotropic resolution, 384x384 matrix, 7/8 PF phase/slice, BW 500 Hz/px, PAT 3, TE/TR/TA = 2.48 ms/5.5 ms/7:04 min.
For water-selective excitation, the zero-crossing of the frequency profile of the RF pulse would coincide with the lipid resonance frequency resulting in only water excitation (for the lipid-selective acquisition vice-versa). [5] The signal decay of the multi-gradient echo acquisition was used to calculate any computed echo time image set (example at cTE = 3 ms), an R2* relaxation rate image and an image set with the root-sum-of-squares addition of all signals together.

RESULTS

The 3D water-selective mGRE acquisition provided proper water excitation in the center of the body (Fig. 1). At the central coronal partition, only water is excited as B0 homogeneity is sufficient. Even though the TIAMO shims are not optimized to the volunteer (basic CP^{+}/CP^{2+} was used), there were no signal dropouts because of missing excitation throughout the large FOV. Without the use of bowel relaxant, intestinal motion causes blur and artefacts. At superficial anterior and posterior parts of the volunteer, lipid excitation is visible caused by B0 inhomogeneity.

Observing the same slices for the short TE lipid-selective GRE acquisition it appeared that lipid excitation was more difficult as water had not completely been suppressed (Fig. 2). Contrast between water and lipids is present, although inhomogeneous over the large FOV. Subcutaneous and visceral lipid tissue is very bright and even some lipid signal is visible within the bones.

DISCUSSION AND CONCLUSION

High resolution large FOV images with a reasonably homogeneous signal distribution and high SNR were obtained in the pelvis for lipid- and water-selective acquisitions using a software-based TIAMO implementation. In this work, we used the standard CP^{+}/CP^{2+} shim modes, but the flexibility of the software implementation allows to easily incorporate any pair of (universal complementary) shim settings into the sequence. Room for improvement is in better B0-shimming and in estimating the attained flip angle with the two excitations with different B1 shims settings [6]. The concept can also be transferred to other sequences for general use. Furthermore, the software-based approach enables the possibility to easily and independently distribute the TIAMO technique to different sites and MR scanners which was not possible with the previous hardware solution.

REFERENCES

[1] Wu, Liucheng, et al. "Diagnostic performance of USPIO-enhanced MRI for lymph-node metastases in different body regions: a meta-analysis." *European journal of radiology* 80.2 (2011): 582-589.

[2] Orzada, Stephan, et al. "RF excitation using time interleaved acquisition of modes (TIAMO) to address B1 inhomogeneity in high-field MRI." Magnetic resonance in medicine 64,2 (2010): 327-33.

[3] Orzada, Stephan, et al. "Mitigation of B1+ inhomogeneity on single-channel transmit systems with TIAMO." *Magnetic resonance in medicine* 70.1 (2013): 290-294.

[4] Rietsch, Stefan HG, et al. "7T ultra-high field body MR imaging with an 8-channel transmit/32-channel receive radiofrequency coil array." *Medical physics* 45.7 (2018): 2978-2990.

[5] Philips, Bart WJ, et al. "High resolution MR imaging of pelvic lymph nodes at 7 Tesla." *Magnetic resonance in medicine* 78.3 (2017): 1020-1028.

[6] Brunheim, Sacha, et al. "Fast and accurate multi-channel B1+ mapping based on the TIAMO technique for 7T UHF body MRI." Magnetic resonance in medicine 79.5 (2018): 2652-2664.

Acknowledgments / Funding Information: This project has received funding from the European Union in the EFRO program, project number PROJ-01009. The 7T MRI system at the ELH Institute has been funded by the Deutsche Forschungsgemeinschaft (DFG, German Research Foundation) – Project number 432657511.

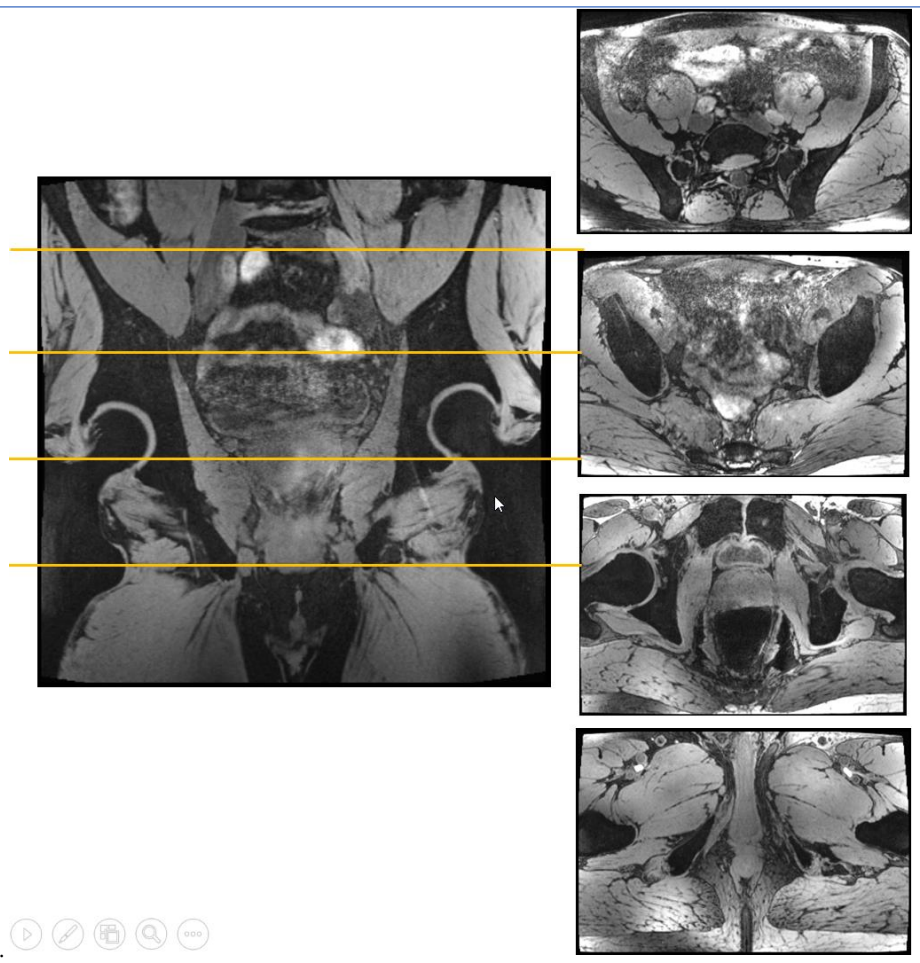

Figure 1.

Figure 1: A coronal (left) and different axial views (right) of the 3D water-selective GRE acquisition reconstructed at cTE = 3 ms with good B0 homogeneity in the central partition and some remaining lipid signal in the anterior and posterior parts of the body of the volunteer.

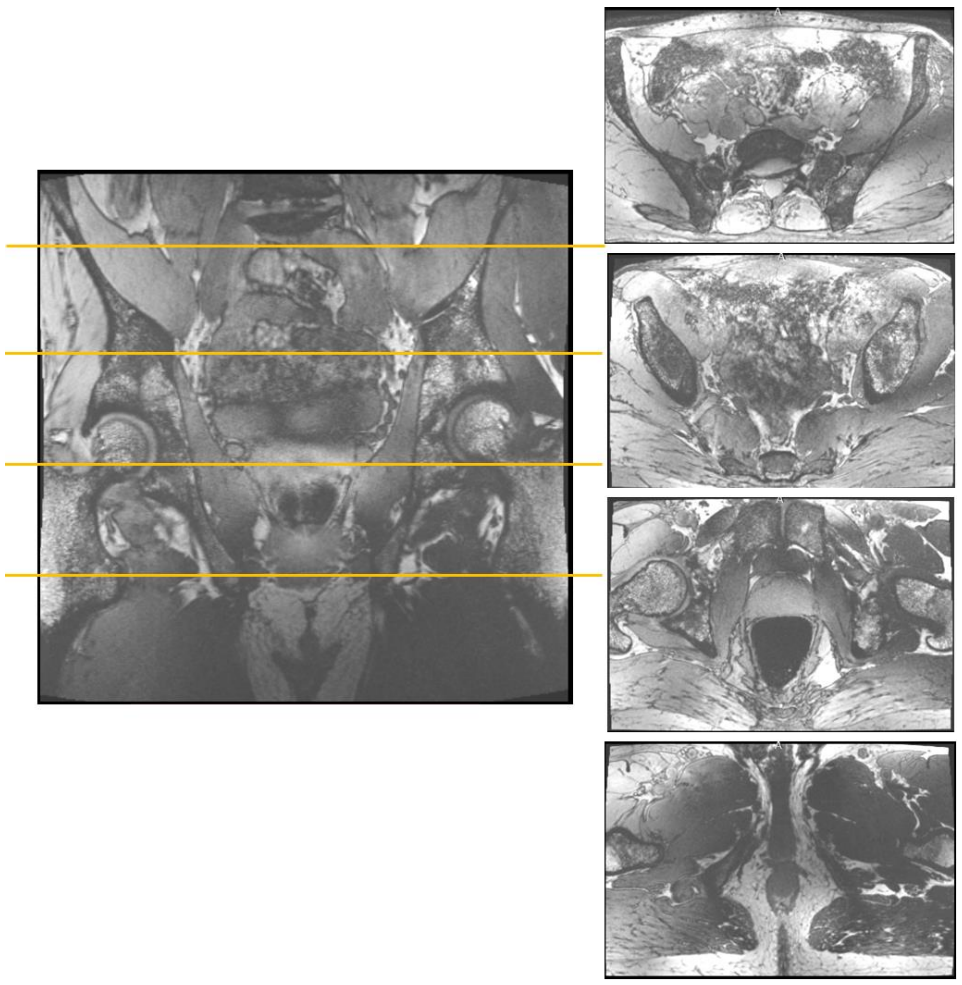

Figure 2.

Figure 2: A coronal (left) and different axial views (right) of the 3D lipid-selective GRE acquisition. The water signal is not completely suppressed. Subcutaneous and visceral lipid tissue is very bright and even some lipid signal is visible in the bones.

Semi-supervised learning for fast multi-compartment relaxometry myelin water imaging (MCR-MWI)

K.-S. Chan[1], T.H. Kim[2,3], B. Bilgic[2,3], J.P. Marques[1]

[1]Donders Centre for Cognitive Neuroimaging, Radboud University, Nijmegen, The Netherlands; [2]Athinoula A. Martinos Center for Biomedical Imaging, Charlestown, MA, United Sates, [3]Department of radiology, Harvard Medical School, Boston, MA, United States

Synopsis: Myelin water imaging using multi-compartment relaxometry (MCR-MWI) improves the GRE-MWI robustness and accuracy but suffered from slow processing speed. In this study, we incorporate both supervised and self-supervised machine learning for fast MCR-MWI that is generalisable to a wide range of acquisition parameters without the need to re-train the network. We demonstrate its application on single compartment fitting and MCR-MWI. Results show that the proposed method can produce comparable high SNR results with a 62-fold shorter processing time.

Introduction: Gradient echo myelin water imaging (GRE-MWI) is a promising myelination measurement method, yet highly ill-conditioned[1-3]. A multi-compartment relaxometry method for MWI (MCR-MWI)[4] incorporating variable flip angle (VFA), multi-echo GRE acquisition was recently introduced to overcome GRE-MWI limitations: accounting for distinct free water (IEW) and myelin water (MW) signal saturation, and ensuring fitting convergence. In MCR-MWI, the steady-state signal is modelled by the extended phase graph with exchange (EPG-X) framework[5] to account for inter-compartmental magnetisation exchange. However, using EPG-X with non-linear least squares (NLS) fitting is computationally expensive. Without parallelisation, one 1.5-mm isotropic resolution brain volume requires ~350 computation hours.

Using fully-connected artificial neural networks (FC-ANN) to speed-up parameter mapping was previously implemented for MWI[6-7]. However, these trained networks are protocol-specific and are not generalisable to new acquisition parameters (e.g., echo times). This would be even more critical with MCR-MWI where repetition time (TR), and (number of different) flip angles (α) have to be considered.

Self-supervised learning has been successful on rapid parameter mapping without the necessity of training data[8,9]. We propose a semi-supervised learning method for MCR-MWI. An FC-ANN is trained as a fast EPG-X simulator to generate the IEW and MW steady-state signal. The trained FC-ANN is then embedded in the MCR-MWI model in the self-supervised network for parameter mapping[10], utilising its computational efficiency to perform optimisation for a large number of voxels without extra training data, making it applicable across a variety of acquisition settings.

Methods

FC-ANN for EPG-X

The FC-ANN[6] architecture for EPG-X is described in Fig.1. The network takes six inputs: myelin sheath volume fraction (f_M), $T_{1,IEW}$, $T_{1,M}$, exchange rate (k_{IEWM}), α, and TR, and returns the magnitude steady-state IEW and MW signals that match the EPG-X simulations.

Training data was generated from $1.5x10^6$ random parameter sets ($\boldsymbol{\theta}$) with the 4 parameters described in Fig.1b. Training was performed using Adam optimiser with 100 epochs. The training loss was defined as a sum of three mean squared errors (MSE):

$$loss = MSE_{\theta,\alpha} + MSE_{\theta,1-90} + \lambda MSE_{dS_\theta/d\alpha}$$

corresponding to the MSE between the FC-ANN predictions and the EPG-X signal (1) given $\boldsymbol{\theta}$ at a single α ($MSE_{\theta,\alpha}$) and (2) for all 90 flip angles ($MSE_{\theta,1-90}$), and (3) the first derivative of the signal to flip angle ($MSE_{dS_\theta/d\alpha}$).

Self-supervised learning for parameter mapping

To perform parameter mapping, we deployed a simplistic physics-informed self-learning approach[10] (Fig.2). The network is initialised with random (and/or constant) values for the MR parameters (which are the network parameters to be optimised) and the acquired MR data is given as input. During the learning process, signal is simulated given the parameters and the signal model (Fig.2b,c), and the MR parameters are updated using an Adam optimiser based on a loss function of the MSE between simulated and actual signal.

Both networks were created and trained using the Deep Learning Toolbox in Matlab R2021b (Natwick, US) with an NVIDIA Tesla P100 GPU (Santa Clara, CA).

In vivo imaging

Data acquisition was performed at 3T (Siemens, Erlangen) on 2 healthy volunteers. A monopolar 3D ME GRE sequence was used to acquire VFA data using two distinct sets of protocols

1) TR/TE1/ΔTE/nTE=38/2.2/3.07ms/12, TA=2.8min/α;
2) TR/TE1/ΔTE/nTE =55/2.68/3.95ms/13, TA=4min/α,

res=1.5mm iso., α=[5,10,20,50,70]°, R_{CAIPI}=5. B_1 map was acquired to correct the B_1 field inhomogeneity. The complex data of all different α datasets and the B_1 map were co-registered before further processing.

Single Compartment Relaxometry

As a reference standard fast processing pipeline, R_2* was estimated on each dataset using trapezoidal integration[11], followed by DESPOT1 R_1 mapping on the extrapolated S_0 images[12]. Mean R_2* map was computed across flip angles. The self-supervised learning method shown in (Fig.2a,b) was used to demonstrate the network ability to perform simple parameter mapping.

Multi-Compartment Relaxometry

MWF maps were obtained as in [4] using an NLS fitting on a voxel-wise basis and compared to the self-supervised learning method described in (Fig.2a,c), processing ~12000 voxels simultaneously per batch.

The resulting maps between standard and self-supervised data were compared.

Results and Discussion: Fig.3 shows that the FC-ANN can generate the EPG-X signal for a variety of protocols and tissue parameters with the maximum percentage difference being below 3%.

Fig. 4 shows that the M_0, R_1* and R_2* maps derived from self-learning and standard relaxometry deliver comparable results, but the normalised MSE between the simulated and measured data is lower with the self-supervised method benefiting from its explicit MSE cost function.

Fig. 5 shows that the semi-supervised approach results in comparable MWF maps to voxel-wise fitting but 62-fold faster. Banding artefacts are observed in the most SNR sensitive measurements ($R^*_{2,MW}$ and k_{IEWM}) in regions corresponding to different processing batches. Although no explicit spatial regularization was used, the maps obtained are less prone to noise enhancement which is attributed to the learning gradients being computed over a large number of pixels.

Conclusions: We present a semi-supervised framework for MCR-MWI using an FC-ANN that is flexible to protocol settings (TR, TE and α) without re-training. Future work will explore the impact of learning rates associated with the various maps and introduce a 3DTV loss function to allow higher resolution MCR-MWI protocols. This framework can be adapted to complex non-linear fitting approaches as quantitative CEST or MT.

References: 1. Nam, et. al., Neuroimage 2015;116:214–221. 2. Alonso-Ortiz, et. al., Neuroimage 2018;182:370–378. 3. Lee et. al., NMR in Biomedicine 2016;30:e3513. 4. Chan et. al., Neuroimage 2020;221:117159. 5. Malik et. al., MRM 2017;3:125. 6. Lee et. al., MRM 2019;31:673. 7. Jung et. al. MRM 2021;85:380–389. 8. Kang, et. al. MRM 2021;85:2040–2054. 9. So at. al., In. Proc. ISMRM 30, Virtual meeting 2021;3027. 10. Kim at. al., Workshop on MRI Acquisition & Reconstruction, Virtual meeting 2021. 11. Gil et. al., NMR in Biomedicine 2016; 29:1780–1790. 12. Deoni et. al., MRM 2003;49:515–526.

Acknowledgments / Funding Information: This work is part of the research programme with project number FOM-N-31/16PR1056/RadboudUniversity, which is financed by the Netherlands Organisation for Scientific Research (NWO). BB and THK are supported by research grants NIH R01 EB028797, R03 EB031175, U01 EB025162, P41 EB030006, U01 EB026996, and the NVidia Corporation for computing support.

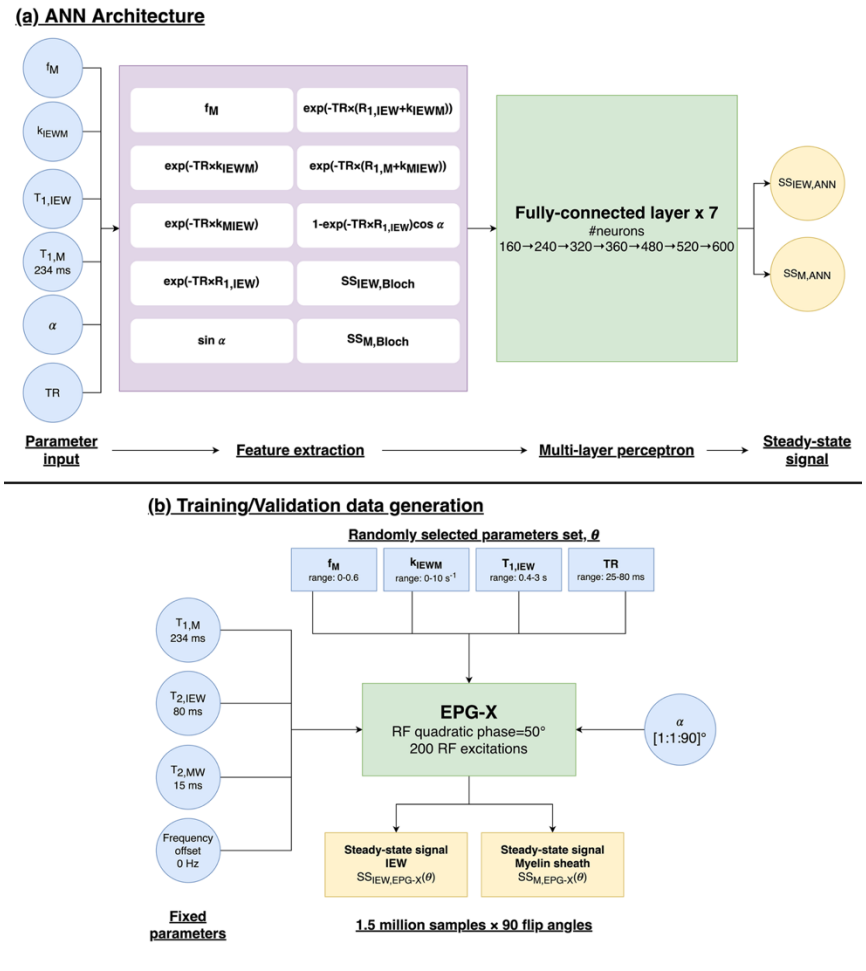

Fig. 1: a) The EPG-X steady-state FC-ANN is preceded by a feature extraction step to derive 10 input features that are both normalized to [0,1] and are related with different terms of the Bloch-McConnell equations. The network core comprises 7 hidden fully-connected layers and a leaky RELU (scale factor=0.01) function. The network parameters are trained with a hybrid strategy of increasing batch size and reducing learning rate as a function of the training iterations to ensure convergence. b) Illustration of the parameters and their ranges to generate training and validation data. ↑

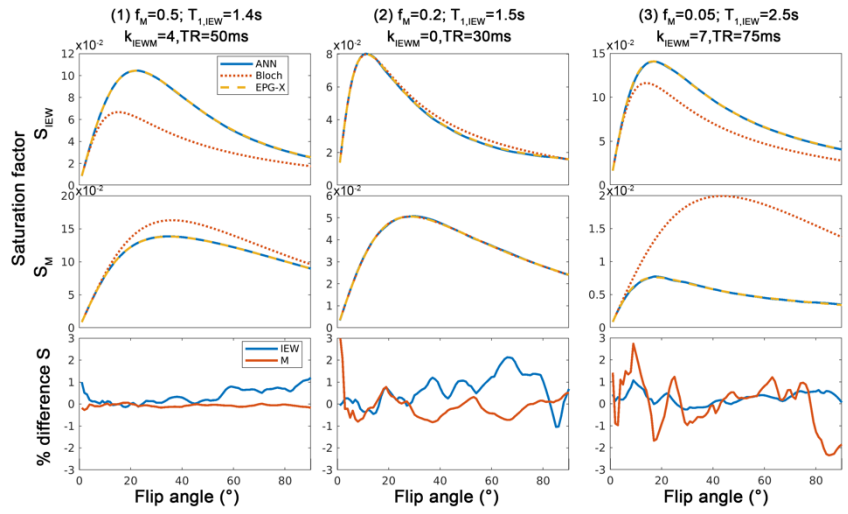

Fig. 3: Plots of the steady-state signal (at TE=0) using the standard Bloch equations (dot), EPG-X (dashed) and FC-ANN (solid) as a function of flip angle. The columns show the simulations of 3 samples in the validation set with different TR and tissue properties. The top row shows the signal of free water, the middle row shows the signal of the myelin water. The bottom row shows the percentage difference of the FC-ANN in respect to EPG-X for the free water (blue) and myelin water (red) respectively. In most cases, the percentage difference from FC-ANN output is below 3%. ↑

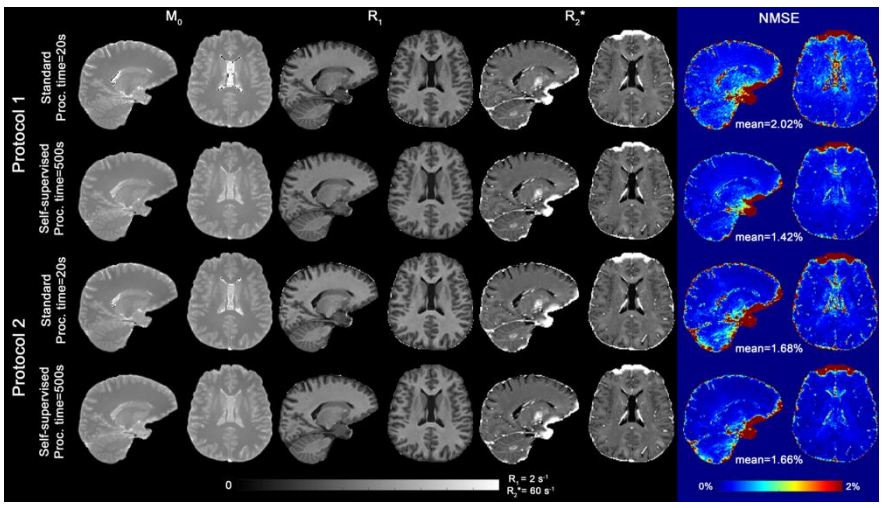

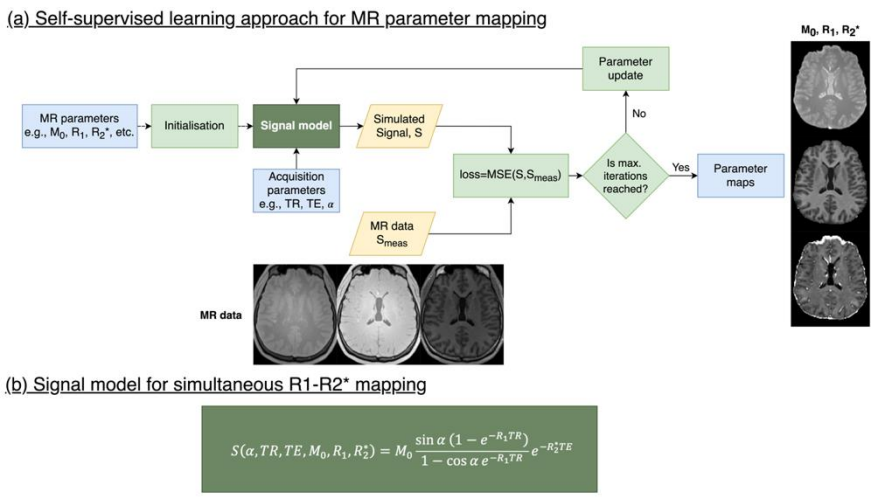

Fig. 2: (a) Illustration of the self-supervised method for parameter mapping. This network uses a signal model to generate simulated data that minimises the MSE to the measured data, and MR parameters are updated until the maximum number of iterations is reached. This method can be adopted for various parameter mapping methods by incorporating the corresponding signal model. We demonstrated its applications on (b) single compartment mapping and (c) MCR-MWI incorporating the network in Fig.1. Contrary to voxel-wise fitting, the proposed method operates on volumetric inputs. ↑

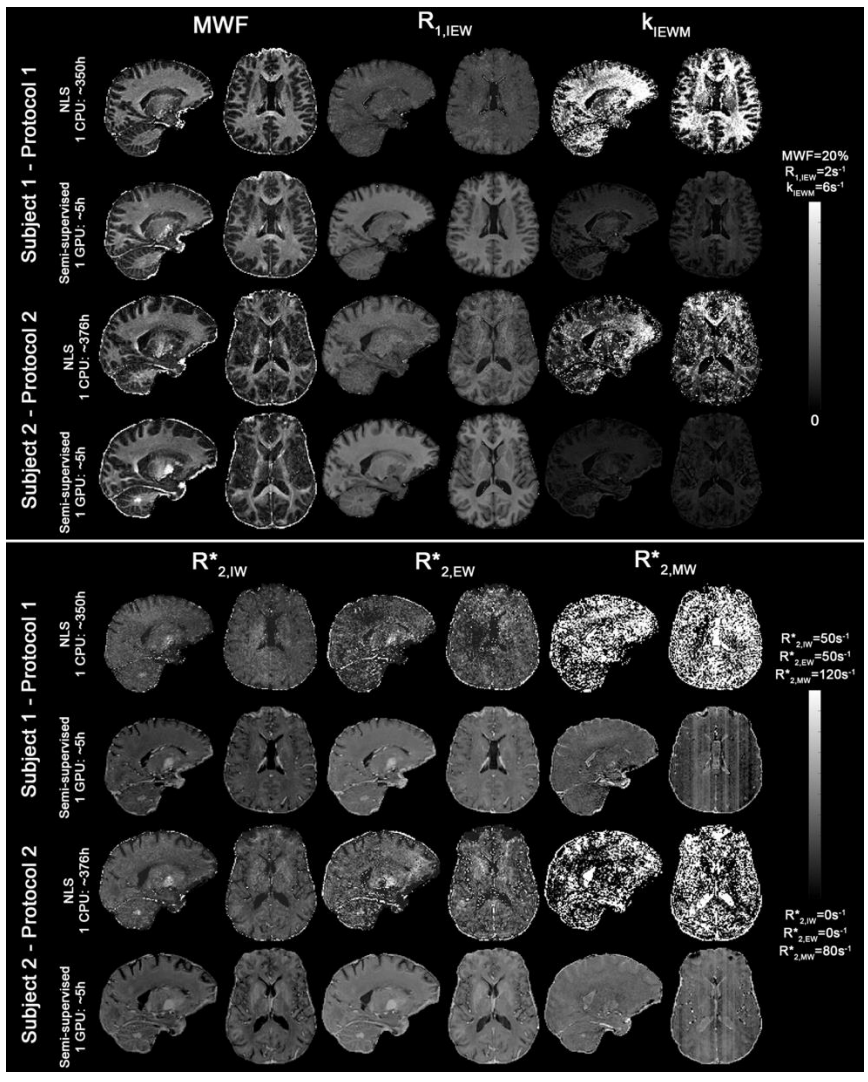

Fig. 5: MCR-MWI results from voxel-wise fitting and semi-supervised learning on 2 subjects (only 1 protocol is shown). MWF maps from both methods share similar contrast in white matter. Significantly different $R_{1,IEW}$ and k_{IEWM} are observed with semi-supervised learning, and its $R_{1,IEW}$ looks closer to the R_1 in Fig.4. The compartmental R_2* show higher SNR with the proposed method, which likely benefits from having more data in the optimisation that makes the results less error-prone. Banding artefacts in $R_{2,MW}$* & k_{IEWM} are related to different processing batches. ↑

Fig. 4: Single compartment mapping using standard method (1st & 3rd rows) and self-supervised learning (2nd & 4th rows). Unsurprisingly, both methods produce maps with very similar contrast since the signal model is not ill-conditioned. Overall, lower normalised MSE can be observed in self-supervised results, particularly in CSF. In a simple problem likes this, the self-supervised method does not show the advantage of computational time. ←

Multi-echo gradient echo sequences: which is best for thermometry?

T.V. Feddersen[1,2], D.H.J. Poot[2], M.M. Paulides[1,3], G.C. van Rhoon[1,4], J.A. Hernandez-Tamames[2,5]

[1]Department of Radiotherapy, Erasmus MC Cancer Institute, University Medical Center Rotterdam, Rotterdam, The Netherlands,[2]Department of Radiology and Nuclear Medicine, Erasmus MC Cancer Institute, University Medical Center Rotterdam, Rotterdam, The Netherlands, [3]EM4C&C, Center for Care and Cure Technologies Eindhoven (C3Te), Department of Electrical Engineering, Eindhoven University of Technology, Eindhoven, The Netherlands, [4]Department of Applied Radiation and Isotopes, Reactor Institute Delft, Delft University of Technology, Delft, The Netherlands, [5]Department of Imaging Physics, Applied Physics Faculty, Delft University of Technology, Delft, The Netherlands

Synopsis: To optimally use our novel head&neck HT applicator, MR thermometry (MRT) needs to become more reliable and it's stability needs to be demonstrated in vivo. We compared the MRT performance across different multi-echo gradient echo sequences in phantom and 10 volunteers on a 1.5T MR scanner (Signa MR450, GE). The sequences investigated were: DEGRE(2D-2echo), ME-FGRE(2D-11echo) and IDEAL IQ(3D-11echo). Regarding accuracy and stability, IDEAL IQ outperformed the other sequences, with values of 0.60°C and 0.75°C respectively. Hence, IDEAL IQ is most promising for MRT during HT applications. Probably, this is due to the design of the sequence and it's 3D nature.

Introduction: During hyperthermia therapy (HT), tissue temperature is increased towards 43°C to stimulate radio-, chemo- or immunotherapy. The HT effect is strongly temperature dependent so real-time monitoring is crucial for treatment quality. MR thermometry (MRT) is a promising tool to measure the temperature distribution during treatment non-invasively, but it's not yet established in clinical routine. By using multi-channel receive coils instead of the single channel body coil, the SNR can be increased and consequently the thermometry is improved. This motivated the development of a novel MR-compatible head&neck HT applicator, integrating a multi-channel receive coil: the MRcollar[1]. In order to optimally use our device, we study the achievable PRFS based MRT performance using multi-echo gradient-echo sequences for their accuracy in a phantom and for their stability in volunteers.

Methods: Figure 1 presents a flowchart of the method. We investigated: Double-Echo Gradient Echo (DEGRE: 2D, 2 echoes), Multi-Echo Fast Gradient Echo (ME-FGRE: 2D, 11 echoes), and a three point Dixon multi echo sequence (IDEAL IQ2: 3D, 11 echoes). All acquisitions were made using a 22-channel head&neck coil on a 1.5T MR scanner (Signa MR450, GE Healthcare). A phantom was imaged during cooling down from 50°C to 30°C, while MR compatible temperature probes continuously measured the true temperature. 10 healthy volunteers were imaged in a non-heated condition, where two scans of the brain were made with all sequences in interleaved fashion. To compensate displacements between the repeats, in-plane motion was compensated by rigid body image registration for all sequences. When displacement in the slice direction was >20% of the slice thickness for the 2D acquisitions (DEGRE + ME-FGRE), the scan was excluded. For each ME-FGRE and IDEAL IQ scan the off-resonance frequency and proton density water/fat maps were calculated by a multi-peak fitting tool3. A new automatic method to select the internal body fat was developed to correct for the B0 drift in the volunteer scans. Figure 2 shows an example of a selected fat mask, as well as the change of off-resonance maps before and after drift correction. When the fat mask contains too few voxels the linear fit is degenerate and hence the correction cannot be applied. Such slices were excluded. An important advantage of this method is that it needs no user input, as it uses the fat & water proton density maps from the multi-peak fitting tool. Additional constraints were added to improve the fat mask, such as correcting for water/fat swapped voxels. The temperature change from baseline was computed from the change in off-resonance frequency after drift correction. The ROI selected to evaluate the MRT in the brain of the volunteers was a fixed ellipse made to cover an area as large as possible to fit all slices in all volunteers (Figure 5). The accuracy of MRT in the phantom was calculated in a circular ROI (radius=12pixels) drawn around the probe-tip, as the average absolute difference between the probe measurement and MRT temperature. In-vivo stability was calculated as the mean absolute deviation from zero of the temperature change in the ROI.

Results: Figure 3 shows an example of temperature maps that can be observed in the phantom whilst cooling down, the MRT accuracy for all sequences is presented in Figure 4. IDEAL IQ outperformed all other sequences with an accuracy of 0.60°C. The volunteer results are presented in Figure 5. All scans from one volunteer and one ME-FGRE scan series from another volunteer were excluded due to z-displacement. About 4-6 slices were excluded per sequence due to too few voxels in the fat mask. The benefit of our exclusion criteria for all sequences can be observed in Figure 5. After exclusion, IDEAL IQ achieves the best stability of 0.75°C. The IDEAL IQ data was most robust concerning the fat mask selection, with only 5% of slices having to be excluded, compared to up 30% for other sequences.

Discussion: With some volunteers, there was substantial motion in the z-direction. Since the 2D acquisitions had a slice gap, 3D image registration was not possible. We expect that exclusion of data due to prominent motion is not an issue during HT treatments, as such motion will be restricted by the water bolus of the HT applicator. In the future we seek to improve our automatic fat selection further so that less slices need to be excluded because of non-reliable drift correction calculation. We notice that this is most prominent in the slices at the edge of the acquisition. In order to still get a reliable drift correction in the slices of interest, a slightly larger volume could be acquired. IDEAL already includes 4 extra slices on each side of the FOV, which is one possible explanation for the superior MRT performance. Additionally, the 3D multi-echo sequence has a higher SNR than the other 2D sequences investigated.

Conclusion: To conclude, IDEAL IQ is deemed the most promising sequence for HT applications for our MRcollar. Its better accuracy and stability in vivo enable reliable detection of small temperature increases during the relatively long treatment times. Since IDEAL IQ is already commercially available it can be easily implemented in the HT acquisition protocol.

References:

1. Drizdal, T., et al., Simulation guided design of the MRcollar: a MR compatible applicator for deep heating in the head and neck region. International Journal of Hyperthermia, 2021. 38(1): p. 382-392.

2. Reeder, S.B., et al., Iterative decomposition of water and fat with echo asymmetry and least-squares estimation (IDEAL): application with fast spin-echo imaging. Magnetic Resonance in Medicine: An Official Journal of the International Society for Magnetic Resonance in Medicine, 2005. 54(3): p. 636-644.

3. Salim, G., et al. Multipeak multiecho modeling for improved PRF-based thermometry. in 32nd Annual Scientific Meeting of the ESMRMB. 2015.

Acknowledgments / Funding Information: This research is funded by the KWF

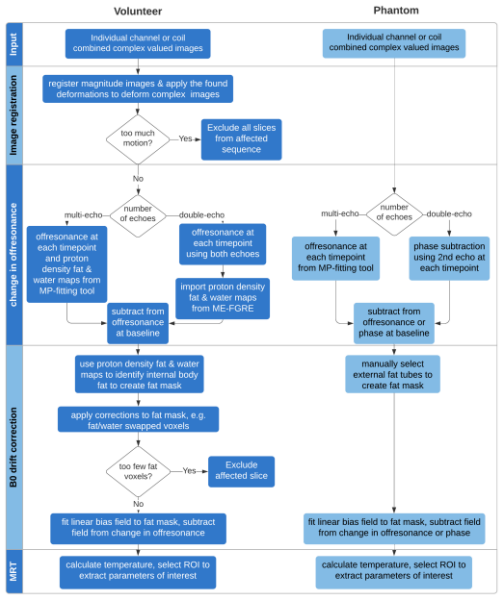

Figure 1. Flow chart showing the post processing and exclusion steps for the volunteer data (left) and phantom data (right).

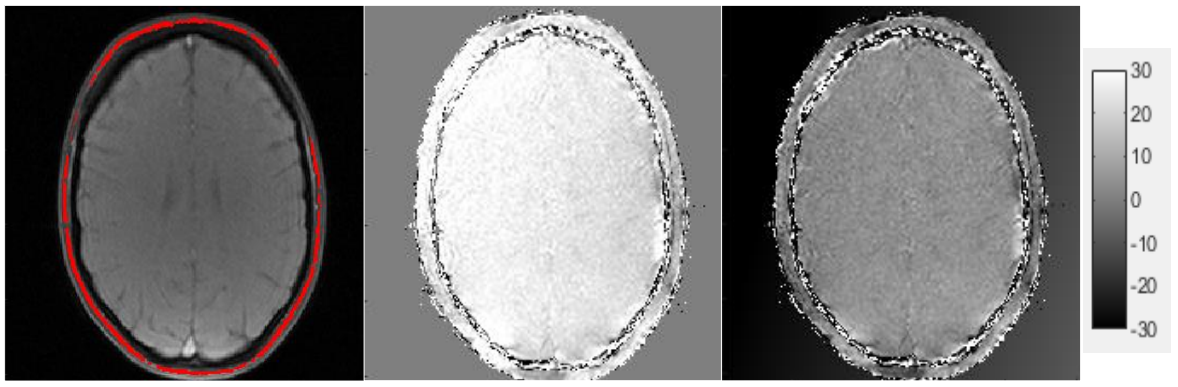

Figure 2. Example of fat mask selected for B0 drift correction with our automatic selection using proton density maps of fat and water. From left to right: a magnitude IDEAL IQ image (volunteer 10, slice 1, echo 1, TP1) underneath the final fat mask in red; change in off-resonance map before B0 drift correction; change in off-resonance map after B0 drift correction. Both changes in off-resonance frequency are plotted on the same scale, the importance of the B0 correction for the true change in temperature becomes apparent.

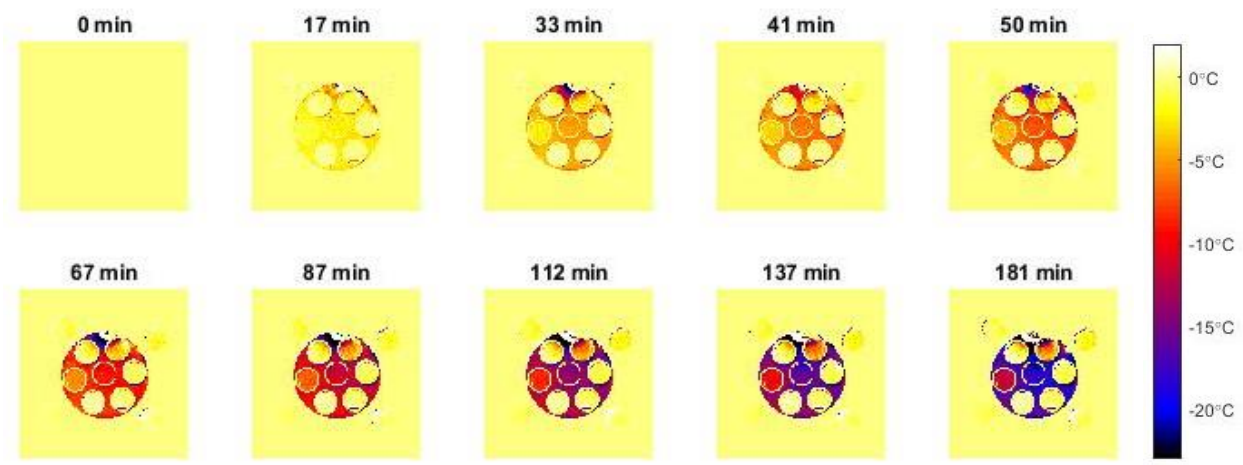

Figure 3. MRT temperature change maps obtained with DE-GRE visualizing the phantom cooling down ~20°C over time. The center vial contains water and was used for evaluation. At the top of the phantom an air bubble is creating artefacts.

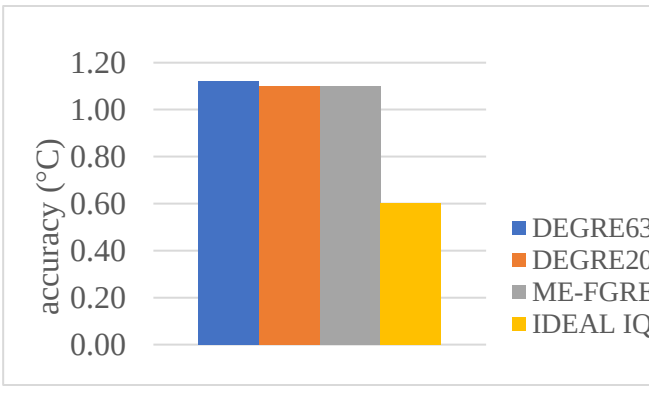

Figure 4. Accuracy achieved for all sequences in the phantom experiments. Accuracy values are obtained by taking the average of the absolute difference between MRT and temperature probe measurement (a low accuracy in this case means a smaller deviation from the 'true' temperature i.e. a more accurate description of the result).

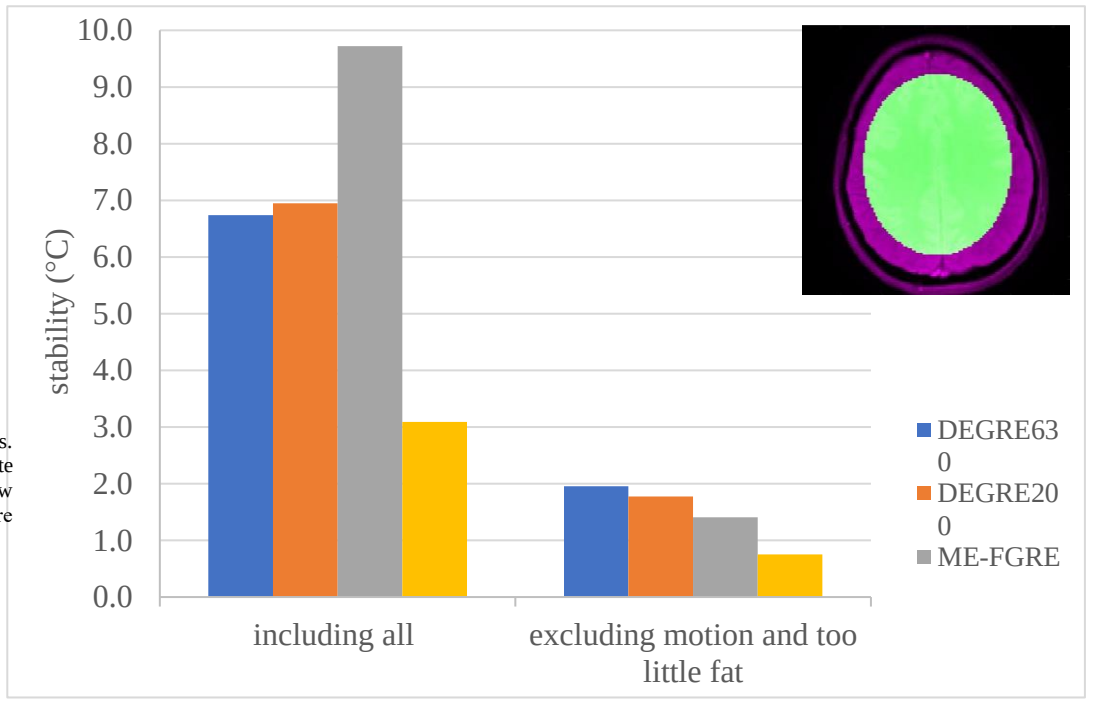

Figure 5. Stability achieved for all sequences in the volunteer experiments, including all scans and excluding scans with too much motion in slice direction and too little fat voxels selected for B0 drift calculation. Stability is measured as the mean in the ROI of the absolute deviation from zero in the temperature change maps. The ROI selected is shown in the top right corner.

The first MR Electrical Properties Tomography (MR-EPT) reconstruction challenge

S. Mandija[1,2], C.A.T. van den Berg[1,2]

[1]Department of Radiotherapy, Division of Imaging and Oncology, University Medical Center Utrecht, Utrecht, The Netherlands; [2]Computational Imaging Group for MR Diagnositcs and Therapy, Center for Image Sciences, University Medical Center Utrecht, Utrecht, The Netherlands

Synopsis: This work announces the initial design of the first Electrical Properties (EPs) reconstruction challenge and opens up the call for ideas to finalize its implementation and to define the organizing committee members. Several EPs reconstruction methods have been presented in the last decade. However, as emerged from the last EPs workshop (IMEP-Utrecht'19), testing on common data has not been performed yet, nor data are publicly available. The scope of this challenge is therefore to benchmark current reconstructions on the same data. These data will also be made available to favor benchmarking of new methods in the future.

Purpose: MR-Electrical Properties Tomography (MR-EPT) aims at reconstructing tissue electrical properties (EPs), (mostly) conductivity and permittivity, at megahertz frequencies from non-invasive MRI measurements. In the last decade, several reconstruction methods have been presented, however the reported EPs values show substantial differences[1,2,3]. This was recognized during the last EPT workshop (IMEP-Utrecht-2019)[4], demonstrating the need of a common dataset to benchmark current reconstruction algorithms and future physics/deep-learning based reconstruction methods. For this purpose, the Utrecht group set out to provide such dataset (simulated and measured phantom/in-vivo data) fulfilling the community-shared key requirements: use of a clinical MRI system (3 T), standard MRI sequences and clinical coil setup to ease future clinical implementation.

Additionally, during that workshop it was recognized the need to objectively compare the current reconstruction methods to understand their strengths and weaknesses in a systematic manner. In consultation with the future EMTP workshop organizers (Lucca-2022), it seems that launching the first MR-EPT reconstruction challenge in the context of this workshop would help reaching these overarching goals.

Here, we therefore present the initial design of the first MR-EPT reconstruction challenge. We also invite the EPT community to provide suggestions to be discussed during the upcoming ISMRM Meeting (London-2022) through the call for ideas and to candidate for the organizing committee (see below).

Methods:

Challenge Phases: Following the lessons learned in the QSM reconstruction challenges[5,6], the EPT reconstruction challenge will comprise of three independent phases (see **Fig.1** for description, data provided, and evaluation strategy of each phase).

Timeline: We foresee that the challenge can be launched in the context of the EMTP workshop (Lucca-2022) and results can be presented in the following ISMRM Meeting.

Dataset: As for the QSM challenges, we aim at providing different type of data for brain EPs reconstructions at 3 T:

1) In-silico brain data (noiseless and with noise) from Sim4Life simulations:
    a. B_1^+ magnitude, phase and receive phase (for transceive phase-based reconstructions), source fields
    b. Ground-truth (GT) EPs maps
2) MRI cylindrical phantom data:
    a. B_1^+ magnitude and transceive phase
    b. GT-EPs maps
    c. MRI magnitude data (e.g. T1-weighted images)
3) MRI 3D-printed brain-like phantom data:
    a. B_1^+ magnitude and transceive phase
    b. GT-EPs maps
    c. MRI magnitude data (e.g. T1-weighted images)
4) MRI in-vivo brain data (3 healthy volunteers):
    a. B_1^+ magnitude and transceive phase
    b. MRI magnitude data (e.g. T1-weighted images)

Data Management: As for the QSM challenge 2.0, data evaluation will be implemented to allow a fully blinded analysis. Only two committee members will have access to the identifying information of the participants. Upon submission of the reconstruction results, participants will also be asked to answer a questionnaire similar to the one presented in the QSM challenge 2.0 providing further information on the type of reconstruction performed and used data (e.g. phase-only).

Metrics: As learned in the QSM challenges, we will not only implement quantitative, global error metrics (e.g. NRMSE). In addition, region specific analysis and visual rating will also be considered. Such rating will provide a quality assessment of the reconstructed EPs maps, lack of reconstruction artifacts (boundary errors / blurring), presence of wrong morphological structures.

Open Science: We also strive for open science. Therefore, we will aim at making our database publicly available (downloadable after registration and user verification). Also, analogously to the QSM challenge 2.0, we will encourage all the participating groups to make available the codes and/or to report about their willingness to provide them upon request.

Results: Quantitative and qualitative analyses (**Fig.1**) will be performed by the committee members and results will ideally be presented at the ISMRM Annual Meeting 2023. Decisions on the final design and metrics will be taken by the organizing committee after reviewing the input from the EPT community (**Fig.2**).

Discussion: Through this challenge, we expect to achieve the following major goals:

1) Provide the first dataset for MR-EPT reconstructions fulfilling the main requirement of: using a clinical MRI system (3 T), standard MRI sequences and clinical coil setup to ease future clinical implementation
2) Evaluate the state-of-the-art of EPT reconstructions methods using the same test data
3) Allow benchmarking of future EPT reconstruction methods

At the current stage, we are looking forward to hearing possible suggestions from the EPT community (e.g. MRI sequences to be used) as well as understanding the overall interest in participating in such a challenge. For this purpose, we invite the readers interested in participating to such a challenge to fill in the following survey (Google form: https://forms.gle/XJV2C65b8wrUGpUg7 – call for ideas, **Fig.2**). We aim at discussing the collected ideas during the upcoming ISMRM Annual Meeting (London-2022). Also, if you would like to be part of the organizing committee, we kindly invite you to candidate via the same form.

Conclusion: This work presents the initial design of the first MR-EPT reconstruction challenge and opens up the call for ideas to finalize its implementation and to define the organizing committee members.

References:

1) Hancu I, Liu J, Hua Y, Lee SK, 'Electrical Properties Tomography: Available contrast and reconstruction capabilities.' Magn Reson Med 2019; 81: 803-810.

2) McCann H, Pisano G, Beltrachini L, 'Variation in reported human head tissue electrical conductivity values.' Brain Topography 2019; 32: 825-858 (original article)

3) Mandija S, Petrov PI, Vink JJT, Neggers SFW, van den Berg CAT, 'Brain tissue conductivity measurements with MR-Electrical Properties Tomography: An in vivo study.' Brain Topography 2021; 34: 56-63

4) Event recorded in the EMTP community website: EMTP Hub - https://www.emtphub.org/events/

5) Milovic C, Tejos C, et al, 'The 2016 QSM Challenge: Lessons learned and considerations for a future challenge design.' Magn Res Med 2020; 84: 1624-1637

6) QSM Challenge 2.0 Organizing Committee, et al, 'QSM reconstruction challenge 2.0: Design and report of results.' Magn Res Med 2021; 86: 1241-1255

Acknowledgments / Funding Information: This work was supported by the Netherlands Organisation for Scientific Research (NWO-Veni), grant number:18078.

Phase 1 – in-silico brain data		
Data	***Evaluation***	***Description***
BLINDED in-silico brain data (with noise): no GT-EPs provided	*Quantitative evaluation:* Global and ROI specific with respect to GT-EPs data	Assess the quality of state-of-the-art reconstructions on unknown data, thus impeding ad-hoc tuning of reconstruction parameters: in-line with QSM challenge 2.0 and standard procedure for deep-learning approaches
Phase 2 – in-silico brain data		
Data	***Evaluation***	***Description***
In-silico brain data (noiseless and with noise); with GT-EPs for the training set and without GT-EPs for the test set	1) *Quantitative evaluation:* Global and ROI specific with respect to GT-EPs data 2) *Qualitative evaluation:* visual rating	Assess the reconstruction performance on a test dataset (4 brain models, GT-EPs not provided) after ad-hoc tuning of algorithm-specific parameters based on EPs reconstructions on a training set (2 brain models, GT-EPs provided)
Phase 3 – MRI measurements		
Data	***Evaluation***	***Description***
Cylindrical phantom MRI data with GT-EPs for the training set and without GT-EPs for the test set	*Quantitative evaluation:* Global and ROI specific with respect to GT-EPs data	Assess the reconstruction performance on measured data (clinical 3 T MRI) on a test dataset (1 phantom model, GT-EPs not provided) after ad-hoc tuning of algorithm-specific parameters based on EPs reconstructions on a training set (1 phantom model, GT-EPs provided)
3D-printed brain MRI data without GT-EPs	1) *Quantitative evaluation:* Global and ROI specific with respect to GT-EPs data 2) *Qualitative evaluation:* visual rating	Assess the reconstruction performance on a more realistic test dataset (3 brain-like models, GT-EPs not provided)
In-vivo brain MRI data	1) *Quantitative evaluation:* Global and ROI specific with respect to GT-EPs data 2) *Qualitative evaluation:* visual rating	Assess the reconstruction performance on a test dataset (3 healthy volunteers)

Fig.1: Description of the 3 phases of the challenge. GT-EPs = ground-truth electrical properties.

https://forms.gle/XJV2C65b8wrUGpUg7

Personal information

[Name]

[Surname]

[email address]

[Institute]

[Country]

Academic title

[MSc, PhD, Postdoc, Assistant/Associate Professor, full Professor, other-specify]

Interested in participating to the challenge

[yes/no]

Interested in becoming member of the organizing committee

[yes/no]

Provide here any comment on the challenge idea

[text field]

Provide here any comment on the data to be shared

[text field]

Provide here any comment on the data simulations (Sim4Life simulations)

[text field]

Provide here any comment on the data acquisitions (MRI, 3T)

[text field]

Provide here any comment on the data analysis

[text field]

Provide here any comment on the timeline

[text field]

Provide here any comment on making data/reconstruction methods available

[text field]

Provide here any other comment

[text field]

Will you be joining ISMRM in London?

[yes/no]

If yes, would you like to participate in a discussion session?

[yes/no]

Fig.2: List of questions present in the Google form to collect suggestions and to candidate for the organizing committee.

A semi-relatistic and reusable 3D printed brain phantom for MR-based Electrical Properties Tomography

T.G. Meerbothe[1,2], S. Florczak[3], P.R.S. Stijnman[1,2], C.A.T. van den Berg[1,2], R. Levato[3,4], S. Mandija[1,2]

[1]Department of Radiotherapy, Division of Imaging and Oncology, University Medical Center Utrecht, Utrecht, The Netherlands; [2]Computational Imaging Group for MR Diagnositcs and Therapy, Center for Image Sciences, University Medical Center Utrecht, Utrecht, The Netherlands; [3]Department of Othopaedics, University Medical Center Utrecht, Utrecht University, Utrecht, The Netherlands; [4]Department of Clinical Sciences, Faculty of Veterinary Medicine, Utrecht University, Utrecht, The Netherlands;

Synopsis: This work presents a semi-realistic and reusable 3D printed brain phantom to benchmark MR-Electrical-Properties-Tomography reconstruction methods. We show that the hollow compartments of this phantom can be refilled multiple times with different water-based solutions of known electrical properties, which are otherwise not available from in-vivo measurements. Additionally, these brain phantoms can be used inside electromagnetic simulation software, allowing for MR-EPT reconstructions in controlled, simulation settings. In this way, a database comprising of simulated and measured data using these brain models and corresponding 3D printed phantoms will be generated and shared for the first MR-EPT reconstruction challenge.

Purpose: In MR-based electrical properties tomography (EPT), electrical properties (EPs, conductivity σ and relative permittivity ε_r) are derived from non-invasive MR measurements. Several reconstruction methods have been presented, however the reported in-vivo results often lack agreement[1,2]. Benchmarking of in-vivo EPs reconstructions is hampered by the lack of knowledge of ground-truth (GT) EPs values. Therefore, these reconstruction methods are often evaluated on phantom measurements, where GT-EPs values are available. However, by using simplified phantoms (e.g. spheres/cylinders), the validity of certain assumptions made by the reconstruction approaches (e.g. symmetry) and the impact of realistic tissue structures (e.g. tissue boundaries) may not be thoroughly studied[3,4].

In this work, we present the first 3D printed, brain-like, MR compatible phantom, in which white/gray matter and cerebrospinal fluid structures can be filled independently with liquids of known EPs. This will allow benchmarking of MR-EPT reconstruction algorithms in a more realistic scenario. Additionally, we show that the 3D printed, brain-like geometry can be easily imported in electromagnetic (EM) simulation software for EPT reconstructions on in-silico data. This allows direct comparison between reconstruction performance in ideal (simulations) and realistic (MR) settings. All the measured and simulated data that will be generated with these phantoms/models will be used to create a database that will be shared with the EPT community to favor benchmarking of EPT reconstruction algorithms.

Materials and Methods: The overall workflow describing the procedure to go from brain MRI data to a 3D printed brain-like phantom, and the creation of the MR-EPT database comprising of MRI measurements and EM simulations is shown in **Fig.1**. The brain data was taken from the BigBrain dataset[5] (voxels labeled as white matter (WM), gray matter (GM) and cerebrospinal fluid (CSF)). Using 3DSlicer[6], the segmented model was modified (smoothing, expansion, island filling and logical operations) to create a model with smooth surfaces and 4 compartments: WM, GM, CSF, and ventricles. The obtained 3D model was used for both EM simulations and 3D printing.

Structural cylinders were added to the surface model to prevent structural breakdown (**Fig.2**). To make all compartments fillable, various pipes and holes were added. The 3D model was imported in Cura[7] for slicing and conversion to GCode and printed via fuse deposition modelling on an Ultimaker S3 3D printer (layer height 0.2mm). Surfaces were printed with polylactic acid (PLA), while a water-soluble support material polyvynil alcohol (PVA) was used to enable printing of overhanging structures. Printing time was about 2 days, after which the phantom was put in a water-bath for 2 days to wash out the support material. The compartments of the phantom were then filled with water/gelatin-based solutions (**Fig.3**[8]).

MRI measurements were performed on a clinical 3 T MRI system (**Fig.3**). The original brain model and the simplified one (used for printing) were also used for EM simulations in Sim4Life[9] (**Fig.4**: simulation setup and EM fields). Helmholtz-EPT reconstructions were performed on both measured and simulated data.

Results and Discussion: From the contrast difference in the T_1-weighted images of **Fig.3**, it can be seen that the compartments of the phantom can be individually filled, washed, and refilled. This allows the creation of a database of measured data using the same 3D printed phantom model but different, known, EPs values. This can be exploited for training deep-learning methods for EPT reconstructions (otherwise difficult for in-vivo data due to lack of GT-EPs knowledge[10]). For illustration, B_1^+ magnitude and transceive phase maps obtained from MRI measurements using this 3D printed phantom are shown.

From the performed measurements, we did not observe any imaging artifact created by the phantom or the materials used for its construction. A few bubbles were left within the gelatin, which may be avoided by slower phantom filling. A small leakage from the phantom surface was also observed. This issue may be overcome by increasing the printing resolution, temperature and thickness of the outer layer.

In **Fig.4**, simulated EM fields illustrate that the model simplification does not have a major effect on the resulting fields.

In **Fig.5**, conductivity maps reconstructed from simulated (controlled settings) and measured (realistic settings) data using the same phantom are shown, demonstrating similar quality and, therefore, the feasibility of using a 3D printed brain phantom for benchmarking EPT reconstructions.

By using the same phantom model, EPT reconstructions from EM simulations and MR measurements can be directly compared. Also, measurement related reconstruction issues of different MR-EPT methods can be accurately characterized. Furthermore, this allows testing the (noise) robustness and generalizability of emerging deep-learning EPT methods (trained on simulated data) with realistic MR measurements on brain models with known GT-EPs values (otherwise not available for in-vivo data).

The measured and simulated data generated with this type of phantoms will be shared with the EPT community allowing future reproducibility and standardization studies, together with the first MR-EPT reconstruction challenge.

Conclusion: A reusable, 3D printed, brain-like, MR compatible phantom is presented for the first time for benchmarking MR-EPT reconstructions from MRI measurements as this allows knowledge of GT-EPs. All the measured/simulated data obtained from such brain models/3D printed phantoms will be shared with the MR-EPT community in the context of the first MR-EPT challenge.

References:

1. McCann, Hannah, Giampaolo Pisano, and Leandro Beltrachini. "Variation in reported human head tissue electrical conductivity values." *Brain topography* 32.5 (2019): 825-858. Original manuscript
2. Mandija, Stefano, et al. "Brain Tissue Conductivity Measurements with MR-Electrical Properties Tomography: An In Vivo Study." *Brain topography* 34.1 (2021): 56-63.
3. Duan, Song, et al. "Quantitative analysis of the reconstruction errors of the currently popular algorithm of magnetic resonance electrical property tomography at the interfaces of adjacent tissues." *NMR in Biomedicine* 29.6 (2016): 744-750.
4. Mandija, Stefano, et al. "Error analysis of helmholtz-based MR-electrical properties tomography." *Magnetic resonance in medicine* 80.1 (2018): 90-100.
5. Amunts K, Lepage C, Borgeat L, Mohlberg H, Dickscheid T, Rousseau M-É, Bludau S, Bazin PL, Lewis LB, Oros-Peusquens AM, Shah NJ, Lippert T, Zilles K, Evans AC. BigBrain: An ultrahigh-resolution 3D human brain model. Science. 2013; 340(6139):1472-1475. doi: 10.1126/science.1235381. PMID: 23788795.
6. Fedorov, Andriy, et al. "3D Slicer as an image computing platform for the Quantitative Imaging Network." Magnetic resonance imaging 30.9 (2012): 1323-1341.
7. Ultimaker, “Cura 3D Printing Slicing Software,” (Accessed: 2021-10-26). [Online]. Available: https://ultimaker.com/en/products/cura-software
8. Duan, Qi, et al. "Characterization of a dielectric phantom for high-field magnetic resonance imaging applications." *Medical physics* 41.10 (2014): 102303.
9. Sim4Life (ZMT AG, Zurich, CH)
10. Hampe, Nils, et al. "Investigating the challenges and generalizability of deep learning brain conductivity mapping." *Physics in Medicine & Biology* 65.13 (2020): 135001.
11. Gosselin M C, Neufeld E, Moser H, Huber E, Farcito S, Gerber L, Jedensjö M, Hilber I, Di Gennaro F, Lloyd B, Cherubini E, Szczerba D, Kainz W, Kuster N, Development of a new generation of high-resolution anatomical models for medical device evaluation: the Virtual Population 3.0, Physics in Medicine and Biology, 59(18):5287-5303, 2014.
12. Yarnykh, Vasily L. "Actual flip-angle imaging in the pulsed steady state: a method for rapid three-dimensional mapping of the transmitted radiofrequency field." Magnetic Resonance in Medicine: An Official Journal of the International Society for Magnetic Resonance in Medicine 57.1 (2007): 192-200.

Acknowledgments / Funding Information: This work was supported by the Netherlands Organisation for Scientific Research (NWO-Veni), grant number:18078.

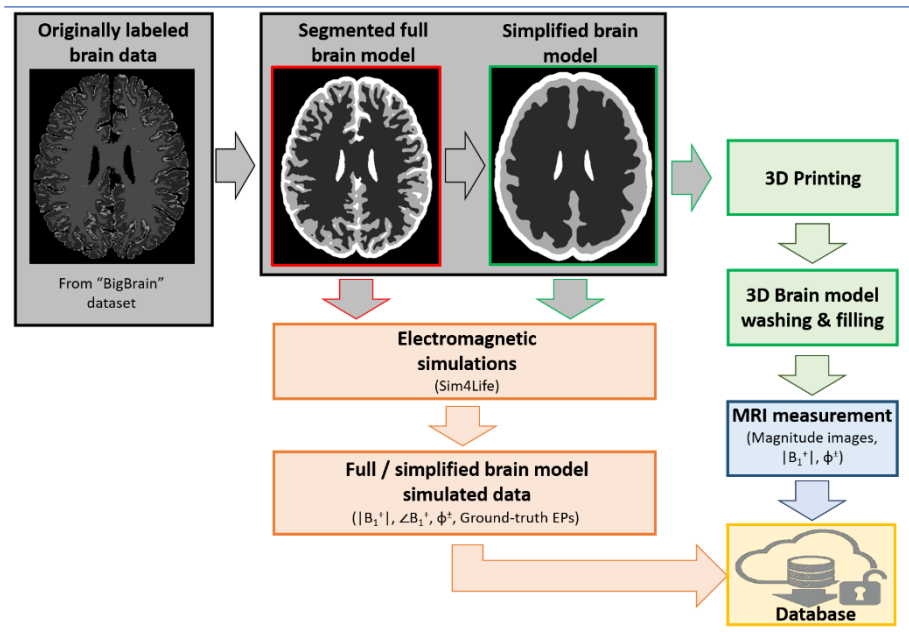

Fig.1: Workflow describing the MR-EPT database creation starting from MRI brain data. The database comprises of simulated data on full/simplified brain models as well as measured data from 3D printed brain models (simplified models). Finally, in-vivo brain data will also be part of the database. This database will be made available and will be instrumental for the first MR-EPT reconstruction challenge.

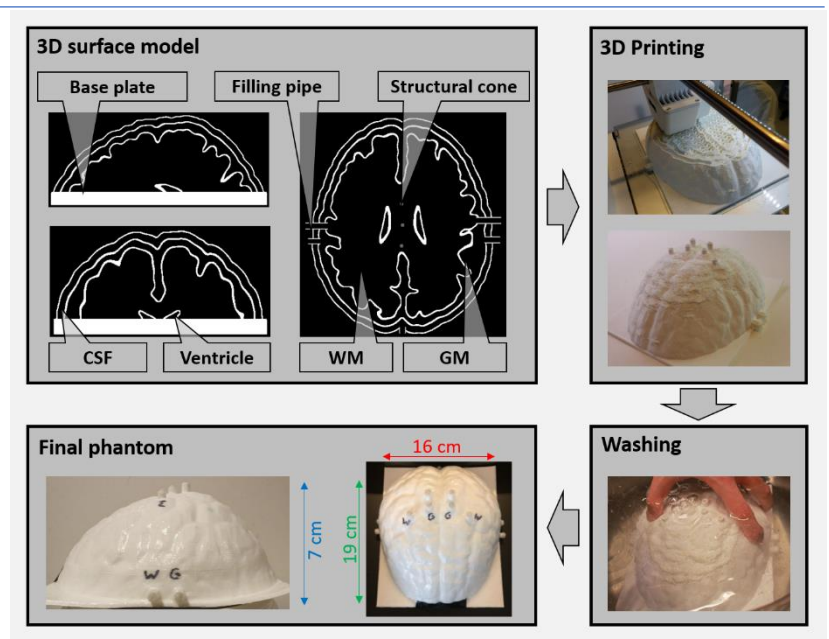

Fig.2: Workflow depicting the 3D printing process from a 3D surface model. In the printing procedure, two components were used, one of which (used as support) was washed out by submerging the phantom in water for 2 days. The final model also shows few small pipes exiting the brain. These were used for filling, washing and refilling of the phantom (see **Fig.3**).

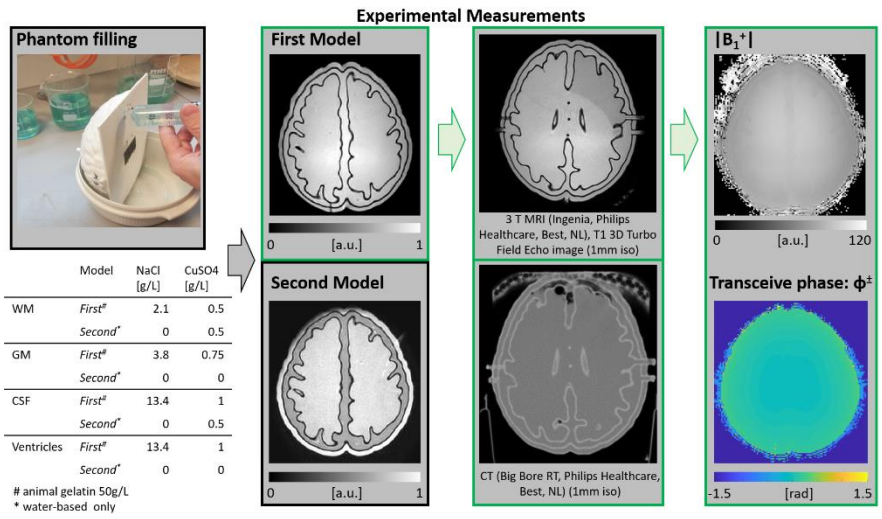

	Model	NaCl [g/L]	CuSO4 [g/L]
WM	First#	2.1	0.5
	Second*	0	0.5
GM	First#	3.8	0.75
	Second*	0	0
CSF	First#	13.4	1
	Second*	0	0.5
Ventricles	First#	13.4	1
	Second*	0	0

animal gelatin 50g/L
* water-based only

Fig.3: *Left:* Preparation of two brain phantoms with different water-based solutions (see table for used materials and concentrations). *Middle*: example MRI images of the two differently filled brain phantoms (different tissue contrast between the two models) and MRI/CT images of the first model. *Right*: example of acquired B_1^+ magnitude and transceive phase maps from 3 T MRI measurements. These are used for conductivity reconstructions.

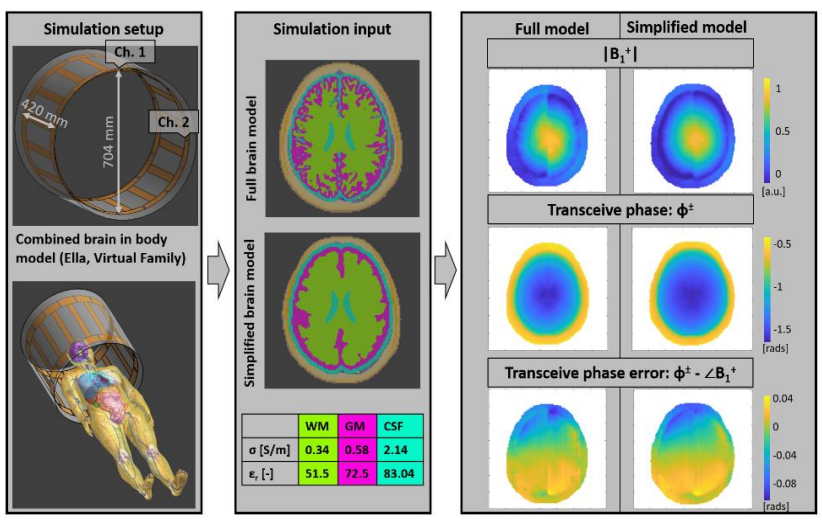

	WM	GM	CSF
σ [S/m]	0.34	0.58	2.14
ε_r [-]	51.5	72.5	83.04

Fig.4: Sim4Life simulations on the full/simplified brain models. *Left*: the birdcage coil model and the adopted brain models inserted in the Ella body model (VirtualFamily[11]). *Middle*: example of conductivity maps for the full/simplified brain models and adopted tissue conductivity values. *Right*: simulated B_1^+ magnitude and transceive phase maps (used for conductivity reconstructions) for both brain models. Error maps showing the error introduced by the transceive phase assumption are also shown.

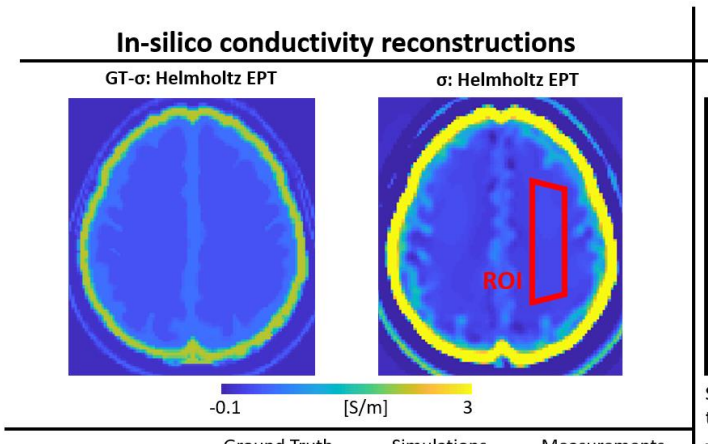

	Ground Truth Mean (SD)	Simulations Mean (SD)	Measurements Mean (SD)
White Matter Conductivity [S/m]	0.34 (-)	0.27 (0.03)	0.24 (0.14)

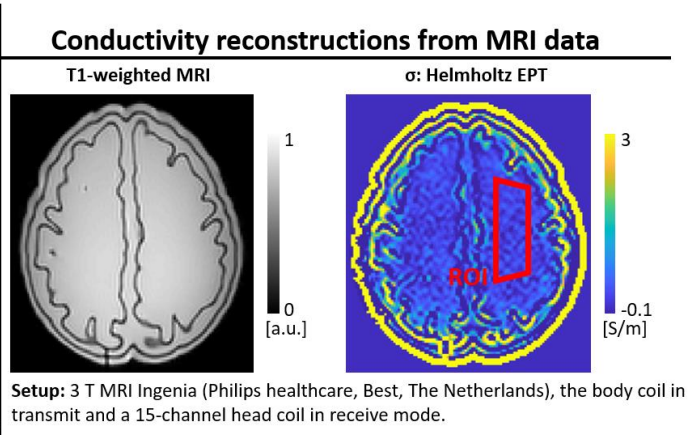

Setup: 3 T MRI Ingenia (Philips healthcare, Best, The Netherlands), the body coil in transmit and a 15-channel head coil in receive mode.

Transceive phase: 2x multi-slice Spin-Echo with opposite read-out directions: FOV:216x216x67mm; voxel size: 1.5x1.5x2mm; TR/TE:800/8ms; slice gap: 0.5mm.

$|B_1^+|$ map: Actual Flip Angle Imaging[12]: 3D T1 Fast Field Echo: FOV:216x216x67mm; voxel size: 1.5x1.5x2.5mm; TR1/TR2/TE:50/250/3.3ms; Flip Angle: 65° .

Fig.5: Helmholtz-based 2D conductivity reconstructions from simulated data and MRI measurements. For these reconstructions, an in-plane 7x7 derivative kernel was used[4]. The ground-truth conductivity map and a T_1-weighted image are also shown as a reference. Measurements setup and MR sequence parameters are reported in the figure (bottom right). Average reconstructed conductivity value for the WM in the region of interest (ROI) is shown (bottom left).

Intra- and inter-scanner variability at 3T of brain segmentation using the 3D-QALAS sequence in volunteers

M. Naeyaert[1], T. Vanderhasselt[1] , B. Raeymaekers[1]
[1]Radiology, Universitair Ziekenhuis Brussel / VUB, Brussel, Belgium

Synopsis: Six volunteers were scanned two times on two different 3T scanners (GE, Philips) using the 3D-QALAS sequence. The intracranial and brain parenchymal volume and myelin content were determined and the brain segmented in cerebrospinal fluid and white and grey matter using synthetic MRI. Bland-Altman plots, Dice coefficient and coefficient of variation indicate that the test-retest variability is very small, but there is an inter-vendor bias for CSF, GM and WM. MyC, BPV and ICV have only a very limited inter-vendor bias. At least for GM and BPV, the expected inter-scanner variation, besides the bias, is below the clinically relevant threshold.

Introduction: Measuring relaxometric properties in the brain has become possible due to a number of new sequences which were introduced, first in 2D 1,2, but now also in 3D such as the 3D-QALAS sequence 3. This relaxometry data can be used to segment the brain and create synthetic images. The increased resolution of the 3D sequences results in less partial volume effect, significantly increasing the accuracy of the measured values and the possibility for clinically relevant applications.

It is important to know the accuracy of these sequences, as well as the influence of the scanner, in order to correctly assess deviations from previous or normative values. To this end, a test-retest was done on volunteers in this research, on two different scanners, such that both inter- and intra-scanner variability could be determined.

Methods: Six healthy volunteers (3 male, age range 28-69 year, average 47 years) were scanned twice using the 3D-QALAS sequence on two different 3T scanners (Philips Ingenia and GE Premier), for a total of four scans, each time with repositioning between scans and with a random order of the scans for each subject. Parameters were kept the same where possible. Common parameters of the scans were: axial scans, resolution: 1x1x1.2 mm^3, FoV 25.6x25.6x16.3 cm^3, TI=100ms, echo train length=150, flip angle=4°. GE specific settings were: TE=2.032ms, TR=5.372ms, bandwidth=390.6Hz/pixel, 48 channel head coil, acceleration 2.6 using hypersense, acquisition time = 6min 38s. Philips specific settings were TE=2.129ms, TR=4.710ms, bandwidth=431 Hz/pixel, 32 channel head coil, acceleration factor 2 using CSense, acquisition time = 6min 57s.

Segmentation in cerebrospinal fluid (CSF) and grey and white matter (GM, WM), and determination of myelin content (MyC), intracranial volume (ICV) and brain parenchymal volume (BPV) was done using SyMRI prototype version 21Q1 4,5 (SyntheticMR AB, Linköping, Sweden). Synthetic T1-weighted images with TE=5ms and TR=100ms were constructed and coregistered to a randomly chosen T1-weighted image using SPM12 6. The segmentation maps were warped along with their respective T1 images. Dice scores were then calculated between the binarized segmentation maps.

The coefficient of variation (CV) was calculated for test-retest variability, using the two measurements per scanner per volunteer. For the inter-scanner variability the CV was calculated using the average of the two measurements per scanner as input values.

Results: The Bland-Altman plots for the intra-scanner results are shown in figure 1. The bias is -1.38% for WM, 1.38% for GM, and <0.1% for the other segments. The limits of agreement (LA) are largest for CSF (-3.53% to 3.73%), WM (-4.58% to 1.83%),GM (-0.67% to 3.43%) and MyC (-3.31% to 3.23%). For BPV and ICV they are <1%.

The inter-scanner Bland-Altman plots are shown in figure 2. For WM there is -8.60% difference on average, while this is 5.88% and -6.13% for GM and CSF respectively. For MyC the bias is -1.89%, BPV has -1.54%, and for the ICV it is -2.15%. The LA are smaller as in the test-retest results for WM, CSF, MyC, BPV and ICV but larger for GM.

The Dice scores are shown in table 1 and indicate better agreement with the GE retest compared to the Philips measurements, except for MyC. The Dice score indicates good to excellent levels of agreement, with the lowest score in MyC.

The CVs are shown in table 2. Both vendors score similarly in the test-retest comparisons, with the ICV and BPV masks being extremely similar, and MyC having CV<1% in all cases. For the inter-scanner results, the largest variability is observed for WM, followed by CSF, GM, ICV, MyC and BPV.

Discussion: The Bland-Altman plots, CV and Dice similarity score all indicate that the intra-scanner variability is very low, yielding very similar volumetric results and segmented maps, with the CV being lower than the expected yearly GM and BPV atrophy in AD 7,8. These results are also in line with earlier findings at 1.5T 9. The slight biases seen in the plots for WM and GM are likely statistical noise.

The CV and Bland-Altman plots indicate an inter-vendor bias: using Philips, more GM is found, but less WM and CSF. For MyC, BPV and ICV the bias is not clinically relevant. The Dice scores from different scanners are slightly lower, except for MyC. These facts indicate that MyC might be a robust quantitative measure across scanners. If the bias is taken into account, both the standard deviations of the CV and the LA in the plots are within clinical limits 7,8. The lower Dice scores for the MyC segments are natural, due to its complexity 10. The reason for the bias will be investigated further, but previous work in phantoms found a slight inter-vendor effect in the T1 estimations 11, used for the tissue segmentation. A possible improvement of the sequence would be prospective motion correction.

Conclusion: The first inter-vendor results for 3D-QALAS in volunteers at 3T are presented. Our test-retest results show that 3D-QALAS reliably estimates WM, GM, CSF and MyC, in line with results at 1.5T. Despite a bias between the vendors for GM, WM and CSF, with up to 8.60% difference on average for WM, the standard deviations are within clinical limits. MyC, BPV and ICV are estimated reliably.

References:

1. Ma, D., Gulani, V., Seiberlich, N., Duerk, J. & Griswold, M. MR Fingerprinting : Rapid Simultaneous Quantification of T1, T2, Proton Density and Off-resonance using a Spiral Trajectory. in Proceedings of the International Society of Magnetic Resonance in Medicine annual meeting 21, 0018 (2013).

2. Blystad, I. et al. Synthetic MRI of the brain in a clinical setting. Acta radiol. 53, 1158–1163 (2012).

3. Kvernby, S. et al. Simultaneous three-dimensional myocardial T1 and T2 mapping in one breath hold with 3D-QALAS. J. Cardiovasc. Magn. Reson. 16, 102 (2014).

4. Warntjes, M. et al. Modeling the Presence of Myelin and Edema in the Brain Based on Multi-Parametric Quantitative MRI. Front. Neurol. 7, 1–15 (2016).

5. West, J., Warntjes, J. B. M. & Lundberg, P. Novel whole brain segmentation and volume estimation using quantitative MRI. Eur. Radiol. 22, 998–1007 (2012).

6. Statistical Parametric Mapping. (Elsevier, 2007). doi:10.1016/B978-0-12-372560-8.X5000-1

7. Anderson, V. M. et al. Gray matter atrophy rate as a marker of disease progression in AD. Neurobiol. Aging 33, 1194–1202 (2012).

8. Sluimer, J. D. et al. Whole-brain atrophy rate in Alzheimer disease: Identifying fast progressors. Neurology 70, 1836–1841 (2008).

9. Fujita, S. et al. Three-dimensional high-resolution simultaneous quantitative mapping of the whole brain with 3D-QALAS: An accuracy and repeatability study. Magn. Reson. Imaging 63, 235–243 (2019).

10. Taha, A. A. & Hanbury, A. Metrics for evaluating 3D medical image segmentation: analysis, selection, and tool. BMC Med. Imaging 15, 29 (2015).

11. Naeyaert, M., Vanderhasselt, T., Warntjes, M. J. B. & Raeymaekers, H. Reproducibility and Multi-vendor Comparison of Simultaneous T1- and T2- Mapping Using 2D and 3D Synthetic MRI with GRAPPA, SENSE and Compressed Sense at 3T. in Proceedings 29th Scientific Meeting, International Society for Magnetic Resonance in Medicine 1288 (2021).

Acknowledgments / Funding Information: We thank GE and Philips for making their sequences available, and SyMRI for their prototype software.

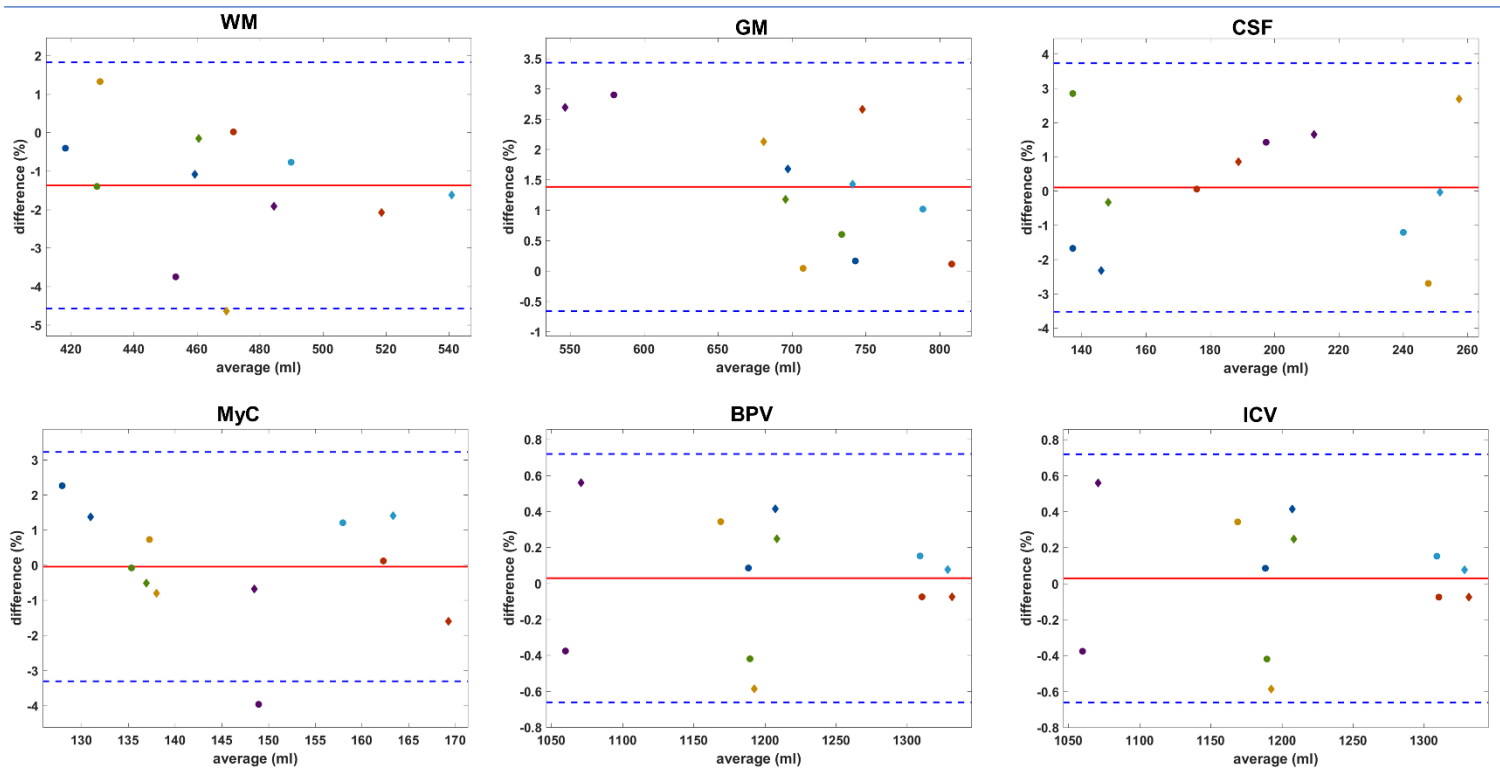

Figure 1: Bland-Altman plots showing the test-retest results, with different colours denoting different volunteers. The red line indicates the average difference (bias), the blue dotted line are at bias ± 1.96 x standard deviation. Diamonds indicate the GE measurements, circles are used for Philips. The biases are <1.5%, indicating excellent test-retest variability, with the 1.96 x standard deviation values for BPV and ICV being <1.0% and well under 5% for the other segments.

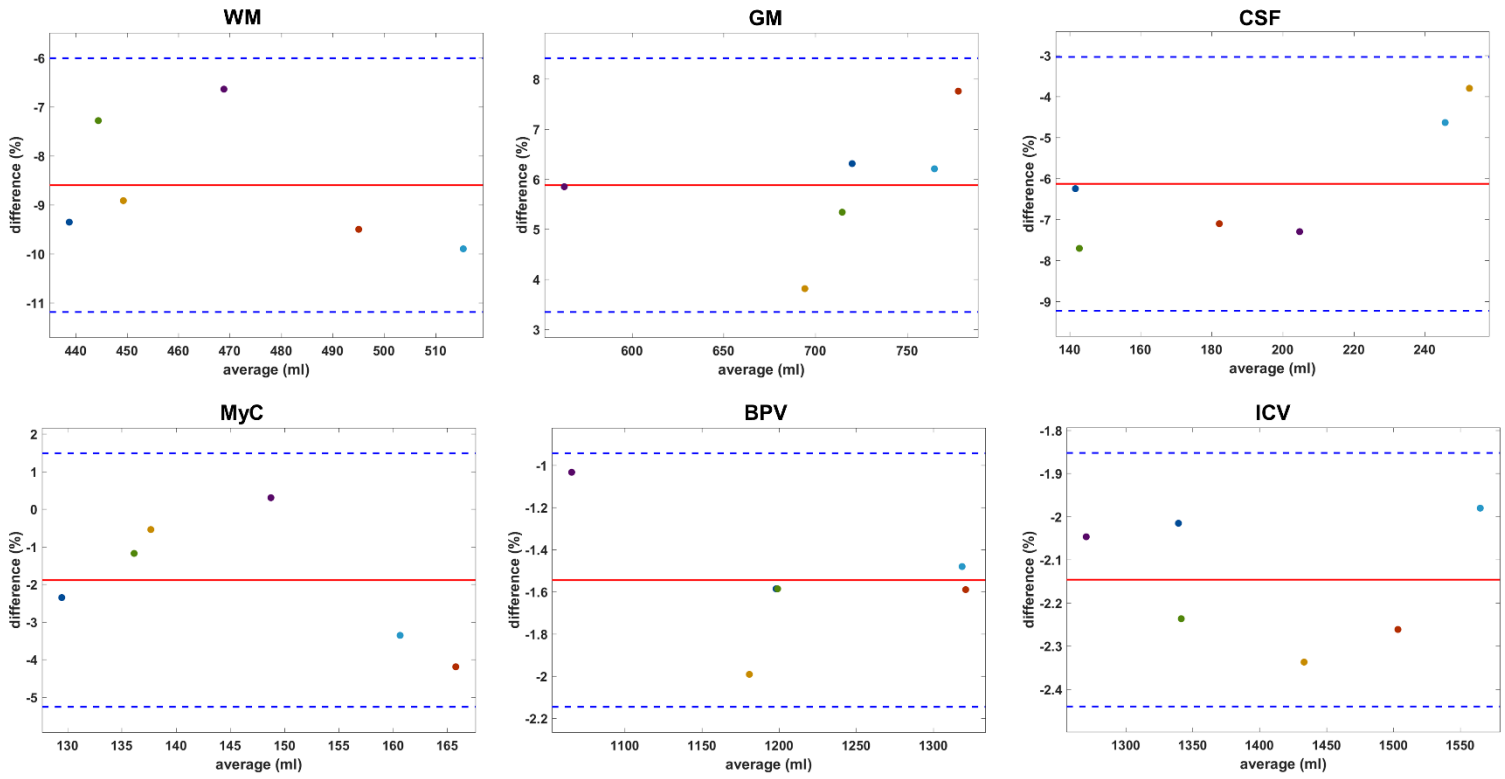

Figure 2: Bland-Altman plots showing the results for the inter-vendor comparison, with each volunteer in a different colour. The red line indicates the average difference (bias), the blue dotted line are at bias ± standard deviation. The mean of the test-retest measurement for each vendor is used in the plots. The y-axis shows the percentage difference between Philips-GE. For GM this gives a positive bias, for all other measures this bias is negative. The difference is small for BPV, ICV and MyC, but larger for WM, GM and CSF.

Dice scores vs GE test	WM	GM	CSF	MyC	BPV	ICV
GE retest	0.92 ± 0.01	0.91 ± 0.01	0.91 ± 0.01	0.78 ± 0.01	0.97 ± 0.00	0.99 ± 0.00
Philips test	0.89 ± 0.01	0.87 ± 0.01	0.84 ± 0.02	0.82 ± 0.01	0.96 ± 0.01	0.98 ± 0.00
Philips retest	0.89 ± 0.01	0.87 ± 0.02	0.83 ± 0.02	0.82 ± 0.01	0.96 ± 0.00	0.98 ± 0.00

Table 1: Dice scores of various segments with reference to a randomly chosen measurement. The scores are calculated from binary masks generated using a threshold of 30% for all segments except for MyC, where the threshold was 10%. The scores indicate good to excellent agreement. An inter-scanner effect can be observed, causing somewhat lower scores for Philips compared to GE. Only for MyC this is not the case.

Coefficient of variation	WM	GM	CSF	MyC	BPV	ICV
test-retest GE	1.36 ± 0.97	1.39 ± 0.41	0.93 ± 0.70	0.75 ± 0.29	0.23 ± 0.17	0.14 ± 0.17
test-retest Philips	0.91 ± 0.85	0.57 ± 0.70	1.17 ± 0.67	0.98 ± 0.97	0.17 ± 0.10	0.08 ± 0.04
inter-vendor	4.30 ± 0.60	2.94 ± 0.59	3.07 ± 0.72	0.99 ± 0.72	0.77 ± 0.14	1.07 ± 0.07

Table 2: Coefficient of variation of the volumetric results, both for the test-retest measurements (top two lines) as for the inter-vendor comparison (bottom line). The average values of the test-retest measurements were used to calculate the inter-vendor CV. The intra-vendor measurements show a CV<1.5%, indicating an excellent agreement. For the inter-vendor comparison, the CV is still good, ranging between 0.77% for BPV to 4.30% for WM.

A preliminary investigation into the contribution of Amines to the CEST contrast at 2 ppm and 3 ppm in glioblastomas at 7T

Bárbara Schmitz-Abecassis[1], Chloé Najac[1], Jeroen de Bresser[1], Linda Dirven[2,3], Martin J. B. Taphoorn[2,3], Matthias J.P. van Osch[1], Johan A. F. Koekkoek[2,3], Ece Ercan[1]

[1]Department of Radiology, Leiden University Medical Center, Leiden, Netherlands
[2]Department of Neurology, Leiden University Medical Center, Leiden, Netherlands
[3] Department of Neurology, Haaglanden Medical Center, The Hague, Netherlands

Synopsis: CEST allows to non-invasively image metabolites and proteins. Although the role of APT and NOE-CEST in gliomas has been widely investigated, the contribution of amines to the CEST-signal at 2 and 3ppm, and its relationship to creatine and glutamate concentrations, remain unclear. We evaluated the amineCEST contrast in tumor and CLWM in three glioma patients, and compared it to the MRS data. Overall we found a decrease in amineCEST alongside a decrease in total creatine and glutamate in the tumor compared to the CLWM.

Introduction: Chemical exchange saturation transfer (CEST) is a non-invasive MRI technique which can provide contrast originating from endogenous metabolites and proteins[1]. The usefulness of CEST imaging, specifically amide proton transfer (APT) and nuclear overhauser effect (NOE)[2,3], has been widely explored in glioma patients. More recently, the role of amines, such as glutamate-weighted CEST (at 3ppm) has been explored in relation to metabolic changes in diffuse gliomas and epilepsy at 7T[4]. Moreover, the contribution of creatine, with amine protons (at 2ppm), has also been explored in patients with glioma and on pre-clinical glioma models[5,6]. Despite the evidence that amines at both 2 and 3ppm provide relevant information on gliomas, no study has yet directly compared them and investigated the metabolic origin of the signal from these pools using MR Spectroscopy (MRS). In this preliminary work, we assessed the amine CEST-contrast at 2 and 3ppm in three glioma patients and compared the CEST-signal with the current gold standard of metabolite imaging, MRS.

Methods: We prospectively included three glioblastoma IDH-wild-type patients (2-Males, 1-Female, Mean age: 57+9). CEST, MRS and T_2-weighted scans were acquired on a 7TMRI scanner. The T_2-FLAIR was acquired as part of the clinical workflow at 3T. T_2-weighted images were used to plan CEST and MRS scans. Slices of interest for CEST and volumes of interest (VOIs) for MRS included the largest tumor-lesion, excluding necrotic tissue. MRS data were also collected from a VOI positioned in contralateral white matter (CLWM). For quantitative comparisons of CEST contrast and MRS data, the MRS VOIs in the tumor and CLWM were used as a mask on the CEST-maps. Image acquisition details can be found in Table1.

CEST images were corrected for B_0 inhomogeneities by interpolation followed by shifting the Z-spectra based on the minimum Z; and B_1 inhomogeneities, using a linear correction per voxel by using the B_1-maps. The CEST Z-spectra and magnetization transfer ratio (MTR) asymmetry were calculated

per voxel, for amines at 2 and 3ppm: $MTR_{asym} = [Z(-x\ ppm) - Z(+x\ ppm)] / Z(-x\ ppm)$

Water-suppressed MRS spectra were corrected for eddy-currents using a custom-built MATLAB routine and fitted with LCModel[7,8]. A basis-set was generated using FID-A toolbox[9]. Concentration and cramer-rao lower bounds (CRLBs) for total creatine (Cr+PCr) and glutamate were obtained from LCModel output. In Figure1, the fitted spectra from the tumor lesion and CLWM of each patient are shown in red and green, respectively, as well as the corresponding VOI.

Results: Figure2 shows the CEST results of one patient, where the MTR asymmetry maps for amines at 2 and 3ppm have been overlaid on the T_2-FLAIR. In Figure 3A, we display the MTR asymmetry values for each patient. MTR asymmetry values at 2ppm (orange squares - Subject1:10.79; Subject2:16.34; Subject3:8.36) are lower for tumors compared to CLWM (orange circles – Subject1:13.22; Subject2:17.88; Subject3:12.08). In Figure3B, the concentration of total creatine and glutamate are shown for both the tumor-lesion and CLWM. It can also be seen that the tCr concentration is lower in the tumor (orange squares – Subject1:12.85; Subject2:9.51; Subject3:9.33) when compared to CLWM (orange circles – Subject1:10.82; Subject2:11.24; Subject3:14.57) except for Subject1. Figure4 shows the ratios between tumor and CLWM, for CEST and MRS, per subject. In orange, tCr and amines at 2ppm illustrate comparable ratios, contrarily to glutamate and amines at 3ppm (in blue).

Discussion and conclusion: This work aimed at assessing the amineCEST-contrast at 2 and 3ppm in glioblastoma compared to CLWM and their relationship to metabolite concentration measured by MRS at 7T.

Contrarily to a recent study[4], our results show a decrease in MTR asymmetry at 2 and 3ppm in tumors compared to CLWM. Neal et al. investigated the CEST-contrast of glutamate (at 3ppm) in mainly IDH mutant glioma patients (WHO grade-II/III) with epilepsy, supporting the role of glutamate in the biology of diffuse lower-grade gliomas[4]. Differently from this study, our patient population consisted of only glioblastoma, IDH wild type patients. This could explain why we did not see a higher CEST-signal from tumors compared to CLWM. In line with our results, a recent study showed lower CEST-signal at 2ppm in high-grade glioma patients, and concluded that amineCEST at 2ppm could be useful for glioma stratification together with molecular markers[6]. Moreover, Cai et al. have previously shown a lower CEST-signal at 2ppm in a pre-clinical model of brain tumors and its correlation to creatine distribution[5]. Similarly, our results based upon MRS also suggest that creatine is the main contributor to the CEST-contrast at 2ppm. In conclusion, our results suggest that the amine pool at 2ppm relates to creatine distribution and can be used as a more prominent marker for glioblastomas. Work in progress includes collecting data from a larger group of patients to confirm our preliminary results.

References:

1. Wu B, Warnock G, Zaiss M, et al. An overview of CEST MRI for non-MR physicists. *EJNMMI Phys*. 2016;3(1). doi:10.1186/s40658-016-0155-
2. Zaiss M, Windschuh J, Paech D, et al. Relaxation-compensated CEST-MRI of the human brain at 7T: Unbiased insight into NOE and amide signal changes in human glioblastoma. *Neuroimage*. 2015;112:180-188. doi:10.1016/j.neuroimage.2015.02.040
3. Wen Z, Hu S, Huang F, et al. MR imaging of high-grade brain tumors using endogenous protein and peptide-based contrast. *Neuroimage*. 2010;51(2):616-622. doi:10.1016/j.neuroimage.2010.02.050
4. Neal A, Moffat BA, Stein JM, et al. Glutamate weighted imaging contrast in gliomas with 7 Tesla magnetic resonance imaging. *NeuroImage Clin*. 2019;22(June 2018):101694. doi:10.1016/j.nicl.2019.101694
5. Cai K, Singh A, Poptani H, et al. CEST signal at 2ppm (CEST at 2ppm) from Z-spectral fitting correlates with creatine distribution in brain tumor. *NMR Biomed*. 2015;28(1):1-8. doi:10.1002/nbm.3216
6. Su C, Xu S, Lin D, et al. Multi-parametric Z-spectral MRI may have a good performance for glioma stratification in clinical patients. *Eur Radiol*. Published online 2021. doi:10.1007/s00330-021-08175-3
7. Provencher SW. Estimation of metabolite concentrations from localized in vivo proton NMR spectra. *Magn Reson Med*. 1993;30(6):672-679. doi:10.1002/mrm.1910300604
8. Klose U. In vivo proton spectroscopy in presence of eddy currents. *Magn Reson Med*. 1990;14(1):26-30. doi:10.1002/mrm.1910140104
9. Simpson R, Devenyi GA, Jezzard P, Hennessy TJ, Near J. Advanced processing and simulation of MRS data using the FID appliance (FID-A)—An open source, MATLAB-based toolkit. *Magn Reson Med*. 2017;77(1):23-33. doi:10.1002/mrm.26091

Acknowledgments / Funding Information: A work funded by: Medical Delta Cancer 3.0 program, NWO grant #16862

Acquisition parameters

Imaging parameters	Amine CEST	DREAM B_1 map	sLASER single-voxel MRS	T_2 weighted scan	T_2-FLAIR
TR/TE (ms)	3.3 / 1.82	8.0 / 1.97	6000/38	3000/278	11000 / 125
Field of view (FOV) (mm^3)	246 x 246 x 32 mm^3	246 x 246 x 32 mm^3	-	250 x 250 x 189 mm^3	220 x 175 x 27 mm^3
Voxel size (mm^3)	2 x 2 x 4	1.5 x 1.5 x 1.5	20x 20 x 20	0.75 x 0.75 x 0.75	5 x 5 x 5
RF B_1 amplitude	3.52μT	-	-	-	-
RF duration/interval/repetition (ms)	50/50/10	-	-	-	-
Number of averages (NSA)	1	1	32	1	1
Total scan time	05:06 min	00:09 min	03:36 min	04:06 min	02:12 min

Table 1. Image acquisition parameters for CEST, MRS and T_2-weighted scan at 7T and clinical T_2-FLAIR.

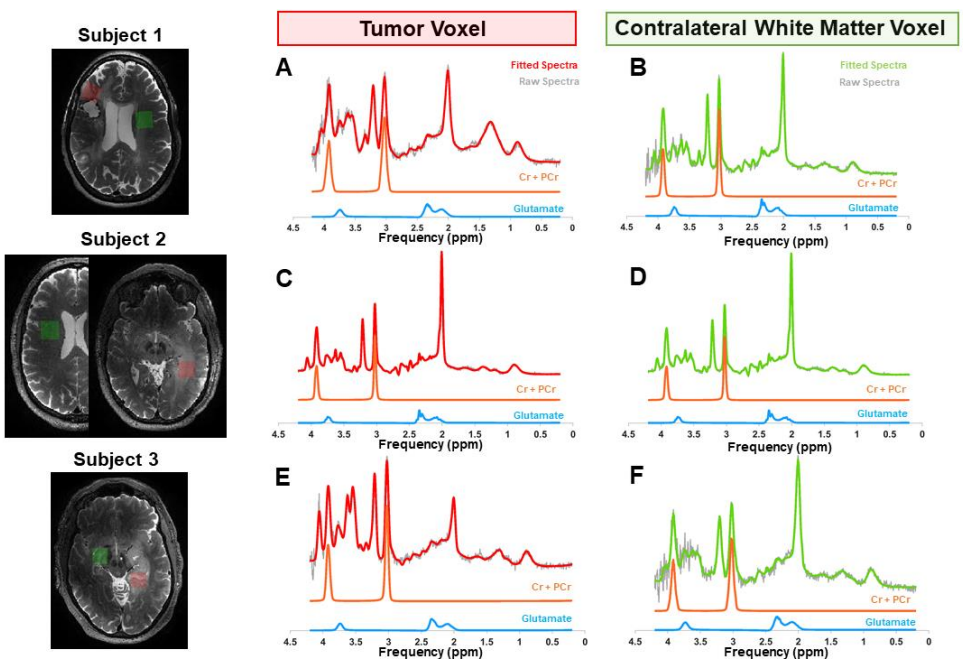

Figure 1. Magnetic resonance spectroscopy (MRS) spectra: In red the voxel of interest (VOI) in the tumor and the correspondent fitted tumor spectra overlaid on T_2-weighted images, for subjects 1, 2 and 3 (A, C and E, respectively). In green the VOI for the CLWM and the correspondent spectra, for subjects 1, 2 and 3 (B, D and F, respectively).

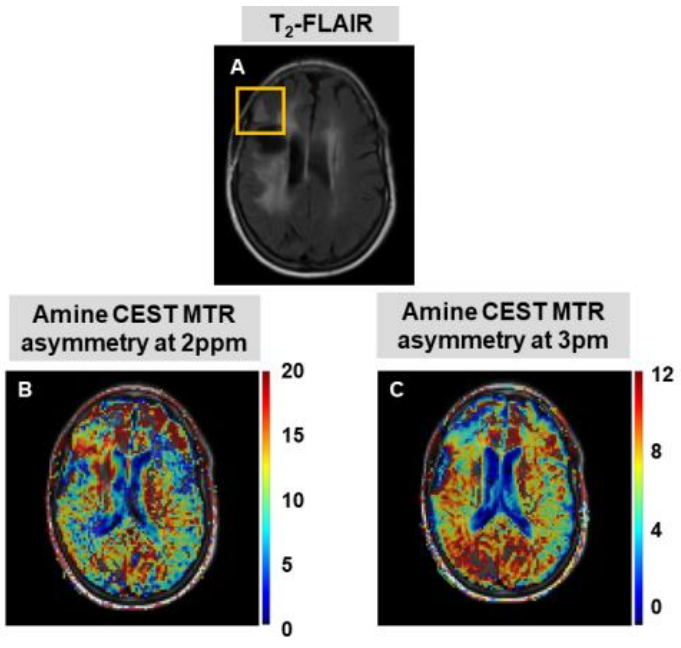

Figure 2. An example of CEST result for subject 1. A. The T_2-FLAIR image where the tumor lesion is highlighted in yellow. B, C. CEST MTR asymmetry maps overlaid on the clinical T_2-FLAIR. The maps correspond to the amines pool at 2ppm and 3ppm on the left and right, respectively.

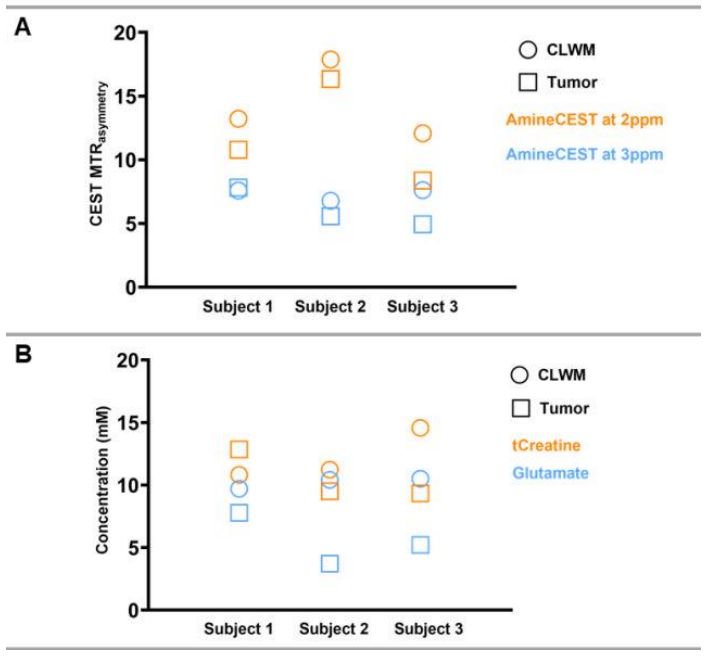

Figure 3. A. Mean CEST MTR asymmetry values for each patient individually extracted from the MRS VOI. Tumor values are represented with a square and CLWM with a circle, for amines at 2ppm and at 3ppm, in orange and blue, respectively. B. Concentration values of tCreatine and glutamate derived from MRS, displayed for each the patient individually from the VOI, in orange and blue, respectively. Tumor values are represented with a square and the ones for the CLWM with a circle.

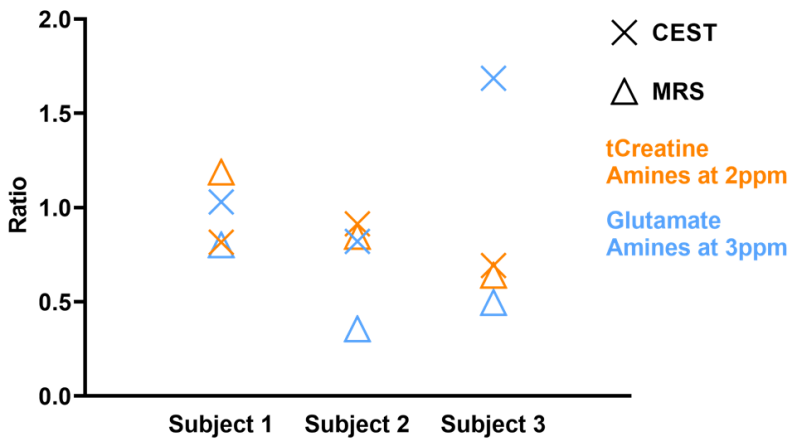

Figure 4. The ratio between the tumor and CLWM values illustrated by a cross and triangle, for CEST and MRS, respectively. Each column represents the data from one subject. Ratios for tCreatine (in MRS) and amines at 2 ppm (in CEST) are in orange, and in blue for Glutamate (MRS) and amines at 3 ppm (CEST).

Nodal detection in head and neck cancer by USPIO enhanced MRI: Where are the USPIOs in the blood?

Jack JA van Asten[2], Daphne Driessen[1], Esther D Kers-Rebel[1], Gosse J Adema[1], Johannes HAM Kaanders[1], Tom WJ Scheenen[2]

[1]Department of Radiation Oncology, [2]Department of Medical Imaging, Radboud university medical centre, Nijmegen, the Netherlands

Synopsis: USPIO-enhanced MRI is a promising imaging method to detect metastatic lymph nodes in patients with head and neck cancer. In the validation process of the USPIO-enhanced MRI technique, it is of interest to determine whether phagocytic uptake occurs in the blood. Therefore this work investigates which blood compartments contain the USPIO particles after infusion. T2 relaxometry established that intravenously injected USPIOs are present in the serum and plasma compartments of the blood.

Introduction: In patients with head and neck cancer, accurate detection of lymph node metastases is of great relevance regarding prognosis and treatment [1,2]. USPIO-enhanced MRI is a promising imaging method to detect metastatic lymph nodes. After intravenous administration, USPIOs accumulate in cells of the immune system residing within healthy (parts of) lymph nodes [3], attenuating MR signal intensity in T2*-weighted pulse sequences. Suspicious lymph nodes retain MR signal intensity. In the validation process of this technique it is of interest to determine whether phagocytic uptake occurs in the blood or inside the lymph nodes. The aim of the present work is therefore to investigate which blood compartments contain the USPIO particles after infusion.

Methods: Blood samples were collected from five head and neck cancer patients at two different timepoints. The baseline sample was obtained prior to the slow-drip USPIO infusion, the second sample 45 minutes after the start of USPIO infusion. The blood was separated into six components: serum (SER), plasma (PLA), full blood (FB), peripheral blood mononuclear cells (PBMC), and granulocytes with and without red blood cells (GRA+RB, GRA-RB). The presence of USPIOs influences the relaxivity of the blood compartments and therefore the transverse relaxation times (T2) were measured, performing the Carr Purcell Meiboom Gill (CPMG) sequence [4,5] with 16 echo time points ranging from 1 – 100 ms, up to 2 – 5000 ms, depending on the a priori estimated T2. The relaxometry measurements were performed at a Bruker Avance 11.7 Tesla magnet, at room temperature (298K). After fourier transform of the 16 free induction decays, the decay curves of the integrated NMR signals of water were fitted with a mono exponential, using the Bruker Topspin software. Shorter T2 relaxation times indicate the presence of USPIOs.

Results: After infusion, significantly shorter T2 times were observed in full blood, serum and plasma indicating the presence of USPIOs, which seem absent in other compartments. The decay of the NMR signal of water is depicted in Figure 1. Averaged transverse relaxation times of the six blood compartments with and without USPIOs are presented in Table 1.

Discussion: Intravenously injected USPIOs are present in the serum and plasma compartments. These data indicate that USPIOs are not phagocytosed by the white blood cells present in the blood within 45 minutes after administration, but rather remain in the serum/plasma fraction. The full blood component represents the other compartments all together and therefore also shows significant difference in T2 times between blood with and without USPIOs.

References:

[1] Snow GB, et al. Clin Otolaryngol Allied Sci. 1982;7(3):185-92.

[2] Leemans CR, et al. Cancer. 1993;71(2):452-6.

[3] Weissleder R, et al. Radiology. 1990;175(2):494-8.

[4] H. Y. Carr and E. M. Purcell, Phys. Rev. 94, 630 (1954).

[5] S. Meiboom and D. Gill, Rev. Sci. Instrum. 29, 688 (1958).

Acknowledgments / Funding Information:

Figure 1. Pseudo 2D of decaying NMR signal of water in blood variant.

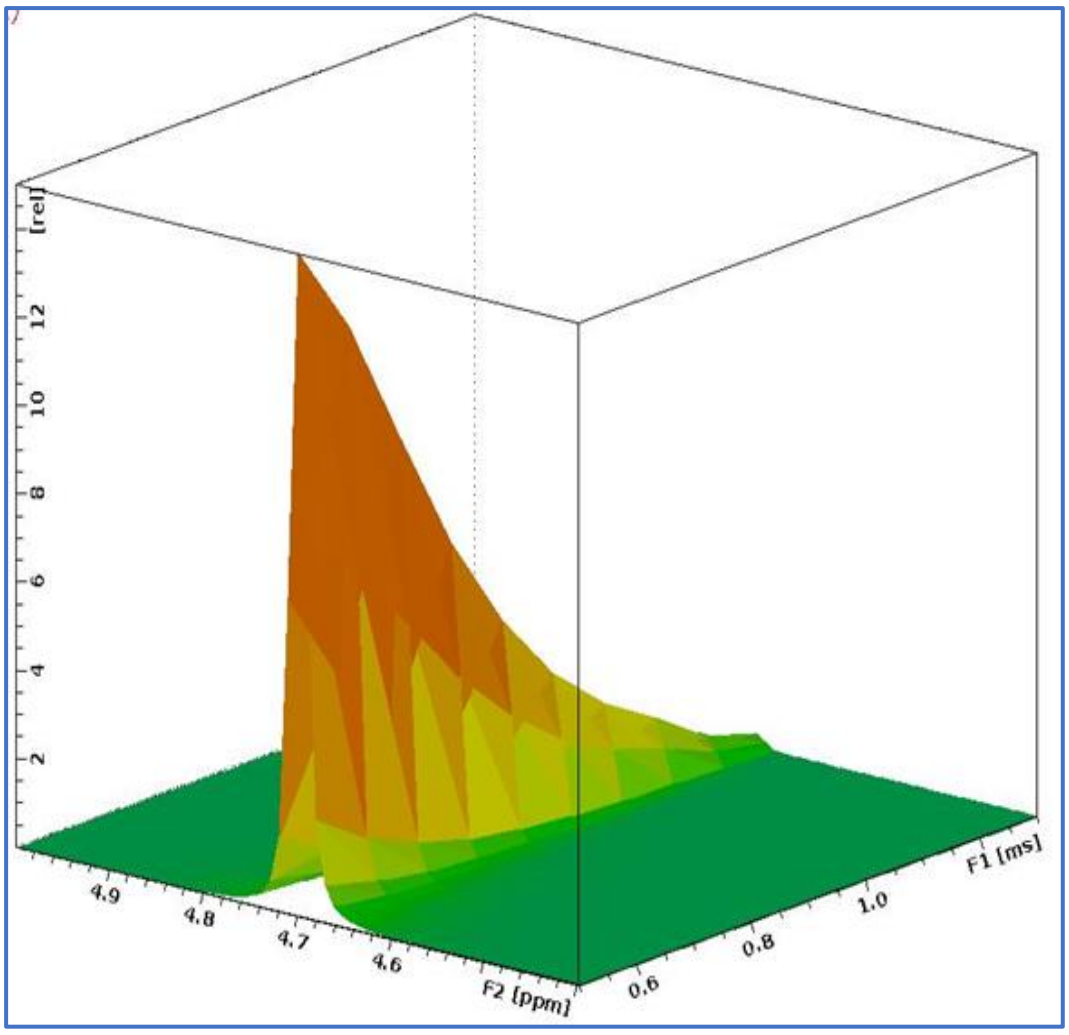

Table 1. Mean T2 times (+/- SE), of six blood components with and without USPIOs. Statistical significant difference by t-test, indicated by * ($p<0.05$).

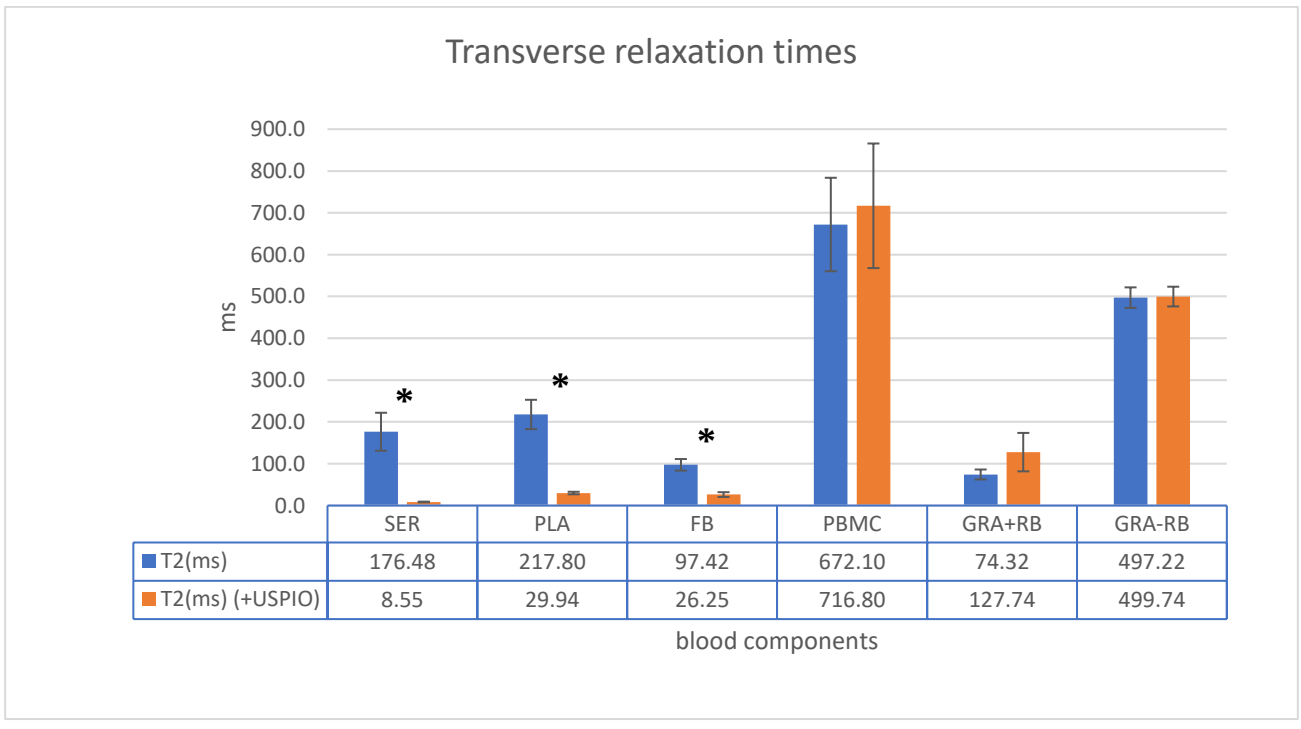

	SER	PLA	FB	PBMC	GRA+RB	GRA-RB
T2(ms)	176.48	217.80	97.42	672.10	74.32	497.22
T2(ms) (+USPIO)	8.55	29.94	26.25	716.80	127.74	499.74

Optimal acquisition settings for simultaneous diffusion kurtosis, free water fraction and T2 estimation

V. Anania[1,2], B. Jeurissen[1,3], J. Morez[1], A.E. Buikema[1], T. Billiet[2], J. Sijbers[1,3], A.J. den Dekker[1,3]
[1]imec-Vision Lab, Department of Physics, University of Antwerp, Antwerp, Belgium; [2]icometrix, Leuven, Belgium;
[3]μNEURO Research Centre of Excellence, University of Antwerp, Antwerp, Belgium

Synopsis: Fitting the diffusion kurtosis imaging free water elimination model (DKI-FWE) to diffusion MRI data represents an ill-conditioned problem. Fortunately, the conditioning of the model fitting can be improved by explicitly modeling the T2 relaxation dependency of the signal. As a benefit, diffusion and kurtosis metrics robust to partial volume effects can be estimated with conventional techniques. In this work, we use Cramér-Rao lower bound (CRLB) theory to identify optimal acquisition settings that maximize the precision of the model parameter estimates.

Purpose: The two-compartment diffusion kurtosis imaging free water elimination model (DKI-FWE)[1] allows to mitigate the bias induced by partial volume effects on tissue-related diffusion parameters. The incorporation of the compartmental T_2 relaxation times helps stabilize the FWE model fitting problem[2]. Therefore, accurate and precise parameter estimates can be obtained by using standard nonlinear least squares (NLLS) estimation techniques. However, DKI is a lengthy imaging protocol, implying that the choice of the data acquisition protocol plays a crucial role to achieve reliable quantification of the tissue properties in competitive acquisition times. In this work, we optimize the diffusion weighting strengths (b-values) and echo time (TEs) in terms of the Cramér-Rao lower bound (CRLB) variances of the model parameters and derived metrics[3].

Methods: DKI-FWE with explicit T_2 dependency (in short T_2-DKI-FWE) models the T_2 and diffusion weighted signal as:

$$S = S_{00}\left((1-f)\exp\left(-\frac{\mathrm{TE}}{T_2^{\mathrm{tissue}}}\right)S_{\mathrm{tissue}}(b,\boldsymbol{g};\boldsymbol{\theta}_{\mathrm{DKI}}) + f\exp\left(-\frac{\mathrm{TE}}{T_2^{\mathrm{fw}}}\right)\exp\left(-bd\right)\right),$$

with S_{00} the non-diffusion weighted signal at TE = 0 ms, f the TE-independent free water signal fraction, $\boldsymbol{g}$ the diffusion weighting direction, $\boldsymbol{\theta}_{\mathrm{DKI}}$ the diffusion and kurtosis tensor parameter vector and d the diffusivity of free water fixed to 3 μm²/ms. While T_2^{tissue} is estimated as an unknown model parameter, T_2^{fw} is fixed to a constant value of 1573 ms derived from literature[4]. In this work, the acquisition schemes resulting from two different CRLB-based optimality criteria (O_1 and O_2) are compared with each other and with a reference scheme (R) consisting of four fixed b-values (0, 0.5, 1 and 2 ms/μm²) acquired at two different TEs (63 and 120 ms). The optimized scheme O_1, previously suggested by the authors[5], was obtained by minimizing the sum of the CRLB variances of $\boldsymbol{\theta}_{\mathrm{DKI}}$, f and the weighted CRLB variance of T_2^{tissue}. In the current work, we assess an additional optimized protocol resulting from the minimization of the sum of the weighted CRLB variances of the fractional anisotropy (FA), mean diffusivity (MD), the linear part of the mean kurtosis ($\bar{K}^*_{app}$), f and T_2^{tissue}. In line with our previous work[5], 120 uniformly distributed gradient directions were kept fixed during the optimization while b-values and TEs were free to vary in the range 0-2 ms/μm² and 63-121 ms, respectively. The optimality criteria were averaged over 500 white matter voxels with a certain degree of free water contamination ($0.05 \leq f \leq 0.03$) and extracted from the T_2-DKI-FWE model fits of a real dataset. The weights applied in the optimization procedure were set equal to the inverse of the ground truth value of the parameter or metric of interest. The performance of all schemes was assessed both in terms of the maximum attainable precision (i.e. the CRLB) and the sample variances of relevant metrics (FA, MD, $\bar{K}^*_{app}$, f and T_2^{tissue}). The sample variances were evaluated in a single-voxel Monte Carlo simulation framework and an unconstrained NLLS fitting routine was used to prevent the introduction of any source of bias due to the position of constraints. In all experiments, Gaussian data distribution was assumed and the signal-to-noise ratio (SNR) was defined on the non-diffusion weighted signal of a non-free water contaminated voxel (f = 0) at the lowest TE (i.e. 63 ms).

Results: Figure 1 shows the distribution of the b-values and TEs for each acquisition scheme and a clustered version of the optimized schemes O_1 and O_2 is proposed for practical reasons. In Figure 2, the CRLB variances and the sample variances assessed in single-voxel experiments are compared for different metrics and for each scheme as a function of the SNR. Finally, in Figure 3, the sample variances of the FA, MD and mean kurtosis (MK) estimates are reported for the reference scheme R and the clustered versions of O_1 and O_2.

Discussion: The good agreement between theoretical bounds and sample variances (Fig. 2) suggests that minimizing the CRLB variances of the parameters of interest is an appropriate criterion for optimal design. Our results highlight that, depending on the parameters included in the cost function and the weighting strategy, the precision of a specific set of metrics can be favored. As a proof of concept, we compare the schemes resulting from two different optimality criteria, O_1 and O_2. Both schemes outperform the conventional acquisition protocol R in terms of the precision of FA, MD, $\bar{K}^*_{app}$ and f in a range of medium/high SNR values. When comparing O_1 and O_2, it is clear that O_2 leads to a gain in precision for MD, f and T_2^{tissue} while more precise FA and $\bar{K}^*_{app}$ estimates can still be achieved with O_1. Finally, clustering the optimal settings in fixed b-TE combinations does not affect the precision of the diffusion derived metrics (Fig. 3) and allows to set up a more practical acquisition.

Conclusion: This study shows that precise T_2-DKI-FWE parameter estimates can be achieved in reasonable acquisition times (< 10 minutes) by using CRLB-optimized settings. A validation of these findings on *in vivo* datasets will be subject of future work.

References:

1. Collier Q, Veraart J, Jeurissen B, Vanhevel F, Pullens P, Parizel PM, den Dekker AJ, Sijbers J. Diffusion kurtosis imaging with free water elimination: A bayesian estimation approach. Magnetic Resonance in Medicine. 2018;80(2):802-13.
2. Collier Q, Veraart J, den Dekker AJ, Vanhevel F, Parizel PM, Sijbers J. Solving the free water elimination estimation problem by incorporating T2 relaxation properties. In Proceedings of 25th Annual Meeting of ISMRM, Honolulu, Hawaii, USA 2017 (p. 1783).
3. Poot DHJ, den Dekker AJ, Achten E, Verhoye M, Sijbers J. Optimal experimental design for diffusion kurtosis imaging. IEEE Transactions on Medical Imaging. 2010;29(3):819-29.
4. Qin Q. A simple approach for three-dimensional mapping of baseline cerebrospinal fluid volume fraction. Magnetic Resonance in Medicine. 2011;65(2):385-91.
5. Anania V, Jeurissen B, Morez J, Buikema AE, Billiet T, Sijbers J, den Dekker AJ. Optimal experimental design for the T2-weighted diffusion kurtosis imaging free water elimination model. Book of Abstracts ESMRMB 2021 Online 38th Annual Scientific Meeting 7–9 October 2021. Magn Reson Mater Phy 34, 1–204 (2021), pp. 54-55.

Acknowledgments / Funding Information: This project has received funding from the European Union's Horizon 2020 research and innovation program under the Marie Skłodowska-Curie grant agreement No 764513. The work was also supported by the Research Foundation Flanders (FWO Belgium) through project funding (G084217N and 12M3119N).

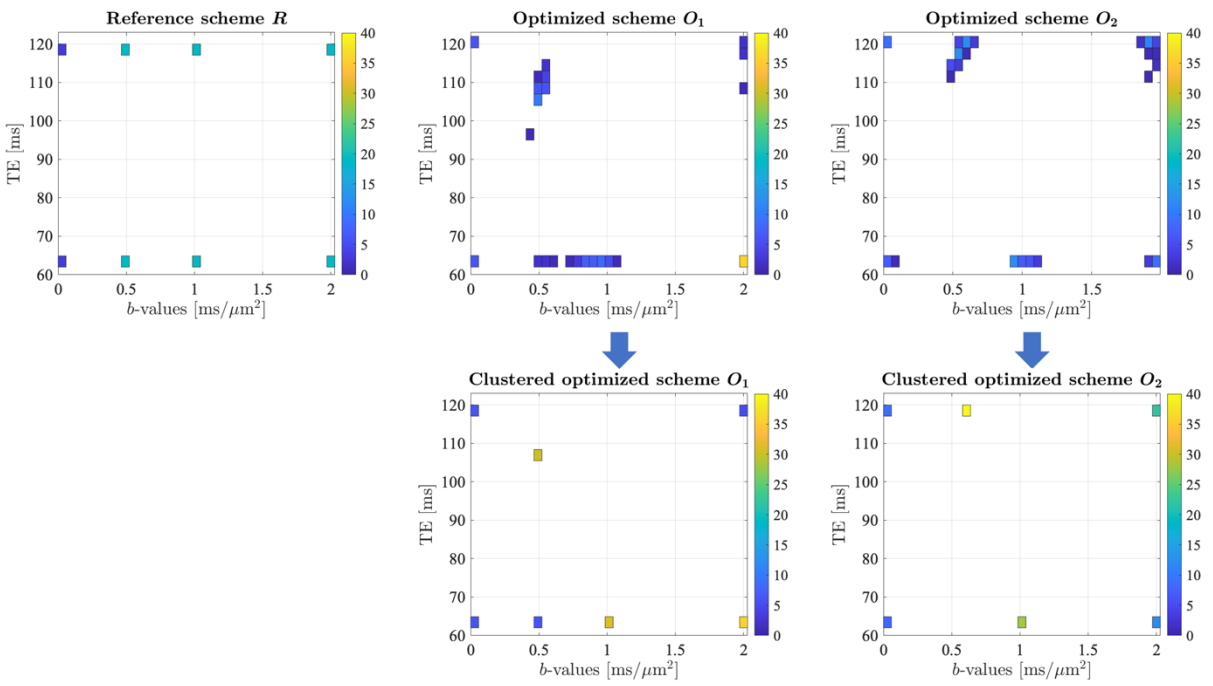

Figure 1. Top row: distribution of b-values and TEs for the reference scheme R (left) and the optimized schemes O_1 (center) and O_2 (right). Bottom row: a more practical version of the acquisition schemes O_1 (center) and O_2 (right) is proposed.

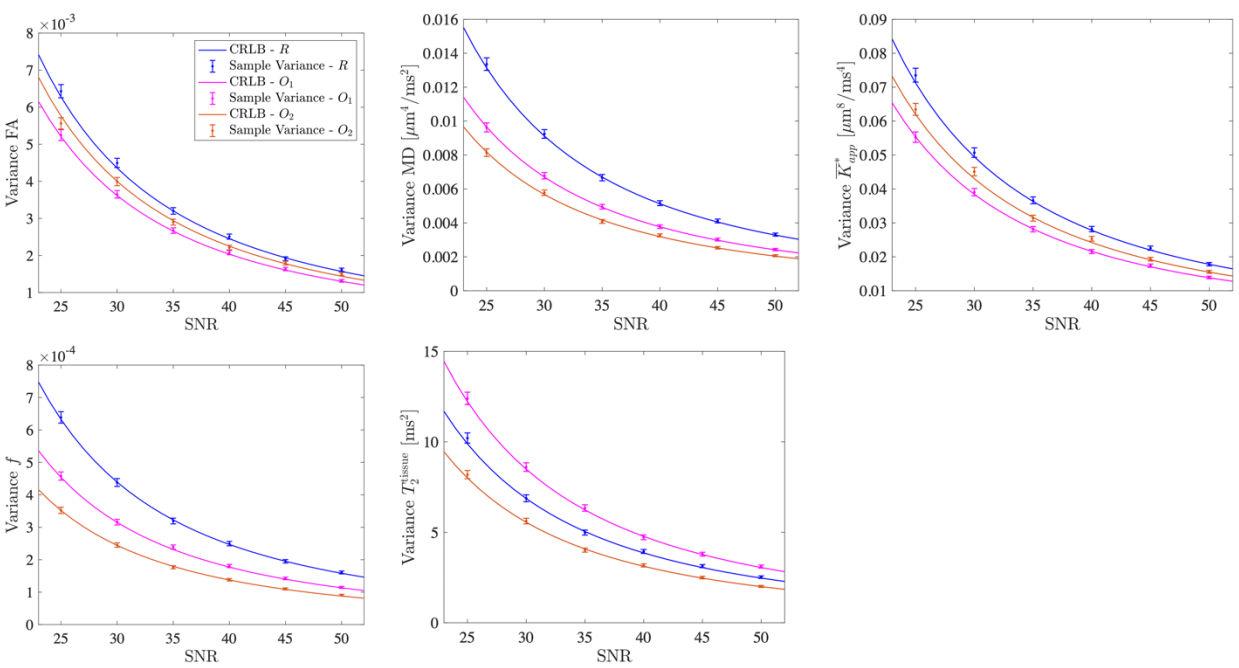

Figure 2. Top row: CRLB variances and sample variances with 95% confidence interval of FA (top row, left), MD (top row, center), $\overline{K}^*_{app}$ (top row, right), f (bottom row, left) and T_2^{tissue} (bottom row, center) as a function of the SNR and for each acquisition scheme (R, O_1 and O_2). A single voxel was simulated with ground truth FA = 0.60, MD = 0.89 μm^2/ms, MK = 0.91, f = 0.1 and T_2^{tissue} = 70 ms. The fitting was repeated for 10^4 noise realizations.

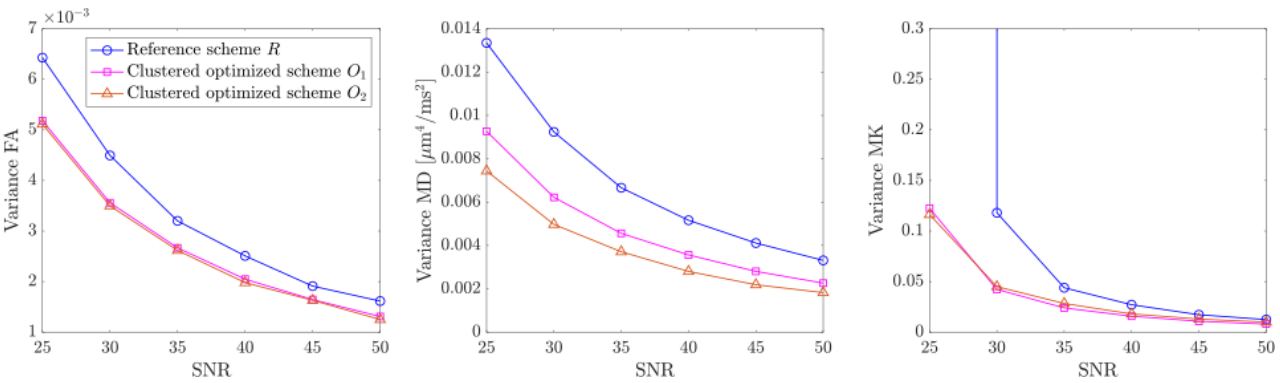

Figure 3. Sample variances of the FA, MD and MK estimates as a function of the SNR for the reference scheme R and the clustered versions of the optimized schemes O_1 and O_2. A single voxel was simulated with ground truth FA = 0.60, MD = 0.89 μm^2/ms, MK = 0.91, f = 0.1 and T_2^{tissue} = 70 ms. The fitting was repeated for 10^4 noise realizations.

Correlating neurite density and synaptic density in the human brain in vivo with diffusion-weighted PET-MR

D. Christiaens[1,6], T. Vande Casteele[2,3,6], M. Laroy[3,6], M. Van Cauwenberge[2,3,6], J. Van den Stock[2,3], F. Bouckaert[2,3], S. Sunaert[4,5,6], M. Vandenbulcke[2,3], F. Maes[1,6], L. Emsell[2,3,4,6]

[1]KU Leuven, Department of Electrical Engineering, ESAT-PSI, Leuven, Belgium; [2]Geriatric Psychiatry, UPC KU Leuven, Leuven, Belgium; [3]KU Leuven, Leuven Brain Institute, Department of Neurosciences, Neuropsychiatry, Leuven, Belgium; [4]KU Leuven, Department of Imaging & Pathology, Translational MRI, Leuven, Belgium; [5]Radiology, University Hospitals Leuven, Leuven, Belgium; [6]Medical Imaging Research Center, University Hospitals Leuven, Leuven, Belgium

Synopsis: ^{11}C-UCB-J PET offers a unique imaging modality to map synaptic density in the human brain in vivo with high specificity. Here, we investigate its correlation with several diffusion MRI metrics and microstructure model parameters in diffusion-weighted PET-MR. We report moderate negative correlation of ^{11}C-UCB-J uptake with measures of anisotropy, consistent with a hypothesis that higher synaptic density is associated with a more disorganised neurite configuration. We also find weak positive correlation to the intra-axonal signal fraction in cortical grey matter. As such, UCB-J PET-MR can further the interpretation and in vivo validation of more advanced microstructure models of grey matter.

Introduction: Microstructure modelling with diffusion MRI (dMRI) can probe measures of neural and glial microstructure in the brain, based on models of tissue compartments and their contribution to the dMRI signal. However, the interpretation of current dMRI metrics and model parameters in relation to underlying biological effects often remains in question. Independent imaging modalities with higher specificity can aid our understanding of microstructure model parameters and offer a potential path toward their *in vivo* validation.

The ^{11}C-UCB-J radiotracer is a novel PET imaging tracer that binds with high specificity to the synaptic vesicle glycoprotein 2A [1], a protein that is expressed ubiquitously in presynaptic vesicles.^{11}C-UCB-J PET imaging therefore can serve as a proxy for synaptic density in the human brain [2]. Synaptic density may, in turn, be expected to correlate with neurite (axon and dendrite) density in grey matter.

Here, we explore to what extent conventional and more advanced dMRI metrics, including model estimates of neurite density, correlate regionally with ^{11}C-UCB-J uptake in multi-shell diffusion-weighted PET-MR imaging data acquired *in vivo*.

Materials and Methods:

Data. We retrospectively selected imaging data of 8 healthy controls (4M, 4F; age 61-73y) with good quality data that were originally scanned for a clinical study on a GE Signa 3T PET-MR system. dMRI data were acquired with 2.5 x 2.5 x 2.5 mm resolution; TE = 87ms; TR = 6600ms; multiband (hyperband) factor 2; GRAPPA (ARC) factor 2; *b*-values 0, 700, 1000 and 2000 s/mm^2 with 12, 20, 32 and 60 isotropically distributed gradient directions respectively. dMRI data were preprocessed with denoising [3], Gibbs ringing suppression [4], motion and distortion correction [5,6], and bias field correction [7] using MRtrix3 [8]. ^{11}C-UCB-J PET imaging was simultaneously acquired with spatial resolution of 4 x 4 x 4 mm; Standardized Uptake Value Ratio (SUVR) images were calculated relative to the centrum semiovale. A T1w image with 1mm isotropic resolution was segmented into white matter (WM), cortical grey matter (CGM), and deep grey matter (DGM) using FSL FAST [9].

dMRI metrics. We calculated 4 sets of dMRI parameters, shown in Figure 1:

- Signal metrics: The mean dMRI signal in each shell and the generalised fractional anisotropy (GFA) in each shell, defined as the standard deviation of the signal intensity divided by the root mean square signal intensity.
- DTI metrics: mean diffusivity (MD) and fractional anisotropy (FA) of the diffusion tensor [10], fitted to the $b <= 1000$ s/mm^2 data.
- MT-CSD metrics: the total apparent fibre density (AFD), defined as the integral of the WM fibre orientation distribution function (ODF), which was estimated using multi-shell multi-tissue constrained spherical deconvolution (MT-CSD) [11].
- Microstructure metrics: parameters of the standard 2-compartment model of WM microstructure, which consists of an intra-axonal *stick* compartment with fraction f and axial diffusivity D_i, and an extracellular *zeppelin* compartment with axial and radial diffusivity $D_e^{/\!/}$ and $D_e^{\perp}$ (parametrized by the trace $D_e = D_e^{/\!/} + 2D_e^{\perp}$ and difference $\Delta D_e = D_e^{/\!/} - D_e^{\perp}$), and which also models fibre crossings and dispersion in a ODF [12,13]. The microstructure parameters and the ODF spectral power p_L, $L=0,2,4,...$ are jointly estimated in Bayesian fashion using Monte Carlo integration based on rotation-invariant signal features [14].

Correlations. The dMRI and PET contrast were rigidly coregistered to the T1w image. We evaluated linear correlation coefficients (Pearson's R) between the dMRI metrics and the ^{11}C-UCB-J SUVR maps in segmented CGM, DGM and WM in all subjects individually as well as aggregated across the cohort.

Results: Figure 2 shows boxplots of the correlation coefficients in each of the dMRI contrasts. We find moderate ($|R| > 0.5$) negative correlation with measures of tissue anisotropy (GFA, FA, and the spectral power ratio p_2/p_0) in most tissues, with high consistency across subjects.

In CGM, where ^{11}C-UCB-J uptake is highest, we also find a weak positive correlation with the intra-axonal fraction f ($R = 0.35$), the intra-axonal diffusivity D_i ($R = 0.45$), and the anisotropy of the extra-axonal compartment ΔD_e ($R = 0.47$).

The correlation with signal-level GFA measures exceeds model-based metrics. These correlations were also the most consistent across tissues and subjects.

Joint histograms of ^{11}C-UCB-J uptake and the dMRI metrics, shown in Figure 3 for signal, DTI and MT-CSD metrics and in Figure 4 for standard model parameters, reveal nonlinear codependencies but also confirm the correlation with dMRI measures of anisotropy.

Discussion and Conclusion: The moderate correlation with dMRI anisotropy is consistent with a hypothesis that higher synaptic density is associated with a more disorganised neurite configuration (dendritic branching etc.). Evidence of a positive correlation with neurite density in grey matter, measured indirectly by the intra-axonal fraction f or AFD, is weak or inconclusive.

Due to the low spatial resolution of PET and dMRI relative to cortical thickness, partial volume effects are a limiting factor in the analysis. Furthermore, the standard WM model does not account for additional signal contributions in grey matter, notably due to soma presence [15] and inter-compartmental exchange [16]. Future work can explore these and other more advanced microstructure models for grey matter with bespoke dMRI acquisition strategies.

References:

1. Nabulsi NB, Mercier J, Holden D, et al. Synthesis and Preclinical Evaluation of 11C-UCB-J as a PET Tracer for Imaging the Synaptic Vesicle Glycoprotein 2A in the Brain. J Nucl Med. 2016;57(5):777-784. doi:10.2967/jnumed.115.168179
2. Finnema SJ, Nabulsi NB, Eid T, Detyniecki K, Lin SF, Chen MK, Dhaher R, Matuskey D, Baum E, Holden D, Spencer DD, Mercier J, Hannestad J, Huang Y, Carson RE. Imaging synaptic density in the living human brain. Sci Transl Med. 2016 Jul 20;8(348):348ra96. doi: 10.1126/scitranslmed.aaf6667.
3. Veraart J, Novikov DS, Christiaens D, Ades-Aron B, Sijbers J, Fieremans E. Denoising of diffusion MRI using random matrix theory. Neuroimage. 2016;142:394-406. doi:10.1016/j.neuroimage.2016.08.016
4. Kellner E, Dhital B, Kiselev VG, Reisert M. Gibbs-ringing artifact removal based on local subvoxel-shifts. Magn Reson Med. 2016;76(5):1574-1581. doi:10.1002/mrm.26054
5. Andersson JL, Skare S, Ashburner J. How to correct susceptibility distortions in spin-echo echo-planar images: application to diffusion tensor imaging. Neuroimage. 2003;20(2):870-888. doi:10.1016/S1053-8119(03)00336-7
6. Andersson JLR, Sotiropoulos SN. An integrated approach to correction for off-resonance effects and subject movement in diffusion MR imaging. Neuroimage. 2016;125:1063-1078. doi:10.1016/j.neuroimage.2015.10.019
7. Tustison NJ, Avants BB, Cook PA, et al. N4ITK: improved N3 bias correction. IEEE Trans Med Imaging. 2010;29(6):1310-1320. doi:10.1109/TMI.2010.2046908
8. Tournier JD, Smith R, Raffelt D, et al. MRtrix3: A fast, flexible and open software framework for medical image processing and visualisation. Neuroimage. 2019;202:116137. doi:10.1016/j.neuroimage.2019.116137
9. Zhang Y, Brady M, Smith S. Segmentation of brain MR images through a hidden Markov random field model and the expectation-maximization algorithm. IEEE Trans Med Imaging. 2001;20(1):45-57. doi:10.1109/42.906424
10. Basser PJ, Mattiello J, LeBihan D. MR diffusion tensor spectroscopy and imaging. Biophys J. 1994;66(1):259-267. doi:10.1016/S0006-3495(94)80775-1
11. Jeurissen B, Tournier JD, Dhollander T, Connelly A, Sijbers J. Multi-tissue constrained spherical deconvolution for improved analysis of multi-shell diffusion MRI data. Neuroimage. 2014;103:411-426. doi:10.1016/j.neuroimage.2014.07.061
12. Novikov DS, Veraart J, Jelescu IO, Fieremans E. Rotationally-invariant mapping of scalar and orientational metrics of neuronal microstructure with diffusion MRI. Neuroimage. 2018;174:518-538. doi:10.1016/j.neuroimage.2018.03.006
13. Reisert M, Kellner E, Dhital B, Hennig J, Kiselev VG. Disentangling micro from mesostructure by diffusion MRI: A Bayesian approach. Neuroimage. 2017;147:964-975. doi:10.1016/j.neuroimage.2016.09.058
14. Christiaens D, Veraart J, Cordero-Grande L, et al. On the need for bundle-specific microstructure kernels in diffusion MRI. Neuroimage. 2020;208:116460. doi:10.1016/j.neuroimage.2019.116460
15. Palombo M, Ianus A, Guerreri M, et al. SANDI: A compartment-based model for non-invasive apparent soma and neurite imaging by diffusion MRI. Neuroimage. 2020;215:116835. doi:10.1016/j.neuroimage.2020.116835
16. Jelescu IO, de Skowronski A, Palombo M, Novikov DS. Neurite Exchange Imaging (NEXI): A minimal model of diffusion in gray matter with inter-compartment water exchange. arXiv. 2021;2108.0612

Acknowledgments / Funding Information: DC is supported by the Flemish Research Foundation (FWO), grant number 12ZV420N. ML is supported by the FWO grant number 1168821N. FB, MV and LE are supported by the FWO grant G0C0319N, and along with JVdS by KU Leuven grant C24/18/095 and The Sequoia Fund.

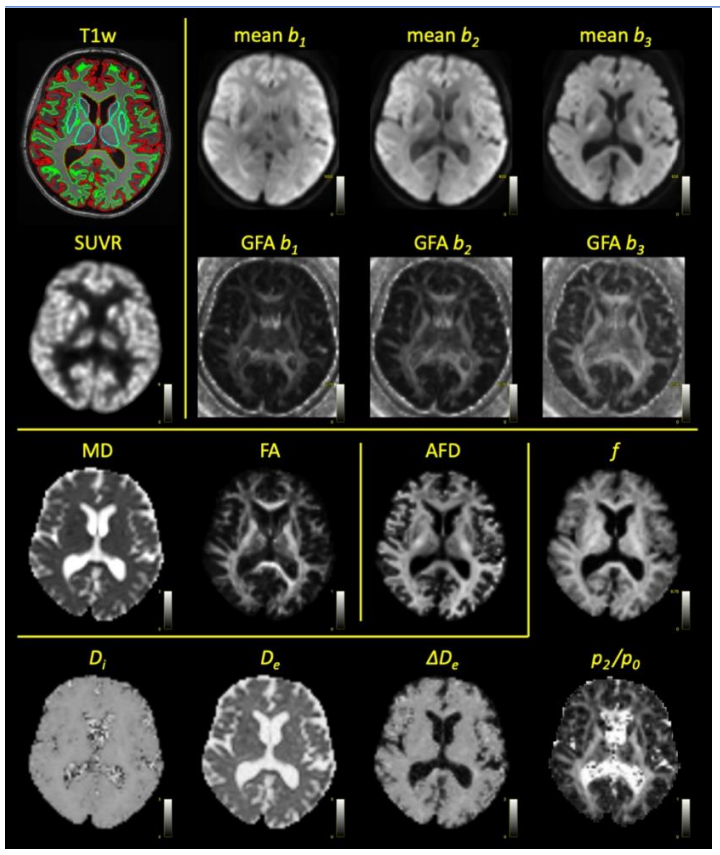

Figure 1. Overview of the PET-MR parameter maps in a single subject: segmented T1w (WM, CGM & DGM); SUVR map of ^{11}C-UCB-J uptake; mean and GFA of each shell of the dMRI data; DTI parameters mean diffusivity (MD) and fractional anisotropy (FA); apparent fibre density (AFD) estimated with MT-CSD; and the standard model parameters intra-axonal volume fraction f and diffusivity D_i, extra-axonal diffusivity D_e and ΔD_e, and the ODF spectral power ratio p_2/p_0.

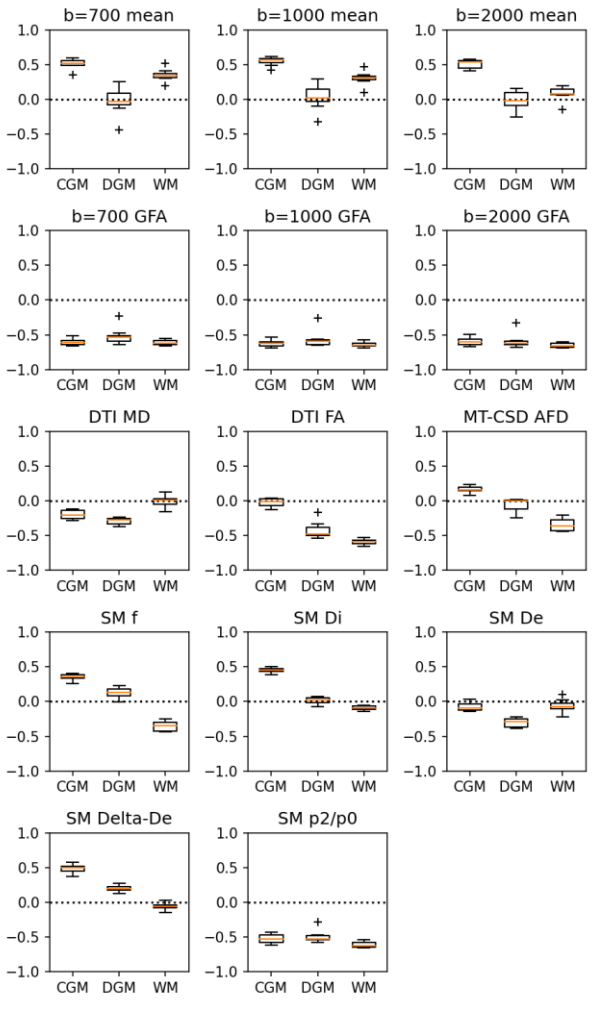

Figure 2. Boxplots of the correlation coefficients between SUVR and each of the listed parameter maps in segmented CGM, DGM and WM. The boxplots display the distribution across subjects; showing high consistency in most parameters and tissue classes.

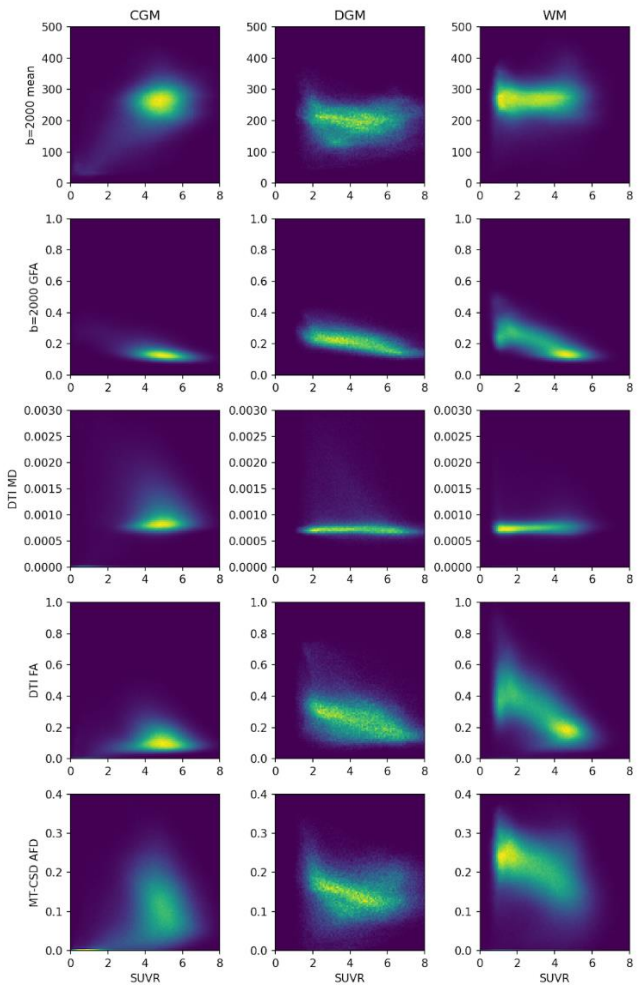

Figure 3. Joint histograms of selected signal, DTI, and MT-CSD metrics with ^{11}C-UCB-J SUVR in CGM, DGM and WM, here shown for all subjects combined.

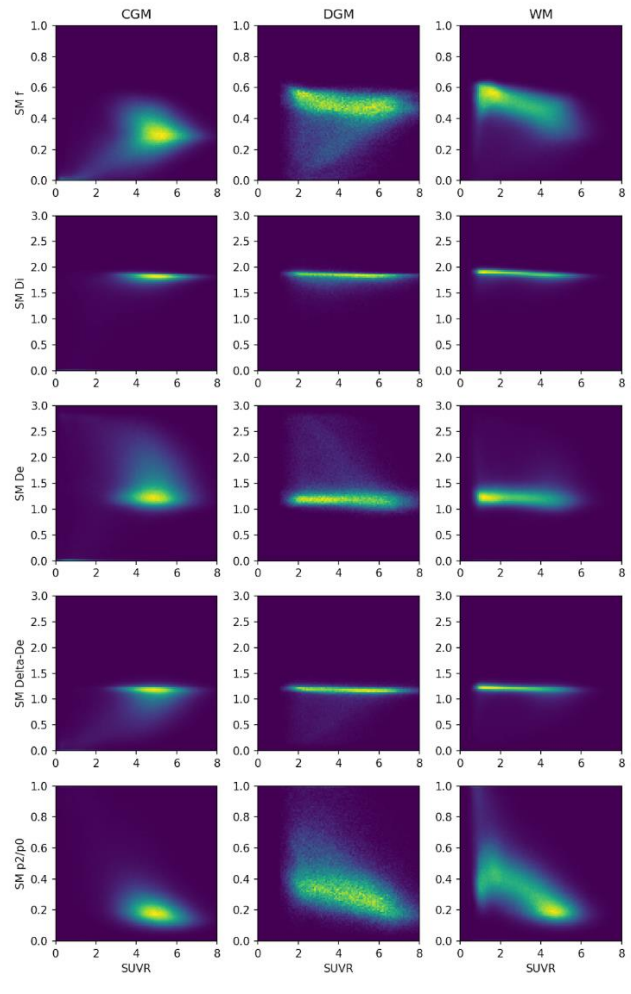

Figure 4. Joint histograms of standard model parameters with ^{11}C-UCB-J SUVR in CGM, DGM and WM, here shown for all subjects combined.

Resolving heterogeneous crossing fibers with Adaptive modelling and Generalized Richardson Lucy spherical deconvolution (AGRL)

A. De Luca[1,2], A. Leemans[2], C.M.W. Tax[2,3], K.G. Schilling[4], G.J. Biessels[1]

[1]Neurology Department, UMC Utrecht Brain Center, UMC Utrecht, Utrecht, The Netherlands; [2]Image Sciences Institute, UMC Utrecht, Utrecht, The Netherlands; [3]Cardiff University Brain Centre Imaging, Cardiff University, Cardiff, UK; [4]Department of Electrical Engineering and Computer Science, Vanderbilt University, Nashville, TN, USA; 4

Synopsis: We evaluate the benefits of shifting from a global white matter (WM) model to an adaptive (voxel-wise) model in the Generalized Richardson Lucy (GRL) framework. Using simulations, we show that GRL with an adaptive model (AGRL) could resolve crossing fiber configurations with heterogeneous properties, whereas conventional GRL did not. In in-vivo data, AGRL simultaneously used different deconvolution models. Compared to GRL, fiber orientation distributions of AGRL showed remarkable angular differences, especially for the second and third peak. Tractography with AGRL resulted in a more extensive reconstruction of the arcuate fasciculus, suggesting adaptive modelling as a promising future direction.

Introduction

Spherical deconvolution methods[1,2] leverage high-angular resolution brain diffusion MRI (dMRI) data to determine the orientation of crossing fibers in white matter (WM). Most spherical deconvolution methods use a global model of single-fiber WM (i.e., response function) across the brain to determine the fiber orientation distribution (FOD), implicitly assuming WM to be homogeneous. However, different WM fibers can exhibit heterogeneous properties[3–5]. In this work, we extend a recently introduced model-based spherical deconvolution framework[6] to account for heterogeneous WM properties, and show proof-of-concept of its performance with synthetic and in-vivo MRI data.

Methods

Adaptive spherical deconvolution: The starting point of this work is the Generalized Richardson Lucy (GRL) deconvolution framework[6]. In GRL, we aim to solve the signal (S) equation $S = K * \mathrm{FOD}$. The columns of the deconvolution matrix K contain possible solutions to the deconvolution problem, e.g., projections of a single-fiber WM model along several directions uniformly distributed on the unit sphere. Instead of using a single K, with Adaptive GRL (AGRL) we propose to account for heterogeneous WM properties by generating N instances of K (K_i) corresponding to different parametrizations of a chosen signal model. In a first iteration, GRL is repeatedly performed for each K_i, and the columns of K_i that do not contribute to the FOD are removed. In a second iteration, the retained columns of all K_i are joined in a final deconvolution matrix $\boldsymbol{K}$, and GRL is applied one final time to determine the final FOD.

Experiments: In all experiments, we used the diffusion tensor imaging (DTI) model to simulate signals. Ten possible K_i were generated by varying the axial diffusivity in 10 steps between $1.2\text{x}10^{-3}$mm^2/s and $2.1\text{x}10^{-3}$mm^2/s while keeping the radial diffusivity fixed to a value estimated per dataset as previously described[6].

Experiment I: two crossing fibers (angle 45°) were generated with homogeneous (identical fractional anisotropy and mean diffusivity) and heterogeneous WM properties (different fractional anisotropy), respectively, with signal to noise ratio (SNR) at b = 0 s/mm^2 equal to 30 using ExploreDTI[7]. The FOD was determined with GRL and AGRL, then deterministic fiber tractography was performed with step size 1mm, angle threshold 30°.

Experiment II: We compared AGRL to GRL using 1 dataset from the Human Connectome Project[8]. We evaluated the spatial distribution of the signal fractions associated to each of the 10 WM-models, then evaluated the prevalence of each WM-model in the whole WM mask (segmented from a co-registered T1-weighted image using FSL[9]). Subsequently, the peaks associated to each FOD were extracted[10] to determine their orientation and amplitude. Peaks with amplitude below 0.05 were discarded. Finally, fiber tractography of the arcuate fasciculus was performed with both GRL and AGRL using a deterministic approach with step-size 0.6mm, angle threshold 45° and 60°.

Results

Experiment I

Results in Fig. 1 show that GRL could only resolve homogeneous crossing fibers. Conversely, AGRL could correctly reconstruct both the homogeneous and heterogeneous configurations, albeit with a small angular error (white arrow, Fig. 1). This results suggest that a global WM model leads to erroneous FOD estimation when it does not match the underlying tissue properties, as expected[3].

Experiment II

The signal fractions associated to each K_i when applying AGRL to in-vivo data are shown in Fig. 2. Part of the corpus callosum and of the deep WM are better described by K_i with lower axial diffusivity (corresponding to about 20% of the WM, Fig. 3C), whereas most superficial WM is better described by a K_i with higher axial diffusivity (~80% of WM, Fig. 3C). In most WM voxels, 3 to 4 WM-models are simultaneously used by AGRL (Fig. 3A-B).

When comparing at the first FOD peak estimated with GRL and AGRL (Fig. 4), we observed little angular differences in deep WM. However, differences above 10° were observed for the first peak in regions with 3+ crossing fibers such as the centrum semiovale, and in proximity of (deep) gray matter. In over 10% of WM, angular differences for the second and third peaks were larger than 10°. In Fig. 5, we evaluated the impact of adaptive modelling fiber tractography of the arcuate fasciculus. In general, tractography with AGRL resulted in longer projections in the anterior part of the tract, larger coverage of the frontal lobe, and a more consistent representation of the bending part of the tract (see orange arrows in Fig. 5). These results were observed for both tested angular thresholds.

Discussion and conclusion

In this work, we have shown that using a global WM-model can lead to failures at detecting crossing fiber configurations when the underlying WM properties are largely different from those of the employed model. When applying AGRL in in-vivo data, we observe that multiple WM-models are simultaneously used in most WM voxels (>90%). While recent work suggests a global WM-model is sufficient to perform spherical deconvolution[11], we observed considerable angular differences between GRL and AGRL. Angular differences are more apparent in the second and third peak than in the first peak and might thus be unobserved if not using high quality dMRI that allows to disentangle 2+ peaks robustly. Altogether, our results suggest that a spatially adaptive WM-model might improve the FOD estimation, and be beneficial for fiber tractography of the arcuate fasciculus and likely other tracts.

References

1. Tournier, J. D., Calamante, F. & Connelly, A. Robust determination of the fibre orientation distribution in diffusion MRI: Non-negativity constrained super-resolved spherical deconvolution. *Neuroimage* **35**, 1459–1472 (2007).
2. Dell'Acqua, F. *et al.* A model-based deconvolution approach to solve fiber crossing in diffusion-weighted MR imaging. *IEEE Trans. Biomed. Eng.* **54**, 462–72 (2007).
3. Guo, F. *et al.* Fiber orientation distribution from diffusion MRI: Effects of inaccurate response function calibration. *J. Neuroimaging* 1–17 (2021) doi:10.1111/jon.12901.
4. Schilling, K. G., Landman, B. A., Leemans, A., Anderson, A. W. & Tax, C. M. Diffusion MRI response function estimates vary more across pathways than across subjects. in *International Society for Magnetic Resonance in Medicine* (2020).
5. de Almeida Martins, J. P. *et al.* Computing and visualising intra-voxel orientation-specific relaxation–diffusion features in the human brain. *Hum. Brain Mapp.* **42**, 310–328 (2021).
6. Guo, F., Leemans, A., Viergever, M. A., Dell'Acqua, F. & De Luca, A. Generalized Richardson-Lucy (GRL) for analyzing multi-shell diffusion MRI data. *Neuroimage* **218**, 116948 (2020).
7. Leemans, A., Jeurissen, B., Sijbers, J. & Jones, D. K. ExploreDTI: a graphical toolbox for processing, analyzing, and visualizing diffusion MR data. in *17th annual meeting of the International Society for Magnetic Resonance in Medicine, Honolulu, Hawaii, USA* 3537 (2009).
8. McNab, J. A. *et al.* The Human Connectome Project and beyond: initial applications of 300 mT/m gradients. *Neuroimage* **80**, 234–45 (2013).
9. Jenkinson, M., Beckmann, C. F., Behrens, T. E. J., Woolrich, M. W. & Smith, S. M. FSL. *Neuroimage* **62**, 782–90 (2012).
10. Jeurissen, B., Leemans, A., Tournier, J.-D., Jones, D. K. & Sijbers, J. Investigating the prevalence of complex fiber configurations in white matter tissue with diffusion magnetic resonance imaging. *Hum. Brain Mapp.* **34**, 2747–66 (2013).
11. Christiaens, D. *et al.* On the need for bundle-specific microstructure kernels in diffusion MRI. *Neuroimage* **208**, 116460 (2020).

Acknowledgments / Funding Information: The research of AdL and GJB is supported by Vici Grant 918.16.616 from ZonMw, The Netherlands, Organisation for Health Research and Development (PI, GJ Biessels). KS is supported by the National Institutes of Health under award numbers R01EB017230, and T32EB001628, and in part by ViSE/VICTR VR3029 and the National Center for Research Resources, Grant UL1 RR024975-01. CMWT is supported by a Sir Henry Wellcome Fellowship (grant no. 215944/Z/19/Z) and VENI grant (no. 17331) from the Dutch Research Council (NWO).

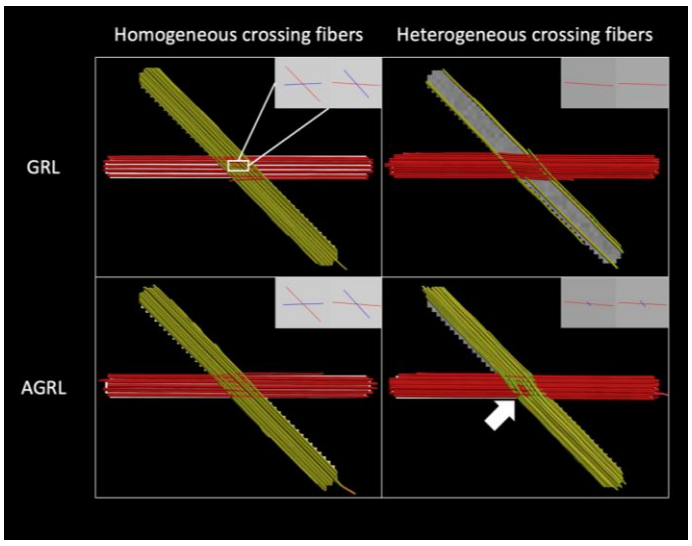

Fig. 1: Synthetic simulations of 2 crossing fibers (angle = 45°) with homogeneous properties (left, fractional anisotropy = 0.9, mean diffusivity = $0.7x10^{-3}mm^2/s$) and heterogeneous properties (right fractional anisotropy = 0.9 / 0.4, mean diffusivity = $0.7x10^{-3}mm^2/s$). AGRL can resolve heterogeneous crossing fibers, whereas GRL only identifies the fiber with higher fractional anisotropy.

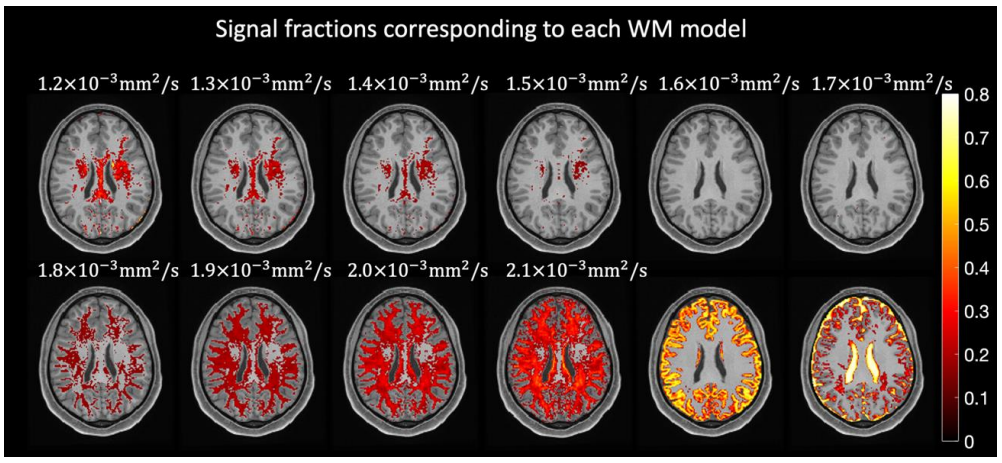

Fig. 2: Signal fractions corresponding to 10 WM models with increasing values of axial diffusivity from 1.2x10-3mm2/s to 2.1x10-3mm2/s. The last two signal fractions correspond to isotropic diffusion classes (gray matter and cerebrospinal fluid).

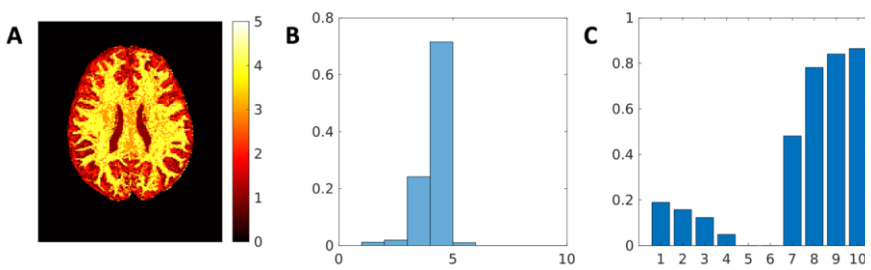

Fig. 3: A) a visual representation of the number of K_i simultaneously used by AGRL per voxel; B) The probability distribution function (PDF) of the number of K_i used in the whole WM and C) the PDF of each K_i in the whole WM.

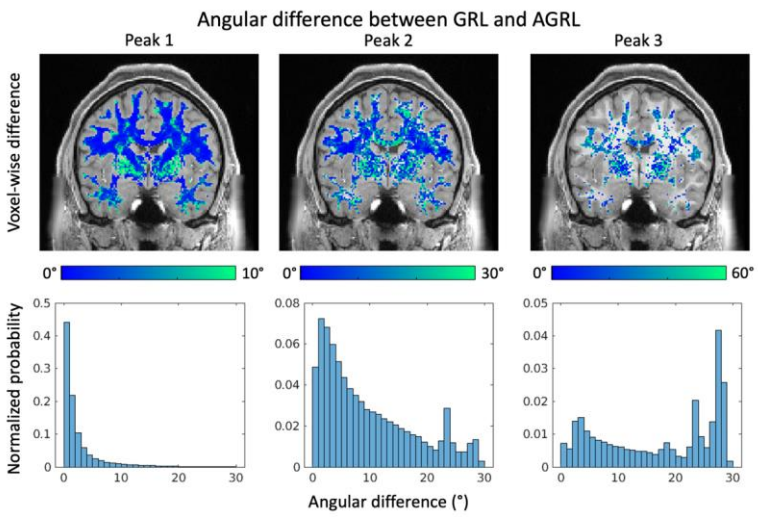

Fig. 4: The first row shows an example coronal slice of the angular difference between GRL and AGRL, whereas the second row shows the histogram of the difference in the whole WM mask.

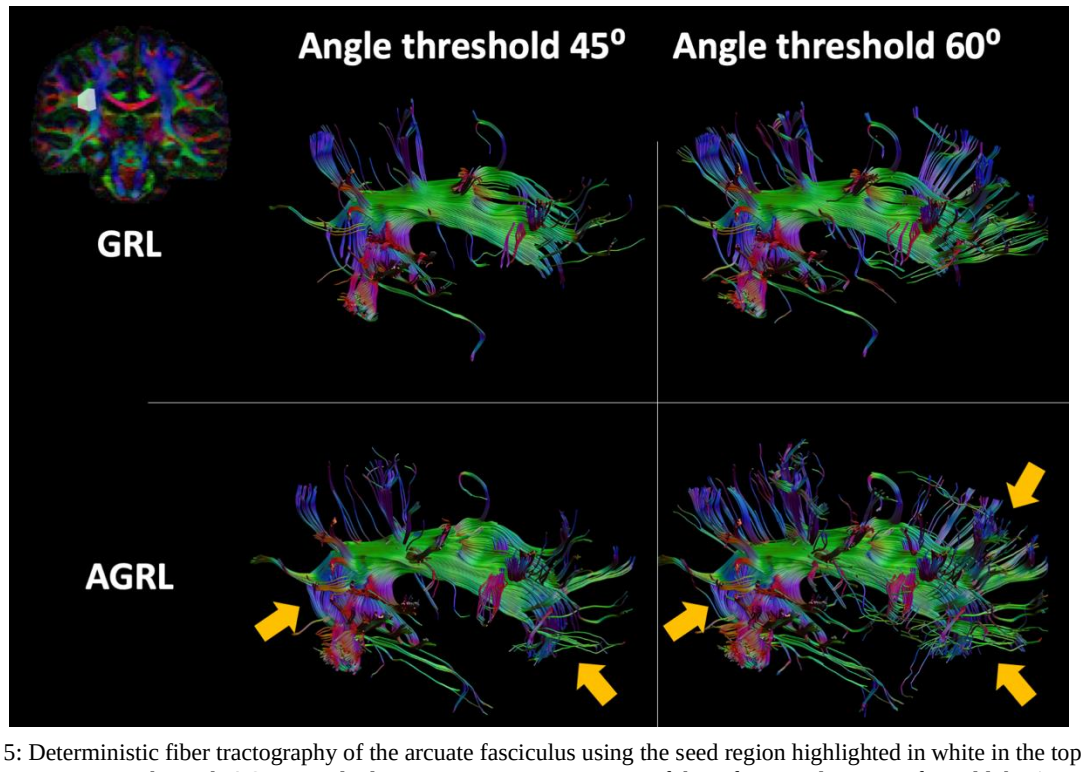

Fig. 5: Deterministic fiber tractography of the arcuate fasciculus using the seed region highlighted in white in the top left corner. Tractography with AGRL resulted in more extensive coverage of the inferior and superior frontal lobe (orange arrows), but also in a slightly larger number of spurious fibers.

Optimal b-value sampling for interstitial fluid estimation in cerebral IVIM imaging, a genetic algorithm approach

G.S. Drenthen[1,2], J.F.A. Jansen[1,2], M.M. van der Thiel[1,2], P.H.M. Voorter[1,2], W.H. Backes[1,2]
[1]School for Mental Health & Neuroscience, Maastricht University, Maastricht, Netherlands; [2]Department of Radiology & Nuclear Medicine, Maastricht University Medical Center, Maastricht, Netherlands

Synopsis - Besides the parenchymal diffusion and microvascular pseudo-diffusion, a third diffusion component was previously found in cerebral intravoxel incoherent motion (IVIM),representing interstitial fluid. However, estimating this intermediate IVIM component can be challenging, since spectral decomposition techniques have strong dependence on the number of samples (i.e. acquired b-values) and SNR. Therefore, it is important to know which b-values are essential to be acquired. In this study, an optimal b-value sampling for estimating the intermediate component is derived using a genetic algorithm. The optimal sampling (0,20,100,270,280,370,540,650,660,710,720,790,980,990,1000 s/mm^2) was shown to outperform linear and logarithmic samplings, for both simulated and in vivo data.

Introduction

Cerebral intravoxel incoherent motion (IVIM) is a diffusion-weighted MR imaging technique that has the potential to simultaneously measure the parenchymal diffusivity and microvascular perfusion[1]. Recently, it was shown that a third, intermediate, IVIM-component can be extracted from the IVIM signal[2]. This additional component is thought to be related to the interstitial fluid (ISF) in the extracellular or perivascular spaces[3].

Estimating the intermediate IVIM component can be challenging, since spectral decomposition using the non-negative least squares (NNLS) is an ill-posed technique with strong dependence on the number of samples (i.e. acquired b-values) and SNR. Since acquisition time limits the total number of acquired b-values, it is important to know which b-values are essential to be acquired. Therefore, in this study we will assess an optimal b-value sampling strategy for estimating the intermediate component. The optimal sampling will be derived using a genetic algorithm[4] and simulated data. Subsequently, the performance of the optimal sampling will be compared to a linear and logarithm sampling using simulations and in vivo data.

Methods

Numerical simulations

To evaluate the optimal b-value sampling scheme, ground-truth IVIM signals were synthesized using, $S(b) = S_0[(1 - f_{int} - f_{mv})e^{-bD_{par}} + f_{int}e^{-bD_{int}} + f_{mv}e^{-bD_{mv}}] + \varepsilon_b$, where, f_{int} and f_{mv} are amplitude fractions of the intermediate and microvascular components. D_{par}, D_{int} and D_{mv} are the diffusivities for the parenchymal, intermediate and microvascular components. Decay curves were synthesized with diffusivity values randomly sampled from a uniform distribution with the following ranges, $D_{par} = .1 \cdot 10^{-3} \leq D < 1.5 \cdot 10^{-3}\ mm^2/s$, $D_{int} = 1.5 \cdot 10^{-3} \leq D \leq 4.0 \cdot 10^{-3}\ mm^2/s$ and $D_{mv} = 4.0 \cdot 10^{-3} < D \leq 200.0 \cdot 10^{-3}\ mm^2/s$. Similarly, the amplitude fractions were randomly sampled from a uniform distribution, where $.0 \leq f_{mv} \leq .1$ and $.0 \leq f_{int} \leq .3$. To simulate the effect of noise, 100.000 Gaussian noise realizations were performed with an SNR of 100 at b=0 s/mm^2.

In vivo MRI

A single subject (67y, male) underwent high-field MRI (7T Magnetom, Siemens Healthcare, Erlangen, Germany). IVIM images were acquired using a multi-shot spin-echo echo-planar-imaging sequence (TR/TE=22800/57.6ms; resolution=1.5x1.5mm, slice thickness=3.5mm, acceleration factor=2, acquisition time=49 minutes), after cerebrospinal fluid suppression (TI=2330ms). 101 diffusion sensitive b-values were acquired, ranging from 0 to 1000 with increments of 10 s/mm^2. The IVIM images were corrected for head displacements.

IVIM analysis

The IVIM data is analysed with the NNLS algorithm, using a basis set of 200 logarithmically spaced functions. From the obtained spectrum, the f_{int} is calculated as the ratio of the intermediate components (D_{int}) to the amplitude of all components. For the in vivo data, the resulting amplitude fractions were subsequently corrected for T1 and T2 relaxation effects[2].

Genetic Algorithm

First, a random population (i.e., first generation) will be initialized as 100 binary vectors of length 101 with 15 non-zero elements (b-values ranging from 0 up to 1000 s/mm^2 with increments of 10 s/mm^2). Second, the performance of each b-value sampling scheme will be assessed by the root mean squared error (RMSE) of the estimation of f_{int}, $FF = \sqrt{1/N \cdot \sum(\widehat{f_{int}} - f_{int})^2}$, where FF is the fitness function, N is the number of noise realisations, $\widehat{f_{int}}$ is the ground-truth and f_{int} is the estimated amplitude fraction of the intermediate component. The 20 sampling schemes with the best performance, i.e. the parents, will be kept for the next generation, while the other 80 will be replaced by 40 new sampling schemes obtained using cross-over and 40 using mutations (Figure 1). This process is repeated up to the 250th generation. The only constraint is that the b-value samplings must include b=0 s/mm^2, since this is required normalizing the IVIM signal.

Evaluation

The performance of the optimal b-value sampling strategy was compared to a linear and logarithmic sampling in terms of the RMSE of f_{int}. For the in vivo data, a ground-truth is calculated as the mean f_{int} of the white matter (WM) as well as the gray matter (GM) using a voxel-wise fit where all 101 b-values are included. Subsequently, the mean f_{int} of the optimal sampling is compared to the ground-truth, as well as to the linear and logarithmic b-value samplings.

Results

The evolution of the population (i.e. the b-value sampling schemes) over several generations is shown in Figure 2. The optimal b-value sampling is found to be; 0,20,100,270,280,370,540,650,660,710,720,790,980,990,1000 s/mm^2. For the simulated data, the optimal b-value sampling strategy was found to be at least 1.24 times more accurate compared to the linear and logarithmic sampling in terms of RMSE (optimal: .29 vs reference: .36 vs linear: .36). For the in vivo data, the optimal sampling strategy resulted in a mean f_{int} that is very close to the ground-truth for both WM and GM. Moreover, the mean f_{int} of the optimal sampling best approximates the ground-truth compared to the linear and logarithmic sampling (Table 1). An IVIM decay curve of the in vivo data, including the optimal sampling, is shown in Figure 3.

Discussion and Conclusion

This study presents an optimal b-value sampling for estimating f_{int}. The optimal sampling was shown to outperform linear and logarithmic sampling strategies, for both simulations and in vivo data. From previous work on mono-exponential decaying functions[5], we expect that the b-value range corresponding to $D_{int} \cdot b \approx 1.3$ would be especially beneficial for estimating f_{int}. Since the intermediate component is expected to be $1.5 \cdot 10^{-3} \leq D \leq 4.0 \cdot 10^{-3}\ mm^2/s$, this would correspond to the range b=325 to 867 s/mm^2. Indeed, our results show that this b-value range is important, since almost half of the 'optimal' b-values span this range.

References

1 D. Le Bihan et al., "Separation of diffusion and perfusion in intravoxel incoherent motion MR imaging.," Radiology, vol. 168, no. 2, pp. 497–505, 1988.
2 S. M. Wong et al., "Spectral Diffusion Analysis of Intravoxel Incoherent Motion MRI in Cerebral Small Vessel Disease," J. Magn. Reson. Imaging, vol. 51, no. 4, pp. 1170–1180, 2020.
3 M. M. Van Der Thiel et al., "Neurobiology of Aging Associations of increased interstitial fluid with vascular and neurodegenerative abnormalities in a memory clinic sample," Neurobiol. Aging, vol. 106, pp. 257–267, 2021.
4 D. E. Goldberg, Genetic Algorithms in Search, Optimization & Machine. Boston, MA: Addison-Wesley Publishing Company, 1989.
5 J. A. Jones et al., "Optimal sampling strategies for the measurement of spin-spin relaxation times," J. Magn. Reson. - Ser. B, vol. 113, no. 1, pp. 25–34, 1996.

Acknowledgments / Funding Information: Nothing to declare.

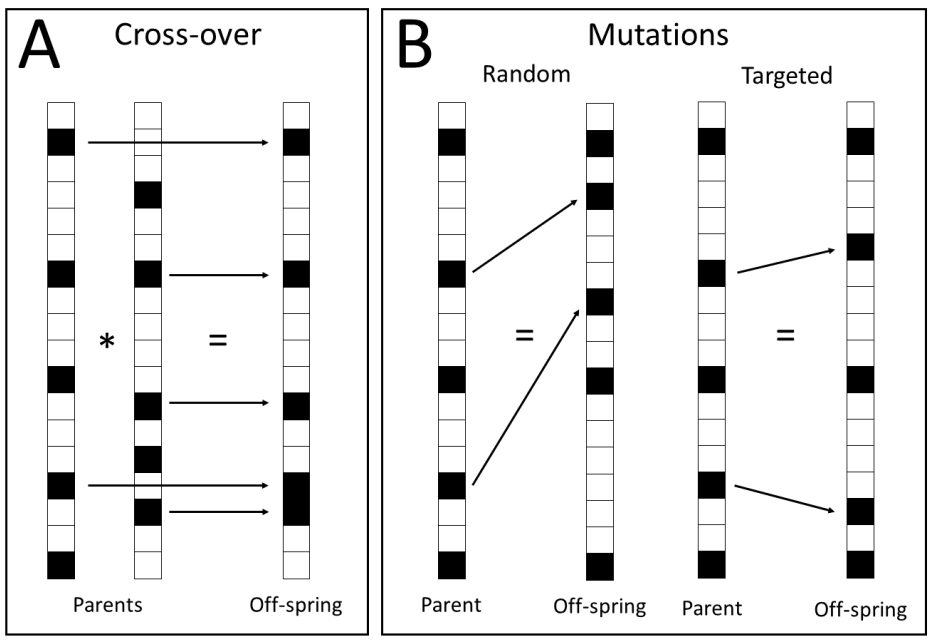

Figure 1: A) Cross-over. To define a new sampling scheme, two random parents are chosen and elements (b-values) from both parents are used to create off-spring. B) Mutations. Mutations are divided into two separate mutation methods, random mutations and targeted mutations. In both cases a random number of b-value samples in the sampling scheme is replaced by another b-value. For random mutations, the replacement is random, while for targeted mutations the b-value will be replaced by a proximal b-value with a distance ranging from -50 up to50 s/mm^2.

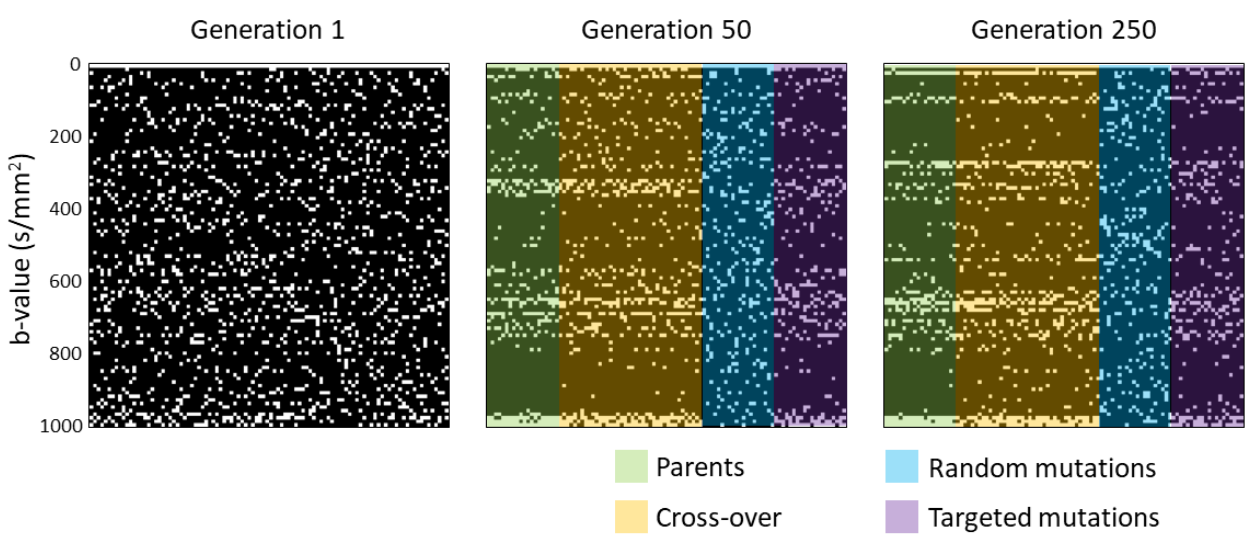

Figure 2: Evolution of the b-value sampling strategies, for generation 1, 50 and 250. The parents selected based on their fitness are shown in green, while the off-spring created using cross-over, random and targeted mutations are shown in yellow, blue and purple, respectively.

Table 1: Means f_{int} of for all the 101 b-values (ground-truth), the optimal, linear and logarithmic sampling strategies. Abbreviations: WM, white matter; GM, gray matter.

	Mean f_{int}			
	Ground-truth	Optimal	Linear	Logarithmic
WM	.070	.071	.081	.067
GM	.067	.065	.086	.061

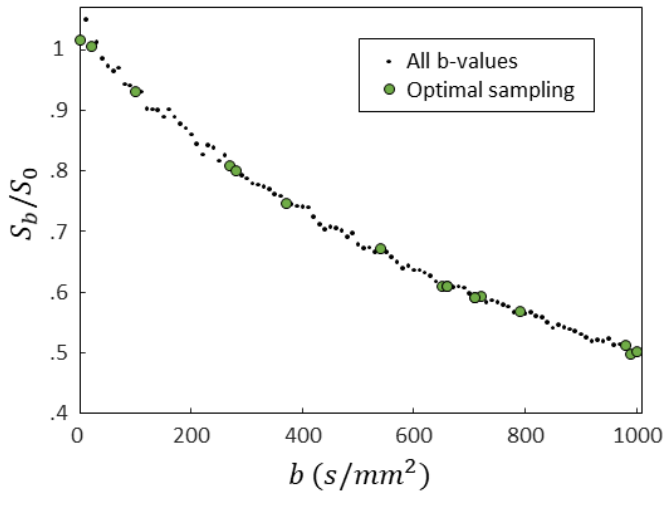

Figure 3: IVIM-signal decay curve for a single voxel from the in vivo 7T data. Optimal b-value sampling is visually indicated as the larger, green, dots.

Accelerating IVIM and DTI for assessing microstructural changes after acute hamstring injury

S. Rauh[1], J. Monte[2], M. Hooijmans[2], J. Suskens[3], O. Gurney-Champion[2], J. Tol[3], M. Maas[2], A. Nederveen[2], G. Strijkers[1]

[1]Department of Biomedical Engineering and Physics, Amsterdam UMC, Amsterdam, The Netherlands; [2]Department of Radiology and Nuclear Medicine, Amsterdam UMC, Amsterdam, The Netherlands, [3]Department of Orthopedic Surgery, Amsterdam UMC, Amsterdam, The Netherlands

Synopsis: DTI and IVIM are sensitive to hamstring injuries, but suffer from long scan times. Using b-values above a certain threshold only (high-b DTI) or a simplified IVIM approach (sIVIM-DTI), which estimates the perfusion fraction and diffusion tensor, can reduce the scan time while inherently correcting DTI-indices for IVIM effects. We showed in this work that those methods provide similar sensitivity to hamstring injuries in comparison to a full IVIM-DTI fit while reducing acquisition time up to 42%. Since no difference in perfusion fraction was found between injury states, we suggest high-b DTI is the method of choice in this application.

Introduction: Hamstring injuries are amongst the most common injuries in elite athletes and show high recurrence rates[1,2]. Diffusion tensor imaging (DTI) and intravoxel incoherent motion (IVIM) are sensitive to muscle micro damage[3,4] and may be able to assess acute muscle injury recovery and predict return-to-play (RTP). IVIM-corrected DTI has an improved reproducibility compared to conventional DTI[5]. A downside of IVIM-correction is the substantial increase in scan time. Applying the DTI fit only to high b-values above a certain threshold or using a simplified IVIM-DTI approach may significantly reduce scan time while inherently correcting DTI indices for IVIM effects. The goal of this work was to evaluate the sensitivity of accelerated DTI and IVIM-DTI to acute hamstring injuries compared to a full IVIM-DTI fit.

Methods: MRI datasets were acquired in 41 elite athletes (2 female, mean age 27.3 years) with acute hamstring injury using a 3T-MRI (Philips Ingenia) at three time points (**Error! Reference source not found.**). The scan protocol included an anatomical Dixon scan (1.5x1.5x2.5mm³, 80 slices, 6 echoes) and a DTI-IVIM scan (duration 11:08min, SE-EPI; 3x3x5mm³, 40 slices, TE/TR=55ms/5914ms, SPAIR and gradient-reversal fat suppression, SENSE=1.5) with 10 b-values (range 0-600s/mm², 8x b=0s/mm²) and 56 diffusion directions. The DTI data was PCA-denoised and registered to the anatomical scan using QMRTools[6]. The diffusion tensor was calculated using three different fitting methods:

1. IVIM-corrected DTI (in the following called '**conventional**'), consisting of four steps:
   a. IVIM fit the mean data.
   b. Voxel-wise IVIM fit with fixed pseudo-diffusion coefficient D* obtained from step a.
   c. IVIM-component subtraction from signal:
   $$S_{DTI} = S - S_{0,IVIM} \cdot f \cdot e^{-b \cdot D^*}$$
   d. DTI fit to S_{DTI} using all b-values.
2. **High-b DTI**. The data was retrospectively undersampled, discarding all b-value<200s/mm², resulting in b=200,400,600s/mm² and 32 diffusion directions. Then a DTI fit was applied.
3. **sIVIM-DTI**: The same high-b-values and directions as in high-b DTI were used (32 directions) and b=0s/mm² data (8 scans) were included to estimate the perfusion fraction f, yielding 40 b-value/direction combinations. A simplified IVIM-DTI approach was applied:

$$S(b) = S_0 \cdot (f \cdot \delta(b) + (1-f) \cdot e^{-b \cdot g^T \underline{\underline{D}} g}$$

Manual segmentation of the injured and contralateral muscle was performed in ITK-snap (www.itksnap.org). ROIs consisted of 7 slices overlaying the origin of the injury and a closely matching region in the contralateral muscle. The mean and standard deviations of the DTI parameters (tensor eigenvalues (λ_1–λ_3), mean diffusivity (MD), fractional anisotropy (FA), perfusion fraction (f)) were calculated within the segmentation for the injured and contralateral muscle and for each method and time point. A repeated measures Anova was used to evaluate the three methods (SPSS). The sensitivity of the methods to injury was assessed by comparing the difference between the injured and contralateral muscle (Δ injured-healthy). The stability of the methods was evaluated by comparing the standard deviations of the DTI parameters in the healthy muscle. The difference between the methods and injury states was assessed for both injury states separately.

Results: The proposed methods yield a scan time reduction of 42% (high-b DTI) and 28% (sIVIM-DTI) compared to the conventional method. Parameter maps are shown in **Error! Reference source not found.**. Sensitivity: At baseline, a larger Δ injured-healthy was found with high-b DTI and sIVIM-DTI for λ_1–λ_3 and MD compared to the conventional method. No difference was found for FA or between sIVIM-DTI and high-b DTI. The difference between the methods disappeared at 2-weeks and RTP. After 2-weeks, Δ injured-healthy of FA was higher for sIVIM-DTI than high-b DTI (**Error! Reference source not found.**). Stability: The standard deviations of λ_2,λ_3,MD,FA and f were significantly higher in high-b DTI and sIVIM-DTI compared to the conventional fit at baseline and 2-weeks. No differences were found for λ_1 (**Error! Reference source not found.**). The standard deviation for FA was higher in sIVIM-DTI than high-b DTI. No differences were found at RTP. Injury sensitivity and method differences: At baseline and 2-weeks, the injured muscle had higher MD and eigenvalues than the healthy muscle for all methods. No effect for injury was found in FA and f. The difference disappeared at RTP. An offset between conventional fitting and accelerated fit outcome measures was found (**Error! Reference source not found.**). λ_1–λ_3 and MD were highest with conventional fitting and higher in high-b DTI than sIVIM-DTI. The opposite effect held for FA and f.

Discussion: Our data showed that the sensitivity to hamstring injuries is preserved with our accelerated high-b DTI and sIVIM-DTI methods. The increased Δ injured-healthy values at baseline might indicate improved sensitivity. The higher standard deviation with accelerated methods could be a result of higher noise contribution in the high b-value data. The overall offset between the conventional and accelerated approaches at all time points might be due to more noise at high b-values, reduced data used for the fit or a suboptimal fixed D* value in the conventional fit which might result in remaining IVIM signal in S_{DTI}. With both conventional IVIM-DTI and sIVIM-DTI methods, no difference was observed in f between injury states. This might indicate that f is not sensitive to hamstring injuries.

Conclusion: High-b DTI and sIVIM-DTI reduce scan time and preserve sensitivity to hamstring injuries. Since f shows no sensitivity to injury, the high-b DTI method may be considered the best method for this application.

References

1. Koulouris G, Connell DA, Brukner P, Schneider-Kolsky M. Magnetic resonance imaging parameters for assessing risk of recurrent hamstring injuries in elite athletes. *Am J Sports Med*. 2007;35(9):1500-1506. doi:10.1177/0363546507301258
2. Slavotinek JP, Verrall GM, Fon GT. Hamstring injury in athletes: Using MR imaging measurements to compare extent of muscle injury with amount of time lost from competition. *Am J Roentgenol*. 2002;179(6):1621-1628. doi:10.2214/ajr.179.6.1791621
3. Hooijmans MT, Monte JRC, Froeling M, et al. Quantitative MRI Reveals Microstructural Changes in the Upper Leg Muscles After Running a Marathon. *J Magn Reson Imaging*. 2020. doi:10.1002/jmri.27106
4. Froeling M, Oudeman J, Strijkers GJ, et al. Muscle changes detected with diffusion-tensor imaging after long-distance running. *Radiology*. 2015;274(2):548-562. doi:10.1148/radiol.14140702
5. Monte JR, Hooijmans MT, Froeling M, et al. The repeatability of bilateral diffusion tensor imaging (DTI) in the upper leg muscles of healthy adults. *Eur Radiol*. 2019. doi:10.1007/s00330-019-06403-5
6. Froeling M. QMRTools: a Mathematica toolbox for quantitative MRI analysis. *J Open Source Softw*. 2019;4(38):1204. doi:10.21105/joss.01204

Acknowledgments / Funding Information: The authors would like to thank Martijn Froeling for help with the scan protocol and the pre-processing pipeline. The study was partly funded by a grant from 'NBA&GE Orthopedics and Sports Medicine Collaboration', USA.

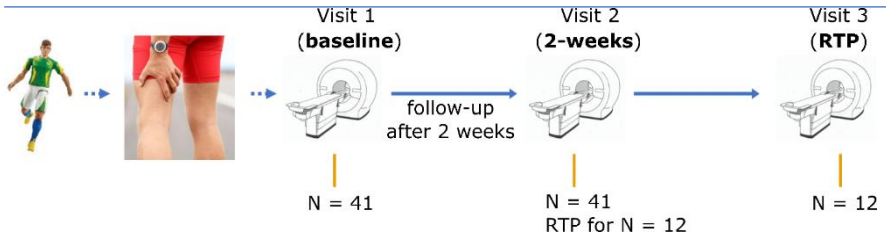

Figure 1. Workflow of the MRI measurements of patients with acute hamstring injury. The patients were scanned within 7 days after the injury (Visit 1, baseline scan), 2 weeks after visit 1 (Visit 2, 2-weeks scan) and within 7 days after Return-to-Play (Visit 3, RTP). 41 patients were included and completed the baseline and 2-weeks follow-up scan. 12 patients completed the RTP scan. For 12 patients 2-weeks follow-up coincided with RTP. 17 patients had no RTP scan.

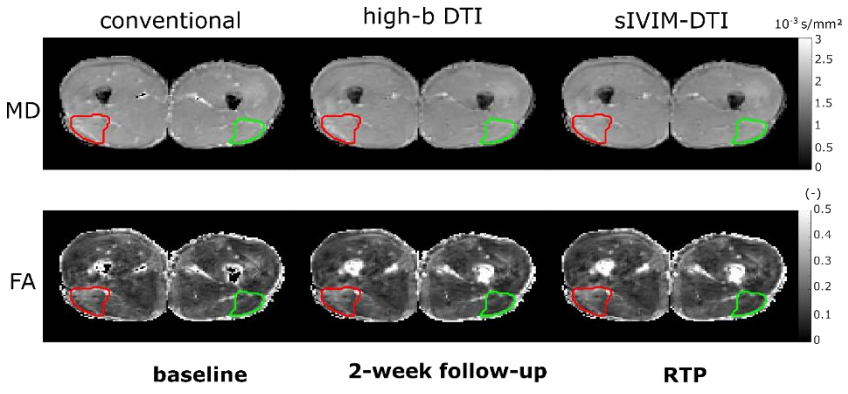

Figure 2. Parameter maps of Mean Diffusivity (MD) and Fractional Anisotropy (FA) from all three fit methods of one representative patient at baseline. Segmentations of the injury (red) and the healthy contralateral muscle (green) are overlaid. No clear difference between the parameter maps obtained from the different fitting methods can be observed.

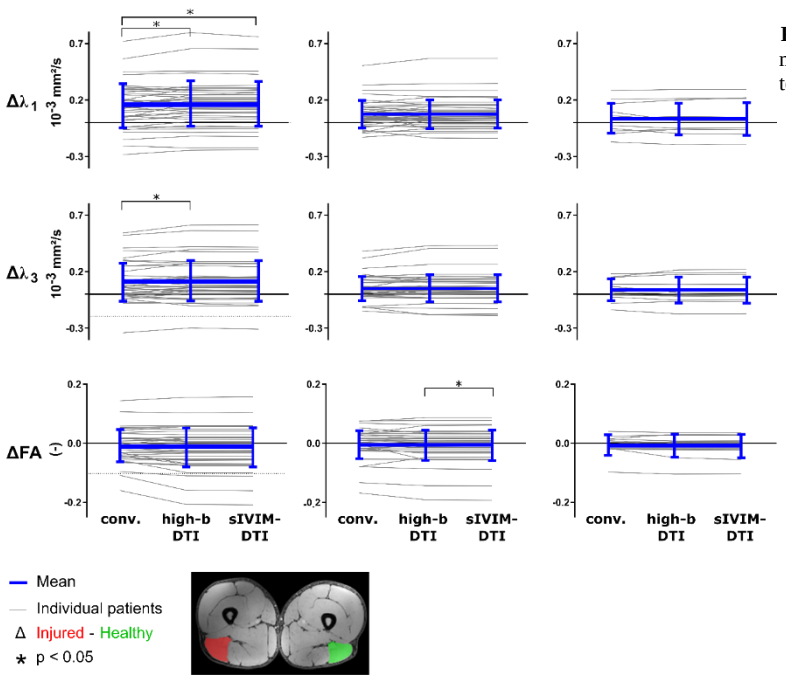

Figure 3. Difference between the injured–healthy parameters (Δ) for all three methods and time points. For all methods, Δ injured-healthy values lie in a similar range without obvious outliers, indicating preserved sensitivity to injury of accelerated DTI and IVIM-DTI methods compared to the conventional fit. A significantly higher Δ injured-healthy was found at baseline for high-b DTI and sIVIM in λ_1, for high-b DTI in λ_3 and after 2-weeks for sIVIM compared to high-b DTI in FA. (conv. = conventional)

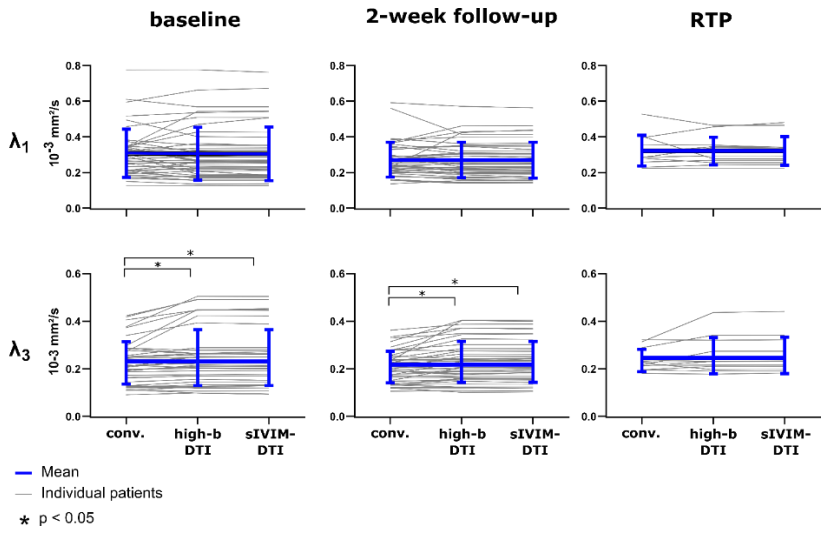

Figure 4. Standard deviations of λ_1 and λ_3 in the contralateral healthy muscle for all three time points and methods. No difference was found for λ_1. For λ_3, standard deviations were significantly higher with the accelerated methods, however, the absolute differences were small (mean difference λ_3 between conventional and high-b DTI/sIVIM: 0.23/0.23, 0.22/0.22, 0.20/0.21, for baseline, 2-week follow-up and RTP respectively). (conv. = conventional)

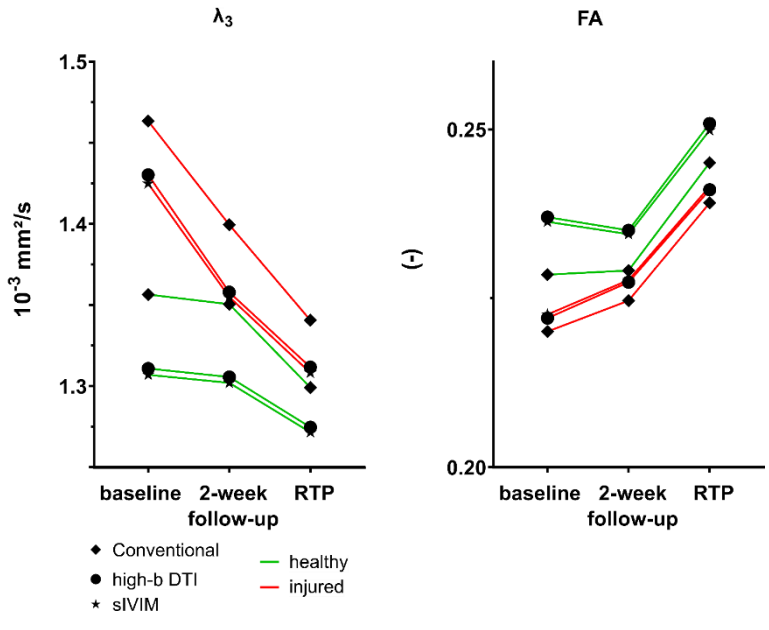

Figure 5. Time course of λ_3 and FA for the injured and healthy muscle for all fitting methods (mean values plotted). The healthy values stay almost constant between baseline and 2-week follow-up for all methods, while the injured values converge towards the healthy. The change in the healthy values at RTP might be explained by less data (N=12 at RTP). An offset between the conventional and proposed methods can be observed for both, injured and healthy muscle at all three time points. Only a minor difference is visible between high-b DTI and sIVIM-DTI.

dtiRIM: A recurrent inference machine for diffusion tensor estimation

E.R. Sabidussi[1], S. Klein[1], B. Jeurissen[2], D.H.J. Poot[1]
[1]Radiology,, Erasmus Medical Center, Rotterdam, The Netherlands; [2]Department of Physics, Imec-Vision Lab, University of Antwerp, Antwerp, Belgium

Synopsis: In Diffusion MRI, the large variability of acquisition schemes limits broader use of Deep Learning for parameter estimation, with data-specific models needed for high-quality predictions. To reduce dependency on training data, we present dtiRIM, a recurrent neural network that learns a regularized solution to a model-based inverse problem. Using the diffusion model allows independent parameters (e.g. gradient directions) to also influence the estimation. We show that a single dtiRIM model predicts diffusion parameters for multiple datasets with lower error than the current state-of-the-art. Our study suggests that dtiRIM has the potential to be the first general learning method for DTI.

Introduction: An outstanding challenge when using Deep Learning (DL) for Diffusion Tensor Imaging (DTI) is the large variability of acquisition settings (e.g. number of q-space samples, gradient directions and strength) between datasets. Existing works[1-3] applied DL to estimate diffusion properties (e.g fractional anisotropy (FA), mean diffusivity (MD)) from diffusion-weighted (DW) images, but different acquisition schemes required training new models.

In this study, we propose to use the Recurrent Inference Machine (RIM) framework[4] to estimate the diffusion tensor parameters with low dependency on scan settings. RIMs learn to minimize a model-based likelihood function, allowing for greater variability of fixed model parameters (e.g. gradient directions). We evaluated our model in simulation and in-vivo experiments.

Methods: Our RIM for DTI ($dti\mathbf{RIM}$) is shown in Figure 1. The RIM is a recurrent neural network function $\hat{\boldsymbol{\theta}} = H_\gamma(\tilde{\boldsymbol{S}}; \boldsymbol{b}, \boldsymbol{g})$ that has learned to predict the parameters $\boldsymbol{\theta} = [S_0, D_{11}, D_{12}, D_{22}, D_{13}, D_{23}, D_{33}]$ that maximize the Rice likelihood $L(\boldsymbol{S}(\boldsymbol{\theta}; \boldsymbol{b}, \boldsymbol{g})|\tilde{\boldsymbol{S}})$, given acquired DW images $\tilde{\boldsymbol{S}}$, gradient strength ($\boldsymbol{b}$) and directions ($\boldsymbol{g}$); here, S_0 is the non-diffusion-weighted signal and $\boldsymbol{D} = (D_{ij})$ is the diffusion tensor. The network weights $\boldsymbol{\gamma}$ are trained on simulation data, by minimizing the differences between ground-truth noiseless DW images $\boldsymbol{S}^{GT}$ and predicted images $\boldsymbol{S}(\hat{\boldsymbol{\theta}}; \boldsymbol{b}, \boldsymbol{g})$: $\hat{\boldsymbol{\gamma}} = \arg\min_{\boldsymbol{\gamma}} \frac{1}{N} \sum_{n=0}^{N-1} (\boldsymbol{S}_n^{GT} - \boldsymbol{S}_n(\hat{\boldsymbol{\theta}}; \boldsymbol{b}, \boldsymbol{g}))^2$, where N is the number of images in the training set.

Training samples $T_i^F = \{\tilde{\boldsymbol{S}}, \boldsymbol{S}^{GT}, \boldsymbol{b}, \boldsymbol{g}\}$ were generated with the Numerical Fiber Generator[5] (NFG). For each sample i, $\boldsymbol{S}^{GT}$ was simulated with uniformly sampled FA$\sim \mathcal{U}(0.05, 1)$ and MD $\sim \mathcal{U}(0.0003, 0.003)$, $b = 1000 s/mm^2$, and $\boldsymbol{g}$ and N randomly sampled from a pre-determined set $\boldsymbol{G}$. To ensure approximately uniform sets of gradient directions of size $N \in [7, 13, ..., 55, 61]$ (in steps of 6), we selected 10 unique subsets $\boldsymbol{g} \in G$ with the lowest electrostatic repulsion[6] (ER) among 1000 random subsets of size N. Finally, Rician noise was added. In total, 400.000 noisy training samples were created.

Two validation sets were used to tune the RIM's hyperparameters. The first ($\mathbf{NFG}_{val}$) was also created with NFG, but with a different configuration of fibers, $\boldsymbol{g} \in \boldsymbol{G}, N = 31$ and SNR 25. The second ($\mathbf{Diffantom}$), was created using the Diffantom simulator[7], with gradients $\boldsymbol{G}, N = 129, b = 2000 s/mm^2$ and SNR 30.

In contrast to voxel-wise methods, RIMs also learn a spatial regularization[8] that might provide robustness to small deviations between signals and the diffusion model. To evaluate this, we created additional $\mathbf{NFG}_{val}$ and $\mathbf{Diffantom}$ datasets with (slightly) misaligned images. Random rigid transformations were applied when generating $\tilde{\boldsymbol{S}}$ from $\boldsymbol{S}^{GT}$, with translations and rotations independently sampled from $\mathcal{N}(0.0, \sigma_d)$, with small $\sigma_d = \{0.25, 0.5\}$ to simulate sub-voxel misalignment. Fifty realizations of motion and noise were created per data set. The bias, standard deviation and RMSE of the FA and MD maps were evaluated. Ground-truth maps were defined as the least-squares solution of $\boldsymbol{\theta}$ on $\boldsymbol{S}^{GT}$.

The testing data ($\mathbf{AOMIC}$) is composed of 1 subject from the AOMIC-ID1000 dataset[9], acquired with gradient directions $\boldsymbol{G_t} \notin \boldsymbol{G}, N = 33$, and $b = 1000 s/mm^2$. To evaluate our method's precision, we emulated repeated scans by creating 4 datasets from the original data with varying number of images ($N = [13, 19, 25, 31], \boldsymbol{g_t} \in \boldsymbol{G_t}$). Each contained 5 unique DW sets, with $\boldsymbol{g_t}$ selected by minimizing the ER among 100 random subsets of $\boldsymbol{G_t}$. Ground-truth maps were obtained from the full set ($G_t, N = 33$) with the state-of-the-art $\mathbf{IWLLS}$[10] from MRTrix3[11], also used here as baseline in all experiments. Statistical significance was evaluated with an unpaired t-test ($p < 0.001$).

Results: Figure 2 shows the results of the FA for all datasets. On $\mathbf{NFG}_{val}$ datasets, $dti\mathbf{RIM}$ presented lower bias, STD and RMSE than $\mathbf{IWLLS}$. On $\mathbf{Diffantom}$ datasets, $dti\mathbf{RIM}$ had lower STD and RMSE, but higher bias. Additionally, $dti\mathbf{RIM}$ errors increased slower than $\mathbf{IWLLS}$ for larger σ_d. For $\mathbf{AOMIC}$, $dti\mathbf{RIM}$ had lower STD ($\forall N$), but larger bias and RMSE for $N \leq 18$.

Figure 3 shows the results of the MD for all datasets. $dti\mathbf{RIM}$ had lower bias, STD and RMSE than $\mathbf{IWLLS}$ in all validation datasets. In $\mathbf{AOMIC}$, $dti\mathbf{RIM}$ had lower STD, but higher RMSE compared to $\mathbf{IWLLS}$, while no significant differences were found for bias.

Figures 4 and 5 show FA and MD maps from $\mathbf{IWLLS}$ and $dti\mathbf{RIM}$ (data $\boldsymbol{G_t}, N = 33$) alongside RMSE maps computed for different N. $dti\mathbf{RIM}$ FA estimates are less dependent on N than $\mathbf{IWLLS}$'s, while MD maps are smoother, and with lower accuracy in high diffusivity regions (e.g. ventricles).

Discussion: We showed that a single RIM model can be used with DW images acquired with different number of q-space samples, gradient directions and strength. The $dti\mathbf{RIM}$ reduced FA and MD errors compared to the state-of-the-art $\mathbf{IWLLS}$ for most datasets. The negative FA bias on in-vivo data can be (mainly) attributed to lower FA estimates in gray matter and CSF, while smaller differences were observed on white matter. MD maps from $dti\mathbf{RIM}$ are slightly blurred compared to $\mathbf{IWLLS}$'s, promoting higher estimation precision, at the cost of higher total error. Additionally, (slight) robustness to misaligned images was shown.

Conclusion: This work presented a novel approach to estimate DTI parameters. Our Recurrent Inference Machines method provides estimates with similar or lower error than IWLLS. It showed robustness to anatomy and variation in scan protocol, including q-space sampling. Although more validation is needed (e.g. larger in-vivo datasets, pathology), our study suggests that the RIM can provide diffusion parameters that are robust and of higher quality than the current state-of-the-art.

References

1. H. Li, Z. Liang, C. Zhang, R. Liu, and et al.,"SuperDTI: Ultrafast dti and fiber tractography with deep learning," MRM,vol. 86, p. 3334–3347, Jul 2021.

2. V. Golkov, A. Dosovitskiy, J. I. Sperl, and et al., "q-Space Deep Learning: Twelve-Fold Shorter and Model-Free Diffusion MRI Scans," IEEE-TMI,vol. 35, pp. 1344–1351,May 2016.

3. E. Aliotta, H. Nourzadeh, and S. H. Patel, "Extracting diffusion tensor fractional anisotropy and mean diffusivity from 3-direction DWI scans using deep learning," MRM,vol. 85, pp. 845–854, Aug. 2020.

4. P. Putzky and W. Welling, "Recurrent inference machines for solving inverse problems," 2017. arXiv:1706.04008

5. T. G. Close, J.-D. Tournier, F. Calamante, L. A. Johnston, I. Mareels, and A. Connelly, "A software tool to generate simulated white matter structures for the assessment of fibre-tracking algorithms," NeuroImage, vol. 47, pp. 1288–1300, Oct. 2009.

6. P. A. Cook, M. Symms, P. A. Boulby, and D. C. Alexander, "Optimal acquisition orders of diffusion-weighted MRI measurements," JMRI, vol. 25, no. 5, pp. 1051–1058,2007.

7. O. Esteban, E. Caruyer, A. Daducci, M. Bach-Cuadra, M. J. Ledesma-Carbayo, and A. Santos, "Diffantom: Whole-Brain Diffusion MRI Phantoms Derived from Real Datasets of the Human Connectome Project," Frontiers in Neuroinformatics, vol. 10, Feb. 2016.

8. E. Sabidussi, S. Klein, M. Caan, S. Bazrafkan, A. den Dekker, J. Sijbers, W. Niessen, and D. H. J. Poot,"Recurrent inference machines as inverse problem solvers for MR relaxometry," Medical Image Analysis,vol. 74, p. 102220, Dec.2021.

9. L. Snoek, M. van der Miesen, A. van der Leij, T. Beemsterboer, A. Eigenhuis, and S. Scholte, ""aomic-id1000"," OpenNeuro 2021. DOI: 10.18112/openneuro.ds003097.v1.2.1

10. J. Veraart, J. Sijbers, S. Sunaert, A. Leemans, and B. Jeurissen, "Weighted linear least squares estimation of diffusion MRI parameters: Strengths, limitations, and pitfalls," NeuroImage, vol. 81, pp. 335–346,Nov. 2013.

11. J.D. Tournier, R. Smith, D. Raffelt, R. Tabbara, T. Dhollander, M. Pietsch, D. Christiaens, B. Jeuris-sen, C.H. Yeh, and A. Connelly, "Mrtrix3: A fast, flexible and open software framework for medical image processing and visualisation," NeuroImage, vol. 202, p. 116137, 2019.

Acknowledgments / Funding Information: This project was funded by the European Union's Horizon 2020 programme, under the grant agreement No 764513.

Acknowledgments / Funding Information: Continue on this line

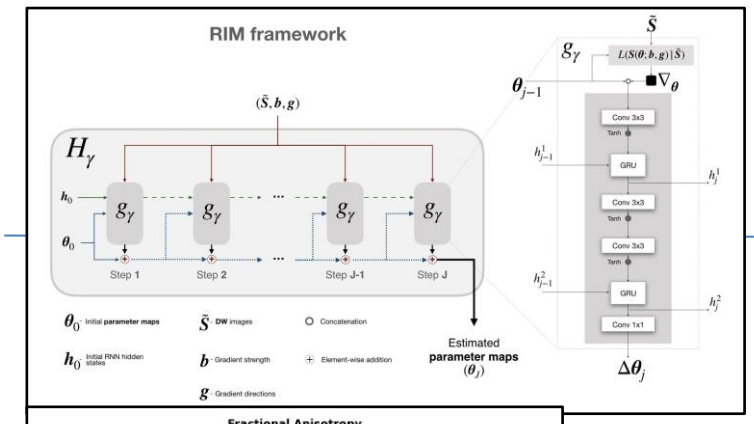

Figure 1. RIM framework ($\hat{\boldsymbol{\theta}} = H_\gamma(\tilde{\boldsymbol{S}}; \boldsymbol{b}, \boldsymbol{g})$). At a given step $j \in \{1, ..., J\}$, the neural network g_γ receives the current parameter estimates $\hat{\boldsymbol{\theta}}_{j-1}$, the gradient of a likelihood, $\nabla_{\boldsymbol{\theta}}$, and a vector of memory states $\boldsymbol{h}_{j-1}$ the RIM can use to keep track of optimization progress. The network outputs an update to the current estimate ($\Delta\boldsymbol{\theta}_j$).

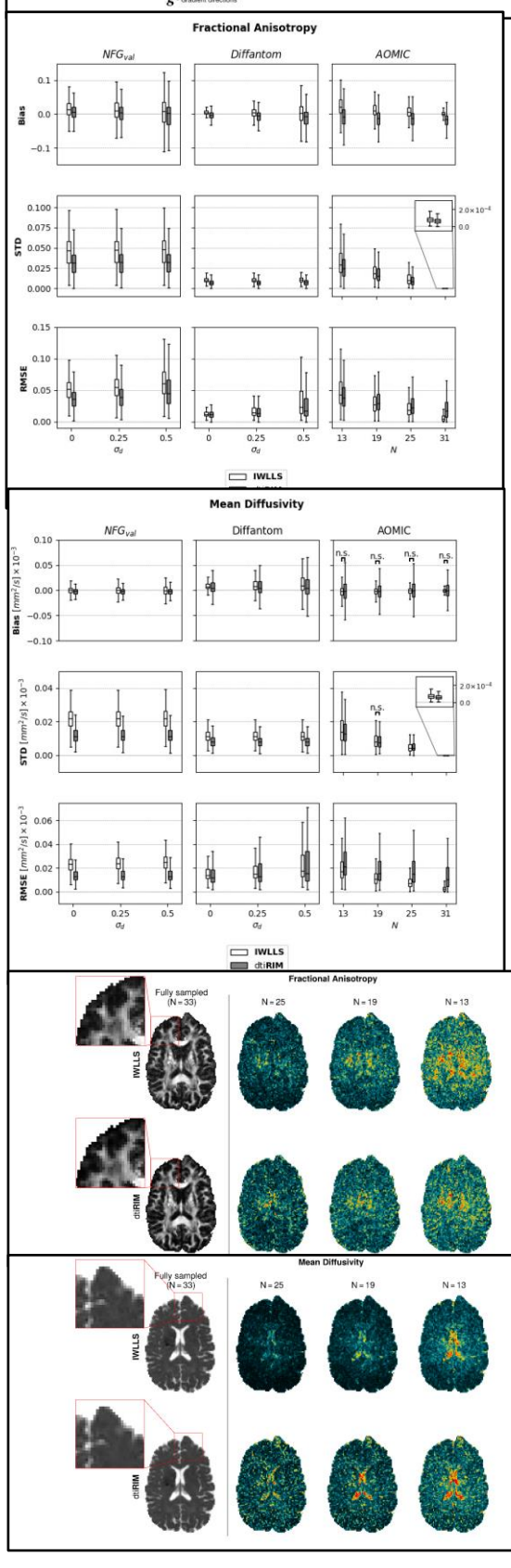

Figure 2. Error measurement in Fractional Anisotropy estimation for different motion severity (σ_d) with simulation ($\mathbf{NFG}_{val}$, $\mathbf{Diffantom}$) and in-vivo datasets ($\mathbf{AOMIC}$). Measures of bias, standard deviation (STD) and root-mean-square error (RMSE). Whiskers represent the 95-percentile and outliers are not shown. All mean differences between $dti\mathbf{RIM}$ and $\mathbf{IWLLS}$ are significant (unpaired t-test, $p < 0.001$)

Figure 3. Error measurement in Mean Diffusivity estimation for different motion severity (σ_d) with simulation ($\mathbf{NFG}_{val}$, $\mathbf{Diffantom}$) and in-vivo datasets ($\mathbf{AOMIC}$). Measures of bias, standard deviation (STD) and root-mean-square error (RMSE). Whiskers represent the 95-percentile and outliers are not shown. $\mathbf{n.s.}$ denotes non-significant mean differences (unpaired t-test, $p < 0.001$).

Figure 4. Left column shows estimated fractional anisotropy (FA) maps for $dti\mathbf{RIM}$ and $\mathbf{IWLLS}$. RMSE maps for different number of q-samples (N) are shown on the right. RMSE was defined, per pixel, as $\sqrt{\frac{1}{C}\sum_{c=1}^{C}\left(\hat{\phi}^c - \phi\right)^2}$, where $c = [1, ..., C]$ is the repetition index, $\hat{\phi}$ is the estimated FA map and ϕ is the $\mathbf{IWLLS}$ FA estimate using fully-sampled set ($N = 33$).

Figure 5. Left column shows estimated mean diffusivity (MD) maps for $dti\mathbf{RIM}$ and $\mathbf{IWLLS}$. RMSE maps for different number of q-samples (N) are shown on the right. RMSE was defined, per pixel, as $\sqrt{\frac{1}{C}\sum_{c=1}^{C}\left(\hat{\phi}^c - \phi\right)^2}$, where $c = [1, ..., C]$ is the repetition index, $\hat{\phi}$ is the estimated MD map and ϕ is the $\mathbf{IWLLS}$ MD estimate using fully-sampled set ($N = 33$).

Comparison of arterial input functions obtained through back-to-back acquistion of DCE and DSC MRI

Chih-Hsien Tseng[1], Jaap Jasper[2], Alejandra Mendez Romero[2], Piotr Wielopolski[3], Matthias van Osch[4], Frans Vos[1, 3]

[1]Department of Imaging Physics, Delft University of Technology, Delft, the Netherlands; [2]Department of Radiation Oncology, Erasmus Medical Center, Rotterdam, the Netherlands; [3]Department of Radiology, Erasmus Medical Center, Rotterdam, the Netherlands; [4]Department of Radiology, Leiden University Medical Center, Leiden, the Netherlands

Synopsis: We aimed to compare the AIF determined from DCE-MRI with the AIF from DSC-MRI in back-to-back imaging, using the same dose of Gadobutrol. The DCE-driven AIFs showed the same 'pattern' as the DSC-driven AIFs, but had smaller variance of the shape and peak value. A linear relation was found between the contrast agent concentration from DCE and ΔR_2*, but the linear coefficients showed large variation across regions and subjects. Our findings show that the DCE-driven AIF has the potential to serve as an alternative for the DSC-driven AIFs for quantitative perfusion assessment.

Purpose: The Arterial Input Function (AIF) plays a crucial role in estimating perfusion properties from Dynamic Susceptibility Contrast MRI (DSC-MRI). An important issue, however, is that measuring the AIF's absolute contrast concentration is challenging due to uncertainties in the relation with the measured R_2*-weighted signal[1–3]. In addition, several experimental difficulties hinder measuring the AIF in DSC-MRI. First, the AIF can become distorted due to partial volume effects[4]. Second, the signal in large arteries tends to reach the noise floor during the passage of contrast agent[5]. Third, signal can be shifted, especially during the peak, due to local resonance frequency changes as induced by the high concentration of contrast agent[6]. A potential solution could be to derive the AIF from separately acquired Dynamic Contrast Enhanced MRI (DCE-MRI) data, which provides higher spatial resolution, has a known relation between signal-change and Gd-concentration[7], and is not susceptible to signal saturation nor vessel displacement[6]. Such a DCE-scan could be measured during a pre-loading bolus injection, potentially with similar duration as the DSC-scan.

In this study, we aim to systematically compare (1) the AIF determined from DCE-MRI with the AIF from DSC-MRI in back-to-back imaging and (2) assess the linearity of the contrast concentration measured from DCE-MRI and the ΔR_2* from DSC-MRI.

Methods: Subjects: 4 patients with histologically confirmed, IDH mutated glioma (WHO grade 2 or 3) were recruited as part of the associated RIGEL study (trial identifier: NCT04304300).

Imaging: MRI scans were acquired two months before radiotherapy by using a 48-channel head coil in a 3T MRI (Signa Premier, GE Healthcare, Waukesha, WI, USA) in Erasmus Medical Center (Rotterdam, Netherlands). A single dose of Gadobutrol (0.1mmol/kg, Gadovist®, Bayer, Germany) was injected at 5mL/s followed by a 15mL NaCl flush (same injection rate) using a power injector 10 seconds after the start of both DCE and DSC acquisition, respectively. DCE images were acquired using a differential subsampling with cartesian ordering sequence[8] with TR/TE: 2.7/0.9ms, flip angle: 14°, FOV: 220×220×142mm^3, matrix size: 128×128, 72 slices, in-plane resolution: 1.7×1.7mm^2, slice thickness: 2mm, and temporal resolution: 2s, 183 dynamics. DSC images were obtained with a T_2*-weighted gradient echo echo-planar imaging sequence with TR/TE: 2000/45ms, FOV: 220×220×140mm^3, matrix size: 100×100, 29 slices, in-plane resolution: 2.2×2.2mm^2, slice thickness: 5mm, temporal resolution: 2s, 50 dynamics.

Analysis: Rigid-body registration was performed to align all DSC images to the first volume of DCE images by SPM12[9]. AIFs were selected manually and semi-automatically: (1) five Region-Of-Interests (ROIs) were annotated in the DCE images, each in a different artery and on a different slice; (2) these selected ROIs were then projected onto the registered DSC images; all voxels included within the ROI were used for AIF-determination (3) a semi-automatic approach[10], based on a clustering approach favoring early bolus arrival time, high peak value and fitting with a gamma function, was implemented to derive five AIFs from the same DSC slices as previous step. The DCE-driven AIF (1) was derived from the annotated region according to a previously published approach[11], in which Orton's model was used to estimate the perceived number of excitation pulses to compensate inflow effects. The DSC-driven AIFs (2)(3) were estimated by assuming a linear relation between ΔR_2* and contrast agent concentration[12]. Subsequently, the AIFs were plotted to visually explore their characteristics. Furthermore, the linearity of the relation between the DCE-driven and DSC-driven AIFs was assessed.

Results: Fig.1 shows the DSC and DCE AIFs, obtained from multiple voxels in a representative vessel. It demonstrates that while the mean curves had similar shapes, the DCE-AIF yielded much more consistent curves (less variation) (Fig.1c,d). Furthermore, the DCE-AIFs from different arteries, from different slices, and from different subjects exhibited more reproducible results than the DSC-AIFs (Fig.2). Finally, the semi-automatically selected DSC-AIFs demonstrated higher peak values and narrower width than derived from manually selection and as compared to the DCE-AIF (Fig.3). Fig.4 shows the scatter plot of the DCE-AIF and DSC-AIF for one artery in each of the four patients. The DCE-based contrast agent concentration correlated significantly ($P<0.05$) to the ΔR_2^* in each plot, although the linear coefficients varied from 4.2 to 11.2 over the 4 patients.

Discussion: The shape and the peak value of the AIF are key factors for quantitative estimation of perfusion parameters from DSC-MRI. However, true quantification of the contrast agent concentration is a challenging problem in DSC-MRI due to susceptibility effects resulting in non-linear partial volume and vessel-shifting artefacts. It can be observed that the DCE-driven AIFs show the same 'pattern' as the DSC-driven AIFs, but had smaller variance of the shape and peak value. This is an indication that the DCE-driven AIF could be a more reliable option for quantifying perfusion properties from DSC-MRI. We found a strong linear relation between the contrast agent concentration from DCE and ΔR_2*, but the linear coefficients showed large variation, again pointing to poor quantification of the AIF by DSC.

Conclusion: Our findings show that the DCE-driven AIF has the potential to serve as an alternative for the DSC-driven AIFs for quantitative perfusion assessment. Also, the semi-automatic method did not prevent erroneous AIF selection from DSC images.

Reference:

1. Knutsson et al., 2010, Magn Reson Mater Phy 23(1):1–21
2. Akbudak et al., 2004, ISMRM workshop on quantitative cerebral perfusion imaging. Italy, pp 10–11
3. Kjølby et al., 2006, Magn Reson Med 56(1):187–197
4. van Osch et al., 2001, Magn Reson Med 45(3):477–485
5. Ebinger et al., 2010, Stroke 41 (2010) 95–101.
6. Rausch et al., 2000, Magn Reson Imaging 18(10):1235–1243.
7. Shen et al., 2015, Invest Radiol. 2015 May;50(5):330-8.
8. Saranathan et al., 2012, *J Magn Reson Imaging*. 2012;35(6):1484-1492.
9. Friston et al., 1994, *Human Brain Mapping*, **2**(4), 189–210.
10. Peruzzo et al., 2011, *Comput Methods Programs Biomed*. 2011;104(3):e148-e157.
11. van Schie et al., 2017, *Journal of Magnetic Resonance Imaging*, 47(5), pp.1190-1196.
12. ØStergaard et al., 1996, *Magnetic Resonance in Medicine*, *36*(5), 715–725.

Acknowledgments / Funding Information: We are thankful to HollandPTC-Varian consortium for financial support.

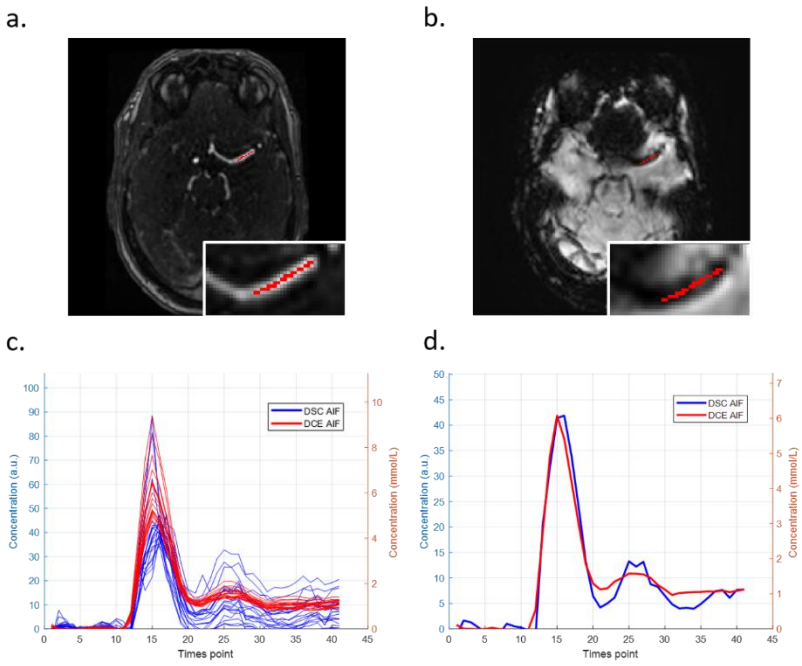

Figure 1. The illustration of AIF measurements in one representative patient in one particular region. This region was manually selected in the DCE images (a) and subsequently projected onto registered DSC images (b). Contrast concentration change measured in the DCE and DSC series in the voxels from the selected region (c) and the mean curve (d). Blue lines are measurements from DSC MRI (left y axis); red lines represent measurements from DCE MRI (right y axis).

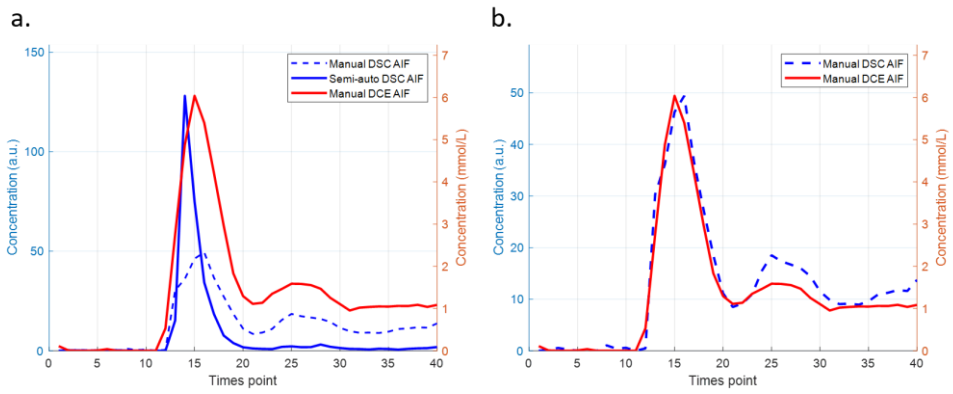

Figure 3. Comparison of the AIF obtained with a semi-automatic algorithm (blue solid line) and manually derived AIFs. The peak of the manual DCE AIF was aligned with the peak of the semi-automatic AIF (a) and the manual DSC AIF (b), respectively. Notice that the semi-automatically determined DSC-AIF has higher peak value than the manual one (blue dash line). However, it has around twice less full width at half maximum than the DCE-driven AIF (red solid line) has. (Only AIFs from one vessel of the representative patient were plotted in this graph.)

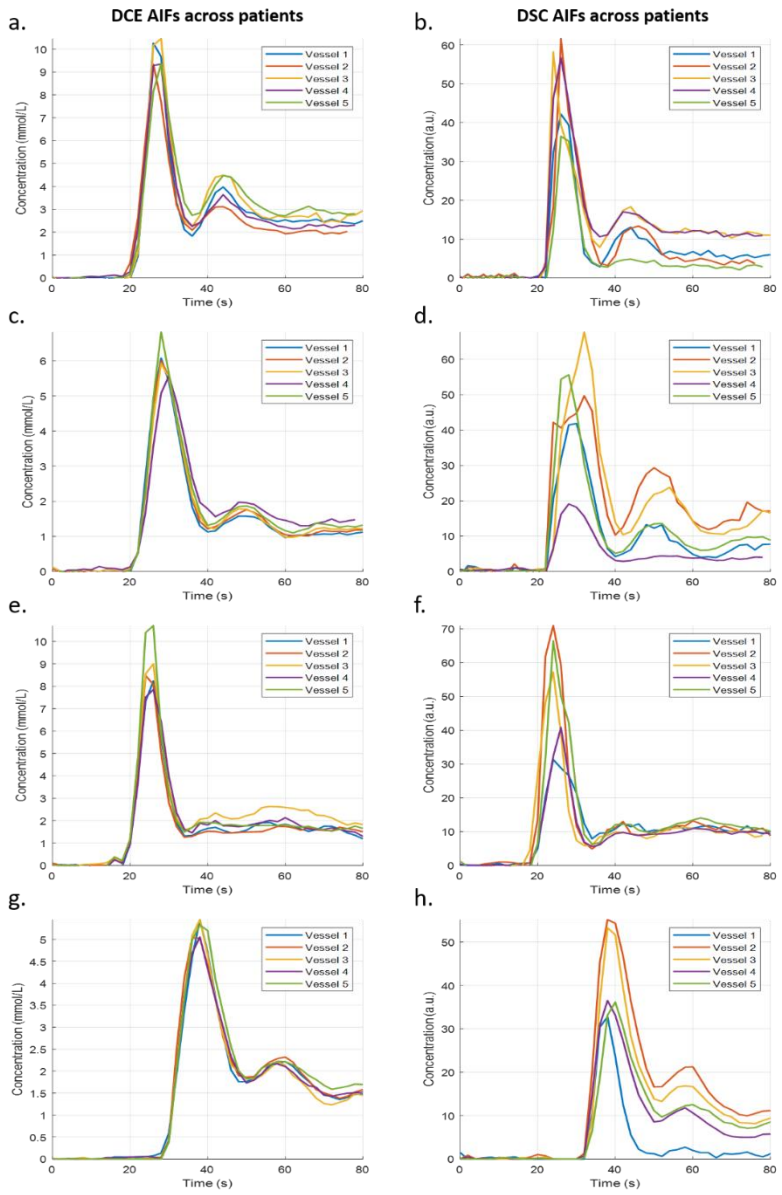

Figure 2. AIFs measured from five vessels in 4 patients (top to bottom) were plotted to test the reproducibility and stability of accessing AIFs from DCE images and DSC images. Observe that the DCE-driven AIFs (a, c, e, g) showed less variation than the DSC-driven AIFs did (b, d, f, h).

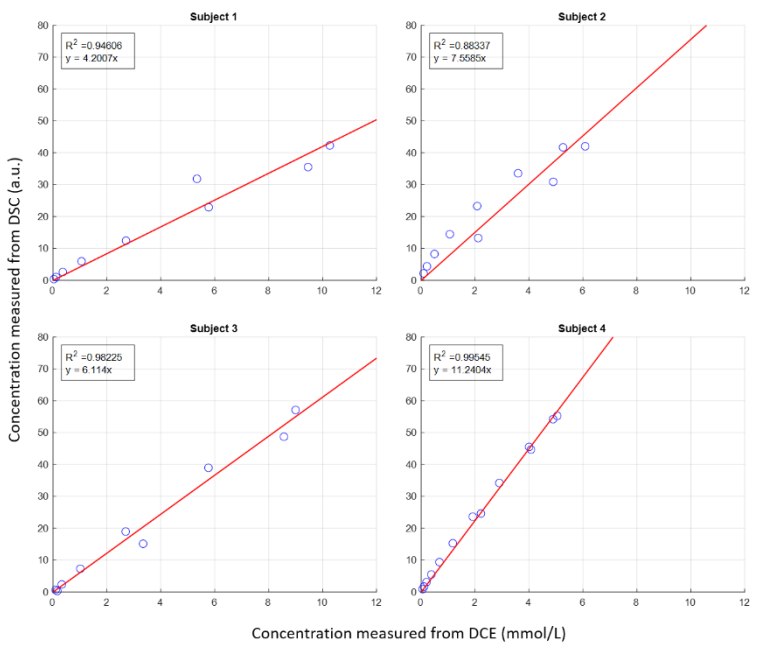

Figure 4. Linear regression model was used to estimate the linearity between the transverse relaxivity change (y-axis) and the contrast concentration change (x-axis) in one vessel which had the highest R-squared value in the 4 patients (a-d). The linear relation is significant but with varied linear coefficients in different patients.

F0 determination at the labeling plane: the neglected factor for successful pCASL perfusion MRI

L. Vaclavu[1], K.C.C. van de Ven[2] , M.J.P. van Osch[1]

[1]C.J. Gorter Center for High Field MRI, Department of Radiology, Leiden University Medical Center, Leiden, The Netherlands; [2]Philips Healthcare, Best, The Netherlands

Synopsis:

In perfusion imaging with arterial spin labeling (ASL), the labeling plane is located further away from the isocenter of the scanner than the imaging volume. This can result in offsets in resonance frequencies which can lead to imperfect inversion and hence lower labeling efficiency. In this study, a perfusion phantom is used to study the influence of off-resonance on two arterial spin labeling schemes, balanced and unbalanced labelling. The results show that additional F0 determination at the labelling plane is the redeeming factor for successful ASL MRI independent of the labeling scheme used.

Introduction:

Pseudo-continuous arterial spin labeling (PCASL) enables the non-invasive assessment of brain perfusion by utilizing the inflowing blood as an endogenous tracer. The inversion of flowing spins is performed at the level of the neck, typically 90 mm below the center of the brain (the isocenter of the scanner). While the magnetic field in the brain region is typically shimmed to provide optimal quality, the labeling plane is often the overlooked or at least unspoken of factor for implementing successful ASL measurements. More specifically, off-resonance (ΔF0) effects at the location of the labeling plane are well-known causes of labeling errors leading to underestimation or even negative cerebral blood flow measurements. Proposed solutions include multi-phase PCASL[1], Optimized PCASL[2], unbalanced PCASL[3] and use of a separate B0-map[4]. The use of the much simpler approach of an additional F0-measurement at the labeling plane, has maybe been used by many, but remains rather unspoken of in literature and ASL recommendations. The purpose of this study was to investigate the sensitivity of balanced (bPCASL) and unbalanced (ubPCASL) implementations to off-resonance at the labeling plane, and whether this depends on an F0 determination at the labelling plane.

Methods:

Images were acquired on a phantom as well as in a healthy female volunteer on a 3T clinical MR system (Achieva, Philips Healthcare, Best, NL) using a 32-channel head-coil and body-coil transmission. Two PCASL schemes were compared: 1) bPCASL, where both the control and label conditions have a net average gradient (G_{mean}) over the labeling duration, and 2) ubPCASL3, where the control condition has $G_{mean,control} = 0$. G_{mean} was 0.36 T/m, gradient strength was 5.0 mT/m and the RF interval of the Hanning-shaped RF pCASL pulses was 1.21 ms with a flip angle of 27.81 degrees. The total label duration was 1800 ms, post-label delay was 2000 ms, and images were acquired with a 4-shot 3D GRaSE readout, with 3.75 x 3.75 x 6 mm^3 voxels, TR/TE 4250/11 ms, flip angle 80°, 4 background suppression pulses, 5 inferior saturation pulses, and scan duration of 04:56 mins. B0 maps were acquired to estimate ΔF0 (Hz) using a delta TE of 1ms, multi-slice FFE read-out with 7 slices, 3.75 x 3.75 mm^2 voxels, 4 mm slice thickness, TR/TE 650/7 ms, flip angle 80° and scan duration of 02:20 mins. A perfusion phantom (QASPER, Gold Standard Phantoms, London, UK) was used to investigate the susceptibility-induced off-resonance effects of pyrolytic graphite sheets secured to the outer tube of the 'neck' region of the phantom as shown in Figure 1. The flow rate was set to 350 mL/min (default).

The main metric for evaluation was the observed signal difference between control-label, and whether the difference resulted in positive ASL signal.

Results:

Figure 1 shows the effects of placing the pyrolytic graphite material on the neck of the phantom. We found that a stack of 4 sheets secured perpendicular to the B0 field had the strongest effect on the B0 maps. The red profile shown in the magnitude images (along the inflow tube) and B0 maps is plotted in the bottom row to illustrate the frequency offset induced by the diamagnetic graphite material for each orientation of the graphite stack of sheets with respect to the B0 field.

The PCASL results for different conditions are shown in Figure 2 for a single slice/location of the perfusion phantom and in the volunteer. First, when no shimming was performed and the same F0 was assumed for labeling as for imaging, that ubPCASL performed well, despite the -246Hz off-resonance at the labeling plane, which was not optimal for bPCASL as seen by the negative ASL signal. Next, the additional F0 determination in the labeling plane resulted in positive ASL signal in all situations except in the presence of graphite and no shimming in bPCASL. The additional F0 determination proved crucial for successful PCASL imaging.

The in vivo results are somewhat more subtle but show higher ASL signal when F0 was determined at the labeling plane compared to no additional F0 determination. This suggests a greater difference between control and label due to more optimal inversion conditions.

Discussion:

Overall, ubPCASL was more robust, but not immune, to off-resonance offsets at the labeling plane. The additional F0 determination greatly improved the ASL signal for both bPCASL and ubPCASL schemes. The lower sensitivity to off-resonance of ubPCASL is known from theory as well as experimental evidence[5,6]. However, applying bPCASL in combination with an F0 determination at the labeling plane also enabled robust perfusion imaging across the brain and in the phantom. The experiments carried out here were limited by the fact that the perfusion phantom only has a single inflow tube in the centre of the cylinder, which precludes left-right comparisons of off-resonance effects on ASL signal. Our findings could guide implementation of PCASL at higher field strengths, but future studies are also needed at clinical field-strengths to demonstrate the influence of more realistic off-resonance and non-uniform effects on different ASL implementations.

References:

1. Jung, Wong, and Liu (2010), Multiphase pseudocontinuous arterial spin labeling (MP-PCASL) for robust quantification of cerebral blood flow. Magn. Reson. Med., 64: 799-810.
2. Shin, Liu, Wong, Shankaranarayanan, and Jung (2012), Pseudocontinuous arterial spin labeling with optimized tagging efficiency. Magnetic Resonance Medicine, 68: 1135-1144.
3. Dai, Garcia, de Bazelaire, Alsop. Continuous flow-driven inversion for arterial spin labeling using pulsed radio frequency and gradient fields. Magn Reson Med 2008;60:1488–1497.
4. Jahanian, Noll, and Hernandez-Garcia (2011), B0 field inhomogeneity considerations in pseudo-continuous arterial spin labeling (pCASL): effects on tagging efficiency and correction strategy. NMR Biomed., 24: 1202-1209.
5. Zhao, Vidorreta, Soman, Detre, and Alsop, "Improving the robustness of pseudo-continuous arterial spin labeling to off-resonance and pulsatile flow velocity," Magn Reson Med, vol. 78, no. 4, pp. 1342-1351, Oct 2017
6. Wu, Fernandez-Seara, Detre, Wehrli, and Wang, "A theoretical and experimental investigation of the tagging efficiency of pseudocontinuous arterial spin labeling," Magn Reson Med, vol. 58, no. 5, pp. 1020-7, Nov 2007.

Acknowledgments / Funding Information: Continue on this line

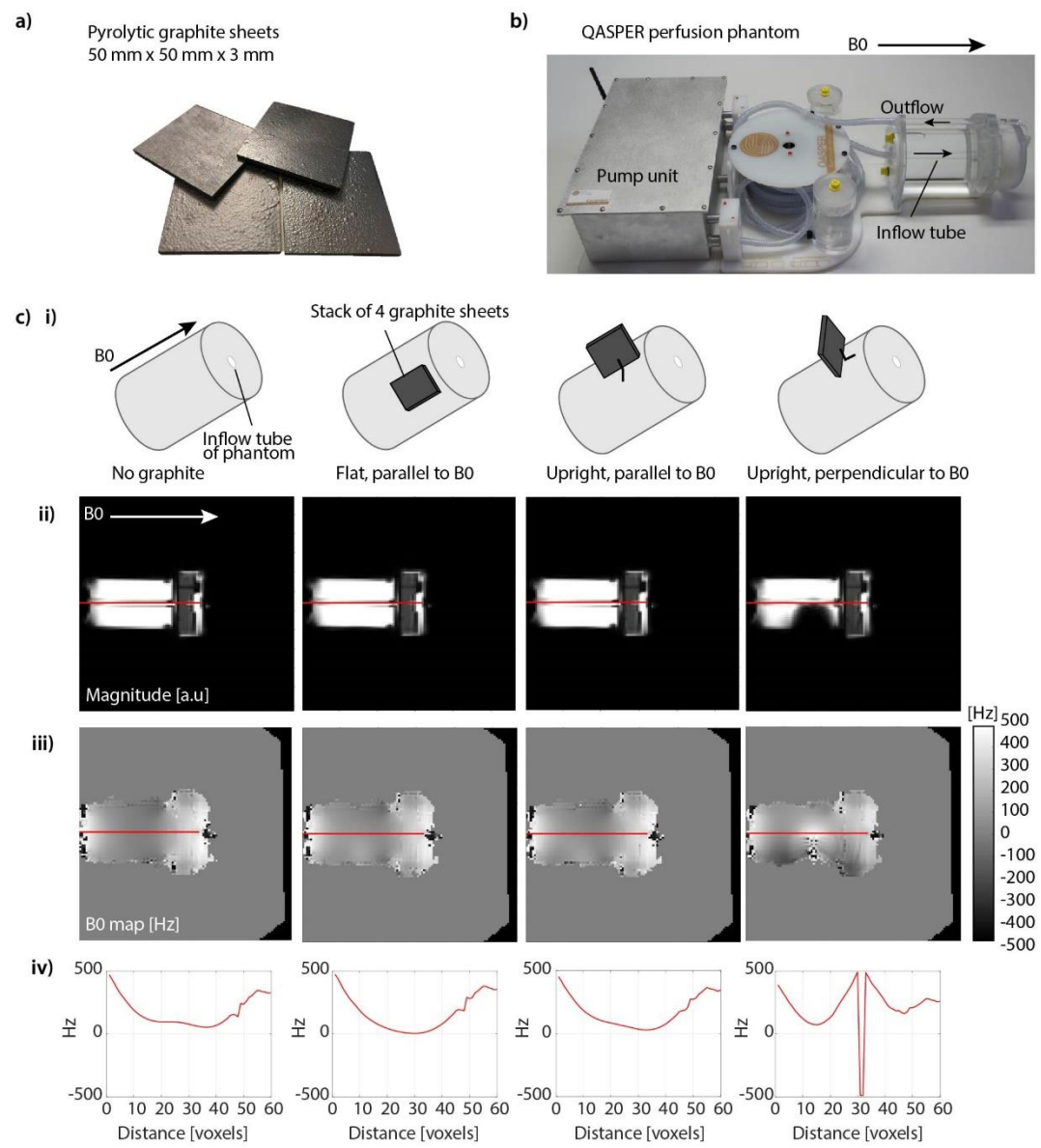

Figure 1. Pyrolytic graphite sheets introduce susceptibility-induced off-resonance on B0 maps. A stack of 4 pyrolytic graphite sheets photographed in (a) were secured to the neck region of the QASPER perfusion phantom (b) where the inflowing perfusate undergoes PCASL labeling. (c) (i) shows different orientations of the graphite which have different off-resonance effects, (c)(ii) shows the effects of graphite on the magnitude images of a B0 map, with graphite perpendicular to the B0 field having the strongest effect. (c) (iii) shows the off resonance effects on the B0 maps in frequencies, and (c) (iv) shows the profiles of the red lines shown in (ii-iii). When the graphite was upright and perpendicular to the B0 field, the off-resonance effect was the strongest. This is the orientation we proceeded with in subsequent experiments with graphite.

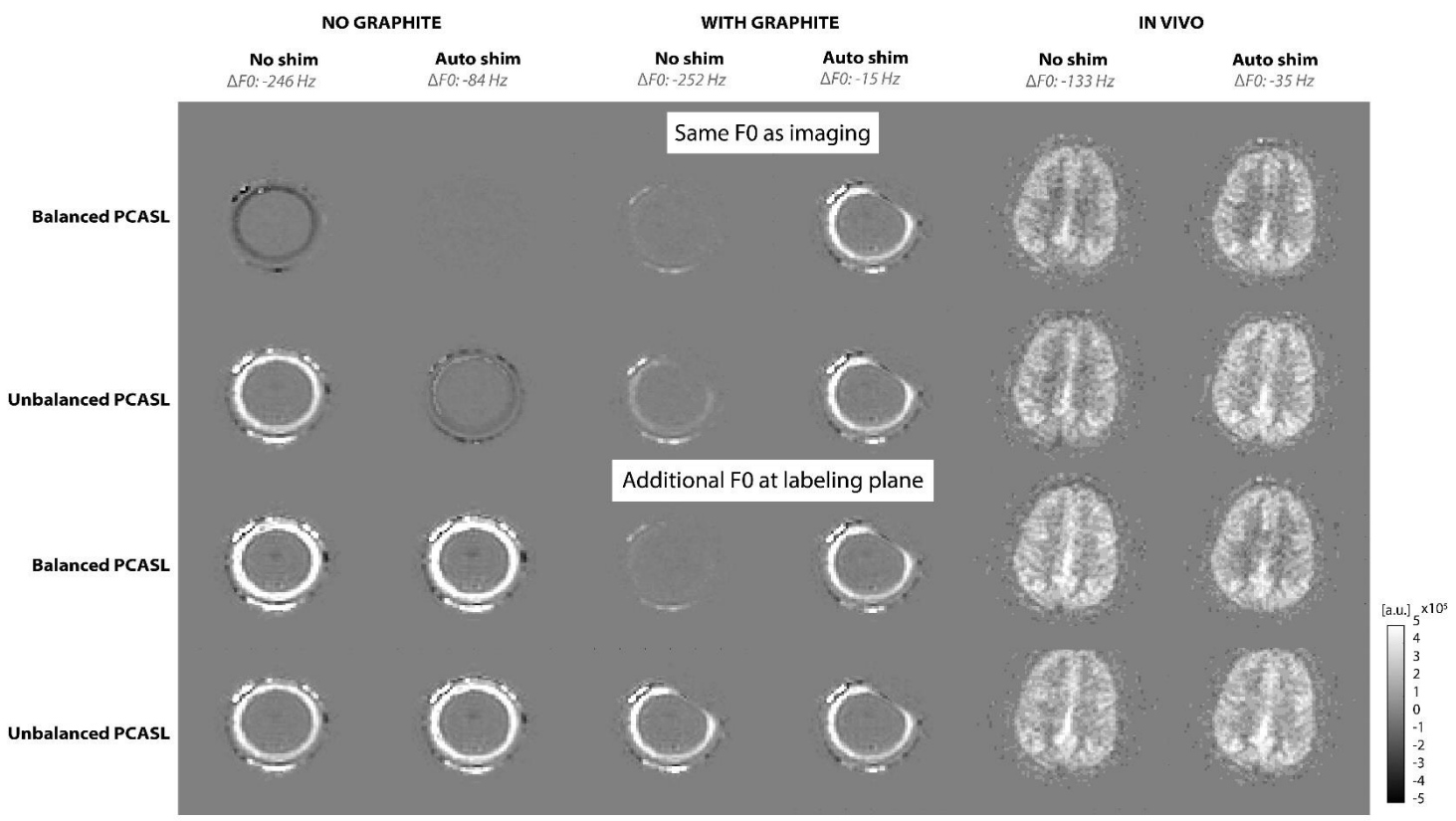

Figure 2. ASL signal from QASPER perfusion phantom without and with graphite and *in vivo*. In the upper panel, when the F0 was set the same for the labeling and imaging volumes, balanced PCASL showed degraded ASL signal especially when no shimming was applied to the field. Note the different off-resonance offsets (ΔF0) of the labeling plane for each scan at the top. The second row shows that unbalanced PCASL performed slightly better.

The bottom panel shows the effect of the additional F0 determination at the labeling plane, with improved ASL signal for balanced PCASL and especially for unbalanced PCASL (bottom row) which performed well in all situations, even with graphite. Note that the presence of graphite resulted in a distorted perfusion ring.

Feasibility of T1-weighted USPIO-enhanced MR imaging of pelvic lymph nodes using stack-of-spirals UTE

M.C. Maas[1], P. Zámecnik[1], M.J. Schneider[2,3], T. Gaass[2,4], T. Benkert[5], J. Dinkel[2,4] and T.W.J. Scheenen[1]

[1]Department of Medical Imaging, Radboudumc, Nijmegen, The Netherlands; [2]Comprehensive Pneumology Center, German Center for Lung Research (DZL), Munich, Germany; [3]Antaros Medical AB, Mölndal, Sweden; [4]Department of Radiology, Ludwig-Maximilians-University Munich (LMU), Munich, Germany; [5]MR Application Predevelopment, Siemens Healthcare GmbH, Erlangen, Germany

Synopsis: Detection of lymph node (LN) metastases benefits from using the ultrasmall superparamagnetic particles of iron oxide (USPIO) contrast agent Ferumoxtran-10. T2* contrast is commonly used to distinguish between normal LNs (high USPIO uptake, low signal) and metastases (low uptake, high signal). T1-weighted imaging may offer complementary information, but is challenging because of the strong T2* effects of the contrast agent. This work investigates whether ultrashort echotime (UTE) imaging with stack-of-spirals sequence can mitigate this issue. High-resolution USPIO-enhanced T1-weighted UTE of the pelvis was achieved, and T1-mediated signal hyperintensities were indeed observed in LNs in patients with prostate cancer.

Introduction: Detection of pelvic lymph node (LN) metastases can be improved using the ultrasmall superparamagnetic particles of iron oxide (USPIO) contrast agent Ferumoxtran-10[1]. The contrast agent accumulates in healthy lymph nodes by uptake by cells of the immune system, while in metastatic LNs particle accumulation is much lower. USPIO-enhanced MRI for detection of LN metastases is primarily based on T2*w imaging, in which LNs with high USPIO uptake exhibit signal loss while LNs with low uptake retain a high signal intensity. T1-weighted imaging may offer complementary information to T2*-weighted imaging in this context, as the R1 and R2* relaxivities of Ferumoxtran-10 differ in their dependency on the microscopic distribution of the USPIO nanoparticles[2]. Thus, T1w imaging may potentially aid in improving the specificity of USPIO enhanced LN diagnostics. However, obtaining unambiguous USPIO-enhanced T1 contrast is challenging using conventional echo-type sequences, because of the strong T2* effect of the contrast agent. Ultrashort echo time (UTE)-type sequences may mitigate this issue by minimizing T2* relaxation effects. Before any additional value of T1w UTE for LN diagnostics can be investigated, the feasibility of obtaining the desired contrast at sufficiently high resolution[3] and image quality must be established. Therefore, the purpose of this study was to assess whether T1-mediated signal enhancement due to USPIO uptake can be observed in pelvic lymph nodes in prostate cancer patients at high isotropic spatial resolution using a stack-of-spirals UTE sequence.

Methods: All measurements were performed on a 3T system (MAGNETOM PrismaFit, Siemens Healthcare, Erlangen, Germany) with standard body and spine phased array coils. The prototypical UTE sequence used a stack-of-spirals k-space trajectory with non-selective excitation and variable-duration slice encoding to minimize the effect of T2* decay[4,5]. We optimized the acquisition protocol in 2 healthy male volunteers (age 30 and 44 years) without USPIO infusion, resulting in the following parameters: coronal slab orientation, TR/TE = 4.3/0.05ms, flip angle 15°, FOV 400 mm, matrix 512, 432 spiral interleaves (corresponding to an undersampling factor of 2) with linear reordering, spiral duration 1160 µs, stack of 256 partitions interpolated to 320, acquisition time 8 minutes. The sequence looped over partitions and spiral angles in its inner and outer loops, respectively. Patients with prostate cancer scheduled for USPIO-enhanced MRI as part of their clinical diagnostic workup were enrolled. Stack-of-spirals UTE was added to the end of their clinical examination, which also included a 3D T1-weighted GRE sequence and a 3D T2*-weighted water-selective MEDIC sequence, both at 0.73 mm isotropic resolution. UTE images were reconstructed offline using the L1-ESPIRiT implementation of the BART toolbox[6], employing manual coil selection to reduce streaking artifacts originating from structures outside the FOV. Images were assessed on the presence of signal hyperintensity in LNs, and scored on image quality, visibility of LNs and blood vessels, and artifacts on 5-point scales by a radiologist and a physicist in consensus, both with 7 years of experience in USPIO-enhanced pelvic MRI.

Results: After protocol optimization, four male patients with prostate cancer (age 54-75 years) were included. One of these had had an intraprostatic injection of superparamagnetic iron oxide (SPIO) particles 3 weeks prior to USPIO infusion, and one had surgical clips in the area of interest. Imaging was successful in all 4 patients. Image quality was rated good to excellent in all patients (Table 1, Figure 1), with excellent and strongly hyperintense depiction of the vasculature and high SNR. Although the overall visibility of LNs varied between patients, T1-mediated hyperintensities were observed in at least 1 LN in all patients (Figure 2). Some variations in contrast behavior in T2*-weighted MEDIC and T1-weighted UTE were observed between LNs (Figure 2). Artifacts due to respiratory or bowel motion, streaks, or foldover into the pelvic region were minor (Figure 3). Blooming artifacts were observed in the patients with intraprostatic SPIO injection and surgical clips, but not in the other patients. Chemical shift related artifacts were observed at the borders between watery and lipid tissues (e.g. between muscle and surrounding lipid tissue, Figure 3).

Discussion: This work shows that high-resolution T1w USPIO-enhanced MRI of pelvic LNs is feasible in patients with prostate cancer, and that intranodal T1-mediated signal enhancement can indeed be observed. The observed variations in contrast behavior between T2*-weighted and T1-weighted UTE support the hypothesis that T1w imaging may provide complementary information, but larger studies are needed to investigate this further. The fat-water artifact observed at the boundary between muscle and lipid tissue may mimic T1-induced signal enhancement at the boundary between the watery LNs and surrounding lipid tissue. This may be mitigated by using fat suppression techniques, or by decreasing the duration of the spiral readouts. Both would likely lead to an increase in scanning time; however, the high SNR obtained suggests that further acceleration of the acquisition may be possible.

Conclusions: T1-mediated signal hyperintensities can be observed within pelvic LNs of patients post-USPIO infusion using a stack-of-spirals UTE sequence, at 0.8mm isotropic resolution in less than 10 minutes. Although further optimization is warranted, this opens the possibility of investigating the possible additional value of T1w UTE imaging for the diagnosis of LN metastases.

References:

1. Harisinghani MG, Barentsz J, Hahn PF, et al. Noninvasive Detection of Clinically Occult Lymph-Node Metastases in Prostate Cancer. New England Journal of Medicine. 2003;348(25):2491–2499.

2. Brisset J-C, Desestret V, Marcellino S, et al. Quantitative effects of cell internalization of two types of ultrasmall superparamagnetic iron oxide nanoparticles at 4.7 T and 7 T. European Radiology. 2010;20(2):275–285.

3. Fortuin AS, Philips BWJ, Leest MMG van der, et al. Magnetic resonance imaging at ultra-high magnetic field strength: An in vivo assessment of number, size and distribution of pelvic lymph nodes. PLOS ONE. 2020;15(7):e0236884.

4. Qian Y, Boada FE. Acquisition-weighted stack of spirals for fast high-resolution three-dimensional ultra-short echo time MR imaging. Magnetic Resonance in Medicine. 2008;60(1):135–145.

5. Mugler III JP, Fielden SW, Meyer CH, et al. Breath-hold UTE Lung Imaging using a Stack-of-Spirals Acquisition. In: Proc. Intl. Soc. Mag. Reson. Med.Vol 23.; 2015:1476.

6. BART Toolbox for Computational Magnetic Resonance Imaging. Available at: DOI: 10.5281/zenodo.592960.

Acknowledgments / Funding Information: N/A

	Median	Range
Image Quality		
Overall image quality	4.5	4-5
Visibility of lymph nodes	3.0	2-5
Visibility of blood vessels	5.0	5-5
SNR	4.0	4-5
Artifacts		
Respiratory / intestinal motion	1.5	1-2
Streaks	2.0	1-2
Blooming (susceptibility)	3.5	1-4
Fold-over	1.0	1-1

Table 1: Overview of image quality and artifact measures of 4 patients with prostate cancer scanned with T1w USPIO-enhanced stack-of-spirals UTE. Scale used for image quality measures: 1 - not evaluable; 2 - poor; 3 - moderate; 4 - good; 5 – excellent. Scale used for artifacts: 1 - absent; 2 - minimal; 3 - moderate; 4 - significant ; 5 – severe.

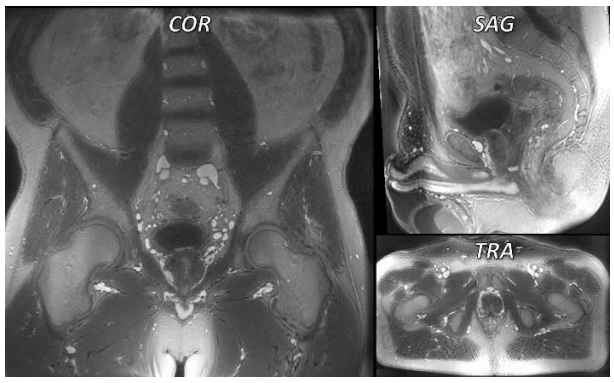

Figure 1: Multi-planar reformats in 3 orthogonal orientations of USPIO-enhanced stack-of-spirals UTE with 0.8 mm isotropic voxels in a 54-year-old patient with prostate cancer, showing the high image quality attainable with this sequence and the strong T1-induced hyperintensity of the blood vessels.

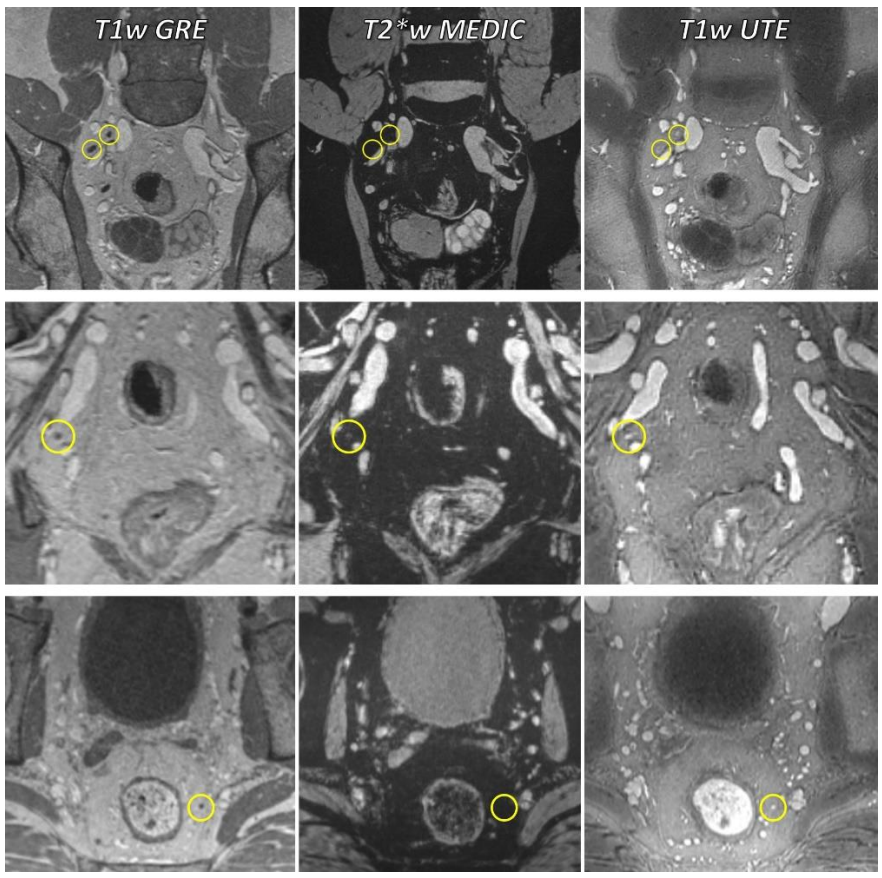

Figure 2: Examples of USPIO-induced T1 signal enhancement in LNs in patients with prostate cancer. Top row: coronal T1w GRE and T2*w MEDIC show strong USPIO-induced signal loss in 2 para-iliacal lymph nodes in a 54-y.o. patient with prostate cancer, while T1w UTE shows signal enhancement in these nodes. Middle row: para-iliacal LN in the same patient retaining some signal on T1w GRE and T2*w MEDIC, while showing strong hyperintensity on T1w UTE. Bottom row: para-rectal lymph node showing strong signal loss on transverse T1w GRE and T2*w MEDIC, while showing hyperintensity on T1w UTE.

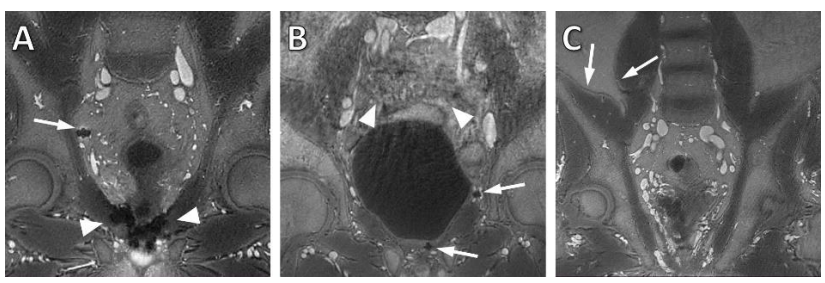

Figure 3: Examples of observed artifacts. A: Susceptibility-induced blooming around the prostate (arrowheads) and a nearby LN (arrow) due to SPIOs injected intraprostatically 3 weeks prior to USPIO infusion; B: Respiratory and bowel motion (arrowheads) and blooming due to surgical clips; C: Water-fat signal interference at interface between muscle and adipose tissue (arrows).

High temporal-resolution MRI during mild-cold exposure enables the assessment of brown adipose tissue with a low inter-image variability

A.S.D. Sardjoe Mishre[1,2], M.E. Straat[1], B.M. Martinez-Tellez[1], M.R. Boon[1], O. Dzyubachyk[3,4], A.G. Webb[2], P.C.N. Rensen[1], H.E. Kan[2]

[1]Department of Medicine, Division of Endocrinology and Einthoven Laboratory for Experimental Vascular Medicine, Leiden University Medical Center (LUMC), Leiden, The Netherlands; [2]Department of Radiology, C.J. Gorter Center for High Field MRI, LUMC, Leiden, The Netherlands; [3]Department of Radiology, Division of Image Processing (LKEB), LUMC, Leiden, The Netherlands; [4]Department of Cell and Chemical Biology, Electron Microscopy section, LUMC, Leiden, The Netherlands.

Synopsis: Brown adipose tissue (BAT) is considered to be a potential therapeutic target against cardiometabolic diseases. Activated BAT combusts intracellular fatty acids leading to a reduction in fat fraction . Both cold exposure and pharmacological stimuli can activate BAT, but the short-term dynamics of BAT activation are unknown. To assess supraclavicular BAT fat fraction dynamics during cold-exposure, we developed a 1-minute-time-resolution MRI protocol using breath-holds and co-registration to minimize motion-artefacts. We demonstrated the validity and feasibility of our image analysis method, and found an inter-image variability of less than 0.1% fat fraction.

Introduction

Brown adipose tissue (BAT) is involved in energy metabolism by combusting glucose and fatty acids to produce heat. BAT activation is a potential treatment against cardiometabolic diseases[1,2]. Cold exposure is the most established physiological stimulus to activate BAT very rapidly[3], but pharmacological alternatives have also been proposed[4]. BAT activity is usually indirectly quantified via glucose uptake using [^{18}F]fluorodeoxglucose (FDG)-PET-CT, but this modality has a poor temporal resolution due to radiation exposure[5]. MRI of the supraclavicular BAT region (scBAT) is a promising radiation-free alternative[6]. Most scBAT MRI studies have either used pre- and post-cooling assessments of the MRI-derived fat fraction (FF) or studied FF dynamics at a low temporal resolution[7-11]. This does not provide sufficient insights into the short-term dynamics of BAT activation, which may be needed for assessing the kinetics of BAT stimuli. Here, we developed an MRI protocol with a high temporal resolution for assessing scBAT FF, minimized variability due to breathing by applying non-rigid image registration, and applied these in a cold exposure study.

Methods

Ten healthy volunteers (age: 24.8±3.0 years; BMI: 21.2±2.1kg/m^2) underwent a standardized cooling procedure for BAT activation using a water-circulating blanket. After 20 minutes at thermoneutrality (32°C), the temperature was set to 18°C for one hour. Images were acquired at 3T using a 16-channel anterior and 12-channel posterior array and a 16-channel head-and-neck coil. Scans were acquired during the last 10 minutes of thermoneutrality and for 60 minutes during cooling using a 3D gradient-echo 12-point Dixon sequence: TR/TE1/ ΔTE/FA/resolution/FOV/breath-hold duration=12ms/1.12ms/ 0.87ms/3°/2.1 mm isotropic/400x×229×134 mm^3/16 s, mDIXONQuant and scanner reconstructions. The acquisition time per scan was 1.03 mins.

For analysis, we co-registered first-echo magnitude images of each dynamic to the first thermoneutral scan (reference scan) using Elastix[12] (Fig. 1). FF of the scBAT depot was obtained from ROIs, which were coarsely delineated on the reference scan and using a mutual FF thresholding approach, wherein voxels were included if their FF was above 30% in both the reference scan and in the registered dynamic (Fig. 1). Voxel-wise FF differences between the reference scan and each dynamic *i*: $\Delta FF_i\,(x,y,z) = FF_i\,(x,y,z) - FF_{TN1}\,(x,y,z)$ were calculated and averaged over the ROI. ROIs were also drawn in the trapezius muscle for reference.

The validity of the co-registration was assessed for each subject by registering the reference scan to each dynamic, and applying the inverse transform to deform the registered reference scan back to its original coordinates, and then analyzing the voxel-wise FF overlap in the scBAT area. The feasibility of the registration was determined by assessing scBAT FF dynamics and ROI sizes between registered and non-registered data. Subsequently, we compared the scBAT FF dynamics to the FF dynamics obtained in the trapezius muscle. The validity, feasibility and reference tissue analyses were evaluated by quantifying the intra-individual variability along the FF dynamics. This was done for all subjects by calculating a moving average using a [-3,3] time window along the FF dynamics, after which the mean squared error (MSE) of the residuals was calculated between the moving average and the FF data. In the feasibility analysis, we also used the moving average method to calculate the MSE for averaged scBAT FF dynamics of registered and non-registered data as a measure for the inter-individual variability.

Results

All subjects were able to adhere to the protocol. The validation analysis resulted in small FF differences over time (MSE=0.003%±0.002%; Fig. 2A). The feasibility analysis resulted in lower MSE values for registered scBAT FF dynamics compared to non-registered data (MSE: 0.09%±0.08% versus MSE:0.14%±0.12%; Fig. 2B-C). scBAT ROIs were on average larger for registered data compared to non-registered data (8259±3272 versus 7571±2378 voxels). The MSE values for the averaged scBAT FF dynamics were 0.008% and 0.02% for registered and non-registered data, respectively. scBAT FF showed a gradual decrease in response to mild-cooling, whereas no response was seen in the trapezius muscle (MSE=0.02%±0.02%; Fig. 3).

Discussion

Our data show a high registration accuracy, as evidenced by the low variability in the validation analysis. Also, the registration feasibility showed a lower variability along the FF dynamics in registered versus non-registered data. This difference is likely the result of motion-induced variation, which increases spatial mismatches between the dynamic image and the reference image, and decreases the number of co-located voxels with a FF higher than 30%. On average, registered scBAT FF dynamics showed a 2.5 lower inter-individual variability compared to non-registered FF dynamics. The absence of any dynamic FF pattern in skeletal muscle indicates that the scBAT FF response is not influenced by temporal changes that may be induced by the scanner's hardware. In comparison to reported scBAT FF changes in response to cold exposure in literature (−1.6%[7], -2.9%[9]), we found relatively small (~ -0.5%) and slowly changing FF dynamics in response to mild-cooling. This is likely caused by differences in the cooling procedure, such as cooling garments, cooling strength and duration. The temporal resolution may therefore be increased or decreased since the temporal evolution of scBAT FF dynamics may differ per stimulus.

Conclusion

We showed the feasibility of obtaining 1-minute-resolution data of scBAT using breath-holds during cooling in healthy subjects and we demonstrated the validity and feasibility of our MRI protocol.

References

1. Berbeé JFP, Boon MR, Khedoe PPSJ, et al. Brown fat activation reduces hypercholesterolaemia and protects from atherosclerosis development. *Nat Commun*. 2015;6. doi:10.1038/ncomms7356
2. Becher T, Palanisamy S, Kramer DJ, et al. Brown adipose tissue is associated with cardiometabolic health. *Nat Med*. 2021;27(1):58-65. doi:10.1038/s41591-020-1126-7
3. Reber J, Willershäuser M, Karlas A, et al. Non-invasive Measurement of Brown Fat Metabolism Based on Optoacoustic Imaging of Hemoglobin Gradients. *Cell Metab*. 2018;27(3):689-701.e4. doi:10.1016/j.cmet.2018.02.002
4. Cypess AM, Kahn CR. Brown fat as a therapy for obesity and diabetes. *Curr Opin Endocrinol Diabetes Obes*. 2010;17(2):143-149. doi:10.1097/MED.0b013e328337a81f
5. Ouellet V, Labbé SM, Blondin DP, et al. Brown adipose tissue oxidative metabolism contributes to energy expenditure during acute cold exposure in humans. *J Clin Invest*. 2012;122(2):545-552. doi:10.1172/JCI60433
6. Karampinos DC, Weidlich D, Wu M, Hu HH, Franz D. Techniques and Applications of Magnetic Resonance Imaging for Studying Brown Adipose Tissue Morphometry and Function. *Handb Exp Pharmacol*. 2019;251:299-324. doi:10.1007/164_2018_158
7. Oreskovich S, Ong F, Ahmed B, et al. Magnetic resonance imaging reveals human brown adipose tissue is rapidly activated in response to cold. *J Endocr Soc*. October 2019. doi:10.1210/js.2019-00309
8. Gashi G, Madoerin P, Maushart CI, et al. MRI characteristics of supraclavicular brown adipose tissue in relation to cold-induced thermogenesis in healthy human adults. *J Magn Reson Imaging*. 2019;50(4):1160-1168. doi:10.1002/jmri.26733
9. Stahl V, Maier F, Freitag MT, et al. In vivo assessment of cold stimulation effects on the fat fraction of brown adipose tissue using DIXON MRI. *J Magn Reson Imaging*. 2017;45(2):369-380. doi:10.1002/jmri.25364
10. Lundström E, Strand R, Johansson L, Bergsten P, Ahlström H, Kullberg J. Magnetic resonance imaging cooling-reheating protocol indicates decreased fat fraction via lipid consumption in suspected brown adipose tissue. *PLoS One*. 2015;10(4). doi:10.1371/journal.pone.0126705
11. Coolbaugh CL, Damon BM, Bush EC, Welch EB, Towse TF. Cold exposure induces dynamic, heterogeneous alterations in human brown adipose tissue lipid content. *Sci Rep*. 2019;9(1):13600. doi:10.1038/s41598-019-49936-x
12. Klein S, Staring M, Murphy K, Viergever MA, Pluim JPW. Elastix: A toolbox for intensity-based medical image registration. *IEEE Trans Med Imaging*. 2010;29(1):196-205. doi:10.1109/TMI.2009.2035616

Figure 1.

The first thermoneutral scan was used as a reference image, and all subsequent dynamic scans were co-registered to the first scan. First echo magnitude images were used for co-registration and the resulting transformation matrix was used to deform the FF map of each dynamic to match the image coordinates of the first thermoneutral scan. ROIs were only drawn on the first thermoneutral scan and voxels below 30% fat were excluded in both fixed and dynamic scans to avoid inclusion of non-fatty tissue for scBAT, whereas no thresholds were used for muscle.

Acknowledgments / Funding Information: Continue on this line

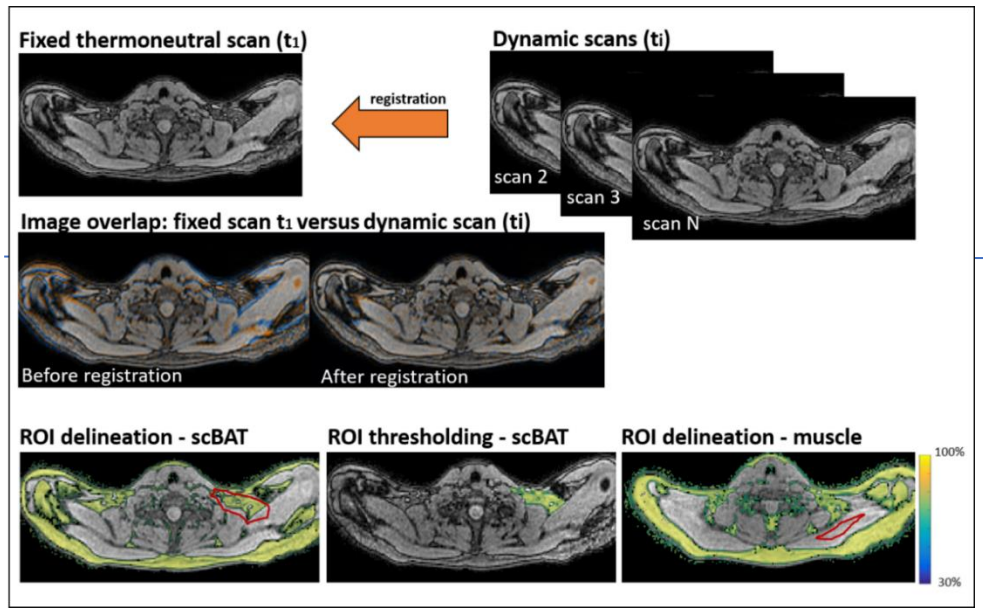

Figure 2. Fat fraction changes (%) for the registration validation (A), non-registered data (B) and registered data (C). scBAT FF changes above 1% are shown in red in (A). Image overlap between the first thermoneutral (reference) scan and the last dynamic are shown for B and C, where the reference scan and the last dynamic are shown in blue and orange. Red denotes thermoneutrality. The mean squared error and the number of voxels in the scBAT volume are reported.

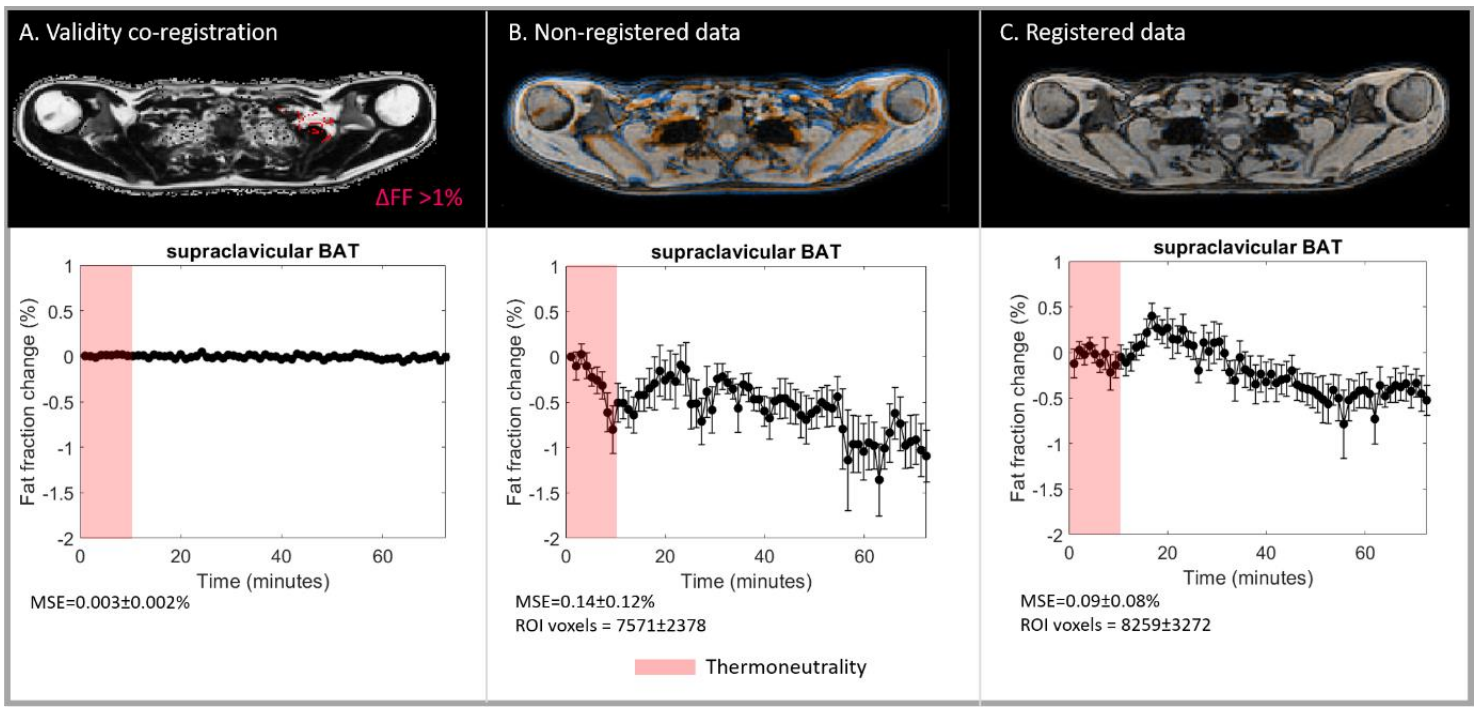

Figure 3. Fat fraction differences from registered data plotted as a function of time for the trapezius muscle. The red-shaded area indicates the thermoneutral period and the mean squared error is reported.

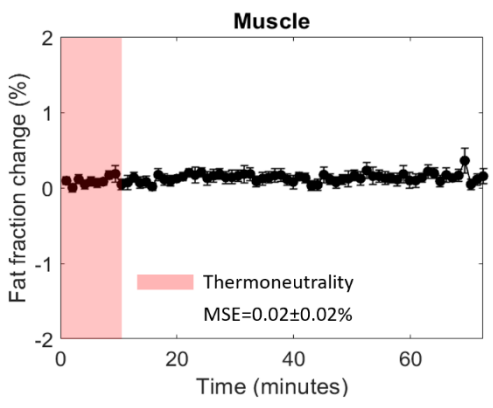

Comprehensive 3D quantitative transient response MRI

G. Kotek[1], W. van Valenberg[1], L. Nunez-Gonzalez[1], D. H. J. Poot[1], M. W. Vogel[2], J. A. Hernandez-Tamames[1]
[1]Radiology and Nuclear Medicine, Erasmus MC, Rotterdam, Netherlands, [2]GE Healthcare, Hoevelaken, Netherlands

Synopsis: Unlike multi-parametric methods as MR Fingerprinting and quantitative transient imaging we present a quantitative MRI method based on the transient response without variation of experimental parameters (FA…). Our method is based on the exact solution of the recursive equation for the magnetization along an acquisition train. Based on this analytical approach we determine the requirements for the features and parameters of a repeated acquisition block to allow simultaneous estimation of experimental (B0, B1) and intrinsic (PD, T1, T2) parameters. The feasibility of the technique on clinical scanners is demonstrated by acquiring a comprehensive set of 3D in vivo parametric maps.

Introduction

Several transient-response-based quantitative methods were proposed in recent years[1,2]. These methods rely on specific variation of acquisition parameters such as excitation flip angle and repetition time along the train of excitation pulses. With such variations, the time dependent Bloch equation, as well as its discretized version describing the signal evolution in an acquisition train, do not have a closed-form analytical solution. Hence, these methods have to resort to iterative forward modelling or dictionary matching for parameter estimation and sequence optimization. In contrast to these methods, we propose a constant propagator (defined as the cumulative effect of the acquisition block on the magnetization as a linear operator) along the echo train in order to enable an exact analytical description of the signal[3]. The explicit analytical expression of the signal evolution reveals critical conceptual elements in the experimental design: 1) enhance or suppress sensitivity to intrinsic and experimental parameters; 2) avoid potential loss of information in the signal evolution; and 3) species can be identified by their unique signal behaviour. We demonstrate this design process of the propagator, that ultimately allows a comprehensive parameter estimation in the transient phase, including experimental confounding quantities such as B0 and B1. We propose a novel, balanced free precession sequence that avoids banding artefacts. We demonstrate the method's sensitivity to intrinsic and experimental parameters with phantoms and the its applicability of the technique in the clinical settings by 3D in vivo acquisition and parameter estimation.

Methods

Theoretical foundations

We describe the evolution of the magnetisation $\boldsymbol{m}_n$ for a species characterised by intrinsic and experimental parameters with the Putzer's algorithm[4,5]. This allows an analytical and always real-valued expression for $\boldsymbol{\mu}_n = \boldsymbol{m}_n - \boldsymbol{m}_{steadystate}$ without the diagonalization of the propagator[6,7], instead using its eigenvalues and avoiding its often-complex eigenvectors[3]:

$$\boldsymbol{\mu}_n = \rho^n \cdot sin(n\varphi) \cdot \boldsymbol{n}_1 + \rho^n \cdot cos(n\varphi) \cdot \boldsymbol{n}_2 + \eta^n \cdot \boldsymbol{n}_3,$$

where the real-valued normal mode (not eigenvectors) vectors are determined by the initial state, the propagator and the eigenvalues $\rho \cdot e^{i\varphi}$, $\rho \cdot e^{i\varphi}$ and η. A generally valid expression for the signal in the quadrature complex notation follows: $s_n = a \cdot \rho^n \cdot e^{i(n\varphi+\delta)} + b \cdot \eta^n \cdot e^{i\xi}$

Propagator design for parametric mapping

The goal of the propagator design in parametric mapping is to produce a signal evolution that allows parameter estimation. There are three main aspects to consider: 1. The effect of B_0 inhomogeneity is suppressed; 2. The signal evolution carries full information; 3. Species can be identified by their unique signal evolution. Our choice of for a propagator that satisfies these requirements consists of four excitations with alternating phases 0, π/2, π/2, 0 with flip angles 30, 175, 30, 175 degrees. Requirement 2. is provided by the different phases in the excitation scheme. Requirements 1. and 3. are explained and demonstrated in Kotek et al.[3].

Implementation on a clinical scanner, acquisition and parameter estimation

The acquisition was done in-vivo and on a phantom (Caliber MRI System Phantom Lite) by 3D stack of spirals balanced GRE: 22 slices, 6mm thickness, stack of spirals: 32 arms, 1024 readout points, FoV 25 and 30 for in-vivo and phantom acquisition. Image reconstruction was done with a non-uniform FFT with density compensation[8], and parameter estimation through the least-squares fitting of the single-species signal model.

Results

The in vivo parametric maps produced with our design are depicted in Figure 1. The T_2 values are in good agreement of literature references, while the T_1 maps show systematic underestimation of T_1. In contrast with the in vivo results, results from phantoms show good agreement between our derived T_1 and T_2 and reference values as shown in Figure 2 and 3.

Discussion

We approached transient state quantitative imaging from a simple algebraic perspective. We challenged the necessity of flip angle or repetition time variation. We investigated if in the case of a constant propagator the signal evolution contains sufficient and exploitable information about intrinsic and experimental parameters. This is the only obvious case when there is a closed-form analytical solution to the Bloch equation. We identified conceptual requirements for the propagator through simple algebraic considerations. The design concept resulted in the following: 1. a novel balanced free precession technique that produces banding artefact free transient state and steady state images; 2. A comprehensive set of parametric maps: T_1, T_2, PD, B_0, B_1. Here we focus mainly on the conceptual details of our method and its direct implementation. For applicability in a clinical workflow further steps are necessary towards acceleration of the acquisition. Furthermore, the underestimation of T_1 from in vivo data requires further investigation to find confounding biologically relevant processes. The technique can be developed further where such processes are enhanced or suppressed by the design of the propagator.

Conclusion

The analytical description provided insight to a proper experimental design that otherwise was not obvious or available when a simulation-based optimization is performed. Among transient state quantitative imaging methods, conceptually and also technically the simplest case is with constant propagator (the one of two cases with analytical solution). Here we demonstrated with an implementation in clinical settings, that no variation of the experimental parameters is necessary in multi-parametric transient response imaging.

References

1. Ma D, Gulani V, Seiberlich N, et al. Magnetic resonance fingerprinting. Nature. 2013;495(7440):187-192.
2. Gómez, P. A., Molina-Romero, M., Buonincontri, G., Menzel, M. I. & Menze, B. H. Designing contrasts for rapid, simultaneous parameter quantification and flow visualization with quantitative transient-state imaging. Sci. Rep. 9(1), 8468 (2019)
3. Kotek, G., Nunez-Gonzalez, L., Vogel, M. W., Krestin, G. P., Poot, D., & Hernandez-Tamames, J. A. (2021). From signal-based to comprehensive magnetic resonance imaging. Scientific reports, 11(1), 17216.
4. Elaydi,S.N. An Introduction To Difference Equation (Springer,2020)
5. Putzer, E. J. Avoiding the Jordan canonical form in the discussion of linear systems with constant coefficients. Am. Math. Mon. 73(1), 2–7 (1966).
6. Hargreaves, B. A., Vasanawala, S. S., Pauly, J. M., & Nishimura, D. G. (2001). Characterization and reduction of the transient response in steady-state MR imaging. Magnetic resonance in medicine, 46(1), 149–158.
7. Ganter C. (2004). Off-resonance effects in the transient response of SSFP sequences. Magnetic resonance in medicine, 52(2), 368–375.
8. Pruessmann, K. P., Weiger, M., Börnert, P., & Boesiger, P. (2001). Advances in sensitivity encoding with arbitrary k-space trajectories. Magnetic resonance in medicine, 46(4), 638–651.

Acknowledgments / Funding Information: This work was supported partially by GE Healthcare (Work statements: B-GEHC-8-2018 and B-GEHC-10_SETI II).

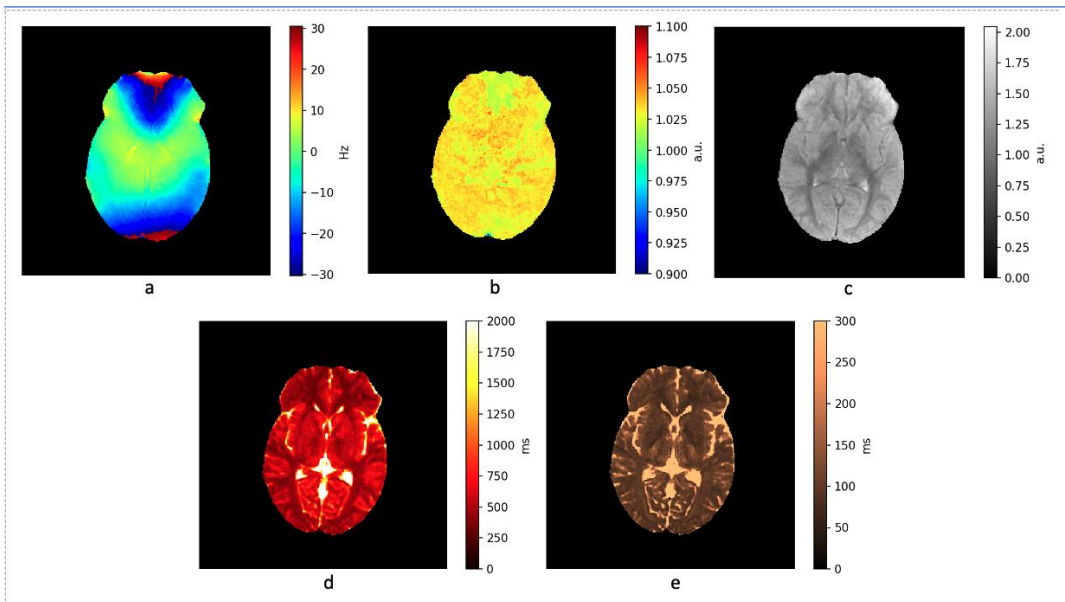

Figure 1. In vivo parametric maps from volunteer data. a: B_0 , b: B_1, c: PD, d: T_1, e: T_2. Acquisition parameters: 24 channel head coil, 30x-175y-30y-175x scheme, T_R=17ms, 6.3mm slice thickness, 22 slices, FoV = 25 cm, bw = 125, acquisition train length 60, 32 spiral arms, 1024 readout points per arm. Despite the fully balanced free precession acquisition sequence, no banding artefacts are present due to the composite operator consisting of excitations along various axes. The $T_1$and T_2 maps are free of B_0 or B_1 inaccuracies.

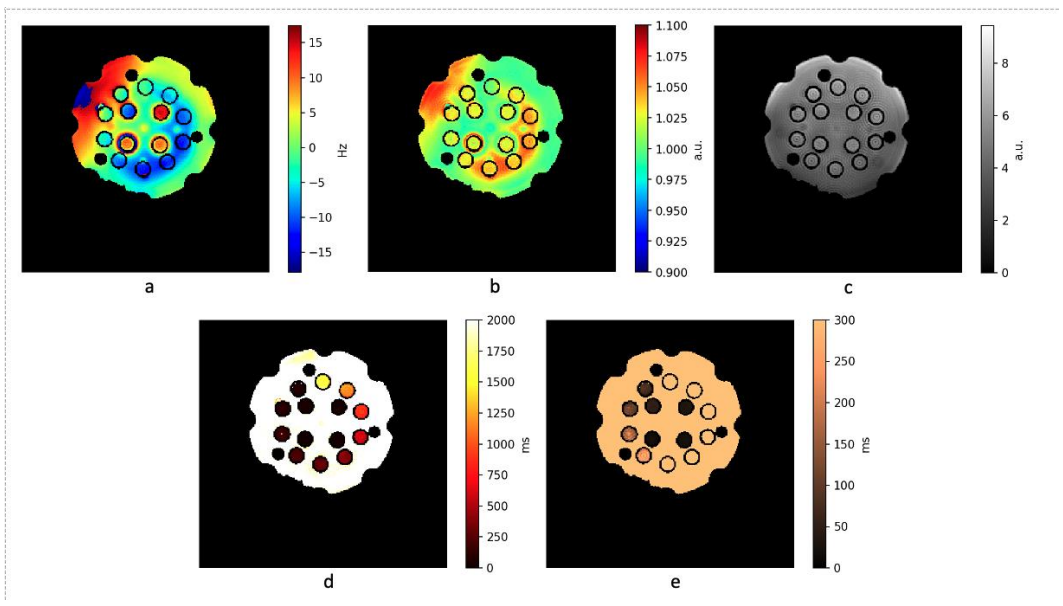

Figure 2. Parametric maps with the Calibre System Phantom Lite - T_1 contrast layer, a: B_0 , b: B_1, c: PD, d: T_1, e: T_2. Acquisition parameters are the same as in the in vivo acquisition except the FoV = 30 cm. The B_1 map shows a similar pattern to the B_0 map, emphasized only by the fine scale of the colormap. The ringing pattern on the PD map is due to the limited resolution of the acquisition. Despite the usual strong B_0 inhomogeneity in the frontal area, it shows only a minor effect on PD, T_1 and T_2 maps. Despite showing good contrast in vivo, the T_1 values are systematically underestimated.

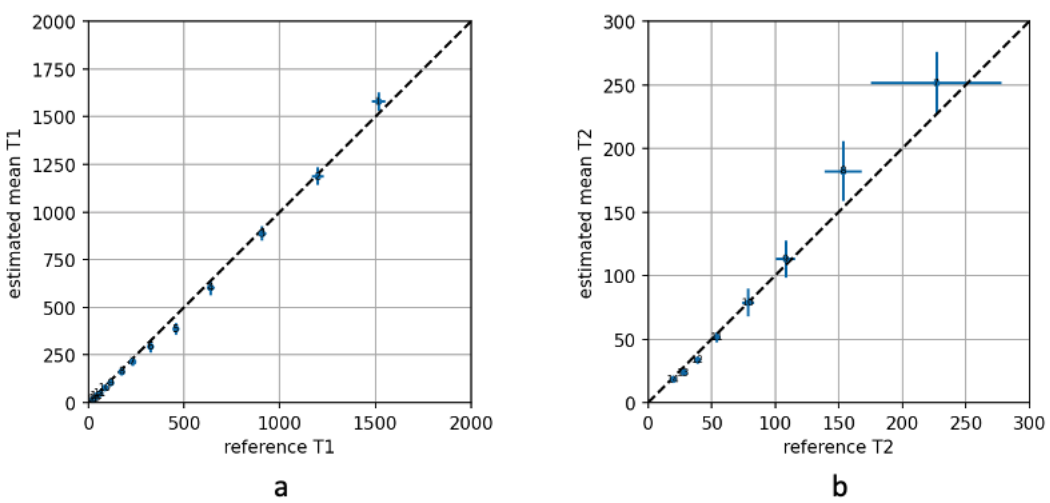

Figure 3. The proposed method's T_1 and T_2 values of the Calibre System Phantom Lite are compared to the reference values. The reference values were determined by standard inversion recovery and echo time variation SE methods. The numbers indicate the phantom's samples. Both T_1 and T_2 values are in good agreement with the reference values. Unlike in the in vivo results, T_1 is not underestimated.

FEASIBILITY OF COMPRESSED SENSING ACCELERATED RISTRETTO MAGNETIC RESONANCE ELASTOGRAPHY IN THE PANCREAS

A. van Schelt[1], N.P.M. Wassenaar[1], J.H. Runge[1], M.A. Troelstra[1,3], J.L. Nelissen[1], C. Guenthner[2], R. Sinkus[3,4], J. Stoker[1], A.J. Nederveen[1], E.M. Schrauben[1]

[1] Department of Radiology and Nuclear Medicine, Amsterdam University Medical Centers, Amsterdam, The Netherlands;
[2] Department of Biomed, ETH Zurich, Zurich, Switzerland;
[3] Department of Imaging Sciences and Biomedical Engineering, King's Colleg, London, United Kingdom; [4] Inserm U1148, LVTS, Univeristy Paris Diderot, Paris, France

Synopsis: Magnetic resonance elastography (MRE) allows for non-invasive determination of pancreatic visco-elastic properties in four consecutive breath-holds. The aim of this study was to develop and test a single breath-hold MRE acquisition accelerated using prospective undersampling and compressed sensing (CS) reconstruction. Testing was done on a retrospective undersampled phantom dataset and *in-vivo*. These showed that CS accelerated (R< 8.7), single breath-hold MRE is feasible without hampering visco-elastic reconstruction in tissues with low shear stiffness (|G*|<1.6kPa). Further research is necessary to guarantee accuracy of the measured shear stiffness, notably for high stiffness tissues such as tumors, and at higher acceleration factors.

Introduction

Magnetic resonance elastography (MRE) allows for non-invasive determination of tissue visco-elastic properties, which differ for healthy and diseased tissues. Longitudinal changes in tissue stiffness in the course of pancreatitis, endocrine dysfunction or pancreatic cancer could reveal new insights in the disease pathophysiology[1]. However, assessing the pancreas with MRE remains challenging due to its small size, elongated shape, and central abdominal location. The quantitative accuracy of MRE in small structures depends on the local stability of the tissue being imaged over all wave-offsets and motion-encoding directions. However, current pancreatic MRE requires four consecutive (16s) breath-holds[2]. These may introduce errors in pancreas location, limit spatial and temporal resolution, and can be particularly uncomfortable for patients.

The aim of this study was to develop and test a single breath-hold MRE acquisition accelerated using prospective undersampling and compressed sensing (CS) reconstruction in the pancreas.

Methods

We modified the 3D Ristretto GRE-MRE acquisition to accommodate for compressed sensing acceleration[3,4]. Feasibility of CS-accelerated MRE was first established by retrospective undersampling (factors:R=0-15) and reconstruction of a 3D MRE dataset of a CIRS phantom with inclusions (CIRS,Inc.,Norfolk,USA). Data was acquired by Guenthner et al. using 36Hz vibration frequency and eight wave-phase offsets in 14 slices (FOV:192x156x42mm)[3]. Scan parameters are reported in Figure 1a.

In-vivo testing was performed on six healthy volunteers (female=6, mean age=27±3 years). A gravitational transducer [5] with a 3D-printed curved polyactic-plate was strapped to the right flank at the level of the pancreas head (Figure.1c). High-resolution T2-weighted images were made for anatomical reference. MRE acquisitions were performed using 40Hz vibration frequency, nine slices (FOV:336x192x27mm) and five wave-phase offsets. Six consecutive pancreatic MRE scans were performed: (I)standard Multi-Slice (MS), (II)3D SENSE-accelerated four breath-hold acquisition, (III)3D CS-accelerated four breath-hold acquisition and (IV-VI)three 3D CS-accelerated single breath-hold acquisitions. Scan parameters are reported in Figure 1a.

Incoherent undersampling was achieved using variable-density Poisson disks with half-scan in both k_y (67%) and k_z (89%) directions(Figure.1b). Five different undersampling patterns with different undersampling factors (R=3.6,8.7,9.8,13.4) were used for each wave-phase offset and were repeated for each encoding direction. For CS acquisitions, reconstruction was performed offline using ReconFrame (Gyrotools,Zurich,Switzerland) in MATLAB (MathWorks,Natick,MA,USA) together with the Berkeley Acquisition Advanced Reconstruction Toolbox (BART) using total variation sparsifying transform in the wave-offset dimension (λ=0.001, 20 iterations)[6,7,8].

Phantom post-processing was performed using MATLAB. The shear stiffness of each inclusion and background was calculated and compared to the non-accelerated stiffness. *In-vivo* MRE post-processing was performed using dedicated software(ROOT,KIR). Phase data are unwrapped and smoothed before 3D transformation using a 3D Blackman-Harris window. The shear wave displacement was calculated per voxel and visco-elastic parameters were extracted with a finite element method. Shear wave speed (SWS) and shear stiffness (|G*|) was calculated by manually drawn region-of-interest over the pancreatic head and liver on MRE magnitude images guided by anatomical high-resolution T2-weighted images.

Mean SWS, |G*| and the nonlinearity (ratio of the second harmonic over the first harmonic) in both the pancreas head and liver were analyzed, with 3D-SENSE-MRE allocated as index test for CS. Statistical analysis was done using repeated measures ANOVA and pairwise comparison with a Bonferroni correction(p<.05) for SWS and nonlinearity parameters of the pancreas and liver.

Results

Mean |G*|and example elastograms of the phantom data are shown in Figure 2. *In-vivo* examples of SWS-maps in the pancreas are shown in Figure 3. The mean SWS, |G*| and nonlinearity for the pancreas and liver are given in Figure 4. Mean SWS and nonlinearity of each method for the pancreas and liver are shown in Figure 5. Repeated measures ANOVA showed no significant differences in SWS overall(f=5/1,p=0.07). Exploratory pairwise comparison showed significant difference between mean SWS of MS and CS13.4(p=.03) in the pancreas and nonlinearity in the liver between CS3.6 and CS8.7(p=.02).

Discussion

Phantom retrospective undersampling showed accurate results for low stiffness inclusions and background (|G*|<1.6kPa) up to an acceleration factor of 15 (Figure.2). However, for the two stiff inclusion the apparent stiffness deviated from non-accelerated R0 values, with underestimation increasing for higher acceleration factors. The relative low mechanical frequency (and hence long wavelength) could explain this disparity[9].

CS-accelerated MRE gave comparable stiffness values in-vivo up to an acceleration factor of 8.7. The nonlinearity showed no significant difference between all scans in the pancreas, indicating that higher acceleration does not significantly hamper visco-elastic reconstruction. However, accuracy of MRE inversion is only guaranteed for a nonlinearity below 50%, therefore CS acceleration of 13.4 (nonlinearity=50.5%) could be considered borderline acceptable.

Liver nonlinearity shows a significant difference between CS3.6 and CS8.7, however, this is not seen for higher acceleration. This could be caused by the large spread observed at CS13.4. A large spread in quality parameters, such as nonlinearity, could indicate loss in accuracy and thereby reproducibility. Additionally, while acceleration of CS=8.7 displayed no difference in SWS and nonlinearity compared to MS, the breath-hold duration (20s) may be too long for some patients.

Conclusion

Phantom and *in-vivo* testing shows that compressed sensing accelerated, single breath-hold MRE is feasible without hampering visco-elastic reconstruction in tissues with low shear stiffness (|G*|<1.6kPa). Further research is necessary to guarantee accuracy of the measured shear stiffness, notably for high stiffness tissues such as tumors, and at higher acceleration factors.

References

[1] MacCurtain BM, Quirke NP, Thorpe SD, Gallagher TK. Pancreatic Ductal Adenocarcinoma: Relating Biomechanics and Prognosis. JOURNAL OF CLINICAL MEDICINE. 2021; 10(12):2711. https://doi.org/10.3390/jcm10122711

[2] van Schelt A, Wassenaar N, Schrauben E, Troelstra M, Nelissen J, Sinkus R, Stoker J, Nederveen A, Runge J. (2021) Optimization of GRE-MRE in the pancreas. ISMRM Abstract number 1021

[3] Guenthner C, Sethi S, Troelstra M, Dokumaci AS, Sinkus R, Kozerke S. Ristretto MRE: A generalized multi-shot GRE-MRE sequence. NMR Biomed. 2019;32(5). doi:10.1002/nbm.4049

[4] Christian Guenthner, Sweta Sethi, Ayse Sila Dokumaci, Ralph Sinkus, and Sebastian Kozerke (2018) ISMRM Abstract number 5584

[5] Runge, J. H., Hoelzl, S. H., Sudakova, J., Dokumaci, A. S., Nelissen, J. L., Guenthner, C., ... Sinkus, R. (2019). A novel magnetic resonance elastography transducer concept based on a rotational eccentric mass: Preliminary experiences with the gravitational transducer. Physics in Medicine and Biology, 64(4):045007. doi: 10.1088/1361-6560/aaf9f8.

Acknowledgments / Funding Information:

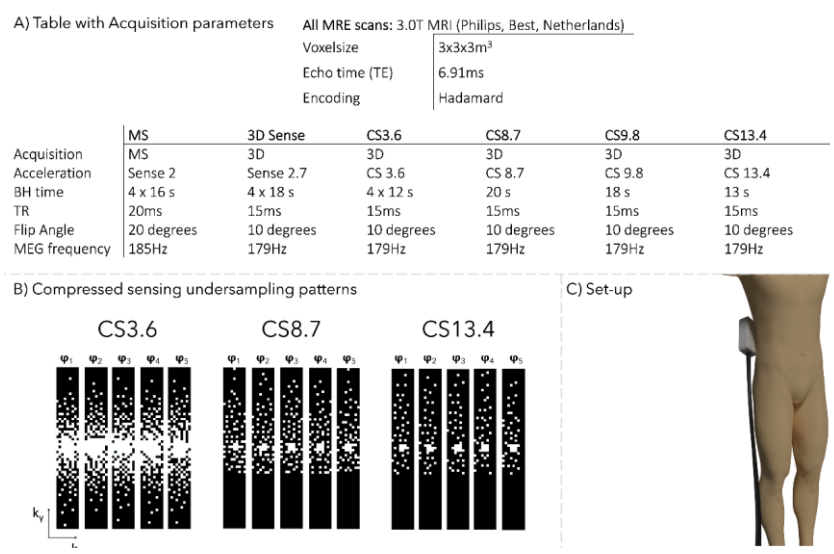

Figure 1 A) Imaging parameters across undersampled datasets for *in-vivo* measurements. Top table shows imaging parameters for both the phantom acquisition and *in*-vivo acquisition. B) Example Poisson disk prospective undersampling patterns for compressed sensing accelerated MRE scans, shown for all individual wave-phase offsets. Undersampling through halfscan (middle: ky=67%; right: k_y=67% and k_z=89%) is also used. C) MRE transducer placement.

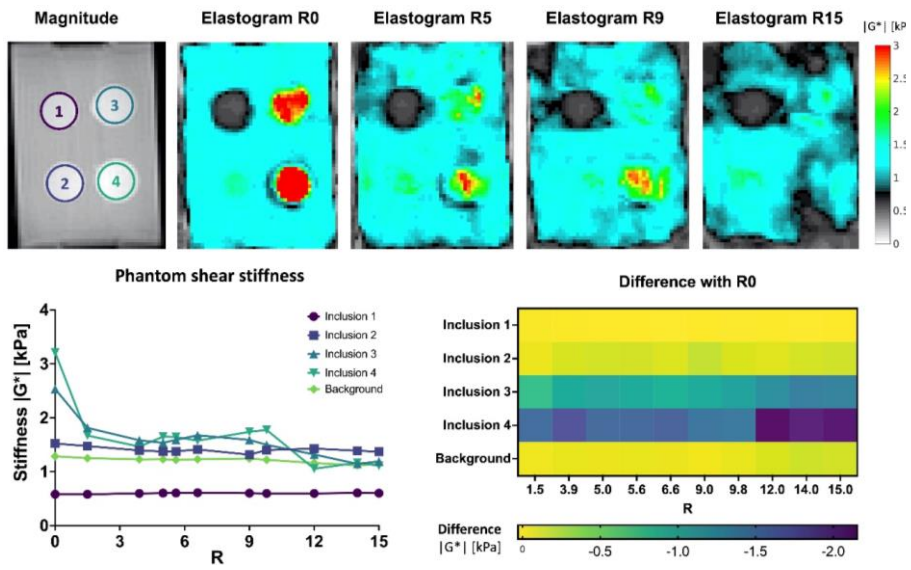

Figure 2 top: Retrospective undersampling phantom magnitude data with four inclusions and corresponding elastograms for undersampling patterns. Bottom left Reconstructed shear stiffness as a function of undersampling factor. Bottom right: Difference between measured shear stiffness and the known shear stiffness of the inclusion.

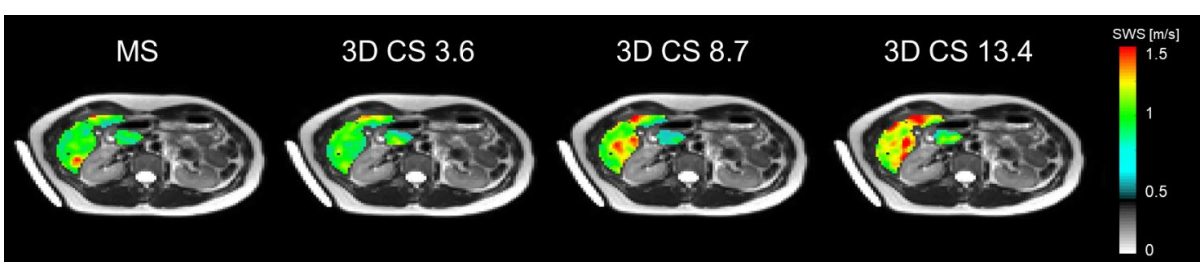

Figure 3 Shear wave speed map (SWS) of all methods of the pancreas and liver overlayed on high resolution T2-weighted images for anatomical reference.

		MS	3D Sense	CS3.6	CS8.7	CS9.8	CS13.4	
Pancreas	Shear Wave Speed	0.97±0.06	1.05±0.06	1.05±0.11	1.09±0.13	1.10±0.06	1.15±0.13	[m/s]
	|G*|	0.88±0.11	0.98±0.12	1.00±0.19	1.09±0.26	1.11±0.15	1.18±0.26	[kPa]
	Nonlinearity	54.8±8.6	36.5±13.2	41.9±10.6	42.0±5.0	43.7±13.5	50.5±15.0	[%]
Liver	Shear Wave Speed	1.11±0.11	1.23±0.14	1.19±0.08	1.16±0.08	1.20±0.07	1.21±0.03	[m/s]
	|G*|	1.30±0.17	1.30±0.16	1.33±0.17	1.36±0.11	1.37±0.15	1.38±0.06	[kPa]
	Nonlinearity	30.6±6.2	28.7±6.8	25.6±7.3	31.2±7.8	32.9±7.8	36.4±11.5	[%]

Figure 4 Table showing the mean shear wave speed (SWS), shear stiffness (|G*|) and nonlinearity for the pancreas and liver. All methods are analyzed and reported.

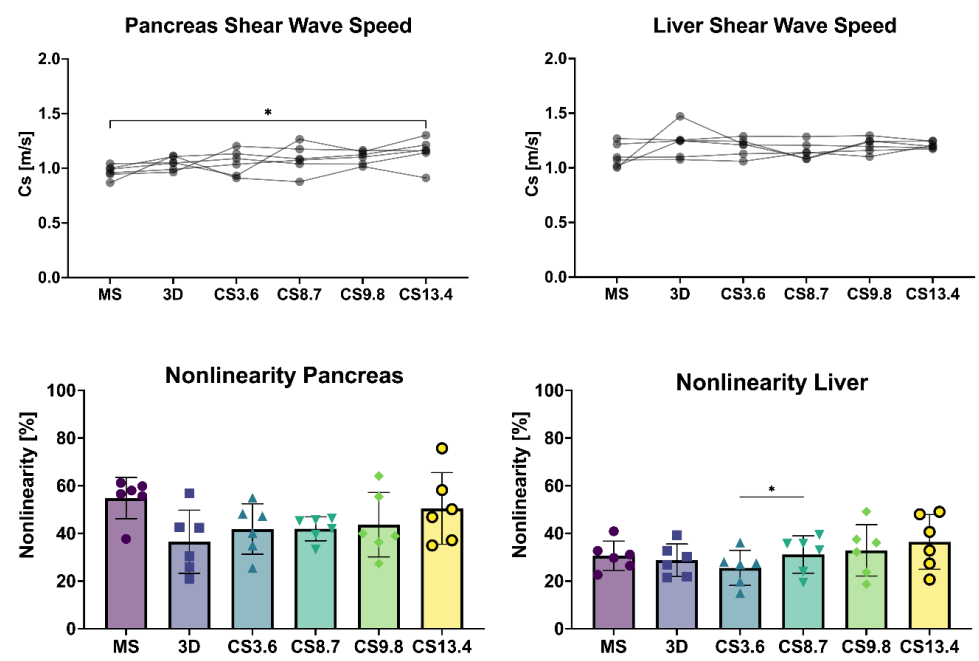

Figure 5 Mean shear wave speed (top) of the pancreas and liver with the corresponding mean nonlinearity (bottom). There is a significant difference between the pancreatic SWS of MS and CS13.4 and the hepatic nonlinearity of CS3.6 and CS8.7.

Impact of Bowel-preparation methods on pancreatic Magnetic Resonance Elastography

E.M. Schrauben[1], A. van Schelt[1], N.P.M. Wassenaar[1], J.L. Nelissen[1], J. Guo[2], I. Sack[2], J. Stoker[1], A.J. Nederveen[1], J.H. Runge[1]
[1] Department of Radiology and Nuclear Medicine, Amsterdam University Medical Centers, Amsterdam, The Netherlands;
[2] Department of Radiology, Charité – Universitätsmedizin Berlin, Berlin, Germany

Synopsis

Pancreas magnetic resonance elastography (MRE) allows non-invasive estimation of tissue stiffness for multiple pathophysiological diseases. MRE reproducibility and the effect of bowel-preparation (butylscopolaminebromide and drinking water) for increased MRE data quality were assessed for the pancreas. Shear wave speed and MRE quality were determined for the pancreas, liver and kidneys. Intrasession and intersession reproducibility showed a coefficient-of-variation of 6.59% and 13.10%. Repeated measures ANOVA showed no significant difference in SWS of all organs ($f=3/11, p>0.05$). Bowel-preparation methods for pancreatic MRE do not increase MRE quality. Drinking water increases the MRE quality for kidneys and liver whilst not altering the measured SWS.

Introduction

Magnetic resonance elastography (MRE) in the pancreas has the potential to elucidate multiple pancreatic pathologies[1], such as pancreatic adenocarcinoma. To characterize tumor microenvironment and estimate stromal disposition in the pancreas a high quality and reproducible MRE is imperative. However, its central abdominal location presents two potential issues as bowel movement may interfere with the shear wave resulting in low quality MRE data while the presence of gas in the gastrointestinal tract surrounding the pancreas inhibits shear wave propagation.

To address these challenges, we hypothesize the effects of two MRE patient preparation methods: 1) drinking 0.5L of water decreases the amount of air in the stomach and increases wave penetration, and 2) using butylscopolaminebromide (Buscopan:20mg/ml,Eureco-PharmaB.V) increases MRE quality through inhibition of smooth-muscle contraction. The aim of this study was to assess test-retest of reproducibility of non-prepared pancreatic MRE and to see if patient preparation improves MRE quality.

Methods

MRE reproducibility of the pancreas was studied in a group of 10 healthy volunteers (♀=6,mean age=26±3years). Both intrasession and intersession reproducibility were investigated (figure.1a). Different subject preparations were evaluated in 15 healthy volunteers (♀=7,mean age=41±16years), following the preparation steps as indicated in Figure 1b; No preparation (TOMO1), Buscopan (TOMO2), water (TOMO3), water and Buscopan (TOMO4). Buscopan was injected via IV to temporarily (~4min) decrease bowel movement.

All scanning was performed at 3.0T (Ingenia,Philips,Best,Netherlands) in combination with body transmit, anterior, and posterior receive coils. Volunteers were positioned prone, head first. Four compressed-air driven MRE-transducers were placed on the lower thoracic cage, two anterior and two posterior (figure.1d)[2]. Elastography images were acquired with a multi-frequency free-breathing SE-EPI sequence at four frequencies (MRE_{freq}=30,40,50,60Hz)[2]. Sequence parameters were: nslices=29, voxelsize=2.7x2.7x5mm , SENSE=2.5, TE/TR=55/2400ms, number of MRE-offsets=8, MEG_{dir}=3, and acquisition-time≈4 min. All subjects fasted four hours prior to scanning.

Post-processing was accomplished using the *k*MDEV inversion algorithm resulting in shear-wave-speed (SWS) maps of the abdomen[3]. Volumes-of-interest were manually drawn on the mean magnitude images to assess the mean pancreatic SWS, along with the kidneys and liver to assess influence on other organs. Strain-SNR and attenuation of the shear wave were evaluated as quality parameters[4].

The reproducibility and repeatability of TOMO1 was assessed by Bland-Altman plots. Repeated measures ANOVA and pairwise comparison ($p<.05$). were used to determine intra-subject variability for all parameters for the preparation methods (SPSS,Statistics,Version26,IBM,USA). The differences in pancreatic SWS throughout preparation methods were compared to the within- and between-session reproducibility.

Results

Intrasession and intersession reproducibility are shown using Bland-Altman plots in Figure 2, with an mean SWS of 1.10±0.10m/s overall and coefficient-of-variation: $CV_{intrasession}$=6.59% and $CV_{intersession}$=13.10%. Figure 3 shows magnitude images and corresponding elastograms for a single volunteer over all preparation scans. Repeated measures ANOVA showed no significant difference for SWS of all organs ($f=3/11, p>.05$). However, exploratory pairwise comparison for the pancreas showed significant difference between TOMO1 and TOMO2 ($p=.005$). Mean SWS of the pancreas were 1.13±0.26, 1.19±0.28, 1.15±0.27 and 1.18±0.27m/s for TOMO1,2,3 and 4, respectively (figure.4). Strain-SNR and attenuation showed no significant differences between different scans for the pancreas (figure.5). However, there is a difference between before and after drinking water in the kidneys and liver, with the exception between TOMO2 and TOMO4 in the liver. There was no significant difference in attenuation of the shear wave for all scans.

Discussion

Mean SWS in the pancreas were in line with previously published literature[2]. Pairwise comparison showed that there is a significant difference between the SWS in the pancreas of TOMO1 and TOMO2. Buscopan injection increases the mean SWS of the pancreas compared to non-prepared-MRE. However, this difference was not observed between other preparation scans or in the kidneys and liver. The pancreas is surrounded by the hepatopancreatic ampulla, which is a smooth-muscle sphincter controlling inflow and inhibiting reflux of duodenal substances into the ampulla. Buscopan could have an influence on the ductal pressure and thereby apparent SWS, because it inhibits spontaneous smooth-muscle activity and thereby the hepatopancreatic ampulla. Nevertheless, differences observed between the non-prepared-MRE and Buscopan SWS is within the limits of the repeatability, indicating that this effect is negligible.

Quality parameters showed no significant difference in the pancreas, suggesting that there is no increased wave penetration when drinking 0.5L of water or decrease of shear-wave interference using Buscopan. However, there is an observed difference in the strain-SNR in the kidney and liver. For the kidneys there seems a difference between before and after drinking water, with an increase in strain-SNR after drinking water. In the liver this is also observed, except between TOMO2 and TOMO4. Previous work showed similar results for the mean SWS in the pancreas (1.20±0.12m/s) and no change in SWS of the pancreas, liver and kidney at different hydration states (an hour after drinking water)[2].

Conclusion

Bowel-preparation methods for pancreatic MRE does not increase MRE quality. Repeated measures ANOVA showed no significant difference in SWS for all organs($f=3/11, p>0.05$). Exploratory pairwise comparison for the pancreas showed significant difference between TOMO1 and TOMO2($p=.005$). This could be due to Buscopan having an effect on the hepatopancreatic ampulla. However, this effect is within the limits of the repeatability of the non-prepared-MRE and therefore clinically irrelevant. Drinking water increases the MRE quality for kidneys and liver whilst not altering the measured SWS.

References

[1] MacCurtain BM, Quirke NP, Thorpe SD, Gallagher TK. Pancreatic Ductal Adenocarcinoma: Relating Biomechanics and Prognosis. Journal of Clinical Medicine. 2021; 10(12):2711. https://doi.org/10.3390/jcm10122711

[2] 1. Dittmann F, Tzschätzsch H, Hirsch S, et al. Tomoelastography of the abdomen: Tissue mechanical properties of the liver, spleen, kidney, and pancreas from single MR elastography scans at different hydration states. Magn Reson Med. 2017;78(3):976-983. doi:10.1002/mrm.26484

[3] H. Tzschatzsch, J. Guo, F. Dittmann, S. Hirsch, E. Barnhill, K. Johrens, J. Braun, I. Sack, Tomoelastography by multifrequency wave number recovery from time-harmonic propagating shear waves, Medical Image Analysis 30 (2016) 1-10.

[4] Bertalan, G, Guo, J, Tzschätzsch, H, et al. Fast tomoelastography of the mouse brain by multifrequency single-shot MR elastography. Magn Reson Med. 2019; 81: 2676– 2687. https://doi.org/10.1002/mrm.27586

Acknowledgments / Funding Information: Continue on this line

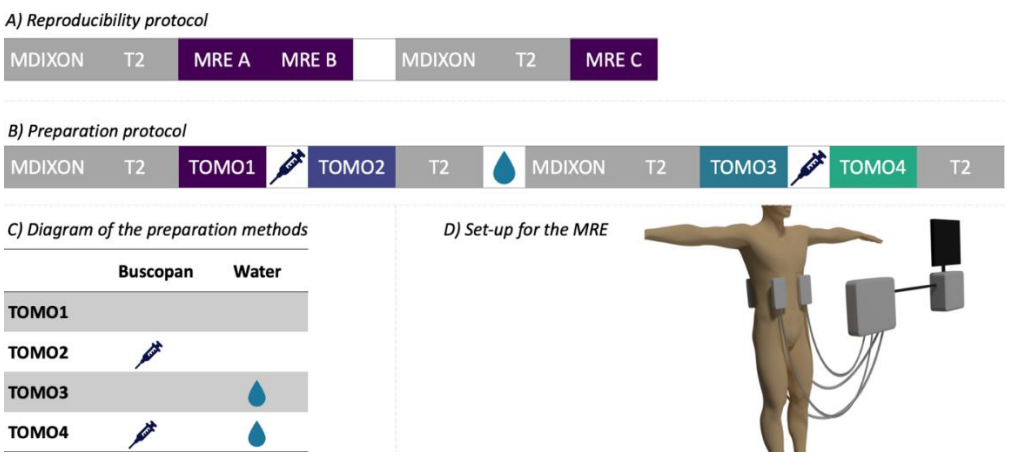

Figure 1 A) To assess intrasession and intersession reproducibility the MRE scan is completed thrice, where the volunteer is taken out of the scanner after the second MRE scan. High-resolution T2 scans are done for anatomical reference. B and C) During the preparation study an MRE scan is first performed without any additional preparations after which Buscopan is injected through an IV with the volunteer stationary on the table. In between the volunteer is asked to drink ½ a liter of water and the same protocol is followed as in the first half of the scan session. D) MRE set-up

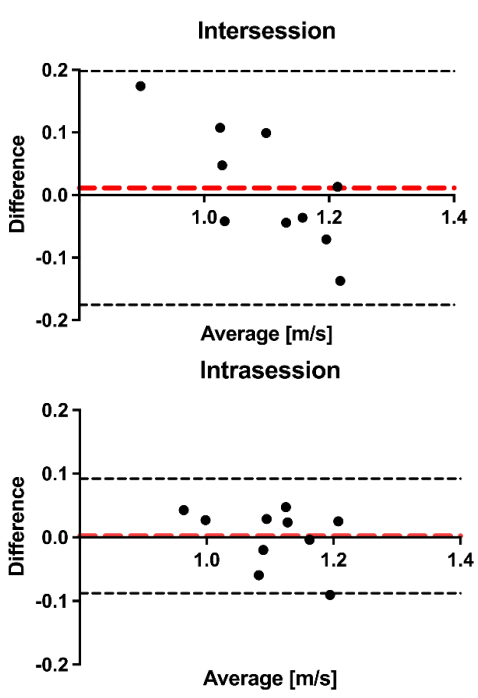

Figure 2 Bland-Altman analysis of the mean shear wave speed of the pancreas within- and between session reproducibility. 95% Limits of agreement were [-0.088 0.092], [-0.18 0.20] and for intrasession and intersession reproducibility respectively. Coefficients of variation were $CV_{intrasession}$=6.59% and $CV_{intersession}$=13.10%.

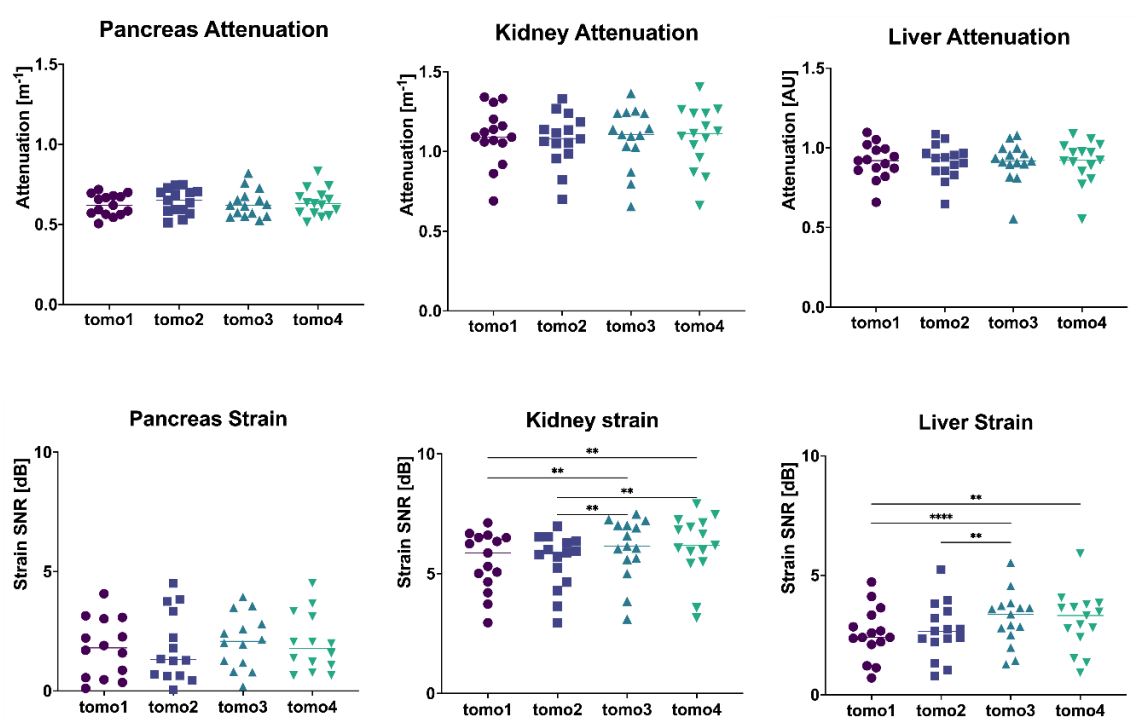

Figure 5 Mean attenuation (top) and strain-SNR (bottom) in the pancreas, kidney, and liver. There is no significant difference in attenuation in all three organs between all preparation MRE scans. There is no significant difference between the strain-SNR in the pancreas. However, there is a difference between before and after drinking water in the kidneys and liver (except between TOMO2 and 4 in the liver). (**p<.01,***p<0.005).

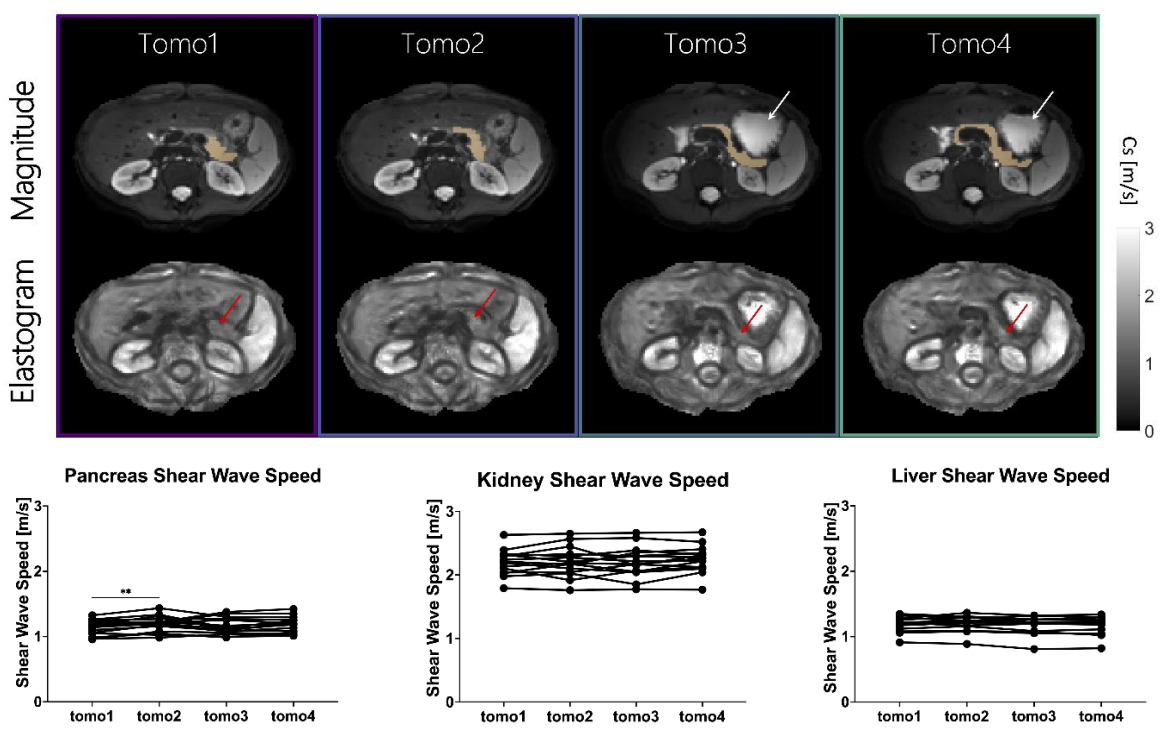

Figure 3 Anatomical magnitude images and corresponding elastograms of a representative volunteer for all preparation methods. The manually drawn volumes-of-interest of the pancreas are overlayed on the magnitude images. The white arrows show the filled stomach after drinking water. The red arrows represent the location of the pancreas on the elastogram.

Figure 4 Shear wave speed for each subject and Bowel-preparation method across abdominal organs. Significant differences were only observed in the pancreas between the nonprepared-MRE and the use of Buscopan (TOMO1 and TOMO2 respectively) (p=.005).

Single Breath-hold Simultaneous T_2 and T_{RAFF2} Mapping for Approximate Spin-lock Dispersion Mapping in the Myocardium at 3T

J. Tourais[1], Ö B. Demirel[2,3], Q. Tao[1], I. Pierce[4], G. Thornton[4], T. Treibel[4], S. Weingärtner[1], M. Akcakaya[2,3]

[1]Department of Imaging Physics, TU Delft, Delft, Netherlands; [2]Department for Electrical and Computer Engineering, Minneapolis, MN, USA; [3]Center for Magnetic Resonance Research, University of Minnesota, Minneapolis, MN, USA; [4]Barts Heart Centre, Barts Health NHS Trust, London, United Kingdom;

Synopsis: Spin-lock (SL) dispersion is a promising biomarker for the assessment of myocardial infarction. However, at 3T, the required range of T1ρ maps acquired at different amplitudes suffers from specific absorption rate (SAR) limitations and off-resonance artifacts. Relaxation Along a Fictitious Field (RAFF) is an alternative to SL preparations with lower SAR requirements while still sampling relaxation in the rotating frame. Thus, a single breath-hold simultaneous T_{RAFF2} and T_2 mapping sequence is proposed for SL dispersion mapping at 3T. High visual quality maps and accurate T_2, T_{RAFF2}, and SL dispersion values are achieved in phantoms and in vivo.

Introduction: Spin-lock (SL) dispersion has recently been proposed as a new imaging biomarker for the detection of myocardial infarction[1]. SL dispersion is usually obtained by acquiring a range of T1ρ maps at different amplitudes (frequencies). However, at 3T, specific absorption rate (SAR) limits the use of high-frequency SL pulses, and long SL preparations suffer from strong off-resonance induced artifacts. Adiabatic T1ρ may be used to avoid off-resonance effects, but its use in dispersion mapping is hampered as variable effective field strengths and sweep durations complicate the relation to a well-defined SL frequency. Relaxation Along a Fictitious Field (RAFF) is an alternative to SL pulses with lower SAR requirements[2]. RAFF operates in a sub-adiabatic regime with constant effective field strength and an identical, constant fictitious field strength leading to uniform sweeps. In previous studies, RAFF has been shown to preserve excellent sensitivity to acute myocardial infarction and chronic scar[3], but its use for dispersion mapping remains unstudied. In this work, we sought to provide a method for the assessment of myocardial SL dispersion at 3T using RAFF in a single breath-hold (BH). The proposed technique is evaluated in phantom measurements and initial in vivo images of a healthy subject.

Methods: In the proposed simultaneous T_{RAFF2} and T_2 mapping sequence, 5 balanced SSFP images with different magnetization preparations were acquired during a single 16s BH (Fig. 1). A first image acquired with no preparation is followed by images prepared with 2 RAFF2 preparation blocks[2] (T_{RAFF2}^P with different duration) and 1 T_2 preparation (T_2^P) duration, each preceded by a 4s rest period. A saturation-prepared image was acquired in the subsequent heartbeat to capture the effect of imaging pulses on the magnetization curve. Simultaneous T_{RAFF2} and T_2 maps were obtained using a 3-parameter fit:

$$S\left(T_{RAFF}^P, T_2^P, A, B\right) = \begin{cases} A \cdot e^{-\frac{T_{RAFF}^P}{T_{RAFF}}} + B \\ A \cdot e^{-\frac{T_2^P}{T_2}} + B \end{cases}$$

SL dispersion maps were calculated by the difference between T_2 (zero-frequency SL) and T_{RAFF2} (approximation for SL relaxation) times normalized by the RAFF frequency as the assumed SL frequency. Phantom and in vivo measurements were performed on a 3T MRI scanner (Prisma, Siemens Healthineers, Erlangen, Germany) with a 28-channel receiver coil array. Phantom measurements were performed on the T1MES4 phantom to evaluate the accuracy and precision of the proposed sequence against regular T_{RAFF2} and T_2 mapping. Simultaneous T_{RAFF2} and T_2 maps were obtained using the proposed sequence with T_{RAFF2}^P times of 12.9 and 25.7 ms (RF pulse power of 625 Hz) and T_2^P of 50 ms. To assess intra-scan reproducibility, 3 scan repetitions were performed in separate acquisitions in the phantom experiments and the coefficient of variation (CV) across all the measurements was computed. A reference T_{RAFF2} map was obtained using T_{RAFF2}^P = 0, 12.9, 25.7, and 38.6 ms and an image preceded by a saturation pulse. Reference T_2 map was acquired with T_2^P of 0, 50, 50, 50 ms, followed by an image preceded by a saturation pulse[5]. Correlation and Bland-Altman plots were obtained to compare the joint and the individual T_{RAFF2}, T_2, and SL dispersion values. In vivo T_{RAFF2} and T_2 maps were obtained using the proposed sequence and individual reference methods for one healthy subject (male, 35y) in a BH of 16s for each sequence. All baseline in vivo images were registered using group-wise registration to minimize motion within and across the separate BH[6] and SL dispersion was computed. Standard deviation (SD) maps in ms were obtained from the fit residuals to obtain a spatially resolved estimation of the precision of the proposed sequence[7]. The imaging parameters were kept constant for phantom and in vivo measurements: FOV: 320x255mm^2; In-plane resol.: 1.7x1.7mm^2; Slice thick.: 8mm; GRAPPA factor/Ref. lines: 2/24; TE 1.6ms; Readout type: bSSFP.

Results: T_{RAFF2} and T_2 values obtained with the proposed simultaneous sequence exhibited excellent correlation (R^2 = 1.00) with the reference T_{RAFF2} and T_2 for the phantom vials (Fig. 2). Dispersion maps yield good sensitivity to changes in the vials of the T1MES phantom. In addition, excellent reproducibility (CV < 10% for the majority of the vials) was observed in the phantom measurements (Fig. 3). In vivo T_{RAFF2} and T_2 maps with the proposed sequence were obtained with high visual map quality, and no B_1^+ or B_0 related artifacts were visible (Fig. 4-5). The average (± std) myocardial T_{RAFF2} and T_2 obtained with the proposed sequence (68.0 ± 10.7 and 44.0 ± 4.0 ms, respectively) were comparable to the reference methods (62.7 ± 11.7 and 41.2 ± 2.4 ms, respectively). The myocardial SL dispersion map resulted in an excellent depiction of the myocardium with a small increase in variability when compared to the SL dispersion obtained with the single-parameter reference maps (0.4 ± 0.2 and 0.3 ± 0.2 x 10^{-4} s^2, respectively).

Discussion: In this work, we propose a method for approximate SL dispersion mapping in the heart by measuring T_{RAFF2} and T_2 in a single 16s BH at 3T. Homogeneous T_{RAFF2}, T_2, and SL dispersion maps of high visual quality were obtained for phantom and in-vivo. By combining multiple contrasts with RAFF2-, T_2- and saturation-prepared images with a three-parameter fit, the consistency of the relaxation time measurements and the resilience of changes in scan parameters and other confounders is increased[5]. RAFF may be more reflective of a single SL frequency component as compared to adiabatic T1ρ, while still enabling the use of high field strengths. T1ρ relaxation depends on the orientation of the magnetization and the effective field, as well as the effective field strength. T1ρ relaxation is non-constant throughout adiabatic T1ρ preparation pulses. In RAFF preparations, the effective field strength, as well as the fictitious field components, giving rise to the sweep, are kept constant and identical throughout the preparation. RAFF does not suffer from the same susceptibilities as off-resonance and the high SAR burden as continuous wave SL. Thus, the proposed simultaneous T_{RAFF2} and T_2 mapping sequence is an excellent candidate for the clinical application of SL dispersion rate due to the lower requirements in SAR while still providing exchange rate information.

Conclusion: Our results show a promising potential for myocardial spin-lock dispersion in a single BH using T_{RAFF2} mapping with clinically tolerable SAR and without the use of contrast agents. The proposed sequence obtains simultaneous T_{RAFF2} and T_2 maps and yields high visual image quality, homogeneous signal, no B_1^+ or B_0 artifacts, and excellent reproducibility. Clinical sensitivity to pathological remodeling, such as for the non-contrast assessment of scar, will be the subject of future studies.

References: [1] Han, Y., Liimatainen, T., Gorman, R.C. et al. (2014), Assessing Myocardial Disease Using T1ρ MRI. Curr Cardiovasc Imaging Rep 7, 9248. [2] Liimatainen, T., Sorce, D.J., O'Connell, R. et al. (2010), MRI contrast from relaxation along a fictitious field (RAFF). Magn. Reson. Med., 64: 983-994. [3] Yla-Herttuala, E., Laidinen, S., Laakso, H. et al. (2018), Quantification of myocardial infarct area based on TRAFFn relaxation time maps - comparison with cardiovascular magnetic resonance late gadolinium enhancement, T1ρ and T2 in vivo. J Cardiovasc Magn Reson 20, 34. [4] Captur, G., Gatehouse, P., Keenan, K.E. et al. (2016) A medical device-grade T1 and ECV phantom for global T1 mapping quality assurance—the T1 Mapping and ECV Standardization in cardiovascular magnetic resonance (T1MES) program. J Cardiovasc Magn Reson 18, 58. [5] Akcakaya, M., Basha, T.A., Weingartner, S., et al. (2015) Improved quantitative myocardial T2 mapping: impact of the fitting model. Magn Reson Med 2015;74:93–105. [6] Tao, Q., van der Tol, P., Berendsen, F.F. et al. (2018), Robust motion correction for myocardial T1 and extracellular volume mapping by principle component analysis-based groupwise image registration. J. Magn. Reson. Imaging, 47: 1397-1405. [7] Kellman, P., Arai, A.E., Xue, H. (2013) T1 and extracellular volume mapping in the heart: estimation of error maps and the influence of noise on precision. J Cardiovasc Magn Reson. 15:56.

Acknowledgments / Funding Information: S.W. acknowledges funding from the 4TU Precision Medicine program, an NWO Start-up STU.019.024, and ZonMW OffRoad 04510011910073. M.A. acknowledges funding from the NIH R01HL153146, NIH P41EB027061, NIH R21EB028369

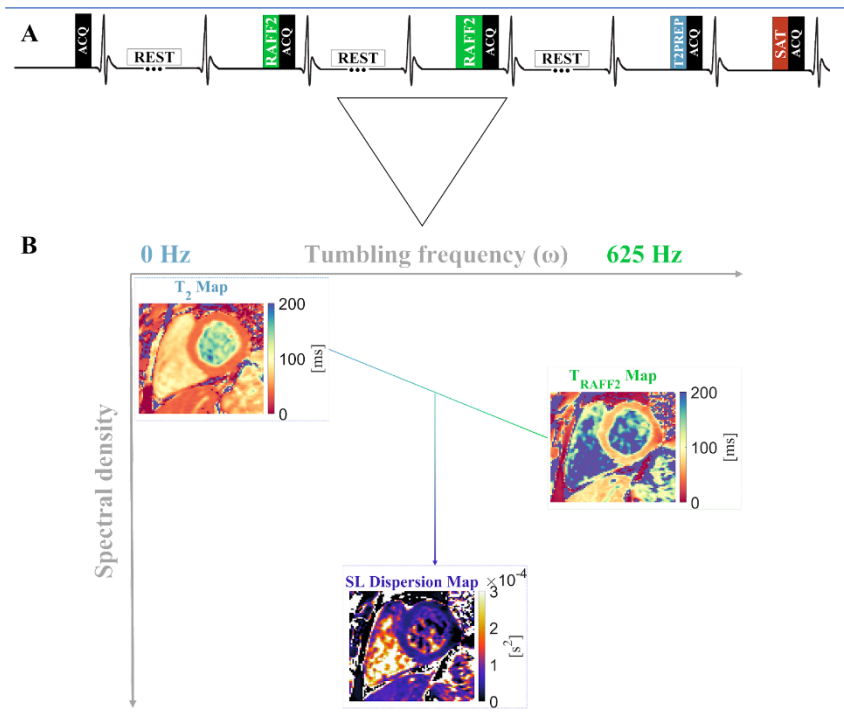

Fig. 1. A) Pulse sequence diagram for the proposed simultaneous myocardial T_{RAFF2} and T_2 mapping sequence. B) The difference between the T_{RAFF2} (max frequency) and T_2 (0 frequency) map divided by the RAFF2 pulse amplitude results in an approximation for a spin-lock (SL) dispersion map.

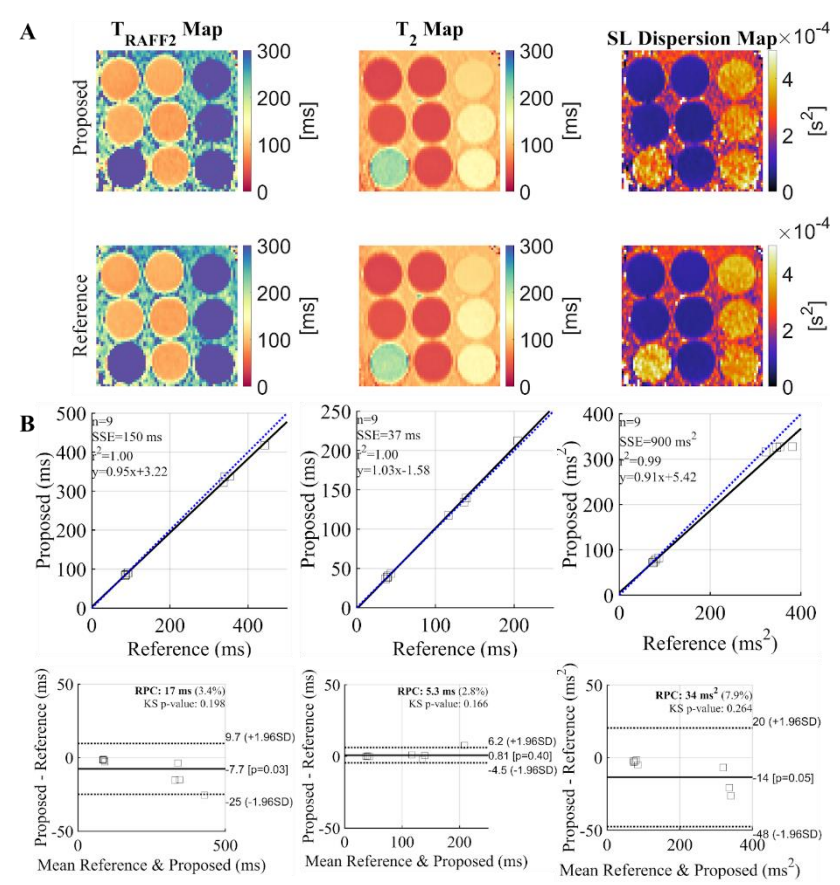

Fig. 2. A) T_2, T_{RAFF2}, and spin-lock (SL) dispersion maps for the T1MES phantom using the proposed simultaneous sequence (top row) and the single-parameter reference maps (bottom row). B) Correlation and Bland-Altman plots for each parameter, showing an excellent correlation between the relaxation properties in phantom, in the expected in vivo range.

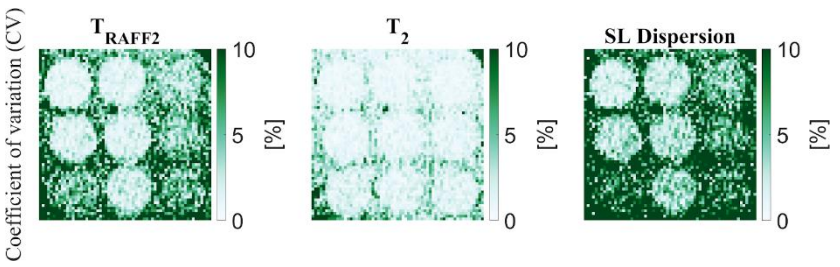

Fig 3. Coefficient of variation (CV) across 3 measurements using the proposed simultaneous T_{RAFF2} and T_2 mapping sequence. All vials show a CV lower than 10% demonstrating excellent reproducibility of the proposed sequence.

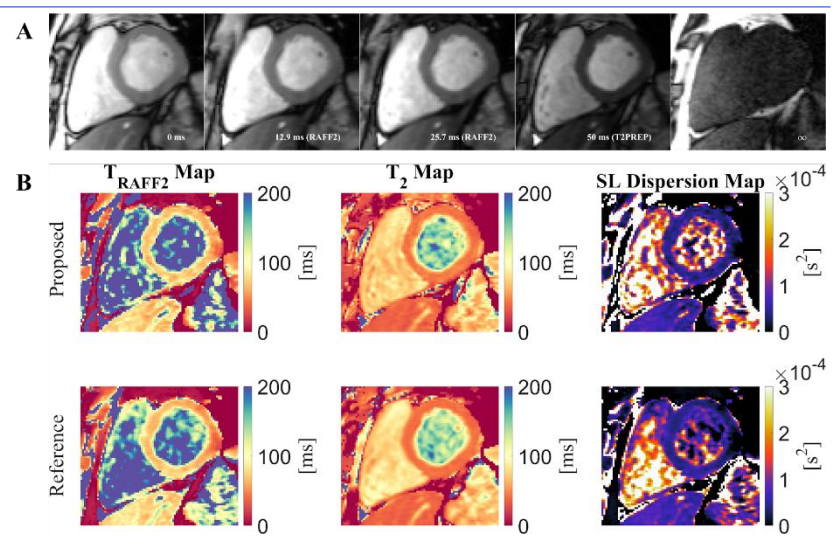

Fig. 4. A) Baseline images for the proposed simultaneous T_{RAFF2} and T_2 mapping sequence with the corresponding preparation times. B) In vivo myocardial T_{RAFF2}, T_2, and spin-lock (SL) dispersion maps were obtained with the proposed sequence and with the single-parameter sequences (Reference). Following image registration, the dispersion map is obtained by subtracting T_2 from T_{RAFF2} and dividing by the RAFF2 pulse power. All maps present high visual image quality, homogeneous myocardial signal and no B_1^+ or B_0 artifacts are visible.

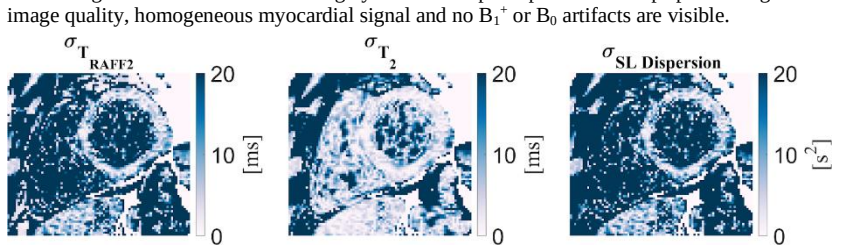

Fig. 5. Standard deviation (SD) maps obtained from the fit residuals show a spatially resolved estimation of the precision of each measured parameter.

Reproducibility of aortic diameter and displacement derived from free-breathing 3D balanced steady-state free precession CINE images at 3T

R. Merton[1], E.M. Schrauben[1], G.J. Strijkers[2], A.J.Nederveen[1], P. van Ooij[1,3]

[1]Radiology and Nuclear Medicine, Amsterdam University Medical Centers, Amsterdam, the Netherlands; [2]Biomedical Engineering and Physics, Amsterdam University Medical Centers, Amsterdam, the Netherlands.[3]Radiology, University Medical Center Utrecht, Utrecht, the Netherlands.

Synopsis: Capturing 3D aortic motion over the heart cycle may give insight into a new biomarker for aortic disease and potentially improve the measurement of aortic hemodynamic parameters. An isotropic, free-breathing, respiratory-corrected 3D CINE balanced steady-state free precession imaging technique of the thoracic aorta was developed to investigate scan-rescan reproducibility of aortic diameter and displacement measures in nine healthy volunteers. Scan-rescan diameter was highly reproducible (CV<10% , ICC=0.85-0.86 and Pearson's ρ=0.87) while displacement was more variable (CV=34-42%, ICC=0.34-0.50, ρ=0.59-0.72). These results are encouraging for future studies investigating aortic motion in health and aortopathy.

Introduction: The motion of the aorta over the cardiac cycle has not often been considered as a biomarker for aortic disease. However, it is possible that aortapathy is exacerbated by increased aortic resistance to heart motion (expressed as decreased aortic displacement over the cardiac cycle), for example in Marfan disease. Therefore, it is of interest to investigate whether the motion of the aorta over the cardiac cycle can be reliably quantified.

CINE balanced steady-state free precession (bSSFP) provides excellent blood-tissue contrast to study motion of the heart and aorta, but is clinically acquired in multiple breath-holds and thick slices, hindering accurate quantification of 3D diameter and motion. Therefore, the aim of this study was to create an isotropic, free-breathing, respiratory-corrected 3D CINE bSSFP imaging technique of the thoracic aorta, and to investigate aortic scan-rescan reproducibility of diameter and displacement measurements.

Methods: Nine healthy control subjects (7 women, age 28 ± 3 years) were enrolled and underwent two MRI examinations separated by a break of 2-5 minutes that included repositioning and replanning. All 3D CINE bSSFP exams were performed during free breathing with PROspective Undersampling in multiple Dimensions[1] (PROUD CINE) with an undersampling factor of R = 10 in a sagittal oblique orientation. MRI acquisitions used retrospective electrocardiogram (ECG) gating on an Ingenia 3T MRI scanner (Philips Healthcare, Best, Netherlands) using a 16-channel torso and 8 channel posterior coil. Pulse sequence parameters for the PROUD CINE scan were: field of view = 256 × 256 × 88 mm3; acquired/reconstructed spatial resolution = 1.6 × 1.6 × 1.6 mm3; temporal resolution ~67 msec (15 timeframes); TR/TR=3.4/1.7 msec; FA=30°; free-running acquisition time ~3 min:48 s.

For respiratory correction of PROUD CINE, the $k_{0,0}$ readout in the foot-head direction (sampled at ~3.9 Hz) was used to extract the respiratory self-gating signal[2]. K-space data were then re-sorted into a 5D dataset with 15 cardiac frames and 4 respiratory frames. Subsequently, a compressed sensing[3,4] reconstruction of the data was applied using a sparsifying total variation operator along the cardiac and respiratory dimensions with regularization parameters $\lambda_C=\lambda_R=0.1$ and number of iterations set to 20[5]. To correct for respiratory motion, non-rigid registration[6] of cardiac-averaged reconstructions to the end-expiration phase was performed. Each respiratory phase of the 5D set was then transformed to end-respiration using the displacement fields retrieved with the registration and the average over the respiratory dimension was used for further analysis. In post-processing, inspection was used to determine the last cardiac phase showing contraction and this phase was selected for the 3D end-systolic images. The diastolic images were systematically selected 5 cardiac phases later and both were manually segmented using Mimics v24 (Materialise, Leuven, Belgium).

The segmentations were transformed into surface objects in Matlab and diameter was calculated per surface vertex as the length of the vector along the normal of the surface to the opposing side[7]. Aortic displacement was calculated following non-rigid registration of the systolic segmentation surface to the diastolic segmentation surface using an iterative closest point (ICP) method[8]. The distance between the registered and source surface vertices represents displacement, where source coordinate values were subtracted from registered coordinate values.

Diameter and displacement results are given as mean ± standard deviations. To quantify scan-rescan reproducibility of these metrics, the rescan data was rigidly registered and interpolated[9] to the scan data using FLIRT (FMRIB's Linear Image Registration Tool[10]), after which voxel-by-voxel Bland-Altman (mean difference, limits of agreements (LoA) and coefficient of variation (CV)) and orthogonal regression (slope, intercept, Pearson's ρ and intra-class correlation coefficient (ICC)) analysis were calculated per subject and subsequently averaged over the subjects. A sub-analysis for the ascending aorta was performed.

Results: Figure 1 shows the data acquisition and reconstruction pipeline and an example of healthy aortic motion. In Figure 2 segmentation contours are provided for systolic and diastolic scan and rescan aortic slices. Figure 3 displays the displacement calculation method and an example of an aortic 3D diameter and displacement map. Figure 4 shows an example of scan-rescan systolic and diastolic diameter and displacement maps as well as Bland-Altman and orthogonal regression plots. Table 1 provides the results of the voxel-by-voxel Bland-Altman and orthogonal regression analysis over all subjects.

For all diameter and displacement measurements, the absolute mean differences were smaller than 0.5 mm with LoA=2.5-3.5 mm. The reproducibility for diameter measurements was good (CV<10% , ICC=0.85 and ρ=0.87) while the reproducibility for voxel-by-voxel displacement was poor (CV=42%, ICC=0.34, ρ=0.59). Displacement reproducibility was higher for the ascending aorta (CV=34%, ICC=0.50, ρ=0.72).

Discussion: Three-dimensional aortic diameter maps showed good reproducibility. For displacement, the result of ICP registration might be sensitive to small differences in segmentation, especially on a voxel-by-voxel basis. Comparison of initial segmentation differences with corresponding displacement map differences supports this suggestion, which was also reflected in the better agreement for the ascending aorta. Automatic machine learning segmentation may mitigate this problem after more data is acquired[11].

Conclusion: Systolic and diastolic segmentations of the aorta from high isotropic spatial resolution free-breathing, respiratory-corrected 3D CINE PROUD scans showed good reproducibility for diameter, while the moderate reproducibility of displacement metrics needs further investigation. This technique may be useful for future studies investigating aortic motion in health and disease.

References:

1. Gottwald LM, Peper ES, Zhang Q, et al. Pseudo-spiral sampling and compressed sensing reconstruction provides flexibility of temporal resolution in accelerated aortic 4D flow MRI: A comparison with k-t principal component analysis. NMR in Biomedicine. 2020;33(4). doi:10.1002/nbm.4255

2. Pang J, Sharif B, Fan Z, et al. ECG and navigator-free four-dimensional whole-heart coronary MRA for simultaneous visualization of cardiac anatomy and function. Magnetic Resonance in Medicine. 2014;72(5):1208-1217. doi:10.1002/mrm.25450

3. Lustig M, Donoho D, Pauly JM. Sparse MRI: The application of compressed sensing for rapid MR imaging. Magnetic Resonance in Medicine. 2007;58(6):1182-1195. doi:10.1002/mrm.21391

4. Lustig M, Donoho DL, Santos JM, Pauly JM. Compressed sensing MRI: A look at how CS can improve on current imaging techniques. IEEE Signal Processing Magazine. 2008;25(2):72-82. doi:10.1109/MSP.2007.914728

5. Uecker M, Ong F, Tamir JI, et al. Berkeley Advanced Reconstruction Toolbox. Proc Intl Soc Mag Reson Med 23. Published online 2015. doi:10.5281/zenodo.12495

6. Vercauteren T, Pennec X, Perchant A, Ayache N. Diffeomorphic demons: efficient non-parametric image registration. NeuroImage. 2009;45(1 Suppl). doi:10.1016/j.neuroimage.2008.10.040

7. van Ooij P, Collins J, Fedak P, et al. 3D Linear Regression Analysis Reveals Relationships of 4D flow MRI-derived Aortic Dimensions with Age, Gender and Wall Shear Stress in Patients with Aortopathy. In: Proc. Intl. Soc. Mag. Reson. 25. ; 2017:0288.

8. Audenaert EA, van Houcke J, Almeida DF, et al. Cascaded statistical shape model based segmentation of the full lower limb in CT. Computer Methods in Biomechanics and Biomedical Engineering. 2019;22(6):644-657. doi:10.1080/10255842.2019.1577828

9. van Ooij P, Powell AL, Potters W v., Carr JC, Markl M, Barker AAJ. Reproducibility and interobserver variability of systolic blood flow velocity and 3D wall shear stress derived from 4D flow MRI in the healthy aorta. Journal of Magnetic Resonance Imaging. 2016;43(1):236-248. doi:10.1002/jmri.24959

10. Jenkinson M, Smith S. A Global Optimisation Method for Robust Affine Registration of Brain Images. Vol 5.; 2001. www.elsevier.com/locate/media

11. Berhane H, Scott M, Elbaz M, et al. Fully automated 3D aortic segmentation of 4D flow MRI for hemodynamic analysis using deep learning. Magnetic Resonance in Medicine. 2020;84(4):2204-2218. doi:10.1002/mrm.28257

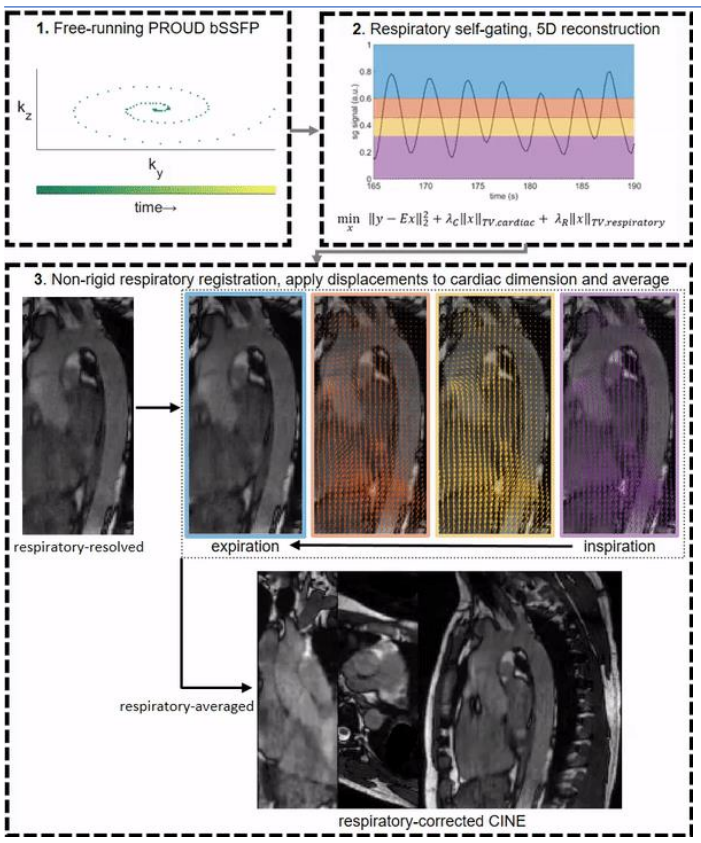

Figure 1: Data acquisition and reconstruction pipeline

1. A free-running prospectively undersampling bSSFP acquires data in ~4 minutes.

2. From the $k_{0,0}$ line, respiratory self-gating is performed and data are sorted into a 5D dataset with 15 cardiac and 4 respiratory phases. CS reconstruction uses total variation over cardiac and respiratory dimensions.

3. Images are averaged over the cardiac dimension, followed by 3D non-rigid registration to end-expiration (vector overlays). Respiratory displacements are then applied to the 5D images and data is respiratory-averaged.

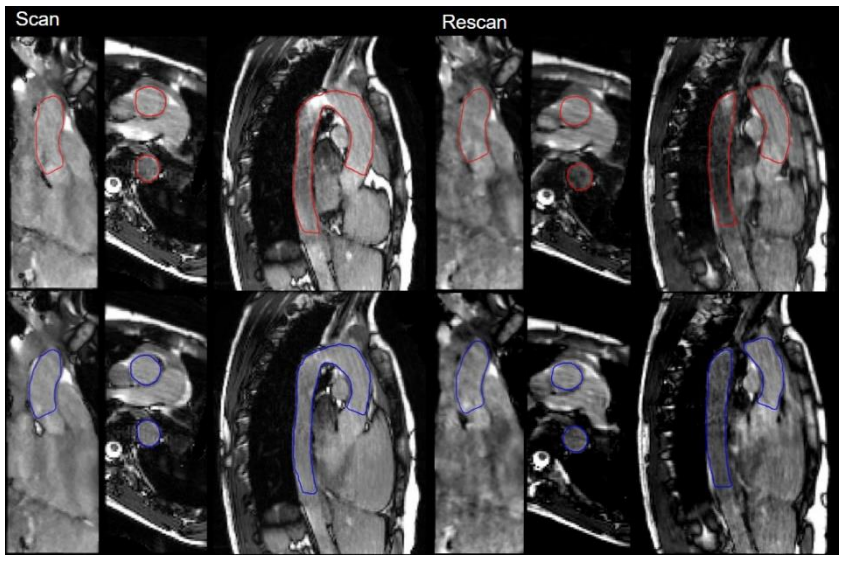

Figure 2: Reconstruction of PROUD CINE with segmentation contour of diastolic (blue) and end-systolic phase (red) of the scan and rescan in one volunteer in coronal, axial and sagittal view.

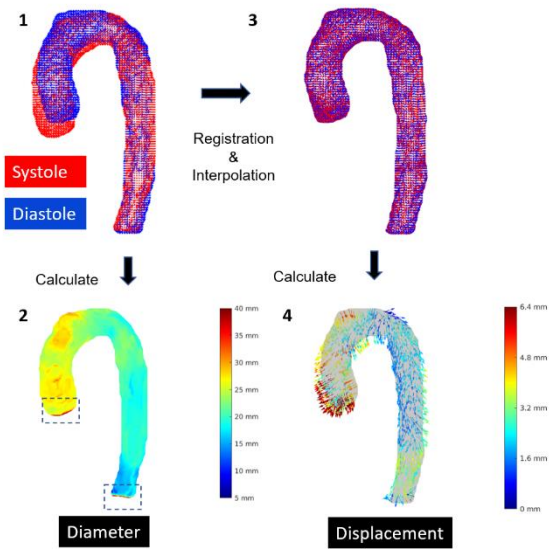

Figure 3: Post processing pipeline

1.The systolic and diastolic aorta segmentations are transformed to a surface in Matlab. 2. For each surface vertex the diameter is calculated. For the final analysis a fixed extend of the surfaces are discarded to remove erroneous diameter calculations from face-end vertices. 3. The systolic surface is non-rigidly registered to the diastolic surface using iterative closest point method and diameter values interpolated[8]. 4. Displacement is calculated by subtracting the old systolic vertex coordinates from the new vertex coordinates.

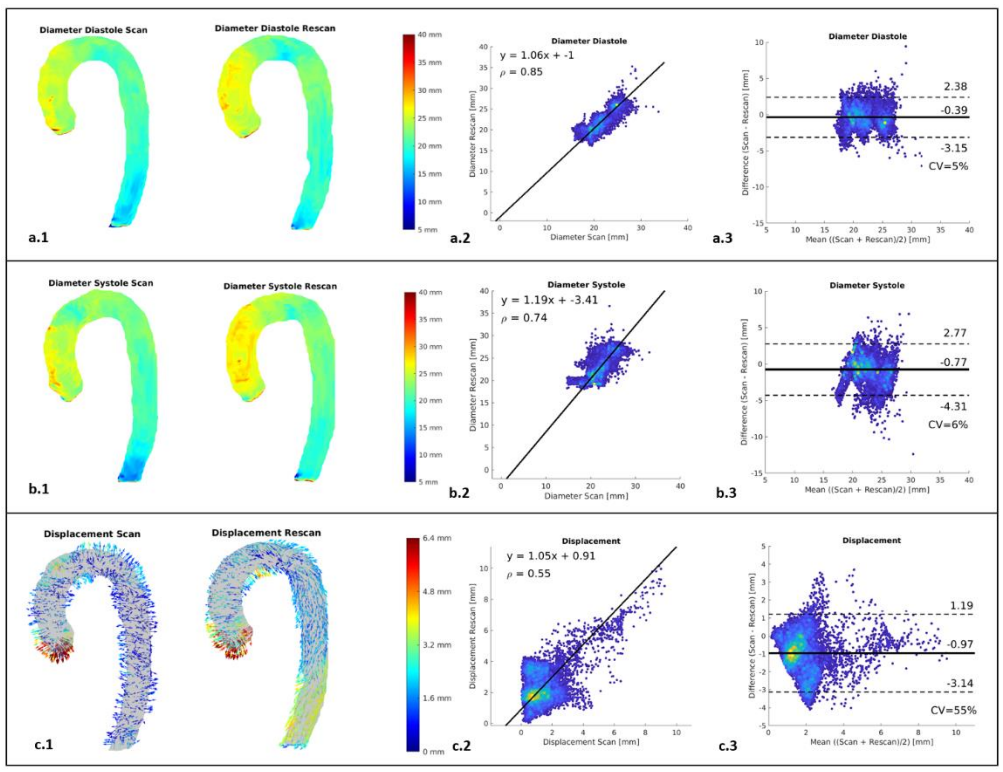

Figure 4: Scan-rescan diameter and displacement analysis in one volunteer of diastolic diameter (a) systolic diameter (b) and displacement (c). 1: The 3D diameter and displacement fields used for the voxel-by-voxel analysis. 2: voxel-by-voxel analysis: Bland-Altman comparison, 3: orthogonal regression.

Table 1: Results of scan-rescan statistical analyses

	Scan	Rescan	Bland-Altman			Regression			
	Mean (mm)	Mean (mm)	Mean difference (mm)	LOA (mm)	CV (%)	Slope (-)	Intercept (mm)	ICC (-)	Pearson (-)
Diameter Systole	20.4 ± 1.9	20.7 ± 2.1	-0.4 ± 0.4	3.5 ± 0.9	6.4 ± 1.9	1.1 ± 0.2	-1.6 ± 2.9	0.85 ± 0.09	0.87 ± 0.08
Diameter Diastole	20.1 ± 1.9	20.1 ± 2.2	0.0 ± 0.7	3.3 ± 1.2	6.8 ± 2.5	1.2 ± 0.4	-0.8 ± 2.9	0.85 ± 0.10	0.87 ± 0.08
Displacement Total Aorta	2.9 ± 1.3	2.9 ± 0.7	0.0 ± 1.4	2.5 ± 0.7	41.5 ± 14.0	1.2 ± 1.0	0.0 ± 1.4	0.34 ± 0.35	0.59 ± 0.20
Displacement Ascending Aorta	3.7 ± 1.5	3.6 ± 0.8	0.1 ± 1.3	2.5 ± 0.6	33.7 ± 9.4	1.1 ± 0.5	0.1 ± 1.0	0.50 ± 0.41	0.72 ± 0.20

Table 1: Scan and rescan mean, mean difference, limits of agreement, Coefficient of Variation, slope, intercept, Intraclass Correlation Coefficient and Pearson's correlation coefficient ρ for systolic and diastolic diameter measurements and 3D displacement for total aorta and ascending aorta averaged over all subjects. For the ascending aorta a ROI from root to the location of the first branch in the aortic-arch was used to create a subset of displacement values.

Single breath-hold native myocardial T1 and T2 mapping using SENSE and a 72-channel cardiac receive array.

Hugo Klarenberg[*1], Mark Gosselink[2], Tim Leiner[2], Bram F. Coolen[1], Aart J. Nederveen[3], Adrianus J. Bakermans[3], Hildo J. Lamb[4], S. Matthijs Boekholdt[5], Gustav J. Strijkers[1], Martijn Froeling[2]

1 Department of Biomedical Engineering and Physics, University Medical Centers, Amsterdam Cardiovascular Sciences, University of Amsterdam, Amsterdam, The Netherlands
2 Department of Radiology, University Medical Center Utrecht, Utrecht, The Netherlands 3 Department of Radiology and Nuclear Medicine, Amsterdam University Medical Centers, Amsterdam, University of Amsterdam, Amsterdam, The Netherlands 4 Department of Radiology, Leiden University Medical Center, Leiden, The Netherlands 5 Department of Cardiology, Amsterdam University Medical Centers, Amsterdam Cardiovascular Sciences, University of Amsterdam, Amsterdam, The Netherlands

INTRODUCTION: Quantitative Magnetic Resonance Imaging (qMRI) via T1 and T2 mapping is increasingly being used in cardiac imaging to guide clinical care [1]. Currently T1 maps are typically acquired using a Modified Look Locker sequence (MOLLI) [2]. T2 maps are commonly acquired using a Gradient-Spin-Echo (GraSE) sequence [3]. Both methods would benefit from scan acceleration to reduce the number of breath holds (BHs) required, as currently a single BH only permits acquisition of a single slice. T1 and T2 mapping methods can be accelerated using Sensitivity encoding (SENSE) which benefits from a high density receive array. Currently SENSE=2 is applied in our clinic in combination with the vendor-supplied 16-channel anterior receiver array. In recent years we have developed a 72 channel receive array which would allow for higher acceleration factors and thus potentially faster T1 and T2 mapping acquisition [4].

The goal of this study was to accelerate native cardiac T1 and T2 mapping using a dedicated 72-channel receive array. SENSE factors up to 4 and 6 were explored to facilitate native T1 and T2 mapping of 3 slices in 1 and 2 BHs, respectively.

METHODS: 20 healthy subjects (10 female), aged 34 ± 7 years, body weight 76 ± 9 kg, heart rate 57 ± 10 beats/min (bpm) where included. MR examinations were performed with a 3T MR scanner (Ingenia, Philips Healthcare, Best, The Netherlands). A novel 72-channel cardiac array coil was used which has 2 flexible arrays of 36 coils which were placed on top of the chest of the subject, as shown in Figure 1.

For MOLLI, a shared inversion pulse interleaved approach was designed to acquire 3 slices after the same inversion (Figure 2). Thereby, only 1 BH was needed to acquire the 3 slices. We took into account that because all slices share the same inversion pulse, the inversion time for the 3 slices was slightly different. For T2 mapping we used a multi-shot GraSE acquisition. With higher acquisition factors less shots, and thus heartbeats, are needed to acquired one image. Therefore multiple slices can be acquired within one BH. For both T1 and T2 mapping acquisition we acquired 3 axial slices covering the basal, mid-ventricular and apical myocardium.

Images with different inversion times (T1 mapping) and for different echo-times (T2 mapping) were aligned (Elastix) using a b-spline registration and pixel-wise fitted to provide T1 and T2 maps. Average T1 and T2 values were determined in 16 segments of the 17-segment AHA model (excluding the apical segment) and compared per slice and per segment between SENSE=2, 4, and 6 accelerated acquisitions. To quantify the differences, average T1 and T2 values were statistically compared on a slice and segment level. Normality of data was checked and a two-way factor ANOVA analysis was applied with acceleration factor and segments as factors. All statistical analyses were performed using R (v. 4.0.3) and Rstudio (2021.09.0.351). P-values of < 0.05 were considered significant.

RESULTS: Figure 3a shows a representative example of native T1 maps acquired with SENSE=2 (3BHs x 11 sec at 60 bpm), 4 (1BH x 11 sec at 60 bpm) and 6 (1BH x 11 sec at 60 bpm). Similarly, Figure 3b shows typical T2 maps acquired with SENSE=2 (3BHs x 13 sec at 60 bpm), 4 (3BHs x 9 sec at 60 bpm) and 6 (2BHs x 10 sec at 60 bpm). Figure 4c shows the descriptive statistics of the native T1 and T2 map acquisitions using SENSE=2, 4 and 6. Mean T1 and T2 values per segment are shown in figures 5a-b. The two-factor ANOVA revealed no difference in mean and segmental T1 values per slice: no significant differences were found in any of the 16 segments between SENSE=2 and 4 and SENSE=2 and 6 and no interaction was present (figure 5a).

The two-factor ANOVA revealed statistical differences per slice in mean T2 values due to PI factor and segments, and an interaction effect was present between both conditions. For T2 on segmental level, significant differences were seen between SENSE=2 and 4 in segments 1, 3 ($p<0.05$) and 2, 8 ($p<0.01$) . For SENSE=6 this was in segments 1, 2, 5 ($p<0.001$), 3, 6, 7, 8, 12 ($p<0.01$) and 13, 14 ($p<0.05$) (figure 5b).

DISCUSSION: Generally, both T1 and T2 maps have a noisier appearance with increasing acceleration, particularly for the basal slices. However, 16-segmental multislice native myocardial T1 mapping acquired in a single BH using an accelerated acquisition with PI factors up to 6 were similar to reference values acquired in 3 BHs. The accelerated cardiac T2 mapping values significantly deviated from reference values particularly for the basal slices which we believe could be due to motion sensitivity of the T2 mapping sequence. Currently a second 72 channel coil has been build doubling the total of receive elements to 144.

CONCLUSION: Native myocardial T1 mapping quantification of 3 slices in just 1 BH is possible using a modified MOLLI sequence in combination with a new 72-channel receive array and SENSE=4 or 6. The myocardial T2 mapping protocol can be accelerated to achieve fewer BHs. However, this goes at the expense of decreased accuracy of the T2 values in specific segments.

SUMMARY OF MAIN FINDINGS: MOLLI native myocardial T1 mapping in 3 slices is possible in as few as 1 BH using SENSE=4 or 6 and a 72 channel receive array.

Synopsis: Single breath-hold native MOLLI T1 mapping in 3 slices is possible using SENSE=4 & 6 and a 72 channel receive array. T1 values in 16 segments of the 17-segment AHA model (excluding the apical segment) were similar compared to SENSE=2 using 3 breath-holds measured in 20 healthy subjects (10 female). Myocardial T2 GRaSE mapping with fewer breath-holds in 3 slices is possible, though at the expense of decreased accuracy of the T2 values in specific segments.

References

1. Messroghli, D.R., et al., Clinical recommendations for cardiovascular magnetic resonance mapping of T1, T2, T2* and extracellular volume: A consensus statement by the Society for Cardiovascular Magnetic Resonance (SCMR) endorsed by the European Association for Cardiovascular Imaging (EACVI). J Cardiovasc Magn Reson, 2017. 19(1): p. 75.

2. Messroghli, D.R., et al., Modified Look-Locker inversion recovery (MOLLI) for high-resolution T1 mapping of the heart. Magn Reson Med, 2004. 52(1): p. 141-6.

3. Feinberg, D.A. and K. Oshio, GRASE (gradient- and spin-echo) MR imaging: a new fast clinical imaging technique. Radiology, 1991. 181(2): p. 597-602.

4. Gosselink M., K., H., Lamb, H.J., Strijkers, G.J., Leiner, T., Klomp, D.W.J., Froeling, M., Highly accelerated cardiac imaging using a high-density 72 channel local receiver array at 3 Tesla. ISMRM, 2019.

Acknowledgments / Funding Information: Continue on this line

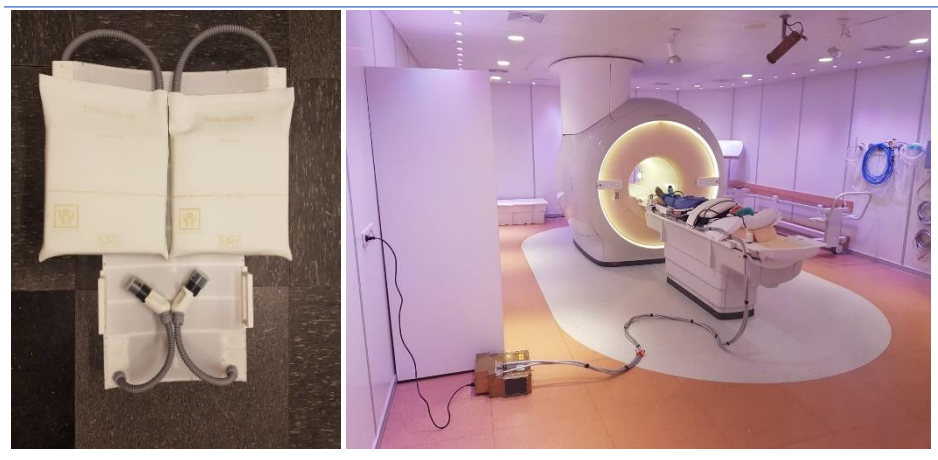

Figure 1: New 72 channel local array setup. (Left) The 2x36 channel arrays are visible attached to the interface box. (Right) Subject in the scanner with the 2 channel arrays positioned on the chest of the subject.

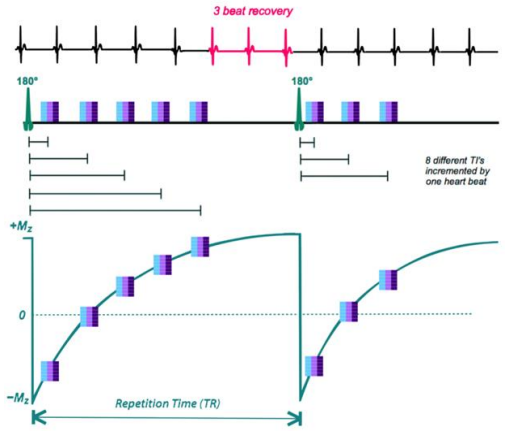

Figure 2: Acquisition timing scheme of the interleaved MOLLI sequence with shared inversion pulses. Light blue = apical slice, light purple = mid-ventricular slice, deep purple = basal slice. TI = time intervals

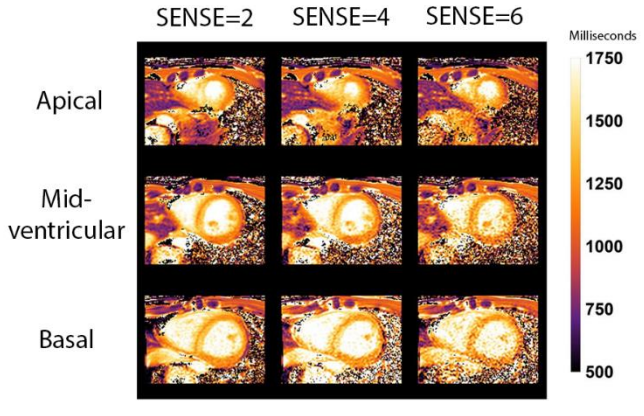

Figure 3a: Example of T1 maps acquired with SENSE 2, 4 and 6 for an apical, mid-ventricular, and basal slice.

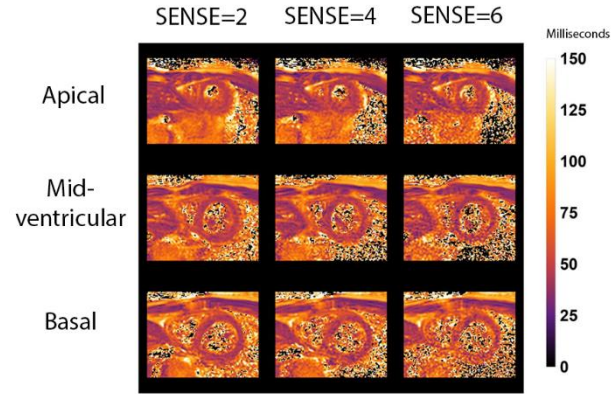

Figure 3b: Example of T2 maps acquired with SENSE 2, 4 and 6 for an apical, mid-ventricular, and basal slice.

Figure 4a: Acquisition parameters MOLLI and GRaSE sequence. mm = millimeter, ms = millisecond

Parameters	MOLLI T1	GRaSE T2
Slice thickness	8 mm	8 mm
Slice gap	16 mm	16 mm
TR/TE/FA	3.6 ms / 1.6 ms / 20°	833 ms / 93.4 ms / 90°
FOV	300 x 300 mm	350 x 350
Spatial resolution	1.17 x 1.17 cm^2	1.22 x 1.22 cm^2
Trigger delay	longest	longest
MOLLI Scheme	5(3)3	n.a.

PI factor	Time readout (ms)	Shared inversions	Breath holds
2	216.6	No	3
4	107.1	Yes	1
6	74.8	Yes	1

Figure 4b: Time resolutions MOLLI sequence. PI = parallel imaging, ms = milliseconds

Figure 4c: Myocardial relaxation times T1, T2 in milliseconds for SENSE=2, SENSE=4 and SENSE=6. PI = parallel imaging, CI = confidence interval, SD = standard deviation

	PI factor	All segments (n)	Min.	Max.	Mean	SD
T1	SENSE=2	253	60.6	4007.1	1269.5	247.0
	SENSE=4	247	345.2	3425.4	1299.6	217.1
	SENSE=6	245	93.5	3939.7	1313.6	267.7
T2	SENSE=2	272	39.1	97.4	53.4	8.31
	SENSE=4	272	39.5	103	54.9	9.56
	SENSE=6	272	37.4	95.5	59.7	12.0

Figure 5a: Boxplots with mean native T1 (ms) values per segment for (green) SENSE 2, (purple) SENSE 4, and (red) SENSE 6, accelerated scans.

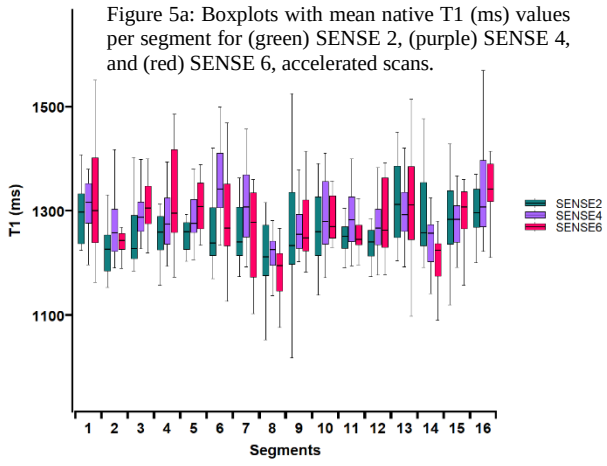

Figure 5b: Boxplots illustrating mean T2 (ms) values per segment during each accelerated acquisition. Green is SENSE=2, purple is SENSE=4, red is SENSE=6

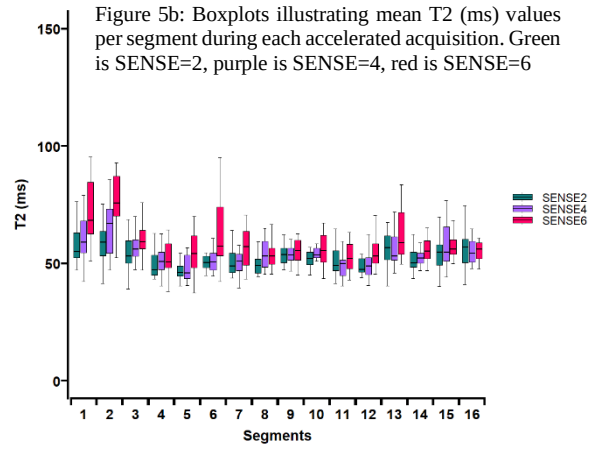

Accelerated deep learning reconstruction of highly-undersampled 3D FLAIR in acute neurological deficit

L.C. Liebrand[1], D. Karkalousos[1], E. Poirion[2], H. Marquering[1], C.B. Majoie[3], J.Savatovsky[2], M.W.A. Caan[1]

[1]Dept. of Biomedical Engineering and Physics, Amsterdam University Medical Centers, location AMC, Amsterdam, Netherlands; [2]Fondation Rothschild Hospital, Paris, France; [3] Dept. of Radiology and Nuclear Medicine, Amsterdam University Medical Centers, location AMC, Amsterdam, The Netherlands

Synopsis: Time is of the utmost importance in diagnosis and treatment of acute ischemic stroke. Compressed-sensing (CS) inference times are currently limiting the clinical workflow. Deep learning reconstruction may allow for faster inference time than iterative CS. Here, we evaluated two variants of the recurrent inference machine (RIM) which were trained on a different dataset of T1-images for reconstructing highly-undersampled (12X) 3D FLAIRs of patients with acute neurological deficit and compared them to CS. Both RIM variants showed good reconstruction quality and faster inference times than CS, while diagnostic interpretability was preserved according to an expert neuroradiologist.

Introduction: Time is of the utmost importance in diagnosis and treatment of acute ischemic stroke. In most countries, CT is used to perform stroke diagnosis instead of MRI. Our aim is to improve the acquisition and reconstruction times of MRI to be more competitive with CT while preserving MRI's rich diagnostic information. Compressed-sensing (CS) iterative reconstruction allows for reconstructing highly accelerated data based on image sparsity and has become commonplace in the clinic. Clinically desired zero-filling by a factor of two yields inference times that exceed measurement time, posing limitations in the clinical workflow. Here, we investigate potentially faster deep learning reconstruction for stroke by retrospectively reconstructing highly-undersampled (12X) 3D FLAIR imaging used in the setting of acute neurological deficit, and evaluate image quality and reconstruction times.

Methods:

Data acquisition

Data were routinely acquired from patients with acute neurological deficits (N=6) who were admitted to the Fondation Rothschild Hospital in Paris, France. The hospital's IRB approved this study. Informed consent was not required for this study with anonymized clinical data.

The stroke examination consisted of multiple scans, of which the sagittally acquired 3D TSE FLAIR is analyzed here. All scans were acquired on a Philips Ingenia Elition 3T equipped with a 32-channel head coil. Scan parameters were as follows: 1.15mm³ isotropic resolution, TR=8000ms, TE=311ms, TI=2400ms, turbo factor=186, scan time=1m52s. The data were prospectively undersampled with a variable density mask with a radial shutter to a factor of approximately 12. Sensitivity-reference scan data were used for coil sensitivity estimation.

Pre-processing

All data were preprocessed in a custom pipeline in Matlab (version R2019b, Mathworks). The FLAIR k-space data were loaded and corrected with MRecon (version 4.4.4, GyroTools), before removing oversampling in the read-out direction and clinically desired zero-filling by approximately a factor of two in all directions – leading to an eightfold increase in matrix size. The sensitivity-reference scan was upsampled and brought into alignment with the FLAIR scan. Sensitivity maps were calculated with caldir (range 50) implemented in the BART toolbox[1].

Deep learning reconstruction models

The basis of our deep-learning reconstruction methods is the Recurrent Inference Machine (RIM)[2]. The RIM is a physics-based model, where the prior information is explicitly formulated through the forward model for solving the inverse problem of accelerated-MRI reconstruction. Its recurrent nature allows it to have a notion of memory and share parameters over time-steps for unrolled optimization by gradient descent.

We chose the Independently Recurrent Neural Network (IndRNN) layer[3] and call this model IRIM. Furthermore, we implemented cascades and built RIM blocks connected sequentially to create the Cascades of Independently Recurrent Variational Inference Machine (CIRVIM), see Figure 1. We used the l1-norm to calculate our loss on normalized magnitude images.

Pretraining and parameters

Models were pretrained on a T1-weighted brains dataset[2] with 64 input channels, 8 time-steps, and for the CIRVIM 8 cascades. We compared the performance of these models to Parallel-Imaging Compressed Sensing (PICS) reconstructions done with BART. We used an l1- wavelet sparsity transform, setting the regularization parameter to 0.05 and the maximum number of iterations to 60. For a fair comparison, PICS reconstructions were conducted on GPU rather than CPU. All experiments were performed on an Nvidia Tesla V100 GPU-card with 32GB of memory.

Results: We were able to reconstruct all subjects' data with all models (see Figure 2 for three examples with visible lesions).

All reconstructions were blindly rated by an expert neuroradiologist (JS) and deemed suitable for clinical reading with good diagnostic confidence (Interpretability, Table 1). Image quality was similar across models, with our models scoring higher on subjective SNR at the cost of sharpness compared to CS.

Moreover, both deep learning models had a shorter inference time than the CS iterative reconstruction, as can be seen in Table 2. Of note is the reconstruction time of the IRIM (32.1 sec), which was twenty-seven times shorter than PICS (872.3 sec) and five times shorter than the CIRVIM (143.3 sec).

Discussion: Our results show the feasibility of reconstructing raw MRI data with deep learning models that are able to speed up reconstruction while preserving diagnostic interpretability, despite training on a completely different sample. The state-of-the-art in image reconstruction is moving towards models with an increasingly large number of parameters. Our results show a potential benefit in using smaller models for time-critical applications such as stroke. We suspect this speed difference is most noticeable for large (zero-filled) matrices.

Possibly, the decision on which reconstruction method eventually to use on-scanner will be made in the future by weighing the trade-off between visual fidelity and reconstruction times. This would be similar to weighing the trade-off between scan quality and acquisition time during acquisition.

Our study was limited by the lack of a fully-sampled ground truth. However, it would be unethical to acquire data without acceleration in the time-critical context of acute neurological deficit. In future work, we aim to extend our results to other sequences used in acute neurological deficit MRI.

Conclusion: Our models are able to reconstruct raw acute ischemic stroke FLAIRs out-of-sample, at a benefit in reconstruction time compared to CS reconstruction whilst preserving diagnostic interpretability.

References:

1. Uecker M, Ong F, Tamir JI, et al. Berkeley Advanced Reconstruction Toolbox. In: Proc. Intl. Soc. Mag. Reson. Med. 23. ; 2015:2486.

2. Lønning K, Putzky P, Sonke JJ, Reneman L, Caan MWA, Welling M. Recurrent inference machines for reconstructing heterogeneous MRI data. Med Image Anal. 2019;53:64-78. doi:10.1016/j.media.2019.01.005

3. Li S, Li W, Cook C, Zhu C, Gao Y. Independently Recurrent Neural Network (IndRNN): Building A Longer and Deeper RNN. Proc IEEE Comput Soc Conf Comput Vis Pattern Recognit. 2018:5457-5466. doi:10.1109/CVPR.2018.00572

Acknowledgments / Funding Information: This study was supported by a TKI-PPP program grant of Health~Holland.

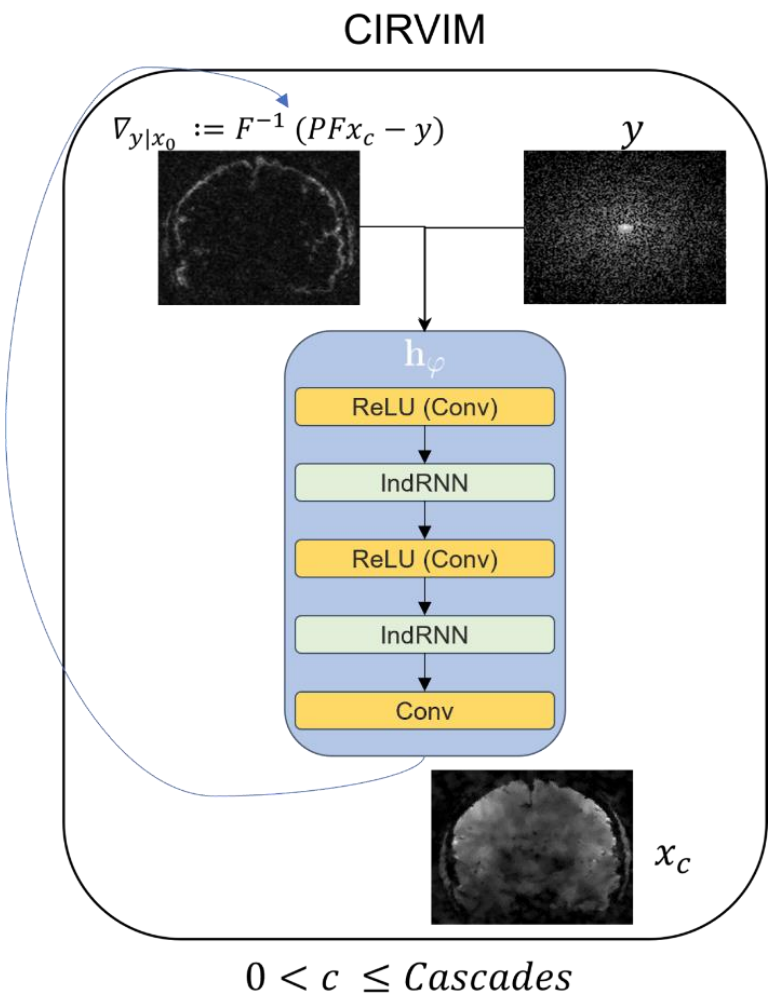

Figure 1: Cascades of Independently Recurrent Variational Inference Machine (CIRVIM). The inputs to the model are the subsampled kspace measurements (top-right) and the computed log-likelihood gradient (llg, top-left). The llg is calculated with respect to the initial estimation xc. Through a sequence of alternating convolutional and recurrent layers (IndRNN) the model targets optimization through time-steps, and for a total number of Cascades.

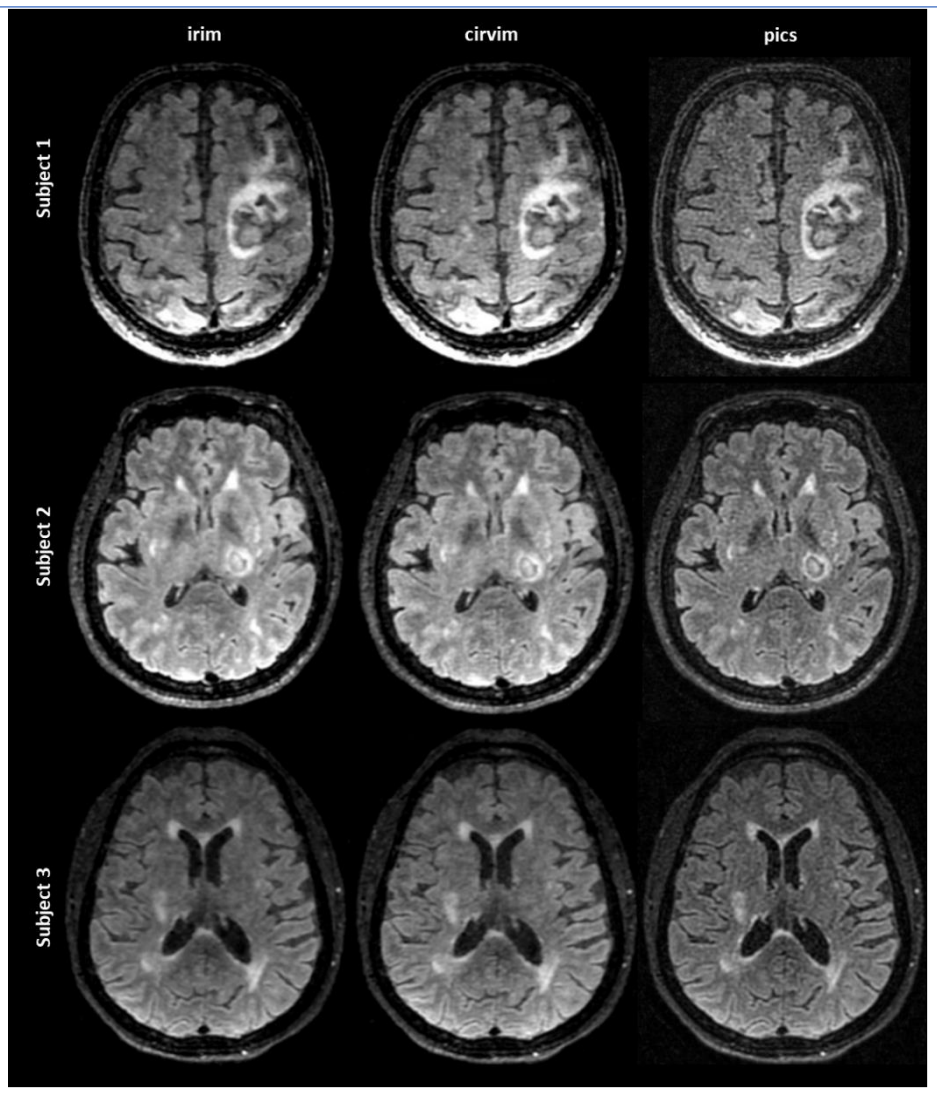

Figure 2: Comparison of FLAIR reconstructions using three models (IRIM, CIRVIM, PICS) from three subjects having an acute neurological deficit and a visible lesion.

Table 1. Mean (standard deviation) image quality rating by an expert neuroradiologist for all six patients. The neuroradiologist was blinded to the reconstruction models used. Scales range between 0 (poorest) and 5 (best). Images were rated on clinical interpretability with good diagnostic confidence, subjective signal-to-noise ratio (SNR), subjective image homogeneity (bias), and subjective sharpness. Image quality was defined as the average of the other scores.

	Interpretability	**Subjective SNR**	**Homogeneity**	**Sharpness**	**Image quality**
IRIM	5.0 (±0.0)	4.3 (±1.2)	2.3 (±1.2)	3.5 (±1.2)	3.8 (±0.5)
CIRVIM	5.0 (±0.0)	4.0 (±0.9)	2.5 (±1.0)	3.8 (±1.0)	3.8 (±0.3)
PICS	5.0 (±0.0)	1.8 (±0.8)	4.0 (±0.6)	5.0 (±0.0)	4.0 (±0.2)

Table 2. Comparison of reconstruction times and number of parameters for all modalities used. The reconstruction times were determined for clinically desired zero-filled volumes at 0.58 mm3 resolution. Note that these reconstruction times do not include data loading and pre-processing.

	IRIM	**CIRVIM**	**PICS**
No. of Parameters	56k	420k	-
Mean reconstruction time (seconds)	32.1	143.3	872.3

Retrospective motion correction with structural priors for conventional clinical MRI protocols

G. Rizzuti[1], A. Sbrizzi[2], T. van Leeuwen[3]
[1]Utrecht University, Utrecht, The Netherlands; [2]Universitair Medisch Centrum Utrecht, Utrecht, The Netherlands; [2]Centrum Wiskunde & Informatica, Amsterdam, The Netherlands

Synopsis: We present a retrospective rigid motion correction and reconstruction scheme for brain MRI with the aid of structural priors. The proposed framework is designed to be applied to a clinical protocol including multiple scans for multiple contrasts, of which some scans are corrupted due to motion during the acquisitions, but at least one is uncorrupted and exploited as an additional prior. We envision a practical workflow that can easily fit into the existing clinical practice without the need for changing the MRI acquisition protocols.

Introduction: We propose a retrospective technique for the removal of rigid motion artifacts from brain MR reconstructions[1,2]. The main goal is to provide a post-processing method that can be readily deployed in practical clinical settings (which are mostly based on conventional Cartesian acquisition schemes), with no alterations to the current clinical workflow. We picture the following scenario: in multi-contrast imaging, a trained technician can indicate that some contrasts are severely affected by motion, while other contrasts are deemed acceptable. Instead of repeating the corrupted scan, we propose a technique for a technique that aims at improving the contrast most severely affected by motion by leveraging the prior anatomical information provided by the well-resolved contrasts (since they share the same anatomy). Extensive synthetic datasets and a preliminary in-vivo study indicate that the method is potentially mature for multi-slice 2D protocols, and promising for more general 3D acquisition.

Theory: We frame our work in the context of retrospective joint motion correction and reconstruction methods[1,2], which can be casted as a constrained bi-level optimization problem. Here, the unknowns of interest are the reconstructed image and the rigid motion parameters associated with each readout line (no intra-readout motion is considered). Despite considering nominal Cartesian sampling, spatial rotations result in effective irregular sampling in the k-space. The optimization problem is tackled via inexact variable projection schemes[3]. We employ conventional regularization methods for the motion parameters (although one should consider phase-wrapping issues), and structure-guided TV regularization for image reconstruction[4]. This term enforces the spatial gradient field of the target reconstruction to align with the normalized spatial gradient field of known prior contrast devoid of motion artifacts. We note that the prior and the target contrasts do not need to be co-registered.

Experiment description: We consider the following synthetic examples:

- numerical BrainWeb[5] T1w and T2w phantoms (256x256 images, 1mm in-plane);
- in-vivo reconstructions with the following specifications:
  - FOV = 224x224x133.5 mm , resolution = 1x1x3 mm , gap = 1.5mm, slices = 30;
  - T1w: multi-slice Spin Echo, TR/TE = 451/14 ms, flip angle = 70;
  - T2w: multi-slice Turbo Spin Echo, TR/TE = 3400/80 ms, flip angle =90, TSE factor = 15.

In both these cases, we retrospectively simulate artificial rigid motion artifacts for the T2w contrast and use the T1w contrast as the (uncorrupted) structural prior. The k -space data is acquired according to nominal Cartesian sampling. The motion type considered here is 2D in-plane "sudden" motion, which consists of two discrete positions where the change of position happens roughly halfway through the scan. Furthermore, we consider an

- in-vivo experiment with the following specifications:
  - T1w: Fast Field Echo, FOV = 260x260x260 mm , resolution = 0.77x0.77x1 mm , gap = 1 mm, slices = 520, TR/TE = 25/2 ms, flip angle = 30;
  - T2w: multi-slice Fast Field Echo, FOV = 260x260x260 mm , resolution = 0.81x0.81x3 mm , gap = 3 mm, slices = 174, TR/TE = 2804/23 ms, flip angle = 18.

  Motion-corruption was induced on the T2w image by instructing the volunteer to replicate 2D in-plane sudden motion, as described previously.

Again, the T1w image is used as prior, and nominal Cartesian sampling is considered. In Figures 1,2,3 we compare different reconstruction methods:

- conventional: inverse Fourier transform of corrupted data;
- joint: joint motion estimation and reconstruction with plain TV regularization;
- proposed: joint motion estimation and reconstruction with structure-guided TV regularization.

Discussion of the results: The results of the experiments described in the previous section aim at demonstrating the added value of structural priors compared to standard joint motion estimation and reconstruction schemes. These findings are consistent over a wide range of motion types. In particular, we compared a traditional joint estimation method and the proposed technique (the main difference being the use of structure-guided regularization) for sudden motion. We were able to consistently improve on the plain joint reconstruction results by several dB's in PSNR, and several points in SSIM, with higher resolution and fewer motion defects. The gain in resolution can be qualitatively assessed in all the "detail" comparisons in Figures 1,2,3. Some ghosting effects are more effectively removed by structure-guided regularization, as can be seen particularly in Figure 2.

Conclusions: Including structural prior information gleaned from well-resolved contrasts allows a more effective resolution of motion artifacts, which we demonstrated with synthetic and in-vivo studies. In the future, we aim at further assessments of the capabilities of the proposed method with more extensive clinical studies. For a more flexible tool, we also aim at including out-of-plane motion.

Acknowledgements: This publication is part of the project "Reducing re-scans in clinical MRI exams" (with project number 104022007 of the research program "IMDI, Technologie voor bemensbare zorg: Doorbraakprojecten") which is financed by The Netherlands Organization for Health Research and Development (ZonMW). The project is also supported by Philips Medical Systems Netherlands BV.

References:

1. Zaitsev, M., Maclaren, J., & Herbst, M. (2015). Motion artifacts in MRI: A complex problem with many partial solutions. Journal of Magnetic Resonance Imaging, 42(4), 887-901.
2. Godenschweger, F., Kägebein, U., Stucht, D., Yarach, U., Sciarra, A., Yakupov, R., ... & Speck, O. (2016). Motion correction in MRI of the brain. Physics in Medicine & Biology, 61(5), R32.
3. van Leeuwen, T., & Aravkin, A. Y. (2021). Variable Projection for NonSmooth Problems. SIAM Journal on Scientific Computing, (0), S249-S268.
4. Ehrhardt, M. J., & Betcke, M. M. (2016). Multicontrast MRI reconstruction with structure-guided total variation. SIAM Journal on Imaging Sciences, 9(3), 1084-1106.
5. Cocosco, C. A., Kollokian, V., Kwan, R. K. S., Pike, G. B., & Evans, A. C. (1997). Brainweb: Online interface to a 3D MRI simulated brain database. In NeuroImage.

Acknowledgments / Funding Information: Continue on this line

Figure 1. Delete this page if there are no figures or tables

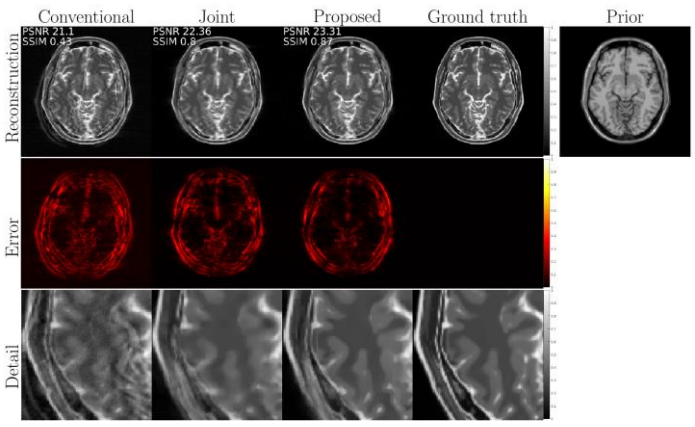

Figure 1: BrainWeb phantom: reconstruction results for different techniques. PSNR and SSIM metrics are computed after a preliminary rigid registration with the ground truth.

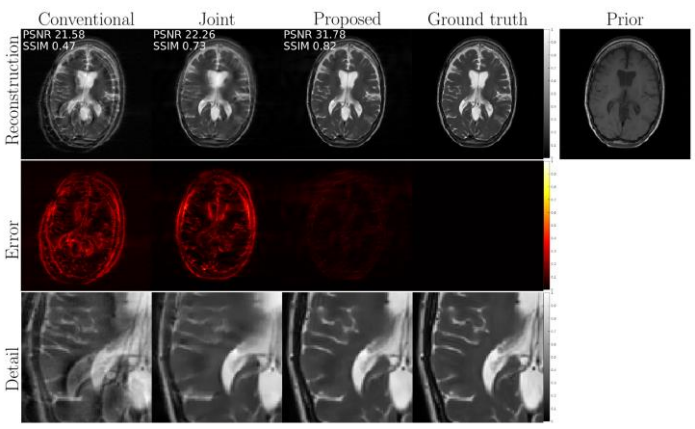

Figure 2: In-vivo data with retrospectively simulated motion artifacts: reconstruction results for different techniques. PSNR and SSIM metrics are computed after a preliminary rigid registration with the ground truth.

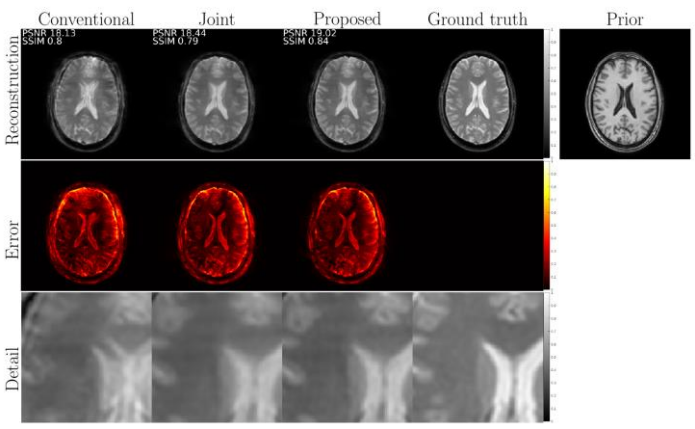

Figure 3: In-vivo data with motion perturbation induced by deliberate voluntary movement: reconstruction results with different techniques. PSNR and SSIM metrics are computed after a preliminary rigid registration with the reference image (obtained without voluntary motion).

DeepFLAIR: a neural network approach to mitigate signal loss in temporal lobe regions of 7 Tesla FLAIR images

D. Uher[1], J.F.A. Jansen[1,2], G.S. Drenthen[1,2], B.A. Poser[3], C.J. Wiggins[4], P.A.M. Hofman[2,5], L.G. Wagner[5], R.H.G.J. van Lanen[6], C.M. Hoeberigs[2,5], A.J. Colon[5], O.E.M.G. Schijns[1,5,6], and W.H. Backes[1,2]

[1]School for Mental Health and Neuroscience, Maastricht University, Maastricht, Netherlands; [2]Department of Radiology & Nuclear Medicine, Maastricht University Medical Centre, Maastricht, Netherlands; [3]Department of Cognitive Neuroscience, Maastricht University, Maastricht, Netherlands; [4]Scannexus, Maastricht, Netherlands; [5]Academic Centre for Epileptology, Kempenhaeghe/Maastricht University Medical Centre, Heeze/Maastricht, Netherlands; [6]Department of Neurosurgery, Maastricht University Medical Centre, Maastricht, Netherlands

Synopsis: In this study, we aimed to improve the 7T FLAIR image quality, especially within the temporal lobe regions which are often attenuated due to field inhomogeneities. A neural network using MP2RAGE and T_2-weighted images as inputs was set up to generate a new FLAIR-like image. The training was performed on the extratemporal-lobe voxels of the acquired 7T FLAIR image. The deepFLAIR showed a significant improvement in the signal-to-noise ratio and contrast-to-noise ratio in the temporal lobe regions in a number of cases. This study showed the potential to generate FLAIR-like images with reduced inhomogeneity artifacts and improved image quality.

Purpose: Epilepsy affects approximately 1% of the world-wide population, with temporal lobe epilepsy (TLE) being the most common focal epilepsy type[1]. In recent years, Ultra High Field Magnetic Resonance Imaging (UHF MRI) has been shown to improve the detection of subtle potential epileptogenic lesions in patients with focal epilepsy[2,3]. Unfortunately, the higher magnetic field strength in UHF imaging introduces increased inhomogeneities in B_0 and B_1 fields leading to image artifacts and signal attenuations[3,4]. The T_2-weighted FLAIR sequence is of particular interest to clinicians involved in the presurgical workup for epilepsy surgery due to its strong contrast and suppressing the cerebral spinal fluid, however it uses an inversion pulse and refocusing pulses which suffer from these inhomogeneities[4,5]. For the FLAIR sequence, the (inferior) temporal lobe area is often affected by signal attenuation (see Figures 1C-E, 3A). In this study, we attempt to improve the signal loss due to UHF inhomogeneities in temporal regions by creating a neural-network-generated FLAIR image ("deepFLAIR") which could potentially reveal subtle temporal neocortical lesions.

Methods: Eight patients (mean age 31y; range 21-46y; 5 females) with chronic, drug-resistant epilepsy with a suspected epileptogenic zone (2 patients with 3T-positive lesions) were selected for this study. All patients were scanned on a 7T MRI (Siemens Healthcare, Erlangen, Germany) with a 32-element channel phased-array head coil and bilaterally positioned dielectric pads. The following structural brain scans were acquired: MP2RAGE (0.7x0.7x0.7mm; TE=2.47ms; TR=5030ms; TI_1=900ms; TI_2=2750ms), T_2-weighted (transverse slices, 0.6x0.6x2.0mm; TE=283ms; TR=4000ms), SPACEFLAIR (0.8x0.8x0.8mm; TE=303ms; TR=8000ms; TI=2330ms). All scans were coregistered to the quantitative T_1 map and the T_1 map was segmented into grey matter (GM) and white matter (WM).

A non-linear regression multilayer perceptron (MLP) has been set up to reconstruct the 7T FLAIR images and boost the signal in the temporal lobe areas which are being affected by the signal attenuations due to the field inhomogeneities. The MLP was trained on 4 input images (see Figure 1A-D) and consisted of 4 hidden layers (16; 64; 32; 8 neurons). The output layer consisted of a single neuron. The MLP works on a voxel-wise basis, meaning that each voxel in the generated FLAIR-like image is determined by the corresponding voxels from the input images. The training was done on slices outside the temporal lobe region. The training lasted for 10 epochs with batch size=100. After the training, the entire scanned area was reconstructed using the trained model to form the deepFLAIR image.

Right and left temporal lobe regions-of-interest (ROIs) sized 28x28x28mm were manually delineated to facilitate the evaluation (see Figure 2B). The quality of the output image was evaluated by calculating the signal-to-noise ratio (SNR) of the WM and contrast-to-noise ratio (CNR) between the GM and WM in the temporal lobe ROIs using the following equations:

$$1)\ SNR = \frac{\mu}{\sigma} \qquad 2)\ CNR = \frac{|\mu_{GM} - \mu_{WM}|}{\sqrt{\frac{\sigma_{GM}^2 + \sigma_{WM}^2}{2}}}$$

where μ and σ are the mean voxel intensity and the standard deviation from the selected tissue (GM or WM) within the ROI, respectively. The SNR and CNR from right and left ROIs were statistically compared via a Wilcoxon signed-rank test between the originally acquired 7T FLAIR and the deepFLAIR images.

Results: Figure 3 shows the generated deepFLAIR image compared with the acquired 7T FLAIR images for a representative subject. When visually assessing the acquired images, the right temporal lobes seemed to be more affected by the magnetic inhomogeneities than their left counterparts. The statistical test revealed a significant improvement in the deepFLAIR image in SNR_{WM} ($p=0.016$) and CNR ($p=0.023$) in the right temporal lobe area. The deepFLAIR approach showed an increase in both SNR_{WM} and CNR for 10 out of 16 temporal lobes. The SNR_{WM} and CNR results were visualized in a paired line plot in Figure 4.

Discussion: This study demonstrated a concept of neural-network-informed improvement of the 7T FLAIR image contrast. A statistically significant improvement was found for both SNR_{WM} and CNR in the right temporal lobes. This suggests that the deepFLAIR approach could have a significant impact in the more severely attenuated temporal lobe regions and therefore facilitate a more confident diagnosis. The per-subject nature of the deepFLAIR provides independence from an extensive subject database but also limits the training data to merely a single brain. The concept seems promising and utilizing more sophisticated network architectures, alterations of the training data or extension across multiple subjects could result in further improvements. This work also needs to be expanded with more varied cases including specific types of epileptogenic lesions and careful prior evaluation by an independent neuroradiologist. The deepFLAIR, despite its qualities, should still be interpreted with care. The main limitation is the lack of a golden standard in the temporal lobe regions, which could be potentially provided with the use of Universal Pulses[4].

Conclusion: This conceptual study presented a possibility to generate FLAIR-like images with reduced inhomogeneity artifacts in the inferior anterior/lateral temporal lobe and overall improved tissue contrast. Further optimizations of the network and the training dataset might provide a significant boost in the image quality and its ability to fully reconstruct the attenuated temporal lobe areas.

References:

1. Fiest KM, Sauro KM, Wiebe S, et al. Prevalence and incidence of epilepsy: A systematic review and meta-analysis of international studies [published correction appears in Neurology. 2017 Aug 8;89(6):642]. Neurology. 2017;88(3):296-303. doi:10.1212/WNL.0000000000003509

2. Wang I, Oh S, Blümcke I, et. al. Value of 7T MRI and post-processing in patients with nonlesional 3T MRI undergoing epilepsy presurgical evaluation. Epilepsia. 2020 Nov;61(11):2509-2520. doi: 10.1111/epi.16682.

3. Opheim G, van der Kolk A, Markenroth Bloch K, et. al. 7T Epilepsy Task Force Consensus Recommendations on the Use of 7T MRI in Clinical Practice. Neurology. 2021 Feb 16;96(7):327-341. doi: 10.1212/WNL.0000000000011413

4. Gras V, Mauconduit F, Vignaud A, et. al. N. Design of universal parallel-transmit refocusing kT-point pulses and application to 3D T2-weighted imaging at 7T. Magn. Reson. Med. 2018; 80: 53-65. https://doi.org/10.1002/mrm.27001

5. van Lanen RHGJ, Colon AJ, Wiggins CJ, et. al. Ultra-high field magnetic resonance imaging in human epilepsy: A systematic review. NeuroImage: Clinical. 2021;30. 102602. https://doi.org/10.1016/j.nicl.2021.102602

Acknowledgments / Funding Information: Funded by the Dutch Epilepsy Foundation, grant nr. 20-09

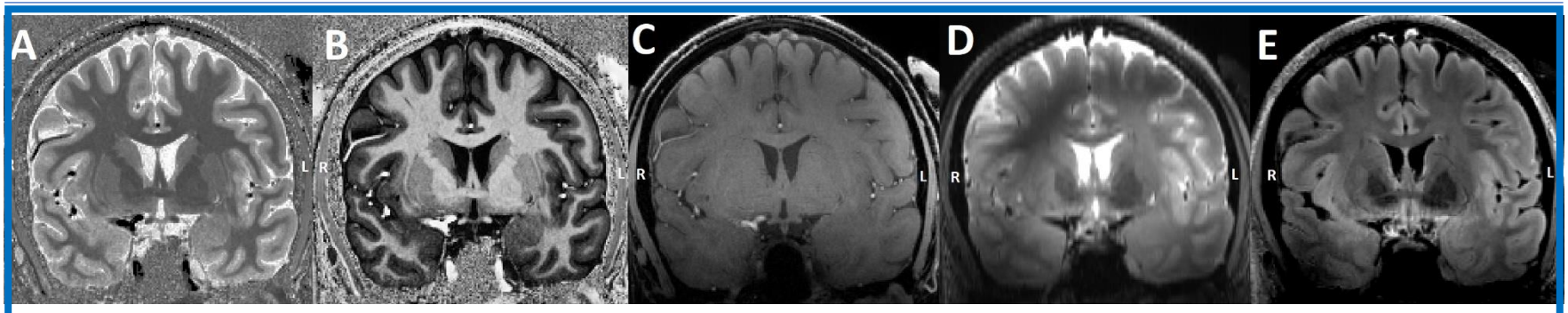

Figure 1: Neural network training input brain scans. A: MP2RAGE derived quantitative T_1 map; B: MP2RAGE derived unified image; C: MP2RAGE second inversion image; D: T_2-weighted image; E: acquired 7T FLAIR image. Note the signal loss in the temporal lobe on images C,D and E. The network learns to predict the voxel intensities in E from the voxel intensities in A,B,C and D.

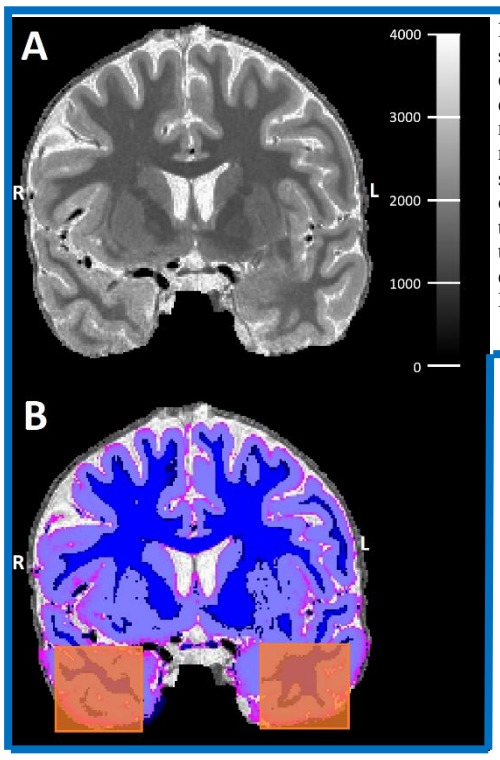

Figure 2: Visualization of the T_1 map segmentation and the selected ROIs for evaluation. A: MP2RAGE derived quantitative T_1 map with a color bar in milliseconds; B: Grey matter and white matter segmentation output with the selected ROIs (orange rectangles) overlayed. ROIs were sized 28x28x28mm to encapsulate majority of the inferior temporal lobe. The segmentation was done using SPM12, a free toolbox for Matlab (Mathworks Inc., 2020)

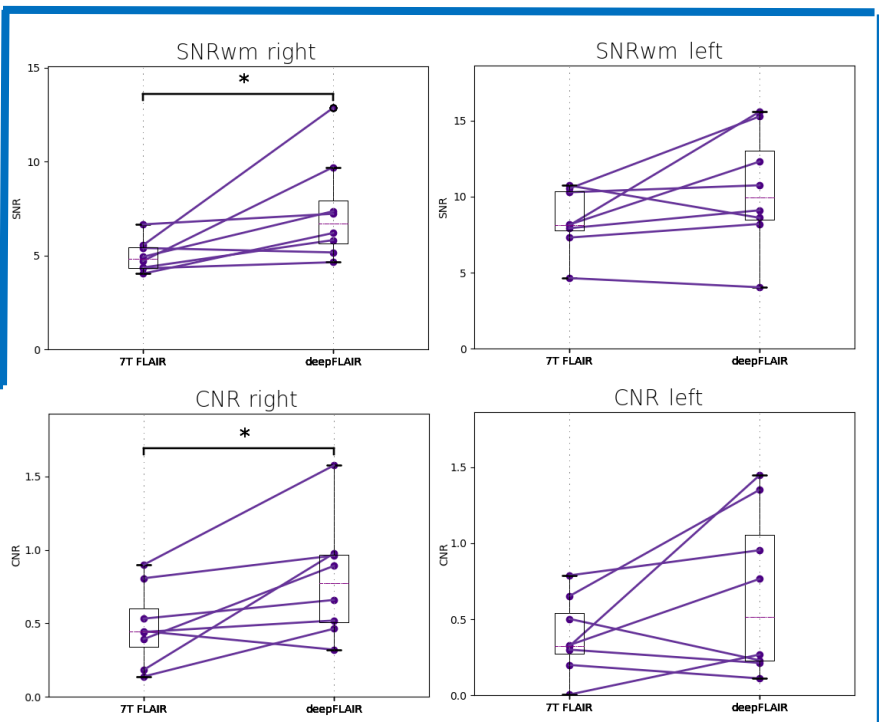

Figure 4: Paired line chart representing the improvement in temporal lobes in terms of signal-to-noise and contrast-to-noise ratios by utilizing the deepFLAIR approach. Each purple line represents a single subject and the change in SNR/CNR between the acquired 7T FLAIR and the generated deepFLAIR. Asterisk * indicates a significant difference by Wilcoxon signed-rank test ($p<0.05$). SNR – signal-to-noise ratio; CNR – contrast-to-noise ratio

Figure 3: Representative example of the deepFLAIR results.
A: acquired 7T FLAIR images;
B: generated deepFLAIR images;
C: detail of the temporal lobe area with strong signal loss in the 7T FLAIR image;
Detail of the temporal lobe area in the generated deepFLAIR image.
R-right; L-left.

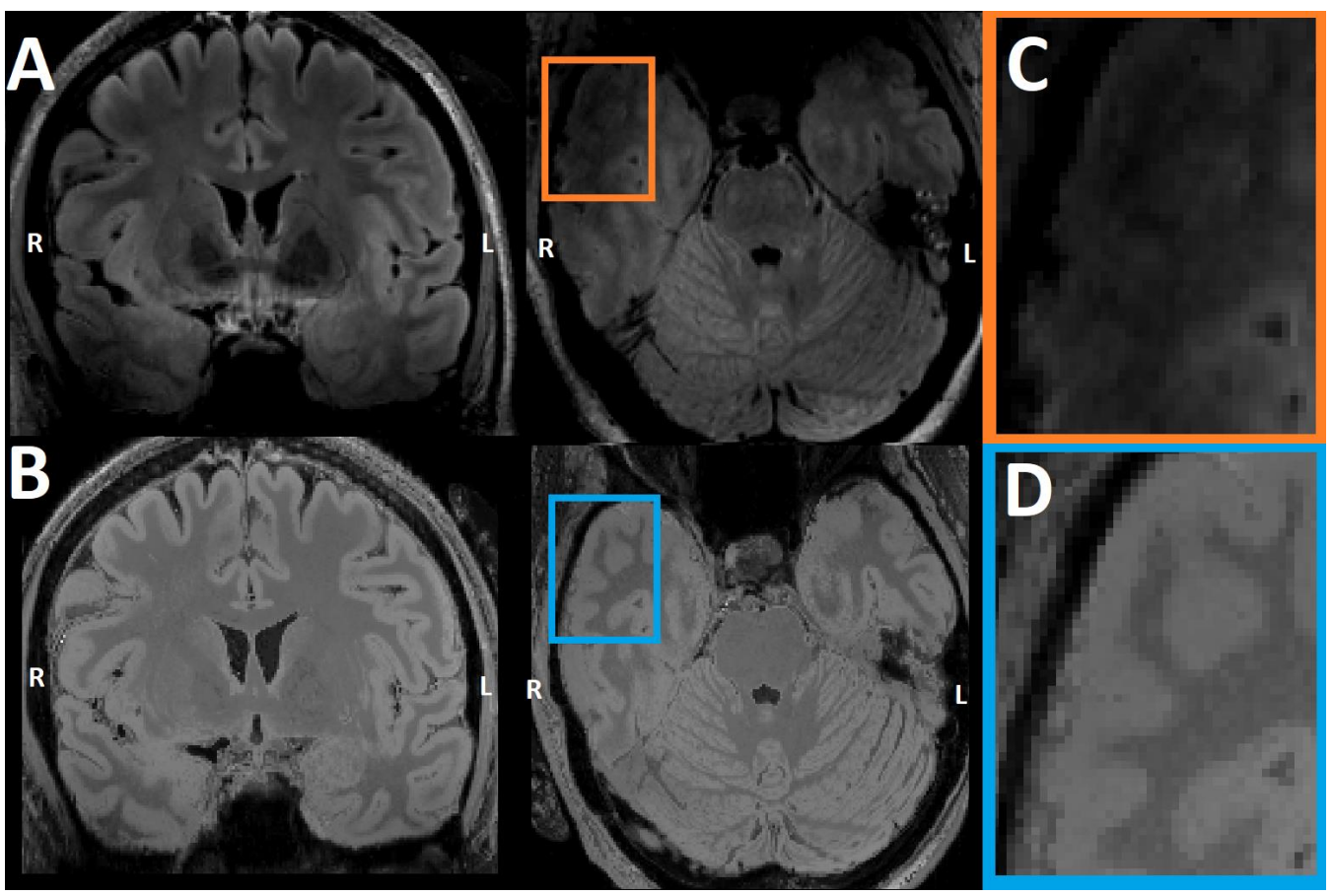

Cross-sectional robustness of 6 freely available software packages for brain volume measurements in multiple sclerosis

D.R. van Nederpelt[1], H. Amiri[1,2], A. Mariyampillai[1], I. Brouwer[1], S. Noteboom[3], F. Barkhof[1,4], J.P.A. Kuijer[1], H. Vrenken[1]

[1] Department of Radiology and Nuclear Medicine, MS Center Amsterdam, Amsterdam Neuroscience, Amsterdam UMC, location VUmc, De Boelelaan 1118, 1081 HZ Amsterdam, The Netherlands. [2] Neuroscience Research Center, Institute of Neuropharmacology, Kerman University of Medical Sciences, Kerman, Iran. [3] Department of Anatomy and Neurosciences, Amsterdam UMC, location VUmc, The Netherlands.[4] Institutes of Neurology and Healthcare Engineering, UCL London, London, UK.

Synopsis: Automated segmentation of brain MR images has paved the way for large cohort atrophy studies in multiple sclerosis (MS). A variety of automated software packages is available. Here we aimed to quantify brain volume differences measured by six freely available software packages on data from 21 MS patients all scanned thrice on three different MR scanners. While intra-class correlation coefficients were high, systematic differences between scanners were found for every software. This suggests that direct comparison of volumes acquired with different scanners is not possible and standardization is needed.

Summary of Main Findings: ICCs for volume measurements in MS were high; however, systematic differences between scanners were found for every software. This suggests that direct comparison of volumes acquired with different scanners is not possible and standardization is needed.

Introduction: Brain atrophy measurement using magnetic resonance imaging (MRI) is an important way to assess disease progression in multiple sclerosis (MS)[1, 2]. Automated brain segmentation techniques enable effective processing of images instead of the time-consuming manual segmentation. However, brain volumetry in MS is still challenging, e.g. due to differences in acquisition protocols, analysis software and disease-related factors such as lesions[3]. Furthermore, segmentation is also affected by technological differences between scanner vendors, models or field strength[4]. These effects are more pronounced in multi-center trials and especially in the clinical setting, where MR scanners and acquisition protocols can vary frequently. Quantifying differences will provide an improved understanding of the resulting variability in atrophy measures, as well as mitigation of that variability. For the segmentation, several automated methods have been proposed, applying different approaches. Here we perform a comparison of reliability and repeatability between three different MR-scanners applying six freely available brain volume segmentation techniques. Additionally, we analyze the effect of lesion-filling on robustness in MS-brain volumetry.

Methods: 21 subjects with MS (relapsing remitting MS n=16; secondary progressive MS n=1; and primary progressive MS n=4), underwent a scan and rescan on three 3T MRI scanners (GE MR750, Philips Ingenuity, Toshiba Vantage Titan). The acquired images were 3D T1-weighted and on the GE an additional 3D FLAIR was scanned, using locally optimized acquisition protocols. Details of the acquisition have been described elsewhere[5]. Lesion segmentation on the FLAIR images was performed with nicMS lesions using an optimal threshold of 0.5[6, 7]. The lesion probability maps were registered to the vendor-specific T1 space with FLIRT[8]. Thereafter, lesion filling was performed using LEAP[3]. Both filled and un-preprocessed 3D T1 images were segmented with FreeSurfer (v7.1), FSL (SIENAX & FIRST), Sequence Adaptive Multimodal SEGmentation (SAMSEG), FastSurfer (a deep learning approach based on FreeSurfer), CAT-12 and SynthSeg (a deep learning approach trained on synthetic data)(**Figure 1**) [9-16]. For all software packages the latest version and the recommended options were used (e.g. in FreeSurfer -3T –all). Both repeatability and reproducibility were assessed cross-sectionally using the intra-class correlation coefficient (ICC) based on the 95% confidence interval for absolute agreement and for consistency, respectively. The ICC-values were classified according to the standards of Koo and Li (2016)[17]. Reproducibility was additionally assessed with repeated measures ANOVA or Friedmann test for non-parametric data. If appropriate, post-hoc testing was performed using pairwise t-tests or Wilcoxon signed rank tests. Reported p-values are Bonferroni corrected.

Results: The overall between-scanner ICC for consistency was good to excellent (>0.7) for all the software, except for some small structures such as the accumbens. **Figure 2** shows that SAMSEG seems to have the highest ICC for between scanner agreement, followed by FastSurfer and SynthSeg. The within-scanner agreement is on average higher than the between-scanner agreement. However, systematic differences in volume measurements between-scanners are found in all the software in both gray and white matter (**Figure 3** and **Figure 4**). For every software package the white matter for GE has a lower volume compared to Toshiba and Philips (p<0.001, except for SynthSeg). Conversely, the volume of gray matter segmented from GE scans was significantly higher compared to both Toshiba and Philips scanners (p<0.001 and for SynthSeg p<0.05). Lesion filling did not significantly improve the ICC score, but we did see an increase in WM volumes, as expected.

Discussion: In this study we compared the repeatability and reliability of 6 freely available software packages on three different 3T MR-scanners. The within-scanner agreement was higher than the between-scanner agreement. Furthermore, systematic differences exist between scanners for each software. This implies that in a clinical setting or a cross-sectional multi-center/multi-scanner trial the patients have to be scanned on the same scanner to detect relatively small yearly atrophy rate in MS[18]. Our results concerning between-scanner differences are consistent with previous similar studies in MS[19, 20]. On average the between-scanner ICC scores are higher in SAMSEG suggesting that sequence adaptive software has a better reproducibility for multi-scanner studies. The FSL and FreeSurfer ICC scores were lower compared to other software. Noticeably, FastSurfer ICCs were higher than FreeSurfer, even though FastSurfer has been trained on FreeSurfer segmentation output instead of manual segmentations. A disadvantage of CAT-12 is that it does not explicitly segment the deep gray matter structures, but uses an atlas to get white matter and gray matter volumes. We unfortunately did not have manually outlined segmentations to check the quality of the segmentation of the images. In addition, not every segmentation was visually inspected for correctness, but abnormal volumes were excluded from the analyses.

Conclusions: Although both between- and within ICCs are high, systematic differences between scanners are present suggesting the need for standardization for between-scanner volume-measurements. It is worth mentioning that there are several more available software packages and that their accuracy assessment is warranted.

References:

1. Andravizou, A., et al., *Brain atrophy in multiple sclerosis: mechanisms, clinical relevance and treatment options.* Autoimmunity Highlights, 2019. **10**(1): p. 7.
2. Liu, Y., et al., *Different patterns of longitudinal brain and spinal cord changes and their associations with disability progression in NMO and MS.* Eur Radiol, 2018. **28**(1): p. 96-103.
3. Chard, D.T., et al., *Reducing the impact of white matter lesions on automated measures of brain gray and white matter volumes.* J Magn Reson Imaging, 2010. **32**(1): p. 223-8.
4. Amiri, H., et al., *Urgent challenges in quantification and interpretation of brain grey matter atrophy in individual MS patients using MRI.* Neuroimage Clin, 2018. **19**: p. 466-475.
5. Weeda, M.M., et al., *Validation of mean upper cervical cord area (MUCCA) measurement techniques in multiple sclerosis (MS): High reproducibility and robustness to lesions, but large software and scanner effects.* Neuroimage Clin, 2019. **24**: p. 101962.
6. Weeda, M.M., et al., *Comparing lesion segmentation methods in multiple sclerosis: Input from one manually delineated subject is sufficient for accurate lesion segmentation.* NeuroImage. Clinical, 2019. **24**: p. 102074-102074.
7. Valverde, S., et al., *One-shot domain adaptation in multiple sclerosis lesion segmentation using convolutional neural networks.* Neuroimage Clin, 2019. **21**: p. 101638.
8. Jenkinson, M., et al., *Improved optimization for the robust and accurate linear registration and motion correction of brain images.* Neuroimage, 2002. **17**(2): p. 825-41.
9. Dale, A.M., B. Fischl, and M.I. Sereno, *Cortical surface-based analysis. I. Segmentation and surface reconstruction.* Neuroimage, 1999. **9**(2): p. 179-94.
10. Fischl, B., M.I. Sereno, and A.M. Dale, *Cortical surface-based analysis. II: Inflation, flattening, and a surface-based coordinate system.* Neuroimage, 1999. **9**(2): p. 195-207.
11. Smith, S.M., et al., *Accurate, robust, and automated longitudinal and cross-sectional brain change analysis.* Neuroimage, 2002. **17**(1): p. 479-89.
12. Patenaude, B., et al., *A Bayesian model of shape and appearance for subcortical brain segmentation.* NeuroImage, 2011. **56**(3): p. 907-922.
13. Puonti, O., J.E. Iglesias, and K. Van Leemput, *Fast and sequence-adaptive whole-brain segmentation using parametric Bayesian modeling.* NeuroImage, 2016. **143**: p. 235-249.
14. Henschel, L., et al., *FastSurfer - A fast and accurate deep learning based neuroimaging pipeline.* NeuroImage, 2020. **219**: p. 117012.
15. Gaser, C. and R. Dahnke. *CAT-A Computational Anatomy Toolbox for the Analysis of Structural MRI Data*. 2016.
16. Billot, B., et al., *SynthSeg: Domain Randomisation for Segmentation of Brain MRI Scans of any Contrast and Resolution.* arXiv e-prints, 2021: p. arXiv: 2107.09559.
17. Koo, T.K. and M.Y. Li, *A Guideline of Selecting and Reporting Intraclass Correlation Coefficients for Reliability Research.* J Chiropr Med, 2016. **15**(2): p. 155-63.
18. De Stefano, N., et al., *Establishing pathological cut-offs of brain atrophy rates in multiple sclerosis.* Journal of Neurology, Neurosurgery & Psychiatry, 2016. **87**(1): p. 93-99.
19. Guo, C., et al., *Repeatability and reproducibility of FreeSurfer, FSL-SIENAX and SPM brain volumetric measurements and the effect of lesion filling in multiple sclerosis.* Eur Radiol, 2019. **29**(3): p. 1355-1364.
20. Biberacher, V., et al., *Intra- and interscanner variability of magnetic resonance imaging based volumetry in multiple sclerosis.* NeuroImage, 2016. **142**: p. 188-197.

Acknowledgments / Funding Information: This research was funded by ZonMW and the Dutch MS Research Foundation. Data acquisition was part of a project sponsored by Novartis.

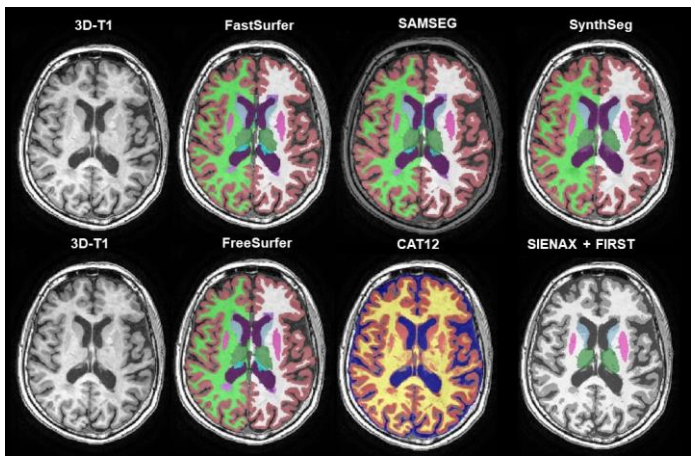

Figure 1. Example of segmentations for 1 subjects on the 3T GE scanner and the first scan (un-preprocessed). Please note that CAT12 and SIENAX+FIRST have different color scales.

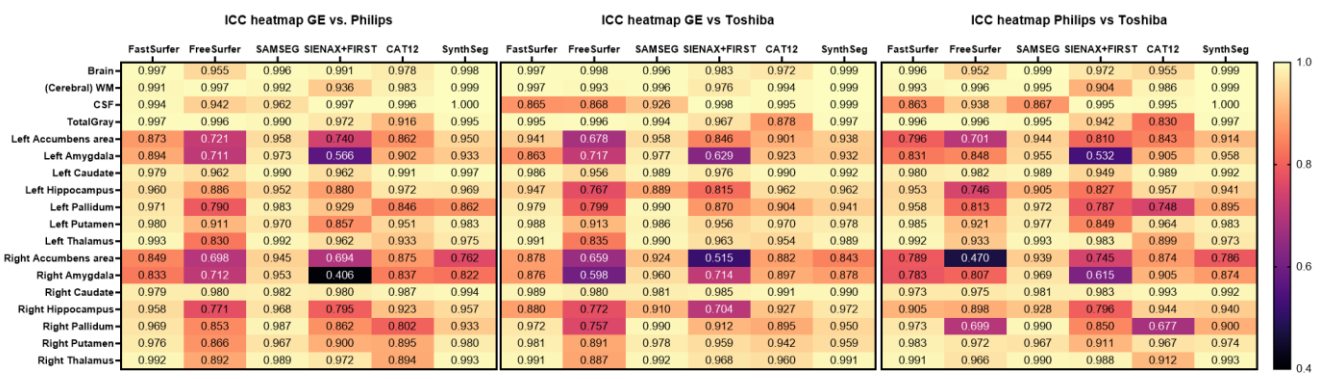

Figure 2. Heatmap of the ICC for Consistency (95% confidence interval) for all three pairwise scanner combinations for the un-preprocessed T1w images.

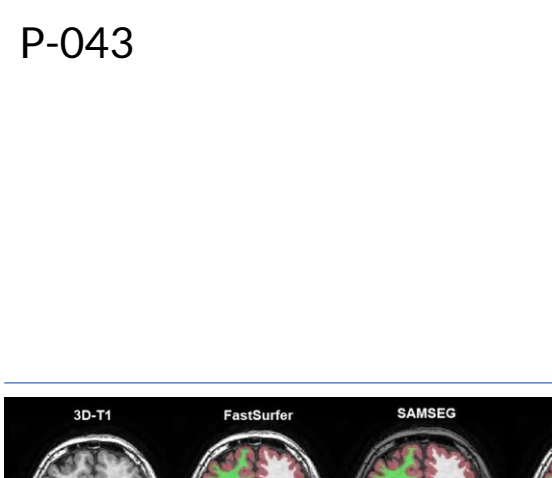

Figure 3. Boxplot (Tukey, line at median) of the total gray matter volume measurements grouped per scanner and software for the un-preprocessed images. * p<.05, ** p<.01, *** p<.001.

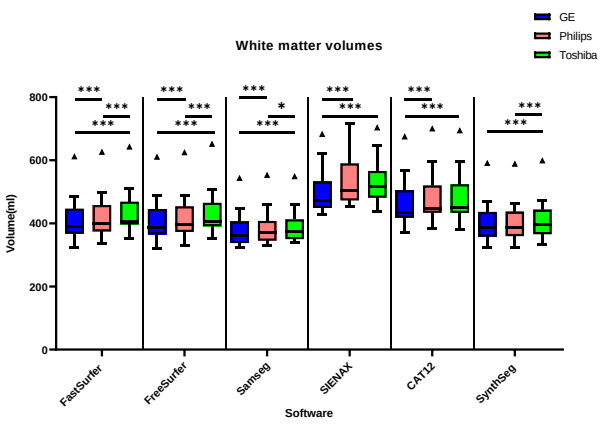

Figure 4. Boxplot (Tukey, line at median) of the white matter volume measurements grouped per scanner and software. Note that the volumes for FastSurfer, FreeSurfer, SAMSEG and SynthSeg are lower because these only consider the cerebral white matter. * p<.05 ** p<.01 *** p<.001.

M-Estimator for Robust Parameter Fitting in Quantitative Cardiac T1 Mapping

Y. Zhao [1], C. Yang[1], L. Huang[2], L. Xia[2], S. Weingärtner[1] and Q. Tao[1]

[1]Department of Imaging Physics, Technische Universiteit Delft, Delft, Netherlands; [2]Department of Radiology, Tongji Hospital, Tongji Medical College, Huazhong University of Science and Technology, Wuhan, China

Synopsis: Quantitative cardiac T1 mapping involves nonlinear parameter estimation after MR acquisition. The widely used minimum mean square error (MMSE) estimator assumes Gaussian additive noise, and can be sensitive to outliers of non-Gaussian nature, such as those caused by cardiac motion. In this work, we propose to apply robust loss functions, which are part of the M-estimator family, with increased robustness to outliers. Experiments on MOLLI and SAPPHIRE sequences showed that the M-estimators were able to improve the T1 estimation robustness, significantly reducing the standard deviation (SD) error of the estimated T1 map in comparison to MMSE.

Introduction: In cardiac T1 Mapping, the signal intensity is commonly modelled as a non-linear function of inversion time, parameterized by a set of variables. Estimation of these parameters involves a non-linear parametric fitting procedure. The minimum mean square error (MMSE) estimator is most widely used and can be interpreted as a maximum likelihood estimator under the assumption that the additive measurement noise is a zero-mean stationary Gaussian process. However, in the MR T1 mapping data, the noise may not follow a Gaussian model, especially as cardiac motion (or imperfect motion correction) can give rise to outliers (i.e. misalignment in structure) for fitting.

To achieve a robust T1 estimate with improved robustness to motion-induced outliers, we propose to employ M-estimators [1] for non-linear parameter estimation of cardiac T1 mapping. The loss function of an M-estimator is designed in a way that outliers will have a reduced impact on the final estimate. In this work, we evaluate three M-estimator variants on two types of MR T1 mapping sequences: Modified Look-Locker Inversion Recovery (MOLLI) [2] and Saturation Pulse Prepared Heart rate independent Inversion-Recovery (SAPPHIRE) sequence [3].

Methods An M-estimator replaces the ℓ_2-norm in MMSE with a robust loss function ρ:

$$\theta^* = \arg\min \sum_k \rho\left(|y_k - f_\theta(t_k)|^2\right) = \arg\min \rho(r_k^2)$$

where y_k is the measurement at t_k, f is the nonlinear signal intensity model parameterized by θ, and r_k denotes the k-th fitting residual. We evaluated three M-estimator variants, namely, the Huber, Cauchy and Welsch losses:

$$\rho_{Huber}(r_k^2) = r_k^2 \cdot \mathbb{I}(|r_k| < S) + (2S \cdot |r_k| - S^2) \cdot \mathbb{I}(|r_k| \geq S)$$

$$\rho_{Cauchy}(r_k^2) = S^2 \cdot \ln(1 + \frac{r_k^2}{S^2})$$

$$\rho_{Welsch}(r_k^2) = S^2 \cdot (1 - \exp(-\frac{r_k^2}{S^2}))$$

where $\mathbb{I}(\cdot)$ is the indicator function, and S is a user-defined parameter to adjust the tolerance to the residual error. In this work, we set S adaptively: $S = r_{mid} \cdot \mathbb{I}(r_{mid} < r_{th}) + S_{min} \cdot \mathbb{I}(r_{mid} \geq r_{th})$, where r_{mid} is the median of the absolute MMSE residual error. The error median r_{mid} reflects the residual distribution of inliers in the presence of a moderate number of outliers. However, a high proportion of outliers may cause severe failure of MMSE, and consequently an elevated r_{mid} much higher than a predefined threshold r_{th}. In such cases, we set S as a limited value S_{min} to curb the estimator's tolerance to residual errors. The Huber loss is a combination of ℓ_1- and ℓ_2-norm losses, which suppresses the influence of outliers if r_k is large. In contrast, the other two loss functions, the *redescending* functions, ignore outliers completely as the residual error approaches infinity (hence enforcing sparsity). The Welsch loss tends to ignore more outliers than the Cauchy loss at a fixed S.

In our experiments, we solved the optimization problem with non-derivative based simplex-search solver, with the initial value set as the MMSE estimate. The MMSE and M-estimator variants were evaluated on 50 MOLLI scans (3.0T Ingenia, Philips Healthcare, Best, The Netherlands), in total 131 short-axis slices, with or without motion correction (MOCO) [4] , and on 12 SAPPHIRE scans (3.0T Siemens Magnetom Prisma, Siemens Healthineers, Erlangen, Germany) without MOCO, in total 119 short-axis slices. The SD error map was estimated for each T1 map using the definition in [5]. The myocardium regions were manually delineated as the region of interest (ROI).

Results and Discussions: Figure 1-a) illustrates an example of parametric fitting with motion-induced outliers, where the Cauchy M estimator yields a robust fitting to the majority of measurements. The statistics of the mean SD error in the myocardium ROI are shown in Figure 1-b) and 1-c), respectively. For the MOLLI scans without MOCO, all three M-estimator variants reduced the mean myocardial SD error significantly. The largest reduction is observed for the redescending variants, the Cauchy and Welsch losses, from 49.3 ± 16.6 ms (MMSE) to 41.6±16.6 ms (Cauchy), $p < 0.001$ by paired T-test. On the SAPPHIRE scans, the mean myocardial SD decreased slightly from 72.6±8.3 ms to 70±6.5 ms with the Cauchy loss, with $p=0.02$. In comparison to the MMSE estimator, the Cauchy estimator had a bias of -12.9 ± 14.3 ms on motion-corrected MOLLI scans and 20 ± 12.2 ms on SAPPHIRE scans, in terms of the estimated myocardial T1 values. Figure 3 shows the estimated T1 and SD maps of an exemplar MOLLI and SAPPHIRE acquisition, both without MOCO. From the MOLLI images, it can be observed that the sharpness of the myocardial border (lower septum) slightly improved when using the M-estimators, with reduced SD error in the same region. However, the Welsch variant can potentially introduce noise susceptible voxels in the estimated T1 map, as the fit may become instable if too many measurement points are discounted.

Conclusion: Nonlinear parameter estimation in quantitative cardiac T1 mapping can be realized by the M-estimators, which are more robust to non-Gaussian noises and motion-induced outliers than the conventional MMSE. Our study showed that M-estimators were able to significantly reduce the SD error in T1 map estimation for both MOLLI and SAPPHIRE sequences, in comparison to the MMSE estimator. The Cauchy variant outperformed other variants in terms of SD error reduction and solution stability.

References

1. De Menezes, D. Q. F., et al. "A review on robust M-estimators for regression analysis." Computers & Chemical Engineering (2021): 107254.
2. Messroghli, D.R., et al. "Modified Look‐Locker inversion recovery (MOLLI) for high‐resolution T1 mapping of the heart." Magnetic Resonance in Medicine: An Official Journal of the International Society for Magnetic Resonance in Medicine 52.1 (2004): 141-146.
3. Weingärtner, S., et al. "Combined saturation/inversion recovery sequences for improved evaluation of scar and diffuse fibrosis in patients with arrhythmia or heart rate variability." Magnetic resonance in medicine 71.3 (2014): 1024-1034.
4. Tao, Q., et al. "Robust motion correction for myocardial T1 and extracellular volume mapping by principle component analysis‐based groupwise image registration." Journal of Magnetic Resonance Imaging 47.5 (2018): 1397-1405.
5. Kellman, P. et al. "T1 and extracellular volume mapping in the heart: estimation of error maps and the influence of noise on precision." Journal of Cardiovascular Magnetic Resonance 15.1 (2013): 1-12.

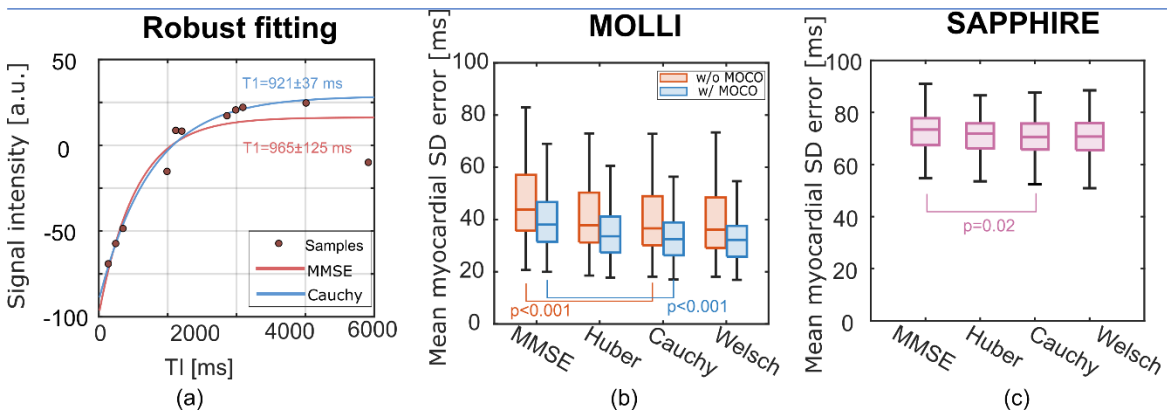

Figure 1. (a) A robust fitting example with outliers induced by motion; (b) Mean SD error within the myocardium region of all MOLLI scans (N=131); (c) Mean SD error within the myocardium region of all SAPPHIRE scans (N=119).

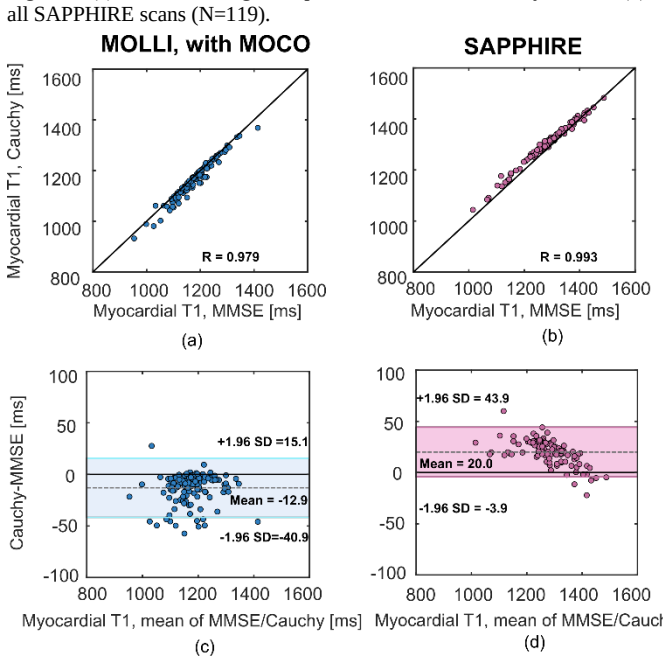

Figure 2. The correlation and Bland-Altman plots of estimated myocardial T1 medians using MMSE and Cauchy on MOLLI (left) and SAPPHIRE (right) scans.

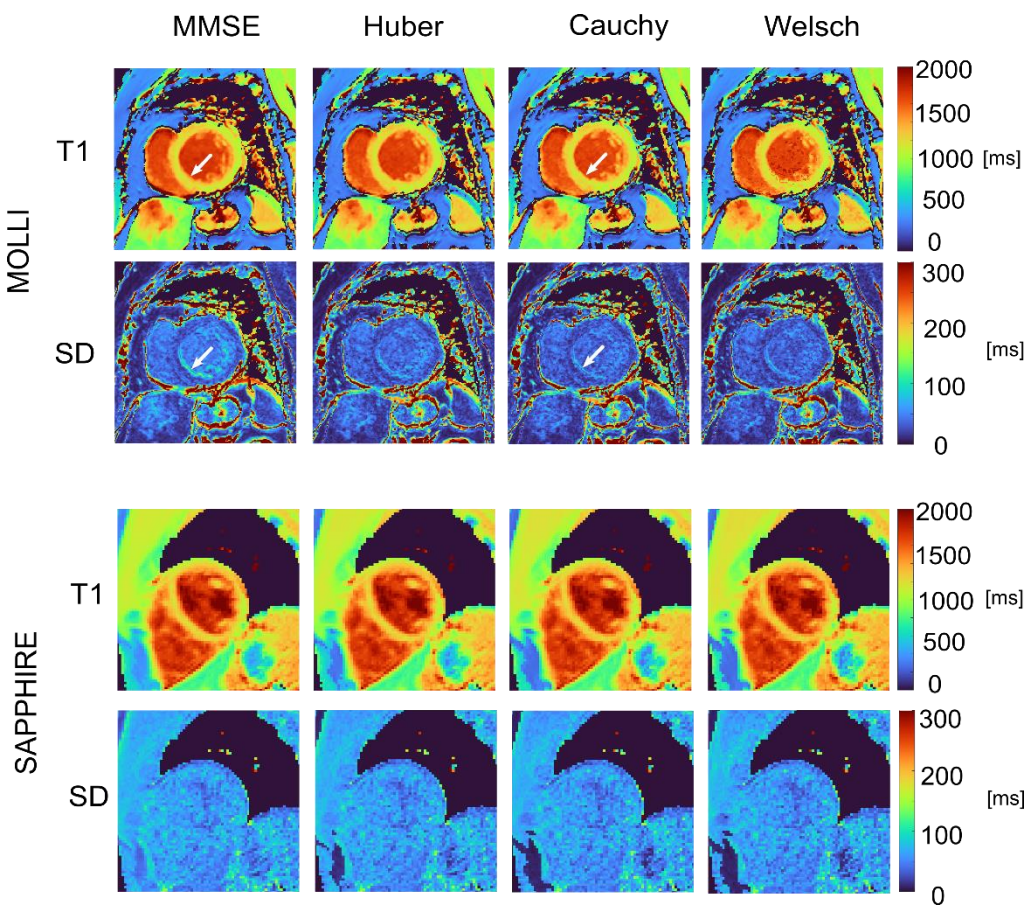

Figure 3. Two examples of the estimated T1 map and SD error map from MOLLI and SAPPHIRE, respectively. White arrow in the upper panel indicates region of improvement in fitting.

Repeatability and accuracy of MR-STAT quantitative T1 and T2 measurements

O. van der Heide[1,2], M. Fuderer[1,2], H. Liu[1,2], C.A.T. van den Berg[1,2], A. Sbrizzi[1,2]
[1]Computational Imaging Group for MR Diagnostics and Therapy, Center for Image Sciences, University Medical Center Utrecht, Utrecht, The Netherlands
[2]Department of Radiology, Division of Imaging and Oncology, University Medical Center Utrecht, Utrecht, The Netherlands

Synopsis: MR-STAT is a quantitative MRI technique that obtains multiple tissue parameter maps (e.g. T1, T2) from a single short scan. In this study we perform an accuracy and repeatability assessment using a Cartesian FISP based sequence by repeatedly scanning Europsin gel tubes and comparing the results against reference measurements. We observe coefficients of variation between 0.5% and 1.9% for T1 and between 2.0% and 7.2% for T2. The mean relative errors as compared to the reference measurements are -1.5% for T1 and 5.8% for T2.

Introduction: MR-STAT[1] is a quantitative MRI technique that allows multiple quantitative tissue parameter maps (e.g. T1, T2 and proton density) to be reconstructed from a single, short transient-state scan. A large-scale non-linear inversion problem is solved in which the parameter maps are directly fitted against the measured time-domain data. In previous work, the feasibility of the MR-STAT approach has been demonstrated in-vivo[2]. For clinical adoption of MR-STAT, accuracy, repeatability and reproducibility of reconstructed quantitative values is of high importance.[3] In this study we perform an accuracy and repeatability study of MR-STAT using a Cartesian FISP-based sequence by scanning a phantom consisting of gel tubes over multiple sessions and comparing the results against reference measurements.

Methods: A 2D gradient-spoiled gradient-echo pulse sequence with a linear, Cartesian gradient encoding scheme was employed. At each TR, the flip angle changed according to an optimized pattern that was generated using the BLAKjac[4] technique (Fig. 1). The TR and TE remained fixed throughout the sequence at 7.5 ms and 3.8 ms, respectively. The sequence was preceded by a non-selective adiabatic inversion pulse. Per scan, a total of 1344 readouts were acquired in 10 s.

Twelve tubes with gadolinium-doped gel (TO5, Eurospin II test system, Scotland, Fig. 2) were scanned on two different days on a 3T MR system (Elition, Philips Healthcare, Best, The Netherlands) using thirteen channels of the vendors receive headcoil. Each day, the gel phantoms were scanned four times over two separate sessions. Between the sessions, the phantom was removed and repositioned resulting in sixteen separate measurements. The scanner room temperature was measured at approximately 22 degrees celcius each session.

Prior to reconstruction, an SVD compression was used to combine the measured data of all channels to single virtual coil data. The MR-STAT reconstructions were then performed on an NVIDIA Tesla V100-PCIE-16GB GPU card[5] and the reconstruction software was written in the Julia programming language[6]. Flip-angle dependent slice profile corrections were applied as well as a B1 correction based on a separate B1 reference measurement[7]. ROIs were drawn manually in the T1 and T2 maps to compute mean values per tube.

Gold standard measurements to obtain reference values for T1 and T2 were also performed. To obtain reference values for T1, a single-echo inversion recovery scan with inversion times of [100, 200, 400, 700, 1100, 1600, 2200, 2900] ms was performed. To obtain reference values for T2, a single-echo spin-echo scan with echo times of [20, 30, 50, 80, 120, 170, 230, 300] ms was performed. The T1 and T2 maps were obtained by voxel-wise fitting of a mono-exponential signal model to the data.

Results: In Fig. 3 mean T1 and T2 values in the ROIs in each tube are plotted for the sixteen measurements. For each tube, the coefficient of variation is computed as the standard deviation of these values, divided by the mean. The coeffcients of variations are between 0.5% and 1.9% for T1 and between 2.0% and 7.2% for T2.

In Fig. 4 Bland-Altman plots of relative differences of the mean values per ROI as compared to the ground truth reference measurements are shown. The mean bias for T1 is -1.5 % and for 5.8 % for T2. Almost measurements fall within the 95 % limits of agreement, which is determined as the mean difference +- 1.96 times the standard deviation.

Discussion: The coeffcients of variation as well as the mean relative errors for T1 are generally lower than for T2. We hypothesise that, on the one hand, this is due to the strong T1 encoding coming from the inversion pre-pulse. On the other hand, inaccuracies in the measured B1 maps[8] mostly propagate into the T2 maps. Since repositioning the phantom changes the B1 field in each tube, higher errors compared to the reference method as well as higher variations between the MR-STAT scans are therefore expected for T2. Furthermore, inaccuracies in the slice profile estimation also have a stronger impact T2 than on T1. The results for T2 could potentially be improved by using a more accurate slice profile model[9], employing T2-prep pulses[10] and/or incorporating phase based T2 mapping techniques[11].

In future work, the reproducibility of MR-STAT on the Eurospin phantom across different MR systems will also be assessed, as well as a comparison study against other qMRI methods like MR Fingerprinting[12]. In-vivo assessments will also be performed because, compared to gel phantom scans, additional signal model imperfections are present (due to e.g. ow, motion, partial volume effects) that may impact the outcomes.

Conclusion: The MR-STAT scans show high repeatability (coefficients of variation between 0.5% and 1.9% for T1 and between 2.0% and 7.2% for T2) and accuracy (mean relative error of -1.5 % for T1 and 5.8 % for T2) across a wide range of T1 and T2 values in gel phantom measurements.

References:

[1] Sbrizzi, A et al. Fast quantitative MRI as a nonlinear tomography problem. Magnetic Resonance Imaging 46 (2018): 56-63.

[2] van der Heide, O et al. High-resolution in vivo MR-STAT using a matrix-free and parallelized reconstruction algorithm. NMR in Biomedicine 33.4 (2020): e4251.

[3] QIBA Technical Performance Working Group. Quantitative Imaging Biomarkers: A Review of Statistical Methods for Technical Performance Assessment. Stat Methods Med Res. 24.1 (2015): 27–67.

[4] Fuderer, M et al. BLAKJac - A computationally e2cient noise-propagation performance metric for the analysis and optimization of MR-STAT sequences. Proc. Intl. Soc. Mag. Reson. Med., 2021: 3059.

[5] van der Heide, O et al. Faster Bloch simulations and MR-STAT reconstructions on GPU using the Julia programming language. Proc. Intl. Soc. Mag. Reson. Med., 2021: 3063.

[6] Bezanson, J et al. Julia: A fresh approach to numerical computing. SIAM review 59.1 (2017): 65-98.

[7] Nehrke, K et al. DREAM - a novel approach for robust, ultrafast, multislice B1 mapping. Magn Reson Med 68.5 (2012): 1517-1526.

[8] Olsson, H et al. Reducing bias in DREAM ip angle mapping in human brain at 7T by multiple preparation ip angles. Magnetic Resonance Imaging 72 (2020): 71-77.

[9] Liu, H. et al. Fast and accurate modeling of transient-state, gradient-spoiled sequences by recurrent neural networks. NMR in Biomedicine 34.7 (2021): e4527 [10] Hamilton. J.I. et al. MR ngerprinting for rapid quanti2cation of myocardial T1, T2, and proton spin density. Magn Reson Med. 77 (2017):1446– 1458.

[11] Wang, X et al. Phase-based T2 mapping with gradient echo imaging. Magn Reson Med 84 (2020):609–619.

[12] Ma, D et al. Magnetic resonance ngerprinting. Nature 495 (2013): 187–192.

Acknowledgments / Funding Information: The authors would like to thank Mariya Doneva for fruitful discussions on the experimental setup. This research has been financed by NOW under grant #17986.

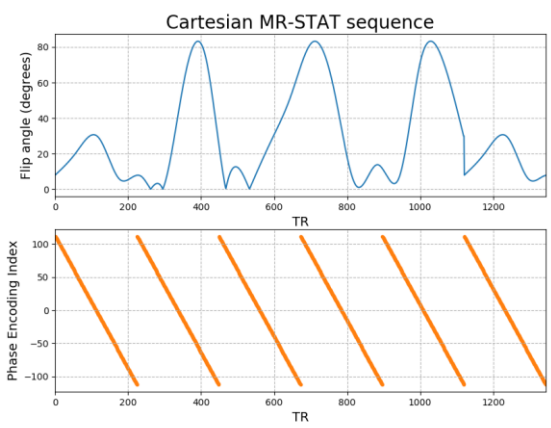

Figure 2: Flip angle train and gradient encoding scheme used in the MR-STAT acquisition. The sequence was preceded by and adiabatic inversion pulse and the TR and TE remained fixed throughout the sequence at 7.5 ms and 3.8 ms, respectively. Per measurement, a total of 1344 readouts were acquired in 10 s of scan time.

Figure 1: Setup of the twelve Eurospin gel tubes that were scanned in four sessions spread over two days, with four scans per session, resulting in a total of sixteen measurements.

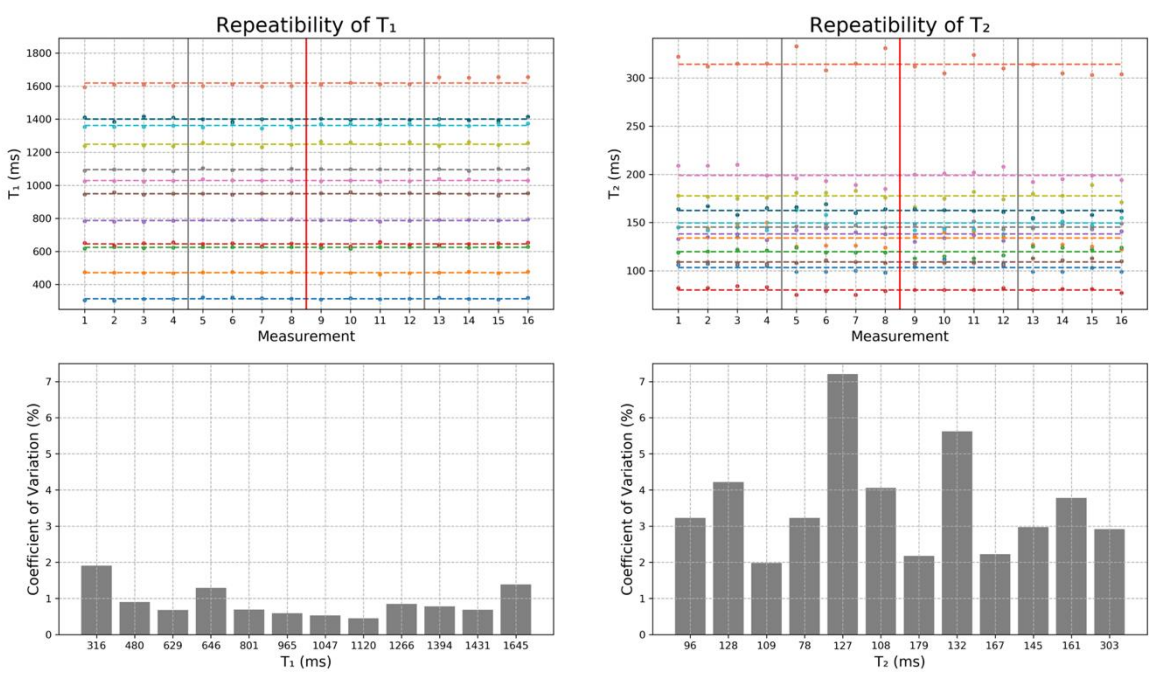

Figure 3: Repeatability assessment of the MR-STAT scans. Mean T1 and T2 values per manually drawn ROIs in the tubes were computed for each of the sixteen measurements and are shown in the top row. The four sessions (with four measurements each) are separated by vertical lines: the gray lines separate sessions within one day, the red line separates the two days. The coefficients of variation (relative standard deviations) are shown in the bottom row.

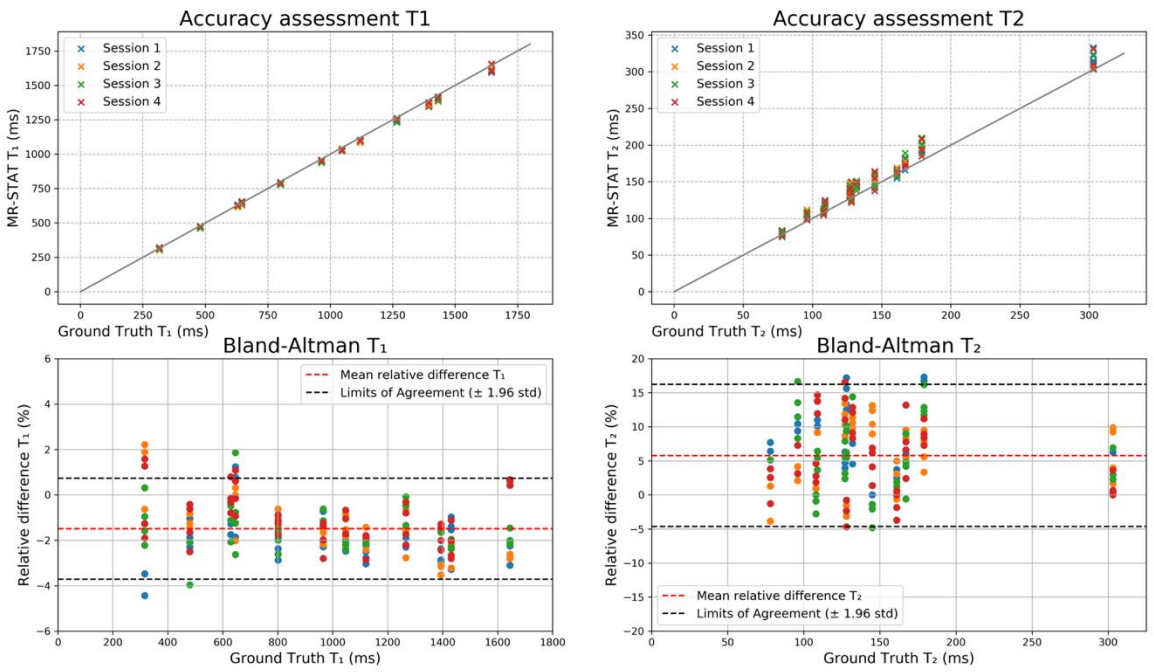

Figure 4: Mean T1 and T2 values per tube obtained with MR-STAT are compared against the reference values in the top row. The four sessions (with four measurements each) are indicated with different colors Blant-Altman plots showing relative differences of mean T1 and T2 values are presented in the bottom row. The mean relative differences are indicated by the red dashed lines. Almost all measurements are observed to fall within the limits of agreement (1.96 times the standard deviation of the relative errors).

Automatic 3D bladder segmentation from low-field MR images using 3D U-Net

L. Straetemans[1], D. Alblas[2], L.M. Morsinkhof[1], J.M. Wolterink[2], F.F.J. Simonis[1]
[1]Magnetic Detection & Imaging, TechMed Centre, University of Twente, Enschede, Netherlands; [2]Applied Mathematics, TechMed Centre, University of Twente, Enschede, Netherlands

Synopsis: Pelvic organ prolapse (POP) is a common problem in women, but little is known about treatments. Automatic 3D segmentation of pelvic organs would be useful for improving research in this area. This study successfully applies a 3D U-Net for automatic bladder segmentation of upright and supine low-field MRI scans from asymptomatic women. The resulting network will probably also perform well on data from POP patients. Further improvements are expected when the training data is completed. Future work will focus on segmentation of additional pelvic organs.

Introduction: Pelvic organ prolapse (POP) is a common problem in women.[1] Several treatments exist, but these often result in recurrences.[2,3] Therefore, we perform research to gain more insight in POP, using low-field MRI.[4] Currently, POP is quantified in 2D MR images, but this is not sufficient to analyze the complexity of this pelvic pathology.

Additional information on organ position and orientation can be obtained from 3D segmentation, as shown in Figure 1. Furthermore, 3D organ segmentation is useful for surgical planning and finite element simulation for biomechanical analysis of POP.[5]

Since manual segmentation is time-consuming (± 6 hours for Figure 1), an automatic method is desired. Research by Feng et al.[6] has shown promising results for automatic segmentation of pelvic organs with blurry boundaries from 1.5 tesla (T) images, scanned in supine position. Upright MRI scanning provides better insight into the true degree of prolapse[7], but this is only possible with low-field MRI, resulting in lower image quality. Moreover, the variety in bladder shapes makes automatic segmentation challenging.

This study investigates the application of a 3D U-Net for automatic segmentation of pelvic organs from 0.25T supine and upright MRI. This project focuses on the segmentation of the bladder, which is a relevant marker for POP as it is prolapsed in most POP patients.

Methods: In order to assess the healthy anatomic situation, the pelvic organ position was first analyzed in asymptomatic subjects. The study included 44women without POP symptoms, between 19 and 65 years of age. Subjects were scanned in upright and supine position using a 0.25T MRI scanner(G-scan Brio, Esaote SpA, Italy) with a 3D bSSFP sequence (TE/TR: 4/8 ms, flip angle: 60°, acquired resolution: 2.02x2.02x2.5mm³, FOV: 250x250x122mm³, total scan time: 5:02 min). Images in both body positions are acquired in the same image orientation.

In total, 88 scans were made (one supine and one upright scan per participant). Manual annotations of the bladder were obtained in 58 scans by a single expert using 3D Slicer (v.4.11.2021-02-26). These data were randomly divided into a training (24 scans), validation (18 scans), and test set (16scans), ensuring that scans from a single subject were in the same set. The proposed architecture is a modified 3D U-Net[8] (Figure 2), implemented with MONAI[9]. The network was optimized using an Adam optimizer with Dice loss, a learning rate of 5e-4 and a weight decay of 1e-6. We used early stopping during training, which resulted in 658 epochs.

For evaluation of our network, we used the Dice Similarity Coefficient (DSC) and Hausdorff Distance (HD) in mm. The resulting network was also applied to a scan from an asymptomatic subject whose bladder had prolapsed to emulate the future performance of the network on scans of POP patients.

Results & Discussion: Table 1 shows the performance metrics of the 3D U-Net on the validation and test datasets. Figure 3 shows that the manual segmentation and the automatic segmentation by U-Net in three slices of a 3D upright scan from a single woman correctly align (DSC=0.93, HD=12.09 mm). These results show that bladder segmentation from 3D low-field MRI is promising.

Figure 4 shows the scans of four different situations (upright, supine, prolapsed, and unsuccessful) overlayed with the manual and automatic segmentation. Figure 4a and 4b show that segmentation is successful in both supine and upright positions. Furthermore, Figure 4c indicates successful automatic segmentation of a prolapsed bladder in an asymptomatic woman. This suggests that the resulting network will also be applicable to scans from POP patients, with little or even without additional training on POP scans. Moreover, segmentation time was greatly reduced, from 10-60 minutes for a manual bladder segmentation, to only a few seconds by U-Net.

Figure 4d shows an example of incomplete segmentation. In the near future, we will extend our training set with additional annotated images, what will probably improve the robustness of the model.

Future research will focus on the automatic segmentation of additional pelvic organs (uterus, rectum, os pubis, spine) with the same model to further facilitate pelvic research on, e.g., prolapse, pessary positioning and before and after POP treatment comparisons.

Conclusion: This research shows promising results for automatic segmentation of the bladder from low-field upright and supine 3D MRI in asymptomatic women, leading to an enormous reduction in segmentation time. This allows comparing bladder position before and after treatment in 3D, which is useful for research on improving therapy for POP.

References:

1. Slieker-ten Hove, M. C. P. et al. Symptomatic pelvic organ prolapse and possible risk factors in a general population. Am. J. Obstet. Gynecol. 200,184.e1-184.e7 (2009).

2. Sarma, S., Ying, T. & Moore, K. H. Long-term vaginal ring pessary use: discontinuation rates and adverse events. BJOG An Int. J. Obstet. Gynaecol.116, 1715–1721 (2009).

3. Fialkow, M. F., Newton, K. M. & Weiss, N. S. Incidence of recurrent pelvic organ prolapse 10 years following primary surgical management: a retrospective cohort study. Int. Urogynecol. J. 19, 1483–1487 (2008).

4. Morsinkhof, L. M., Grob, A. T. M., Veenstra van Nieuwenhoven, A. L. & Simonis, F. F. J. Upright MR imaging of daily variations in pelvic organ position for assessment of pelvic organ prolapse. Proc. Intl. Soc. Mag. Reson. Med. 29 3691, (2021).

5. Chen, L., Ashton-Miller, J. A. & DeLancey, J. O. L. A 3D finite element model of anterior vaginal wall support to evaluate mechanisms underlying cystocele formation. J. Biomech. 42, 1371–1377 (2009).

6. Feng, F., Ashton-Miller, J. A., DeLancey, J. O. L. & Luo, J. Convolutional neural network-based pelvic floor structure segmentation using magnetic resonance imaging in pelvic organ prolapse. Med. Phys. 47, 4281–4293 (2020).

7. Grob, A. T. M. et al. Underestimation of pelvic organ prolapse in the supine straining position, based on magnetic resonance imaging findings. Int. Urogynecol. J. 30, 1939–1944 (2019).

8. Kerfoot, E. et al. Left-Ventricle Quantification Using Residual U-Net BT - Statistical Atlases and Computational Models of the Heart. Atrial Segmentation and LV Quantification Challenges. In (eds. Pop, M. et al.) 371–380 (Springer International Publishing, 2019).

9. Consortium, M. MONAI: Medical Open Network for AI. (2021). doi:10.5281/zenodo.4323058

Acknowledgments / Funding Information: -

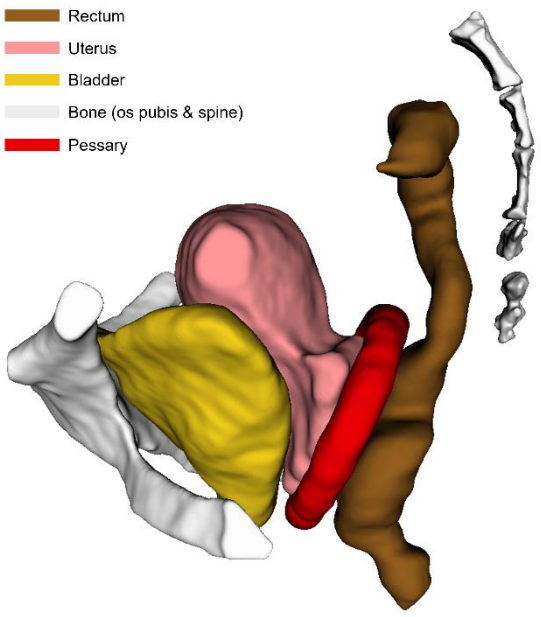

Figure 1: Sagittal view on 3D model of the pelvic area, manually segmented from a 3D scan of a POP patient, wearing a pessary.

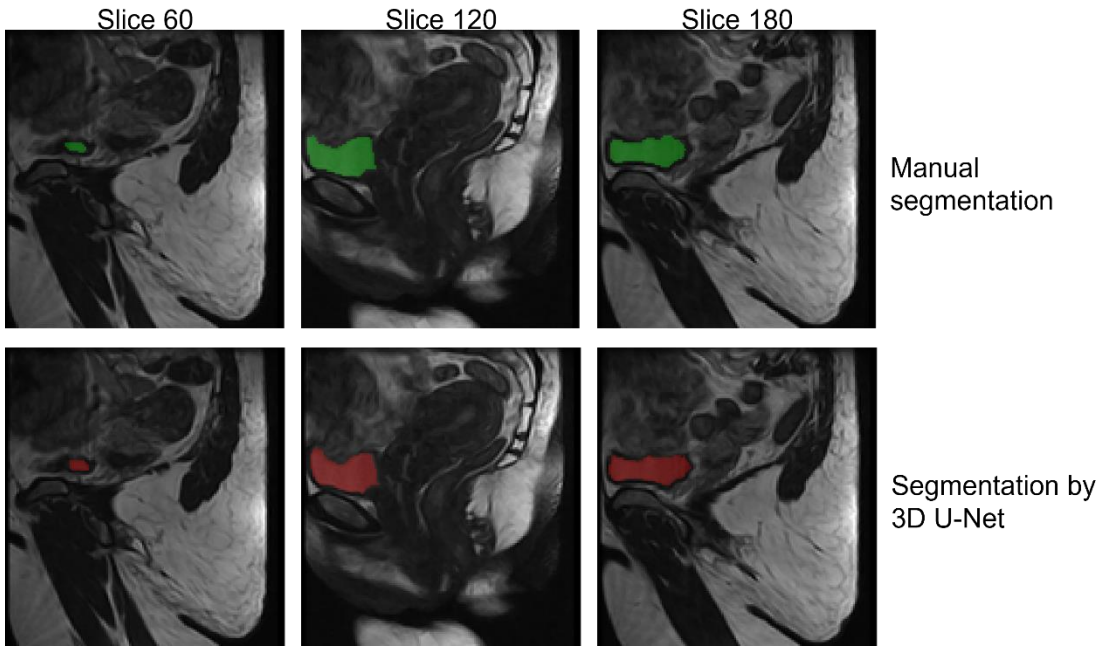

Figure 3: The manual segmentation (green) and automatic segmentation by U-Net (red) in three slices of a 3D upright scan from a single woman. DSC=0.93, HD=12.09 mm.

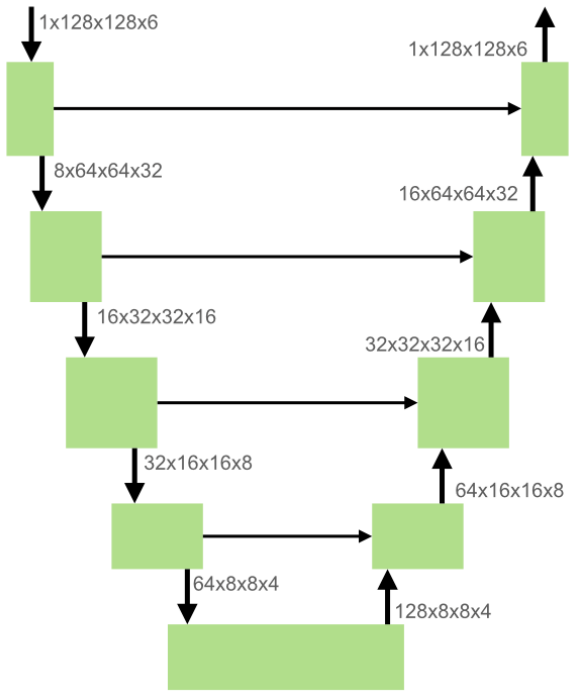

Figure 2: The architecture of the 3D U-Net and its dimensions.

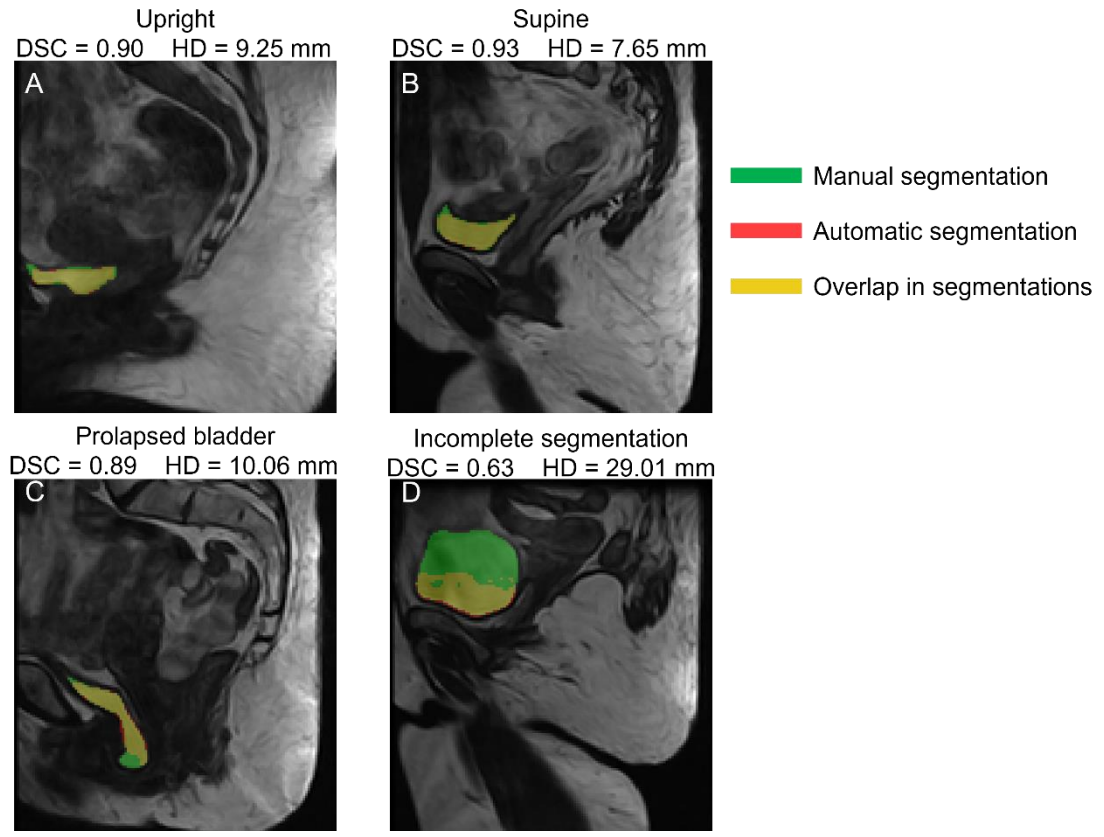

Figure 4: The scans of four different situations (A: upright, B: supine, C: prolapsed, D: unsuccessful) overlayed with the manual (green) and automatic (red) segmentation, as well as the overlap of these two segmentations (yellow).

Table 1: The mean Dice score, Hausdorff distance (in mm), and their standard deviations for the validation and test data.

	Dice Score (± SD)	Hausdorff Distance (mm) (± SD)
Validation set	0.83 (0.12)	25.67 (22.71)
Test set	0.85 (0.09)	18.89 (7.06)

A Multi-Dimensional Compressed Sensing Model for ^{23}Na Multi-Quantum Coherences MRI

C. Licht[1], E. Ilicak[1], L. R. Schad[1], S. Rapacchi[2]
[1]Computer Assisted Clinical Medicine, Heidelberg University, Mannheim, Germany; [2]CRMBM, Aix Marseille University, CNRS, Marseille, France

Synopsis: Sodium MRI offers great potentials to be a clinical marker for disease states. Besides the single quantum signal, the triple quantum signal of sodium could provide novel and complementary information. 3D volumetric sodium multi-quantum coherences imaging, however, is inherently slow as it requires specific phase cycling. In this work we show that compressed sensing can be applied to triple-quantum imaging and in addition, we present a multi-dimensional compressed sensing model that is specifically suited for triple-quantum imaging. The model jointly reconstructs multi-dimensional multi-quantum coherences data by utilizing total variation to optimally exploit sparsity in each imaging dimension.

Introduction/ Purpose: The signal of sodium (^{23}Na) MRI is correlated to the vitality of cells and therefore, offers great potentials as an important clinical marker for disease states[1]. ^{23}Na nuclei exhibit a quadrupolar moment, that in a multi-radiofrequency experiment, resolves single and triple quantum signals (SQ and TQ). The TQ signal is very sensitive to its sodium environment and especially to the intracellular compartment[2], yielding the potential to provide further important information about the tissue and the state of the disease[3].

^{23}Na multi-quantum coherences (MQC) imaging is an inherently slow process and thus not suited for the clinical routine yet. Owed to this, its clinical value remains yet unknown. Compressed Sensing (CS) has been established to speed up MR imaging by randomly undersampling k-space and iteratively reconstructing the data by assuming sparsity in some transform domain[4]. 3D MQC imaging, despite the low SNR, is well suited for CS reconstruction as it produces very sparse data in its multi-dimensional space. Improved reconstruction results are achieved by exploiting sparsity in all imaging dimensions simultaneously[5]. In 3D multi-echo multi-quantum imaging, a temporal and a phase cycle dimension are added. Conclusively, by exploring ^{23}Na MQC undersampling to reach acceleration and leveraging CS a priori to maintain image quality enables to accelerate ^{23}Na MQC imaging. We present phantom and in-vivo results to show for the first time applicability of conventional 3D and multi-dimensional 5D CS to accelerate ^{23}Na MQC imaging.

Methods: Imaging was performed on 3T MRI (Siemens Trio, Erlangen, Germany) system with a 1Tx/Rx dual-tuned ^{23}Na/^{1}H head coil (Rapid Biomedical GmbH, Rimper, Germany). Prior to the MQC scans, B0 shimming was repeated with a ^{1}H-based vendor provided 3D shimming routine until accurate convergence. A home-built flip angle calibration sequence was used to calibrate global 90°RF pulses. The optimal evolution time τ was determined from a global TQTPPI spectroscopic prescan, followed by an offline fit. Cartesian imaging of simultaneous single and triple quantum ^{23}Na (CRISTINA[6]), a multi-echo three-pulse sequence was extended to 3D and improved to only sample the first echo asymmetrically. Triple-quantum filtered images were obtained with the following parameters: 10 TEs with TE= 1.66ms (asymmetric first echo) with ΔTE=4.9ms and receiver bandwidth 200Hz/px. Time between second and third RF pulse was kept as short as possible and RF pulse duration was set to 500ms.

Phantom: FoV 260x260x240mm, matrix size 32x32x12, TR=140ms, evolution time τ_{Evo}=8.1ms. Phase increment $\Delta\phi$=60° averaged over 8 acquisitions, TA=80min.

In-vivo: Two volunteers (25±1 year), FoV 234x234x200mm, matrix size 24x24x10, TR=150ms, the evolution time τ_{Evo}=8.9ms. Phase increment $\Delta\phi$=60° averaged over 7 acquisitions, TA=54min.

The phantom and in-vivo data were retrospectively undersampled with 3D variable density Cartesian patterns[7] varying along the phase-cycle and averaging dimension. Undersampling masks were density-adapted weighted according to Schoormans et al.[8]. The constrained optimization problem for 3D total variation CS is described as:

$$\textbf{3D CS}: \min_{u} \lambda_{x,y,z} \left\| \nabla_x u, \nabla_y u, \nabla_z u \right\|_2 \; s.t. \left\| \Phi_{\mathrm{F}}(u) - f \right\|_2^2 < \sigma^2$$

Due to MQC's multi-dimensional structure, the constrained problem for multi-quantum imaging, however, can be jointly solved by adding two additional regularization terms yielding the following optimization problem:

$$\textbf{5D CS}: \min_{u} \lambda_{x,y,z} \left\| \nabla_x u, \nabla_y u, \nabla_z u \right\|_2 + \lambda_{TE} \left\| \Psi_{TE} u \right\|_2 + \lambda_{pc} \left\| \Psi_{Rep} u \right\|_2 \; s.t. \left\| \Phi_{\mathrm{F}}(u) - f \right\|_2^2 < \sigma^2$$

with u being the image one wants to reconstruct, $\nabla_{\mathrm{x,y,z}}$, Ψ_{TE} and Ψ_{pc} representing the sparsifying transform operators for total variation and Fourier transform along the dimensions, respectively. $\lambda_{x,y,z}$, λ_{TE} and λ_{pc} are spatial, temporal and phase cycle sparsity weighting parameters, respectively, which enable to control sparsity weightings for each dimension separately. The second term represents the data fidelity term with Φ_F indicating the partial Fourier transform followed by random undersampling, f representing the measured data in frequency domain and σ being the signal variance noise. The Split Bregman Method[9] was used to solve the stated optimization problems. All computations were performed in MATLAB (MATLAB R2020a, MathWorks, Natick, MA) within ~400 seconds utilizing GPU computing. Reconstruction quality was evaluated by computing the coefficient of determination (R^2) between signals' average intensity and ^{23}Na concentration in the phantom vials.

Results: Figure 1 shows retrospectively undersampled phantom data that was reconstructed with conventional zero-filling followed by an inverse Fourier transform, standard 3D CS and the proposed multi-dimensional 5D CS model. Figure 2 depicts retrospectively undersampled in-vivo brain data from volunteer a) that was reconstructed with conventional zero-filling followed by an inverse Fourier, 3D CS and the proposed 5D CS model. For phantom as well as in-vivo data, the 5D CS model provides superior artefact suppression when compared to conventional 3D CS. Figure 3 shows retrospectively undersampled in-vivo brain data from two volunteers that were reconstructed with the proposed 5D CS model.

Discussion: Retrospective undersampling only was chosen, because the TQ signal changes rapidly due to inhomogeineities or heating of the tissue, which makes similarity comparison impossible. Denoising is enhanced in the 5D CS model, from sparsity being promoted with two additional regularization terms. Furthermore, additional information captured in the TE dimension enables to preserve image information, see arrow 1 Figure 3b. Further improvements are expected by conducting measurements on 7T as well as utilizing a multi-channel receive coil with parallel imaging techniques.

Conclusion: We have shown that the CS scheme can be used for ^{23}Na MQC. Furthermore, we developed a TQ-specific CS model that provides superior artefact suppression while robustly reducing acquisition time in-vivo by a factor of 2.

References:

1. Huhn K, Engelhorn T, Linker RA, Nagel AM. Potential of Sodium MRI as a Biomarker for Neurodegeneration and Neuroinflammation in Multiple Sclerosis. Front Neurol. 2019 Feb 11;10:84. doi: 10.3389/fneur.2019.00084. PMID: 30804885; PMCID: PMC6378293.
2. LaVerde G, Nemoto E, Jungreis CA, Tanase C, Boada FE. Serial triple quantum sodium MRI during non-human primate focal brain ischemia..Magn Reson Med. 2007 Jan;57(1):201-5. doi: 10.1002/mrm.21087. PMID: 17191243.
3. Hoesl MAU, Kleimaier D, Hu R, et al. 23Na Triple-quantum signal of in vitro human livercells, liposomes, and nanoparticles: cell vi- ability assessment vs. separation of intra- and extracellular signal. J Magn Reson Imaging. 2019;50:435-444.
4. Lustig M, Donoho D, Pauly JM. Sparse MRI: The application of compressed sensing for rapid MR imaging. Magn Reson Med. 2007Dec;58(6):1182-95. doi: 10.1002/mrm.21391. PMID: 17969013.
5. Montesinos P, Abascal JF, Cussó L, Vaquero JJ, Desco M. Application of the compressed sensing technique to self-gated cardiac cine sequences in small animals. Magn Reson Med. 2014 Aug;72(2):369-80. doi: 10.1002/mrm.24936. Epub 2013 Sep 16. PMID: 24105815.
6. Hoesl, M.A.U., L.R. Schad, and S. Rapacchi, Efficient 23Na triple-quantum signal imaging on clinical scanners: Cartesian imaging of single and triple-quantum 23Na (CRISTINA).Magnetic Resonance in Medicine, 2020. 84(5): p. 2412-2428.
7. Kuestner, T. ,et al Compressed Sensing LAB: An MR acquisition and reconstruction system. *Proceedings of the ISMRM Workshop on Data Sampling and Reconstruction*. Sedona, AZ, USA, 2016.
8. Schoormans, J., Strijkers, G. J., Hansen, A. C., Nederveen, A. J., & Coolen, B. F. (2020). Compressed sensing MRI with variable density averaging (CS-VDA) outperforms full sampling at low SNR. *Physics in medicine and biology*, *65*(4), 045004. https://doi.org/10.1088/1361-6560/ab63b7
9. Goldstein, T. & Osher, S. The split bregman method for l1-regularized problems. SIAM Journal on Imaging Sciences 2, 323–343 (2009). URLhttps://doi.org/10.1137/080725891 SMASH.

Acknowledgments / Funding Information: -

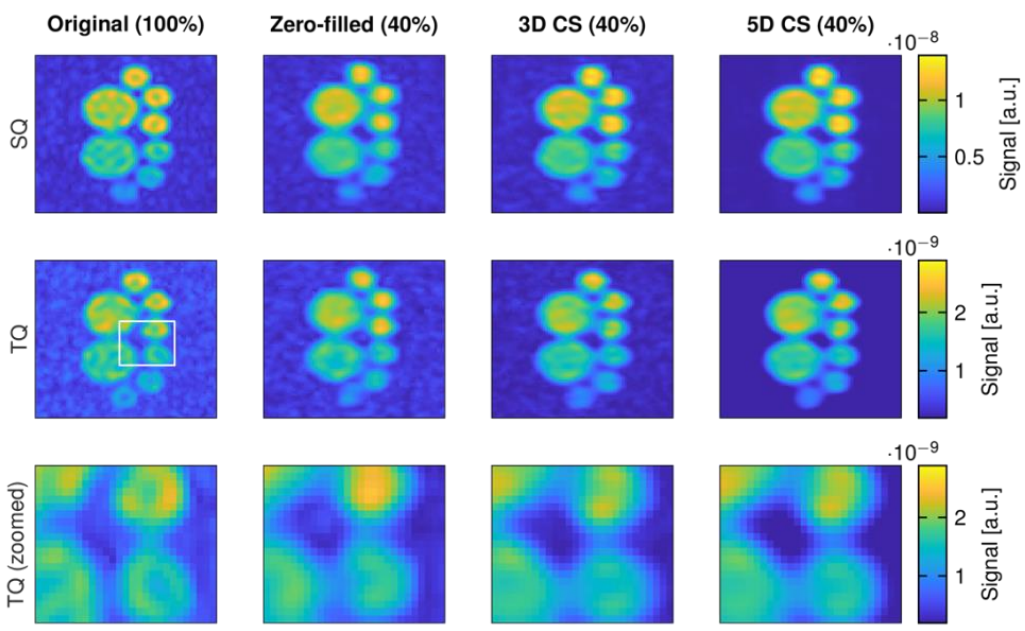

Figure 1: The fully sampled acquisition was retrospectively undersampled by preserving 40% of phase-encode steps and then reconstructed. Compared to competing methods, the proposed 5D CS technique improves aliasing artefact suppression. Linear relationship between signals' average intensity and ^{23}Na concentrations were: fully sampled $R^2_{original,SQ}$= 0.95 and $R^2_{original,TQ}$= 0.93, $R^2_{3DCS,SQ}$= 0.90 and $R^2_{3DCS,TQ}$= 0.91, $R^2_{5DCS,SQ}$= 0.91 and $R^2_{5DCS,SQ}$= 0.92. All vials contain 4% agar and NaCl concentrations ranging from 60 to 154mM

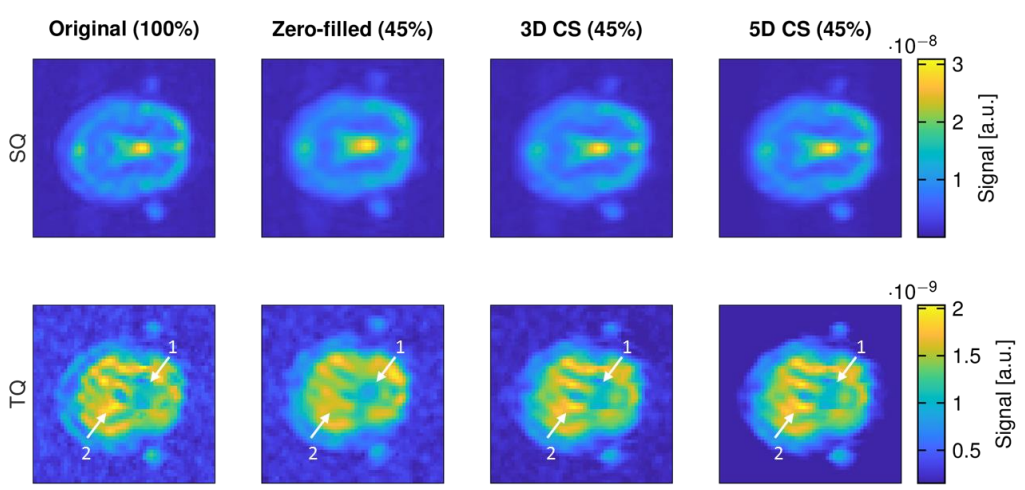

Figure 2: Reconstruction results of in-vivo brain SQ and TQ data for different reconstruction algorithms for volunteer a. The fully sampled acquisition was retrospectively undersampled by preserving 45% of phase-encode steps and then reconstructed. Compared to competing methods, the proposed 5D CS technique improves aliasing artefact suppression. The arrows indicate regions with the most significant changes. When compared to the zero-filled reconstruction, it is observable that CS enables to reconstruct images more accurately (arrows 1, 2).

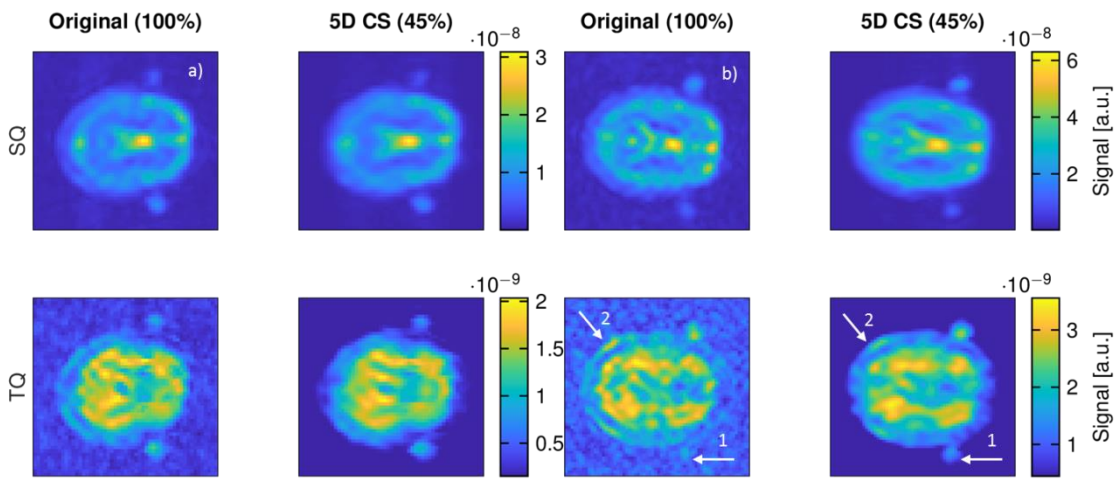

Figure 3: CS reconstruction results for two volunteers (a, b) with the proposed 5D CS model. Arrow 1 indicates a well preserved reference vial, which is barely observable in the original data. The 5D CS model takes advantage of exploiting sparsity in all imaging dimensions, which provides more information for the reconstruction of the image, when compared to 3D CS. However, the reconstruction results for volunteer B exhibits slight blurring as well as lower signal intensity peaks (see arrow 2).

Estimating brain tissue stiffness from cardiac-induced 7T MRI displacement measurements using 3D subzone-based reconstruction

M. Burman Ingeberg[1], E.W. Van Houten[2] J.J.M. Zwanenburg[1]

[1]Department of Radiology, University Medical Center Utrecht, Utrecht, The Netherlands; [2]Department of Mechanical Engineering, University de Sherbrooke, Sherbrooke, Canada

Synopsis: Mechanical properties of the human brain can be altered by a variety of pathologies. These properties can be estimated from in vivo MRI measurements of brain tissue displacements as induced by the heartbeat. Previously obtained 7T MRI displacements measurements were used to reconstruct stiffness parameters using a subzone-based non-linear inversion scheme. Various structures of the brain can be observed in the reconstructed parameter distributions, and the results show good test-retest reliability. The preliminary results show promise of this approach to yield non-invasive assessment of brain tissue microstructure as a tool to investigate brain disease.

Purpose: A variety of pathologies can alter the microstructure of human brain tissue. In general, changes in human tissue can be quantified using Magnetic Resonance Elastography (MRE), where harmonic steady-state mechanical waves are induced at a region of interest. The resulting tissue displacements can then be measured using phase-contrast MRI measurements and can be used to reconstruct mechanical properties of the tissue. However, the brain is enveloped in cerebral meninges and the cranium, which dampen extrinsically applied vibrations. Alternatively, mechanical properties of the brain can be estimated from *in vivo* MRI measurements of brain tissue deformation as induced by the heartbeat[1,2]. Recently, the quality of these deformation measurements was improved significantly using ultrahigh field (7T) MRI[3]. This data, however, has not yet been tested for its usability for reconstruction of brain tissue stiffness. The purpose of this project is therefore to reconstruct brain stiffness parameters from 7T MRI measurements of the displacements resulting from intrinsic, cardiac-induced vibrations, and to assess the test-retest reliability.

Methods: We used data from a previously described 7T MRI study, which used Displacement Encoding with Stimulated Echoes (DENSE)[3]. The data consisted of 3D displacement measurements (1.95x1.95x2.2 mm resolution), time-resolved over the cardiac cycle (15 cardiac phases), for eight subjects, including a repeated scan after repositioning of the subject. The tissue displacements over the cardiac cycle were converted to the harmonic domain by Fourier Transformation of each voxel. Stiffness parameters were then reconstructed at the first harmonic frequency (approximately 1 Hz) by applying a 3D subzone-based non-linear inversion (NLI) scheme[4]. A viscoelastic model of the brain was used, yielding the complex parameters shear storage modulus, shear loss modulus, λ-modulus, and damping ratio as stiffness parameters of interest. In this model for low frequencies, only relative distributions of these stiffness parameters can be recovered for reasons described elsewhere[4], resulting in arbitrary units of the reconstructed parameters. They were therefore normalized between zero and one and the unit of stiffness is renamed from Pa to $\widetilde{\text{Pa}}$. Finally, the shear stiffness μ can be calculated from the reconstructed stiffness parameters as

$$\mu = \frac{2|G^*|^2}{G' + |G^*|},$$

where G^* is the complex dynamic modulus and G' is the shear storage modulus.

Results: Figure 1 shows representative preliminary results of the shear stiffness distribution compared to magnitude images for four subjects, while Figure 2 shows preliminary results of the real part of λ-modulus for the same four subjects with repeat scans. Similarly, preliminary results of the damping ratio for four subjects with repeats can be seen in Figure 3. The mean and standard deviation over all subjects of each quantity is presented in Table 1, where they are calculated separately for the grey and white matter.

Discussion: The shear stiffness distribution in Figure 1 shows structural similarities to the magnitude images. In particular, structure around the ventricles show consistency between the shear stiffness and the magnitude images as well as between subjects. The consistency of the reconstruction between repeat scans can be observed in the λ-modulus distributions in Figure 2 where each scan is directly compared to the repeat scan. Due to the repositioning of subjects between repeats, the orientation of the slices might deviate in this preliminary analysis, as the dataset are not yet co-registered. The damping ratio in Figure 3 shows more consistency between repeat scans then between subjects. There tends to be a higher damping ratio around the ventricles for each subject, likely due to the tissue around the cerebrospinal fluid absorbing a greater amount of vibrational energy. The results reported in Table 1 show similar values for the stiffness parameters between the grey and white matter, where the shear stiffness is slightly higher in the grey matter while the λ-modulus is slightly lower. These differences are consistent across all subjects, i.e., each subject had higher gray matter shear stiffness and lower gray matter λ-modulus relative to the respective white matter values of the same subject.

The use of a viscoelastic brain model results in a non-unique solution that renders the units of the stiffness parameters arbitrary. This is not a problem in terms of determining structure and relative differences but could lead to significant inaccuracies when clinical elastography depends on quantitative property estimates[4]. One option is thus to move from the viscoelastic model to a poroelastic model, where instead the brain is modeled as an elastic matrix with a porous fluid flow. Not only has this been shown to produce better reconstructions that the viscoelastic model at lower frequencies, but also provides unique solutions at such frequencies[5].

Conclusion: In conclusion, 7T MRI measurements of cardiac-induced brain tissue deformation allow for non-invasive estimation of brain stiffness, with good test-retest repeatability. Stiffness parameters of the brain was reconstructed where the grey and white matter exhibit similar values. This method may be valuable for studying the effects of brain disease on tissue microstructure. Further optimization of the NLI reconstruction is still necessary, including testing a poroelastic model instead of the currently used viscoelastic model.

References:

1. Zorgani A. et al. Brain palpation from physiological vibrations using MRI, PNAS, 2015;112(42):12917-21.

2. Weaver J. et al. Brain mechanical property measurement using MRE with intrinsic activation, PMB, 2012;57(22):7275-87.

3. Adams A. et al. Validating faster DENSE measurements of cardiac-induced brain tissue expansion as a potential tool for investigating cerebral microvascular pulsations, Neuroimage, 2020;208:116466.

4. McGarry M. et al. Uniqueness of poroelastic and viscoelastic nonlinear inversion MR elastography at low frequencies, PMB, 2019;64(7):075006.

5. McGarry M. et al. Suitability of poroelastic and viscoelastic mechanical models for high and low frequency MR elastography, Med Phys., 2015;42(2):947-57

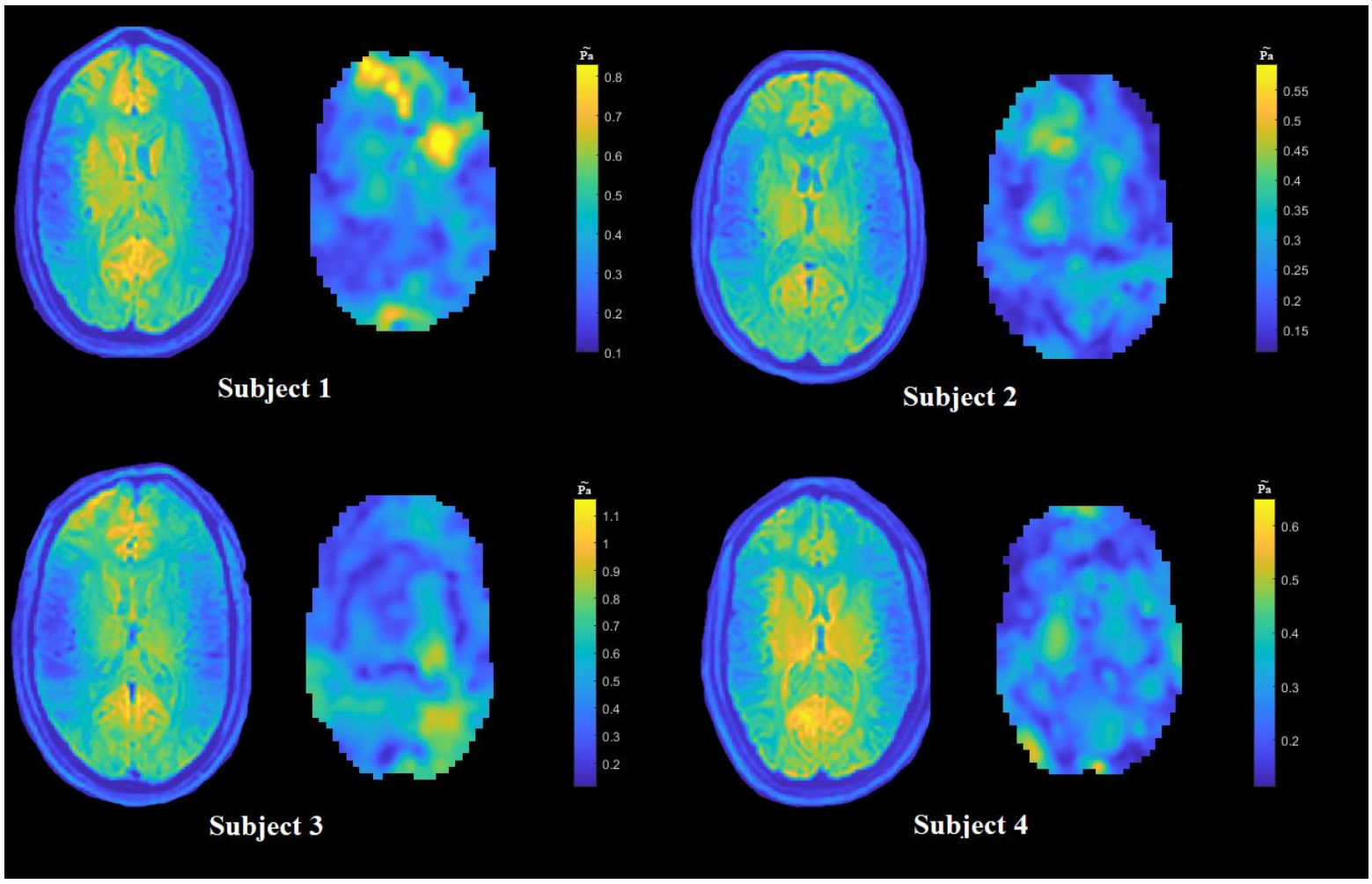

Figure 1: Representative preliminary results of the shear stiffness distribution (right) compared to magnitude images (left) for four subjects. The color bar corresponds only to the shear stiffness distribution.

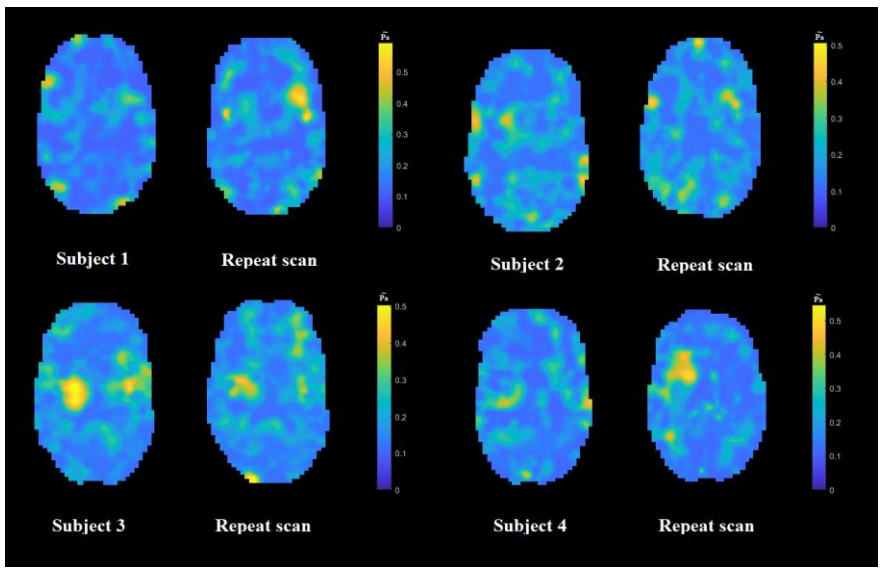

Figure 2: Preliminary results of the real part of λ-modulus for four subjects with repeat scans. The displayed slices are chosen to be approximately the same slice between repeat scans.

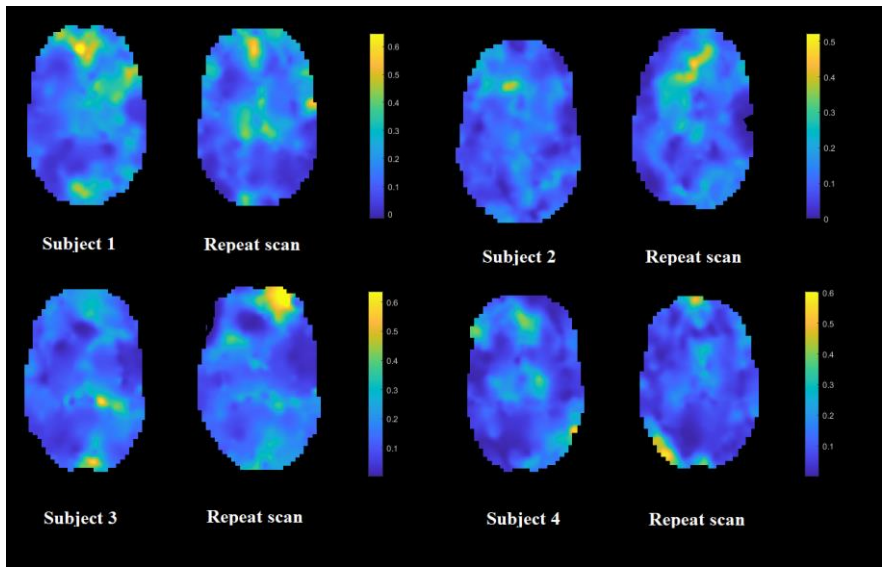

Figure 3: Preliminary results of the damping ratio for four subjects with repeat scans. The displayed slices are chosen to be approximately the same slice between repeat scans.

Table 1: The mean and standard deviation (mean±std) over all subjects of each reconstructed quantity, separated for the grey and white matter.

	Grey matter		White matter	
Scan	1	2	1	2
Shear Stiffness [$\widetilde{\mathbf{Pa}}$]	0.36±0.09	0.38±0.10	0.35±0.09	0.36±0.10
λ-modulus (real part) [$\widetilde{\mathbf{Pa}}$]	0.174±0.003	0.172±0.002	0.178±0.004	0.179±0.005
Damping ratio	0.155±0.021	0.167±0.014	0.135±0.021	0.142±0.015

A separation between motor and sensory somatotopic maps in the human cerebellum

E. Brouwer[1], N. Priovoulos[1], W. van der Zwaag[1]
[1]Spinoza Centre for Neuroimaging, Amsterdam, The Netherlands;

Synopsis: We investigated the organisation of the cerebellar digit map with three distinct tasks (flexing/extending/stroking) using B1-shimmed, high-resolution fMRI at 7T. For all tasks, the positions of the COG of the digit representations formed an orderly progression in at least one of the lobules. The distance between the motor task activations for flexing and extending of the digits were smaller than from either motor task to stroking clusters, indicating a separation between somatosensory and motor clusters in cerebellar lobule V.

Introduction: The human cerebellum is an important part of the sensory and motor networks, though largely unexplored compared to the neocortex, due to its highly-foliated cortex and challenging B1 profile at higher fields. There is a sensory somatotopic digit map in the anterior and posterior lobules of the cerebellum[1] which has been suggested to overlap with cerebellar motor digit representations[2]. By comparison, in the primary motor cortex, flexing and extending are known to result in distinct digit maps[3]. The precise sensory-motor digit organisation in the cerebellar cortex has not yet been explored in adequate spatial resolution. Here, we investigated the organisation of the cerebellar digit map with three distinct tasks (flexing/extending/stroking) using RF-shimmed, high-resolution fMRI at 7T.

Methods: Five right-handed participants (22-42years) were scanned in a 7T Achieva (Phillips) with an 8Tx/32Rx (Nova Medical) whole-head coil. An RF-shim was calculated following B1 mapping. A 3D-EPI slab covering the cerebellum (1mm isotropic, TR/TE=3300ms/21ms, $SENSE_{y/z}$= 2.6/3.27, FOV=182x60x186mm, partial-$fourier_{y/z}$ =0.8, flip-angle=20°) was used for functional acquisitions. Each session consisted of three 15-minute functional runs in which right-hand digit 1, 3 or 5 was flexed into a ball (motor), extended against an elastic band (motor) or stroked with a toothbrush (sensory); 12s ON and 6s OFF (Fig-1). fMRI data were motion/distortion-corrected, the cerebellum was segmented and a GLM (finger-stimulus>rest) was fitted (FSL, SPM12 and ANTs). Dominant clusters ($p<0.05$) in lobule V and VIII for each of the three tasks and digits were identified by visual inspection. When the cluster extended into the left hemisphere of the cerebellum, the zstat threshold was raised to 4 (n=2). For each cluster, the peak z-stat value and the centre of gravity (COG) and direction of the somatotopic gradient in the individual space were extracted. A winner-takes-all (WTA) map was generated for each task and participant. For each participant, the median distance between COGs of each digit were calculated for each task, as well as the distance between groups of COGs for the different tasks.

Results: Stroking, flexing and extending typically resulted in individual-digit significant clusters in both lobule V (anterior lobe) and lobule VIII (posterior lobe) (Fig-2a). The winner takes all (WTA) maps presented all three digits in a semi-orderly progression, but not in consistent direction, for most subjects and tasks. While a posterior-anterior (P-A) progression can be seen in Figure 2a in lobule V for all tasks, a P-A direction is found for flexing in lobule VIII and a superior-inferior (S-I) direction for extending and stroking. Interestingly, we found consistent bilateral activation in lobule VIII during the extending task (Fig-2b), but not for flexing or stroking.
In lobule V, during the flexing task, a consistent organisation in the P-A direction was found in the COG positions for all participants (Fig-3), though not for extending and stroking. In lobule VIII, P-A gradients were found for two participants in all tasks and a left-right gradient for 2/3/3 participants for flexing, extending and stroking respectively. The S-I gradient was inconsistent for all participants and tasks.
The distinct tasks resulted in separated series of COGs within the same lobules. Median distances between digit COGs were largest for the flexing task (Fig-4a). Between task groups, the largest distances were found between the two motor and stroking task in lobule V (Fig-4b). In lobule VIII, groups of COGs were closer together.

Discussion: All three tasks reliably engaged the cerebellar motor regions in lobule V and VIII at single-digit level. More consistently organised activation in lobule V and larger distances between tasks compared to lobule VIII indicate that the digit regions cover more cortical surface in the anterior lobe, though both regions demonstrated digit maps.
The flexing and stroking tasks showed mostly unilateral results. In comparison, the extending task resulted in bilateral clusters. This could be due to the higher complexity of the task, as more difficult movements have been shown to yield more bilateral activation in M1[4].
Larger distances between the stroking task and the two motor tasks could potentially indicate a separation between motor and sensory organisation in the cerebellum similar the neocortex, where distinct sensory (S1) and motor digit maps (M1) exist[3]. A separation between flexing and extending, as has been reported in M1[3], was not apparent in this cerebellar data, though flexing demonstrated a more distinct digit progression compared to extending.
With the current 1mm spatial resolution, individual digit representations could be distinguished, but areas responding to different tasks were close and overlapping. To further investigate the intralobular organisation of lobule VIII, a higher spatial resolution and/or surface-based approaches might be required.

Conclusion: To conclude, we employed an RF-shimmed high-resolution 7T fMRI acquisition to demonstrate that digit-maps exist both in the anterior (Lobule V) and posterior (Lobule VIII) part of the cerebellum, across motor and sensory tasks. We found a separation between motor and sensory digit maps, indicating a similar organisation to the neocortex.

References:

1. Van der Zwaag W, Kusters R, Magill A, et al. Digit somatotopy in the human cerebellum: A 7T fMRI study. Neuroimage. 2013;67:354-362. doi:10.1016/j.neuroimage.2012.11.041
2. Wiestler T, McGonigle DJ, Diedrichsen J. Integration of sensory and motor representations of single fingers in the human cerebellum. J Neurophysiol. 2011;105(6):3042-3053. doi:10.1152/JN.00106.2011
3. Huber L, Finn ES, Handwerker DA, et al. Sub-millimeter fMRI reveals multiple topographical digit representations that form action maps in human motor cortex. Neuroimage. 2020;208:116463. doi:10.1016/J.NEUROIMAGE.2019.116463
4. Chettouf S, Rueda-Delgado LM, de Vries R, Ritter P, Daffertshofer A. Are unimanual movements bilateral? Neurosci Biobehav Rev. 2020;113:39-50.

Acknowledgements: This study was supported by an NWO-TTW VIDI grant (VI.Vidi.198.016).

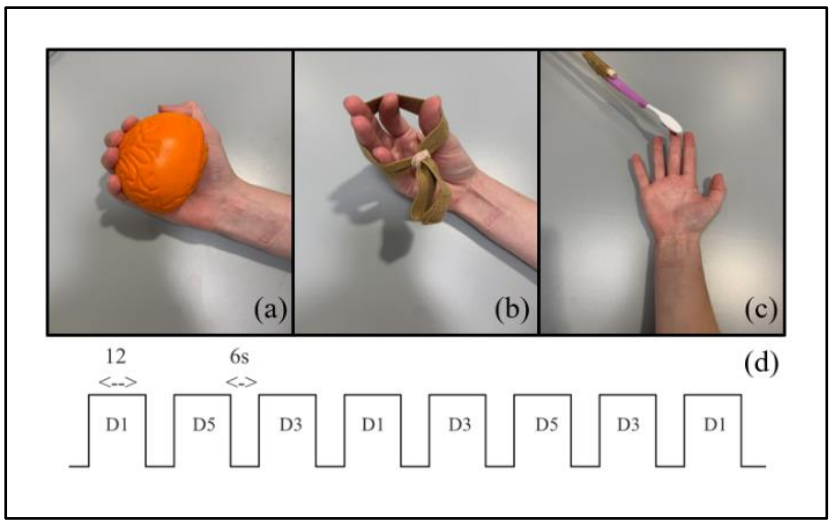

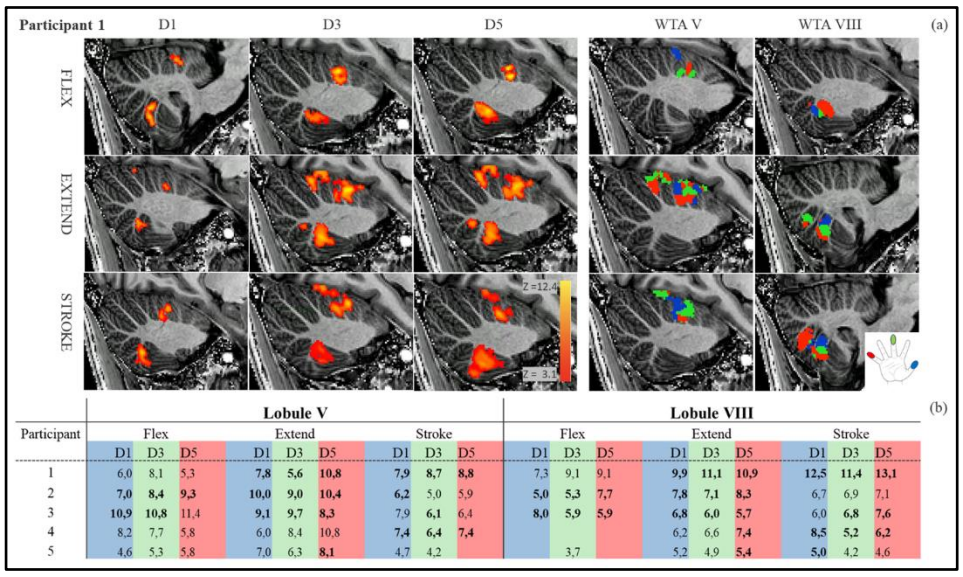

(b)

Participant	Lobule V									Lobule VIII								
	Flex			Extend			Stroke			Flex			Extend			Stroke		
	D1	D3	D5	D1	D3	D5	D1	D3	D5	D1	D3	D5	D1	D3	D5	D1	D3	D5
1	6,0	8,1	5,3	**7,8**	**5,6**	**10,8**	**7,9**	**8,7**	**8,8**	7,3	9,1	9,1	**9,9**	**11,1**	**10,9**	**12,5**	**11,4**	**13,1**
2	**7,0**	**8,4**	**9,3**	**10,0**	**9,0**	**10,4**	**6,2**	5,0	5,9	**5,0**	**5,3**	**7,7**	**7,8**	**7,1**	**8,3**	6,7	6,9	7,1
3	**10,9**	**10,8**	11,4	**9,1**	**9,7**	**8,3**	7,9	**6,1**	6,4	**8,0**	**5,9**	**5,9**	**6,8**	**6,0**	**5,7**	6,0	**6,8**	**7,6**
4	8,2	7,7	5,8	6,0	8,4	10,8	**7,4**	**6,4**	**7,4**				6,2	6,6	**7,4**	**8,5**	**5,2**	**6,2**
5	4,6	5,3	5,8	7,0	6,3	**8,1**	4,7	4,2			3,7		5,2	4,9	**5,4**	**5,0**	4,2	4,6

Figure 1. (a) Flexing (b) Extending (c) Stroking (d) Stimulus timeline

Figure 2. (a) The significant cluster activation in the sagittal slice of participant 1 for each task and digit. A winner takes all (WTA) map of digit 1, 3 and 5 for each task and lobule. (b) The maximum zstat in the significant cluster, the zstat is bold if significant bilateral activation is reported

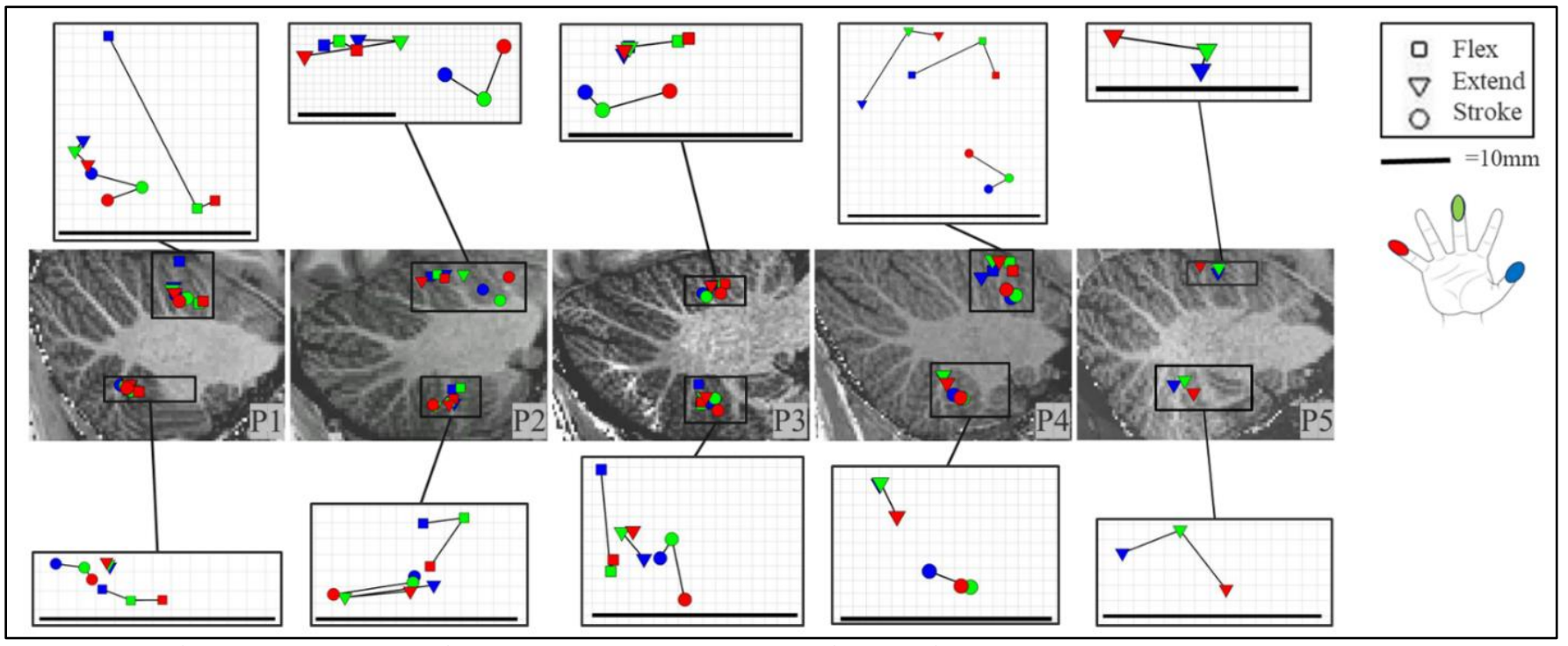

Figure 3. The COGs for each digit cluster are presented for each participant and lobule. All tasks with significant results for all three digits were projected onto the sagittal plane, overlaid on a sagittal slice of the cerebellum. The black bar indicates 10mm. Notice the predominant posterior-anterior orientation of the somatotopic gradient in lobule V.

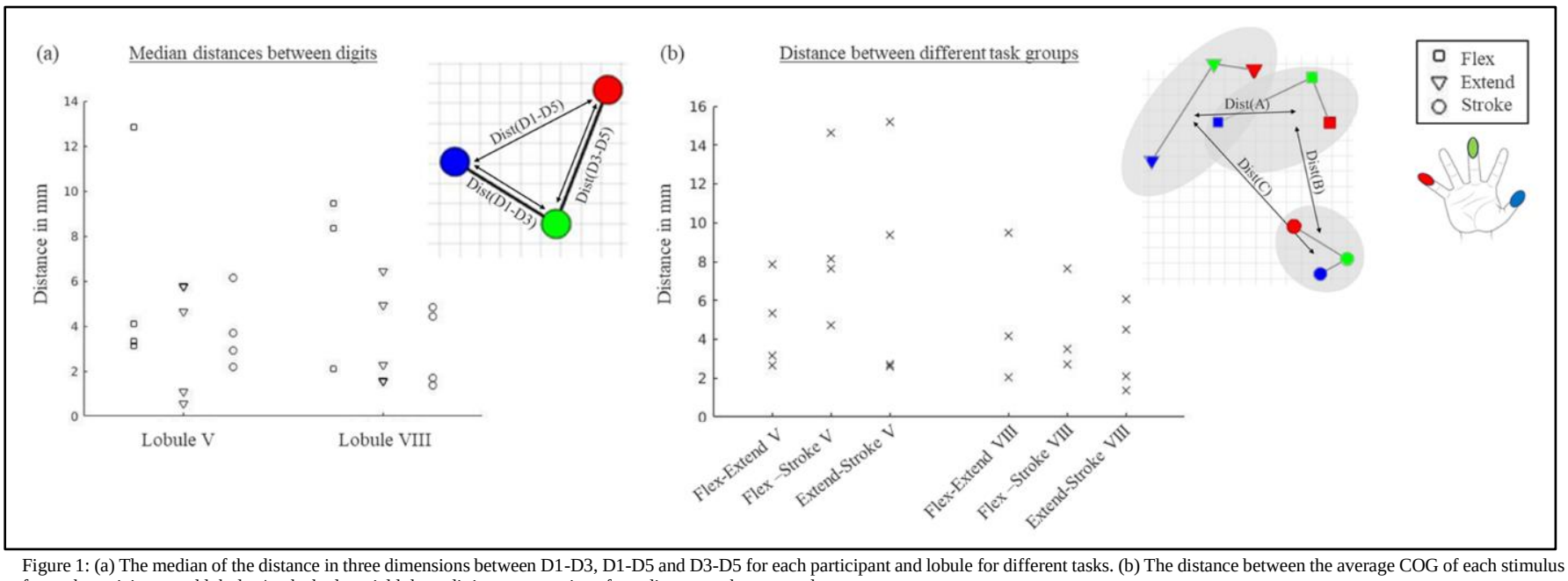

Figure 1: (a) The median of the distance in three dimensions between D1-D3, D1-D5 and D3-D5 for each participant and lobule for different tasks. (b) The distance between the average COG of each stimulus for each participant and lobule. *tasks had to yield three digit representations for a distance to be reported.

Network efficiency of structural covariance networks relate to cognitive performance in children with childhood absence epilepsy

M.J.A. Eussen[1,2], J.F.A. Jansen[2,3], T. Voncken[4], M.H.J.A. Debeij-Van Hall[5], J.G.M. Hendriksen[4,5], R.J. Vermeulen[4], S. Klinkenberg[4], W.H. Backes[2,3], G.S. Drenthen[2,3]

[1] Department of Biomedical Technology, Eindhoven University of Technology, Eindhoven, the Netherlands; [2]Department of Radiology & Nuclear Medicine, Maastricht University Medical Center, Maastricht, the Netherlands; [1] School for Mental Health and Neuroscience, Maastricht University Medical Center, Maastricht, The Netherlands; [4] Department of Neurology, Maastricht University Medical Center, Maastricht, the Netherlands; [5] Department of Behavioral Sciences, Epilepsy Center Kempenhaeghe, Heeze, The Netherlands.

Synopsis: Cognitive deficits have been reported in children with childhood absence epilepsy (CAE). Regional alterations in morphology in children with CAE are likely related to the changes in the underlying network structure. Structural covariance networks (SCNs) based on interregional correlations of cortical thicknesses can describe these changes. To relate cognitive performance to network efficiency, individual SCNs are derived from anatomical MR images of the control group and one patient. The global efficiency calculated from the resulting SCNs showed a negative relation with cognitive performance for children with CAE.

Purpose:

Childhood absence epilepsy (CAE) is a generalized epilepsy and is a common form of epilepsy in school-aged children, typically between 6 and 12 years old. These children experience frequent, brief absence seizures during which the child is not aware or responsive. CAE has been considered as a benign condition, since most children become seizure-free when reaching adulthood. However, various cognitive impairments have been previously reported in children with CAE compared to controls[1,2,3]. Moreover, a previous neuroimaging study also revealed regional alterations in cortical thickness in children with CAE[4]. Possibly, these regional changes are not independent, but are related to an underlying network structure, which can be described by the structural covariance network (SCN). The SCN is constructed using interregional correlations of morphological properties, such as cortical thicknesses, and rests on the assumption that functional and/or axonal connected regions share similar patterns of morphology[5]. The SCNs can subsequently be characterized using graph theoretic analysis, which can provide measures related to network efficiency. The aim of this study is to investigate the potential relation between network efficiency of individual SCNs and cognitive performance of children with CAE.

Methods:

Data acquisition

Sixteen children with clinically diagnosed CAE (6-12y, 12 male) and 15 healthy, age- and sex-matched control subjects (6-12y, 11 male) were included[6]. The Full Scale Intelligence Quotient (FSIQ) of all participants was assessed using the Wechsler Intelligence Scale for Children third edition (WISC-III). All subjects were scanned on a 3.0T (Philips Achieva) scanner using a 32-element phased-array coil. Structural MR images were acquired for each subject using a T1-weighted three-dimensional turbo field echo sequence (TR = 8.4 ms, TE = 3.8 ms, FA = 8°, voxel size 1 mm3).

Preprocessing

As part of the Freesurfer pipeline, T1-weighted images were parcellated into 68 cortical regions based on the Desikan-Killiany atlas, and for each region the mean cortical thickness was determined. Subsequently, for each region, potential effects of age, sex and total intercranial volume on the cortical thickness were regressed out via linear regression models.

SCN construction

For the SCN analysis, each brain region is treated as a node in the network, while the connection strength between the nodes was calculated by the Pearson coefficient across a group of subjects. Therefore, an individual SCN cannot be obtained directly. Previously, Saggar et al.[7] introduced the Add-One-Patient approach to estimate the individual contribution of a patient on the SCN of the control group. In short, the SCN is generated for the control group including one patient. Next, the graph metric is calculated from the resulting SCN. This process is repeated for all subsequent patients, resulting in individual graph metrics for each patient. Negative and non-significant correlations were not considered, to cope with false positive connections. Subsequently, the resulting adjacency matrix is binarized using sparsity thresholds ranging from 85.5%-90% with increments of 0.5%. This allows for comparisons of networks with the same number of connections, which is important since the graph metrics are influenced by the sparsity of the network (i.e. the number of connections). The graph metric used to characterize the network efficiency is the global efficiency, which is inversely related to the mean path lengths between all pairs of nodes in a sparse graph[8]. This metric is normalized with respect to 100 random networks with a preserved degree and strength distribution. A graphical representation of the method is given in Figure 1. All preprocessing and SCN analyses were performed in Matlab.

Statistical analysis

After visual assessment, a Box-Cox transformation is performed on the non-normally distributed global efficiency values. To investigate whether the global network efficiency relates significantly to the FSIQ of children with CAE, a linear regression model was applied. Age and sex are added to the model as covariates. Statistical significance was inferred when $p < 0.05$.

Results:

A significant negative relation between global efficiency and FSIQ was found at a sparsity level of 88.5% ($\beta = -1.21$, $p = 0.03$) and 89% ($\beta = -1.21$, $p = 0.04$). This indicates that at both sparsity levels, a lower FSIQ is associated with a higher global efficiency in children with CAE. A scatterplot of the Box-Cox transformed global efficiency as function as FSIQ at sparsity level 88.5% is shown in Figure 2.

Discussion & Conclusion:

This study demonstrates that the global efficiency calculated from individual cortical thickness derived SCNs is significantly related to the FSIQ of children with CAE. The negative relation for global efficiency and FSIQ indicates that for a more efficient network the FSIQ score is lower. This is in line with the findings of a prior SCN study in epilepsy, which reported that higher clustered (i.e. more efficient) networks related to epilepsy severity, in terms of lower cognitive performance scores, younger age at onset and higher seizure frequency[9]. From the results presented here, a relation between global efficiency and epilepsy severity cannot be formally drawn, therefore, this needs to be further investigated in future work.

References

1. Fonseca Wald ELA, Hendriksen JGM, Drenthen GS, Kuijk SMJV, Aldenkamp AP, Vles JSH, Vermeulen RJ, Debeij-van Hall MHJA, Klinkenberg S. Towards a Better Understanding of Cognitive Deficits in Absence Epilepsy: a Systematic Review and Meta-Analysis. *Neuropsychol Rev.* 2019;29(4):421-449.
2. Caplan R., Siddarth P, Stahl L, Lanphier E, Vona P, Gurbani S, Koh S, Sankar R, Shields W. Childhood absence epilepsy: Behavioral, cognitive, and linguistic comorbidities. *Epilepsia*. 2008;49(11):1838–1846.
3. Fonseca Wald ELA, Klinkenberg S, Voncken TPC, Ebus SCM, Aldenkamp AP, Vles JSH, Vermeulen RJ, Hendriksen JGM, Debeij-Van Hall MHJA. Cognitive development in absence epilepsy during long-term follow-up. *Child Neuropsychol*. 2019;25(8):1003-1021.
4. Kim E, Shim W, Lee J, Yoon H, Ko T, Yum M. Altered structural network in newly onset childhood absence epilepsy. *Journal of Clinical Neurology*. 2020;16(4):573.
5. Wright IC, Sharma T, Ellison ZR, McGuire PK, Friston KJ, Brammer MJ, Murray RM, Bullmore ET. Supra-regional brain systems and the neuropathology of schizophrenia, *Cerebral Cortex.* 1999;9(4):366-378.
6. Drenthen GS, Fonseca Wald EL, Backes WH, Debeij-Van Hall MH, Hendriksen JG, Aldenkamp AP, Vermeulen RJ, Klinkenberg S, Jansen JF. Lower myelin-water content of the frontal lobe in childhood absence epilepsy. *Epilepsia*. 2019;60(8):1689–1696.
7. Saggar M, Hossein, SMH, Bruno JL, Quintin EM, Raman MM, Kesler SR, Reiss AL. Estimating individual contribution from group-based Structural Correlation Networks. *NeuroImage*. 2015;120:274–284
8. Rubinov M, Sporns O. Complex network measures of brain connectivitiy: Uses and interpretations. *NeuroImage*. 2010;52(3):1059-1069.
9. Drenthen GS, Backes WH, Rouhl RPW, Vlooswijk MCG, Majoie MHJM, Hofman PAM, Aldenkamp AP, Jansen JFA. Structural covariance networks relate to the severity of epilepsy with focal-onset seizures. *NeuroImage: Clinical*. 2018;20:861–867.

Acknowledgments / Funding Information: Nothing to disclose.

Figures:

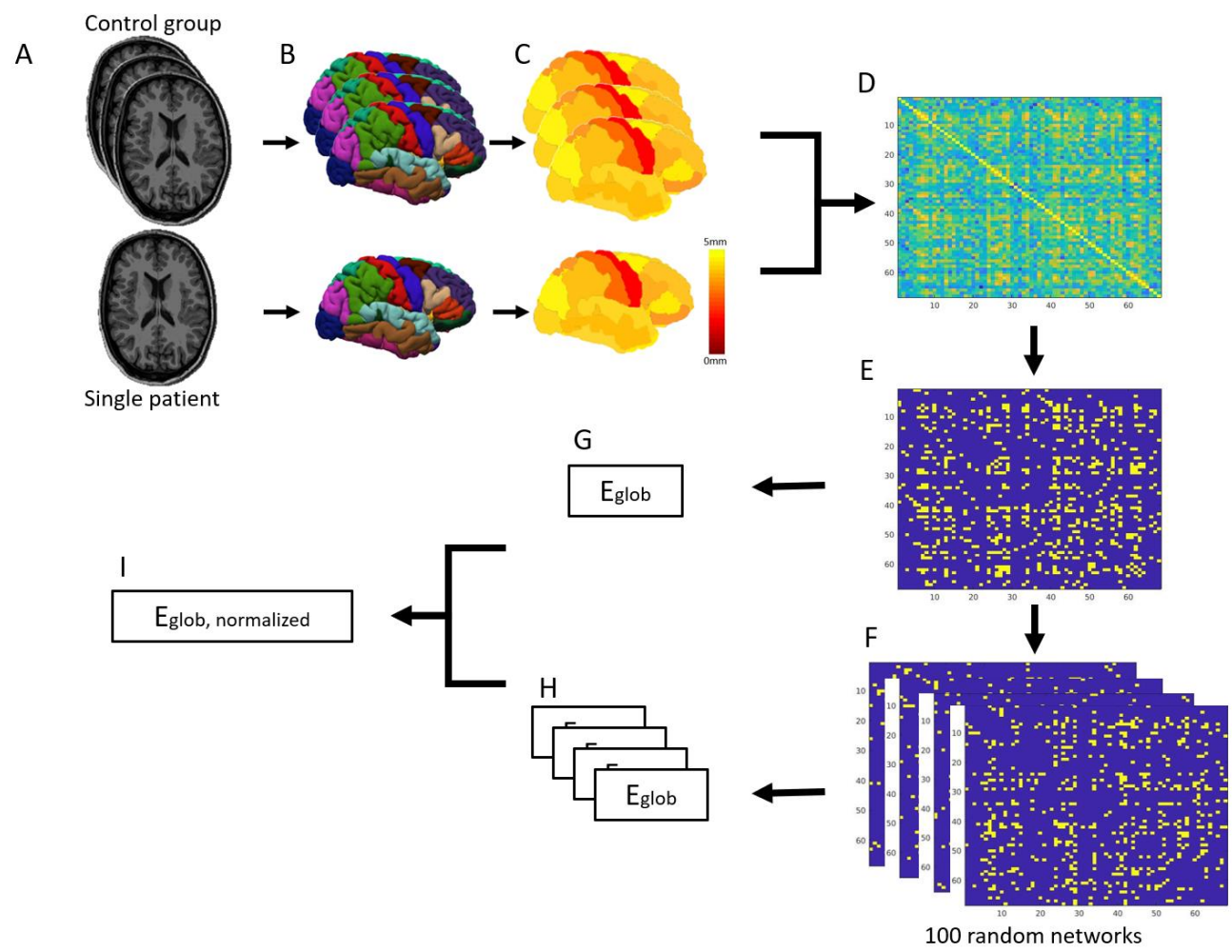

Figure 1 Graphical representation of the method that estimates the individual contribution of a single patient on the SCN of the control group from which the global efficiency is determined. (A) T1-weighted images. (B) Parcellated images. (C) Derive mean cortical thickness for each parcellated region. (D) Adjacency matrix of the SCN based on the control group including one patient. (E) Binarized matrix. (F) Random networks derived from original SCN. (G,H) Global efficiency metrics calculated from the binarized adjacency matrices. (I) Global efficiency metric for one individual patient.

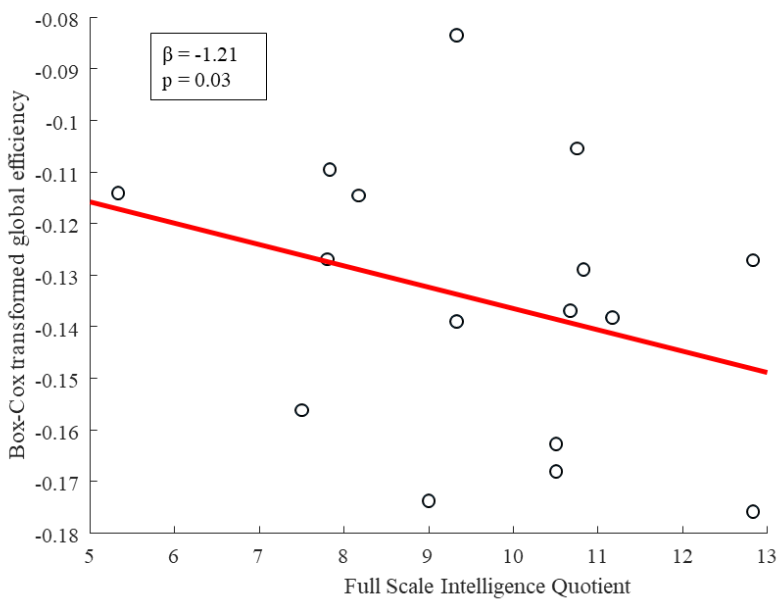

Figure 2 Scatter plot of Box-Cox transformed global efficiency vs Full Scale Intelligence Quotient for a sparsity level of 88.5%. A least squares regression line is added for visualisation.

Effects of the cardiac and respiratory cycles on CSF-mobility in human subarachnoid and perivascular spaces

L. Hirschler[1], B.A. Runderkamp[2], S.J. van Veluw[1,3], M.W.A.Caan[4], and M.J.P. van Osch[1]
[1]C.J. Gorter Center for high Field MRI, Department of Radiology, Leiden University Medical Center, Leiden, The Netherlands
[2] Department of Radiology, Amsterdam University Medical Center, Amsterdam, The Netherlands
[3] Department of Neurology, Massachusetts General Hospital, Harvard Medical School, 175 Cambridge Street, Suite 300, Boston, MA 02114, USA
[4] Department of Biomedical Engineering & Physics, Amsterdam University Medical Center, Amsterdam, The Netherlands

Synopsis: Although research into brain waste clearance has recently gained increasing attention, the driving force(s) as well as the physiological processes involved still remain strongly debated. Here, we assess the influence of the cardiac cycle and of respiration on the mobility of cerebrospinal fluid (CSF), thought to be an important waste carrier. We found that the cardiac cycle was inducing higher CSF-mobility changes than respiration.

Introduction

Despite the increasing evidence that cerebrospinal fluid (CSF)-mediated brain waste clearance is key for cerebral homeostasis, the driving force(s) involved in this process still remain unknown[1,2]: active driving forces have been suggested, such as cardiac pulsations[3], respiration[4], or vasomotion[5], whereas other studies show that drainage only occurs via passive mixing mechanisms[6,7]. Moreover, current knowledge on brain clearance mechanisms is mostly based on experimental studies performed in rodents[3,5,8,9]. However, findings in rodents might not completely reflect CSF-motion in humans since physiological parameters, such as the cardiac or respiratory frequencies, are different between species. Altogether this could influence the relative contribution of the different proposed driving forces of CSF-mobility. In summary, getting a better understanding of the underlying mechanisms driving CSF-mobility is crucial in order to better comprehend human brain clearance.

We previously showed that it was possible to use retrospective binning in k-space to measure CSF-mobility changes over the cardiac cycle[10]. Here we follow up on that work and provide quantitative measures of the influence of the cardiac cycle on CSF-mobility and compare it to that of respiration and to a random binning (negative control) in five regions of interest (ROIs).

Methods

Seven healthy subjects (age: 30±9y) were scanned at 7T (Philips, The Netherlands) using a head transmit coil and a 32-channel receive coil. All provided written informed consent for this IRB-approved study. High-resolution (0.45mm isotropic), whole-brain 3D images were acquired with a long echo time turbo-spin echo sequence (TSE) using a pseudo-random undersampling scheme[10,11] (TSE-factor=146, TE/TR=497/3486ms). As previously described[10,12], seven sets of images were acquired for each volunteer to create a tensor: one without crushers and six with crushers (velocity encoding gradients of 5mm/s) applied in different directions (T_{acq}=40 min).

During the acquisition, the heart rate was recorded using a peripheral pulse unit and the respiration rate using a belt wrapped around the subject's chest. After acquisition, each scan was reconstructed three times using the BART toolbox[13]: the k-space profiles were retrospectively binned in 6 phases, using retrospective binning to either (1) the cardiac cycle, or (2) the respiratory cycle or (3) to random phases (negative control).

Intra-subject images were registered using Elastix[5]. CSF-mobility and fractional anisotropy (FA) were modelled for each (cardiac/respiration/random) phase by computing the mean eigenvalue of a rank-two positive definite tensor, analogous to Diffusion Tensor Imaging.

The CSF-signal intensity, the average CSF-mobility and FA as well as the dependence of the CSF-mobility and FA on cardiac/respiration/random phases were evaluated in five manually delineated ROIs: fourth ventricle, subarachnoid spaces (SAS) around the middle cerebral artery (MCA), motor cortex sulci, perivascular spaces (PVS) in the basal ganglia (BG) and around penetrating arteries of the cortex (Fig.1).

To quantitatively estimate and compare how CSF-mobility varies across the proposed driving forces, the CSF-mobility change was fitted voxel-wise to a sinus function. The fit quality, the maximum amplitude as well as the phase of the maximum amplitude were the output parameters (Fig.4a).

Results

CSF-mobility is highest in the SAS around the MCA (0.041±0.006 mm^2/s, Fig.2b) and 2-3 times lower in PVS of the BG and of penetrating arteries of the cortex.

In large CSF-spaces close to the base of the brain (SAS MCA, 4th ventricle) and in PVS of penetrating arteries in the cortex (Fig.2), CSF-mobility fluctuates with the cardiac cycle but not with respiration (no difference with random binning). At the surface of the brain, in the SAS of the motor cortex sulci, and in the BG-PVS no dependence with either cardiac or respiratory effects is found. The post-processing itself does not artificially generate the observed CSF-mobility changes, since a random binning did not result in a clear pattern across phases (Fig.2-3), also shown by the fit quality which was lower than that of cardiac and respiration (Fig.5). Moreover, the percentage of voxels that presented a good fit (R^2>0.7) to the sinusoidal pattern in the random binning condition was lower than both the cardiac and respiration binning (Fig.4).

In the regions where the cardiac cycle has an effect on CSF-mobility, an opposite effect in FA is observed (Fig.3), albeit at a smaller scale.

The amplitude of the CSF-mobility change induced by the cardiac cycle ranges from 4-12% (Fig.5).

Discussion and conclusion

The cardiac cycle has the highest influence on CSF-mobility in the SAS around large arteries, in the fourth ventricle and in the PVS of penetrating arteries of the cortex. No or minor effects of the respiratory cycle were observed.

The presence of a wave pattern along a vessel or PVS is the subject of further investigations, and might have smoothed potential stronger effects if CSF-mobility varies with different phases within the ROI (e.g. in Figs2&3 that show average profiles over ROIs).

The opposite effects observed on the FA suggest that the cardiac cycle induces CSF motion perpendicularly to the original motion direction.

A strength of our dataset is that a direct comparison can be made between the cardiac/respiration/random phases as they all originate from the same datasets (i.e. one dataset reconstructed in different ways).

Future steps will include studying cardiac and respiratory influence on SAS around veins, since it is hypothesized that respiration induced pressure changes mainly affect the venous system[14].

REFERENCES

1. Dolgin, E. Brain's drain. *Nat. Biotechnol.* (2020) doi:10.1038/s41587-020-0443-1. 2. Mestre, H., Mori, Y. & Nedergaard, M. The Brain's Glymphatic System: Current Controversies. *Trends Neurosci.*, 1–9 (2020). **3.** Mestre, H. *et al.* Flow of cerebrospinal fluid is driven by arterial pulsations and is reduced in hypertension. *Nat. Commun.* (2018) doi:10.1038/s41467-018-07318-3. **4.** Vinje, V. *et al.* Respiratory influence on cerebrospinal fluid flow – a computational study based on long-term intracranial pressure measurements. *Sci. Rep.* (2019) doi:10.1038/s41598-019-46055-5. **5.** van Veluw, S. J. *et al.* Vasomotion as a Driving Force for Paravascular Clearance in the Awake Mouse Brain. *Neuron* (2020) doi:10.1016/j.neuron.2019.10.033. **6.** Smith, A. J. & Verkman, A. S. The 'glymphatic' mechanism for solute clearance in Alzheimer's disease: Game changer or unproven speculation? *FASEB J.* (2018) doi:10.1096/fj.201700999. **7.** Bakker, E. N. T. P., Naessens, D. M. P. & VanBavel, E. Paravascular spaces: entry to or exit from the brain? *Exp. Physiol.* (2019) doi:10.1113/EP087424. **8.** Iliff, J. J. *et al.* A paravascular pathway facilitates CSF flow through the brain parenchyma and the clearance of interstitial solutes, including amyloid β. *Sci. Transl. Med.* (2012) doi:10.1126/scitranslmed.3003748. **9.** Albargothy, N. J. *et al.* Convective influx/glymphatic system: tracers injected into the CSF enter and leave the brain along separate periarterial basement membrane pathways. *Acta Neuropathol.* (2018) doi:10.1007/s00401-018-1862-7. **10.** Hirschler, L. *et al.* The driving force of glymphatics: influence of the cardiac cycle on CSF mobility in perivascular spaces in humans. in *Proceedings of the 29th Annual Meeting of ISMRM, Sydney, Australia, 2020. Abstract 2127.* **11.** Mazzoli, V. *et al.* Accelerated 4D phase contrast MRI in skeletal muscle contraction. *Magn. Reson. Med.* 80, (2018). **12.** Hirschler, L. *et al.* High resolution T2-prepared MRI enables non-invasive assessment of CSF flow in perivascular spaces of the human brain. in *Proceedings of the 28th Annual Meeting of ISMRM, Montréal, Canada, 2019. Abstract 0746.* **13.** Uecker, M., Tamir, J. I., Ong, F. & Lustig, M. The BART Toolbox for Computational Magnetic Resonance Imaging. *Ismrm* (2016). **14.** Rasmussen, M. K., Mestre, H. & Nedergaard, M. Fluid Transport in the Brain. *Physiol. Rev.* (2021) doi:10.1152/physrev.00031.2020.

Acknowledgments / Funding Information: This work is part of the research program Innovational Research Incentives Scheme Vici with project number 016.160.351, which is financed by NWO. It was also supported by Alzheimer Nederland.

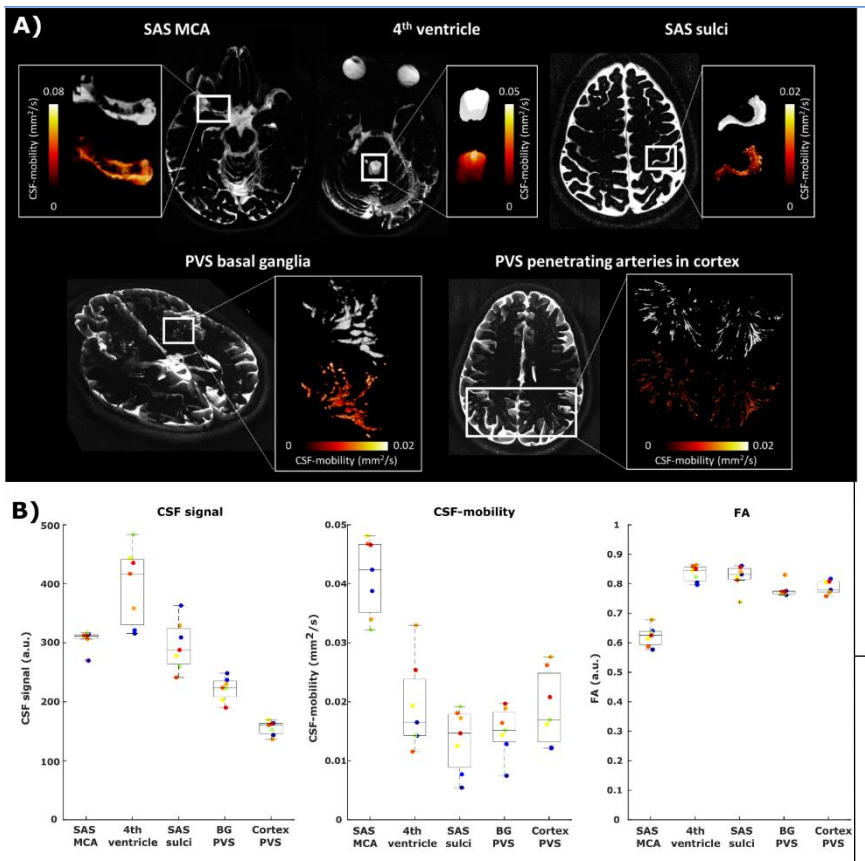

Figure 1: (A) Example of the location of the regions of interest. In each insert, the extracted ROI is shown (top of the inserts) next to the CSF-mobility within the ROI (bottom of the inserts). (B) Average CSF signal (a.u.) (left), CSF-mobility (in mm^2/s) (middle) and FA (a.u.) (right) in the different ROIs. Each point represents the mean value over voxels in a given ROI in one subject.

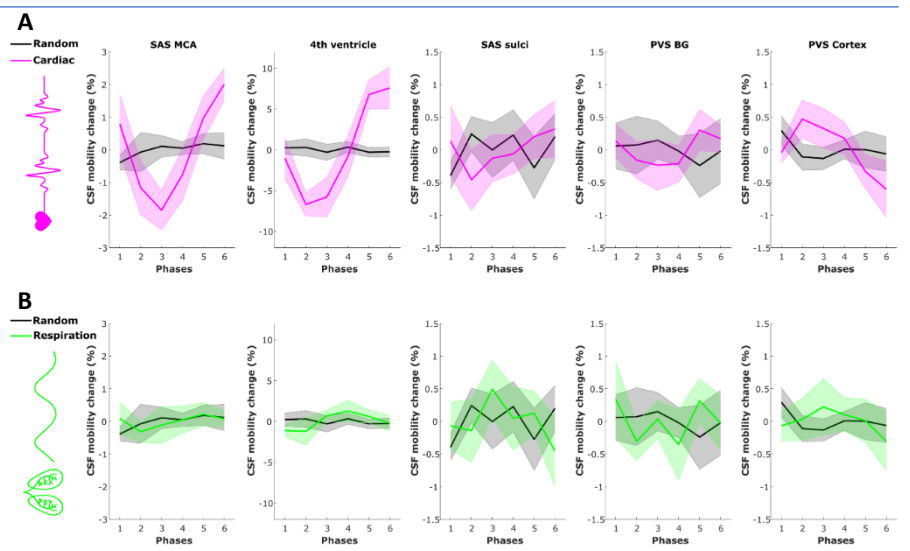

Figure 2: CSF-mobility change from the mean value over phases (in %) across different driving forces in five regions of interest. CSF-mobility change as a function of (A) the cardiac cycle (pink) and random phases (grey) and of (B) respiration (green) and random (grey) phases.

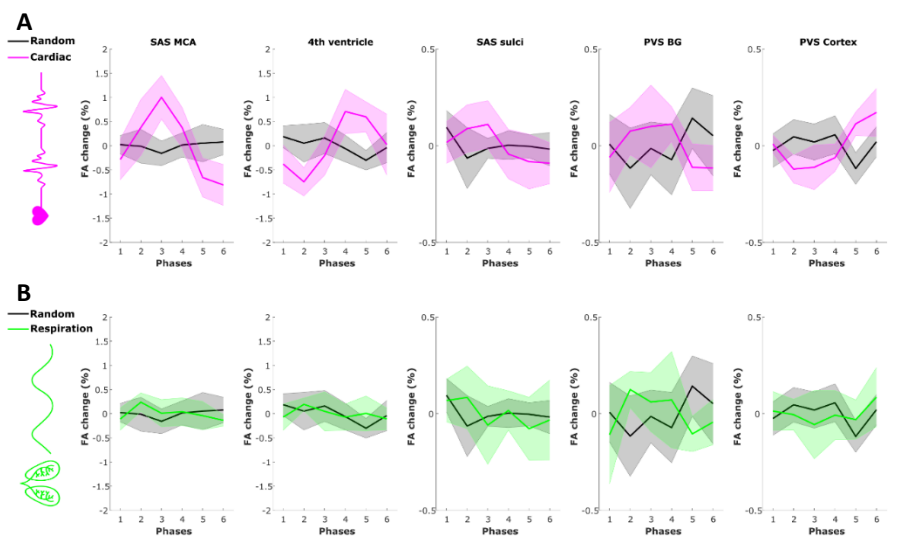

Figure 3: Fractional anisotropy (FA) change from the mean value over phases (in %, mean±1.96*SEM over volunteers) across driving forces in five regions of interest. FA change as a function of (A) the cardiac cycle (pink) and random (grey) phases and of (B) respiration (green) and random (grey) phases.

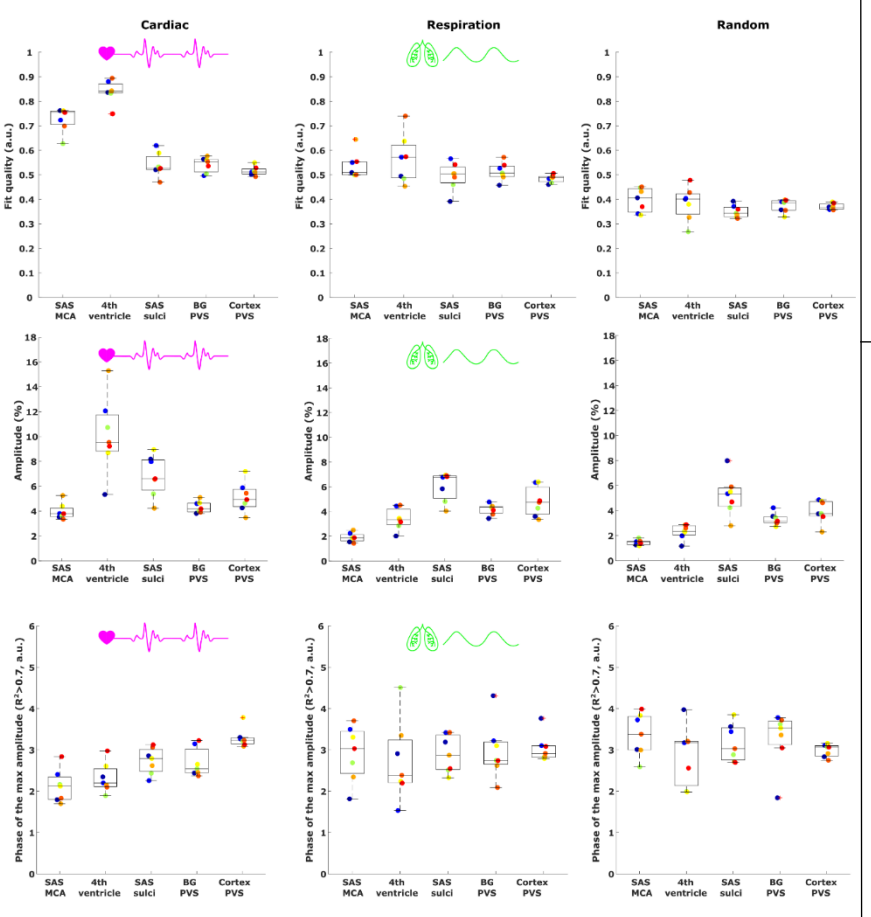

Figure 5: Comparison between the effect of the cardiac (left), respiration (middle) and random (right) binning on the fit output parameters: fit quality (top), amplitude of the maximum (%) (middle) and phase of the maximum CSF-mobility change (bottom) (see Fig.4A). For the phase, only voxels presenting a good fit quality (>0.7) were included. Each colored point represents the value in one subject.

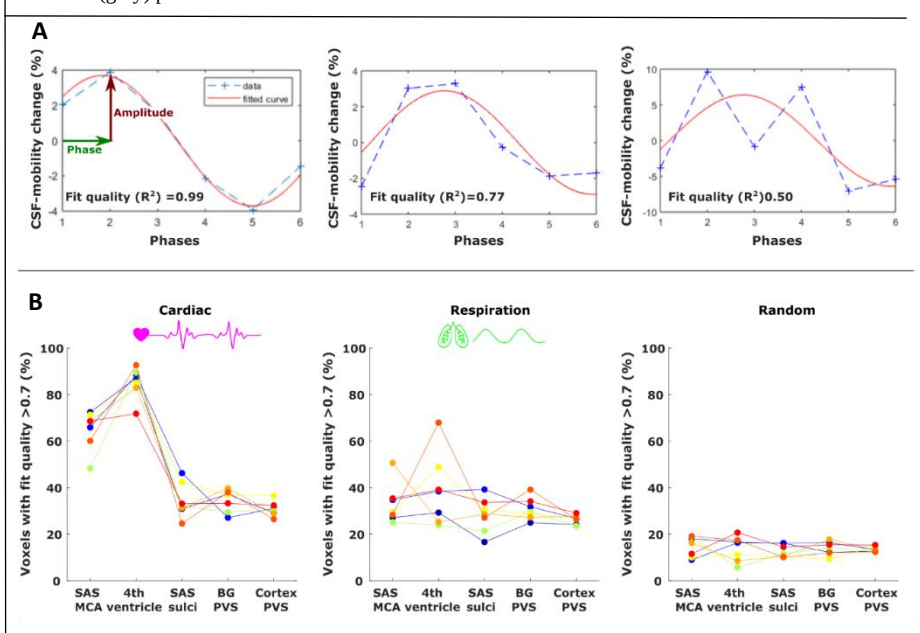

Figure 4: (A) Example of the sinusoidal fit applied (in red) to the signal across phases (dotted blue line) in three different voxels. The associated fit quality is shown in the insert. (B) Percentage of voxels that show a good fit ($R^2 > 0.7$) to the sinusoidal model (relative to the total amount of voxels in the ROI) for the cardiac (left), respiration (middle) and random (right) binning in five ROIs. Every colored line corresponds to the values in one subject.

Towards whole-brain layer-fMRI connectivity: methodological advancements for functional layer connectomics

K. Koiso[1,2], S. Dresbach[1], C. J. Wiggins[3], O. F. Gulban[1,4], Y. Miyawaki[2,5], B. A. Poser[1], R. Huber[1]

[1]Faculty of Psychology and Neuroscience, Maastricht University, Maastricht, NL; [2]Graduate School of Informatics and Engineering, The University of Electro-Communications, Tokyo, Japan; [3]Scannexus, Maastricht, NL; [4]Brain Innovation, Maastricht, NL; [5]Center for Neuroscience and Biomedical Engineering, The University of Electro-Communications, Tokyo, Japan

Synopsis: Laminar-specific fMRI allows neuroscientists to address research questions of directional functional connectivity within and across brain areas. While recent sequence developments allow improvements in coverage and mitigations of venous biases, previous attempts of whole-brain connectome datasets turned out to be too artifact-dominated (Mueller 2021) to be neuroscientifically applicable. Here we present a new and improved sequence used for acquiring a relatively large open dataset of whole-brain laminar connectivity. Its purpose is to: 1) investigate the reproducibility of laminar connectivity results, 2) to benchmark and develop processing pipelines, 3) and to explore which type of new neuroscientific research questions become addressable with laminar fMRI.

Purpose: Laminar-specific fMRI allows neuroscientists to address questions of directional functional connectivity within and across brain areas. While recent sequence developments allow improvements in coverage and mitigations of venous biases, previous attempts of whole-brain connectome datasets turned out to be too artifact-dominated (Mueller 2021) to be neuroscientifically applicable.

Here, we describe our efforts to achieve a new and improved sequence for whole-brain layer-dependent functional connectome mapping. The developed methodology is used to acquire a large openly available dataset of cerebral blood volume and BOLD contrast. The purpose of this public dataset is multifold:

1.) At last year's ISMRM, we proposed a whole-brain protocol (https://cds.ismrm.org/protected/21MPresentations/abstracts/0630.html), which turned out to be unusable due to physiological and scanner artifacts (inflow and traveling wave artifact with long TRs Fig. 1). In this year's work, we aim to present solutions to those artifacts.

2.) We seek to provide a test bed for developing and benchmarking new layer-dependent preprocessing and analysis tools.

3.) We aim to characterise the layer-dependent signatures of common connectivity networks (Pais-Roldán, 2020) and their replicability.

4.) We aim to provide at least 50 runs of movie watching clips (14min each) to quantify reliability of laminar connectivity results.

5.) We want to explore which type of new neuroscientific research questions will become addressable with laminar fMRI.

Methods: Scanning was performed on a SIEMENS MAGNETOM "Classic" 7T scanner while subjects were watching a Human Connectome Project (HCP) movie. For layer-fMRI scanning without venous biases, a blood volume sensitive VASO (Lu 2003) sequence was used. We used the MAGEC VASO approach to maintain the VASO T1-weighting across long echo trains (Huber 2020).

Scanning: This study is based on prior experiments (shown in (Mueller 2021)). In order to find an improved sequence/reconstruction framework for the current study, 9 two-hour sessions in eight participants were performed (shown in Fig. 1-2). These newly improved scan/reconstruction parameters were then used for 8 two-hour sessions in the main single participant. These data are openly accessible on OpenNeuro (Markiewicz 2021): https://openneuro.org/datasets/ds003216. 5 more two-hour sessions datasets will be available soon. The final parameters that we used are: resolution = 0.842mm iso, TR = 5.1s (alternating 5.1s/5.2s), 3D-EPI (Poser 2010), GRAPPA 3x2, two segments and 3D-CAIPI 1 (equivalent to GRAPPA 6x1 with pre-phased CAIPI 3) (Poser 2013, Stirnberg 2021), TA = 14 min, 5 runs per session, the last two TRs were NORDIC (Vizioli 2021) noise scans (not included in reconstruction so far). This sequence is available via SIEMENS' C2P 'app store' Teamplay. Further acquisition parameters: https://layerfmri.page.link/WBprotocol. Respiratory and cardiac traces were recorded for vascular reactivity analyses.

Data processing: Motion correction (ANTS, Avants 2008), BOLD correction in LayNii (Huber 2021), and segmentation of GM and WM were initially performed in FreeSurfer and then manually corrected.

Layer-connectivity analysis: To investigate connectivity networks across layers, we performed ICA on run-averaged functional time series independently on three layer groups. For the columns of specific layer-profiles, we defined columns (LayNii LN2_COLUMNS), calculated 'hubness' (AFNI 3dTcorrMap) and performed PCA (AFNI 3dpc). Then, we highlighted individual layer-profiles and presented their columnar distribution across the brain.

Results and Discussion:

Fig. 1 shows the newly incorporated and tested sequence advancements compared to previous work. The reduction of spatial and temporal artifacts with segmentation and shorter TRs are clearly visible. Fig. 2 depicts results from pilot experiments to find the best acceleration scheme (the winner was six-fold acceleration). Fig. 3 depicts the preprocessing quality (alignment to anatomy, layerification in EPI, and alignment across runs). Fig. 4 and Fig. 5 exemplify the neuroscientific applicability of the provided data. Fig. 4 depicts the layer-dependent differences of common ICA networks. While the Parieto-Frontal network, the Visual network, and the Auditory network show consistent topographical distributions across depths, the 'default mode network' is interestingly showing considerable deviations. We find that the visual and auditory networks show stronger z-scores in superficial and deep layers, compared to middle layers (Fig. 4). This finding might be related to the fact that neurons even in those uni-modal areas have more feedback synapses from cortical areas compared to feedforward input. When analyzing each session's data separately, we see consistent layer signatures, demonstrating high reliability (Fig. 5A).

We used PCA analyses across all layer profiles in all columns to explore data-driven approaches of consistent layer profiles across areas. Doing so for movie watching tasks, we find that columns that exhibit layer-profiles of inverted U-shapes (feedforward-like) tend to be stronger represented in the parieto-frontal area. Whereas columns with U-shaped (feedback-like) layer-profiles tend to be strongly represented in visual areas.

Conclusion:

At last year's ISMRM, we presented an attempt to acquire a whole-brain layer-specific connectivity protocol, with mixed success. This year, we went through a second iteration of re-considering all acquisition and reconstruction choices to reduce the TR, improve the artifact level, and provide another new and improved dataset of 25 runs of whole-brain layer-specific movie watching.

The open dataset provided here, will be useful for benchmarking developing laminar preprocessing strategies. Furthermore, with the large number of runs provided of the same 14 min movie clips, this dataset will be helpful for a comprehensive characterization of the reproducibility layer-fMRI connectivity results.

References:

Avants BB, Epstein CL, Grossman M, Gee JC. Symmetric diffeomorphic image registration with cross-correlation: Evaluating automated labeling of elderly and neurodegenerative brain. Med Image Anal. 2008;12(1):26-41. doi:10.1016/j.media.2007.06.004

Guidi M, Huber L, Lampe L, Merola A, Ihle K, Möller HE. Cortical laminar resting-state fluctuations scale with the hypercapnic bold response. HBM. 2020;41:2014-2027. doi:10.1002/hbm.24926

Havlicek M, Uludag K. A dynamical model of the laminar BOLD response. Neuroimage. 2019;204:116209. doi:10.1101/609099

Huber L, Finn ES, Chai Y, et al. Layer-dependent functional connectivity methods. Prog Neurobiol. 2020:in print. Doi:j.pneurobio.2020.101835

Huber L (Renzo), Poser BA, Bandettini PA, et al. LayNii: A software suite for layer-fMRI. Neuroimage. 2021;237:118091. doi:10.1016/j.neuroimage.2021.118091

Lu H, Golay X, Pekar JJ, van Zijl PCM. Functional magnetic resonance imaging based on changes in vascular space occupancy. Magn Reson Med. 2003;50:263-274. doi:10.1002/mrm.10519

Markiewicz CJ, Gorgolewski KJ, Feingold F, et al. OpenNeuro: An open resource for sharing of neuroimaging data. Elife. 2021:10:e71774. doi: https://doi.org/10.7554/eLife.71774.

Mueller et al, 2021, ISMRM #0630,

Poser BA, Koopmans PJ, Witzel T, Wald LL, Barth M. Three dimensional echo-planar imaging at 7 tesla. Neuroimage. 2010;51(1):261-266. doi:10.1016/j.neuroimage.2010.01.108

Poser BA, Ivanov D, Kemper VG, Kannengiesser SA, Uludag K, Barth M. CAIPIRINHA-accelerated 3D EPI for high temporal and / or spatial resolution EPI acquisitions. Esmrmb. 2013:226.

Pais-Roldán P, Yun SD, Palomero-Gallagher N, Shah NJ. Cortical depth-dependent human fMRI of resting-state networks using EPIK. bioRxiv. 2020:1-26. doi:10.1101/2020.12.07.414144

Stirnberg R, Stöcker T. Segmented K-Space Blipped-Controlled Aliasing in Parallel Imaging (Skipped-CAIPI) for High Spatiotemporal Resolution Echo Planar Imaging. Magn Reson Med. 2020;85(0):1540-1551. doi:10.1101/2020.06.08.140699

Shadlen MN, Kiani R. Decision making as a window on cognition. Neuron. 2013;80(3):791-806. doi:10.1016/j.neuron.2013.10.047

Vizioli L, Moeller S, Dowdle L, et al. Lowering the thermal noise barrier in functional brain mapping with magnetic resonance imaging. Nat Commun. 2021;12:5181. doi:10.1038/s41467-021-25431-8

Acknowledgments / Funding Information: Help with scanning: These data were acquired with the kind support of Scannexus at their 7T MAGNETOM "Classic" SIEMENS scanner. We thank Mathilde Kennis for assistance with after hour scans. Funding: Kenshu Koiso is funded by Japan Public-Private Partnership Student Study Abroad Program (TOBITATE! Young Ambassador Program), by Japan Student Services Organization (JASSO) and by UEC fund. Laurentius Huber was funded by the NWO VENI project 016.Veni.198.032. Benedikt Poser is partially funded by the NWO VIDI grant 16.Vidi.178.052, by the National Institute for Health grant R01MH/111444 (PI David Feinberg) and by the H2020 FET-Open AROMA grant agreement no. 88587. Yoichi Miyawaki is funded by JSPS KAKENHI (20H00600, 18KK0311). Ethics: The scanning procedures have been approved by the Ethics Review Committee for Psychology and Neuroscience (ERCPN) at Maastricht University, following the principles expressed in the Declaration of Helsinki.

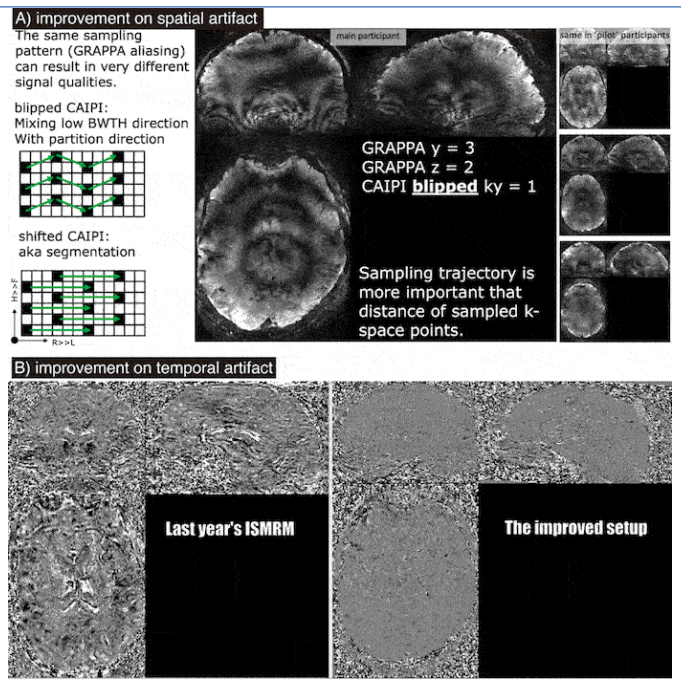

Figure 1. New and improved artifact level (GIF animation)

Panel A: Segmentation and kz-CAIPI can shorten TRs without ghosting artifacts that are common when mixing the low bandwidth direction with the partition direction. This insight allowed us to reduce the volume TR from 8.9 s to 5.1 s.

Panel B: Temporal artifact level of the improved sequence/reconstruction approach. This figure presents the temporal VASO signal evolution (demeaned) of movie watching data averaged across 20 runs (across 4 days).

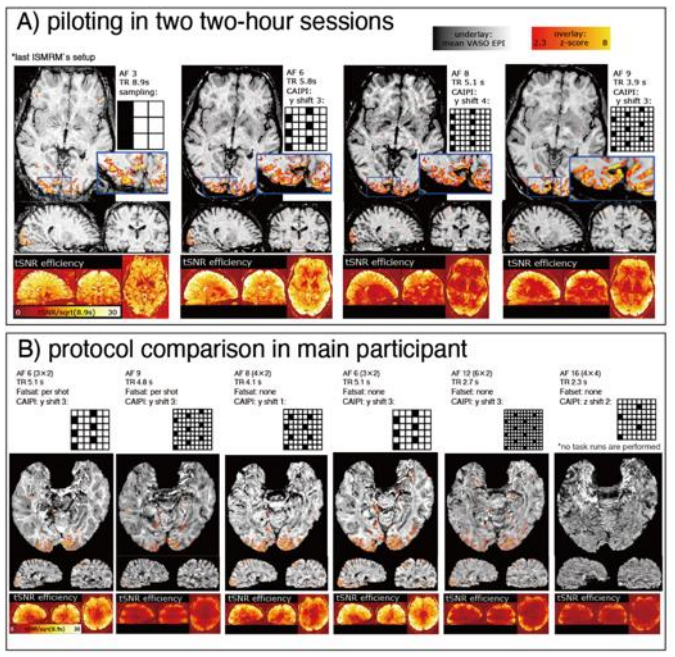

Figure 2. Finding the best sampling approach

Panel A: Piloting before scanning the main participant. The middle left sequence (AF = 6, TR = 5.8 s, CAIPI y shift 3) has an advantageous tSNR efficiency.

Panel B: Protocol comparison in the main participant. The third column (AF = 6, TR = 5.1 s without fat saturation) depicts a good compromise of TR and artifact level. We decided to use this sequence for all subsequent scans.

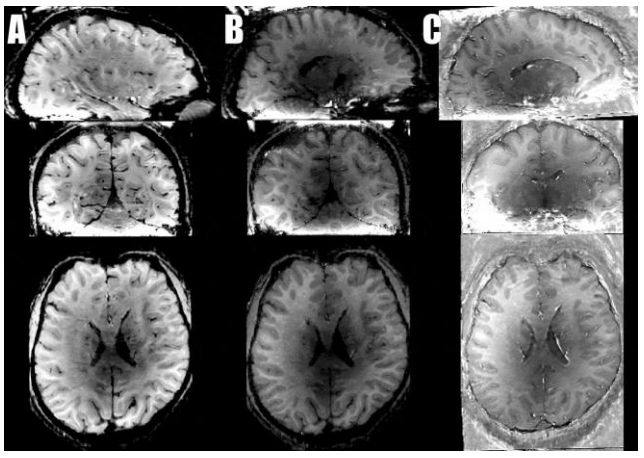

Figure 3. Preprocessing quality (GIF animation)

Panel A: Non-linear alignment quality of a 3T MPRAGE to VASO EPI. Most of the brain is of usable quality.

Panel B: Layerification quality in the EPI space.

Panel C: Session-to-session alignment quality. The gif animation cycles across 5 separate sessions of multiple days.

Note that the spatially heterogeneous brightness level of the T1-weighted EPI is a feature of variable flip angles in the MAGEC-VASO approach and does not affect the functional contrast.

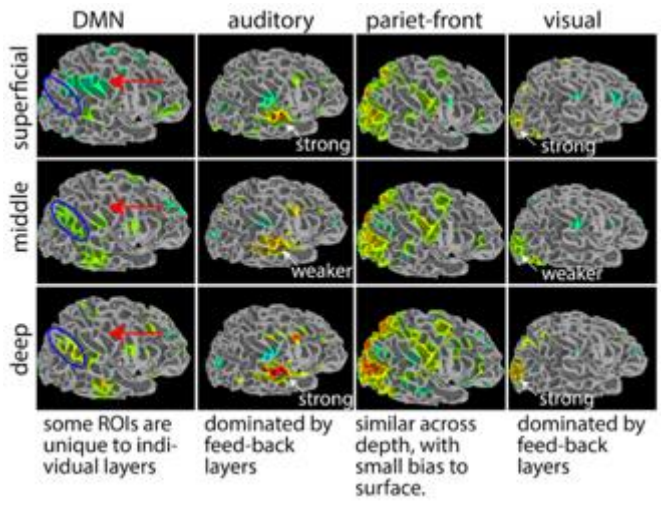

Figure 4. Layer-dependent differentiation of ICA-determined connectivity networks

We find that the primary areas (e.g., visual and auditory) are showing stronger z-scores for superficial and deep layers. The DMN seems to subdivide into different sub-ROIs for different layers. Other networks (e.g., parietal-frontal) are relatively consistent across depths with minimal layer-differentiation. Note that the purpose of this figure is to exemplify the neuroscientific usability of the provided data.

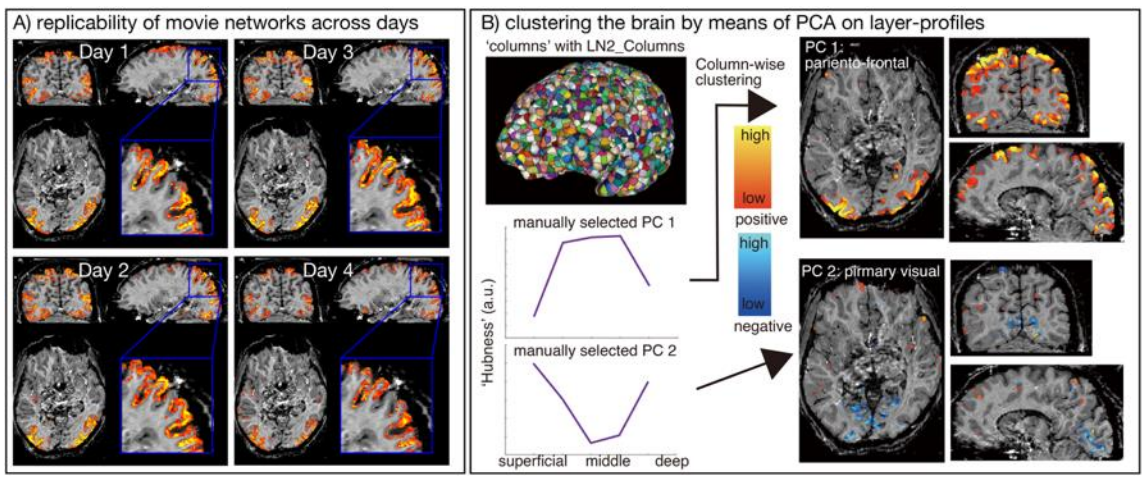

Figure 5. Network detection replicability and layer-profile analysis

Panel A: GLM results of a representative brain network shown independently for each day. We can see consistent layer signatures for each day's result.

Panel B: PCA extracted columns with feedforward-like and feedback-like layer-profiles. The columns (top left in B) are generated with the LayNii command "LN2_Columns". The lower left graphs are the two representative layer-profile PCs. The right figures in panel B are the columns with the selected layer-profile PCs accordingly.

MAGiC in glioma: Are pre-contrast quantitative MRI parame-ters different in tumors with versus without contrast-enhancement?

Laura Nunez-Gonzalez[1], Karin A. van Garderen[1,2], Marion Smits[1,2], Jaap Jaspers[3], Alejandra Méndez Romero[3], Dirk H.J.Poot[1], and Juan A. Hernandez-Tamames[1,4]

[1] Radiology and Nuclear Medicine, Erasmus MC - University Medical Center Rotterdam; The Netherlands;
[2] Brain Tumor Center, Erasmus MC Cancer Institute, Rotterdam, The Netherlands;
[3]Department of Radiotherapy, Erasmus MC Cancer Institute, Rotterdam, The Netherlands;
[4]Department of Imaging Physics, Faculty of Applied Physics, TU Delft, Delft, The Netherlands;

Synopsis: We analyze quantitative values in glioma obtained with MAGiC, which allows obtaining quantitative T1, T2 and PD maps in one single acquisition of less than 6 minutes for a whole brain. The maps were obtained before contrast-agent injection in 14 patients with glioma. We investigated the possibility of characterizing tumor regions based on quantitative maps acquired without contrast-agent. The results showed significant differences among tumoral tissue, tissue with T1w-enhancement, and normal white matter. Voxel-wise, this allowed to distinguish tumoral tissue but did not allow to accurately predicting T1w-enhancement. However, promising results were found predicting T1w-enhancement inside the tumor.

1. Introduction. The standard assessment of gliomas includes several weighted images[1,2]. Fast quantitative MR imaging could improve these protocols by reducing scan-time andsystem-variability[3–5] but must be validated. Characterization of tumor tissue and enhancement prediction using quantitative maps wereereported[6–9], but focusing only on T1[6,7] or T2[8,9]. In this work, we characterized gliomas using parametric maps obtained using MAGiC acquired before contrast injection and investigated its T1w-enhancement prediction capability.

2. Methods. Acquisitions were performed after Institutional Review Board approval with GE 3.0T systems (General Electric Medical Systems, USA):GE-MR750 and GE-Signa-Premier. A 16-channel Head and Neck array coil was used. After giving informed consent, 14 patients were scanned. The whole brain was acquired in 5min and 34s using MAGiC before contrast-agent injection, with TE=92.24ms, TR=4000ms, FOV=224mm, slice-thickness=4 mm and voxel-size=0.875x0.875x5mm^3.

The T1w, T1c, T2Wand T2-FLAIRwere used to segment the gliomas using HD-GLIO[10,11]. Regions of interest (ROIs) were defined for the non-enhancing-T2-weighted-hyperintensities (T2h) and for T1w-enhancement (T1e). Also, an ROI1cm around the tumor for the peritumoral area (PER)was defined, other for normal white matter (nWM), and another joining T2h and T1e (TUM).The mean, standard deviation (STD), Skewness, and Kurtosis for T1 and T2 was computed inside each ROI. The average across patients and 95% confidence interval (CI) were computed and signed-rank Wilcoxon test used to detect differences between ROIs.

Receiver operating characteristic curve (ROC) analysis[12] was performed to distinguish between TUM and nWM; T1e and the rest; and T1e and T2h. We considered T1, T2, the Euclidian norm of T1 and T2 (normT1T2) and the Euclidian norm of the logarithm of T1 and T2 (normlog). The optimal operating point was calculated as the highest Youden's index[13]. The threshold obtained was applied to the quantitative maps.

A cross-validated ROC analysis was performed to distinguish T1w-enhancement in tumors by the leaving-pair-out[14] method. The threshold associated with the Youden's index was applied to classify the left-out-pair. Then the average AUC, sensitivity, specificity and accuracy were calculated.

3. Results. Tables 1 and 2 report tables with the ROIs statistics.

Voxel-wise. To discriminate between TUM and nWM, normlog was the metric with the highest AUC (0.95), with sensitivity=92.03%, specificity=86.88% at threshold=8.44. For distinguishing T1w-enhancement, normT1T2 had the highest AUC (0.85), with a priori sensitivity=81.79%, specificity= 71.99% at threshold= 1344ms.

Figure 1 shows the segmentations for one patient using HD-GLIO and applying the thresholds from the ROC analysis. Voxels with normlog> 8.44 were classified as tumor (TUM*), and with normT1T2>1344ms as T1w-enhancement (T1e*).

T1w-enhancement. The PDF of the T1, T2, normT1T2 and normlog are plotted for patients with and without T1w-enhancement (Figure 2). Table 3 shows a table with the mean AUC, sensitivity, specificity and accuracy obtained from the leave-pair-out analysis. The highest AUC was obtained using T1 and the normT1T2 (0.68).

4. Discussion. The results show that the distributions of T1 and T2 values differentiates tumor from normal white matter. Regarding voxel-wise T1w-enhancement, the amount of misclassified voxels without enhancement as T1e* could lead to false positives. It could be that pre-contrast quantitative images deviate in the enhancing tumor due to some leakage in the blood brain barrier (BBB) not appreciable in conventional images[15,16], or something else correlated with BBB leakage. However, it is possible that only applying a threshold to the pre-contrast quantitative images has moderate ability to detect T1w-enhancement[15].

The analysis done on tumors showed that it could be possible to discriminate between enhanced and no-enhanced tumors. It seems that the process of contrast leakage is correlated with the structural information obtained in the pre-contrast scans. But further investigation is needed, with larger cohort of patients. Avoiding contrast agent could mean an improvement for brain tumor patients who need to undergo repeated MRI acquisitions.

Classification of voxels could probably be improved with more advanced techniques.

5. Conclusions. We showed clear differences in quantitative values for the tumoral and healthy tissue. In glioma, the pre-contrast normT1T2 is predictive for the post-contrast enhancing tumor. This work encourages further exploration of quantitative imaging in gliomas with the possibility of reducing scan-time and avoiding contrast-agent administration.

References

1. Ellingson BM, Bendszus M, Boxerman J, et al. Consensus recommendations for a standardized Brain Tumor Imaging Protocol in clinical trials. *Neuro-Oncology*. Published online August 6, 2015. doi:10.1093/neuonc/nov095

2. Weller M, van den Bent M, Preusser M, et al. EANO guidelines on the diagnosis and treatment of diffuse gliomas of adulthood. *Nat Rev Clin Oncol*. 2021;18(3):170-186. doi:10.1038/s41571-020-00447-z

3. Deoni SCL. Quantitative Relaxometry of the Brain: *Topics in Magnetic Resonance Imaging*. 2010;21(2):101-113. doi:10.1097/RMR.0b013e31821e56d8

4. Gómez PA, Cencini M, Golbabaee M, et al. Rapid three-dimensional multiparametric MRI with quantitative transient-state imaging. *arXiv:200107173 [physics]*. Published online June 27, 2020. Accessed July 7, 2020. http://arxiv.org/abs/2001.07173

5. Warntjes JBM, Leinhard OD, West J, Lundberg P. Rapid magnetic resonance quantification on the brain: Optimization for clinical usage. *Magnetic Resonance in Medicine*. 2008;60(2):320-329. doi:10.1002/mrm.21635

6. Hattingen E, Müller A, Jurcoane A, et al. Value of quantitative magnetic resonance imaging T1-relaxometry in predicting contrast-enhancement in glioblastoma patients. *Oncotarget*. 2017;8(32):53542-53551. doi:10.18632/oncotarget.18612

7. Kleesiek J, Morshuis JN, Isensee F, et al. Can Virtual Contrast Enhancement in Brain MRI Replace Gadolinium?: A Feasibility Study. *Investigative Radiology*. 2019;54(10):653-660. doi:10.1097/RLI.0000000000000583

8. Laule C, Bjarnason TA, Vavasour IM, et al. Characterization of brain tumours with spin–spin relaxation: pilot case study reveals unique T 2 distribution profiles of glioblastoma, oligodendroglioma and meningioma. *Journal of Neurology*. 2017;264(11):2205-2214. doi:10.1007/s00415-017-8609-6

9. Pirkl CM, Nunez-Gonzalez L, Kofler F, et al. Accelerated 3D whole-brain T1, T2, and proton density mapping: feasibility for clinical glioma MR imaging. *Neuroradiology*. Published online April 9, 2021. doi:10.1007/s00234-021-02703-0

10. Kickingereder P, Isensee F, Tursunova I, et al. Automated quantitative tumour response assessment of MRI in neuro-oncology with artificial neural networks: a multicentre, retrospective study. *The Lancet Oncology*. 2019;20(5):728-740. doi:10.1016/S1470-2045(19)30098-1

11. Isensee F, Jäger PF, Kohl SAA, Petersen J, Maier-Hein KH. Automated Design of Deep Learning Methods for Biomedical Image Segmentation. *arXiv:190408128 [cs]*. Published online April 2, 2020. Accessed December 3, 2020. http://arxiv.org/abs/1904.08128

12. Streiner DL, Cairney J. What's under the ROC? An Introduction to Receiver Operating Characteristics Curves. *Can J Psychiatry*. 2007;52(2):121-128. doi:10.1177/070674370705200210

13. Youden WJ. Index for rating diagnostic tests. :5.

14. Airola A, Pahikkala T, Waegeman W, De Baets B, Salakoski T. An experimental comparison of cross-validation techniques for estimating the area under the ROC curve. *Computational Statistics & Data Analysis*. 2011;55(4):1828-1844. doi:10.1016/j.csda.2010.11.018

15. Blystad I, Håkansson I, Tisell A, et al. Quantitative MRI for Analysis of Active Multiple Sclerosis Lesions without Gadolinium-Based Contrast Agent. *American Journal of Neuroradiology*. 2016;37(1):94-100. doi:10.3174/ajnr.A4501

16. Blystad I, Warntjes JBM, Smedby Ö, Lundberg P, Larsson EM, Tisell A. Quantitative MRI using relaxometry in malignant gliomas detects contrast enhancement in peritumoral oedema. *Scientific Reports*. 2020;10(1). doi:10.1038/s41598-020-75105-6

Acknowledgments / Funding Information: This research was funded by General Electric Healthcare, grant number B-GEHC-5 GE for the project "MR Physiological Signature" and "The APC was funded by Erasmus Medical Center". Part of the study was funded by HollandPTC-Varian consortium-confined call 2018, grant number 2018013, for the project "Improving toxicity modelling, patient selection and clinical outcome of proton therapy in low grade glioma".

Table 1. Table withstatistics of the T1 values from all the patients. Column 3: Mean over patients of the T1 ROI statistics. Column 4: 95% CI of the mean over patients. Column 5: P-values of the Wilcoxon signed-rank test with the nWM (P-val ROI vs nWM). Column 6: P-values of the Wilcoxon signed-rank test with the tumoral tissue without T1w-enhancement (P-val ROI vs T2h). Column 7: P-values of the Wilcoxon signed-rank test with the T1w-enhancement voxels (P-val ROI vs T1e). * indicates $p < 0.05$.

ROI	ROI statistic	Mean (ms)	95% CI (ms)	Pval (ROI vs nWM)	Pval (ROI vs T2h)	Pval (ROI vs T1e)
nWM	Mean	993.16	± 38.20	-	< 0.01*	0.02*
	STD	294.04	± 39.61	-	0.95	0.02*
	Skewness	2.64	± 0.57	-	< 0.01*	0.02*
	Kurtosis	16.19	± 6.13	-	< 0.01*	0.02*
T2h	Mean	1353.78	± 92.41	< 0.01*	-	0.02*
	STD	294.68	± 39.78	0.95	-	0.02*
	Skewness	1.23	± 0.39	< 0.01*	-	0.16
	Kurtosis	6.00	± 1.73	< 0.01*	-	0.08
T1e	Mean	1713.30	± 53.19	0.02*	0.02*	-
	STD	448.03	± 51.00	0.02*	0.02*	-
	Skewness	1.00	± 0.19	0.02*	0.16	-
	Kurtosis	4.30	± 0.86	0.02*	0.08	-
PER	Mean	1056.78	± 60.48	0.01*	< 0.01*	0.02*
	STD	315.16	± 65.47	0.24	0.33	0.03*
	Skewness	2.27	± 0.54	< 0.01*	< 0.01*	0.03*
	Kurtosis	13.50	± 6.28	< 0.01*	0.01*	0.03*

Table 2. Table with statistics of the T2 values from all the patients. Column 3: Mean over patients of the T1 ROI statistics. Column 4: 95% CI of the mean over patients. Column 5: P-values of the Wilcoxon signed-rank test with the nWM (P-val ROI vs nWM). Column 6: P-values of the Wilcoxon signed-rank test with the tumoral tissue without T1w-enhancement (P-val ROI vs T2h). Column 7: P-values of the Wilcoxon signed-rank test with the T1w-enhancement voxels (P-val ROI vs T1e). * indicates $p < 0.05$.

ROI	ROI statistic	Mean (ms)	95% CI (ms)	Pval (ROI vs nWM)	Pval (ROI vs T2h)	Pval (ROI vs T1e)
nWM	Mean	92.33	± 4.43	-	< 0.01*	0.02*
	STD	48.90	± 10.61	-	0.04*	0.02*
	Skewness	10.72	± 1.75	-	< 0.01*	0.02*
	Kurtosis	184.88	± 57.84	-	< 0.01*	0.02*
T2h	Mean	152.25	± 16.06	< 0.01*	-	0.30
	STD	64.63	± 12.34	0.04*	-	0.02*
	Skewness	4.62	± 1.13	< 0.01*	-	0.08
	Kurtosis	42.38	± 13.60	< 0.01*	-	0.08
T1e	Mean	180.05	± 22.52	0.02*	0.30	-
	STD	130.81	± 45.67	0.02*	0.02*	-
	Skewness	3.57	± 0.95	0.02*	0.08	-
	Kurtosis	24.92	± 11.51	0.02*	0.08	-
PER	Mean	103.82	± 9.75	< 0.01*	< 0.01*	0.02*
	STD	63.56	± 24.05	0.01*	0.50	0.16
	Skewness	8.10	± 1.99	< 0.01*	< 0.01*	0.03*
	Kurtosis	111.55	± 54.74	< 0.01*	< 0.01*	0.03*

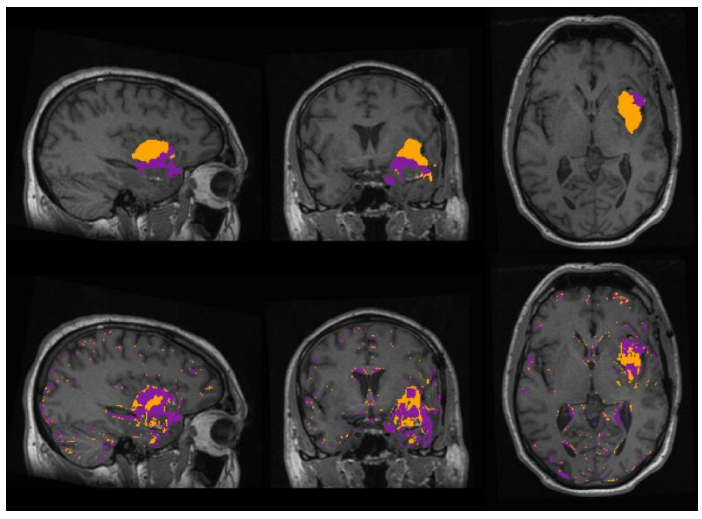

Figure 1. Patient 3. Sagittal, coronal and axial planes of the segmentations overlaid on the T1w scan from. Top: segmentation from HD-GLIO, T2-hyperintensity (T2h) in orange and T1-enhancement (T1e) in purple. Bottom: using thresholding, voxels classified as tumor (TUM*) in orange and voxels classified as T1w-enhanced (T1e*) in purple. The purple T1e* region is overlapped with the orange TUM*.

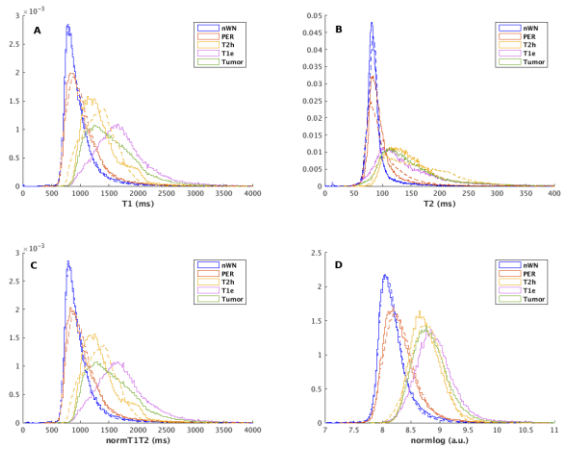

Figure 2. Probability density functions of the T1 values (A), T2 values (B), the norm of T1 and T2 values –normT1T2- (C), and the norm of the logarithm of T1 and T2 values –normlog- (D) for all the patients showing T1w-enhancement (solid line) and for all the patients without T1w-enhancement (dashed line) for each region of interest (ROI) (Blue->normal white matter -nWM-, Red->peritumoral area –PER-, Yellow-> T2 hyperintensity -T2h-, Purple -> T1w-enhancement -T1e-, Green -> T2h + T1e -TUMOR-)

	Param	Mean AUC (STD)	Sensitivity	Specificity	Accuracy
T1	Mean	0.62 (0.03)	59 %	71 %	65 %
	STD	0.65 (0.03)	45 %	86 %	65 %
	Skewness	0.65 (0.03)	59 %	73 %	66 %
	Kurtosis	0.68 (0.03)	73 %	73 %	73 %
T2	Mean	0.54 (0.04)	41 %	43 %	42 %
	STD	0.58 (0.03)	29 %	100 %	64 %
	Skewness	0.58 (0.03)	61 %	43 %	52 %
	Kurtosis	0.56 (0.03)	65 %	35 %	50 %
normT1T2	Mean	0.62 (0.03)	59 %	71 %	65 %
	STD	0.65 (0.03)	45 %	86 %	65 %
	Skewness	0.66 (0.03)	61 %	63 %	62 %
	Kurtosis	0.68 (0.03)	73 %	73 %	73 %
normlog	Mean	0.61 (0.03)	71 %	71 %	71 %
	STD	0.52 (0.04)	73 %	31 %	52 %
	Skewness	0.61 (0.03)	57 %	86 %	71 %
	Kurtosis	0.66 (0.03)	61 %	63 %	62 %

Table 3. Table with the averaged area under the curve (AUC) of the receiver operating characteristic(ROC) analysis on distinguishing between tumors with and without T1w-enhancement and its standard deviation between brackets from all the leave-pair-out sets used for cross-validation for each statistical parameter. Last three columns report the sensitivity, specificity and accuracy taking into account all the sets and the results of the leave-pair-out analysis.

Repeatability of APTw imaging at 7T

I.V. Obdeijn[1], L. Alic[2], M.H. Lequin[1,3], S.L.A. Plasschaert[3], W.J.M. van der Kemp[1], J.H. Hoogduin[1], D.W.J. Klomp[1], J.P. Wijnen[1], and E.C. Wiegers[1]

[1]Department of Radiology, University of Medical Centre Utrecht, Utrecht, the Netherlands; [2]Magnetic Detection and Imaging Group, Technical Medical Centre, University of Twente, Enschede, the Netherlands; [3]Department of paediatric neuro-oncology, Princess Maxima Centre, Utrecht, the Netherlands

Synopsis: APTw imaging is a potential imaging biomarker to assess treatment effects in brain tumours, especially at high field MRI (7T) due to improved signal-to-noise-ratio enabling the assessment of APTw values in heterogenous tumours. Embedding of APTw imaging in clinical decision making requires insight in the repeatability of APTw imaging. Therefore, we evaluated the repeatability of APTw imaging at 7T by using a phantom and in vivo in the human brain subjects. Repeatable and specific APTw maps were obtained at 7T, which facilitate the potential of detecting metabolic changes in brain tumours due to treatment.

Introduction:

Amide proton transfer weighted (APTw) imaging is based upon chemical exchange saturation transfer (CEST) and enables in vivo assessment of tissue-bound mobile proteins and peptides[1,2]. Promising applications of APTw imaging in neuro-oncology include differentiation between high and low grade glioma and between true progression and pseudoprogression[3]. Furthermore, APTw imaging is reported as a potential imaging biomarker for the assessment of treatment effects in brain tumours[4,5]. At 7T MRI, the improved signal-to-noise-ratio and spectral resolution and prolonged T1 relaxation time enables APTw imaging at higher resolution which in turn makes it possible to measure heterogeneity of APTw values in brain tumours relevant for the evaluation of treatment effects[1,6,7]. For application of APTw imaging in clinical decision making regarding treatment effects in brain tumours insight in the repeatability is required. Therefore, the aim of this study is to assess the repeatability of APTw imaging at 7T in a phantom and in vivo in the human brain.

Methods:

A 7T MRI scanner (Achieva, Philips Healthcare, Best, The Netherlands) was used in combination with a 32-channel receive and 8-channel transmit head coil (Nova Medical, Wilmington (MA), United States). The APTw images were acquired with a 3D gradient echo sequence with 35 frequency offsets [$\Delta\omega$=0,±0.20,±0.27,±0.50,±1.17,±1.84,±2.60,±2.80,±3.00,±3.20 ±3.34,±3.65,±3.80,±4.20,±6.71,±20.00,±40.00 and S_0, $\Delta\omega$=±600.00 ppm] and the following imaging parameters: saturation time= 1.4 (56 block pulses (alternating between two 4-channel quadrature B_1 shim settings) of 25 ms); TFE shot-interval of 8s (overall TR); $B_{1,rms}{}^{+}$= 2.1 µT; SENSE factor AP of 2.4, matrix= 128x128x12; FOV= 256x256x24 mm^3; voxel size= 2.0x2.0x2.0 mm^3; TR/TE= 3.75/1.8 ms; flip angle= 5°. Image protocol based on a protocol optimized to measure multiple metabolites[8].

A cylindrical phantom filled with 0.9% saline solution and five submerged falcon tubes (Figure 1-A), at pH ~7.0 (range 6.8-7.2; measured with indicator strips), contained solutions of nicotinamide (NAM; 20, 50 and 100 mM), glutamate (Glu; 10 mM) and glycine (Gly; 20 mM). APTw images in supratentorial and infratentorial brain region were acquired in five healthy subjects (2m/3f; age: 25.8±1.7 years). T1w-images were used to position the two CEST slabs along the AC-PC line for the supratentorial slab, and a line between the superior pontine notch and the inferior edge of the quadrigeminal plate for the infratentorial slab. The phantom and subjects were scanned twice, with an interval of one week.

Processing

Z-spectra were normalized with respect to the unsaturated z-spectral point (S_0). B_0-correction was performed pixel-wise by defining the position of the minimum of the z-spectrum, shifting, and resampling the z-spectrum accordingly. The z-spectra were fitted pixel-wise with a five (in vivo) or six-pool (phantom) Lorentzian model (direct water saturation (DS), magnetization transfer (MT), nuclear overhauser effect (NOE), amines, amides (APT), and hydroxyl) using a Levenberg-Marquardt algorithm (see Table 1 for the fitting parameters). All image processing was performed with MATLAB (R2019b, The MathWorks, Natick: MA).

Data analysis

The fitted APTw values were used to generate APTw maps. For the phantom, circular regions of interest (ROIs) were drawn manually for each solute and APTw map was averaged per ROI. The repeatability of the phantom was assessed based on het averaged APTw map of the five solutes by defining the root-mean-squared-deviation (RSMD) and within-coefficient-of-variation (wCV). For the healthy subjects, ROIs were defined by applying atlas-based segmentation using the MNI-152 atlas[9,10] and Elastix[11], see Figure 1. The repeatability was assessed in supratentorial and infratentorial brain regions separately by measuring RMSD and wCV per tissue type (i.e. grey matter (GM) ROI, (small) white matter (WM) ROI, and (small) pons ROI (only infratentorial)).

Results:

Representative averaged z-spectra of a ROI with corresponding Lorentzian fits are shown in Figure 2-A for the phantom, supratentorial and infratentorial brain region. Figure 2-B shows the APTw maps for the two individual acquisitions, and for both datasets (i.e. phantom and brain). The boxplots (Figure 3) illustrate similar APTw levels for both timepoints for all ROIs, supported by the wCV for the supratentorial and infratentorial brain tissue types (Table 2). The phantom data showed that increasing amide concentration resulted in an increase of the APTw values. The repeatability metrics of the phantom shows a RMSD of 0.52 and wCV of 14.28%. For the healthy subjects, the wCV ranged between 4.42% (small ROIs of the pons) and 19.98% (small ROIs of infratentorial WM).

Discussion: :

APTw imaging at 7T can be considered repeatable and specific for amides which is of high value in clinical decision making. A preclinical study of orthotopic glioblastoma[4] and a clinical study in breast cancer patients[12] showed a decrease in APTw values of ~25% , in response to cancer treatment. Even within our small ROIs the wCV is lower, which would enable monitoring of treatment effects in heterogeneous tumours.

This study uses no B_1-correction which may affect the accuracy of APTw values, but is considered not to influence the repeatability as our B_1-maps showed no significant change over time within one person. However, B_1-correction is necessary when evaluating APTw values between the patients, between different hardware configurations or in a long term follow-up.

In conclusion, we showed that APTw imaging at 7T is specific and repeatable thus potentially enabling detection of metabolic changes in brain tumours due to treatment.

References

[1] van Zijl PCM, Yadav NN. Chemical exchange saturation transfer (CEST): What is in a name and what isn't? Magnetic Resonance in Medicine 2011;65:927–48. https://doi.org/10.1002/mrm.22761.

[2] Wu B, Warnock G, Zaiss M, Lin C, Chen M, Zhou Z, et al. An overview of CEST MRI for non-MR physicists. EJNMMI Physics 2016;3. https://doi.org/10.1186/s40658-016-0155-2.

[3] Zhou J, Heo HY, Knutsson L, van Zijl PCM, Jiang S. APT-weighted MRI: Techniques, current neuro applications, and challenging issues. Journal of Magnetic Resonance Imaging 2019;50:347–64. https://doi.org/10.1002/JMRI.26645.

[4] Sagiyama K, Mashimo T, Togao O, Vemireddy V, Hatanpaa KJ, Maher EA, et al. In vivo chemical exchange saturation transfer imaging allows early detection of a therapeutic response in glioblastoma. Proceedings of the National Academy of Sciences 2014;111:4542–7. https://doi.org/10.1073/PNAS.1323855111.

[5] Meissner JE, Korzowski A, Regnery S, Goerke S, Breitling J, Floca RO, et al. Early response assessment of glioma patients to definitive chemoradiotherapy using chemical exchange saturation transfer imaging at 7 T. Journal of Magnetic Resonance Imaging 2019;50:1268–77. https://doi.org/10.1002/jmri.26702.

[6] Barisano G, Sepehrband F, Ma S, Jann K, Cabeen R, Wang D, et al. Clinical 7 T MRI: Are we there yet? A review about magnetic resonance imaging at ultra-high field. The British Journal of Radiology 2019;92. https://doi.org/10.1259/BJR.20180492.

[7] Morrison M, Lupo J. 7-T Magnetic Resonance Imaging in the Management of Brain Tumors. Magnetic Resonance Imaging Clinics of North America 2021;29:83–102. https://doi.org/10.1016/J.MRIC.2020.09.007.

[8] Khlebnikov V, Bhogal A, Mougin O, Boer V, Wijnen J, Gowland P, et al. Multicolor metabolic quantitative CEST (mmqCEST) imaging: possibility and limitations (ISMRM), Montréal: 2019.

[9] Fonov V, Evans A, McKinstry R, Almli C, Collins D. Unbiased nonlinear average age-appropriate brain templates from birth to adulthood. NeuroImage 2009;47:S102. https://doi.org/10.1016/S1053-8119(09)70884-5.

[10] Fonov V, Evans AC, Botteron K, Almli CR, McKinstry RC, Collins DL. Unbiased average age-appropriate atlases for pediatric studies. NeuroImage 2011;54:313–27. https://doi.org/10.1016/J.NEUROIMAGE.2010.07.033.

[11] Klein S, Staring M, Murphy K, Viergever M, Pluim J. elastix: a toolbox for intensity-based medical image registration. IEEE Transactions on Medical Imaging 2010;29:196–205. https://doi.org/10.1109/TMI.2009.2035616.

[12] Krikken E, Khlebnikov V, Zaiss M, Jibodh RA, van Diest PJ, Luijten PR, et al. Amide chemical exchange saturation transfer at 7T: A possible biomarker for detecting early response to neoadjuvant chemotherapy in breast cancer patients. Breast Cancer Research 2018;20. https://doi.org/10.1186/s13058-018-0982-2.

Acknowledgments / Funding Information: We acknowledge funding from WKZ Research Fund.

	Start	Lower	Upper
A_{water}	0.9	0.02	1.0
Γ_{water}	1.4	0.3	10
δ_{water}	0.0	-1.0	1.0
A_{MT}	0.1	0.0	1.0
Γ_{MT}	25	10	100
δ_{MT}	-2.0	-4.0	-2.0
A_{amide}	0.025	0.0	0.2
Γ_{amide}	0.5	0.4	3.0
δ_{amide}	3.5	3.0	4.0
A_{NOE}	0.02	0.0	0.4
Γ_{NOE}	3.0	1.0	5.0
δ_{NOE}	-3.5	-4.5	-2.0
A_{amine}	0.01	0.0	0.2
Γ_{amine}	0.5	0.4	3.0
δ_{amine}	2.2	1.0	2.5
$A_{hydroxyl}$ †	0.01	0.0001	0.1
$\Gamma_{hydroxyl}$ †	0.2	0.0	0.9
$\delta_{hydroxyl}$ †	0.9	0.8	1.0
δ: chemical shift; Γ: FWHM † fitting of hydroxyl only used in phantom			

Table 1. Lorentzian fitting parameters for six endogenous contrast pools at 7T. A is the amplitude of the z-spectrum (S_{sat}/S_0) at a specific pool defined by a chemical shift and FWHM given in ppm

		ROI/ Segment	Mean ± STD T=1	Mean ± STD T=2	RMSD	wCV (%)
Phantom		NAM 20 mM	1.36±0.93	1.11±0.67	-	-
		NAM 50 mM	4.36±1.32	3.76±0.78	-	-
		NAM 100 mM	6.35±1.38	6.02±0.46	-	-
		GLU 10 mM	1.01±1.27	0.84±1.21	-	-
		GLY 20 mM	0.11±0.32	1.01±0.79	-	-
In vivo brain	Supratentorial	GM	6.47±0.28	6.78±0.50	0.69	7.35
		WM	5.39±0.39	5.40±0.49	0.70	9.14
		WM small	4.82±0.78	5.19±0.86	1.12	15.83
	Infratentorial	GM	6.71±0.59	7.11±0.48	0.55	5.61
		WM	5.98±0.91	5.46±0.83	1.03	12.74
		WM small	6.10±1.21	5.23±0.97	1.60	19.98
		Pons	5.70±0.68	5.54±0.75	0.61	7.68
		Pons small	6.05±0.60	5.95±0.37	0.38	4.42

Table 2. Mean ± standard deviation and repeatability metrics of APTw maps of the ROIs belonging to the phantom, supratentorial brain region and infratentorial brain region.

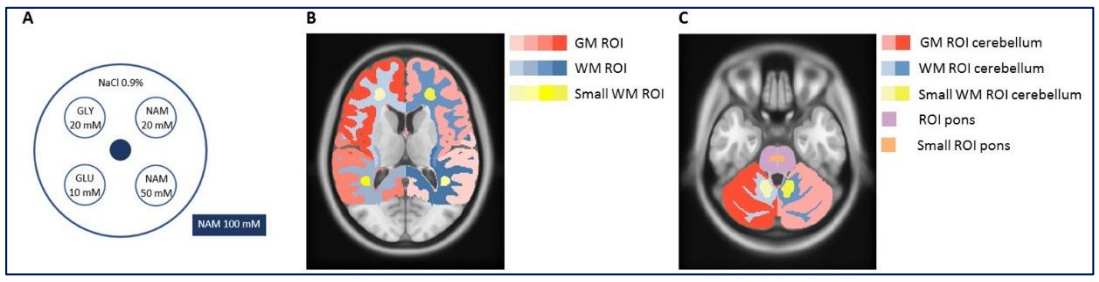

Figure 1. ROIs for the phantom (A), supratentorial brain region (B) and infratentorial brain region (C). The colour bars for the different brain tissue types indicate multiple ROIs per tissue type created within one subject. Supratentorial:4 ROIs (i.e frontal/ parietal and left/ right) for each tissue type. Infratentorial:2 ROIs (i.e. left/right) for each tissue type in the cerebellum and two ROIs for the pons.

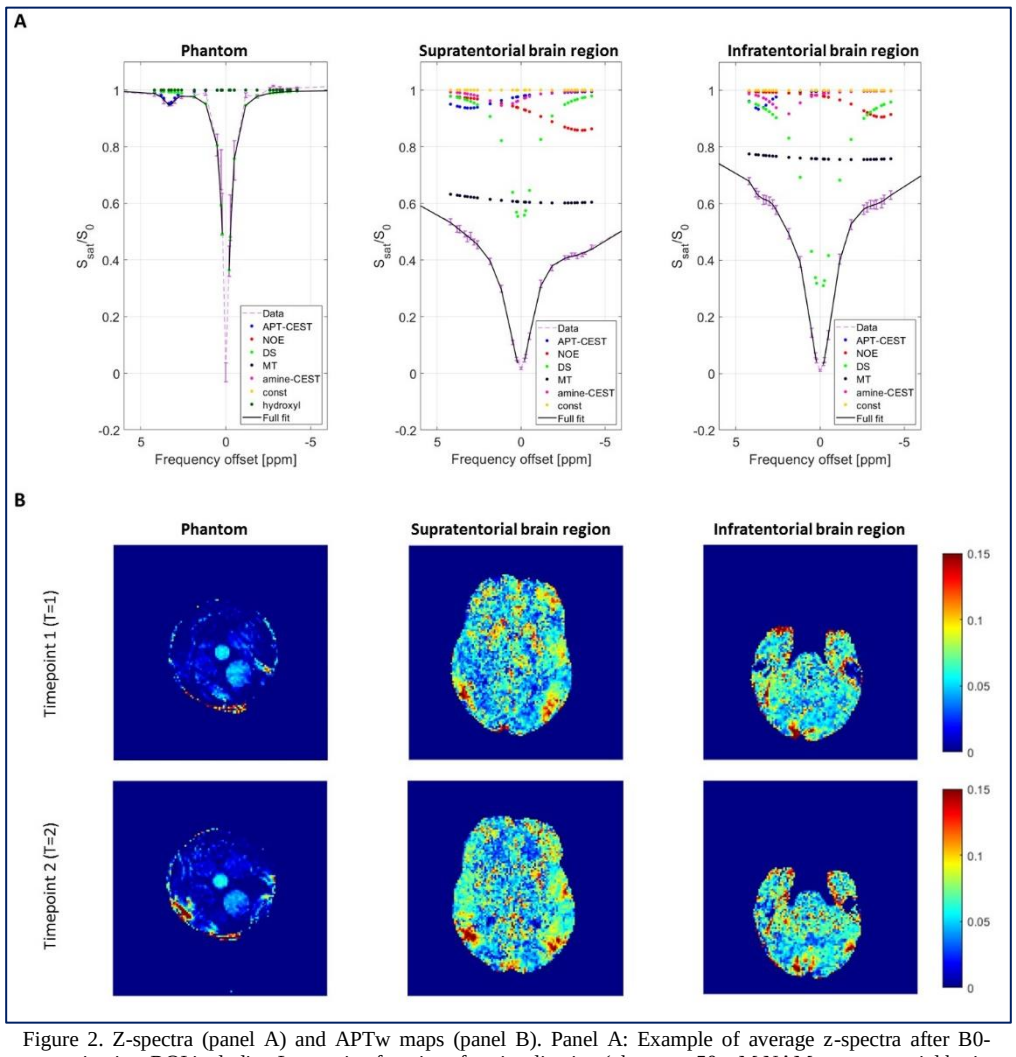

Figure 2. Z-spectra (panel A) and APTw maps (panel B). Panel A: Example of average z-spectra after B0-correction in a ROI including Lorentzian functions for visualization (phantom: 50 mM NAM, supratentorial brain region: WM parietal lobe, infratentorial brain region: WM cerebellum. Panel B: APTw maps for both timepoints illustrated by phantom, supratentorial brain region and infratentorial brain region of one subject.

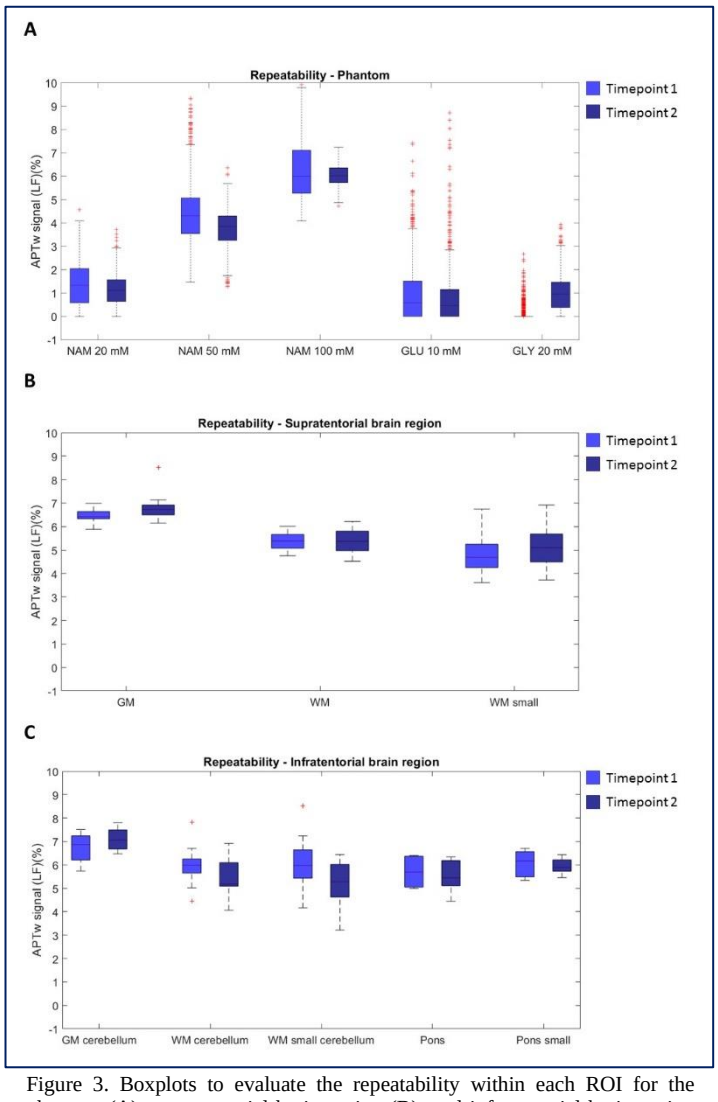

Figure 3. Boxplots to evaluate the repeatability within each ROI for the phantom (A), supratentorial brain region (B), and infratentorial brain region (C). The two boxes for every ROI represent measurement at timepoint 1 (light blue) and timepoint 2 (dark blue).

Comparing population Receptive Field mapping using VASO-CBV and BOLD

I.A.F. Oliveira[1, 2], Yuxuan Cai[1, 2], Shir Hofstetter[1], J.C.W. Siero[1, 4], W. van der Zwaag[1], S.O. Dumoulin[1,2,3]

[1]Spinoza Centre for Neuroimaging, Amsterdam, Netherlands; [2]Experimental and Applied Psychology, VU University, Amsterdam, Netherlands; [3]Experimental Psychology, Helmholtz Institute, Utrecht, Netherlands; [4]Radiology, University Medical Centre Utrecht, Utrecht, Netherlands

Synopsis: We extended the use of VASO-CBV to pRF mapping modelling. We show that VASO-CBV data can be used reliably to map polar angle and eccentricity, similar to BOLD-based data. In addition, the pRF size increased systematically from V1 to V3 similarly for BOLD and VASO-CBV estimates. The higher microvascular specificity of VASO-CBV did not result in smaller pRF size estimates. This result suggests that the vascular contribution to the pRF size is not dominant in either VASO-CBV and BOLD-based pRF mapping.

Introduction: The 7T VASO-CBV method has proven to be highly effective for high-resolution fMRI, especially for depth-dependent applications[1-5]. However, the feasibility of using VASO-CBV for advanced cognitive neuroimaging applications has not yet been widely evaluated. We evaluated the feasibility of VASO-CBV in the visual cortex using population receptive field (pRF) modeling[7]. The pRF analysis is a popular method to study the topographic organization of primary sensory neural populations[8]. Since pRF size has both vascular and neuronal contributions, we hypothesize that the higher specificity of VASO-CBV would result in smaller pRF sizes than BOLD. In the present study, we first determined the optimal slice orientation for VASO-CBV in the visual cortex. With the optimized slice orientation, we extended the use of VASO-CBV to the pRF modeling.

Methods: Six healthy volunteers (5 females, age 32±7 years) participated in the study. Imaging was performed on a 7T scanner (Philips) using a 32Rx8Tx (Nova Medical). SS-SI VASO data were recorded using a 3D EPI readout [TI1/TI2/TE/$TR_{SS\text{-}SIVASO}$ = 1100/2600/15/3000ms]. Voxel-size 1.75mm isotropic (FOV=196x196x32mm^3, matrix=112x112, 18 slices). PF=0.78, fat-suppression-SPAIR.

The protocol optimization was necessary since the slab positioning can affect the amount of inflow and, therefore, tissue signal. We compared four different orientations of the slab together with a change in the direction of the readout gradient. The slice orientation that yielded the highest level of activation represented by the highest average Z-score was the one used in the subsequent pRF experiments (Fig1).

Stimuli

We used a flickering checkerboard stimulus with 24s on/off blocks, with an extra 12 seconds of fixation at the start for the slice orientation comparison. The pRF paradigm consisted of sweeping bar apertures at four orientations (0°, 45°, 90°, and 135°) with two different motion directions for each orientation[7].

In both experiments, motion correction was performed separately for BOLD and VASO, followed by the BOLD contamination correction[6]. We used z-scores from GLM analysis (FEAT in FSL, v.6.0) to assess the optimization slice orientation.

We estimated the pRF position and sizes using the conventional Gaussian pRF model[7] with an additional HRF fit step[9] using vistasoft[10]. The pRF analysis was limited to those voxels with a p-value<0.05 in the VASO data. The comparison was performed between each BOLD run separately against the averaged VASO (14 runs) to maintain a similar variance explained. A one-way Bayesian ANOVA was used to assess the statistical differences.

We used Temporal SNR and variance explained as a function of the number of runs to assess the noise level. The tSNR was calculated across cumulatively averaged runs for GM and WM. The variance explained was estimated per voxel by computing the variance after fitting the BOLD and VASO-CBV time series separately with the model prediction of a given voxel.

Results: Fig.1.B shows VASO-CBV activated voxels within the shared volume of all orientations, overlaid on the anatomical data. Orientation III showed higher responses than all other orientations (ANOVA, p-value<0.05). Fig.2 shows the fMRI signal quality captured by the pRF model depicted in R^2 maps and time courses. The 14-run averaged BOLD shows more high R2 voxels compared to 14-run VASO-CBV and single-run BOLD.

We found similar eccentricity and polar angle maps for VASO-CBV and BOLD (Fig3), with a tight relationship for the eccentricity. Regarding the noise level, the tSNR increases with the number of runs for all regions and participants, although with higher values for BOLD than VASO-CBV (Fig4). The R^2 curves also show the same pattern, increasing with the number of runs, with higher values for BOLD than VASO-CBV. The pRF size increases with the eccentricity for both VASO-CBV and BOLD similarly (Fig5). In the Bayesian framework, we define the alternative hypothesis as the difference between VASO-CBV pRF sizes and the individual BOLD run pRF sizes. The Bayesian ANOVA indicated weak evidence in V1 (BF_{10}=2.687). And no evidence in V2 (BF_{10}=1.044) and V3 (BF_{10}=0.477).

Discussion & Conclusion: We observed a robust VASO-CBV activation pattern for all orientations and no inflow artifacts in any orientation planes.

The tSNR curves (Fig4A) reveal that, in general, a single BOLD run is equivalent to 4-5 averages runs of VASO-CBV. Although in different ratios, the R^2-curves increase with runs, with BOLD reaching a plateau earlier than VASO-CBV. Therefore, we compared the 14-VASO-CBV with individual BOLD runs.

All pRF properties (Polar angle, eccentricity, and pRF size) measured with VASO-CBV showed similar behavior compared to BOLD. The expected higher microvascular specificity of VASO-CBV does not directly result in smaller pRF size estimates. The pRF size depends on a combination of two types of signal components; neural and non-neural[7]. Neural includes the position scatter. Since the comparison was performed in the same cortical location, the position scatter is not expected to differ in VASO-CBV compared to BOLD. We also exclude eye and head motion as potential explanations since VASO-CBV and BOLD are nearly simultaneously acquired. The high SNR case of 14-run average BOLD shows no difference in observed pRF size. We, therefore, do not think that SNR was a factor of influence. Together, these results suggest that the vascular component of the pRF size is not dominant in either VASO-CBV or BOLD.

Reference

[1]. Beckett, A.J.S., Dadakova, T., Townsend, J., Huber, L., Park, S., Feinberg, D.A., 2020. Comparison of BOLD and CBV using 3D EPI and 3D GRASE for corticallayer functional MRI at 7 T. Magn. Reson. Med. mrm.28347.

[2]. Huber, L., Goense, J., Kennerley, A.J., Trampel, R., Guidi, M., Reimer, E., Ivanov, D., Neef, N., Gauthier, C.J., Turner, R., Möller, H.E., 2015. Cortical lamina-dependent blood volume changes in human brain at 7T. Neuroimage 107, 23–33.

[3].Huber, L., Handwerker, D.A., Jangraw, D.C., Chen, G., Hall, A., Stüber, C., Gonzalez-Castillo, J., Ivanov, D., Marrett, S., Guidi, M., Goense, J.B.M., Poser, B.A.,Bandettini, P.A., 2017. High-resolution CBV-fMRI allows mapping of laminar activity and connectivity of cortical input and output in human M1. Neuron 1–11.

[4].Persichetti, A.S., Avery, J.A., Huber, L., Merriam, E.P., Martin, A., 2019. Layer-Specific Contributions to Imagined and Executed Hand Movements in HumanPrimary Motor Cortex. SSRN Electron. J. 1–5.

[5].Yu, Y., Huber, L., Yang, J., Jangraw, D.C., Handwerker, D.A., Molfese, P.J., Chen, G., Ejima, Y., Wu, J., Bandettini, P.A., 2019. Layer-specific activation of sensory input and predictive feedback in the human primary somatosensory cortex. Sci. Adv. 5, eaav9053.

[6].Huber, L., Ivanov, D., Krieger, S.N., Streicher, M.N., Mildner, T., Poser, B.A., Möller, H.E., Turner, R., 2014. Slab-selective, BOLD-corrected VASO at 7 tesla provides measures of cerebral blood volume reactivity with high signal-to-noise ratio. Magn. Reson. Med. 72, 137–148.

[7].Dumoulin, S.O., Wandell, B.A., 2008. Population receptive field estimates in human visual cortex. Neuroimage 39, 647–660.

[8].Dumoulin, S.O., Knapen, T., 2018. How visual cortical organization is altered by ophthalmologic and neurologic disorders. Annu. Rev. Vis. Sci. 4, 357–379.

[9].Harvey, B.M., Dumoulin, S.O., 2011. The relationship between cortical magnification factor and population receptive field size in human visual cortex:Constancies in cortical architecture. J. Neurosci. 31, 13604–13612.

Acknowledgments / Funding Information: Continue on this line

[10]. (https://github.com/vistalab/vistasoft)

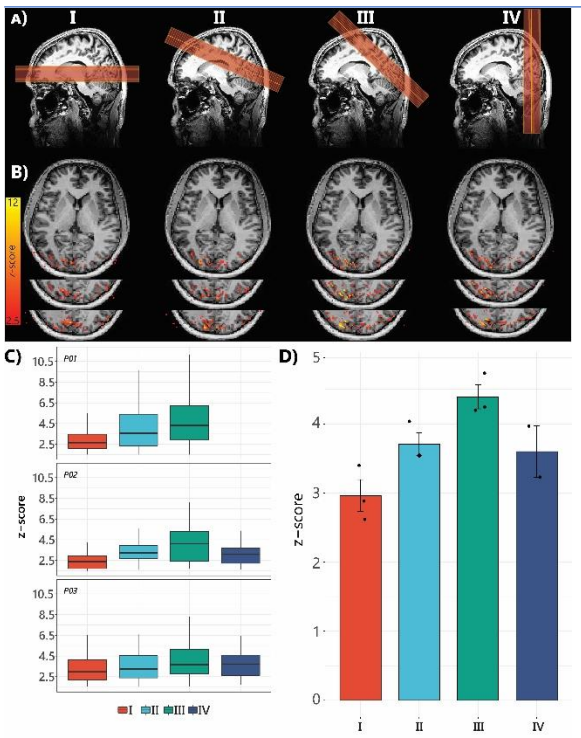

Fig1. The slice orientation was defined as follows: I) Aligned with the ACPC-axis, with the phase encoding in the A-P. II) Aligned with the calcarine sulcus with phase encoding in the A-P. III) Aligned with the superior surface of the cerebellum, with phase encoding in the R-L. IV) Purely coronal slices, with phase encoding in the R-L. B) VASO-CBV activated voxels within the shared volume of all orientations, overlaid on the anatomical data. C) Average Z-scores per participant. D) Z-score averaged across participants. Slice orientation (III) yielded the strongest signals.

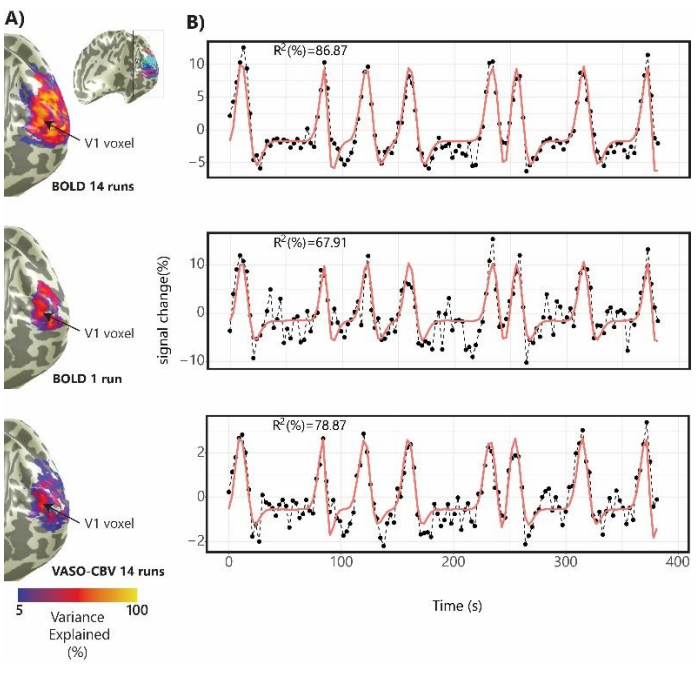

Fig2. Example of time courses and variance explained maps for VASO-CBV and BOLD. V1 is outlined on top of a polar angle map. A) Map of the variance explained by the pRF model for 14-run average VASO-CBV and two BOLD examples, one averaged over 14 runs and a single run. B) An example pRF fMRI responses from a voxel located in V1, for VASO-CBV, averaged over 14 runs and two BOLD examples, one averaged over 14 runs and a single run. The dashed lines represent the measured response, and the red line represents the model prediction. R denotes variance explained by the model for the selected voxel.

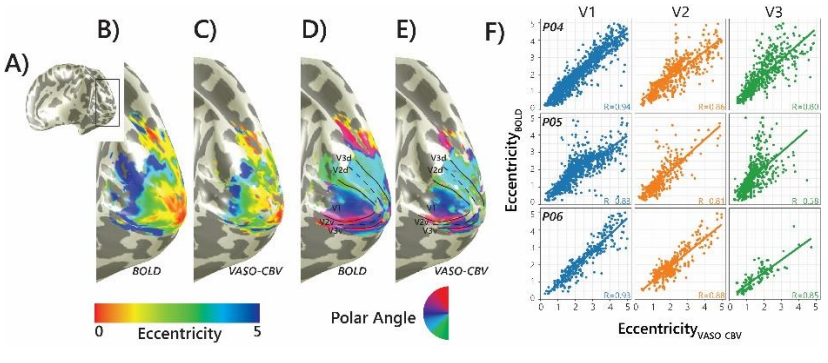

Fig3. pRF position estimates on an inflated cortical surface. A) The visual area(occipital pole) is indicated on the inflated cortical surface. The eccentricity maps are shown for BOLD (B) and VASO-CBV (C). Polar angle maps are likewise compared between BOLD (D) and VASO-CBV (E). Maps are threshold at a variance explained of 5%. F) Correlations between eccentricity values obtained from BOLD and VASO-CBV indicate a similar progression of pRF values across eccentricity between the two sequences. R-value is the Pearson correlation coefficient.

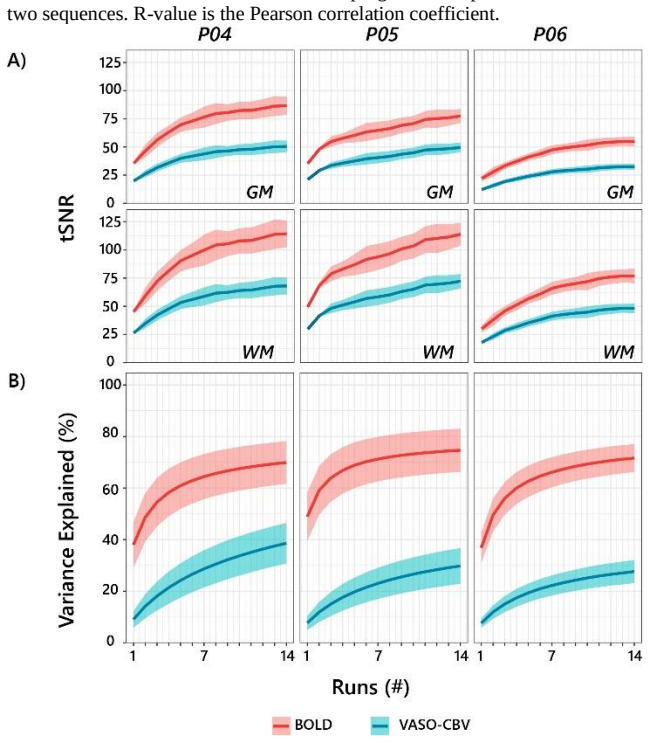

Fig4. Noise level assessed by tSNR and variance explained as a function of the number of runs. A) The tSNR increases with the number of averaged runs for all participants and both tissue types in similar proportions. BOLD tSNR is higher than VASO-CBV for all regions and participants. B) For BOLD, variance explained plateaus earlier than the VASO-CBV variance explained, but the levels of variance explained by BOLD are consistently higher.

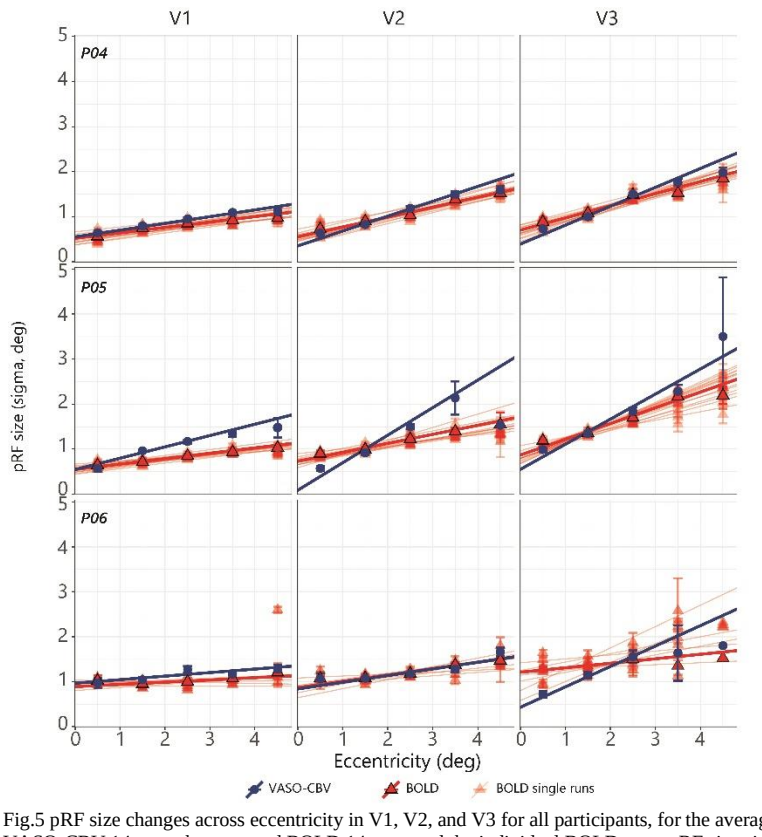

Fig.5 pRF size changes across eccentricity in V1, V2, and V3 for all participants, for the averaged VASO-CBV 14 runs, the averaged BOLD 14 runs, and the individual BOLD runs. pRF sizes increase with visual field eccentricity and across the visual area hierarchy.

Laminar and columnar functional organization of human area MT using VASO at 7T

A. Pizzuti[1,2], R. Huber[1], O. F. Gulban[1,2], A. Benitez-Andoegui[1,3], J. Peters[1], R. Goebel[1,2]
[1]Department of Cognitive Neuroscience, Faculty of Psychology and Neuroscience, Maastricht, Netherlands; [2]Brain Innovation, Maastricht, Netherlands, MEG Core Facility, National Institutes of Mental Health, Bethesda, United States

Synopsis: We investigate the feasibility of using CBV-sensitive VASO fMRI at ultra-high field to study the selective columnar organization to axes of motion stimuli in human area MT.

For 5 subjects we found:

- BOLD and VASO both reveal characteristic tuning curves for axes of motion.
- VASO results are more specific and less sensitive than BOLD results.
- VASO layer profiles are less distorted by superficial veins than BOLD.
- Columnar analysis is feasible using VASO.

Purpose: Ultra-high field (>=7T) functional magnetic resonance imaging (fMRI) provides a unique opportunity to investigate the columnar and laminar organization of the human brain in vivo. The middle temporal area in humans (hMT) shows a selective columnar response to directions or axes of motion as revealed by conventional BOLD fMRI contrast with rapid gradient-echo (GE) imaging[1,2]. Although GE-BOLD has been widely applied in fMRI studies, its spatial specificity is reduced by oxygenation changes in draining veins[3]. Alternatives like SS-SI-VASO sensitive to cerebral blood volume (CBV) offer higher spatial specificity to the microvasculature and improved quantifiability, at the cost of reduced signal sensitivity and increased acquisition time with respect to GE-BOLD[4,5]. Here, we investigated, for the first time, the feasibility of mapping axes of motion in hMT and its laminar-columnar functional organization using VASO compared to conventional BOLD.

Methods: Five volunteers were scanned at a 'classical' MAGNETOM 7T (Siemens Healthineers) with a 32-channel Rx head coil (Nova) at Scannexus B.V. (Maastricht, Netherlands). We collected 3-4 functional runs at 0.8 mm iso-voxel resolution to map four different axes of motion using SS-SI VASO (3D EPI readout[6], TR/TE/FA=2410ms/25ms/26+°, TI=1530ms, 26 slices, GRAPPA=3 and in-plane partial Fourier 6/8) while presenting 4 repetitions of moving dots (12s, each) in 4 different directions (0°-180°, 45°-225°, 90°-270°, 135°-315°), alternated with flickering dots (12s) (Figure 1, A shows the slab coverage). In the same session we collected a functional localizer run with GE-BOLD[7] at 2mm iso (TR/TE/FA=1000ms/22ms/55°, 57 slices and multi band factor=3) to locate area hMT presenting 28 repetitions of outward/inward motion of dots (10s), followed by static dots (10s) and an anatomical MP2RAGE[8] (0.7mm iso;TR/TE=6000ms/2.39ms, TI=800ms/2750ms, FA=4°/5°, GRAPPA=3). Functional localizer data were processed as follows: slice time correction, motion correction, high-pass filtering, geometric EPI distortion correction (BrainVoyager), co-registration to the high-resolution VASO data (Syn, ANTS). A region of interest (ROI) for the left hMT was obtained combining significant voxels [p<0.00001] to the "moving vs static dots" contrast of the localizer run (using a General Linear Model) with a sphere centred around the activity (radius=16mm). Anatomical data were co-registered to the same space (SyN, ANTS), upsampled to 0.2 mm isovoxel (AFNI) and segmented (FSL BET, FSL FAST, ITK-SNAP). On both motion corrected BOLD and VASO time series from SS-SI VASO, we evaluated the tSNR (Figure 1 B) and then ran a GLM (BrainVoyager) restricted to the hMT-ROI (Figure 1 C); the initial set of activated voxels obtained from the contrast map "all axes of motion vs flickering dots" was cross-validated using a leave-one-run out approach[1,2]. Motion direction preference was assigned for each voxel based on the maximum t-value in the vector of t-values resulting from contrasting each direction vs flickering dots ('preference map'). A voxel-wise measure of *sensitivity* (norm of t-values vector) and *specificity* (averaged angle between winner t-value and the rest) was derived. Equi-volume normalized cortical depths and a flattening algorithm were used to investigate the laminar and columnar profile of hMT (LayNii LN2_LAYERS, LN2_MULTILATERATE, LN2_PATCH_FLATTEN)[9,10].

Results: We found axes-of-motion specific tuning curves for all cross-validated voxels in all analyzed subjects for both BOLD and VASO contrast. Figure 2 A shows that for both BOLD and VASO a characteristic peak at the preferred axis of motion can be observed in the group result, showing that the averaged voxel response exhibits a clear preference towards a single axis of motion. Moreover, VASO shows a higher ratio of t-values between the preferred vs non-preferred axes confirming its higher specificity compared to BOLD (on average for VASO=4.1, for BOLD=1.7). Figure 2 B quantifies that BOLD cross-validated voxels are more *sensitive* in terms of the overall response strength, but less specific than VASO, as expected. We plot 2D histograms of cross-validated voxels showing percent signal change across cortical depth and layer profiles (Figure 3 and 4): an overall lower mean and variance towards superficial layers is observed for VASO compared to BOLD, indicating that the draining vein effects on the pial surface are mitigated. Finally, Figure 5 visualizes *preference maps* of each subject across 3 cortical depths allowing the qualitative exploration of the columnar functional organization in hMT.

Discussion & Conclusion: This study shows for the first time the feasibility of measuring axes of motion and its laminar-columnar organization in extrastriate area hMT using SS-SI-VASO. As shown in Figure 2, voxel-specific selectivity for different axes of motion confirms previous results for BOLD and VASO contrasts. Despite the reduced signal sensitivity, VASO shows higher spatial specificity in comparison to BOLD contrast. In addition, unlike BOLD, the percent signal change for VASO data does not increase towards superficial layers in the layer profiles, indicating that the draining vein effects are mitigated as expected (Figure 3, 4). Further investigations are needed to quantify the functional columnar organization of hMT and highlight differences between the BOLD and VASO contrasts (Figure 5).

References:

1. Schneider M, Kemper VG, Emmerling TC, De Martino F, Goebel R. Columnar clusters in the human motion complex reflect consciously perceived motion axis. PNAS 2019; vol. 116, no. 11. doi:10.1073/pnas.1814504116

2. Zimmermann J. et al. (2011), 'Mapping the Organization of Axis of Motion Selective Features in Human AreaMT Using High-Field fMRI'. PLOS ONE. vol. 6, no. 12. doi:10.1371/journal.pone.0028716

3. Beckett AJS, Dadakova T, Townsend J, Huber L, Park S, Feinberg DA. Comparison of BOLD and CBV using 3D EPI and 3D GRASE for cortical layer functional MRI at 7 T. Magn Reson Med. 2020; 84(6):3128-3145. doi:10.1002/mrm.28347

4. Huber L, Uludag K, Moller HE. Non-BOLD contrast for laminar fMRI in humans: CBF, CBV, and CMRO2. Neuroimage. 2019; vol.197, pp. 742-760. doi:10.1016/j.neuroimage.2017.07.041

5. Lu H, Golay X, Pekar JJ, van Zijl PCM. Functional magnetic resonance imaging based on changes in vascular space occupancy. Magnetic Resonance in Medicine 2003; vol. 50, no. 2, pp. 263-274. doi:https://doi.org/10.1002/mrm.10519

6. Poser et al.,. Three dimensional echo-planar imaging at 7 tesla. Neuroimage. 2010;51(1):261-266. doi:10.1016/j.neuroimage.2010.01.108

7. Moeller S et. al. Multiband multislice GE-EPI at 7 tesla, with 16-fold acceleration using partial parallel imaging with application to high spatial and temporal whole-brain fMRI. Magnetic Resonance in Medicine 2010; vol. 63, no. 5, pp.1144-1153. doi:10.1002/mrm.22361

8. Marques JP et al. MP2RAGE, a self bias-field corrected sequence for improved segmentation and T1-mapping at high field. Neuroimage 2010; vol. 49, no. 2, pp. 1271-1281. doi:10.1016/j.neuroimage.2009.10.002

9. Huber L et al. LAYNII: A software suite for layer-fMRI. bioRxiv 2020; doi:10.1101/2020.06.12.148080

10. Gulban OF, Wagstyl K, Goebel R, Huber L (2021): Patch flattening for high resolution topographical surveys of MRI & histology without surface meshes. figshare. Conference contribution. https://doi.org/10.6084/m9.figshare.14813172.v1

Acknowledgments / Funding Information: This project was funded by the EU-project H2020-860563 euSNN; This study was approved by the local ethics committee. RH was funded from the NWO VENI project 016.Veni.198.032. OFG is an employee of Brain Innovation and has financial interest tied to the company. RG has financial interest tied to Brain Innovation.

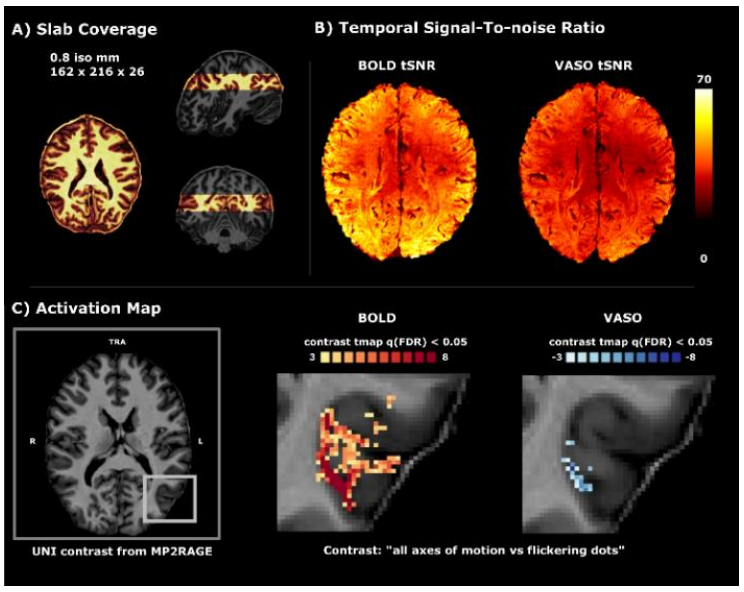

Figure 1. SS-SI VASO functional images for a selected subject. **A)** Slab coverage relative to a whole brain MP2RAGE**. B)** Temporal Signal-To-Noise Ratio. **C)** Activation map for BOLD and VASO time series for the contrast: "all axes of motion vs flickering dots" (q(False Discovery Rate) < 0.05).

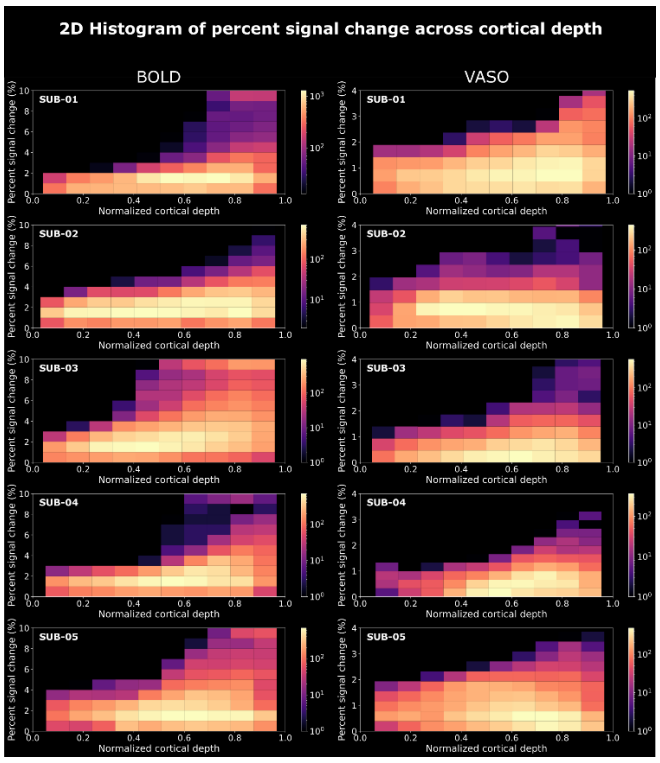

Figure 3. Single-subject 2D histogram (of cross-validated voxels) showing percent signal change across cortical depth for BOLD (left) and VASO (right). On the x-axes 0=deep layer, 1=superficial layer. Colors indicate the number of voxels in each bin in log scale. BOLD shows an overall higher mean value and variability towards superficial layers (normalized cortical depth=1) with respect to VASO.

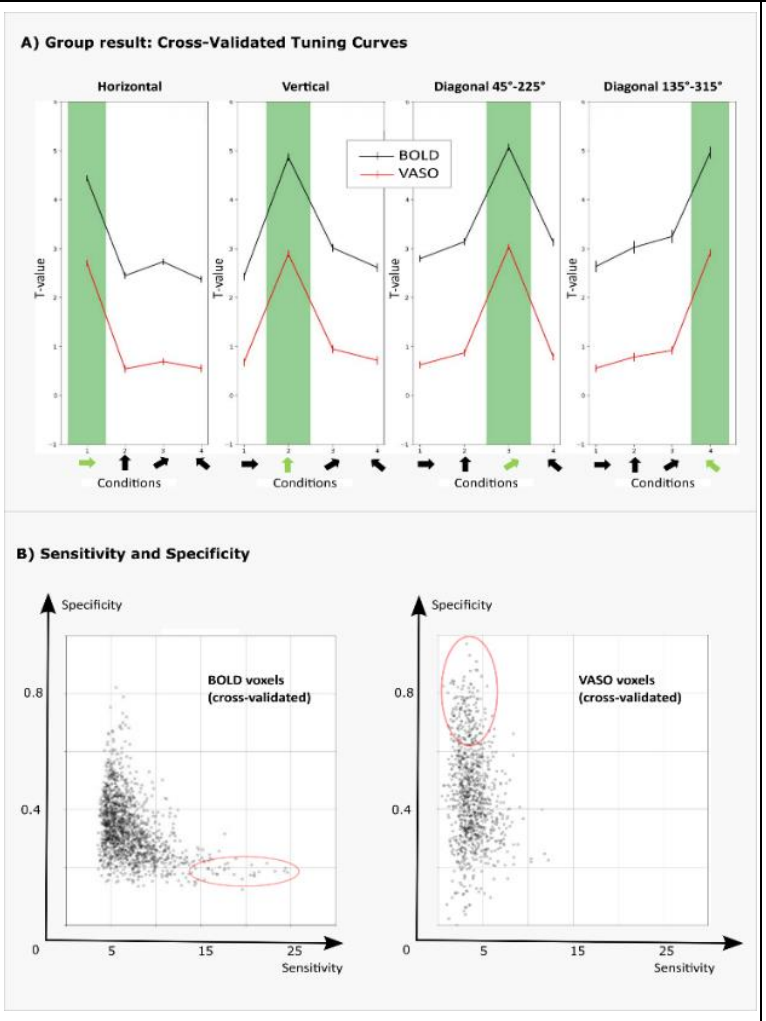

Figure 2. A) Group average axis of motion selectivity tuning curves for each axis of motion. Tuning curves are computed by averaging t-values of all cross-validated voxels sharing the same preferred axis of motion. The plot depicts the mean and the standard error of all voxels per each category. **B)** Sensitivity and specificity quantify cross-validated voxel behavior of all participants for both BOLD and VASO. Red circles highlight the main difference between contrast types.

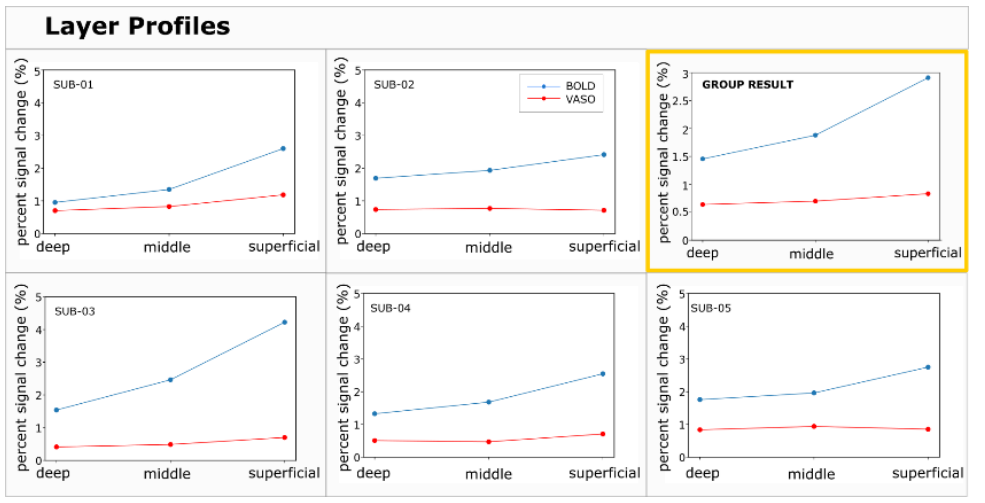

Figure 4. Layer profiles across three cortical depths: deep (25%), middle (50%), superficial (75%) with respect to the white-gray matter boundary. For each cortical depth, the averaged percent signal change of all cross-validated voxels is reported for both BOLD and VASO. The yellow box shows the group result of all five subjects.

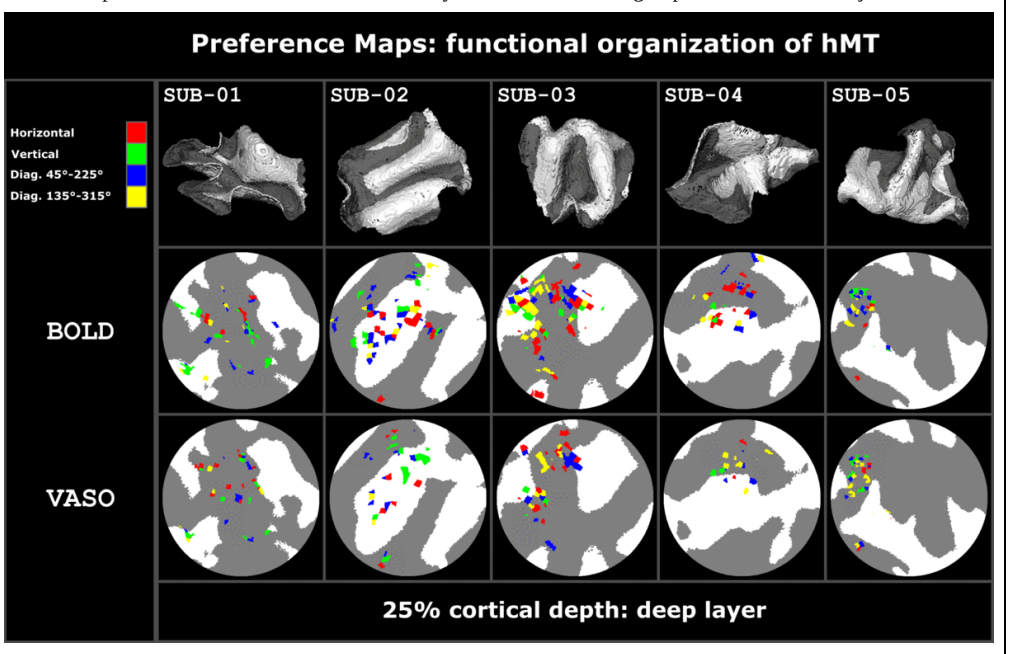

Figure 5. *Preference maps* of each subject in a flattened surface for three cortical depths. The first row shows hMT, colors reflect the curvature of the region (white: gyri, dark gray: sulci). Second and third rows show the preference maps (colors indicate axis-of-motion, see legend at top-left) of all cross-validated voxels in a flat representation, respectively for BOLD and VASO (curvature colormap consistent with the first row).

Vascular reactivity measurements are insensitive to changes in visual stimulus presentation method

M.R. Schipper[1], T.W. van Harten[1], M. van Bronkhorst[1], M.C.E. van der Plas, M.J.H., Wermer[1], M.A.A., van Walderveen[1], and M.J.P., van Osch[1].

[1]Radiology, Leiden University Medical Center, Leiden, The Netherlands

Synopsis: Vascular reactivity to a visual stimulus is an early marker in Cerebral Amyloid Angiopathy. Robustness against stimulus delivery setup changes is of importance for comparison between cohorts and for longitudinal comparison within groups. For us, this became relevant due to different stimulus setup between our scanners (in-room monitor vs. projector&screen). With both setups, BOLD fMRI reactivity scans were acquired during an 8 Hz checkerboard stimulus paradigm. Five healthy participants were included in the study. The commonly used outcome parameters of vascular reactivity, i.e. amplitude, time to peak, and time to baseline, appeared to be resilient against changes in stimulus setup.

INTRODUCTION: Measuring the blood-oxygen-level-dependent (BOLD) response to a stimulus, relates to the level of deoxygenated hemoglobin, blood volume and blood flow[1]. Through these mechanisms, fMRI can be used as a readout measure of vascular reactivity with especially promising findings in Cerebral Amyloid Angiopathy (CAA). CAA is caused by excessive amyloid β deposition in the vasculature of the brain. CAA is amongst others associated with intracerebral hemorrhage (ICH), lobar cerebral microbleeds (CMBs), cortical superficial siderosis (cSS), and cognitive impairment[2,3]. The visual cortex of patients with CAA has an early and high cerebrovascular amyloid burden[5]. This leads to an impaired vascular reactivity, which was demonstrated in sporadic CAA patients as well as in symptomatic and presymptomatic gene carriers of Dutch-type CAA (D-CAA), the most common hereditary form of CAA[6,7]. CAA-patients showed a decreased amplitude, delayed time to peak, and a delayed time to baseline of the BOLD response. This way, the affected BOLD response to a visual stimulus forms an important early marker of CAA. The current study aimed to assess the reproducibility of BOLD responses in healthy subjects, between two scanners with different stimulus presentation methods. This study was initiated, because our natural history study of symptomatic and presymptomatic D-CAA subjects needed to move from one scanner to another, with the two scanners relying on different stimulus delivery hardware.

METHODS: Five healthy subjects (age varied from 21-56yrs, median of 27yrs; all female subjects) were scanned twice, at two different 3T Philips scanners. The presentation of the visual stimulus in scan room A was through a projector that projects onto a screen at the end of the bore. The presentation in scan room B was through an in-room monitor at the end of the bore (Figure 1). At each scan session a T1-weighted scan (TE = 5ms; TR = 9.76ms; flip angle 8 degrees; 130 slices; FoV = 217.71x217.71x156 mm; voxel size 1.00x.85x.85 mm) and a gradient echo echo-planar imaging fMRI scan were acquired (TE = 38ms; TR = 1500ms; flip angle = 78 degrees; 18 slices on scanner A and 17 slices on scanner B; FoV = 210x210x60 mm on scanner A and 210x210x56.27 mm on scanner B; voxel size = 1.64x1.64x3.31 mm; 224 dynamics). fMRI scans were acquired during a 20s on and 28s off 8 Hz checkerboard stimulus paradigm. Data processing was done by FSL Feat (fMRI Expert Analysis Tool, Version 6.00)[8] and included MCFLIRT rigid body transformations[9], slice-timing correction using Fourier-space time-series phase-shifting, non-brain removal using BET[10], spatial smoothing using a Gaussian kernel of FWHM 3mm; grand-mean intensity normalization of the entire 4D dataset by a single multiplicative factor, high-pass temporal filtering (Gaussian-weighted least-squares straight line fitting, with sigma=24.0s). To investigate the possible presence of unexpected artefacts or activation, MELODIC ICA was carried out[11] and large components were removed in the presence of unexpected artefacts of activation. A registered thresholded V1[12] ROI from the Julich histological atlas was overlaid onto individual fMRI images and mean activation per timeseries were calculated. A trapezoid fit was applied to the normalized averaged BOLD response for a standardized measure of time to peak, time to baseline, and amplitude of the BOLD response[6].

RESULTS: Figure 2 shows the BOLD response curves per subject for both scanners. Figure 3 presents a table with the outcome measures time to peak, time to baseline, and amplitude for all subjects. There was no significant difference in the time to peak, time to baseline, or amplitude of the BOLD response between scanner A and scanner B (absolute mean difference = 0.350, 3.106, and 0.003, SD = 0.702, 2.696, and 0.0024 respectively). The Bland-Altman plots comparing the two methods (Figure 4) show that all observations of the parameters fall within the limits of agreement (the mean +/- 1.96 SD). In addition, the observations are randomly scattered above and below the mean difference, without a consistent change in homogeneity. This indicates no consistent bias of one approach to the other.

DISCUSSION: The most important finding of this study is the resilience of the amplitude, time to peak, and time to baseline to a change in the stimulus delivery setups. This may extrapolate to the possibility to compare vascular reactivity measures in (D-)CAA from scanners with different stimulus delivery hardware, and may allow for comparisons between cohorts. Limits of this study are that only five participants were included as well as only two different setups. In addition, all participants were healthy controls. A patient with (progressed) CAA may respond differently to different stimulus presentations or could be more sensitive to differences in light intensity. In addition, one participant showed significant motion during the fMRI, causing noise in the measured BOLD response.

CONCLUSION: This data indicates that the vascular reactivity measurements may be insensitive to the method of stimulus presentation. This finding may pave the road for the combined analyses of multiple data sets and allow for flexibility in the use of different stimulus delivery setups for studies on disease progression in CAA or ultimately for treatment trials.

REFERENCES:

1. Raichle, M.E. (1998). Behind the scenes of functional brain imaging: A historical and physiological perspective. Proceedings of the National Academy of Sciences, 95(3), 765-772. https://doi.org/10.1073/pnas.95.3.765
2. Charidimou, A., Boulouis, G., Gurol, M. E ., Ayata, C., Bacskai, B. J., Frosch, M. P., Viswanathan, A., & Greenberg, S. M. (2017). Emerging concepts in sporadic cerebral amyloid angiopathy. *Brain*, *140*(7), 1829-1850. https://doi.org/10.1093/brain/awx047
3. Greenberg, S. M., Al-Shahi, S. R., Biessels, G. J., van Buchem, M., Cordonnier, C., Lee, J, Montaner, J., Schneider, J. A., Smith, E. E., Vernooij, M., & Werring, D. J. (2014). Outcome markers for clinical trials in cerebral amyloid angiopathy. *Lancet Neurology*, *13*(4), 419-428. http://doi.org/10.1016/S1474-4422(14)70003-1
4. Levy, E., Carman, M. D., Fernandez-Madrid, I. J., Power, M. D., Lieberburg, I., van Duinen, S. G., Bots, G. T., Luyendijk, W., & Frangione, B. (1990). Mutation of the Alzheimer's disease amyloid gene in hereditary cerebral hemorrhage, Dutch type. *Science*, *248*(4959), 1124-1126. https://doi.org/10.1126/science.2111584
5. Johnson, K. A., Gregas, M., Becker, J. A., Kinnecom, C., Salat, D. H., Moran, E. K., Smith, E. E., Rosand, J., Rentz, D. M., Klunk, W. E., Mathis, C. A., Price, J. C., DeKosky, S. T., Fischman, A. J., & Greenberg, S. M. (2007). Imaging of amyloid burden and distribution in cerebral amyloid angiopathy. *Annals of Neurology*, *62*(3), 229-234. https://doi.org/10.1002/ana.21164
6. Dumas, A., Dierksen, G. A., Gurol, M. E., Halpin, A., Martinez-Ramirez, S., Schwab, K., Rosand, J., Viswanathan, A., Salat, D. H., Polimeni, J. R., & Greenberg, S. M. (2012). Functional magnetic resonance imaging detection of vascular reactivity in cerebral amyloid angiopathy. *Annals of Neurology*, *72*(1), 76-81. https://doi.org/10.1002/ana.23566
7. van Opstal, A. M., van Rooden, S., van Harten, T., Ghariq, E., Labadie, G., Fotiadis, P., Gurol, M. E., Terwindt, G. M., Wermer, M. J. H., van Buchem, M. A., Greenberg, S. M., & van der Grond, J. (2017). Cerebrovascular function in presymptomatic and symptomatic individuals with hereditary cerebral amyloid angiopathy: a case-control study. *The Lancet Neurology*, *16*(2), 115-122. https://doi.org/10.1016/S1474-4422(16)30346-5
8. FMRIB's Software Library, www.fmrib.ox.ac.uk/fsl
9. M. Jenkinson and P. Bannister and M. Brady and S. Smith. Improved optimisation for the robust and accurate linear registration and motion correction of brain images. NeuroImage 17:2(825-841) 2002.
10. S. Smith. Fast Robust Automated Brain Extraction. Human Brain Mapping 17:3(143-155) 2002.
11. F. Beckmann and S.M. Smith. Probabilistic Independent Component Analysis for Functional Magnetic Resonance Imaging. IEEE Trans. on Medical Imaging 23:2(137-152) 2004.
12. Amunts, K et al. (2000). Neuroimage. 11, 66-84

Acknowledgments / Funding Information: There are no acknowledgements for this study.

Figure 1. Setup of the stimulus delivery hardware; a) stimulus view from within the bore for method A, b) stimulus delivery hardware with projector and screen in method A, c) stimulus view from within the bore for method B, and d) stimulus delivery hardware with in-room monitor in method B.

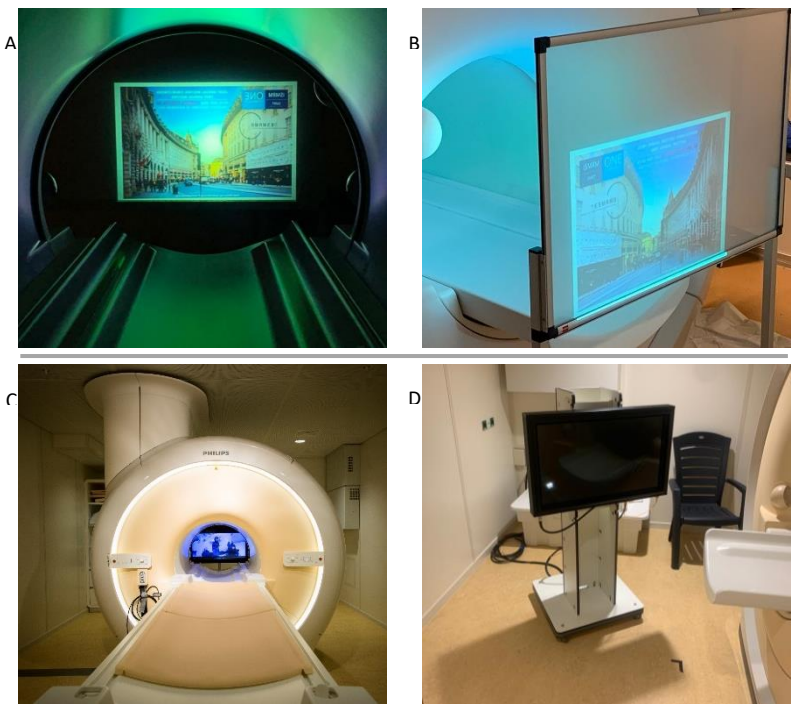

*Figure 2. Normalized mean and 1.96 times the standard deviation of the BOLD response per subject (a-e) for both visual stimulus projection methods. Red represents method A. Blue represents method B. The grey box indicates the presentation of the stimulus.

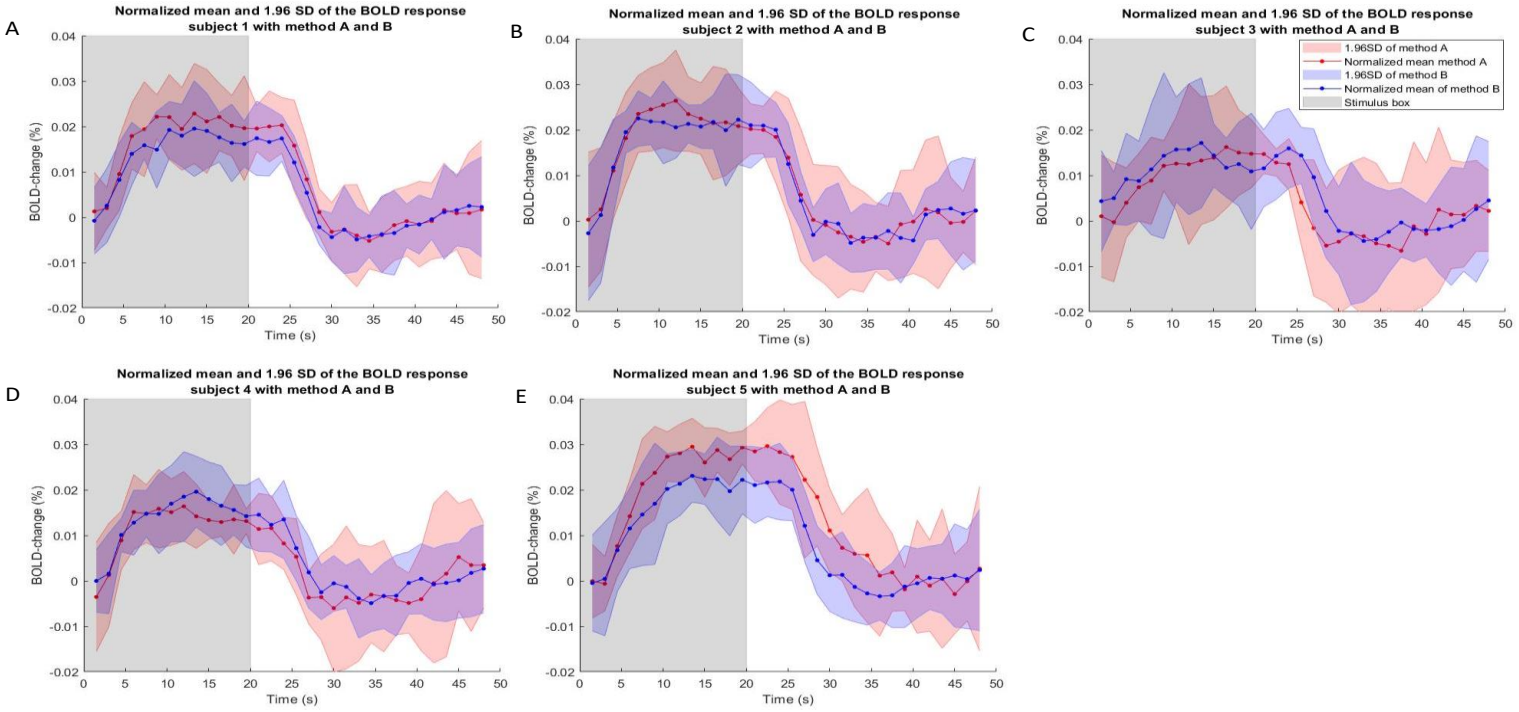

Figure 3. Table of the BOLD parameters time to peak, time to baseline, and amplitude for both stimulus presentation methods in all subjects.

	Subject 1	Subject 2	Subject 3	Subject 4	Subject 5
Time to peak					
Method 1	6.532	6.881	11.247	5.613	9.590
Method 2	6.882	6.224	9.114	6.748	10.229
Mean	6.7069	6.5527	10.1808	6.1803	9.9095
Mean difference	-0.3500	0.6567	2.1333	-1.1348	-0.6398
Time to baseline					
Method 1	8.7111	8.7430	3.9081	6.9955	15.8052
Method 2	8.1100	7.8690	9.0746	8.8542	9.2275
Mean	8.4105	8.3060	6.4914	7.9248	12.5164
Mean difference	0.6012	0.8739	-5.1665	-1.8587	6.5777
Amplitude					
Method 1	0.02073	0.02300	0.01430	0.0146	0.0282
Method 2	0.0173	0.0213	0.0140	0.0165	0.0216
Mean	0.0190	0.0222	0.0141	0.0156	0.0249
Mean difference	0.0034	0.0017	0.0003	-0.0020	0.0066

Figure 4. Bland-Altman plots of the BOLD parameters a) time to peak, b) time to baseline and c) amplitude. Method A is the projection of the visual stimulus through a beamer onto a screen. Method B is the projection of the visual stimulus through a monitor. Limits of agreement are defined by mean +/- 1.96 standard deviation.

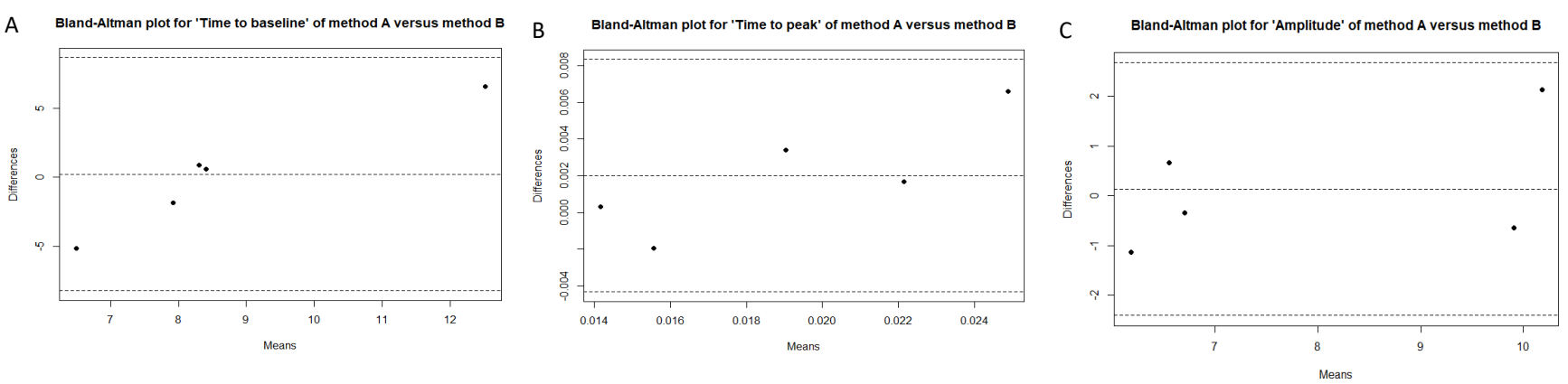

Monte Carlo simulations of weighted overlap map thresholds to reduce the risk for type I errors in fMRI

P. Van Schuerbeek [1]
[1] Department of Radiology, UZ Brussel (VUB), Brussel, Belgium

Synopsis: We performed Monte Carlo Simulations to show that the risk for type I errors decreases if a minimum overlap between the individual results is set in addition to the significance of the group results. The activation maps of a real fMRI experiment showed that the combination of a weighted overlap map threshold in combination with a voxel significance threshold seems to lead to less type II errors compared to applying a family wise error (FWE) correction.

Introduction: In fMRI, the common practice is to report the significance of the found group results only. However, a significant group effect is not always supported by effects observed in the individual subjects1,2,3. Seghier et al. (2016) showed that weighted overlap maps (WOM) can aid the interpretation of group effects by looking at the variability of the effects observed at subject's level. In this study, we illustrate how WOM help reducing the chance for false positive results using Monte Carlo simulations (MCS) and real fMRI data.

Methodology:

Monte Carlo Simulations: The MCS were done in RepSim4. We performed 1000 MCS simulating the statistical activation maps per subject for 5 fMRI experiments (sample sizes 15, 20, 28, 50 and 100 subjects). In each simulation, a WOM was calculated based on the statistical significance p:

$$WOM = \frac{1}{N}\sum_{i=1}^{N} w_i \; with \; w_i = \begin{cases} 1 \; if \; p_i < 0.001 \\ e^{-\frac{1}{2}\left(\frac{p_i - 0.001}{0.001}\right)^2} \; if \; p_i \geq 0.001 \end{cases}$$

(N: number of subjects)

Per MCS, a group analysis was performed and the resulting statistical map was thresholded at p<0.001.

Per fMRI experiment, we calculated the chance per voxel for overlapping false positive activations in n subjects (n∈[0…N]) and the chance for an additional false positive group effect.

fMRI Experiment: To illustrate the effect of applying a WOM based mask on fMRI results, we used data of 28 subjects (24 females, age 25□3) participating in an episodic future thinking (EFT) fMRI experiment. In this experiment, the participants were asked to imagine an event that could happen in their own future associated with the words presented on a screen (e.g. word: car, event: driving to a friend next weekend). The multi-echo fMRI scan was done on a GE MR750W scanner (18 trials lasting 20s with 4s rest, 210 dynamics, TR=2s, TE=17/39.2/61.4ms).

After processing the individual fMRI scans in SPM125, a 1-sample T-test on the activation maps was performed and a WOM was calculated. The group activation map for EFT was thresholded at p(uncorrected)<0.001, p(FWE)<0.05 and p(uncorrected)<0.001 combined with WOM>0.15 (at least 5 subjects).

Results:

Monte Carlo Simulations: The MCS showed that for all sample sizes, in each voxel the chance of having a false positive result at group level not supported at subject's level was 0.001. The chance of having a false positive activation in only 1 subject was 0.030 for N=15, 0.040 for N=20, 0.056 for N=28, 0.095 for N=50 and 0.173 for N=100. The chance that a false positive result in only 1 subject is also significant at group level was 0.000 for N=15 and N=20, 1.02E-7 for N=28, 3.99E-6 for N=50 and 3.33E-5 for N=100. The largest overlap seen between false positive subject's results was 5 for N=15, 6 for N=20, 5 for N=28, 6 for N=50 and 7 for N=100. The largest overlap seen between individual results that also showed a significant group results was 1 for N=15 and N=20, 2 for N=28 and 3 for N=50 and N=100. The results of the MCS are summarized in table 1.

fMRI Experiment: The maximum WOM of the individual activation maps for EFT was 0.73. Figure 1 shows the overlap between the activation map thresholded at p(uncorrected)<0.001, p(FWE)<0.05 and p(uncorrected)<0.001 combined with WOM>0.15.

Discussion: Our Monte Carlo simulations showed that the risk for false positive results repeatedly observed in multiple subjects increased with sample size. However, the chance of having a significant false positive group result supported by false positive results in multiple subjects, decreased with the overlap between the individual results. This observation supports the call of Chen et al. (2017) and Seghier et al. (2016) that it is interesting to give more attention at the individual effects underlying observed group effects.

The activation maps of a real fMRI experiment showed that our proposed group significance combined with a minimum WOM threshold resulted in more and larger activation areas compared to the family wise error (FWE) correction, while large parts of the activations found with p(uncorrected)<0.001 were filtered out as possibly false positives. Since the FWE correction is known to inflate the risk for type II errors6, our results suggest that our combined threshold method makes a better balance between type I and type II errors. However, task related activations occurring in a few subjects only, will be misted due to the WOM threshold.

Conclusion: As illustrated in this study, using a WOM based on the individual activation maps in combination with the significance of group results can help reducing the risk for false positive results in a fMRI study.

References

1. Chen G., Taylor A., Cox W., 2017. Is the statistical value all we should care about in neuroimaging? NeuroImage 147: 952-959

2. Seghier M.L., Price C., 2016. Visualising inter-subject variability in fMRI using threshold-weighted overlap maps. Sci Rep 6: 20170

3. Van Schuerbeek P. 2018. Effect size and result overlap between individual and group results in fMRI studies. ISMRM 2018 (Paris, France), Abstract 881

4. https://github.com/P-VS/RepSim

5. http://www.fil.ion.ucl.ac.uk/spm/

6. Lieberman M., Cunningham W., 2009. Type I and Type II error concerns in fMRI research: re-balancing the scale. Soc. Cogn. Affect. Neurosci. 4(4): 423-8

Acknowledgments / Funding Information: Continue on this line

n subjects (n=WOM*N)	N=15		N=20	
	Chance overlapping false positive results	Chance false positive group effect	Chance overlapping false positive results	Chance false positive group effect
0	0.969	0.001	0.959	0.001
1	0.030	0.000	0.040	0.000
2	3.14E-6	0.000	7.31E-4	0.000
3	4.44E-9	0.000	7.63E-6	0.000
4	0.000	0.000	6.22E-8	0.000
5	0.000	0.000	4.44E-9	0.000
6	0.000	0.000	0.000	0.000
7	0.000	0.000	0.000	0.000
8	0.000	0.000	0.000	0.000
9	0.000	0.000	0.000	0.000
10	0.000	0.000	0.000	0.000

n subjects (n=WOM*N)	N=28		N=50	
	Chance overlapping false positive results	Chance false positive group effect	Chance overlapping false positive results	Chance false positive group effect
0	0.943	0.001	0.900	0.001
1	0.056	1.02E-7	0.095	3.99E-6
2	0.001	0.000	0.005	4.44E-9
3	2.35E-5	0.000	1.31E-4	0.000
4	3.55E-7	0.000	2.77E-6	0.000
5	0.000	0.000	3.11E-8	0.000
6	0.000	0.000	0.000	0.000
7	0.000	0.000	0.000	0.000
8	0.000	0.000	0.000	0.000
9	0.000	0.000	0.000	0.000
10	0.000	0.000	0.000	0.000

n subjects (n=WOM*N)	N=100	
	Chance overlapping false positive results	Chance false positive group effect
0	0.809	0.001
1	0.173	3.33E-5
2	0.017	4.35E-7
3	0.001	0.000
4	4.41E-5	0.000
5	1.43E-6	0.000
6	1.33E-8	0.000
7	0.000	0.000
8	0.000	0.000
9	0.000	0.000
10	0.000	0.000

Table 1. Summary of the MCS presenting the chance per voxel to show a false positive result overlapping in n subjects and additionally showing a false positive group effect. N is the sample size of the simulated fMRI experiments. To compare the results, the WOM values were transformed in number of subjects as n=WOM*N.

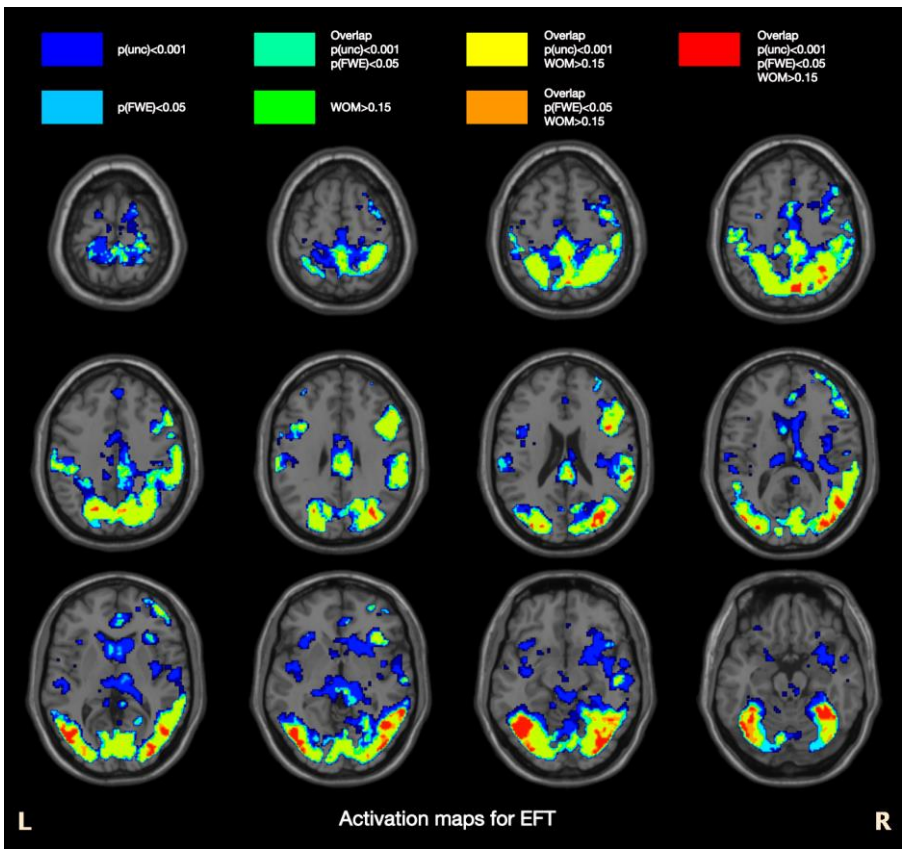

Figure 1. The overlap between the EFT activation maps thresholded at p(uncorrected)<0.001, p(FWE)<0.05 and p(uncorrected)<0.001 combined with WOM>0.15.

Comparison of Language Areas determined by Resting State and Task Based fMRI using healthy subjects HCP data.

Robert Pretorius[1], Stefan Sunaert[1,2,3], Ahmed Radwan[1]
[1] KU Leuven, Department of Imaging and pathology, Translational MRI, Leuven, Belgium
[2] KU Leuven, Leuven Brain Institute, Department of Neurosciences, Leuven, Belgium
[3] Department of Radiology, University Hospitals Leuven, Leuven, Belgium

Synopsis

Adding to the literature of resting state fMRI (rsfMRI) in preoperative planning, we investigated the similarity of a task based fMRI (tbfMRI) language protocol to a pan-language functional connectivity map in 10 healthy subjects. When comparing the whole brain there is relatively low Jaccard and Sorensen-Dice similarity between rsfMRI and tbfMRI language activity, however when looking at separate cortical anatomical regions the language areas are among those having the highest similarity. Additionally, there is a significantly higher similarity in the left IFG pars triangularis. This suggests that rsfMRI could be used reliably to determine Broca's area in preoperative planning.

Purpose

Determining the location of Broca's area, Wernicke's area and general language laterality is imperative in pre-operative planning. Task based fMRI (tbfMRI) is currently used to help determine this, but what if your patients cannot complete such tasks? Recent works have described resting state fMRI (rsfMRI) as a possible alternative[1–4]. However, the data is limited, mostly including clinical patients and the conclusions are variable[5]. Further building on this work, we investigate the similarity in language area activity in tbfMRI and rsfMRI in 10 healthy subjects.

Methods

The data used was available from the S1200 release of the WU-Minn Human Connectome Project consortium (HCP)[6]. Anatomical data, resting state, and task-based language conditions for 10 subjects were chosen for analysis.

The resting state data was acquired with a TR of 720 ms. The language task was organized as described by Binder et al.[7] For each subject one run per tbfMRI and rsfMRI condition was used.

Data analysis (summarised in Fig. 1) consisted of preprocessing steps, first level analysis and comparative analysis. Software packages used to achieve this were CONN-toolbox[8], Statistical Parametric Mapping (SPM) and custom scripting in MATLAB (MathWorks). Preprocessing was done using CONN's 'default-MNI' preprocessing pipeline. A spatial smoothing kernel with FWHM of 6 was used.

The same preprocessing was applied to rsfMRI and tbfMRI data with the sole difference being the bandpass filter used in the denoising step. The results are mapped to MNI space.

For rsfMRI data, after denoising, seed based connectivity (SBC) was calculated using the default conn network parcellation atlas. The left and right Inferior Frontal Gyrus (IFG) and posterior superior temporal gyrus (pSTG) language networks were chosen as seeds. The p-maps were thresholded at $p<0.05$. A combined pan-language functional connectivity (FC) map was created by selecting only those voxels present in all 4 SBC p-maps.

For first level analysis of tbfMRI data, a Math < Story contrast (vector: [-1,1] for [math, story] conditions) was created. The corresponding t-map was converted to p-maps and thresholded at $p<0.05$.

The above was repeated for each subject and comparisons were made between subject specific tbfMRI first level results and the pan-language FC maps. Jaccard index and Sorensen-Dice index were used as similarity metrics. The comparison was made for the whole brain volume and for separate cortical ROIs. These regions were determined by parcellating the MNI space with the Harvard-Oxford atlas[9-12].

Results

First level results of tbfMRI show activation in Broca's area (IFG) and Wernicke's area (pSTG) as expected (Fig. 2A). The resting state first level seed-based correlation results also show expected activation patterns for each of the four language networks results. The pan-language FC map shows a slightly asymmetric activity pattern in the language areas. (Fig. 2B).

When comparing the whole brain volumes of tbfMRI and the pan-language FC maps the Jaccard index values are 0.0653 ± 0.0191 and Sorensen Dice indices are 0.1220 ± 0.0339 (Fig. 3).

Looking at separate brain regions, there are 28 regions with higher Sorensen Dice indices and 30 regions with higher Jaccard indices than the whole brain values. For Both Jaccard and Dice values the language areas are among the highest scoring areas (Fig. 4). A significantly higher value for Dice and Jaccard can be found in the left IFG pars triangularis ($p<0.001$, Wilcoxon rank sum test).

Discussion

The tbfMRI first level activity map and pan-language FC map seem quite widespread. FDR correction of the p-maps could solve this, however more subjects would be needed to increase the power of the analysis.

The dice and Jaccard scores when comparing the whole brain are relatively low. This might indicate that the four chosen language networks are not sufficient as correlates for task-based language area determinants. The choice of analysis using the pan-language FC map might also not be optimal. In addition, the Story > Math contrast as described by Binder et al.[7] might not be as good an indicator of language laterality as other protocols that are used in the clinic such as verb-to-noun generation, sentence completion or object naming.

However, when separating out the cortical anatomical regions, the language areas are among the highest scoring areas, albeit with relatively low scores. A marked exception to this is the left sided IFG pars triangularis, which scores significantly higher than the rest. This could indicate that the localization of Brocca's area using rsfMRI in healthy subjects might be valid. However, a limitation of this finding is that there was no information available at the time about the handedness of the subjects.

Conclusion

When comparing language in tbfMRI and rsfMRI in healthy subjects there is a low similarity when looking at the whole brain. However when looking at separate cortical areas the language areas score the highest in similarity. Moreover there is a significantly higher similarity index for the left IFG pars triangularis compared to other areas.

This work further opens the door towards determining language localisation using rsfMRI in preoperative planning. Future work includes a bigger sample size, the addition of motor networks and development of predictive models.

References

1. Catalino MP, Yao S, Green DL, Laws ER, Golby AJ, Tie Y. Mapping cognitive and emotional networks in neurosurgical patients using resting-state functional magnetic resonance imaging. Neurosurg Focus. 2020 Feb 1;48(2):E9.

2. Branco P, Seixas D, Deprez S, Kovacs S, Peeters R, Castro SL, et al. Resting-state functional magnetic resonance imaging for language preoperative planning. Front Hum Neurosci. 2016;10(FEB2016):1–14.

3. Tie YM, Rigolo L, Norton IH, Huang RY, Wu WT, Orringer D, et al. Defining language networks from resting-state fMRI for surgical planning-a feasibility study. Hum Brain Mapp. 2014;35(3):1018–30.

4. Rolinski R, You X, Gonzalez-Castillo J, Norato G, Reynolds RC, Inati SK, et al. Language lateralization from task-based and resting state functional MRI in patients with epilepsy. Hum Brain Mapp. 2020;41(11):3133–46.

5. Manan HA, Franz EA, Yahya N. The utilisation of resting-state fMRI as a pre-operative mapping tool in patients with brain tumours in comparison to task-based fMRI and intraoperative mapping: A systematic review. Eur J Cancer Care (Engl). 2021;30(4):1–15.

6. HCP Young Adult - Connectome - Publications [Internet]. Humanconnectome.org. 2017 [cited 10 November 2021]. Available from: https://www.humanconnectome.org/study/hcp-young-adult

7. Binder J, Gross W, Allendorfer J, Bonilha L, Chapin J, Edwards J et al. Mapping anterior temporal lobe language areas with fMRI: A multicenter normative study. NeuroImage. 2011;54(2):1465-1475.

8. Whitfield-Gabrieli S, Nieto-Castanon A. Conn: A Functional Connectivity Toolbox for Correlated and Anticorrelated Brain Networks. Brain Connectivity. 2012;2(3):125-141.

9. Makris N, Goldstein JM, Kennedy D, Hodge SM, Caviness VS, Faraone SV, Tsuang MT, Seidman LJ. Decreased volume of left and total anterior insular lobule in schizophrenia. Schizophr Res. 2006;83(2-3):155-171.

10. Frazier JA, Chiu S, Breeze JL, Makris N, Lange N, Kennedy DN, Herbert MR, Bent EK, Koneru VK, Dieterich ME, Hodge SM, Rauch SL, Grant PE, Cohen BM, Seidman LJ, Caviness VS, Biederman J. Structural brain magnetic resonance imaging of limbic and thalamic volumes in pediatric bipolar disorder.Am J Psychiatry 2005;162(7):1256-1265

11. Desikan RS, Ségonne F, Fischl B, Quinn BT, Dickerson BC, Blacker D, Buckner RL, Dale AM, Maguire RP, Hyman BT, Albert MS, Killiany RJ. An automated labeling system for subdividing the human cerebral cortex on MRI scans into gyral based regions of interest. Neuroimage 2006;31(3):968-980

12. Goldstein JM, Seidman LJ, Makris N, Ahern T, O'Brien LM, Caviness VS Jr, Kennedy DN, Faraone SV, Tsuang MT Hypothalamic abnormalities in schizophrenia: sex effects and genetic vulnerability. Biol Psychiatry 2007;61(8):935-945

Acknowledgments / Funding Information: Continue on this line

Figure 1. Delete this page if there are no figures or tables

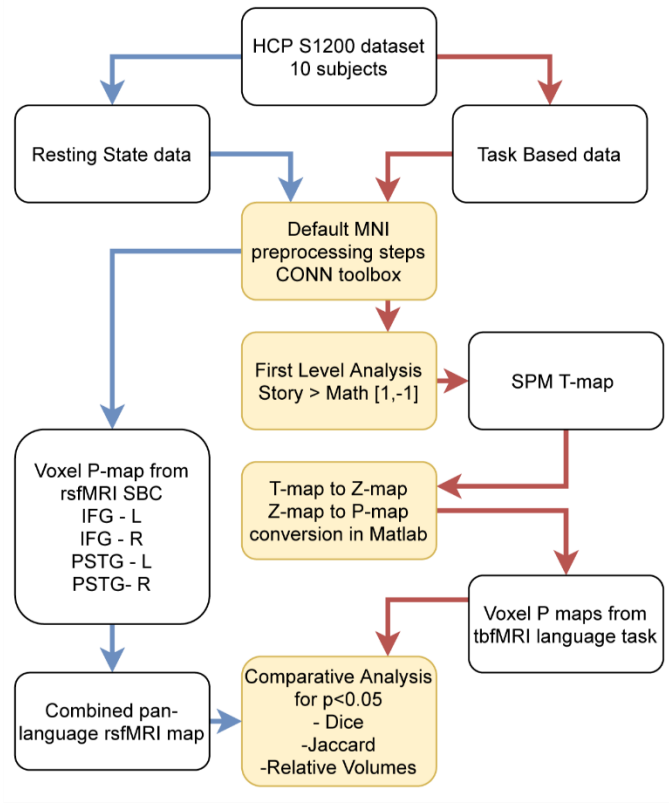

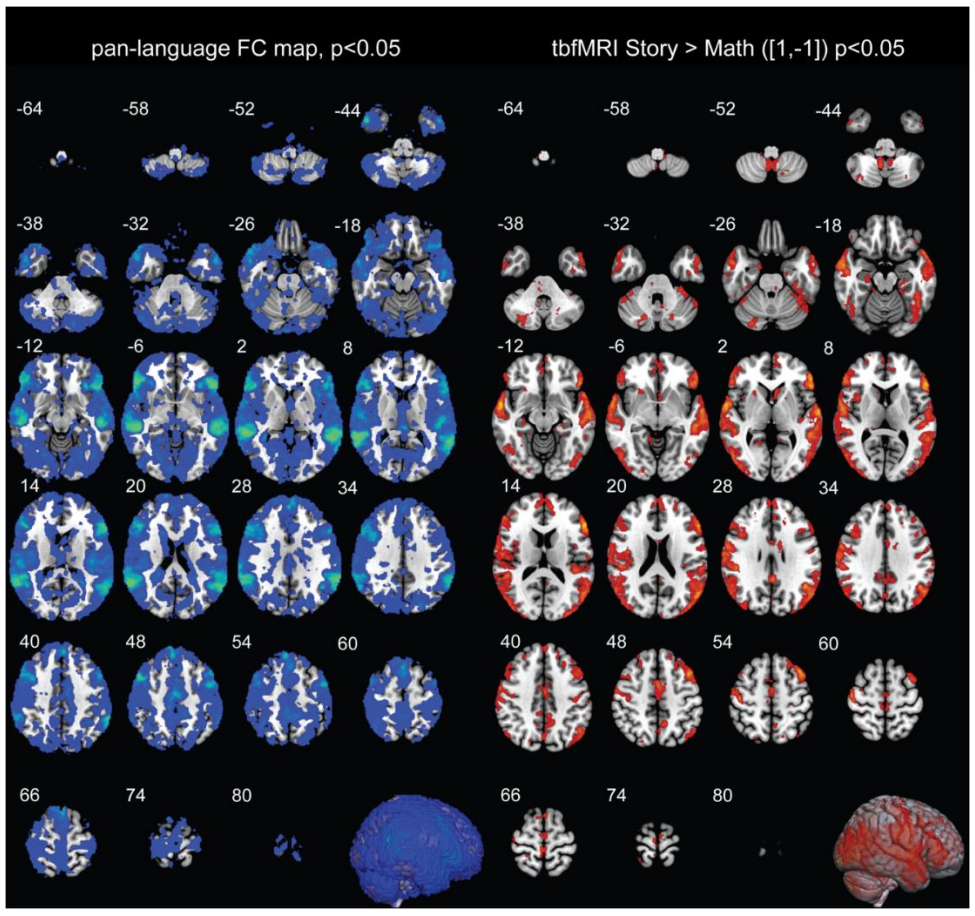

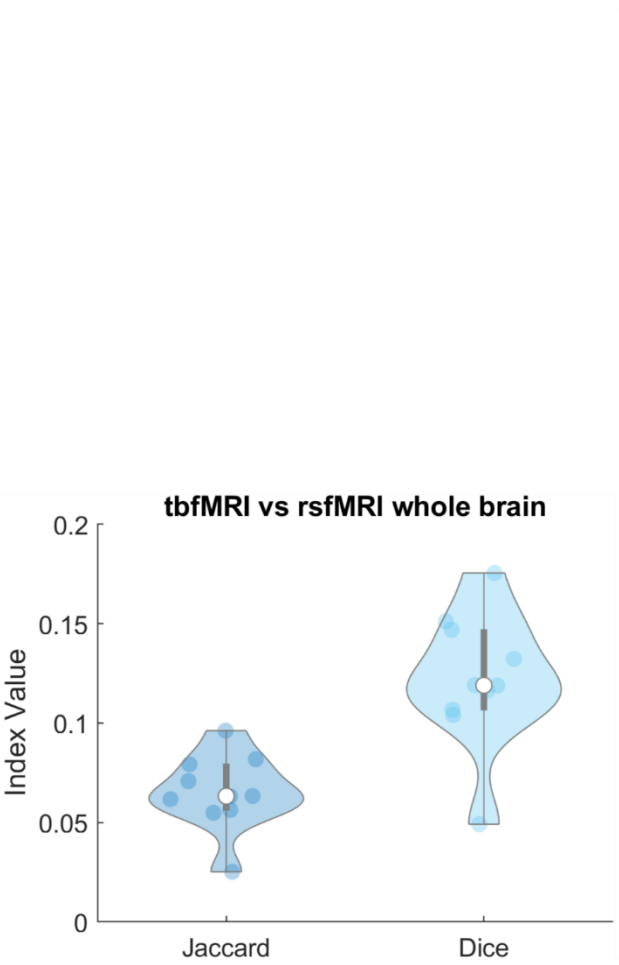

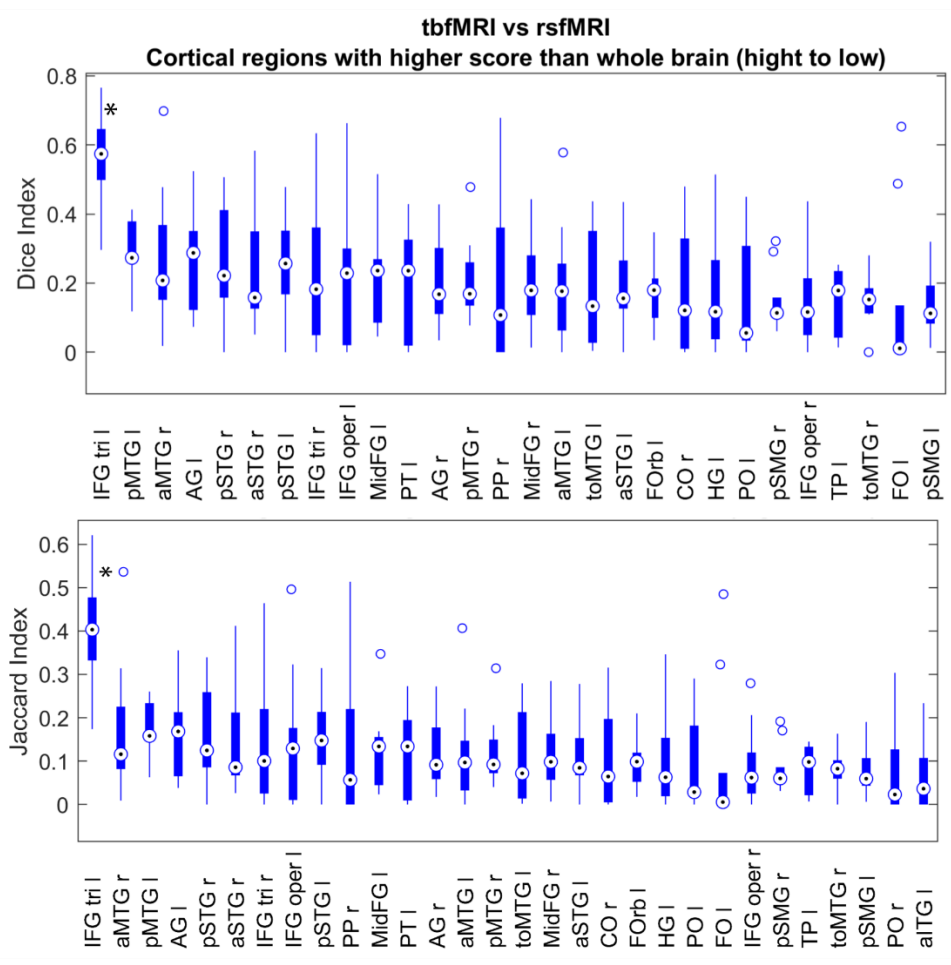

(Top Left – flowchart) Figure 1. Flow chart of the preprocessing and analysis steps. The blue path corresponds to the rsfMRI data and the red path to the tbfMRI data.

(Top Right – the brain mosaic) Figure 2. Average activity (n=10). Red: first level tbfMRI for a Story > Math language task (contrast:[1, -1]) thresholded at p<0.05. Blue: pan-language activity for rsfMRI map for L and R, IFG and pSTG language networks thresholded at p<0.05. Corresponding axial z values are shown in the top left corners.

(Bottom Left – the 2 violin plots) Figure 3. Jaccard and Sorensen-Dice index for tbfMRI and pan-language rsfMRI maps when comparing the whole brain volume.

(Bottom Right – the many boxplots) Figure 4. Jaccard and Sorensen-Dice indices for tbfMRI and pan-language FC maps for n=10 subjects when comparing separate cortical regions. Regions are sorted from high to low going from left to right (n=28 for Sorensen-Dice index, n=30 for Jaccard index). Significance is noted by an asterix.

Quantification of microvascular properties of gliomas using DSC – Hybrid EPI based MR Vascular Fingerprinting (MRVF) compared with Vessel Size Imaging (VSI)

K. Venugopal[1], F. Arzanforoosh[1], D. van Dorth[2], M. Smits[1], J. A. Hernandez-Tamames[1], E.A.H. Warnert[1], M. J. P. van Osch[2], D. H. J. Poot[1]

[1]Erasmus MC, University Medical Center Rotterdam, Department of Radiology and Nuclear Medicine, Rotterdam, Netherlands

[2]Leiden University Medical Center, C. J. Gorter Center for High-Field MRI, Department of Radiology, Leiden, Netherlands

Synopsis: This study uses an MRVF approach to analyze the time evolution of a DSC hybrid -EPI (HEPI) sequence that simultaneously acquires gradient and spin echo images. HEPI properties are incorporated from the scanner into simulations including contrast agent extravasation, diffusion, and MR signal evolution and for varying the outcome parameters: CBV, mean vessel-size, and leakage. In vivo data of six glioma patients are used to compare MRVF output maps to those obtained from conventional VSI modelling. The results show reasonable agreement. Also, the noise sensitivity of both techniques was investigated.

Introduction: Perfusion parameters derived from Dynamic Susceptibility Contrast (DSC) MRI are increasingly utilized as image-based biomarkers for management of patients with glioma[1]. Of particular interest is relative cerebral blood volume (rCBV), which is the most widely used parameter for predicting tumor grade and has the potential to predict overall survival of glioma patients[2]. Hybrid EPI (HEPI)[3] is a fast acquisition technique that combines gradient (GRE) and spin echo (SE) read-outs which are sensitive to all vessels (micro and macro) and only microvasculature, respectively. Using HEPI for DSC imaging can therefore provide additional information of blood vessel architecture, including estimates of vessel radius (R)[4]. To disentangle R and rCBV, a vascular fingerprinting[5] (MRVF) approach based on DSC HEPI acquisition is proposed in this work. Quantitative information retrieved about the underlying microvasculature of glioma using a HEPI dictionary specific for the DSC technique is compared with those obtained using conventional Vessel Size Imaging (VSI) processing[6]. To test the hypothesis that MRVF is more robust to noise than VSI, R and rCBV are estimated after adding noise to the raw in-vivo data.

Methods: HEPI-DSC images were acquired at 3T (MR750, GE) from 6 patients with confirmed diagnosis of glioma (Table 1). Dynamic images ($TR/TE_{GRE}/TE_{SE}$ 1.5s/20ms/70ms, 15 slices) were acquired during bolus injection of 7.5ml of GBCA (Gadovist, Bayer, GE) after a preload of equal size[7,8]. We imported the HEPI sequence as played out on the scanner into a simulation (DCESim) tool[9] that simulates CA extravasation, diffusion, and MR signal. A dictionary was created by simulating a 2D voxel with 5 vessels having 10, 50 and 40 logarithmically spaced values of permeability (k) [0, $7*10^{-3}$] s^{-1}, R [5, 150] µm and rCBV [0.5, 10]% respectively[9,10]. For each dictionary atom the simulation included a time range of 400s to cover pre-bolus and delay, followed by 100s of the main bolus and HEPI-acquisition. The dictionary was matched to the patient data using a separate scaling factor for the GRE and SE parts to compensate for baseline signal differences between dictionary and in-vivo signals. The vessel parameters corresponding to the match from the dictionary to the data are retrieved. Conventional VSI modelling to obtain rCBV and R maps was done after conversion of GRE & SE time courses into changes in transverse relaxation rates over time[6]. Here, leakage correction was included as previously described[11]. Structural Similarity Index Measure (SSIM) was used to assess the similarity between the corresponding parameter maps obtained using MRVF and VSI. To perform noise analysis, independent Gaussian random noise was added to three of the patient datasets and the absolute percentage difference was calculated as error-measure.

Results: The vessel parameters of the dictionary match to the in-vivo data are shown in Table 1 for a representative voxel within the tumor region for each of the datasets. Non-zero permeability values were obtained only for the enhancing tumor voxels as seen on T1-Gd. Figure 1 shows for each patient a representative T2 FLAIR image with the R and rCBV parametric maps obtained using the two methods. It is observed that both techniques show similar patterns, although the tumor rCBV in patient 3 is more hyperintense for MRVF than for VSI. R estimates are comparatively noisy in MRVF maps due to very small differences in the HEPI signals simulated for varying R above 70µm. The SSIM values are shown in Table 1, illustrating that both the techniques are similar as concluded from the moderate to high SSIM-values. Figure 2 shows GRE (A,B,C) and SE (D,E,F) signals for a representative tumor voxel in three of the datasets, before and after adding noise, and their corresponding dictionary match. R and rCBV maps were also estimated using both the techniques from the noisy data. They were compared with the corresponding maps from the raw data by evaluating the percentage difference values between them which are shown in Figure 3. Low percentage error values were obtained for the rCBV maps in both the techniques, while the difference values for R were comparatively higher for VSI compared to MRVF.

Discussion: The proposed DSC-HEPI based fingerprinting approach retrieves quantitative information on microvasculature of gliomas with the advantage of acquiring a single time course during passage of a bolus of contrast agent compared to the conventional MRVF based on pre- and post-contrast asymmetric spin-echo data[5]. Time-course data show good correspondence between dictionary and in-vivo data. We compared the quantitative maps of R and rCBV from MRVF to VSI values and found similar patterns, although some differences should be noted. In the experiments MRVF and VSI appeared to be robust against noise in estimating rCBV, while the apparent improved robustness of MRVF in estimating R needs to be further studied.

References:

1. Shiroishi, Mark S., et al., *Journal of Magnetic Resonance Imaging* 41.2 (2015): 296-313.
2. Calamante, Fernando, et al, " *Journal of cerebral blood flow & metabolism* 19.7 (1999): 701-735.
3. P. F. Ferreira, P. D. Gatehouse, and D. N. Firmin, *J. Cardiovasc. Magn. Reson.*, 2012, doi: 10.1186/1532-429X-14-44.
4. Troprès, I. *et al*. Vessel size imaging. *Magn. Reson. Med.* 45, 397–408 (2001).
5. Christen, Thomas, et al., *Neuroimage* 89 (2014): 262-270.
6. E. Kellner *et al.*, *J. Magn. Reson. Imaging*, 2015, doi: 10.1002/jmri.24864
7. S. R. van der Voort *et al.*, *Clin. Cancer Res.*, 2019, doi: 10.1158/1078-0432.CCR-19-1127.
8. Paulson, Eric S., and Kathleen M. Schmainda, *Radiology* 249.2 (2008): 601-613.
9. Pannetier, Nicolas Adrien, et al," *PloS one* 8.3 (2013): e57636.
10. Beaumont, Marine, et al., *Journal of Cerebral Blood Flow & Metabolism* 29.10 (2009): 1714-1726.
11. J. L. Boxerman, K. M. Schmainda, and R. M. Weisskoff, *Am. J. Neuroradiol.*, 2006.

Acknowledgments / Funding Information: NA

Patient	Histopathological Diagnosis (grade)	Parameters in Tumor voxel			SSIM (MRVF vs VSI)	
		K (s^{-1})	R (µm)	rCBV (%)	Vessel Size	rCBV
1 (65Y, Male)	Glioblastoma (IV) (Enhancing)	$1.2*10^{-3}$	13.2	2.71	0.7856	0.7879
2 (32Y, Male)	Oligodendroglioma (III) (Non-enhancing)	0	11.4	3.21	0.7282	0.7714
3 (24Y, Male)	Oligodendroglioma (III) (Enhancing)	$1.8*10^{-3}$	39.5	5.38	0.7786	0.7745
4 (22Y, Female)	Oligodendroglioma (II) (Non-Enhancing)	0	5	4.3	0.8860	0.8067
5 (37Y, Male)	Astrocytoma (III) (Enhancing)	$0.3*10^{-3}$	81	2	0.7948	0.7924
6 (8Y, Female)	Astrocytoma (II) (Non-Enhancing)	0	26	1.47	0.8940	0.7917

Table 1: Diagnosis of the patient datasets and the vessel parameters, k, R and rCBV values obtained from the best match of the HEPI signals in a tumor voxel. The last two columns show the SSIM obtained between MRVF and VSI for R and rCBV maps for each of the dataset.

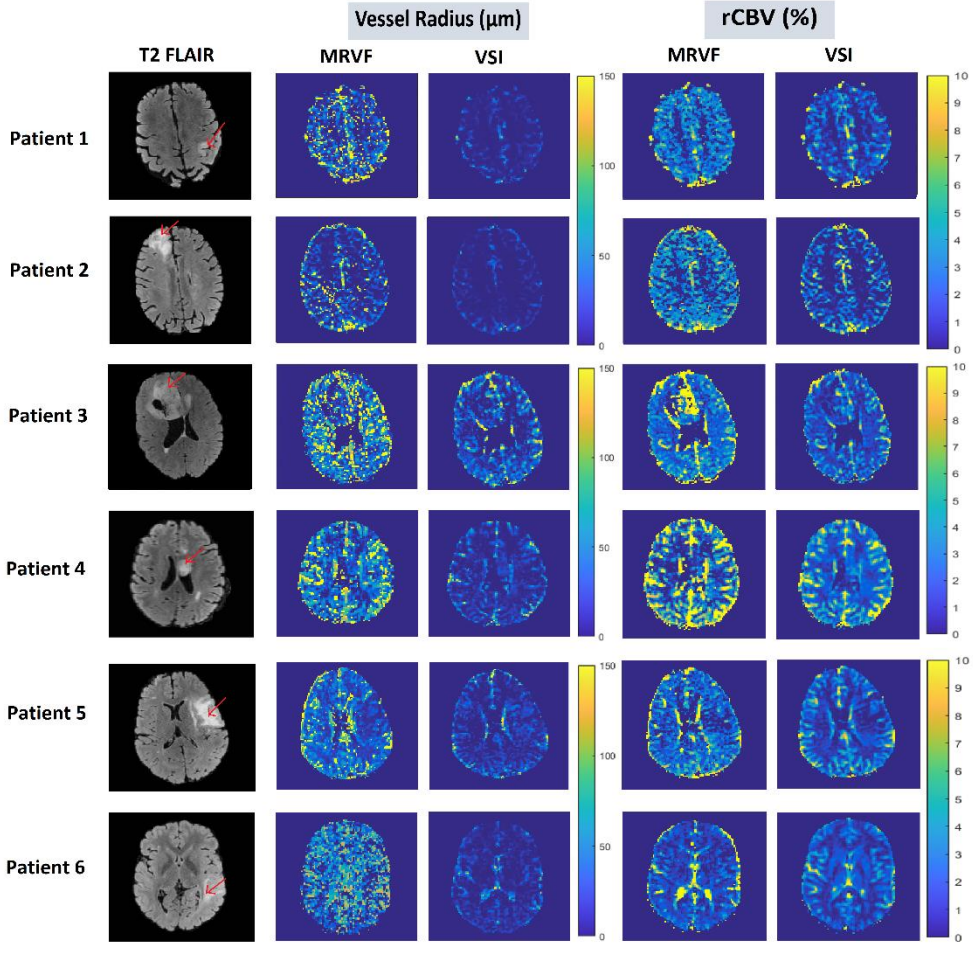

Figure 1: T2 FLAIR images of 6 patient datasets of slices showing the glioma (marked by the red arrows) and the corresponding vessel radius and rCBV maps obtained using the MRVF and the VSI methods.

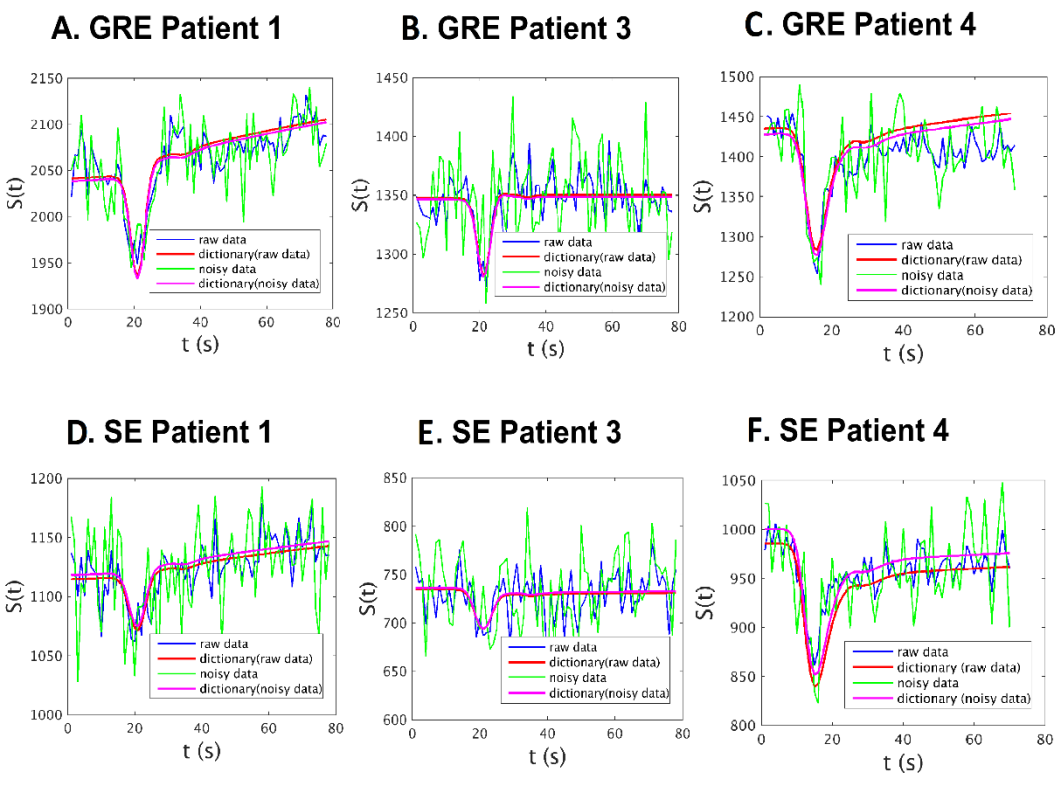

Figure 2: Raw GRE and SE signals (blue) in a voxel in one of the voxels, compared with the corresponding signals after adding noise (green), of patient datasets, 1 (A, D), 3 (B,E) and 4 (C,F). For each GRE and SE raw and noisy data, corresponding match obtained from the respective GRE and SE of the dictionary atoms is also shown.

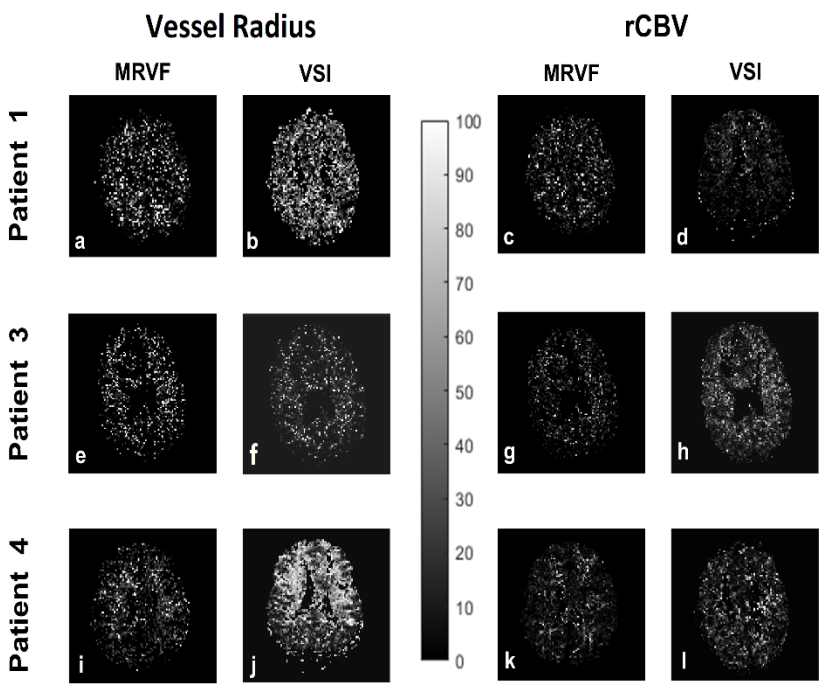

Figure 3: Error (%) maps in R (a,b,e,f,i,j) and rCBV (c,d,g,h,k,l) estimation from raw and noisy data using MRVF (a,c,e,g,i,k) and VSI (b,d,f,h,j,l) for patients 1(a-d), 3(e-h) and 4(i-l).

Measuring CSF net flow velocities in the human brain with 7T MRI

E.C. van der Voort[1], M.C.E. van der Plas[1], J.J.M Zwanenburg[1]
[1]Radiology, University Medical Center Utrecht, Utrecht, The Netherlands

Synopsis: This work provides a framework to measure CSF net flow in vivo in humans whilst accounting for the pulsatile motion due to cardiac effects. CSF motion contributes to the clearance of waste products in the brain and has been proven to be impaired in Alzheimer patients. A slice-selective single shot Displacement encoding with stimulated echoes sequence was used to measure these CSF motions. Preliminary results show that more work is needed in order to accurately estimate the CSF net flow.

Purpose

Motion of cerebrospinal fluid (CSF) contributes to removal of waste products and has been proven to be impaired in Alzheimer patients [1,2]. CSF motion, which is in the order of µm/s to mm/s, can be measured using stimulated echo sequences[3]. However, it remains challenging to measure this motion in vivo due to other effects such as the cardiac and respiratory cycle. These effects also induce CSF motions, while CSF production and absorption induce a net flow that is very small compared to the higher-frequency motions[4]. Our end-goal is to measure this net flow of CSF while correcting for confounding effects from higher-frequency components in the CSF motion. Here we describe the approach and provide preliminary results targeting net CSF-flow at end-exhalation breath holds as proof-of-concept.

Methods

We propose to use a slice-selective single shot Displacement encoding with stimulated echoes (DENSE) sequence[5] without cardiac triggering and long mixing time (TM, delay between encoding and decoding) to maximize sensitivity to slow flow (see Figure 1). The measured phase, φ, can be modeled as a linear combination of cardiac effects, φ_c, CSF net velocity effect, $\dot{\varphi}_{net}$, and static confounders, φ_0, yielding the model:

$$\varphi(r) = \varphi_0 + \sum_{i=1}^{10} x_{c,i}\varphi_{c,i} + \dot{\varphi}_{net}TM$$

where i is the number of the cardiac bin. The $x_{c,i}$ and TM are known based on physiology trace and scan parameters respectively. The φ_0, $\varphi_{c,i}$ and $\dot{\varphi}_{net}$ are estimated using a least squares optimization. The cardiac induced displacement is calculated from the average cardiac phase of the ROI by:

$$d_{c,i} = \frac{DENC}{\pi}\varphi_{c,i}$$

And the net velocity is calculated from the average net phase of the ROI by:

$$v_{net} = \frac{DENC}{\pi}\dot{\varphi}_{net}$$

Where DENC is the motion encoding sensitivity in mm.

We obtained preliminary results of this approach from one healthy volunteer (male, 26 years) scanned at a 7T (Philips Healthcare) using a 8-channel transmit and 32-channel receive coil (Nova Medical). Written informed consent was obtained in accordance with the Ethical Review Board of our institution. Acquisition was performed during breath hold after exhalation to obtain a stable respiratory effect which will be part of $\dot{\varphi}_{net}$. A total of 50 slices in coronal orientation were acquired in two cycles (odd and even), which were obtained during the same breath hold. DENSE measurements were repeated 51 times with the following parameters: motion encoding sensitivity 0.3 mm in FH direction, mixing time 1250/1350 ms, cycle duration: 2500/2700 ms, SENSE = 2.3, resolution of 3x3x3 m^3, TR/TE = 5000/(5400)/24 ms. Physiological data was simultaneously recorded using a respiration belt to trace abdominal breathing and a peripheral pulse transducer (PPU) to trace the cardiac cycle. For reference of the CSF, a T2-weighted scan was acquired using 2 refocusing pulses and an echo time of 250 ms. 2D phase unwrapping was performed per slice for all dynamics.

During post-processing all acquisitions were retrospectively binned into ten cardiac phases using the PPU data. The T2-weighted scan was used to create a mask for the different ROI's that were investigated. Within these ROI's (see Figure 2) mean phase values were calculated which were used as input for the least squares optimization.

Results and Discussion

Figure 3 shows the displacement over the cardiac cycle for the fourth ventricle and a mixing time of 1250 ms. Table 1 shows net velocities of the CSF for the different ROIs and the two mixing times. All velocities are small at most 33 µm/s. Most velocities are negative indicating flows towards the spinal canal, which is to be expected during exhalation. However, the velocity at the fourth ventricle did not have consistent sign between the two mixing times and is lower than expected (similar numbers as found in the brain stem tissue).

Future work is needed to further develop and validate the proposed approach. The model needs to be extended to include respiration- and vasomotion-induced CSF motion. The effect of eddy currents needs to be considered as well. We intend to validate the approach with simulations for which the ground truth is known, and by setting up a dedicated phantom with creep flow. A challenge for the measurements is to balance the motion sensitivity for the slow net velocities and the sensitivity to phase wraps due to the high velocities from heartbeat-related CSF motion. A multi-DENC approach might solve this issue. It is promising that with the current DENC (0.3 mm) very low net velocities seem to be detectable, as seen in the brain stem tissue. The apparently wrong estimates for the net CSF velocity in the fourth ventricle might be due to phase wraps in the data, although phase-unwrapping was applied to avoid such errors.

Conclusion

A framework was set up to measure CSF net flow in vivo whilst accounting for pulsatile confounding motions. Preliminary results show that more work is needed.

References

1. Bakker, E. N., Bacskai, B. J., Arbel-Ornath, M., Aldea, R., Bedussi, B., Morris, A. W., ... & Carare, R. O. (2016). Lymphatic clearance of the brain: perivascular, paravascular and significance for neurodegenerative diseases. *Cellular and molecular neurobiology*, *36*(2), 181-194.
2. Peng, W., Achariyar, T. M., Li, B., Liao, Y., Mestre, H., Hitomi, E., ... & Deane, R. (2016). Suppression of glymphatic fluid transport in a mouse model of Alzheimer's disease. *Neurobiology of disease*, *93*, 215-225.
3. Magdoom, K. N., Zeinomar, A., Lonser, R. R., Sarntinoranont, M., & Mareci, T. H. (2019). Phase contrast MRI of creeping flows using stimulated echo. *Journal of Magnetic Resonance*, *299*, 49-58.
4. Spijkerman, J. M., Geurts, L. J., Siero, J. C., Hendrikse, J., Luijten, P. R., & Zwanenburg, J. J. (2019). Phase contrast MRI measurements of net cerebrospinal fluid flow through the cerebral aqueduct are confounded by respiration. *Journal of Magnetic Resonance Imaging*, *49*(2), 433-444.
5. Sloots et al. Dynamic Changes in Brain Tissue Strain and ADC over the Cardiac Cycle quantified at 7T MRI, In proceedings of ISMRM 2021 #0648

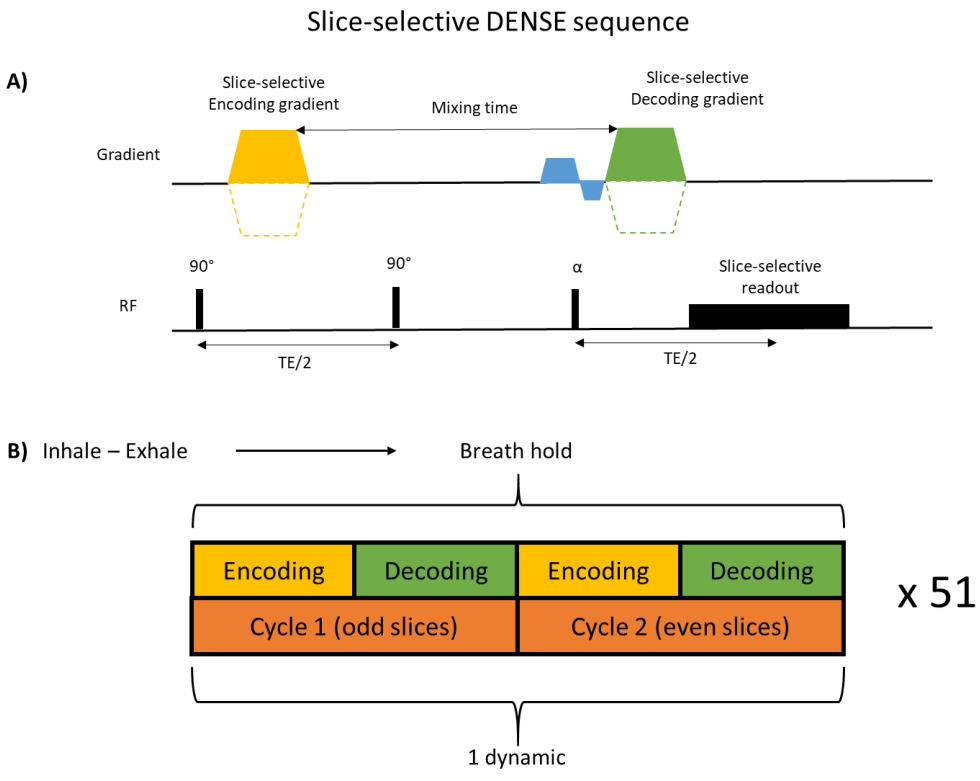

Figure 1. Overview of slice-selective DENSE sequence. A) DENSE employs an encoding and decoding gradient, which is alternated over the multiple dynamics. A phase shift during the mixing time corresponds to tissue displacement along the direction of the motion encoding gradients. B) Schematic overview of the sequence that was acquired. A total of 50 slices was acquired in two cycles (odd and even) during a breath hold after exhalation.

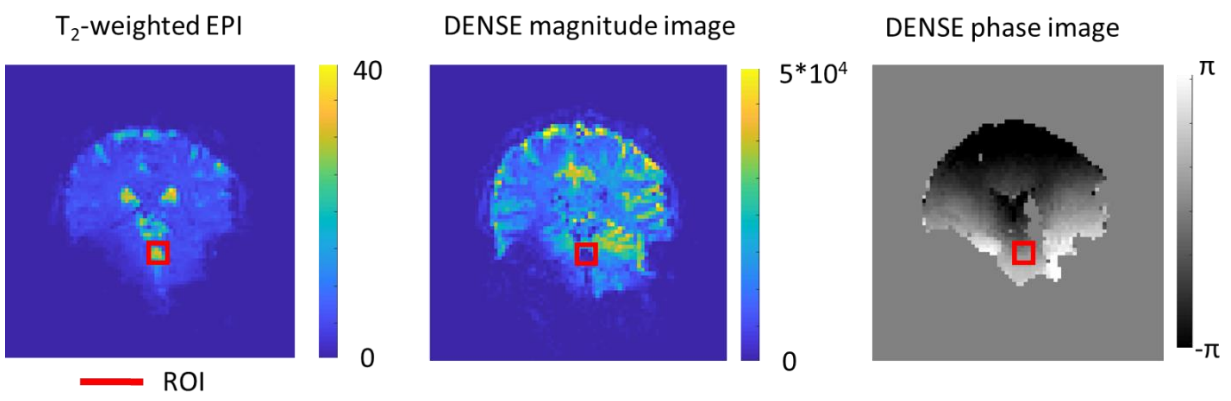

Figure 2. T_2-weighted EPI, DENSE magnitude image and DENSE phase image. The ROI is drawn in the fourth ventricle, for which the cardiac cycle is also shown in Figure 3

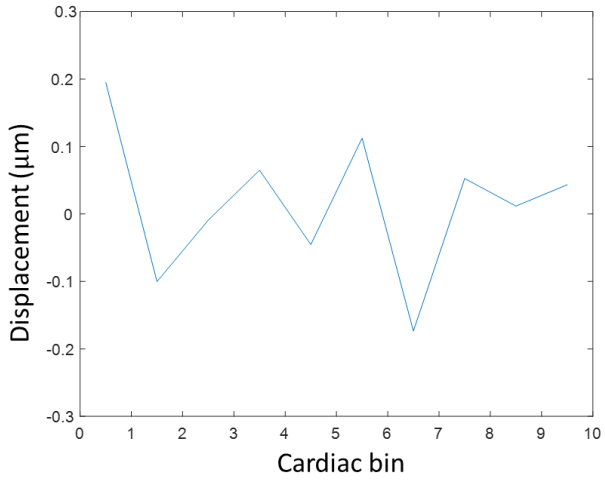

Figure 3. The displacement (μm) measured for every cardiac bin in the fourth ventricle for a mixing time of 1250 ms.

Table 1. Velocity (µm/s) of net CSF flow for the five different ROIs and the two mixing times.

	TM = 1250 ms	**TM = 1350 ms**
Left Ventricle	22.8	8.4
Right Ventricle	-3.9	-25.6
Fourth Ventricle	10.9	-25.5
Superior CSF ROI	-12.0	-33.2
Brain Stem Tissue	-14.0	-8.2

Combining Arterial Blood Contrast with BOLD improves fMRI laminar specificity

N. Priovoulos[1], I.A.F. Oliveira[1], B.A. Poser[2], D.G. Norris[3,4], W. van der Zwaag[1]

[1]Spinoza Centre for Neuroimaging, Amsterdam, Netherlands; [2]MR-Methods group, MBIC, Faculty of Psychology and Neuroscience, Maastricht University, the Netherlands; [3]Donders Institute for Brain, Cognition and Behaviour, Radboud University Nijmegen, Nijmegen, The Netherlands; [4]Erwin L. Hahn Institute for MRI, University of Duisburg-Essen, Essen, Germany

Synopsis: BOLD fMRI is widely applied in human neuroscience, but is limited in its spatial specificity compared to cerebral blood volume approaches due to its venous bias. Here we added cerebral blood-volume weighting based on magnetization transfer (Arterial Blood Contrast) to a BOLD submillimeter acquisition at 7T. Adding Arterial Blood Contrast helped differentiate the deep and superficial cortical responses in the human primary motor cortex. The results suggest that combining Arterial Blood Contrast with BOLD can improve the fMRI spatial specificity while retaining high sensitivity.

Summary of main findings: Suppressing grey matter using magnetization transfer (Arterial Blood Contrast) in a BOLD acquisition better differentiated the deep and superficial cortical fMRI signal. Adding Arterial Blood Contrast may increase specificity compared to BOLD alone.

Introduction: fMRI allows imaging the neural underpinnings of behavior in-vivo and has seen therefore widespread application[1]. fMRI contrast is typically produced using blood deoxyhemoglobin as an endogenous contrast agent (BOLD), which biases spatial sensitivity towards vein-rich areas, like the superficial layer of the cortex[2]. Cerebral blood volume (CBV) approaches are more spatially specific, showing increased intracortical functional contrast[3], but are less sensitive. Arterial Blood Contrast (ABC) is a newly-introduced technique[4] that produces a CBV-weighted functional signal by preferentially suppressing the tissue through the saturation of the macromolecular pool and the transfer of spin coherence to the free water pool[5]. The spatial-specificity benefits of ABC are currently unexplored. In this study, we employ a task paradigm thought to elicit intracortical functional contrast[6] to examine the specificity of a submillimeter BOLD technique with added ABC-weighting.

Methods: All six participants (4 female) were scanned in a Philips Achieva 7T with a 8Tx/32Rx whole-head coil (Nova Medical). The participants performed two counterbalanced runs of a finger-flexing task (right index finger, ON=13.5s, OFF=13.5s, run-duration=6min:40s), while a segmented submillimeter 3D-EPI was recorded (FOV=120x131x31mm3, voxel-size=0.9mm isotropic, TA/TR/TE=2700ms/52ms/18ms, flip-angle=20o, SENSEy/z=3.5/1.5, partial-Fouriery/z=0.7, shot-duration=218ms) (Figure 1A,B). Between each segment either a saturation train (7 hard rectangular on-resonance phase-modulated pulses, B1=10μT, duration=1ms, 95% SAR limit[4],[7]) or an equivalent wait was inserted, to achieve ABC- or BOLD-weighting. The ratio between ABC and BOLD showed 64% remaining signal in white-matter (WM), 72% in grey-matter (GM), and no signal loss in cerebrospinal fluid (CSF), implying minimal direct saturation. A distortion-matched, T1-weighted 3D-EPI was obtained by replacing the saturation train with an adiabatic inversion pulse (TI=1100ms). The 3D-EPIs were placed approximately perpendicular to the left primary motor cortex to optimally visualize the handknob (Figure 1B), including the lateral side (M1-BA4a) that has been reported to show a double-stripe CBV fMRI response to finger flexing (Figure 1C,D)[6]. The fMRI data were motion-corrected and projected to the T1-weighted-EPI with a single interpolation. A GLM (finger-tapping>rest) was fitted (FSL6.0.1) and the percent signal change was calculated. Cortical depth profiles of the GM from WM to pial surface were extracted from a manually drawn ROI in M1-BA4a (LAYNII[8]). For two participants, a second session was recorded on a different day to examine the reproducibility of the results.

Results: Cortical depth sampling of the M1-BA4a during finger flexing showed an increased percent signal change close to WM for ABC compared to BOLD, resulting in a consistent between participants activation bump in deep GM (peak percent signal change ranging from 0.75 to 1.3% between participants in deep GM). This stripe pattern was visually obvious in the unsmoothed data in 4 out of 6 participants (Figure 2A-C). In the superficial GM, a second peak was not readily visible, though in 2 participants a second peak was observed in both BOLD and ABC. The ABC response, including the stripe pattern, was reproducible in different days (Figure 3A). The mean cortical depth response across participants showed an increased percent signal change close to WM for ABC compared to BOLD (Figure 4D). ABC and BOLD average timecourses were similar, with a potentially slightly earlier peak in the outer and middle GM for ABC compared to BOLD within M1-BA4a (Figure 4A-C). The mean number of active voxels ($p<0.05$) across the whole slab was similar between BOLD and ABC, implying similar sensitivity, with a slight increase in deep GM (Figure 4E).

Discussion: Increasing the fMRI spatial specificity within the human cerebral cortex is an important target for human neuroscience. Here, we showed that adding ABC-weighting elicited a differential deep and superficial cortical response that was not detected with standard BOLD weighting in most participants. The ABC approach offers high sensitivity, straightforward implementation and high temporal efficiency, despite the SAR-constrained 7T environment. High-resolution ABC may therefore have widespread application in in-vivo neuroscience. The ABC-weighting as implemented here is added to the underlying BOLD contrast. Preferentially saturating the GM tissue may increase spatial specificity and sensitivity due to an increased arteriole and capillary contribution through the suppression of the (negative) tissue signal change, as well as due to increased water signal (arterioles upstream to the point of activation). This is supported by the potential slightly earlier peak of the ABC response in the superficial and middle GM, in agreement with added arterial weighting, though experiments with longer interstimulus intervals would be needed to test this. The perfusion of saturated water from the tissue to the capillaries and further downstream may further decrease the venous contribution. Despite the increased specificity, a substantial venous bias remains in the current implementation, as evidenced by the close agreement between BOLD and ABC close to the pial surface. Exploring the TE space to reduce the venous contribution (either through fully center-out readouts or at TEs where the short T2* venous signal has decayed) may further increase specificity in the future.

Conclusion: BOLD fMRI is widely applied in human neuroscience, but is limited in its spatial specificity. Here, we showed that adding ABC-weighting to a submillimeter BOLD-weighted 7T acquisition increases intracortical contrast, while retaining high sensitivity.

References:

[1]Glover, (2011) Neurosurg Clin N Am. 22: 133-9

[2]Uludag, et al., (2009) Neuroimage. 48: 150-65

[3] Huber, et al., (2018) Neuroimage. 164: 131-43

[4]Schulz, et al., (2020) Biorxiv.

[5]Kim, et al., (2008) Magn Reson Med. 60: 1518-23.

[6]Huber, et al., (2017) Neuron. 96: 1253-63.

[7]Priovoulos, et al., (2021) Proc. Intl. Soc. Mag. Reson. Med. 29: Paris.

[8]Huber, et al., (2021) Neuroimage. 237: 1180-91.

Acknowledgments / Funding Information: This work was supported by a TTW VI.Vidi.198.016 awarded to dr. Wietske van der Zwaag

Figure 1. A, Overview of ABC, BOLD and T1w anatomical-reference using the same segmented 3D-EPI. B, BOLD, ABC and MTR=ABC/BOLD at the handknob (primary motor cortex). C, Two runs of a finger-flexing task were recorded, where participants were instructed to flex their right index finger without touching their palm or rest while fixating on a cross. D, Finger-flexing elicits a double-stripe intracortical fMRI response in M1-BA4a with CBV methods[6], thought to relate to input and output cortical responses.

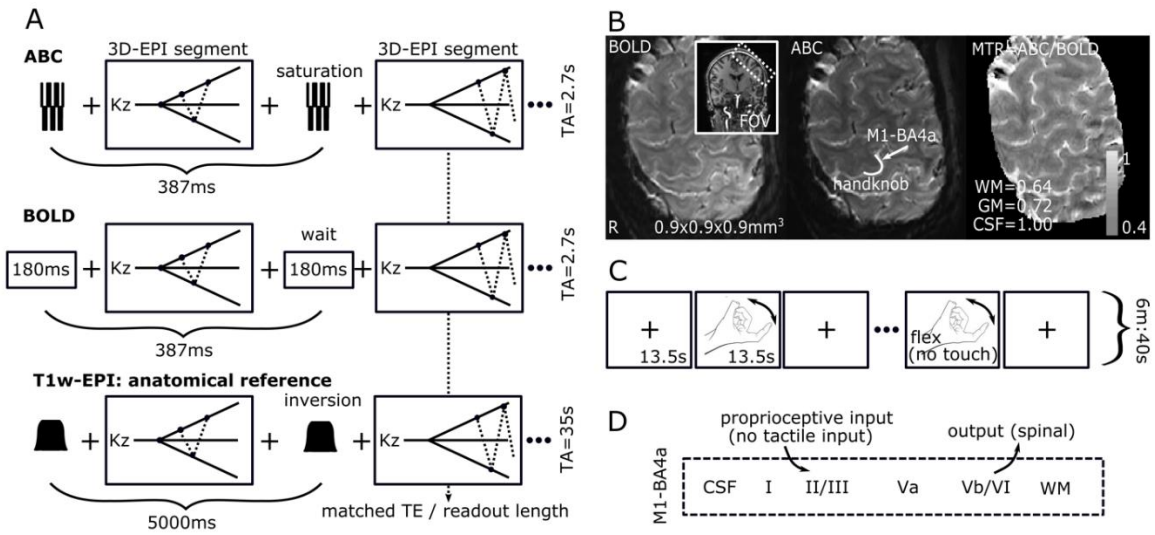

Figure 2: fMRI signal change in the left handknob during right index finger flexing. Each column represents a participant. Top row, ABC signal change. Middle row, BOLD. The white box highlights the M1-BA4a, where a double-striped activation pattern is expected[7]. The black lines represent the WM, middle GM and pial surface. Bottom row, mean cortical depth sampling within the M1-BA4a (red=ABC, blue=BOLD). The cortical depth profiles show increased signal change close to WM for ABC.

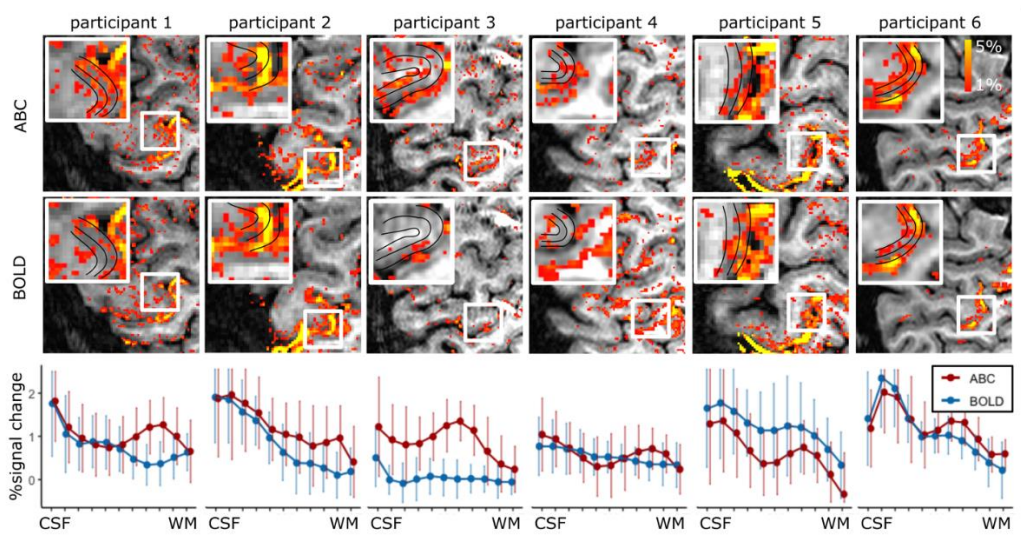

Figure 3. Reproducibility of the fMRI percent-signal-change in the left handknob during right index finger flexing. A, B: Participant 1 and 2. Top row, ABC, bottom row, BOLD. The white box highlights M1-BA4a, where a double-striped activation pattern is expected[7]. The black lines represent the WM, mid-GM and pial surface. Note that for participant 1 the deep GM activation stripe in ABC is consistent across days.

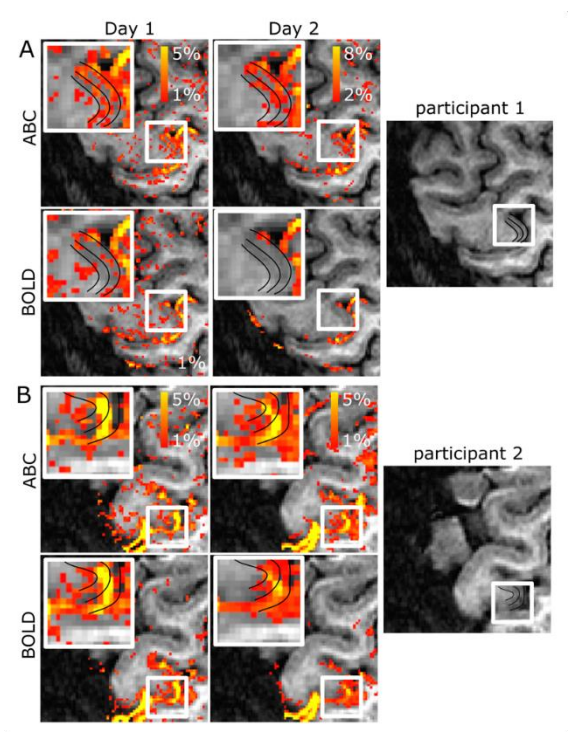

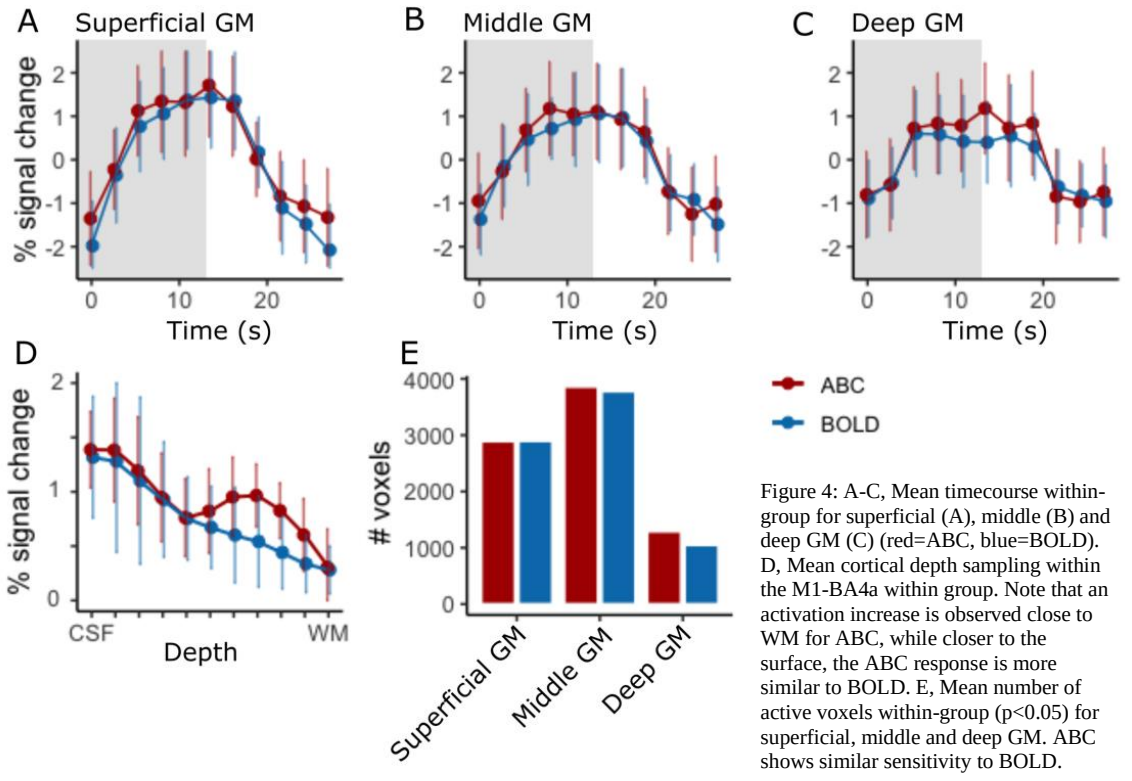

Figure 4: A-C, Mean timecourse within-group for superficial (A), middle (B) and deep GM (C) (red=ABC, blue=BOLD). D, Mean cortical depth sampling within the M1-BA4a within group. Note that an activation increase is observed close to WM for ABC, while closer to the surface, the ABC response is more similar to BOLD. E, Mean number of active voxels within-group ($p<0.05$) for superficial, middle and deep GM. ABC shows similar sensitivity to BOLD.

Probing diffusion of water and metabolites to assess white matter microstructure in Duchenne muscular dystrophy

E.M. Broek[1], N. Doorenweerd[1], M. Tamsma[1], I. Ronen[1], C. Najac[1], K.G. Hollingsworth[2], E.H. Niks[3], V. Straub[4], H.E. Kan[1]

[1]Department of Radiology, Leiden University Medical Center, Leiden, Netherlands
[2]Newcastle Magnetic Resonance Centre, Translational and Clinical Research Institute, Faculty of Medical Sciences, Newcastle University, Newcastle upon Tyne, UK
[3]Department of Neurology, Leiden University Medical Center, Leiden, Netherlands
[4]John Walton Muscular Dystrophy Research Centre, Newcastle University and Newcastle Hospitals NHS Foundation Trust, Newcastle Upon Tyne, UK

Synopsis: Many patients with Duchenne muscular dystrophy (DMD) experience cognitive and behavioral symptoms. Altered white matter microstructure has been shown with diffusion tensor imaging (DTI) in this population. In the present study, brain involvement in DMD was investigated with diffusion-weighted spectroscopy (DWS) and DTI to gain insight into the tissue compartments involved. Results indicated preserved diffusion of N-acetyl aspartate (NAA), choline, and creatine and similar NAA/creatine and choline/creatine ratios in patient with DMD compared to healthy controls. This suggests that the altered diffusivity of water may be due to extracellular, rather than intracellular processes.

Introduction: DMD is a progressive X-linked recessive neuromuscular disorder caused by the absence of functional dystrophin protein[1,2]. Dystrophin is expressed in both muscles and brain[3]. Approximately 30% of patients with DMD experience behavioral and cognitive deficits[4], which have a large impact on quality of life. Reduced fractional anisotropy (FA) and increased mean diffusivity (MD), detected with DTI, were reported in the brains of patients with DMD compared to healthy controls (HC)[5,6,7]. However, the water molecules that are detected with DTI are non-specific, as they are present in almost all microscopic tissue subcomponents and diffuse quickly between intra- and extracellular environments[8]. DWS allows for compartment-specific assessment of the diffusion properties of neuronal and glial markers, such as N-acetyl aspartate (NAA), creatine (Cr), and choline (Cho). Here, we aimed to assess the properties of these markers to gain a better understanding of cell-type specific contributions to the diffusion signal.

Materials and methods: DWS scans were obtained in N=21 genetically confirmed patients with DMD and N=11 age- and sex-matched HC in a two-center study (Leiden University Medical Center, the Netherlands; Newcastle University, the United Kingdom). Scans were obtained at 3 Tesla (Philips Achieva, Best, the Netherlands) using an 8-channel head coil. 3D T_1-weighted scans (TE/TR 4.6/9.8 ms; spatial resolution 1.17x0.92x1.17 mm; 4:55 min) were obtained for anatomical reference. DWS data were acquired with and without water suppression using a cardiac-triggered DW-PRESS sequence (TE=125 ms, TR=2 cardiac cycles; volume-of-interest (VOI)=30x20x15 mm; 24 signal averages; 3:20 min; b=0 and b=3765 mm/s^2; three diffusion directions; non-water suppressed two signal averages, 24s) to determine diffusion and metabolite levels. The VOI was positioned in the white matter (see Figure 1). DTI scans (TE/TR 59/9440 ms; spatial resolution 1.96x2x2 mm; 32 directions, b=0 and b=1000 s/mm^2; 6:40 min) were obtained to determine water diffusion metrics.

DWS spectra were analyzed using an in-house Matlab routine, including corrections for individual frequency and phase drifts and eddy currents, and subsequently fitted using LCModel[9]. For total NAA (tNAA=NAA + N-acetyl-aspartyl-glutamate (NAAG)), choline compounds (tCho=Cho + phosphocholine (PCho) + glycerophosphocholine (GPC)), and total creatine (tCr=Cr + phosphocreatine (PCr)) the apparent diffusion coefficients (ADC) were calculated. Volume fractions of cerebrospinal fluid, white matter, and grey matter within the VOI were determined using an overlay of the VOI with the tissue maps derived from FSL[10]. Mean white matter fraction, mutation status, study center, and age were correlated with the ADCs of the metabolites to inspect the need to include them as covariates. Metabolite ADCs were then compared between groups using a multivariate general linear model in SPSS. The ratios of tNAA/tCr and tCho/tCr were calculated from the fitted non-diffusion weighted spectrum. Differences between groups were inspected using a Student's t-test. DTI preprocessing steps included signal drift, Gibbs ringing, subject motion, eddy current, and echo planar imaging corrections, carried out using ExploreDTI[11]. DTI scans were co-registered with T_1 and DWS to obtain the FA and MD of water within the VOI (results pending).

Results: DWS data from n=20 patients with DMD and n=10 HC passed quality control (signal-to-noise ratio >6; full-width half-maximum of NAA <.030 ppm; Cramer-Rao Lower Bounds <6% for NAA, <10% for choline and creatine). See Table 1 for participant characteristics. Corresponding DTI scans were available of all participants, but n=2 contained artifacts leading to exclusion. This resulted in n=18 patients with DMD and n=10 HC. Mean white matter fraction (80%±8.9%), mutation status, study center, and age did not significantly correlate with the ADCs of the metabolites ($p>.05$), and were therefore not included as covariates. No significant differences in mean ADCs were found between patients with DMD and HC ($p>.05$; see Table 2). No significant differences were found between groups for tNAA/tCr and tCho/tCr ratios ($p>.05$; see Table 3). Water FA and MD within the VOI results are pending.

Discussion and conclusion: Results from this study indicate preserved diffusion of tNAA, tCho, and tCr with ADC values similar to the literature[12]. The ratios of tNAA/tCr and tCho/tCr in patients with DMD compared to HC are consistent with our previous results, indicating intact biochemical composition in patients with DMD[13]. If the reduced FA and increased MD is replicated within the VOI in this cohort, then the findings may suggest that the microstructural alterations represent changes in the extracellular space rather than cell-specific intracellular space in patients with DMD. In future studies, these findings could be related to the behavioral and cognitive deficits in this population, to further clarify and explain their origin.

[1] Banihani, R., Smile, S., Yoon, G., Dupuis, A., Mosleh, M., Snider, A., & McAdam, L. (2015). Cognitive and neurobehavioral profile in boys with Duchenne muscular dystrophy. *Journal of Child Neurology*, *30*(11), 1472-1482.

[2] Naidoo, M., & Anthony, K. (2020). Dystrophin Dp71 and the neuropathophysiology of Duchenne muscular dystrophy. *Molecular neurobiology*, *57*(3), 1748-1767.

[3] Doorenweerd, N., Mahfouz, A., van Putten, M., Kaliyaperumal, R., t'Hoen, P. A., Hendriksen, J. G., ... & Lelieveldt, B. P. (2017a). Timing and localization of human dystrophin isoform expression provide insights into the cognitive phenotype of Duchenne muscular dystrophy. *Scientific Reports*, *7*(1), 1-12.

[4] Doorenweerd, N. (2020a). Combining genetics, neuropsychology and neuroimaging to improve understanding of brain involvement in Duchenne muscular dystrophy-a narrative review. *Neuromuscular Disorders*, *30*(6), 437-442.

[5] Doorenweerd, N., Straathof, C. S., Dumas, E. M., Spitali, P., Ginjaar, I. B., Wokke, B. H., ... & Kan, H. E. (2014). Reduced cerebral gray matter and altered white matter in boys with Duchenne muscular dystrophy. *Annals of Neurology*, *76*(3), 403-411.

[6] Preethish-Kumar, V., Shah, A., Kumar, M., Ingalhalikar, M., Polavarapu, K., Afsar, M., ... & Saini, J. (2020). In vivo evaluation of white matter abnormalities in children with Duchenne muscular dystrophy using DTI. *American Journal of Neuroradiology*, *41*(7), 1271-1278.

[7] Fu, Y., Dong, Y., Zhang, C., Sun, Y., Zhang, S., Mu, X., ... & Wu, S. (2016). Diffusion tensor imaging study in Duchenne muscular dystrophy. *Annals of Translational Medicine*, *4*(6).

[8] Palombo, M., Shemesh, N., Ronen, I., & Valette, J. (2018). Insights into brain microstructure from in vivo DW-MRS. *Neuroimage*, *182*, 97-116.

[9] Provencher, S. W. (1993). Estimation of metabolite concentrations from localized in vivo proton NMR spectra. *Magnetic Resonance in Medicine*, *30*(6), 672-679.

[10] Tamsma, M., Ronen, I., Najac, C., Hollingsworth, K. G., Niks, E. H. Straub, V., Kan, H. E., Doorenweerd, N. (2020). *Diffusion weighted spectroscopy in Duchenne muscular dystrophy brain.* [Conference presentation abstract]. ISMRM Benelux Chapter meeting 2020, online.

[11] Leemans A, Jeurissen B, Sijbers J, Jones DK. "ExploreDTI: A graphical toolbox for processing, analyzing, and visualizing diffusion MR data". Proceedings of the 17th Scientific Meeting, International Society for Magnetic Resonance in Medicine, Honolulu, USA, p. 3537, 2009.

[12] Najac, C., Branzoli, F., Ronen, I., & Valette, J. (2016). Brain intracellular metabolites are freely diffusing along cell fibers in grey and white matter, as measured by diffusion-weighted MR spectroscopy in the human brain at 7 T. *Brain Structure and Function*, *221*(3), 1245-1254.

[13] Doorenweerd, N., Hooijmans, M., Schubert, S. A., Webb, A. G., Straathof, C. S., van Zwet, E. W., ... & Kan, H. E. (2017b). Proton magnetic resonance spectroscopy indicates preserved cerebral biochemical composition in Duchenne muscular dystrophy patients. *Journal of Neuromuscular Diseases*, *4*(1), 53-58.

Acknowledgments / Funding Information: This research is supported by the Duchenne Parent Project-NL and Muscular Dystrophy UK.

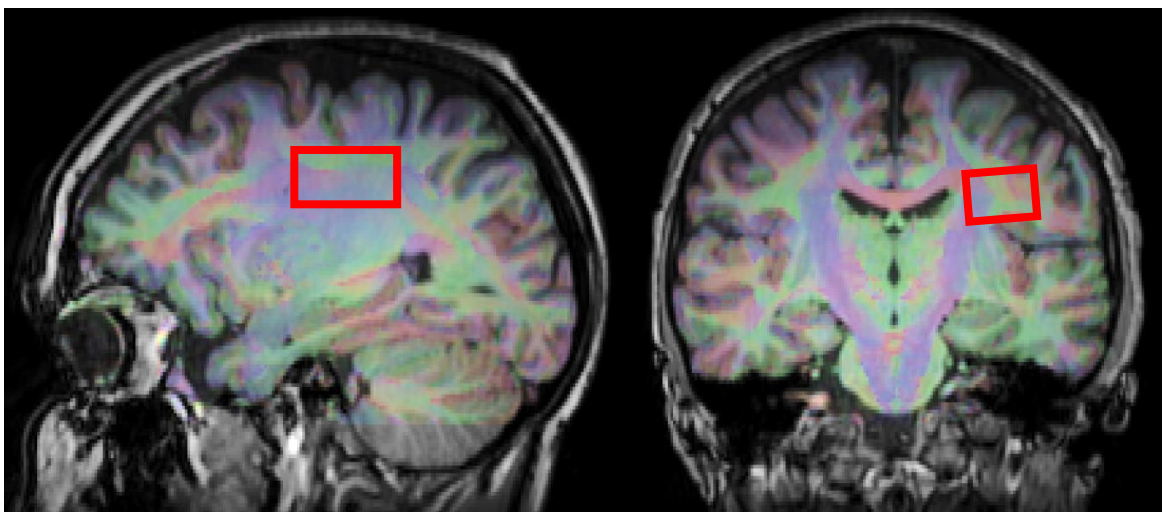

Figure 1. Representative illustration of a merged T_1, DTI FA map, and volume of interest (red box) of the DWS scan.

	DMD			Control		
	Total	NL	UK	**Total**	NL	UK
n =	**20**	9	11	**10**	6	4
Age mean, ± SD (years	**15.6 ± 4.6**	16.0 ± 4.3	15.3 ± 5.0	**16.3 ± 3.3**	16.2 ± 2.6	16.5 ± 4.6
Age, range (years)	**10 – 23**	10 – 22	10 – 23	**11 – 22**	11 – 18	11- 22
White matter fraction, ± SD (%)	**77.7 ± 9.5**	77.9 ± 10.7	77.6 ± 8.9	**80.1 ± 9.7**	77.4 ± 10.7	84.3 ± 7.4

Table 1. Participant characteristics of the DWS dataset (n=30). Independent samples t-tests were performed to compare patients versus controls and NL versus UK study centers for age and white matter fraction. No significant differences were found between groups.

	DMD patients *Mean (SD)* ($*10^{-4}$)	Controls *Mean (SD)* ($*10^{-4}$)
tNAA ADC *p = .57*	1.7 (.2)	1.6 (.2)
tCr ADC *p = .32*	1.7 (.2)	1.7 (.2)
tCho ADC *p = .17*	1.2 (.4)	1.4 (.2)

Table 2. Mean ADC and standard deviation for patients with DMD and healthy controls. Statistics were done using a general linear model.

	DMD patients *Mean (SD)*	Controls *Mean (SD)*
tNAA/tCr *p = .36*	2.5 (.2)	2.4 (.1)
tCho/tCr *p = .12*	.4 (.1)	0.3 (.03)

Table 3. Mean ratios and SD of tNAA/tCr and tCho/tCr for patients with DMD and healthy controls. Statistics were done using a Student's t-test.

3D MRI vs conventional ultrasound tumour measurements for treatment planning of eye tumours

L. Klaassen[1,2,3], M.G. Jaarsma-Coes[1,2], T.A. Ferreira[2], T.H.K. Vu[1], M. Marinkovic[1], G.P.M. Luyten[1], C.R.N. Rasch[3], J.W.M. Beenakker[1,2,3]

[1] Leiden University Medical Center, Department of Ophthalmology, Leiden, Netherlands
[2] Leiden University Medical Center, Department of Radiology, Leiden, Netherlands
[3] Leiden University Medical Center, Department of Radiation Oncology, Leiden, Netherlands

Synopsis: The aim of this study was to compare ultrasound and MRI dimension measurements for eye tumours and to determine the most suitable measurement modality. MRI and ultrasound yield similar prominence measurements (median absolute difference 0.3mm) when tumour extent is visible on both modalities. However, in anteriorly located tumours, MRI measurements are more accurate, and using US for these tumours might lead to an underestimation of tumour diameter. MRI provided insight in 3D tumour geometry, even when tumour extent was difficult to visualize on US, enabling more accurate therapy planning and selection for uveal melanoma patients.

Introduction: Uveal melanoma (UM) is the most frequently occurring malignant primary eye tumour, with approximately 6 cases per million person-years[1]. Ocular MRI, enabling 3D tumour imaging and providing a better soft tissue contrast than conventional 2D ultrasound (US), is increasingly used for the diagnosis, therapy planning and follow-up of UM[2-4]. Tumour prominence (thickness) and largest basal diameter (LBD) are the primary determinants for the brachytherapy applicator size and application time and are used to define the 3D clinical target volume in proton beam therapy. Within this study, we aim to compare US and MRI dimension measurements for UM and determine the most suitable measurement modality.

Methods: Data of 25 UM patients with a wide range in size and location were analysed retrospectively after approval of the local ethics committee. Patients were scanned at 3 Tesla MRI according to the protocol of Ferreira[5]. The tumour was semi-automatically delineated on the 3D fat-suppressed contrast-enhanced T1-weighted images (T1gd: acquisition voxel size 0.8x0.8x0.8mm^3, TE/TR 26/400 ms, scan time 02:07 min) and on the 3D turbo-spin echo T2-weighted images (acquisition voxel size 0.8x0.8x0.8mm^3, TE/TR 330/2500 ms, scan time 02:57 min) in MeVisLab (MeVis Medical Solutions, Bremen, Germany). Tumours were delineated by an ophthalmic MRI expert with 7 years of experience.

Prominence and largest basal diameter (LBD) were computed automatically from the MRI contours. The measurements from the T1gd contours were compared to the clinical US measurements, as the contrast between tumour and surrounding structures is largest on this sequence.

Differences between T1gd and US measurements were related to tumour location in the anteroposterior direction. Tumours that were not completely visible on US or where the extent of flat tumour components was difficult to assess on MRI were assessed separately. We furthermore compared the prominence and LBD between T1gd and T2-weighted scans.

Results: For 7/25 patients, the prominence and/or LBD measurement did not fit into the US FOV or the tumour top was not visible on US. All these tumours were located in the anterior 50% of the eye. In 3 of the 4 patients with an US prominence <4 mm, tumour extent was difficult to assess on MRI (Fig 1).

When tumour extent was visible on both imaging modalities, median absolute differences were 0.3 mm (range 0.0-1.3 mm) for prominence and 1.1 mm (range 0.1-2.8 mm) for LBD, respectively (Fig 2). For the LBD, 80% of measurements were more than 0.5 mm larger on MRI, possibly caused by difficulty in manually finding the optimal measurement plane with US, and choroidal enhancement at the tumour edge that was considered tumour on T1gd but not visible on US.

For patients for whom the tumour extent was difficult to assess on one imaging modality or both, the median absolute difference for the prominence and LBD were 0.7 mm (range 0.5-1.6 mm) and 1.4 mm (range 0.1-7.6 mm). Here, the larger differences in tumour prominence could be caused by an oblique cut through the tumour with US, due to tumour location and tissues surrounding the eye limiting an optimal probe placement. Furthermore, for patients with flat tumours or tumours with flat extensions, differences may be caused by difficulty assessing the extent of the tumour on both MRI and US.

For the T1gd-T2 comparison, the median absolute difference for the prominence was 0.3 mm. For 19/25 patients, the difference between T1gd and T2 prominence was <0.5mm. For the LBD, the median absolute difference was 1.6 mm, with T1gd>T2 for 23/25 patients.

Discussion: MRI and US yield similar prominence measurements (median absolute difference 0.3 mm at an acquisition voxel size of (0.8mm)^3 and an ultrasound intra-observer variability of 0.6 mm [5]) when tumour extent is visible on both modalities. However, in anteriorly located tumours, MRI measurements are more accurate, and using US for these tumours might lead to an underestimation of tumour diameter. In this study, choroidal enhancement at the tumour edge is considered tumour, since no histopathological evidence is known that suggests otherwise. MRI gave insight in 3D tumour geometry, even when tumour extent was difficult to visualize on US, potentially enabling more accurate therapy planning and selection for uveal melanoma patients.

The extent of flat tumours can be difficult to assess on MRI, although, the distinction between tumour and healthy tissue may not be evident on US either. For these tumours, tumour measurements may be supported by fundoscopic imaging.

Furthermore, this study shows that differences exist between measurements performed on T1gd and T2-weighted scans. Without histopathological confirmation of the underlying cause of choroidal enhancement, it is difficult to conclude which measurement is correct. For now, we advise to perform measurements on T1gd to ensure no tumour tissue is missed.

References:

1. Jager MJ, Shields CL, Cebulla CM et al. Uveal melanoma. Nat Rev Dis Primers. 2020;6(1):24.
2. Ferreira TA, Fonk LG, Jaarsma-Coes MG et al. (2019) MRI of uveal melanoma. Cancers (Basel) 11:1–20.
3. Niendorf T, Beenakker JWM, Langner S et al. (2021) Ophthalmic Magnetic Resonance Imaging: Where Are We (Heading To)? Curr Eye Res. doi: 10.1080/02713683.2021.1874021
4. Aziz S, Taylor A, McConnachie A et al. (2009) Proton beam radiotherapy in the management of uveal melanoma: Clinical experience in Scotland. Clin Ophthalmol 3:49–55.
5. Ferreira TA, Jaarma-Coes MG, Marinkovic M et al. (2021) MR imaging characteristics of uveal melanoma with histopathological validation. Neuroradiology. doi: 10.1007/s00234-021-02825-5
6. Haritoglou C, Neubauer AS, Herzum H et al. (2002) Interobserver and intraobserver variability of measurements of uveal melanomas using standardised echography. Br J Ophthalmol 86:1390 LP – 1394.

Acknowledgments / Funding Information: Research support by Philips

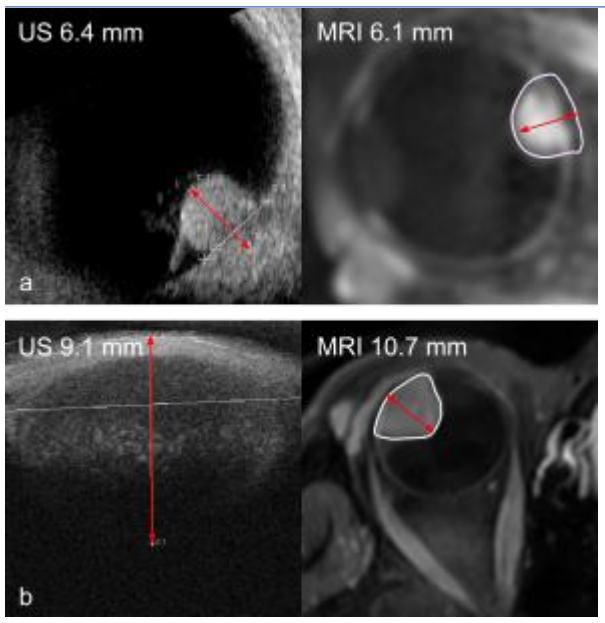

Figure 1: Examples of prominence measurements on US and MRI. a: Measurements fit into field of view and extent is visible. b: Tumour top is not visible on US.

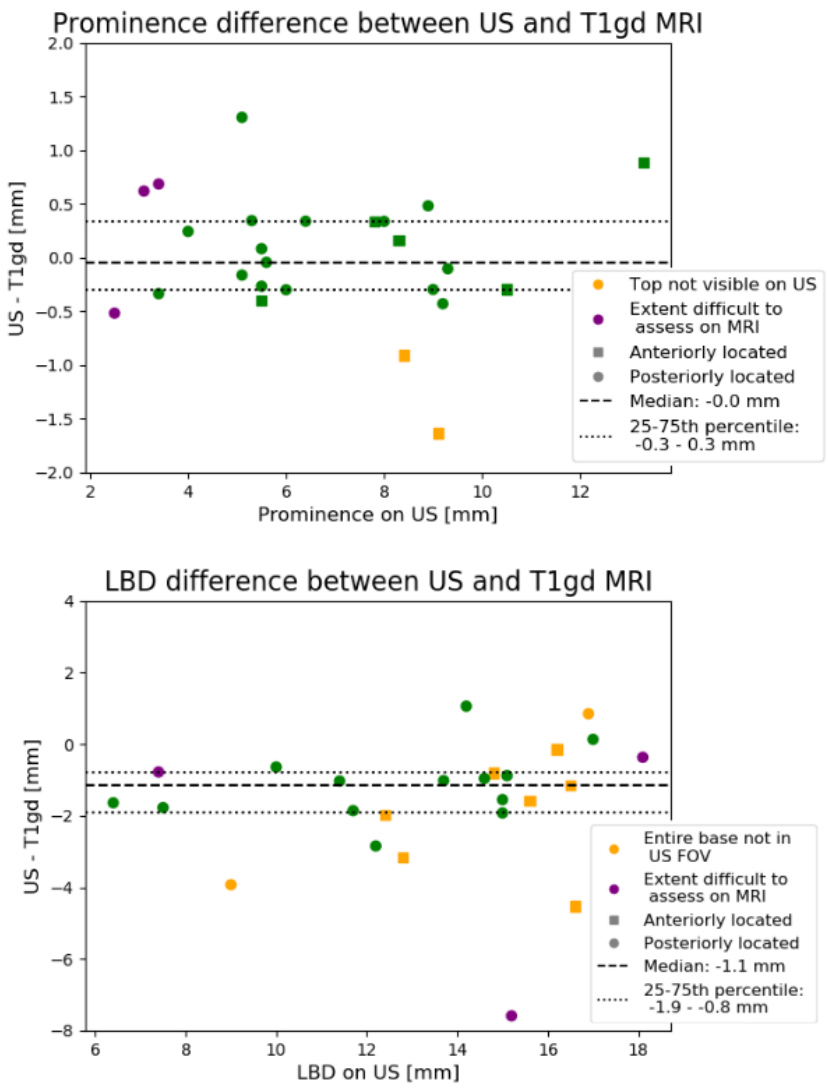

Figure 2. Difference between MRI and US measurements for prominence and LBD related to measurement on US and to location in AP direction (anterior: tumour center of mass in anterior 50% of the eye, posterior: tumour center of mass in posterior 50% of the eye).

Personalized MRI contrast for treatment guidance on an MRI-linac in patients with liver metastases

R.J.M. Navest[1], V.W.J. van Pelt[1], T.N. van de Lindt[1], T. Janssen[1], M.E. Nowee[1], J.-J. Sonke[1], U.A. van der Heide[1], P.J. van Houdt[1]
[1]Department Radiation Oncology, The Netherlands Cancer Institute, Amsterdam, The Netherlands

Synopsis:

Lesion visibility is unsatisfactory in approximately 30% of patients with liver metastases. This causes 4D-MRI guided treatment to become more challenging. The heterogeneity of T1 and T2 values was investigated in 23 patients by T1 and T2 mapping. Based on individual T1 and T2 values of the metastasis and surrounding liver tissue, personalized 4D-MRI sequence settings were calculated. These personalized 4D-MRI sequences improved the contrast between a metastasis and surrounding liver tissue in patients prospectively.

Purpose:

MRI-guided stereotactic body radiation therapy (SBRT) is an upcoming local treatment for liver metastases. The visibility of liver metastases during MRI-guided SBRT, however, is unsatisfactory in approximately 30% of patients[1]. Consequently, set-up correction and motion monitoring during treatment are challenging. We therefore propose to personalize the 4D-MRI sequence settings based on patient specific T1 and T2 values of the lesion(s) and surrounding liver tissue.

Methods:

23 patients with up to 3 liver metastases received 4D-MRI guided liver SBRT on a 1.5T MRI-linac. A 4D T2 TSE or 4D balanced GRE was used for set-up correction and motion monitoring. Additionally, before the first treatment fraction a sagittal T1 map (variable flip angle series) and transversal T2 map (k-t-T2 technique) were acquired for all patients during free breathing.

The mean and standard deviation of T1 and T2 were calculated for regions-of-interest (ROIs) within the metastases and healthy liver tissue (excluding large vessels). These T1 and T2 values were used to determine the MRI sequence settings that yield optimal contrast between the lesion and surrounding liver tissue, through Bloch simulations. Contrast was defined as the relative difference of the mean MR signal intensity of the lesion ROI with respect to the liver ROI (i.e. $C = (SI_{lesion} - SI_{liver}) / SI_{liver}$).

Optimal values of the echo time, refocusing angle and parallel imaging (PI) factor for the 4D T2 TSE and number of startup echoes, flip-angle, PI factor and partial Fourier factor for the 4D balanced GRE were calculated. The optimal 4D-MRI sequences were tested prospectively on a subset of four patients at the end of a treatment fraction. To compare the contrast between the clinically used and optimized 4D-MRI sequences, the absolute ratio between them was calculated (i.e. $|C_{opt} / C_{clin}|$).

Results & Discussion:

The measured T1 and T2 values are shown in Fig. 1 for all metastases. The median (range) T1 value of the liver and lesions across all patients were 659 (450-892) and 1105 (578-2466) ms, respectively. T2 values of 58 (40-82) ms for liver and 85 (46-242) ms for metastases were found.

The absolute contrast ratio, and thus lesion visibility, improved for all patients. A minimum and maximum absolute contrast ratio of 1.1 and 4.4 for T2 TSE and 1.02 and 5.9 balanced GRE were found. Fig. 2 shows the lesion visibility improvement of the optimized compared to the clinically used 4D-MR images for the prospective test. Note brighter rim around the lesion in patient 2 and heterogeneous MR signal intensity within the lesion in patient 3 and 4. This makes delineation and contrast estimation more difficult.

Conclusion:

Based on the measured T1 and T2 of metastases and surrounding liver tissue, optimal MRI sequence settings could be calculated. Personalized 4D-MRI sequence settings improved the contrast between a metastasis and surrounding liver tissue in patients prospectively.

References:

1. Weykamp et al. Magnetic Resonance-Guided Stereotactic Body Radiotherapy of Liver Tumors: Initial Clinical Experience and Patient-Reported Outcomes. Front. Oncol. 2021;11:2103

Acknowledgments / Funding Information: Continue on this line

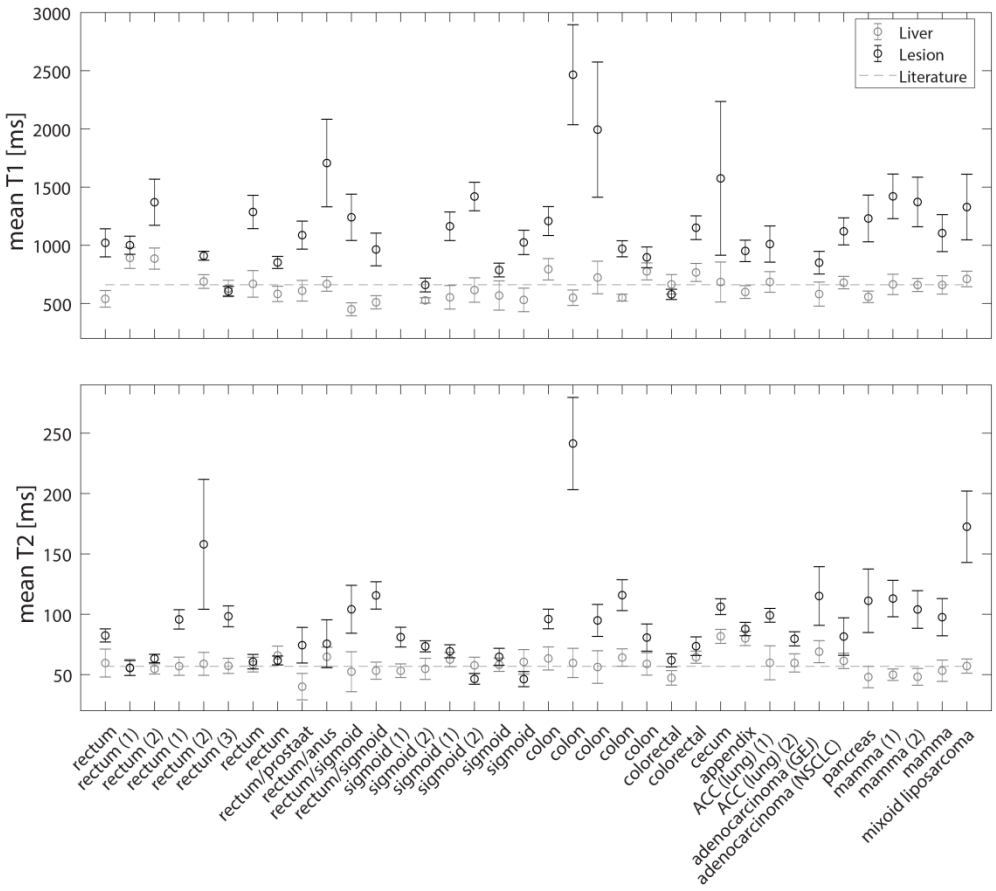

Fig. 1: The T1 (upper) and T2 (lower) values measured in the metastases (black) and surrounding liver tissue (gray). The error bars indicate the standard deviation. The literature value of the liver is indicated by the dashed gray line. The primary tumor where the metastasis originated from is reported on the x-axis. The number between brackets behind de primary tumor indicates it is one of multiple metastases in the same patient

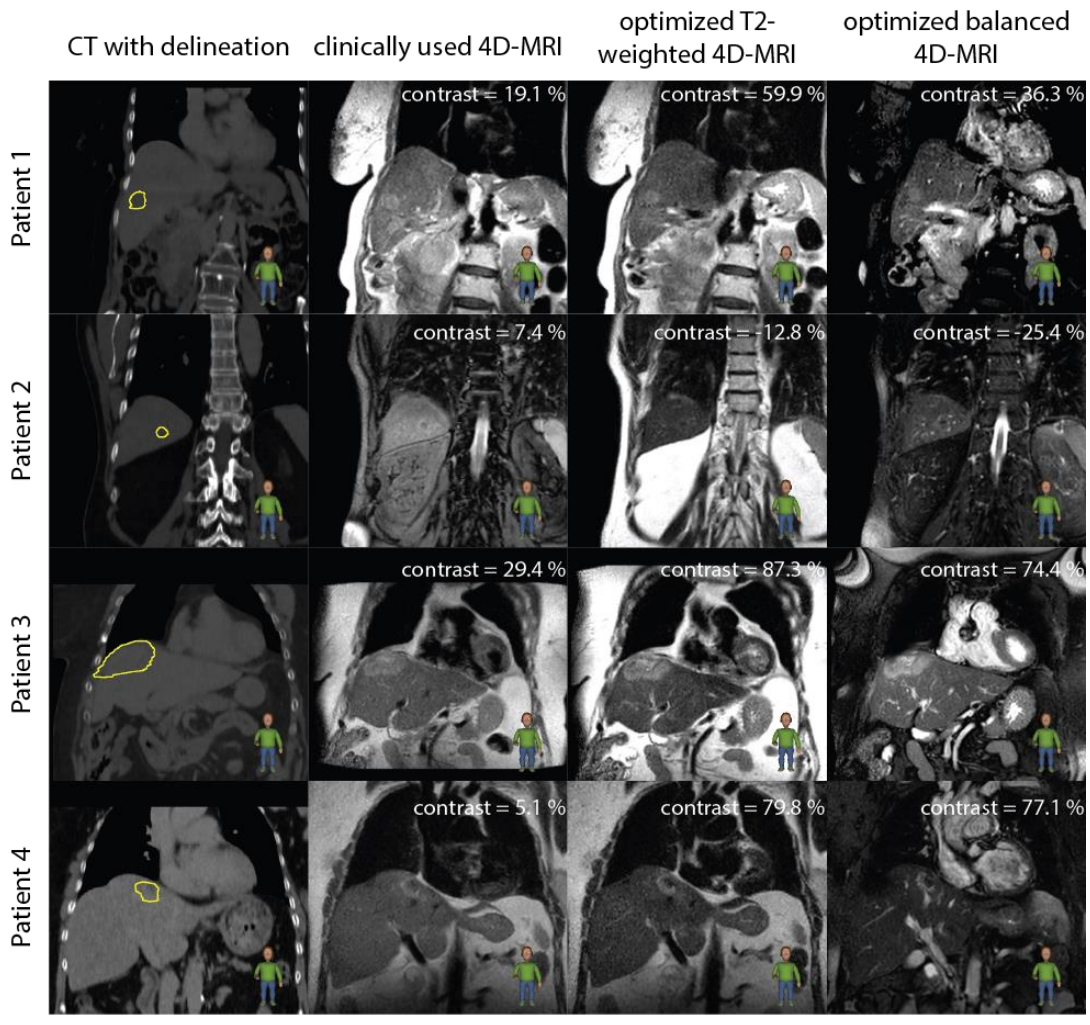

Fig. 2: In each row from left to right, the CT with delineation, clinically used 4D-MRI (either T2 or balanced contrast), optimized T2-weighted 4D-MRI and optimized balanced 4D-MRI is shown for one of the prospective patient tests. The measured contrast between the metastasis and surrounding liver tisue is reported at the top right of each MR scan.

Open Science Initiative for Perfusion Imaging (OSIPI): A community-led, open-source code library for analysis of DCE/DSC-MRI

P.J. van Houdt[1], S. Ragunathan[2], M. Berks[3], Z. Ahmed[4], L. Kershaw[5], O. Gurney-Champion[6], S. Tadimalla[7], J.F. Kallehauge[8], J. Arvidsson[9], B. Dickie[10], S. Lévy[11], L. Bell[12], S. Sourbron[13], M.J. Thrippleton[5]

[1]the Netherlands Cancer Institute, Amsterdam, the Netherlands; [2] Barrow Neurological Institute, Phoenix, United States Department, Institution, City, Country; [3]University of Manchester, Manchester, UK; [4]Mayo Clinic, Rochester, USA; [5]University of Edinburgh, Edinburgh, United Kingdom; [6]Amsterdam UMC, Amsterdam, Netherlands; [7]The University of Sydney, Sydney, Australia; [8]Aarhus University, Aarhus, Denmark; [9]The University of Gothenburg, Gothenburg, Sweden; [10]The University of Manchester, Manchester Academic Health Science Centre, Manchester, UK;[11]University Hospital Erlangen, Erlangen, Germany; [12]Genentech, Inc, South San Francisco, USA; [13]University of Sheffield, Sheffield, UK

Synopsis: A lack of validated, open-source code reduces the reliability of perfusion MRI, resulting in duplicate development. To address this problem, the Open Science Initiative for Perfusion Imaging (OSIPI) established a taskforce to collect, validate and harmonise such code. To date, 74 code contributions have been collected, with 14 of these tested. Source code and tests are published in an open-access repository. The OSIPI DCE/DSC-MRI code collection constitutes a valuable resource for researchers, and will ultimately be developed into a standardised, community-driven open-source code library.

Introduction

Perfusion MRI results show substantial variability dependent on the processing software used [1,2]. Furthermore, researchers expend substantial effort in writing bespoke code for their analyses because existing solutions are unavailable, unvalidated, difficult to use or provide insufficient functionality. Taskforce 2.3 of the Open Science Initiative for Perfusion Imaging (OSIPI) was therefore established to *collect*, *validate* and *harmonise* open-source code snippets for processing dynamic contrast-enhanced (DCE-) and dynamic susceptibility contrast (DSC-) MRI, as a resource for researchers and developers. Here we present initial results of code collection and validation.

Methods

A public call for code was made via the ISMRM Perfusion Study Group in February 2021, and contributions were published in a public repository [3]. To provide greatest utility for the most users, code to perform the most common steps of DCE- and DSC-MRI processing pipelines was prioritised. Initial code collection was restricted to the Python language, since it is open-source, widely used and has many high quality scientific computing libraries.

To validate code contributions, automated scientific testing was implemented within the online repository using the *Pytest* package and the Github *Actions* feature. The aim is to verify that code outputs match previously defined or measured reference values to within an acceptable tolerance defined by the taskforce, and to document the outputs of each contribution. Test data was taken from digital reference objects (DROs) and clinical scans. Reference values for in-vivo test data were obtained using separate, trusted software; for DRO data, reference values supplied with the DRO were used. Code for variable flip angle T_1 mapping was validated using a Quantitative Imaging Biomarker Alliance DRO (version 3 [4]), and in-vivo brain [5] and prostate [6] scans. Code contributions implementing the extended Tofts pharmacokinetic model were validated using data from an anthropomorphic DRO [7].

Results

As of 1 November 2021, the repository hosts 74 distinct units of perfusion functionality contributed by 11 individuals and groups. This includes code implementing all core aspects of DCE- and DSC-MRI processing, for example T_1 mapping, concentration estimation and perfusion parameter derivation, as shown in Table 1. Details of all collected code can be viewed in the online repository [3].

Validation is in-progress across all core areas of functionality (Table 1). Preliminary results for seven T_1 mapping implementations are shown in Figure 1. All results matched the reference values to within the tolerance, and multiple implementations of equivalent algorithms generated similar outputs. For the extended Tofts pharmacokinetic model, five different code contributions were validated. The resulting estimates of K^{trans}, v_e and v_P were within the tolerances (Figure 2).

Discussion

DSC-MRI functionality is currently underrepresented in the repository; we therefore encourage new code contributions in this area. We also aim to collect code implementing additional aspects of perfusion processing, such as model selection, multiple pulse sequences and water exchange effects. Where Python code is unavailable, the taskforce may decide to translate or provide wrappers to contributions written in other languages such as Matlab and C++.

Contributions tested thus far yielded results in good agreement with reference values. Testing is currently being expanded to cover broader parameter ranges, different pharmacokinetic models and other processing steps. A challenge of the pass-fail testing approach is that tolerances are subjective and difficult to determine, and binary test outputs provide limited useful information to potential users. We are therefore exploring complementary approaches for automated documentation and visualisation of code outputs.

Finally, the taskforce aims to enhance the value of the repository by integrating contributions into the *OSIPI Perfusion Analysis Library*, which will be maintained by the perfusion community to facilitate standardised processing and reporting of perfusion MRI.

Conclusion

The OSIPI Taskforce 2.3 code collection constitutes a valuable and growing resource to benefit researchers using contrast-based perfusion imaging. Our approach, which is based on open-source tools and free web-based services, may be a valid model for open science initiatives in other MRI subfields.

References

1. Beuzit et al., Dynamic contrast-enhanced MRI: Study of inter-software accuracy and reproducibility using simulated and clinical data. JMRI 2016; 43:1288.

2. Kudo et al., Accuracy and Reliability Assessment of CT and MR Perfusion Analysis Software Using a Digital Phantom. Radiology 2013; 267:201

3. https://github.com/OSIPI/DCE-DSC-MRI_CodeCollection/wiki

4. Daniel Barboriak, https://qidw.rsna.org/#collection/594810551cac0a4ec8ffe574

5. Clancy et al., Rationale and design of a longitudinal study of cerebral small vessel diseases, clinical and imaging outcomes in patients presenting with mild ischaemic stroke: Mild Stroke Study 3. Eur Stroke J 2020; 6:81.

6. Klawer et al., Improved repeatability of dynamic contrast-enhanced MRI using the complex MRI signal to derive arterial input functions: a test-retest study in prostate cancer patients. MRM 2019; 81:3358

7. Bosca and Jackson, Creating an anthropomorphic digital MR phantom—an extensible tool for comparing and evaluating quantitative imaging algorithms. Phys. Med. Biol. 2016; 61:974

8. https://github.com/OSIPI/OSIPI-Perfusion-Analysis-Library/blob/develop/docs/OPAL_design_specification.md

Acknowledgments / Funding Information: We acknowledge the OSIPI membership and leadership for their suggestions and feedback, Ole Gunnar Johansen (University of Oslo) and Matthew Orton (The Royal Marsden NHS Foundation Trust) for contributing additional code and Joanna M. Wardlaw (University of Edinburgh) for providing test data.

Table 1: Core functionality initially targeted by the taskforce, showing the number of implementations collected and tested to date. AATH: adiabatic approximation to the tissue homogeneity, C: concentration, CBF: cerebral blood flow, CBV: cerebral blood volume, MTT: mean transit time, DESPOT1-HIFI: driven equilibrium single pulse observation of T1 with High-speed Incorporation of RF Field Inhomogeneities, NOVIFAST: NOn-linear VarIable Flip Angle data baSed T1 estimator, 2CUM: two-compartment uptake model, 2CXM: two-compartment exchange model.

Technique	Functionality	Available methods	Collected	Tested
DCE-MRI	T_1 mapping	variable flip angle (linear, non-linear, NOVIFAST), DESPOT1-HIFI	9	6
	C estimation	signal-to-concentration (spoiled gradient echo)	6	4
	vascular input functions	population functions (Georgiou, McGrath, Parker, Wong), patient-specific, parametrized	12	0
	pharmacokinetic models	Tofts, extended Tofts, Patlak, 2CXM, 2CUM, AATH, steady-state, dual-inlet; forward model, fitting of concentration and signal	29	4
DSC-MRI	C estimation	single- and dual- gradient echo	1	0
	vascular input function	automated AIF selection	1	0
	leakage correction	Boxerman–Schmainda–Weiskoff	2	0
	parameter derivation	deconvolution; CBV, CBF and MTT estimation	2	0

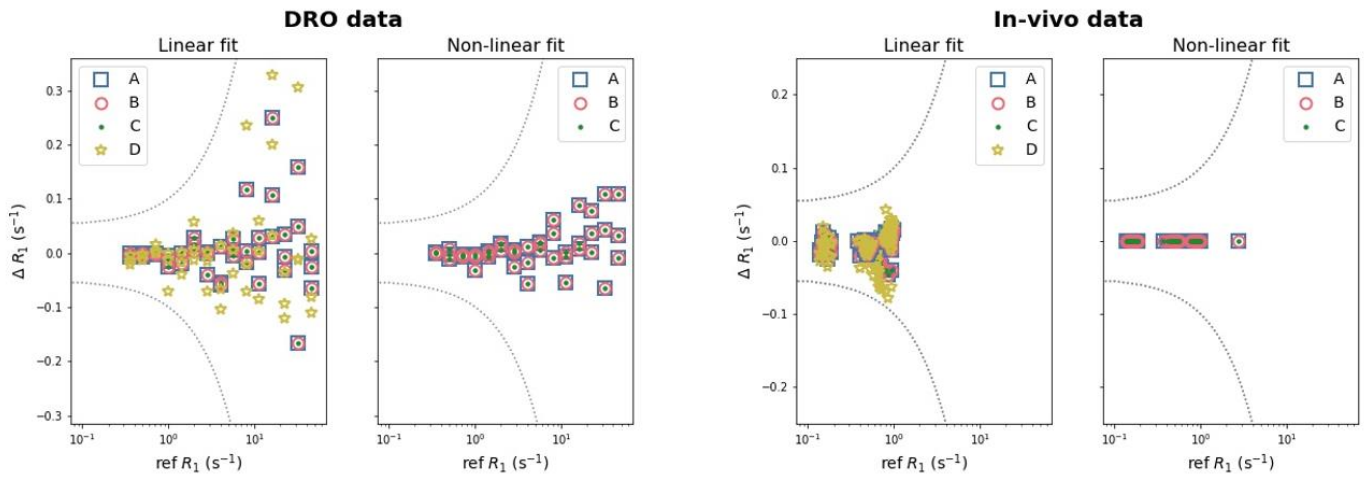

Figure 1: Preliminary validation results for T_1-fitting algorithms, showing deviation from reference R_1 values for DRO and in-vivo voxels for patients with prostate cancer (healthy prostate and tumour voxels) and small vessel disease (white matter, gray matter and cerebrospinal fluid.

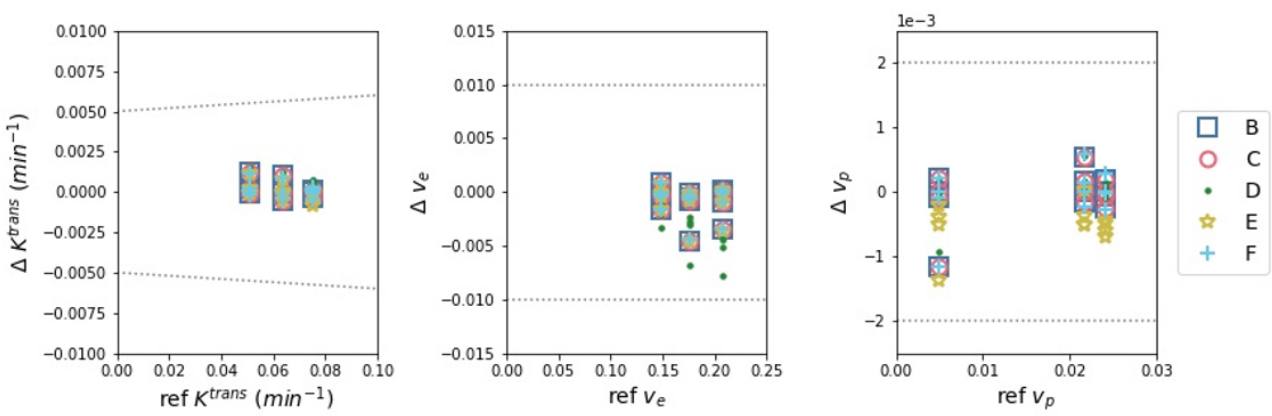

Figure 2: Preliminary validation results for implementations of the extended Tofts model. Data points indicate the deviations from reference values for DRO voxels representing normal tissues and tumour. Markers B-F correspond to different code contributions. Dashed lines indicate the tolerances (K^{trans}: 0.005 min^{-1} absolute + 1% relative; v_e: 0.05 absolute; v_p: 0.002 absolute). DRO signals were converted to concentration using code by D.S. Smith (https://github.com/welcheb/pydcemri).

Multi-level fiber tractography evaluation using transcranial magnetic stimulation (TMS) mapping

Andrey Zhylka[1], Josien Pluim[1], Florian Kofler[2,3,4], Ahmed Radwan[5,6], Alberto De Luca[7,8], Axel Schroeder[9], Benedikt Wiestler[2,4], Jan S. Kirschke[2,10], Bjoern Menze[3,11], Stefan Sunaert[5,6,12] Alexander Leemans[7], Sandro M. Krieg[9,13], and Nico Sollmann[2,13,14]

Biomedical Engineering, Eindhoven University of Technology, Eindhoven, Netherlands, Diagnostic and Interventional Neuroradiology, School of Medicine, Klinikum rechts der Isar, Munich, Germany, [3]Informatics, TU Munich, Munich, Germany, [4]TranslaTUM - Central Institute for Translational Cancer Research, TU Munich, Munich, Germany, [5]Department of Imaging and Pathology, Translational MRI, KU Leuven, Leuven, Belgium, [6]Neuroscience, Leuven Brain Institute (LBI), Leuven, Belgium, [7]Image Sciences Institute, UMC Utrecht, Utrecht, Netherlands, [8]Neurology, UMC Utrecht Brain Center, Utrecht, Netherlands, [9]Neurosurgery, School of Medicine, Klinikum rechts der Isar, Munich, Germany, [10]TUM-Neuroimaging Center, Klinikum rechts der Isar, Munich, Germany, [11]Quantitative Biomedicine, University of Zurich, Zurich, Switzerland, [12]Radiology, UZ Leuven, Leuven, Belgium, [13]TUM-Neuroimaging Center, Klinikum rechts der Isar, Munich, Germany, [14]Diagnostic and Interventional Radiology, University Hospital Ulm, Ulm, Germany

Synopsis: Navigated transcranial magnetic stimulation (nTMS) motor mapping allows locating function in the individual patient pre-operatively and, to a certain extent, decreases the false-positive rate for fiber tractography. However, the false-negative rate is still high. In this work we evaluate novel multi-level fiber tractography (MLFT) along with conventional deterministic algorithms in patients with motor-eloquent high-grade glioma, combined with nTMS mapping-based region of interest (ROI) placement. The results were compared based on the coverage of nTMS motor maps, revealing reconstruction of the corticospinal tract (CST) with significantly higher volume and better coverage of the eloquent motor cortex for MLFT.

Purpose: Despite diffusion MRI (dMRI) offers an in-vivo insight into neuroanatomy by performing white-matter fiber tractography[1]. However, conventional approaches are known to have limitations and may produce false-positive and false-negative pathways[2]. Furthermore, placement of regions of interest (ROIs) for subsequent tractography can be challenging. This holds in particular for the common case of patients with functionally eloquent brain tumors, (due to altered anatomo-functional architecture and functional reallocation[3,4,5]). nTMS allows locating function in the individual patient pre-operatively and enables ROI definition based on the individual functional motor map[6,7]. Combined with fiber tractography, nTMS can provide valuable input for surgery planning in patients with motor-eloquent lesions[6,7]. However, the false-negative rate is still high in tractography. In this work we evaluate recently proposed MLFT[8] along with deterministic diffusion tensor imaging (DTI)-based as well as constrained spherical deconvolution (CSD)-based tractography in patients with motor-eloquent high-grade glioma. Pre-operative nTMS motor mapping was used for ROI definition. We evaluated the aforementioned algorithms based on their coverage of the nTMS motor maps and explored the effect of an angular-deviation threshold (ADT) as well as fractional anisotropy threshold (FAT).

Methods: We used pre-operative data of 31 adult patients diagnosed with high-grade glioma in motor-eloquent location. All patients underwent functional mapping of upper and lower extremity motor function using nTMS (Nexstim eXimia NBS system, Nexstim Plc.), providing an individual motor map based on motor-evoked potentials elicited by neuronavigated single-pulse stimulation[6,7]. 3-Tesla dMRI (Achieve dStream, Philips Healthcare) was acquired with one volume at b=0s/mm^2 and 32 volumes at b=1000s/mm^2 with uniformly distributed gradient directions and a voxel size of 2 mm isotropic. Brain parcellation was performed using FreeSurfer[9], preceded by lesion segmentation and lesion filling[10,11,12]. The dMRI data were corrected for motion and eddy currents, and co-registered to the corresponding T1-weighted images using ExploreDTI[13]. The fiber orientation distributions (FODs) were estimated using recursive calibration of the response function[14]. A spherical harmonics order of $L_{max} = 6$ was used[15]. We performed tractography using MLFT, deterministic CSD-based, and deterministic DTI-based algorithms. Three ADTs (20°/45°/60°) and a FOD peak threshold of 0.08 (for MLFT and CSD-based tractography) was used. For DTI-based tractography, three FATs (25%/50%/75% FAT) were considered, referring to the minimum threshold enabling reconstructing a minimum fiber course (i.e., 100% FAT)[16]. The seed region was defined as a cross-section at the anterior pontine level of the brain stem[17] . The target region for tractography was obtained by enlarging each motor-positive nTMS point by a hull of 2 mm radius[6,7,18]. The ratio of connected spots was counted per each algorithm and parameter configuration, providing the coverage of the nTMS motor map, where connected spots are motor-positive nTMS points (with 2-mm hulls) visited by at least one pathway of a reconstructed bundle. The significance of the parameter changes was estimated using Wilcoxon tests. In addition, we calculated the volumes of the reconstructed CST.

Results: Compared to DTI- and CSD-based algorithms, MLFT was capable of reconstructing the CST with higher volumes than the DTI- and CSD-based algorithms, (Figure 1). Moreover, coverage of the nTMS motor map (i.e., motor-positive nTMS spots with their hull that are visited by reconstructed fibers) was highest for MLFT, with statistically significant differences compared with DTI- and CSD-based algorithms (in all comparisons using Wilcoxon tests with alternative hypothesis that MLFT-produced coverage is lower: $p<0.01$ each). The CSD-based algorithm showed performance comparable to the DTI-based algorithm at the lowest ADT, while the nTMS motor map coverage achieved with DTI-based tractography primarily varied with the change in FAT. Additionally, the change in ADT showed to be statistically significant in almost all instances (except for 75% FAT for DTI-based reconstruction).

Discussion and Conclusion: The newly proposed MLFT provides reconstruction of the CST in patients with motor-eloquent high-grade glioma with larger bundle volume and coverage of the nTMS motor map than deterministic DTI- and CSD-based tractography. It was also shown to consistently gain the coverage by increasing the ADTs**Error! Reference source not found.**, similar to CSD-based tractography. DTI-based tractography, however, did not show practically significant changes with ADT alteration, despite the results at different ADTs being statistically significant in most cases, which may be an illustration of the model's inability to resolve complex fiber configurations[19]. Given that DTI is widely applied in the distinct pre-operative setup of patients with functionally eloquent tumors but has well-known shortcomings[20,21], MLFT may provide a more detailed and complete reconstruction of the CST compared to DTI-based fiber tractography. Furthermore, the results show the importance of the parameter setting choice for clinical application. Given that MLFT is capable of estimating high-angular fiber distributions, changing ADTs appears to be promising and should be tested and verified by intraoperative direct electrical stimulation as the next step. In case of DTI, experiments with FAT appear to be more beneficial for the improvement of the extent of reconstruction. In conclusion, MLFT could improve fiber tracking of the CST in patients with brain tumors beyond DTI, but attention has to be paid to the distinct parameter settings to obtain optimal results.

References:

1. Jeurissen B., Descoteaux M., Mori S., Leemans A. Diffusion MRI tractography of the brain. *NMR Biomed*, 32(4):e3785 (2019)
2. Maier-Hein KH, Neher PF, Houde JC, Cote MA, Garyfallidis E, Zhong J, et al. The challenge of mapping the human connectome based on diffusion tractography. *Nat Commun* 8, 1349 (2017)
3. Gibb W.R., Kong N.W., Tate M.C. Direct Evidence of Plasticity within Human Primary Motor and Somatosensory Cortices of Patients with Glioblastoma. *Neural Plast* 2020:8893708 (2020)
4. Bulubas L., Sardesh N., Traut T., Findlay A., Mizuiri D., Honma S.M., Krieg S.M., Berger M.S., Nagarajan S.S., Tarapore P.E. Motor Cortical Network Plasticity in Patients with Recurrent Brain Tumors. *Front Hum Neurosc*, 14:118 (2020)
5. Conway N., Wildschuetz N., Moser T., Bulubas L., Sollmann N., Tanigawa N., Meyer B., Krieg S.M. Cortical plasticity of motor-eloquent areas measured by navigated transcranial magnetic stimulation in patients with glioma. *J Neurosurgery*, 127(5):981-991 (2017)
6. Sollmann N, Krieg SM, Säisänen L, Julkunen P. Mapping of Motor Function with Neuronavigated Transcranial Magnetic Stimulation: A Review on Clinical Application in Brain Tumors and Methods for Ensuring Feasible Accuracy. *Brain Sci*, 11(7):897 (2021)
7. Sollmann N, Meyer B., Krieg S. Implementing Functional Preoperative Mapping in the Clinical Routine of a Neurosurgical Department: Technical Note. *World Neurosurg*, 103:94-105 (2017)
8. Zhylka A., Leemans A., Pluim J., De Luca A. Anatomically informed multi-level fiber tractography for improved sensitivity of white matter bundle reconstruction in diffusion MRI. ISMRM (2020), p0855
9. Fischl B. FreeSurfer. *NeuroImage*, 62(2):774-81 (2012)
10. Radwan AM, Emsell L, Blommaert J, Zhylka A, Kovacs S, Theys T, et al. Virtual brain grafting: Enabling whole brain parcellation in the presence of large lesions. *NeuroImage*, 229:117731 (2021)
11. Kofler F, Berger C, Waldmannstetter D, Lipkova J, Ezhov I, Tetteh G, et al. BraTS Toolkit: Translating BraTS Brain Tumor Segmentation Algorithms Into Clinical and Scientific Practice. *Front Neurosci*, 14:125 (2020)
12. Menze BH, Jakab A, Bauer S, Kalpathy-Cramer J, Farahani K, Kirby J, et al. The Multimodal Brain Tumor Image Segmentation Benchmark (BRATS). *IEEE Trans Med Imaging*, 34(10):1993-2024 (2015)
13. Leemans, A., Jeurissen, B., Sijbers, J., Jones, D. K. ExploreDTI: a graphical toolbox for processing, analyzing, and visualizing diffusion MR data. *ISMRM;* 3537 (2009).
14. Tax CM, Jeurissen B, Vos SB, Viergever MA, Leemans A. Recursive calibration of the fiber response function for spherical deconvolution of diffusion MRI data. *NeuroImage*, 86:67-80 (2014)
15. Tournier JD, Calamante F, Gadian DG, Connelly A. Direct estimation of the fiber orientation density function from diffusion-weighted MRI data using spherical deconvolution. *NeuroImage*, 23(3):1176-85 (2004)
16. Frey D, Strack V, Wiener E, Jussen D, Vajkoczy P, Picht T. A new approach for corticospinal tract reconstruction based on navigated transcranial stimulation and standardized fractional anisotropy values. *NeuroImage*, 62(3):1600-9 (2012)
17. Weiss C, Tursunova I, Neuschmelting V, Lockau H, Nettekoven C, Oros-Peusquens AM, et al. Improved nTMS- and DTI-derived CST tractography through anatomical ROI seeding on anterior pontine level compared to internal capsule. *NeuroImage Clinical*, 7:424-37 (2015)
18. Sollmann N, Wildschuetz N, Kelm A, Conway N, Moser T, Bulubas L, et al. Associations between clinical outcome and navigated transcranial magnetic stimulation characteristics in patients with motor-eloquent brain lesions: a combined navigated transcranial magnetic stimulation-diffusion tensor imaging fiber tracking approach. *Journal of neurosurgery*, 128(3):800-810 (2018)
19. Farquharson S., Tournier J.-D., Calamante F., Fabinyi G., Schneider-Kolsky M., Jackson G. D., Connelly A. White matter fiber tractography: why we need to move beyond DTI. *J of Neurosurgery* 118(6): 1367-1377 (2013)
20. Duffau H. Diffusion tensor imaging is a research and educational tool, but not yet a clinical tool. *World Neurosurg*, 82(1-2):e43-5 (2014)
21. Nimsky C. Fiber tracking--we should move beyond diffusion tensor imaging. *World Neurosurg*, 82(1-2):35-6 (2014)

Acknowledgments / Funding Information: Andrey Zhylka is supported by the funding from the European Union's Horizon 2020 research and innovation program under the Marie Sklodowska-Curie grant agreement No 765148.

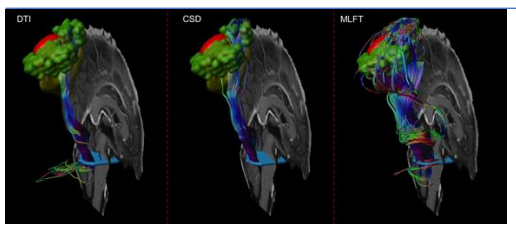

Figure 1. Exemplary case of nTMS-based reconstruction of the CST. A cross-section of the brain stem (light blue) placed at the anterior pontine level was used as a seed region for tractography. The nTMS-based motor map (green; single motor-positive nTMS points with a 2-mm hull) was used as the target region for reconstruction in the vicinity of a tumor (red).

		DTI, (mm^3) (25% FAT)	DTI, (mm^3) (50% FAT)	DTI, (mm^3) (75% FAT)	CSD, (mm^3)	MLFT, (mm^3)
ADT = 20°	Max. Volume	18734	13111	10097	11021	26219
	Min. Volume	0	0	0	0	6.4
	Mean Volume	7480	5788	3094	4057	12761
ADT = 45°	Max. Volume	34538	21190	12410	14897	44989
	Min. Volume	0	0	0	0	4680
	Mean Volume	14545	8970	4334	6686	24711
ADT = 60°	Max. Volume	40927	23710	13950	16219	61681
	Min. Volume	0	0	0	189	9715
	Mean Volume	17749	10157	4706	7982	32067

Table 1. Volumes of the bundles reaching the nTMS motor map. For DTI three angular thresholds as well as three FA thresholds are included.

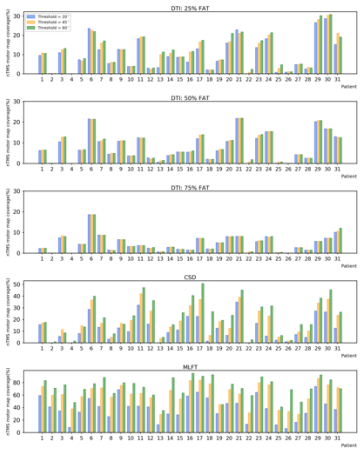

Figure 2. Ratio of the nTMS motor maps that is visited by fiber bundles reconstructed with DTI-based (with 25, 50, and 75% of the individual fractional anisotropy threshold [FAT]), CSD-based, and MLFT tractography. Change of the angular-deviation thresholds (ADTs) appears to only have visible effect on the result of CSD-based tractography and MLFT.

		DTI, (%) (25% FAT)	DTI, (%) (50% FAT)	DTI, (%) (75% FAT)	CSD, (%)	MLFT, (%)
ADT = 20°	Max. Coverage	28.7	21.7	18.5	34.8	73.7
	Min. Coverage	0	0	0	0	6.4
	Mean Coverage	9.8	7.8	4.4	11.9	38.7
ADT = 45°	Max. Coverage	30.4	21.8	18.5	42	86.2
	Min. Coverage	0	0	0	0	28.9
	Mean Coverage	11.1	8.1	4.5	18	60.8
ADT = 60°	Max. Coverage	30.8	21.8	18.5	50.6	94.7
	Min. Coverage	0	0	0	1	35
	Mean Coverage	11.7	8.2	4.6	22.6	71.8

Table 2. The nTMS motor map coverage by the three algorithms given varied angular threshold as well as varied FA threshold in case of DTI.

	20° - 45°	20° - 60°	45° - 60°
DTI (25% FAT)	$6.748 * 10^{-5}$	0.0005	0.0026
DTI (45% FAT)	0.00028	0.0012	0.0076
DTI (75% FAT)	0.011	0.061	0.31
CSD	$1.17 * 10^{-6}$	$2.56 * 10^{-6}$	$1.04 * 10^{-5}$
MLFT	$1.17 * 10^{-6}$	$1.17 * 10^{-6}$	$1.92 * 10^{-6}$

Table 3. P-values obtained from comparing the nTMS motor map coverage given varied angular deviation thresholds (ADTs) using paired Wilcoxon tests. Using a significance level $\alpha = 0.05$, the difference caused by changing the ADT is significant for all cases except at 75% of the individual fractional anisotropy threshold (FAT) for DTI-based tractography.

Cerebrovascular brain-age

M.B.J. Dijsselhof[1], M. Barboure[1], M. Stritt[2], W. Nordhøy[3], A.M. Wink[1], L.T. Westlye[4,5,6], J.H. Cole[7], F. Barkhof[1,8], J. Petr[9], H.J.M.M. Mutsaerts[1]

[1]Department of Radiology & Nuclear Medicine, Amsterdam University Medical Center, Amsterdam, Netherlands; [2] Mediri GmbH, Heidelberg, Germany; [3]Department of Diagnostic Physics, Oslo University Hospital, Oslo, Norway; [4]Norwegian Centre for Mental Disorders Research, Oslo University Hospital, Oslo, Norway; [5]Department of Psychology, University of Oslo, Oslo, Norway; [6]KG Jebsen Centre for Neurodevelopmental Disorders, University of Oslo, Oslo, Norway; [7]Dementia Research Centre & Centre for Medical Image Computing, University College London, London, United Kingdom; [8]Queen Square Institute of Neurology & Centre for Medical Image Computing, University College London, London, United Kingdom; [9]Helmholtz-Zentrum Dresden-Rossendorf, Dresden, Germany

Synopsis

The structural brain-age makes predictions based on changes in tissue integrity. Adding cerebrovascular MRI biomarkers may add sensitivity to physiological and metabolic changes, hence complementing structural brain-age, and possibly improving its early pathology sensitivity. Baseline and follow-up T1w, FLAIR, and ASL data of 233 healthy participants and combinations of features and algorithms were used to predict 'Cerebrovascular brain-age'.
The ExtraTrees algorithm utilising T1w, ASL, and FLAIR features performed best and showed good longitudinal reproducibility.

Introduction

The brain-age method is able to estimate the biological brain age using structural MRI images, with a mean absolute error (MAE) of 5.3 years [1].The brain-age offset to the chronological age — the age gap — is associated with cognitive pathology in healthy and cognitively impaired cohorts [2]. The structural brain-age makes predictions based on changes in brain-tissue integrity and irreversible structural changes. Adding vascular or functional MRI biomarkers may add sensitivity to physiological and metabolic changes, hence complementing and improving structural brain-age, and possibly improving its sensitivity to earlier disease changes. Arterial spin labeling (ASL) MRI is a potential early biomarker displaying changes in both blood supply and demand, and was shown to correlate with the initial stages of cognitive pathology [3]. First results by Rokicki et al. showed that ASL-derived features do improve brain-age prediction (r2=0.77,MAE = 6.4 years) [4]. It remains to be studied whether the use of other ASL-derived parameters, such as the spatial Coefficient of Variation (CoV) and vascular-territory derived (VT) CBF, may improve brain-age estimation even further [5,6]. These features incorporate ASL imaging properties that reflect age, such as arterial transit artefacts (ATA), in VT's that are directly related to cerebrovascular health. In this study, we propose the 'Cerebrovascular brain-age' as a combination of T1w, FLAIR, and ASL image features. We will compare its performance between different machine learning methods and image features, and estimate its long-term reproducibility.

Methods

Methods-study design/data

Baseline and follow-up (1.7±0.5 years) T1w, FLAIR, and 3D spiral PCASL data of 233 healthy participants (36.8% male, age: 61.4±13.5 years) were drawn from the NORMENT (Norwegian Centre for Mental Disorders Research) StrokeMRI dataset [4], of which image acquisition specifics were described previously [4]. Image processing was performed with ExploreASL (Figure 1A) [7]. All images were registered to T1w and spatially normalised to MNI.

Comparison of machine learning models & image features

We compared different features (Figure 1A), feature sets (Figure 1B), and machine learning algorithms readily available within Python packages scikit-learn version 0.23.1, xgboost library version 1.2.0, and sklearn_rvm library version 0.1.1 (Figure 1C). To correct for individual physiological differences, CBF features were normalised by deep WM CBF [7], which was not associated with age. Model performance was assessed for each algorithm and feature set combination, using MAE of age gaps — chronological minus predicted brain age —and 300 Monte-Carlo cross-validation simulations using a 70%:30% train-test split (n=326 : n=140). The optimal combination of machine learning method and image features was used in subsequent analyses, described below.

Comparison with existing brainageR model

Model performance was compared to brainageR (trained on 3337 healthy individuals, age: 40.6±21.4 years, age-range 18-92 years [8]) using the best-performing model and feature set using a single 70%:30% train-test split.

Validation with follow-up data

The best-performing model was selected based on the lowest MAE and assessed for robustness by looking at back-to-back repeatability. Age gaps were calculated for baseline and follow-up in the same train-test split mentioned above. Next, we tested if the age gaps at follow-up differed fromage gaps at baseline using the paired t-test and intra-class correlation coefficient (ICC). Lastly, we compared the age gaps of the best performing model and T1w feature set using the paired t-test.

Results

Comparison of machine learning models & image features

The ExtraTrees algorithm showed the lowest MAE for most feature sets, lowest for T1w+FLAIR+ASL (MAE = 4.47) (Figure 2).

Comparison with brainageR

The ExtraTrees algorithm with T1w+FLAIR+ASL features performed better than brainageR (MAE = 5.36 and 5.67 respectively) in the single 70:30 split, but the difference was not significant (p = 0.06) (Figure 3).

Reproducibility in follow-up data

The ExtraTrees results showed very good reproducibility. The average baseline and follow-up age gaps were similar, respectively -1.18 ± 6.7 and-1.31 ± 6.2 years (p=0.38) with an average difference of 0.135 ± 3.8 years only (ICC = 0.83) (Figure 4). Reproducibility of T1w+FLAIR+ASL features, assessed as the average age gap differences between baseline and follow-up (p=0.17), was equally good as for only T1w features (Figure 5).

Discussion

Our results show that the addition of ASL and FLAIR features to structural brain-age can improve the prediction of brain-age and shows good long-term reproducibility. Out of the algorithms we compared, ExtraTrees performed the best. However, we could not improve the biological age prediction significantly from the existing brainageR model; probably because the brainageR model was trained with a larger population and wider age range. Furthermore, our model slightly overestimated young age and underestimated old age, which is the opposite to brainageR. Despite our relatively small population and the physiological variability of CBF, our cerebrovascular brain-age prediction remained relatively consistent from baseline to follow-up. Our potential limitations include the relatively small, single-site, training and validation set. Future studies are encouraged to include multiple(longitudinal) cohorts and scanners to improve generalisation, and try to determine correlations between Cerebrovascular brain-age and cognitive decline.

References

[1] James H Cole, Stuart J Ritchie, Mark E Bastin, MC Valdés Hernández, S Muñoz Maniega, Natalie Royle, Janie Corley, Alison Pattie, Sarah E Harris,Qian Zhang, et al. Brain age predicts mortality. Molecular psychiatry, 23(5):1385– 1392, 2018.
[2] B. Manor, M. Gorges, Y. Cruz-Almeida, K. Franke, and C. Gaser, "Ten Years of brain-age as a Neuroimaging Biomarker of Brain Aging: What Insights Have We Gained?," Front. Neurol., vol. 1, p. 789, 2019, doi: 10.3389/fneur.2019.00789.
[3] Y Iturria-Medina, Sotero RC, Toussaint PJ, Mateos-Pérez JM, Weiner MW, Aisen P, Petersen R, et al. Early role of vascular dysregulation on late-onset Alzheimer's disease based on multifactorial data-driven analysis. Nat Commun. doi:10.1038/ncomms11934
[4] Rokicki J, Wolfers T, Nordhøy W, Tesli N, Quintana DS, Alnaes D, Richard G, de Lange AG, Lund MJ, Norbom L, Agartz I, Melle I, Naerland T, Selbaek G, Persson K, Nordvik JE, Schwarz E, Andreassen OA, Kaufmann T, Westlye LT. Multimodal imaging improves brain age prediction and reveals distinct abnormalities in patients with psychiatric and neurological disorders. Hum Brain Mapp. 2021 Apr 15;42(6):1714-1726. doi:10.1002/hbm.25323. Epub 2020 Dec 19. PMID: 33340180; PMCID: PMC7978139.
[5] Henri JMM Mutsaerts, Jan Petr, Lena Václav, Jan W Van Dalen, Andrew D Robertson, Matthan W Caan, Mario Masellis, Aart J Nederveen, Edo Richard, and Bradley J MacIntosh. The spatial coefficient of variation in arterial spin labeling cerebral blood flow images. Journal of Cerebral Blood Flow & Metabolism, 37(9):3184–3192, 2017
[6] Tatu L., Moulin, T., Bogousslavsky, J. & Duvernoy, H. Arterial territories of the human brain: cerebral hemispheres. Neurology 50, 1699–1708(1998)
[7] H. J. M. M. Mutsaerts et al., "ExploreASL: An image processing pipeline for multi-center ASL perfusion MRI studies," Neuroimage, vol. 219, Oct.2020, doi: 10.1016/j.neuroimage.2020.117031.
[8] Biondo, F., Jewell, A., Pritchard, M., Aarsland, D., Steves, C. J., Mueller, C., & Cole, J. H. (2021). Brain-age predicts subsequent dementia in memory clinic patients. medRxiv, 2021.2004.2003.21254781

Acknowledgments / Funding Information: We acknowledge the following grants: the Dutch Heart Foundation 2020T049 — M.B.J. Dijsselhof and H.J.M.M. Mutsaerts — the Eurostars-2 jointprogramme with co-funding from the European Union Horizon 2020 research and innovation programme (ASPIRE E!113701), provided by theNetherlands Enterprise Agency (RvO) — H.J.M.M. Mutsaerts and M. Stritt — and the EU Joint Program for Neurodegenerative Disease Research,provided by the Netherlands Organisation for Health Research and Development and Alzheimer Nederland DEBBIE JPND2020-568-106 — H.J.M.M.Mutsaerts., Helmholtz-Zentrum Dresden-Rossendorf, Dresden, Germany

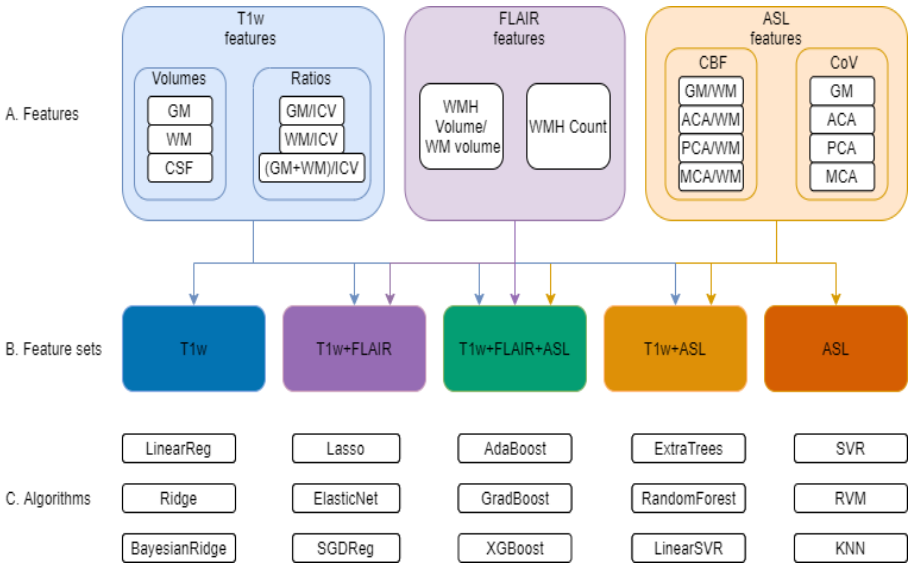

Figure 1: Systematic overview of different features (A), feature sets (B) and different algorithms (C) used to predict brain age. CBF = cerebral blood flow; CoV = coefficient of variation; GM = grey matter; WM = white matter; WMH = white matter hyperintensity; CSF = cerebrospinal fluid; ICV =intracranial volume; ACA = anterior cerebral artery territory; MCA = middle cerebral artery territory; PCA = posterior cerebral artery territory.

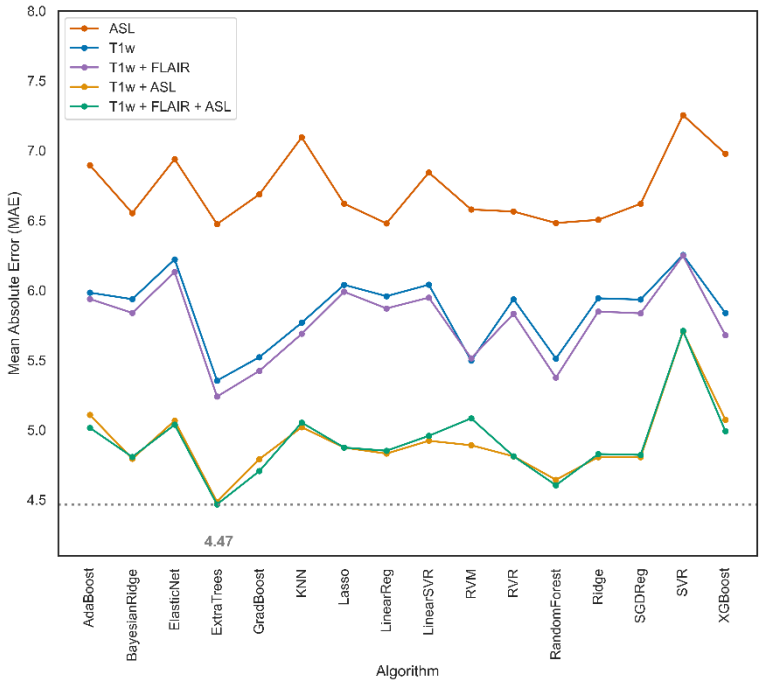

Figure 2: MAE for various algorithms and different feature sets after 300 rounds of Monte-Carlo cross-validation.

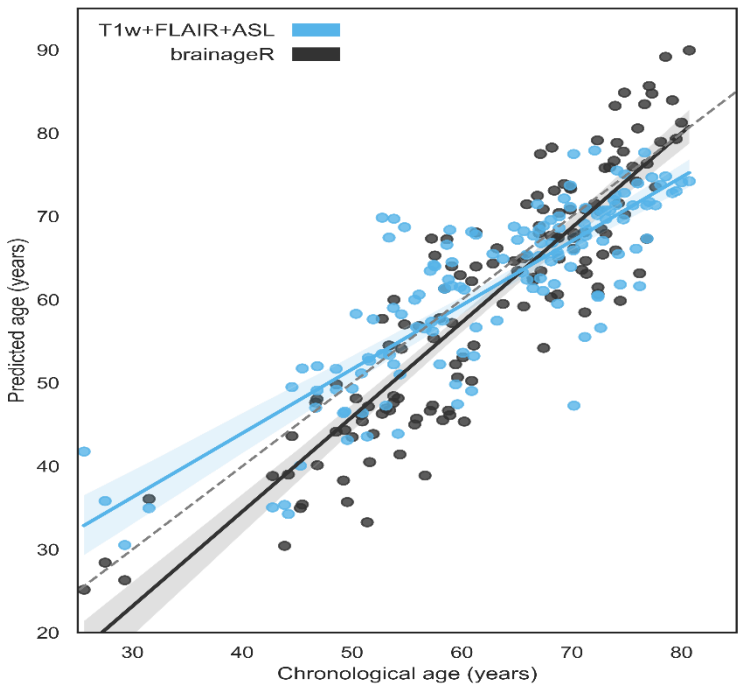

Figure 3: Predicted brain ages of the ExtraTrees, using the T1w+FLAIR+ASL features, and brainageR algorithms.

Figure 4: Age gaps of baseline and follow-up sessions obtained with the ExtraTrees algorithm using the T1w+FLAIR+ASL features.

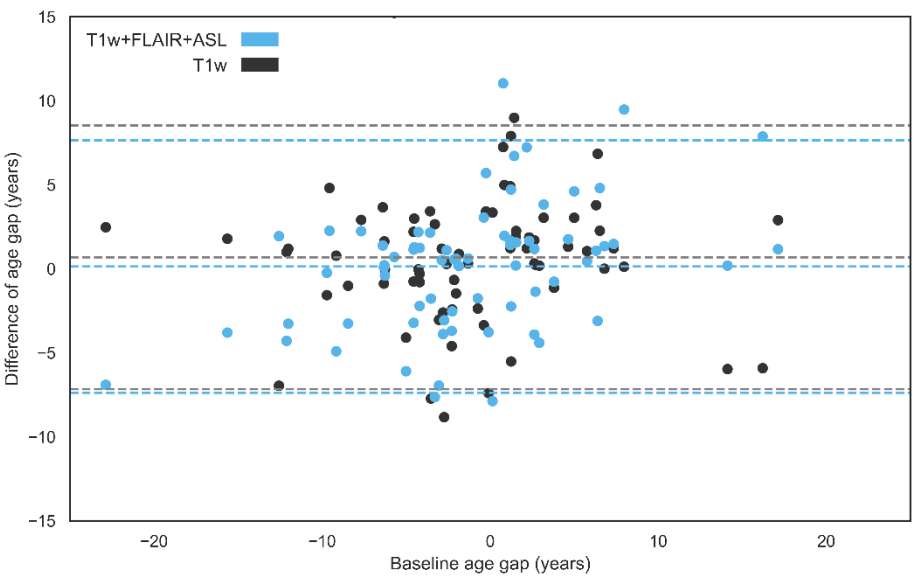

Figure 5: Bland-Altman plot showing the difference of age gaps between baseline and follow-up for T1w and T1w+FLAIR+ASL features, per baseline age gap.

The association between white matter hyperintensity shape and long-term dementia outcome in community-dwelling older adults

Jasmin A. Keller[1], Sigurður Sigurdsson[2], Kelly Klaassen[1], Eveline Scholte[1], Lydiane Hirschler[1], Mark A. van Buchem[1], Lenore J. Launer[3], Matthias J.P. van Osch[1], Vilmundor V. Gudnason[2], and Jeroen de Bresser[1]

[1]Department of Radiology, Leiden University Medical Center, Leiden, Netherlands, [2]Icelandic Heart Association, Kopavogur, Iceland, [3]Laboratory of Epidemiology and Population Science, National Institute on Aging, Bethesda, MD, United States

Synopsis: Recently white matter hyperintensity (WMH) shape was introduced as a promising novel marker that may provide a more detailed characterization of WMH than volume alone. We aimed to investigate the association between WMH shape and the occurrence of dementia later in life in community dwelling older adults. WMH shape markers and WMH volumes were determined for periventricular/confluent, and deep WMH. A more complex shape of periventricular/confluent WMH (higher fractal dimension), as well as total and periventricular/confluent WMH volume, were associated with a greater risk of dementia. These results may indicate a prognostic value of WMH shape markers.

Introduction: Cerebral small vessel disease (SVD) is a key contributor to the development of dementia [1]. White matter hyperintensities (WMH) are a key imaging marker of SVD and become evident as hyperintense lesions on fluid-attenuated inversion recovery (FLAIR) MRI images [1]. Previous research has shown that WMH volume is related to the occurrence of dementia [2]. Recently WMH shape was introduced as a promising novel marker that may provide a more detailed characterization of WMH than volume alone. WMH shape has been associated with the occurrence of future stroke and increased mortality in patients with an increased vascular burden [3]. However, the association of WMH shape and occurrence of dementia later in life remains unknown. Therefore, we aimed to investigate the association between WMH shape and the occurrence of dementia later in life in community dwelling older adults.

Methods:

Participants & study design

This abstract includes a randomly selected subset (n=350) of the AGES Reykjavik study [4]. At baseline, FLAIR and T1-weighted brain MRI scans were acquired on a 1.5 Tesla Signa Twinspeed device (General Electric Medical Systems, Waukesha, Wisconsin). Dementia outcome was determined as a binary variable (yes/no) by contacting the nursing homes 10.2 ± 2.4 years after the baseline MRI scan. The inclusion and exclusion of participants from the AGES-Reykjavik study for the current research are illustrated in Figure 1.

WMH markers

WMH were segmented automatically using the registered FLAIR images in the LST toolbox in SPM12. The lateral ventricles were segmented using the T1 scan and subsequently inflated with both 3 and 10 mm. The inflated ventricle masks were used to classify WMH into periventricular, confluent, and deep WMH (see Figure 2). WMH shape markers were calculated based on the WMH segmentation. Convexity, solidity, concavity index, and fractal dimension were determined for periventricular/confluent WMHs [5]. A lower convexity and solidity, and higher concavity index and fractal dimension indicate more irregularly shaped periventricular or confluent WMH. For deep WMHs, fractal dimension and eccentricity were calculated [5]. Mean shape values across all WMHs per participant were determined [5]. A higher eccentricity and fractal dimension indicate a more complex shape of deep WMH. We also calculated the volumes of periventricular/confluent, deep, and total WMH. WMHs consisting of less than 5 voxels were not further analysed, since WMH shape markers cannot be calculated accurately on small volume WMH [6].

Statistical analysis

Cox regression was performed for z-scores of WMH shape markers, controlled for age and sex. Solidity and WMH volumes were natural log-transformed due to non-normal distribution. For WMH volumes, regression models were additionally controlled for intracranial volume.

Results: Baseline characteristics of the study sample can be found in Table 1. A higher fractal dimension of periventricular/confluent WMH was associated with a greater risk of developing dementia later in life (HR 1.50, 95% CI (1.09–2.07); p=0.013). A higher fractal dimension indicates a more complex shape. No significant associations were found for the other WMH shape markers (Table 2). Total WMH volume (HR 1.88, 95% CI (1.21–2.70); p=0.001) and volume of periventricular/confluent WMH (HR 1.80, 95% CI (1.28–2.54); p=0.001) were associated with a greater risk of developing dementia later in life (Table 3). No association was found for deep WMH volume.

Discussion: We found that a more complex shape of periventricular/confluent WMH as measured by the fractal dimension was associated with a higher risk of dementia later in life in community-dwelling older adults. Moreover, total WMH volume, as well as the volume of periventricular/confluent WMH, were associated with dementia status at follow-up, which is in line with previous studies [2]. Due to a heterogeneous aetiology of WMH in SVD, the MRI phenotypes associated with different underlying pathophysiological processes may appear as distinguishable WMH shape patterns [7]. The shape of periventricular/confluent WMH, for instance, may depend on the macrostructure of the small vessels surrounding the lateral ventricles. Determination of WMH shape may aid prognostic differentiation, which is currently only possible in a limited way with WMH volume or count alone [7]. We are the first to study the association between WMH shape markers and dementia outcome. It should be noted that these are preliminary results on a smaller subset of our dataset. The results may differ when the whole dataset is considered. Therefore, a final conclusion can be drawn when the ongoing analysis has been completed.

References:

1. Wardlaw JM, Smith C, Dichgans M. Mechanisms of sporadic cerebral small vessel disease: Insights from neuroimaging. Lancet Neurol. 2013;12(5):483-497,
2. Bos D, Wolters FJ, Darweesh SKL, et al. Cerebral small vessel disease and the risk of dementia: A systematic review and meta-analysis of population-based evidence. Alzheimer's Dement. 2018;14(11):1482-1492,
3. Ghaznawi R, Geerlings MI, Jaarsma-Coes M, et al. Association of White Matter Hyperintensity Markers on MRI and Long-term Risk of Mortalityand Ischemic Stroke. Neurology. 2021;96(17):e2172-e2183,
4. Harris TB, Launer LJ, Eiriksdottir G, et al. Age, gene/environment susceptibility-reykjavik study: Multidisciplinary applied phenomics. Am J Epidemiol. 2007;165(9):1076-1087,
5. Ghaznawi R, Geerlings MI, Jaarsma-Coes MG, et al. The association between lacunes and white matter hyperintensity features on MRI: The SMART-MR study. J Cereb Blood Flow Metab. 2019;39(12):2486-2496,
6. De Bresser J, Kuijf HJ, Zaanen K, et al. White matter hyperintensity shape and location feature analysis on brain MRI; Proof of principle study in patients with diabetes. Sci Rep. 2018;8(1):1-10,
7. Alber J, Alladi S, Bae H, et al. White matter hyperintensities in vascular contributions to cognitive impairment and dementia (VCID): Knowledge gaps and opportunities. Alzheimer's Dement Transl Res Clin Interv. 2019;5(1):107-117.

Acknowledgments / Funding Information: This work was funded by an Alzheimer Nederland grant (WE.03-2019-08).

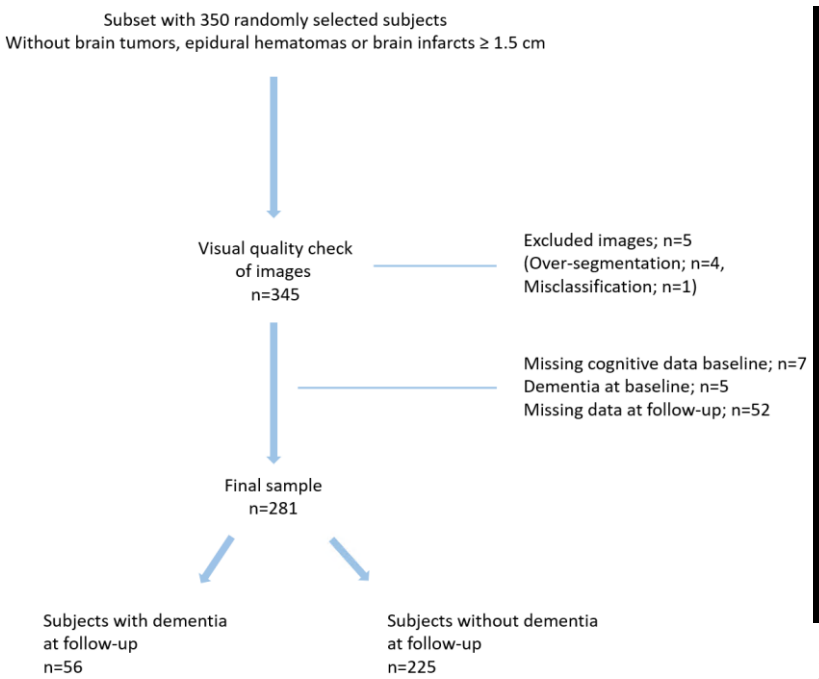

Figure 1. Flowchart illustrating the inclusion and exclusion of participants.

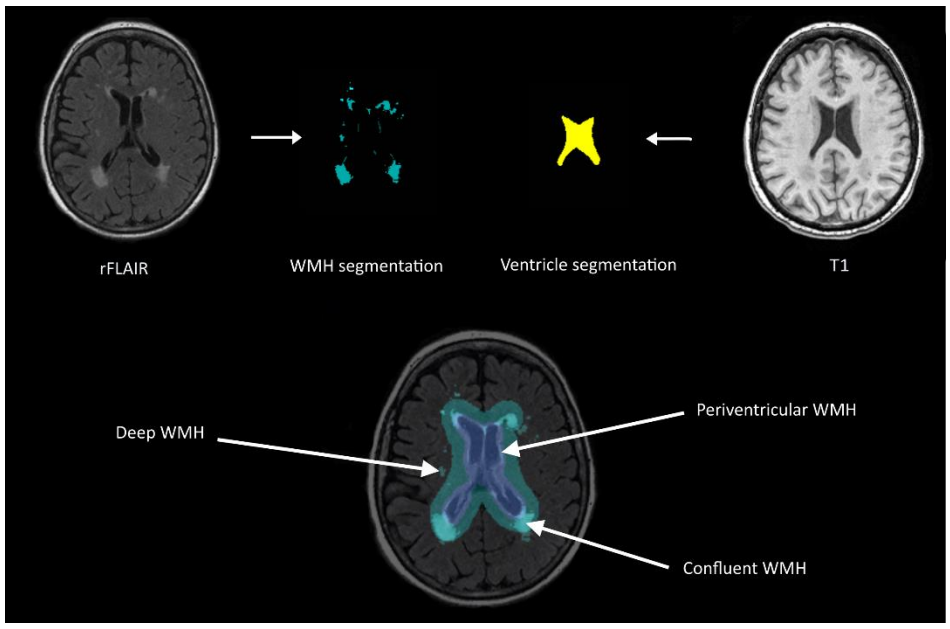

Figure 2. Illustration of the image processing pipeline. Lateral ventricles were segmented using T1-weighted MRI images. WMH segmentation was performed on the registered FLAIR (rFLAIR) images. Using two different inflated ventricle masks, WMH were classified into three types (deep, periventricular and confluent). Based on the resulting WMH type, different WMH shape markers were calculated.

	Total n=281
Age (years)	75.4 ± 5.1
Dementia at follow-up	56 (20%)
Time to follow-up (years)	10.2 ± 2.4
Education level [a]	2.14 ± 0.89
Females	213 (64%)
BMI (kg/m^3)	27.2 ± 4.1

Table 1. Baseline characteristics of the study sample. Data are indicated as mean ± standard deviation or n (percentage). [a] Education level is the highest level of education that has been completed, where 1 = primary school, 2 = secondary school, 3 = college, and 4 = university. BMI: Body mass index.

		Dementia at follow-up (mean ± SD)	No dementia at follow-up (mean ± SD)	Hazard ratio (95% CI)
Periventricular/ Confluent WMH				
	Solidity	0.15 ± 0.06	0.20 ± 0.12	0.76 (0.55–1.06)
	Convexity	0.96 ± 0.19	1.04 ± 0.17	0.86 (0.65–1.13)
	Concavity Index	1.34 ± 0.14	1.26 ± 0.15	1.26 (0.96–1.67)
	Fractal dimension	1.79 ± 0.12	1.70 ± 0.16	1.50 (1.09–2.07) *
Deep WMH				
	Eccentricity	0.40 ± 0.06	0.39 ± 0.07	1.12 (0.84–1.51)
	Fractal dimension	1.71 ± 1.22	1.70 ± 0.14	1.11 (0.83–1.48)

Table 2. Cox regression results of WMH shape markers. * p<0.05

	Dementia at follow-up (mean ± SD)	No dementia at follow-up (mean ± SD)	Hazard ratio (95% CI)
Total WMH Volume	28.21 ± 24.28	16.46 ± 16.18	1.88 (1.21–2.70) **
Periventricular/confluent WMH Volume	26.40 ± 24.07	15.09 ± 15.78	1.80 (1.28–2.54) **
Deep WMH Volume	1.81 ± 1.31	1.37 ± 1.23	1.29 (0.96–1.73)

Table 3. Cox regression results of WMH volumes. Volumes are given in millilitres. ** p<0.01

Measurement of gastric emptying with dynamic 3D DMI using a deuterium body array at 7 T

A. Gursan[1], A.D. Hendriks[1], D. Welting[1], D.W.J. Klomp[1], J.J. Prompers[1]
[1]Department of Radiology, University Medical Center Utrecht, Utrecht, The Netherlands

Synopsis: Gastric emptying abnormalities are frequently observed in diabetes patients. Here we explored whether dynamic 3D DMI could be a radiation-free alternative for scintigraphy to measure the gastric emptying rate. One volunteer was scanned after oral intake of deuterated glucose and proximal and distal gastric emptying was monitored. The distribution of the glucose load in the proximal and distal parts of the stomach and the rate of gastric emptying agreed well with scintigraphy results. DMI has potential to investigate gastric emptying abnormalities in patients with diabetes, while at the same time providing information on glucose uptake and metabolism in the liver.

Introduction: Gastric emptying is the process of nutrients moving from the stomach into the duodenum at a regulated rate[1]. Gastric emptying abnormalities are frequently observed in diabetes and include both slow/delayed and fast gastric emptying[2]. While delayed gastric emptying can cause hypoglycemia in diabetes patients using exogenous insulin, rapid gastric emptying is emerging as major determinant of postprandial hyperglycemia[2]. The current gold standard for the assessment of gastric emptying is scintigraphy[3]. Deuterium metabolic imaging (DMI)[4–10] with deuterated glucose could potentially be used as a radiation-free alternative to assess gastric emptying, while at the same time providing information on glucose uptake and metabolism in surrounding tissues, such as the liver. Previously, we have demonstrated the feasibility of monitoring liver glucose uptake and metabolism with DMI using a dedicated 4-channel deuterium body array at 7T. In the current study, we measured gastric emptying with dynamic 3D DMI using the same setup.

Methods: The study was approved by the local medical ethics committee. DMI measurements were performed at a 7T whole-body MRI system (Philips Healthcare, Best, Netherlands), with a dedicated setup consisting of 4 deuterium (^{2}H) transmit/receive loop coils and 4 proton (^{1}H) transmit/receive dipole antennas. Image-based B_0 shimming and acquisition of coronal and axial T_1w reference images for DMI planning were performed with the ^{1}H antennas. DMI measurements were performed with a pulse-acquire sequence using a 1 ms block pulse, followed by phase encoding gradients for 3D spatial encoding, and TE/TR=1.95/333 ms, nominal voxel size=30x30x30 mm^3, matrix size=8(AP)x10(LR)x9(FH), NSA=4, and temporal resolution=5:08 min. DMI acquisitions were made using a Hamming-weighted k-space acquisition pattern. No respiratory gating was applied. One healthy volunteer was scanned after an overnight fast. A load of 50 grams of [6,6'-$^2H_2$]glucose was dissolved in 200 ml water and administered orally through a tube while the subject was laying in the scanner. Two baseline scans at natural abundance were acquired before deuterated glucose intake and DMI scans were continued up to 130 min after intake. Reconstruction and processing of the raw DMI data was performed with an in-house written MATLAB script (MathWorks, Natick, MA, USA). Channel combination was performed using the Roemer equal noise algorithm[11]. The deuterated glucose signal (3.8 ppm) was fitted using AMARES[12]. Glucose maps were created using the amplitude of the fitted glucose signals. Axial T_1w images were used to draw ROI's for proximal and distal parts of the stomach and the sum of the two ROI's was used as total stomach ROI. Glucose signal amplitudes were added within each ROI, and the glucose signal in the first measurement after glucose intake in the total stomach ROI was set to 100%. For the total stomach ROI, the time course of glucose signal amplitudes was fitted to a mono-exponential function to determine the emptying half time (T_{50}).

Results: A very strong deuterated glucose signal was observed in the proximal part of the stomach immediately after administration of deuterated glucose and, although it was slowly decreasing thereafter, the glucose signal stayed high until the last measurement at 130 min after glucose intake (Figures 1 and 2). In contrast, in the distal stomach the glucose signal disappeared almost completely 20 min after intake (Figure 2). Figure 3 shows the ROI's for the proximal and distal parts of the stomach on the T_1w axial images. Figure 4 shows the distribution and time courses of glucose signal in the proximal and distal parts of the stomach, relative to the total stomach glucose signal. About 80% of the glucose signal was initially observed in the proximal stomach, which then decreased more or less linearly over time. In the distal stomach, the glucose signal decayed rapidly during the first 20 min and then remained at a constant low value (~7%) up to 130 min. For the total stomach glucose signal, the fitted T_{50} was 80 min (Figure 5).

Discussion/Conclusion: We demonstrated the measurement of gastric emptying with dynamic 3D DMI. Using scintigraphy, it has been shown that both the nutrient load and the volume of the load affects the gastric emptying rate, as the regulation is dependent on the amount of calories entering the duodenum[13,14]. Moreover, intragastric distribution of a labeled glucose drink is different between seated and lying positions, and especially the distal gastric emptying rate is affected by posture[15]. However, it was shown that the overall gastric emptying rate is not significantly different for seated and lying positions[15]. Compared to a scintigraphy study in seated subjects using a similar glucose load and volume as in our study, we observed a slightly shorter T_{50} for the whole stomach (80 vs 103 min)[16]. The intragastric distribution of the glucose load and the different patterns for proximal and distal gastric emptying agree well with scintigraphy results of subjects in a lying position[15].In conclusion, dynamic 3D DMI allows monitoring of proximal and distal gastric emptying without radiation burden. This technique could be applied to investigate gastric emptying abnormalities in patients with diabetes, and results can be linked directly to hepatic glucose uptake and metabolism, through simultaneous measurement with a deuterium body array setup.

References:

1. Hellström PM et al. *Best Pract Res Clin Anaesthesiol*. 2006;20(3):397-407. doi:10.1016/j.bpa.2006.02.002
2. Goyal RK. *N Engl J Med*. 2021;384(18):1742-1751. doi:10.1056/nejmra2020927
3. Griffith GH eta al. *Lancet*. 1966;287(7449):1244-1245. doi:10.1016/s0140-6736(66)90247-9
4. De Feyter HM et al. *Sci Adv*. 2018;4(8):1-12. doi:10.1126/sciadv.aat7314
5. Lu M et al. *J Cereb Blood Flow Metab*. 2017;37(11):3518-3530. doi:10.1177/0271678X17706444
6. Kreis F et al. *Radiology*. 2020;294(2):289-296. doi:10.1148/radiol.2019191242
7. Riis-Vestergaard MJ et al. *Int J Obes*. 2020;44(6):1417-1427. doi:10.1038/s41366-020-0533-7
8. De Feyter HM et al. *Magn Reson Med*. 2021;86(1):62-68. doi:10.1002/mrm.28717
9. Hesse F et al. *Proc Natl Acad Sci U S A*. 2021;118(12):e2014631118. doi:10.1073/pnas.2014631118
10. von Morze C et al. *Magn Reson Med*. 2021;85(4):1795-1804. doi:10.1002/mrm.28612
11. Roemer PB et al. *Magn Reson Med*. 1990;16(2):192-225. doi:10.1002/mrm.1910160203
12. Vanhamme L et al. *J Magn Reson*. 1997;129(1):35-43. doi:10.1006/jmre.1997.1244
13. Gentilcore D et al. *Neurogastroenterol Motil*. 2006;18(12):1062-1068. doi:10.1111/j.1365-2982.2006.00830.x
14. Jones KL et al. *Am J Physiol - Gastrointest Liver Physiol*. 2005;289(2):G240-G248. doi:10.1152/ajpgi.00030.2005
15. Jones KL et al. *Dig Dis Sci*. 2006;51(8):1331-1338. doi:10.1007/s10620-005-9010-3
16. Frank JW et al. *Gastroenterology*. 1995;109(3):755-765. doi:10.1016/0016-5085(95)90382-8

Acknowledgments / Funding Information: This work was funded by a HTSM grant from NWO TTW (project number 17134) and by a FET Innovation Launchpad grant from the EU (grant number 850488).

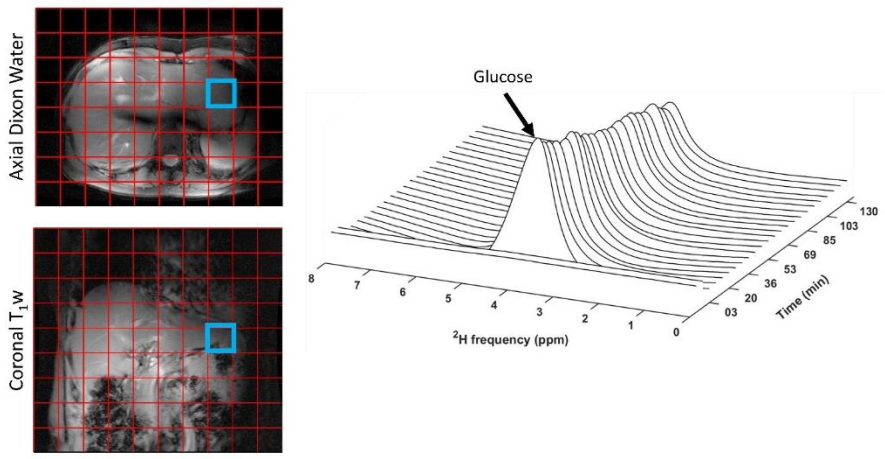

Figure 1. Deuterium spectra from a voxel located in the proximal part of the stomach at baseline and 0-130 min after oral administration of [6,6'-$^2H_2$] glucose. A high deuterated glucose signal was observed in the stomach immediately after glucose intake, which decreased gradually, but stayed high until the end of the scan.

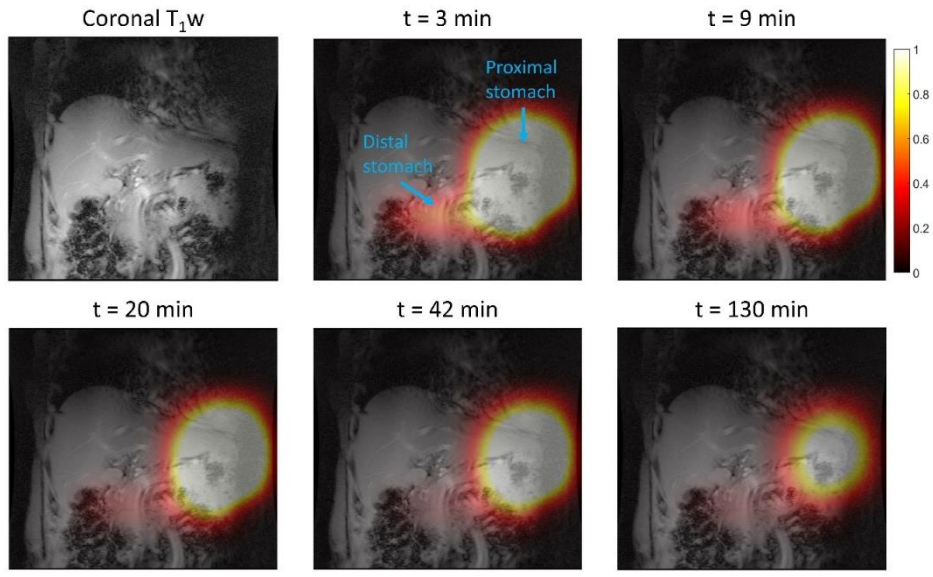

Figure 2. Coronal color maps of fitted deuterated glucose signal amplitudes (in AU) from 5 selected 3D DMI measurements between 0 and 130 min after oral administration of [6,6'-$^2H_2$]glucose. Signal amplitudes larger than 1 are represented in white. The color maps are overlaid on the T_1w images. The signal in the distal part of the stomach faded around 20 min after administration, while it remained hyperintense in the proximal stomach until the end of the experiment.

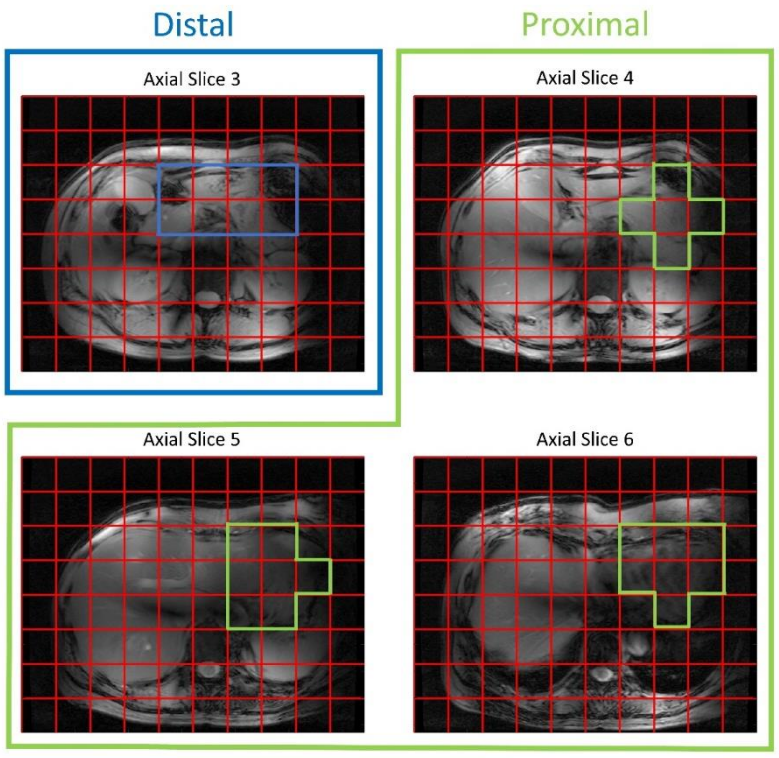

Figure 3. ROI's for distal (blue) and proximal (green) parts of the stomach. Masks were drawn on T_1w axial images. The ROI for the distal part of the stomach was drawn in the axial slice in which both kidneys were visible.

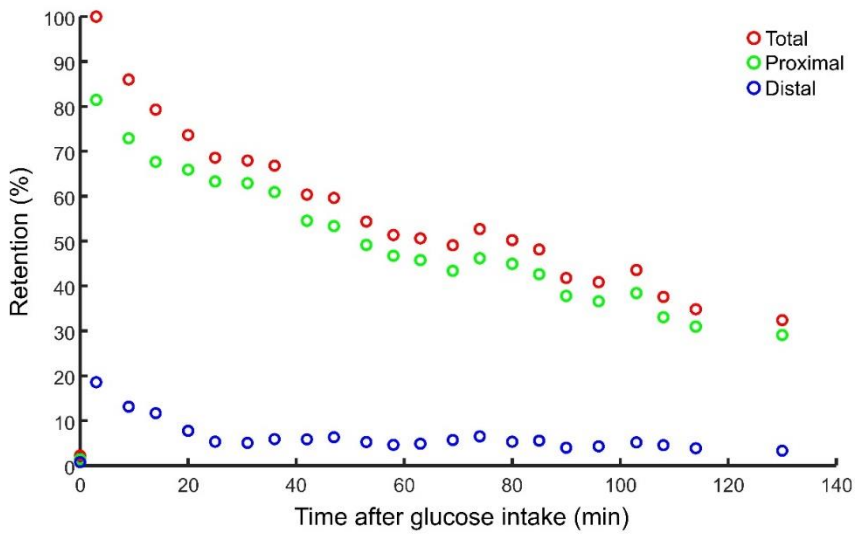

Figure 4. Glucose retention graph for total, proximal and distal stomach. Glucose retention is defined as the sum of the deuterated glucose signal amplitudes within each ROI, expressed as a percentage of the glucose signal in the total stomach ROI in the first measurement after deuterated glucose intake (=100%).

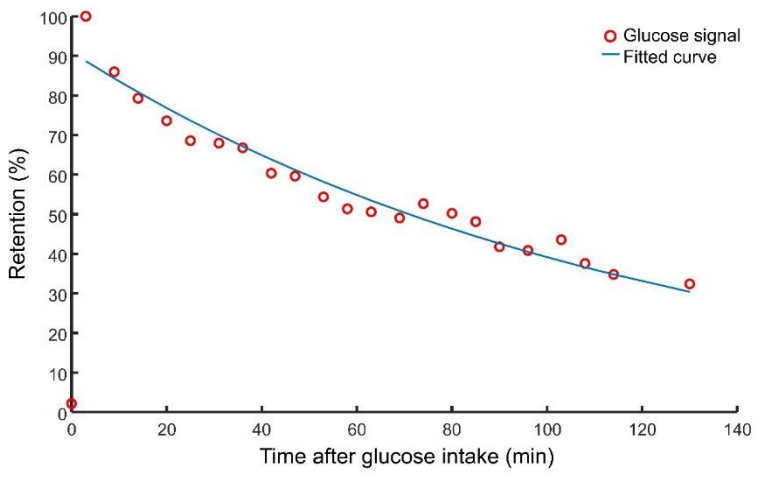

Figure 5. Mono-exponential fit of the time course of the deuterated glucose signal in the total stomach ROI. The gastric emptying half time (T_{50}) determined from the fit was 80 min.

3D Deuterium Metabolic Imaging (DMI) of the Human Liver at Using Low-rank and Subspace Modeling

Kyungmin Nam[1], Ayhan Gursan[1], Namgyun Lee[2], Jannie Wijnen[1], Dennis Klomp[1], Jeanine Prompers[1], Alex Bhogal[1] and Arjan Hendriks[1]

[1]Department of Radiology, University Medical Center Utrecht, Utrecht, The Netherlands, [2]Department of Biomedical Engineering, University of Southern California, Los Angeles, USA

Synopsis: Deuterium metabolic imaging (DMI) is an emerging technique to spatially map metabolism in vivo through the intake of deuterium labeled substrates such as [6,6′-$^2H_2$]-glucose. Although DMI has the potential to become a powerful tool to assess liver metabolism, it has limitations due to its long scan time, and low signal-to-noise ratio (SNR) for high spatial resolution in the human body. In this work, we demonstrated the feasibility of low-rank and subspace modeling (LRSM) reconstruction to increase SNR by reducing spectral noise, allowing high spatiotemporal resolution for 3D DMI of the human liver at 7T.

Purpose: Deuterium metabolic imaging (DMI)[1] is an emerging metabolic imaging technique that can spatially map metabolism in vivo through the intake of deuterium-labeled substrates such as [6,6′-$_2H^2$]-glucose. At ultra-high fields (≥ 7T), deuterium MRSI (DMRSI) benefits from a significantly increased signal-to-noise ratio (SNR) and improved spectral resolution[2]. However, achieving full coverage of the human liver with high spatial resolution within a short acquisition time is challenging. The subspace imaging framework SPICE[3,4] was proposed to enable fast acquisition of 3D MRSI with high resolution. The subspace-based image reconstruction[5] was shown to reduce spectral noise in 3D ^{31}P MRSI data of the human brain. In this work, we demonstrate the application of low-rank and subspace model reconstruction (LRSM) for effective denoising of 3D DMRSI data from the human liver at 7T.

Methods: (1) Experiments Two healthy volunteers were scanned at a 7T MR system (Achieva, Philips, Netherlands) using a transmit-receive body array, including 4 proton dipole antennas and 4 deuterium loop coils. For one volunteer, a 3D DMRSI scan was obtained 2.5 hours after oral intake of deuterated glucose. Scan parameters: DMRSI in the human liver at natural abundance: 20×20×20mm^3 voxels, FOV=240×360×300mm^3, TR/TE=371/1.0ms, 1ms block pulse, spectral bandwidth=1443Hz, average=1, and acquisition time=20min 8s. DMRSI after oral glucose intake: 25×25×25mm^3 voxels, FOV=250×300×300mm^3, TR/TE=333/1.95ms, spectral bandwidth=5000Hz, weighted averages=4, acquisition time=10min 35s. **(2) Numerical simulation** A 3D high-resolution image (matrix size=256x256x12) was generated with three distinct compartments for numerical simulation: liver, stomach, and the rest of the body (including a subcutaneous fat layer). Metabolite signals for water, glucose, Glx, and lipids were generated by varying the amplitude of each signal using a Lorentzian lineshape. Deuterium spectra were simulated with a 10kHz spectral bandwidth and 2048 points. The high-resolution was down-sampled to the resolution of a typical DMI acquisition. Complex Gaussian noise (i.e., N(0, 1)) was added to the simulated deuterium signals with increasing noise standard deviation (0.01-0.2). **(3) Reconstruction** Our approach employs a low-rank and subspace modeling reconstruction where a temporal subspace is estimated from the fully sampled 5×5×5 k-space center region. Specifically, the unknown spatial basis U is estimated by solving the following least-squares problem:

$$\check{U} = \underset{U}{\operatorname{argmin}} \|d - \Omega(FUV)\|_2^2,$$

where $d \in U^{P\times 1}$denotes the vector of k-space data and $\Omega(\cdot)$: $\mathbb{C}^{N\times M} \rightarrow \mathbb{C}^{P\times 1}$ is a linear operator that concatenates the measured data into a vector, $F \in \mathbb{C}^{N\times N}$ is the Fourier encoding matrix, and the columns of U and rows of V span the spatial and temporal subspaces of the Casorati matrix. The Roemer equal noise algorithm[8] was used for channel combination. **(4) Analysis** After phase correction, the SNR was calculated according to $\mathrm{SNR} = I_{water}/\sigma(I_{noise})$, where I_{water} is the water signal intensity and $\sigma(I_{noise})$ the standard deviation of the noise (8-12 ppm). Glucose and water maps were calculated by fitting the signal using the AMARES algorithm[9].

Results and Discussion: Figure 1 shows the generated numerical phantom mask in high-resolution and after down-sampling to low-resolution (Fig. 1A). The SNR (Fig. 2A) was calculated for different additive noise after applying two reconstruction methods: LRSM and FFT reconstruction. The LRSM reconstruction increased the SNR approximately 5-fold at noise level 10 (i.e., a noise standard deviation of 0.1). The metabolite maps of water and glucose (Fig. 2C) are similar to the ground truth when using either FFT or LRSM reconstruction with noise level 10. The Glx maps were noisier than the ground truth, especially for the FFT reconstruction (Fig. 2C). The average SNR (Fig. 3C) in the ROI of the liver (natural abundance DMRSI) was approximately 5-fold higher for LRSM compared to FFT reconstruction. While the natural abundance deuterated water signal was barely visible in some voxels with FFT reconstruction, LRSM reconstruction clearly showed signals in the liver. Figure 4 shows DMI data in the liver after oral intake of deuterated glucose for both reconstructions. The noise (Fig. 4B) is high and could be misinterpreted as a Glx signal for the FFT reconstruction, which is not the case for the LRSM reconstruction. The average SNR (Fig. 4C) of the deuterated water signal in the liver was about 3.5 times higher for the LRSM reconstruction. Glucose and water metabolite maps were created for both reconstruction methods (Fig. 5). The glucose map generated from the data with a single average showed more noise for the FFT reconstruction than for the LRSM reconstruction.

Conclusion: This work demonstrates the implementation of low-rank and subspace modeling reconstruction of 3D DMI data of the human body at 7T. The reconstruction method reduces the noise level in the spectra, enabling metabolite detection in low SNR data. The enhanced metabolite detection could potentially increase spatial resolution and/or decrease acquisition time of 3D DMRSI, for example in combination with fast acquisition techniques such as DEPSI[10].

References:

1. De Feyter HM, Behar KL, Corbin ZA, et al. Deuterium Metabolic Imaging (DMI) for MRI-Based 3D Mapping of Metabolism in Vivo. Vol 4.; 2018.

2. de Graaf RA, Hendriks AD, Klomp DWJ, et al. On the magnetic field dependence of deuterium metabolic imaging. NMR Biomed. 2020;33(3).

3. Lam F, Liang ZP. A subspace approach to high-resolution spectroscopic imaging. Magn Reson Med. 2014;71(4):1349-1357.

4. Lam F, Ma C, Clifford B, Johnson CL, Liang ZP. High-resolution 1H-MRSI of the brain using SPICE: Data acquisition and image reconstruction. Magn Reson Med. 2016;76(4):1059-1070.

5. Wiesner HM, Guo R, Li Y, et al. High-resolution 3D Phosphorus Metabolic Imaging of the Human Brain at 7T using SPICE. Proc Intl Soc Mag Reson Med 29 (2021), #0235.

6. Lam F, Li Y, Guo R, Clifford B, Liang ZP. Ultrafast magnetic resonance spectroscopic imaging using SPICE with learned subspaces. Magn Reson Med. 2020;83(2):377-390.

7. Liang Z-P. Spatiotemporal Imaging with Partially Separable Functions. IEEE Int Symp Biomed Imaging. 2007;2:988-991.

8. Roemer PB, Edelstein WA, Hayes CE, Souza SP, Mueller OM. The NMR phased array. Magn Reson Med. 1990;16(2):192-225.

9. Vanhamme L, Van Den Boogaart A, Van Huffel S. Improved Method for Accurate and Efficient Quantification of MRS Data with Use of Prior Knowledge. J Magn Reson. 1997;129(1):35-43.

10. Nam KM, Gursan A, Bhogal A, et al. Deuterium Echo-Planar Spectroscopic Imaging to Dynamically Monitor Deuterated Glucose in the Liver at 7T. Proc Intl Soc Mag Reson Med 29 (2021), #0231.

Acknowledgments / Funding Information: This project has received funding from the European Union's Horizon 2020 research and innovation program under the Marie Sklodowska-Curie grant agreement (No. 813120) and was funded by an HTSM grant from NWO TTW (project number 17134) and by a FET Innovation Launchpad grant from the EU (grant number 850488).

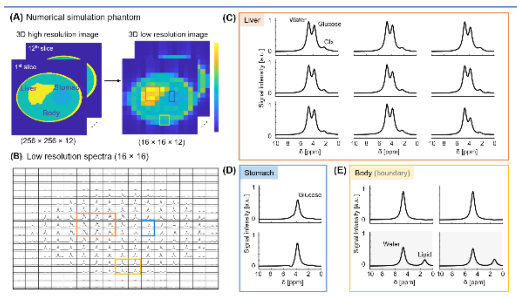

Fig. 1: Schematic overview of the numerical simulation and representative spectra of each region. **(A)** 3D high-resolution phantom mask (A, left) was transformed to 3D k-space and truncated to a lower resolution (A, right). **(B)** In the deuterium spectrum, regions of interest (ROI) are shown, including the liver (orange box), stomach (blue box), and the boundary of the body (yellow box). **(C, D, E)** Representative spectra in each ROI: Water, glucose, and Glx signals are shown in the liver (C), glucose only in the stomach (D), and water in the body, and water and lipids in the body boundary (E)

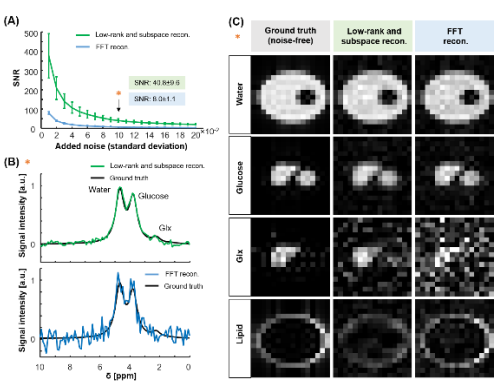

Fig. 2: Results from the numerical simulation phantom, when using two different reconstruction methods: Low-rank and subspace modeling (green) and Fast Fourier Transform (FFT) (blue). **(A)** The average SNR of the water peak of 108 voxels in the liver region was calculated for 20 different levels of added Gaussian noise. **(B)** Deuterium spectra from a liver voxel containing water, glucose, and Glx signals overlaid with the ground truth spectrum (i.e., noise-free). **(C)** Metabolite maps of both reconstructions are shown at noise level 10.

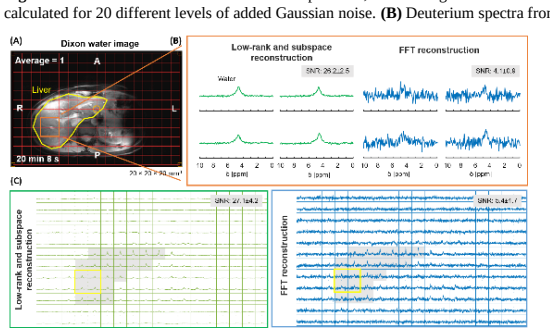

Fig. 3: 3D deuterium MRSI dataset of the human liver at natural abundance processed by two reconstruction methods: low-rank and subspace modeling (green) and FFT (blue). **(A)** The ^{1}H MRI image (Dixon) shows the liver which is contoured by a yellow line. **(B)** Deuterium spectra of four voxels are shown in the liver for both reconstruction methods. **(C)** The average SNR of the water peak was calculated for 22 voxels in the liver region (grey) of the middle slice.

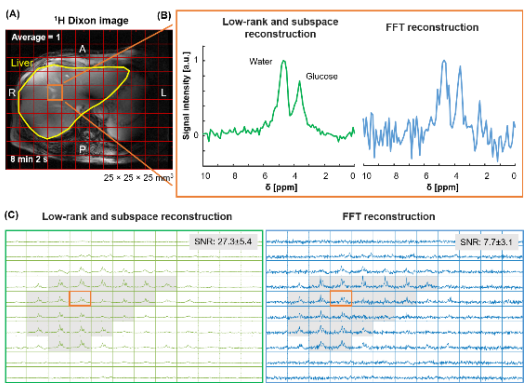

Fig. 4: 3D deuterium MRSI datasets of the human liver acquired 2.5 hours after oral glucose intake, processed by two reconstruction methods: low-rank and subspace modeling (green) and FFT (blue). **(A)** The ^{1}H MRI image (Dixon) shows the liver which was contoured by a yellow line. **(B)** Deuterium spectrum of one voxel in the liver for both reconstruction methods. **(C)** The average SNR of the water peak was calculated for 23 voxels in the liver region (grey) of the middle slice. The DMI dataset was retrospectively reduced to one average.

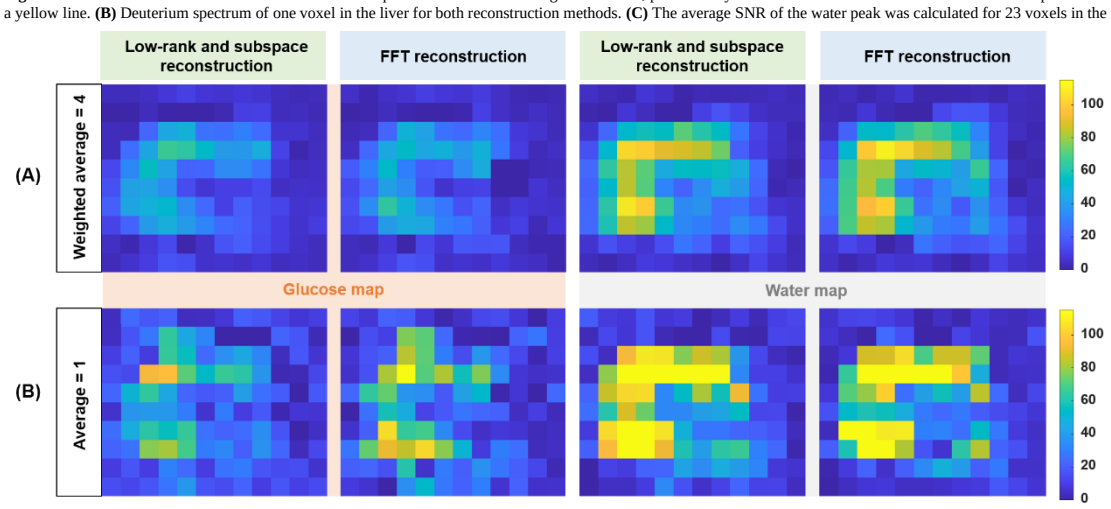

Fig.5: Deuterated glucose and water maps of the DMI data in the transverse plane without a smoothing filter. Metabolite maps were created by fitting the signal amplitude. Datasets of 4 weighted averages (A) and 1 average (B) were fitted. These maps showed the glucose and water signal intensity 2.5 hours after oral glucose intake and are processed using two reconstruction methods: low-rank and subspace modeling and FFT. **(A)** Note that for the data with 4 averages, metabolite maps looked similar. **(B)** For a single average, the glucose map was more noisy for FFT compared to LRSM reconstruction.

^{31}P multi-echo imaging with low B1^{+} dual-band refocusing pulses

Z. Shams[1], W.J.M. van der Kemp[1], E.C. Wiegers[1], J.J.M. Zwanenburg[1], J.P. Wijnen[1], D.W.J Klomp[1]
[1]Department of Radiology, University Medical Center Utrecht, Utrecht, Netherlands

Synopsis: We developed a multi-echo sequence to detect phosphomonoesters (PME) and phosphodiesters (PDE), aiming for high signal-to-noise and T_2-contrast to noise ratio per unit of time, with the constraint of a maximum available B_1 of ~15μT. In line with MRI, the candidates were multi-echo MRSI with 180° pulses (full refocusing) and fast spin echo (FSE) with modulated variable flip angles. Multi-echo MRSI resulted in higher SNR at the same SAR level compared to a FSE with modulated refocusing flip angles. Using 9 dual-band echo pulses improved the SNR for PDE and PME more than two-fold compared to the FID signal alone.

Purpose

^{31}P MRS can spectrally resolve phospholipid metabolites involved in phospholipid metabolism which are altered in many cancers[1]. 7 Tesla facilitates the detection of PMEs (phosphocholine (PC), phosphoethanolamine (PE)) and PDEs (glycerophosphocholine (GPC), glycerophosphoethanolamine (GPE)) with increased SNR and spectral resolution. Multi-echo MRSI allows T_2-weighted SNR enhancement, for an increased metabolite sensitivity, or T_2 information per metabolite[2,3]. In MR imaging, a widely incorporated method to increase SNR per unit of time is the use of three-dimensional FSE with modulated refocusing flip angles (FA)[4,5]. This employs a very long echo train length (ETL; more than 100 in the brain) using variable, low FAs . We aimed to transfer this method to ^{31}P MRS imaging. We simulated the use of variable FAs FSE in the ^{31}P regime as a new approach for gaining SNR per unit of time within specific absorption rate (SAR) limits. The results were compared with a multi-echo technique with full refocusing pulses. However, the block pulses for this purpose require a high B_1 (i.e. much higher than 15 μT which is maximal available with our ^{31}P body-coil) to excite the frequency range of interest. As a solution, we have designed a dual-band refocusing pulse to be used at a maximum available B_1 of ~15 μT[6]. This pulse selectively hits the two frequency ranges of interest (PDEs and PMEs) with the potential utilization for multi-echo sequences with more than 100 echo pulses. Finally, we implemented the dual-band pulse in a multi-echo MRSI sequence and validated the approach in a phantom and in vivo.

Methods

Simulations

We simulated the effect of extending the ETL on the PDE and PME signals by using refocusing FA modulated FSE technique[5]. T_1 and T_2 of the metabolites used in simulation are listed in Figure 1A. TR=5.5s, nominal FA=15, maximum FA=130, and echo spacing=15ms. Weighted average SNR_{wa} was calculated as in Eq. 1.

$$S_{wa} = S_0 \frac{1+2\sum_{i=1}^{n} S_i w_i}{1+2\sum w_i}, SNR_{wa} = \frac{S_{wa}}{\sigma_{wa}} = SNR_0 \frac{1+2\sum_{i=1}^{n} S_i w_i}{\sqrt{1+2\sum w_i^2}} \quad \text{Eq.1}$$

Where S_0, SNR_0, w_i, S_{wa} and σ_{wa} represent free induction decay (FID) signal, FID SNR, signal weight, weighted average signal and noise, respectively. The signal itself was used as signal weight. To compare, SNR_{wa} and SAR of a multi echo sequence with full refocusing 180s with the same echo spacing of 15ms and the same number of echo pulses (100) was calculated as previously described[2]. FA squared was calculated as an alternative to SAR.

Data Acquisition

MRS measurements were carried out on a 7Tesla MR system (Philips, Best, NL) equipped with a double tuned ^{1}H/^{31}P head coil. We acquired spectra from a phantom containing PME, PDE and inorganic phosphate (Pi) and from a healthy volunteer (female, age: 28). The AMESING[2] sequence (multi-echo) was modified such that the excitation was performed by a block 90° pulse, followed by 180° Shinnar-LeRoux dual-band refocusing pulses (7ms) at 14.8 μT, with two refocusing bandwidths of 166Hz to hit the PDE and PME at 3.0-3.5 ppm and 6.2-6.8 ppm, respectively. A single FID by means of a pulse-acquire and 5 and 9 full echoes in one k-space step where acquired while k-space data were sampled spherically. As a reference, we performed the same experiments on a phantoms using the sequence with adiabatic pulses requiring high B_1 of ~100 μT, which could only be obtained on the phantom surface with a homebuilt dual-tuned surface coil set-up[2,7]. $(B_{1,rms}^{+})^2$ of the dual-band and adiabatic pulses were calculated as: $SAR \propto (B_{1,rms}^{+})^2 = 1/T_p \int_0^{T_p} B_1^{+}(t)^2 \, dt$. All multi-echo MRSI experiments were performed with a matrix size of 8 × 8 × 8, isotropic resolution of 20 mm, 1 average, 256 data points, spectral width 8200 Hz, ΔTE 45 ms (3-fold larger than simulated to minimize truncation artifacts in spectral domain), TR 5 s (in vivo) and 4 s (phantom).

Results

Figure 1 shows the simulated signals of PDE and PME by using modulated FA FSE approach. It produces a refocusing flip angle train that rapidly brings the signals into pseudo-steady-state (PSS) conditions. Figure 2 shows SNR comparison for GPC signal. Multi-echo method with a number of 20 full refocusing 180 pulses resulted in SNR weighted average of 2.13 (considering T_1 relaxation effect). FSE with modulated FAs gave an SNR weighted average of 1.76 at the same FA squared of 673. The spectra acquired from the adiabatic and dual-band ME implementations are shown in Figure 3A and B. Using just 9 pulses increased SNR by more than a factor of 2 (Figure 3D). Figure 4 shows ^{31}P spectra from the brain with PDE and PME signals being refocused by each echo pulse.

Discussion and Conclusion

Simulations showed that we can achieve higher SNR with a full 180 multi-echo sequence than a modulated FAs FSE sequence. Compared to the imaging FSE implementation, the echo spacing in our ^{31}P FSE is much longer (15 ms vs 3 ms) resulting in signal loss due to T_2 relaxation. Using the very low power dual-band pulses, within a TR of 5s the number of echo pulses could be increased when compared to adiabatic pulses ($(B_{1,rms}^{+})^2$ of 0.246 μT^2 compared to 62.277 μT^2), which would result in higher SNR. In addition to increased SNR, T_2 information of the metabolites can be estimated with this implementation. The in vivo results indicated the feasibility of using low power ^{31}P dual-band pulses in multi-echo approaches instead of high power demanding adiabatic pulses.

References

[1] Glunde K, Bhujwalla ZM, et al., Choline metabolism in malignant transformation. Nat. Rev. Cancer, 2011; 11: 835–848.

[2] van der Kemp WJM, Boer VO, et al., Adiabatic Multi-Echo P Spectroscopic ImagiNG (AMESING) at 7 tesla for measuring transverse relaxation times and regaining sensitivity in tissues with short T2* values. NMR Biomed. 2013; 26:1299–1307.

[3] van Houtum Q, Welting D, et al., Low SAR 31P (multi-echo) spectroscopic imaging using an integrated whole-body transmit coil at 7T. NMR in Biomed. 2019;

[4] Busse R, Hariharan H, et al., Fast Spin Echo Sequences With Very Long Echo Trains: Design of Variable Refocusing Flip Angle Schedules and Generation of Clinical *T*2 Contrast. MRM, 2006; 55:1030–1037.

[5] Busse R, Brau A, et al., Effects of Refocusing Flip Angle Modulation and View Ordering in 3D Fast Spin Echo. MRM, 2008; 60:640–649.

[6] Klomp DWJ, van de Bank BL, et al., 31P MRSI and 1H MRS at 7 T: initial results in human breast cancer. NMR Biomed, 2011; 24: 1337–1342.

[7] Shams Z, Wiegers EC, van der Kemp WJM, Klomp DWJ, Wijnen JP, ^{31}P dual-band pulse for selective refocusing of phosphomonoesters and phosphodiesters at low B1 and low SAR. In Proceedings of the 31st Annual Meeting ISMRM, 2021; 4569.

Acknowledgments / Funding Information: We would like to thank EU-Eurostars! 12921 VM-Biopsy for financial support.

	T1 (ms) [1]	T2 (ms) [2]
GPC	5820	213
GPE	6790	214
PC	4310	129
PE	6330	202

1. Jimin Ren, NMRBiomed, 2015
2. Van der Kemp, MRM, 2018

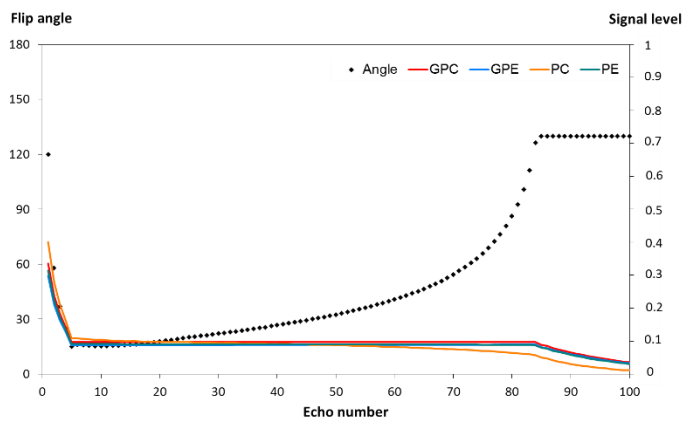

Figure 1.Simulated signals of GPC,GPE, PC and PE, and modulated FA series. The simulated variable echo train is depicted in black. GPC, GPE and PE signal is constant until 1260 ms (echo 84), the PC signal starts to decrease at ~900 ms. Echo-spacing= 15 ms, TR = 5500 and ETL =100.

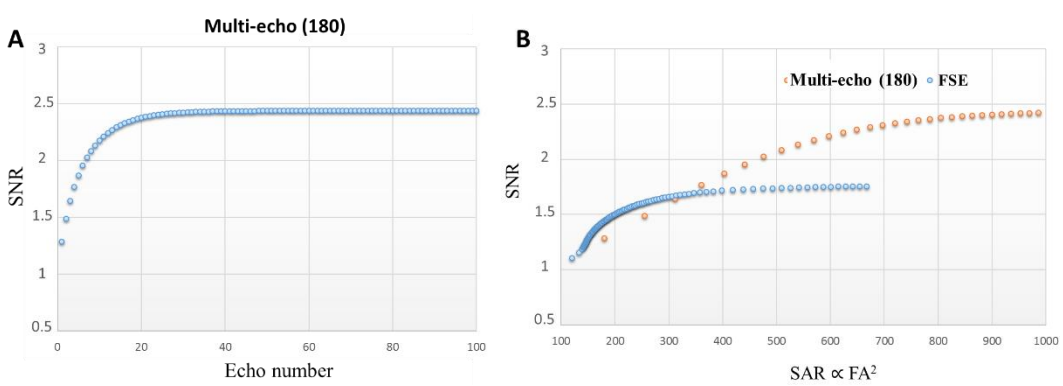

Figure 2. (A) SNR of GPC as a function of number of echo pulses in multi-echo MRSI with 180° pulses. The noise is taken into account with the same T_2 decay weighting as the signal. (B) SNR as a function of SAR in multi-echo MRSI compared with FSE with low FAs. SAR is proportional to the square of the flip angle. The maximum SNR of 1.76 was achieved for FSE with maintaining the signal for relatively long time of 1260 ms. SNR values were calculated from Equations 1. For multi-echo MRSI, the maximum SNR Was 2.13 after taking T_2 relaxation effect into account.

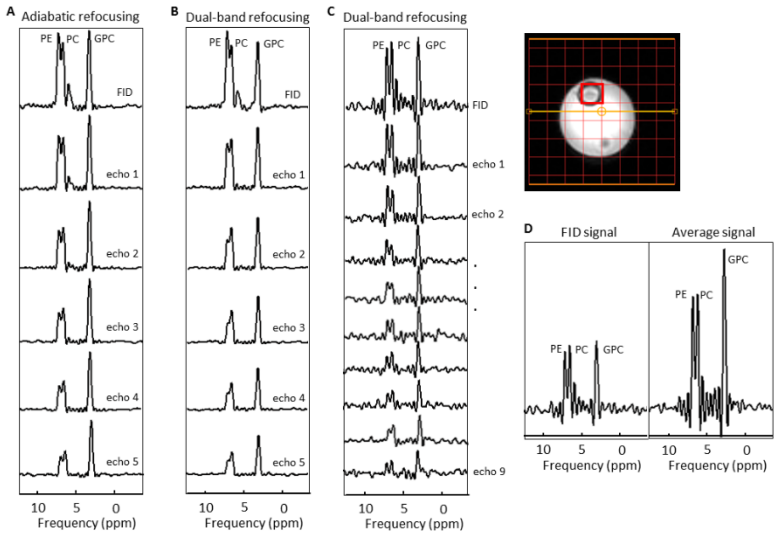

Figure 3. Spectra from a phantom containing PE, PC and GPC using adiabatic (A) and dual-band (B and C) pulses in the multi-echo spectralimaging for the voxel (contains GPC, PC and PE) shown in red. (D) SNR increased by more than 2 after implementing 9 echoes compared to the FID signal. Experiments corresponding to A and B were performed using a surface coil at B_1 of ~100 μT (adiabatic excitation and refocusing) and B_1 of 15 μT (block excitation and dual refocusing), respectively. Experiment C was done utilizing a quadrature head coil at B_1 = 15 μT.

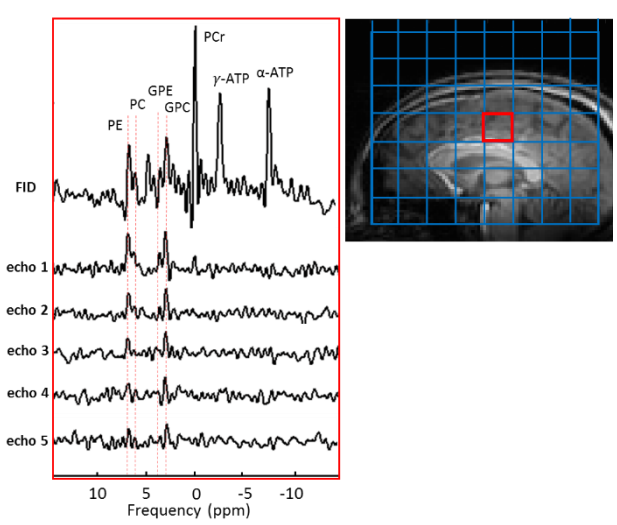

Figure 4. In vivo spectra acquired with dual-band multi-echo (5 echoes) sequence, showing resolved signal of PDE and PME.

Integral 2-dimensional HP-MRS model-fitting with an advanced Levenberg-Marquardt algorithm

D. van Ormondt[1], J.W. van der Veen[2], D. Graveron-Demilly[3]
[1]jMRUI-Branch Delft, Delft, The Netherlands; [2]MRS Core Facility, NIMH, NIH, Bethesda, USA; [3]Université Claude Bernard, Lyon 1,France

Synopsis: MRS of hyperpolarised (HP-MRS) molecules yields 2-dimensional data. One dimension pertains to the FID of the HP-MRS signal at N_{FID} time-points, the other to the concentrations of HP-molecules at N_{HP} time-points. The task is to estimate the N_{PAR} model-parameters of the combined HP-MRS model-function from the data. Assuming the form of this model-function to be known, this estimation is best done with an advanced Levenberg-Marquardt algorithm. This involves computation of $N_{PAR}\times N_{FID}\times N_{HP}$ partial derivatives of the model-function w.r.t. the model-parameters, which is time-consuming. Here we compute >100 times fewer partial derivatives and expect a corresponding reduction of the computing time.

Introduction: For dynamic quantification of hyperpolarised (HP) metabolites[1] with non-linear least-squares (NLLS) model-fitting[2], one needs to derive formulas of the HP-metabolite-concentrations as a function of time. In addition, partial derivatives of the formulas w.r.t. the HP model-parameters must be provided. Despite availability of symbolic algebra-toolboxes, the latter is tedious and error-prone for non-experts. Therefore, it is wise to invoke so-called Automatic Differentiation (AD) which is numeric, accurate, and fast. An advanced Levenberg-Marquardt version of NLLS, featuring AD, is GADfit[3], which we used earlier for 1-dimensional data[4]. We recall that simultaneous processing of all 2-dimensional data together, is more precise than processing 1-dimensional subsets of the data successively[2]. In order to take advantage of relations between data-points of the **2**-dimensional HP-MRS signal, we have adapted the original (real-valued) code of GADfit. This reduced the computation-time drastically.

Methods: The heart of NLLS model-fitting is the computation of the Jacobian matrix $\boldsymbol{J}$ [5]. In the present case, $\boldsymbol{J}$ has N_{PAR} columns and $N_{FID}\times N_{HP}$ rows. The elements of $\boldsymbol{J}$ are the partial derivatives of the HP-MRS model-function w.r.t. the HP-MRS model-parameters. At first sight, as many as $N_{PAR}\times N_{FID}\times N_{HP}$ partial derivatives need be calculated. However, owing to the **2**-dimensional nature of the HP-MRS model-function, each FID-formula occurs N_{HP} times and each concentration-formula of a HP-molecule N_{FID} times. Consequently, the number of *independent* partial derivatives is much smaller than $N_{PAR}\times N_{FID}\times N_{HP}$. Only *independent* partial derivatives need be computed; they serve as building-blocks from which one can assemble a complete Jacobian. Implementation of this fact in the existing code of GADfit necessitated separation of AD of the HP-formulas from that of the NMR-formulas, while preserving parallel computing with co-arrays. Also, we added an alternative AD-algorithm that can handle *complex-valued* NMR-formulas. GADfit is freely down-loadable from https://github.com/raullaasner/gadfit/releases. We use release 1.3 which is based on state-of-the-art Fortran 2018[6]; release 1.4 is an adaptation of 1.3 for use by the C++ community. The HP-MRS signal was simulated as described in Ref.2; see **Fig.1** for the corresponding spectra. The signal used for actual fitting was noise-free, enabling us to establish that the estimated parameter-values equalled the true values with high precision.

Results: The main results are listed in rows 2 and 3 (of 4) of **Table 1**. N_{HP} was set to 100 and N_{FID} to 2048 real-valued points, implying that the HP-MRS model-function was fitted to as many 204800 data-points simultaneously. When using only 1 CPU, *i.e.*, parallel computing turned *off*, the execution time of 1 iteration is reduced from 56 s in the original version to 67 ms in our version, amounting to *acceleration by a factor of* 836. When using all 4 CPUs of the same PC, *i.e.*, parallel computing turned *on*, the acceleration factor is less, but still as high as 366. (From Table 1, one would expect $t_{iteration}$=0.067×15/56=0.019.) Apparently, our version does not yet optimally implement parallel computing. Furthermore, note that convergence of the fit needs 9 iterations in the original version, *vs* 22 iterations in our version; see row 4.

Discussion: This Abstract concerns work in progress. The main goal, reduction of the computing-time by at least two orders of magnitude by exploiting relations between data-points of the 2-dimensional HP-MRS signal, has been achieved. This needed some drastic adaptation of the use of AD which is intertwined with parallel computing via co-arrays, in object-oriented fashion. As mentioned in **Results,** parallel computing in our version does not yet live up to its potential. Yet, we aim to preserve all advanced Levenberg-Marquardt features implemented in GADfit's original version. The latter and convergence-speed will be addressed in future research.

Conclusion: We accelerated the advanced Levenberg-Marquardt program GADfit by two orders of magnitude for application to HP-MRS data. This enabled fitting to all 204800 data-points simultaneously within a second. The acceleration can be increased further by improving our handling of parallel computing with co-arrays.

References:

1. Larson PEZ, Vigneron DB, Kurhanewicz, J, *et al*. Clinical translation of hyperpolarized **13**C pyruvate and urea MRI for simultaneous metabolic and perfusion imaging. MAGN RESON MED. 10 August 2021. https://doi.org/10.1002/mrm.28965.

2. van Ormondt D, de Beer R, van der Veen JW, Graveron-Demilly D. Simultaneous processing of two-dimensional hyperpolarised ^{13}C-MRS data directly in the time-domain. Proc. ISMRM-Benelux, 2017.

3. Laasner R. Global nonlinear optimization with automatic differentiation and coarrays. https://github.com/raullaasner/gadfit.

4. van Ormondt D, de Beer R, van der Veen JW, Graveron-Demilly D. Reduction of MRSI postprocessing-time by using Co-array-Semantics. Proc. ISMRM-Benelux, 2019.

5. van Ormondt D, de Beer R, van der Veen JW, Graveron-Demilly D. Concatenating all data acquired in hyperpolarised ^{13}C-MRS increases precision. Proc. ISMRM-Benelux, 2018.

6. Curcic M. Modern Fortran. eBook, Manning, Shelter Island, 2020.

Acknowledgments / Funding Information: No funding.

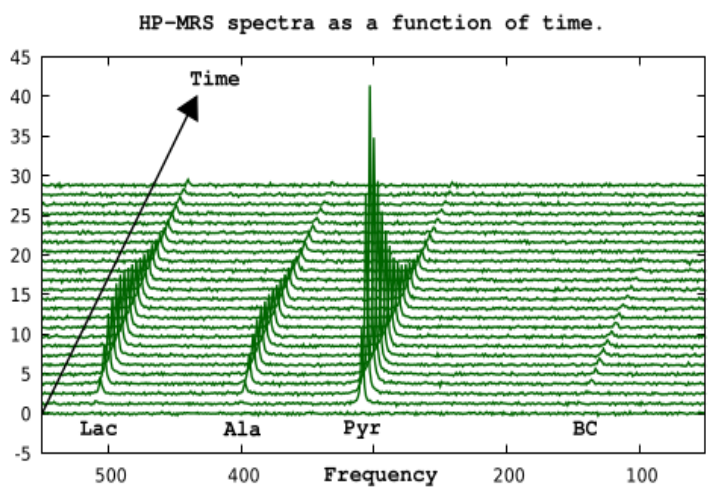

Figure 1. Evolution of the FFT of the simulated HP-MRS signal, after injection of HP ^{13}C-Pyr, using the same parameters as in Ref.2, plus added Gaussian noise. Frequency in arbitrary units.

***Table 1**: Computation-times per iteration for the original and present versions of GADfit, and number of iterations used in each.*

GADfit	original	present
$t_{\text{iteration}}$ using 1 CPU	56 s	0.067 s
$t_{\text{iteration}}$ using 4 CPUs	15 s	0.041 s
iterations	9	22

Single-shot 3T ^{1}H MRS with dual water/lipid VAPOR suppression for intrahepatic acetylcarnitine detection

M.Buitinga[1,2], J. Mevenkamp[1], F. Haans[1], K. Brouwers[1], P. Schrauwen[2], L. Lindeboom[1,2], J.E. Wildberger[1], V.B. Schrauwen-Hinderling[1,2]

[1] *Department of Radiology & Nuclear Medicine*, Maastricht University Medical Center, Maastricht, The Netherlands; [2] *Department of Nutrition & Movement Sciences*, University of Maastricht, Maastricht, The Netherlands

Synopsis: We have developed a novel 3T ^{1}H-MRS sequence to detect acetylcarnitine. Acetylcarnitine has been investigated by ^{1}H-MRS in muscle and is thought to play an important role in maintaining metabolic flexibility and insulin sensitivity. As decreased metabolic flexibility and insulin sensitivity are hallmarks of metabolic disease, techniques to study acetylcarnitine levels non-invasively are of great interest. The advantage of the new approach is the absence of subtraction schemes and a high signal intensity, while lipid resonances are sufficiently suppressed to uncover acetylcarnitine. This makes the sequence suitable for acetylcarnitine detection in tissues susceptible to respiratory motion, such as the liver.

Purpose: The conversion of excessive acetyl-coA into acetylcarnitine has been suggested to play an important role in maintaining metabolic flexibility and insulin sensitivity under conditions of excessive substrate supply to the mitochondria.[1,2] As decreased metabolic flexibility and insulin sensitivity are early indicators of the development of metabolic disease, such as type 2 diabetes mellitus (T2D)[3] and non-alcoholic fatty liver disease (NAFL)[4], the development of non-invasive techniques to quantitatively assess acetylcarnitine concentrations *in vivo*, are of great interest. We previously quantified acetylcarnitine levels by 3T ^{1}H-MRS in skeletal muscle of healthy and metabolically compromised individuals[5,6]. Our results in skeletal muscle clearly support the premise that acetylcarnitine concentrations associate with insulin sensitivity. To further unravel the role of acetylcarnitine in the development of metabolic diseases, we sought to develop a ^{1}H-MRS sequence that enables the study of this metabolite in the liver. Reliable detection of acetylcarnitine by MRS techniques is hampered by overlapping broad lipid resonances, Our previously developed editing sequences made use of differences in spin-lattice (T_1) and transversal (T_2) relaxation times between acetylcarnitine and lipids[5,6]. The most effective lipid suppression was obtained by a subtraction-based T_1 editing approach with a long TE of 350ms[6]. However, as the liver moves with respiration, such a subtraction-based method is sensitive to motion-induced artifacts and therefore infeasible. Here, we propose a single-shot approach with dual water/lipid suppression based on the variable pulse power and optimized relaxation delays (VAPOR) scheme.

Methods: The VAPOR scheme is originally designed to only suppress water[7]. The advantage of the VAPOR sequence is its relative insensitivity to inhomogeneities in transmit B_1 field of the RF coil and variations in T_1. The original sequence consists of eight frequency-selective RF pulses of which the timing and flip angles were optimized to null a large range of water T_1[7]. To get dual water and lipid suppression, two of the RF pulses were exchanged for inversion pulses (BW75Hz) of which the frequency was set at 2.13ppm (acetylcarnitine region). The timing of the two inversion pulses and the timing and relative flip angles of the remaining six VAPOR pulses were optimized through computer simulations in MATLAB (MATLAB 2018b, The MathWorks,Inc.). The voxel used was 40mm x 20mm x 60mm. All spectra were acquired with a TR of 7500 ms, TE of 266ms, number of acquired data points of 2048, and number of averages (NSA) of 16. The TE equals $2/J_{\alpha\text{-carbonyl}}$ and was chosen to refocus J-coupling of $\alpha-$carbonyl, the resonance closest to acetylcarnitine. The optimized sequence with the simulations are depicted in figure 1. To test the MRS sequence, we acquired ^{1}H-MRS spectra (Achieva 3T MRI, Philips Health Care) of phantoms with 10% intralipid (a soybean oil emulsion (Fresenius Kabi)) in physiological salt including 0mM, 2mM, or 5mM of acetylcarnitine (Sigma Aldrich) and 2% agar (Invitrogen). A regular PRESS with a TE of 266ms and without water and lipid suppression was acquired to use the unsuppressed water signal as an internal reference. To assess the performance of our newly developed sequence (iVAPOR) in comparison to the formerly established sequences for the muscle, we also acquired spectra with the subtraction-based T_1 editing sequence with a TE of 350ms[6]. All obtained spectra were post-processed in a custom-written MATLAB script as previously described[8]. Acetylcarnitine content was calculated after T_2 correction relative to the unsuppressed water resonance.

Results: The PRESS spectrum of the phantom with 10% intralipid and 5mM acetylcarnitine (figure 2a) clearly demonstrates the broad lipid resonances that overlap the acetylcarnitine resonance when no lipid suppression is applied. The acetylcarnitine peaks could be revealed in the phantoms containing 2mM and 5mM acetylcarnitine by supressing the lipid resonances using either the subtraction-based T_1 editing sequence (figure 2b) or the iVAPOR sequence (figure 2c). Due to the lower TE of the iVAPOR sequence, the signal intensity of the acetylcarnitine peak was higher (figure 2c) when compared with the acetylcarnitine peak obtained with the subtraction-based T_1 editing sequence (figure 2b). Integration of the peaks resulted in comparable values when corrected for T_2 decay, indicating that both methods work effectively. Measured acetylcarnitine levels by the iVAPOR sequence strongly correlated with the known phantom concentrations.

Discussion and conclusion: Our iVAPOR approach allows the detection of acetylcarnitine in a single-shot, circumventing subtraction artefacts associated with our previously developed T_1 editing sequence[6]. The use of inversion pulses makes the iVAPOR approach intrinsically more sensitive to variations in T_1 relaxation times, though the absence of a subtraction scheme and a higher signal intensity make this sequence more suitable for detection in tissues susceptible to respiratory motion, such as the liver. Future studies should focus on reproducibility measurements and *in vivo* validation steps in the muscle and liver.

References:

1. Noland RC, Koves TR, Seiler SE, et al. Carnitine insufficiency caused by aging and overnutrition compromises mitochondrial performance and metabolic control. *J Biol Chem*. 2009;284(34):22840-22852. doi:10.1074/jbc.M109.032888
2. Muoio DM, Noland RC, Kovalik JP, et al. Muscle-specific deletion of carnitine acetyltransferase compromises glucose tolerance and metabolic flexibility. *Cell Metab*. 2012;15(5):764-777. doi:10.1016/j.cmet.2012.04.005
3. Czech MP. Insulin action and resistance in obesity and type 2 diabetes. *Nat Med*. 2017;23(7):804-818. doi:10.1038/nm.4350.Insulin
4. Manco M. Insulin Resistance and NAFLD: A Dangerous Liaison beyond the Genetics. *Children*. 2017;4(8):74. doi:10.3390/children4080074
5. Lindeboom L, Nabuurs CI, Hoeks J, et al. Long-echo time MR spectroscopy for skeletal muscle acetylcarnitine detection. *J Clin Invest*. 2014;124(11):4915-4925. doi:10.1172/JCI74830
6. Lindeboom L, Bruls YMH, van Ewijk PA, et al. Longitudinal relaxation time editing for acetylcarnitine detection with 1H-MRS. *Magn Reson Med*. 2017;77(2):505-510. doi:10.1002/mrm.26149
7. Tkáč I, Deelchand D, Dreher W, et al. Water and lipid suppression techniques for advanced 1H MRS and MRSI of the human brain: Experts' consensus r ecommendations. *NMR Biomed*. 2021;34(5):1-25. doi:10.1002/nbm.4459
8. Roumans KHM, Lindeboom L, Veeraiah P, et al. Hepatic saturated fatty acid fraction is associated with de novo lipogenesis and hepatic insulin resistance. *Nat Commun*. 2020;11(1):1-11. doi:10.1038/s41467-020-15684-0

Acknowledgments / Funding Information: Vera Schrauwen-Hinderling was supported by an ERC starting grant (grant no. 759161 'MRS in diabetes')

Figure 1.

Figure 1: iVAPOR sequence with six water suppression pulses and 2 inversion pulses at the acetylcarnitine resonance. Calculated time dependence of the water, lipid and acetylcarnitine resonances for three different values of the flip angle (different B1 of the RF coil (β))(90°(red), 60° (black), 130°(blue)). Optimized time delays t1= 100 ms, t2= 100 ms, t3= 43 ms, t4= 67 ms, t5= 43 ms, t6= 164 ms, t7= 43 ms, t8= 48 ms.

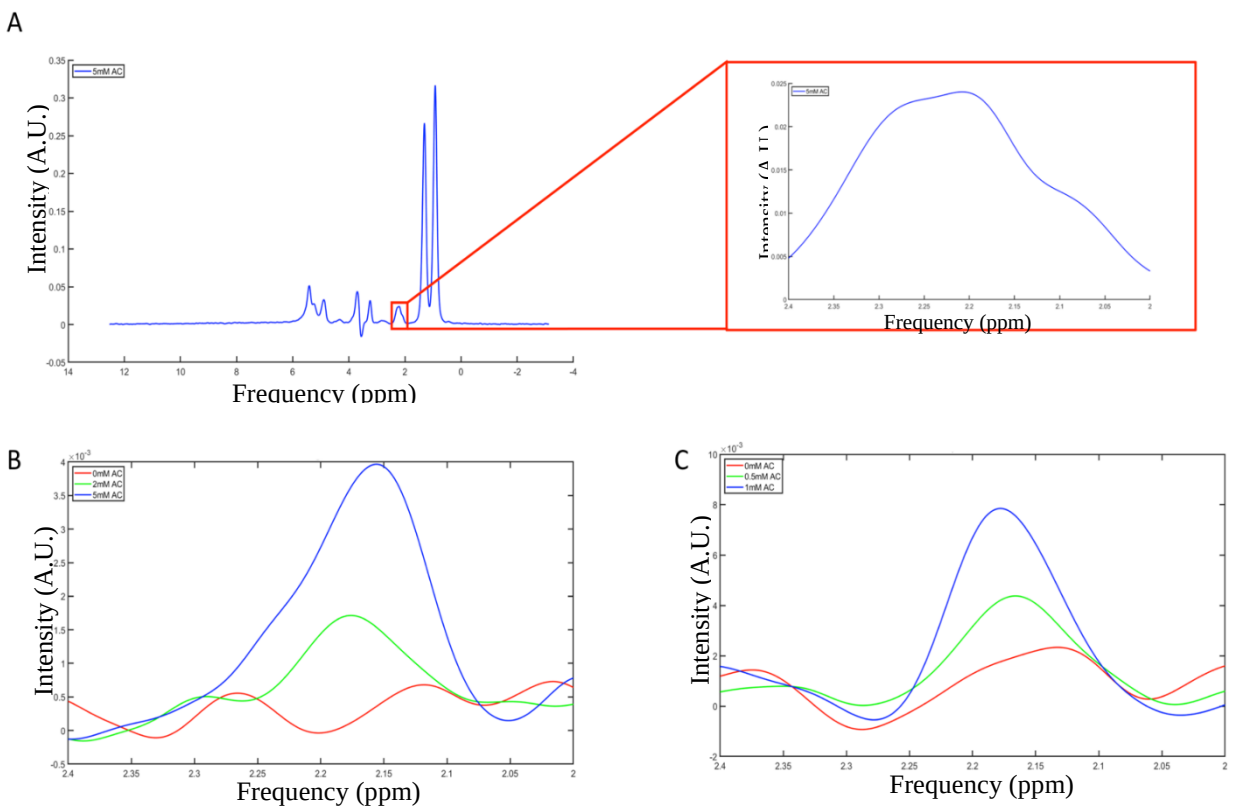

Figure 2: Spectra obtained in phantoms containing 10% intralipid and 0mM (red), 2mM (green), or 5mM (blue) acetylcarnitine. a) PRESS sequence with a TE of 266ms of a phantom with 10% intralipid and 5mM acetylcarnitine. b) Subtraction-based T_1 editing sequence with a TE of 350ms. c) iVAPOR sequence with a TE of 266ms

Protocol Optimization of Spectro-Dynamic MRI

M.H.C. van Riel[1], N.R.F. Huttinga[1], T. Bruijnen[1], and A. Sbrizzi[1]
[1]Department of Radiotherapy, Computational Imaging Group for MR diagnostics and therapy, UMC Utrecht, Utrecht, Netherlands

Synopsis: Inferring dynamical information from (bio)mechanical systems at a high temporal resolution can be very valuable for cardiovascular or musculoskeletal applications. Spectro-dynamic MRI is a recently proposed method that combines a measurement model and a dynamical model to characterize dynamical systems directly from k-space data. Both the displacement fields and the underlying dynamical parameters are estimated. In this work, different sampling trajectories and acquisition orderings are used to investigate the trade-off between temporal resolution and k-space coverage. A phantom experiment shows that it is possible to reconstruct a moving image from the estimated dynamics at a temporal resolution of 4.4 ms.

Introduction: The human body can be seen as an aggregate of dynamical systems (e.g. the cardiac and musculoskeletal systems). 3D dynamic information about these systems is important for scientific and diagnostic purposes[1,2], but acquiring this data at high spatial and temporal resolutions is extremely challenging.

We have developed spectro-dynamic MRI[3] as a method to estimate time-resolved dynamic information directly from k-space data. Using a particular repeating sampling strategy, the motion fields and the underlying mechanical parameters can be reconstructed from highly undersampled k-space data.

In this work, we investigate several sampling patterns for spectro-dynamic MRI. A rigidly moving object was simulated with different sampling patterns and data orderings. The displacement fields and dynamic system parameters (the natural frequency) were estimated. Furthermore, we reconstructed time-resolved images of a phantom from the motion-corrupted k-space data at a temporal resolution of 4.4 ms.

Theory: Assuming conservation of magnetization, a measurement model G can be constructed, explicitly describing the impact of motion on the MR signal. G contains spatial and temporal derivatives of the steady-state magnetization $m(\mathbf{r},t)$ and the displacement field $\mathbf{u}(\mathbf{r},t)$[3]:

$$G(\mathbf{u}, m, \mathbf{r}, t) = \frac{\partial}{\partial t} m(\mathbf{r}, t) + \nabla m(\mathbf{r}, t) \cdot \frac{\partial}{\partial t}\mathbf{u}(\mathbf{r}, t) + m(\mathbf{r}, t)\left[\nabla \cdot \frac{\partial}{\partial t}\mathbf{u}(\mathbf{r}, t)\right] = 0.$$

To evaluate the temporal derivatives, finite difference schemes can be used, but the accuracy depends on the time difference Δt between two successive measurements at the same coordinates. Acquiring fully sampled 3D images within a few milliseconds is impossible, but repeated sampling of the same k-space point can be done within that time frame. By transforming G to the spectral domain (k-space), we obtain the measurement model in terms of the measured k-space data $M(\mathbf{k},t)$ and the Fourier transform of the displacement field $\mathbf{U}(\mathbf{k},t)$:

$$G(\mathbf{U}, M, \mathbf{k}, t) = \frac{\partial}{\partial t} M(\mathbf{k}, t) + i2\pi \sum_{j=1}^{d} k_j \, M(\mathbf{k}, t) * \frac{\partial}{\partial t} U_j(\mathbf{k}, t) + i2\pi \sum_{j=1}^{d} M(\mathbf{k}, t) * k_j \frac{\partial}{\partial t} U_j(\mathbf{k}, t) = 0,$$

with summations over the d spatial dimensions (2 in our experiments). To allow for heavily undersampled data, a dynamical model F is added, describing the dynamics of the underlying system. As a simple test scenario, we use a spherical pendulum:

$$F(\mathbf{u}, \boldsymbol{\theta}, t) = \frac{d^2}{dt^2}\mathbf{u}(t) + \omega^2 \mathbf{u}(t) = 0.$$

F is parameterized by the displacement field, which is spatially independent in this example, and a set of dynamical parameters $\boldsymbol{\theta}$, in this case the natural frequency $\omega = \sqrt{g/l}$ of the pendulum.

By solving a single optimization problem, the displacement field $\mathbf{u}$ and the dynamical parameters $\boldsymbol{\theta}$ can be estimated simultaneously:

$$\min_{\mathbf{u},\boldsymbol{\theta}} |G(\mathbf{u}, M, \mathbf{k}, t)|_2^2 + \lambda |F(\mathbf{u}, \boldsymbol{\theta}, t)|_2^2.$$

Methods: *Simulation:* A spherical pendulum with rigid harmonic oscillatory motion in both the *x*- and *y*-directions and friction was simulated. The friction was not included in the reconstruction to study the effect of model imperfections.

Cartesian, Radial and Spiral sampling trajectories were considered to investigate the trade-off between the temporal resolution Δt and the k-space coverage per time point (Fig. **Error! Reference source not found.**(a)). Furthermore, each trajectory was simulated with three different orderings (Fig. **Error! Reference source not found.**(b)): Repeated ($\Delta t = TR$), interleaved ($\Delta t = 3 \cdot TR$) and linear ($\Delta t = N \cdot TR$), with a TR of 4.4 ms. The repeated ordering has the highest temporal resolution, at the cost of less k-space coverage per time point. We used $N = 12$, which is too low to reconstruct images at a useful spatial resolution (as shown by the artifacts in Fig. **Error! Reference source not found.**), but sufficient to estimate dynamic information.

The estimated displacements were compared to the ground truth values using the root mean square error (RMSE).

Phantom: A spherical pendulum made from Lego (Fig. **Error! Reference source not found.**) with a gel-filled tube was used to acquire MR data with a 1.5T MRI scanner (Ingenia, Philips Healthcare). A 2D coronal spoiled gradient echo (SPGR) scan with a repeated Cartesian trajectory was used ($TR/TE = 4.4/2.1$ ms, $FA = 9°$). Time-resolved images were reconstructed by correcting the k-space data with the estimated displacements.

Results: *Simulation:* The estimated displacements (Fig. **Error! Reference source not found.**) for the linear ordering show an error at the start of each experiment, where the amplitude and velocity are highest. The radial repeated pattern fails, since the measurements lack dynamic information in the direction perpendicular to the readout direction. This does not occur for spiral trajectories, and for Cartesian patterns it only occurs for the line through the center of k-space.

The Cartesian trajectory has the lowest $RMSE_x$ (Table **Error! Reference source not found.**), but results in a slightly larger error in the phase encode direction. For all trajectories, the interleaved ordering results in the highest accuracy.

Phantom: Fig. **Error! Reference source not found.** shows the reconstructed images of the moving phantom at one point in time. The undersampling in the phase encode direction causes artifacts. Since the repeated ordering was used, the temporal resolution is equal to the TR (4.4 ms).

Discussion: The RMSE values show that interleaved acquisitions result in the highest accuracy. Furthermore, unlike Cartesian trajectories, non-Cartesian trajectories do not suffer from systematically lower accuracy in the phase encode direction.

In the future, we would like to explore joint estimation of the dynamics and image reconstruction, and extend spectro-dynamic MRI to non-rigid motion and 3D acquisitions. In order to model more complex in-vivo systems, techniques employed in data-driven discovery of dynamical systems[4–6] could be leveraged to provide dynamical models with reduced complexity from measured data.

Conclusion: We have extended the spectro-dynamic MRI framework to more flexible sampling strategies. An interleaved ordering showed the highest accuracy. The displacement fields and the dynamical parameters could be estimated from k-space data, in simulation and in a phantom experiment. Moving images could be reconstructed from the data and the estimated displacements. These results can be used in further developments of spectro-dynamic MRI toward in-vivo applications.

References:

1. Amzulescu MS, de Craene M, Langet H, et al. Myocardial strain imaging: Review of general principles, validation, and sources of discrepancies. European Heart Journal Cardiovascular Imaging. 2019;20(6):605-619. doi:10.1093/ehjci/jez041

2. Shapiro LM, Gold GE. MRI of weight bearing and movement. Osteoarthritis and Cartilage. 2012;20(2):69-78. doi:10.1016/j.joca.2011.11.003

3. van Riel MHC, Huttinga NRF, Sbrizzi A. Spectro-Dynamic MRI: Characterizing Bio-Mechanical Systems on a Millisecond Scale. Proceedings of the 29th Annual Meeting of ISMRM. 2021;0904.

4. Daniels BC, Nemenman I. Automated adaptive inference of phenomenological dynamical models. Nature Communications. 2015;6:1-8. doi:10.1038/ncomms9133

5. Brunton SL, Kutz JN. Data-Driven Science and Engineering. Cambridge University Press; 2019. doi:10.1017/9781108380690

6. Rudy SH, Kutz JN, Brunton SL. Deep learning of dynamics and signal-noise decomposition with time-stepping constraints. Journal of Computational Physics. 2019;396:483-506. doi:10.1016/j.jcp.2019.06.056

Acknowledgments / Funding Information: We would like to thank Nico van den Berg and Hannah Liu for their help and advice regarding the execution of the experiments and the analysis of the data.

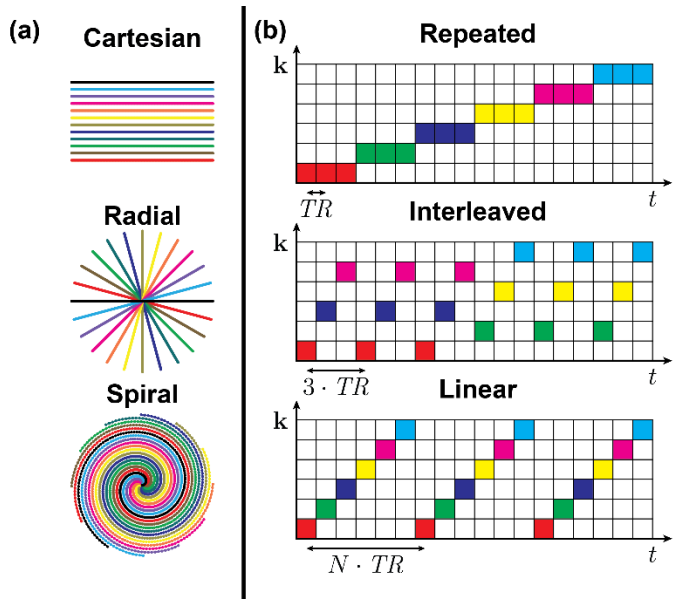

Figure 1: (a) Cartesian (top), radial (middle) and spiral (bottom) sampling trajectories. (b) Schematic representations of the repeated (top), interleaved (middle) and linear (bottom) sampling orderings. Each colored square represents one readout. The repeated ordering samples the same readout multiple times (3 times in this simple schematic, typically dozens of times in practice), while the linear ordering samples all N readouts (12 in our experiments) before repeating. The interleaved ordering is a hybrid between the other two orderings.

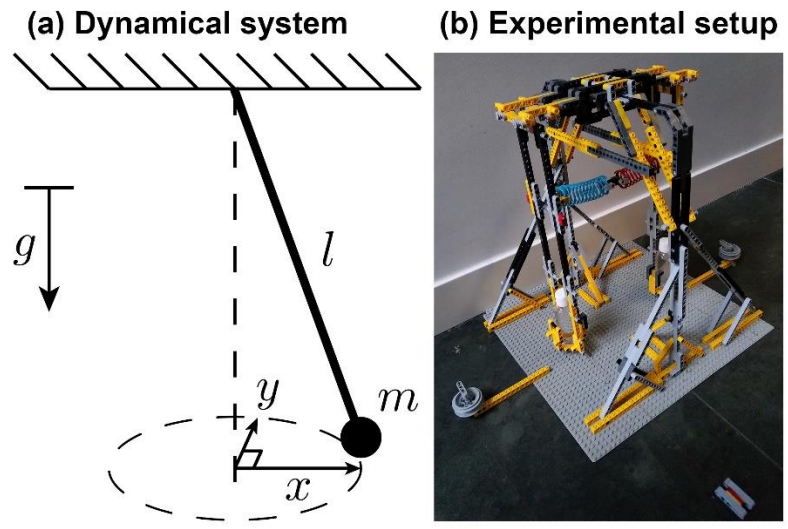

Figure 2: (a) Schematic overview of a spherical pendulum with length l, mass m, and gravitational acceleration g. The pendulum is able to swing in the x- and y-directions, and its tip traces the shape of an ellipse. (b) Experimental setup of the spherical pendulum, with a tube at the end of the pendulum generating MR contrast.

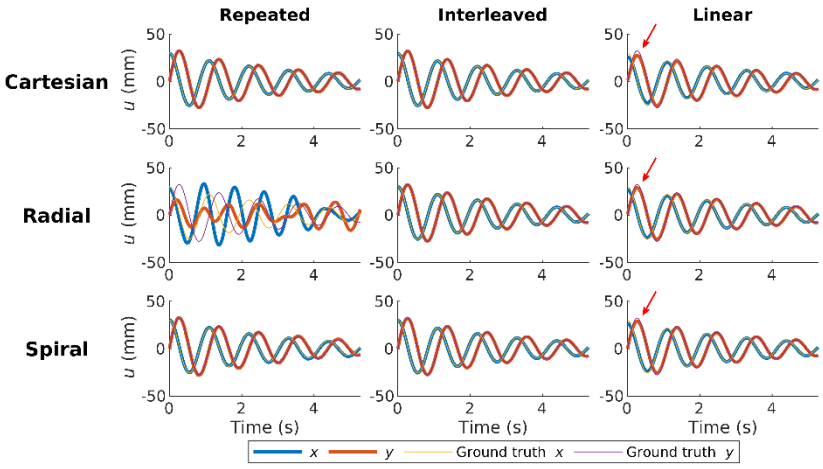

Figure 3: Estimated and ground truth x- and y-displacements for each sampling pattern. The reconstruction for the repeated radial pattern fails since a single radial spoke that crosses the center of k-space does not encode motion perpendicular to the readout direction. The linear ordering has a reduced accuracy for all trajectories (see the errors at the red arrows), as the Δt becomes too large for accurate finite differences.

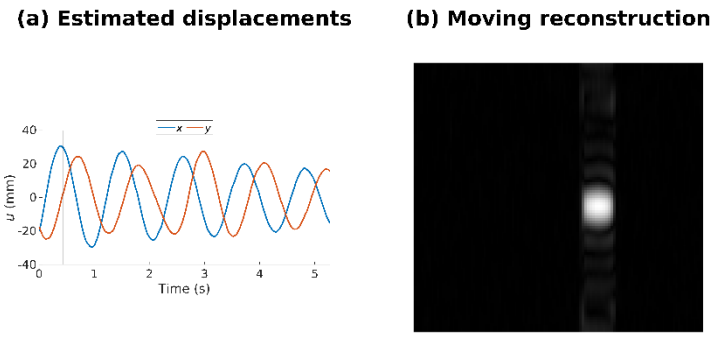

Figure 4: (a) Estimated displacements of the spherical pendulum. (b) Reconstructed image at one point in time. The vertical line in (a) indicates the time of the current image. For each time point, all readout lines were corrected to the estimated position as shown in (a), followed by a Fast Fourier transform. The artifacts in the phase encode (vertical) direction are caused by the high undersampling in that direction, while the temporal resolution is equal to the TR (4.4 ms).

Trajectory	Ordering	$\mathbf{RMSE}_x$ [mm]	$\mathbf{RMSE}_y$ [mm]	ω [rad/s]
Cartesian	Repeated	0.17	0.29	5.80
	Interleaved	**0.12**	0.15	**5.72**
	Linear	1.09	1.51	5.79
Radial	Repeated	17.94	11.93	7.37
	Interleaved	0.13	0.13	5.75
	Linear	0.87	1.05	5.66
Spiral	Repeated	0.58	0.57	5.82
	Interleaved	0.20	**0.11**	5.72
	Linear	0.86	1.02	5.68

Table 1: RMSE of the estimated displacements in both directions compared to the ground truth, and the estimated frequencies of the dynamical system. The true frequency during simulation was 5.72 rad/s. Bold values indicate the estimations with the smallest error (the estimated frequency for the Cartesian interleaved pattern was slightly more accurate than for the spiral interleaved pattern). The interleaved ordering has the highest accuracy for all trajectories. Also note that the Cartesian trajectory systematically performs worse in the phase encode (y) direction.

Glycogen accumulation in the brain of classic-infantile Pompe patient measured with single-voxel ^{1}H MRS and 2D-MRSI at 7T

C. Najac[1], V.O. Boer[2], N.A.M.E. van der Beek[3], A.T. van der Ploeg[4], I. Ronen[1], J.M.P. van den Hout[4], H.E. Kan[1]

[1]C.J. Gorter Center for High Field MRI, Dept of Radiology, Leiden University Medical Center, Leiden, Netherlands, [2]Danish Research Centre for Magnetic Resonance, Centre for Functional and Diagnostic Imaging and Research, Copenhagen University Hospital Amager and Hvidovre, Copenhagen, Denmark, [3]Center for Lysosomal and Metabolic diseases, Dept of Neurology, Erasmus MC University Medical Center, Rotterdam, Netherlands, [4]Center for Lysosomal and Metabolic diseases, Dept of Pediatrics, Erasmus MC University Medical Center, Rotterdam, Netherlands

Synopsis: Pompe disease is caused by an abnormal accumulation of glycogen in the lysosomes of multiple tissues including the brain due to a deficit in acid α-glucosidase (GAA). The development of enzyme replacement therapy with recombinant human GAA (rhGAA) has dramatically improved patients' survival, however, rhGAA does not reach the brain which remains untreated. Consequently, classic-infantile Pompe patients may develop progressive white matter lesions and cognitive problems. Here, we used single-voxel ^{1}H MRS and spectroscopic imaging and found an accumulation of glycogen and significant decrease in total-N-acetyl-aspartate in the brain of classic-infantile patients (n=3) when compared to age-matched healthy controls (n=3).

Introduction:

Glycogen storage disease type II, also known as Pompe disease, is a rare autosomal recessive disorder caused by a deficit in the lysosomal glycogen degradation enzyme, acid α-glucosidase (GAA)[1]. Classic-infantile Pompe patients are the most affected and do not reach the age of one year, if untreated. Enzyme replacement therapy with recombinant human acid α-glucosidase (rhGAA) has dramatically improved patient survival[2]. rhGAA, however, does not cross the blood-brain-barrier (BBB) and thus the brain remains unaffected by the treatment. As classic-infantile patients get older, a new phenotype appears, showing hampering or even decline of cognitive development[3,4]. Conventional brain imaging has shown white matter (WM) lesions in the brain of classic-infantile patients, which progressively spread with increasing age[3,4]. Post-mortem studies in Pompe disease demonstrated that glycogen accumulates in lysosomes within neurons of the cerebral cortex, brainstem, and spinal cord and in glial cells of the WM and the cerebral cortex[5]. This suggests that cell-specific neurochemical profile might be affected in Pompe disease. Here, we investigated the potential of single-voxel ^{1}H MRS (SVS) and spectroscopic imaging (MRSI) at 7T to provide a non-invasive readout of glycogen accumulation and other metabolic alterations in the brain of classic-infantile Pompe patients.

Materials and methods:

Subjects: Three classic-infantile patients (9, 14, and 16yo) and three age-matched healthy controls participated in this study so far. Patient diagnosis was confirmed by enzyme activity assays and mutation analysis in the first 6 months after birth, and patients were treated with a dose of rhGAA of 40mg/kg/week at the time of the MRI/MRS scans. Patient characteristics and longitudinal neuropsychological evaluations are given in **Fig.1**. MRI performed at 3T showed that all patients already presented abnormal WM lesions one year before our study. Study protocols were approved by the institutional review board and written informed consent was obtained.

MR setup: Experiments were conducted on a 7T whole-body MRI scanner (Philips Healthcare, The Netherlands) equipped with a volume transmit/32-channel receive head coil (Nova Medical, USA).

In vivo MR protocol and post-processing: A 3D-T_1W gradient-echo (TR/TE=5.5/2.5ms, resolution 1x1x1mm^3) and a multi-slice multi-echo (TR/TE_1/TE_2=4385/27/100ms, resolution 1.3x1.3x4mm^3) acquisitions were performed and used for positioning of the volume-of-interest (VOI). SVS data were acquired using a sLASER sequence (TR/TE=6500/34ms, NSA=32, acq. time~5min) from a 18x18x18mm^3 VOI positioned in the left frontal periventricular WM region (**Fig.2B**). For 2D-MRSI acquisition, volume pre-selection was performed using sLASER (TR/TE=5000/36-38ms, volume dimensions (AP,RL,FH)=130x90x10mm^3). Spatio-spectral encoding for the spectroscopic imaging was done using a concentric rings readout trajectory[6] (FOV (AP,RL)=240x240mm^2, voxel size=10x10mm^2, slice thickness (FH)=10mm, acq. time~11min). FOCI refocusing pulses were used both for SVS and 2D-MRSI acquisitions to minimize in-plane chemical shift displacement errors Outer-volume-suppression targeting lipid signal was performed using ten saturation bands interleaved with the water suppression and positioned circularly around the selected volume. SVS and 2D-MRSI data were reconstructed using in-house Matlab routines[7] and spectra were fitted with LCModel[8] with respective basis-sets.

Glycogen phantom: A 28mM glycogen solution was prepared by mixing glycogen from rabbit liver (Sigma) with water. Data were acquired using same protocol as for SVS *in vivo* acquisition. The spectrum was corrected for frequency-drift and the residual water peak was removed with a linear prediction singular value decomposition Matlab-based routine. The resulting glycogen spectrum was added to the LCModel basis-sets to fit glycogen signal *in vivo*.

Statistical analysis: Statistical significance was tested using an unpaired Student's *t*-test with Welch's correction and assuming unequal variance (*$p < 0.05$, **$p < 0.01$, ***$p < 0.001$, GraphPad Software, USA).

Results and discussion:

As illustrated in **Fig.1&2**, Pompe patients presented a decline in total intelligence and performance test scores, and showed widespread WM lesions on conventional T_2-weighted images at time of the MRI. This is in agreement with previous reports[3,4]. **Fig.3A** shows SVS data acquired in Pompe patients (*panels A/C*) and healthy controls (*panels B/D*). A clear shift in the neurochemical profile is observed in all three patients, particularly, a large increase in signal between 3.5-4ppm attributed to glycogen, in agreement with expected glycogen accumulation in the brain of Pompe patients. The significant increase in glycogen was observed in combination with a significant increase in myo-inositol (Ins) and decrease in tNAA (NAA+NAAG) in patients compared to healthy controls (**Fig.3B**). As the signal of glycogen and Ins partially overlap at 3.6ppm (**Fig.3A**), quantification of Ins in patients is possibly compromised. The decrease in tNAA reflects neuronal damage in WM lesions and corroborates previous reports[9]. MRSI results were in line with the SVS data and showed a significant presence of glycogen as well as a significant lower level of tNAA across the slice in patients (**Fig.4**). On the T_2-weighted images, WM in the patients showed large hyperintense areas, possibly reflecting tissue damage associated with the glycogen accumulation seen on the MRSI.

Conclusion:

We illustrated the potential of MRS, both in SVS and in 2D-MRSI mode, to monitor the accumulation of glycogen in the brain of Pompe patients. As innovative treatment strategies which target both muscles and the brain are currently under development, MRS(I) could serve as a non-invasive readout to monitor disease progression and response to treatment. In addition, as neurochemical changes often precede macrostructural damages, MRS(I) might serve as an early biomarker for the effect of Pompe disease on the brain.

References:

[1] van der Ploeg, A.T., Reuser, A.J.J. Lysosomal storage disease 2 - Pompe's disease. Lancet (2008).
[2] Van den Hout, J.M.P. et *al.*, Recombinant human alpha-glucosidase from rabbit milk in Pompe patients. Lancet (2000).
[3] Ebbink, B.J. et *al.*, Cognitive decline in classic infantile Pompe disease: An underacknowledged challenge. Neurology (2016).
[4] Ebbink, B.J. et *al.*, Classic infantile Pompe patients approaching adulthood: a cohort study on consequences for the brain. Dev Med Child Neurol (2018).
[5] Dasouki, M. et *al.*, Pompe disease: literature review and case series. Neurol Clin (2014).
[6] Emir, U.E. et *al.*, Non-water-suppressed short-echo-time magnetic resonance spectroscopic imaging using a concentric ring k-space trajectory. NMR Biomed (2017).
[7] Magnusson, P.O. et *al.*, Gamma-aminobutyric acid edited echo-planar spectroscopic imaging (EPSI) with MEGA-sLASER at 7T. Magn Reson Med (2019).
[8] Provencher, S.W. Estimation of metabolite concentrations from localized in vivo proton NMR spectra. Magn Reson Med (1993).
[9] Chien, Y.H. et *al.*, Brain development in infantile-onset Pompe disease treated by enzyme replacement therapy. Pediatr Res (2006).

Acknowledgments / Funding Information: This project has received funding from the Leiden University Fund (W-19356-2-32), and the H2020-MSCA-COFUND-LEaDing Fellow Programme (The Netherlands) under the Marie Skłodowska-Curie grant agreement No 707404.

A

Patient	Age start of ERT (y:m:d)	Age at time of MRI (y:m)	Mutations	CRIM status	Last motor function
P1	0:6:0	9:1	c.525delT c.525delT	N	sitting
P2	0:2:0	13:10	c.525delT c.2481+102_2646+31del538	P	sitting
P3	0:0:16	16:2	c.2481+102_2646+31del538 c.2481+102_2646+31del538	P	walking

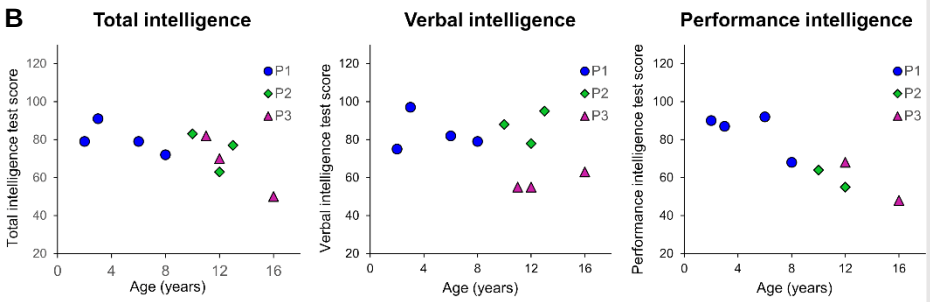

Figure 1. (A) Patients characteristics. All ages are stated in years (y), months (m) and days (d). CRIM: cross-reactive immunological material; P: positive; N: negative. **(B)** Results from neuropsychological evaluations over time showing total intelligence (*left*), verbal intelligence (*middle*) and performance intelligence (*right*) test scores for the three patients. P1: patient 1 (*blue*); P2: patient 2 (*green*); P3: patient 3 (*pink*).

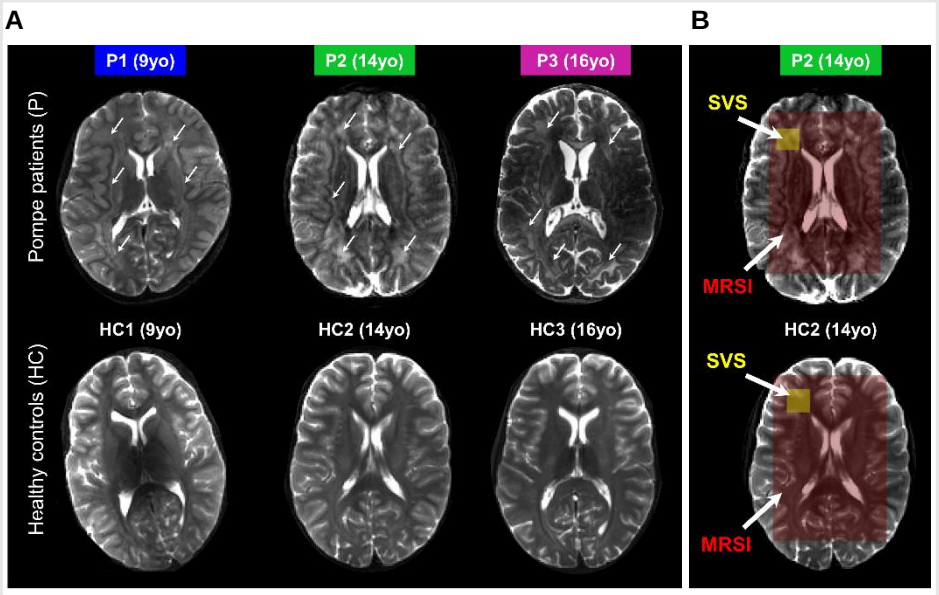

Figure 2. (A) T_2-weighted images of Pompe patients (*top*) and age-matched healthy controls (*bottom*), highlighting the widespread WM lesions (*arrows*) in all three Pompe patients. **(B)** Example of positioning of the VOI for SVS (*yellow*) and MRSI (*red*) acquisitions.

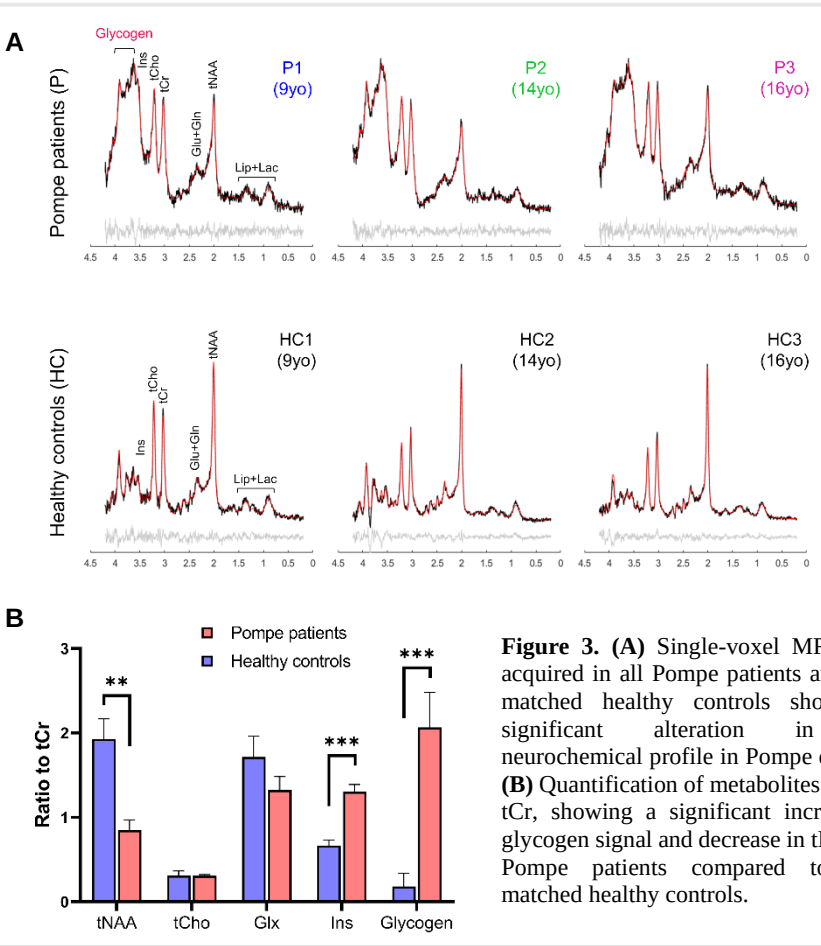

Figure 3. (A) Single-voxel MRS data acquired in all Pompe patients and age-matched healthy controls showed a significant alteration in the neurochemical profile in Pompe disease. **(B)** Quantification of metabolites ratio to tCr, showing a significant increase in glycogen signal and decrease in tNAA in Pompe patients compared to age-matched healthy controls.

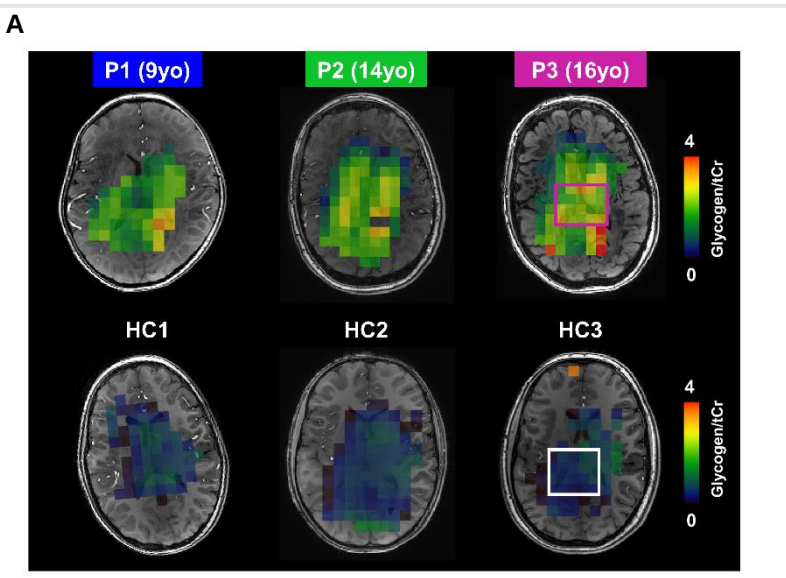

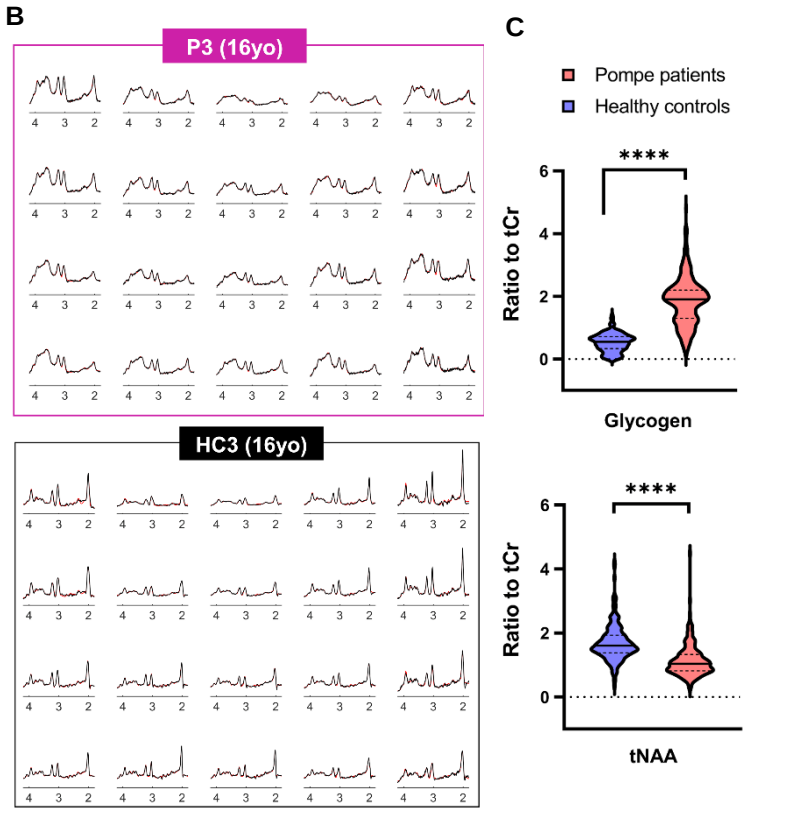

Figure 4. (A) Glycogen maps obtained following LCModel fitting for all Pompe patients (*top*) and age-matched healthy controls (*bottom*). A threshold was applied to remove spectra with low SNR quality or large lipid contamination and **(B)** Example of MRSI data from a Pompe patient (P3, *top*) and healthy control (HC3, *bottom*). **(C)** Quantification of glycogen and tNAA (all voxels from all Patients vs. healthy controls), showing glycogen accumulation and a large decrease in tNAA in Pompe patients when compared to healthy controls.

Effect of PCA-based denoising on quantification of in-vivo 31P MRSI test-retest data from the whole human liver at 7 Tesla

L. van den Wildenberg[1], A. Gursan[1], M. Froeling[1], L.W.F. Seelen[1], T.A. van der Velden[1], W.J.M. Gosselink[1], W.J.M. van der Kemp[1], D.W.J. Klomp[1], J.J. Prompers[1]

[1]Imaging and Oncology, UMC Utrecht, Utrecht, the Netherlands

Synopsis: ^{31}P MRS can be used in liver disease diagnosis and treatment monitoring. However, ^{31}P MRS has a low intrinsic sensitivity and the concentrations of liver ^{31}P metabolites are in the low millimolar range. Ultra-high field (≥7T) MRI and new developments in RF coil design can mitigate the low SNR, but additionally advanced reconstruction strategies including denoising could be used. In this study we show that principal component analysis (PCA)-based denoising of 7T liver ^{31}P MRSI data enhances the SNR 3.8-fold, but also slightly changes quantified ^{31}P metabolite concentrations, while not affecting the test-retest reliability with the used fitting prior knowledge.

Introduction: Phosphorus magnetic resonance spectroscopy (^{31}P MRS) is a non-invasive technique allowing assessment of hepatic energy metabolism and membrane turnover[1,2], which could potentially be used in liver disease diagnosis and treatment monitoring[3–6]. However, ^{31}P has a low gyromagnetic ratio and thus low intrinsic sensitivity, and *in-vivo* concentrations of potentially observable ^{31}P metabolites in the liver are only in the range of 0.7-2.7mM[7]. Ultra-high field strength (≥7T) MRI scanners and an integrated ^{31}P whole-body transmit coil[8] in combination with a multi-channel ^{31}P receive array improve the sensitivity of whole-liver ^{31}P MR spectroscopic imaging (MRSI). In addition to these hardware developments, improvements can also be achieved during reconstruction of the ^{31}P MRSI data, for example by using principal component analysis (PCA)-based denoising to enhance the SNR[9]. However, it is unclear whether denoising benefits ^{31}P MRSI data quantification. In this study, we investigated the effect of applying PCA-denoising before or after channel combination on the quantification of test-retest, 16-channel whole-liver ^{31}P MRSI data from healthy subjects and the derived repeatability parameters.

Methods: Ten healthy volunteers (four females and six males, age 34±12 (range: 25-62) years, BMI 24±4.0kg/m^2) were scanned twice in supine position using a whole-body 7T MR system (Philips Healthcare, Best, NL) with an in-house designed ^{31}P whole-body birdcage transmit coil (diameter 60cm, 120.6MHz[8]). ^{31}P signals were received with a local body array, containing 16 ^{31}P loop coils integrated with 8 fractionated ^{1}H dipole antennas[10,11]. Image-based B_0 shimming was performed and transversal and coronal T_1-weighted images were acquired. ^{31}P spectra were acquired with a pulse-acquire sequence with a block pulse (carrier frequency set to phosphocreatine, B_1=6μT), followed by phase encoding gradients for 3D spatial encoding. Acquisitions were made with Hamming weighted k-space sampling without respiratory gating. The following parameters were used: FOV=500(LR)×280(AP)×360(FH)mm^3, nominal resolution=20mm isotropic, TR=60ms, TE=0.56ms, FA=12°, BW=5000Hz, NSA=20, acquisition time=22:37min. A full liver mask was manually drawn on the transversal T_1-weighted images. ^{31}P MRSI data were reconstructed in Matlab (The Mathworks Inc., Natick, MA) and metabolites were fitted with AMARES[12] using OXSA[13,14]. Three reconstruction strategies were compared with each other: 1) Roemer channel combination without denoising (ND-Roemer), 2) PCA-denoising applied before Roemer channel combination (D-Roemer) and 3) PCA-denoising applied after Roemer channel combination (Roemer-D). Signals from α-, β-, and γ-ATP, inorganic phosphate (Pi), glycerophosphocholine (GPC), glycerophosphoethanolamine (GPE), phosphocholine (PC), phosphoethanolamine (PE), nicotinamide adenine dinucleotide (NADH), uridine diphosphate glucose (UDPG), phosphatidylcholine (PtdC), and phosphocreatine (PCr) were fitted with Lorentzian line shapes with equal line widths, with soft constraints for the chemical shifts and fixed J-couplings for the ATP doublets and triplets. Only voxels in the liver mask with a fitted PCr amplitude smaller than the α-ATP amplitude (to filter out muscle-contaminated voxels) based on the ND-Roemer reconstruction were taken into account for the statistical analyses. Signal amplitudes were expressed as percentage of the sum of all fitted signals and results were averaged over all selected voxels. One-way ANOVA for repeated measures with Bonferroni post-hoc analyses was performed to assess significant differences in SNR (based on α-ATP) and metabolite signal amplitudes between the three reconstruction methods. Next to this, for each reconstruction method repeatability was assessed from Bland-Altman analyses (coefficients of repeatability (CR) and bias), within-subject coefficients of variation (CoV)[15], and intraclass correlation coefficients (ICC). Significant differences in the repeatability parameters for the different metabolites (excluding β-ATP and PCr) among the three reconstruction methods were assessed with a one-way ANOVA for repeated measures with Bonferroni post-hoc analyses. Statistical significance was set at $p<0.05$.

Results: On average 140±32 voxels per subject were used for quantification of liver ^{31}P metabolites. An illustration of the ^{31}P MRSI grid is shown in Figure 1, together with ^{31}P MR spectra from one selected voxel reconstructed with ND-Roemer, D-Roemer and Roemer-D. AMARES fitting results for the different reconstructions are shown in Figure 2. PCA-denoising in both D-Roemer and Roemer-D reconstructions significantly increased the SNR of the ^{31}P MR spectra compared to ND-Roemer (Figure 3). In addition, the average SNR for D-Roemer was higher than for Roemer-D, but this difference was only significant for the second scan. Quantified metabolite levels were very similar among the three methods, but the small (absolute) differences were nevertheless significant for almost all metabolites and between all methods (Figure 4). However, no significant differences were found for the repeatability parameters among the three reconstruction methods (Figure 5).

Discussion and conclusion: PCA-denoising significantly increases the SNR of ^{31}P MRSI data and denoising before channel combination seems to enhance the SNR more than denoising after channel combination (3.8-fold vs 3.0-fold). In addition, PCA-denoising significantly affects quantified metabolites levels as determined by AMARES fitting, although the actual (absolute) differences are small. It is impossible to determine which results are most accurate, as there is no ground truth, but simulated data could help to resolve this[9]. Importantly, we found no significant differences between the repeatability parameters among the different reconstruction methods, indicating that PCA-denoising does not improve the test-retest reliability for the quantification of ^{31}P metabolites from our liver ^{31}P MRSI data with the used fitting constraints. Effects of PCA-denoising on data quantification with less prior knowledge or of data with lower SNR remain to be investigated.

References

1. Liu Y, Gu Y, Yu X. Assessing tissue metabolism by phosphorous-31 magnetic resonance spectroscopy and imaging: a methodology review. *Quant Imaging Med Surg*. 2017;7(6):707-726.
2. Valkovic L, Chmelik M, Krššák M. In-vivo 31P-MRS of skeletal muscle and liver: A way for non-invasive assessment of their metabolism. *Anal Biochem*. 2017;529:193-215.
3. Panda A, Jones S, Stark H, et al. Phosphorus liver MRSI at 3 T using a novel dual-tuned eight-channel 31P/1H coil. *Magn Reson Med*. 2012;68(5):1346-1356. doi:10.1002/mrm.24164
4. Brinkmann G, Melchert UH. A study of T1-weighted 31Phosphorus MR-spectroscopy from patients with focal and diffuse liver disease. *Magn Reson Imaging*. 1992;10:949-956.
5. Cox IJ, Menon DK, Sargetoni J, et al. Phosphorus-31 magnetic resonance spectroscopy of the human liver using chemical shift imaging techniques. *J Hepatol*. 1992;14:265-275.
6. Rivera D, Kalleveen I, de Castro CA, et al. Inherently decoupled 1H antennas and 31P loops for metabolic imaging of liver metastasis at 7 T. *NMR Biomed*. 2020;33(4):1-10. doi:10.1002/nbm.4221
7. Purvis LAB, Valkovič L, Robson MD, Rodgers CT. Feasibility of absolute quantification for 31P MRS at 7 T. *Magn Reson Med*. 2019;82(1):49-61. doi:10.1002/mrm.27729
8. Löring J, van der Kemp WJM, Almujayyaz S, van Oorschot JWM, Luijten PR, Klomp DWJ. Whole-body radiofrequency coil for 31P MRSI at 7T. *NMR Biomed*. 2016;29(6):709-720. doi:10.1002/nbm.3517
9. Froeling M, Prompers JJ, Klomp DWJ, van der Velden TA. PCA denoising and Wiener deconvolution of 31P 3D CSI data to enhance effective SNR and improve point spread function. *Magn Reson Med*. 2021;85:2992-3009.
10. Raaijmakers AJE, Italiaander M, Voogt IJ, et al. The fractionated dipole antenna: A new antenna for body imaging at 7 Tesla. *Magn Reson Med*. 2016;75(3):1366-1374. doi:10.1002/mrm.25596
11. van Houtum Q, Mohamed Hoesein FAA, Verhoeff JJC, et al. Feasibility of 31P spectroscopic imaging at 7 T in lung carcinoma patients. *NMR Biomed*. 2019;(May 2019):1-8. doi:10.1002/nbm.4204
12. Vanhamme L, Van Den Boogaart A, Van Huffel S. Improved Method for Accurate and Efficient Quantification of MRS Data with Use of Prior Knowledge. *J Magn Reson*. 1997;129(1):35-43. doi:10.1006/jmre.1997.1244
13. Purvis LAB, Clarke WT, Biasiolli L, Robson MD, Rodgers CT. Line-width constraints in Matlab AMARES using pre-Metabolite T2 and per-Voxel Delta B0. In: *In Proceedings of the 22nd Annual Meeting of ISMRM*. ; :2885.
14. Purvis LAB, Clarke WT, Biasiolli L, Valkovic L, Robson MD, Rodgers CT. OXSA: An open-source magnetic resonance spectroscopy analysis toolbox in MATLAB. *PLoS One*. 2017;12(9).
15. Hyslop NP, White WH. Estimating Precision Using Duplicate Measurements. *J Air Waste Manage Assoc*. 2009;59:1032-1039. doi:10.3155/1047-3289.59.9.1032

Acknowledgments / Funding Information: H2020-FETopen:NICI

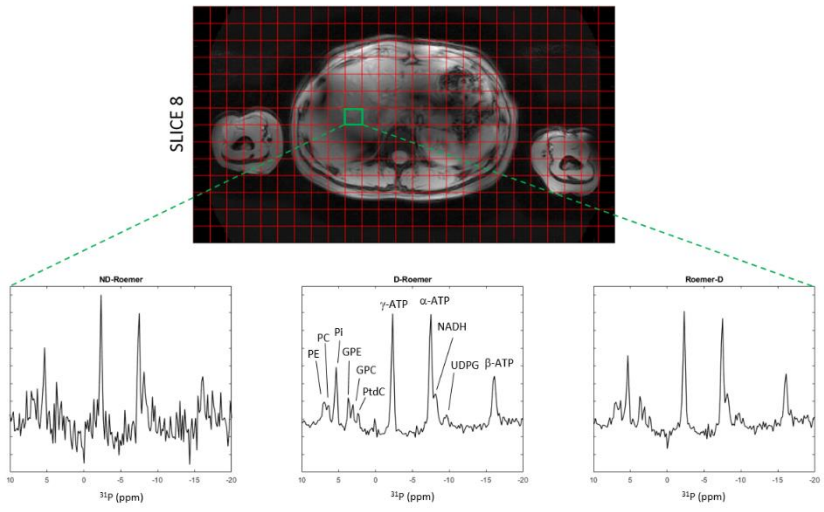

Figure 1: One slice of a transversal T_1-weighted MRI scan of subject 1 overlaid with the ^{31}P MRSI grid. ^{31}P MR spectra of one voxel in the liver are shown reconstructed with 1) Roemer channel combination without PCA-denoising (ND-Roemer) (left), 2) PCA-denoising before channel combination (D-Roemer) (middle) and 3) PCA-denoising after channel combination (Roemer-D) (right). No apodization was applied.

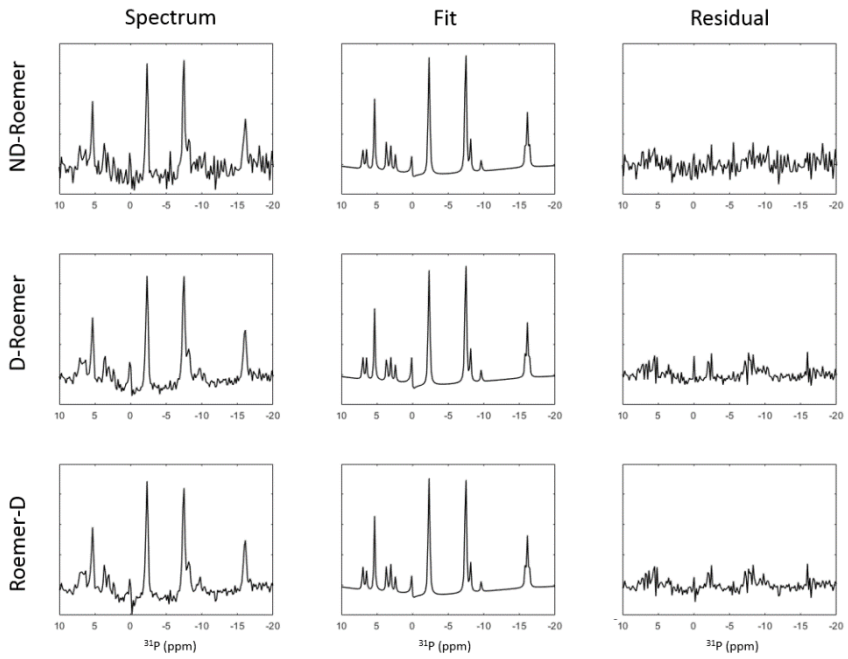

Figure 2: ^{31}P MR spectra of one voxel in the liver of scan 1 from subject 1 (first column) together with AMARES fit results (middle column) and residuals (last column) for the three different reconstruction methods.

SNR	ND – Roemer		D – Roemer		Roemer – D	
	Scan 1	Scan 2	Scan 1	Scan 2	Scan 1	Scan 2
V1	7.61 (4.1)	6.98 (2.7)	26.11 (6.4)	23.06 (5.6)	22.27 (9.2)	22.31 (6.3)
V2	5.00 (2.5)	5.66 (2.2)	21.86 (6.5)	22.78 (6.2)	18.13 (6.9)	19.35 (5.3)
V3	7.56 (3.4)	7.40 (3.5)	30.50 (9.9)	27.28 (7.8)	24.59 (7.9)	24.15 (7.1)
V4	5.96 (2.6)	6.51 (3.1)	20.28 (5.0)	21.68 (5.5)	17.38 (5.8)	20.62 (6.7)
V5	6.85 (3.7)	6.44 (3.4)	22.26 (3.9)	19.10 (5.0)	20.00 (6.8)	18.67 (5.8)
V6	7.44 (3.6)	6.89 (3.8)	24.29 (6.5)	22.83 (7.6)	23.41 (6.7)	20.64 (8.3)
V7	6.19 (2.5)	5.52 (2.2)	19.66 (4.2)	17.90 (3.8)	18.60 (4.7)	16.29 (5.2)
V8	8.43 (3.8)	7.54 (3.6)	24.80 (6.6)	24.34 (7.5)	23.23 (6.5)	22.79 (8.0)
V9	3.38 (1.3)	6.56 (3.0)	27.69 (5.8)	26.27 (8.0)	7.64 (4.4)	20.85 (6.4)
V10	5.69 (3.8)	7.16 (3.3)	26.91 (5.3)	24.43 (6.5)	14.59 (10.4)	21.47 (5.9)
MEAN (SD)	6.41 (1.5)	6.67 (0.7)	24.44 (3.5) *	22.97 (2.9) *	18.99 (5.1) *	20.71 (2.2) *§

Figure 3: SNR for the α-ATP signal for each scan for the ten different volunteers (V), averaged over all selected voxels within the liver mask, for ND-Roemer (no PCA-denoising), D-Roemer (PCA-denoising before channel combination) and Roemer-D (PCA-denoising after channel combination). SD's are given between parentheses. * $p < 0.05$ vs. ND-Roemer of the same scan; § $p < 0.05$ vs. D-Roemer of the same scan.

Metabolites	ND – Roemer		D – Roemer		Roemer – D	
	Scan 1	Scan 2	Scan 1	Scan 2	Scan 1	Scan 2
β-ATP	13.18 (1.7)	13.25 (1.3)	14.49 (1.8) *	14.92 (1.4) *	13.83 (1.8)	14.02 (1.4)
α-ATP	22.07 (1.3)	21.93 (1.0)	23.57 (1.1) *	23.46 (1.0) *	22.94 (1.3) *§	22.85 (1.1) *§
γ-ATP	22.18 (1.4)	21.97 (1.0)	22.92 (1.1) *	22.89 (1.0) *	23.99 (1.0) *§	23.91 (0.8) *§
Pi	9.02 (1.0)	8.93 (1.1)	9.07 (1.0)	9.08 (1.1) *	9.55 (1.0) §	9.49 (1.0) *§
GPC	5.01 (1.4)	5.00 (1.2)	4.54 (1.4) *	4.39 (1.5) *	4.64 (1.5) *	4.59 (1.5)
GPE	4.69 (0.8)	4.67 (0.7)	4.35 (0.8) *	4.18 (1.0) *	4.24 (0.9) *	4.12 (1.0) *
PC	3.54 (0.6)	3.50 (0.3)	2.80 (0.5) *	2.73 (0.4) *	3.03 (0.4) *§	2.94 (0.4) *§
PE	4.54 (0.3)	4.63 (0.2)	4.31 (0.3)	4.31 (0.3) *	4.39 (0.3)	4.33 (0.4) *
NADH	5.72 (0.8)	6.13 (1.0)	6.11 (1.1)	6.62 (1.4) *	5.36 (0.9) *§	5.80 (1.0) *§
UDPG	2.55 (0.3)	2.57 (1.1)	1.71 (0.4) *	1.83 (0.3) *	1.83 (0.4) *	1.96 (0.5) *
PtdC	3.82 (1.5)	3.74 (0.5)	2.09 (1.0) *	1.93 (0.9) *	2.65 (1.2) *§	2.43 (1.0) *§
PCr	3.66 (0.5)	3.67 (0.5)	4.03 (0.9)	3.66 (0.8)	3.55 (0.7) §	3.54 (0.7)

Figure 4: Fitted signal amplitudes for each metabolite, averaged over all volunteers, using ND-Roemer (no PCA-denoising), D-Roemer (PCA-denoising before channel combination) and Roemer-D (PCA-denoising after channel combination). SD's are given between parentheses. * $p < 0.05$ vs. ND-Roemer of the same scan; § $p < 0.05$ vs. D-Roemer of the same scan.

	ND – Roemer	D – Roemer	Roemer – D
CoV (%)	6.26 (3.0)	7.85 (4.8)	8.03 (4.5)
ICC	0.86 (0.1)	0.87 (0.1)	0.84 (0.2)
CR (%)	16.17 (8.1)	21.29 (12.7)	21.53 (12.6)
Bias (%)	-0.31 (2.6)	0.39 (4.8)	0.34 (4.8)

Figure 5: Repeatability parameters for ^{31}P metabolite levels determined from the two scans in the ten volunteers, averaged over all metabolites except β-ATP and PCr, using ND-Roemer (no PCA-denoising), D-Roemer (PCA-denoising before channel combination) and Roemer-D (PCA-denoising after channel combination). SD's are given between parentheses. There were no significant differences among the three methods.

Post-mortem T_2*-weighted imaging of the mouse brain for plaque or microbleed detection

A.van der Toorn[1], M. Derksen[1], C. Borrmann[2], M. Hernández-Guillamon[3], M. Fatar[2], R.M. Dijkhuizen[1]

[1]Biomedical MR Imaging and Spectroscopy group, Center for Image Sciences, University Medical Center Utrecht, Utrecht University, Utrecht, Netherlands. [2]Department of Neurology, UniversitätsMedizin Mannheim, University of Heidelberg, Mannheim, Germany. [3]Neurovascular Research Laboratory, Vall d'Hebron Research Insitute, Universitat Autònoma de Barcelona, Barcelona, Spain.

Synopsis: T_2* weighted images were obtained in post-mortem brains of wild-type and two transgenic mouse strains. The transgenic mice develop cerebral amyloid angiopathy (CAA) during their lifetime. MR imaging was used to observe developmental changes and the occurrence of amyloid beta plaque formation and/or bleedings in the brain as a result of age and condition (pre or post middle cerebral artery occlusion and with or without CAA). It is hypothesized that the presence of stroke increases plaque incidence and vice versa. Results show an increase in hypointensities in mice brains developing CAA. This might be caused by plaque formation or by microbleeds. Morphological differences of the hippocampus become apparent in the aging APP23 mice compared to wild-type. Effects of stroke on the incidence of hypointensities in the brains still have to be determined.

Introduction

Alzheimer's Disease (AD) is characterized by amyloid β (Aβ) depositions that trigger neuronal dysfunction and cell death. Aβ accumulates inside neuronal cells as well as extracellularly, where it aggregates into plaques. Plaques can be found in the brain parenchyma and in cerebral blood vessels, where it is known as cerebral amyloid angiopathy (CAA), which causes vascular degeneration and neuroinflammation [1] [2]. Despite increasing insights in the pathophysiology of AD, the spatiotemporal development of parenchymal and vascular pathology in AD remains incompletely characterized. Therefore, we applied whole-brain high-resolution MRI to assess development of microbleeds and/or plaques in APP23 mice, a widely used mouse model for evaluating vascular changes during amyloid deposition, at different ages. Since an interaction between the occurrence of stroke and the (increased) development of CAA is suspected, identical experiments were also performed in another transgenice mice model of Alzheimer's, TgSwDI mice, before and after stroke at 8 months of age. Comparison of the described groups of mice with different pathologies will lead to more information on possible interactions between the spatio-temporal development of plaques and/or microbleeds and stroke.

Materials & Methods

APP23, TgSwDI and wild-type mice were euthanized at different ages and brains were perfusion-fixed with PFA. After two weeks all tissue outside the skull was removed, however, the brains were left in the skull to prevent deformations. Brains were then soaked in PBS for at least a week before the MR experiments. Three brains were scanned together during a MRI session in a 9.4 T Varian MR scanner with gradients up to 1000 mT/m and a three-turn solenoid coil of 2 cm diameter. At least two MR volumes were obtained : one using a balanced ssfp acquisition (TR/TE 15.4/7.708 ms,FOV 19.7*18*19.7 mm3 262*240*263 points, coronal 90, isotropic spatial resolution of 75 um, flip angle 40°,6 averages at each of 4 phase-shifts (0°90°180°270°), acquisition duration of 6.5 hrs) and another one using a 3D multi gradient echo acquisition (TR/TE/TE2 100/3.2/4.3 ms, 22 echoes ,FOV 19.7*18*19.7 mm3 262*240*263 points, coronal 90, isotropic spatial resolution of 75 um, flip angle 25°,8 averages , acquisition duration of 14 hrs). The BSSFP images were linearly and non-linearly registered to an average mouse brain using FLIRT and FNIRT (FMRIB's software library [3] [4]). T_2* weighted images were summed to give a single high SNR image which was linearly registered to the BSSFP image for each mouse. Non-linear registration to any average image was performed by applying the registration of the BSSFP image. For each timepoint an average brain image was generated using the wild-type animals at that age. The transgenic mouse brains were registered to the average mouse brains of their age group. This made the generation of average mouse brain images per age group possible for the APP23 mice. Images were normalized by setting the median image intensity in the cortex of the mice to one. The individual transgenic mouse brains were also compared to the average wild-type brains. In the summed T_2*-weighted data each pixel was checked with the corresponding pixel in the average image obtained from the wild-type mice. Each pixel with a signal intensity lower than the average signal intensity + 2.5 times the standard deviation of the intensity of that pixel in the corresponding wild-type volumes was denoted as a plaque/microbleed pixel. The number of such pixels was quantified for each group. The processing pipeline for the mice with stroke (induced by transient occlusion of the middle cerebral artery) was more or less identical. However, in this case the stroke lesion was sometimes so large that the registration suffered in the ipsilesional part of the brain. Therefore comparisons were only made in ROIs in the contralesional hemisphere.

Results & Discussion

As compared to wild-type control brains, APP23 brains appeared more granular-like on the anatomical bSSFP scans starting at ~15 months of age. Focal hypointensities were detected in the summed T_2*-weighted images of APP23 brains from an age of 15 months onwards (see figure 1). A lower degree of contrast in the hippocampus of APP23 mice was observed starting at 15-18 months of age (figure 2). T2* maps revealed plaques/microbleeds in APP23 mice, which were less frequent in wild-type brains, starting at 7 months of age. In TgSwDI mice at ages of 8 or 12 months, plaques/microbleeds were less prominent (see figure 3). Stroke lesions distorted the images too much to reliably count low intensity pixels.

Conclusion

Our data reveal the occurrence of morphological changes in the hippocampus at a relatively early stage in APP23 mice, before the formation of microbleeds or plaques. Quantitative analysis of high-resolution MRI data may provide important insights into the progression of markers that inform on the development of AD. The effect of stroke on the occurrence of plaques or microbleeds is currently being investigated.

References: 1.Ballard, C., et al., *Alzheimer's disease.* Lancet, 2011. **377**(9770): p. 1019-31. 2. Miao, J., et al., *Cerebral microvascular amyloid beta protein deposition induces vascular degeneration and neuroinflammation in transgenic mice expressing human vasculotropic mutant amyloid beta precursor protein.* Am J Pathol, 2005. **167**(2): p. 505-15. 3.Smith, S.M., et al., *Advances in functional and structural MR image analysis and implementation as FSL.* Neuroimage, 2004. **23 Suppl 1**: p. S208-19. 4. Jenkinson, M., et al., *Fsl.* Neuroimage, 2012. **62**(2): p. 782-90.

Acknowledgments / Funding Information: Research was funded by the Joint Programming Initiative Neurodegenerative Diseases

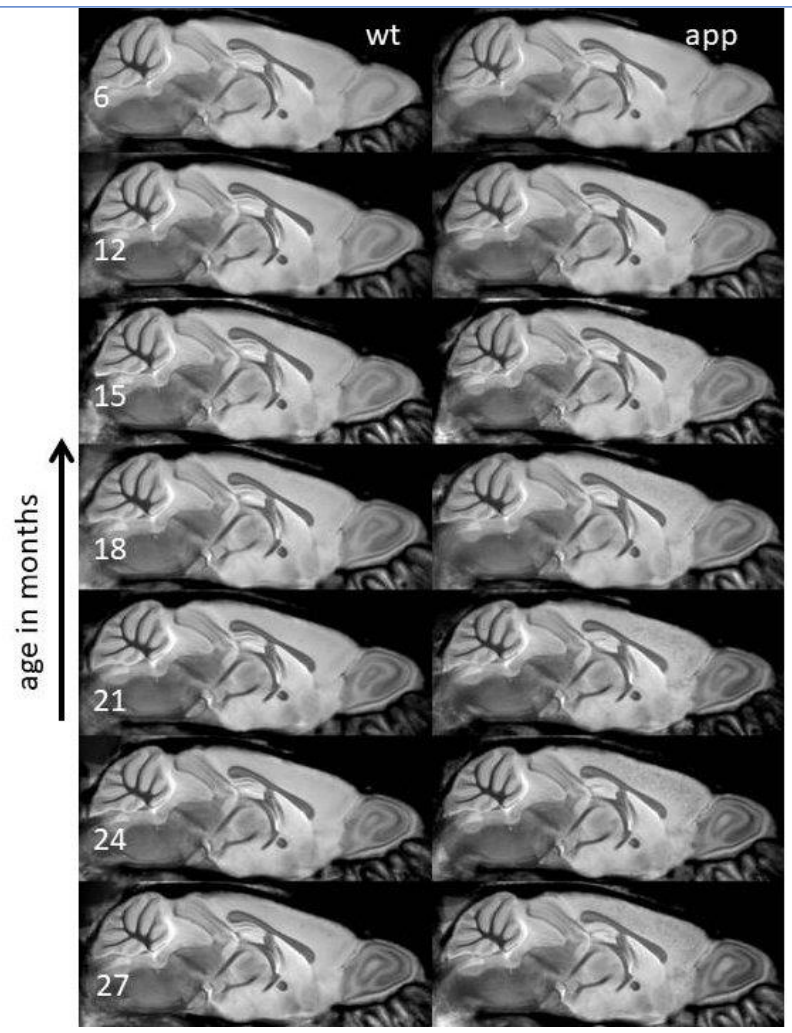

Figure 1. Median images of wild-type and APP23 mouse brains at different ages. Increased occurrence of hypointensities can be observed in the cortex of the APP23 mice.

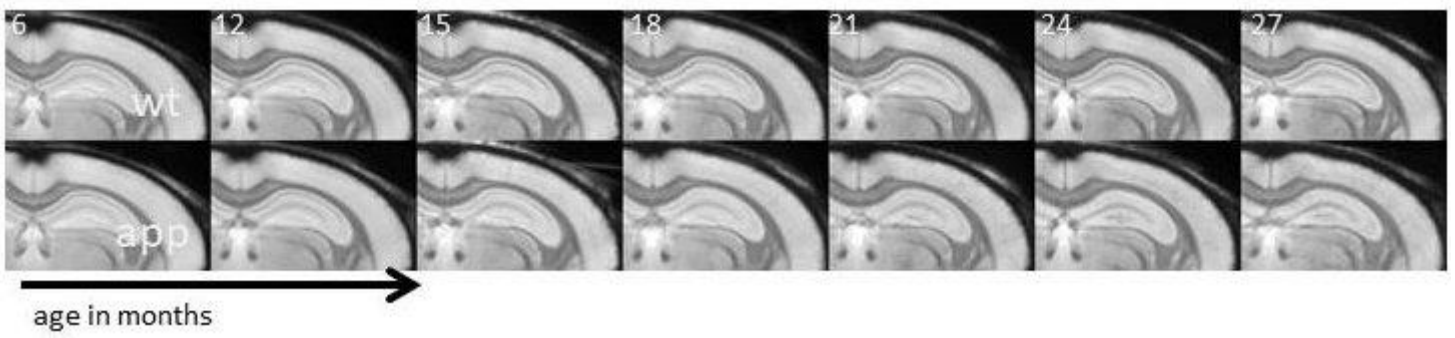

Figure 2. Median images of wild-type (top) and APP23 (bottom) hippocampal region. Note changes in the pattern within the hippocampus.

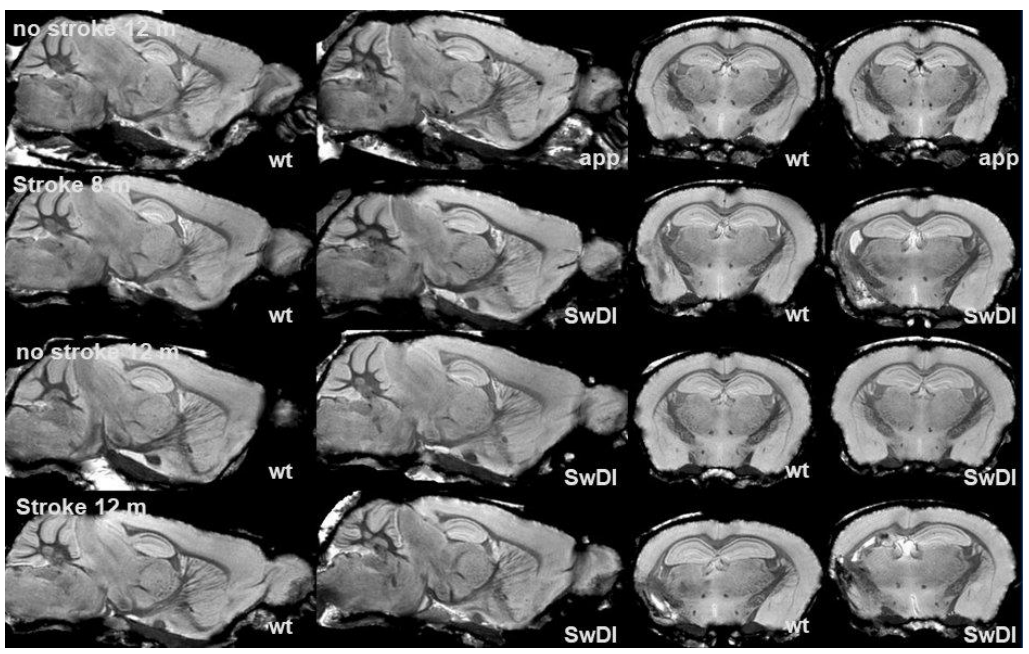

Figure 3. Summed T2*-weighted saggital and coronal slices from individual animals after linear registration (non-linear registration deforms the images too much in the case of stroke). Note the absence of low intensity spots in the wild-type and TgSwDI animals, while stroke lesions can be clearly observed.

Deep-learning based passive marker detection for MRi-guided endovascular interventions in a pulsatile flow phantom

J. Nijsink[1], C.G. Overduin[1], P. Brand[1], M.C. Warlé[1], J.J. Fütterer[1]
[1]Department of Radiology and Nuclear Medicine, Radboudumc, Nijmegen, Netherlands

Synopsis: Automatic passive marker detection is required for continuous device tracking during MRI-guided endovascular interventions. This study elaborates marker detection performance of a deep learning-based model in GRE images in a pulsatile flow phantom at 3T and its robustness to alterations in imaging parameters and marker concentrations. The model correctly detected on average 4.1±1.1 out of 5 markers. The performance was highest for images resembling the training dataset and worsened for images with deviating marker appearance, e.g., due to high echo times, marker concentrations or adjusted phase-encoding direction. Further model optimization is required to make it more robust and clinically relevant.

Introduction: MRI-guidance offers several advantages during endovascular procedures, such as high soft-tissue contrast, three-dimensional (3D) volume imaging and functional imaging, but endovascular device manipulation under real-time MRI still remains complex.[1,2] To continuously visualize the moving guidewire through a vascular trajectory, the imaging scan planes need to be aligned and updated. Manual plane adjustment in 3D is challenging and time-consuming, hence automation of imaging plane adjustment could facilitate easier device navigation.[2] For automatic plane adjustment, automatic marker detection is required. Several studies implemented automatic passive marker detection using traditional digital image processing.[1,3,4] Where adjustments in, for example, guidewire or marker design may require manual updating of the algorithm in conventional methods, deep learning methods can be easily retrained to adjust to the new marker appearance.

Therefore, this study evaluated the feasibility of deep learning to automatically detect passive markers during real-time MRI in a pulsatile flow phantom and its robustness to alterations in imaging parameters and marker concentrations.

Methods: In previous work[5], we have demonstrated that passive iron(II,III)oxide (Fe_3O_4) marker enhanced guidewires were adequately displayed at 3T MRI (Magnetom Skyra, Siemens, Erlangen, Germany) in a pulsatile flow phantom using a near-real time (up to 3.3 frames per second (fps)) gradient echo sequence (GRE). In short, an 8-mm tube was immersed within an agar solution and connected to a heart-lung machine to generate a realistic pulsatile flow (Figure 1). Four different guidewires (Nano4Imaging GmbH, Düsseldorf, Germany) with each having different iron(II,III)oxide concentration (6.25, 12.5, 25, and 50mg/mL) markers were imaged using 2D GRE sequence (echo time (TE)/ repetition time (TR): 2.48/4.6ms, framerate: 3.3fps, matrix size: 144x144, flip angle: 12^{O}, pixel size: 1.74x1.74mm, slice orientation: sagittal, phase encoding direction (PED): perpendicular to B0, slice thickness (ST): 5mm), further specified as the baseline image. Imaging was repeated for the different guidewires with alterations in imaging parameters and identical guidewires with different marker concentrations (Table 1).

In the current study, an U-net[6] deep learning model was trained to detect markers in the images acquired as described above. Markers were manually annotated and a 2D Gaussian kernel with a variance of (1,1) was placed at annotated locations to generate a likelihood map. The train set consisted of thirty baseline GRE images that additionally underwent rotation, translation, scaling and cropping augmentation techniques. The validation test consisted of ten images. The detection performance of the trained model was validated using 25 images from the datasets with different parameters. To analyse the performance, local maxima were calculated for a range of likelihood thresholds (0.1-0.9 with 0.05 steps). If the distance between annotated and detected marker was two voxels or smaller (3.5mm), the marker was specified as correctly detected. Mean number of true positive and false positive detected markers for the different thresholds were calculated and tabulated together with the standard deviation (SD).

Results: The time to analyse one image (inference time) with an Nvidia GTX1080Ti graphics card was approximately 4ms. Figure 2 shows examples of the automatic marker detection using the trained deep learning model for the baseline image and the parallel PED image. The performance of the automatic marker detection algorithm for the different image datasets is displayed in Table 2 and Figure 3. The overall mean true positive detected markers was 4.1±1.1. The mean number of true positive (4.9±0.2) and false positive (0.0±0.0) detected markers for the images scanned with low TE and with larger slice thickness was similar to the baseline images (4.9±0.3). Detection performance decreased for images with larger marker concentrations and high TE, as well as for images with parallel PED. The highest marker concentration resulted in the lowest performance, with a mean number of correctly detected markers of 4.1±1.1.

Discussion: This study shows that passive marker artifacts on endovascular guidewires can be adequately detected by a trained deep learning model within approximately 4ms. Detection performance was not affected by minor adjustments in TE (<1ms) and doubled slice thickness, however higher marker concentrations, high TE and switched PED most pronouncedly resulted in decreased performance. This is to be expected as these parameters directly affect artefact appearance through, amongst others, increased magnetic susceptibility artifacts.[7,8]

Our findings provide insight into the robustness of automatic detection models and care should be taken to alter imaging parameters when such techniques are applied clinically. Improved robustness of the detection model can likely be realized by training the model with a larger dataset and with MRI images acquired with different parameters. Furthermore, for translation to the clinical setting MRI images of the device in humans should be acquired to train the deep learning model.

Our results appear promising towards designing a fully automated marker detection and real-time imaging protocol. Ideally, such an algorithm should use a bi-directional communication protocol to retrieve the real-time image stream, determine marker location and update the ideal imaging scan plane. Ultimately, this may improve usability and facilitate studies on MRI-guided endovascular interventions in clinical practice.

Conclusion: Deep learning based automatic marker detection of passive markers in near real-time imaging was feasible. Adjusting parameters such as TE, PED and marker concentration reduced the performance of the marker detection.

References:

George A, Derbyshire J, Saybasili H, et al. Visualization of active devices and automatic slice repositioning (“SnapTo”) for MRI-guided interventions. *Magnetic resonance in medicine*. 2010;63(4):1070-1079. doi:10.1002/MRM.22307

2. Bock M, Volz S, Zühlsdorff S, et al. MR-guided intravascular procedures: real-time parameter control and automated slice positioning with active tracking coils. *Journal of magnetic resonance imaging : JMRI*. 2004;19(5):580-589. doi:10.1002/JMRI.20044

3. van Weide R der, Bakker HJG, Viergever MA. Localization of intravascular devices with paramagnetic markers in MR images. *IEEE Transactions on Medical Imaging*. 2001;20(10):1061-1071. doi:10.1109/42.959303

4. Hoinkiss D, Nijsink H, Borm P, et al. Real-Time Slice Steering for MR-Guided Interventions Using Endovascular Devices Equipped with Passive MRI Markers. In: *Proc Int Soc Magn Reson*. 2021:0854.

5. Nijsink H, Overduin K, Overduin S, et al. Optimized passive marker device visibility for MRI-guided endovascular interventions at 3T: a pulsatile flow phantom study. In: *Proc Int Soc Magn Reson*. 2021:4006.

6. Ronneberger O, Fischer P, Brox T. U-net: Convolutional networks for biomedical image segmentation. In: *Lecture Notes in Computer Science (Including Subseries Lecture Notes in Artificial Intelligence and Lecture Notes in Bioinformatics)*. Vol 9351. Springer Verlag; 2015:234-241. doi:10.1007/978-3-319-24574-4_28

7. Lewin JS, Duerk JL, Jain VR, Petersilge CA, Chao CP, Haaga JR. Needle localization in MR-guided biopsy and aspiration: Effects of field strength, sequence design, and magnetic field orientation. *American Journal of Roentgenology*. 1996;166(6):1337-1345. doi:10.2214/ajr.166.6.8633445

8. Bos C, Viergever MA, Bakker CJG. On the artifact of a subvoxel susceptibility deviation in spoiled gradient-echo imaging. *Magnetic Resonance in Medicine*. 2003;50(2):400-404. doi:10.1002/mrm.10505

Acknowledgments / Funding Information: This research was financially supported by the Eurostars - Eureka program (SPECTRE E! 11263). We thank Nano4Imaging for their contribution in the guidewire design and the donation of the guidewires.

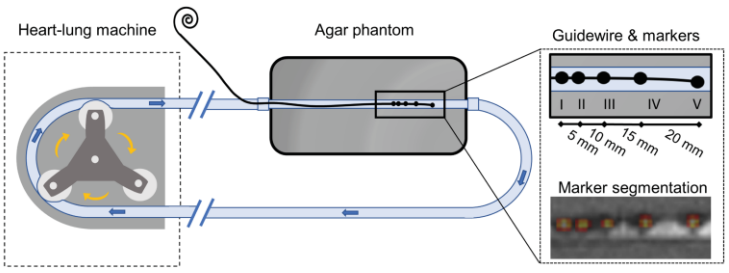

Figure1: Schematic drawing of the guidewire with markers inserted in the flow phantom.

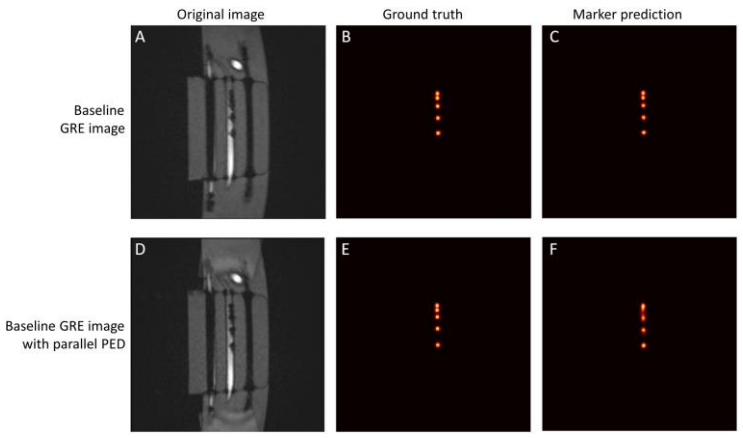

Figure 2: Original baseline **(A)** and parallel PED **(D)** GRE MRI images with corresponding ground-truth annotations **(B)** and **(E)**, respectively. **(C)** and **(F)** show the probability map generated by the deep learning model of the original and parallel PED image, respectively. Note that the marker prediction of the top three markers is less distinct for the parallel PED image compared to the baseline image.

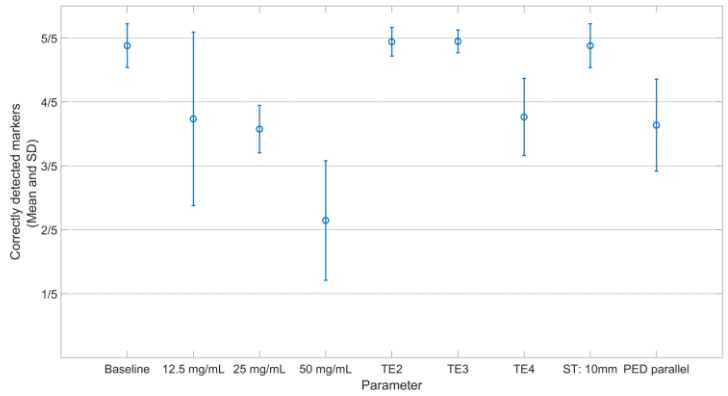

Figure 3: Detection performance of the deep learning model displayed by mean correctly detected markers and corresponding standard deviation. Detection performance decreased for larger marker concentration, echo time and parallel PED.

Table 1: Evaluated parameters with corresponding baseline and varied values

Evaluated parameters	Baseline value	Varied values		
Iron(II,III)oxide concentration (mg/mL)	6.25	12.5	25	50
GRE: TE / TR (ms)[1]	TE 1: 2.48 / 4.6	TE 2: 2.54 / 4.8	TE 3: 3.05 / 5.8	TE 4: 6.49 / 12.1
Slice thickness (mm)	5	10		
Phase encoding direction	Perpendicular	Parallel		

GRE: gradient echo, TE: echo time, TR: repetition time

[1] Bandwidth for TE1-TE4 is 1445, 990, 505, 130 Hz/pixel, respectively.

Table 2: Mean (SD) number of correctly and wrongly detected markers for each threshold per dataset.

Evaluated parameters of GRE images	Mean correctly detected markers (SD)[1]	Mean false positive detected markers (SD)
baseline	**4.9 (0.3)**	**0.0 (0.0)**
Conc. 12.5 mg/mL	3.7 (1.4)	0.1 (0.0)
Conc. 25 mg/mL	3.6 (0.4)	0.2 (0.6)
Conc. 50 mg/mL	2.1 (0.9)	0.0 (0.0)
TE2	4.9 (0.2)	0.0 (0.0)
TE3	4.9 (0.2)	0.0 (0.0)
TE4	3.8 (0.6)	0.0 (0.0)
ST: 10 mm	4.9 (0.3)	0.0 (0.0)
PED: parallel	3.6 (0.7)	0.0 (0.0)

GRE: gradient echo, TE: echo time, TR: repetition time, SD: standard deviation, ST: slice thickness, PED: phase encoding direction, [1] maximum markers to be detected was 5

Imaging white matter changes in alternate motor fibers after experimental focal stroke in rats

V.H. Wielenga[1], C.H. van Heijningen[1], A. Van der Toorn[1], T.H. Rietberg[1], J.S. van der Mannen[1], M. Froeling[2], G.A.F. van Tilborg[1], R.M. Dijkhuizen[1]

[1]Biomedical MR Imaging & Spectroscopy group, Center for Image Sciences, University Medical Center Utrecht, Utrecht, The Netherlands;
[2]Division of Imaging and Oncology, University Medical Center Utrecht, Utrecht, The Netherlands

Background: After ischemic stroke, many patients experience poor recovery of motor function, which is caused by damage to the motor system. Whilst the corticospinal tract, the brain's major motor pathway, is well studied, the role of alternate motor fibers in the rubrospinal tract and reticulospinal tract remains incompletely understood[1,2]. Animal models provide opportunities for in-depth longitudinal investigation of white matter tract conditions in relation to motor dysfunction and recovery after stroke. In this project, we aim to elucidate the role of the rubrospinal tract and reticulospinal tract in functional recovery in a novel experimental focal stroke model using serial multiparametric in vivo MRI.

Materials and Methods: Unilateral focal stroke in the corticospinal tract of female Long-Evans rats is induced through intracerebral injection of the vasoconstrictive agent N5-(1-iminoethyl)-L-ornithine (L-NIO). Combined injection with Gadovist is done to confirm the location of injection with MRI directly after stroke (Fig. 1A). In vivo MRI sessions with multiparametric imaging protocol are performed on a preclinical 9.4T MRI scanner to measure changes in the brain in various phases after stroke. Diffusion MRI is executed with 220 diffusion-weighted directions, increasingly divided over 5 b-values (0, 600, 1200, 1800, 2400) to enable complex fibre orientation estimation[3]. A batch of behavioural tests is performed to assess functional recovery.

Results: Figure 1 shows examples of preliminary data. A lesion in the internal capsule at day 3 can be detected with T2-weighted MRI. A decrease in fractional anisotropy (FA) in surrounding white matter suggests tract degeneration. Signs of injury were not detected in sham rats.

Discussion: The results from this study can provide more information about the role of the rubrospinal and reticulospinal tract in loss and recovery of motor function after ischemic stroke. This information may contribute to development of new diagnosis and treatment methods for recovering stroke patients.

References:

[1] Ishida A, Kobayashi K, Ueda Y, Shimizu T, Tajiri N, Isa T, Hida H. Dynamic interaction between cortico-brainstem pathways during training-induced recovery in stroke model rats. *J Neurosci*, 2019, 39(37), 7306-7320.

[2] Senesh MR, Barragan K & Reinkensmeyer DJ. With reduced ability to move in synergy after stroke: evidence of competition between corticoreticulospinal and corticospinal tracts? *Neurorehabil Neural Repair*, 2020, 34(10), 904-914.

[3] Tournier JD, Calamante F, Connelly A. Robust determination of the fibre orientation distribution in diffusion MRI: non-negativity constrained super-resolved spherical deconvolution. *Neuroimage*, 2007, 35(4), 1459-1472.

Acknowledgments / Funding Information: Funded by NWO Graduate Programme (022.006.001)

Figure 1. (A) Focal stroke in the corticospinal tract is achieved by LNIO injection in the internal capsule. Co-injection with Gadovist confirms correct injection from contrast enhancement on a balanced steady-state free precession scan. (B) At day 3, stroke-induced damage is apparent from changes in T2 and diffusion measures.

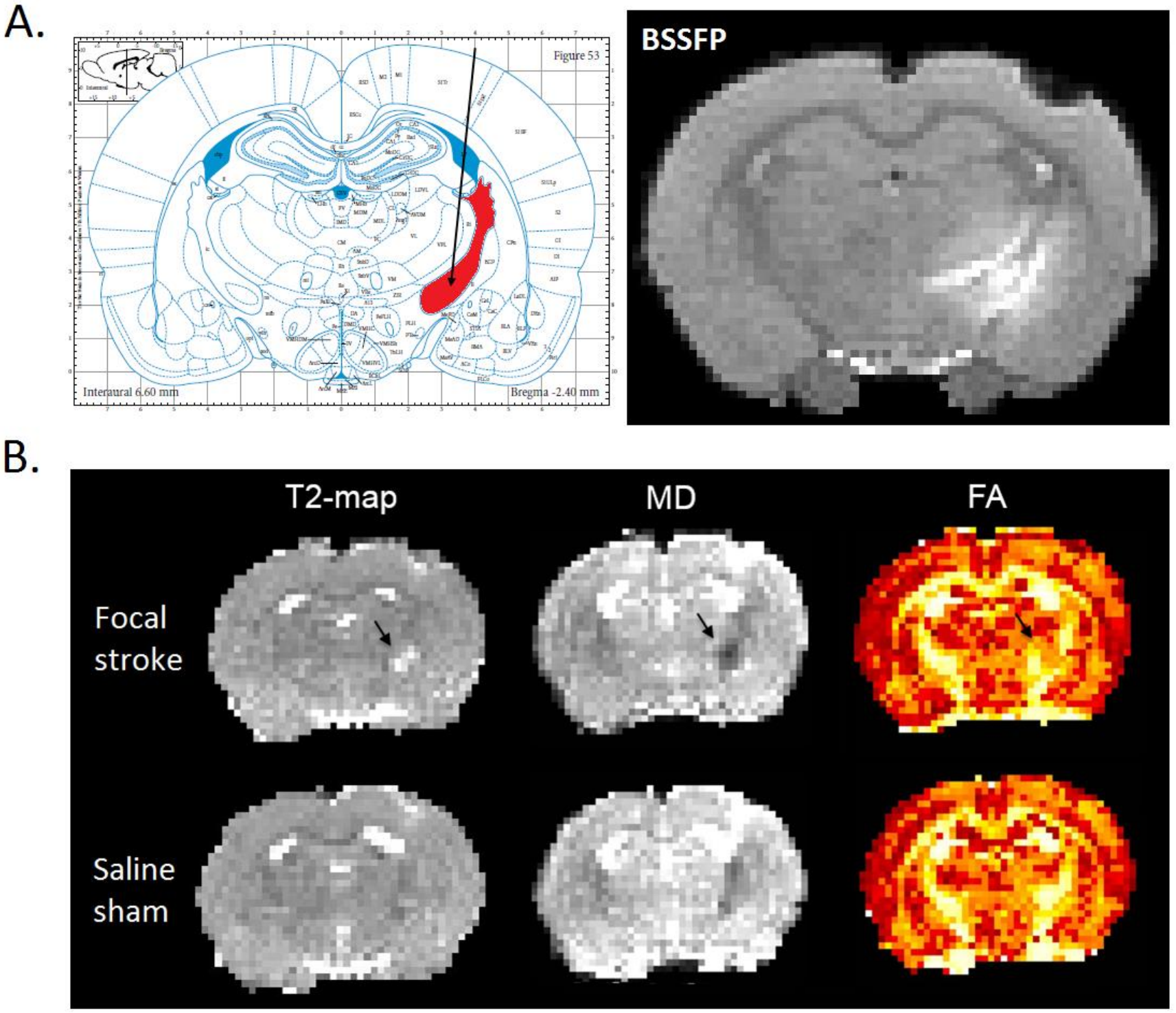

Fast Subject-Specific Local SAR and B_1^+ Prediction for PTx at 7T using only an Initial Localizer

W.M. Brink[1], M. Staring[2], R.F. Remis[3], A. Webb[1]

[1]C.J. Gorter Center for High Field MRI, dept. Radiology, Leiden University Medical Center, Leiden, Netherlands; [2]Division of Image Processing, dept. Radiology, Leiden University Medical Center, Leiden, Netherlands; [3]Circuits and Systems Group, dept. Microelectronics, Delft University of Technology, Delf, Netherlands

Synopsis: This work presents a method for local SAR and B_1^+ prediction using only a 9 seconds long localizer as an input. The total procedure can be executed in less than 30 seconds for a birdcage configuration and less than 45 seconds for a PTx configuration, which enables seamless integration into the MR workflow.

Introduction: Ultra-high field (UHF) MRI (B_0>7T) shows great promise to yield higher resolution structural and physiological information than available at 3T, particularly in the brain. Parallel RF transmission (PTx) is a key technology for UHF-MRI to address the increased spatial variations in the radiofrequency (RF) field distribution. However, currently it has failed to reach widespread clinical adoption. The main factors include the intersubject variability in local specific absorption rate (SAR), which leads to large safety margins to ensure compliance with regulatory limits in all subjects,[1,2] and time-consuming B_1^+ calibration procedures required for tailored RF pulse design. Together, these technological challenges limit the clinical impact of PTx and the utilization of UHF-MRI.

In this work, we demonstrate a fast subject-specific method based on deep learning and a fast EM solver for predicting both local SAR and B_1^+ fields using only a 9 second long localizer scan. A schematic overview of the approach is shown in Figure 1.

Methods: MR protocol: Data was acquired in 20 healthy volunteers (10 male, 10 female, age range 21-66 years) on a Philips Achieva 7T MRI system equipped with a Nova Medical birdcage head coil and integrated 32-channel receive coil array. The imaging protocol consisted of a 3D T_1-weighted MP-RAGE sequence acquired at 1 mm isotropic resolution in 3 min, followed by a fast 3D T_1-weighted localizer acquired at 2 mm isotropic resolution in 9 s.

The 1 mm T_1-weighted data were first used to generate subject-specific dielectric body models with eight tissue classes using our recently developed deep learning segmentation method.[3] The resulting material parameter maps (i.e. permittivity, conductivity, density) were subsequently downsampled to 2 mm and used as 'ground truth' data for training the deep learning network with the localizer as input.

Deep Learning: A 2.5D convolutional neural network was implemented based on the ForkNET topology.[4] The network was designed to have one input and 5 outputs, consisting of the three tissue parameters and additional masks for the background and internal air. The network was implemented using TensorFlow and trained in 100 epochs using a mean squared error loss function. To ensure generalizability, the results were tested in a leave-one-out manner, in which the test subject was excluded from the training data.

EM Solver: The B_1^+ field and 10g-averaged SAR distribution (SAR_{10g}) in the ground truth and localizer-based body models were simulated using a previously developed custom EM solver based on the volume integral equation method.[5] The solver employs a numerical Green's tensor computed via FDTD and includes a pre-computed coil response library to account for the loading of the RF coil. Incident fields for a quadrature birdcage as well as a PTx loop array were simulated using FDTD (XF7.4, Remcom inc., State College, PA) and the method was implemented in Matlab (2021a, Mathworks inc., Natick, MA) facilitating parallel computing and GPU acceleration through an Nvidia K40 GPU. Channelwise E-fields were combined to construct Q-matrices, averaged over 10 g and processed into a SAR oracle format to facilitate efficient SAR evaluation.[6,7]

Results: Training of the deep learning network took approximately 160 min and final inference took approximately 1s to evaluate per subject. A comparison between ground truth and localizer-based dielectric body models is shown in Figure 2.

Figure 3 shows a convergence analysis of the EM solver with respect to discretization step size, evaluated in the birdcage configuration. The peak local SAR error drops below ~1% on average for spatial resolutions of 4.0 mm and higher, which strikes an appropriate balance with an average computation time of 12s. In the eight-channel PTx configuration, the average computation time was 32s, including parallel computing overhead.

Quadrature birdcage simulations in five of the ground truth and localizer-based body models are shown in Figure 4. Overall, peak SAR_{10g} values obtained in the network generated body models are within 5% of those obtained in the ground truth body models.

Peak SAR_{10g} predictions in 1000 random PTx excitations were evaluated against those obtained in the corresponding ground truth body models, summarized in Figure 5. The average peak SAR_{10g} overestimation in the localizer-based models was 2.2% and an additional 6.3% safety margin would be required to ensure conservative local SAR estimate in 95% of the cases. This is a considerable improvement compared to the average overestimation of 45.2% that would be obtained by accounting for the worst-case local SAR within the current dataset.

Discussion and Conclusion: This work presents a method for local SAR and B_1^+ prediction using only a short localizer as an input. The total procedure can be executed in less than 30 seconds for the birdcage configuration and less than 45 seconds for the PTx configuration, which enables seamless integration into the MR workflow. As a localizer is acquired at the start of any MR protocol, and the resulting B_1^+ information can replace B_1^+ calibration procedures, the procedure does not place a time burden on the MR workflow. The resulting SAR information can be used to personalize the safety margins, design SAR-optimized RF pulses and increase the headroom in allowed sequence parameters.

References:

1. Le Garrec M, Gras V, Hang MF, Ferrand G, Luong M, Boulant N. Probabilistic analysis of the specific absorption rate intersubject variability safety factor in parallel transmission MRI. Magnetic Resonance in Medicine 2017;78:1217–1223 doi: 10.1002/mrm.26468.
2. Ajanovic A, Hajnal J V, Malik S. Positional Sensitivity of Specific Absorption Rate in Head at 7T. In: Proceedings of the 28th Annual Meeting of ISMRM; p. 4251.
3. Brink W, Yousefi S, Bhatnagar P, Staring M, Remis R, Webb A. Numerical Body Model Inference for Personalized RF Exposure Prediction in Neuroimaging at 7T. In: Proceedings of the 29th Annual Meeting of the ISMRM, Virtual Meeting; 2021.
4. Rashed EA, Diao Y, Hirata A. Learning-based estimation of dielectric properties and tissue density in head models for personalized radio-frequency dosimetry. Physics in medicine and biology 2020;65 doi: 10.1088/1361-6560/AB7308.
5. Brink WM, van Gemert JHF, Remis RF, Webb AG. Accelerated SAR Computations by Exploiting Sparsity in the Anatomical Domain. In: Proceedings of the 27th Annual Meeting of ISMRM, Montreal; 2019. p. 0735.
6. Kuehne A, Seifert F, Ittermann B. GPU-Accelerated SAR Computation with Arbitrary Averaging Shapes. In: Proceedings of the 20th Annual Meeting of ISMRM, Melbourne, Australia; 2012. p. 2735.
7. Pendse M, Stara R, Khalighi MM, Rutt B. IMPULSE: A scalable algorithm for design of minimum specific absorption rate parallel transmit RF pulses. Magnetic Resonance in Medicine 2019;81:2808–2822 doi: 10.1002/MRM.27589.

Acknowledgments / Funding Information: The authors thank Dr. Chloé Najac and Kevin Keene for assistance in data acquisition. This work was supported by the Nederlandse Organisatie voor Wetenschappelijk Onderzoek (NWO) through a VENI fellowship (TTW.16820).

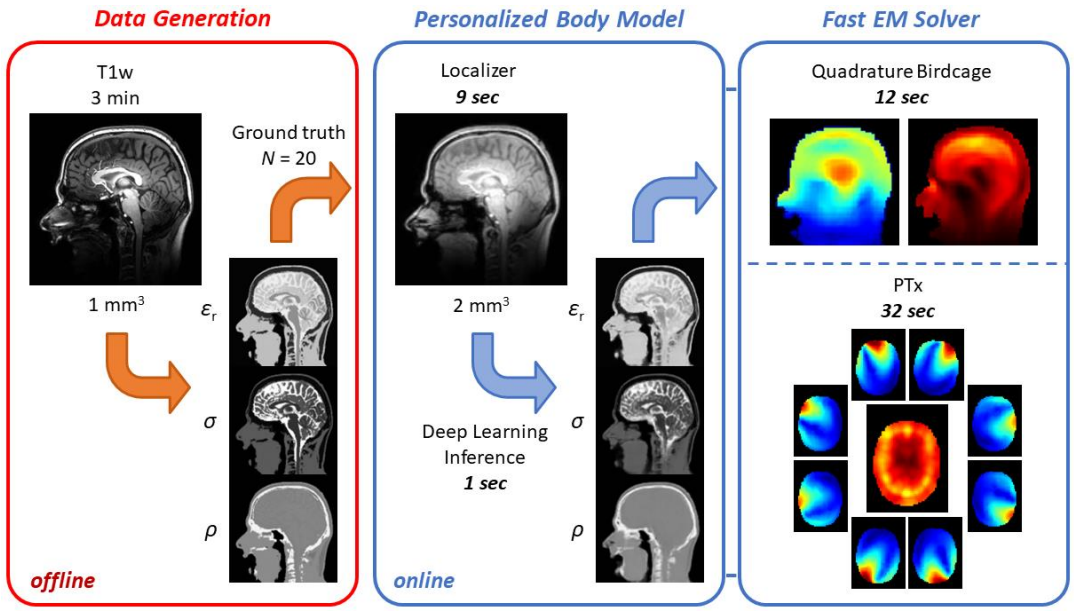

Fig. 1. Schematic overview of the approach. Ground truth dielectric body models (N=20) were generated from T_1-weighted datasets acquired at 1 mm³ resolution. The deep learning method was then trained using the corresponding 9s localizer image with a resolution of 2 mm³ as input. Local SAR and B_1^+ fields are finally simulated using a custom EM solver.

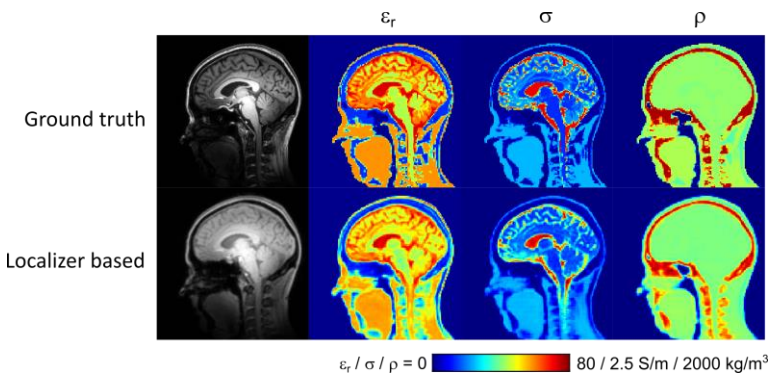

Fig. 2. Example of a subject-specific dielectric body model derived from the 9s localizer compared to the ground truth. Shown are sagittal cross sections of the T_1-weighted and localizer data, and corresponding material property maps.

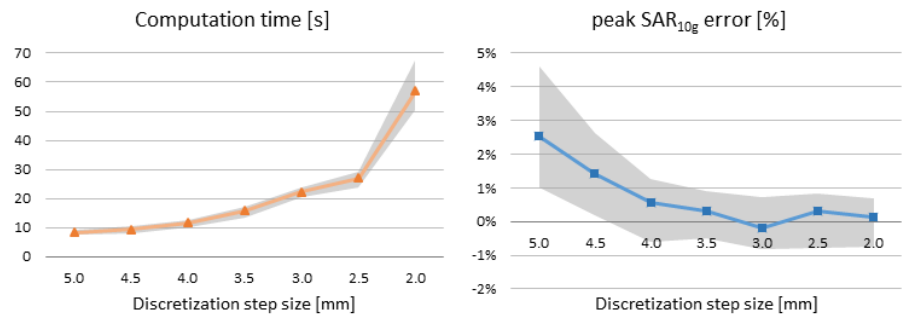

Fig. 3. Numerical convergence analysis of the EM solver evaluated in the birdcage configuration (N=5). Shown are the average computation time and average peak SAR_{10g} error with min/max error bands compared to results obtained at 1.5 mm.

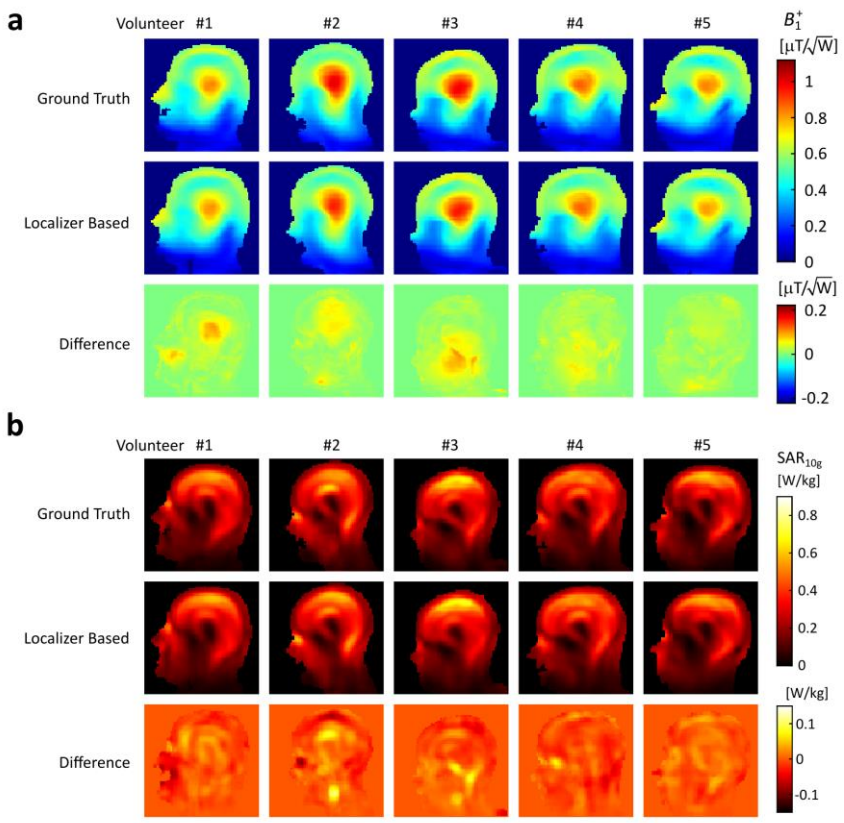

Fig. 4. B_1^+ (a) and SAR_{10g} (b) simulations in the birdcage configuration, comparing predictions obtained in the ground truth body models against those obtained in localizer-based body models.

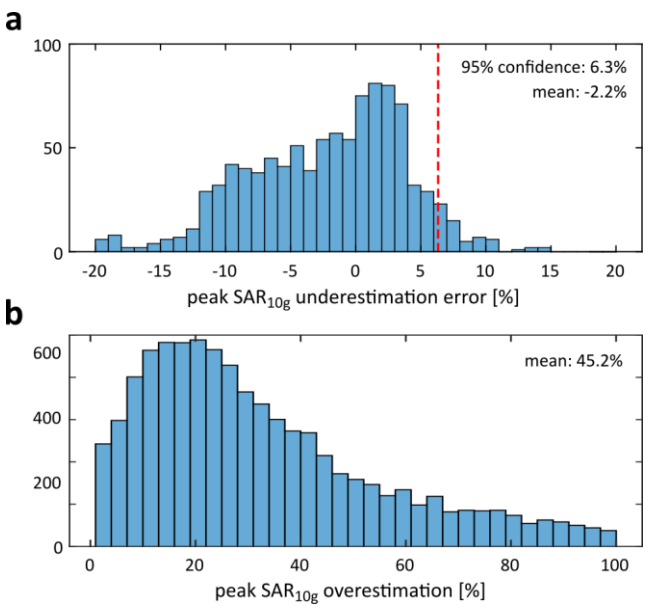

Fig. 5. PTx peak SAR_{10g} predictions evaluated in 1000 random excitations, showing prediction errors in the personalized approach (a) and overestimations when assuming worst case values (b). The data indicate that the localizer-based approach results in an effective safety margin of 8.5%, compared to an average overestimation of 45.2% in the 'worst case' approach.

Investigation of correlation between surface current and coupling using conventional coils and shielded coaxial cable coils operating at 7T

G. Costa[1], S. Güler[2,3] , P. Baltus[1], M. Paulides[1], I. Zivkovic[1]

[1]Department of Electrical Engineering, Technology University of Eindhoven, Eindhoven, Netherlands; [2]Department of Electrical Engineering, Technical University of Denmark, Kongens Lyngby, Denmark; [3]Danish Research Centre for Magnetic Resonance, Centre for Functional and Diagnostic Imaging and Research, Copenhagen University Hospital Amager and Hvidovre, Copenhagen, Denmark

Synopsis: One of the major challenges in the design of multichannel arrays for UHF MRI is minimizing coupling between elements. Shielded-coaxial-cable (SCC) coils have been recently proposed as highly decoupled elements per se: however, the decoupling mechanism of SCC coils is still not determined. In this work, we examined the relationship between coupling, surface current density uniformity, and the total current on coil conductor through measuring and simulating three different 2-coils arrays. While no correlation was observed between surface current density uniformity and interelement coupling, a negative correlation was observed between the coupling and the total current on coil conductor.

Purpose: One of the major challenges in the design of multichannel arrays for UHF MRI is minimizing coupling between elements. A summary of the existing decoupling techniques can be found in[1]. Use of the shielded-coaxial-cable (SCC) coil as array elements is convenient since no additional decoupling is needed[2,3]. However, the exact decoupling mechanism of SCC coils is still not determined. One assumption was that interelement coupling is related to surface current distribution (SCD) on the coil shield. In this work, we examine the relationship between coupling, SCD uniformity, and Total Loop Currents (TLC) using Conventional Coils (CC) (1 mm and 3 mm wire diameter) and SCC coils at 300MHz (7T MRI).

Methods: Square CC (arm length D=85mm) were fabricated using wires with two different diameters, 1 mm and 3 mm (Figure 1). The coils were tuned and matched at 12mm distance from a rectangular phantom using distributed capacitors and pi-matching networks. The phantom dimensions were 270x350x370mm, and the phantom was filled with a water-salt solution (2.5g/l of NaCl). 1mm and 3mm CC were placed into 2-coil array configurations, and a VNA (Agilent Fieldfox) was used to measure the S-parameters of the arrays for different separation distances between elements (0.5cm to 5cm with 5mm step) and for different amount of overlap (0% to 100% with 10% step). The normalized S_{21} parameter[4] (nS_{21}) was used to evaluate the total coupling between the array elements. Simulations have been performed in CST Microwave Studio software (Darmstadt, Germany), using a frequency domain solver with tetrahedral mesh. The simulation setup was the same as the measurement setup, with phantom properties ε_r=78 and σ=0.6 S/m. The maximum (*max*) and minimum (*min*) values of SCD have been exported from simulations. The parameter *max/min* was used to evaluate the uniformity of SCD along the two loops, while port currents were used to evaluate the TLC. The correlation between nS_{21} and *max/min*, and the correlation between nS_{21} and TLC has been examined using scatter plots. Fabricated SCC coils (as in [2]) have been used for comparison. The nS_{21} and TLC of SCC were simulated and measured, then compared with the 1mm and 3mm case. *max/min* data of SCC were not included, as *max/min* data of SCC also included the contribution from the inner conductor. Anyway, Figure 1c) shows good agreement between the SCD on the shield of an isolated 3mm SCC and the SCD on a 3mm wire.

Results: Figure 2 shows the results for the nS_{21} parameter. In Figure 2a) agreement between simulations and experiments is shown. In Figure 2b) the simulation results for the nS21 in the 1mm, 3mm, and SCC case are compared. SCC were always better decoupled than 3mm CC, while 1mm CC were sometimes better decoupled than SCC in the overlapping region. Figure 3 shows the results for the TLC and for the maximum and the minimum value of *max/min* plots. As of TLC, Figure 3a) shows a comparison between the TLC on port1 (port1 and port2 signals showed good agreement) in the 1mm, 3mm, and SCC case. For every value of the distance between the coils, $TLC_{SCC} > TLC_{3mm} > TLC_{1mm}$. Figure 3b) shows a comparison between the *max/min* parameter in the 1mm and 3mm case. The behaviour of the *max/min* parameter was noisy in both cases. Figure 4 shows the scatter plots relating nS_{21} to the TLC, and nS_{21} to the *max/min* parameter. While there was no evidence of correlation between *max/min* and nS_{21} (Figure 4b), a negative correlation between nS_{21} and the TLC was found (Figure 4a). The relationship between the TLC and nS_{21} was very different in the 3 examined cases, and was therefore non-generalizable. Suspecting that the negative correlation between nS_{21} and the TLC derived from mismatching, scatter plots of S_{11} versus the TLC were made, and are shown in Figure 4c).

Discussion: The correlation between the coupling and the current on coil conductor was investigated. To quantify coupling, the nS_{21} parameter was used. To characterize the loop current, two synthetic parameters were extracted from the simulated design: port currents, and the max/min parameter. Port currents were used to quantify TLC, while the *max/min* parameter was used to evaluate SCD uniformity. While TLC was the highest for SCC coils, the coupling was the lowest: therefore, there was no positive correlation between the TLC and coupling. The noisy behaviour of the *max/min* parameter suggested no correlation between the max/min and nS_{21} instead. A more accurate evaluation was carried using the scatter plots. Results from the scatter plots confirmed the hypothesis of no correlation between the nS_{21} and *max/min* in all the examined cases, while a negative relationship between the total loop current and nS_{21} was found. We showed that negative correlation between nS_{21} and TLC could be partially attributed to coil mismatch.

Conclusion: No correlation existed between the SCD uniformity (measured through *max/min*) and nS_{21}, while a negative correlation existed between the coupling and TLC. The negative correlation could be partially attributed to mismatch. Further investigations are needed to understand the coupling mechanism of SCC.

References:

1. Zivkovic I., "*Interelement decoupling strategies at UHF MRI*" , in Frontiers in Physics, October 2021, doi: 10.3389/fphy.2021.717369
2. Ruytenberg T. et al, "*Shielded-coaxial-cable coils as receive and transceive array elements for 7T human MRI*", in Magnetic Resonance in Medicine, 2020; 83(3) : pp. 1135–1146, doi: 10.1002/mrm.27964
3. Ruytenberg T. et al, "*A flexible five-channel shielded-coaxial-cable (SCC) transceive neck coil for high-resolution carotid imaging at 7T*", in Magnetic Resonance in Medicine, 2020;84: pp 1672–1677, doi: 10.1002/mrm.28215
4. Xinqiang Yan et al, "*Self-decoupled radiofrequency coils for magnetic resonance imaging*", in Nature Communications, (2018) 9:3481 | DOI: 10.1038/s41467-018-05585-8

Acknowledgments / Funding Information: No Acknowledgments

Figure 1. Design of experiments and simulations (a) Geometry of fabricated coils (b) Geometry of the experiments and simulations (c) Surface current distribution for a 3mm wire square coil and a 3mm shielded coaxial cable

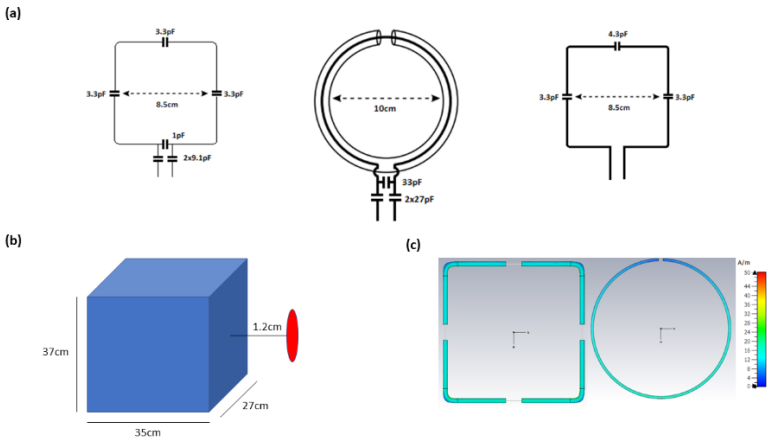

Figure 2. Normalized S21 vs relative coil position. (a) Experimental vs simulated: the red curve represents simulated values, the blue curve represents experimental values (b) Normalized S21 values for 1mm (blue curve) 3mm (red curve) and SCC (yellow curve) coils. In all the proposed plots, x represents the distance between the coil centers, while D represents either the length of the coil arm (in the square coil case) or the loop diameter (in the case of a SCC)

Figure 3. Synthetic current parameters vs relative position. (a) Total loop current for 1mm (blue curve) 3mm (red curve) and scc (yellow curve) coils. (b) max/min parameter for 1mm (blue curve) and 3mm (red curve) coils. In all the proposed plots, x represents the distance between the coil centers, D represents either the length of the coil arm (in the square coil case) or the loop diameter (in the case of a SCC)

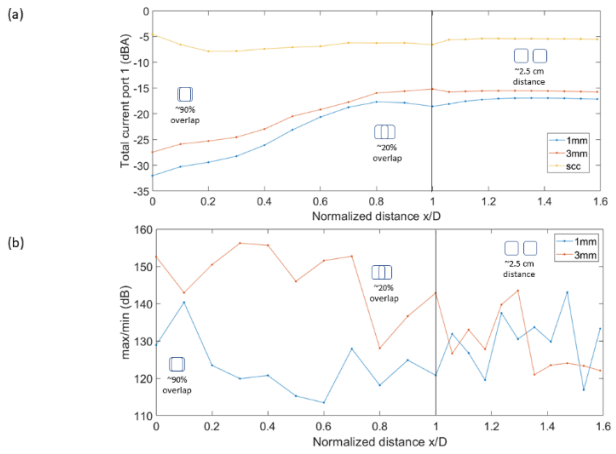

Figure 4. Scatter plots (a) TLC vs nS21 (left graph) and max/min vs S21 for 1mm (blue dots) 3mm (red dots) and scc (yellow dots) coils. (b) S11 vs TLC for 1mm (leftmost graph), 3mm (center graph) and SCC (rightmost graph) coils

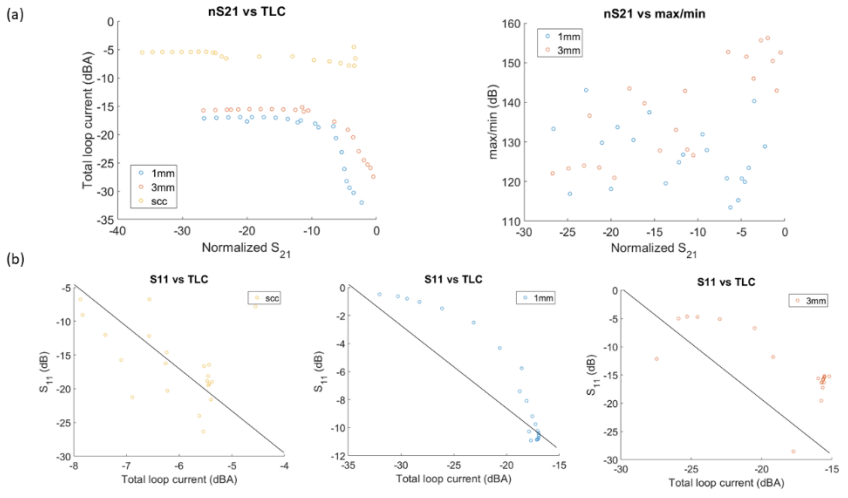

Feasibility study of novel 8-channel stacked $^{1}H/^{31}P$ transceiver coil as PET insert for 7T MRI

R. Forner[1], W. Branderhorst[1], D. Rivera[2], A. Raaijmakers[1,2], D. Welting[1], D. Klomp[1]
[1]UMC Utrecht, Utrecht, Netherlands; [2]Eindhoven University of Technology, Eindhoven, Netherlands

Synopsis: In this study, we aim to assess the feasibility of achieving simultaneous 1H&31P MR and PET imaging in an existing 7T MRI system. Due to space constraints, an integrated whole-body coil is not feasible. Instead, we investigate the possibility of using a 31P&1H array, and positioning the PET detectors between the RF shield in the patient tube and the gradient coil. 31P simulations with the dipole setup showed higher B1+ efficiency than with the body coil, and only ~5% degradation of the PET sensitivity, while the impact of the new setup was insignificant for the

INTRODUCTION

Recently, the integration of a wide-bore 1.5T body birdcage in a PET system has been demonstrated(1)

but this is feasible for MR imaging for 1H at 7T due to the shortened wavelength. Alternatively, dipole arrays have been popularly used for 1H imaging. 31P-MRSI provides insight into the energy metabolism and cell proliferation and is thus invaluable for tumour characterisation. However, at low field strengths the low SNR necessitates large MRSI voxels in vivo. With the development of ultra-high field systems, in vivo ^{31}P spectroscopy is practicable(2).

However, the RF shield of the birdcage reduces the available room for PET detectors in the bore of the magnet.

The main goal of this study is to achieve simultaneous 7T 31P/1H and PET imaging, with PET detectors integrated into an existing 7T MR system. Figure 1 displays our current design of the system. By positioning the PET detectors between the RF shield and the gradient coil, we can omit further shielding of the PET crystals and electronics to save space. Furthermore, we aim to use a dipole array consisting of eight 31P elements stacked onto the 1H elements for 31P MRSI, since a whole-body birdcage coil would limit space for the PET detectors.

We assess the effects of:

1) using an array of eight 31P/1H dipoles instead of a body birdcage coil on B1 and SNR for 31P
2) adding a RF shield at radius 29.5 cm on B1 at both frequencies, and
3) the presence of an array of eight 31P/1H elements on PET sensitivity

METHODS

The PET performance is evaluated at our 7T system (Philips Achieva, Best, The Netherlands). The influence of the shield at both frequencies is simulated using a hexagonal 26 litre salt-water phantom. Finally, the performance of a whole-body birdcage is compared to that of an 8-channel array for 31P at 7T in a scanner.

MRI simulations

RF coil simulations were first performed for both the proton and the phosphorus coils in the presence of each other. The simulations are performed with the software Sim4Life (ZMT, Zurich, CH).

For each frequency's simulations, the ports of the elements for the other frequency are terminated by 50Ω. B1 maps are used to compare the influence of the presence of the shield on the array performance. The ports are then combined with a successively increasing phase of 45 degrees across all 8 elements to give CP performance. The simulations for B_1^+ are normalised to 1W of total input power to simplify comparison.

MRI-Scanner

For the 31P 7T phantom scans, identical sequences are used for both setups. The array is shimmed by means of custom-made cable lengths to obtain optimal constructive B1+ interference in the voxel containing the phosphorous-rich phantom (contained within the larger 26L phantom). The SNR is evaluated for both setups for a matched flip angle.

PET-Scanner

A cylindrical Ge-68 source (⌀20 cm, total activity: 34.1 MBq) was placed on the patient bed of a PET/CT system (Biograph mCT40, Siemens Healthcare, Erlangen, Germany). Two 3-minute PET scans were made with a single bed position centered on the phantom: one with and one without the presence of the 1H/31P stacked setup. Data were obtained from the raw PET data in the Siemens acquisition console.

RESULTS

MRI: Simulations

The presence of the shield has no appreciable influence on the performance of the 1H/31P array for either frequency as in figures 3 for 1H and 4 for 31P.

Scanner

SNR comparison of shimmed 8-channel array (SNR of 233) and 31P birdcage (SNR of 126) from figure 5 shows that the B1 shimmed array outperforms the birdcage scanned.

PET: Scanner

The total number of true coincidences obtained from the PET scan of the cylindrical phantom with the stacked 1H/31P setup was 28321883, versus 29830146 for the phantom without the dipoles. This suggests that the PET sensitivity would be reduced by only ~5% when the current prototype dipole array would be used for 1H/31P MRI/PET.

DISCUSSION

While the 8-channel 31P array seems to outperform the birdcage coil, it is to be noted that the array may require subject specific shimming. Shimming was performed for the specific voxel containing the phantom.

Also of note is the relatively strong non-uniformity of the 31P field compared to the 1H field. It is conceivable that the flux is contained in the near-field of the elements and a further optimisation of the 31P elements may enhance B1+ uniformity.

Effect of PET setup on MRI performance:

The presence or absence of the shield led to insignificant changes in the B1 performance of the dipoles. However, with patients that are closer to the shield, the interaction is expected to increase.

Effect of MRI hardware on PET performance:

A ~5% degradation for the PET sensitivity was observed when this novel 8-channel 1H/31P setup for MRI at 7T is placed inside an existing MR-PET system.

CONCLUSION

31P imaging can be performed with stacked elements, with an insignificant impact of the shield on the MRI performance for both frequencies. The impact of the array coils on the PET sensitivity was only ~5%. Using our design, obtaining 1H and 31P MRSI and PET data is feasible for simultaneous 1H/31P MR-PET imaging at 7T.

REFERENCES

1. Branderhorst W, Steensma BR, Beijst C, Huijing ER, Alborahal C, Versteeg E, et al. Evaluation of the radiofrequency performance of a wide-bore 1.5 T positron emission tomography/magnetic resonance imaging body coil for radiotherapy planning. Phys Imaging Radiat Oncol [Internet]. 2021 Apr 1 [cited 2021 Nov 12];17:13–9. Available from: http://phiro.science/article/S2405631620300786/fulltext
2. Van Cappellen Van Walsum AM, Rijpkema M, Heerschap A, Oeseburg B, Nijhuis JG, Jongsma HW. Cerebral 31P Magnetic Resonance Spectroscopy and Systemic Acid-Base Balance during Hypoxia in Fetal Sheep. Pediatr Res 2003 545 [Internet]. 2003 Nov [cited 2021 Nov 12];54(5):747–52. Available from: https://www.nature.com/articles/pr2003491

Acknowledgments / Funding Information: European Union's Horizon 2020 grant number: 801075, 'NICI' and NWO's open competition XS21-1 programme, OCENW.XS21.1.128

Figure 1. Delete this page if there are no figures or tables

FIGURES

1. Setup: PET

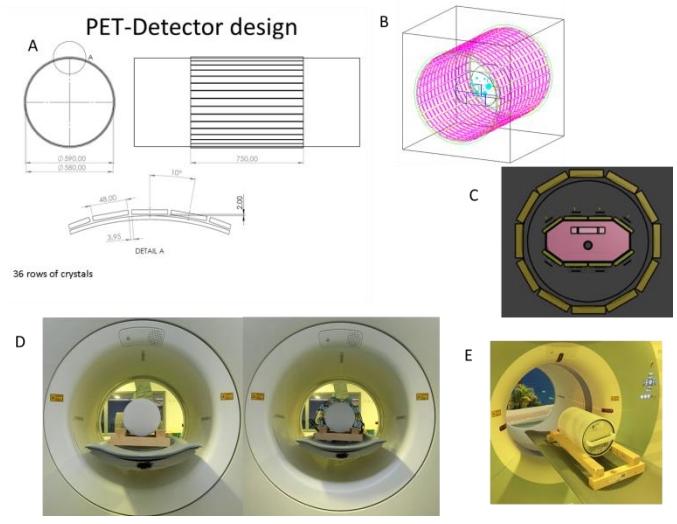

A: The PET detector design with 36 rows of crystals

B: 3D model of PET setup

C: EM simulation model showing PET detector ring, RF shield, RF 1H/31P stacked array and phantom – moving inwards

D: The PET scan setup consists of the phantom alone (left) and the phantom with the 1H/31P stacked element arrays arranged radially with the cables routed along the z-axis (right)

E: PET phantom positioning

2. Simulations: Setup of stacked array on phantom

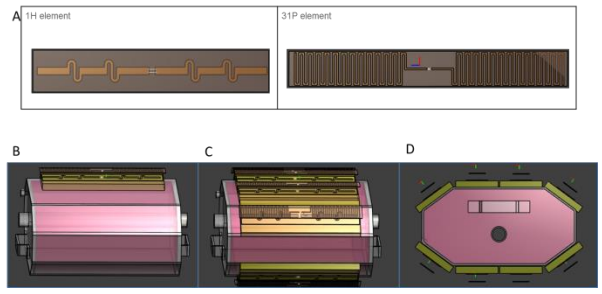

3. Simulation results 1H: Difference in the B1+ in the phantom when the setup is simulated with the shield vs without the shield for 1H

1H B1+ in phantom with shield (left) vs B1+ in phantom without shield (right)

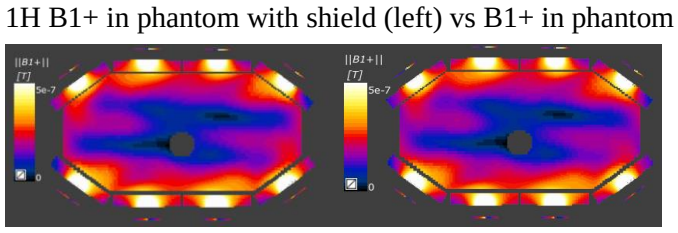

4. Simulation results: Difference in the B1+ in the phantom when the setup is simulated with the shield vs without the shield for 31P

31P B1+ in phantom with shield (left) vs B1+ in phantom without shield (right)

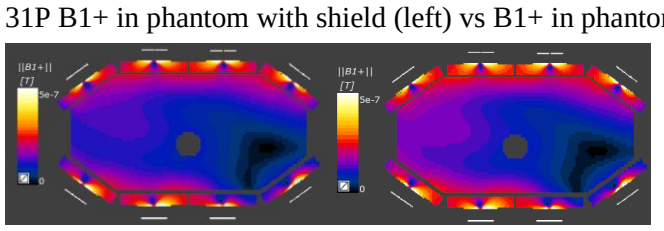

5. Scanner results: SNR comparison of shimmed 8-channel array (left, SNR of 233) and 31P birdcage (right, SNR of 126) shows that the B1 shimmed array outperforms the birdcage

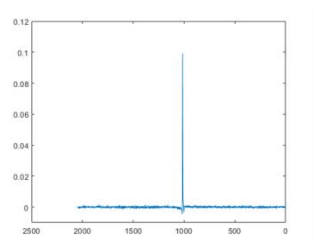

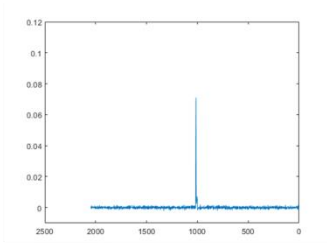

A New Approach to Shimming Halbach Arrays Using Higher Order Halbach Array Inserts

T. O'Reilly, W. Teeuwisse, A. Webb
C.J. Gorter for High-Field MRI, Department of Radiology, Leiden University Medical Center, Leiden, the Netherlands

Introduction

Halbach arrays are an appealing approach for low field MRI due to low cost and weight [1,2] but typically suffer from poor B0 homogeneity. B0 imperfections can be introduced by variations in the magnetization strength and direction of the individual magnets[3] or manufacturing tolerances in the magnet formers. Arrays typically need several shimming iterations, involving the addition of magnetic material inside the magnet, with positioning often calculated using stochastic algorithms.

We present a new shimming approach that exploits the field patterns created by higher-order Halbach shim-arrays to correct for distinct spherical harmonic B0-inhomogeneity terms. A homogenous B_0 field (degree (l) = 0, order (m) = 0 spherical harmonic) is generated using a cylindrical dipolar (k=1) Halbach array where the magnetization direction rotates twice over circumference of the cylinder. A transverse linear gradient (l=1, m=|1| spherical harmonics) can be created using a quadrupolar (k=2) (see figure 1) Halbach array comprising three rotations over the surface, etc. For spherical harmonics where l > m, the field can be approximated by varying the magnetization of the Halbach array along its length. For example, to create a linear gradient along the bore (l=1, m=0) one could use a k=1 Halbach array with the sign of the magnetization reversing (smoothly) along its length. As such, given a sufficiently long Halbach array, a k=1 shim can be used to generate all spherical harmonics of order 0. We demonstrate this concept on a new custom-built 47 mT, head system where we improve the homogeneity of the magnet by 50% by only correcting for the m=2 spherical harmonics.

Method

A 50 cm long, 31 cm diameter bore Halbach array based magnet was designed using the variable diameter homogeneity optimisation described previously [6]. The magnet consists of 25 rings, with 20 mm centre-to-centre spacing, of 12 mm cuboid N48 magnets: the central 19 rings have two layers of magnets and the three rings at each end have 3 layers. The magnetic field was mapped over a 250 mm diameter spherical volume (DSV) with a Teslameter attached to a 3D positioning robot. The acquired field maps were fitted to up to 20th order spherical harmonics to reduce noise. The inhomogeneity over a 25 cm DSV was measured to be 11723 ppm (figure 3). The l=2 , m=2 spherical harmonic term was the most significant contributor with a magnitude of 10245 ppm and as such we designed a k=3 Halbach shim array.

Shim magnets (up to 6 mm) are placed in 12 holders located on the outside of the magnet (see figure 2): each holder can accommodate 49 trays of magnets with 10 mm spacing between the trays. For the first shim iteration we filled only 13 trays (40 mm spacing) to allow for later iterations. Magnets were placed on a cylindrical radius with up to seven magnets per tray segment (84 in total for each position along the magnet). The field distribution generated by each ring of magnets was calculated, and a least squares fit of the field performed to calculate the total magnetization needed in each ring. This was then approximated by varying the size and number of magnets in each ring. An experimental field map was acquired after shimming and we simulated a correction of up to 5th order spherical harmonics based on this map.

To show the impact of the shim insert, spectra and images of an 8 centimeter spherical phantom were acquired. In both cases the field was shimmed using the linear gradients prior to data acquisition. Images were acquired using a 3D TSE sequence with the following scan parameters: FoV: 150x150x150 mm, resolution: 1.5x1.5x1.5 mm, TR/TE: 600ms/15ms, ETL: 20, bandwidth: 20kHz, duration: 5 minutes

Result

Figure 2c shows the magnet configuration after optimisation with a single populated shim tray shown in 2b. The initial field (figure 3) shows the characteristic Z2 – Y2 spherical harmonic field. The correction field created by a k=2 Halbach shim array closely matches this inhomogeneity. There is good agreement between the simulated (6156 ppm) and measured (5879 ppm) fields after shimming. Simulations of corrections show the B0 homogeneity can be improved to 2771 ppm using shim arrays up to k=6 with only high frequency perturbations at the outer bore remaining, over a 20 cm DSV, sufficient for brain coverage, homogeneity improves to 282 ppm. Figure 5 shows that the acquired spectra and images are significantly improved after the shims are inserted.

Discussion

In this work we show a new approach to shimming Halbach-array magnets using higher order Halbach shim arrays to correct for spherical harmonic inhomogeneities. We achieve a 50 % reduction in inhomogeneity by correcting only for the m=2 order, with excellent agreement between simulations and measurements, showing promise for using this approach for correcting a larger set of spherical harmonics. There are practical limits to the highest order spherical harmonics one can correct due to discretization errors associated with the very high number of rotations needed. While we have applied this method to shimming an existing magnetic field, the basic principle could also be used to optimize the field distribution of new magnets designs.

References

[1] Cooley C. et al. A portable scanner for magnetic resonance imaging of the brain. Nat. Biomed. Eng. 2020

[2] O'Reilly T et al. In vivo 3D brain and extremity MRI at 50 mT using a permanent magnet Halbach array. Magn. Reson. Med. 2020;85:495-505

[3] Hugon C et al. Design of arbitrarily homogeneous permanent magnet systems for NMR and MRI: Theory and experimental developments of a simple portable magnet. J. Magn Reson. 2010;205:75-85

[4] O'Reilly T, A. Webb. The role of non-random magnet rotations on main field homogeneity of permanent magnet assemblies. Proc Intl Soc Mag Reson Med (2021) 4042.

[5] Blümler P. Proposal for a permanent magnet system with a constant gradient mechanically adjustable in direction and strength. Concepts Magn Reson Part B Magn Reson Eng. 2016; 46(1);41-48

[6] O'Reilly et al. Three-dimensional MRI in a homogenous 27 cm diameter bore Halbach array magnet. J. Magn Reason. 2019; 307; 106578

Acknowledgments / Funding Information: This work is supported by ERC Advanced Grant PASMAR and Simon Stevin Meester Award

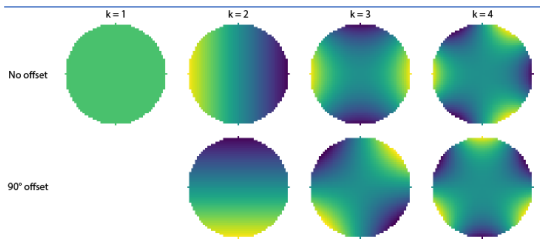

Figure 1. Transverse views of magnetic field patterns created by cylindrical Halbach arrays of different orders: in the bottom row the magnet rotations are offset by 90 degrees. The field patterns correspond to spherical harmonics of order m = 0 for k=1 up to m = |3| for k = 4, where the 90 degree offset changes the sign of the order (i.e. for k = 3 with no offset the field corresponds to the l = 2, m = 2 spherical harmonic, and with a 90 degree offset to l = 2, m = -2).

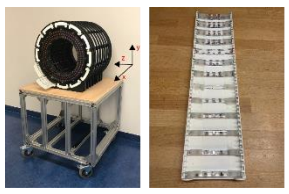

Position [mm]	Magnet size [mm]	Num. Magnets.
-240	6	84
200	6	84
-160	6	84
-120	6	84
-80	5	54
-40	6	72*
0	6	84
40	5	78*
80	3	24*
120	6	84
160	6	84
200	6	84
240	6	84

Figure 2. Left) A photo of the constructed magnet with a 31 cm bore, the 12 shim inserts are visible in white on the outside. Middle) A table with the ring configuration for the magnet. Right) A photo of a single 3D printed shim tray with 13 of the 49 positions filled with magnets. The shim magnets are placed in plexiglass holders and click in to place. Once filled the shim trays can be slid in to the magnet frame.

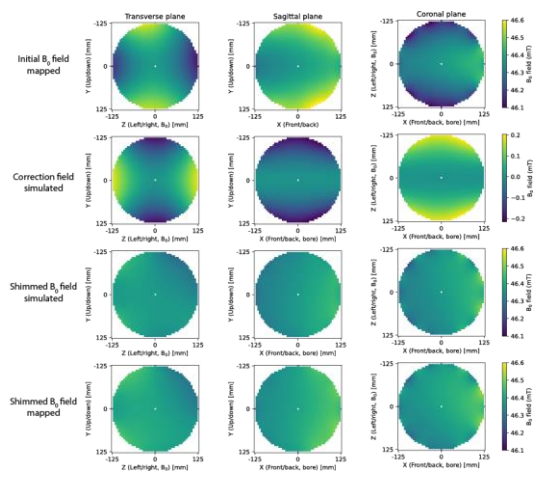

Figure 3. 1st row) Initial B_0 field map shown in the three planes of the 25 cm diameter spherical volume. Inhomogeneities in the transverse plane are dominated by the 2nd order $Z^2 – Y^2$ spherical harmonic term. 2nd row) The simulated shim field created by a k=3 (quadrupolar) Halbach shim configuration. 3rd row) Simulated B0 field map after applying the shims. 4th row) The measured field map after the shims are applied, showing excellent agreement with the simulated field maps. The initial inhomogeneity over a 25 cm sphere was 11723 ppm, the simulated shimmed field was 6156 ppm and the measured field after shimming was 5879 ppm.

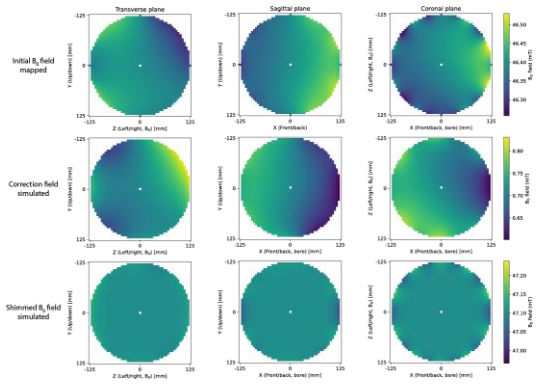

Figure 4. Simulations of the shimming performance when correcting for up to m=5 shims. The initial inhomogeneity over a 25 cm DSV is 5879 ppm which is decreased to 2771 ppm after shimming. The remaining perturbations have a relatively high spatial frequency which may be difficult to correct with shim trays placed on the outside of the magnet and may require the placement of magnetic material on the inside of the magnet.

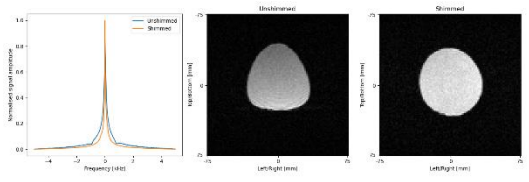

Figure 5. Left) Spectra acquired of an 8cm spherical phantom with an without the shim inserts added. Middle and right) Images acquired using a TSE sequence of the same ball phantom. In all cases additional shimming was performed using the gradient coils. The line width and the image distortions are substantially improved after the shims are added to the system.

Radiofrequency Safety of External Defibrillation Electrodes at 1.5T

Ralph Oosterveld[1], Ruud Verdaasdonk[1] and Wyger Brink[2]
[1]Biomedical Photonic Imaging group, dept. of Science and Technology, University of Twente, Enschede, Netherlands
[2]Magnetic Detection & Imaging group, dept. of Science and Technology, University of Twente, Enschede, Netherlands

Synopsis:

In this work, we evaluate the RF safety of external defibrillator electrodes at a field strength of 1.5T through phantom measurements and EM simulations. Electrode design considerations are identified and evaluated in terms of RF heating, and a modified electrode design is proposed which aims to mitigate the risk of RF heating.

Introduction:

Rapid application of external defibrillation to patients with ventricular fibrillation (VF) or cardiac arrest in an MRI environment is challenging due to the lack of commercially available external defibrillators that can be used in the MRI environment. In such situations, the patient is typically removed from the MR suite, involving time-consuming steps such as disconnecting RF coils and other peripherals, and then moved to another room. Finally, paddle electrodes are applied and the defibrillation procedure can commence, starting with diagnostic test procedures such as pulse detection and impedance measurement between the electrodes. Due to these time-consuming steps, and the rapid decrease in survival rate within minutes of onset of VF, higher-risk patient populations are typically denied from MRI access.

Recently, interest has grown for developing MRI-compatible external defibrillator systems which can provide immediate in-bore defibrillation. Pilot animal studies with porcine models have demonstrated the feasibility of high-energy (360 J) in-bore defibrillation discharges, using modified high voltage twisted pair cables equipped with RF baluns for MR compatibility[1,2]. Limited insights have yet been established in terms of MR safety of these devices, in particular, radiofrequency (RF) heating from exposure to high SAR sequences was evaluated only for relatively short durations of 6-11 minutes. Despite these short exposure durations, in some cases skin alterations such as redness but also deeper lesions were observed, indicating potential deleterious effects depending on the electrode type and design.

In this work, we evaluate the RF safety of external defibrillator electrodes at a field strength of 1.5T through phantom measurements and EM simulations. Electrode design considerations are identified and evaluated in terms of RF heating, and a modified electrode design is proposed which aims to mitigate the risk of RF heating.

Methods:

Phantom and Defibrillation Electrode: A 5L rectangular phantom was made consisting of agarose gel (2% w/w) with 3 g/L NaCl for electrical conductivity adjustment. A generic AED electrode (Heartstart FR2, Philips Healthcare, Best, the Netherlands) of size 10 × 18 cm was positioned on top of the phantom, and subsequently replaced by a modified electrode first with slits in the feet-head direction and secondly with slits in the left-right direction.

RF Heating: A high-SAR protocol was performed in a Siemens Aera 1.5T MRI system. The protocol consisted of a T1-weighted FSE sequence with minimized TR and 180° refocusing pulses to maximize RF exposure, with a duration of 20 min. Before and after each heating period, thermographic images of the phantom surface were obtained using an infrared camera (Flir One Pro-Series, Teledyne FLIR, Wilsonville, OR) after removal of the electrode.

EM simulations: A generic quadrature body coil model was simulated at 64 MHz using FDTD (XF7.4, Remcom inc., State College, PA) in a 2-mm grid. The resolution around the phantom interface ($\varepsilon_r = 50$, $\sigma = 0.5$ S/m) was increased to 0.5 mm in order to accurately represent the electrode adhesive ($\varepsilon_r = 2.5$, $\sigma = 0.05$ S/m). All simulated data were normalized to an average B_1^+ of 2 μT in the transverse cross-section of the phantom.

Results:

Thermographic images are shown in Figure 1, indicating that electrode modifications with slits in the feet-head direction show different RF heating patterns. Local RF heating was doubled when vertical slits were introduced and decreased when horizontal slits were introduced.

EM simulations of the phantom setup are shown in Figure 2, showing very similar heating patterns as observed via the thermographic camera. A considerable increase in local SAR_{10g} was observed when the slits were oriented in the longitudinal direction, while having slits in the transverse direction reduced SAR_{10g}.

Discussion and Conclusion:

In this preliminary study we have evaluated the RF safety of defibrillation electrodes used in in-bore defibrillation setups. When RF exposure levels are increased for example in high-SAR FSE or bSSFP sequences, these data indicate that RF heating underneath the electrode can take place and reach levels considerably higher than previously reported while complying with global SAR limits.[1,2] The relative heating patterns on the surface of a phantom showed a strong correlation with EM simulation, reflecting also a strong dependence on electrode design parameters, warranting further evaluation for the development of MR compatible external defibrillators.

References

1. Shusterman V, Hodgson-Zingman D, Thedens D, et al. High-energy external defibrillation and transcutaneous pacing during MRI: Feasibility and safety. *Journal of Cardiovascular Magnetic Resonance*. 2019;21(1):1-14. doi:10.1186/S12968-019-0558-Z/FIGURES/10

2. Schmidt EJ, Watkins RD, Zviman MM, Guttman MA, Wang W, Halperin HA. A Magnetic Resonance Imaging-Conditional External Cardiac Defibrillator for Resuscitation Within the Magnetic Resonance Imaging Scanner Bore. *Circulation Cardiovascular imaging*. 2016;9(10). doi:10.1161/CIRCIMAGING.116.005091

Acknowledgments / Funding Information: The authors thank Wim Leppink for help with phantom fabrication and providing the AED electrode used in this study.

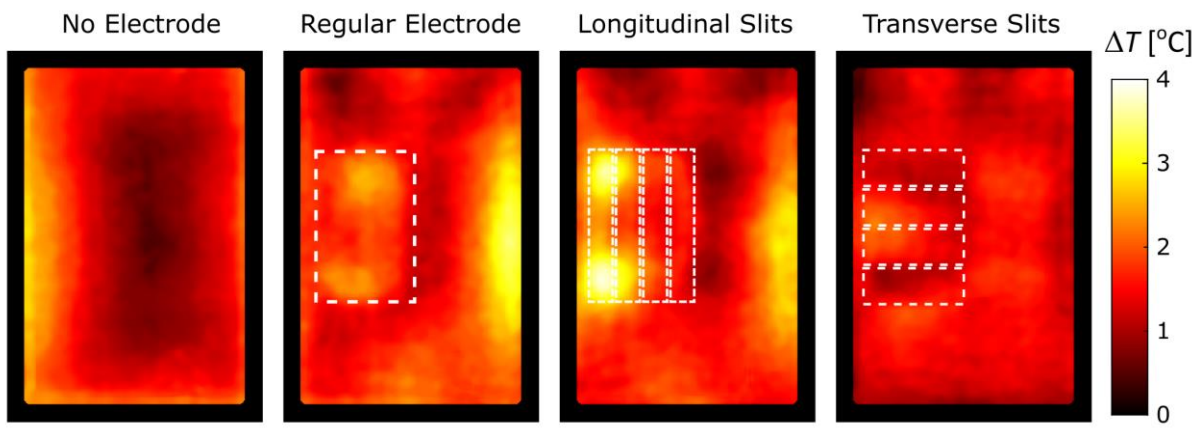

Fig.1 Thermographic images showing temperature increases in different defibrillation electrode configurations. RF heating was considerably higher when vertical slits were introduced and decreased for horizontal slits.

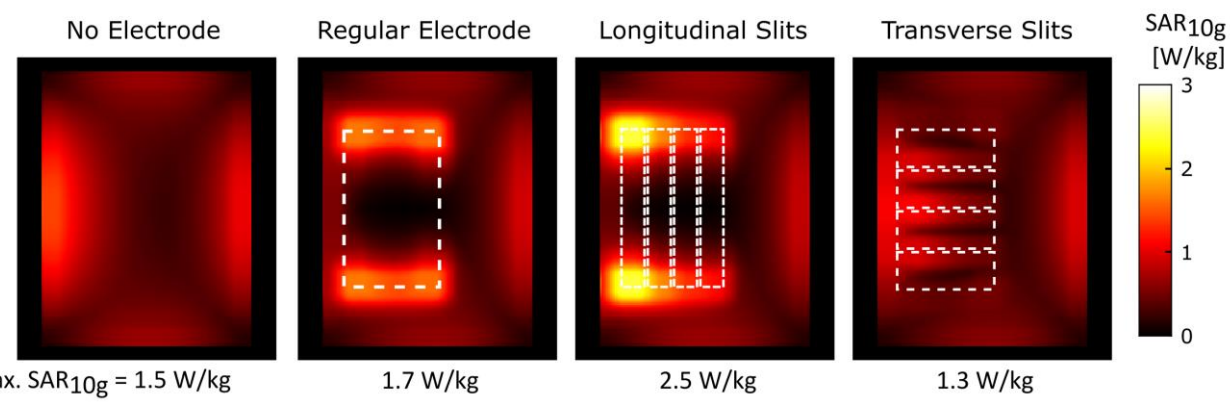

Fig.2 EM simulation results showing considerable changes in SAR_{10g} in different defibrillation electrode configurations. When vertical slits were introduced, local SAR_{10g} was almost doubled in comparison to having no electrode, while decreasing for the case of having horizontal slits.

A new single channel method for electromagnetic interference reduction on a 50 mT permanent magnet system

Javad Parsa[1,2], Thomas O'Reilly[1], and Andrew Webb[1]
[1]Leiden University Medical Center, Leiden, Netherlands
[2]Percuros B. V, Leiden, Netherlands.

Synopsis: External electromagnetic interference (EMI) in the unshielded low field and portable MRI systems can swamp the signal, and various multi-detector methods have been developed to minimize it. A new EMI cancellation method designed for a single-channel receiver-system has been implemented on a 50 mT system by using the MR-inactive channel of a birdcage coil and a 180o power hybrid. This method results in up to a 97% reduction in the standard deviation of external EMI.

Introduction: Low field MRI has received much attention in recent years due to its low cost and portability [1-3], along with the possibility of its use outside of RF shielded environments in unconventional locations. However, this increases the potential for substantial electromagnetic interference (EMI) created by equipment close to the scanner, in the image. Many different methods to reduce EMI for MRI/NMR have been explored in the past[4-10], mostly by using external sensors, with impressive results shown recently for a multi-channel low field system[10]. In this work, we test a simple single-channel approach on a Halbach-based low field MRI system operating at 2.15 MHz[1] , using a birdcage coil with the MR-inactive port detecting only the EMI. Phantom and in vivo images with and without EMI have been acquired to evaluate the approach.

Methods: The concept of the EMI-cancellation scheme is shown in figure 1. One channel of a circularly-polarized birdcage coil with the B_1-field orthogonal to the transvere B_0-field acquires signal plus EMI, while the other channel with the B_1-field parallel to B_0 only detects the EMI. For a simple acquisition system which only has one receive channel, the signals are subtracted using a 180° power combiner which makes the overall cost and complexity of the total system as low as possible.

A 16-leg low-pass transmit/receive birdcage for knee and calf muscle imaging was designed, simulated, and constructed (Figure 1). The coil dimensions were 19 cm × 16 cm × 16 cm to accommodate the human knee. The birdcage coil was constructed on a plexiglass cylinder using copper tape with 13 mm width and 0.06 mm thickness (Figure 1). A 180º power splitter/combiner (SBTCJ-1W+, Mini-Circuits, NY, USA), placed inside an aluminum shielded box, was connected to the two ports.

To test the method three different imaging setups were considered. First, the normal operating mode in which the subject's torso is covered by a conductive blanket (Holland Shielding Systems, Dordrecht, the Netherlands) and all other sides of the Faraday cage are closed. Second, an unshielded state (no blanket, Faraday cage open) with a 2.15 MHz sine wave produced by a function generator (33500 Series waveform generators, Agilent Technologist, US) acting as a narrow band EMI. Finally, unshielded as for the previous case, with a broadband EMI broadcast over a frequency range 0-3 MHz. For each of these setups, the following data were acquired. First, with only the MRI signal (S) port connected directly to the spectrometer, second with only the EMI port connected, and third the full setup with both the S and EMI ports connected via the power combiner to the spectrometer (Figure 1). A 3D turbo spin-echo (TSE) sequence was used to obtain images. The sequence parameters for the phantom (water-containing cylinder with diameter 14 cm, length 90 cm) imaging were TR/TE: 1000 ms/15 ms, ETL: 20, FOV: 150x150x300 mm, 2x2x5 mm resolution, and one average. In-vivo TSE parameters were TR/TE: 250 ms/15 ms, ETL: 4, FOV: 160x160x200 mm, 2x2x5 mm resolution, two averages, and two volunteers.

Results: Reflection coefficients (S_{11}) for each port and coupling between two ports (S_{12}) were lower than -27 dB,. Power splitter evaluation gave less than 0.2 dB insertion loss, 0.5º phase unbalance, and -25 dB inter-channel isolation. Figure 2 shows results acquired from the first shielded setup. The ratio of the signal from the S port to that of the EMI port was 45:1, representing a greater than 97% isolation between the ports. The signal from the combined port was reduced by ~40% compared to that of the S-port without the combiner present due to the inherent 3 dB reduction in signal and noise from the 180° hybrid. In the second experiment (figure 3), the standard deviation of the single line of narrowband EMI throughout the image was measured, and resulted in 97% and 71% reduction for the phantom and in vivo images, respectively. Figure 4 shows the third setup in which broadband EMI cancellation was 97% for the phantom and 90% for the in vivo images, respectively.

Discussion and Conclusion: A new EMI cancellation method has been introduced and tested for a 50 mT Halbach-based portable MRI system under different EMI conditions. A significant reduction in EMI was achieved using the new design. This simple approach has both advantages and limitations with respect to other methods. It does not require external sensors or extensive signal processing and can be implemented on a single receiver console. However, the use of a 180° power combiner does reduce the signal by 40%. The approach also relies on the external interference having essentially random polarization. Finally, the birdcage coil used here does have lower sensitivity than an equivalently-sized solenoid, although the solenoid also picks up a much larger EMI signal than the birdcage due to its B_1 spatial distribution which extends out of the magnet.

References

1. O'Reilly T, Teeuwisse W M, and Webb A G, In vivo 3D brain and extremity MRI at 50 mT using a permanent magnet Halbach array. Magn Reson Med. 2020;00:1-11.
2. Hyperfine - Portable MR Imaging: Bringing MRI to the Patient. https://hyperfine.io/?gclid=Cj0KCQiAx9mABhD0ARIsAEfpavS44Ax2KT5LfC36K95GbfZRUMXzf jyhkn0uwexFSyjqf933fxu5qAaAszcEALw_wcB. Accessed Jan. 31, 2021.
3. Cooley C Z, et al. A portable scanner for magnetic resonance imaging of the brain. Nature Biomedical Engineering. 2021; 5:229–239.
4. T Brosnan, F. Graham Sommer, Noise reduction in magnetic resonance imaging, Magn Reson Med. 1988; 08:394-409.
5. S. Vaishali, K. K. Rao and G. V. S. Rao, "A review on noise reduction methods for brain MRI images," 2015 International Conference on Signal Processing and Communication Engineering Systems; 2015: 363-365.
6. M. K. Laudon, J. G. Webster, R. Frayne and T. M. Grist, "Minimizing interference from magnetic resonance imagers during electrocardiography," in IEEE Transactions on Biomedical Engineering, 1998; 45: 160-164.
7. D.V. Trushkin, O.A. Shushakov, A.V. Legchenko. The potential of a noise-reducing surface NMR groundwater surveys in the earth's magnetic field Geophys. Prospect. 1994: 855-862.
8. E. Dalgaard, E. Auken, J.J. Larsen Adaptive noise cancelling of multichannel magnetic resonance sounding signals. Geophys. 2012; 19: 88-100
9. T. Kremer, J.J. Larsen, F. Nguyen Processing harmonic EM noise with multiple or unstable frequency content in surface NMR surveys Geophys. J. Int. 2019; 119: 753-775.
10. Sai Abitha Srinivas, and et al. External Dynamic InTerference Estimation and Removal (EDITER) for low field MRI. Magnetic Resonance in Medicine 2021, https://doi.org/10.1002/mrm.28992.

Acknowledgments / Funding Information: This work was funded by H2020-MSCA-ITN-ETN-2019 (NOVA-MRI 859908) and a Horizon 2020 ERC Advanced Grant (670629), Horizon 2020 ERC Advanced NOMA-MRI 670629.

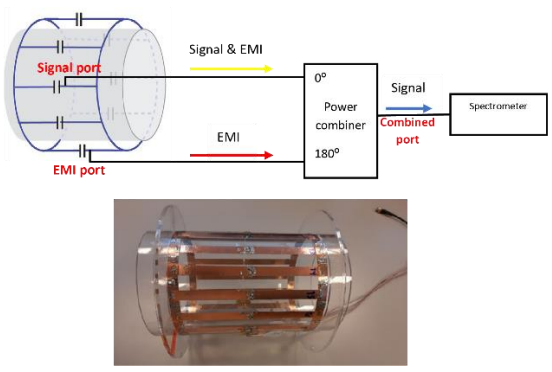

Figure 1. Top: A schematic of the method used to cancel EMI. The RF coil has two orthogonal ports, one of which is orthogonal to B_0 and the other coincident. Signals from the MR-inactive and MR-active ports are combined with a 180° phase shifter to remove the EMI. Bottom: Constructed birdcage coil.

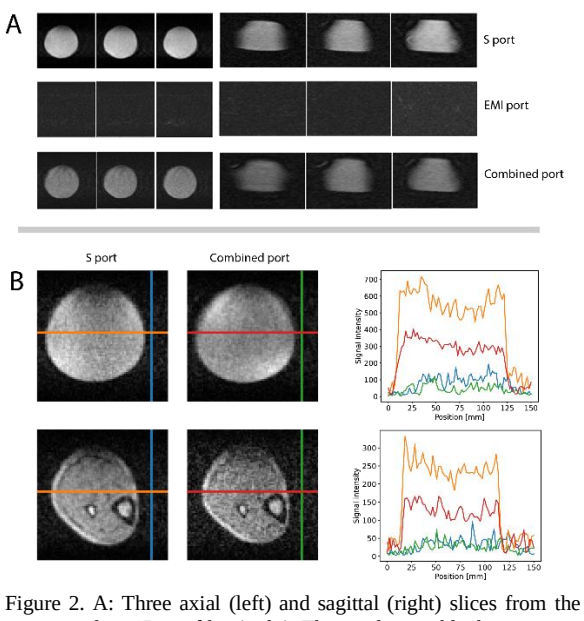

Figure 2. A: Three axial (left) and sagittal (right) slices from the phantom. B: Central-slice of phantom (top) and in vivo (bottom) images from the combined port (left) and the S port (middle) with corresponding 1D-profiles (right). The conducting blanket is present, the faraday shield is closed, and there is no external EMI applied.

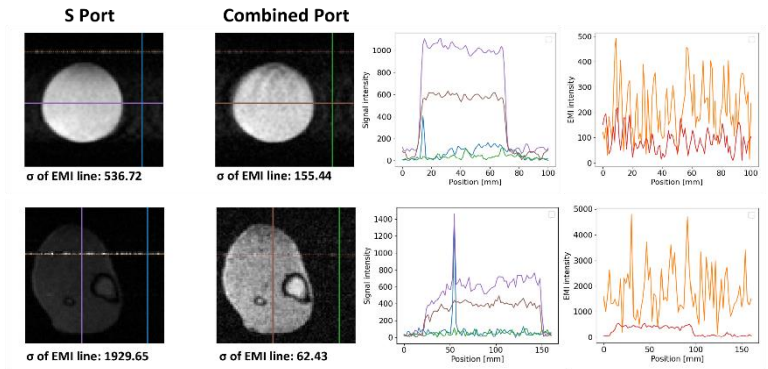

Figure 3. Phantom (top) and in vivo (bottom) with a single frequency EMI applied within the imaging bandwidth, apparent as the line through the image in the phase encoding direction. On the right, the orange lines show a projection along the line of the EMI from the S port, and the red lines from the combined port. The standard deviation (σ) of the EMI signal is also shown. There is no conducting blanket and the Faraday shield is open.

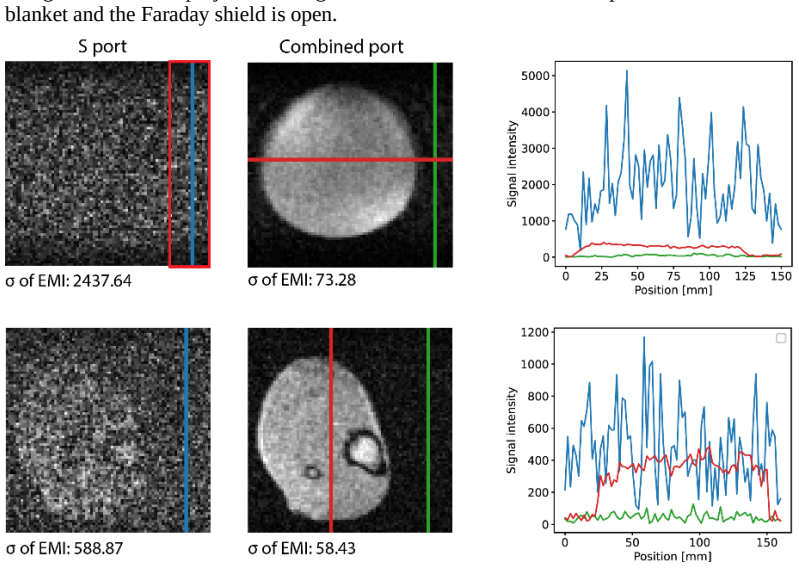

Figure 4. In vivo and phantom results using an external 0-3 MHz broadband EMI noise source. There is no conducting blanket and the Faraday shield is open. The red rectangle shows the region of interest that was used to measure the standard deviation (σ) of the EMI.

Measuring stroke volume with wearable RF antennas: a validation study with EM simulations and MRI

B.R. Steensma[1], C.A. Louka[1,2], A.J.E. Raaijmakers[3], C.A.T. van den Berg[1]

[1]Center for Image Sciences, University Medical Center Utrecht, Utrecht, The Netherlans; [2]Department of Physics, National Technical University of Athens, Athens, Greece, [3]Department of Biomedical Engineering, Eindhoven University of Technology, Eindhoven, The Netherlands

Synopsis: We developed a wearable setup to detect heart motion and stroke volume with an RF antenna connected to a miniature network analyzer. EM simulations were used to demonstrate the possibility of measuring changes in stroke volume with an RF antenna and to investigate the spatial sensitivity of the antenna. A Valsalva manoeuver was used to provoke changes in stroke volume, which were observed with the RF antenna and in cine MRI acquisitions.

Purpose: RF coils in MRI can be used to measure physiological motion during MR acquisitions[1–4]. In general, various types of RF antennas can be used as wearable motion sensors outside of the MRI system[5–7]. Since the input impedance of an RF antenna is modulated by conductivity of the tissue load[8], we hypothesize that RF antennas are sensitive to the amount of blood pumped by the heart per stroke (stroke volume). To investigate this hypothesis, we performed electromagnetic simulations of RF antenna impedance on a moving phantom and human body model. Impedance measurements were performed with an RF antenna before and after a Valsalva manoeuver (decreases the stroke volume[9]) and validated with MRI. To our knowledge, accurate non-invasive measurement of stroke volume is currently only possible with MRI or echo[10]. Our aim is to develop a low-cost wearable device that can be used to monitor stroke volume at home, for example in patients with heart failure.

Methods: Electromagnetic simulations were performed in a phantom to investigate the origin of sensitivity to motion in an RF antenna (Sim4Life, Zurich Medtech, Zurich, Switzerland). A dipole antenna was positioned on a cylindrical phantom with inside a sphere with the properties of blood (Figure 2). The sphere moved and/or increased in volume in 20 simulations. EM simulations were also performed on an XCAT model[11] (10 simulated cardiac phases, no respiratory motion). To visualize spatial sensitivity of the antenna, we used the reaction theorem, which expresses the change in complex antenna impedance in terms of electromagnetic fields with respect to a "dielectric" reference state at time t=0[12]:

$$Z(t) - Z_0 = -\frac{j\omega}{I^2}\int_V [\epsilon(r,t) - \epsilon(r,0)]E(r,t)\cdot E(r,0)dV = -\frac{j\omega}{I^2}\int_V dZdV \quad (1)$$

Simulations were performed at various transmit frequencies to investigate the effect of operating frequency on spatial sensitivity of the signal, which was visualized by plotting dZ. A 12cm diameter loop coil (Figure 1a) was matched at 128 MHz. The loop was placed in a neoprene (1b) belt to ensure proximity to the chest. Measurements were performed with a tabletop network analyzer (Planar TR1300/1, Copper Mountain Technologies, IN, US). An example of raw measurement data is shown in Figure 1c, both cardiac and respiratory motion are observed. To provoke changes in the stroke volume, 4 volunteers (3 male/ 1 female, age 21-30, BMI 18.4 – 22.0) performed a Valsalva manoeuver, while continuously measuring RF impedance. The same procedure was performed in the MRI scanner (1.5T Philips Achieva, Philips Healthcare, Best, The Netherlands), where a stack of transverse cine slices (2*2*10 mm^3, TR/TE 2.40/1.19 ms, FA 60°, 10-15 slices) was acquired before and at the end of the Valsalva manoeuver.

Results: Figure 2 shows the results of phantom simulations. There is a linear relationship between the volume of the sphere and changing antenna impedance. The antenna is most sensitive when the sphere moves closer to the antenna. Figure 3a shows the spatial sensitivity dZ of the antenna to heart motion. Signal only comes from regions where motion causes changes in the dielectric properties, which is caused by the $(\epsilon(r,t) - \epsilon(r,0))$ term in equation 1. Figure 3b shows that magnitude of the signal is comparable between frequencies, but the cardiac waveform differs strongly. The dipole antenna is more sensitive to cardiac motion than the loop coil. After bench testing with loop coils and dipole antennas at various frequencies, a loop coil at 128 MHz was used because this provided the most stable cardiac signal over multiple volunteers. Figure 4 shows measurement results on a single volunteer during Valsalva. The raw signal of the loop coil in a single volunteer is shown in Figure 4a. Both respiratory and cardiac components are visible in the signal. We consistently found in experiments that there is an almost 90° phase shift between the respiratory and cardiac component in the complex impedance signals. Figure 4c and 4d show that the area under the curve (AUC) and the root-mean-square (RMS) value of the signal decrease during Valsalva, which is also expected from physiology[9]. A decreasing stroke volume is also observed during Valsalva in the MRI acquisitions (Figure 5a/b). 5c and d show a comparison of the change in the RF impedance and in the stroke volume before and during Valsalva. A strong correlation is observed for volunteer 2-4 (M), but not for V1 (F).

Discussion: Simulation results indicate that the RF antenna impedance is sensitive to motion of interfaces close to the antenna. Indirectly, antenna impedance can therefore be used to estimate volume changes of organs close to the antenna, such as the heart or the lungs. The spatiotemporal sensitivity of the antenna to heart motion makes it strongly affected by transmit frequency, as indicated in figure 3. By using the Valsalva manoeuver, it is possible to provoke a decrease in stroke volume that is observable with a loop coil. Inter-subject variation of the sensitivity to changing stroke volume and the design of a flexible[3–15] setup are subject for further investigation.

Conclusion: We demonstrated through EM simulations and experiments that RF antennas are sensitive to changes in stroke volume. This enables the development of a low-cost wearable based on RF technology which can constantly monitor stroke volume, for example in patients with heart failure.

References:

1. Buikman D, Helzel T, Röschmann P. The rf coil as a sensitive motion detector for magnetic resonance imaging. Magn Reson Imaging. 1988;6(3):281-289. doi:10.1016/0730-725X(88)90403-1

2. Jaeschke SHF, Robson MD, Hess AT. Cardiac gating using scattering of an 8-channel parallel transmit coil at 7T. Magn Reson Med. 2018. doi:10.1002/mrm.27038

3. Andreychenko A, Crijns S, Raaijmakers A, et al. Noise variance of an RF receive array reflects respiratory motion: a novel respiratory motion predictor. In: International Society for Magnetic Resonance in Medicine (ISMRM). ; 2014.

4. Ludwig J, Speier P, Seifert F, Schaeffter T, Kolbitsch C. Pilot tone–based motion correction for prospective respiratory compensated cardiac cine MRI. Magn Reson Med. 2021. doi:10.1002/mrm.28580

5. Lin JC, Kiernicki J, Kiernicki M, Wollschlaeger PB. Microwave apexcardiography. IEEE Trans Microw Theory Tech. 1979. doi:10.1109/TMTT.1979.1129682

6. Hui X, Kan EC. Monitoring vital signs over multiplexed radio by near-field coherent sensing. Nat Electron. 2018. doi:10.1038/s41928-017-0001-0

7. Vas R. Electronic Device for Physiological Kinetic Measurements and Detection of Extraneous Bodies. IEEE Trans Biomed Eng. 1967. doi:10.1109/TBME.1967.4502453

8. Navest RJM, Mandija S, Andreychenko A, Raaijmakers AJE, Lagendijk JJW, van den Berg CAT. Understanding the physical relations governing the noise navigator. Magn Reson Med. 2019. doi:10.1002/mrm.27906

9. Inan OT, Etemadi M, Wiard RM, Kovacs GTA, Giovangrandi L. Non-invasive measurement of Valsalva-induced hemodynamic changes on a bathroom scale ballistocardiograph. In: Proceedings of the 30th Annual International Conference of the IEEE Engineering in Medicine and Biology Society, EMBS'08 - "Personalized Healthcare through Technology." ; 2008. doi:10.1109/iembs.2008.4649242

10. Borzage M, Heidari K, Chavez T, Seri I, Wood JC, Blüml S. Measuring stroke volume: Impedance cardiography vs phasecontrast magnetic resonance imaging. Am J Crit Care. 2017. doi:10.4037/ajcc2017488

11. Segars WP, Sturgeon G, Mendonca S, Grimes J, Tsui BMW. 4D XCAT phantom for multimodality imaging research. Med Phys. 2010. doi:10.1118/1.3480985

12. Richmond JH. A Reaction Theorem and Its Application to Antenna Impedance Calculations. IRE Trans Antennas Propag. 1961. doi:10.1109/TAP.1961.1145068

13. Port A, Luechinger R, Brunner DO, Pruessmann KP. Elastomer coils for wearable MR detection. Magn Reson Med. 2021. doi:10.1002/mrm.28662

14. Zhang B, Sodickson DK, Cloos MA. A high-impedance detector-array glove for magnetic resonance imaging of the hand. Nat Biomed Eng. 2018. doi:10.1038/s41551-018-0233-y

15. Vincent JM, Rispoli J V. Conductive Thread-Based Stretchable and Flexible Radiofrequency Coils for Magnetic Resonance Imaging. IEEE Trans Biomed Eng. 2020. doi:10.1109/TBME.2019.2956682

Acknowledgments / Funding Information: NWO open mind grant 18802, University Medical Center Utrecht circulatory health grant

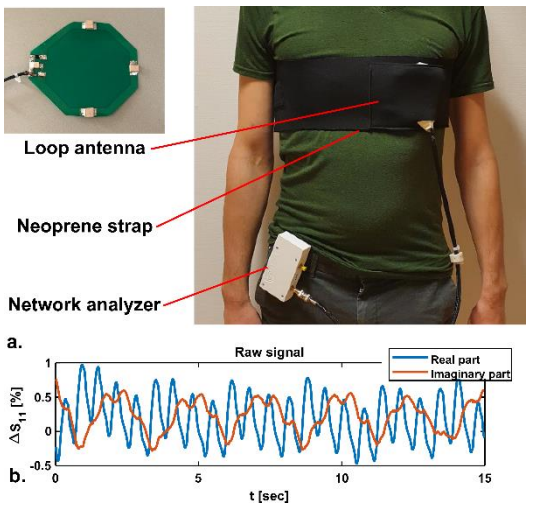

Figure 1: 1a. Wearable setup for monitoring stroke volume, including a 128 MHz loop coil, which is placed in a neoprene strap on the chest of the subject. To make the device completely wearable, a NanoVNA (nanovna.com) was used was adapted (Wavetronica, Utrecht, The Netherlands) to transmit data to a PC with a Bluetooth dongle. 1b. Raw complex signal as measured with the loop coil, showing both cardiac (real, blue) and respiratory motion components (imaginary, red).

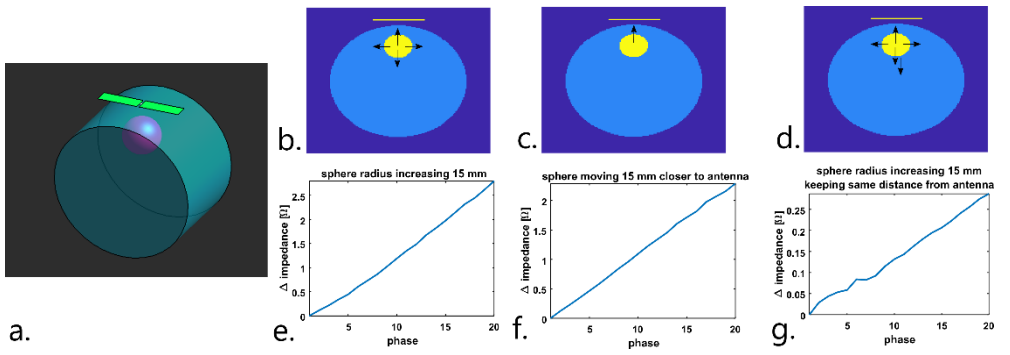

Figure 2: 2a. Setup used in phantom simulations, containing a cylinder with average electrical properties of the torso (ε_r=40, σ = 0.4 S/m), and a sphere with the electrical properties of blood (ε_r=62 σ = 1.42 S/m). The sphere either increases in radius (2b), moves towards the antenna (2c) or increases in radius but remains at the same distance from the antenna (2d). Figure 2e-g show the respective changes in antenna impedance.

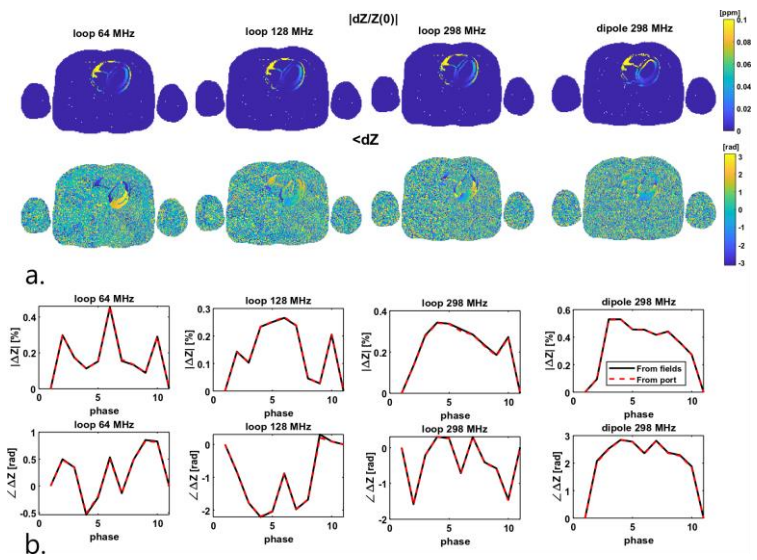

Figure 3: 3a. spatial maps of the magnitude and phase of the antenna sensitivity dZ to cardiac motion, for various operating frequencies and antennas. Respiratory motion was not included in the model. 3b. impedance change for the different phases in the heart cycle as calculated from the fields with the reaction theorem and as extracted from the ports in the simulation.

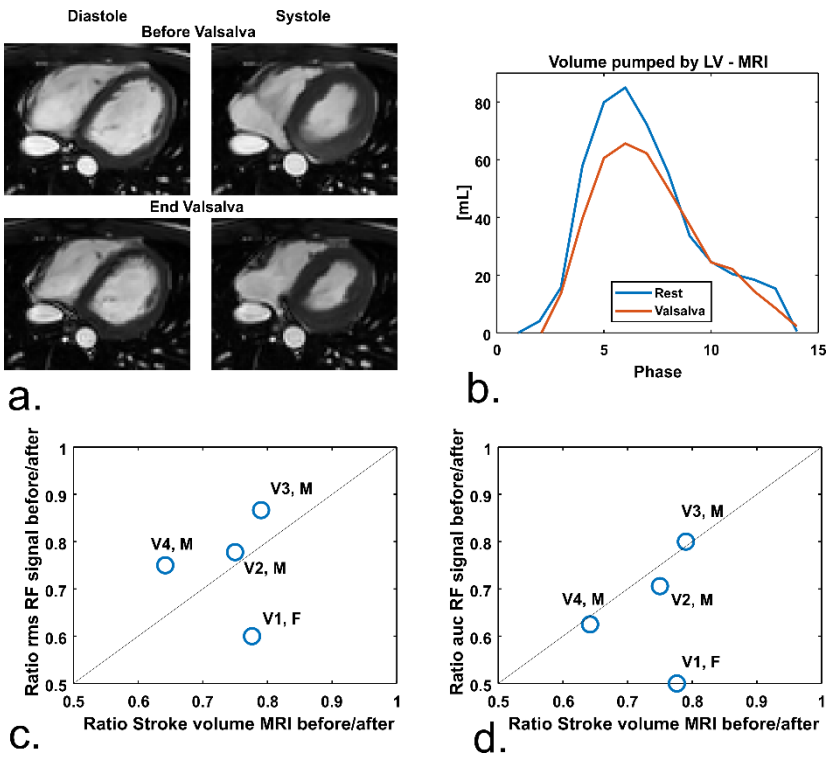

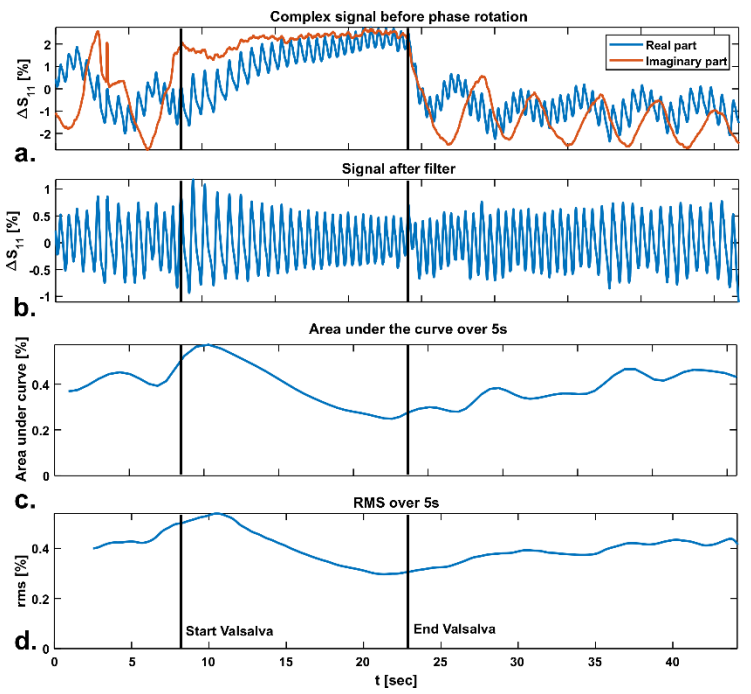

Figure 4: Exemplary signals during Valsalva manoeuver in V4 (M, 22y, BMI 18.4). 4a Raw signal, where the heart motion is visible in the real part and the breathing motion is visible in the imaginary part of the signal. 4b Cardiac signal after filtering. Time of the Valsalva manoeuver is indicated by the lines. During the Valsalva manoeuver, the RMS value (4c) and the AUC (4d) decrease.

Figure 5: 5a center slice of a transverse cine acquisition from which stroke volume was calculated. Clear differences are visible in the size of the heart before and after Valsalva. 5b. Stroke volume before and after Valsalva, as calculated from a stack of cine images covering the left ventricle. 5c and 5d. Ratio of the RMS value and the AUC of the RF signal before/after Valsalva, plotted against the ratio of stroke volumes before/after Valsalva as calculated from the MR images.

ATowards motion robust MRT during Microwave Hyperthermia by integrating an 8-channel receiver coil array into the MRcollar

Kemal Sumser[1], Gennaro G Bellizzi[1], Juan A Hernandez-Tamames[2], Gerard C van Rhoon[1], and Margarethus M Paulides[1,3]
[1]Department of Radiotherapy, Erasmus Medical Center Rotterdam, Rotterdam, Netherlands, [2]Department of Radiology and Nuclear Medicine, Erasmus Medical Center Rotterdam, Rotterdam, Netherlands, [3]Department of Electrical Engineering, Eindhoven University of Technology, Eindhoven, Netherlands

Synopsis: In the head and neck region, precise heating and temperature monitoring is a challenge. The MRcollar, an MR compatible head and neck microwave hyperthermia applicator has been developed for conformal heating and to enable MR thermometry (MRT) during the treatment. To deliver on the needs of accurate temperature monitoring, the MRcollar has been equipped with 8-channel receiver coil array. This coil array improves increased the SNR by 5 times compared to the body coil of the MRcollar. Increase in the SNR also led to improvement in the MRT precision, from 0.91 °C to 0.37 °C.

Introduction

In the head and neck region, precise heating and temperature monitoring is a challenge. The MRcollar, an MR compatible head and neck microwave hyperthermia applicator has been developed for conformal heating and to enable MR thermometry (MRT) during the treatment. MRT has great potential to deliver on temperature monitoring needs but the precision and speed requirements demand high signal-to-noise-ratio (SNR) measurements. Hereto, we developed an integrated applicator-multichannel receiver coil array concept for high SNR performance and parallel imaging by near-skin receiving the radio frequency signals of the MR imaging [1]. This concept was used in the MRcollar that has twelve antennas for heating and now incorporates eight MR-receive coils. Herein, we quantify the SNR and MRT precision gain that the integrated receive coils offer against receiving the signals by the body coil of the MR scanner.

Methods

The MRcollar (fig. 1a) consists of two crescent moon-shaped shells each consisting of six antenna modules in a 2 x 3 arrangement placed around the head and neck for 12 antenna setup. Every module contains a printed Yagi-Uda antenna submerged in water and operating at 433.92 MHz. The MRcollar houses 8-channel MR receiver coil array tuned to 63.89 MHz for MR imaging at 1.5 T. Each of the moon-shaped shells include a 3-channel receive coil array (a bottom (15 x 8 cm), a central (15 x 12 cm) and a top (15 x 8 cm) rectangular shaped loops) and the head rest includes a 2-channel receive coil array (butterfly coil 20 x 9 cm and 9 x 9 cm rectangular shaped loops).

The cylindrical phantom provided by the MR vendor as well as the standard MRT sequence, i.e. a fast gradient echo sequence was used for the evaluation with the following parameters: TR: 100 ms, TE: 19.2 ms, flip angle 30°, resolution 1.25 x 1.25 x 3 mm3, matrix resolution 256 x 256, total acquisition time 25.6 s. In total, 12 acquisitions were made. SNR was calculated in a region of interest (ROI) (fig. 1b) using the dual image subtraction method [2]. Temporal MRT precision was calculated for each voxel assuming that the temperature remained constant during the experiments. PRFS thermometry was calculated using the first acquisition as the baseline, the voxels which are highlighted in red in fig. 1c were used for field drift correction [3].

Results

Example magnitude images for the body coil as receiver and the MRcollar receiver coil array are visualized in the first column of fig. 2, and example MRT and precision maps are given in the columns 2-4 of fig 2. SNR was 23 when the phantom was imaged using the body coil as a receiver and SNR was improved around five-fold to 120 for the 8-channel receiver coil of the MRcollar. Since MRT is a differential method, improvement in the SNR also led to an improved MRT precision. The lowest measured standard deviation reduced from 1.8 °C for the body coil acquisition to 0.55 °C for the MRcollar receiver coils. The average standard deviation in the ROI reduced from 0.91 °C for the body coil to 0.37 °C for the MRcollar coils.

Conclusion

Integrating the receiver coils in the MRcollar led to the an important improvement in SNR. The 5-fold increase in the SNR improves the accuracy and the precision of the MRT results since MRT is a differential measurement method which amplifies the effect of the noise. In addition to the SNR benefits, the integrated receiver coil array also allows for the use of advanced MR techniques, such as parallel imaging, to enable faster acquisition times for correction of the impact of respiratory motion. Hence, integration of the receiver arrays close to the skin into MR hyperthermia devices provides a crucial step towards reliable temperature monitoring during hyperthermia.

References

[1] Sumser K, Bellizzi GG, Forner R, Drizdal T, Tamames JA, Van Rhoon GC, Paulides MM. Dual-Function MR-guided Hyperthermia: An Innovative Integrated Approach and Experimental Demonstration of Proof of Principle. IEEE Transactions on Biomedical Engineering. 2020 Jul 29.

[2] Goerner FL, Clarke GD. Measuring signal-to-noise ratio in partially parallel imaging MRI. Medical physics. 2011 Sep;38(9):5049-57.

[3] Sumser K, Bellizzi GG, van Rhoon GC, Paulides MM. The potential of adjusting water bolus liquid properties for economic and precise MR thermometry guided radiofrequency hyperthermia. Sensors. 2020 Jan;20(10):2946.

Acknowledgments / Funding Information: This work was developed within the framework of COST Action MyWAVE CA17115312 and it was funded by the Dutch Cancer Society grants EMCR 2012-5472 and 11368.

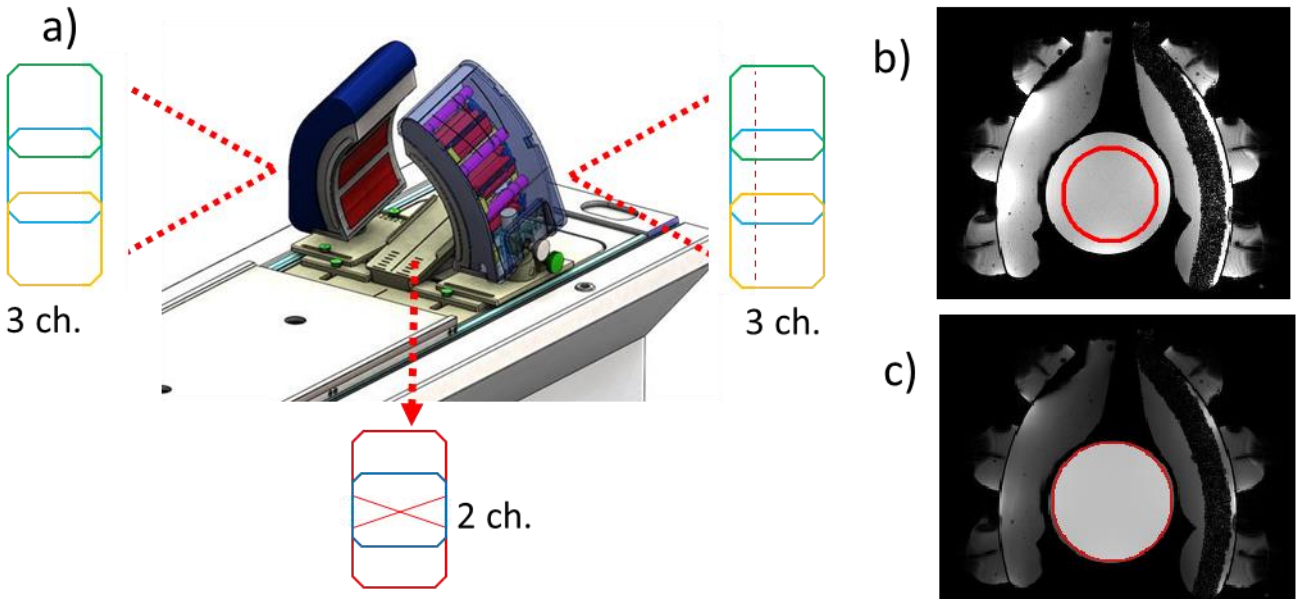

Figure 1. a) The MRcollar and the locations of the 8-channel coil array, b) the ROI that was used for SNR calculation, c) the voxels that was used for B0 drift correction.

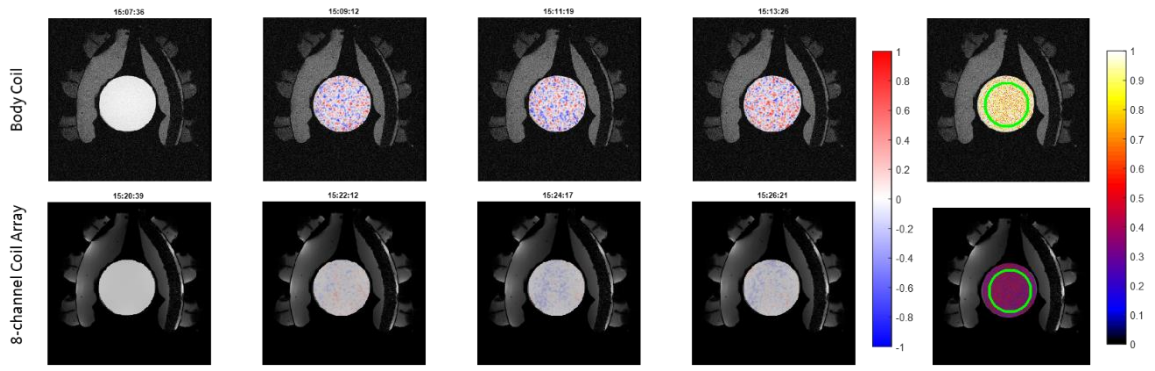

Figure 2. Example MRT maps (first four columns) and temporal precision map for MRT (last row) for the body coil (top row) and for the 8-channel coil array (bottom row)

A lightweight silent gradient axis with integrated 32 channel receive array for fast and quiet brain imaging at 3 Tesla

E. Versteeg[1], M. van Uden[2], L. van der Hofstad[2], K. Bax[2], M. Borgo[2,3], W. Schuth[3], J. Siero[1,4], Mark Gosselink[1], D. Klomp[1]
[1]Department of Radiology, University Medical Center Utrecht, Utrecht, The Netherlands; [2]Tesla Dynamic Coils, Zaltbommel, The Netherlands; [3]Futura Composites, Heerhugowaard, The Netherlands; [4]Spinoza Centre for Neuroimaging, Amsterdam, The Netherlands

Synopsis: The sound level in MRI can be lowered by using a silent gradient axis that adds extra soundless encoding. In this work, we present the field characteristics and first images for a silent gradient designed for a clinical 3 tesla system. This silent gradient featured a built-in 32-channel receive coil and weighs 21 kg. The gradient field could be oscillated at 23.5 kHz and featured a linear region of 20 cm. The coil had limited interactions with the transmit B1 field and did not affect B1 homogeneity, which was showcased in phantom and in-vivo images.

Purpose: Most MR-exams intrinsically feature loud acoustic noise as the imaging gradients need to be switched fast and at high amplitude to ensure short acquisition times. Together with claustrophobia these loud sounds are the main sources of patient anxiety during MR-exams, which might lead to a degradation of the image quality (1,2). Previously, we have presented a silent gradient axis that aims to lower sound levels by providing extra soundless spatial encoding and allow the other imaging gradients to be switched slower, which reduces the sound level without loss of imaging time(3). In this work, we present the field characteristics and first images for a silent gradient designed for a clinical 3 tesla MR-system.

Methods:

Gradient design

An open and lightweight design was targeted for the silent gradient (Futura composites, Heerhugowaard & Tesla DC, Zaltbommel). The silent gradient coil consisted of 32 windings distributed in two groups (16 windings per group), which were spaced 25 cm apart and produced a z-gradient field. By grouping the windings like this, the amount of epoxy needed to pot the gradient coil was minimized resulting in a weight of 21 kg of the whole coil, which facilitates easy installation comparable to a standard head coil. The gradient coil was made resonant at 23.5 kHz using two capacitors and combined with a modified gradient amplifier (NG500, Prodrive Technologies, Son) to maximize the silent encoding (4). Furthermore, a 32-channel receive coil array was integrated into the coil with the receive elements distributed over 4 rows extending in the feet-head direction to facilitate parallel imaging along the direction of the silent gradient. This receive array consisted of two attached PCB's containing all coils which were decoupled based on a predetermined overlap. Figure 1 shows the final coil design.

Characterization

The gradient field distribution was calculated using Biot-Savart and was used to determine gradient efficiency and field linearity. The exact resonance frequency and spatiotemporal gradient field behavior were measured using a dynamic field camera (Skope Magnetic Resonance Technologies AG, Switzerland). During these measurements the gradient coil was positioned in a 7T MR-system (Philips, The Netherlands). To investigate transparency of the setup to the transmit field of the 3T RF body-coil, B1-mapping was performed with the same subject, once with the setup and once with the standard Philips head coil.

Images

For imaging experiments, the RF coil array with the embedded silent gradient was positioned in a 3T MR-system (Ingenia CX, Philips, Best). A phantom consisting of a water-filled bottle was imaged to investigate the imaging performance along the linear region of the gradient. Here, a modified 2D gradient-echo sequence that plays out the silent gradient during readout was used with the following imaging parameters: coronal slice orientation, in-plane resolution = 2 x 2 mm^2, FOV = 256 x 512 (RL x FH) mm^2, slice-thickness = 4 mm, TE = 5.6 ms, TR = 60 ms, and flip angle = 16°. Additionally, a similar sequence was used to image a volunteer with the following imaging parameters: coronal slice orientation, in-plane resolution = 1 x 1 mm^2, FOV = 256 x 256 (RL x FH) mm^2, slice-thickness = 6 mm, TE = 21 ms, TR = 60 ms, and flip angle = 21°. All images were acquired with the silent gradient operating at 22.5 mT/m. Reconstruction was performed off-line in MATLAB using the field camera data and a non-uniform Fourier transform.

Results and Discussion: Figure 2a shows the field distribution of the silent gradient. Here, the gradient efficiency was determined to be 0.56 mT/m/A. Figure 2b shows the deviation from a perfectly linear gradient field for the silent gradient, which shows that the gradient field has less than 10% deviation from linearity in a 20 cm DSV. The field measurements in figure 2C shows the gradient field oscillating at 23.5 kHz and at an amplitude of 22.5 mT/m. Additionally, the silent gradient needs about 1.5 ms to reach a steady state and ~1 ms to return back to zero.

The B1-maps (Fig 3ab) shows similar performance with both setups in the MR-system suggesting that the interaction with the gradient coil is limited. On average the B1 measured with the silent gradient system was ~10% lower. However, the B1-field homogeneity was not affected as the spread in B1-values (Figure 3c) was similar for both setups ($\sigma_{B1\text{-silent gradient}}$ = 2.3 μT vs $\sigma_{B1\text{-standard coil}}$ = 2.4 μT).

Figure 4a shows that no significant distortion is observed over the 20 cm linear region. However, some signal loss was seen outside this region, which might be recovered by incorporating the field non-linearity in the reconstruction. In Figure 4b, the in-vivo image shows that the whole-brain fits in the 20 cm linear region.

Earlier work on silent gradient axes was performed at 7 tesla, where a 26 dB reduction in sound level was achieved for a T1-weighted anatomical scan (5). Translating the concept of the silent gradient axis to 3 tesla is expected to yield similar or lower sound levels as the Lorentz forces at 3 tesla are intrinsically lower.

Conclusion: We have presented a silent gradient designed for 3 tesla MR-system, which can enable quiet and fast brain imaging.

References:

1. McNulty JP, McNulty S. Acoustic noise in magnetic resonance imaging: An ongoing issue. Radiography 2009;15:320–326 doi: 10.1016/j.radi.2009.01.001.

2. Dewey M, Schink T, Dewey CF. Claustrophobia during magnetic resonance imaging: Cohort study in over 55,000 patients. J. Magn. Reson. Imaging 2007;26:1322–1327 doi: 10.1002/jmri.21147.

3. Versteeg E, Klomp DWJ, Siero JCW. A silent gradient axis for soundless spatial encoding to enable fast and quiet brain imaging. Magn. Reson. Med. 2021;00:1–12 doi: 10.1002/MRM.29010.

4. Welting D, Versteeg E, Voogt I, et al. Towards 8ch multi transmit with high power ultrasonic spirals and 72ch receive setup for ultimate spatial encoding at 7T. In: Proceedings of the 29th Annual Meeting of ISMRM. ; 2021. p. 0563.

5. Versteeg E, Jacobs SM, Oliveira ÍAF, Klomp DWJ, Siero JCW. Fast and quiet 3D MPRAGE using a silent gradient axis- sequence development. In: Proceedings of the 29th Annual Meeting of ISMRM. ; 2021. p. 0842.

Acknowledgments / Funding Information: This project was funded by EUROSTARS Beyond 11362

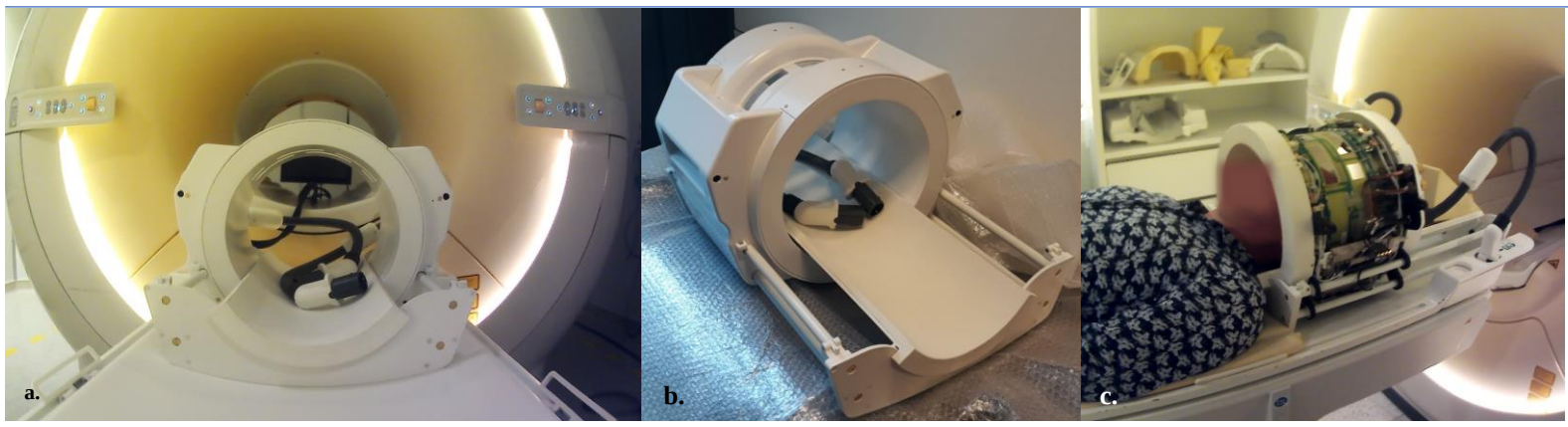

Figure 1 The final gradient design. This shows the silent gradient in a 3T MR system (**a.**) and the open design of the coil (**b.**). **c.** shows the silent gradient without covers and with a volunteer for scale. Note the open PCB design which enables the use of a mirror system to look at images/movies during scanning.

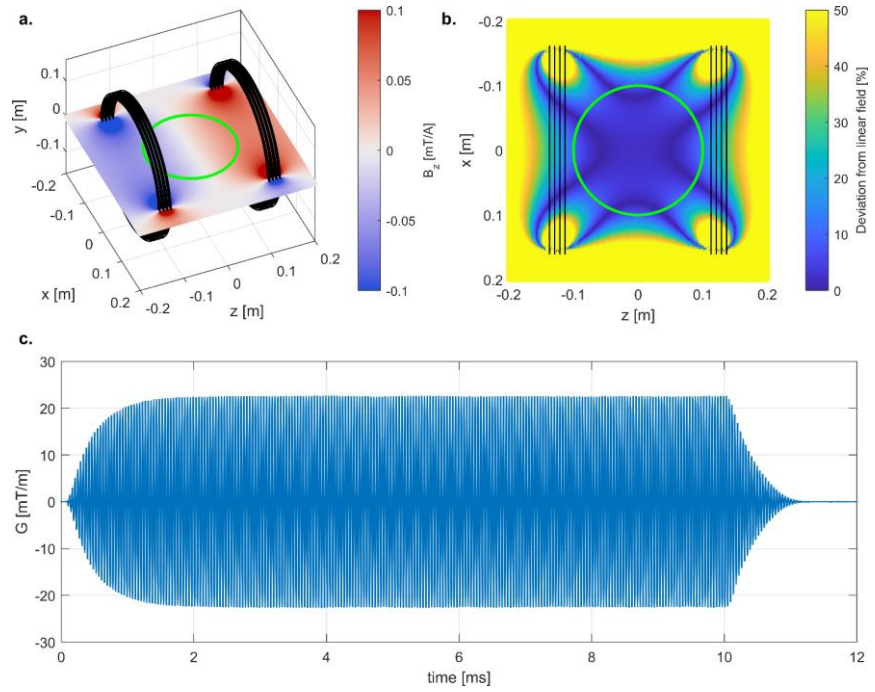

Figure 2 Characterization of the silent gradient. **a.** field distribution for 1 A of current with in green the DSV with <10% deviation from linearity. **b.** the deviation from linearity with in green the DSV with < 10% deviation from linearity. **c.** The field camera measurement of the silent gradient.

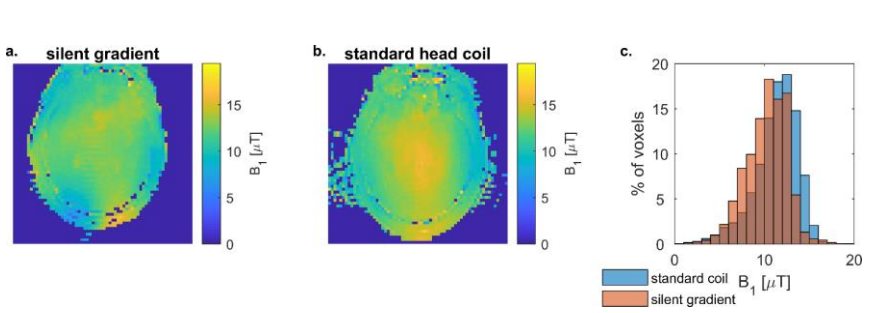

Figure 3 B1-mapping results for a target B1 of 13.49 µT: **a.** with the silent gradient in the MR-system **b.** with the standard head coil in the MR-system **c.** histogram of the B1 measured in the whole-brain for both setups. Note that the B1-distributions of both measurements look similar (similar B1 homogeneity).

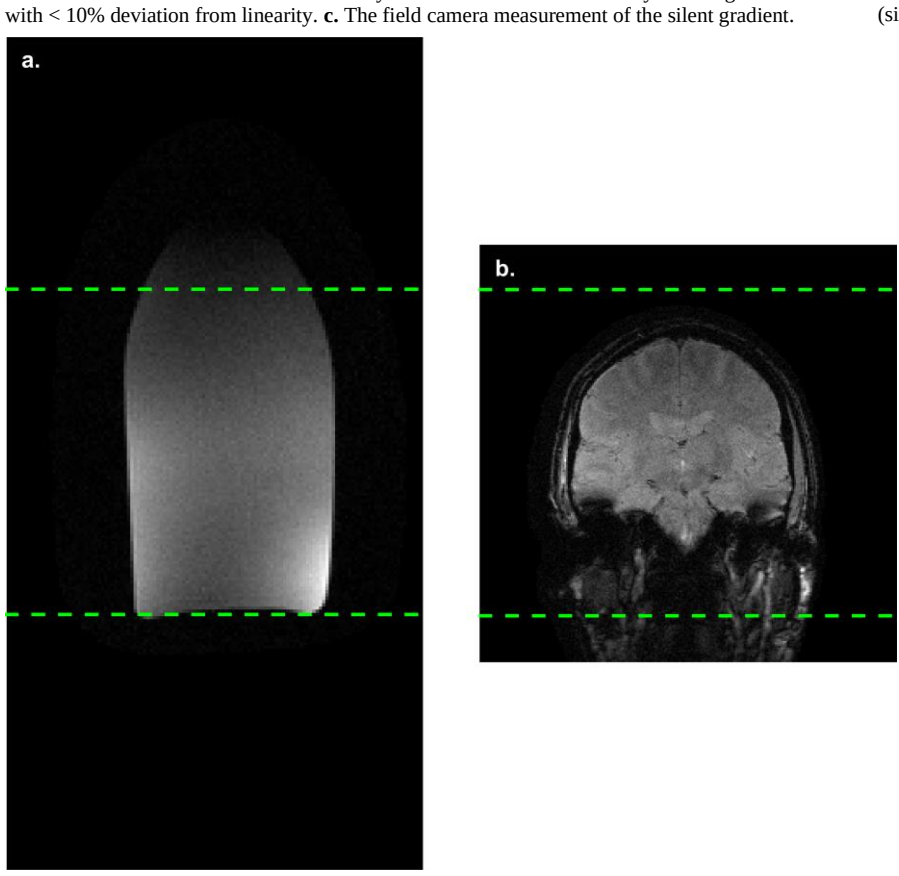

Figure 4 Images acquired with the silent gradient. **a.** Bottle phantom with a large field-of-view in the direction of the silent gradient. The green lines indicate the edges of the 20 cm DSV with <10% linearity. **b.** in-vivo image with the green lines indicating the DSV with <10% linearity.

Three-dimensional magnetic resonance fingerprinting at 50 mT with integrated estimation and correction for image distortions due to B_0 inhomogeneities

K. Koolstra[1], T. O'Reilly[2], P. Börnert[2,3], A. Webb[2]

[1]Division of Image Processing, Radiology, Leiden University Medical Center, the Netherlands

[2]C.J. Gorter Center for High Field MRI, Radiology, Leiden University Medical Center, the Netherlands

[3]Philips Research Hamburg, Hamburg, Germany

Introduction

Magnetic resonance fingerprinting (MRF) offers a way to acquire relaxation time maps in an efficient manner and has shown its use in many 1.5T and 3T applications[1]. The T_1 and T_2 relaxation times can potentially be used to generate a variety of image contrasts retrospectively[2]. This could be particularly relevant at low field[3], where scans take many minutes due to a lower signal-to-noise ratio (SNR). Portable point-of-care permanent magnet systems often have large B_0 inhomogeneities, which can cause image distortions and signal dropout. MRF is a flexible acquisition framework[4] that can encode the B_0 field inhomogeneities in the acquisition process, to incorporate them in the reconstruction process. In this work, we use an alternating TE pattern in the MRF sequence that supports ΔB_0 estimation from the MRF data. We use the reconstructed ΔB_0 map to correct for B_0-induced image distortions of the MRF images, before matching them to the calculated dictionary. This method reduces distortions in the relaxation time maps without needing to acquire an additional ΔB_0 map.

Methods

Hardware: We used a 50 mT Halbach magnet consisting of 23 rings filled with neodymium boron iron magnets, shown in Fig. 1A, with custom-built RF and gradient amplifiers and a Magritek Kea2 spectrometer (Fig. 1B). A 15 cm diameter, 15 cm long solenoid coil was used in transceive mode (Fig. 1C). A mechanical robot with a magnetic field probe was used to map the B_0 field during system installation.

*Fingerprinting implementation***:** MRF data were acquired with a FISP sequence[5], using an optimized flip angle pattern of 240 RF shots, a constant TR of 12 ms and an alternating TE pattern to support ΔB_0 estimation, shown in Fig. 2A. The dictionary was generated using the extended phase graph formalism, with T_1 values ranging from 20-500 ms (5 ms steps), T_2 values ranging from 10-500 ms (5 ms steps) and B_1^+ fraction ranging from 0.05-1.50 (0.05 steps).

MR Data acquisition: Experiments were performed in the lower leg of 2 healthy volunteers with informed consent obtained. Three-dimensional MRF scans were acquired with a Cartesian sampling scheme shown in Fig. 2B. Scan parameters: FOV = 170×150×99 mm^3, resolution = 2.5×2.5×3.0 mm^3, $TE_1/TE_2/TR$ = 6.00/6.15/12.0 ms, imaging bandwidth (BW) = 294 Hz/pixel, undersampling factor = 8.6, scan time = 13 min and 6 s. Inversion recovery (inversion times = 25/50/75/100/150/300 ms) and multi-echo-spin-echo (TEs = 20/40/60/80/100/120/140/160/180/200 ms) were used for reference T_1 and T_2 mapping, respectively. A TSE-based ΔB_0 map was acquired for comparison[6].

Reconstruction: MRF images were reconstructed using a matrix completion-based reconstruction on the two separate TE series[7]. A ΔB_0 map was estimated from the two series using total variation regularization and spherical harmonic decomposition and used in a model-based reconstruction framework to correct for image distortions[6]. The resulting combined image series were matched to the dictionary using the simulated B_1^+ excitation profile (Fig. 1E) as prior information for each slice. This pipeline is schematically shown in Fig. 2C.

Results

Figure 3 shows that the relaxation times obtained with MRF (constant TE, without distortion correction) are close to those obtained with the reference techniques, but the SNR of the MRF maps is lower compared to that of the reference maps, as expected. Using an alternating TE pattern results in very similar parameter maps compared to using a constant TE (both without distortion correction), as shown in Fig. 4. Estimating a ΔB_0 map from the alternating TE pattern and using it in a model-based MRF reconstruction results in matched parameter maps with reduced distortions. The estimated ΔB_0 map is in the same range as that estimated from a TSE sequence, with a maximum error of 105 Hz.

Discussion

The acquired MRF ΔB_0 map corresponds with the map measured with a robot and that measured with a fully encoded TSE sequence. The difference between the MRF-based ΔB_0 map and the TSE-based ΔB_0 map could have been introduced by hardware imperfections (spectrometer timing jitter, eddy currents, etc.) leading to phase errors in the MRF sequence or by heating of the magnet during the imaging session. Using the ΔB_0 map in a model-based reconstruction framework reduces the image distortions along the readout direction of the parameter maps. The remaining signal void at the left side of the M_0 map is a result of through-plane B_0-induced dephasing, for which the current reconstruction algorithm does not correct. Future work could resolve this by incorporating a ΔB_0 map with a higher through-plane resolution into the signal model.

Conclusion

It is possible to integrate ΔB_0 estimation and correction in an MRF acquisition and reconstruction framework for a 50 mT permanent magnet MR system. The proposed framework reduces the image distortions of the MRF relaxation time maps without increasing the scan time.

References

[1]Panda, Ananya, et al. "Magnetic resonance fingerprinting–an overview." Current opinion in biomedical engineering (2017) 3:56-66.

[2]Blystad, Ida, et al. "Synthetic MRI of the brain in a clinical setting." Acta radiologica (2012) 53(10): 1158-1163.

[3]O'Reilly, Thomas, and Andrew G. Webb. "In vivo T1 and T2 relaxation time maps of brain tissue, skeletal muscle, and lipid measured in healthy volunteers at 50 mT." Magnetic Resonance in Medicine (2021).

[4]Sarracanie, Mathieu. "Fast Quantitative Low-Field Magnetic Resonance Imaging With OPTIMUM-Optimized Magnetic Resonance Fingerprinting Using a Stationary Steady-State Cartesian Approach and Accelerated Acquisition Schedules." *Investigative Radiology* (2021).

[5]Jiang, Yun, et al. "MR fingerprinting using fast imaging with steady state precession (FISP) with spiral readout." Magnetic resonance in medicine (2015) 74(6):1621-1631.

[6]Koolstra, Kirsten, et al. "Image distortion correction for MRI in low field permanent magnet systems with strong B0 inhomogeneity and gradient field nonlinearities." Magnetic Resonance Materials in Physics, Biology and Medicine (2021):1-12.

[7]Doneva, Mariya, et al. "Matrix completion-based reconstruction for undersampled magnetic resonance fingerprinting data." Magnetic resonance imaging (2017) 41:41-52.

[8]Koolstra, Kirsten, et al. "Water–fat separation in spiral magnetic resonance fingerprinting for high temporal resolution tissue relaxation time quantification in muscle." Magnetic resonance in medicine (2020) 84(2):646-662.

Acknowledgments / Funding Information: This work is supported by the following grants: Horizon 2020 ERC FET-OPEN 737180 Histo MRI, Horizon 2020 ERC Advanced NOMA-MRI 670629, Simon Stevin Meester Award and NWO WOTRO Joint SDG Research Programme W 07.303.101. We would also like to thank Hanna Liu for sharing the optimized flip angle train with us.

Figure 1. Experimental setup. (A) Halbach magnet. (B) Gradient amplifiers (left), RF amplifier (middle) and spectrometer (right). (C) solenoid transceive RF coil. (D) ΔB_0 field in Hz with respect to the center frequency, measured with a robot. (E) RF excitation profile along the bore.

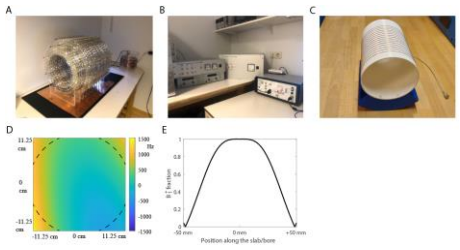

Figure 2. Fingerprinting sequence and reconstruction pipeline. (A) The MRF sequence uses a flip angle train of 240 RF shots and an alternating TE pattern similar to that in Ref. 8. (B) The 3D sampling pattern. The sampled phase encoding numbers are plotted for each of the RF shots. (C) The MRF data is reconstructed using matrix completion, after which a ΔB_0 map is estimated from the TE difference. The ΔB_0 map is used to correct for B_0-induced image distortions in the MRF images, before matching the data to the dictionary.

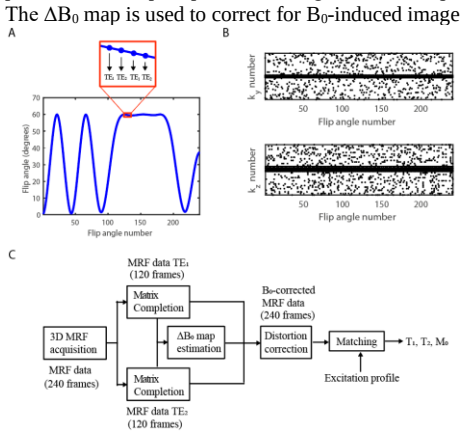

Figure 3. Comparison of relaxation time maps obtained with MRF and with reference techniques in the lower leg. The muscle T_1 times measured with MRF are in the same range as those measured with an inversion recovery sequence (175 ms vs 165 ms), but the muscle T_2 times measured with MRF are longer than those measured with MESE (60 ms vs 40 ms). The SNR of the MRF maps is lower, as expected. Scan parameters for inversion recovery: TE/TR = 12/900 ms, echotrain length (ETL) = 5. Scan parameters for multi-ech-spin-echo: TR = 1250 ms, echotrain length (ETL) = 5.

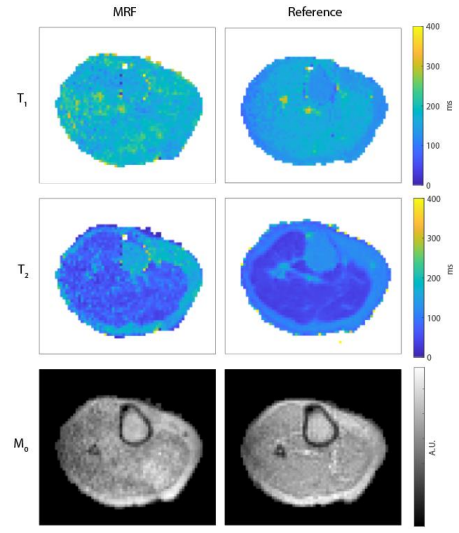

Figure 4. Comparison between uncorrected MRF data with constant TE and uncorrected and corrected MRF data with alternating TE. The relaxation time maps obtained from the MRF scan with an alternating TE pattern (without distortion correction) are very similar to those obtained with a constant TE pattern. A ΔB_0 map was estimated from the alternating TE data and used to correct for image distortions along the readout direction before matching. The effects are small, but visible in the M_0 maps and in the subcutaneous fat region in the T_2 maps.

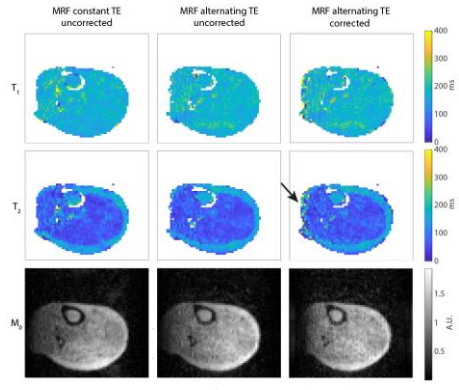

Figure 5. Comparison of the MRF-based ΔB_0 map estimation with a standard TSE-based technique. The ΔB_0 map estimated from the B_0-MRF data is close to that obtained with a TSE sequence. The maximal difference is 105 Hz, which could be caused by phase errors in the MRF sequence due to system imperfections or temperature induced B_0 drift, which can be as much as 1500 Hz/hour during in-vivo imaging. Scan parameters for the TSE sequence: resolution = 2.5×2.2×3.0 mm^3, TE/TR = 12/300 ms, readout gradient shift = 150 µs, echotrain length (ETL) = 5, scan time = 9 min.

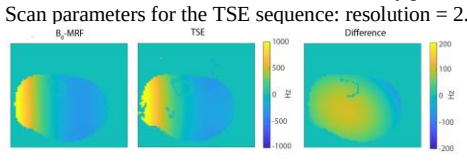

Model-based self-navigated water/fat decomposition for segmented diffusion-weighted EPI

Yiming Dong[1], Malte Riedel[2], Kirsten Koolstra[3], Matthias J.P. van Osch[1], Peter Börnert[1,4]

[1]C.J. Gorter Center for High Field MRI, Department of Radiology, LUMC, The Netherlands; [2] University and ETH Zurich, Zurich, Switzerland;

[3] Division of Image Processing, Department of Radiology, LUMC, The Netherlands; [4]Philips Research Hamburg, Germany

Synopsis: Multi-shot EPI readout-approaches provide high spatial resolution at reduced geometric distortions and improved SNR in diffusion weighted imaging (DWI). As a specific challenge, multi-shot acquisition data require corrections for motion-induced, shot-specific phase errors, e.g. using additional navigator signals or appropriate self-navigation. Furthermore, proper fat-suppression is challenging in DWI, especially at B0 critical regions, making the use of chemical-shift encoding interesting. Therefore, an iterative, model-based reconstruction algorithm with self-navigation and water/fat decomposition, is proposed in this work. In-vivo examples in the leg and head-neck regions demonstrate improved water/fat separation as compared to acquisition-navigator approaches, while measurement times can be shortened.

Introduction: Fat is a confounding factor for EPI-based diffusion-weighted imaging (DWI)[1] due to the large chemical-shift effect. To overcome the imperfections of conventional fat-suppression techniques, chemical-shift encoding[2,3] has been recently proposed[4-6] to handle even multipeak fat spectra in EPI[5,6]. Multi-shot EPI has gained growing popularity[7,8] in DWI to reduce geometric distortion, making motion-induced shot-to-shot phase errors correction via extra-navigated[7,8] or self-navigated[9-11] approaches necessary. However, when combined with chemical-shift encoding, the presence of shifted fat in the navigator signal can impair image reconstruction and degrade the quality of final water images. To circumvent such artefacts, we propose an extended model-based self-navigated water/fat decomposition resolved EPI (MSDE) image reconstruction algorithm to jointly estimate water and fat while correcting for the motion-induced shot-to-shot phase variations. The adverse effects of the shifted fat is successfully mitigated, and no extra navigator[8] signal is required.

Methods: The DWI signal model $s_{n,l,j}$ for a k-space sample k_t at the n-th chemical-shift encoding point ΔTE_n, shot l and coil j can be written as:

$$s_{n,l,j}(t) = \int \left[c_j(r)\,\rho_w(r) + \sum_{m=1}^{M} \alpha_m c_j(r)\,\rho_f(r) e^{i\psi_{f,m}(\Delta TE_n + t)} \right] e^{i2\pi\psi_B(r)\Delta TE_n} e^{i\phi_{n,l}(r)}\, e^{-ik_t r}\, dr$$

where ρ_w and ρ_f denote the complex-valued water/fat components, c_j the coil sensitivities, α_m and $\psi_{f,m}$ the relative amplitude and chemical-shift for each peak m of the M-peak fat model, and r the spatial position. ψ_B is the B_0 inhomogeneity map and $\phi_{n,l}$ the motion-induced phase map, which are modulated in image-space avoiding the computational burden[12,13] imposed by equivalent k-space convolutions. The extended model-based water/fat separation can be solved with the conjugate gradient method (CG), by minimizing:

$$\{P_w, P_f\} = \underset{P_w, P_f \in \mathbb{C}^Q}{\operatorname{argmin}} \left\| \hat{A}X - S \right\|_2^2$$

where Q is the number of voxels, $\hat{A}$ the coefficient matrix, $X = [P_w, P_f]^T = \left[{\rho_w}^1, \dots, {\rho_w}^Q, {\rho_f}^1, \dots, {\rho_f}^Q\right]^T$ the water/fat images, and S the joint vectorized representation of all signals for N chemical-shift encoding points, L shots, and J coils. The sequence and general reconstruction pipeline are illustrated in Figure 1. It is the aim to fully leverage all data sampled in a usual DWI scan. Thus, from chemical-shift encoded non-DWI measurements, a B_0 map, and water and fat threshold-based masks can be derived using an image-based water/fat decomposition approach for EPI (IDE)[6]. Furthermore, those non-DWI data are used to estimate coil-sensitivity maps (CSM) that match the EPI scan data conditions (geometric distortion). This is done by 1) using water-fat-JSENSE[14], or 2) through ESPIRiT[15] by performing water/fat separation for data acquired by each coil individually (with the estimated B_0 map from previous step), and estimating the merged water/fat (position-corrected) CSM.

For the diffusion measurements, a Gauss-Newton solver is implemented to jointly estimate water, fat, and shot-to-shot phase maps. Using first-order Taylor expansion, the phase term error can be approximated as $e^{i\Delta\phi_{n,l}(r)} \approx 1 + i\Delta\phi_{n,l}(\boldsymbol{r})$ and updated for the next iteration. The number of iterations is empirically chosen to be 10. The unknown vector ΔY can be determined by minimizing,

$$\{\Delta P_w, \Delta P_f, \Delta\Phi_{1,1}, \dots, \Delta\Phi_{N,1}, \dots, \Delta\Phi_{N,L}\} = \underset{\substack{\Delta\Phi_{n,l} \in \mathbb{R}^Q \\ \Delta P_w, \Delta P_f \in \mathbb{C}^Q}}{\operatorname{argmin}} \left\| \hat{B}\Delta Y - \Delta S \right\|_2^2$$

where $\hat{B}$ is the coefficient matrix of the Gauss-Newton system,

$\Delta\Phi_{n,l} = \left[{\Delta\phi_{n,l}}^1, \dots, {\Delta\phi_{n,l}}^Q\right]^T$ for $n = 1, \dots, N; l = 1, \dots, L$, and $\Delta S = S - \hat{A}\bar{X}$ with the current estimated $\bar{X}$. The pre-calculated water/fat masks are applied to the pre-estimated CSM to stabilize the estimation. To enforce smoothness of the estimated phase maps, a 2D triangular window[14] (width set empirically to 5/6 of the matrix size) is applied in k-space for each Gauss-Newton iteration.

Experiments were conducted both in head-neck regions and in the lower leg (4 subjects, 3T, Philips, Best, The Netherlands), using a spin-echo DW segmented EPI sequence with three b-values (0, 200, 400 s/mm^2)/(0, 300, 600 s/mm^2) sampling 4/6 interleaves at TE=64/59ms using 16-channel head-neck/8-channel knee coils, TR=2000 ms at resolution: $1.4 \times 1.5 \times 4$ mm^3. The three ΔTE were chosen as 0.2/1.0/1.8 ms with respect to the spin echo. For comparison, an extra 2D-navigator[8] was acquired for each diffusion shot. A multi-peak fat model[6] was used for all reconstructions.

Results: Figure 2 shows a DWI data set reconstructed using the proposed MSDE approach with the CSM obtained from respectively SENSE pre-scan, ESPIRIT, and water-fat-JSENSE. The two approaches using the self-calibrated CSM show improved water images compared to the one with the pre-scan. Figure 3 shows results of one subject's leg, comparing IDE, the extended model-based water/fat separation with extra navigators, and the proposed self-navigated (MSDE). The artefacts shown in the water/ADC maps of the first two methods can be eliminated by using self-navigation. Figure 4 shows estimated phase maps from MSDE at one ΔTE and the phase/magnitude of the extra navigators which contain shifted fat signal for comparison. Figure 5 shows the performance of the three approaches in the head-neck region. The examples show that the MSDE can avoid signal cancellations in the extra-navigated results.

Discussion and conclusion: The proposed MSDE algorithm provides more reliable water/fat separation for DWI compared to IDE. This is guaranteed by (1) the model-based reconstruction with fat off-resonance modulation in k-space, (2) the reduction of the spatial mismatch between CSM and EPI data, via integrated CSM estimation, (3) self-navigation to avoid measuring extra navigators which prolong acquisition times, suffer from poor SNR (acquired at TE > 100ms) and contain shifted fat signal, and (4) chemical-shift encoding, as an intelligent way of signal averaging, providing more data that help to better condition the inverse problem. This also supports the self-navigation to deal with the increased g-factor effects at large shots number.

References:

1. Le Bihan D, Mangin J-F, Poupon C, et al. Diffusion tensor imaging: concepts and applications. JMRI. 2001;13(4):534–546.

2. Glover G. Multipoint Dixon technique for water and fat proton and susceptibility imaging, J Magn Reson Imaging 1991;1:521 - 530.

3. Reeder SB, Pineda AR, Wen Z, Shimakawa A, Yu H, Brittain JH, Gold GE, Beaulieu CH, Pelc NJ. Iterative decomposition of water and fat with echo asymmetry and least-squares estimation (IDEAL): application with fast spin-echo imaging. Magn Reson Med. 2005 Sep;54(3):636-44.

4. Burakiewicz J, Charles-Edwards DG, Goh V, Schaeffter T. Water-fat separation in diffusion-weighted EPI using an IDEAL approach with image navigator. Magn Reson Med. 2015 Mar;73(3):964-72.

5. Hu Z, Wang Y, Dong Z, Guo H. Water/fat separation for distortion-free EPI with point spread function encoding. Magn Reson Med. 2019;82(1):251-262.

6. Dong Y, Koolstra K, Riedel M, van Osch MJP, Börnert P. Regularized joint water–fat separation with B0 map estimation in image space for 2D-navigated interleaved EPI based diffusion MRI. Magn Reson Med. 2021; 00: 1– 18. https://doi.org/10.1002/mrm.28919

7. Butts, K., Pauly, J., De Crespigny, A. and Moseley, M. (1997), Isotropic diffusion-weighted and spiral-navigated interleaved EPI for routine imaging of acute stroke. Magn. Reson. Med., 38: 741-749.

8. Jeong H-K, Gore JC, Anderson AW. High-resolution human diffusion tensor imaging using 2D navigated multishot SENSE EPI at 7 T. MRM. 2013;69(3):793-802.

9. Chen NK, Guidon A, Chang HC, Song AW. A robust multi-shot scan strategy for high-resolution diffusion weighted MRI enabled by multiplexed sensitivity-encoding (MUSE). Neuroimage. 2013 May 15;72:41-7.

10. Truong TK, Guidon A. High-resolution multishot spiral diffusion tensor imaging with inherent correction of motion-induced phase errors. Magn Reson Med 2014;71:790–796.

11. Guo H, Ma X, Zhang Z, Zhang B, Yuan C, Huang F. POCS-enhanced inherent correction of motion-induced phase errors (POCS-ICE) for high-resolution multishot diffusion MRI. Magn Reson Med. 2016 Jan;75(1):169-80.

12. Brodsky, E. K., Holmes, J. H., Yu, H., & Reeder, S. B. (2008). Generalized K-space decomposition with chemical-shift correction for non-Cartesian water-fat imaging. Magnetic Resonance in Medicine, 59(5), 1151–1164.

13. Honorato, J.L., Parot, V., Tejos, C., Uribe, S. and Irarrazaval, P. (2012), Chemical species separation with simultaneous estimation of field map and T2* using a k-space formulation. Magnetic Resonance Medicine, 68: 400-408.

14. Uecker, M. & Lustig, M. Making SENSE of Chemical Shif: Separating Species in Single-Shot EPI using Multiple Coils. In Proc. Intl.
Soc. Mag. Reson. Med., 20, 2490 (Melbourne, 2012).

15. Uecker M, Lai P, Murphy MJ, Virtue P, Elad M, Pauly JM, Vasanawala SS, Lustig M. ESPIRiT--an eigenvalue approach to autocalibrating parallel MRI: where SENSE meets GRAPPA. Magn Reson Med. 2014 Mar;71(3):990-1001.

Acknowledgments / Funding Information: The authors would like to acknowledge NWO-TTW (HTSM-17104).

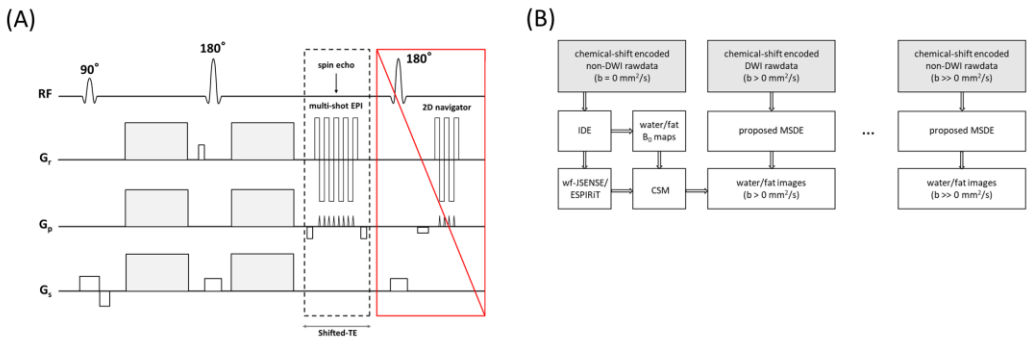

Figure 1. Sequence diagram and the schematic reconstruction pipeline. (A) Chemical-shift encoded segmented DW-EPI sequence6 equipped with extra navigators for comparison. In this work we want to eliminate the navigator. (B) First, a B_0 map and water/fat images are estimated from the b = 0 s/mm^2 data. Second, self-calibrated CSM can be calculated by water-fat JSENSE[18] or ESPIRiT[19] and masked by water/fat regions obtained by thresholding. Finally, DW water/fat images with corrected phase can be jointly calculated using the proposed MSDE method for each individual DW data set.

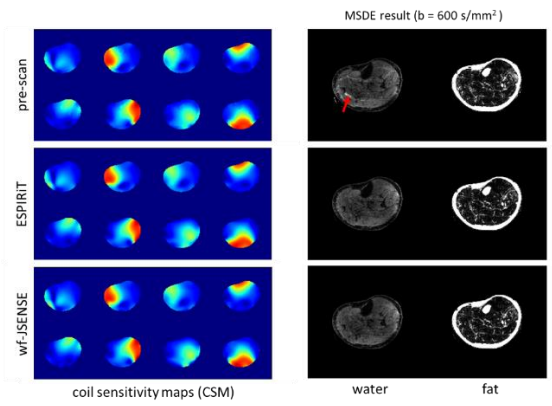

Figure 2. Impact of CSM quality. Normalized coil sensitivity maps acquired from a (non-EPI) pre-scan, from ESPIRiT, and water-fat JSENSE using the actual 6-shots (b = 0 s/mm^2) data, are shown along with the corresponding DW water/fat images estimated via MSDE. Some artefacts can be seen in the water image with pre-scan CSM (marked by red arrow), which may result from the B_0 introduced geometric distortion mismatch with the EPI image. ESPIRiT/water-fat JSENSE can avoid this bias with the help of CSM self-calibration and provide improved results.

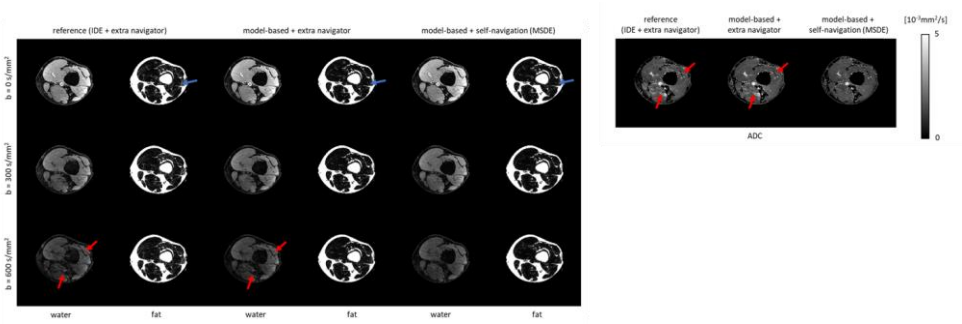

Figure 3. Comparison of three different methods in the lower leg of a normal volunteer. The IDE and model-based with extra navigator show some artefacts in the final water images, mainly due to the lower SNR (at TE>100 ms) and presence of shifted fat in the navigator. This can be mitigated through MSDE using self-navigation. Besides, with model-based reconstruction, the latter two results show improved fat images without fat aliasing results from EPI alternating trajectory[6] (blue arrows). Corresponding ADC maps are shown in the lower panel, which underline the above findings (red arrows).

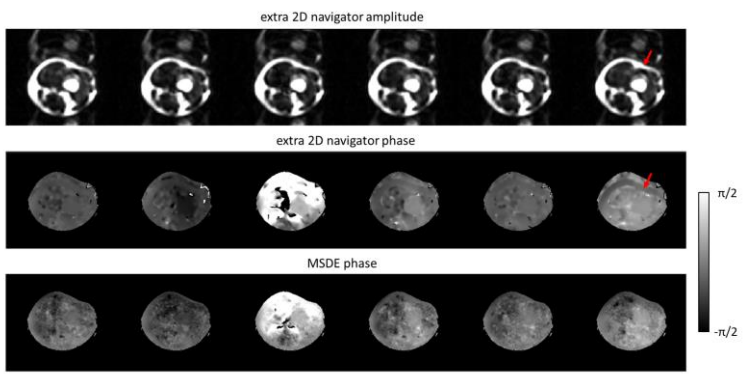

Figure 4. Comparison of the extra DW navigators and self-navigation for six shots. The navigator amplitude/phase (b = 600 s/mm^2) and the phase estimated by self-navigation at one given ΔTE_n are displayed. The extra navigator was acquired at TE = 104 ms showing a relatively low water amplitude compared to fat due to the respective diffusion properties. In addition, the fat is shifted with respect to the water (red arrows), which results in the marked artifacts in Figure 3. These effects can be mitigated by the joint model-based estimation and self-navigation of MSDE.

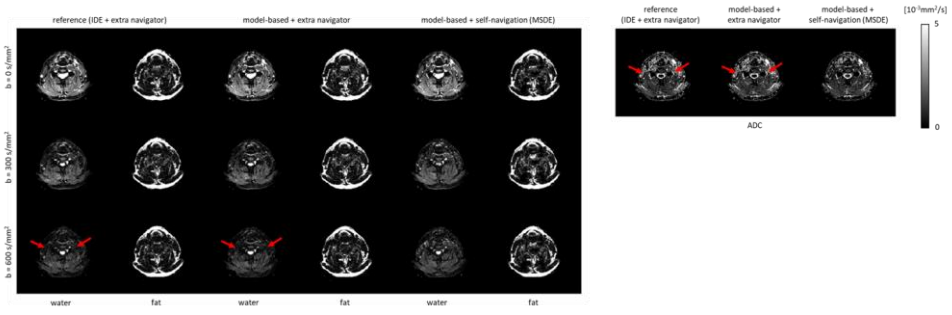

Figure 5. Comparison of three different methods in one subject's head-neck region for 4 shots. Signal cancellations can be seen in both image reconstructions using the extra 2D navigators for the diffusion water images (red arrows). The MSDE can avoid this signal loss and produce reliable water images, even at the highest b-value. The consequences can also be seen in the ADC mapping below.

The impact of learning rate, network size, and training time on unsupervised deep learning for intravoxel incoherent motion (IVIM) model fitting

Misha P.T. Kaandorp1,2, Frank Zijlstra[1,2], João P. de Almeida Martins[1,2,] Christian Federau[3,4], Peter T. While[1,2]

[1]Department of Radiology and Nuclear Medicine, St. Olav's University Hospital, Trondheim, Norway, [2]Department of Circulation and Medical Imaging, NTNU – Norwegian University of Science and Technology, Trondheim, Norway, [3]Institute for Biomedical Engineering, University and ETH Zürich, Zürich, Switzerland, [4]AI Medical, Zürich, Switzerland

Synopsis

We demonstrate that a high learning rate, small network size, and early stopping in unsupervised deep learning for IVIM model fitting can result in sub-optimal solutions and correlated parameters. In simulations, we show that prolonging training beyond early stopping resolves these correlations and reduces parameter error, providing an alternative to exhaustive hyperparameter optimization. However, extensive training results in increased noise sensitivity, tending towards the behavior of least squares fitting. In in-vivo data from glioma patients, fitting residuals were almost identical between approaches, whereas pseudo-diffusion maps varied considerably, demonstrating the difficulty of fitting D* in these regions.

Introduction

The intravoxel incoherent motion (IVIM)[1] model for diffusion-weighted imaging (DWI) is a biexponential model composed of diffusion coefficient (D), pseudo-diffusion coefficient (D*), and perfusion fraction (F). Despite the various IVIM fitting approaches available[2,3], IVIM remains challenging in the in-vivo brain due to low signal-to-noise ratio (SNR) and low F[4]. Recently, deep neural networks (DNN) were introduced[5] as a promising alternative for IVIM fitting. Kaandorp et al.[6] demonstrated unexpected correlations between the perfusion parameters with this approach, and resolved these by optimizing various hyperparameters (IVIM-NET$_{optim}$). Although IVIM-NET$_{optim}$ showed promising results in the pancreas[6], applying it to brain data showed poor anatomy generalization and high D* values[7].

In this work, we explore the impact of learning rate, network size, and training time on the convergence behavior of the unsupervised DNN loss term, and on the accuracy of the parameter estimates. We demonstrate the possible pitfalls associated with both early stopping and extensive training, using both simulations and in-vivo data from glioma patients.

Methods

We implemented the original DNN architecture of Barbieri et al.[5] in Pytorch 1.8.1. The network architecture was a multi-layer perceptron with 3 hidden layers. The network input consisted of the measured DWI signal at each *b* value, and the network output consisted of the three IVIM parameters plus an extra parameter S0, also considered in IVIM-NET$_{optim}$. These parameters were constrained by absolute activation functions and scaled to appropriate physical ranges (below). The network was trained using the mean-squared error (MSE) loss between the input signal and the predicted IVIM signal.

Training and validation IVIM curves were simulated by uniformly sampling the parameters between: $0 \leq S0 \leq 1$, $0.5\times10^{-3} \leq D \leq 5\times10^{-3}$ mm^2/s, $0 \leq F \leq 50\%$, and $10\times10^{-3} \leq D^* \leq 100\times10^{-3}$ mm^2/s, and considering 16 *b* values[4]. Validation data consisted of 100,000 random IVIM curves. Training was performed for 4000 epochs with 500 batches per epoch and batch size 128, similar to previous approaches[5,6]. Rician noise was added to the signals such that at S0=1 the SNR was 200. Four networks were evaluated by considering two different numbers of hidden units in each layer (#units = 16, 64) and two different learning rates (lr = 1×10^{-3}, 1×10^{-4}). For each network, we computed the MSE loss, Spearman's correlation (ρ) and normalized parameter MSEs at the end of each epoch.

The performance of the most stable network in terms of validation convergence was evaluated by examining the distribution of individual datapoints in predicted-target scatter plots, and using in-vivo data from glioma patients (white matter SNR=30)[4]. Performance was assessed at three points during training: (i) when the validation loss did not improve over 10 epochs (NN$_{Earlystop10}$), representing early stopping as used in previous approaches[5,6]; (ii) when MSE-D* was at a minimum (NN$_{Min(MSE\text{-}D^*)}$); (iii) at the last epoch (NN$_{Epoch4000}$), representing extensive training. Comparisons were also made to Least Squares (LSQ) and IVIM-NET$_{optim}$.

Results

Using lower #units reduced convergence speed, whereas higher learning rate resulted in spiky convergence of the unsupervised loss term, which could result in sub-optimal solutions (Figure 1). Therefore, using #units=64 and lr=1×10^{-4} was considered the most stable network.

The early stopping criterion (patience=10 epochs) resulted in sub-optimal solutions prior to true convergence (Figure 1), where parameters were strongly correlated (Figure 2A). Prolonging training resolved these correlations and reduced parameter MSEs (Figure 2). However, training substantially longer resulted in increased parameter MSEs, particularly for D* (Figure 2B). Figure 3 shows that at NN$_{Earlystop10}$, the predicted parameters for low SNR (low S0) signals are apparently biased towards the center of the simulated distributions, particularly for D*. As training progresses, the estimates corresponding to low SNR signals exhibit higher variability and display a distribution tending towards that of LSQ.

For the in-vivo data, prolonging training also improved DNN fitting and reduced root-mean-square error (RMSE), which became increasingly similar to the RMSE of LSQ as training progressed (Figure 4). However, although the RMSE-maps were similar between approaches, the D*-maps differed substantially, particularly for low SNR regions. As found in the simulations, at NN$_{Earlystop10}$, the DNN tended to estimate D* towards the center of the simulated distribution, whereas prolonging training resulted in greater variability. In contrast, IVIM-NET$_{optim}$ displayed inferior RMSE and high D*, as reported elsewhere for the brain[7].

Discussion and Conclusion

The development of advanced estimators for IVIM modelling is often motivated by a desire to produce smoother parameter maps than LSQ, with higher accuracy and precision[3]. The introduction of DNNs for IVIM fitting shows promise to this end[5], yet performance may be conditional on a myriad of choices regarding network architecture and training strategy[6,7]. In this work, we showed that high learning rate and early stopping may lead to correlated parameter estimates and sub-optimal model fitting. We showed that a lower learning rate results in more stable convergence, and extending training time leads to reduced parameter correlations and parameter error. However, extensive training resulted in an increased sensitivity to noise, somewhat akin to LSQ fitting. While this may be undesirable, it could also be argued that the corresponding variability observed in the parameter maps is indicative of the underlying uncertainty, which is indeed useful information. This uncertainty is exemplified by the contrasting D*-maps between approaches, despite the similar RMSE, and illustrates the difficulty in estimating D* in the brain.

1. Le Bihan D, Breton E, Lallemand D, Aubin M, Vignaud J LM. Separation of diffusion and perfusion in intravoxel incoherent motion MR imaging. *Radiology*. 1988;168:497–505.
2. Gurney-Champion OJ, Klaassen R, Froeling M, Barbieri S, Stoker J, Engelbrecht MRW, Wilmink JW, Besselink MG, Bel A, van Laarhoven HWM, Nederveen AJ. Comparison of six fit algorithms for the intravoxel incoherent motion model of diffusion-weighted magnetic resonance imaging data of pancreatic cancer patients. *PLoS One*. 2018;13(4):1-18. doi:10.1371/journal.pone.0194590
3. While PT. A comparative simulation study of bayesian fitting approaches to intravoxel incoherent motion modeling in diffusion-weighted MRI. *Magn Reson Med*. 2017;78(6):2373-2387. doi:10.1002/mrm.26598
4. Federau C, Meuli R, O'Brien K, Maeder P, Hagmann P. Perfusion measurement in brain gliomas with intravoxel incoherent motion MRI. *Am J Neuroradiol*. 2014;35(2):256-262. doi:10.3174/ajnr.A3686
5. Barbieri S, Gurney-Champion OJ, Klaassen R, Thoeny HC. Deep learning how to fit an intravoxel incoherent motion model to diffusion-weighted MRI. *Magn Reson Med*. 2020;83(1):312-321. doi:10.1002/mrm.27910
6. Kaandorp MPT, Barbieri S, Klaassen R, van Laarhoven HWM, Crezee H, While PT, Nederveen AJ, Gurney-Champion OJ. Improved unsupervised physics-informed deep learning for intravoxel incoherent motion modeling and evaluation in pancreatic cancer patients. *Magn Reson Med*. 2021;86(4):2250-2265. doi:https://dx.doi.org/10.1002/mrm.28852
7. Spinner GR, Federau C, Kozerke S. Bayesian inference using hierarchical and spatial priors for intravoxel incoherent motion MR imaging in the brain: Analysis of cancer and acute stroke. *Med Image Anal*. 2021;73:102144. doi:https://dx.doi.org/10.1016/j.media.2021.102144

Acknowledgments / Funding Information: This work was supported by the Research Council of Norway (FRIPRO Researcher Project 302624).

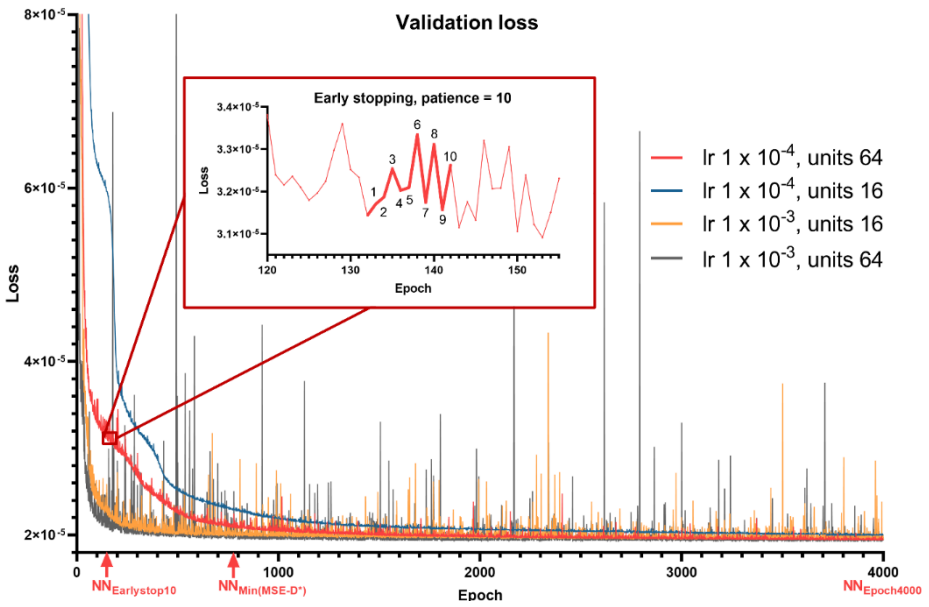

Figure 1: Validation loss curve of the four trained networks with different #units [16, 64] and lr [1×10^{-3}, 1×10^{-4}] evaluated for 4000 epochs, where each epoch consisted of 500x128 training batches. The red square highlights where the validation loss did not improve over 10 epochs and the early stopping criterion would have ended the training, showing sub-optimal convergence of the unsupervised loss term. The arrows indicate the three validation points ($NN_{Earlystop10}$, $NN_{Min(MSE-D*)}$, and $NN_{Epoch4000}$) for the network trained with #units=64 and lr=1×10^{-4}.

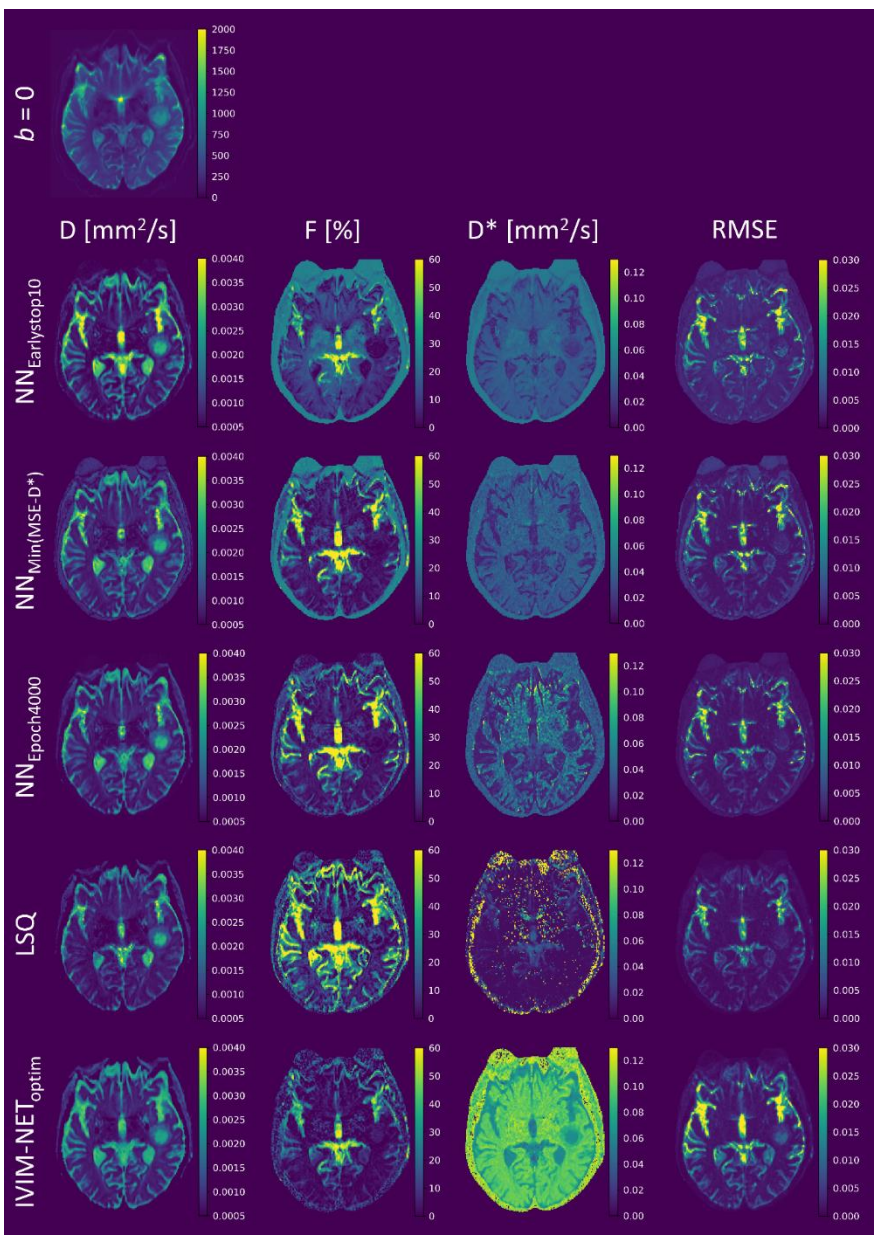

Figure 2: IVIM parameter maps and RMSE-maps (with corresponding b = 0 map) generated for in-vivo data from a glioma patient, when fitted by the DNN at each of the three validation points ($NN_{Earlystop10}$, $NN_{Min(MSE-D*)}$, and $NN_{Epoch4000}$) for the network trained with #units=64 and lr=1×10^{-4}, as well as for LSQ and $IVIM\text{-}NET_{optim}$. The tumor is in the center of the right hemisphere.

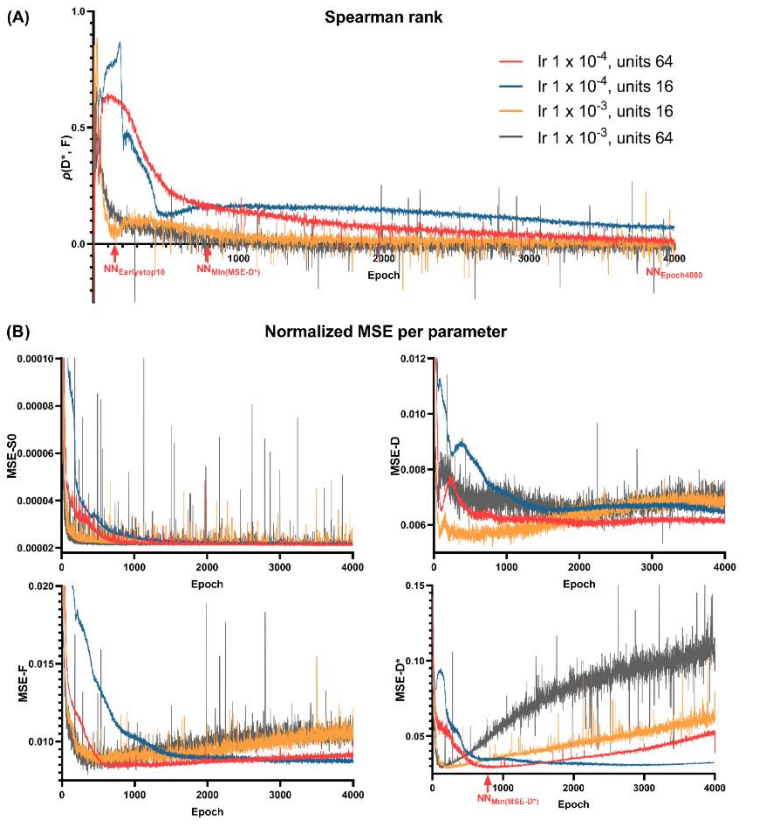

Figure 1: (A) Spearman rank correlation plot of the perfusion parameters (ρ(D*,F)) for the four trained networks with different #units [16, 64] and lr [1×10^{-3}, 1×10^{-4}] evaluated for 4000 epochs, showing that emerging correlations are resolved during training. (B) Plots of normalized MSE for each parameter, showing that each parameter has an optimum solution during unsupervised training. As training proceeds, the MSE for each parameter eventually increases, especially for D*.

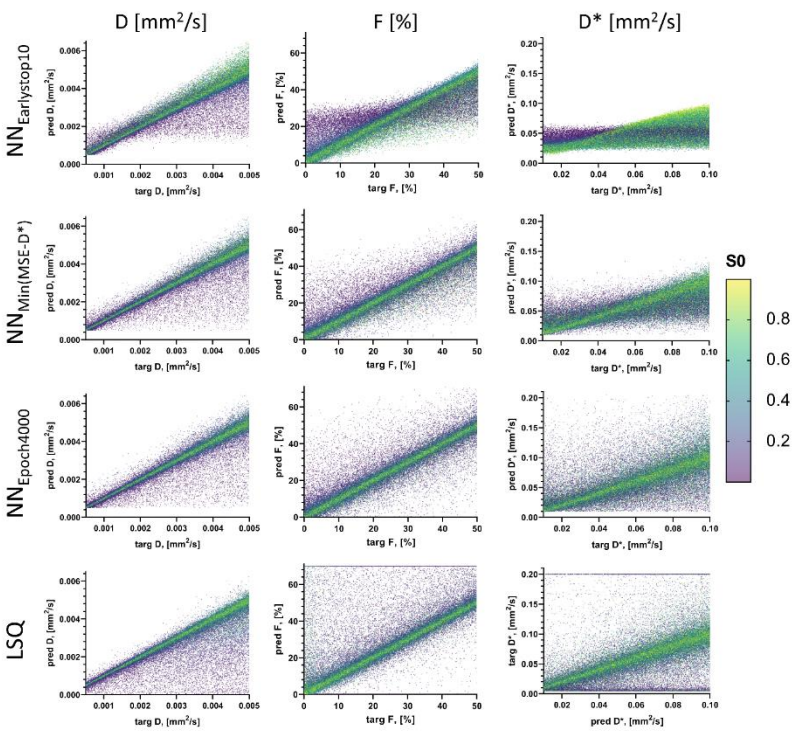

Figure 3: Scatter plots of ground-truth parameters (targ) against predictions (pred) for each of the three validation points ($NN_{Earlystop10}$, $NN_{Min(MSE-D*)}$, and $NN_{Epoch4000}$) for the network trained with #units=64 and lr=1×10^{-4}, as well as for LSQ. All plots have S0 as color variable where S0=1 corresponds to SNR=200, with dark blue the lowest S0 and green/yellow the highest S0. During training, the network initially predicts estimates close to the center of the simulated distributions ($NN_{Earlystop10}$), whereas after extensive training ($NN_{Epoch4000}$) it shows similar behavior to LSQ.

Three-component IVIM fitting in cerebrovascular disease using physics-informed neural networks: repeatability and accuracy

P.H.M. Voorter[1,2], W.H. Backes[1,2,3], O.J. Gurney-Champion[4], S.M. Wong[1], J. Staals[3,5], R.J. van Oostenbrugge[2,3,5], M.M. van der Thiel[1,2], J.F.A. Jansen[1,2,6], G.S. Drenthen[1,2]

[1]Department of Radiology & Nuclear Medicine, Maastricht University Medical Center, Maastricht, the Netherlands; [2]School for Mental Health & Neuroscience, Maastricht University, Maastricht, the Netherlands; [3]School for Cardiovascular Disease, Maastricht University, Maastricht, the Netherlands, [4]Department of Radiology and Nuclear medicine, Amsterdam University Medical Center, Cancer Center Amsterdam, University of Amsterdam, Amsterdam, the Netherlands, [5]Department of Neurology, Maastricht University Medical Center, Maastricht, the Netherlands, [6]Department of Electrical Engineering, Eindhoven University of Technology, Eindhoven, the Netherlands

Synopsis: Next to parenchymal diffusion and microvascular pseudo-diffusion, a third diffusion component is present in cerebral intravoxel incoherent motion (IVIM) imaging, representing interstitial fluid. Fitting the three-component IVIM model using conventional fitting methods strongly suffers from image noise. Therefore, we explored the applicability of a physics-informed neural network (PI-NN) fitting approach, previously shown to be more robust to noise. Using test-retest data from sixteen patients with cerebrovascular disease, we found higher repeatability of all IVIM parameters using PI-NN. Furthermore, simulations showed that PI-NN provided more accurate IVIM parameters. Hence, using PI-NN is promising to obtain tissue markers of cerebrovascular disease.

Introduction

Intravoxel incoherent motion (IVIM) imaging is a diffusion-weighted MR technique, which can simultaneously measure the parenchymal diffusion (D_{par}) and microvascular pseudo-diffusion (D_{mv}).[1] Recently, the presence of a third, intermediate diffusion component (D_{int}) was revealed, which was suggested to represent interstitial fluid (ISF) within the parenchyma.[2,3] D_{int} was furthermore found to be related to cerebral small vessel disease (cSVD) markers, such as white matter hyperintensities (WMH).[2] However, with current fitting techniques, extracting accurate voxel-wise measures for the three diffusion components is extremely hard due to the strong influence of noise. Recently, Troelstra et al.[4] showed that fitting a tri-exponential IVIM model using an unsupervised physics-informed neural network (PI-NN) resulted in more robust voxel-wise IVIM parameters compared to the conventional least squares (LSQ) method in the liver.

In this study, we have adapted the three-component PI-NN to estimate the cerebral diffusion components (D_{par}, D_{int} and D_{mv}). We aimed to assess the performance of our PI-NN compared to conventional LSQ in terms of test-retest repeatability (using in-vivo data of patients with cerebrovascular disease) and accuracy (using simulations).

Methods

In-vivo data: Sixteen patients with cerebrovascular disease (cSVD (n=11) and cortical stroke (n=5)) underwent brain MRI twice on separate days (Philips Achieva 3.0T). IVIM images were acquired with diffusion sensitization in three orthogonal directions, and included an inversion pulse for cerebrospinal fluid suppression (single-shot spin-echo echo-planar-imaging (EPI), 2.4mm cubic voxel size, b-values: 0,5,7,10,15,20,30,40,50,60,100,200,400,700,1000 s/mm^2). Additionally, T_2-weighted FLAIR and T_1-weighted images were acquired for anatomical reference.

Image analysis: The IVIM images were corrected for head displacement, EPI and eddy current distortions (ExploreDTI). The three-component cerebral IVIM model, accounting for the inversion recovery, was described as:[2]

$$S(b) = S(0) \cdot \left[\frac{(1 - f_{mv} - f_{int}) E_{1,par} E_{2,par} e^{-bD_{par}} + f_{int} E_{1,int} E_{2,int} e^{-bD_{int}} + f_{mv} E_{1,mv} E_{2,mv} e^{-bD_{mv}}}{(1 - f_{mv} - f_{int}) E_{1,par} E_{2,par} + f_{int} E_{1,int} E_{2,int} + f_{mv} E_{1,mv} E_{2,mv}} \right] \quad \text{[Eq. 1]}$$

$$\text{with } E_{1,k} = \left(1 - 2e^{-\frac{TI}{T_{1,k}}} + e^{-\frac{TR}{T_{1,k}}}\right) \text{for } k = par, int;\ E_{1,mv} = \left(1 - e^{-\frac{TR}{T_{1,blood}}}\right);\ E_{2,k} = \left(e^{-\frac{TE}{T_{2,k}}}\right) \text{for } k = par, int, mv$$

Here, f_{mv} and f_{int} are the volume fractions of the D_{mv} and D_{int} components, respectively. Both LSQ and PI-NN fitting approaches were applied to the Trace images in a voxel-wise manner. For the LSQ approach, a two-step Levenberg-Marquardt algorithm was used with lower and upper bounds equal to typical ranges found with IVIM in the human brain (Table 1).[2] For the PI-NN approach, the hyperparameters and training features were based on a previous study with some small adjustments to make it suitable for brain data.[5] For example, the loss function was changed according to Equation 1. The diffusivity parameters were constrained by sigmoid functions, and the fractions were constrained to be positive (Table 1). To mitigate the problem of variable results due to repeated training, we trained 20 instances of the PI-NN model on all brain voxels in the in-vivo dataset and averaged the corresponding predictions.[5]

The white matter (WM) and cortical gray matter (cGM) were automatically segmented from the T_1-weighted images (Freesurfer), whereas WMH were semi-automatically segmented from the FLAIR images.[6]

Statistical analysis: After voxel-wise fitting, the IVIM parameters were averaged over all brain voxels per subject scan. As a measure of precision, the test-retest repeatability of these IVIM parameters was quantified using the within-subject coefficient of variation (CV) and the intraclass correlation coefficient (ICC) (calculated using a one-way random model).[7] Statistical difference between CVs obtained with LSQ and PINN was tested with a paired Wilcoxon signed-rank test. Furthermore, Bland-Altman plots were created to visually compare the effect of PI-NN and LSQ on the repeatability.

Simulations: 10.000 IVIM signal curves were generated using Equation 1, while randomly sampling the five IVIM parameters from a Gaussian distribution (97.7% within the ranges given in Table 1). Gaussian noise was added, similar to the noise level in our in-vivo data (signal-to-noise ratio at b=0 s/mm^2 was 35).[8] An ensemble of 20 PI-NN models was trained on 1.000.000 noisy IVIM signal decay curves. Subsequently, the PI-NN and LSQ fitting approaches were applied to the synthesized curves to predict the IVIM parameters. The accuracy of both methods was quantified with the normalized root-mean-square error (NRMSE) between all predicted and ground-truth IVIM parameters.

Results

In-vivo data: The IVIM parameter maps obtained with the PI-NN and LSQ fitting approach of a representative cSVD patient are shown in Figure 1. The PI-NN maps appear smoother, while still retaining reasonable contrast between different tissue types, e.g. higher D_{par}, higher f_{int} and lower D_{mv} in WMH compared to normal-appearing WM (NAWM). The PI-NN method was more precise than the LSQ, as it showed higher test-retest repeatability in terms of lower CV and higher ICC values (Table 2). This was also illustrated by the smaller differences between the test-retest of the PI-NN measurements using Bland-Altman plots (Figure 2).

Simulated data: Figure 3 shows scatterplots of the ground-truth and predicted IVIM parameters. Overall, the PI-NN was more accurate as it had lower NRMSE than LSQ (Table 2).

Discussion

In this study, we demonstrated the applicability of a PI-NN for three-component cerebral IVIM fitting in patients with cerebrovascular disease. The PI-NN method resulted in more precise (repeatable) and more accurate IVIM parameters as compared to the LSQ method. The high-quality parameter maps generated with PI-NNs are needed for visual evaluation of increased ISF (D_{int}, f_{int}), microstructural damage (D_{par}) and microvascular alterations (D_{mv}, f_{mv}) within patients, and enables assessment of these parameters in small brain structures, such as small WMH lesions or peri-lesional WM.

References

1. Le Bihan D, Breton E, Lallemand D, Grenier P, Cabanis E, Laval-Jeantet M. MR imaging of intravoxel incoherent motions: application to diffusion and perfusion in neurologic disorders. Radiology. 1986;161(2):401-7.

2. Wong SM, Backes WH, Drenthen GS, Zhang CE, Voorter PH, Staals J, et al. Spectral diffusion analysis of intravoxel incoherent motion MRI in cerebral small vessel disease. Journal of Magnetic Resonance Imaging. 2020;51(4):1170-80.

3. van der Thiel MM, Freeze WM, Verheggen IC, Wong SM, de Jong JJ, Postma AA, et al. Associations of increased interstitial fluid with vascular and neurodegenerative abnormalities in a memory clinic sample. Neurobiology of Aging. 2021;106:257-67

4. Troelstra M, Witjes J, van Dijk AM, Mak AL, Runge J, Verheij J, et al. Physics-informed deep neural network for tri-exponential intravoxel incoherent motion fitting in non-alcoholic fatty liver disease. Proceedings of the 30th annual meeting of the ISMRM 2021:0312

5. Kaandorp MP, Barbieri S, Klaassen R, van Laarhoven HW, Crezee H, While PT, et al. Improved unsupervised physics-informed deep learning for intravoxel incoherent motion modeling and evaluation in pancreatic cancer patients. Magnetic Resonance in Medicine. 2021;86(4):2250-65.

6. De Boer R, Vrooman HA, Van Der Lijn F, Vernooij MW, Ikram MA, Van Der Lugt A, et al. White matter lesion extension to automatic brain tissue segmentation on MRI. Neuroimage. 2009;45(4):1151-61.

7. Liljequist D, Elfving B, Skavberg Roaldsen K. Intraclass correlation–A discussion and demonstration of basic features. PloS one. 2019;14(7):e0219854.

8. National Electrical Manufacturers Association. Determination of signal-to-noise ratio (SNR) in diagnostic magnetic resonance imaging. NEMA Standards Publication MS 1-2008. 2008.

Acknowledgments / Funding Information: This work has received funding from the European Union's Horizon 2020 research and innovation programme 'CRUCIAL' under grant number 848109.

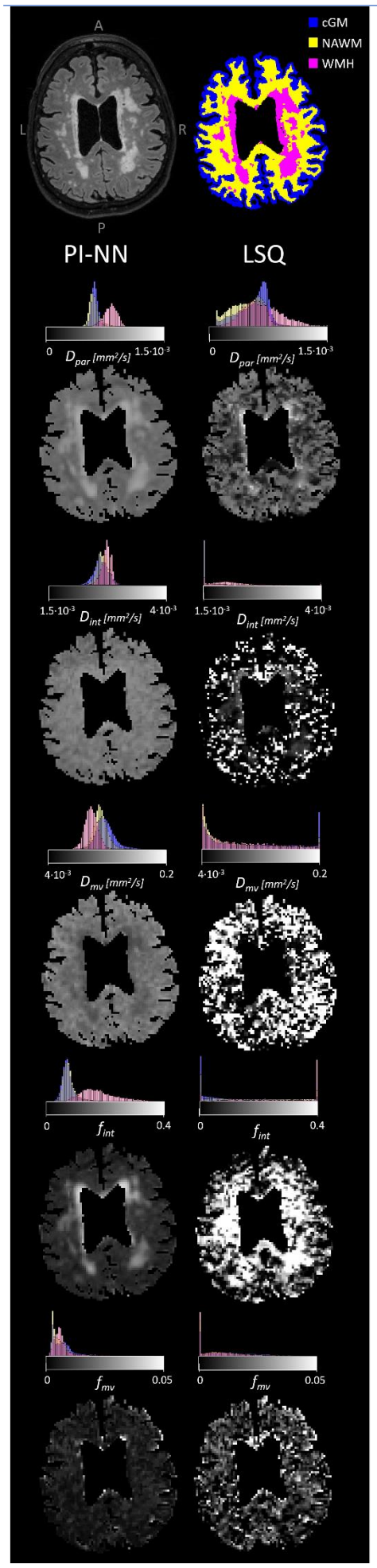

Figure 1. An example of the FLAIR image and the cGM, NAWM and WMH segmentation (top row). The corresponding IVIM parameters maps are shown, obtained with the PI-NN fitting approach (left column) as well as the LSQ fitting approach (right column). The histograms above the colorbars visualize the IVIM parameter distribution in cGM (blue), NAWM (yellow) and WMH (pink) of the whole cerebrum. The PI-NN maps appear less noisy, while still retaining contrast between different tissue types (e.g. higher D_{par}, higher f_{int} and lower D_{mv} in WMH compared to NAWM).

Table 1. Typical IVIM parameter ranges found in the human brain[2], and additional information about the LSQ and PI-NN fitting approach. For LSQ, a two-step Levenberg-Marquardt algorithm was used: 1) D_{par} was estimated by fitting a mono-exponential function using b≥200 s/mm²; 2) all IVIM parameters were fitted with Eq. 1 using all b-values (with D_{par} from step 1 as starting value and upper bound). For PI-NN, the diffusion parameters were constrained by a sigmoid function with 60% wider ranges than the reported typical ranges, whereas the fractions were constrained to be positive.

	Typical range in human brain	LSQ			PI-NN
		Starting value	***Lower bound***	***Upper bound***	***Constraints***
D_{par} [mm²/s]	$0.1\cdot10^{-3}$ – $1.5\cdot10^{-3}$	D_{par} from step 1	$0.1\cdot10^{-3}$	D_{par} from step 1	Sigmoid
D_{int} [mm²/s]	$1.5\cdot10^{-3}$ – $4\cdot10^{-3}$	$2.75\cdot10^{-3}$	$1.5\cdot10^{-3}$	$4\cdot10^{-3}$	Sigmoid
D_{mv} [mm²/s]	$4\cdot10^{-3}$ – $200\cdot10^{-3}$	$102\cdot10^{-3}$	$4\cdot10^{-3}$	$200\cdot10^{-3}$	Sigmoid
f_{int} [-]	0 – 0.4	0	0	0.4	≥ 0
f_{mv} [-]	0 – 0.2	0.05	0	0.2	≥ 0

Table 2. The repeatability and accuracy as a measure of performance for the PI-NN fitting approach versus the LSQ fitting approach. The repeatability was determined by the coefficient of variation (CV) and the intraclass correlation coefficient (ICC) for all IVIM parameters. Low CV values and ICC values close to 1 represent good test-retest repeatability. The paired Wilcoxon signed-rank test showed significantly lower CV values for PI-NN compared to LSQ. The accuracy was expressed in the normalized root-mean-square error (NRMSE). Low NRMSE values represent high accuracy.

IVIM parameter	Repeatability						Accuracy	
	PI-NN	LSQ			PI-NN	LSQ	PI-NN	LSQ
	CV *Median (Q1-Q3)*	CV *Median (Q1-Q3)*	Z	*p*-value	ICC	ICC	NRMSE	NRMSE
D_{par}	0.14 (0.03-0.37)	0.80 (0.41-1.27)	-2.275	0.023	0.90	0.71	0.19	0.40
D_{int}	0.22 (0.15-0.39)	1.45 (0.69-1.94)	-3.516	<0.001	0.72	0.46	0.16	0.39
D_{mv}	0.38 (0.09-0.54)	2.42 (0.77-6.49)	-3.361	0.001	0.57	0.46	0.27	0.42
f_{int}	1.75 (1.51-2.40)	2.40 (1.60-3.56)	-2.947	0.003	0.85	0.52	0.35	0.83
f_{mv}	2.70 (2.00-5.24)	3.90 (2.20-6.36)	-2.068	0.039	0.83	0.76	0.16	0.21

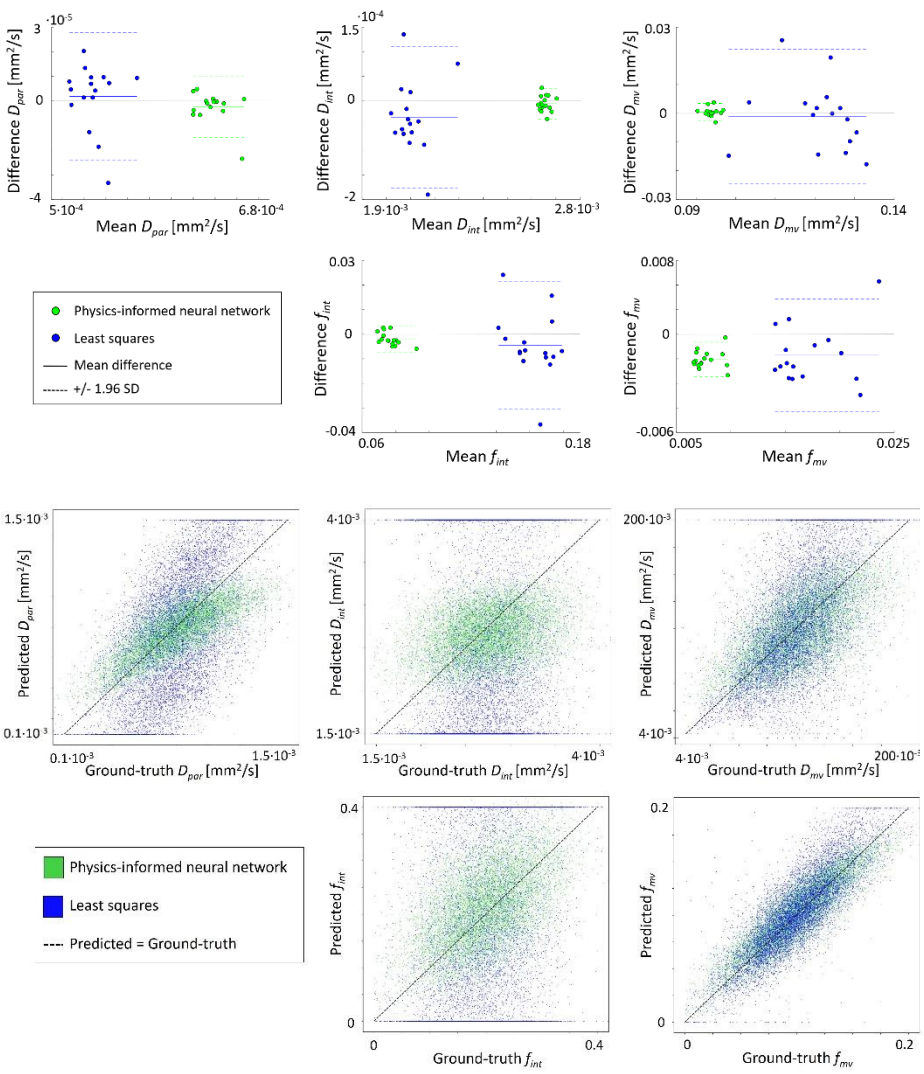

Figure 2. The Bland-Altman plots of the test-retest IVIM parameters. The difference between test-retest IVIM parameter measurements is smaller when using the PI-NN fitting approach (green) compared to the LSQ fitting approach (blue), which is indicated by the distance between the dotted lines. A systematic offset can be observed between the PI-NN and LSQ fitting approaches, probably due to the lower accuracy of the LSQ method (revealed by the simulations).

Figure 3. The scatter plots show the ground truth IVIM parameters of the simulated data on the horizontal axis and the predicted IVIM parameters on the vertical axis using the PI-NN method (green) as well as the LSQ method (blue). The LSQ method regularly finds the optimal solution in the minimum or maximum bound that was given as constraint, which is far from the ground-truth IVIM values. The point clouds of the PI-NN appear more coherent and closer to the dashed predicted=ground-truth line compared to the LSQ method, hence showing higher accuracy of the PI-NN method.

Investigating the stability of the extended IVIM-DTI tensor model: Accuracy and precision as function of SNR and f

S. de Jong[1], S. Rauh[1], O. Gurney-Champion[2], M.T. Hooijmans[2], A.J. Nederveen[2], G.J. Strijkers[1]
[1]Department of Biomedical Engineering and Physics, Amsterdam UMC, Amsterdam, The Netherlands; [2]Department of Radiology and Nuclear Medicine, Amsterdam UMC, Amsterdam, The Netherlands

Synopsis: The stability of the extended Intravoxel Incoherent Motion Diffusion Tensor Imaging (IVIM-DTI) model was tested both by a simulation using realistic kidney parameter values and in-vivo in a healthy volunteer. The extended model describes both, the diffusion and perfusion components as a tensor to account for directionality. From the simulations, it was found that the interquartile range is below 10% for the diffusion-derived parameters with an SNR > 25, but an SNR > 35 is needed to be within 15% for the pseudo-diffusion parameters. In-vivo results support those findings.

Introduction: Intravoxel-incoherent motion (IVIM) imaging can provide information about the diffusion and perfusion processes of underlying tissue[1]. It describes the signal loss in dependency of b-values as a function of the signal at b=0 s/mm² (S_0), the perfusion fraction (f), the diffusion coefficient (D) and the pseudo-diffusion coefficient (D^*).

$$S(b) = S_0 \cdot ((1-f) \cdot e^{-b \cdot D} + f \cdot e^{-b \cdot D^*}) \qquad [1]$$

In organs with ordered microstructure, such as the kidneys or skeletal muscle, a combination with diffusion tensor imaging (DTI) can be used to account for anisotropic diffusion processes. However, in this combined IVIM-DTI model the perfusion component is assumed to be isotropic, although there is evidence that the vessel structure is also anisotropic[2]. Therefore, an extended IVIM model was recently proposed which accounts for anisotropic perfusion:

$$S(b) = S_0 \cdot ((1-f) \cdot e^{-b\underline{g}^T \underline{\underline{D}} \underline{g}} + f \cdot e^{-b\underline{g}^T \underline{\underline{D^*}} \underline{g}}) \qquad [2]$$

where $\underline{g}$ is the diffusion gradient directions vector, $\underline{\underline{D}}$ the diffusion tensor and $\underline{\underline{D^*}}$ the perfusion tensor[3,4]. From the tensors the mean diffusivity (MD_{diff} and MD_{pseudo}) and fractional anisotropy (FA_{diff} and FA_{pseudo}) for the diffusion and pseudo-diffusion component can be derived. While this model was applied in the heart and kidneys already, little is known about its stability in different SNR regions and perfusion states[3,4]. The aim of this work was to quantify the fit stability for the different parameters.

Methods: Simulations have been performed in Matlab (2021a). The signal was calculated for each unique parameter set using equation 2 and 32 different directions distributed over the positive hemisphere for all b-values ranging from 0 to 600 s/mm^2. As ground truth parameters we used values typically found in the kidneys: $MD_{diff} \in [1.6; 2.2]\ 10^{-3} mm^2/s$, $f \in [0.15; 0.25]$ and $MD_{pseudo} \in [20; 120] 10^{-3} mm^2/s$ with each four equidistantly distributed values[4,5]. For each MD we sampled three random eigenvalues with the condition that FA<0.5. Rician noise was added to the signal and the IVIM-DTI tensor model was fitted to the signal using a two-step algorithm: First, the diffusion tensor was fitted to b≥200 s/mm², then the diffusion tensor was fixed and f and D*-tensor were estimated. 100 iterations, adding of Rician noise, were performed and the relative error ($e_{re} = \frac{\theta_{est} - \theta_{true}}{\theta_{true}}$) of the parameters was calculated for each iteration and parameter . The simulations were performed for SNR values ranging from 5 to 1000, where from 5 to 60 steps of 5 were taken.

To investigate the influence of perfusion fraction on the parameters, simulations with SNR=25 were performed with six equidistantly spaced values between [0.15 0.4]. For each value of f the same method as described above was applied.

A healthy volunteer (male, 23 years) underwent MRI examination (3T, Philips Ingenia) of the kidneys in free breathing. The same b-values and directions as in the simulations were used. The scan parameters are listed in Table 1. A voxel-wise fit was performed. Segmentations were drawn in the kidney cortex and medulla in ITK snap[6].

Results: Figure 1 shows the dependence of the IVIM-DTI tensor parameters on SNR. The bias for diffusion-tensor derived parameters and f are below 1% for SNR > 25 and the interquartile range (IQR) stays below 6%. Increased bias was found for the pseudo-diffusion-tensor derived parameters. For MD_{pseudo} and FA_{pseudo} the IQR was below 20% for the same SNR. For an SNR > 35 the bias of the pseudo-diffusion parameter were below the 5% and the IQR stays below 13%.

Figure 2 shows the dependence of the bias of parameters on f. Both diffusion-tensor derived parameters show a slight increase in the IQR, while the MD_{pseudo} and f show a decrease in IQR. Over the span of f values the IQR of MD_{pseudo} and f decreases by a factor of 1/3.

In the volunteer scan, an SNR of 33 and 29 was found in the cortex and medulla, respectively. The mean parameter values are displayed in Table 2 and parameter maps are shown in Figure 3. The parameter maps of MD_{diff}, FA_{diff} and f are homogeneous, while MD_{pseudo} and FA_{pseudo} show more outliers, visible as noisy pixels. This matches the expectations from the simulations.

Discussion:. We found that diffusion-tensor derived parameters can be estimated accurately with an SNR>25. This is in line with the findings Froeling *et al.* found in skeletal muscle[7]. Higher SNR is necessary to estimate the pseudo-diffusion tensor accurately (SNR>35). D^* is strongly dependent on the perfusion fraction, which influences the amount of data available for the pseudo-diffusion parameter estimation. The perfusion related parameters, except FA_{pseudo}, increase in stability for increasing f.

The diffusion-derived values found in the kidney cortex and medulla are in line with literature[3,4]. With the mean SNR of 31 found in our kidney data we expect the diffusion-derived parameters to be estimated accurately. More research into the dependence of the IVIM-DTI tensor model on different factors, such as motion blur or varying perfusion fraction, is needed to be able to understand the stability of the fit and to find the optimal measurement conditions.

(Yushkevich, et al. 2006)

Conclusion: Our simulations revealed that for precise and accurate results of the extended IVIM-DTI tensor model an SNR>35 is required and that a greater value of f increases the stability of the MD_{pseudo} and f estimation. However, more research is needed to investigate all possible influences on the fit stability.

References

1. Bihan, Denis Le, E. Breton, D. Lallemand, M. L. Aubin, and J. Vignaud. “Separation of diffusion and perfusion in intravoxel incoherent motion MR imaging.” *Radiology*, 1988: 497-505.
2. Abdullah, Osama M., A. D. Gomez, S. Merchant, M. Heidinger, S. Poelzing, and E. W. Hsu. “Orientation dependence of microcirculation-induced diffusion signal in anisotropic tissues.” Magnetic resonance in medicine, 2016: 1252-1262.
3. Zhang, Xiu-Shi, et al. “Investigation of intravoxel incoherent motion tensor imaging for the characterization of the in vivo human heart.” *Magnetic Resonance in Medicine*, 2021: 1414-1426.
4. Hilbert, Fabian, et al. “An intravoxel oriented flow model for diffusion-weighted imaging of the kidney.” *NMR in Biomedicine*, 2016: 1403-1413.
5. Notohamiprodjo, Mike, et al. “Combined intravoxel incoherent motion and diffusion tensor imaging of renal diffusion and flow anisotropy.” *Magnetic resonance in medicine* 73, no. 4 (2015): 1526-1532.
6. Yushkevich, Paul A., et al. “User-guided 3D active contour segmentation of anatomical structures: significantly improved efficiency and reliability.” *Neuroimage* 31, no. 3 (2006): 1116-1128.
7. Froeling, Martijn, A. J. Nederveen, K. Nicolay, and G. J. Strijkers. “DTI of human skeletal muscle: the effects of diffusion encoding parameters, signal-to-noise ratio and T2 on tensor indices and fiber tracts.” *NMR in biomedicine* 26, no. 11 (2013): 1339-1352.

Table 1. The MRI sequence parameters used for the in vivo measurement.

Echo Time [ms]	Repetition Time [ms]	Resolution [mm^3]	SENSE factor	Slice thickness [mm]	Number of slices
55.181	2772.04	2.5 x 2.5 x 5	2	5 (0.3 gap)	18

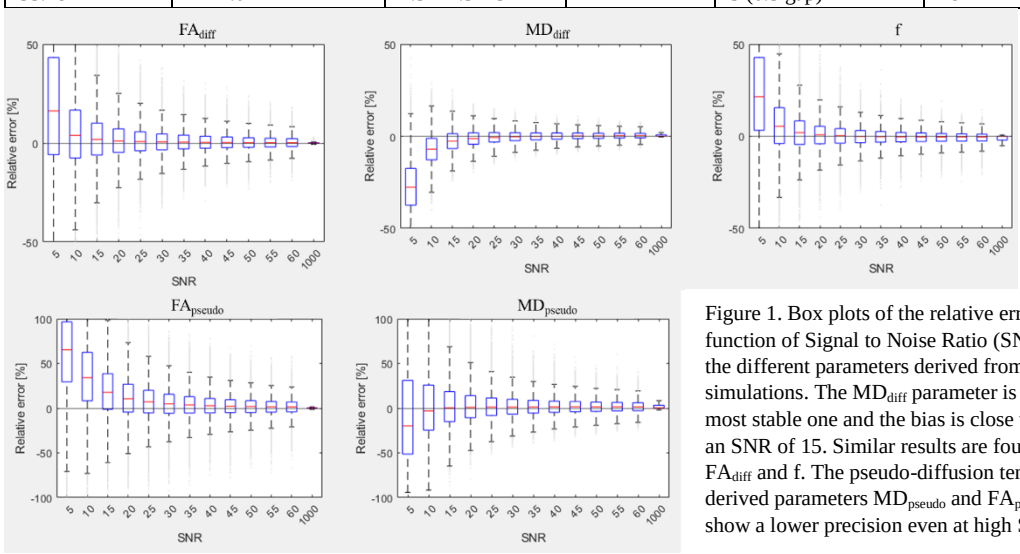

Figure 1. Box plots of the relative errors as a function of Signal to Noise Ratio (SNR) for the different parameters derived from the simulations. The MD_{diff} parameter is the most stable one and the bias is close to 0 at an SNR of 15. Similar results are found for FA_{diff} and f. The pseudo-diffusion tensor derived parameters MD_{pseudo} and FA_{pseudo} show a lower precision even at high SNR.

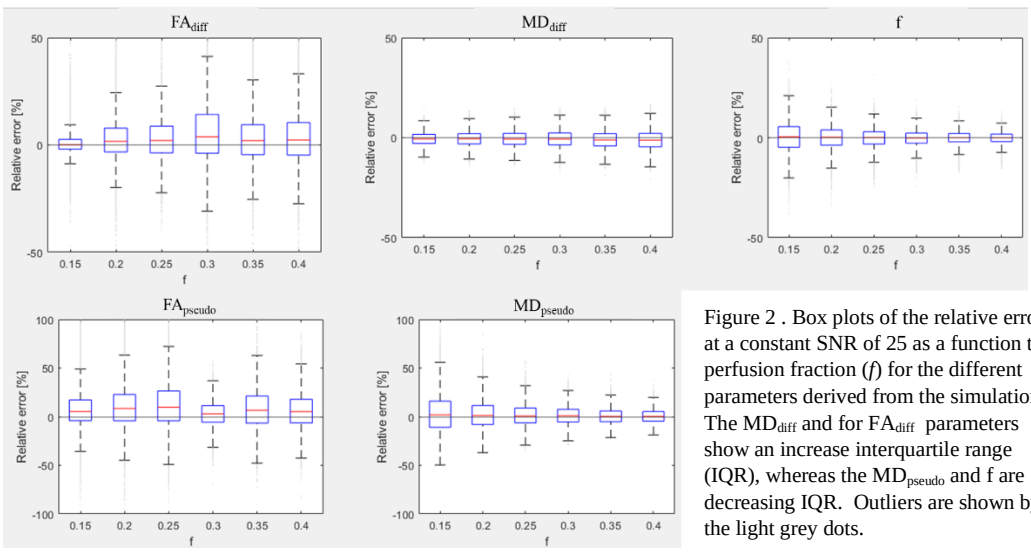

Figure 2 . Box plots of the relative errors at a constant SNR of 25 as a function the perfusion fraction (*f*) for the different parameters derived from the simulations. The MD_{diff} and for FA_{diff} parameters show an increase interquartile range (IQR), whereas the MD_{pseudo} and f are decreasing IQR. Outliers are shown by the light grey dots.

Table 2. The mean values ± standard deviation of the outcome measure for both the kidney cortex and medulla are shown.

Param	FA_{diff}	MD_{diff}	f	FA_{pseudo}	MD_{pseudo}
Cortex	0.31195 ± 0.16133	2.0175 ± 0.67276	0.23752 ± 0.24658	0.45137 ± 0.33983	37.0125 ± 51.1199
Medulla	0.29534 ± 0.13081	2.0726 ± 0.52397	0.17895 ± 0.18016	0.50062 ± 0.34289	44.6947 ± 56.9836

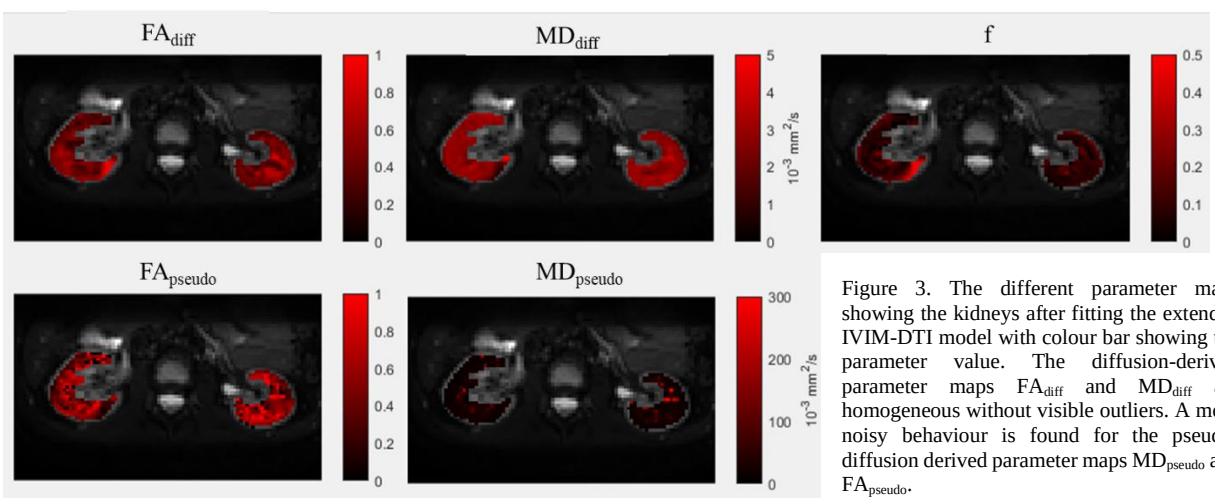

Figure 3. The different parameter maps showing the kidneys after fitting the extended IVIM-DTI model with colour bar showing the parameter value. The diffusion-derived parameter maps FA_{diff} and MD_{diff} are homogeneous without visible outliers. A more noisy behaviour is found for the pseudo-diffusion derived parameter maps MD_{pseudo} and FA_{pseudo}.